frontiers | Research Topics

Emerging technologies for musculoskeletal disease modeling and regenerative medicine

Edited by
Andrea Vernengo, Dmitriy Sheyn, Rahul Gawri and Mark Buckley

Published in
Frontiers in Bioengineering and Biotechnology

FRONTIERS EBOOK COPYRIGHT STATEMENT

The copyright in the text of individual articles in this ebook is the property of their respective authors or their respective institutions or funders. The copyright in graphics and images within each article may be subject to copyright of other parties. In both cases this is subject to a license granted to Frontiers.

The compilation of articles constituting this ebook is the property of Frontiers.

Each article within this ebook, and the ebook itself, are published under the most recent version of the Creative Commons CC-BY licence. The version current at the date of publication of this ebook is CC-BY 4.0. If the CC-BY licence is updated, the licence granted by Frontiers is automatically updated to the new version.

When exercising any right under the CC-BY licence, Frontiers must be attributed as the original publisher of the article or ebook, as applicable.

Authors have the responsibility of ensuring that any graphics or other materials which are the property of others may be included in the CC-BY licence, but this should be checked before relying on the CC-BY licence to reproduce those materials. Any copyright notices relating to those materials must be complied with.

Copyright and source acknowledgement notices may not be removed and must be displayed in any copy, derivative work or partial copy which includes the elements in question.

All copyright, and all rights therein, are protected by national and international copyright laws. The above represents a summary only. For further information please read Frontiers' Conditions for Website Use and Copyright Statement, and the applicable CC-BY licence.

ISSN 1664-8714
ISBN 978-2-8325-3312-3
DOI 10.3389/978-2-8325-3312-3

About Frontiers

Frontiers is more than just an open access publisher of scholarly articles: it is a pioneering approach to the world of academia, radically improving the way scholarly research is managed. The grand vision of Frontiers is a world where all people have an equal opportunity to seek, share and generate knowledge. Frontiers provides immediate and permanent online open access to all its publications, but this alone is not enough to realize our grand goals.

Frontiers journal series

The Frontiers journal series is a multi-tier and interdisciplinary set of open-access, online journals, promising a paradigm shift from the current review, selection and dissemination processes in academic publishing. All Frontiers journals are driven by researchers for researchers; therefore, they constitute a service to the scholarly community. At the same time, the *Frontiers journal series* operates on a revolutionary invention, the tiered publishing system, initially addressing specific communities of scholars, and gradually climbing up to broader public understanding, thus serving the interests of the lay society, too.

Dedication to quality

Each Frontiers article is a landmark of the highest quality, thanks to genuinely collaborative interactions between authors and review editors, who include some of the world's best academicians. Research must be certified by peers before entering a stream of knowledge that may eventually reach the public - and shape society; therefore, Frontiers only applies the most rigorous and unbiased reviews. Frontiers revolutionizes research publishing by freely delivering the most outstanding research, evaluated with no bias from both the academic and social point of view. By applying the most advanced information technologies, Frontiers is catapulting scholarly publishing into a new generation.

What are Frontiers Research Topics?

Frontiers Research Topics are very popular trademarks of the *Frontiers journals series*: they are collections of at least ten articles, all centered on a particular subject. With their unique mix of varied contributions from Original Research to Review Articles, Frontiers Research Topics unify the most influential researchers, the latest key findings and historical advances in a hot research area.

Find out more on how to host your own Frontiers Research Topic or contribute to one as an author by contacting the Frontiers editorial office: frontiersin.org/about/contact

Emerging technologies for musculoskeletal disease modeling and regenerative medicine

Topic editors

Andrea Vernengo — AO Research Institute, Switzerland

Dmitriy Sheyn — Regenerative Medicine Institute, Cedars Sinai Medical Center, United States

Rahul Gawri — McGill University, Canada

Mark Buckley — University of Rochester, United States

Citation

Vernengo, A., Sheyn, D., Gawri, R., Buckley, M., eds. (2023). *Emerging technologies for musculoskeletal disease modeling and regenerative medicine*. Lausanne: Frontiers Media SA. doi: 10.3389/978-2-8325-3312-3

Table of contents

06 Sex Differences in Mesenchymal Stem Cell Therapy With Gelatin-Based Microribbon Hydrogels in a Murine Long Bone Critical-Size Defect Model
Masaya Ueno, Ning Zhang, Hirohito Hirata, Danial Barati, Takeshi Utsunomiya, Huaishuang Shen, Tzuhua Lin, Masahiro Maruyama, Ejun Huang, Zhenyu Yao, Joy Y. Wu, Stefan Zwingenberger, Fan Yang and Stuart B. Goodman

18 Estrogen Receptor α Signaling in Osteoblasts is Required for Mechanotransduction in Bone Fracture Healing
Lena Steppe, Benjamin Thilo Krüger, Miriam Eva Angelica Tschaffon, Verena Fischer, Jan Tuckermann, Anita Ignatius and Melanie Haffner-Luntzer

33 Establishment of an *Ex Vivo* Inflammatory Osteoarthritis Model With Human Osteochondral Explants
Kaihu Li, Penghui Zhang, Yong Zhu, Mauro Alini, Sibylle Grad and Zhen Li

43 Interleukin-1β More Than Mechanical Loading Induces a Degenerative Phenotype in Human Annulus Fibrosus Cells, Partially Impaired by Anti-Proteolytic Activity of Mesenchymal Stem Cell Secretome
Raquel M. Gonçalves, Taryn Saggese, Zhiyao Yong, Joana R. Ferreira, Anita Ignatius, Hans-Joachim Wilke, Cornelia Neidlinger-Wilke and Graciosa Q. Teixeira

55 Engineered Human Meniscus in Modeling Sex Differences of Knee Osteoarthritis *in Vitro*
Zhiyao Ma, David Xinzheyang Li, Melanie Kunze, Aillette Mulet-Sierra, Lindsey Westover and Adetola B. Adesida

71 *In Vitro* Cellular Strain Models of Tendon Biology and Tenogenic Differentiation
Shannon Y. Wu, Won Kim and Thomas J. Kremen Jr

86 Toward Development of a Diabetic Synovium Culture Model
Neeraj Sakhrani, Andy J. Lee, Lance A. Murphy, Hagar M. Kenawy, Christopher J. Visco, Gerard A. Ateshian, Roshan P. Shah and Clark T. Hung

102 Disulfiram Suppressed Peritendinous Fibrosis Through Inhibiting Macrophage Accumulation and Its Pro-inflammatory Properties in Tendon Bone Healing
Qi Zhou, Wei Wang, Fujun Yang, Hao Wang, Xiaodong Zhao, Yiqin Zhou, Peiliang Fu and Yaozeng Xu

113 Human Organ-on-a-Chip Microphysiological Systems to Model Musculoskeletal Pathologies and Accelerate Therapeutic Discovery
Raquel E. Ajalik, Rahul G. Alenchery, John S. Cognetti, Victor Z. Zhang, James L. McGrath, Benjamin L. Miller and Hani A. Awad

136 Three-Dimensional Modeling and *In Silico* Kinematic Evaluation of Interspinous Ligament Desmotomy in Horses
Adam Henry Biedrzycki and George Louis Elane

143 3D Bioprinted Scaffolds for Bone Tissue Engineering: State-Of-The-Art and Emerging Technologies
Zahra Yazdanpanah, James D. Johnston, David M. L. Cooper and Xiongbiao Chen

168 Research Progress of Exosomes in Bone Diseases: Mechanism, Diagnosis and Therapy
Fanying Meng, Xu Xue, Zhifeng Yin, Fei Gao, Xiuhui Wang and Zhen Geng

185 Cryogel Scaffold-Mediated Delivery of Adipose-Derived Stem Cells Promotes Healing in Murine Model of Atrophic Non-Union
Katherine R. Hixon, Dakota B. Katz, Jennifer A. McKenzie, Anna N. Miller, Farshid Guilak and Matthew J. Silva

200 Synoviocyte-Derived Extracellular Matrix and bFGF Speed Human Chondrocyte Proliferation While Maintaining Differentiation Potential
Rachel D. Truong, Megan A. Bernier, James E. Dennis and Thomas J. Kean

211 Electrical Stimulation of Acute Fractures: A Narrative Review of Stimulation Protocols and Device Specifications
Peter J. Nicksic, D'Andrea T. Donnelly, Nishant Verma, Allison J. Setiz, Andrew J. Shoffstall, Kip A. Ludwig, Aaron M. Dingle and Samuel O. Poore

222 Bone Marrow Microenvironment-On-Chip for Culture of Functional Hematopoietic Stem Cells
Azmeer Sharipol, Maggie L. Lesch, Celia A. Soto and Benjamin J. Frisch

237 Tendon mechanical properties are enhanced *via* recombinant lysyl oxidase treatment
Phong K. Nguyen, Aniket Jana, Chi Huang, Alison Grafton, Iverson Holt, Michael Giacomelli and Catherine K. Kuo

252 Biomechanical evaluation of a short-rod technique for lumbar fixation surgery
Ze-Bin Huang, Mao-Dan Nie, Ning-Ze Zhang, Shu Liu, Jia-Bin Yuan, Xu-Miao Lin, Cheng-Kung Cheng, Zhi-Cai Shi and Ning-Fang Mao

268 Human mesenchymal stromal cells release functional mitochondria in extracellular vesicles
Matthew A. Thomas, Megan J. Fahey, Brenna R. Pugliese, Rebecca M. Irwin, Marc A. Antonyak and Michelle L. Delco

280 *In Situ* Assessment of Porcine Osteochondral Repair Tissue in the Visible–Near Infrared Spectral Region
Shital Kandel, William Querido, Jessica M. Falcon, Hannah M. Zlotnick, Ryan C. Locke, Brendan Stoeckl, Jay M. Patel, Chetan A. Patil, Robert L. Mauck and Nancy Pleshko

292 Electrospun aligned poly(ε-caprolactone) nanofiber yarns guiding 3D organization of tendon stem/progenitor cells in tenogenic differentiation and tendon repair
Qiao Yang, Jianfeng Li, Weiwei Su, Liu Yu, Ting Li, Yongdi Wang, Kairui Zhang, Yaobin Wu and Ling Wang

309 Angle-stable interlocking nailing in a canine critical-sized femoral defect model for bone regeneration studies: In pursuit of the principle of the 3R's
W. B. Saunders, L. M. Dejardin, E. V. Soltys-Niemann, C. N. Kaulfus, B. M. Eichelberger, L. K. Dobson, B. R. Weeks, S. C. Kerwin and C. A. Gregory

324 Influence of the parameters of the convolutional neural network model in predicting the effective compressive modulus of porous structure
Yongtao Lu, Yi Huo, Zhuoyue Yang, Yibiao Niu, Ming Zhao, Sergei Bosiakov and Lei Li

335 Development of 2-D and 3-D culture platforms derived from decellularized nucleus pulposus
Marco A. Herrera Quijano, Nadia Sharma, Pascal Morissette Martin, Cheryle A. Séguin and Lauren E. Flynn

354 Stable human cartilage progenitor cell line stimulates healing of meniscal tears and attenuates post-traumatic osteoarthritis
Salomi Desai, Mark Dooner, Jake Newberry, John Twomey-Kozak, Janine Molino, Jay Trivedi, Jay M. Patel, Brett D. Owens and Chathuraka T. Jayasuriya

366 Engineering collagenous analogs of connective tissue extracellular matrix
Philip A. P. Brudnicki, Matthew A. Gonsalves, Stephen M. Spinella, Laura J. Kaufman and Helen H. Lu

386 Chondrogenic differentiation of human bone marrow MSCs in osteochondral implants under kinematic mechanical load is dependent on the underlying osteo component
Graziana Monaco, Feras Qawasmi, Alicia J. El Haj, Nicolas R. Forsyth and Martin J. Stoddart

399 Primary sternal tumour resection and reconstruction with LARS mesh-bone cement sandwich by 3D-printing: Case reports
He Zhang, Bo Hou, Tienan Xia, Lu Ji, Jiatong Li, Ting Chen and Guanning Shang

frontiers in Bioengineering and Biotechnology

ORIGINAL RESEARCH
published: 19 October 2021
doi: 10.3389/fbioe.2021.755964

Sex Differences in Mesenchymal Stem Cell Therapy With Gelatin-Based Microribbon Hydrogels in a Murine Long Bone Critical-Size Defect Model

*Masaya Ueno[1,2†], Ning Zhang[1†], Hirohito Hirata[1], Danial Barati[1], Takeshi Utsunomiya[1], Huaishuang Shen[1], Tzuhua Lin[1], Masahiro Maruyama[1], Ejun Huang[1], Zhenyu Yao[1], Joy Y. Wu[3], Stefan Zwingenberger[4], Fan Yang[1,5] and Stuart B. Goodman[1,5]**

[1]Department of Orthopaedic Surgery, Stanford University, Stanford, CA, United States, [2]Department of Orthopaedic Surgery, Faculty of Medicine, Saga University, Saga, Japan, [3]Department of Medicine, Stanford University, Stanford, CA, United States, [4]University Center for Orthopaedics, Traumatology, and Plastic Surgery, University Hospital Carl Gustav Carus at Technische Universität Dresden, Dresden, Germany, [5]Department of Bioengineering, Stanford University, Stanford, CA, United States

OPEN ACCESS

Edited by:
Rahul Gawri,
McGill University, Canada

Reviewed by:
Derek H. Rosenzweig,
McGill University, Canada
Patricia Miguez,
University of North Carolina at Chapel Hill, United States

***Correspondence:**
Stuart B. Goodman
goodbone@stanford.edu

†These authors have contributed equally to this work

Specialty section:
This article was submitted to Biomaterials, a section of the journal Frontiers in Bioengineering and Biotechnology

Received: *09 August 2021*
Accepted: *04 October 2021*
Published: *19 October 2021*

Citation:
Ueno M, Zhang N, Hirata H, Barati D, Utsunomiya T, Shen H, Lin T, Maruyama M, Huang E, Yao Z, Wu JY, Zwingenberger S, Yang F and Goodman SB (2021) Sex Differences in Mesenchymal Stem Cell Therapy With Gelatin-Based Microribbon Hydrogels in a Murine Long Bone Critical-Size Defect Model. Front. Bioeng. Biotechnol. 9:755964. doi: 10.3389/fbioe.2021.755964

Mesenchymal stem cell (MSC)-based therapy and novel biomaterials are promising strategies for healing of long bone critical size defects. Interleukin-4 (IL-4) over-expressing MSCs within a gelatin microribbon (μRB) scaffold was previously shown to enhance the bridging of bone within a critical size femoral bone defect in male Balb/c mice. Whether sex differences affect the healing of this bone defect in conjunction with different treatments is unknown. In this study, we generated 2-mm critical-sized femoral diaphyseal bone defects in 10–12-week-old female and male Balb/c mice. Scaffolds without cells and with unmodified MSCs were implanted immediately after the primary surgery that created the bone defect; scaffolds with IL-4 over-expressing MSCs were implanted 3 days after the primary surgery, to avoid the adverse effects of IL-4 on the initial inflammatory phase of fracture healing. Mice were euthanized 6 weeks after the primary surgery and femurs were collected. MicroCT (μCT), histochemical and immunohistochemical analyses were subsequently performed of the defect site. μRB scaffolds with IL-4 over-expressing MSCs enhanced bone healing in both female and male mice. Male mice showed higher measures of bone bridging and increased alkaline phosphatase (ALP) positive areas, total macrophages and M2 macrophages compared with female mice after receiving scaffolds with IL-4 over-expressing MSCs. Female mice showed higher Tartrate-Resistant Acid Phosphatase (TRAP) positive osteoclast numbers compared with male mice. These results demonstrated that sex differences should be considered during the application of MSC-based studies of bone healing.

Keywords: sex differences, bone healing, mesenchymal stem cell, microribbon hydrogel, interleukin-4

INTRODUCTION

Sex is one of the critical factors that influences the types and frequencies of diseases in the musculoskeletal system. For example, osteoporosis is more prevalent in women than in men (Cawthon, 2011). Osteoporosis affects up to 30% of women but only 12% of men at some point in their lives (Ralston and de Crombrugghe, 2006). The risk of fracture is also higher in women than

in men (Cawthon, 2011); women show a greater incidence of stress fractures early in life and fragility fractures later in life (Cummings et al., 2002; Beck et al., 2000). In a clinical study, female sex was found to be associated with a reduced fracture union rate (Chang et al., 2006), and was identified as a major risk factor for compromised bone healing in several clinical studies (David et al., 2006; Li et al., 2006; Parker et al., 2007). Thus, it is prudent to consider the premise that the treatment of musculoskeletal disorders including bone healing should be tailored to the patient's sex.

Mesenchymal stem cell (MSC) therapies have shown great potential to facilitate bone healing (Shi et al., 2010; Liu et al., 2014a; Sui et al., 2019; Zhang et al., 2021). MSCs are one of the most investigated adult stem cell populations and are involved in the continuous maintenance and repair of many tissue types (Kern et al., 2006; Jin et al., 2013). For example, systemic transplantation of MSCs has shown remarkable efficacy in preventing and treating estrogen deficiency-induced bone loss in pre-clinical studies (Cho et al., 2009; Lee et al., 2011; An et al., 2013; Liu et al., 2014b; Sui et al., 2017).

We have encapsulated MSCs within gelatin microribbon (μRB)-based scaffolds to enhance the efficacy of mesenchymal stem cell delivery to a bone defect site with high cell survival and adequate supply of nutrients and provide primary structural support (Han et al., 2016; Conrad et al., 2018). μRB building blocks can be homogeneously mixed with cells with high cell viability and can inter-crosslink into macroporous scaffolds (Han et al., 2013). Macroporous gelatin μRB-based scaffolds increased cartilage formation in a murine subcutaneous implantation model (Rogan et al., 2020). In a murine cranial defect, μRB-based scaffolds significantly improved stem cell survival, vascular ingrowth, and accelerated bone formation (Han et al., 2016).

It is recognized that inflammation and the innate immune system including macrophages play crucial roles in the differentiation and activation of MSCs, and are essential for normal bone growth, repair, and homeostasis (Chow et al., 2019; Maruyama et al., 2020). Acute injury damages bone, the local soft tissues, and the neurovascular system, leading to the production of a pro-inflammatory microenvironment. This inflammatory milieu is the first stage of bone healing and determines the delicate balance between bone formation and bone degradation (Loi et al., 2016a). The inflammatory cascade polarizes macrophages to a proinflammatory M1 phenotype; M1 macrophages produce cytokines and chemokines that recruit MSCs, vascular progenitors and other cells, and activates or licenses MSCs to a new state facilitating resolution, re-vascularization, reconstruction, and homeostasis. As the acute inflammatory response subsides, M2 anti-inflammatory macrophages further stimulate tissue regeneration.

IL-4 is an anti-inflammatory cytokine; when IL-4 was added in monoculture of mouse MSCs acutely, IL-4 decreased cell proliferation and osteogenic differentiation (Lin et al., 2017a; Zhang et al., 2021). However, IL-4 stimulates the polarization of macrophages from an M1 to an M2 phenotype (Shapouri-Moghaddam et al., 2018), and crosstalk between MSCs and macrophages is critical for successful bone healing (Pajarinen et al., 2019). Interestingly, IL-4 over-expressing MSCs enhanced osteogenesis in MSC-macrophage cocultures if the IL-4 was added after 48–72 h (Lin et al., 2019). To aid in this reparative response, we developed IL-4 over-expressing MSCs using lentiviral vectors. IL-4 over-expressing MSCs within μRB scaffolds, delivered locally 3 days after the acute injury, enhanced bone formation using a long bone defect in young, male mice (Ueno et al., 2020) in an established femoral diaphyseal critical size bone defect model (Zwingenberger et al., 2013). Whether this biological approach is comparable in female mice having a different hormonal profile is unknown.

In the current study, we compare the healing potential of IL-4 over-expressing MSCs in male and female mice using an established murine long bone critical size defect model. We evaluated the healing defect using comprehensive histologic and immunohistochemical analyses, and μCT of the bone defect site.

MATERIALS AND METHODS

Isolation and Manipulation of MSCs

Bone marrow derived MSCs from each sex were isolated according to a previously published method (Peister et al., 2004; Lin et al., 2015). Briefly, we collected bone marrow from both femurs and tibias of 8–10-week-old BALB/c male and female mice. Then bone marrow was carefully suspended and filtered through a 70 μm strainer, spun down and resuspended in alpha-minimal essential medium (α-MEM, Thermo Fisher Scientific, Waltham, MA, United States) supplied with 10% fetal bovine serum (FBS, Invitrogen, Carlsbad, CA, United States) and antibiotic antimycotic solution (100 units of penicillin, 100 μg of streptomycin and 0.25 μg of Amphotericin B/ml; Hyclone, Thermo Fisher Scientific, Waltham, MA, United States). The unattached cells were removed by replacing the culture media after 24 h and defined as passage 1. The immunophenotype of isolated MSCs according to International Society for Cell Therapy (ISCR) (Dominici et al., 2006) (CD105+ /CD73+ /CD90.2+ /Scal + CD45−/ CD34−CD11b−) was characterized by flow cytometry (LSR II, Stanford Shared FACS Facility, Stanford, CA, United States) at passage 4. MSCs between passage four to eight were used in the current study. Based on our protocol (Ueno et al., 2020), we produced genetically modified MSCs that over-express IL-4 by infecting MSCs with the lentiviral vector carrying murine IL-4 gene. Briefly, the lentivirus vectors were generated in HEK293T cells by co-transfecting with the transfer plasmid (pCDH-CMV-mIL-4-EF1-copGFP), packaged plasmid (psPAX2), and enveloped plasmid (pMD2G VSVG) using a calcium phosphate transfection kit (Takara Bio United States Inc., Mountain View, CA, United States) with 25 mmol/L chloroquine. We then collected the supernatants of the culture media 48 h after the transfection, and the cellular debris was removed by centrifugation at 4,000 g for 20 min. The virus was mixed in MSC culture medium supplemented with 6 μg/ml of polybrene (Sigma Aldrich, St. Louis, MO, United States) with the multiplicity of infection 100 for MSC infection (Ricks et al., 2008; Lin et al., 2017b; Zhang et al., 2021). ELISA kits for mouse IL-4 (R&D system, Minneapolis, MN, United States) were used to

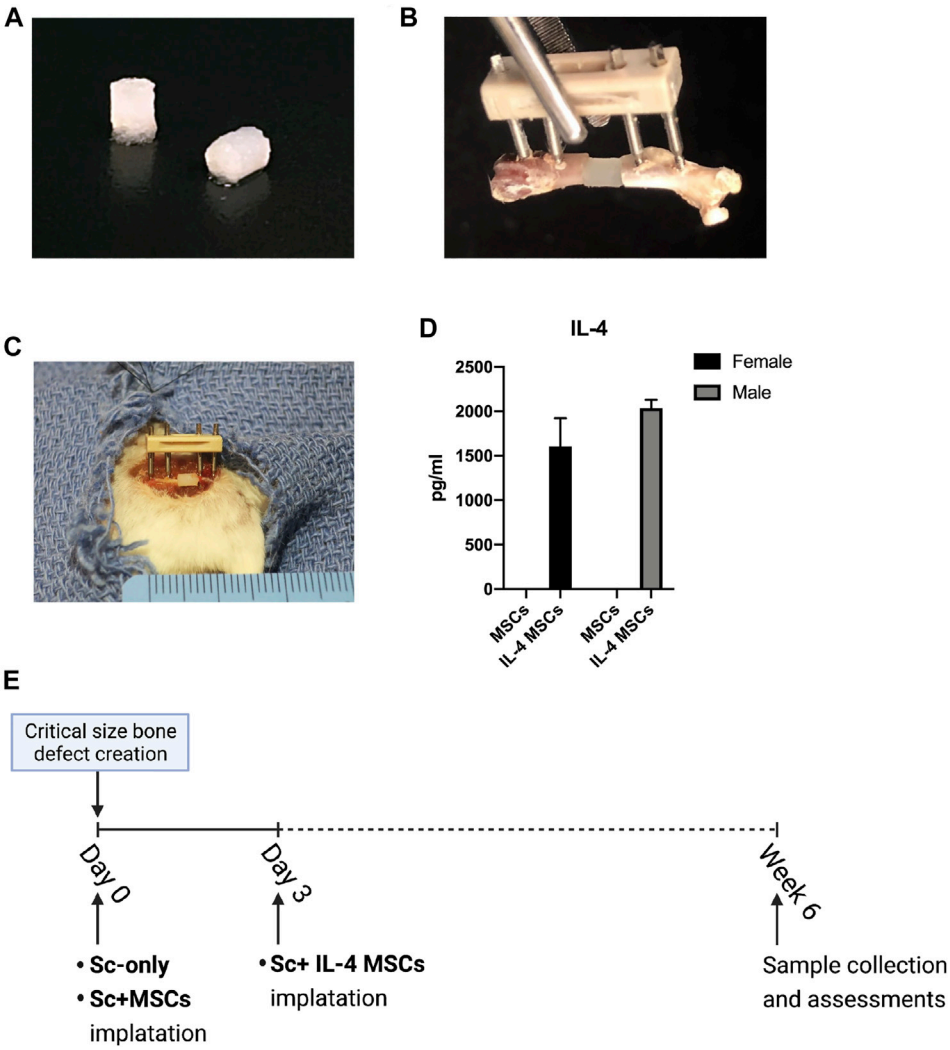

FIGURE 1 | Animal model and surgical procedure. **(A)** MSC-seeded μRBs scaffolds. **(B)** A model of the external fixator and μRBs. **(C)** Implantation of a μRBs scaffold in a mouse femur critical size bone defect with an external fixator. **(D)** IL-4 secreting levels detected by ELISA in the culture media of IL-4 MSCs and MSCs for 24 h (2039.01 ± 90.73 pg/ml in male IL-4 MSCs and 1607.25 ± 313.58 pg/ml in female IL-4 MSCs. The IL-4 concentration could not be detected by ELISA in male and female MSC alone groups). **(E)** Surgical procedure. The IL-4 overexpressing MSCs (IL-4 MSCs) were added day 3 after creation of the surgical defect, whereas in the other groups, namely scaffold only (Sc-only), scaffold with unmodified MSCs (Sc + MSCs), were added immediately after the surgery (day 0).

quantify IL-4 expression by the infected MSCs (IL-4 MSCs) or non-infected MSCs (MSCs) for 24 h culture. The manufacturers' protocols were carefully followed. The optical densities were determined using SpectraMax M2e Microplate Readers (Molecular Devices, San Jose, CA, United States) set at 450 nm with wavelength correction set to 540 nm.

Gelatin μRB-Based Scaffold

The fabrication of gelatin μRBs (**Figure 1A**) using a wet spinning process was conducted according to a previous report (Conrad et al., 2018). Briefly, gelatin was stirred in dimethyl sulfoxide (20 wt%) at 60°C for 18 h at 60 rpm to form a viscous solution. Then the gelatin solution was transferred to a 60 ml syringe and ejected using a syringe pump set to 5 ml/h into ethanol located 1.8 m under the syringe being stirred at 500 rpm. The precipitated gelatin microfiber was transferred to acetone for 3 h to dry and form μRBs. The μRBs were chopped to short length using a homogenizer after transferred back to ethanol. The μRBs were transferred to methanol containing methacrylic acid N-hydroxysuccinimide ester (15 wt%) and stirred for 18 h at room temperature to functionalize them. Next, the μRBs were transferred to fresh methanol containing glutaraldehyde (0.1 wt%) and stirred vigorously for 18 h at room temperature. The glutaraldehyde was neutralized by adding L-lysine hydrochloride (1% in 200 ml PBS) and stirring for 2 h. The product was washed eight times using PBS and three times using deionized water to remove the reagents, thereafter, the product was freeze-dried and stored at −20°C.

To fabricate scaffolds, the μRBs were rehydrated using PBS containing 0.05% LAP photo-initiator. After incubation for 1 h at

37°C, the μRBs were gently mixed with trypsinized MSCs suspended in PBS. The cell concentrations were 10 million cells/mL. The μRBs containing cells were filled to 2 mm diameter cylindrical mold and exposed to ultraviolet light (365 nm, 2 mW/cm^2) for 4 min to produce macroporous scaffolds. The scaffolds were then gently pushed out from the mold and kept in PBS for further applications. Cell properties after encapsulation into the same scaffold prior to placement of this construct into the bone defect, as well as cell viability in the scaffolds after placement into a defect site in a mouse cranial defect model were tested and reported previously (Han et al., 2016). Bioluminescence imaging (BLI) showed that 81.1 ± 21.3% of stem cells in the μRB scaffold were alive at day 1, compared to 26.6 ± 10.1% in the hydrogel scaffold group. After 6 weeks, almost 40% of stem cell still showed BLI positive signals.

Animals

Stanford's Administrative Panel on Laboratory Animal Care (APLAC) approved this animal experiment protocol (APLAC 26905). Guidelines for the Care and Use of Laboratory Animals were followed in all aspects of the current project. Male and female Balb/c mice (Jackson Laboratory, Bar Harbor, ME) between 10 and 12 weeks old were used. These mice were kept on a 12-h light-and-dark cycle, and they were able to access a standard diet with food and water ad libitum.

Surgical Procedure and Postoperative Care

The surgery was conducted on mice who were given preoperative analgesia by subcutaneously injection of 0.1 mg/kg of buprenorphine. Mice were anesthetized using inhalation anesthesia with isoflurane in 100% oxygen at a flow of 1 L/min on a warm surgery station for small animals during the surgical procedures. The surgery was conducted by at least two experienced surgeons in each case, and one non-operative surgeon assistant. A 2-mm critical-sized diaphyseal bone defect was made in the femur, as previously described (**Figures 1B,C**) (Zwingenberger et al., 2013). Briefly, we approached the right femur *via* a longitudinal lateral incision, then implanted the femoral external fixation device (MouseExFix, RISystem AG, Landquart, Switzerland) onto the right femur. Then, a special jig was used to generate a 2 mm critical-size bone defect in the midshaft of the femur using a Gigli saw (Zwingenberger et al., 2013). There were three groups for each sex: μRB scaffold without any implantation of cells (Sc-only group), μRB scaffold with unaltered MSCs (Sc + MSCs group), and μRB scaffold with IL-4 over-expressing MSCs (Sc + IL-4-MSCs group). Mice were implanted with MSCs which were isolated from the same sex. Male recipient mice received male donor MSCs or IL-4 MSCs, whereas female recipient mice received female donor MSCs or IL-4 MSCs.

The surgical procedure and scaffold implantation for Sc-only group and Sc + MSCs group were performed at time zero. Since the previous *in vitro* study demonstrated that administration of the anti-inflammatory cytokine IL-4 during the first 48 h of culture significantly mitigated acute inflammation, decreased cell proliferation and downregulated oncostatin M which is recognized to enhance osteogenesis (Guihard et al., 2012; Loi et al., 2016b), the scaffolds with IL-4 over-expressing MSCs were implanted 3 days after the primary surgery (**Figure 1D**). We closed the surgical incisions with 5–0 Ethilon sutures and injected BuprenorphineSR (0.1 mg/kg) subcutaneously for analgesia after surgery.

Micro-Computational Tomography and Radiographic Analysis

6 weeks after the primary surgery, mice were euthanized by exposure to CO_2 followed by cervical dislocation. Both lower limbs from each animal were collected. μCT scans were performed using a TriFoileXplore CT 120 (TriFoil Imaging, Chatsworth, CA) with 50 μm resolution (Ueno et al., 2020; Utsunomiya et al., 2021a; Utsunomiya et al., 2021b). In the left femur (the healthy side), a 3 × 3 × 2 mm rectangular region in the center of femur was scanned (**Figure 2A**). For the right femur containing the 2 mm critical-size bone defect surgery, we measured the original length of defect based on the μCT images case by case to set the size of ROI (3 mm × 3 mm × original length) (**Figure 2C**). Final length of the defect was also measured case by case. We calculated the tissue mineral content of the newly formed bone from the original bone defect area. The length of the bone defect healing was also calculated by this formula: defect healing (mm) = original length (mm)—final length (mm) (**Figure 2**).

Histologic and Immunohistochemical Analysis

The tissue samples were fixed in 4% paraformaldehyde overnight after the μCT scans, then decalcified in 0.5 M ethylenediaminetetraacetic acid (EDTA) for 2 weeks, then embedded in optimal cutting temperature compound (OCT) and frozen at −80°C. Embedded samples were cut into 10 μm-thick sections. Hematoxylin and Eosin (H&E) staining was performed for histological analysis. To evaluate the status of bone healing, the contents of the defect were graded according to the scoring system of Huo et al., (1991) (**Table.1**). 1-Step NBT/BCIP Substrate Solution (Thermo Fisher Scientific Rockford, IL) was used for Alkaline phosphatase (ALP) staining. After staining with 1-Step NBT/BCIP Substrate Solution, the ALP-positive area based on the entire area of the scaffold was calculated using the image analysis software program ImageJ (National Institutes of Health, Bethesda, MD, United States) (Schneider et al., 2012). Osteoclast-like cells were determined using a leukocyte tartrate resistant acid phosphatase (TRAP) staining kit (Sigma Aldrich, St. Louis, MO, United States) and counted as TRAP positive multi-nucleated cells located in the bone defect area. To identify the macrophages, the sections were blocked by 5% BSA buffer for 30 min at room temperature, followed by 1 h primary and secondary antibody incubation at room temperature. Macrophages were stained by rat anti-CD11b antibody (Abcam, Cambridge, MA, United States) followed by Alexa Fluor® 647 conjugated donkey anti-rat IgG (Abcam, Cambridge, MA, United States). M1 pro-inflammatory macrophages were identified using mouse anti-inducible nitric oxide synthase (iNOS) antibody (Abcam, Cambridge, MA, United States) followed by Alexa Fluor® 488

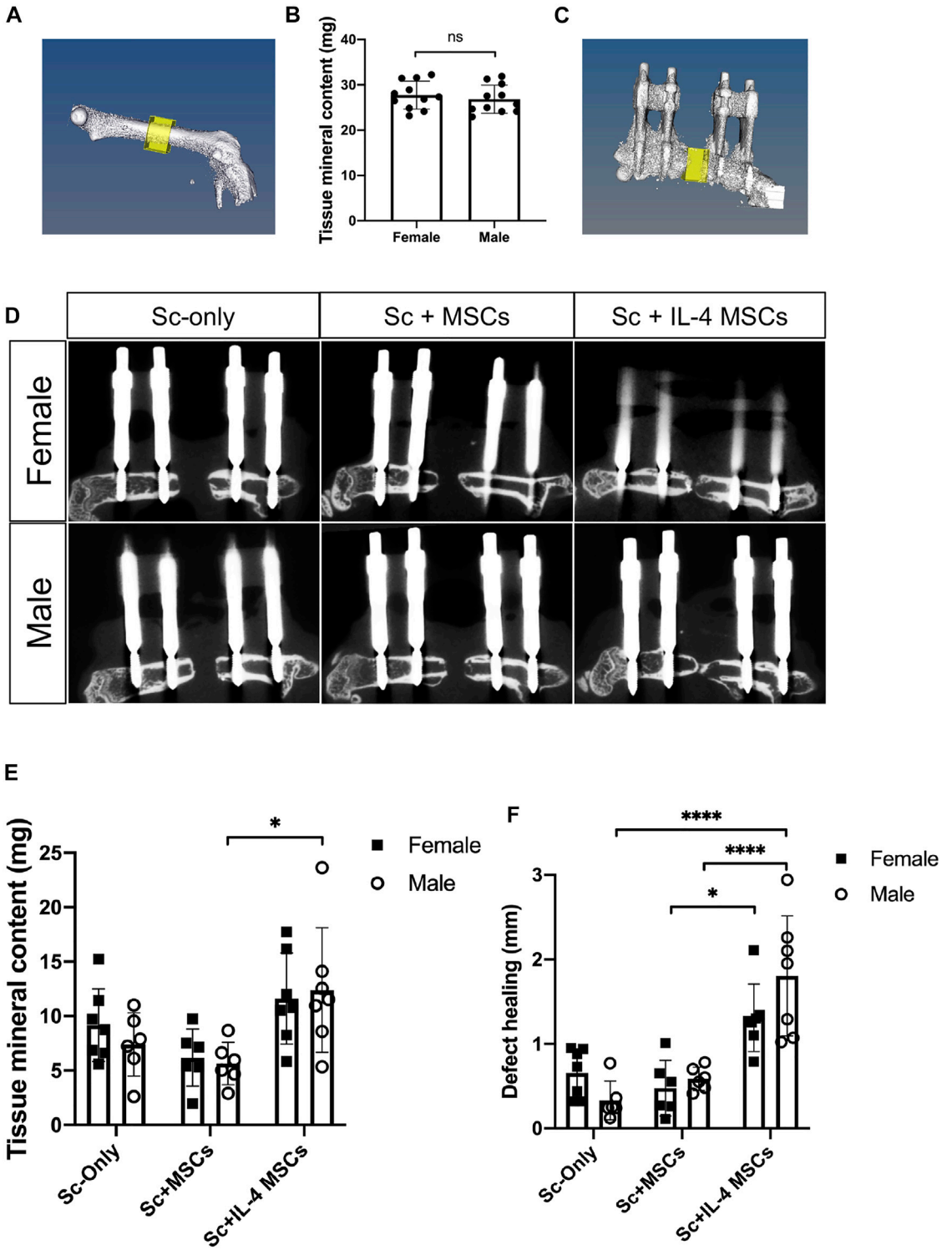

FIGURE 2 | μCT -based reconstructions of the femurs in male and female mice. **(A)** μCT -based reconstructions of the healthy side of femur and the region of interest. **(B)** Tissue mineral content (mg) of the region of interest. female, $n = 16$; male, $n = 16$. IL-4 MSCs in μRBs decreased the sizes of bone defects in both sexes. **(C)** μCT -based reconstructions of the initial defect area and the region of interest. **(D)** μCT -based reconstructions of femurs and defect areas of three groups. **(E)** Tissue mineral content (mg) of the bone defect area and **(F)** defect healing at 6 weeks (mm) calculated by the μCT. Female Sc-only, $n = 7$; female Sc + MSCs, $n = 6$; female Sc + IL-4 MSCs, $n = 7$; male Sc-only, $n = 6$; male Sc + MSCs, $n = 6$; male Sc + IL-4 MSCs, $n = 7$. *: $0.01 \leq p < 0.05$, ****: $p < 0.0001$.

TABLE 1 | The numerical scoring scheme used for the histologic evaluation of fracture healing according to Huo et al. (1991).

Score	Associated finding at fracture site
1	Fibrous tissue
2	Predominantly fibrous tissue with small amount of cartilage
3	Equal mixture of fibrous tissue and cartilaginous tissue
4	Predominantly cartilage with small amount of fibrous tissue
5	Cartilage
6	Predominantly cartilage with small amount of immature bone
7	Equal mixture of cartilage and immature bone
8	Predominantly immature bone with small amount of cartilage
9	Union of fracture by immature bone
10	Union of fracture fragments by mature bone

conjugated goat anti-mouse IgG (Invitrogen, CA, United States). M2 anti-inflammatory macrophages were stained by rabbit anti-liver Arginase (Arg1) antibody (Abcam, Cambridge, MA, United States) followed by Alexa Fluor® 555 conjugated donkey anti-rabbit IgG (Invitrogen, Carlsbad, CA, United States). Slides were mounted by prolong gold antifade mount with DAPI (Life Technologies, Grand Island, NY, United States). Slides were imaged using a fluorescence microscope (BZ-X800, Keyence, IL, United States). Positive cells in all slides were counted double blinded in three randomly selected areas by two independent researchers. All the samples were recorded as digital images with 200x magnification using a microscope (BZ-X800, Keyence, Itasca, IL, United States).

Statistical Analysis

Statistical analyses were conducted using GraphPad Prism 7 (GraphPad Software, San Diego, CA). Data are presented as mean ± SD. Student t-tests were to compare the tissue mineral content of non-operated femurs between female and male mice. Two-way ANOVA with Bonferroni's post hoc test was conducted for the multiple statistical comparisons among groups. The difference was considered significant when the p-value was < 0.05.

RESULTS

Micro-Computational Tomography of the Non-Operative Femur

To determine whether there were differences between sex, the tissue mineral contents of the non-operated femurs were compared. 16 mice of both sexes were measured for this experiment. There were no statistically significant differences in the tissue mineral content between femurs of the non-operative sides of males vs. females ($p = 0.506$) (**Figure 2B**).

Micro-Computational Tomography of the Bone Defect Area on the Operative Side

To assess the degree of bone regeneration in the defect area, μCT analysis was performed after 6 weeks to analyze the size and tissue mineral content of the region of interest (**Figure 2C**). For both sexes, the Sc + IL-4-MSCs groups displayed increased bone healing and decreased bone defect size (**Figure 2F**). Three of seven male mice receiving Sc + IL-4-MSCs and one of seven female mice receiving Sc + IL-4-MSCs showed bony bridging on μCT; in contrast, none of the other groups showed bony bridging (**Figure 2D**). The male Sc + IL-4-MSCs group showed higher tissue mineral content compared to the male Sc-only group (**Figure 2E**).

Histological Analysis

The same trends for the results of μCT were seen with histomorphometric analysis of H&E-stained sections (**Figure 3**). There was increased bone formed in the periphery of the defect area in Sc + IL-4-MSCs groups of both sexes than in other groups. Three of seven specimens from the male Sc + IL-4-MSCs group and one of seven from the female Sc + IL-4-MSCs group showed bone bridging. None of the mice of the other groups showed bone bridging of the defect. The grade of defect healing quantified by the scoring system of Huo et al., in the male Sc + IL-4-MSCs group (score: 5.4 ± 2.3) was significantly higher compared with the male Sc-only group (score: 1.8 ± 0.4, $p = 0.0005$) and the male Sc + MSC group (score: 2.8 ± 0.4, $p = 0.022$). No significant difference was detected between male and female groups using the same treatment.

Expression of Alkaline Phosphatase

Male groups showed higher ALP positive staining than the female groups for the same treatment, but the values did not reach statistical significance (female vs. male in Sc-only groups: $p = 0.520$, in Sc + MSCs groups: $p = 0.737$). However, the male Sc + IL-4-MSCs group showed a strong trend compared to the female Sc + IL-4-MSCs group ($p = 0.0536$). Comparing the groups in same sex, the Sc + IL-4-MSCs group showed a higher level of ALP positive staining, but this did not reach statistical significance (**Figure 4**).

Tartrate Resistant Acid Phosphatase Staining

For the TRAP staining, the number for female Sc-only group was significantly higher than female Sc + MSCs group: $p = 0.044$). No significant differences were detected among female and male of Sc-only groups, Sc + MSCs groups and Sc + IL-4-MSCs groups (**Figure 5**).

Immunohistochemistry for Macrophage Phenotype

The number of macrophages (CD11b+/DAPI+) in the male Sc + IL-4-MSCs group was significantly higher than the female Sc + IL-4-MSCs group ($p = 0.0097$). No significant differences were detected among female and male mice in the Sc-only or Sc + MSCs groups. The macrophage number of male Sc + IL-4-MSCs group was significantly increased compared with that in male Sc + MSCs and male Sc-only group ($p = 0.0002$, $p = 0.0002$ respectively). There were no significant differences among the groups of female mice (female Sc-only, female Sc + MSCs, female Sc + IL-4-MSCs) (**Figure 6**). For the M1 pro-inflammatory

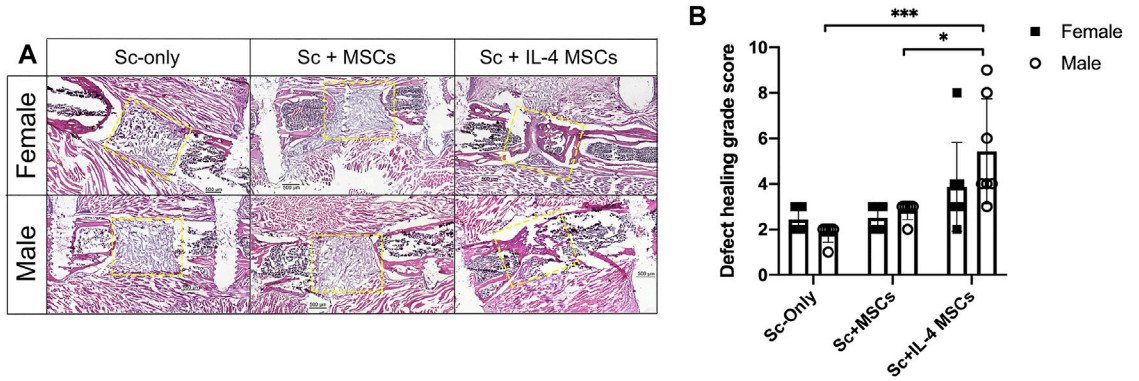

FIGURE 3 | Histology analysis of critical size bone defect healing after 6 weeks in female and male mice. **(A)** H&E stained representative images of the bone defect images (scaffolds ± cells) at 200x magnification. The yellow dotted frames show the original bone defect area. **(B)** Defect healing grade score based on the histological evaluation. *: $0.01 \leq p < 0.05$, ***: $0.0001 \leq p < 0.001$.

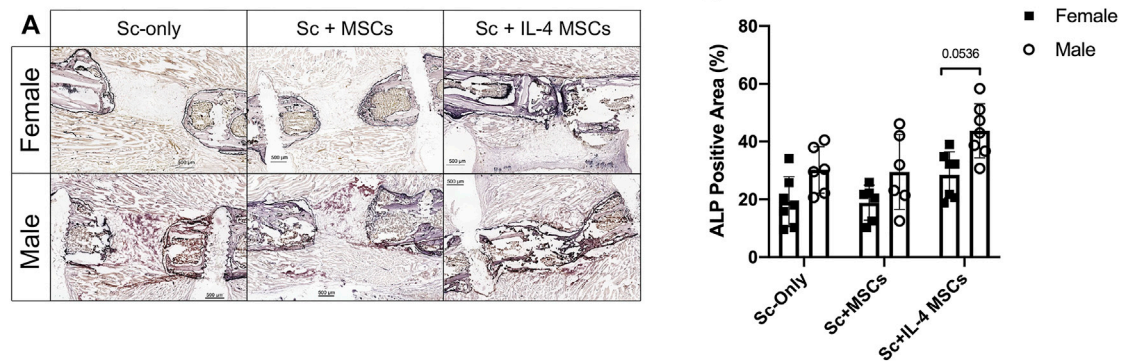

FIGURE 4 | ALP staining and analysis of critical size bone defect healing in female and male mice. **(A)** The ALP-stained bone defects representative images of all groups after 6 weeks with 200 times magnification. **(B)** ALP positive area calculated.

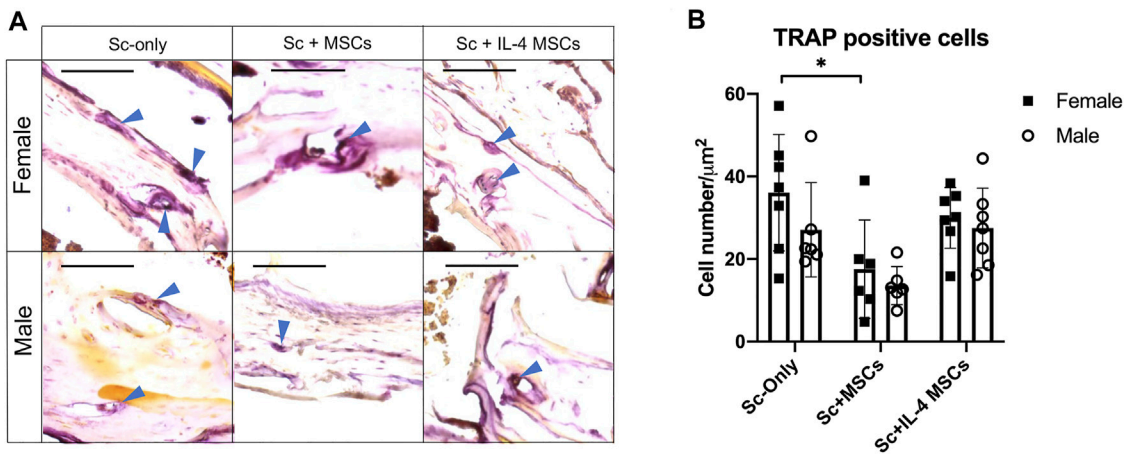

FIGURE 5 | TRAP staining and analysis of critical size bone defect healing after 6 weeks in female and male mice. **(A)** The TRAP-stained bone defects representative images of all groups with 200 times magnification (red arrows showed the TRAP positive cells, bar = 100 μm). **(B)** TRAP positive cell number calculated per μm^2. *: $0.01 \leq p < 0.05$.

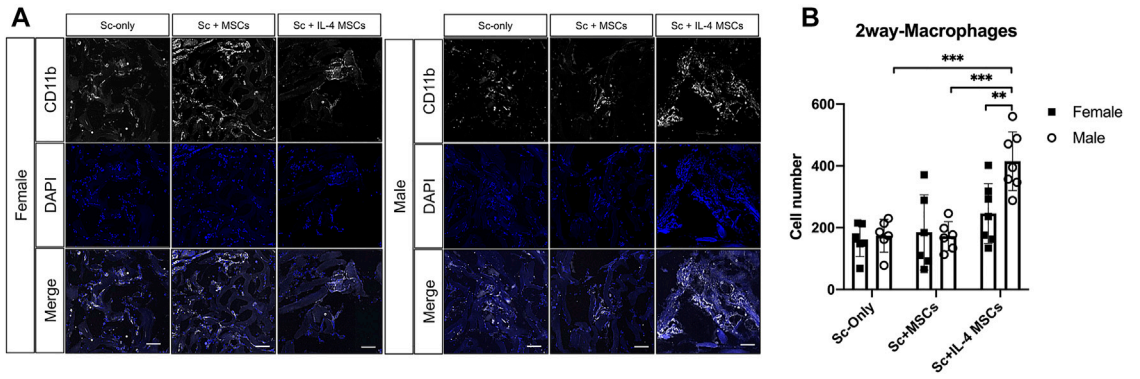

FIGURE 6 | Immunohistochemistry staining and analysis of CD11b/DAPI inside the scaffolds of critical size bone defect healing after 6 weeks in female and male mice. **(A)** Representative images of CD11b/DAPI stained macrophages in all groups. (Blue: DAPI/nucleus; White: CD11b/Macrophage marker. Bar = 100 μm). **(B)** Number of cells counted from the immunohistochemistry images. Female Sc-only, $n = 6$; female Sc + MSCs, $n = 6$; female Sc + IL-4 MSCs, $n = 7$; male Sc-only, $n = 6$; male Sc + MSCs, $n = 6$; male Sc + IL-4 MSCs, $n = 7$. **: $0.001 \leq p < 0.01$, ***: $0.0001 \leq p < 0.001$, ****: $p < 0.0001$.

macrophage (iNOS+/DAPI+) number, the male Sc + IL-4-MSCs group was significantly higher than the male Sc + MSCs group ($p = 0.0483$); the female Sc + IL-4-MSCs was significantly higher than female Sc + MSCs group ($p = 0.001$) and female Sc-only group ($p = 0.0002$). The number of M2 macrophages in the female Sc + IL-4-MSCs group was significantly increased compared with that in female Sc + MSCs group ($p < 0.0001$) and with that in the female Sc-only group ($p < 0.0001$). M2 macrophage number in male mice showed a similar trend. M2 macrophage number in male Sc + IL-4-MSCs group was significantly increased compared with that in male Sc + MSCs group ($p < 0.0001$) and the male Sc-only group ($p < 0.0001$). The M2/M1 ratio in male Sc + IL-4-MSCs group was significantly higher compared with that in male Sc + MSCs group ($p < 0.0001$) and in the male Sc-only group ($p < 0.0001$). The M2/M1 ratio in female Sc + IL-4-MSCs group showed an increased trend compared with that in male Sc + MSCs group ($p = 0.0605$) and the male Sc-only group ($p = 0.0913$). However, no significant differences of M1 macrophage number, M2 macrophage number or M2/M1 ratio were observed between female and male mice with same implantation treatment (female Sc-only vs. male Sc-only group; female Sc + MSCs vs. male Sc + MSCs group; female Sc + IL-4-MSCs vs. male Sc + IL-4-MSCs group) (**Figure 7**).

DISCUSSION

MSCbased bone tissue engineering has been proposed as a potential substitutive intervention to promote bone repair, instead of bulk autologous bone grafting. Recently, we have investigated the healing of bone defects by modulating the immune system (Loi et al., 2016a; Loi et al., 2016b; Goodman et al., 2019; Pajarinen et al., 2019; Maruyama et al., 2020). IL-4 is the most effective anti-inflammatory cytokine that polarizes M1 macrophages to an M2 phenotype (Lin et al., 2017a; Lin et al., 2018; Lin et al., 2019). We previously reported that IL-4 over-expressing MSCs within a μRB scaffold enhanced macrophage migration into the scaffolds and subsequent bone formation to aid in the bridging of a 2 mm a critical size femoral defect in male Balb/c mice, compared to μRB scaffold with or without unmodified MSCs (Ueno et al., 2020). The crosstalk between local MSCs and recruited immune cells at the appropriate time point decreases inflammation and the facilitates bone healing; this enhancement of bone formation by manipulating immune regulation with IL-4 appears to be a generalized phenomenon regardless of sex.

Sex differences have been observed in musculoskeletal diseases. Although the reasons for these differences are complex and largely unknown, one of the possible reasons is the sex-based differences in cells' response to the local microenvironment (Knewtson et al., 2021). Sex differences have been shown to affect the MSC-based therapeutic potential for bone healing. Katsara et al. found that bone marrow MSCs from male mice had higher osteogenic and adipogenic potential than female mice, without affecting their proliferative abilities (Katsara et al., 2011). Strube et al. reported that female bone marrow contained significantly fewer MSCs, as indicated by lower colony-forming unit (CFU) numbers in femora and tibias using a rat bone defect model (Strube et al., 2009). Male muscle-derived stem cells were more effective than female derived cells in the healing of defects in bone and cartilage (Matsumoto et al., 2008; Meszaros et al., 2012). Mehta et al., demonstrated that male rats showed larger bone callus and advanced healing compared to females using a bone defect model (Mehta et al., 2011). However, little is known concerning the influence of sex on long bone defect healing using MSC-based interventions. Previously, we have compared the gold standard bone-graft (positive control), μRB scaffold only, μRB scaffold with unaltered MSCs and μRB scaffold with IL-4 over-expressing MSCs in the same bone defect model in male mice. The group with bone graft showed enhanced bone formation, however the scaffold only and scaffold with unaltered MSCs groups showed fibrous tissue with virtually no bone formation (Ueno et al., 2020). The group with IL-4 MSCs plus scaffold showed enhanced bone formation. In the current study, we investigated the outcomes of the MSC-based therapy

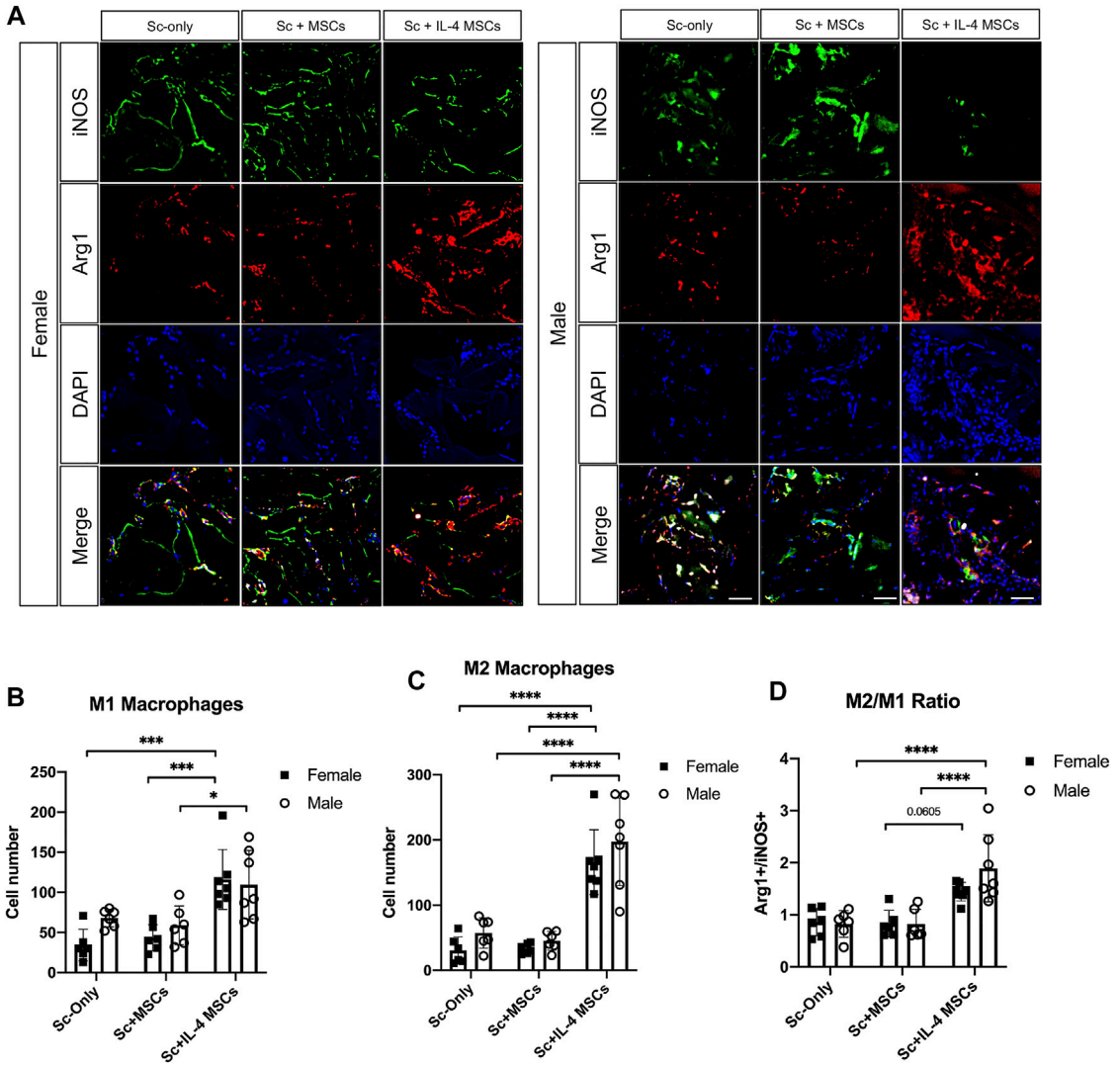

FIGURE 7 | Immunohistochemistry staining and analysis of iNOS/Arg1/DAPI inside the scaffolds of critical size bone defect healing after 6 weeks in female and male mice. **(A)** Representative images of iNOS/Arg1/DAPI stained macrophages in all groups. (Blue: DAPI/nucleus; Green: iNOS/M1 macrophage marker; Red: Arg-1/M2 macrophage marker. Bar = 50 μm). **(B)** Number of cells counted from the immunohistochemistry images. Female Sc-only, $n = 6$; female Sc + MSCs, $n = 6$; female Sc + IL-4 MSCs, $n = 7$; male Sc-only, $n = 6$; male Sc + MSCs, $n = 6$; male Sc + IL-4 MSCs, $n = 7$. *: $0.01 \leq p < 0.05$, ***: $0.0001 \leq p < 0.001$, ****: $p < 0.0001$.

using a μRB scaffold in female and male Balb/c mice subjected to a critical size femoral bone defect.

The current results suggest that IL-4 over-expressing MSCs are an effective way to enhance bone healing in a critical size bone defect model in both female and male mice compared with scaffold only and scaffold with unmodified MSCs. Although the μCT and histological analysis of the bone defect area showed no significant differences between females and males with the same treatment, more detailed analysis revealed some differences based on sex in the mice receiving Sc + IL-4-MSCs. Three of seven male mice and one of seven female mice showed bony bridging after receiving IL-4 over-expressing MSC seeded scaffolds. The ALP staining showed that with the IL-4 over-expressing MSCs scaffold treatment, male mice had a strong trend ($p = 0.0536$, **Figure 4B**) of increased ALP positive area. Furthermore, the total macrophage number in the male Sc + IL-4-MSCs group was significantly higher than in female mice with the IL-4 over-expressing MSCs intervention; M2 macrophage number, and M2/M1 macrophage ratio also showed that the male Sc + IL-4-MSCs group had a higher level than female mice with the same treatment. These results suggest that male mice had enhanced bone healing with the IL-4 over-expressing MSC seeded scaffolds compared with female mice with the same treatment. These results may be due to sex differences in the properties of the MSCs or the healing process of different sexes, which have been reported by other groups (Strube et al., 2009; Mehta et al., 2011). It should further be taken into account that male animals of the same age have a higher body weight compared to females. In our study, the average body weights of males were higher than females (mean ± SD; male 29.4 ± 1.5 g, female 24.0 ± 1.3 g) which may result in different loading patterns and thus different healing parameters.

Interestingly, the TRAP staining showed that female mice receiving the empty scaffold (female Sc-only) had significantly higher TRAP positive cell number compared with female mice receiving Sc + MSCs (female Sc + MSCs) and higher than female mice receiving Sc + IL-4 MSCs (female Sc + IL-4 MSCs), although no significant difference was detected. Female mice in Sc-only group showed higher TRAP positive cells than male mice receiving the empty scaffold (**Figure 5**) although no significant differences were found. Similar results have been reported by other researchers using a murine tibial fracture model (Deng et al., 2020). The increased osteoclast numbers (TRAP positive cell number) found in female mice may promote faster remodeling of the fracture calluses.

In the current study, we used IL-4 overexpressing MSCs implanted 3 days after the generation of the critical size bone defect but implanted the scaffold without MSCs and with unmodified MSCs immediately after we created the bone defect. Direct application of anti-inflammatory immunomodulatory cytokines at the critical time can favorably modify the local microenvironment. Administration of IL-4 too early in the bone healing process inhibits the proliferation of human osteoblasts (Frost et al., 2001). Lewis et al. reported that mice overproducing IL-4 had severe osteoporosis primarily due to a marked decrease in osteoblast and ALP activity (Lewis et al., 1993). Our previous *in vitro* study also showed modulation of macrophage phenotype at an appropriate time optimized the proliferation and osteogenic differentiation of MSCs (Loi et al., 2016b). This underscores the concept that the timing of anti-inflammatory cytokine intervention such as IL-4 is critical to facilitating osteogenesis by not interfering with the mandatory pro-inflammatory period of bone healing. Thus, we implanted the scaffolds with IL-4 over-expressing MSCs 3 days after the primary creation of the bone defect.

Autograft is the gold standard for treatment of residual long bone defects however, autologous bone is often limited in quantity and/or quality and can be accompanied by morbidity at the harvest site (Khan et al., 2005). Furthermore, the failure rate of autologous bone grafting to heal a nonunion or other defect ranges from 4 to 25% (Tuchman et al., 2016). Allograft bone is osteoconductive only and may potentially transfer communicable diseases or cause adverse immunological events (Khan et al., 2005). In an effort to find alternative therapies, novel biomaterials were developed. The μRB scaffold used in the current study was reported to enhance the proliferation of stem cells in 3D culture compared with hydrogel scaffold (Han et al., 2016). Cell viability was also promoted in μRB scaffold *in vivo* in a mouse critical-size cranial defect model (Han et al., 2016). In this previous study, BLI results indicated that almost 40% of stem cell survived showed after 6 weeks; this is the same time period after which we implanted the scaffolds in the current study. Together with the addition of MSCs, we showed that the 2-mm defect, which is almost 100% of the femoral diameter in Balb/c mice, was too demanding to bridge the defect after 6 weeks (Ueno et al., 2020). MSC-based therapies using μRB scaffolds are thus promising strategies for healing of bone defects based on the results of this study. However, this treatment was not universally successful in all cases for both sexes.

Limitations to our present study should be recognized. The model represents an acute femoral diaphyseal critical size defect, with harvest at one time point. Ongoing studies using a similar chronic defect will shed further light on these treatments in the face of an established nonunion. The timing of administration of IL-4 over-expressing MSCs was crucial and based on previous *in vitro* and *in vivo* studies. This presents a challenge for clinical translation in which "one-stop" surgical treatment is preferred. Other methods of delivery of the IL-4 payload together with MSCs should be pursued. We also found that the proliferation of female murine MSCs *in vitro* was slower than for males, which is similar to that reported for rat MSCs (Strube et al., 2009). We did not endeavor to detect the specific fate of the implanted MSCs at the end of the current study. A previous report showed an enhancement of cell survival using the μRB scaffold 6 weeks after implantation (Han et al., 2016).

In conclusion, μRB scaffolds with IL-4 over-expressing MSCs improved the healing of critical size femoral diaphyseal bone defects in female and male mice. Male mice had enhanced bone healing using the IL-4 over-expressing MSC seeded scaffolds compared with female mice. These results suggest that sex differences should be considered during the application of MSC-based studies of bone healing.

DATA AVAILABILITY STATEMENT

The raw data supporting the conclusion of this article will be made available by the authors, without undue reservation.

ETHICS STATEMENT

The animal study was reviewed and approved by the Stanford's Administrative Panel on Laboratory Animal Care (APLAC).

AUTHOR CONTRIBUTIONS

MU and NZ contributed in the study design, acquisition, analysis and interpretation of data, drafting and critical revision of the manuscript. HH, DB, TU, HS, TL, MM, and EH, contributed in the acquisition, analysis and interpretation of data. ZY, JW, SZ, and FY contributed in the study design and critical revision of the manuscript. SG contributed in the study conceptualization and design, interpretation of data and critical revision of the manuscript. All authors approved the submitted version of the manuscript.

FUNDING

This work was supported by the NIH grants R01AR073145 and R01AR063717 from NIAMS and the Ellenburg Chair in Surgery at Stanford University.

REFERENCES

An, J. H., Park, H., Song, J. A., Ki, K. H., Yang, J. Y., Choi, H. J., et al. (2013). Transplantation of Human Umbilical Cord Blood-Derived Mesenchymal Stem Cells or Their Conditioned Medium Prevents Bone Loss in Ovariectomized Nude Mice. *Tissue Eng. Part. A.* 19 (5-6), 685–696. doi:10.1089/ten.TEA.2012.0047

Beck, T. J., Ruff, C. B., Shaffer, R. A., Betsinger, K., Trone, D. W., and Brodine, S. K. (2000). Stress Fracture in Military Recruits: Gender Differences in Muscle and Bone Susceptibility Factors. *Bone* 27 (3), 437–444. doi:10.1016/s8756-3282(00)00342-2

Cawthon, P. M. (2011). Gender Differences in Osteoporosis and Fractures. *Clin. Orthop. Relat. Res.* 469 (7), 1900–1905. doi:10.1007/s11999-011-1780-7

Chang, M. A., Bishop, A. T., Moran, S. L., and Shin, A. Y. (2006). The Outcomes and Complications of 1,2-intercompartmental Supraretinacular Artery Pedicled Vascularized Bone Grafting of Scaphoid Nonunions. *J. Hand Surg.* 31 (3), 387–396. doi:10.1016/j.jhsa.2005.10.019

Cho, S. W., Sun, H. J., Yang, J.-Y., Jung, J. Y., An, J. H., Cho, H. Y., et al. (2009). Transplantation of Mesenchymal Stem Cells Overexpressing RANK-Fc or CXCR4 Prevents Bone Loss in Ovariectomized Mice. *Mol. Ther.* 17 (11), 1979–1987. doi:10.1038/mt.2009.153

Chow, S.-H., Chim, Y. N., Chim, Y.-N., Wang, J., Zhang, N., Wong, R.-Y., et al. (2019). Vibration Treatment Modulates Macrophage Polarisation and Enhances Early Inflammatory Response in Oestrogen-Deficient Osteoporotic-Fracture Healing. *eCM* 38, 228–245. doi:10.22203/ecm.v038a16

Conrad, B., Han, L. H., and Yang, F. (2018). Gelatin-Based Microribbon Hydrogels Accelerate Cartilage Formation by Mesenchymal Stem Cells in Three Dimensions. *Tissue Eng. Part. A.* 24 (21-22), 1631–1640. doi:10.1089/ten.TEA.2018.0011

Cummings, S. R., and Melton, L. J. (2002). Epidemiology and Outcomes of Osteoporotic Fractures. *Lancet* 359 (9319), 1761–1767. doi:10.1016/S0140-6736(02)08657-9

David, V., Lafage-Proust, M.-H., Laroche, N., Christian, A., Ruegsegger, P., and Vico, L. (2006). Two-week Longitudinal Survey of Bone Architecture Alteration in the Hindlimb-Unloaded Rat Model of Bone Loss: Sex Differences. *Am. J. Physiol. Endocrinol. Metab.* 290 (3), E440–E447. doi:10.1152/ajpendo.00293.2004

Deng, Z., Gao, X., Sun, X., Cui, Y., Amra, S., and Huard, J. (2020). Gender Differences in Tibial Fractures Healing in normal and Muscular Dystrophic Mice. *Am. J. Transl. Res.* 12 (6), 2640–2651.

Dominici, M., Le Blanc, K., Mueller, I., Slaper-Cortenbach, I., Marini, F. C., Krause, D. S., et al. (2006). Minimal Criteria for Defining Multipotent Mesenchymal Stromal Cells. The International Society for Cellular Therapy Position Statement. *Cytotherapy* 8 (4), 315–317. doi:10.1080/14653240600855905

Frost, A., Jonsson, K. B., BrändstrÖm, H., Ljunghall, S., Nilsson, O., and Ljunggren, Ö. (2001). Interleukin (IL)-13 and IL-4 Inhibit Proliferation and Stimulate IL-6 Formation in Human Osteoblasts: Evidence for Involvement of Receptor Subunits IL-13R, IL-13Rα, and IL-4Rα. *Bone* 28 (3), 268–274. doi:10.1016/s8756-3282(00)00449-x

Goodman, S. B., Pajarinen, J., Yao, Z., and Lin, T. (2019). Inflammation and Bone Repair: From Particle Disease to Tissue Regeneration. *Front. Bioeng. Biotechnol.* 7, 230. doi:10.3389/fbioe.2019.00230

Guihard, P., Danger, Y., Brounais, B., David, E., Brion, R., Delecrin, J., et al. (2012). Induction of Osteogenesis in Mesenchymal Stem Cells by Activated Monocytes/macrophages Depends on Oncostatin M Signaling. *Stem Cells* 30 (4), 762–772. doi:10.1002/stem.1040

Han, L.-H., Yu, S., Wang, T., Behn, A. W., and Yang, F. (2013). Microribbon-Like Elastomers for Fabricating Macroporous and Highly Flexible Scaffolds that Support Cell Proliferation in 3D. *Adv. Funct. Mater.* 23 (3), 346–358. doi:10.1002/adfm.201201212

Han, L.-H., Conrad, B., Chung, M. T., Deveza, L., Jiang, X., Wang, A., et al. (2016). Winner of the Young Investigator Award of the Society for Biomaterials at the 10th World Biomaterials Congress, May 17-22, 2016, Montreal QC, Canada: Microribbon-Based Hydrogels Accelerate Stem Cell-Based Bone Regeneration in a Mouse Critical-Size Cranial. *J. Biomed. Mater. Res.* 104 (6), 1321–1331. doi:10.1002/jbm.a.35715

Huo, M. H., Troiano, N. W., Pelker, R. R., Gundberg, C. M., and Friedlaender, G. E. (1991). The Influence of Ibuprofen on Fracture Repair: Biomechanical, Biochemical, Histologic, and Histomorphometric Parameters in Rats. *J. Orthop. Res.* 9 (3), 383–390. doi:10.1002/jor.1100090310

Jin, H., Bae, Y., Kim, M., Kwon, S.-J., Jeon, H., Choi, S., et al. (2013). Comparative Analysis of Human Mesenchymal Stem Cells from Bone Marrow, Adipose Tissue, and Umbilical Cord Blood as Sources of Cell Therapy. *Int. J. Mol. Sci.* 14 (9), 17986–18001. doi:10.3390/ijms140917986

Katsara, O., Mahaira, L. G., Iliopoulou, E. G., Moustaki, A., Antsaklis, A., Loutradis, D., et al. (2011). Effects of Donor Age, Gender, and *In Vitro* Cellular Aging on the Phenotypic, Functional, and Molecular Characteristics of Mouse Bone Marrow-Derived Mesenchymal Stem Cells. *Stem Cell Develop.* 20 (9), 1549–1561. doi:10.1089/scd.2010.0280

Kern, S., Eichler, H., Stoeve, J., Klüter, H., and Bieback, K. (2006). Comparative Analysis of Mesenchymal Stem Cells from Bone Marrow, Umbilical Cord Blood, or Adipose Tissue. *Stem Cells* 24 (5), 1294–1301. doi:10.1634/stemcells.2005-0342

Khan, S. N., Cammisa, F. P., Jr., Sandhu, H. S., Diwan, A. D., Girardi, F. P., and Lane, J. M. (2005). The Biology of Bone Grafting. *J. Am. Acad. Orthop. Surgeons* 13 (1), 77–86. doi:10.5435/00124635-200501000-00010

Knewtson, K. E., Ohl, N. R., and Robinson, J. L. (2021). Estrogen Signaling Dictates Musculoskeletal Stem Cell Behavior: Sex Differences in Tissue Repair. *Tissue Eng. Part. B Rev.* doi:10.1089/ten.TEB.2021.0094

Lee, K., Kim, H., Kim, J.-M., Kim, J.-R., Kim, K.-J., Kim, Y.-J., et al. (2011). Systemic Transplantation of Human Adipose-Derived Stem Cells Stimulates Bone Repair by Promoting Osteoblast and Osteoclast Function. *J. Cel Mol. Med.* 15 (10), 2082–2094. doi:10.1111/j.1582-4934.2010.01230.x

Lewis, D. B., Liggitt, H. D., Effmann, E. L., Motley, S. T., Teitelbaum, S. L., Jepsen, K. J., et al. (1993). Osteoporosis Induced in Mice by Overproduction of Interleukin 4. *Proc. Natl. Acad. Sci.* 90 (24), 11618–11622. doi:10.1073/pnas.90.24.11618

Li, Z., Zhang, W., Li, Z.-B., and Li, J.-R. (2006). Abnormal union of Mandibular Fractures: a Review of 84 Cases. *J. Oral Maxillofac. Surg.* 64 (8), 1225–1231. doi:10.1016/j.joms.2006.04.018

Lin, T. H., Sato, T., Barcay, K. R., Waters, H., Loi, F., Zhang, R., et al. (2015). NF-κB Decoy Oligodeoxynucleotide Enhanced Osteogenesis in Mesenchymal Stem Cells Exposed to Polyethylene Particle. *Tissue Eng. Part. A.* 21 (5-6), 875–883. doi:10.1089/ten.TEA.2014.0144

Lin, T., Pajarinen, J., Nabeshima, A., Lu, L., Nathan, K., Yao, Z., et al. (2017). Establishment of NF-κB Sensing and Interleukin-4 Secreting Mesenchymal Stromal Cells as an "On-Demand" Drug Delivery System to Modulate Inflammation. *Cytotherapy* 19 (9), 1025–1034. doi:10.1016/j.jcyt.2017.06.008

Lin, T.-h., Gibon, E., Loi, F., Pajarinen, J., Córdova, L. A., Nabeshima, A., et al. (2017). Decreased Osteogenesis in Mesenchymal Stem Cells Derived from the Aged Mouse Is Associated with Enhanced NF-κB Activity. *J. Orthop. Res.* 35 (2), 281–288. doi:10.1002/jor.23270

Lin, T., Kohno, Y., Huang, J. F., Romero-Lopez, M., Pajarinen, J., Maruyama, M., et al. (2018). NFκB Sensing IL-4 Secreting Mesenchymal Stem Cells Mitigate the Proinflammatory Response of Macrophages Exposed to Polyethylene Wear Particles. *J. Biomed. Mater. Res.* 106 (10), 2744–2752. doi:10.1002/jbm.a.36504

Lin, T., Kohno, Y., Huang, J. F., Romero-Lopez, M., Maruyama, M., Ueno, M., et al. (2019). Preconditioned or IL4-Secreting Mesenchymal Stem Cells Enhanced Osteogenesis at Different Stages. *Tissue Eng. Part. A.* 25 (15-16), 1096–1103. doi:10.1089/ten.TEA.2018.0292

Liu, Y., Wu, J., Zhu, Y., and Han, J. (2014). Therapeutic Application of Mesenchymal Stem Cells in Bone and Joint Diseases. *Clin. Exp. Med.* 14 (1), 13–24. doi:10.1007/s10238-012-0218-1

Liu, Y., Wang, L., Liu, S., Liu, D., Chen, C., Xu, X., et al. (2014). Transplantation of SHED Prevents Bone Loss in the Early Phase of Ovariectomy-Induced Osteoporosis. *J. Dent Res.* 93 (11), 1124–1132. doi:10.1177/0022034514552675

Loi, F., Córdova, L. A., Pajarinen, J., Lin, T.-h., Yao, Z., and Goodman, S. B. (2016). Inflammation, Fracture and Bone Repair. *Bone* 86, 119–130. doi:10.1016/j.bone.2016.02.020

Loi, F., Córdova, L. A., Zhang, R., Pajarinen, J., Lin, T.-h., Goodman, S. B., et al. (2016). The Effects of Immunomodulation by Macrophage Subsets on Osteogenesis *In Vitro*. *Stem Cel Res. Ther.* 7, 15. doi:10.1186/s13287-016-0276-5

Maruyama, M., Rhee, C., Utsunomiya, T., Zhang, N., Ueno, M., Yao, Z., et al. (2020). Modulation of the Inflammatory Response and Bone Healing. *Front. Endocrinol.* 11, 386. doi:10.3389/fendo.2020.00386

Matsumoto, T., Kubo, S., Meszaros, L. B., Corsi, K. A., Cooper, G. M., Li, G., et al. (2008). The Influence of Sex on the Chondrogenic Potential of Muscle-Derived Stem Cells: Implications for Cartilage Regeneration and Repair. *Arthritis Rheum.* 58 (12), 3809–3819. doi:10.1002/art.24125

Mehta, M., Duda, G. N., Perka, C., and Strube, P. (2011). Influence of Gender and Fixation Stability on Bone Defect Healing in Middle-Aged Rats: a Pilot Study. *Clin. Orthop. Relat. Res.* 469 (11), 3102–3110. doi:10.1007/s11999-011-1914-y

Meszaros, L. B., Usas, A., Cooper, G. M., and Huard, J. (2012). Effect of Host Sex and Sex Hormones on Muscle-Derived Stem Cell-Mediated Bone Formation and Defect Healing. *Tissue Eng. Part. A.* 18 (17-18), 1751–1759. doi:10.1089/ten.TEA.2011.0448

Pajarinen, J., Lin, T., Gibon, E., Kohno, Y., Maruyama, M., Nathan, K., et al. (2019). Mesenchymal Stem Cell-Macrophage Crosstalk and Bone Healing. *Biomaterials* 196, 80–89. doi:10.1016/j.biomaterials.2017.12.025

Parker, M. J., Raghavan, R., and Gurusamy, K. (2007). Incidence of Fracture-Healing Complications after Femoral Neck Fractures. *Clin. Orthop. Relat. Res.* 458, 175–179. doi:10.1097/blo.0b013e3180325a42

Peister, A., Mellad, J. A., Larson, B. L., Hall, B. M., Gibson, L. F., and Prockop, D. J. (2004). Adult Stem Cells from Bone Marrow (MSCs) Isolated from Different Strains of Inbred Mice Vary in Surface Epitopes, Rates of Proliferation, and Differentiation Potential. *Blood* 103 (5), 1662–1668. doi:10.1182/blood-2003-09-3070

Ralston, S. H., and de Crombrugghe, B. (2006). Genetic Regulation of Bone Mass and Susceptibility to Osteoporosis. *Genes Develop.* 20 (18), 2492–2506. doi:10.1101/gad.1449506

Ricks, D. M., Kutner, R., Zhang, X.-Y., Welsh, D. A., and Reiser, J. (2008). Optimized Lentiviral Transduction of Mouse Bone Marrow-Derived Mesenchymal Stem Cells. *Stem Cell Develop.* 17 (3), 441–450. doi:10.1089/scd.2007.0194

Rogan, H., Ilagan, F., Tong, X., Chu, C. R., and Yang, F. (2020). Microribbon-hydrogel Composite Scaffold Accelerates Cartilage Regeneration *In Vivo* with Enhanced Mechanical Properties Using Mixed Stem Cells and Chondrocytes. *Biomaterials* 228, 119579. doi:10.1016/j.biomaterials.2019.119579

Schneider, C. A., Rasband, W. S., and Eliceiri, K. W. (2012). NIH Image to ImageJ: 25 Years of Image Analysis. *Nat. Methods* 9 (7), 671–675. doi:10.1038/nmeth.2089

Shapouri-Moghaddam, A., Mohammadian, S., Vazini, H., Taghadosi, M., Esmaeili, S. A., Mardani, F., et al. (2018). Macrophage Plasticity, Polarization, and Function in Health and Disease. *J. Cel Physiol.* 233 (9), 6425–6440. doi:10.1002/jcp.26429

Shi, Y., Hu, G., Su, J., Li, W., Chen, Q., Shou, P., et al. (2010). Mesenchymal Stem Cells: a New Strategy for Immunosuppression and Tissue Repair. *Cell Res.* 20 (5), 510–518. doi:10.1038/cr.2010.44

Strube, P., Mehta, M., Baerenwaldt, A., Trippens, J., Wilson, C. J., Ode, A., et al. (2009). Sex-specific Compromised Bone Healing in Female Rats Might Be Associated with a Decrease in Mesenchymal Stem Cell Quantity. *Bone* 45 (6), 1065–1072. doi:10.1016/j.bone.2009.08.005

Sui, B.-D., Hu, C.-H., Zheng, C.-X., Shuai, Y., He, X.-N., Gao, P.-P., et al. (2017). Recipient Glycemic Micro-environments Govern Therapeutic Effects of Mesenchymal Stem Cell Infusion on Osteopenia. *Theranostics* 7 (5), 1225–1244. doi:10.7150/thno.18181

Sui, B.-D., Hu, C.-H., Liu, A.-Q., Zheng, C.-X., Xuan, K., and Jin, Y. (2019). Stem Cell-Based Bone Regeneration in Diseased Microenvironments: Challenges and Solutions. *Biomaterials* 196, 18–30. doi:10.1016/j.biomaterials.2017.10.046

Tuchman, A., Brodke, D. S., Youssef, J. A., Meisel, H.-J., Dettori, J. R., Park, J.-B., et al. (2016). Iliac Crest Bone Graft versus Local Autograft or Allograft for Lumbar Spinal Fusion: A Systematic Review. *Glob. Spine J.* 6 (6), 592–606. doi:10.1055/s-0035-1570749

Ueno, M., Lo, C. W., Barati, D., Conrad, B., Lin, T., Kohno, Y., et al. (2020). Interleukin-4 Overexpressing Mesenchymal Stem Cells Withingelatin-basedmicroribbon Hydrogels Enhance Bone Healing in a Murine Long Bone Critical-size Defect Model. *J. Biomed. Mater. Res.* 108 (11), 2240–2250. doi:10.1002/jbm.a.36982

Utsunomiya, T., Zhang, N., Lin, T., Kohno, Y., Ueno, M., Maruyama, M., et al. (2021). Different Effects of Intramedullary Injection of Mesenchymal Stem Cells during the Acute vs. Chronic Inflammatory Phase on Bone Healing in the Murine Continuous Polyethylene Particle Infusion Model. *Front. Cel Dev. Biol.* 9, 631063. doi:10.3389/fcell.2021.631063

Utsunomiya, T., Zhang, N., Lin, T., Kohno, Y., Ueno, M., Maruyama, M., et al. (2021). Suppression of NF-kappaB-Induced Chronic Inflammation Mitigates Inflammatory Osteolysis in the Murine Continuous Polyethylene Particle Infusion Model. *J. Biomed. Mater. Res. A.* 109, 1828–1839. doi:10.1002/jbm.a.37175

Zhang, N., Lo, C.-W., Utsunomiya, T., Maruyama, M., Huang, E., Rhee, C., et al. (2021). PDGF-BB and IL-4 Co-overexpression Is a Potential Strategy to Enhance Mesenchymal Stem Cell-Based Bone Regeneration. *Stem Cel Res. Ther.* 12 (1), 40. doi:10.1186/s13287-020-02086-8

Zwingenberger, S., Niederlohmann, E., Vater, C., Rammelt, S., Matthys, R., Bernhardt, R., et al. (2013). Establishment of a Femoral Critical-Size Bone Defect Model in Immunodeficient Mice. *J. Surg. Res.* 181 (1), e7–e14. doi:10.1016/j.jss.2012.06.039

Conflict of Interest: The authors declare that the research was conducted in the absence of any commercial or financial relationships that could be construed as a potential conflict of interest.

Publisher's Note: All claims expressed in this article are solely those of the authors and do not necessarily represent those of their affiliated organizations, or those of the publisher, the editors and the reviewers. Any product that may be evaluated in this article, or claim that may be made by its manufacturer, is not guaranteed or endorsed by the publisher.

Copyright © 2021 Ueno, Zhang, Hirata, Barati, Utsunomiya, Shen, Lin, Maruyama, Huang, Yao, Wu, Zwingenberger, Yang and Goodman. This is an open-access article distributed under the terms of the Creative Commons Attribution License (CC BY). The use, distribution or reproduction in other forums is permitted, provided the original author(s) and the copyright owner(s) are credited and that the original publication in this journal is cited, in accordance with accepted academic practice. No use, distribution or reproduction is permitted which does not comply with these terms.

frontiers in Bioengineering and Biotechnology

ORIGINAL RESEARCH
published: 07 December 2021
doi: 10.3389/fbioe.2021.782355

Estrogen Receptor α Signaling in Osteoblasts is Required for Mechanotransduction in Bone Fracture Healing

*Lena Steppe[1†], Benjamin Thilo Krüger[1], Miriam Eva Angelica Tschaffon[1], Verena Fischer[1], Jan Tuckermann[2], Anita Ignatius[1] and Melanie Haffner-Luntzer[1]**

[1]Institute of Orthopedic Research and Biomechanics, University Medical Center Ulm, Ulm, Germany, [2]Institute of Comparative Molecular Endocrinology (CME), Ulm University, Ulm, Germany

OPEN ACCESS

Edited by:
Dmitriy Sheyn, Board of Governors Regenerative Medicine Institute, United States

Reviewed by:
Evan Buettmann, Virginia Commonwealth University, United States
Melodie Metzger, Cedars Sinai Medical Center, United States
Doron Cohn-Schwartz, Rambam Health Care Campus, Israel

***Correspondence:**
Melanie Haffner-Luntzer
melanie.haffner-luntzer@uni-ulm.de

†ORCID ID:
Lena Steppe, orcid.org/0000-0003-0968-5627

Specialty section:
This article was submitted to Biomaterials, a section of the journal Frontiers in Bioengineering and Biotechnology

Received: *24 September 2021*
Accepted: *24 November 2021*
Published: *07 December 2021*

Citation:
Steppe L, Krüger BT, Tschaffon MEA, Fischer V, Tuckermann J, Ignatius A and Haffner-Luntzer M (2021) Estrogen Receptor α Signaling in Osteoblasts is Required for Mechanotransduction in Bone Fracture Healing. Front. Bioeng. Biotechnol. 9:782355. doi: 10.3389/fbioe.2021.782355

Biomechanical stimulation by whole-body low-magnitude high-frequency vibration (LMHFV) has demonstrated to provoke anabolic effects on bone metabolism in both non-osteoporotic and osteoporotic animals and humans. However, preclinical studies reported that vibration improved fracture healing and bone formation in osteoporotic, ovariectomized (OVX) mice representing an estrogen-deficient hormonal status, but impaired bone regeneration in skeletally healthy non-OVX mice. These effects were abolished in general estrogen receptor α (ERα)-knockout (KO) mice. However, it remains to be elucidated which cell types in the fracture callus are targeted by LMHFV during bone healing. To answer this question, we generated osteoblast lineage-specific ERα-KO mice that were subjected to ovariectomy, femur osteotomy and subsequent vibration. We found that the ERα specifically on osteoblastic lineage cells facilitated the vibration-induced effects on fracture healing, because in osteoblast lineage-specific ERα-KO ($ER\alpha^{fl/fl;\ Runx2Cre}$) mice the negative effects in non-OVX mice were abolished, whereas the positive effects of vibration in OVX mice were reversed. To gain greater mechanistic insights, the influence of vibration on murine and human osteogenic cells was investigated *in vitro* by whole genome array analysis and qPCR. The results suggested that particularly canonical WNT and Cox2/PGE_2 signaling is involved in the mechanotransduction of LMHFV under estrogen-deficient conditions. In conclusion, our study demonstrates a critical role of the osteoblast lineage-specific ERα in LMHFV-induced effects on fracture healing and provides further insights into the molecular mechanism behind these effects.

Keywords: osteoblasts, estrogen receptor signaling, whole-body vibration, fracture healing, LMHFV, wnt signaling, prostaglandin signaling

INTRODUCTION

In bone repair, an optimal mechanical environment is required for the successful healing of the fractured bone (Claes et al., 1995; Haffner-Luntzer et al., 2015; Claes, 2017). Long-bone fracture healing critically depends on the stability and type of fracture fixation resulting in different degrees of interfragmentary movement, which either guide intramembranous or endochondral bone formation. A too rigid fixation with less interfragmentary movements results in lower strains around the fracture area and can even hinder successful healing (Perren, 1979; Claes et al., 1998). Clinical and preclinical studies suggest, that the

endocrine status is also important because a disturbed bone formation during fracture healing is commonly observed in postmenopausal osteoporotic patients and OVX rodents (Kim et al., 2001; Nikolaou et al., 2009; Beil et al., 2010; He et al., 2011; Cheung et al., 2016). This can be explained by the importance of the osteoanabolic hormone estrogen for bone health (Cauley, 2015). Therefore, external mechanostimulation applied by whole-body low-magnitude high-frequency vibration (LMHFV) was suggested as a promising approach to improve compromised bone repair in osteoporotic subjects (Thompson et al., 2014; Edwards and Reilly, 2015). Several clinical trials investigating fracture healing and LMHFV are ongoing with no published results yet. Regarding the intact skeleton, clinical studies mainly reports anabolic effects of LMHFV on the osteoporotic skeleton (Rubin et al., 2004), whereas one study demonstrates no effect on bone mineral density (Leung et al., 2014). Preclinical studies demonstrate that LMHFV application provokes positive effects on bone healing in sheep (Li et al., 2018) and in ovariectomy-induced estrogen-deficient rodents (Stuermer et al., 2010; Komrakova et al., 2013; Chung et al., 2014; Wehrle et al., 2015; Wang et al., 2017; Steppe et al., 2020). By contrast, no or negative effects on bone repair were observed in non-OVX rodents (Shi et al., 2010; Stuermer et al., 2010; Chung et al., 2014; Wehrle et al., 2014, 2015; Wang et al., 2017; Steppe et al., 2020).

Therefore, estrogen seems to play an important role in regulating the mechanotransduction of LMHFV during fracture healing. The effect of estrogen on bone is mainly mediated via its interaction with two estrogen receptors (ERs), ERα and ERβ. Both are expressed by chondrocytes and osteogenic cells (Manolagas et al., 1995; Almeida et al., 2017), but regulate the expression of different target genes. In addition to the classic ER pathway involving ligand-binding and the subsequent interaction with transcription factors or estrogen-responsive elements or, also ligand-independent signaling can be exerted by ERα and ERβ in the absence of estrogen. Several studies report that ERα expression is decreased in the fracture callus of OVX mice compared to non-OVX animals (He et al., 2011), whereas mechanical stimulation enhanced ERα expression in the fracture callus particularly in OVX rodents (Wehrle et al., 2015; Chow et al., 2016; Haffner-Luntzer et al., 2018a). Furthermore, other reports showed that ERα is required for mediating the anabolic effects of mechanical strain (Lee et al., 2003; Jessop et al., 2004; Windahl et al., 2013; Chow et al., 2016), indicating that ERα is involved in mechanotransduction in bone. By using a global ERα-knockout (ERα-KO) mouse model, we previously demonstrated that in the absence of ERα, both the improved fracture healing and bone formation upon vibration in OVX animals and the impaired bone regeneration in non-OVX mice were not observed anymore (Haffner-Luntzer et al., 2018a). ERβ-KO did not display any effect, indicating only a minor role of this receptor-however, by using global KO mice we were unable to conclude about systemic versus local effects of ERα during mechanostimulation in fracture healing. Notably, we found that the number and the contact area between osteoblasts and bone (osteoblast surface) in the fracture callus of wildtype mice were decreased in non-OVX but increased in OVX animals by vibration, whereas these parameters were unaltered in ERα-KO OVX mice upon LMHFV treatment (Haffner-Luntzer et al., 2018a). Since osteoblasts are involved in bone regeneration (Dirckx et al., 2013; Bahney et al., 2019) and as ERα is highly expressed by osteoblasts (Haffner-Luntzer et al., 2018a), we hypothesized that osteoblasts are direct target cells of LMHFV via ERα signaling. To investigate this hypothesis, we generated mice with an osteoblast lineage-specific ERα-KO ($ERα^{fl/fl;\ Runx2Cre}$), which underwent ovariectomy followed by a femur osteotomy and LMHFV treatment.

TABLE 1 | Experimental treatment groups per each genotype ($ERα^{fl/fl}$, $ERα^{fl/fl;\ Runx2Cre}$).

Group	OVX	Osteotomy	LMHFV
Non-OVX Sham Vibration	−	+	−
Non-OVX Vibration	−	+	+
OVX Sham Vibration	+	+	−
OVX Vibration	+	+	+

MATERIALS AND METHODS

Animal Care and Animal Models

All experiments were performed according to the German Guidelines of Animal Research on the Protection of Animals as well as the ARRIVE guidelines and were approved by the local ethical committee (No. 1455, Regierungspräsidium Tübingen, Germany). Osteoblast lineage-specific ERα-KO mice (Tg (Runx2-cre)1Jtuc x $Esr1^{tm1.2Mma}$) were generated by crossing Runx2-Cre with $ERα^{fl/fl}$ mice on a C57BL/6 background, both provided by Prof. J. Tuckermann (Ulm University). Cre^{-} littermates ($ERα^{fl/fl}$) were used as control. Cre^{+} mice ($ERα^{fl/fl;\ Runx2Cre}$) were shown to lack the ERα in cells of the osteogenic lineage (**Supplementary Figure S1**) including osteoblasts, osteocytes and hypertrophic chondrocytes. All animals were housed in groups of up to five mice per cage with a 12 h light, 12 h dark rhythm, and received water *ad libitum* as well as a standard mouse feed (Ssniff R/M-H, V1535-300; Ssniff, Soest, Germany) until the day of ovariectomy/sham-ovariectomy. Subsequently, the food was switched to a phytoestrogen-free diet (Ssniff). Mouse genotyping was conducted by lysed ear punch PCR using the primers: 5′-CCAGGAAGACTGCCA GAAGG-3′, 5′-TGGCTTGCAGGT ACAGGAG-3′ and 5′-GGAGCTGCCGAGTCAATAAC-3′ to detect the Cre transgene, whereas the ERα loxP sites were detected using the primers: 5′- TAGGCTTTGTCTCGCTTT CC-3′, 5′- CCCTGG CAAGATAAGACAGC-3′ and 5′-AGGAGAATGAGGTGG CACAG-3′.

Surgical Procedures

When aged 12 weeks, female mice (n = 24 per genotype) were randomly assigned (**Table 1**) to bilateral ovariectomy (n = 12 per genotype) or sham-operated (non-OVX, n = 12 per genotype) as

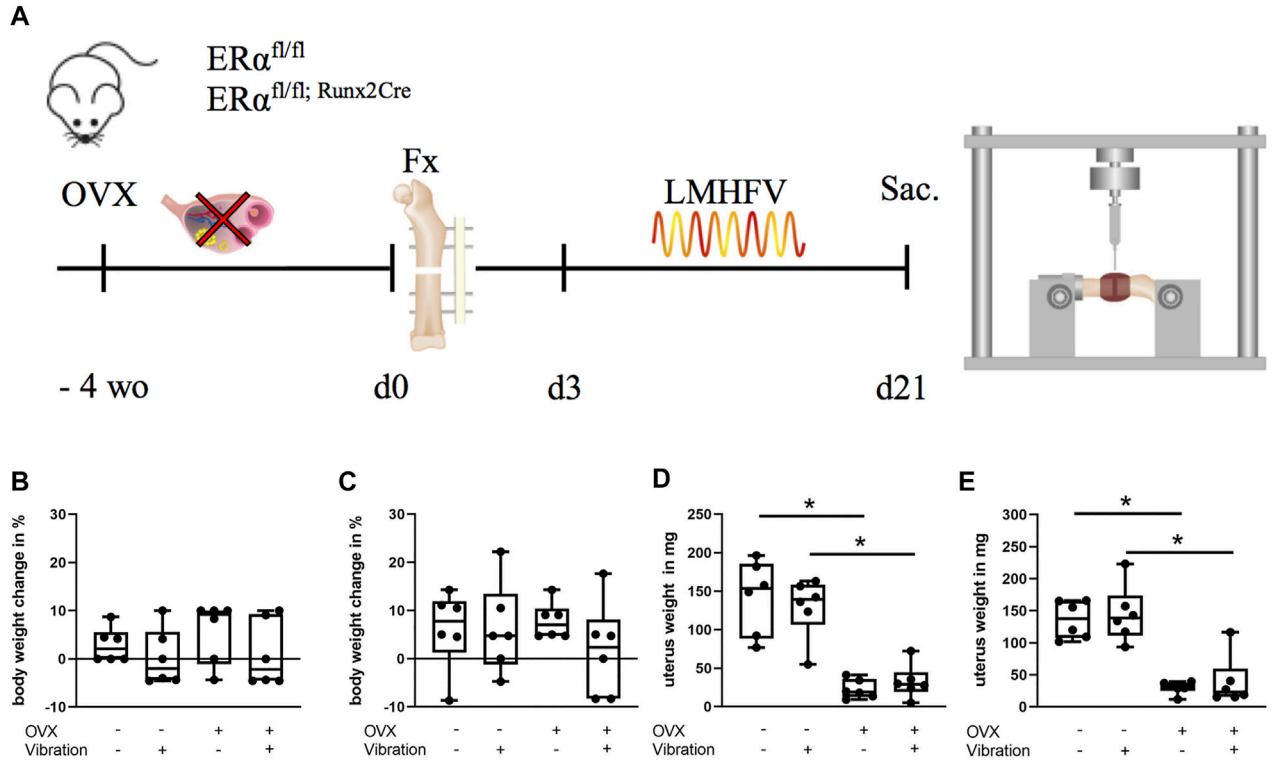

FIGURE 1 | Schematic illustration of the experimental timeline and physiological parameters of ERα$^{fl/fl}$ and ERα$^{fl/fl;\ Runx2Cre}$ mice. **(A)** When aged 12 weeks, mice were ovariectomized (OVX) or sham-operated followed by fracture surgery (Fx) 4 weeks later. Vibration (LMHFV) or sham-vibration treatment started on the third postoperative day for 20 min/day and 5 days/week. On day 21 after fracture, the mice were sacrificed (Sac.) and their bones were analyzed. Body weight of ERα$^{fl/fl}$ **(B)** and ERα$^{fl/fl;\ Runx2Cre}$ **(C)** mice as well as their respective uterus weight [**(D):** ERα$^{fl/fl}$, **(E):** ERα$^{fl/fl;\ Runx2Cre}$] was assessed. Data are shown as box-and-whisker plots (with median and interquartile range) from max. to min., showing all data points. *indicates significant effects with $p \leq 0.05$.

described previously (Haffner-Luntzer et al., 2017). 4 weeks after OVX or non-OVX surgery, all mice underwent standardized unilateral femur osteotomy as described previously (Röntgen et al., 2010; Wehrle et al., 2015; Haffner-Luntzer et al., 2017). Briefly, the osteotomy was created at the right femur diaphysis using a 0.4 mm Gigli wire saw (RISystem, Davos, Switzerland) and stabilized by a semi-rigid external fixator (RISystem). Half of the OVX (n = 6 per genotype) and non-OVX mice received LMHFV. Three weeks after osteotomy surgery (day 21), all mice were sacrificed using an isoflurane overdose and cardiac blood withdrawal.

LMHFV

The LMHFV regimen was chosen due to our previous studies, showing that 45 Hz significantly improved fracture healing in OVX mice (Wehrle et al., 2015; Haffner-Luntzer et al., 2018a). Starting on the third day after osteotomy surgery, mice were placed on custom-made vibration platforms for 20 min per day for 5 days per week and received vertical whole-body vibration with 0.3 g sinusoidal peak-to-peak acceleration and 45 Hz frequency, as described previously (Wehrle et al., 2015) (**Figure 1A**). The amplitude and frequency were continuously recorded using integrated accelerometers at the platform (Sensor KS95B.100, measurement amplifier Innobeamer L2, Software Vibromatrix; IDS Innomic GmbH, Salzwedel, Germany). The control mice were sham-vibrated on the same platforms without activation of the vibration generator. All mice were allowed to move freely on the platforms during the vibration or sham-vibration treatment and afterwards returned to their home cages.

Biomechanical Testing and µCT Analysis

To evaluate the mechanical properties of intact and osteotomized femurs explanted on day 21, a non-destructive three-point bending test was performed as described previously (Röntgen et al., 2010; Wehrle et al., 2015). Briefly, following removal of the fixator, an axial load with a maximum of 2 N was applied on top of the callus side in a cranio-lateral position using a material-testing machine (1454, Zwick GmbH & Co KG, Ulm, Germany). The bending stiffness was calculated from the slope of the load-deflection curve as described previously (Röntgen et al., 2010). If the bones were too fragile for reaching a preload of 0.05 N, the three-point bending test was not performed and a flexural rigidity value of 0 was given. Following biomechanical testing, femora were fixed in 4% phosphate-buffered formaldehyde solution and scanned using a µCT scanning device (Skyscan 1172 version 1.5; Skyscan, Kontich, Belgium) at a resolution of 8 µm using a peak voltage of 50 kV and 200 µA. Analyses and calibration steps were performed according to the guidelines of the American Society

for Bone and Mineral Research (Bouxsein et al., 2010). The volume of interest was defined as the entire callus between the fractured cortices. Within each scan, two phantoms with a defined density of hydroxyapatite (250 and 750 mg hydroxyapatite/cm^3) were included to determine the bone mineral density. To distinguish between mineralized and nonmineralized tissue, a threshold for cortical bone set at 641.9 mg hydroxyapatite/cm^3 was used (Morgan et al., 2009). The trabecular bone of the intact left femora was assessed 200 µm proximal of the metaphyseal growth plate over a length of 280 µm in the distal femur, excluding the cortex. For assessing the trabecular bone parameters, a threshold set at 394.8 mg hydroxyapatite/cm^3 was used (Morgan et al., 2009). Analyses were performed by means of Skyscan software (NRecon version 1.7.1.0, DataViewer version 1.5.1.2, and CTAn version 1.17.2.2). Bony bridging score was determined in two perpendicular planes with one bridged cortex counting for one scoring point. A bony bridging score of 3 or 4 represented successful healing.

Histomorphometry of the Fracture Callus and Immunohistochemical Staining

Following µCT analysis, bone specimens were subjected to decalcified histology as described previously (Haffner-Luntzer et al., 2014). Sections of 7 µm were stained with Safranin O for histomorphometric tissue quantification. The amounts of bone, cartilage and fibrous tissue in the fracture gap were determined using an image analysis software (Leica DMI6000 B; Software MMAF Version 1.4.0 MetaMorph®; Leica, Heerbrugg, Switzerland). The number and surface of osteoclasts (NOc/BPm, OcS/BS) were quantitatively assessed using tartrate-resistant alkaline phosphatase (TRAP) staining. Osteoclasts were defined as TRAP-positive cells with two or more nuclei, directly located on the bone surface with a visible resorption lacuna between the bone matrix and the cell. The number and surface of osteoblasts were determined using Safranin-O staining. Osteoblasts were defined as cubic-shaped cells with visible cytoplasm, located directly on the bone surface. Bone cells and surface were evaluated in a rectangular area (650 × 450 µm) using the Osteomeasure system (Osteometrics, Decatur, United States). Images were obtained using a Leica microscope (DMI 6000B). All analyses were performed according to the American Society for Bone and Mineral Research guidelines for bone histomorphometry (Dempster et al., 2013).

For immunohistochemical staining, paraffin-embedded sections of 4 µm were deparaffinized, enzymatically demasked by trypsin, blocked with 3% peroxidase followed by a serum block with 5% goat serum in TBS-T for 2 h. Staining for ERα was performed at 4°C overnight using the following primary antibody: rabbit anti-mouse ERα (1:75, # PA5-16440, Invitrogen). Rabbit IgG was included as isotype control to confirm specific staining. Next, sections were washed with TBS and incubated with a goat anti-rabbit secondary antibody (1:100, #B2770, Life Technologies) for an hour at RT. After another washing step, horseradish peroxidase (HRP)-conjugated streptavidin (#PK-6100, VECTASTAIN® Elite ABC-HRP Kit, Peroxidase, Vector Laboratories) was applied according to the manufacturer`s guidelines. NovaRED (#SK-4800, Vector® NovaRED® Substrate Kit, Peroxidase (HRP), Vector laboratories) was used as chromogen and the sections were counterstained with hematoxylin (1:5; #2C-306, Waldeck, Münster, Germany) and rinsed. This staining protocol was previously established by using biological negative controls (bone sections from ERα-general KO mice). In ERα-stained sections, osteoblasts were identified by their cubic shape and direct contact to the bone trabeculae, whereas osteocytes were defined as ellipsoidal shaped cells embedded in the mineralized bone matrix. Hypertrophic chondrocytes were identified as spherical or polygonal shaped cells within a population of other chondrocytes.

Cell Culture Experiments and Transcriptome Analysis

Murine MC3T3-E1 cells were purchased from the American Type Culture Collection (ATCC) and seeded at a density of 4,000 cells per cm^2. On day 3 after seeding, cells were differentiated by adding 50 mg/ml ascorbic acid and 10 mM β-glycerophosphate to the phenol-red free culture medium containing 10% charcoal-stripped (estrogen-free) fetal calf serum (FCS), 1% L-glutamine and 1% penicillin/streptomycin (all ThermoFisher Scientific). Half of the cultures were subjected to LMHFV on a custom-made vibration platform at 0.3 g peak-to-peak acceleration/45 Hz for 20 min/day for 5 days. The other half of the cultures (sham-vibrated) were placed on the same platform without turning on the vibration device. Total RNA was isolated as described previously (Haffner-Luntzer et al., 2018b) and microarray-based gene expression analysis with mouse Gene 1.0 ST GeneChip® arrays was performed as published previously (Mödinger et al., 2018). Differentially expressed probesets were determined by *t* test and considered statistically significant when $p < 0.05$ and fold change ≤1.5, as described previously (Zoller et al., 2017). To identify the involved molecular pathways, the GoMINER tool (Zeeberg et al., 2003) was used, whereas functional protein interaction networks were identified using the STRING 10 program (http://string-db.org/). Complete microarray data are available in the **Supplementary Material**. For the Cox2 antagonist experiment, celecoxib was obtained from Sigma (SML3031) and prepared using dimethyl sulfoxide (stock: 2 mg/ml). AH23848 (EP4 antagonist) was purchased from Cayman Chemical (19023) and dissolved in dimethyl sulfoxide (stock: 5 mg/ml). Both antagonists were used at a concentration of 1×10^{-6} M.

Human bone marrow-derived mesenchymal stem cells (hMSCs) were obtained by Lonza (PT-2501) and seeded in 24-well plates (10,000 cells/well) 2 days prior to the differentiation experiments. The medium was changed to differentiation medium (phenol-red free α-MEM, 10% FCS + 1% penicillin/streptomycin + 1% L-glutamine, 50 mg/ml ascorbic acid, 10 mM β-glycerophosphate) at day 0 and the cells were allowed to differentiate for 10 days. At day 10, the medium was switched to estrogen-free medium and vibration was performed 4 h after the medium-switch for 20 min at 45 Hz and 0.3 g. Thirty minutes after the end of the vibration treatment, the experiment was stopped and RNA was isolated (RNeasy Mini kit, Qiagen) for

analyzing gene expression by qPCR and human Gene 1.0 ST GeneChip® arrays.

qPCR

The SensiFAST SYBR Hi-ROX One-Step Kit (Bioline, Mempis, United States) was used according to the manufacturer's guidelines to perform quantitative PCR. *B2M* (murine F: 5′-ATACGCCTGCAGAGTTAAGCA-3′, murine R: 5′-TCACATGTCTCGATCCCAGT-3′, human F: 5′-CTCACGTCATCCAGCAGAGA-3′, human R: 5′-GGATGGATGAAACCCAGACA-3′) was used as the housekeeping gene. Relative gene expression of *Lef1* (murine F: 5′-TCA CCT ACA GCG ACG AG-3′, murine R: 5′-TGACATCTGACGGGATGTGT-3′, human F: 5′ GAGATTTCTCTGTATGGCACC-3′, human R: 5′-CTGCAATGAGACACTTTCTC-3′), *Ptgs2* (murine F: 5′-AGGGGTGTCCCTTCACTTCT-3′, murine R: 5′-CATTGATGGTGGCTGTTTTG-3′, human F: 5′-TAAGGGGAGAGGAGGGAAAA-3′, human R: 5′-CTGCTGAGGAGTTCCTGGAC-3′) and *Mdk* (human F: 5′-TGCCCTGCAACTGGAAGAA-3′, human R: 5′-GCCTGTGCCCCC ATCAC-3′) was calculated using the delta-delta CT method.

Statistics

Group size was $n = 6$ per group and per genotype ($ER\alpha^{fl/fl}$, $ER\alpha^{fl/fl;\ Runx2Cre}$). In one animal, the histological sections were not evaluable, therefore analyzing this group with $n = 5$ (**Figures 3E–H**, second boxplot). Data were tested for normal distribution using the Shapiro-Wilk test, and data sets were normally distributed. Statistical testing between two groups was done using two-tailed Student's t-test, whereas comparisons between more than two groups were performed by one-way ANOVA with post hoc Tukey's test for adjusting the p-value for multiple comparisons using GraphPad Prism 8.4.3 (GraphPad Software, La Jolla, CA). The level of significance was set at $p \leq 0.05$. Results are presented as box-and-whisker plots (with median and interquartile range) from max. to min., showing all data points.

RESULTS

Body Weight and Uterus Weight Changes

All mice received the selected treatments including ovariectomy/sham-operation, fracture and LMHFV/sham-vibration as illustrated in **Figure 1A**. The body weight of the animals was not significantly influenced by the treatments or the genotype during the entire experimental period (**Figures 1B,C**). To control for the success of OVX in $ER\alpha^{fl/fl}$ and $ER\alpha^{fl/fl;\ Runx2Cre}$ mice, uterus weight at day 21 after osteotomy was assessed. In both mouse strains, OVX resulted in a significantly lower uterus weight (**Figures 1D,E**). Additionally, we performed μCT analysis of the intact left femora to determine if our mice developed an osteoporotic bone phenotype after OVX treatment. We found that non-vibrated and vibrated OVX groups from both genotypes displayed lower bone volume fraction and trabecular number, either significantly or by strong trend (**Supplementary Figure S2**).

Fracture Healing in Control ($ER\alpha^{fl/fl}$) Mice

In non-OVX mice that received LMHFV treatment, a significant reduction of flexural rigidity ($p < 0.0001$) and bony bridging ($p = 0.0047$) of the fracture gap was displayed, whereas the bone mineral density and the relative bone volume ratio did not differ significantly (**Figures 2A–D**). Furthermore, histomorphometrical analysis revealed a by trend reduced relative bone area ($p = 0.0923$), an increased cartilage area ($p = 0.0564$) as well as a significantly reduced osteoblast count ($p = 0.0539$) and a significantly lower osteoblast activity ($p = 0.0159$) in vibrated non-OVX $ER\alpha^{fl/fl}$ mice (**Figures 3A–F**). All these data indicated impaired fracture healing at day 21 in non-OVX mice subjected to vibration treatment.

Bone regeneration was also compromised in OVX mice compared to non-OVX mice, as indicated by an inferior flexural rigidity ($p < 0.0001$), significantly reduced bony bridging ($p = 0.0041$) and by trend increased amount of cartilage ($p = 0.1469$) in the fracture callus (**Figures 2**, **3**). Similarly, osteoblast number ($p = 0.0576$) and surface ($p = 0.0296$) were also diminished in OVX mice compared to non-OVX mice (**Figures 3E,F**).

Bone healing was improved by LMHFV in OVX mice in comparison to OVX animals as indicated by significantly enhanced flexural rigidity ($p = 0.0374$), bone mineral density ($p = 0.0108$) and bony bridging ($p = 0.0155$) of the fracture gap and a by trend reduced cartilage area ($p = 0.2248$) (**Figures 2**, **3**). Furthermore, LMHFV resulted in a significantly increased number ($p = 0.0031$) and activity of osteoblasts ($p = 0.0012$) in OVX $ER\alpha^{fl/fl}$ mice compared to OVX animals without vibration (**Figures 3E,F**). The callus size as well as the number and surface of osteoclasts did not differ significantly between all the $ER\alpha^{fl/fl}$ groups (**Figures 3D,G,H**). Overall, these data demonstrated that OVX and LMHFV both disturb bone regeneration in control $ER\alpha^{fl/fl}$ mice, whereas in combination both treatments resulted in an improved fracture healing.

Fracture Healing in Osteoblast-Specific ERα-KO ($ER\alpha^{fl/fl;\ Runx2Cre}$) Mice

Although mice with a specific deletion of the ERα in the osteoblast lineage ($ER\alpha^{fl/fl;\ Runx2Cre}$) were previously shown to have a preexisting bone phenotype with decreased trabecular bone mass in the spine and tibiae (Seitz et al., 2012), we found that this does not influence fracture healing ($p = 0.439$) when directly comparing non-OVX non-vibrated animals of both genotypes (**Supplementary Figure S3**).

Furthermore, LMHFV did not exert negative effects on fracture healing in non-OVX $ER\alpha^{fl/fl;\ Runx2Cre}$ mice, because there were no significant differences in flexural rigidity, bone content or bridging of the fracture gap in comparison to $ER\alpha^{fl/fl;\ Runx2Cre}$ mice that did not receive LMHFV (**Figure 4**). In addition, histomorphometrical parameters were unaltered by LMHFV treatment in non-OVX mice except the osteoblast number ($p = 0.0005$) and surface ($p = 0.0004$) that were significantly increased in vibrated non-OVX mice lacking the ERα in osteoblasts (**Figure 5**).

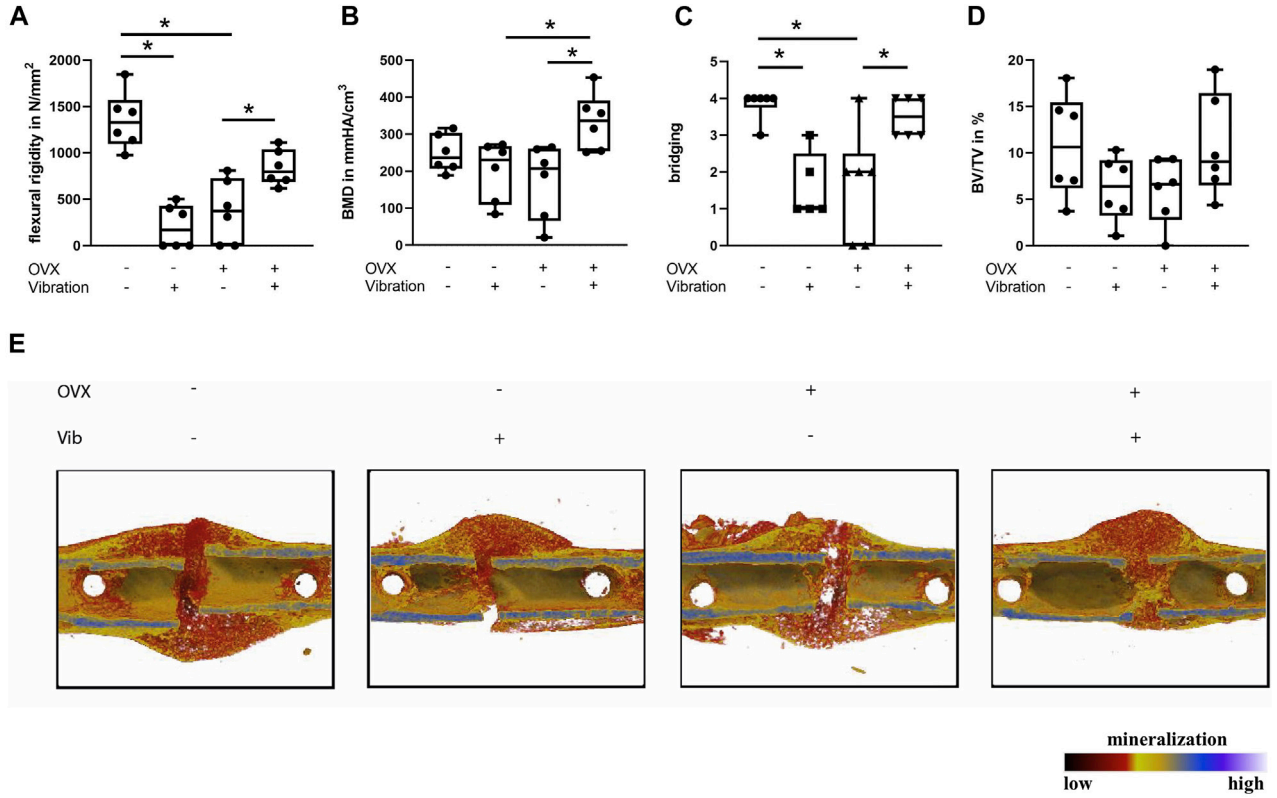

FIGURE 2 | Influence of LMHFV on fracture healing in ERα$^{fl/fl}$ mice on day 21. Biomechanical testing and μCT analysis. **(A)** Bending stiffness of the fracture callus. **(B)** Bone mineral density of the fracture gap. **(C)** Bony bridging of the fracture gap evaluated in two perpendicular planes. **(D)** Relative bone volume (BV/TV) in the fracture gap. **(E)** Representative μCT images from the fractured femurs. Red indicates weakly mineralized bone, whereas yellow and light blue indicate highly mineralized bone. Data are shown as box-and-whisker plots (with median and interquartile range) from max. to min., showing all data points. *indicates significant effects with $p \leq 0.05$.

ERα$^{fl/fl;\ Runx2Cre}$ OVX mice without vibration were protected from impaired fracture healing due to OVX, because a similar flexural rigidity, bony bridging and bone formation in the fracture callus was observed compared to non-OVX ERα$^{fl/fl;\ Runx2Cre}$ mice (**Figure 4**). Furthermore, histomorphometrical analysis did not reveal any significant differences in callus composition or cellular parameters compared to non-OVX ERα$^{fl/fl;\ Runx2Cre}$ mice (**Figure 5**).

Interestingly, reversed effects of vibration on bone formation during fracture healing in OVX ERα$^{fl/fl;\ Runx2Cre}$ mice were observed, which resulted in a considerably reduced flexural rigidity ($p = 0.001$), by trend diminished bone formation ($p = 0.1975$) and significantly reduced bony bridging ($p = 0.0032$) compared to OVX ERα$^{fl/fl;\ Runx2Cre}$ mice (**Figures 4A,C,D**) in contrast to the improved fracture healing seen in vibrated OVX control ERα$^{fl/fl}$ mice. Histomorphometrical analysis further revealed a significantly increased cartilage area ($p = 0.0114$) in the fracture callus of OVX ERα$^{fl/fl;\ Runx2Cre}$ animals subjected to vibration treatment (**Figure 5B**). In addition, the osteoblast surface ($p = 0.0039$) and number ($p = 0.0188$) were significantly decreased in vibrated OVX ERα$^{fl/fl;\ Runx2Cre}$ mice (**Figures 5E,F**), whereas osteoclast activity was significantly reduced ($p = 0.0315$) (**Figure 5H**).

Molecular Mechanisms

We performed whole genome microarray-based gene expression analysis of vibrated and sham-vibrated samples and found that 304 genes were differentially regulated upon LMHFV treatment (**Figure 6**). Among the 184 upregulated genes, the mechanosensitive enzyme Cox2, encoded by the gene *Ptgs2*, appeared in our array (**Table 2**), as well as bone remodeling and extracellular matrix-associated genes (**Table 3**). Downregulated genes were found to be involved in Wnt/β-catenin signaling (**Table 4**), with most of the genes encoding for proteins that act as Wnt inhibitors (*Axin2, Sostdc1, Dkk2*) except the gene encoding for the Wnt receptor *Fzd9*. STRING analysis was performed to investigate the interactions of the respective pathways (**Figures 6A,D**). As expected, the Wnt pathway genes were clustering as well as the genes for extracellular matrix and Cox2/PGE_2 signaling (**Figure 6D**). Confirming the microarray findings, gene expression of Cox2 was validated by qPCR (**Figure 6C**). Consequently, we were interested whether the Cox2/PGE_2 pathway might interact with canonical Wnt signaling. To investigate whether the signaling via the Cox2/EP4 axis might affect downstream signaling of the Wnt pathway, we performed further *in vitro* experiments with MC3T3-E1 cells pretreated with either the EP4

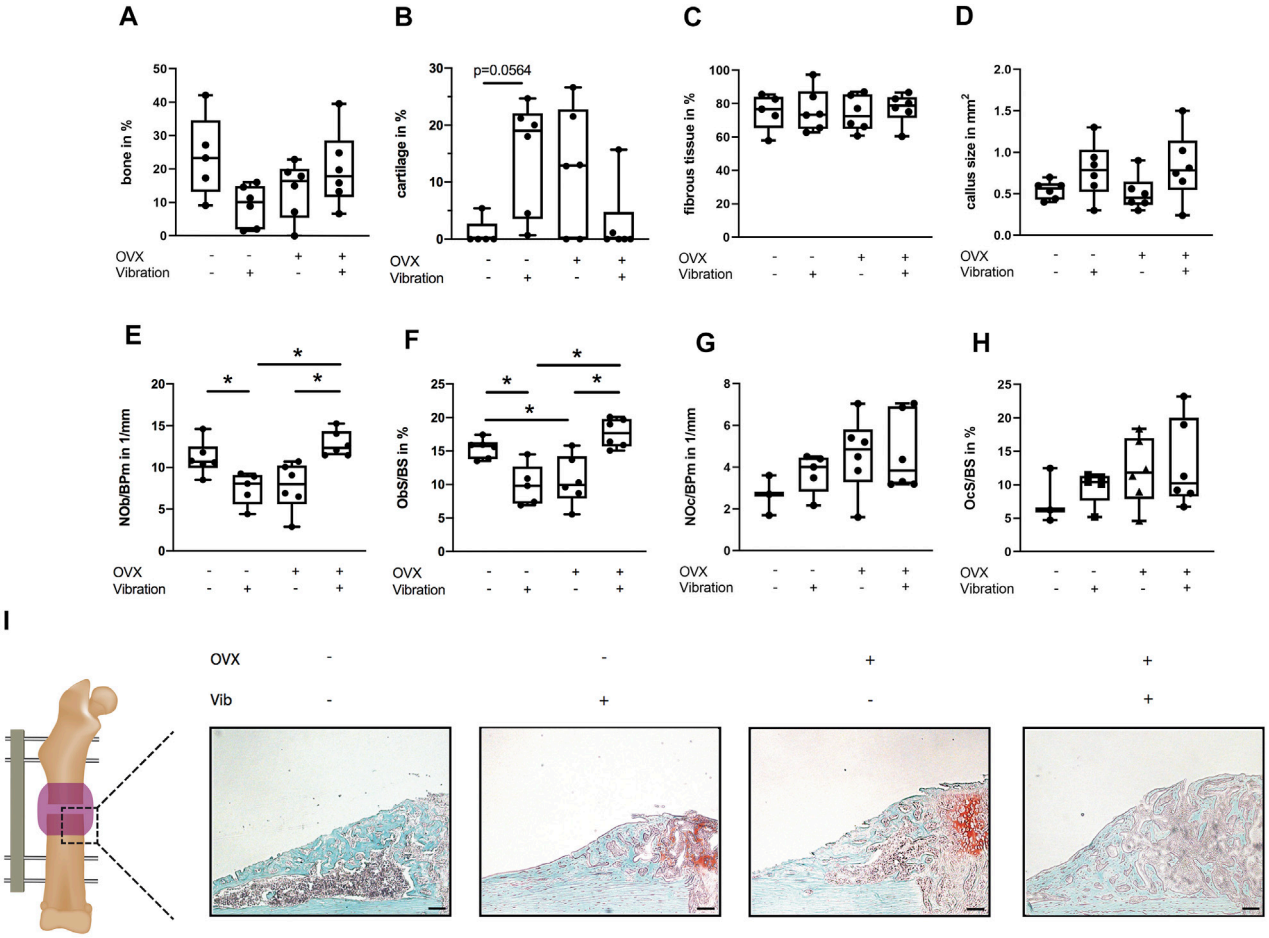

FIGURE 3 | Histomorphometrical analysis of the fracture gap in ERα$^{fl/fl}$ mice on day 21. Paraffin sections of fractured femurs were stained with Safranin O and histomorphometrical analysis was performed to determine **(A)** relative bone area, **(B)** relative cartilage area, **(C)** relative fibrous tissue area and **(D)** callus size. **(E)** Number of –6+s per bone perimeter (NOb/BPm) and **(F)** osteoblast surface per bone surface (ObS/BS) in the fracture gap. **(G)** Number of osteoclasts per bone perimeter (NOc/BPm) and **(H)** osteoclast surface per bone surface (OcS/BS). **(I)** Representative images from the fracture callus at day 21 after surgery stained with Safranin O. Scale bar = 100 µm. Data are shown as box-and-whisker plots (with median and interquartile range) from max. to min., showing all data points. *indicates significant effects with $p \leq 0.05$.

inhibitor AH23848 or the Cox2 inhibitor celecoxib. We demonstrated that the prostaglandin pathway via EP4 positively modulates the Wnt target gene *Lef1* in response to LMHFV, because the EP4 and Cox2 inhibitors abolished the LMHFV-induced *Lef1* upregulation (**Figures 6E–G**). Because we aimed to study the effects of LMHFV also in human cells, hMSCs were subjected to vibration and gene expression was assessed. We demonstrated that Cox2 in hMSCs was also upregulated by vibration (**Figure 6H**). Furthermore, the Wnt inhibitor *Mdk* was downregulated upon LMHFV, whereas the Wnt transcription factor *Lef1* was significantly upregulated (**Figures 6I,J**). In addition, microarray-based gene analysis of vibrated vs. non-vibrated hMSCs revealed that a further 56 genes were differentially regulated upon vibration. After excluding non-coding transcripts, 26 probesets remained for analysis. Among them, there were five micro RNAs (miRNAs) that are known to be involved in regulating bone metabolism, whereof three were upregulated and two downregulated (**Table 5**).

DISCUSSION

Estrogen is a key hormone for bone homeostasis, therefore, estrogen-deficiency in postmenopausal females or after ovariectomy in rodents lead to osteoporosis development. Furthermore, fracture healing was found to be disturbed in osteoporotic women and in female mice after ovariectomy because of impaired endochondral bone formation (Beil et al., 2010; Wehrle et al., 2015; Haffner-Luntzer et al., 2017; Wildemann et al., 2021). Biomechanical stimulation by whole-body vibration was proposed as a readily applicable and non-invasive treatment approach for osteoporotic fracture healing. However, preclinical studies demonstrate that the estrogen and ERα signaling play an important role in the response to vibration treatment. Therefore, the aim of this study was to further investigate the target cells of vibration during fracture healing and the role of estrogen-dependent and -independent ERα signaling particularly in cells of the osteoblast lineage.

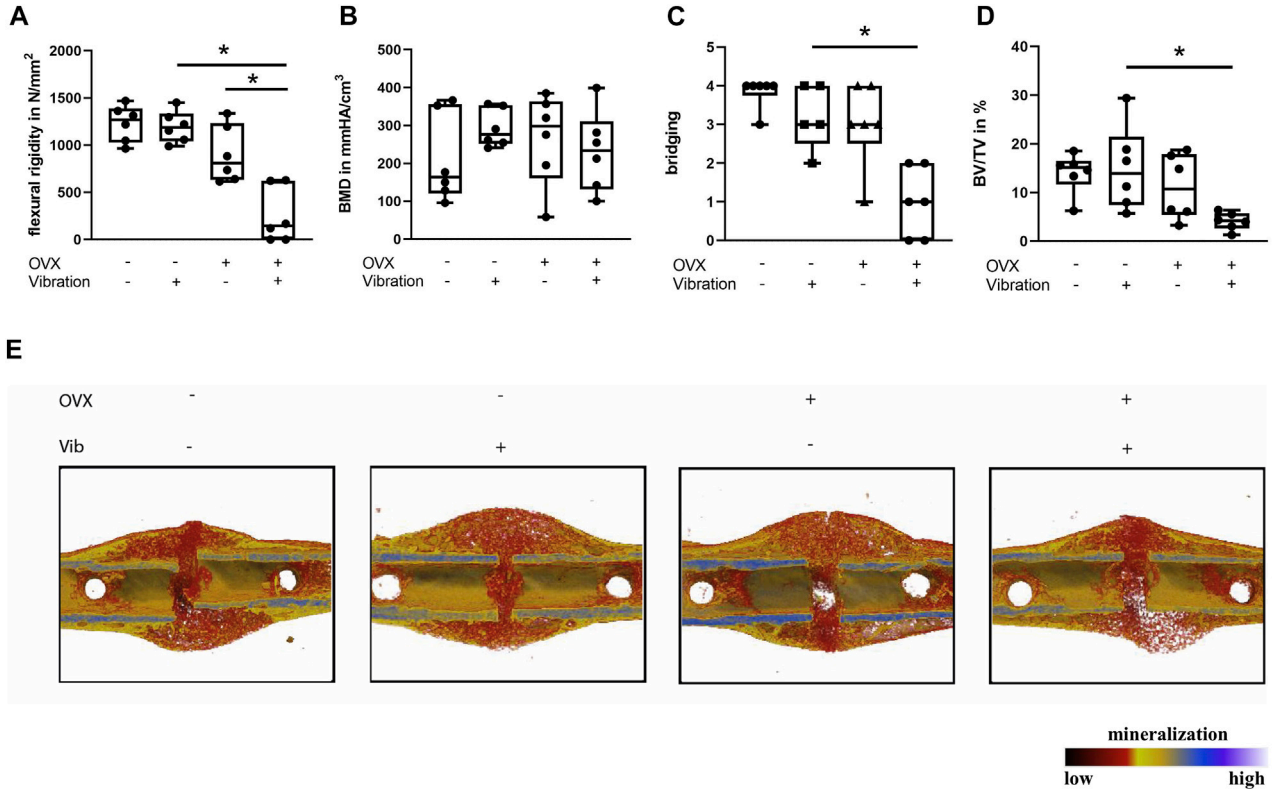

FIGURE 4 | Influence of LMHFV on fracture healing in ERα$^{fl/fl;\ Runx2Cre}$ mice on day 21. Biomechanical testing and μCT analysis. **(A)** Bending stiffness of the fracture callus. **(B)** Bone mineral density of the fracture gap. **(C)** Bony bridging of the fracture gap evaluated in two perpendicular planes. **(D)** Relative bone volume (BV/TV) in the fracture gap. **(E)** Representative μCT images from the fractured femurs. Red indicates weakly mineralized bone whereas yellow and light blue indicate highly mineralized bone. Data are shown as box-and-whisker plots (with median and interquartile range) from max. to min., showing all data points. *indicates significant effects with $p \leq 0.05$.

In the present study, mice lacking the ERα receptors on osteoblast-lineage cells were protected from ovariectomy-induced compromised fracture healing, indicating that the ERα in these cells contributes to the pathomechanisms of osteoporosis-induced impaired bone repair. As expected, osteoblast number and activity were reduced in ERα$^{fl/fl}$ mice after ovariectomy, whereas these parameters were unaltered in OVX ERα$^{fl/fl;\ Runx2Cre}$ mice. This suggests that ligand-independent ERα signaling negatively regulates osteoblast formation and activity in the fracture callus of estrogen-deficient mice during bone regeneration. Regarding the role of ERα during fracture healing, to our knowledge, there is only one other study using mice with an ERα deletion in mature osteoblasts and osteocytes that uses a monocortical defect model on the tibiae of female mice (Ikedo and Imai, 2021). In agreement with our findings, they also reported that the ERα on mature osteoblasts controls osteoblast number and osteoblast surface. However, their defect model does not represent a full fracture of the bone, thus lacking the endochondral ossification process. Another difference between the two studies is that Ikedo et al. deleted the ERα by expressing the Cre recombinase under the control of the osteocalcin promotor, whereas we used the Runx2-Cre model. In comparison to osteocalcin, which is expressed by mature osteoblasts, *Runx2* is necessary for the differentiation of osteoblastic precursors, thus the deletion of the ERα receptors on osteoblast lineage cells affected these cells earlier (Komori et al., 1998).

The presence or absence of estrogen plays a crucial role in regulating the mechanotransduction pathways upon LMHFV. In this study, we confirmed that while the application of LMHFV impaired bone formation in the fracture callus of non-OVX ERα$^{fl/fl}$ mice, it improved the healing outcome in OVX ERα$^{fl/fl}$ animals, consistent with previous reports (Stuermer et al., 2010; Cheung et al., 2012; Wehrle et al., 2014; Wehrle et al., 2015; Chow et al., 2016; Haffner-Luntzer et al., 2018a). We demonstrated that the vibration-induced effects on fracture healing are mediated via osteoblast lineage-specific ERα signaling because the effects of vibration on bone repair were abolished or even reversed in osteoblast lineage-specific ERα-KO animals (ERα$^{fl/fl;\ Runx2Cre)}$. On a cellular level, osteoblast number and surface were unaffected by LMHFV in non-OVX KO animals, whereas a reduction of both parameters was found in the fracture callus of OVX ERα$^{fl/fl;\ Runx2Cre}$ mice that were subjected to LMHFV. Histological characterization of the fractures revealed the persistence of residual cartilage in OVX ERα$^{fl/fl;\ Runx2Cre}$ mice that were subjected to vibration, consistent with the impaired healing

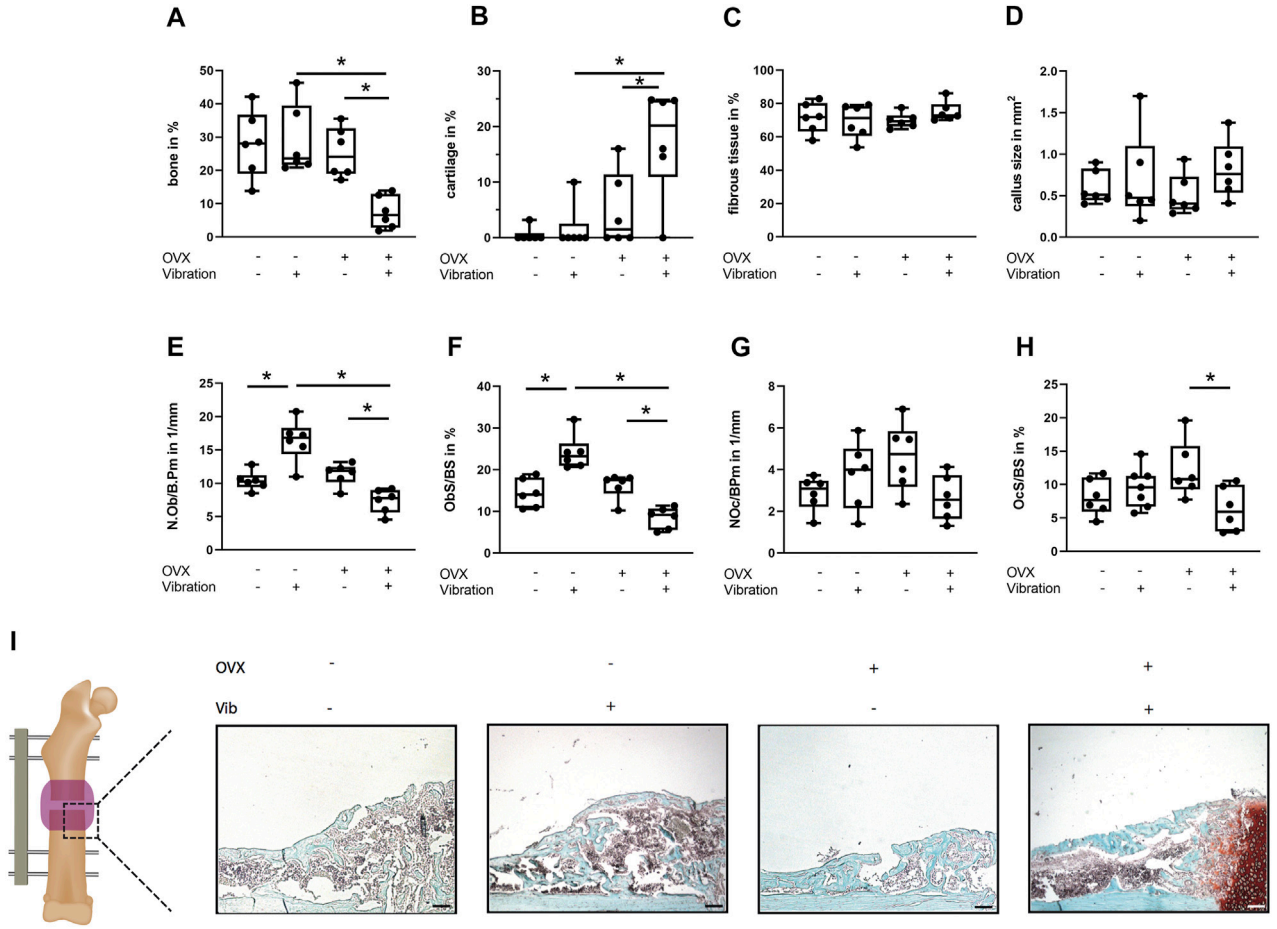

FIGURE 5 | Histomorphometrical analysis of the fracture gap in ERα$^{fl/fl;\ Runx2Cre}$ mice on day 21. Paraffin sections of fractured femurs were stained with Safranin O and histomorphometrical analysis was performed to determine **(A)** relative bone area, **(B)** cartilage area, **(C)** relative fibrous tissue area and **(D)** callus size. **(E)** Number of osteoblasts per bone perimeter (NOb/BPm) and **(F)** osteoblast surface per bone surface (ObS/BS) in the fracture gap. **(G)** Number of osteoclasts per bone perimeter (NOc/BPm) and **(H)** osteoclast surface per bone surface (OcS/BS). **(I)** Representative images from the fracture callus at day 21 after surgery stained with Safranin O. Scale bar = 100 µm. Data are shown as box-and-whisker plots (with median and interquartile range) from max. to min., showing all data points. *indicates significant effects with $p \leq 0.05$.

and the poor biomechanical properties of the fractured bones. We conclude from our data that ligand-dependent ERα signaling in osteoblast lineage cells might be responsible for the negative effects of LMHFV in estrogen-competent mice and that ligand-independent ERα signaling in osteoblast lineage cells is important for the positive effects of LMHFV under estrogen-deficient conditions. The reasons why deletion of the ERα specifically on cells of the osteoblast lineage even reversed the effects of vibration in OVX mice remains to be elucidated.

To further investigate which pathways might contribute to the vibration-mediated improved bone healing under estrogen-deficient conditions, we performed microarray-based gene expression analysis *in vitro* in vibrated osteogenic cells. We identified the Cox2/PGE_2 and Wnt pathway as critical signaling pathways that are regulated by LMHFV under estrogen-deficient conditions in MC3T3-E1 cells. Specifically, our array data revealed that Cox2, involved in prostaglandin biosynthesis, and the prostaglandin receptor EP4 were significantly upregulated. Cox2 is well known to be induced by mechanical strain and was recently reported to be regulated by LMHFV *in vitro* (Haffner-Luntzer et al., 2018b). In this study, siRNA knockdown of ERα in MC3T3 cells followed by LMHFV both with and without estrogen supplementation was performed, showing that Cox2 expression is significantly increased upon LMHFV in the absence of estrogen and significantly reduced by LMHFV in the presence of estrogen (Haffner-Luntzer et al., 2018b). Furthermore, it was demonstrated by Haffner-Luntzer et al., that these effects of LMHFV on Cox2 expression were both abrogated by siRNA knockdown of ERα. Additionally, the metabolic activity was also upregulated by vibration in an estrogen-depleted environment, but not in the presence of estrogen. In primary osteoblasts isolated from C57BL/6J wildtype mice, the significant downregulation of Cox2 upon vibration in estrogen-supplemented medium was confirmed, whereas this effect was abrogated in primary osteoblasts derived from ERα general KO mice (Haffner-Luntzer et al.,

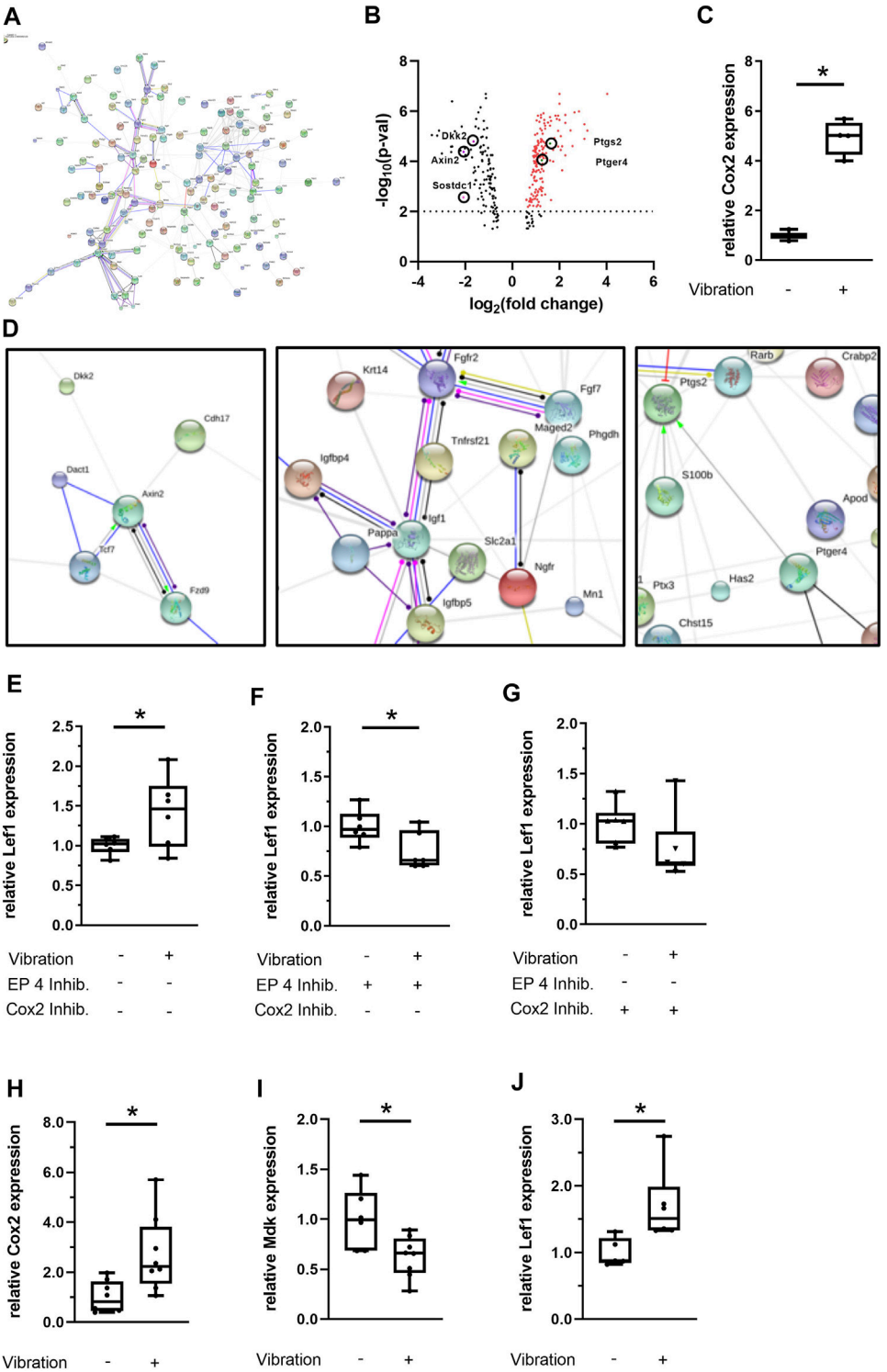

FIGURE 6 | Transcriptome analysis of MC3T3-E1 cells and gene expression analysis of hMSCs upon vibration treatment under estrogen-free conditions. **(A)** Nondetailed STRING protein-association network (action) derived from the MC3T3-E1 microarray data. The image in high quality can be found in the supplemental material (**Supplementary Figure S4**). **(B)** Vulcano plot of differentially regulated genes and **(C)** qPCR validation of Cox2 expression in MC3T3-E1 cells. **(D)** Detailed STRING network (MC3T3-E1 microarray). **(E–G)** Effect of LMHFV in MC3T3-E1 cells pretreated with the EP4 antagonist AH23848 (1×10^{-6} M) or with the Cox2 antagonist celecoxib (1×10^{-6} M). **(H–J)** Effect of LMHFV in hMSCs. Data are shown as box-and-whisker plots (with median and interquartile range) from max. to min., showing all data points. N = 4–6 per group (vibrated and sham-vibrated), *indicates significant effects with $p \leq 0.05$.

TABLE 2 | Selected differentially regulated mechanosensitive genes upon vibration treatment in MC3T3-E1 cells under estrogen-free conditions.

Gene	Description	Pathways	GenBank accession number	*p*-value	Fold change
Ptgs2	Prostaglandin-endoperoxide synthase 2	Eicosanoid metabolism, arachidonic acid metabolism, VEGF signaling pathway	NM_011198	1.92×10^{-5}	3.03 ↑
Ptger4	Prostaglandin E receptor 4 (subtype EP4)	Eicosanoid metabolism	NM_001136079	9.12×10^{-5}	2.38 ↑

TABLE 3 | Selected differentially regulated bone remodeling and ECM-associated genes upon vibration treatment in MC3T3-E1 cells under estrogen-free conditions.

Gene	Description	Pathways	GenBank accession number	*p*-value	Fold change
Igf1	Insulin-like growth factor 1	IGF-1 signaling pathway, focal adhesion	NM_001111274	1.625×10^{-4}	2.04 ↑
Spp1	Secreted phosphoprotein 1	Regulators of bone mineralization, ECM-receptor interaction, focal adhesion, Toll-like receptor signaling pathway	NM_001204201	4.94×10^{-5}	2.13 ↑
Fosl1	Fos-like antigen 1	Osteoclast differentiation, Wnt signaling pathway	NM_010235	1.008×10^{-4}	2.33 ↑
Ctsk	Cathepsin K	Osteoclast differentiation, Toll-like receptor signaling pathway	NM_007802	1.436×10^{-3}	0.60 ↓
Fgf7	Fibroblast growth factor 7	MAPK signaling pathway, regulation of actin cytoskeleton	NM_008008	5.29×10^{-5}	2.56 ↑
Iqgap2	IQ motif containing GTPase activating protein 2	Regulation of actin cytoskeleton	NM_027711	7.42×10^{-5}	2.7 ↑
Itga1	Integrin alpha 1	Integrin signaling	NM_001033228	2.50×10^{-2}	0.58 ↓

TABLE 4 | Selected differentially regulated Wnt signaling genes upon vibration treatment in MC3T3-E1 cells under estrogen-free conditions.

Gene	Description	Pathways	GenBank accession number	*p*-value	Fold change
Axin2	Axin 2	Wnt signaling pathway	NM_015732	4.13×10^{-5}	0.24 ↓
Dkk2	Dickkopf WNT signaling pathway inhibitor 2	Wnt/LRP6 signaling pathway	NM_020265	1.59×10^{-5}	0.32 ↓
Fzd9	Frizzled class receptor 9	Wnt signaling pathway	NM_010246	1.12×10^{-5}	0.47 ↓
Sostdc1	Sclerostin domain containing 1	Wnt signaling pathway	NM_025312	2.71×10^{-3}	0.24 ↓

TABLE 5 | Selected differentially regulated microRNAs in hMSCs upon vibration.

Gene	Description/Function	GenBank accession number	*p*-value	Fold change
miRNA 548a-2	Involved in alveolar bone loss	NR_030317	3.83×10^{-3}	1.76 ↑
miRNA 377	Reduced osteosarcoma proliferation	NR_029869	3.326×10^{-2}	1.54 ↑
miRNA 219a-2	Regulates osteogenic diff	NR_029837	1.088×10^{-3}	1.52 ↑
miRNA 518b	Upregulated in PO	NR_030196	2.255×10^{-2}	0.64 ↓
miRNA 194-2	Reduced osteosarcoma proliferation, increased apoptosis	NR_029829	2.645×10^{-4}	0.43 ↓

2018b). Because of these data and the fact that Cox2 upregulation is indispensable for mechanotranduction, we performed all *in vitro* experiments in an estrogen-depleted environment and with the same vibration regime that was used in our previous study (Haffner-Luntzer et al., 2018b).

Studies using mechanical loading via dynamic cell stretching (Liedert et al., 2010) or via fluid shear stress (Yeh et al., 2010) have shown a synergistic effect of estrogen and mechanical stimulation regarding Cox2 upregulation in osteoblasts, however, this effect might not account for vibration and seems to be dependent on the type of stimulus. Regarding fracture healing, studies with Cox2-selective inhibitors or Cox2-KO mouse models demonstrated a significantly disturbed bone healing (Simon et al., 2002; Zhang et al., 2002), indicating an important role of this pathway during bone regeneration. This is supported by a study with local Cox2 overexpression at the fracture site revealing an acceleration of fracture healing (Lau et al., 2013). Furthermore, the application of EP4 receptor agonist was shown to rescue impaired fracture healing in Cox2-KO mice (Xie et al., 2009), which highlights the importance of Cox2-and EP4 for endochondral bone repair. These studies together with our array data might explain the improved bone healing by LMHFV in our OVX $ER\alpha^{fl/fl}$ animals, possibly mediated via Cox2 upregulation. We have further provided evidence for Cox2 upregulation upon LMHFV in hMSCs and that several miRNAs might also be involved in the effects of LMHFV on hMSCs. However, while these findings regarding the regulation of miRNAs upon vibration are interesting, they still require further detailed investigation in future projects.

Regarding the molecular mechanism that is involved in Cox2-induced osteogenesis, it has been recently demonstrated that the Cox2/PGE_2/EP4 axis is involved in mechanosensing of primary cilia after LMHFV (Li et al., 2021). Primary cilia act as important mechanosensors on osteoblasts, with EP4 was found to be expressed at the bases of these cilia. Under LMHFV treatment, MC3T3-E1 cells were shown to upregulate EP4 and displayed a lower number and length of cilia. By blocking the EP4 receptor, primary cilia mechanotransduction and LMHFV-mediated osteogenesis were abrogated, suggesting a crosstalk of primary cilia and the Cox2/PGE_2/EP4 pathway to facilitate mechanotransduction signaling.

One signaling pathway that might be activated by the Cox2/PGE_2/EP4-mediated mechanotransduction is the Wnt signaling pathway. Wnt signaling plays a crucial role in bone homeostasis and fracture healing, whereby an activated Wnt signaling is associated with an improved fracture repair (Kim et al., 2007; Chen and Alman, 2009), whereas inhibited Wnt signaling led to delayed fracture healing (Huang et al., 2012; Beier et al., 2014; Haffner-Luntzer et al., 2014; Liedert et al., 2014; Haffner-Luntzer et al., 2016; Teng et al., 2018). In our microarray data, we found a downregulation of canonical Wnt/β-catenin pathway inhibitors (*Axin2, Sostdc1, Dkk2*), indicating that the canonical Wnt pathway is activated by LMHFV. This was further substantiated by the study of Gao et al. showing that vibration treatment of primary osteoblasts resulted in an upregulation of the Wnt signaling genes *Wnt3a, Lrp6* and *β-catenin in vitro* (Gao et al., 2017). By contrast, the Wnt receptor Fzd9, which is essential for activating the non-canonical Wnt pathway, was downregulated. It is known that Fzd9-KO mice display an impaired bone strength during fracture healing, whereas it was found that the canonical Wnt signaling was unaffected by Fzd9 deficiency in osteoblasts (Heilmann et al., 2013). Therefore, the mechanism involved in the downregulation of Fzd9 and its effects on osteogenesis after LMHFV is not completely clear. Even so, our data strongly suggests that the canonical Wnt signaling is activated upon LMHFV via downregulation of Wnt inhibitory molecules. Several studies suggested a strong association between Cox2 and the Wnt/β-catenin signaling, showing that Cox2 regulates the transcriptional and translational levels of β-catenin (Zheng et al., 2019) and that Cox2 is important for osteoblast maturation via Wnt pathway genes (Nagano et al., 2017). Other studies reported that PGE_2 is able to induce bone formation via promoting the production of insulin-like growth factor 1 (IGF-1) and activating the protein kinase B (Akt) (Sunters et al., 2010; Xia et al., 2010). Since there is no data available regarding a possible connection between Cox2/PGE_2 and Wnt signaling in the context of LMHFV, we did perform *in vitro* experiments with EP4 or Cox2 inhibitors and could prove that the presence of Cox2 or EP4 is crucial for LMHFV-induced *Lef1* upregulation in MC3T3-E1 cells *in vitro*, indicating an interaction of both pathways upon LMHFV.

We therefore hypothesize that mechanotransduction *in vivo* first requires estrogen-independent ERα signaling in osteoblast lineage cells, which subsequently triggers Cox2 expression and PGE_2 production that might lead to differentially expressed Wnt-related target genes. Ultimately, this might favor an activation of the Wnt pathway, which could further promote fracture healing.

A limitation of our study was that we used the OVX model to induce estrogen-deficiency. Because the ovaries are not the only source of estrogen, small amounts of circulating estrogen might still be present in OVX mice (Haisenleder et al., 2011). Another limitation is that we used a diaphyseal femur fracture model which does not reflect the most common fracture sites (vertebral compression fractures, hip fractures, distal radius fractures, proximal humerus fractures) or the fracture type (metaphyseal), that commonly occur in postmenopausal women. However, it was shown that molecular mechanisms did not differ greatly between diaphyseal and metaphyseal fracture healing (Haffner-Luntzer et al., 2020).

Furthermore, with the performed three-point bending test, we did not evaluate ultimate bone strength. This test is also critically dependent on the callus geometry, which was not consistent between all mice. Therefore, a torsion test would be the best way to analyze mechanical stability, however, there is also evidence that torsion testing is not superior to our three-point bending test in small rodents (Steiner et al., 2015). Also, it should be also considered that hypertrophic chondrocytes in the cartilaginous fracture callus undergoing transdifferentiation to osteoblasts (Zhou et al., 2014) might express the Cre recombinase under the Runx2-promotor and might also be affected by the KO. Therefore, we cannot discriminate in our model between the effects of LMHFV on endochondral ossification and direct ossification, which both occur in the fracture callus in the chosen surgical model. Another limitation is that we did not compare all eight experimental groups to each other to investigate direct interaction between genotype and OVX/vibration treatment. This was due to considerations to reduce the number of needed animals.

In conclusion, our study suggests a critical role of the ERα in osteoblast lineage cells during mechanotransduction in the fracture callus both under estrogen-deficient and -sufficient conditions. This work provides further insights into the molecular mechanism responsible for the effects of estrogen or estrogen-deficiency on mechanostimulation during fracture healing and might result in improved treatment strategies for osteoporotic fracture patients, because we demonstrated that in addition to the estrogen status, the presence of ERα is important for mediating the positive effects of LMHFV on fracture healing. To ensure a safe treatment with LMHFV, further research is needed to define eligible patient cohorts that would benefit most from this treatment.

DATA AVAILABILITY STATEMENT

The original contributions presented in the study are included in the article/**Supplementary Material**, further inquiries can be directed to the corresponding author.

ETHICS STATEMENT

The animal study was reviewed and approved by Regierungspräsidium Tübingen, Germany.

AUTHOR CONTRIBUTIONS

LS: conceptualization, investigation, visualization, data analysis, writing original draft; BK: investigation; MT: visualization; VF: visualization; JT: provided mouse models; AI: conceptualization, funding acquisition, writing original draft, supervision; MH-L: conceptualization, investigation, funding acquisition, writing original draft, supervision.

FUNDING

This research was supported by the German Research Foundation (DFG, Project-ID HA 8470/1-1; Collaborative Research Center CRC1149, Project-ID 251293561) and an ASBMR Rising Star Award to MH-L.

ACKNOWLEDGMENTS

We thank Kristina Karremann, Tina Hieber, Andrea Böhmler and Iris Baum for excellent technical assistance.

SUPPLEMENTARY MATERIAL

The Supplementary Material for this article can be found online at: https://www.frontiersin.org/articles/10.3389/fbioe.2021.782355/full#supplementary-material

Supplementary Figure S1 | : Osteoblasts, osteocytes and hypertrophic chondrocytes are affected by the deletion of ERα, but not bone marrow cells. Immunohistochemical staining for ERα were performed on paraffin sections of **(A,C)** $ER\alpha^{fl/fl}$ and **(B,D)** $ER\alpha^{fl/fl;\ Runx2Cre\ mice}$. Representative images of the fracture callus, growth plate and bone marrow are shown. Scale bar = 100 μm in overview images of the fracture callus and 50 μm in images 1–9; g= gap.

Supplementary Figure S2 | : Influence of OVX treatment on trabecular bone parameters. μCT analysis of the left femora was performed to determine the relative bone volume (BV/TV) in the trabecular bone compartment of $ER\alpha^{fl/fl}$ **(A)** and $ER\alpha^{fl/fl;\ Runx2Cre}$ **(B)** mice. The trabecular number (Tb.N) was also determined in $ER\alpha^{fl/fl}$ **(C)** and $ER\alpha^{fl/fl;\ Runx2Cre}$ **(D)** mice. Data are shown as box-and-whisker plots (with median and interquartile range) from max. to min., showing all data points. *indicates significant effects with $p \leq 0.05$; $n = 4–5$.

Supplementary Figure S3 | : Influence of the respective genotype on fracture healing outcome on day 21. Biomechanical testing data (bending stiffness), bony bridging score and BV/TV of the fracture calli from control groups were directly compared between $ER\alpha^{fl/fl}$ and $ER\alpha^{fl/fl;\ Runx2Cre}$ mice. Data are shown as box-and-whisker plots (with median and interquartile range) from max. to min., showing all data points. *indicates significant effects with $p \leq 0.05$.

Supplementary Figure S4 | : Nondetailed STRING protein-association network (action) derived from the MC3T3-E1 microarray data in high quality.

REFERENCES

Almeida, M., Laurent, M. R., Dubois, V., Claessens, F., O'Brien, C. A., Bouillon, R., et al. (2017). Estrogens and Androgens in Skeletal Physiology and Pathophysiology. *Physiol. Rev.* 97, 135–187. doi:10.1152/physrev.00033.2015

Bahney, C. S., Zondervan, R. L., Allison, P., Theologis, A., Ashley, J. W., Ahn, J., et al. (2019). Cellular Biology of Fracture Healing. *J. Orthop. Res.* 37, 35–50. doi:10.1002/jor.24170

Beier, E. E., Sheu, T.-j., Buckley, T., Yukata, K., O'Keefe, R., Zuscik, M. J., et al. (2014). Inhibition of Beta-Catenin Signaling by Pb Leads to Incomplete Fracture Healing. *J. Orthop. Res.* 32, 1397–1405. doi:10.1002/JOR.22677

Beil, F. T., Barvencik, F., Gebauer, M., Seitz, S., Rueger, J. M., Ignatius, A., et al. (2010). Effects of Estrogen on Fracture Healing in Mice. *J. Trauma* 69, 1259–1265. doi:10.1097/TA.0b013e3181c4544d

Bouxsein, M. L., Boyd, S. K., Christiansen, B. A., Guldberg, R. E., Jepsen, K. J., and Müller, R. (2010). Guidelines for Assessment of Bone Microstructure in Rodents Using Micro-computed Tomography. *J. Bone Miner. Res.* 25, 1468–1486. doi:10.1002/jbmr.141

Cauley, J. A. (2015). Estrogen and Bone Health in Men and Women. *Steroids* 99, 11–15. doi:10.1016/J.STEROIDS.2014.12.010

Chen, Y., and Alman, B. A. (2009). Wnt Pathway, an Essential Role in Bone Regeneration. *J. Cel. Biochem.* 106, 353–362. doi:10.1002/JCB.22020

Cheung, W.-H., Sun, M.-H., Zheng, Y.-P., Chu, W. C.-W., Leung, A. H.-C., Qin, L., et al. (2012). Stimulated Angiogenesis for Fracture Healing Augmented by Low-Magnitude, High-Frequency Vibration in A Rat Model-Evaluation of Pulsed-Wave Doppler, 3-D Power Doppler Ultrasonography and Micro-CT Microangiography. *Ultrasound Med. Biol.* 38, 2120–2129. doi:10.1016/j.ultrasmedbio.2012.07.025

Cheung, W. H., Miclau, T., Chow, S. K.-H., Yang, F. F., and Alt, V. (2016). Fracture Healing in Osteoporotic Bone. *Injury* 47, S21–S26. doi:10.1016/S0020-1383(16)47004-X

Chow, S. K. H., Leung, K. S., Qin, J., Guo, A., Sun, M., Qin, L., et al. (2016). Mechanical Stimulation Enhanced Estrogen Receptor Expression and Callus Formation in Diaphyseal Long Bone Fracture Healing in Ovariectomy-Induced Osteoporotic Rats. *Osteoporos. Int.* 27, 2989–3000. doi:10.1007/s00198-016-3619-2

Chung, S.-L., Leung, K.-S., and Cheung, W.-H. (2014). Low-magnitude High-Frequency Vibration Enhances Gene Expression Related to Callus Formation, Mineralization and Remodeling during Osteoporotic Fracture Healing in Rats. *J. Orthop. Res.* 32, 1572–1579. doi:10.1002/jor.22715

Claes, L. E., Heigele, C. A., Neidlinger-Wilke, C., Kaspar, D., Seidl, W., Margevicius, K. J., et al. (1998). Effects of Mechanical Factors on the Fracture Healing Process. *Clin. Orthopaedics Relat. Res.* 355S, S132–S147. doi:10.1097/00003086-199810001-00015

Claes, L. (2017). Mechanobiologie der Frakturheilung Teil 1. *Unfallchirurg* 120, 14–22. doi:10.1007/s00113-016-0280-3

Claes, L., Wilke, H.-J., Augat, P., Rübenacker, S., and Margevicius, K. (1995). Effect of Dynamization on gap Healing of Diaphyseal Fractures under External Fixation. *Clin. Biomech.* 10, 227–234. doi:10.1016/0268-0033(95)99799-8

Dempster, D. W., Compston, J. E., Drezner, M. K., Glorieux, F. H., Kanis, J. A., Malluche, H., et al. (2013). Standardized Nomenclature, Symbols, and Units for Bone Histomorphometry: A 2012 Update of the Report of the ASBMR Histomorphometry Nomenclature Committee. *J. Bone Miner. Res.* 28, 2–17. doi:10.1002/jbmr.1805

Dirckx, N., Van Hul, M., and Maes, C. (2013). Osteoblast Recruitment to Sites of Bone Formation in Skeletal Development, Homeostasis, and Regeneration. *Birth Defect Res. C* 99, 170–191. doi:10.1002/bdrc.21047

Edwards, J. H., and Reilly, G. C. (2015). Vibration Stimuli and the Differentiation of Musculoskeletal Progenitor Cells: Review of Resultsin Vitroandin Vivo. *Wjsc* 7, 568. doi:10.4252/wjsc.v7.i3.568

Gao, H., Zhai, M., Wang, P., Zhang, X., Cai, J., Chen, X., et al. (2017). Low-level Mechanical Vibration Enhances Osteoblastogenesis via a Canonical Wnt Signaling-Associated Mechanism. *Mol. Med. Rep.* 16, 317–324. doi:10.3892/mmr.2017.6608

Haffner-Luntzer, M., Weber, B., Lam, C., Fischer, V., Lackner, I., Ignatius, A., et al. (2020). A Novel Mouse Model to Study Fracture Healing of the Proximal Femur. *J. Orthop. Res.* 38, 2131–2138. doi:10.1002/jor.24677

Haffner-Luntzer, M., Fischer, V., Prystaz, K., Liedert, A., and Ignatius, A. (2017). The Inflammatory Phase of Fracture Healing Is Influenced by Oestrogen Status in Mice. *Eur. J. Med. Res.* 22, 23. doi:10.1186/s40001-017-0264-y

Haffner-Luntzer, M., Heilmann, A., Rapp, A. E., Beie, S., Schinke, T., Amling, M., et al. (2014). Midkine-deficiency Delays Chondrogenesis during the Early Phase of Fracture Healing in Mice. *PLoS One* 9, e116282. doi:10.1371/journal.pone.0116282

Haffner-Luntzer, M., Kemmler, J., Heidler, V., Prystaz, K., Schinke, T., Amling, M., et al. (2016). Inhibition of Midkine Augments Osteoporotic Fracture Healing. *PLoS One* 11, e0159278. doi:10.1371/journal.pone.0159278

Haffner-Luntzer, M., Kovtun, A., Lackner, I., Mödinger, Y., Hacker, S., Liedert, A., et al. (2018a). Estrogen Receptor α- (ERα), but Not ERβ-Signaling, Is Crucially Involved in Mechanostimulation of Bone Fracture Healing by Whole-Body Vibration. *Bone* 110, 11–20. doi:10.1016/j.bone.2018.01.017

Haffner-Luntzer, M., Lackner, I., Liedert, A., Fischer, V., and Ignatius, A. (2018b). Effects of Low-Magnitude High-Frequency Vibration on Osteoblasts Are Dependent on Estrogen Receptor α Signaling and Cytoskeletal Remodeling. *Biochem. Biophysical Res. Commun.* 503, 2678–2684. doi:10.1016/j.bbrc.2018.08.023

Haffner-Luntzer, M., Liedert, A., and Ignatius, A. (2015). Mechanobiologie und Knochenstoffwechsel. *Unfallchirurg* 118, 1000–1006. doi:10.1007/s00113-015-0102-z

Haisenleder, D. J., Schoenfelder, A. H., Marcinko, E. S., Geddis, L. M., and Marshall, J. C. (2011). Estimation of Estradiol in Mouse Serum Samples: Evaluation of Commercial Estradiol Immunoassays. *Endocrinology* 152, 4443–4447. doi:10.1210/EN.2011-1501

He, Y.-X., Zhang, G., Pan, X.-H., Liu, Z., Zheng, L.-z., Chan, C.-W., et al. (2011). Impaired Bone Healing Pattern in Mice with Ovariectomy-Induced Osteoporosis: A Drill-Hole Defect Model. *Bone* 48, 1388–1400. doi:10.1016/j.bone.2011.03.720

Heilmann, A., Schinke, T., Bindl, R., Wehner, T., Rapp, A., Haffner-Luntzer, M., et al. (2013). The Wnt Serpentine Receptor Frizzled-9 Regulates New Bone Formation in Fracture Healing. *PLoS One* 8, e84232–10. doi:10.1371/journal.pone.0084232

Huang, Y., Zhang, X., Du, K., Yang, F., Shi, Y., Huang, J., et al. (2012). Inhibition of β-catenin Signaling in Chondrocytes Induces Delayed Fracture Healing in Mice. *J. Orthop. Res.* 30, 304–310. doi:10.1002/jor.21505

Ikedo, A., and Imai, Y. (2021). Estrogen Receptor α in Mature Osteoblasts Regulates the Late Stage of Bone Regeneration. *Biochem. Biophysical Res. Commun.* 559, 238–244. doi:10.1016/j.bbrc.2021.04.112

Jessop, H. L., Suswillo, R. F., Rawlinson, S. C., Zaman, G., Lee, K., Das-Gupta, V., et al. (2004). Osteoblast-Like Cells from Estrogen Receptor α Knockout Mice Have Deficient Responses to Mechanical Strain. *J. Bone Miner. Res.* 19, 938–946. doi:10.1359/jbmr.2004.19.6.938

Kim, J.-B., Leucht, P., Lam, K., Luppen, C., Ten Berge, D., Nusse, R., et al. (2007). Bone Regeneration Is Regulated by Wnt Signaling. *J. Bone Miner. Res.* 22, 1913–1923. doi:10.1359/JBMR.070802

Kim, W.-Y., Han, C.-H., Park, J.-I., and Kim, J.-Y. (2001). Failure of Intertrochanteric Fracture Fixation with a Dynamic Hip Screw in Relation to Pre-operative Fracture Stability and Osteoporosis. *Int. Orthopaedics (Sicot)* 25, 360–362. doi:10.1007/s002640100287

Komori, T., Yagi, H., Nomura, S., and Yamaguchi, A. (1998). Targeted Disruption of Cbfa1 Results in a Complete Lack of Bone Formation Owing to Maturational Arrest of Osteoblasts. *Proc. Natl. Acad. Sci. U. S. A.* 95, 8692–8697. doi:10.1073/pnas.95.15.8692

Komrakova, M., Sehmisch, S., Tezval, M., Ammon, J., Lieberwirth, P., Sauerhoff, C., et al. (2013). Identification of a Vibration Regime Favorable for Bone Healing and Muscle in Estrogen-Deficient Rats. *Calcif. Tissue Int.* 92, 509–520. doi:10.1007/s00223-013-9706-x

Lau, K.-H. W., Kothari, V., Das, A., Zhang, X.-B., and Baylink, D. J. (2013). Cellular and Molecular Mechanisms of Accelerated Fracture Healing by COX2 Gene Therapy. *Bone* 53, 369–381. doi:10.1016/J.BONE.2013.01.003

Lee, K., Jessop, H., Suswillo, R., Zaman, G., and Lanyon, L. (2003). Bone Adaptation Requires Oestrogen Receptor-α. *Nature* 424, 389. doi:10.1038/424389a

Leung, K. S., Li, C. Y., Tse, Y. K., Choy, T. K., Leung, P. C., Hung, V. W. Y., et al. (2014). Effects of 18-month Low-Magnitude High-Frequency Vibration on Fall Rate and Fracture Risks in 710 Community Elderly-A Cluster-Randomized Controlled Trial. *Osteoporos. Int.* 25, 1785–1795. doi:10.1007/s00198-014-2693-6

Li, Y., Liu, G., Yu, J., Li, C., Tan, L., Hao, B., et al. (2018). Effects of Continuous or Intermittent Low-Magnitude High-Frequency Vibration on Fracture Healing in Sheep. *Int. Orthopaedics (Sicot)* 42, 939–946. doi:10.1007/s00264-018-3759-4

Li, Y.H., Zhu, D., Yang, T., Cheng, L., Sun, J., and Tan, L. (2021). Crosstalk Between The COX2-PGE2-EP4 Signaling Pathway And Primary Cilia In Osteoblasts After Mechanical Stimulation. *J. Cell Physiol.* 236, 4764–4777. doi:10.1002/jcp.30198

Liedert, A., Röntgen, V., Schinke, T., Benisch, P., Ebert, R., Jakob, F., et al. (2014). Osteoblast-specific Krm2 Overexpression and Lrp5 Deficiency Have Different Effects on Fracture Healing in Mice. *PLoS One* 9, e103250. doi:10.1371/journal.pone.0103250

Liedert, A., Wagner, L., Seefried, L., Ebert, R., Jakob, F., and Ignatius, A. (2010). Estrogen Receptor and Wnt Signaling Interact to Regulate Early Gene Expression in Response to Mechanical Strain in Osteoblastic Cells. *Biochem. Biophysical Res. Commun.* 394, 755–759. doi:10.1016/j.bbrc.2010.03.065

Manolagas, S. C., Bellido, T., and Jilka, R. L. (1995). Sex Steroids, Cytokines and the Bone Marrow: New Concepts on the Pathogenesis of Osteoporosis. *Ciba Found. Symp.* 191, 187–202. doi:10.1002/9780470514757.ch11

Mödinger, Y., Rapp, A., Pazmandi, J., Vikman, A., Holzmann, K., Haffner-Luntzer, M., et al. (2018). C5aR1 Interacts with TLR2 in Osteoblasts and Stimulates the Osteoclast-Inducing Chemokine CXCL10. *J. Cel. Mol. Med.* 22, 6002–6014. doi:10.1111/jcmm.13873

Morgan, E. F., Mason, Z. D., Chien, K. B., Pfeiffer, A. J., Barnes, G. L., Einhorn, T. A., et al. (2009). Micro-computed Tomography Assessment of Fracture Healing: Relationships Among Callus Structure, Composition, and Mechanical Function. *Bone* 44, 335–344. doi:10.1016/j.bone.2008.10.039

Nagano, A., Arioka, M., Takahashi-Yanaga, F., Matsuzaki, E., and Sasaguri, T. (2017). Celecoxib Inhibits Osteoblast Maturation by Suppressing the Expression of Wnt Target Genes. *J. Pharmacol. Sci.* 133, 18–24. doi:10.1016/j.jphs.2016.11.003

Nikolaou, V. S., Efstathopoulos, N., Kontakis, G., Kanakaris, N. K., and Giannoudis, P. V. (2009). The Influence of Osteoporosis in Femoral Fracture Healing Time. *Injury* 40, 663–668. doi:10.1016/j.injury.2008.10.035

Perren, S. M. (1979). Physical and Biological Aspects of Fracture Healing with Special Reference to Internal Fixation. *Clin. Orthop. Relat. Res.* 138, 175–196.

Röntgen, V., Blakytny, R., Matthys, R., Landauer, M., Wehner, T., Göckelmann, M., et al. (2010). Fracture Healing in Mice under Controlled Rigid and Flexible Conditions Using an Adjustable External Fixator. *J. Orthop. Res.* 28, 1456–1462. doi:10.1002/jor.21148

Rubin, C., Recker, R., Cullen, D., Ryaby, J., McCabe, J., and McLeod, K. (2004). Prevention of Postmenopausal Bone Loss by a Low-Magnitude, High-Frequency Mechanical Stimuli: A Clinical Trial Assessing Compliance, Efficacy, and Safety. *J. Bone Miner. Res.* 19, 343–351. doi:10.1359/JBMR.0301251

Seitz, S., Keller, J., Schilling, A. F., Jeschke, A., Marshall, R. P., Stride, B. D., et al. (2012). Pharmacological Estrogen Administration Causes a FSH-independent Osteo-Anabolic Effect Requiring ER Alpha in Osteoblasts. *PLoS One* 7, e50301–9. doi:10.1371/journal.pone.0050301

Shi, H.-F., Cheung, W.-H., Qin, L., Leung, A. H.-C., and Leung, K.-S. (2010). Low-magnitude High-Frequency Vibration Treatment Augments Fracture Healing in Ovariectomy-Induced Osteoporotic Bone. *Bone* 46, 1299–1305. doi:10.1016/j.bone.2009.11.028

Simon, A. M., Manigrasso, M. B., and O'Connor, J. P. (2002). Cyclo-oxygenase 2 Function Is Essential for Bone Fracture Healing. *J. Bone Miner. Res.* 17, 963–976. doi:10.1359/jbmr.2002.17.6.963

Steiner, M., Volkheimer, D., Meyers, N., Wehner, T., Wilke, H.-J., Claes, L., et al. (2015). Comparison between Different Methods for Biomechanical Assessment of *Ex Vivo* Fracture Callus Stiffness in Small Animal Bone Healing Studies. *PLoS ONE* 10, e0119603–16. doi:10.1371/journal.pone.0119603

Steppe, L., Liedert, A., Ignatius, A., and Haffner-Luntzer, M. (2020). Influence of Low-Magnitude High-Frequency Vibration on Bone Cells and Bone Regeneration. *Front. Bioeng. Biotechnol.* 8, 595139. doi:10.3389/fbioe.2020.595139

Stuermer, E. K., Komrakova, M., Werner, C., Wicke, M., Kolios, L., Sehmisch, S., et al. (2010). Musculoskeletal Response to Whole-Body Vibration during

Fracture Healing in Intact and Ovariectomized Rats. *Calcif. Tissue Int.* 87, 168–180. doi:10.1007/s00223-010-9381-0

Sunters, A., Armstrong, V. J., Zaman, G., Kypta, R. M., Kawano, Y., Lanyon, L. E., et al. (2010). Mechano-transduction in Osteoblastic Cells Involves Strain-Regulated Estrogen Receptor α-mediated Control of Insulin-like Growth Factor (IGF) I Receptor Sensitivity to Ambient IGF, Leading to Phosphatidylinositol 3-Kinase/AKT-dependent Wnt/LRP5 Receptor-independent Activation of β-Catenin Signaling. *J. Biol. Chem.* 285, 8743–8758. doi:10.1074/jbc.M109.027086

Teng, J. W., Ji, P. F., and Zhao, Z. G. (2018). MiR-214-3p Inhibits β-catenin Signaling Pathway Leading to Delayed Fracture Healing. *Eur. Rev. Med. Pharmacol. Sci.* 22, 17–24. doi:10.26355/eurrev_201801_14095

Thompson, W. R., Yen, S. S., and Rubin, J. (2014). Vibration Therapy. *Curr. Opin. Endocrinol. Diabetes Obes.* 21, 447–453. doi:10.1097/MED.0000000000000111

Wang, J., Leung, K. S., Leung, K., Chow, S., and Cheung, W. (2017). The Effect of Whole Body Vibration on Fracture Healing - a Systematic Review. *eCM* 34, 108–127. doi:10.22203/eCM.v034a08

Wehrle, E., Liedert, A., Heilmann, A., Wehner, T., Bindl, R., Fischer, L., et al. (2015). The Impact of Low-Magnitude High-Frequency Vibration on Fracture Healing Is Profoundly Influenced by the Oestrogen Status in Mice. *DMM Dis. Model. Mech.* 8, 93–104. doi:10.1242/dmm.018622

Wehrle, E., Wehner, T., Heilmann, A., Bindl, R., Claes, L., Jakob, F., et al. (2014). Distinct Frequency Dependent Effects of Whole-Body Vibration on Non-fractured Bone and Fracture Healing in Mice. *J. Orthop. Res.* 32, 1006–1013. doi:10.1002/jor.22629

Wildemann, B., Ignatius, A., Leung, F., Taitsman, L. A., Smith, R. M., Pesántez, R., et al. (2021). Non-union Bone Fractures. *Nat. Rev. Dis. Primers* 7, 57. doi:10.1038/S41572-021-00289-8

Windahl, S. H., Saxon, L., Börjesson, A. E., Lagerquist, M. K., Frenkel, B., Henning, P., et al. (2013). Estrogen Receptor-α Is Required for the Osteogenic Response to Mechanical Loading in a Ligand-independent Manner Involving its Activation Function 1 but Not 2. *J. Bone Miner. Res.* 28, 291–301. doi:10.1002/jbmr.1754

Xia, X., Batra, N., Shi, Q., Bonewald, L. F., Sprague, E., and Jiang, J. X. (2010). Prostaglandin Promotion of Osteocyte Gap Junction Function through Transcriptional Regulation of Connexin 43 by Glycogen Synthase Kinase 3/β-Catenin Signaling. *Mol. Cel. Biol.* 30, 206–219. doi:10.1128/mcb.01844-08

Xie, C., Liang, B., Xue, M., Lin, A. S. P., Loiselle, A., Schwarz, E. M., et al. (2009). Rescue of Impaired Fracture Healing in COX-2−/− Mice via Activation of Prostaglandin E2 Receptor Subtype 4. *Am. J. Pathol.* 175, 772–785. doi:10.2353/AJPATH.2009.081099

Yeh, C.-R., Chiu, J.-J., Lee, C.-I., Lee, P.-L., Shih, Y.-T., Sun, J.-S., et al. (2010). Estrogen Augments Shear Stress-Induced Signaling and Gene Expression in Osteoblast-like Cells via Estrogen Receptor-Mediated Expression of β1-integrin. *J. Bone Miner. Res.* 25, 627–639. doi:10.1359/jbmr.091008

Zeeberg, B. R., Feng, W., Wang, G., Wang, M. D., Fojo, A. T., Sunshine, M., et al. (2003). GoMiner: a Resource for Biological Interpretation of Genomic and Proteomic Data. *Genome Biol.* 4, R28. doi:10.1186/gb-2003-4-4-r28

Zhang, X., Schwarz, E. M., Young, D. A., Puzas, J. E., Rosier, R. N., and O'Keefe, R. J. (2002). Cyclooxygenase-2 Regulates Mesenchymal Cell Differentiation into the Osteoblast Lineage and Is Critically Involved in Bone Repair. *J. Clin. Invest.* 109, 1405–1415. doi:10.1172/JCI1568110.1172/jci0215681

Zheng, C., Qu, Y. X., Wang, B., Shen, P. F., Xu, J. D., and Chen, Y. X. (2019). COX-2/PGE2 Facilitates Fracture Healing by Activating the Wnt/β-Catenin Signaling Pathway. *Eur. Rev. Med. Pharmacol. Sci.* 23, 9721–9728. doi:10.26355/eurrev_201911_19534

Zhou, X., von der Mark, K., Henry, S., Norton, W., Adams, H., and de Crombrugghe, B. (2014). Chondrocytes Transdifferentiate into Osteoblasts in Endochondral Bone during Development, Postnatal Growth and Fracture Healing in Mice. *Plos Genet.* 10, e1004820. doi:10.1371/journal.pgen.1004820

Zoller, V., Funcke, J.-B., Roos, J., Dahlhaus, M., Abd El Hay, M., Holzmann, K., et al. (2017). Trail (TNF-Related Apoptosis-Inducing Ligand) Induces an Inflammatory Response in Human Adipocytes. *Sci. Rep.* 7, 1–12. doi:10.1038/s41598-017-05932-7

Conflict of Interest: The authors declare that the research was conducted in the absence of any commercial or financial relationships that could be construed as a potential conflict of interest.

Publisher's Note: All claims expressed in this article are solely those of the authors and do not necessarily represent those of their affiliated organizations, or those of the publisher, the editors and the reviewers. Any product that may be evaluated in this article, or claim that may be made by its manufacturer, is not guaranteed or endorsed by the publisher.

Copyright © 2021 Steppe, Krüger, Tschaffon, Fischer, Tuckermann, Ignatius and Haffner-Luntzer. This is an open-access article distributed under the terms of the Creative Commons Attribution License (CC BY). The use, distribution or reproduction in other forums is permitted, provided the original author(s) and the copyright owner(s) are credited and that the original publication in this journal is cited, in accordance with accepted academic practice. No use, distribution or reproduction is permitted which does not comply with these terms.

frontiers in Bioengineering and Biotechnology

ORIGINAL RESEARCH
published: 21 December 2021
doi: 10.3389/fbioe.2021.787020

Establishment of an *Ex Vivo* Inflammatory Osteoarthritis Model With Human Osteochondral Explants

Kaihu Li[1,2], *Penghui Zhang*[2,3], *Yong Zhu*[1], *Mauro Alini*[2], *Sibylle Grad*[2] *and Zhen Li*[2]*

[1]Department of Orthopaedics, Xiangya Hospital of Central South University, Changsha, China, [2]AO Research Institute Davos, Davos, Switzerland, [3]Department of Orthopaedic Surgery, The Seventh Affiliated Hospital, Sun Yat-sen University, Shenzhen, China

Osteoarthritis (OA) is the most common degenerative joint disease without clear pathophysiological mechanism and effective drugs for treatment. Although various animal models exist, the translation of the outcome into clinics remains difficult due to species differences. In this study, an *ex vivo* inflammatory OA model was induced using different concentrations of interleukin one beta (IL-1β) and tumor necrosis factor α (TNF-α) on explants from the human femoral head. In the inflammatory OA groups, the gene expression levels of cartilage catabolism (matrix metalloproteinase 1 (MMP1), matrix metalloproteinase 3 (MMP3)), and inflammation (interleukin 6 (IL-6), interleukin 8 (IL-8)) markers were significantly upregulated, while the anabolic genes (collagen 2 (COL2), aggrecan (ACAN), and proteoglycan 4 (PRG4)) were downregulated compared to the control group. The release of cytokines (IL-6, IL-8) and nitric oxide (NO) in the conditioned medium was also upregulated in inflammatory OA groups. The Safranin O/Fast Green staining showed loss of proteoglycan in the superficial zone cartilage after cytokine treatment. The results indicated that an *ex vivo* inflammation and degeneration model was successfully established using osteochondral explants from the human femoral head. This model can be used to elucidate the in-depth mechanism of inflammatory OA and to screen new drugs for OA treatment.

Keywords: osteoarthritis, *ex vivo*, model, osteochondral explant, inflammation, human

OPEN ACCESS

Edited by:
Rahul Gawri,
McGill University, Canada

Reviewed by:
Amani Hassan,
McGill University, Canada
Jennifer Patterson,
Instituto IMDEA Materiales, Spain

***Correspondence:**
Zhen Li
zhen.li@aofoundation.org

Specialty section:
This article was submitted to Biomaterials, a section of the journal Frontiers in Bioengineering and Biotechnology

Received: *30 September 2021*
Accepted: *25 November 2021*
Published: *21 December 2021*

Citation:
Li K, Zhang P, Zhu Y, Alini M, Grad S and Li Z (2021) Establishment of an Ex Vivo Inflammatory Osteoarthritis Model With Human Osteochondral Explants. Front. Bioeng. Biotechnol. 9:787020. doi: 10.3389/fbioe.2021.787020

INTRODUCTION

Osteoarthritis (OA) is the most common degenerative joint disease, mainly invading knee and hip joints (Martel-Pelletier et al., 2016). Its prevalence and incidence keep rising year by year, leading to increasing burden in most countries (Safiri et al., 2020; Peat and Thomas, 2021). OA mainly manifests progressive and recurrent joint pain, swelling, and restricted activity causing many years lived with disability (YLDs) (Safiri et al., 2020). The underlying pathophysiologic mechanism has not been fully elucidated due to the heterogeneity of the disease and multiple risk factors like trauma, genetics, gender, and aging (Loeser et al., 2016; He et al., 2020; Coryell et al., 2021). Furthermore, there are no effective disease-modifying OA drugs (DMOADs) approved yet, other than medicines for relieving symptoms (Cai et al., 2021; Oo et al., 2021).

To elucidate the pathological mechanism and screen the effectiveness of new drugs, numerous *in vitro* and *in vivo* OA models have been developed (Teeple et al., 2013; McCoy, 2015; Johnson et al., 2016). *In vitro* cell culture models and cytokines, such as interleukin one beta (IL-1β) and tumor

necrosis factor α (TNF-α), have widely been used to establish OA-like conditions, since low-grade inflammatory circumstances are known to play a major regulatory role in the disease progression (Robinson et al., 2016). However, isolated *in vitro* cultured cells lack the environment of cells embedded in their native extracellular matrix. For *in vivo* studies, various animals and surgical methods have been used to establish a destabilized OA model, simulating posttraumatic OA (Teeple et al., 2013; McCoy, 2015). Nonetheless, the translation of animal data to clinical practice is still challenging due to significant variations between animals and humans.

To overcome these limitations and better reflect real circumstances of human OA progression, *ex vivo* explant models have great potential, as they are also in accordance with the 3Rs principle of animal testing: replace, reduce, refine (Schwab et al., 2017; Cope et al., 2019; Humpenoder et al., 2021). Geurts et al. (Geurts et al., 2018) have established an inflammatory OA model induced by lipopolysaccharide with osteochondral plugs from human OA knee and spine joints to assess the effects of potential drugs. The tissue viability of explants from the human OA tibia plateau has been proven stable within a period of at least 2 or 4 weeks (Kleuskens et al., 2021). In addition, different OA-like phenotypes have been established with human osteochondral explants, such as loading-induced models, inflammatory models, and hypertrophy subtypes (Houtman et al., 2021). To date, no study has been reported that comprehensively characterized the *ex vivo* inflammatory OA model with human samples induced with different concentrations of IL-1β and TNF-α in combination.

In this study, we aimed to establish and characterize an *ex vivo* inflammatory OA model using osteochondral explants isolated from human femoral heads. The effects of IL-1β and TNF-α at different doses were investigated. The expression of genes related to cartilage anabolism, catabolism, and inflammation was evaluated by quantitative real-time polymerase chain reaction (qRT-PCR). The glycosaminoglycan (GAG), nitric oxide (NO), and inflammatory cytokine releases into the conditioned medium were quantified. In addition, the cell viability and tissue morphology of explants were assessed by live cell staining and histological methods.

MATERIALS AND METHODS

Osteochondral Explant Isolation

Osteochondral explants were harvested from human femoral heads of patients who underwent hip replacement operation with their informed consent and approval by the cantonal ethical commission (KEK-ZH-NR: 2010-0444/0). The clinical characteristics of donors and the Kellgren–Lawrence classification (Kellgren and Lawrence, 1957) of hip joints used in this study are summarized in **Table 1**. The average age of included patients was 75.75 ± 11.10 years (range from 59 to 89 years). Osteochondral explants (**Figure 1B**) were isolated from the non-tissue wear regions of the femoral heads using a trephine with an inner diameter of 8 mm. The subchondral bone was cut with a circular saw to reach a height of 5 mm (**Figure 1C**). After isolation, the explants were rinsed in phosphate-buffered saline (PBS) three times before culture.

Experimental Design

All explants were first cultured for 1 day at 37°C, 5% CO_2, and 80% humidity in 12-well nontreated plates with 2 ml explant medium per well, which consisted of high-glucose DMEM medium (Gibco, Grand Island, NY, USA), supplemented with 100 μg/ml sodium pyruvate (Sigma-Aldrich, St. Louis, MO, USA), 2.5% HEPES (Gibco), 1% nonessential amino acids (Gibco), 50 μg/ml ascorbic acid (Sigma-Aldrich), 1% ITS + Premix (Corning, Tewksbury, MA, USA), 100 U/ml penicillin, and 100 μg/ml streptomycin. After 1-day preculture, one explant from each donor was processed for further analysis as the normalization baseline. Other explants were randomly divided into four groups and respectively cultured in 1) explant medium (Control), 2) explant medium plus 1 ng/ml IL-1β (PeproTech) + 1 ng/ml TNF-α (R&D Systems, Minneapolis, MN, USA), 3) explant medium plus 5 ng/ml IL-1β + 5 ng/ml TNF-α, or 4) explant medium plus 10 ng/ml IL-1β + 10 ng/ml TNF-α; explants were harvested on day 3 and day 7. The conditioned medium was collected on day 0, day 1, day 5, and day 7 for further analysis (**Figure 1D**).

GAG Measurement

The release of sulfated GAG into the conditioned medium was measured with 1,9-dimethyl-methylene blue (DMMB, Sigma-Aldrich, St. Louis, MO, USA) color reagent. Chondroitin sulfate was used to generate the standard curve (concentration range 0–2.5 μg/50 μl). Briefly, 50-μl standards or samples were added into each well followed by 200 μl DMMB reagent. Absorbance at 535 nm was immediately read by a Tecan microplate reader.

NO Measurement

NO in the conditioned medium was measured by Griess Reagent System (Promega Corporation, Madison, WI, USA). Nitrite was used to generate the standard curve with the maximum concentration of 100 μM. Firstly, 50-μl standards or samples were pipetted into the plate. Secondly, 50 μl Sulfanilamide Solution and NED Solution was successively added into each well with each incubated for 10 min at room temperature and protected from light. The absorbance at 535 nm was read by a microplate reader.

Enzyme-Linked Immunosorbent Assay

The protein concentrations of human IL-6 and IL-8 in the conditioned media were assessed by ELISA (R&D Systems) according to the manufacturer's instructions.

Gene Expression Analysis

The full-thickness cartilage tissue was removed from subchondral bone and then minced into small pieces and digested with 2 mg/ml pronase (Roche, Basel, Switzerland) for 2 h at 37°C as described in a previous study (Caprez et al., 2018). Then, cartilage fragments, precooled with liquid nitrogen, were pulverized before transferring into tubes with TRI Reagent

TABLE 1 | Demographic characteristics of patients included.

No	Gender	Age (years)	Kellgren–Lawrence grade	No. of explants isolated
1	Male	86	2	13
2	Female	81	4	9
3	Male	89	3	11
4	Female	70	3	9
5	Female	76	2	14
6	Female	83	3	10
7	Female	59	3	12
8	Female	62	4	8

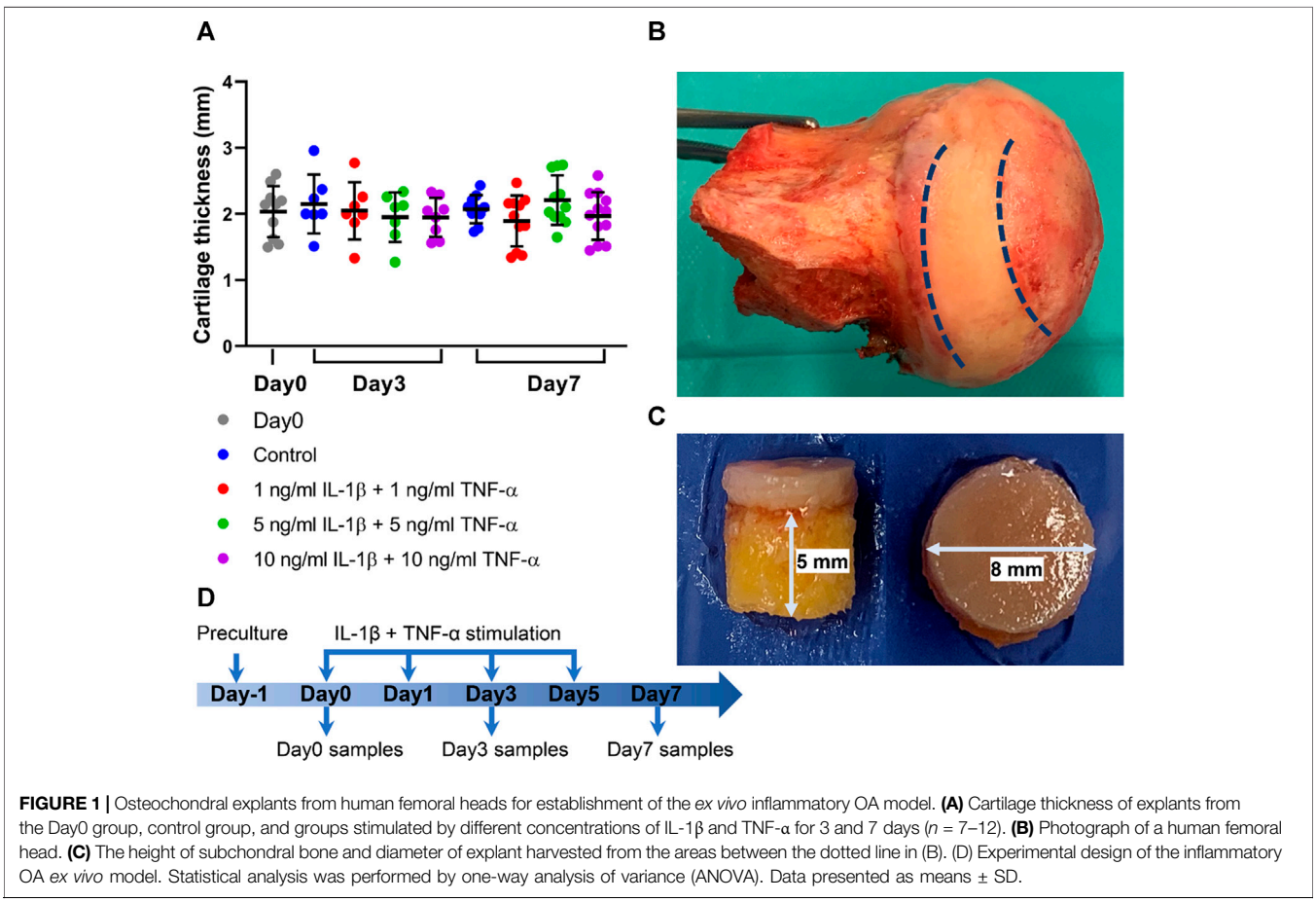

FIGURE 1 | Osteochondral explants from human femoral heads for establishment of the *ex vivo* inflammatory OA model. **(A)** Cartilage thickness of explants from the Day0 group, control group, and groups stimulated by different concentrations of IL-1β and TNF-α for 3 and 7 days (n = 7–12). **(B)** Photograph of a human femoral head. **(C)** The height of subchondral bone and diameter of explant harvested from the areas between the dotted line in (B). (D) Experimental design of the inflammatory OA *ex vivo* model. Statistical analysis was performed by one-way analysis of variance (ANOVA). Data presented as means ± SD.

(Molecular Research Center, Cincinnati, OH, USA). The pulverized cartilage tissue within TRI was then homogenized with a tissue lyser (Retsch). After centrifugation, the supernatant was transferred into fresh tubes. 1-Bromo-3-chloropropane (BCP, Sigma-Aldrich) was then added into each tube. After 15 min of shaking and 15 min of centrifugation, the aqueous phase containing RNA was transferred into fresh tubes. RNA was then purified with RNeasy Mini Kit (Qiagen, Hilden, Germany). The RNA concentration was measured by a NanoDrop spectrophotometer (Thermo Fisher Scientific Inc., Waltham, MA, USA). Reverse transcription was conducted with SuperScript Vilo RT Kit (Thermo Fisher Scientific). PCR to assess gene expression was performed with QuantStudio Flex 7.0 instrument and TaqMan Gene Expression Master Mix (Applied Biosystems, Foster City, CA, USA). The primer and probe sequences of tested genes are listed in **Table 2**. RPLP0 ribosomal RNA was used as endogenous control. Data were analyzed using the $2^{-\Delta\Delta Ct}$ method.

Lactate Dehydrogenase/Ethidium Homodimer Staining

Cartilage of explants was removed from subchondral bone with a scalpel, snap frozen in liquid nitrogen, and stored at -20 °C.

TABLE 2 | Oligonucleotide primers and probes used for qPCR.

Gene	Primer and probe	Sequence/catalog number
RPLP0	Forward primer (5′→3′)	TGG GCA AGA ACA CCA TGA TG
	Reverse primer (5′→3′)	CGG ATA TGA GGC AGC AGT TTC
	Probe (5′FAM/3′TAMRA)	AGG GCA CCT GGA AAA CAA CCC AGC
COL2	Forward primer (5′→3′)	GGC AAT AGC AGG TTC ACG TAC A
	Reverse primer (5′→3′)	GAT AAC AGT CTT GCC CCA CTT ACC
	Probe (5′FAM/3′TAMRA)	CCT GAA GGA TGG CTG CAC GAA ACA TAC
COL10	Forward primer (5′→3′)	ACG CTG AAC GAT ACC AAA TG
	Reverse primer (5′→3′)	TGC TAT ACC TTT ACT CTT TAT GGT GTA
	Probe (5′FAM/3′TAMRA)	ACT ACC CAA CAC CAA GAC ACA GTT CTT CAT TCC
ACAN	Forward primer (5′→3′)	AGT CCT CAA GCC TCC TGT ACT CA
	Reverse primer (5′→3′)	CGG GAA GTG GCG GTA ACA
	Probe (5′FAM/3′TAMRA)	CCG GAA TGG AAA CGT GAA TCA GAA TCA ACT
PRG4		Hs00981633_m1
MMP1		Hs00899658_m1
MMP3		Hs00968305_m1
IL-6		Hs00174131_m1
IL-8		Hs00174103_m1

Primers and probes presented with sequences were custom designed; primers and probes presented with catalogue numbers were from Applied Biosystems.

Sections with thickness of 10 μm were made by cryosection microtome (Leica, Wetzlar, Germany). The lactate dehydrogenase (LDH) solution (10 ml) was prepared as follows (Jahn and Stoddart, 2011): 54 mg lactic acid (Sigma) and 17.5 mg nicotinamide adenine dinucleotide (NAD, Sigma) were added into a beaker and were mixed with 8 ml 40% Polypep solution (Sigma) which was preheated to 37 °C. Then, the pH was adjusted to 8.0 with 10% NaOH and 40% Polypep solution was added to achieve a final volume of 10 ml. Finally, 30 mg nitro blue tetrazolium (NBT, Sigma) was added to the solution before use. After rinsing in deionized water, the sections were incubated in ethidium homodimer (Sigma) for 45 min at room temperature and then incubated in LDH solution at 37°C for 3 h. The sections were then fixed with 4% formalin for 15 min and mounted with an aqueous mounting reagent (Dako, Glostrup, Denmark). In each group, six full-thickness histological slides from three explants were counted, with two inconsecutive sections from each explant. Cells with blue color or combined color (blue and red) were considered as alive, while only reddish-stained cells were considered as dead. The numbers of alive and dead cells were counted with ImageJ software (ImageJ, National Institutes of Health, Bethesda, MD, USA).

Safranin O/Fast Green Staining

Osteochondral explants were fixed in 4% formalin for 48 h and then decalcified with 12.5% EDTA containing 1.25% NaOH for about 2 weeks. After decalcification was accomplished, explants were dehydrated with ascending series of ethanol in an automatic spin tissue processor (Microm, STP 120-2) and embedded manually with the tissue embedding center (Microm, EC 350-1). Sections with thickness of 5 μm were made with paraffin microtome (Microm, HM 355S). For staining, sections were first deparaffinized with xylene and then hydrated with gradient ethanol and deionized water. Sections were stained in Weigert's Hematoxylin (Sigma) for 10 min followed by rinsing in tap water for 10 min. The slides were then stained with 0.02% Fast Green (Sigma) for 6 min followed by differentiation with 1% acetic acid (Fluka) for 30 s. Following that, slides were stained with 0.1% Safranin O (Sigma) for 12 min and then rinsed in deionized water. Sections were then differentiated with 70% ethanol for 10 s and mounted with Eukitt (Sigma) after dehydration. In each group, three staining images (n = 3) of cartilage were quantified with one image per donor using ImageJ software. The cartilage on the whole image (**Figure 3A**) was defined as the total cartilage area. The area on the image (**Figure 3A**) without red staining was defined as the Safranin O-negatively stained area. The percentage of Safranin O-negatively stained area in each image was calculated (Shi et al., 2019) and then normalized to its individual control sample from the corresponding donor.

Statistical Analysis

All the statistical analyses were performed with GraphPad Prism 8.4.0 (GraphPad Software, Inc., La Jolla, CA, USA). The Shapiro–Wilk normality test was used to define whether data were normally distributed. One-way analysis of variance (ANOVA) was conducted to determine differences between three or more groups for continuous variables with normal distribution. The Kruskal–Wallis test was conducted to evaluate the differences for non-normally distributed data. $p < 0.05$ was considered as statistical significance.

RESULTS

Explant Size

Osteochondral explants with 8-mm diameter were obtained using a trephine device. The height of subchondral bone was cut to reach 5 mm with the circular saw (**Figure 1B**). After explants were harvested, cartilage thickness was measured with a caliper. The average cartilage thickness in each group was assessed; the thickness reached 2.03 ± 0.36 mm and was comparable among all the groups (**Figure 1A**).

Tissue Viability

Cell viability in cartilage tissue of explants was evaluated on cryosections stained with LDH/ethidium homodimer

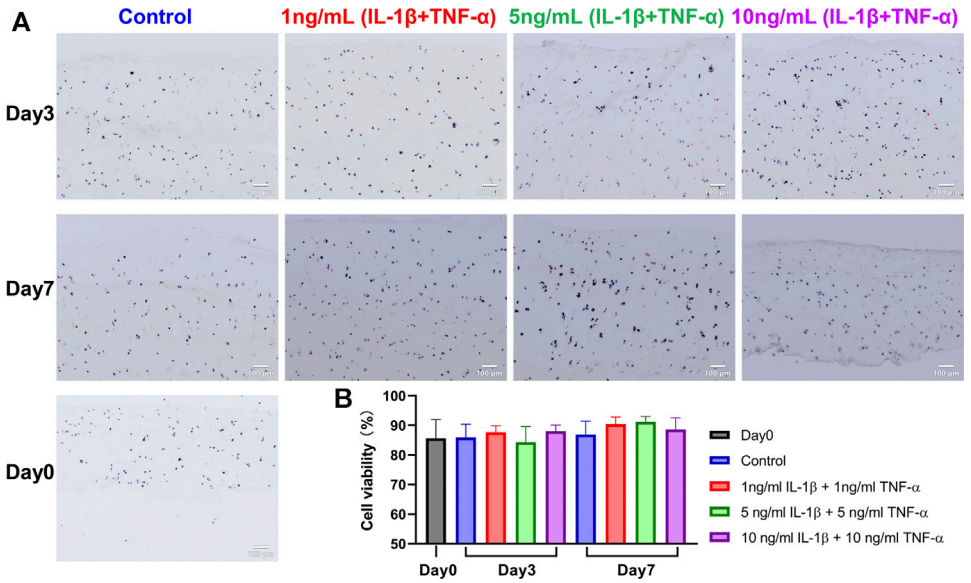

FIGURE 2 | LDH/ethidium homodimer staining on snap-frozen sections of unstimulated and IL-1β- and TNF-α-stimulated osteochondral explants from human femoral heads. **(A)** Representative staining images of cartilage in explants from the Day 0 group, control group, and groups stimulated by different concentrations of IL-1β and TNF-α for 3 and 7 days. Blue and blue/red-stained cells were alive, while red-only-stained cells were dead. Scale bars, 100 μm. **(B)** Quantification analysis of tissue viability among above groups (n = 6). Statistical analysis was performed by one-way analysis of variance (ANOVA). Data presented as means +SD.

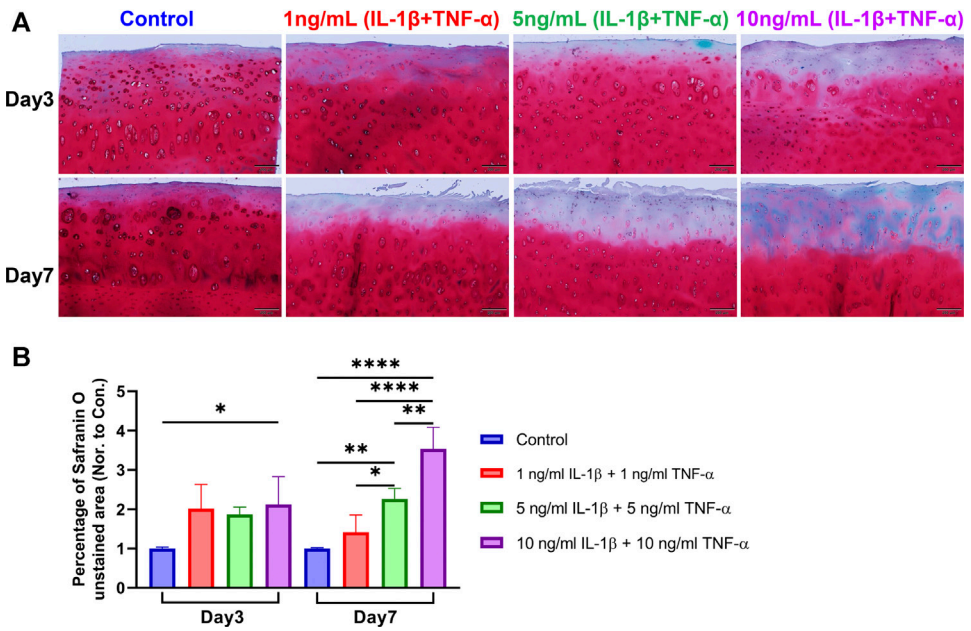

FIGURE 3 | Safranin O/Fast Green staining on sections of unstimulated and IL-1β- and TNF-α-stimulated osteochondral explants from human femoral heads. **(A)** Representative staining images of explants from the control group and groups stimulated by different concentrations of IL-1β and TNF-α for 3 and 7 days. Scale bars, 200 μm. **(B)** Safranin O-unstained area among the above groups was quantified and normalized to the control group of each donor as 1 (n = 3). Statistical analysis was performed by one-way analysis of variance (ANOVA). Data presented as means +SD. ns $p > 0.05$, *$p < 0.05$, **$p < 0.01$, ****$p < 0.0001$.

(**Figure 2A**). Cell viability of the day 0 group was 85.6 ± 6.3%. Data showed that the cell viability was stable during culture and was also unchanged when explants were treated with combined cytokines at different concentrations (**Figure 2B**).

Safranin O/Fast Green Staining

Proteoglycan distribution in the explants was assessed with Safranin O/Fast Green staining using paraffin sections. In the control group, there was no or little proteoglycan loss, while

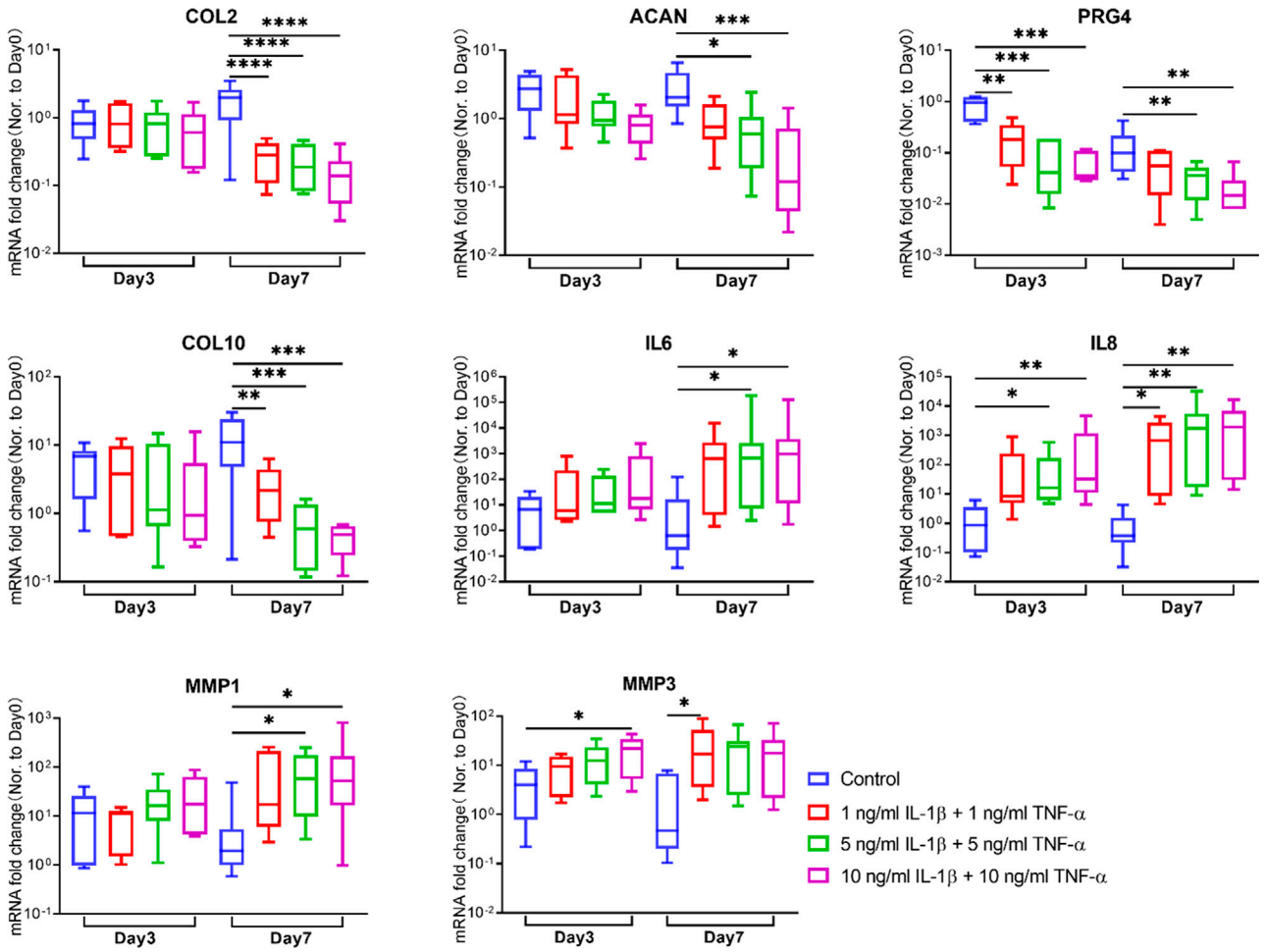

FIGURE 4 | Gene expression changes of chondrocytes in osteochondral explants from human femoral heads stimulated with different concentrations of IL-1β and TNF-α for 3 and 7 days. The relative gene expression levels of COL2, ACAN, PRG4, COL10, IL6, IL8, MMP1, and MMP3 were measured by qRT-PCR (n = 6–8). Statistical analysis was performed by one-way analysis of variance (ANOVA) or Kruskal–Wallis test. Data presented as box and whisker plots with boxes indicating the 25th to 75th percentiles, whiskers indicating the maximum and minimum values, and horizontal lines in the boxes indicating medians. *p < 0.05, **p < 0.01, ***p < 0.001, ****p < 0.0001.

cytokine-stimulated groups presented mild to severe proteoglycan loss in the cartilage (**Figure 3A**). Significant differences were observed in the percentage of the Safranin O-negatively stained area between the control group and inflammatory groups on both day 3 and day 7 (**Figure 3B**). Furthermore, the Safranin O-negatively stained area showed significant differences among different treatment groups on day 7. The histological results indicated that the cytokine stimulation enhanced the loss of proteoglycan in the extracellular matrix of explant cartilage tissue, which is a typical histopathological change in OA cartilage.

Gene Expressions

The gene expression levels of catabolism, anabolism, and inflammation markers in the cartilage tissue were assessed by qRT-PCR (**Figure 4**). For catabolic genes, compared with the respective control group at the same time point, MMP1 was markedly elevated in the 5- and 10-ng/ml cytokine-induced groups on day 7, while MMP3 showed remarkable upregulation in the 10-ng/ml inflammatory group on day 3 and the 1-ng/ml group on day 7. As for anabolism genes, COL2 was significantly decreased in all inflammatory groups on day 7, while ACAN was significantly downregulated in the 5- and 10-ng/ml inflammatory groups on day 7. PRG4 showed an early downregulation on day 3 in all inflammatory groups, and a significantly lower expression in the 5- and 10-ng/ml inflammatory groups compared to the control group on day 7. For pro-inflammation-related genes, IL-6 was significantly upregulated in the 5- and 10-ng/ml inflammatory groups on day 7. IL-8 exhibited a remarkable increase in all inflammatory groups except the 1-ng/ml inflammatory group on day 3. COL10 expression declined in inflammatory groups on day 7.

NO and GAG Release

The conditioned medium of each explant was collected at each medium change. Accumulative amounts of NO, a marker reflecting the inflammation microenvironment, were determined in supernatant medium. From day 1 on, accumulative NO levels were significantly higher in all cytokine-induced groups compared to the

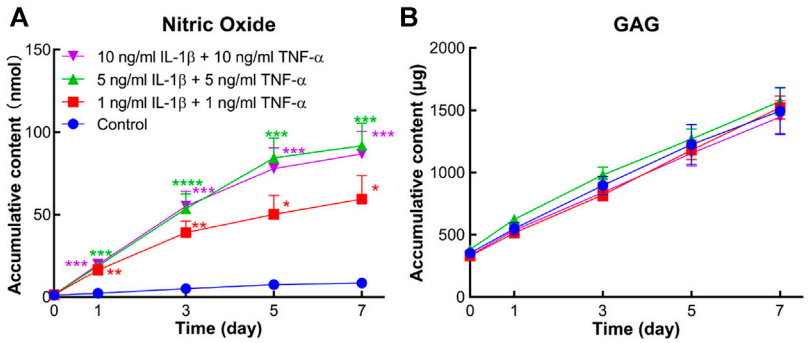

FIGURE 5 | Accumulative amount of nitric oxide (NO) and sulfated glycosaminoglycan (GAG) in the conditioned medium of human osteochondral explants stimulated by different concentrations of IL-1β and TNF-α. **(A)** Accumulative amount of NO in the control group and cytokine-stimulated groups (n = 6–11). **(B)** Accumulative amount of GAG in the above groups (n = 6–11). Statistical analysis at each time point was performed by one-way analysis of variance (ANOVA) or Kruskal–Wallis test. Data presented as means +SEM. *p < 0.05, **p < 0.01, ***p < 0.001, ****p < 0.0001 vs. control group.

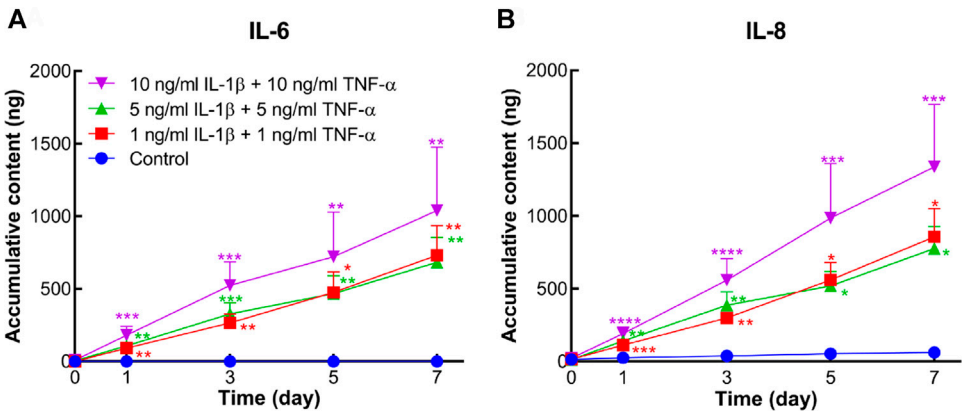

FIGURE 6 | Accumulative amount of IL-6 and IL-8 released into the conditioned medium of human osteochondral explants stimulated by different concentrations of IL-1β and TNF-α. **(A)** Accumulative amount of IL-6 in the control group and cytokine-stimulated groups (n = 6–10). **(B)** Accumulative amount of IL-8 in the above groups (n = 6–10). Statistical analysis at each time point was performed by the Kruskal–Wallis test. Data presented as means +SEM. *p < 0.05, **p < 0.01, ***p < 0.001, ****p < 0.0001 vs. control group.

control group (**Figure 5A**). In contrast, GAG release in the conditioned medium did not show any difference between the groups with or without stimulation by inflammatory factors (**Figure 5B**).

IL-6 and IL-8 Release

Protein levels of IL-6 and IL-8 secreted into the medium were measured by ELISA. In comparison to the control group, accumulative contents of IL-6 and IL-8 were markedly increased in all inflammatory groups from day 1 to day 7 (**Figure 6**).

Summary of the Dose-Dependent Effect of IL-1β and TNF-α on Human Osteochondral Explant Culture

To clearly delineate the effect of the dose and culture period, all the quantitative measurement results are summarized in **Table 3**, including gene expression data, inflammatory molecule release in conditioned medium, and semiquantitative Safranin O staining evaluation. For the 3-day culture period, most cartilage-related gene expression levels were not altered other than PRG4 and IL-8, although inflammatory indicators in conditioned medium were upregulated and proteoglycan degradation was significantly enhanced. For the 7-day culture duration, the changes in the cartilage were obviously significant from aspects of transcription level as well as medium and histological analysis. Moreover, a dose-dependent correlation was presented between gene expression and concentrations of inflammatory cytokines. With 1 ng/ml IL-1β and 1 ng/ml TNF-α, no changes were observed in gene expressions of ACAN, PRG4, MMP1, and IL6, while the concentrations at 5 and 10 ng/ml induced similarly significant results.

DISCUSSION

Through encouraging research and development, several potential DMOADs have been found in experimental OA models based on animal studies (Cai et al., 2021). However,

TABLE 3 | Summary of results in the ex vivo inflammatory OA model.

Groups		Gene expression								ELISA		NO	Safranin O staining
		ACAN	PRG4	COL2	COL10	MMP1	MMP3	IL-6	IL-8	IL-6	IL-8		
Day3	Control												
	1 ng/ml (IL-1β+TNF-α)		↓							↑	↑	↑	
	5 ng/ml (IL-1β+TNF-α)		↓						↑	↑	↑	↑	
	10 ng/ml (IL-1β+TNF-α)		↓				↑		↑	↑	↑	↑	↓
Day7	Control												
	1 ng/ml (IL-1β+TNF-α)			↓	↓		↑		↑	↑	↑	↑	
	5 ng/ml (IL-1β+TNF-α)	↓	↓	↓	↓	↑		↑	↑	↑	↑	↑	↓
	10 ng/ml (IL-1β+TNF-α)	↓	↓	↓	↓	↑		↑	↑	↑	↑	↑	↓

"↓" means significant downregulation vs. control group; "↑" means significant upregulation vs. control group.

their translation to clinical practice is still challenging due to species variances. Cartilage thickness and anatomy of knee/stifle joints vary widely between human and animals (McCoy, 2015). Seok et al. found that genomic responses in mouse models poorly simulated inflammatory diseases in humans (Seok et al., 2013). Establishing an appropriate OA model that could accurately mimic human OA phenotypes is indispensable and invaluable for OA drug development. Given that low-grade inflammation is pivotal in OA initiation and development (Robinson et al., 2016), we sought to establish an *ex vivo* inflammatory OA model with specimens from the human femoral head, which were stimulated by different concentrations of IL-1β in combination with TNF-α. Our results showed that tissue viability could be maintained during the culture period. Cartilage of these explants presented a similar inflammatory response like in human OA joints with respect to findings of histology, gene expression, and analysis of supernatant conditioned medium (Martel-Pelletier et al., 2016; Robinson et al., 2016; Boffa et al., 2020).

Most osteochondral explants previously used as *ex vivo* models have originated from animal joints (Maglio et al., 2019), which could only partially represent the response of human cartilage in joint diseases. It would be ideal to have healthy osteochondral tissue as a control group. However, due to the limited access to healthy human osteochondral explants, this was not feasible in the current study. In this work, only the osteochondral tissue with intact cartilage surface was extracted from the femoral head. For the same donor, one or two explants were disposed into each experimental group to minimize the variation among donors. Furthermore, a single stimulation by IL-1β or TNF-α has represented the most popular method to induce an *in vitro* or *ex vivo* OA-like condition (Johnson et al., 2016; He et al., 2020). However, IL-1β and TNF-α seem to be equivalently important during OA progression (Loeser et al., 2016; Robinson et al., 2016). IL-1β and TNF-α in combination are expected to induce a more extensive response of cartilage cells, which should mimic a microenvironment more similar to the OA joints. Since their combination has not been tested before in an inflammatory *ex vivo* model, different concentrations (1, 5, and 10 ng/ml) and culture durations (3 and 7 days) were assessed in our study to compare their effect on human osteochondral explant cultures. In terms of histology results and conditioned medium analysis, all cytokine-stimulated groups showed different levels of OA-like response at both day 3 and day 7. Furthermore, the Safranin O-negatively stained area in histology showed significant differences among different treatment groups on day 7. As for gene expression, the findings presented a large variance among different donors. This may be inevitable for human samples because each donor owned different age, gender, health condition, and Kellgren–Lawrence OA classification in the hip. For the 3-day culture, PRG4 was the sole gene with a remarkable change in all inflammatory groups. PRG4, also known as lubricin, is predominantly produced by superficial zone chondrocytes to protect the cartilage surface from damage (Li et al., 2007; Jay and Waller, 2014). In our model, chondrocytes in the superficial zone of explants were more vulnerable to inflammatory stimulation supplemented in the medium. Thus, the PRG4 gene expression presented an early downregulation. Groups stimulated by 1 ng/ml IL-1β and 1 ng/ml TNF-α still showed remarkable changes in anabolic gene (COL2), catabolic gene (MMP3), and inflammatory gene expression (IL-8) on day 7. These results suggested that the combination of 1 ng/ml IL-1β and 1 ng/ml TNF-α was sufficient to induce a certain grade of inflammatory and catabolic effect on human osteochondral explants after 7 days of culture. Furthermore, inflammatory cytokines at the concentration of 5 ng/ml demonstrated more profound inflammatory and catabolic effects, as indicated by significant downregulation of ACAN and PRG4 gene expression, upregulation of MMP1 and IL6 gene expression, and depletion of proteoglycan in the cartilage layer. Inflammatory cytokines at the concentration of 10 ng/ml showed comparable results as the 5 ng/ml group. These results indicated that IL-1β and TNF-α at 1 ng/ml may be used to induce a mild inflammatory OA condition, whereas the concentrations of 5 and 10 ng/ml mimic a severe inflammatory OA condition on the human osteochondral explant.

The expression of COL10, a chondrocyte hypertrophy marker (van der Kraan and van den Berg, 2012), was previously reported to be upregulated in OA cartilage (He et al., 2019). However, a decrease in COL10 expression in inflammatory OA groups was observed in the current study. Most research data demonstrating upregulation of COL10 in OA cartilage were based on *in vivo* studies rather than *ex vivo* experiments. This discrepancy on COL10 expression in OA condition may be due to the species or model differences, which need to be further elucidated in future studies. MMP13, ADAMTS4, and ADAMTS5 were all reported to be elevated in OA (Malemud, 2019), but remained unchanged in our study (**Supplementary Figure S1**). We considered the reason to be that the baseline of these genes in the explants may already have been too high to induce remarkable changes within such short stimulation duration. The unchanged

expression of these genes, mainly responsible for disintegrating GAG in cartilage extracellular matrix (Yang et al., 2017; Malemud, 2019), may partially explain the similar GAG amount released into conditioned medium of untreated and cytokine-treated groups. Additionally, there may exist differences in the detection methods between Safranin O staining and DMMB. Safranin O staining can reveal local proteoglycan degradation difference in a small region (superficial zone of the cartilage), while small differences of released GAG into the conditioned medium may not be detectable by the DMMB method. If GAG catabolically released in the medium was comparable in all groups, the proteoglycan in the cartilage after cytokine treatment could also be decreased because the anabolic gene expression level (ACAN) was also downregulated in the treated groups. Houtman *et al.* also reported unchanged GAG amounts in all groups of human osteochondral explants after the 6-day treatment, but a significant elevation among different groups from day 10 (Houtman et al., 2021). These results indicated that a longer culture period may be needed to observe a difference in GAG release in our model.

There are some limitations in the current study. One weakness of the proposed model concerns the scalability, donor variability, and dependency of patients undergoing joint replacement surgery. Another limitation of this work is that it focuses on osteochondral tissue responses in an artificial setting. The role of mechanical loading, angiogenesis, or cross talk with synovial tissue and fluid cannot be considered under the described culture conditions. The influence of synovial inflammation on osteochondral tissues could, however, be investigated by coculture experiments or stimulation with conditioned medium. Adaptation of the explant model to a mechanical loading bioreactor commonly used for 3D-tissue engineering constructs (Li et al., 2010) might enable the evaluation of tissue responses under physiological and pathological joint loading conditions.

In our current study, inflammatory cytokines were added at every medium change. For longer culture periods of more than 7 days, we also suggest this method in order to achieve stable osteoarthritic conditions. One of our previous studies (Du et al., 2020) showed that the inflammatory phenotype of human cartilaginous tissue cells would be mitigated in the group of TNF-α stimulation for 24 h followed by basal medium without TNF-α for 24 h, in comparison to the group of TNF-α stimulation for 48 h. For drug screening using our model, intervention with drugs at the beginning can be performed to assess the anti-inflammatory or inflammation prevention effects of drugs at the early phase of OA, while treatment with drugs after 7 days can evaluate their therapeutic effects on midterm or end-stage OA. The time points of drug application can be selected according to the aim of the specific study.

The inflammatory OA *ex vivo* model established in this study will have many applications in OA research. Firstly, OA-related genes or proteins, discovered by animal studies, could be tested with human osteochondral explant samples to evaluate their clinical relevance. Secondly, novel signaling pathways associated with OA disease mechanisms can be studied. Small molecules or drugs which are potential DMOADs could be evaluated using this preclinical explant model. Future research may include the analysis of the subchondral bone to investigate the interplay between cartilage and bone tissue in OA progression. The osteochondral explants can also be cocultured with synovium or fat tissue to explore the mechanism of OA as a joint disease in a more complex setting. Last but not least, physical stimulations like mechanical loading imposed by bioreactors could be substitutes of cytokines to mimic other clinical OA subtypes or investigated as complementary therapeutic measure (Ossendorff et al., 2018).

CONCLUSION

An *ex vivo* inflammatory OA model was established with explants from the human femoral head by stimulation with IL-1β in combination with TNF-α at a low concentration. The inflammatory OA model could be utilized as a preclinical tool to uncover the underlying OA mechanism and screen new drugs for treatment as there is no species barrier for clinical translation.

DATA AVAILABILITY STATEMENT

The original contributions presented in the study are included in the article/**Supplementary Material**; further inquiries can be directed to the corresponding author.

ETHICS STATEMENT

The studies involving human participants were reviewed and approved by the Swiss Graubünden cantonal ethical commission (KEK-ZH-NR: 2010-0444/0). The patients/participants provided their written informed consent to participate in this study.

AUTHOR CONTRIBUTIONS

PZ, SG, and ZL contributed to the design of the work; KL, PZ, and ZL contributed to the acquisition, analysis, and interpretation of data for the work; KL drafted the manuscript; KL, PZ, YZ, MA, SG, and ZL revised the manuscript critically; and all authors provided approval for publication of the content.

FUNDING

This study was funded by AO Foundation. KL was funded by the China Scholarship Council (CSC).

SUPPLEMENTARY MATERIAL

The Supplementary Material for this article can be found online at: https://www.frontiersin.org/articles/10.3389/fbioe.2021.787020/full#supplementary-material

REFERENCES

Boffa, A., Merli, G., Andriolo, L., Lattermann, C., Salzmann, G. M., and Filardo, G. (2020). Synovial Fluid Biomarkers in Knee Osteoarthritis: A Systematic Review and Quantitative Evaluation Using BIPEDs Criteria. *Cartilage*, 194760352094294. doi:10.1177/1947603520942941

Cai, X., Yuan, S., Zeng, Y., Wang, C., Yu, N., and Ding, C. (2021). New Trends in Pharmacological Treatments for Osteoarthritis. *Front. Pharmacol.* 12, 645842. doi:10.3389/fphar.2021.645842

Caprez, S., Menzel, U., Li, Z., Grad, S., Alini, M., and Peroglio, M. (2018). Isolation of High-quality RNA from Intervertebral Disc Tissue via Pronase Predigestion and Tissue Pulverization. *JOR Spine* 1 (2), e1017. doi:10.1002/jsp2.1017

Cope, P. J., Ourradi, K., Li, Y., and Sharif, M. (2019). Models of Osteoarthritis: the Good, the Bad and the Promising. *Osteoarthritis and Cartilage* 27 (2), 230–239. doi:10.1016/j.joca.2018.09.016

Coryell, P. R., Diekman, B. O., and Loeser, R. F. (2021). Mechanisms and Therapeutic Implications of Cellular Senescence in Osteoarthritis. *Nat. Rev. Rheumatol.* 17 (1), 47–57. doi:10.1038/s41584-020-00533-7

Du, J., Pfannkuche, J. J., Lang, G., Häckel, S., Creemers, L. B., Alini, M., et al. (2020). Proinflammatory Intervertebral Disc Cell and Organ Culture Models Induced by Tumor Necrosis Factor Alpha. *JOR Spine* 3 (3), e1104. doi:10.1002/jsp2.1104

Geurts, J., Jurić, D., Müller, M., Schären, S., and Netzer, C. (2018). Novel *Ex Vivo* Human Osteochondral Explant Model of Knee and Spine Osteoarthritis Enables Assessment of Inflammatory and Drug Treatment Responses. *Ijms* 19 (5), 1314. doi:10.3390/ijms19051314

He, Y., Li, Z., Alexander, P. G., Ocasio-Nieves, B. D., Yocum, L., Lin, H., et al. (2020). Pathogenesis of Osteoarthritis: Risk Factors, Regulatory Pathways in Chondrocytes, and Experimental Models. *Biology* 9 (8), 194. doi:10.3390/biology9080194

He, Y., Manon-Jensen, T., Arendt-Nielsen, L., Petersen, K. K., Christiansen, T., Samuels, J., et al. (2019). Potential Diagnostic Value of a Type X Collagen Neo-Epitope Biomarker for Knee Osteoarthritis. *Osteoarthritis and Cartilage* 27 (4), 611–620. doi:10.1016/j.joca.2019.01.001

Houtman, E., van Hoolwerff, M., Lakenberg, N., Suchiman, E. H. D., van der Linden-van der Zwaag, E., Nelissen, R. G. H. H., et al. (2021). Human Osteochondral Explants: Reliable Biomimetic Models to Investigate Disease Mechanisms and Develop Personalized Treatments for Osteoarthritis. *Rheumatol. Ther.* 8 (1), 499–515. doi:10.1007/s40744-021-00287-y

Humpenöder, M., Corte, G. M., Pfützner, M., Wiegard, M., Merle, R., Hohlbaum, K., et al. (2021). Alternatives in Education-Rat and Mouse Simulators Evaluated from Course Trainers' and Supervisors' Perspective. *Animals* 11 (7), 1848. doi:10.3390/ani11071848

Jähn, K., and Stoddart, M. J. (2011). Viability Assessment of Osteocytes Using Histological Lactate Dehydrogenase Activity Staining on Human Cancellous Bone Sections. *Methods Mol. Biol.* 740, 141–148. doi:10.1007/978-1-61779-108-6_15

Jay, G. D., and Waller, K. A. (2014). The Biology of Lubricin: Near Frictionless Joint Motion. *Matrix Biol.* 39, 17–24. doi:10.1016/j.matbio.2014.08.008

Johnson, C. I., Argyle, D. J., and Clements, D. N. (2016). *In Vitro* models for the Study of Osteoarthritis. *Vet. J.* 209, 40–49. doi:10.1016/j.tvjl.2015.07.011

Kellgren, J. H., and Lawrence, J. S. (1957). Radiological Assessment of Osteo-Arthrosis. *Ann. Rheum. Dis.* 16 (4), 494–502. doi:10.1136/ard.16.4.494

Kleuskens, M. W. A., Donkelaar, C. C., Kock, L. M., Janssen, R. P. A., and Ito, K. (2021). An *Ex Vivo* Human Osteochondral Culture Model. *J. Orthop. Res.* 39 (4), 871–879. doi:10.1002/jor.24789

Li, Z., Kupcsik, L., Yao, S.-J., Alini, M., and Stoddart, M. J. (2010). Mechanical Load Modulates Chondrogenesis of Human Mesenchymal Stem Cells through the TGF-β Pathway. *J. Cel Mol Med* 14 (6A), 1338–1346. doi:10.1111/j.1582-4934.2009.00780.x

Li, Z., Yao, S., Alini, M., and Grad, S. (2007). Different Response of Articular Chondrocyte Subpopulations to Surface Motion. *Osteoarthritis and Cartilage* 15 (9), 1034–1041. doi:10.1016/j.joca.2007.03.001

Loeser, R. F., Collins, J. A., and Diekman, B. O. (2016). Ageing and the Pathogenesis of Osteoarthritis. *Nat. Rev. Rheumatol.* 12 (7), 412–420. doi:10.1038/nrrheum.2016.65

Maglio, M., Brogini, S., Pagani, S., Giavaresi, G., and Tschon, M. (2019). Current Trends in the Evaluation of Osteochondral Lesion Treatments: Histology, Histomorphometry, and Biomechanics in Preclinical Models. *Biomed. Res. Int.* 2019, 1–27. doi:10.1155/2019/4040236

Malemud, C. J. (2019). Inhibition of MMPs and ADAM/ADAMTS. *Biochem. Pharmacol.* 165, 33–40. doi:10.1016/j.bcp.2019.02.033

Martel-Pelletier, J., Barr, A. J., Cicuttini, F. M., Conaghan, P. G., Cooper, C., Goldring, M. B., et al. (2016). Osteoarthritis. *Nat. Rev. Dis. Primers* 2, 16072. doi:10.1038/nrdp.2016.72

McCoy, A. M. (2015). Animal Models of Osteoarthritis. *Vet. Pathol.* 52 (5), 803–818. doi:10.1177/0300985815588611

Oo, W. M., Little, C., Duong, V., and Hunter, D. J. (2021). The Development of Disease-Modifying Therapies for Osteoarthritis (DMOADs): The Evidence to Date. *Dddt* Vol. 15, 2921–2945. doi:10.2147/DDDT.S295224

Ossendorff, R., Grad, S., Stoddart, M. J., Alini, M., Schmal, H., Südkamp, N., et al. (2018). Autologous Chondrocyte Implantation in Osteoarthritic Surroundings: TNFα and its Inhibition by Adalimumab in a Knee-specific Bioreactor. *Am. J. Sports Med.* 46 (2), 431–440. doi:10.1177/0363546517737497

Peat, G., and Thomas, M. J. (2021). Osteoarthritis Year in Review 2020: Epidemiology & Therapy. *Osteoarthritis and Cartilage* 29 (2), 180–189. doi:10.1016/j.joca.2020.10.007

Robinson, W. H., Lepus, C. M., Wang, Q., Raghu, H., Mao, R., Lindstrom, T. M., et al. (2016). Low-grade Inflammation as a Key Mediator of the Pathogenesis of Osteoarthritis. *Nat. Rev. Rheumatol.* 12 (10), 580–592. doi:10.1038/nrrheum.2016.136

Safiri, S., Kolahi, A.-A., Smith, E., Hill, C., Bettampadi, D., Mansournia, M. A., et al. (2020). Global, Regional and National burden of Osteoarthritis 1990-2017: a Systematic Analysis of the Global Burden of Disease Study 2017. *Ann. Rheum. Dis.* 79 (6), 819–828. doi:10.1136/annrheumdis-2019-216515

Schwab, A., Meeuwsen, A., Ehlicke, F., Hansmann, J., Mulder, L., Smits, A., et al. (2017). *Ex Vivo* culture Platform for Assessment of Cartilage Repair Treatment Strategies. *ALTEX* 34 (2), 267–277. doi:10.14573/altex.1607111

Seok, J., Warren, H. S., Cuenca, A. G., Mindrinos, M. N., Baker, H. V., Xu, W., et al. (2013). Genomic Responses in Mouse Models Poorly Mimic Human Inflammatory Diseases. *Proc. Natl. Acad. Sci. U S A.* 110 (9), 3507–3512. doi:10.1073/pnas.1222878110

Shi, Y., Hu, X., Cheng, J., Zhang, X., Zhao, F., Shi, W., et al. (2019). A Small Molecule Promotes Cartilage Extracellular Matrix Generation and Inhibits Osteoarthritis Development. *Nat. Commun.* 10 (1), 1914. doi:10.1038/s41467-019-09839-x

Teeple, E., Jay, G. D., Elsaid, K. A., and Fleming, B. C. (2013). Animal Models of Osteoarthritis: Challenges of Model Selection and Analysis. *AAPS J.* 15 (2), 438–446. doi:10.1208/s12248-013-9454-x

van der Kraan, P. M., and van den Berg, W. B. (2012). Chondrocyte Hypertrophy and Osteoarthritis: Role in Initiation and Progression of Cartilage Degeneration? *Osteoarthritis and Cartilage* 20 (3), 223–232. doi:10.1016/j.joca.2011.12.003

Yang, C.-Y., Chanalaris, A., and Troeberg, L. (2017). ADAMTS and ADAM Metalloproteinases in Osteoarthritis - Looking beyond the 'usual Suspects'. *Osteoarthritis and Cartilage* 25 (7), 1000–1009. doi:10.1016/j.joca.2017.02.791

Conflict of Interest: The authors declare that the research was conducted in the absence of any commercial or financial relationships that could be construed as a potential conflict of interest.

Publisher's Note: All claims expressed in this article are solely those of the authors and do not necessarily represent those of their affiliated organizations, or those of the publisher, the editors and the reviewers. Any product that may be evaluated in this article, or claim that may be made by its manufacturer, is not guaranteed or endorsed by the publisher.

Copyright © 2021 Li, Zhang, Zhu, Alini, Grad and Li. This is an open-access article distributed under the terms of the Creative Commons Attribution License (CC BY). The use, distribution or reproduction in other forums is permitted, provided the original author(s) and the copyright owner(s) are credited and that the original publication in this journal is cited, in accordance with accepted academic practice. No use, distribution or reproduction is permitted which does not comply with these terms.

frontiers in Bioengineering and Biotechnology

ORIGINAL RESEARCH
published: 28 January 2022
doi: 10.3389/fbioe.2021.802789

Interleukin-1β More Than Mechanical Loading Induces a Degenerative Phenotype in Human Annulus Fibrosus Cells, Partially Impaired by Anti-Proteolytic Activity of Mesenchymal Stem Cell Secretome

Raquel M. Gonçalves[1,2,3,4], Taryn Saggese[1], Zhiyao Yong[1], Joana R. Ferreira[2,3,4], Anita Ignatius[1], Hans-Joachim Wilke[1], Cornelia Neidlinger-Wilke[1†] and Graciosa Q. Teixeira[1†]*

[1]Institute of Orthopaedic Research and Biomechanics, Trauma Research Centre, Ulm University, Ulm, Germany, [2]Instituto de Investigação e Inovação Em Saúde (i3S), Universidade Do Porto, Porto, Portugal, [3]Instituto de Engenharia Biomédica (INEB), Universidade Do Porto, Porto, Portugal, [4]Instituto de Ciências Biomédicas Abel Salazar (ICBAS), Universidade do Porto, Porto, Portugal

OPEN ACCESS

Edited by:
Rahul Gawri,
McGill University, Canada

Reviewed by:
Yong-Can Huang,
Peking University Shenzhen Hospital, China
Diane Gregory,
Wilfrid Laurier University, Canada

***Correspondence:**
Graciosa Q. Teixeira
graciosa.teixeira@uni-ulm.de

[†]These authors have contributed equally to this work and share last authorship

Specialty section:
This article was submitted to Biomaterials, a section of the journal Frontiers in Bioengineering and Biotechnology

Received: 27 October 2021
Accepted: 27 December 2021
Published: 28 January 2022

Citation:
Gonçalves RM, Saggese T, Yong Z, Ferreira JR, Ignatius A, Wilke H-J, Neidlinger-Wilke C and Teixeira GQ (2022) Interleukin-1β More Than Mechanical Loading Induces a Degenerative Phenotype in Human Annulus Fibrosus Cells, Partially Impaired by Anti-Proteolytic Activity of Mesenchymal Stem Cell Secretome. Front. Bioeng. Biotechnol. 9:802789. doi: 10.3389/fbioe.2021.802789

Mesenchymal stem/stromal cell (MSC)–based therapies for low back pain and intervertebral disc (IVD) degeneration have been emerging, despite the poor knowledge of their full mechanism of action. As failure of the annulus fibrosus (AF) is often associated with IVD herniation and inflammation, the objective of the present study was to investigate the impact of the MSC secretome on human AF cells exposed to mechanical loading and a pro-inflammatory environment. Human AF cells isolated from IVD biopsies from patients with adolescent idiopathic scoliosis (AIS) or disc degeneration (DD) were exposed to physiological cyclic tensile strain (CTS) for 72 h in a custom-made device, with or without interleukin (IL)-1β medium supplementation. AF cells stimulated with CTS + IL-1β were then treated with secretome from IL-1β–preconditioned MSCs for 48 h. AF cell metabolic activity, gene expression, protein secretion, matrix metalloproteinase (MMP) activity, and tissue inhibitor of MMPs (TIMP) concentration were evaluated. Expanded AF cells from AIS and DD patients revealed similar metabolic activity and gene expression profiles. CTS stimulation upregulated collagen type I (*COL1A1*) expression, while IL-1β significantly stimulated *IL-6*, *IL-8*, *MMP-1*, and *MMP-3* gene expression and prostaglandin E_2 production by AF cells but downregulated *COL1A1*. The combination of CTS + IL-1β had a similar outcome as IL-1β alone, accompanied by a significant upregulation of elastin. The MSC secretome did not show any immunomodulatory effect on CTS + IL-1β–stimulated AF cells but significantly decreased *MMP-1*, MMP-2, *MMP-3*, and *MMP-9*, while increasing the production of TIMP-1. The obtained results demonstrate a stronger impact of the inflammatory milieu on human AF cells than upper physiologic mechanical stress. In addition, a new MSC mechanism of action in degenerated IVD consisting of the modulation

of AF MMP activity was also evidenced, contributing to the advancement of knowledge in AF tissue metabolism.

Keywords: disc degeneration, disc herniation, annulus fibrosus cells, mechanical loading, inflammation, mesenchymal stem cells, secretome, matrix metalloproteinases

INTRODUCTION

Low back pain (LBP) is one of the top 10 disorders in the number of years lived with disability for adolescents and young adults (from 10 to 49 years old), affecting 70–85% of the world population and compromising healthy aging (Vos et al., 2020). LBP can be considered a multifactorial disorder but has been strongly associated with degeneration of the intervertebral disc (IVD). Current therapies include physical therapy or anti-inflammatory drugs, and if LBP does not improve, invasive surgery such as discectomy, spinal fusion, or IVD prosthesis can be used (Maher et al., 2017). Such treatments may alleviate LBP symptoms but reduce patients' mobility, might be temporary, and, overall, do not target the underlying problem.

The outer ring of the IVD, the annulus fibrosus (AF), consists of concentric collagen fibers interconnected by a network of elastin and fibrillin, interrupted at distinct locations by a zone that links the different lamellae, known as the translamellar bridging network (TBLN). AF failure is often associated with structural weakness in restraining the hydrated inner structure, the nucleus pulposus (NP). Factors that induce AF failure include mechanical stress, which has been previously shown to increase pro-inflammatory gene expression in human AF cells (Pratsinis et al., 2016). Mechanical loading appears to act synergistically with a pro-inflammatory environment, weakening the AF through TBLN deregulation (Saggese et al., 2019). But moderate mechanical stress has also shown to rescue pro-inflammatory gene expression of AF cells exposed to a pro-inflammatory stimulus (Zhang et al., 2021). Overall, the pathomechanism of AF mechanical weakening and consequent disc herniation remains to be fully understood.

IVD herniation involves alterations in the AF but also in the NP, including loss of proteoglycans and water content, upregulation of matrix metalloproteinases (MMP-1, -2, -3, -9, among others) and inflammatory mediators (tissue necrosis factor (TNF)-α, interleukin (IL)-1β, etc) that contribute to the weakening and mechanical failure of the disc tissue (Risbud and Shapiro, 2014). More recently, the complement activation product terminal complement complex (TCC), an inflammatory trigger, has also been suggested to be involved in the disease progression (Teixeira et al., 2021a). Unbalanced production of MMPs weakens the IVD extracellular matrix (ECM), which can lead to NP extrusion through the AF, ultimately leading to lumbar disc herniation (LDH). LDH accounts only for 5–15% of LBP cases but can induce sciatica symptoms and loss of bladder/bowel control and is the main cause of spine surgery (Weinstein et al., 2008). Moreover, about 18% of patients present signs of IVD re-herniation after surgery (Shin et al., 2019). Early treatment to reinforce AF in LDH would be an important strategy to prevent disease progression.

Cell-based therapies are emerging to treat LBP and IVD degeneration. In particular, mesenchymal stem/stromal cell (MSC)–based therapies have been shown to promote ECM synthesis in NP and increase disc height in small animal models (Sakai et al., 2006). MSC intravenous administration has also shown to reduce IVD herniation in a rat model of punctured IVD (Cunha et al., 2017). In the clinical trials conducted so far, MSC transplantation appears to be safe and patients reported less pain, but no significant alterations in the IVD were observed (Orozco et al., 2011; Noriega et al., 2017). This discrepancy between animals and humans might be due to the fact that the former lacks the biped position of the human spine and retain a large population of notochordal cells, thus a higher regenerative capacity. In a pro-inflammatory environment characteristic of the degenerated IVD, we have demonstrated that MSCs have been shown to have immunomodulatory features, and we hypothesize that this may occur via a paracrine mechanism (Teixeira et al., 2018). Recently, we have shown that MSC secretome, obtained upon IL-1β preconditioning, also reduces pro-inflammatory markers in both NP and AF organ cultures (Ferreira et al., 2021; Neidlinger-Wilke et al., 2021). Nevertheless, as these studies were conducted in a bovine model, the direct clinical translation may have some restraints. In fact, MSCs and their secretome can be highly influenced by the cells' microenvironment, as reviewed by Ferreira et al. (2018). The degenerated IVD is a harsh biochemical and biomechanical condition, with acidic pH, high concentration of pro-inflammatory factors, and matrix-degrading enzymes, under high and complex mechanical loading. This environment is a challenge for the successful translation of cell therapies, including those with MSCs. Additionally, more complex *in vitro* studies are needed which take the multifaceted IVD environment and the interaction of the different influencing factors into account. In this study, we hypothesized that 1) a synergistic action between mechanical loading and a pro-inflammatory microenvironment can deregulate human AF cell phenotypes, and 2) the MSC secretome has an immunomodulatory impact on human AF cell metabolism.

MATERIALS AND METHODS

MSC Expansion and Secretome Production

Human MSCs (Lonza, $n = 3$, donor information is summarized in **Supplementary Table S1**) were seeded (3,000 cells/cm^2) and routinely expanded in MSC medium composed of low-glucose Dulbecco's modified Eagle medium (DMEM, Gibco) supplemented with 10% fetal bovine serum (FBS, HyClone), 1% penicillin/streptomycin (10,000 U/mL—10 mg/ml, Gibco),

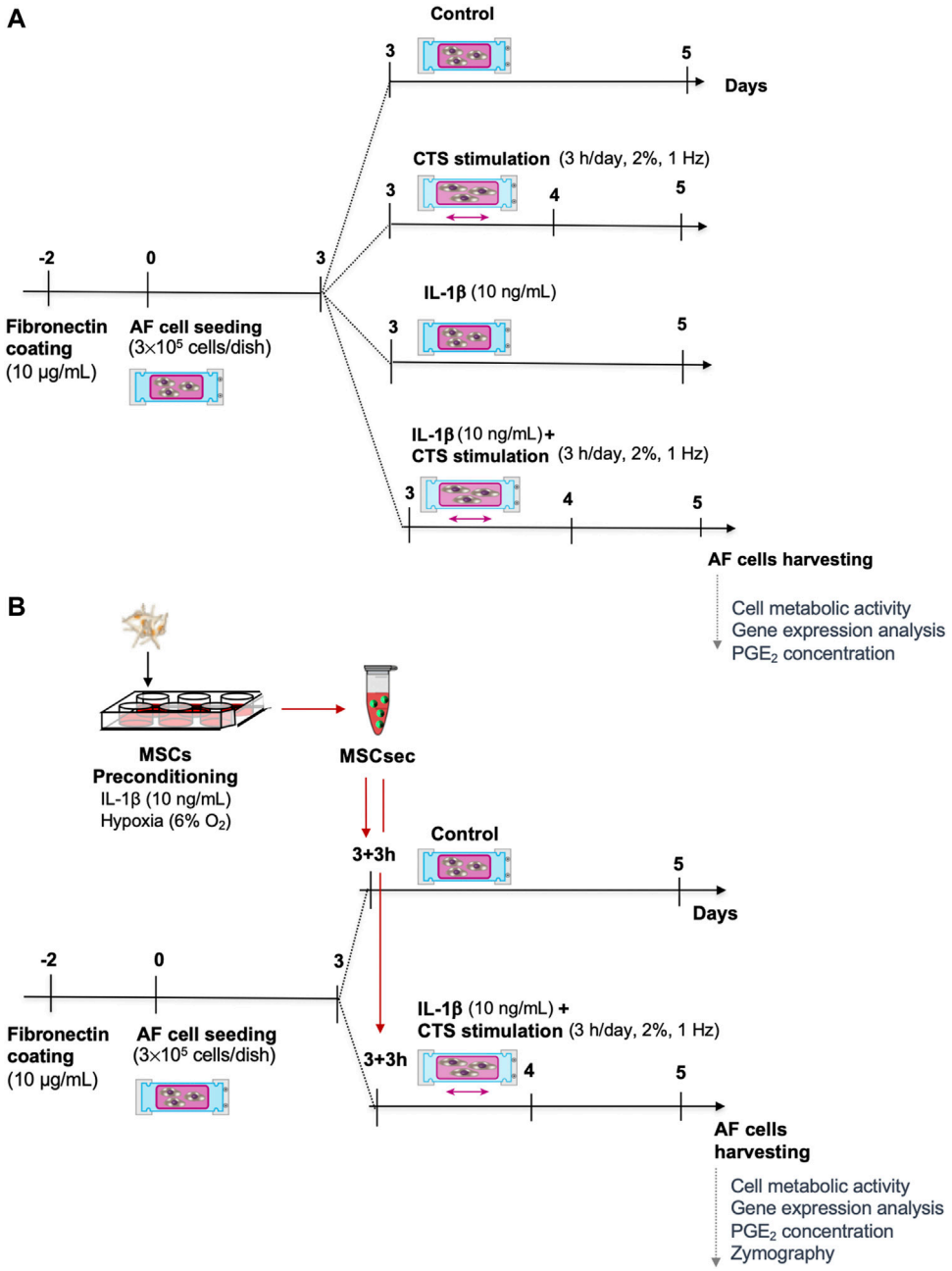

FIGURE 1 | Experimental timeline. **(A)** Human annulus fibrosus (AF) cells were cultured in a custom-made electromechanical device for the application of cyclic tensile strain (CTS) to deformable silicone dishes, with IL-1β (10 ng/ml) or with CTS + IL-1β. **(B)** The CTS + IL-1β–stimulated AF cells were treated with secretome from human bone marrow–derived mesenchymal stem/stromal cells (MSC) upon preconditioning with IL-1β for 48 h.

and 0.5% amphotericin B (250 µg/ml, Gibco), at 37°C, 21% oxygen and humidified atmosphere. The medium was exchanged twice a week, and cells were trypsinized when reaching 70% confluency. For secretome production, $1x10^6$ MSCs (passage 5–9) were seeded in 6-well plates (Corning) and incubated in 5 ml of MSC medium supplemented with recombinant human IL-1β (10 ng/ml, R&D Systems), at 37°C in a humidified atmosphere with 6% O_2 and 8.5% CO_2 for 48 h, as previously optimized for MSC preconditioning (Ferreira et al., 2021). MSC secretome (MSCsec) was collected by centrifugation at 1800 *g* for 5 min, at 4°C, to remove cell debris and then stored at −80°C until further use.

Human AF Cell Isolation and Culture

Human AF cells were isolated from a total of 12 patients undergoing surgery in the lumbar region: six samples from

patients with adolescent idiopathic scoliosis (AIS, age: 16 ± 2 years old, 4 males/2 females), and six samples from patients with disc degeneration (DD, age: 65 ± 11 years old, 5 males/1 female, Pfirrmann grades IV-V). Detailed patient information is summarized in **Supplementary Table S2**. Open surgery was performed to remove the disc tissue. The AF tissue was macroscopically separated from the cartilaginous endplate and NP, as previously described (Teixeira et al., 2021a; Teixeira et al., 2021b). Visibly fibrous tissue with a clearly identifiable lamellar structure was selected for AF cell isolation. AF cells were obtained upon enzymatic digestion of the tissue for 3–5 h in 0.8 mg/ml collagenase type II (Sigma-Aldrich) in IVD medium without FBS: low-glucose DMEM (Gibco) supplemented with 1% non-essential amino acids (Biochrom), 1% penicillin/streptomycin, 5% amphotericin B, and 1.5% 5M NaCl/0.4 M KCl solution (to adjust osmolarity to 400 mOsm), under agitation, reduced oxygen supply (6% O2 and 8.5% CO2), 37°C, and saturated humidity. Cells were then expanded under sterile conditions in IVD medium containing 5% FBS Superior (Biochrom), as previously described (Teixeira et al., 2016).

Stimulation of AF Cells With CTS and IL-1β and Treatment With MSC Secretome

Human AF cells (passages 3 to 4) were seeded in silicone dishes (300,000 cells/dish) coated with fibronectin (10 μg/ml) and placed in a custom-made cyclic tensile strain (CTS) device (Neidlinger-Wilke et al., 1994), previously modified as described (Pratsinis et al., 2016). After 3 days, the medium was exchanged, and the AF cells were stimulated for 48 h as follows: 1) 2% CTS at 1 Hz was applied 3 h/day to the silicone dishes, similar to what was previously optimized (Wuertz et al., 2007); 2) IL-1β (10 ng/ml), as previously seen to induce a pro-inflammatory response in bovine IVD organ culture (Teixeira et al., 2016); and 3) CTS (1 Hz, 3 h/day) + IL-1β (10 ng/ml). Unstimulated AF cells were kept as a control group. The experimental timeline is depicted in **Figure 1A**.

In a subsequent set of experiments, the MSC secretome was added to AF cells stimulated with CTS + IL-1β, 3 h after stretching, in a 1:1 ratio with IVD medium. The MSC secretome addition to unstimulated AF cells was used as a control. The experimental timeline is represented in **Figure 1B**.

After 48 h, AF cells and conditioned medium were collected for different analyses. Conditioned medium was removed and frozen at −80°C for posterior protein analysis by ELISAs and zymography. AF cell metabolic viability was evaluated by resazurin assay, after which cells were immediately shock frozen in RNAlater ICE (Invitrogen) and liquid nitrogen and stored at −80°C for RNA isolation.

Metabolic Activity of AF Cells

The metabolic activity of AF cells was assessed by resazurin reduction assay. AF cells were incubated with 0.02 mg/ml resazurin sodium salt (Sigma-Aldrich) solution in IVD medium for 3 h at 37°C. Fluorescence intensity was measured in a spectrophotometer microplate reader (Tecan), with 530-nm excitation and 590-nm emission filters.

Gene Expression Analysis of AF Cells

AF cells frozen in RNAlater ICE were thawed, the RNAlater was removed, and RNA was isolated using an RNeasy Mini kit (Qiagen). RNA concentration and quality were determined by spectrophotometry (Spark, Tecan). For cDNA synthesis with integrated removal of DNA contamination, 1 μg of RNA was treated with a QuantiTect Reverse Transcription kit (ThermoFisher Scientific). Gene expression analysis was performed with primers for the reference gene human glyceraldehyde 3-phosphate dehydrogenase (*GAPDH*), as well as for the target genes in **Table 1**. The transcribed cDNA was mixed with custom-designed primers and the Platinum SYBR Green qPCR SuperMix-UDG (Invitrogen) and ROX Reference Dye (Invitrogen). The runs were performed in a QuantStudio 3 real-time PCR system (Applied Biosystems). The melt curves were analyzed to confirm the specificity of the reaction and a quantification cycle (Cq) 35 cutoff was used. Relative expression levels were calculated by using the Livak method (using the $2^{-\Delta\Delta Ct}$), where $\Delta\Delta Ct = \Delta Ct_{(\text{sample of interest})} - \Delta Ct_{(\text{control sample})}$ and $\Delta Ct = Ct_{(\text{gene of interest})} - Ct_{(GAPDH)}$ (Livak and Schmittgen, 2001).

Quantification of PGE_2 and TIMPs in AF Culture Supernatants

The concentration of prostaglandin E_2 (PGE_2, Arbor Assays), human TIMP-1, TIMP-2, TIMP-3, and TIMP-4 (RayBiotech) was measured by using enzyme-linked immunosorbent assay (ELISA) kits according to the manufacturers' instructions in AF supernatants, after 5 days of culture.

Zymography

The MMP activity of AF cells was investigated by analyzing the conditioned medium through gelatin zymography, as previously described (Cardoso et al., 2014). Briefly, the total protein content in the conditioned medium was determined by bicinchoninic acid assay (Bio-Rad), and 15–20 mg of protein was mixed with sample buffer (10% sodium dodecyl sulfate, 4% sucrose, and 0.03% bromophenol blue in 0.5 M Tris–HCl, pH 6.8) and separated on 10% polyacrylamide gels containing 0.1% gelatin (Sigma-Aldrich) as substrate. After electrophoresis, gels were washed twice with 2% Triton X-100. Gelatin gels were subsequently incubated for 16 h at 37°C in 50 mM Tris–HCl, pH 7.5, and 10 mM $CaCl_2$. Gels were stained with 0.1% Coomassie Brilliant Blue R-250 (Sigma-Aldrich), 50% methanol, and 10% acetic acid (Merck). The molecular weight and activity of the MMPs were estimated by densitometric analysis.

Statistical Analysis

Results are presented as box plots with the median ± interquartile range. Statistical analysis was performed using GraphPad Prism 9 software (GraphPad Software, Inc, La Jolla, CA, United States). Normal distribution data were tested using the D'Agostino–Pearson omnibus normality test. A non-parametric unpaired Mann–Whitney test was used to compare AIS and DD samples. A non-parametric paired Friedman test, followed by Dunn's multiple comparison test, was used to compare AF cell stimuli and the effect of the MSC secretome. Significance was set at $p < 0.05$.

TABLE 1 | Human oligonucleotide primers used for qRT-PCR. Primers with shown sequence were custom designed. fw: forward; rev: reverse.

Gene	Sequence (forward and reverse primers)	Product size (bp)
BAX	fw: 5′-TGG-AGC-TGC-AGA-GGA-TGA-TTG-3′ rev: 5′-GAA-GTT-GCC-GTC-AGA-AAA-CAT-G-3′	98
CD46	fw: 5′-GTG AGG AGC CAC CAA CAT TT-3′ rev: 5′-GCG GTC ATC TGA GAC AGG T-3′	177
CD55	fw: 5′-CAG CAC CACCAC AAA TTG AC-3′ rev: 5′-CTG AAC TGT TGG TGG GAC CT-3′	215
CD59	fw: 5′-CCG CTT GAG GGA AAA TGA G-3′ rev: 5′-CAG AAA TGG AGT CAC CAG CA-3′	130
COL1A1	fw: 5′- TGA CCT CAA GAT GTG CCA CT -3′ rev: 5′-ACC AGA CAT CCC TCT TGT CC –3′	197
Elastin	fw: 5′- CTG-GCT-TTC-GGA-TTG-TCT-CC-3′ rev: 5′-CGT-TGA-TGA-GGT-CGT-GAG-TC -3′	109
Fibrillin-1	fw: 5′-CAC-CTG-TGA-GTG-TAA-TGA-TGG-3′ rev: 5′-TAG-CAC-CTC-TGT-GAA-GCA-3′	90
GAPDH	fw: 5′-TGC ACC ACC AAC TGC TTA GC-3′ rev: 5′-GGC ATG GAC TGT GGT CAT GAG-3′	87
IL-6	fw: 5′-AGG AGA CTT GCC TGG TGA AA -3′ rev: 5′-CAG GGG TGG TTA TTG CAT CT -3′	188
IL-8	fw: 5′-GTG CAG TTTT GCC AAG GAGT-3′ rev: 5′-CTC TGC ACC CAG TTT TCC TT-3′	196
MMP-1	fw: 5′-ATG CTG AAA CCC TGA AGG TG-3′ rev: 5′-CTG CTT GAC CCT CAG AGA CC-3′	234
MMP-3	fw: 5′-GGA GAT GCC CAC TTT GAT GAT-3′ rev: 5′-CAT CTT GAG ACA GGC GGA AC-3′	187

RESULTS

Viability and Inflammatory Profile of Human AF Cells Exposed to Mechanical and Inflammatory Stimuli

To evaluate the effect of mechanical loading and inflammatory stimuli on human AF cells' inflammatory profile, they were cultured in silicone dishes and stimulated with 1) CTS (2%, 1 Hz, 3 h/day), 2) IL-1β (10 ng/ml), or 3) CTS + IL-1β. Unstimulated AF cells were used as controls (**Figure 1A**). AF cells from both AIS and DD patients were used indiscriminately. We first screened AF cells from different patients for metabolic activity and gene expression profiles regarding apoptosis (*BAX*), cellular complement regulators (*CD46*, *CD55*, *CD59*), inflammatory markers (*IL-6*, *IL-8*), matrix-degrading enzymes (*MMP-1*, *MMP-3*), and ECM proteins (*COL1A1*, elastin, fibrillin-1). No differences were obtained between the different genes in AF cells from the distinct patient groups (**Supplementary Figure S1**).

To investigate whether AF cell viability was affected by the CTS or IL-1β, mitochondrial metabolic activity and gene expression of *BAX*, an apoptosis regulator member of the *BCL-2* gene family, were analyzed (**Figures 2A,B**). No differences were observed between the mitochondrial metabolic activity of the different groups. Moreover, no significant differences were observed in the gene expression of *BAX* when comparing CTS, IL-1β and CTS-IL-1β to the unstimulated control group. However, when comparing CTS + IL-1β with the single stimuli CTS and IL-1β, a significant downregulation was found in comparison to CTS ($*p < 0.05$).

Moreover, CTS + IL-1β stimulation of AF cells significantly increased the expression of the inhibitory complement receptor *CD46*, compared with the IL-1β–stimulated group ($*p < 0.05$), and of the inhibitor *CD55*, compared with the CTS group ($*p < 0.05$) and unstimulated cells ($***p < 0.001$; **Figures 2C,D**). Interestingly, IL-1β by itself also promoted a significant upregulation of *CD55* (**, $p < 0.01$) and a decrease in *CD59*, the major TCC inhibitor ($p = 0.06$), compared with control cells (**Figures 2D,E**).

Regarding the expression of inflammatory markers, as expected, IL-1β stimulation induced the upregulation of *IL-6* and *IL-8* gene expression and PGE_2 secretion by AF cells ($*p < 0.05$, $**p < 0.01$ and $***p < 0.001$, respectively) in comparison to unstimulated cells (**Figures 2F–H**). In contrast, CTS stimulation by itself was not shown to affect the production of these markers. The synergic action of mechanical and inflammatory stimuli (CTS + IL-1β) significantly upregulated *IL-6* and *IL-8* expression, compared with both unstimulated ($****p < 0.0001$) and CTS-stimulated cells ($***p < 0.001$ for *IL-6* and $**p < 0.01$ for *IL-8*), and increased PGE_2 production compared with control ($***p < 0.001$) and with CTS-stimulated cells ($**p < 0.01$).

Matrix Remodeling Capacity of Human AF Cells Exposed to Mechanical and Inflammatory Stimuli

The effect of mechanical loading and inflammatory stimuli on the production of matrix-degrading enzymes and ECM proteins by human AF cells was also evaluated. The results showed that CTS by itself does not interfere with the matrix remodeling capacity of

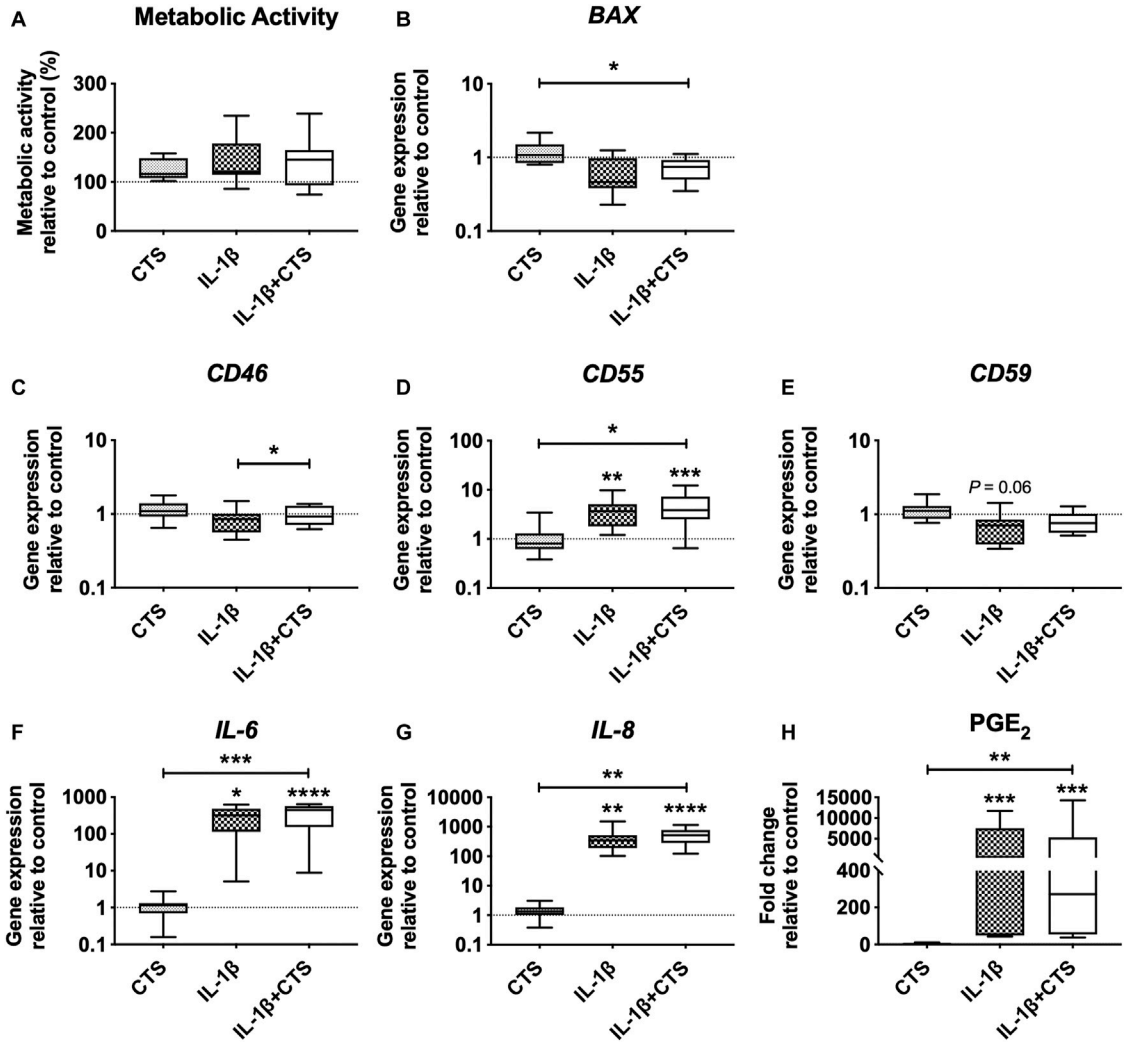

FIGURE 2 | Human annulus fibrosus (AF) cells metabolic activity and gene expression of cell apoptosis marker, complement factors, and pro-inflammatory cytokines, in response to cyclic tensile strain (CTS) and the pro-inflammatory cytokine IL-1β (10 ng/ml) after 48 h. **(A)** AF cells mitochondrial metabolic activity (compared to unstimulated cells). Relative mRNA expression of **(B)** cell apoptosis marker *BAX*, **(C)** complement factors *CD46*, **(D)** *CD55*, and **(E)** *CD59*; pro-inflammatory markers **(F)** *IL-6* and **(G)** *IL-8*. Results were normalized to expression level of *GAPDH* and unstimulated cells. **(H)** Concentration of pro-inflammatory marker PGE_2 in (fold change to unstimulated cells). $n = 10$, $^{*}p < 0.05$, $^{**}p < 0.01$.

AF cells. However, when CTS was combined with IL-1β, it significantly increased *MMP-1* and *MMP-3* expression compared with CTS-treatment ($^{***}p < 0.001$ and $^{**}p < 0.01$, respectively) and with unstimulated cells ($^{**}p < 0.01$ and $^{***}p < 0.001$, respectively; **Figures 3A,B**). A significant upregulation of *MMP-3* expression was also observed by the IL-1β-stimulation in comparison to control. In addition, the CTS + IL-1β treatment significantly downregulated *COL1A1* by AF cells ($^{*}p < 0.05$) and upregulated elastin ($^{**}p < 0.01$), a key AF protein involved in tissue elasticity, compared to CTS-treated cells (**Figures 3C,D**). This trend was also observed in the presence of IL-1β only, with *COL1A1* significantly downregulated ($^{*}p < 0.05$), in comparison with unstimulated cells. In contrast, neither CTS nor IL-1β seemed to affect fibrillin-1, another glycoprotein involved in AF elasticity (**Figure 3E**).

MSC Secretome Treatment of Human AF Cells Under Mechanical and Inflammatory Stimuli

Since a synergistic action between mechanical stimuli and a pro-inflammatory microenvironment in human AF cells was observed, we went further and investigated the regulatory effect of the MSC secretome in AF cells in the presence of CTS + IL-1β stimulus. Unstimulated AF cell cultures supplemented with MSC secretome served as controls.

The MSC secretome treatment of human AF cells did not affect the gene expression of *CD46* and *CD59* but significantly upregulated *CD55* ($^{*}p < 0.05$), *IL-6*, and *IL-8* ($^{**}p < 0.01$) and increased the production of PGE_2 ($^{***}p < 0.001$) compared to unstimulated AF cells (**Figure 4B**, D–F). Regarding the matrix

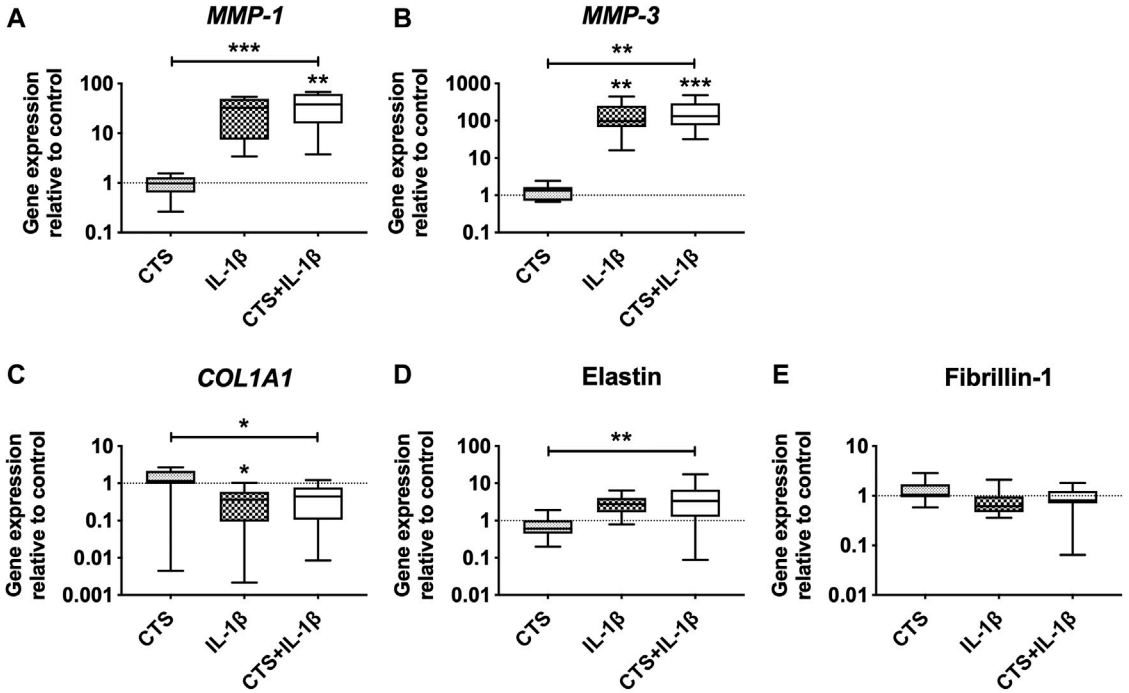

FIGURE 3 | Matrix metalloproteinases (MMPs) and extracellular matrix (ECM) gene expression of human AF cells in response to cyclic tensile strain (CTS) and to pro-inflammatory cytokine IL-1β (10 ng/ml) after 48 h. Relative mRNA expression of matrix-degrading enzymes **(A)** *MMP-1*, **(B)** *MMP-3*, and ECM proteins **(C)** *COL1A1*, **(D)** elastin, and **(E)** fibrillin-1. Results were normalized to expression level of *GAPDH* and unstimulated cells. $n = 10$, $^{*}p < 0.05$, $^{**}p < 0.01$.

remodeling capacity of human AF cells, the secretome downregulated the gene expression of *MMP-1* ($^{*}p < 0.01$) and *MMP-3* ($p = 0.07$) (**Figures 5A,B**) compared to CTS + IL-1β stimulation alone and did not alter *COL1A1*, elastin, or fibrillin-1 expression (**Figures 5C–E**). In accordance with the increase in pro-inflammatory cytokines, the MSC secretome significantly upregulated *MMP-1* ($^{*}p < 0.05$) and *MMP-3* ($^{**}p < 0.05$) gene expression in control AF cells. Furthermore, MMP activity was evaluated by gelatin zymography in AF culture supernatants. The pro- and active forms of the gelatinases MMP-2 (between 72 and 63 kDa) and MMP-9 (between 82 and 92 kDa) (Cardoso et al., 2014), particularly the latter, were identified (**Figure 5F**). The MMP bands were quantified, and a band of MSC secretome as a control was subtracted from the other conditions tested. The results show that the MSC secretome was able to reduce the activity of gelatin-degrading enzymes produced by human AF cells, namely, the active form of MMP-9 ($p = 0.06$; **Figure 5G**).

In addition, the concentration of different tissue inhibitors of MMPs–TIMP-1, TIMP-2, TIMP-3, and TIMP-4—was quantified in all the conditions (**Figure 6**), with the concentrations found in the MSC secretome being subtracted from the AF culture supernatants. The MSC secretome significantly increased the production of TIMP-1 by CTS + IL-1β–treated AF cells ($^{*}p < 0.05$) but did not affect TIMP-2, TIMP-3, or TIMP-4. An increase in TIMP-1 and TIMP-2 was observed in unstimulated cells upon treatment with MSC secretome ($^{**}p < 0.01$ and $^{*}p < 0.05$).

DISCUSSION

In the present study, a pro-inflammatory/catabolic IVD microenvironment was simulated in human AF cell cultures, based on previous *ex vivo* models of bovine NP (Teixeira et al., 2016) and AF (Saggese et al., 2019) organ cultures, which were maintained in low-glucose, iso-osmotic (400 mOsm), and pro-inflammatory conditions with low oxygen supply. In the AF organ cultures, a synergistic action of cyclic tensile strain (CTS) and IL-1β was shown to increase the synthesis of pro-inflammatory mediators and MMP-3 in the AF and to decrease the strength of the tissue (Saggese et al., 2019). In the present study, we evaluated the effects of these stimuli (CTS, IL-1β, and CTS + IL-1β) on the metabolism of human AF cells, as well as possible alterations induced by the treatment with secretome produced by IL-1β–preconditioned MSCs.

For that, AF cells were isolated from patients diagnosed with either AIS or DD and expanded up to passage 3–4, in order to obtain enough cells to culture under different stimuli. Although organ culture models could better mimic the degenerative 3D environment of the IVD, these are difficult to conduct under standardized and reproducible conditions using limited human IVD biopsies, which are small in size and often very fragmented. Therefore, they were used for cell isolation and 2D cultures of AF cells. Despite the differences observed in IVD tissues from disc degeneration compared to AIS patients, namely, increased TCC deposition and expression of *CD59* (a direct TCC inhibitor) (Teixeira et al., 2021a), the expanded AF cells from both

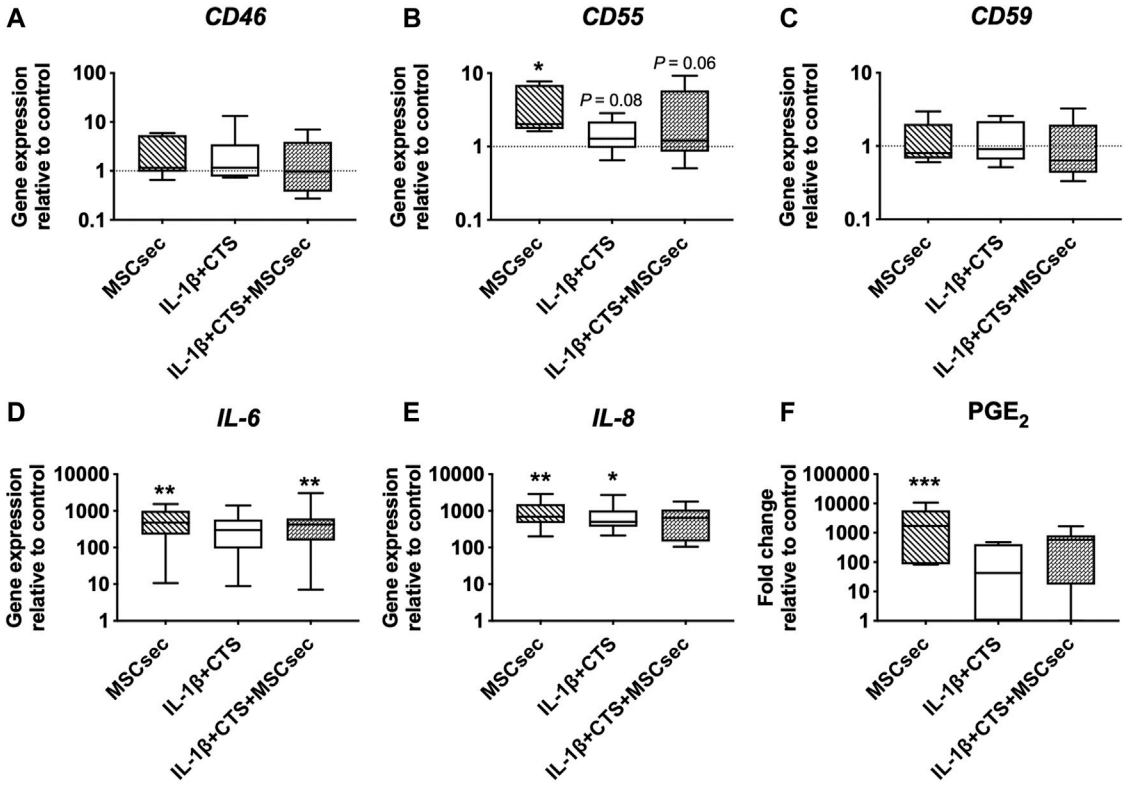

FIGURE 4 | Effect of MSC secretome on human AF cells stimulated with cyclic tensile strain (CTS) and IL-1β (10 ng/ml) in the expression of complement markers and pro-inflammatory cytokines after 48 h. Relative mRNA expression of complement regulatory factors **(A)** *CD46*, **(B)** *CD55*, and **(C)** *CD59*; and pro-inflammatory markers **(D)** *IL-6* and **(E)** *IL-8*. Results were normalized to expression level of *GAPDH* and to unstimulated cells. **(F)** Concentration of pro-inflammatory marker PGE_2 (fold change to unstimulated cells). $n = 7$, $^*p < 0.05$, $^{**}p < 0.01$.

patient groups revealed similar behavior. Primary cells always show a certain variability; however, we expected to see differences between the gene expression profiles of cells from AIS and DD due to the lower age of AIS versus DD patients (an average of 16 ± 2 versus 65 ± 11 years old, respectively) and less degeneration in AIS tissues. However, CTS and/or IL-1β did not induce a significantly different response between the two groups for cells in passages 3 to 4. After expansion in 2D cultures, we hypothesize that the cells from DD patients lose their disease phenotype, behaving similarly to AF cells from AIS patients. This suggests that *in vitro* expansion of AF cells might attenuate cellular changes associated with patients' age and specific disease, in line with recent findings showing similar expression of complement-related markers by AF cells from AIS and DD patients after challenging with IL-1β and cathepsin-D (Teixeira et al., 2021b).

CTS + IL-1β stimulation of human AF cells induced an upregulation of pro-inflammatory cytokines (IL-6, IL-8, and PGE_2) and MMPs (MMP-1, MMP-3), which was observed to a lesser extent in the presence of IL-1β, but not after CTS stimulation by itself. In the present work, 2% strain alone did not seem to be a strong enough stimulus to induce changes in the AF cell gene expression profile. This might be due to the 2D cell cultures, in contrast to previous investigations of human AF cells cultured in 3D collagen gels, in which differences were observed (Neidlinger-Wilke et al., 2005). CTS stimulation of AF cells has been shown to increase *COL2A1* and aggrecan expression and decrease *MMP-3* expression in human AF cells cultured in 3D collagen gels, independently of the strain magnitude (1–8% strain, 1 Hz) (Neidlinger-Wilke et al., 2005). CTS was also shown to promote upregulation of pro-inflammatory genes, like *COX-2*, *IL-6*, and *IL-8* in AF cells (8% strain, 1 Hz) (Pratsinis et al., 2016). Under mild pro-inflammatory stimulation (1 ng/ml IL-1β) and 6% CTS (0.05 Hz), CTS was suggested to have a protective effect on rat AF cells (Sowa and Agarwal, 2008). Since a role for complement-associated factors has recently been suggested in a degenerative/pro-inflammatory environment, we investigated the gene expression of the cellular complement regulators *CD46*, *CD55*, and *CD59* by human AF cells. Here, CD55, but not the other complement factors, was upregulated by CTS + IL-1β stimulation of AF cells. In bovine AF organ cultures, CTS + IL-1β simulation induced upregulation of *CD46*, but not of *CD55* nor *CD59* (Neidlinger-Wilke et al., 2021). IL-1β stimulation of human articular chondrocytes upregulated *CD45*, *CD55* and *CD59* (Hyc et al., 2003). This indicates that the complement cascade is activated by the CTS and IL-1β stimuli; however, different molecules may be regulated at different timepoints.

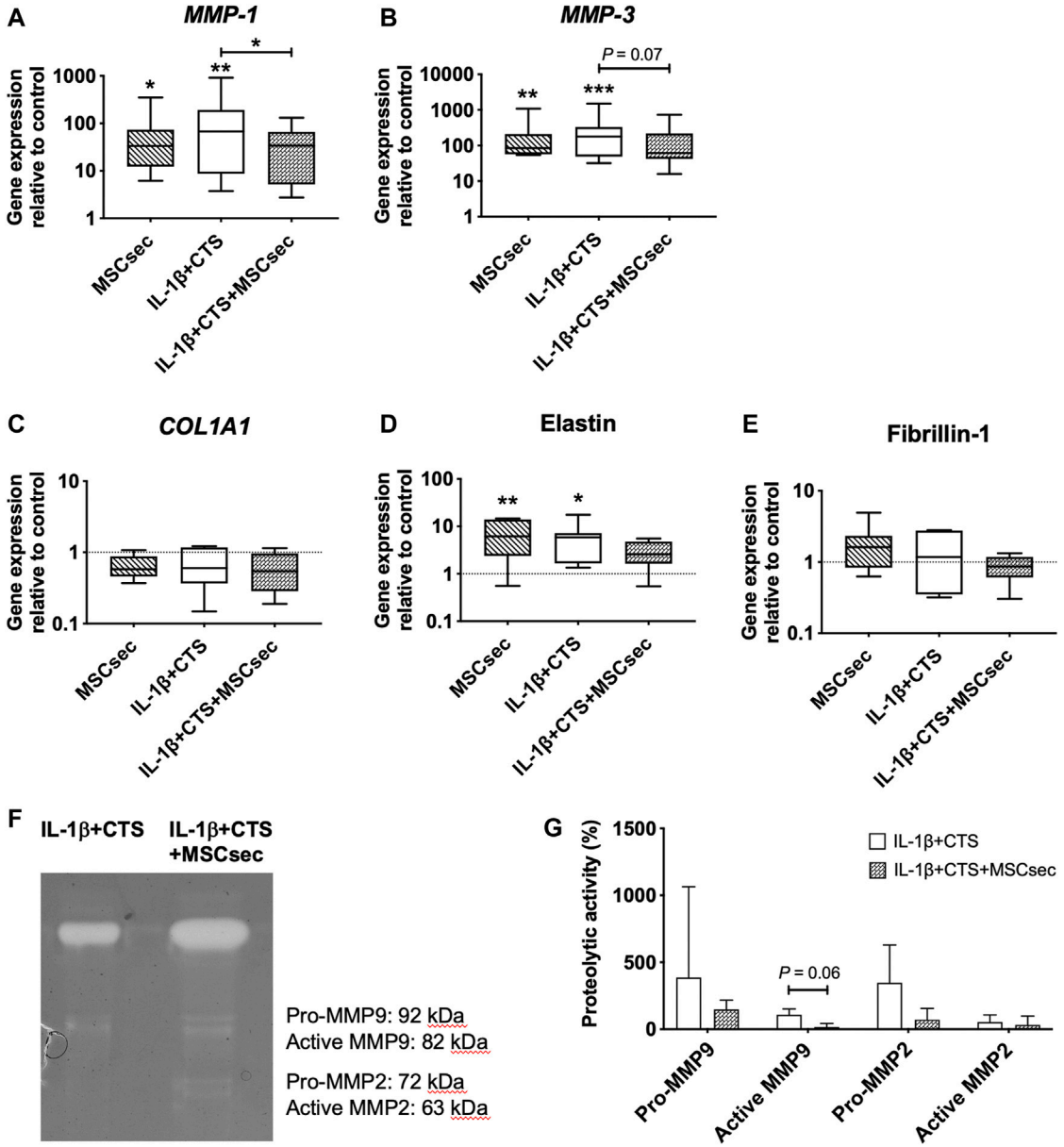

FIGURE 5 | Effect of MSC secretome on human AF cells stimulated with cyclic tensile strain (CTS) and IL-1β (10 ng/ml) in MMPs and ECM proteins after 48 h. Relative mRNA expression of the matrix degrading enzymes **(A)** *MMP-1* and **(B)** *MMP-3*, and of ECM proteins **(C)** *COL1A1*, **(D)** elastin, and **(E)** fibrillin-1. Results were normalized to the expression level of GAPDH and unstimulated cells. $n = 7$, $^{*}p < 0.05$, $^{**}p < 0.01$. **(F)** MMP activity in AF cultures media, determined by gelatin zymography **(G)** Quantification of MMP-2 and MMP-9 activity by densitometry ($n = 3$).

Regarding matrix metabolism, CTS + IL-1β stimulation of human AF cells did not alter *COL1A1* and fibrillin-1 production but seemed to enhance elastin synthesis. The latter was also promoted by CTS and IL-1β individually. Fibrillin-1 production was previously shown to be increased within the translamellar bridging-network of bovine AF organ cultures in the presence of IL-1β but not in the presence of CTS + IL-1β (Saggese et al., 2019). Besides the differences between 2D and 3D (organ culture), this study also used lower IL-1β concentration (1 ng/ml), which could explain the different results of the present study. Concerning elastin, TNF-α stimulation of human tenocytes was shown to reduce COL1 deposition while increased elastin gene expression (John et al., 2010), in agreement to what was observed with AF cells in our study. Moreover, it has been described that elastin increases with IVD degeneration and aging, particularly in the AF, consisting in a response to restore the lamellar structure under radial loads that potentially cause delamination (Cloyd and Elliott, 2007).

Previously, we have demonstrated that MSCs cultured with bovine NP in the presence of IL-1β downregulated the pro-

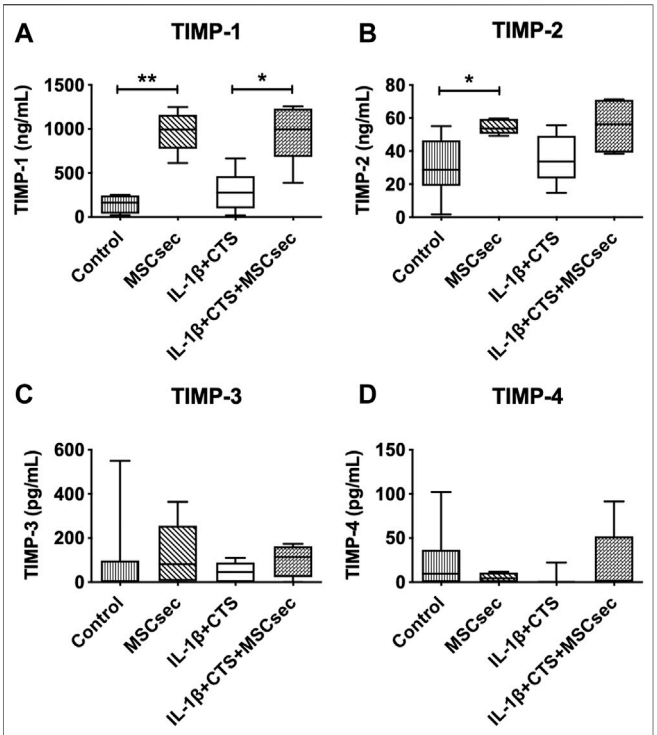

FIGURE 6 | Concentration of tissue inhibitors of metalloproteinases (TIMPs) in the supernatant of AF cultures stimulated with cyclic tensile strain (CTS) and IL-1β (10 ng/ml) and treated with MSC secretome after 48 h, determined by ELISA. **(A)** TIMP-1, **(B)** TIMP-2, **(C)** TIMP-3, and **(D)** TIMP-4. $n = 5–9$, $^{*}p < 0.05$, $^{**}p < 0.01$.

inflammatory markers *bIL-6*, *bIL-8*, and *bTNF-α* by NP cells but did not promote ECM synthesis (Teixeira et al., 2018). MSCs secrete numerous soluble factors in response to microenvironmental cues, which include pro-inflammatory stimulation, 3D environment, or hypoxia. Therefore, the MSC secretome has been explored as a cell-based/cell-free therapy for several disorders (Ferreira et al., 2018). MSC IL-1β preconditioning has been shown to upregulate chemokines (CCL5, CCL20, CXCL1, CXCL3, CXCL5, CXCL6, CXCL10, CXCL11, and CX (3)CL1), interleukins (IL-6, IL-8, IL-23A, IL-32), toll-like receptors (TLR2, TLR4, CLDN1), MMPs (MMP-1, MMP-3), growth factors (CSF2, TNF-α), and adhesion molecules (ICAM1, ICAM4), compared to unstimulated MSCs (Carrero et al., 2012). Moreover, although the cell passage can affect the cellular response, it has been reported that the composition of the MSC secretome does not vary significantly between passages 3 and 12 (Serra et al., 2018).

In the IVD, the MSC secretome has been suggested to stimulate the cellular repair capacity (Brisby et al., 2013). For instance, the secretome of human umbilical cord–derived MSCs was shown to restore the stemness of NP progenitor cells, thus rejuvenating the degenerated NP (Zeng et al., 2020). Moreover, the secretome of IL-1β–preconditioned MSCs, enriched in IL-6, RANTES, MCP-1, IL-1β, TIMP-2, IL-8, GRO α/β/γ, leptin, MIP-3α, and CXCL1, downregulated the expression/production of inflammatory markers by bovine NP, while promoting aggrecan deposition (Ferreira et al., 2021). It was also shown to downregulate the expression/production of inflammatory markers, complement system regulators, MMPs, TIMPs, and collagen by bovine AF cells in an *ex vivo* model (Neidlinger-Wilke et al., 2021). In contrast to the previous findings, in the present study, the MSC secretome did not downregulate the expression of cellular complement regulators and pro-inflammatory cytokines of CTS + IL-1β–stimulated human AF cells but strongly downregulated MMP-1 and MMP-3 gene expression. Furthermore, in this study, it was demonstrated to have reduced MMP-2 and MMP-9 activity of human AF cells in presence of the MSC secretome. MMP-1 and MMP-3 are strongly expressed in the IVD of young adults but not in those of children and adolescents, while MMP-2 and MMP-9 are present in older adults, but in fewer cells (Weiler et al., 2002). Moreover, static compression and annular puncture of rat caudal discs have been shown to stimulate MMP-2 activity with simultaneous AF lamellar disorganization, linking MMP-2 to local matrix degradation and collagen remodeling (Rastogi et al., 2013). Therefore, the MSC secretome could be an interesting approach to modulate matrix remodeling in the AF, although further studies need to be conducted in human IVD to better understand its impact on the tissue biomechanics.

In addition, besides being enriched in TIMP-2 (Ferreira et al., 2021), the MSC secretome also stimulated the production of TIMP-1 and TIMP-2, but not TIMP-3 and TIMP-4, by human AF cells, which could be directly correlated with MMP inhibition. This is in agreement with what was previously observed by Le Maitre et al. (2004), who described an increase in TIMP-1 and TIMP-2, but not TIMP-3, in degenerated human IVD biopsies. Vo et al. (2013) also described sthe upregulation of TIMP-1 with IVD degeneration, as well as a downregulation of TIMP-3. Overall, mechanical and inflammatory stimuli play a crucial role in the modulation of the expression levels of MMPs, ADAMTs, and TIMPs. Inhibition of MMPs and ADAMTSs has demonstrated efficacy and therapeutic potential in slowing osteoarthritis progression (Fosang and Little, 2008), which suggests that therapies proposing the inhibition of matrix-degrading enzymes or stimulation of TIMPs are promising for IVD, although they should be tissue-specific and carefully localized.

Our study shows a therapeutic effect of the MSC secretome on the AF cells challenged with CTS + IL-1β. To induce a pro-inflammatory microenvironment, 10 ng/ml IL-1β was used, but other inflammatory cytokines are known to be widely expressed in IVD degeneration/herniation, such as TNF-α or IL-6, and should be also addressed in future studies. More recently, Wangler et al. (2021) have shown that conditioned medium from traumatically injured versus degenerated IVD has different proteome contents, so different inflammatory cytokine cocktails should be explored in the future to deepen the knowledge of the therapeutic effect of MSC secretome on IVD. *In vivo* experiments that fully recreate the degenerative IVD microenvironment will prove the regulatory effect of the secretome of IL-1β–preconditioned MSCs on the modulation of the immune system response and IVD degeneration.

CONCLUSION

Overall, this study demonstrates that the inflammatory milieu, in synergy with tensile strain, has an impact on human AF cells, promoting upregulation of inflammatory markers, cellular complement regulators, and elastin; increasing MMP activity and TIMP production; and decreasing *COL1A1* expression. Moreover, this study evidences a novel aspect of the mechanism of action of the MSC secretome in degenerated IVD that consists in the modulation of MMP activity and TIMP-1 production by AF cells.

DATA AVAILABILITY STATEMENT

The original contributions presented in the study are included in the article/**Supplementary Material**, further inquiries can be directed to the corresponding author.

ETHICS STATEMENT

The studies involving human participants were reviewed and approved by Ulm University (371/19), Ulm, Germany, and by Heidelberg University (S-051/2016), Heidelberg, Germany. Written informed consent to participate in this study was provided by the participants or by the participants' legal guardian/next of kin (when underage).

AUTHOR CONTRIBUTIONS

RG and GT designed the study, analyzed the data, and wrote the manuscript. TS, ZY, and JF contributed to data collection and revised the manuscript. AI, H-JW, and CN-W helped to optimize the research and proofread the manuscript. All authors read and approved the final manuscript.

FUNDING

The study was supported by Ulm University (L.SBN.0157), German Spine Foundation (*Deutsche Wirbelsäulenstiftung*) and the German Academic Exchange Service (DAAD). RG was supported by the Alexander von Humboldt Foundation and by *Conselho de Reitores das Universidades Portuguesas*.

ACKNOWLEDGMENTS

The authors wish to thank Mrs. Iris Baum for technical support.

SUPPLEMENTARY MATERIAL

The Supplementary Material for this article can be found online at: https://www.frontiersin.org/articles/10.3389/fbioe.2021.802789/full#supplementary-material

REFERENCES

Brisby, H., Papadimitriou, N., Brantsing, C., Bergh, P., Lindahl, A., and Barreto Henriksson, H. (2013). The Presence of Local Mesenchymal Progenitor Cells in Human Degenerated Intervertebral Discs and Possibilities to Influence These *In Vitro*: a Descriptive Study in Humans. *Stem Cell Development.* 22, 804–814. doi:10.1089/scd.2012.0179

Cardoso, A. P., Pinto, M. L., Pinto, A. T., Oliveira, M. I., Pinto, M. T., Gonçalves, R., et al. (2014). Macrophages Stimulate Gastric and Colorectal Cancer Invasion through EGFR Y1086, C-Src, Erk1/2 and Akt Phosphorylation and smallGTPase Activity. *Oncogene.* 33, 2123–2133. doi:10.1038/onc.2013.154

Carrero, R., Cerrada, I., Lledó, E., Dopazo, J., García-García, F., Rubio, M.-P., et al. (2012). IL1β Induces Mesenchymal Stem Cells Migration and Leucocyte Chemotaxis Through NF-Kb. *Stem Cell Rev Rep.* 8, 905–916. doi:10.1007/s12015-012-9364-9

Cloyd, J. M., and Elliott, D. M. (2007). Elastin Content Correlates with Human Disc Degeneration in the Anulus Fibrosus and Nucleus Pulposus. *Spine.* 32, 1826–1831. doi:10.1097/brs.0b013e3181132a9d

Cunha, C., Almeida, C. R., Almeida, M. I., Silva, A. M., Molinos, M., Lamas, S., et al. (2017). Systemic Delivery of Bone Marrow Mesenchymal Stem Cells for *In Situ* Intervertebral Disc Regeneration. *Stem Cell Transl. Med.* 6, 1029–1039. doi:10.5966/sctm.2016-0033

Ferreira, J. R., Teixeira, G. Q., Santos, S. G., Barbosa, M. A., Almeida-Porada, G., and Gonçalves, R. M. (2018). Mesenchymal Stromal Cell Secretome: Influencing Therapeutic Potential by Cellular Pre-conditioning. *Front. Immunol.* 9, 2837. doi:10.3389/fimmu.2018.02837

Ferreira, J., Teixeira, G. Q., Teixeira, G., Neto, e., Ribeiro-Machado, c., Silva, A., et al. (2021). IL-1β-pre-Conditioned Mesenchymal Stem/Stromal Cells' Secretome Modulates the Inflammatory Response and Aggrecan Deposition in Intervertebral Disc. *Eur. Cell Mater.* 41, 431–543. doi:10.22203/ecm.v041a28

Fosang, A. J., and Little, C. B. (2008). Drug Insight: Aggrecanases as Therapeutic Targets for Osteoarthritis. *Nat. Rev. Rheumatol.* 4, 420–427. doi:10.1038/ncprheum0841

Hyc, A., Osiecka-Iwan, A., Strzelczyk, P., and Moskalewski, S. (2003). Effect of IL-1β, TNF-Agr; and IL-4 on Complement Regulatory Protein mRNA Expression in Human Articular Chondrocytes. *Int. J. Mol. Med.* 11, 91–94. doi:10.3892/ijmm.11.1.91

John, T., Lodka, D., Kohl, B., Ertel, W., Jammrath, J., Conrad, C., et al. (2010). Effect of Pro-Inflammatory and Immunoregulatory Cytokines on Human Tenocytes. *J. Orthop. Res.* 28, 1071–1077. doi:10.1002/jor.21079

Le Maitre, C. L., Freemont, A. J., and Hoyland, J. A. (2004). Localization of Degradative Enzymes and Their Inhibitors in the Degenerate Human Intervertebral Disc. *J. Pathol.* 204, 47–54. doi:10.1002/path.1608

Livak, K. J., and Schmittgen, T. D. (2001). Analysis of Relative Gene Expression Data Using Real-Time Quantitative PCR and the 2−ΔΔCT Method. *Methods.* 25, 402–408. doi:10.1006/meth.2001.1262

Maher, C., Underwood, M., and Buchbinder, R. (2017). Non-Specific Low Back Pain. *The Lancet.* 389, 736–747. doi:10.1016/s0140-6736(16)30970-9

Neidlinger-Wilke, C., Ekkerlein, A., Goncalves, R., Ferreira, J., Ignatius, A., Wilke, H., et al. (2021). Mesenchymal Stem Cell Secretome Decreases the Inflammatory Response in Annulus Fibrosus Organ Cultures. *Eur. Cell Mater.* 42, 1–19. doi:10.22203/ecm.v042a01

Neidlinger-Wilke, C., Wilke, H.-J., and Claes, L. (1994). Cyclic Stretching of Human Osteoblasts Affects Proliferation and Metabolism: A New Experimental Method and its Application. *J. Orthop. Res.* 12, 70–78. doi:10.1002/jor.1100120109

Neidlinger-Wilke, C., Würtz, K., Liedert, A., Schmidt, C., Börm, W., Ignatius, A., et al. (2005). A Three-Dimensional Collagen Matrix as a Suitable Culture System for the Comparison of Cyclic Strain and Hydrostatic Pressure Effects on Intervertebral Disc Cells. *J. Neurosurg. Spine.* 2, 457–465. doi:10.3171/spi.2005.2.4.0457

Noriega, D. C., Ardura, F., Hernández-Ramajo, R., Martín-Ferrero, M. Á., Sánchez-Lite, I., Toribio, B., et al. (2017). Intervertebral Disc Repair by Allogeneic

Mesenchymal Bone Marrow Cells. *Transplantation.* 101, 1945–1951. doi:10.1097/tp.0000000000001484

Orozco, L., Soler, R., Morera, C., Alberca, M., Sánchez, A., and García-Sancho, J. (2011). Intervertebral Disc Repair by Autologous Mesenchymal Bone Marrow Cells: a Pilot Study. *Transplantation.* 92, 822–828. doi:10.1097/tp.0b013e3182298a15

Pratsinis, H., Papadopoulou, A., Neidlinger-Wilke, C., Brayda-Bruno, M., Wilke, H.-J., and Kletsas, D. (2016). Cyclic Tensile Stress of Human Annulus Fibrosus Cells Induces MAPK Activation: Involvement in Proinflammatory Gene Expression. *Osteoarthritis and Cartilage.* 24, 679–687. doi:10.1016/j.joca.2015.11.022

Rastogi, A., Kim, H., Twomey, J. D., and Hsieh, A. H. (2013). MMP-2 Mediates Local Degradation and Remodeling of Collagen by Annulus Fibrosus Cells of the Intervertebral Disc. *Arthritis Res. Ther.* 15, R57. doi:10.1186/ar4224

Risbud, M. V., and Shapiro, I. M. (2014). Role of Cytokines in Intervertebral Disc Degeneration: Pain and Disc Content. *Nat. Rev. Rheumatol.* 10, 44–56. doi:10.1038/nrrheum.2013.160

Saggese, T., Teixeira, G. Q., Wade, K., Moll, L., Ignatius, A., Wilke, H.-J., et al. (2019). Georg Schmorl Prize of The German Spine Society (Dwg) 2018: Combined Inflammatory and Mechanical Stress Weakens the Annulus Fibrosus: Evidences from a Loaded Bovine AF Organ Culture. *Eur. Spine J.* 28, 922–933. doi:10.1007/s00586-019-05901-w

Sakai, D., Mochida, J., Iwashina, T., Hiyama, A., Omi, H., Imai, M., et al. (2006). Regenerative Effects of Transplanting Mesenchymal Stem Cells Embedded in Atelocollagen to the Degenerated Intervertebral Disc. *Biomaterials.* 27, 335–345. doi:10.1016/j.biomaterials.2005.06.038

Serra, S. C., Costa, J. C., Assunção-Silva, R. C., Teixeira, F. G., Silva, N. A., Anjo, S. I., et al. (2018). Influence of Passage Number on the Impact of the Secretome of Adipose Tissue Stem Cells on Neural Survival, Neurodifferentiation and Axonal Growth. *Biochimie.* 155, 119–128. doi:10.1016/j.biochi.2018.09.012

Shin, E.-H., Cho, K.-J., Kim, Y.-T., and Park, M.-H. (2019). Risk Factors for Recurrent Lumbar Disc Herniation after Discectomy. *Int. Orthopaedics (Sicot).* 43, 963–967. doi:10.1007/s00264-018-4201-7

Sowa, G., and Agarwal, S. (2008). Cyclic Tensile Stress Exerts a Protective Effect on Intervertebral Disc Cells. *Am. J. Phys. Med. Rehabil.* 87, 537–544. doi:10.1097/phm.0b013e31816197ee

Teixeira, G. Q., Boldt, A., Nagl, I., Pereira, C. L., Benz, K., Wilke, H.-J., et al. (2016). A Degenerative/Proinflammatory Intervertebral Disc Organ Culture: an *Ex Vivo* Model for Anti-inflammatory Drug and Cell Therapy. *Tissue Eng. C: Methods.* 22, 8–19. doi:10.1089/ten.tec.2015.0195

Teixeira, G. Q., Pereira, C. L., Ferreira, J. R., Maia, A. F., Gomez-Lazaro, M., Barbosa, M. A., et al. (2018). Immunomodulation of Human Mesenchymal Stem/Stromal Cells in Intervertebral Disc Degeneration. *Spine (Phila Pa 1976).* 43, E673–E682. doi:10.1097/brs.0000000000002494

Teixeira, G. Q., Yong, Z., Goncalves, R. M., Kuhn, A., Riegger, J., Brisby, H., et al. (2021a). Terminal Complement Complex Formation Is Associated with Intervertebral Disc Degeneration. *Eur. Spine J.* 30, 217–226. doi:10.1007/s00586-020-06592-4

Teixeira, G. Q., Yong, Z., Kuhn, A., Riegger, J., Goncalves, R. M., Ruf, M., et al. (2021b). Interleukin-1β and Cathepsin D Modulate Formation of the Terminal Complement Complex in Cultured Human Disc Tissue. *Eur. Spine J.* 30, 2247–2256. doi:10.1007/s00586-021-06901-5

Vo, N. V., Hartman, R. A., Yurube, T., Jacobs, L. J., Sowa, G. A., and Kang, J. D. (2013). Expression and Regulation of Metalloproteinases and Their Inhibitors in Intervertebral Disc Aging and Degeneration. *Spine J.* 13, 331–341. doi:10.1016/j.spinee.2012.02.027

Vos, T., Lim, S. S., Abbafati, C., Abbas, K. M., Abbasi, M., Abbasifard, M., et al. (2020). Global burden of 369 Diseases and Injuries in 204 Countries and Territories, 1990-2019: a Systematic Analysis for the Global Burden of Disease Study 2019. *Lancet.* 396, 1204–1222. doi:10.1016/S0140-6736(20)30925-9

Wangler, S., Kamali, A., Wapp, C., Wuertz-Kozak, K., Häckel, S., Fortes, C., et al. (2021). Uncovering the Secretome of Mesenchymal Stromal Cells Exposed to Healthy, Traumatic, and Degenerative Intervertebral Discs: a Proteomic Analysis. *Stem Cell Res. Ther.* 12, 11. doi:10.1186/s13287-020-02062-2

Weiler, C., Nerlich, A., Zipperer, J., Bachmeier, B., and Boos, N. (2002). 2002 SSE Award Competition in Basic Science: Expression of Major Matrix Metalloproteinases Is Associated with Intervertebral Disc Degradation and Resorption. *Eur. Spine J.* 11, 308–320. doi:10.1007/s00586-002-0472-0

Weinstein, J. N., Lurie, J. D., Tosteson, T. D., Tosteson, A. N. A., Blood, E. A., Abdu, W. A., et al. (2008). Surgical versus Nonoperative Treatment for Lumbar Disc Herniation. *Spine.* 33, 2789–2800. doi:10.1097/brs.0b013e31818ed8f4

Wuertz, K., Urban, J. P. G., Klasen, J., Ignatius, A., Wilke, H.-J., Claes, L., et al. (2007). Influence of Extracellular Osmolarity and Mechanical Stimulation on Gene Expression of Intervertebral Disc Cells. *J. Orthop. Res.* 25, 1513–1522. doi:10.1002/jor.20436

Zeng, X., Lin, J., Wu, H., Yu, J., Tu, M., Cheang, L. H., et al. (2020). Effect of Conditioned Medium from Human Umbilical Cord-Derived Mesenchymal Stromal Cells on Rejuvenation of Nucleus Pulposus Derived Stem/Progenitor Cells from Degenerated Intervertebral Disc. *Int. J. Stem Cell.* 13, 257–267. doi:10.15283/ijsc20027

Zhang, W., Wang, H., Yuan, Z., Chu, G., Sun, H., Yu, Z., et al. (2021). Moderate Mechanical Stimulation Rescues Degenerative Annulus Fibrosus by Suppressing Caveolin-1 Mediated Pro-inflammatory Signaling Pathway. *Int. J. Biol. Sci.* 17, 1395–1412. doi:10.7150/ijbs.57774

Conflict of Interest: The authors declare that the research was conducted in the absence of any commercial or financial relationships that could be construed as a potential conflict of interest.

Publisher's Note: All claims expressed in this article are solely those of the authors and do not necessarily represent those of their affiliated organizations, or those of the publisher, the editors, and the reviewers. Any product that may be evaluated in this article, or claim that may be made by its manufacturer, is not guaranteed or endorsed by the publisher.

Copyright © 2022 Gonçalves, Saggese, Yong, Ferreira, Ignatius, Wilke, Neidlinger-Wilke and Teixeira. This is an open-access article distributed under the terms of the Creative Commons Attribution License (CC BY). The use, distribution or reproduction in other forums is permitted, provided the original author(s) and the copyright owner(s) are credited and that the original publication in this journal is cited, in accordance with accepted academic practice. No use, distribution or reproduction is permitted which does not comply with these terms.

frontiers in Bioengineering and Biotechnology

ORIGINAL RESEARCH
published: 15 February 2022
doi: 10.3389/fbioe.2022.823679

Engineered Human Meniscus in Modeling Sex Differences of Knee Osteoarthritis *in Vitro*

Zhiyao Ma[1†], *David Xinzheyang Li*[1,2†], *Melanie Kunze*[1], *Aillette Mulet-Sierra*[1], *Lindsey Westover*[3] *and Adetola B. Adesida*[1*]

[1]*Department of Surgery, Divisions of Orthopaedic Surgery, Surgical Research and Otolaryngology-Head and Neck Surgery, Faculty of Medicine and Dentistry, University of Alberta, Edmonton, AB, Canada,* [2]*Department of Civil and Environmental Engineering, University of Alberta, Edmonton, AB, Canada,* [3]*Department of Mechanical Engineering, University of Alberta, Edmonton, AB, Canada*

OPEN ACCESS

Edited by:
Mark Buckley,
University of Rochester, United States

Reviewed by:
Csaba Matta,
University of Debrecen, Hungary
Robert Nims,
Washington University in St. Louis, United States
Jennifer Puetzer,
Virginia Commonwealth University, United States

***Correspondence:**
Adetola B Adesida
adesida@ualberta.ca

[†]*These authors have contributed equally to this work and share first authorship*

Specialty section:
This article was submitted to Tissue Engineering and Regenerative Medicine, a section of the journal Frontiers in Bioengineering and Biotechnology

Received: *29 November 2021*
Accepted: *21 January 2022*
Published: *15 February 2022*

Citation:
Ma Z, Li DX, Kunze M, Mulet-Sierra A, Westover L and Adesida AB (2022) Engineered Human Meniscus in Modeling Sex Differences of Knee Osteoarthritis in Vitro. *Front. Bioeng. Biotechnol. 10:823679. doi: 10.3389/fbioe.2022.823679*

Background: Osteoarthritis (OA) primarily affects mechanical load-bearing joints. The knee joint is the most impacted by OA. Knee OA (KOA) occurs in almost all demographic groups, but the prevalence and severity are disproportionately higher in females. The molecular mechanism underlying the pathogenesis and progression of KOA is unknown. The molecular basis of biological sex matters of KOA is not fully understood. Mechanical stimulation plays a vital role in modulating OA-related responses of load-bearing tissues. Mechanical unloading by simulated microgravity (SMG) induced OA-like gene expression in engineered cartilage, while mechanical loading by cyclic hydrostatic pressure (CHP), on the other hand, exerted a pro-chondrogenic effect. This study aimed to evaluate the effects of mechanical loading and unloading *via* CHP and SMG, respectively, on the OA-related profile changes of engineered meniscus tissues and explore biological sex-related differences.

Methods: Tissue-engineered menisci were made from female and male meniscus fibrochondrocytes (MFCs) under static conditions of normal gravity in chondrogenic media and subjected to SMG and CHP culture. Constructs were assayed *via* histology, immunofluorescence, GAG/DNA assays, RNA sequencing, and testing of mechanical properties.

Results: The mRNA expression of *ACAN* and *COL2A1*, was upregulated by CHP but downregulated by SMG. *COL10A1*, a marker for chondrocyte hypertrophy, was downregulated by CHP compared to SMG. Furthermore, CHP increased GAG/DNA levels and wet weight in both female and male donors, but only significantly in females. From the transcriptomics, CHP and SMG significantly modulated genes related to the ossification, regulation of ossification, extracellular matrix, and angiogenesis Gene Ontology (GO) terms. A clear difference in fold-change magnitude and direction was seen between the two treatments for many of the genes. Furthermore, differences in fold-change magnitudes were seen between male and female donors within each treatment. SMG and CHP also significantly modulated genes in OA-related KEGG pathways, such as mineral absorption, Wnt signalling pathway, and HIF-1 signalling pathway.

Conclusion: Engineered menisci responded to CHP and SMG in a sex-dependent manner. SMG may induce an OA-like profile, while CHP promotes chondrogenesis. The combination of SMG and CHP could serve as a model to study the early molecular events of KOA and potential drug-targetable pathways.

Keywords: disease modelling, human-engineered meniscus, mechanical stimulation, simulated microgravity, cyclic hydrostatic pressure

INTRODUCTION

Osteoarthritis (OA) is the most common form of degenerative disease and primarily affects loading-bearing joints, with the knee joint being the most prevalent (Nicolella et al., 2012; Boyan et al., 2013a). A hallmark feature of knee osteoarthritis (KOA) is the atrophy of articular cartilage. Surrounding joint tissues, including the menisci, will also undergo breakdown (Sun et al., 2010; Blackburn et al., 2016). These abnormal changes can lead to rapid loss of the knee joint's function and mobility, making KOA a leading cause of physical disability (Murray et al., 2012). Although KOA occurs in almost all demographic groups, the prevalence and severity of KOA increases with age and is disproportionately higher in females than males (Badley and Kasman, 2004; Breedveld, 2004; O'Connor, 2007; Boyan et al., 2012; Pan et al., 2016). It has been reported by the World Health Organization that 9.6% of males and 18% of females above the age of 60 years have symptomatic OA (Osteoarthritis, 2014).

The molecular mechanisms and cellular events underlying the pathogenesis and progression of KOA are not well understood. As well, the molecular basis of biological sex matters has not been previously investigated. Currently, there is no consensus model to reflect the pathophysiology of KOA holistically. However, the molecular and cellular characteristics of KOA resemble the hypertrophic differentiation of chondrocytes as they progress to the bone during endochondral ossification (Dreier, 2010). Conveniently, this process includes the upregulation of hypertrophic markers *COL10A1* and *MMP13*, which can be indicators for the KOA phenotype (Aigner et al., 1993; D'Angelo et al., 2000). Healthy chondrocytes, on the other hand, resist hypertrophic differentiation and lack expression of these hypertrophic markers (Leijten et al., 2012). Given the disproportionate incidence of KOA in females as compared to males, we reasonably expect the cellular and molecular characteristics of KOA to show sex-dependent differences.

Mechanical stimulation was reported by an abundance of studies to play a critical role in modulating OA-related responses of loading-bearing tissues. Applying mechanical loading to joints through regular exercise is essential to maintaining healthy cartilage and preventing breakdown from prolonged disuse (Bader et al., 20112011). Cyclic hydrostatic pressure (CHP) as a loading modality mimics physiological loading patterns and can be easily recreated *in-vitro* using specialized bioreactors (Elder and Athanasiou, 2009; Mellor et al., 2017). Studies have shown that CHP applied to engineered tissue constructs has induced a mostly pro-chondrogenic effect. For example, Zellner et al. applied dynamic hydrostatic pressure (cyclic at 1 Hz for 4 h per day, 0.55–5.03 MPa) for 7 days to cellular aggregates generated from inner and outer meniscus fibrochondrocytes (MFCs) (Zellner et al., 2015). After 14 additional days of static culture, aggregates loaded initially for the 7 days showed immunohistochemically enhanced chondrogenesis compared to unloaded controls (Zellner et al., 2015). Further, Gunja et al. applied dynamic hydrostatic pressure (0.1 Hz for 1 h every 3 days, 10 MPa) for 28 days to engineered tissue constructs using MFCs with added TGF-β1 growth factors (Gunja et al., 2009). Loaded tissue constructs with growth factors showed additive and synergistic increases in collagen deposition (approximately 2.5-fold), GAG deposition (2-fold), and enhanced compressive properties compared to unloaded controls without growth factors (Gunja et al., 2009).

Mechanical unloading of joints from long-term immobilization has been shown to induce cartilage atrophy that resembles characteristics of KOA. In a case study by Souza et al., joint immobilization of healthy individuals without prior history of OA resulted in magnetic resonance imaging (MRI) parameters of their knee articular cartilage that resemble KOA (Souza et al., 2012). When returning to standard weight-bearing, the MRI parameters for the joints were restored to baseline values consistent with healthy articular cartilage (Souza et al., 2012). Mechanical unloading has also been modelled by simulated microgravity (SMG) using rotating wall vessel bioreactors (Yu et al., 2011; Jin et al., 2013; Mayer-Wagner et al., 2014; Mellor et al., 2014; Mellor et al., 2017). Mayer-Wagner et al. applied simulated microgravity for 21 days to human mesenchymal stem cell (hMSC) pellets and found a decrease in histological staining of proteoglycans and collagen type-II compared to normal gravity controls (Mayer-Wagner et al., 2014). SMG pellets also showed a lower *COL2A1*/*COL10A1* expression ratio suggesting that mechanical unloading *via* SMG reduced the chondrogenic differentiation of hMSCs (Mayer-Wagner et al., 2014). Finally, in a comparative study, CHP-loaded pellets from human adipose-derived stem cells showed increased expression of *ACAN*, *SOX9*, and *COL2A1*, and a 3-fold increase in GAG productions compared to unloaded SMG groups (Mellor et al., 2017). However, none of the above studies investigated the sex-dependent differences in the magnitude of differential modulation by mechanical loading and unloading *via* CHP and SMG, respectively.

A recent definition of OA from the Osteoarthritis Research Society International includes the menisci of the knee joint as a tissue undergoing breakdown and abnormal changes from the disease (Blackburn et al., 2016). Knee menisci undergoing OA has also been shown to have similar characteristics as knee articular cartilage undergoing OA, such as focal calcification and the

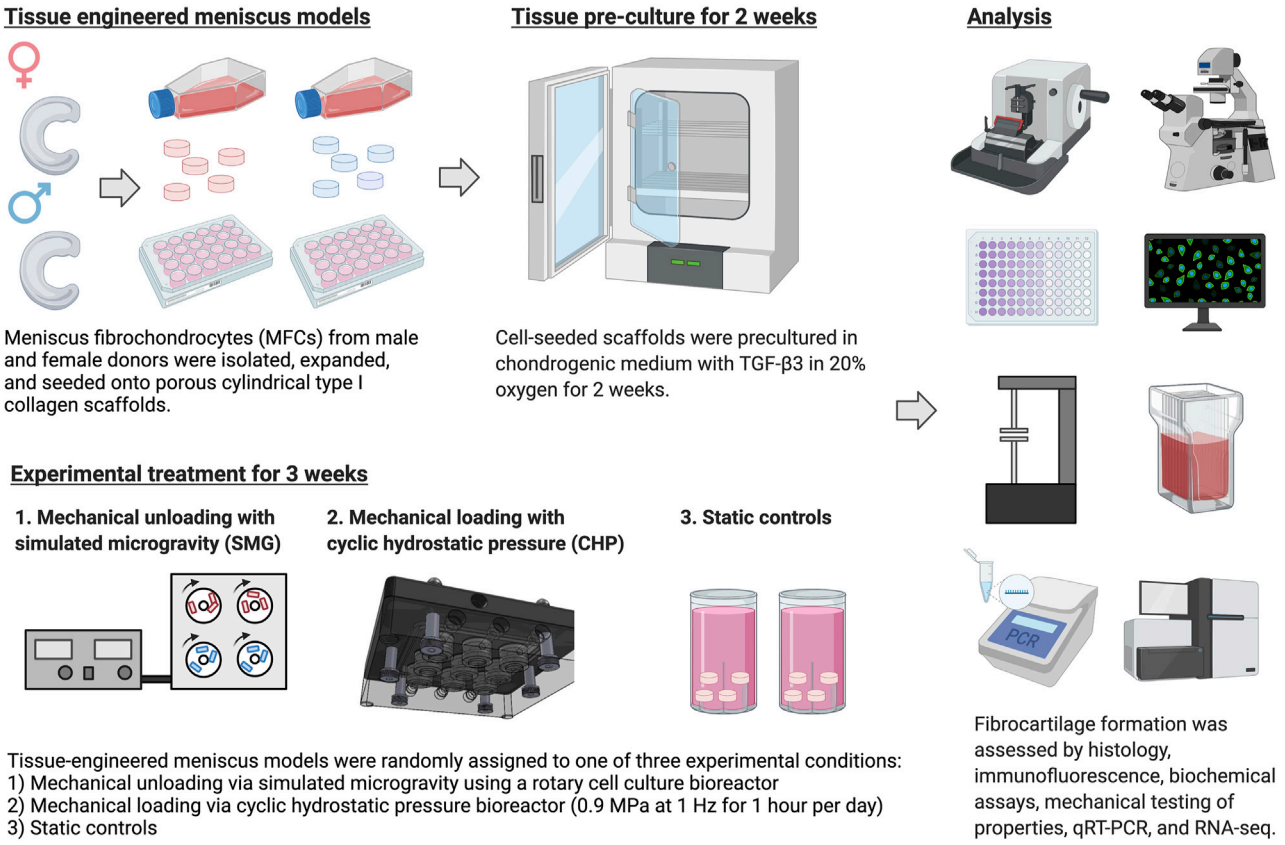

FIGURE 1 | Experiment outlines. Created with Biorender.com (2021).

increased expression of hypertrophic markers *COL10A1* and *MMP13* (Sun et al., 2010; Kiraly et al., 2017). This suggests that MFC may play an active role in the pathogenesis of KOA alongside knee articular chondrocytes, making MFC a reasonable cell option to model OA *in-vitro*.

Taken together, the goal of this study was to evaluate the effects of mechanical loading and unloading *via* CHP and SMG, respectively, and determine sex-dependent differences in the modulation of OA-related characteristics in bioengineered human meniscus tissues. This would serve as an OA disease model *in-vitro* to determine the cellular and molecular profiles responsible for the sex-dependent incidence of the disease.

TABLE 1 | Non-identifying donor information.

Sex	Donor number	Age	Population doubling (PD)
Female	F1	33	2.687
	F2	44	2.380
	F3	30	2.774
	F4	28	3.860
Male	M1	19	3.349
	M2	45	2.699
	M3	22	3.247
	M4	35	2.149

MATERIALS AND METHODS

The experiment is outlined in **Figure 1**. Most culture methods and assays were performed identically to those described in previous work (Liang et al., 2017; Szojka et al., 2021a; Szojka et al., 2021b).

Ethics Statement

Human non-osteoarthritic inner meniscus samples were collected from patients undergoing partial meniscectomies at the University of Alberta Hospital and Grey Nuns Community Hospital in Edmonton. The ethics of this study was approved by the Health Research Ethics Board of the University of Alberta. Non-identifying donor information is listed in **Table 1**.

Cell and Tissue Culture

Meniscus fibrochondrocytes (MFCs) were isolated from inner meniscus tissue samples by type II collagenase (0.15% w/v of 300 units/mg; Worthington) mediated digestion, followed by 48 h recovery. After recovery, cells were replated in tissue culture flasks at the density of 10^4 cells/cm^2 and expanded for 1 week in high glucose Dulbecco's modified Eagle's medium (HG-DMEM)

supplemented with 10% v/v heat-inactivated fetal bovine serum (FBS), 10 mM 4-(2-hydroxyethyl)-1-piperazineethanesulfonic acid (HEPES), 100 U/mL penicillin, 100 μg/ml streptomycin and 2 mM L-glutamine (PSG; Life Technologies, ON, Canada), 5 ng/ml of FGF-2 (Neuromics, MH, United States, catalogue #: PR80001) and 1 ng/ml of TGF-β1 (ProSpec, catalogue #: CYT-716) for 1 week

Expanded MFCs were resuspended in defined chondrogenic medium (HG-DMEM supplemented with HEPES, PSG, ITS +1 premix (Corning, Discovery Labware, Inc, MA, United States), 125 μg/ml of human serum albumin, 100 nM of dexamethasone, 365 μg/ml ascorbic acid 2-phosphate, 40 μg/ml of L-proline, and 10 ng/ml of TGF-β3) and seeded onto bovine type I collagen scaffolds (dimensions: 6 mm diameter, 3.5 mm height; Integra LifeSciences, NJ, United States) at the density of 5×10^6 cells/cm^3. The cell-containing constructs were precultured statically in standard 24-well plates with 2.5 ml/construct of the chondrogenic medium described above for 2 weeks; media changes occurred once per week.

Mechanical Stimulation

After the 2-weeks preculture, tissue constructs were randomly assigned to a mechanical stimulation group. For the static control group, constructs were placed in a tissue culture tube (Sarstedt, Germany). For the mechanical unloading group, a commercially available bioreactor (RCCS-4; Synthecon Inc.) was used to culture tissue constructs in a simulated microgravity (SMG) environment. The rotation speed was adjusted over time to maintain constructs in suspension (30 rpm from day 1–2; 34 rpm from day 3–7; 37 rpm from day 8–13; 40 rpm from day 14–21). For the mechanical loading group, cyclic hydrostatic pressure (CHP) was applied to tissue constructs using a MechanoCulture TR (CellScale, Canada). Constructs were loaded 1 h per day and daily with 0.9 MPa cyclic hydrostatic pressure at the frequency of 1 Hz. When not loaded, tissue constructs were cultured in 6-well plates under static conditions. All experimental groups were cultured with chondrogenic medium with supplemented TGF-β3 growth factor, and the volume of medium per tissue construct (approximately 6.5 ml per tissue construct per week) was equivalent among the different groups. The mechanical stimulation was applied for 3 weeks, and medium change was performed once a week. At the end of the 3-weeks treatment, the CHP group was allowed 30 min of rest following the last loading event for gene expression changes to occur. Tissue replicates for RNA extraction were placed in TRIzol reagent and frozen at −80°C. Constructs from SMG and static control groups were harvested at approximately the same time.

Histology, Immunofluorescence, and Biochemical Analysis

The wet weight of tissue constructs (n = 5–8 replicates) intended for histology and biochemical analysis was recorded at the end of the experiment. Constructs (n = 2 replicates, only one replicate is presented) were then fixed in 1 ml of 10% v/v buffered formalin (Fisher Scientific, MA, United States) overnight at 4°C, dehydrated, embedded in paraffin wax, and sectioned at 5 μm thickness. Tissue sections approximately from the middle region of the constructs were stained with Safranin-O (Sigma-Aldrich, United States, #S2255-25G), Fast Green FGF (Sigma-Aldrich, United States, #F7258-25G), and Haematoxylin (Sigma-Aldrich, United States, #MHS32-1L) for histological examination of cell morphology and extracellular matrix deposition. Briefly, for immunofluorescence staining, tissue sections were labelled with primary antibody against human type I, type II, and type X collagen (1:200 dilution of anti-human rabbit type I collagen, Cedarlane, Canada, #CL50111AP-1; 1:200 dilution of mouse anti-human type II collagen, Developmental Studies Hybridoma Bank, United States, #II-II6B3; 1:100 dilution of rabbit anti-human type X collagen, Abcam, UK, #ab58632) and incubated overnight at 4°C (Anderson-Baron et al., 2021). On the next day, the secondary antibody (1:200 dilution of goat anti-rabbit, Abcam, UK, #ab150080; 1:200 dilution of goat anti-mouse, Abcam, UK, #ab150117) and DAPI (Cedarlane, Canada) was applied to visualize the stained components.

Biochemical assays quantified the total content of glycosaminoglycan (GAG) and DNA. Tissue constructs (n = 4 replicates for donors F1-3 and M1-3; n = 3 replicates for donors F4 and M4) were digested overnight with proteinase K (Sigma-Aldrich, United States, #P2308) at 56°C. GAG content was measured with a 1,9-dimethyl methylene blue assay (DMMB, Sigma-Aldrich, United States, #341088). Chondroitin sulphate (Sigma-Aldrich, United States, #C8529) was used to generate the standard curve. DNA content was measured with a CyQuant cell proliferation assay kit (ThermoFisher Scientific, United States, #C7026) with different dilutions of supplied bacteriophage λ DNA as the standard.

Mechanical Property Assessment

Detailed sequence of the mechanical testing protocol is included in **Supplementary Material S3**. A stepwise stress relaxation test (**Supplementary Figure S1**) was used to assess the mechanical properties of tissue constructs (n = 2 replicates for donor F1-3 and M1-3) with the BioDynamic 5210 system (TA Instruments, United States). The cross-section areas of tissue constructs were measured before mechanical tests. For the test, constructs were placed between two platens and the initial height was determined by bringing tissue to near contact with platens. Constructs were first preconditioned by 15 cycles of sine wave dynamic loading with the amplitude of 5% tissue height at the frequency of 1 Hz. The following stress relaxation test consisted of 3 incremental strain steps. In the first two steps, the constructs were subjected to a 10% strain ramp at the rate of 50% strain/sec followed by 5 min relaxation under constant strain. In the third step, the relaxation time was adjusted to 10 min. All tested constructs were able to reach equilibrium within the given relaxation period. Force was recorded as a function of time, and stress was calculated by normalizing force to construct's cross-section area. The peak modulus was calculated by dividing the maximum stress measured immediately after each strain increment by the strain increment. The strain was applied in 10% increments up to a maximum of 30% strain.

RNA Extraction, qPCR, and Next-Generation Sequencing

Tissue constructs (n = 2 for donors F1-3 and M1-3; n = 3 replicates for donors F4 and M4) intended for transcriptome analysis were preserved in Trizol (Life Technologies, United States) immediately upon harvesting and stored at −80°C until RNA extraction. RNA was extracted and purified from ground constructs using PuroSPIN Total DNA Purification KIT (Luna Nanotech, Canada) following the manufacturer's protocol. RNA was reversely transcribed into cDNA, and genes of interest were amplified by quantitative real-time polymerase chain reaction (RT-qPCR) using specific primers (**Supplementary Table S1**). The expression level of genes of interest was normalized to chosen housekeeping genes (i.e., *B-actin*, *B2M*, and *YWHAZ*) based on the coefficient of variation (CV) and M-value as measures of reference gene stability (Hellemans et al., 2007), and the data was presented using the $2^{-\Delta\Delta CT}$ method (Livak and Schmittgen, 2001; Schmittgen and Livak, 2008). Next-generation RNA-sequencing was performed on the Illumina NextSeq 500 platform with paired-end 42 bp × 42 bp reads, and FastQ files were obtained for further bioinformatics analysis.

Bioinformatics

Next-generation sequencing data were analyzed with Partek® Flow® software (Version 10.0.21.0302, Copyright© 2021, Partek Inc, St. Louis, MO, United States). Raw input reads were first trimmed from the 3′ end to achieve a quality score beyond 20 and then aligned to the reference human genome hg38 using the STAR 2.7.3a aligner. Aligned data were quantified to a transcript model (hg38-RefSeq Transcripts 94–2020–05–01) using the Partek E/M algorithm. Genes with maximum read counts below 50 were filtered out to reduce noise. Quantified and filtered reads were normalized in sequential order using the Add: 1.0, TMM, and Log 2.0 methods. Statistical analysis was performed using analysis of variance (ANOVA) for biological sex and treatment. Within each sex, the donors were assigned as a random variable. Differentially expressed genes (DEGs) for each comparison were determined by *p*-values, adjusted *p*-values (*q*-values), and fold change (FC). Gene ontology enrichment, pathway enrichment, and the visualization of DEGs using Venn diagrams were all conducted in Partek.

Statistical analysis

Statistical analyses were performed in Prism 9 (GraphPad) and Partek® Flow® software. The statistical test used, and *p*-values and *q*-values are indicated in the respective figure legends. For analysis in **Figure 3B**, paired *t*-test were used between SMG and CHP groups within each sex and unpaired *t*-test were used between female and male groups within each mechanical treatment. For analysis in **Figure 4A**, a repeated measurement one-way ANOVA with Geisser-Greenhouse correction was used to compare mechanical treatment groups within each sex and a Tukey's multiple comparison test was used to find the adjusted *p*-value between each comparison. Within each mechanical treatment, unpaired t-tests between female and male groups were used. For the male cohort, no statistical analysis was conducted for the SMG group in contraction due to limited data points. For analysis in **Figure 4B**, repeated measurement one-way ANOVA with Geisser-Greenhouse correction was used to compare different strain levels within each mechanical treatment group and a Tukey's multiple comparison test was used to find the adjusted *p*-value between each comparison. Within each strain level, paired t-tests were used to compare CHP and SMG groups. For the male cohort, no statistical analysis was conducted for the SMG group due to limited data points.

RESULTS

Dataset Overview

Transcriptome analysis included the expression profiles of 8 donors (4 females and 4 males), each individually exposed to static, mechanical loading (CHP), and mechanical unloading (SMG) conditions. After preprocessing as described in the methods, 13,361 genes were preserved for downstream analysis.

Transcriptome Profiles of the Engineered Meniscus to CHP and SMG

We first analyzed the overall effect of mechanical loading and unloading on the transcriptome profiles of all donors combined. Summarized results are shown in **Figure 2**. Fold-change of gene expression levels in the CHP and SMG groups were calculated by normalizing to its corresponding static group. Differentially expressed genes (DEGs) were defined as genes with expression fold-change over 2 and *q*-value less than 0.05. Mechanical loading from CHP significantly modulated 236 genes, while mechanical unloading from SMG significantly modulated 388 genes. The overlay of DEGs between the two mechanical stimulation groups showed only a small proportion of common DEGs (52 genes), whereas the majority of DEGs were uniquely modulated by CHP (184 genes) and SMG (336 genes) (**Figure 2A**). These results indicated that CHP and SMG distinctly modulate the transcriptome profile of donors in this study.

The most significant Gene Ontology (GO) terms enriched by the DEGs for CHP and SMG were examined next (**Figure 2B**). Although the top 3 most significantly enriched Gene Ontology (GO) in biological components were identical for CHP and SMG ("extracellular space," "extracellular region," and "extracellular matrix"), the included gene expression profiles were different between the treatment groups. The top 20 genes with the highest absolute fold change participating in the ECM relevant activities in CHP and SMG groups are listed in **Table 2**. For CHP, most of the genes are signalling molecules or proteins associated with ECM structure remodelling. For SMG, many of the strongly regulated genes played a more general role, such as various growth factors coding genes: *IGFBP1*, *TGFA*, and *NGF*. Among the top regulated genes, only *NETO1* and *OLFML2A* were common between CHP and SMG; these two genes were upregulated in both treatment groups.

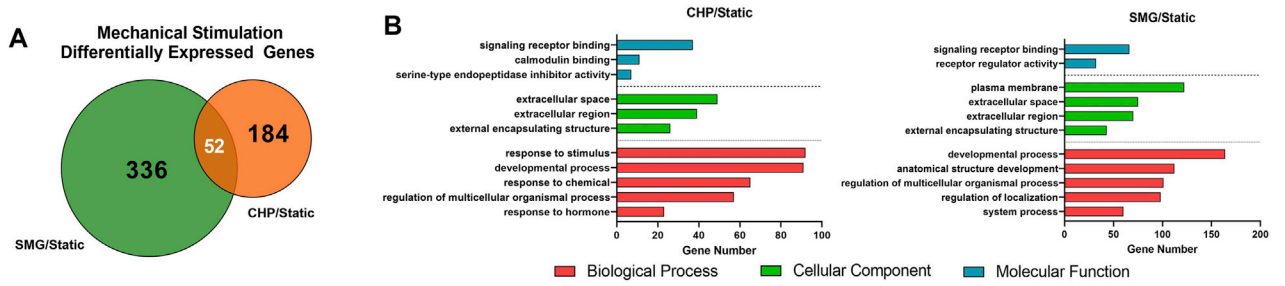

FIGURE 2 | Effect of CHP and SMG on the transcriptome profile alteration of engineered meniscus tissues. **(A)** Overlap of differentially expressed genes (DEGs) by CHP and SMG. **(B)** Top non-redundant Gene Ontology (GO) terms enriched by DEGs of CHP and SMG. DEGs were identified based on all 8 donors. Top significant enriched GO terms were selected by *p*-value and plotted to the number of genes included in each term.

TABLE 2 | Top 20 genes with the highest absolute fold change participating in the ECM relevant activities in CHP and SMG groups as compared to static controls.

Gene	**Description**	***p*-value: CHP vs static**	**Fold change: CHP vs static**
EREG	Epiregulin	1.20E-06	19.10
NET O 1	Neuropilin And Tolloid Like 1	2.53E-08	7.98
MMP3	Matrix metallopeptidase 3	1.22E-06	6.47
MMP10	Matrix metallopeptidase 10	1.14E-03	4.54
SBSPON	Somatomedin B And Thrombospondin Type 1 Domain Containing	7.88E-04	3.97
CCL2	C-C Motif Chemokine Ligand 2	8.18E-07	3.62
UCN2	Urocortin 2	5.86E-05	3.61
PLA2G2A	Phospholipase A2 Group IIA	7.00E-04	3.60
OLFML2A	Olfactomedin Like 2A	1.15E-03	3.45
CXCL13	C-X-C Motif Chemokine Ligand 13	1.00E-03	3.40
SFRP2	Secreted Frizzled Related Protein 2	1.17E-05	−4.07
ADM	Adrenomedullin	1.34E-06	−4.49
CPXM1	Carboxypeptidase X, M14 Family Member 1	1.95E-04	−4.53
SELENOP	Selenoprotein P	3.90E-03	−5.82
FAM20A	FAM20A Golgi Associated Secretory Pathway pseudokinase	2.24E-03	−5.92
MNDA	Myeloid Cell Nuclear Differentiation Antigen	4.02E-03	−5.99
SCUBE1	Signal Peptide, CUB Domain And EGF Like Domain Containing 1	3.28E-03	−7.06
SFRP4	Secreted Frizzled Related Protein 4	6.83E-04	−8.17
ODAPH	Odontogenesis Associated Phosphoprotein	3.30E-03	−9.07
APOE	Apolipoprotein E	3.30E-07	−14.78
Gene	**Description**	***p*-value: SMG vs static**	**Fold change: SMG vs static**
IGFBP1	Insulin Like Growth Factor Binding Protein 1	5.49E-04	15.94
OLFML2A	Olfactomedin Like 2A	2.34E-05	6.34
NET O 1	Neuropilin And Tolloid Like 1	1.26E-06	5.00
ADAMTS14	ADAM metallopeptidase With Thrombospondin Type 1 Motif 14	8.34E-04	3.72
PCSK9	Proprotein convertase Subtilisin/Kexin Type 9	2.20E-03	3.48
VSTM2L	V-Set And Transmembrane Domain Containing 2 Like	3.03E-04	3.47
BMPER	BMP Binding Endothelial Regulator	1.91E-04	3.45
NTM	Neurotrimin	1.30E-04	3.40
HMOX1	Heme oxygenase 1	5.06E-08	3.38
CAPG	Capping Actin Protein, Gelsolin Like	2.94E-07	3.22
LEP	Leptin	8.50E-04	−4.81
R3HDML	R3H Domain Containing Like	8.67E-04	−4.93
APLN	Apelin	8.68E-07	−4.94
STC1	Stanniocalcin 1	8.99E-05	−5.41
NGF	Nerve Growth Factor	7.68E-05	−5.42
TGFA	Transforming Growth Factor Alpha	8.23E-04	−5.47
VEGFA	Vascular Endothelial Growth Factor A	6.33E-06	−5.68
DSCAML1	DS Cell Adhesion Molecule Like 1	3.09E-03	−6.17
ADAMTSL2	ADAMTS Like 2	4.74E-04	−7.23
PDE4C	Phosphodiesterase 4C	2.48E-04	−8.73

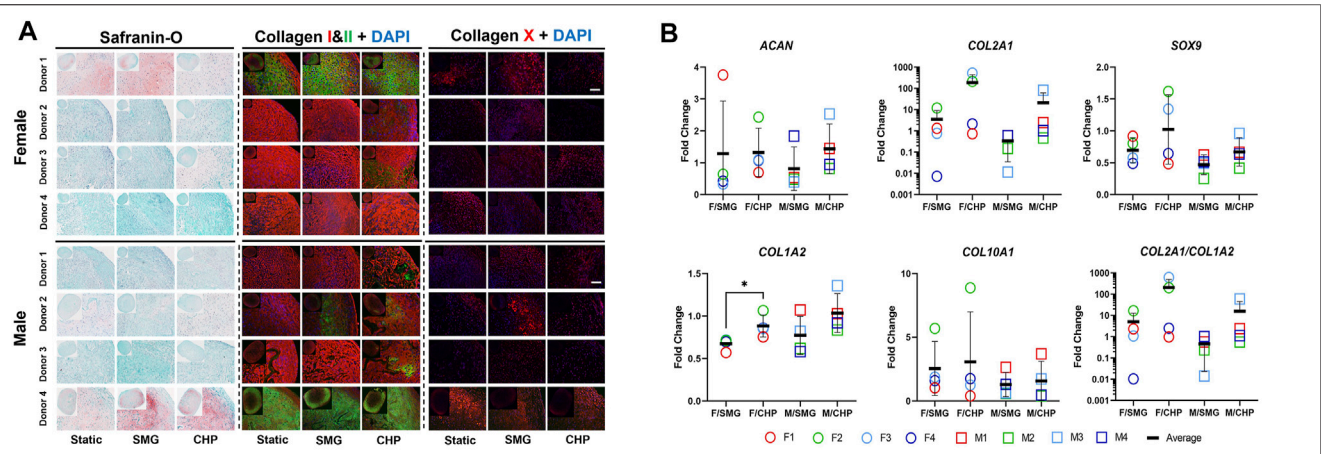

FIGURE 3 | Effect of CHP and SMG on the chondrogenic and hypertrophic differentiation potential of female and male donors. **(A)** Histological and immunofluorescent staining analysis. **(B)** Regulation of selected genes expression level. Gene expression level of individual samples were measured by RT-qPCR. Fold change of expression level was calculated by normalizing expression level in the CHP or SMG group to its corresponding static group. Scale bar: 100 μm *Represents $p < 0.05$.

Sex-Dependent Response of Engineered Meniscus to CHP and SMG

Next, we sought to explore the sex-dependent differences in the engineered meniscus responses to CHP and SMG. Therefore, we separated donors into female and male cohorts and evaluated several factors involved in normal cartilage physiology and OA-related alterations. The GAG and type II collagen content are often used to characterize the degree of chondrogenesis for cartilage tissues, and higher content is linked to higher chondrogenic capacity. Type X collagen, on the other hand, is a hypertrophic marker that suggests an OA-like phenotype. The histological staining for GAG by Safranin-O and immunofluorescence labelled type II collagen (**Figure 3A**) showed highly variable chondrogenic capacities within the female and male cohorts in the baseline static control group. Regardless, tissue constructs exposed to CHP and SMG showed an increase in type II collagen content, with CHP having a generally more pronounced effect. Type X collagen staining intensity was also modulated by mechanical stimulations compared to baseline. A clear increase in type X collagen content was observed in the SMG group, while the CHP group showed comparable type X collagen intensity as the baseline.

To further pursue sex matters in responses to CHP and SMG, the gene expression of selected markers was examined by RT-qPCR (**Figure 3B**). In addition to *COL1A2*, *COL2A1*, and *COL10A1*, the transcription factor *SOX9* and cartilage-specific proteoglycan core protein *ACAN* were also quantified. The observed increase of type II collagen level in the CHP group was confirmed quantitatively by gene expression results. The average *COL2A1* expression level was upregulated 215.9-fold in the CHP group for the female cohort compared to a 21.4-fold increase in CHP for the male cohort. For *ACAN*, *SOX9*, and *COL1A2*, the CHP group had a higher average fold-change than the SMG group, but the differences between the sexes were not significant. For *COL10A1*, the average fold-change of expression level was comparable between the CHP and SMG groups for both females and males. However, when taking individual female donors into account, only female donor 2 showed a significant increase in *COL10A1* expression level in CHP (8.9-fold) compared to SMG (5.7-fold) group. Generally, CHP, as compared to SMG, reduced *COL10A1* expression level for the female cohort. The RT-qPCR data were consistent with the histological observations, providing additional evidence on the cellular and molecular influence of CHP and SMG. The RT-qPCR data also agreed with the RNA-sequencing data, thereby providing additional validation for the observed trends (**Supplementary Figure S2**).

Sex-dependent differences were also assessed in other related aspects (**Figure 4A**). Quantitative GAG/DNA measurements showed that CHP increased while SMG decreased the GAG production per MFC. The tissue wet weights showed similar trends as the GAG/DNA ratios; CHP tissues weighed more, and SMG tissues weighed less on average than the static control groups. This difference in tissue wet weight was significant in only the female cohort between treatments. Further, at the end of the mechanical stimulation period, tissue constructs from all three experimental groups contracted to certain degrees. The percentage of contraction (percentage reduction in area) was quantified, and comparison among groups showed that SMG tissues had increased contraction compared to the CHP tissues. The contraction plot is presented as the percentage contracted in **Supplementary Figure S4**.

The differences among stimulation groups were significant within the female and male cohorts while also significant between female CHP and male CHP groups. For the mechanical properties of tissue constructs, SMG groups showed higher peak modulus at all tested strain levels for both sexes as expected based on contraction results, and the differences of the average fold-change decreased with increasing strain level. No

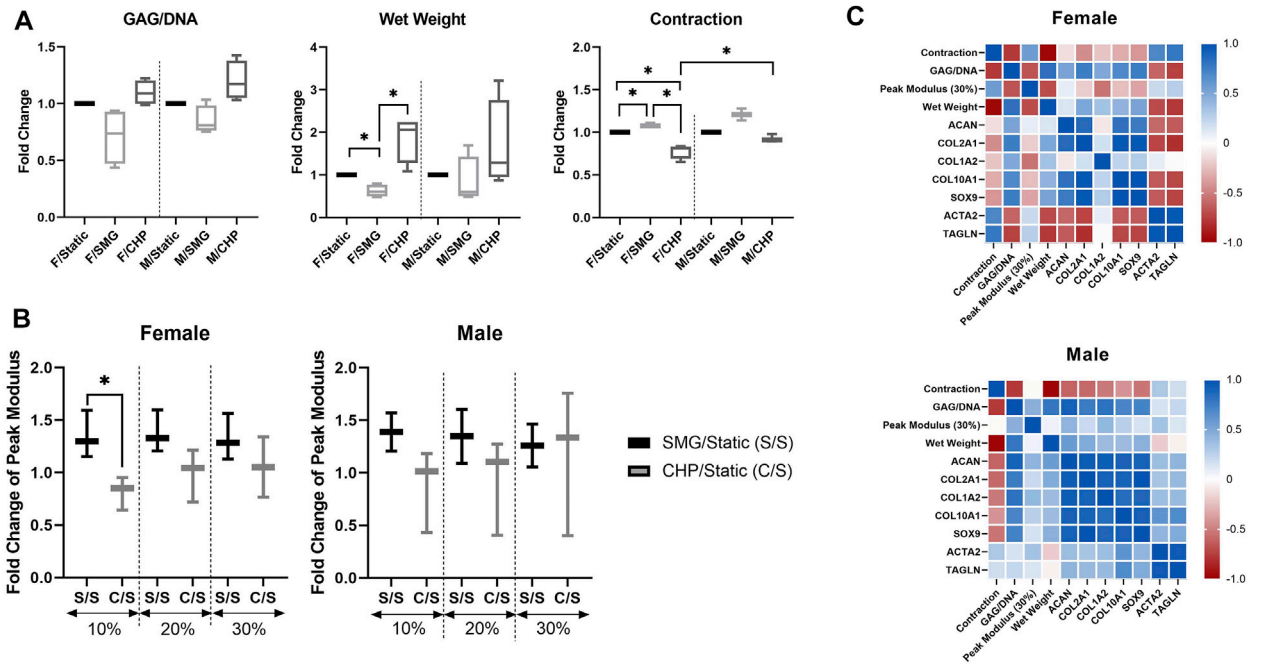

FIGURE 4 | Effect of CHP and SMG on chondrogenesis related factors of female and male donors **(A)** Biochemical and morphological analysis; contraction is calculated as the % of area lost as compared to the original area. No statistical analysis was conducted for the contraction data with the male SMG group due to limited data points **(B)** Mechanical property analysis. No statistical analysis was conducted for the mechanical property data with the male SMG group due to limited data points **(C)** Pearson correlation heatmap of analyzed factors. Fold change value of characterized factors was calculated by normalizing the CHP or SMG group to its corresponding static group. Heatmap was generated by calculating the pairwise Pearson correlation coefficient of included factors. *Represents $p < 0.05$.

significant differences were observed between female and male cohorts (**Figure 4B**).

To better understand the relationship among all factors of interest and the sex-dependent differences, a Pearson correlation network (**Figure 4C**) was generated for both the female and male cohorts with data from all three treatment groups. Some observations mentioned above were further confirmed with correlation coefficients, such as the positive correlation between GAG/DNA and wet weight, the negative correlation between GAG/DNA and contraction, and the positive correlation between *SOX9* and *COL2A1* expression levels. Overall, the correlation analysis yielded different patterns between the female and male cohorts, especially for two examined genes, *ACTA2* and *TAGLN,* that are characteristic of the contractile phenotype in dedifferentiated articular chondrocytes compared to the other factors (Parreno et al., 2017). The level of contraction was positively correlated with *ACTA2* and *TAGLN* expression levels in both female and male groups, confirming their indication for contraction levels. However, the female cohort showed differently a mostly strong negative correlation between the contractile genes and the rest of the factors compared to the male cohort. *ACTA2* and *TAGLN* activity is associated with cytoskeletal composition and structure (Killion et al., 2017; Tang and Gerlach, 2017), and thus results may suggest sex-dependent differences of cytoskeletal activity in response to mechanical stimulation.

Comparison of Female and Male Transcriptome Response to CHP and SMG

Finally, we investigated the sex-dependent difference in the global transcriptome profile in response to mechanical loading and unloading. Consistent with the DEGs analysis for all donors combined, CHP and SMG uniquely regulated a large proportion of genes within each sex group (**Figure 5A**). We identified the top 25 enriched KEGG pathways for female and male tissues under CHP and SMG using the corresponding DEG sets (**Figure 5B**). For CHP, the most enriched KEGG pathway for both female and male groups was “mineral absorption.” Other relevant terms, such as “IL-17 signalling pathway”, “HIF-1 signalling pathway”, and “glycosaminoglycan biosynthesis,” were also observed for both sex groups. Although some of the enriched pathways were shared, a distinct gene profile with different magnitudes and sometimes the direction of modulation was observed for each sex group (**Table 3**). For example, the *NOTUM* gene in the Wnt-signalling pathway was significantly upregulated by 6.7-fold in CHP for the female cohort and only 1.8-fold in CHP for the male cohort. A large proportion of the top 25 KEGG pathways enriched by SMG overlapped with the pathways in CHP, but the corresponding gene profiles were different. For example, SMG did not significantly regulate the *NOTUM*, and it showed the opposite direction between female and male cohorts. The *MMP3* gene was downregulated by SMG but upregulated by CHP. Interestingly, in addition to the

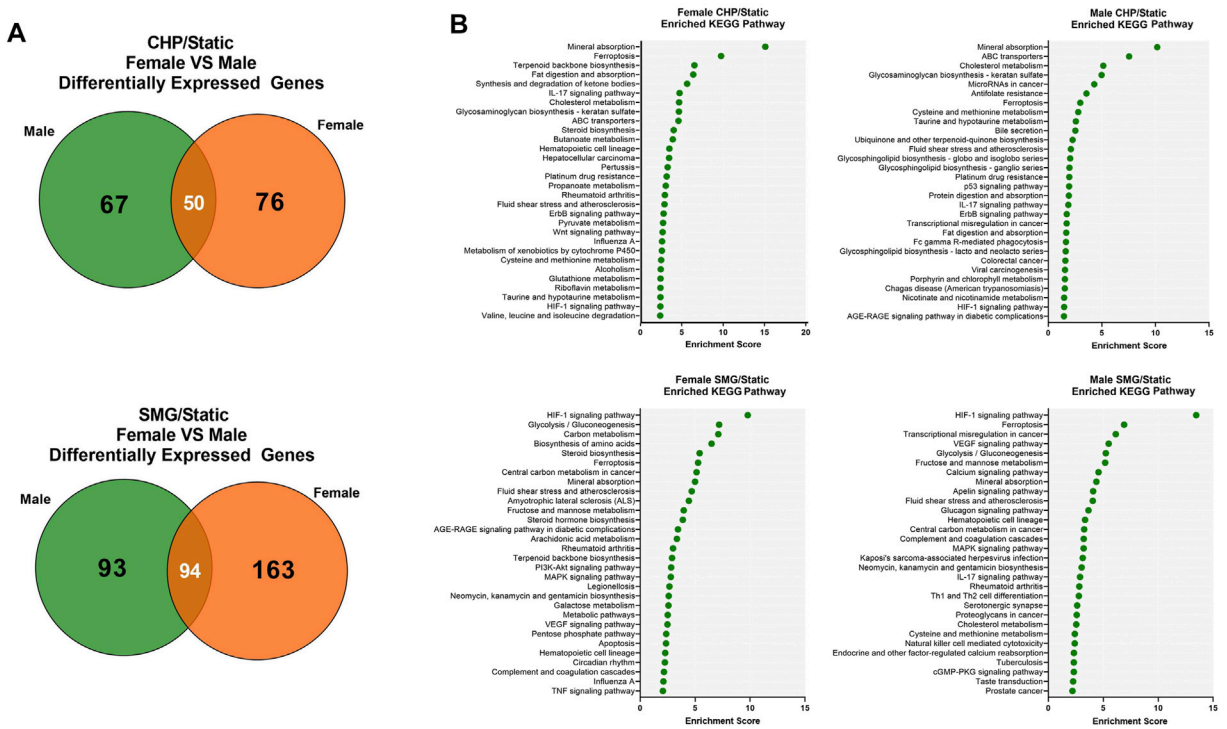

FIGURE 5 | Transcriptome response of female and male donors to CHP and SMG. **(A)** Overlap of DEGs of female and male donors exposed to CHP and SMG. **(B)** Top enriched KEGG pathways by identified DEGs. KEGG terms were selected by *p*-value and plotted to the enrichment score.

OA-related KEGG pathways, the "fluid shear stress and atherosclerosis" pathway was enriched for both female and male cohorts, suggesting an effect of mechanical stimulation from CHP and SMG on engineered meniscus constructs.

In relation to mechanobiology of the meniscus, we investigated the transcriptome profile changes of various mechanosensitive molecules such as *TRPV1/4*, *PIEZO1*, *TMEM63A/B/C*, and *RUNX2* (McNulty and Guilak, 2015; Servin-Vences et al., 2017; Agarwal et al., 2021; Hwang et al., 2021; Lee et al., 2021). Furthermore, the mechanotransduction function of *FOSB* in MFCs (Szojka et al., 2021a) was reported by Szojka et al., and its function in the IL-17 signalling pathway was well demonstrated (Benderdour et al., 2002). Finally, Vyhlidal et al. recognized the potential of caveolae molecules such as *CAV1/2* in the mechanotransductive mechanism of the meniscus, but this needs to be further verified in future studies (Vyhlidal and Adesida, 2021). The transcriptome changes are summarized in **Table 4**. Within our dataset, only *CAV1*, *CAV2*, and *FOSB* are significant by *q*-value for loading regime comparison and sex-based comparison. *CAV2* was regulated in the opposite direction by CHP and SMG. CHP upregulated *FOSB* by 49.5-fold compared to 3.4-fold by SMG. The difference was even larger in female tissues (137.8-fold by CHP and 2.8-fold by SMG), and in comparison, the fold change of *FOSB* expression was similar by CHP and SMG for male tissues (9.7-fold and 3.7-fold). Other mechanosensitive molecules were not significantly modulated from the treatments. The transcriptome profile changes suggest sex-dependent differences in the mechanotransduction mechanisms as well as varying capabilities to sense cytoskeletal structural changes.

DISCUSSION

Currently, there is no existing model to reflect the physiological mechanism of OA holistically, but several *in-vitro* and *in-vivo* models have been developed to answer questions regarding the mechanisms of OA (Cope et al., 2019). This study aimed to evaluate the effects of mechanical loading and unloading *via* CHP and SMG, respectively, on the OA-related profile changes of engineered meniscus tissues and explore biological sex-related differences. This can serve as an *in-vitro* model to investigate the cellular and molecular profiles responsible for the sex-dependent incidence of OA disease.

Cartilage is a highly mechanosensitive tissue, and appropriate levels of mechanical stimulation are crucial for homeostasis and healthy cartilage development. Mechanical stimuli are transmitted by the pericellular matrix (PCM) (Melrose et al., 2006; Youn et al., 2006) to the chondrocyte surface and sensed by mechano-receptors, triggering a cascade of downstream activities (Zhao et al., 2020). The importance of mechanical loading under normal gravity environments has been demonstrated by studies examining the protective effects of moderate loading against tissue degradation as well as investigating the unwanted consequences from unloading. From several *in-vitro* and *in-vivo* models, mechanical loading has been shown to attenuate

TABLE 3 | Key enriched KEGG pathways and associated differentially expressed genes (DEGs) in CHP and SMG groups as compared to static controls within female and male donor cohorts. *q < 0.05, **q < 0.01, ***q < 0.001 represent statistical difference of the two groups in each fold change value.

Gene	Description	Fold change: CHP/Static			Fold change: SMG/Static		
		Female	Male	Combined	Female	Male	Combined
KEGG: Mineral absorption							
FTH1	Ferritin Heavy Chain 1	2.18*	3.47*	1.70*	3.47*	2.32*	2.77***
HMOX1	Heme oxygenase 1	2.94*	3.51**	2.83***	3.51**	3.28**	3.38***
MT1E	Metallothionein 1E	2.79**	1.96*	2.48***	1.96*	−1.09	1.32
MT1G	Metallothionein 1G	8.25*	3.29	9.38**	3.29	1.11	2.21
MT1M	Metallothionein 1M	2.59**	1.89*	2.20***	1.89*	−1.35	1.14
MT2A	Metallothionein 2A	2.59*	1.57	2.79***	1.57	1.18	1.35
SLC30A1	Solute Carrier Family 30 Member 1	2.21**	2.03*	1.70**	2.03*	1.23	1.57**
SLC8A1	Solute Carrier Family 8 Member A1	−2.13	1.15*	−1.44	1.15*	−3.13*	−2.91**
KEGG: Wnt signaling pathway							
FOSL1	FOS Like 1, AP-1 Transcription Factor Subunit	2.99*	3.88**	3.44***	1.16	1.88	1.53
FZD2	Frizzled Class Receptor 2	−2.22*	−1.25	−1.68*	−1.48	−1.12	−1.30
NOTUM	Notum, Palmitoleoyl-Protein carboxylesterase	6.71*	1.77	2.97*	1.17	−1.94	−1.48
SFRP2	Secreted Frizzled Related Protein 2	−6.22*	−3.03*	−4.07**	−2.55	−3.15	−2.82*
KEGG: HIF-1 signaling pathway							
EGLN3	Egl-9 Family Hypoxia Inducible Factor 3	1.00	2.49	1.58	−4.24*	−5.75*	−4.72***
EN O 2	Enolase 2	−1.24	1.48	1.11	−2.96*	−2.51	−2.74**
GAPDH	Glyceraldehyde-3-Phosphate dehydrogenase	−1.14	1.24	1.06	−2.27*	−2.21	−2.24**
HK2	Hexokinase 2	-1.61	1.03	−1.21	−2.20*	−2.66*	−2.41**
HMOX1	Heme oxygenase 1	2.94*	2.74*	2.83***	3.51**	3.28**	3.38***
LDHA	Lactate dehydrogenase A	1.21	1.31	1.26	−1.94*	−2.04*	−1.98***
PDK1	Pyruvate dehydrogenase kinase 1	−1.28	−1.13	−1.20	−2.89**	−3.43**	−3.11***
PFKFB3	6-Phosphofructo-2-Kinase/Fructose-2,6-Biphosphatase 3	−1.80	−1.15	−1.44	−2.33*	−2.34*	−2.33**
PGK1	Phosphoglycerate kinase 1	1.17	1.23	1.20	−2.04*	−2.24*	−2.13***
TFRC	Transferrin Receptor	2.80**	1.36	1.92**	2.55**	2.22*	2.35***
VEGFA	Vascular Endothelial Growth Factor A	−1.57	−1.11	−1.33	−5.48**	-5.95*	−5.68***
KEGG: IL-17 signaling pathway							
CCL2	C-C Motif Chemokine Ligand 2	3.85*	3.48**	3.62***	3.51**	1.41	2.17**
FOSB	FosB Proto-Oncogene, AP-1 Transcription Factor Subunit	137.8*	9.70	49.48**	2.82	3.66	3.40
FOSL1	FOS Like 1, AP-1 Transcription Factor Subunit	2.99*	3.88**	3.44***	1.16	1.88	1.53
MAPK13	Mitogen-Activated Protein kinase 13	−1.51	1.31	−1.07	−3.05*	−3.01*	−3.03***
MMP13	Matrix metallopeptidase 13	1.56*	1.38	1.51	1.64	2.57*	1.89**
MMP3	Matrix metallopeptidase 3	10.5**	4.36	6.47***	−1.80	−3.99*	−2.82**
KEGG: Fluid Shear stress and atherosclerosis							
CCL2	C-C Motif Chemokine Ligand 2	3.85*	3.48**	3.62***	3.51**	1.41	2.17**
HMOX1	Heme oxygenase 1	2.94**	2.74**	2.83***	3.51**	3.28**	3.38***
MAP3K5	Mitogen-Activated Protein kinase kinase 5	−1.37	−1.39	−1.38	2.38*	1.49	1.87**
MAPK13	Mitogen-Activated Protein kinase 13	−1.51	1.31	−1.07	−3.05*	−3.01*	−3.03***
MGST1	Microsomal Glutathione S-Transferase 1	2.21**	1.40	1.65**	1.86*	1.25	1.43**
NQ O 1	NAD(P)H Quinone dehydrogenase 1	3.83***	2.40**	2.88***	4.04***	2.42**	2.97***
PLAT	Plasminogen Activator, Tissue Type	1.51	2.27	1.88*	2.51*	2.43*	2.47**
PRKAA2	Protein kinase AMP-Activated Catalytic Subunit Alpha 2	−1.37	1.44	1.03	−4.63*	-2.90	−3.70**
VEGFA	Vascular Endothelial Growth Factor A	−1.57	−1.11	−1.33	−5.48**	−5.95*	−5.68***

inflammatory cytokine-induced expression of matrix-degrading enzyme (Ohtsuki et al., 2019), upregulating the content of sulphated glycosaminoglycan (sGAG), aggrecan, cartilage oligomeric matrix protein, type II collagen, and lubricin (PRG4) (Antunes et al., 2020), and modulating relevant pathways such as the HIF-1 (Huang et al., 2017) and IL-4 (He et al., 2019) signalling pathways. On the contrary, prolonged mechanical unloading by space flight has been shown to accelerate cartilage degeneration (Herranz et al., 2013; Fitzgerald, 2017; Fitzgerald et al., 2019). Although several studies suggested that SMG was beneficial for preserving a chondrogenic phenotype through induction of 3D aggregates from monolayer cultures (Aleshcheva et al., 2015; Wuest et al., 2018; Wehland et al., 2020) and promoted cartilaginous components deposition for scaffold cultures (Freed and Vunjak-Novakovic, 1997), the degree of hypertrophic

TABLE 4 | Relevant mechanosensitive molecules in CHP and SMG groups as compared to static controls within female and male donor cohorts. *q < 0.05, **q < 0.01, ***q < 0.001 represent statistical difference of the two groups in each fold change value.

Gene	Description	Fold change: CHP/Static			Fold change: SMG/Static		
		Female	Male	Combined	Female	Male	Combined
CAV1	Caveolin 1	1.92*	1.51	1.68**	1.40	1.40	1.40*
CAV2	Caveolin 2	1.42*	1.28	1.34**	1.07	−1.15	−1.04
FOSB	FosB Proto-Oncogene, AP-1 Transcription Factor Subunit	137.8*	9.70	49.48**	2.82	3.66	3.40
PIEZO1	Piezo Type Mechanosensitive Ion Channel Component 1	1.19	1.41	1.30	-1.02	1.09	1.04
RUNX2	RUNX Family Transcription Factor 2	1.13	−1.13	1.02	−1.14	1.07	−1.04
TMEM63A	Transmembrane Protein 63A	−1.05	−1.13	−1.09	1.15	1.22	1.19
TMEM63B	Transmembrane Protein 63B	1.04	1.18	1.11	1.25	1.38	1.32
TMEM63C	Transmembrane Protein 63C	1.43	1.42	1.43	−1.24	−1.20	−1.22
TRPV1	Transient Receptor Potential Cation Channel Subfamily V Member 1	−1.62	−1.21	−1.37	−1.16	−1.03	−1.08
TRPV4	Transient Receptor Potential Cation Channel Subfamily V Member 4	1.25	1.02	1.11	−1.10	−1.16	−1.13

differentiation was not investigated in these studies. Through regulation of key genes and molecular pathways, SMG was also reported to increase activities associated with cartilage catabolism (Stamenković et al., 2010; Wang et al., 2010; Laws et al., 2016) and promoted hypertrophic differentiation of chondrocytes (Jin et al., 2013; Weiss et al., 2017).

In addition to cartilage, the meniscus also plays a critical role in the biomechanics of the knee joint. Evidence has shown that the role of meniscus fibrochondrocytes (MFCs) in response to mechanical signals affects the physiological, pathological, and repair response of the meniscus (McNulty and Guilak, 2015). The PCM of MFCs is also involved in mechanotransduction, although it may play a protective role against larger stresses and strains (Gupta and Haut Donahue, 2006). Various *in-vivo* studies have documented that mechanical stimulation can drive both anti- and pro-inflammatory responses in MFCs (Ferretti et al., 2005; Killian et al., 2014), as well as the detrimental effects of mechanical unloading from joint immobilization on meniscus development, function, and repair (Videman et al., 1979; Klein et al., 1989; Anderson et al., 1993; Djurasovic et al., 1998; Mikic et al., 2000; Bray et al., 2001). Additionally, several *in-vitro* studies have shown the anabolic effect of mechanical loading on MFCs with enhanced meniscus ECM components like *ACAN* expression and collagens and mechanical properties (Aufderheide and Athanasiou, 2006; Puetzer et al., 2012). Finally, there have been various *in-vitro* meniscus repair models that utilized mechanical loading to suppress IL-1 mediated increases in MMP activity, enhance sGAG production, and increase integrative strength of the engineered tissue constructs (McNulty et al., 2007; McNulty and Guilak, 2008; McNulty et al., 2010; Riera et al., 2011; McNulty and Guilak, 2015).

Consistent with these previous reports, our results showed that mechanical loading *via* CHP increased the deposition of type II collagen and aggrecan, supported by immunofluorescence staining and gene expression analysis. In addition, the Safranin-O staining and biochemical quantification of GAG production per cell confirmed that CHP increased the chondrogenic potential of meniscus MFCs. As expected, the wet weight of engineered constructs in the CHP group was the highest among the three treatment groups since the GAG is a major water-binding component of cartilage (KIANI et al., 2002). The ratio of *COL2A1* to *COL1A2* has also been used to evaluate chondrogenic capacity (Wuest et al., 2018; Wehland et al., 2020), and in our results, CHP substantially increased the *COL2A1*/*COL1A2* ratio compared to SMG groups. Although upregulation of type II collagen deposition and *COL2A1* expression was observed in the SMG groups compared to static controls, the magnitude of upregulation was not less than in the CHP groups. The GAG/DNA ratio of the SMG group was also lower than static controls in addition to a stronger intensity of type X collagen staining. Taken together, our data highlights the detrimental effect of SMG on the chondrogenic capacity of the engineered meniscus and suggests that mechanical unloading increases the hypertrophic differentiation of MFCs, driving them to display OA-like characteristics.

To the best of our knowledge, this is one of the first studies to investigate the effect of mechanical loading and unloading on cartilage models by examining global transcriptome profile alterations. The ECM of chondrocytes is crucial for regulating key functions through receptor-mediated matrix-cell interactions. The composition of the ECM and the bound signalling molecules largely influences the chondrogenic capacity of embedded chondrocytes (Gao et al., 20142014). By overlaying the DEGs, we found that CHP and SMG regulated MFC functions through largely different mechanisms. As listed in **Table 2**, several Wnt-signaling pathway-related genes were strongly regulated by CHP, in addition to various matrix remodelling enzymes. But for SMG, the genes with the highest fold-change functioned in more general ways, such as the several growth factors encoding genes identified to regulate general development processes. The KEGG pathway analysis also showed that several chondrogenesis- and OA-related pathways such as mineral absorption, Wnt-signalling pathway, HIF-1 signalling pathways, and IL-17 signalling pathway were enriched by both CHP and SMG. However, the expression profile of related genes in terms of magnitude and direction was quite different (**Table 3**). It is worth mentioning that no sex hormone-related pathways were present in the top enriched pathways. Thus, the observed sex-dependent differences are independent of differences between sex-related hormones. Taken together, the comparative transcriptome analysis

suggested a distinct effect of CHP and SMG on regulating chondrogenesis, but further investigations are needed to determine the specific underlying mechanisms.

The cellular and molecular mechanisms behind the well-documented sex discrepancy in OA incident rates are poorly understood. Many factors are believed to contribute to the higher incidence and severity of OA in females, such as age, psychosocial status, metabolic variables, hormonal differences, anatomical variations, and inflammatory disease (Ferre et al., 2019). While the focus of many previous studies was mainly on bone shape (Yang et al., 2014; Wise et al., 2016; Frysz et al., 2020), gait kinematics (Phinyomark et al., 2016; Ro et al., 2017; Allison et al., 2018), and sex hormones (Zazulak et al., 2006; Brennan et al., 2010; Boyan et al., 2013b; Wang et al., 2013; Antony et al., 2016), little effort was invested into determining differences in the global transcriptome profile. Two studies reported that female OA patients have higher levels of inflammatory cytokines in the synovial fluid than males (Hooshmand et al., 2015; Kosek et al., 2018), but the underlying signalling mechanism was not investigated. To explore the sex-dependent differences in OA pathogenesis, we separated our donor cohort based on sex and compared the OA-related characteristics.

Although the female and male donor cohorts included in this study showed highly variable trends in terms of histological and immunofluorescence staining for cartilage markers like aggrecan and type II collagen, an expected similar trend was observed for *COL2A1*, *SOX9*, *ACAN*, and *COL2A1/COL1A2* average fold-change levels across donor and treatment groups. The average fold change level for *COL10A1* was comparable between the CHP and SMG groups for both sexes. However, one female donor showed significantly higher fold-changes for *COL10A1* while the remaining female cohort showed a generally reduced expression of *COL10A1* in CHP compared to SMG, but not significant. The observed deposition of type X collagen in immunofluorescence staining shows high variability, and sex-dependent differences are difficult to elucidate. Our results suggest overall that at the protein level, the effect of mechanical stimulation is more dominant than sex differences for the deposition of cartilaginous components.

A significant sex-dependent difference was observed for tissue contraction between female and male CHP groups. Additionally, the Pearson correlation network generated for the female and male donor cohorts shows clear sex-dependent differences in expression trends between contractile genes *ACTA2* and *TAGLN* in relation to the other factors investigated in this study. Firstly, the measured contraction based on the percentage of reduction in tissue area positively correlated with *ACTA2* and *TAGLN* expression levels in both female and male cohorts. This suggests that these contractile genes are indeed correlated with physical contraction levels in our study. Interestingly, *ACTA2* and *TAGLN* expression levels in relation to other factors show distinct sex-dependent differences. Among the female cohort, the contractile genes showed a mostly strong negative correlation with the other factors, while the genes in the male cohort showed a generally positive correlation. Mechanical loading has been suggested to mediate the function of chondrocytes by stimulating the reorganization of cytoskeleton (Killion et al., 2017; Tang and Gerlach, 2017). And simulated microgravity was also reported to alter the structure of cytoskeleton components (Wehland et al., 2020) and regulate the expression of several cytoskeletal genes (Aleshcheva et al., 2015). Since *ACTA2* and *TAGLN* activity is associated with cytoskeletal composition and structure, the opposite trend in correlation with other factors between the female and male cohort may suggest sex-dependent differences from cytoskeletal activity in response to varying levels of mechanical stimulation. Furthermore, the mechano-sensitive gene *FOSB* in the IL-17 signalling pathway was identified in our dataset to show a 137.8-fold upregulation from CHP in the female cohort while only observing a 9.7-fold increase in the male cohort. This may suggest sex-dependent differences in the mechanotransduction mechanisms as well as varying capabilities to sense cytoskeletal structural changes arising from mechanical stimulation.

There are several limitations to our model explored in this study. Firstly, we did not have any tissue samples from OA patients to confirm the OA-phenotype observed in our model. However, the modulation of several OA markers (Kiraly et al., 2017) from SMG such as the upregulation of MMP13 and the increased staining of collagen type X, reasonably suggest that the SMG treatment is pushing the engineered tissues constructs towards an OA-phenotype, and this effect is likely to increase with longer treatment periods. Another limitation is that even prolonged joint mobility under normal gravity can induce an OA-phenotype, and thus the static group in this study may also serve as an alternate condition for simulating OA. However, the static group here is meant as a baseline control between the two mechanical treatments and serves to reduce donor-to-donor variability by normalizing measurements to the static control within each donor. Finally, a limitation in our model is that although the engineered meniscus constructs contain the necessary component of fibrocartilage, the tissue microenvironment experienced by the cells is likely different from that of the native meniscus. In particular, the cells in the native meniscus may respond differently to receptor-mediated cell-ECM interactions from mechanical load than in the engineered meniscus models, especially due to differences in the matrix stiffness. We hope to address this limitation in our future studies by evaluating cytoskeleton factors and measurements and using substrates with tunable stiffnesses such as hydrogels.

CONCLUSION

Taken together, our data suggest that engineered meniscus tissues responded to mechanical loading and unloading *via* CHP and SMG in a sex-dependent manner. Mechanical unloading *via* SMG was shown to induce an OA-like profile, while mechanical loading *via* CHP promotes elements of chondrogenesis. Within each mechanical stimulation group, female and male donor cohorts show sex-dependent differences in the magnitude and direction of many differentially expressed genes, as well as tissue contraction and correlation of contractile genes with the other factors investigated in this study. The combination of CHP and SMG can feasibly serve as an *in-vitro* model to study the cellular and molecular mechanisms of KOA and provide a platform for exploring potential drug-targetable pathways as therapeutics.

DATA AVAILABILITY STATEMENT

The datasets presented in this study can be found in online repositories. The names of the repository/repositories and accession number(s) can be found below: GEO and GSE192982.

AUTHOR CONTRIBUTIONS

All listed authors meet the *Frontier in Bioengineering and Biotechnology* criteria for authorship. ZM, DL, and AA designed the study. ZM, DL, and AM-S performed tissue culture. ZM, DL, and MK performed RT-qPCR expression analysis. ZM, DL, and AA were responsible for RNA-seq data analysis with Partek Flow software. ZM, DL, and LW were responsible for mechanical testing and analysis. ZM and DL performed the statistical analysis and prepared tables and figures. ZM, DL, and AA wrote the manuscript with input from all co-authors. LW and AA were responsible for acquiring financial support and supervision of the study.

FUNDING

ZM: NSERC (NSERC RGPIN-2018-06290 Adesida) DL: NSERC Undergraduate Student Research Awards MK: Alberta Cancer Foundation-Mickleborough Interfacial Biosciences Research Program (ACF-MIBRP 27128 Adesida) AM-S: Canadian Institutes of Health Research (CIHR MOP 125921 Adesida) LW: University of Alberta Pilot Seed Grant Program (UOFAB PSGP); University of Alberta Women and Children's Health Research Institute Innovation Grant (UOFAB WCHRIIG 3126) AA: Natural Sciences and Engineering Research Council (NSERC RGPIN-2018-06290); Canadian Institutes of Health Research (CIHR MOP 125921 Adesida); Canada Foundation for Innovation (CFI 33786); University Hospital of Alberta Foundation (UHF; RES0028185 Adesida); Edmonton Orthopaedic Research Committee, Cliff Lede Family Charitable Foundation (RES00045921 Adesida); University of Alberta Pilot Seed Grant Program (UOFAB PSGP); University of Alberta Women and Children's Health Research Institute Innovation Grant (UOFAB WCHRIIG 3126); the Alberta Cancer Foundation-Mickleborough Interfacial Biosciences Research Program (ACF-MIBRP 27128 Adesida). Research grant funding for the work was provided by Natural Sciences and Engineering Research Council (NSERC RGPIN-2018-06290 Adesida), NSERC RTI-2019-00310 Adesida; Canada Foundation for Innovation (CFI 33786); University Hospital of Alberta Foundation (UHF; RES0028185 Adesida); Edmonton Orthopaedic Research Committee, Cliff Lede Family Charitable Foundation (RES00045921 Adesida); University of Alberta Pilot Seed Grant Program (UOFAB PSGP); University of Alberta Women and Children's Health Research Institute Innovation Grant (UOFAB WCHRIIG 3126); the Alberta Cancer Foundation-Mickleborough Interfacial Biosciences Research Program (ACF-MIBRP 27128 Adesida).

ACKNOWLEDGMENTS

We thank Tara Stach and the team at the Biomedical Research Centre from the University of British Columbia for their help with RNA sequencing.

SUPPLEMENTARY MATERIAL

The Supplementary Material for this article can be found online at: https://www.frontiersin.org/articles/10.3389/fbioe.2022.823679/full#supplementary-material

REFERENCES

Agarwal, P., Lee, H.-p., Smeriglio, P., Grandi, F., Goodman, S., Chaudhuri, O., et al. (2021). A Dysfunctional TRPV4-Gsk3β Pathway Prevents Osteoarthritic Chondrocytes from Sensing Changes in Extracellular Matrix Viscoelasticity. *Nat. Biomed. Eng.* 5, 1472–1484. doi:10.1038/s41551-021-00691-3

Aigner, T., Reichenberger, E., Bertling, W., Kirsch, T., Stöß, H., and Mark, K. (1993). Type X Collagen Expression in Osteoarthritic and Rheumatoid Articular Cartilage. *Virchows Archiv B Cell Pathol* 63, 205–211. doi:10.1007/bf02899263

Aleshcheva, G., Wehland, M., Sahana, J., Bauer, J., Corydon, T. J., Hemmersbach, R., et al. (2015). Moderate Alterations of the Cytoskeleton in Human Chondrocytes after Short-term Microgravity Produced by Parabolic Flight Maneuvers Could Be Prevented by Up-regulation of BMP-2 and SOX-9. *FASEB j.* 29, 2303–2314. doi:10.1096/fj.14-268151

Allison, K., Hall, M., Wrigley, T. V., Pua, Y.-H., Metcalf, B., and Bennell, K. L. (2018). Sex-specific Walking Kinematics and Kinetics in Individuals with Unilateral, Symptomatic Hip Osteoarthritis: A Cross Sectional Study. *Gait & Posture* 65, 234–239. doi:10.1016/j.gaitpost.2018.07.179

Anderson, D. R., Gershuni, D. H., Nakhostine, M., and Danzig, L. A. (1993). The Effects of Non-weight-bearing and Limited Motion on the Tensile Properties of the Meniscus. *Arthrosc. J. Arthroscopic Relat. Surg.* 9, 440–445. doi:10.1016/s0749-8063(05)80319-6

Anderson-Baron, M., Liang, Y., Kunze, M., Mulet-Sierra, A., Osswald, M., Ansari, K., et al. (2021). Suppression of Hypertrophy during *in vitro* Chondrogenesis of Cocultures of Human Mesenchymal Stem Cells and Nasal Chondrocytes Correlates with Lack of *in vivo* Calcification and Vascular Invasion. *Front. Bioeng. Biotechnol.* 8. doi:10.3389/fbioe.2020.572356

Antony, B., Venn, A., Cicuttini, F., March, L., Blizzard, L., Dwyer, T., et al. (2016). Association of Body Composition and Hormonal and Inflammatory Factors with Tibial Cartilage Volume and Sex Difference in Cartilage Volume in Young Adults. *Arthritis Care Res.* 68, 517–525. doi:10.1002/acr.22715

Antunes, B. P., Vainieri, M. L., Alini, M., Monsonego-Ornan, E., Grad, S., and Yayon, A. (2020). Enhanced Chondrogenic Phenotype of Primary Bovine Articular Chondrocytes in Fibrin-Hyaluronan Hydrogel by Multi-Axial Mechanical Loading and FGF18. *Acta Biomater.* 105, 170–179. doi:10.1016/j.actbio.2020.01.032

Aufderheide, A. C., and Athanasiou, K. A. (2006). A Direct Compression Stimulator for Articular Cartilage and Meniscal Explants. *Ann. Biomed. Eng.* 34, 1463–1474. doi:10.1007/s10439-006-9157-x

Bader, D. L., Salter, D. M., and Chowdhury, T. T. (20112011). Biomechanical Influence of Cartilage Homeostasis in Health and Disease. *Arthritis* 2011, 1–16. doi:10.1155/2011/979032

Badley, E. M., and Kasman, N. M. (2004). The Impact of Arthritis on Canadian Women. *BMC Women's Health* 4, S18. doi:10.1186/1472-6874-4-s1-s18

Benderdour, M., Tardif, G., Pelletier, J. P., Di Battista, J. A., Reboul, P., Ranger, P., et al. (2002). Interleukin 17 (IL-17) Induces Collagenase-3 Production in Human Osteoarthritic Chondrocytes via AP-1 Dependent Activation: Differential Activation of AP-1 Members by IL-17 and IL-1beta. *J. Rheumatol.* 29, 1262–1272.

Blackburn, S., Research User Group, C., Rhodes, C., Higginbottom, A., and Dziedzic, K. (2016). The OARSI Standardised Definition of Osteoarthritis: A Lay Version. *Osteoarthritis and Cartilage* 24, S192. doi:10.1016/j.joca.2016.01.379

Boyan, B. D., Hart, D. A., Enoka, R. M., Nicolella, D. P., Resnick, E., Berkley, K. J., et al. (2013). Hormonal Modulation of Connective Tissue Homeostasis and Sex Differences in Risk for Osteoarthritis of the Knee. *Biol. Sex Dif* 4, 3. doi:10.1186/2042-6410-4-3

Boyan, B. D., Tosi, L., Coutts, R., Enoka, R., Hart, D. A., Nicolella, D. P., et al. (2012). Sex Differences in Osteoarthritis of the Knee. *J. Am. Acad. Orthopaedic Surgeons* 20, 668–669. doi:10.5435/jaaos-20-10-668

Boyan, B. D., Tosi, L. L., Coutts, R. D., Enoka, R. M., Hart, D. A., Nicolella, D. P., et al. (2013). Addressing the Gaps: Sex Differences in Osteoarthritis of the Knee. *Biol. Sex Dif* 4, 4. doi:10.1186/2042-6410-4-4

Bray, R. C., Smith, J. A., Eng, M. K., Leonard, C. A., Sutherland, C. A., and Salo, P. T. (2001). Vascular Response of the Meniscus to Injury: Effects of Immobilization. *J. Orthop. Res.* 19, 384–390. doi:10.1016/s0736-0266(00)00037-1

Breedveld, F. C. (2004). Osteoarthritis--the Impact of a Serious Disease. *Rheumatology* 43, 4i–8. doi:10.1093/rheumatology/keh102

Brennan, S. L., Cicuttini, F. M., Shortreed, S., Forbes, A., Jones, G., Stuckey, S. L., et al. (2010). Women Lose Patella Cartilage at a Faster Rate Than Men: A 4.5-year Cohort Study of Subjects with Knee OA. *Maturitas* 67, 270–274. doi:10.1016/j.maturitas.2010.07.008

Cope, P. J., Ourradi, K., Li, Y., and Sharif, M. (2019). Models of Osteoarthritis: the Good, the Bad and the Promising. *Osteoarthritis and Cartilage* 27, 230–239. doi:10.1016/j.joca.2018.09.016

D'Angelo, M., Yan, Z, Nooreyazdan, M., Pacifici, M, Sarment, D. S., Billings, P. C., et al. (2000). MMP-13 Is Induced during Chondrocyte Hypertrophy. *J. Cell Biochem.* 77, 678–693.

Djurasovic, M., Aldridge, J. W., Grumbles, R., Rosenwasser, M. P., Howell, D., and Ratcliffe, A. (1998). Knee Joint Immobilization Decreases Aggrecan Gene Expression in the Meniscus. *Am. J. Sports Med.* 26, 460–466. doi:10.1177/03635465980260032101

Dreier, R. (2010). Hypertrophic Differentiation of Chondrocytes in Osteoarthritis: the Developmental Aspect of Degenerative Joint Disorders. *Arthritis Res. Ther.* 12, 216. doi:10.1186/ar3117

Elder, B. D., and Athanasiou, K. A. (2009). Hydrostatic Pressure in Articular Cartilage Tissue Engineering: From Chondrocytes to Tissue Regeneration. *Tissue Eng. B: Rev.* 15, 43–53. doi:10.1089/ten.teb.2008.0435

Ferre, I. M., Roof, M. A., Anoushiravani, A. A., Wasterlain, A. S., and Lajam, C. M. (2019). Understanding the Observed Sex Discrepancy in the Prevalence of Osteoarthritis. *JBJS Rev.* 7, e8. doi:10.2106/jbjs.rvw.18.00182

Ferretti, M., Srinivasan, A., Deschner, J., Gassner, R., Baliko, F., Piesco, N., et al. (2005). Anti-inflammatory Effects of Continuous Passive Motion on Meniscal Fibrocartilage. *J. Orthop. Res.* 23, 1165–1171. doi:10.1016/j.orthres.2005.01.025

Fitzgerald, J. (2017). Cartilage Breakdown in Microgravity-A Problem for Long-Term Spaceflight? *Npj Regen. Med.* 2, 10. doi:10.1038/s41536-017-0016-1

Fitzgerald, J., Endicott, J., Hansen, U., and Janowitz, C. (2019). Articular Cartilage and Sternal Fibrocartilage Respond Differently to Extended Microgravity. *npj Microgravity* 5, 3. doi:10.1038/s41526-019-0063-6

Freed, L. E., and Vunjak-Novakovic, G. (1997). Microgravity Tissue Engineering. In Vitro *Cell.Dev.Biol.-Animal* 33, 381–385. doi:10.1007/s11626-997-0009-2

Frysz, M., Gregory, J., Aspden, R. M., Paternoster, L., and Tobias, J. H. (2020). Sex Differences in Proximal Femur Shape: Findings from a Population-Based Study in Adolescents. *Sci. Rep.* 10, 4612. doi:10.1038/s41598-020-61653-4

Gao, Y., Liu, S, Huang, J., Guo, W, Chen, J., Zhang, L., et al. (20142014). The ECM-Cell Interaction of Cartilage Extracellular Matrix on Chondrocytes. *Biomed. Res. Int.* 1–8. doi:10.1155/2014/648459

Gunja, N. J., Uthamanthil, R. K., and Athanasiou, K. A. (2009). Effects of TGF-B1 and Hydrostatic Pressure on Meniscus Cell-Seeded Scaffolds. *Biomaterials* 30, 565–573. doi:10.1016/j.biomaterials.2008.10.007

Gupta, T., and Haut Donahue, T. L. (2006). Role of Cell Location and Morphology in the Mechanical Environment Around Meniscal Cells. *Acta Biomater.* 2, 483–492. doi:10.1016/j.actbio.2006.05.009

He, Z., Leong, D. J., Xu, L., Hardin, J. A., Majeska, R. J., Schaffler, M. B., et al. (2019). CITED2 Mediates the Cross-talk between Mechanical Loading and IL-4 to Promote Chondroprotection. *Ann. N.Y. Acad. Sci.* 1442, 128–137. doi:10.1111/nyas.14021

Hellemans, J., Mortier, G., de Paepe, A., Speleman, F., and Vandesompele, J. (2007). qBase Relative Quantification Framework and Software for Management and Automated Analysis of Real-Time Quantitative PCR Data. *Genome Biol.* 8, R19. doi:10.1186/gb-2007-8-2-r19

Herranz, R., Anken, R., Boonstra, J., Braun, M., Christianen, P. C. M., de Geest, M., et al. (2013). Ground-Based Facilities for Simulation of Microgravity: Organism-specific Recommendations for Their Use, and Recommended Terminology. *Astrobiology* 13, 1–17. doi:10.1089/ast.2012.0876

Hooshmand, S., Juma, S., Khalil, D. A., Shamloufard, P., and Arjmandi, B. H. (2015). Women with Osteoarthritis Have Elevated Synovial Fluid Levels of Insulin-like Growth Factor (IGF)-1 and IGF-Binding Protein-3. *J. Immunoassay Immunochemistry* 36, 284–294. doi:10.1080/15321819.2014.947431

Huang, Z., Zhou, M., Wang, Q., Zhu, M., Chen, S., and Li, H. (2017). Mechanical and Hypoxia Stress Can Cause Chondrocytes Apoptosis through Over-activation of Endoplasmic Reticulum Stress. *Arch. Oral Biol.* 84, 125–132. doi:10.1016/j.archoralbio.2017.09.021

Hwang, H. S., Park, I. Y., Hong, J. I., Kim, J. R., and Kim, H. A. (2021). Comparison of Joint Degeneration and Pain in Male and Female Mice in DMM Model of Osteoarthritis. *Osteoarthritis and Cartilage* 29, 728–738. doi:10.1016/j.joca.2021.02.007

Jin, L., Feng, G., Reames, D. L., Shimer, A. L., Shen, F. H., and Li, X. (2013). The Effects of Simulated Microgravity on Intervertebral Disc Degeneration. *Spine J.* 13, 235–242. doi:10.1016/j.spinee.2012.01.022

Kiani, C., Chen, L., Wu, Y. J., Yee, A. J., and Yang, B. B. (2002). Structure and Function of Aggrecan. *Cell Res* 12, 19–32. doi:10.1038/sj.cr.7290106

Killian, M. L., Haut, R. C., and Haut Donahue, T. L. (2014). Acute Cell Viability and Nitric Oxide Release in Lateral Menisci Following Closed-Joint Knee Injury in a Lapine Model of post-traumatic Osteoarthritis. *BMC Musculoskelet. Disord.* 15, 297. doi:10.1186/1471-2474-15-297

Killion, C. H., Mitchell, E. H., Duke, C. G., and Serra, R. (2017). Mechanical Loading Regulates Organization of the Actin Cytoskeleton and Column Formation in Postnatal Growth Plate. *MBoC* 28, 1862–1870. doi:10.1091/mbc.e17-02-0084

Kiraly, A. J., Roberts, A., Cox, M., Mauerhan, D., Hanley, E., and Sun, Y. (2017). Comparison of Meniscal Cell-Mediated and Chondrocyte-Mediated Calcification. *Toorthj* 11, 225–233. doi:10.2174/1874325001711010225

Klein, L., Heiple, K. G., Torzilli, P. A., Goldberg, V. M., and Burstein, A. H. (1989). Prevention of Ligament and Meniscus Atrophy by Active Joint Motion in a Non-weight-bearing Model. *J. Orthop. Res.* 7, 80–85. doi:10.1002/jor.1100070111

Kosek, E., Finn, A., Ultenius, C., Hugo, A., Svensson, C., and Ahmed, A. S. (2018). Differences in Neuroimmune Signalling between Male and Female Patients Suffering from Knee Osteoarthritis. *J. Neuroimmunology* 321, 49–60. doi:10.1016/j.jneuroim.2018.05.009

Laws, C. J., Berg-Johansen, B., Hargens, A. R., and Lotz, J. C. (2016). The Effect of Simulated Microgravity on Lumbar Spine Biomechanics: an *in vitro* Study. *Eur. Spine J.* 25, 2889–2897. doi:10.1007/s00586-015-4221-6

Lee, W., Nims, R. J., Savadipour, A., Zhang, Q., Leddy, H. A., Liu, F., et al. (2021). Inflammatory Signaling Sensitizes Piezo1 Mechanotransduction in Articular Chondrocytes as a Pathogenic Feed-Forward Mechanism in Osteoarthritis. *Proc. Natl. Acad. Sci. USA* 118, e2001611118. doi:10.1073/pnas.2001611118

Leijten, J. C. H., Emons, J., Sticht, C., van Gool, S., Decker, E., Uitterlinden, A., et al. (2012). Gremlin 1, Frizzled-Related Protein, and Dkk-1 Are Key Regulators of Human Articular Cartilage Homeostasis. *Arthritis Rheum.* 64, 3302–3312. doi:10.1002/art.34535

Liang, Y., Idrees, E., Andrews, S. H. J., Labib, K., Szojka, A., Kunze, M., et al. (2017). Plasticity of Human Meniscus Fibrochondrocytes: A Study on Effects of Mitotic

Divisions and Oxygen Tension. *Sci. Rep.* 7, 12148. doi:10.1038/s41598-017-12096-x

Livak, K. J., and Schmittgen, T. D. (2001). Analysis of Relative Gene Expression Data Using Real-Time Quantitative PCR and the 2−ΔΔCT Method. *Methods* 25, 402–408. doi:10.1006/meth.2001.1262

Mayer-Wagner, S., Hammerschmid, F., Redeker, J. I., Schmitt, B., Holzapfel, B. M., Jansson, V., et al. (2014). Simulated Microgravity Affects Chondrogenesis and Hypertrophy of Human Mesenchymal Stem Cells. *Int. Orthopaedics (Sicot)* 38, 2615–2621. doi:10.1007/s00264-014-2454-3

McNulty, A. L., Estes, B. T., Wilusz, R. E., Weinberg, J. B., and Guilak, F. (2010). Dynamic Loading Enhances Integrative Meniscal Repair in the Presence of Interleukin-1. *Osteoarthritis and Cartilage* 18, 830–838. doi:10.1016/j.joca.2010.02.009

McNulty, A. L., and Guilak, F. (2008). Integrative Repair of the Meniscus: Lessons from *in vitro* Studies. *Biorheology* 45, 487–500. doi:10.3233/bir-2008-0489

McNulty, A. L., and Guilak, F. (2015). Mechanobiology of the Meniscus. *J. Biomech.* 48, 1469–1478. doi:10.1016/j.jbiomech.2015.02.008

McNulty, A. L., Moutos, F. T., Weinberg, J. B., and Guilak, F. (2007). Enhanced Integrative Repair of the Porcine Meniscus *in vitro* by Inhibition of Interleukin-1 or Tumor Necrosis Factor α. *Arthritis Rheum.* 56, 3033–3043. doi:10.1002/art.22839

Mellor, L. F., Baker, T. L., Brown, R. J., Catlin, L. W., and Oxford, J. T. (2014). Optimal 3D Culture of Primary Articular Chondrocytes for Use in the Rotating Wall Vessel Bioreactor. *Aviat Space Environ. Med.* 85, 798–804. doi:10.3357/asem.3905.2014

Mellor, L. F., Steward, A. J., Nordberg, R. C., Taylor, M. A., and Loboa, E. G. (2017). Comparison of Simulated Microgravity and Hydrostatic Pressure for Chondrogenesis of hASC. *Aerospace Med. Hum. Perform.* 88, 377–384. doi:10.3357/amhp.4743.2017

Melrose, J., Roughley, P., Knox, S., Smith, S., Lord, M., and Whitelock, J. (2006). The Structure, Location, and Function of Perlecan, a Prominent Pericellular Proteoglycan of Fetal, Postnatal, and Mature Hyaline Cartilages. *J. Biol. Chem.* 281, 36905–36914. doi:10.1074/jbc.m608462200

Mikic, B., Johnson, T. L., Chhabra, A. B., Schalet, B. J., Wong, M., and Hunziker, E. B. (2000). Differential Effects of Embryonic Immobilization on the Development of Fibrocartilaginous Skeletal Elements. *J. Rehabil. Res. Dev.* 37, 127–133.

Murray, C. J., Vos, T., Lozano, R., Naghavi, M., Flaxman, A. D., Michaud, C., et al. (2012). Disability-adjusted Life Years (DALYs) for 291 Diseases and Injuries in 21 Regions, 1990-2010: a Systematic Analysis for the Global Burden of Disease Study 2010. *Lancet* 380, 2197–2223. doi:10.1016/S0140-6736(12)61689-4

Nicolella, D. P., O'Connor, M. I., Enoka, R. M., Boyan, B. D., Hart, D. A., Resnick, E., et al. (2012). Mechanical Contributors to Sex Differences in Idiopathic Knee Osteoarthritis. *Biol. Sex Dif* 3, 28. doi:10.1186/2042-6410-3-28

O'Connor, M. I. (2007). Sex Differences in Osteoarthritis of the Hip and Knee. *JAAOS - J. Am. Acad. Orthopaedic Surgeons* 15.

Ohtsuki, T., Shinaoka, A., Kumagishi-Shinaoka, K., Asano, K., Hatipoglu, O. F., Inagaki, J., et al. (2019). Mechanical Strain Attenuates Cytokine-Induced ADAMTS9 Expression via Transient Receptor Potential Vanilloid Type 1. *Exp. Cell Res.* 383, 111556. doi:10.1016/j.yexcr.2019.111556

Osteoarthritis (2014). Bone and Joint Canada. http://boneandjointcanada.com/osteoarthritis/.

Pan, Q., O'Connor, M. I., Coutts, R. D., Hyzy, S. L., Olivares-Navarrete, R., Schwartz, Z., et al. (2016). Characterization of Osteoarthritic Human Knees Indicates Potential Sex Differences. *Biol. Sex. Differ.* 7, 27. doi:10.1186/s13293-016-0080-z

Parreno, J., Raju, S., Wu, P.-h., and Kandel, R. A. (2017). MRTF-A Signaling Regulates the Acquisition of the Contractile Phenotype in Dedifferentiated Chondrocytes. *Matrix Biol.* 62, 3–14. doi:10.1016/j.matbio.2016.10.004

Phinyomark, A., Osis, S. T., Hettinga, B. A., Kobsar, D., and Ferber, R. (2016). Gender Differences in Gait Kinematics for Patients with Knee Osteoarthritis. *BMC Musculoskelet. Disord.* 17, 157. doi:10.1186/s12891-016-1013-z

Puetzer, J. L., Ballyns, J. J., and Bonassar, L. J. (2012). The Effect of the Duration of Mechanical Stimulation and Post-Stimulation Culture on the Structure and Properties of Dynamically Compressed Tissue-Engineered Menisci. *Tissue Eng. A* 18, 1365–1375. doi:10.1089/ten.tea.2011.0589

Riera, K. M., Rothfusz, N. E., Wilusz, R. E., Weinberg, J. B., Guilak, F., and McNulty, A. L. (2011). Interleukin-1, Tumor Necrosis Factor-Alpha, and Transforming Growth Factor-Beta 1 and Integrative Meniscal Repair: Influences on Meniscal Cell Proliferation and Migration. *Arthritis Res. Ther.* 13, R187. doi:10.1186/ar3515

Ro, D. H., Lee, D. Y., Moon, G., Lee, S., Seo, S. G., Kim, S. H., et al. (2017). Sex Differences in Knee Joint Loading: Cross-Sectional Study in Geriatric Population. *J. Orthop. Res.* 35, 1283–1289. doi:10.1002/jor.23374

Schmittgen, T. D., and Livak, K. J. (2008). Analyzing Real-Time PCR Data by the Comparative CT Method. *Nat. Protoc.* 3, 1101–1108. doi:10.1038/nprot.2008.73

Servin-Vences, M. R., Moroni, M., Lewin, G. R., and Poole, K. (2017). Direct Measurement of TRPV4 and PIEZO1 Activity Reveals Multiple Mechanotransduction Pathways in Chondrocytes. *eLife* 6. doi:10.7554/eLife.21074

Souza, R. B., Baum, T., Wu, S., Feeley, B. T., Kadel, N., Li, X., et al. (2012). Effects of Unloading on Knee Articular Cartilage T1rho and T2 Magnetic Resonance Imaging Relaxation Times: A Case Series. *J. Orthop. Sports Phys. Ther.* 42, 511–520. doi:10.2519/jospt.2012.3975

Stamenković, V., Keller, G., Nesic, D., Cogoli, A., and Grogan, S. P. (2010). Neocartilage Formation in 1 G, Simulated, and Microgravity Environments: Implications for Tissue Engineering. *Tissue Eng. Part. A.* 16, 1729–1736. doi:10.1089/ten.tea.2008.0624

Sun, Y., Mauerhan, D. R., Honeycutt, P. R., Kneisl, J. S., Norton, H. J., Zinchenko, N., et al. (2010). Calcium Deposition in Osteoarthritic Meniscus and Meniscal Cell Culture. *Arthritis Res. Ther.* 12, R56. doi:10.1186/ar2968

Szojka, A. R. A., Li, D. X., Sopcak, M. E. J., Ma, Z, Kunze, M, Mulet-Sierra, A., et al. (2021). Mechano-Hypoxia Conditioning of Engineered Human Meniscus. *Front. Bioeng. Biotechnol.* 9. doi:10.3389/fbioe.2021.739438

Szojka, A. R., Marqueti, R. d. C., Li, D. X., Molter, C. W., Liang, Y., Kunze, M., et al. (2021). Human Engineered Meniscus Transcriptome after Short-Term Combined Hypoxia and Dynamic Compression. *J. Tissue Eng.* 12, 204173142199084. doi:10.1177/2041731421990842

Tang, D. D., and Gerlach, B. D. (2017). The Roles and Regulation of the Actin Cytoskeleton, Intermediate Filaments and Microtubules in Smooth Muscle Cell Migration. *Respir. Res.* 18, 54. doi:10.1186/s12931-017-0544-7

Videman, T., Eronen, I., Friman, C., and Langenskiöld, A. (1979). Glycosaminoglycan Metabolism of the Medial Meniscus, the Medial Collateral Ligament and the Hip Joint Capsule in Experimental Osteoarthritis Caused by Immobilization of the Rabbit Knee. *Acta Orthopaedica Scand.* 50, 465–470. doi:10.3109/17453677908989791

Vyhlidal, M. J., and Adesida, A. B. (2021). Mechanotransduction in Meniscus Fibrochondrocytes: What about Caveolae? *J. Cell Physiol.* doi:10.1002/jcp.30616

Wang, Q., Zheng, Y.-P., Wang, X.-Y., Huang, Y.-P., Liu, M.-Q., Wang, S.-Z., et al. (2010). Ultrasound Evaluation of Site-specific Effect of Simulated Microgravity on Articular Cartilage. *Ultrasound Med. Biol.* 36, 1089–1097. doi:10.1016/j.ultrasmedbio.2010.04.018

Wang, X. D., Kou, X. X., Meng, Z., Bi, R. Y., Liu, Y., Zhang, J. N., et al. (2013). Estrogen Aggravates Iodoacetate-Induced Temporomandibular Joint Osteoarthritis. *J. Dent Res.* 92, 918–924. doi:10.1177/0022034513501323

Wehland, M., Steinwerth, P., Aleshcheva, G., Sahana, J., Hemmersbach, R., Lützenberg, R., et al. (2020). Tissue Engineering of Cartilage Using a Random Positioning Machine. *Ijms* 21, 9596. doi:10.3390/ijms21249596

Weiss, W. M., Mulet-Sierra, A., Kunze, M., Jomha, N. M., and Adesida, A. B. (2017). Coculture of Meniscus Cells and Mesenchymal Stem Cells in Simulated Microgravity. *npj Microgravity* 3, 28. doi:10.1038/s41526-017-0032-x

Wise, B. L., Liu, F., Kritikos, L., Lynch, J. A., Parimi, N., Zhang, Y., et al. (2016). The Association of Distal Femur and Proximal Tibia Shape with Sex: The Osteoarthritis Initiative. *Semin. Arthritis Rheum.* 46, 20–26. doi:10.1016/j.semarthrit.2016.02.006

Wuest, S., Caliò, M., Wernas, T., Tanner, S., Giger-Lange, C., Wyss, F., et al. (2018). Influence of Mechanical Unloading on Articular Chondrocyte Dedifferentiation. *Ijms* 19, 1289. doi:10.3390/ijms19051289

Yang, B., Yu, J.-K., Zheng, Z.-Z., Lu, Z.-H., and Zhang, J.-Y. (2014). Comparative Study of Sex Differences in Distal Femur Morphology in Osteoarthritic Knees in a Chinese Population. *PLoS ONE* 9, e89394. doi:10.1371/journal.pone.0089394

Youn, I., Choi, J. B., Cao, L., Setton, L. A., and Guilak, F. (2006). Zonal Variations in the Three-Dimensional Morphology of the Chondron Measured *in situ* Using

Confocal Microscopy. *Osteoarthritis and Cartilage* 14, 889–897. doi:10.1016/j.joca.2006.02.017

Yu, B., Yu, D., Cao, L., Zhao, X., Long, T., Liu, G., et al. (2011). Simulated Microgravity Using a Rotary Cell Culture System Promotes Chondrogenesis of Human Adipose-Derived Mesenchymal Stem Cells via the P38 MAPK Pathway. *Biochem. Biophysical Res. Commun.* 414, 412–418. doi:10.1016/j.bbrc.2011.09.103

Zazulak, B. T., Paterno, M., Myer, G. D., Romani, W. A., and Hewett, T. E. (2006). The Effects of the Menstrual Cycle on Anterior Knee Laxity. *Sports Med.* 36, 847–862. doi:10.2165/00007256-200636100-00004

Zellner, J., Mueller, M., Xin, Y., Krutsch, W., Brandl, A., Kujat, R., et al. (2015). Dynamic Hydrostatic Pressure Enhances Differentially the Chondrogenesis of Meniscal Cells from the Inner and Outer Zone. *J. Biomech.* 48, 1479–1484. doi:10.1016/j.jbiomech.2015.02.003

Zhao, Z., Li, Y., Wang, M., Zhao, S., Zhao, Z., and Fang, J. (2020). Mechanotransduction Pathways in the Regulation of Cartilage Chondrocyte Homoeostasis. *J. Cell Mol Med* 24, 5408–5419. doi:10.1111/jcmm.15204

Conflict of Interest: The authors declare that the research was conducted in the absence of any commercial or financial relationships that could be construed as a potential conflict of interest.

Publisher's Note: All claims expressed in this article are solely those of the authors and do not necessarily represent those of their affiliated organizations, or those of the publisher, the editors and the reviewers. Any product that may be evaluated in this article, or claim that may be made by its manufacturer, is not guaranteed or endorsed by the publisher.

Copyright © 2022 Ma, Li, Kunze, Mulet-Sierra, Westover and Adesida. This is an open-access article distributed under the terms of the Creative Commons Attribution License (CC BY). The use, distribution or reproduction in other forums is permitted, provided the original author(s) and the copyright owner(s) are credited and that the original publication in this journal is cited, in accordance with accepted academic practice. No use, distribution or reproduction is permitted which does not comply with these terms.

frontiers in Bioengineering and Biotechnology

REVIEW
published: 15 February 2022
doi: 10.3389/fbioe.2022.826748

In Vitro Cellular Strain Models of Tendon Biology and Tenogenic Differentiation

Shannon Y. Wu[1], *Won Kim*[2] *and Thomas J. Kremen Jr*[3]*

[1]David Geffen School of Medicine at UCLA, Los Angeles, CA, United States, [2]Department of Rehabilitation Medicine, Asan Medical Center, University of Ulsan College of Medicine, Seoul, South Korea, [3]Department of Orthopaedic Surgery, David Geffen School of Medicine at UCLA, Los Angeles, CA, United States

Research has shown that the surrounding biomechanical environment plays a significant role in the development, differentiation, repair, and degradation of tendon, but the interactions between tendon cells and the forces they experience are complex. *In vitro* mechanical stimulation models attempt to understand the effects of mechanical load on tendon and connective tissue progenitor cells. This article reviews multiple mechanical stimulation models used to study tendon mechanobiology and provides an overview of the current progress in modelling the complex native biomechanical environment of tendon. Though great strides have been made in advancing the understanding of the role of mechanical stimulation in tendon development, damage, and repair, there exists no ideal *in vitro* model. Further comparative studies and careful consideration of loading parameters, cell populations, and biochemical additives may further offer new insight into an ideal model for the support of tendon regeneration studies.

Keywords: mechanotransduction, tendon, tenogenic differentiation, bioreactor, 3D culture, model

OPEN ACCESS

Edited by:
Dmitriy Sheyn,
Cedars Sinai Medical Center,
United States

Reviewed by:
Scott Rodeo,
Hospital for Special Surgery,
United States
Anne Nichols,
University of Rochester, United States
Spencer Szczesny,
The Pennsylvania State University (PSU), United States

***Correspondence:**
Thomas J. Kremen Jr
tjkremen@mednet.ucla.edu

Specialty section:
This article was submitted to Biomaterials, a section of the journal Frontiers in Bioengineering and Biotechnology

Received: *01 December 2021*
Accepted: *17 January 2022*
Published: *15 February 2022*

Citation:
Wu SY, Kim W and Kremen TJ (2022) In Vitro *Cellular Strain Models of Tendon Biology and Tenogenic Differentiation. Front. Bioeng. Biotechnol. 10:826748. doi: 10.3389/fbioe.2022.826748*

INTRODUCTION

Tendons are connective tissues responsible for transmitting the force generated by muscles to bones. Although their structure and composition allow them to tolerate repetitive forces during daily activities, excessive or abnormal applications of force can cause tendon damage or rupture. Tendon repair can be difficult due to the hypocellular and avascular nature of tendon tissue. Emerging tissue engineering strategies continue to be developed with the goal of augmenting current treatment approaches as well as the development of novel therapies for the treatment of tendon injuries. Although exposure to excessive force contributes to tendon injury, mechanical loading of tendon tissue also plays an important role in appropriate tendon healing. As a result, *in vitro* mechanical stimulation studies attempt to understand the effects of mechanical load on tendon and connective tissue progenitor cells that have the potential to differentiate into tendon cells. These models have allowed researchers to observe the effects of mechanical loading on these cells with regard to tendon gene expression, cell morphology, protein production as well as more gross tissue properties including cellular alignment and tensile strength. This review aims to summarize and compare the different cellular mechanical loading models used in the study of tendon mechanobiology and highlight how the designs of these models have evolved over time in the effort to recapitulate the complexity of forces exerted upon tendon tissues *in vivo*. First, we contextualize our discussion with an introduction to current understanding of native tendon structure and biomechanics. We then discuss how explanted tendon, 2D, and 3D models have contributed to our understanding of the effects of mechanical stimulation in the effort to recapitulate the native tendon architecture in the

in vitro setting. We conclude by identifying existing gaps in knowledge and possible directions for future work within the field of *in vitro* mechanical loading research.

STRUCTURE AND BIOMECHANICS OF TENDON

Structure of Tendon

Tendons are hypocellular structures that largely consist of water and extracellular matrix (ECM), with water making up 55–70% of the tissue mass.(Jaiswal et al., 2020). ECM is predominantly composed of various types of collagen protein molecules. Type I collagen accounts for 60–85% of the total dry weight of tendon tissue (Docheva et al., 2015), whereas type III collagen accounts for 1–5% of the total collagen content.(Liu et al., 1995; Lim et al., 2019). There are also small amounts of other collagen proteins, such as type II, IV, V, XII and XIV collagen (Wang, 2006; Wang et al., 2018a). Type III collagen plays an important role in regulating the size of type I collagen fibrils, while type V collagen, found in the center of fibrils, is thought to act as the template for fibrillogenesis. (Thorpe and Screen, 2016).

Tendon's mechanical properties can be attributed to its hierarchical structure of collagen fibrils (Trelstad and Hayashi, 1979; Wang, 2006). At the molecular level, collagen's triple helix structure allows tendon tissues to have sufficient mechanical strength. (Fratzl et al., 1998). The intermolecular sliding of collagen within tendon facilitates deformation in a linear fashion with application of strain (Kelc et al., 2013). Collagen fibrillogenesis, or the formation of fibrils from the collagen molecules, is an important multi-step process that determines the functionality of the overall tendon. There has been debate on how this process unfolds as tendons mature. Some believe that collagen molecules assemble to form fibril intermediates, which then assemble end-to-end to create longer and mechanically functional fibrils. These longer fibrils then interact laterally, forming fibrils of a larger diameter. In contrast, Kalson et al. have suggested that end-to-end and lateral fusion events do not contribute to fibril growth, as serial microscopy has revealed few fusion events during development, and the number of fibrils does not decrease as expected with fusion. (Kalson et al., 2015). Rather, collagen molecules may accrue on fibril ends, growing in a binding site- and structure-specific mechanism as described by the surface-nucleation-and-propagation (SNP) model. (Holmes et al., 1998). Collagen fibril bundles form fibers, which in turn form the fascicles of tendon tissues. These structures are arranged parallel to the long axis of tendon tissues, which give tendon tissue its hallmark tensile strength (Wang, 2006). Some authors have posited that fascicles are further organized into a spiral formation (Kannus, 2000; Ottani et al., 2002). While some argue that such a structure would make transference of force to bone less efficient, this architecture may be better suited to resisting flexion, compression, and multidirectional forces.

Non-collagenous proteins found within tendon extracellular matrix (ECM) consist of a variety of proteoglycan (PG) molecules (e.g. decorin, fibromodulin, lumican, and fibromodulin), glycoproteins (e.g. tenascin C, fibronectin, lubricin, and laminin) and glycosaminoglycans (Humphrey et al., 2014). The hydrophilic nature of these proteins help the structure to retain high water content, which provides some resistance to physiologic compression forces and inter-fascicular sliding (Jozsa et al., 1989; Kirkendall and Garrett, 1997; Martin et al., 2003; Vogel, 2004; Kohrs et al., 2011; Docheva et al., 2015; Wunderli et al., 2020). In addition, proteoglycans play important roles in collagen fibrillogenesis. Lumican, fibromodulin, decorin, and biglycan all play a role in stabilizing fibril formation and maturation, as knockout mouse models demonstrate that elimination of these proteoglycans result in weaker tendons and increased fibrosis (Robbins et al., 1997; Ezura et al., 2000; Zhang et al., 2009). Proteoglycans may also play a role in attenuating strain experienced at the cellular level. Studies have found that the levels of strain transferred to cells in synthetic scaffolds differ from native levels, as significant strain attenuation occurs from the tissue level to the cell level (Cheng and Screen, 2007). At times, levels of strain estimated on synthetic scaffolds can overestimate native tissue strain by 20–60% (Han et al., 2013). The authors further found that cells in the PG-rich portions of the sample experienced less strain than those in more fibrous areas, suggesting that PGs may affect the local mechanical response, possibly through support of collagen fibrillogenesis or facilitation of resistance to compression or sliding forces.

Biomechanical Properties of Tendon

Tendon tissues have specialized mechanical properties and have features of linear elastic material models as well as viscoelastic material models. In fact, mathematical methods termed quasi-linear viscoelasticity models have been used to model tendon tissue's mechanical behavior (Woo et al., 2000).

The stress-strain curves of tendon tissues are of particular interest because they demonstrate their intrinsic tensile strength during pull-to-failure testing. When using linear elastic material models to describe tendon mechanical properties, the stress-strain curves have three regions, including the toe region, the linear region, and the yield or failure region. (Hooley et al., 1980; Lieber et al., 1991). The toe region corresponds with stretching of crimped fiber bundles, which continues until 2% of strain (Wang, 2006). Within the toe region, the crimp pattern of tendon fibers is stretched; it is recovered when the stress disappears (Lim et al., 2019). Within the linear region (2–6% strain), the slope of the stress-strain curve appears to be constant as it is the inflection point where the curve transitions from strain stiffening to strain softening. This region is also the point at which the tangent modulus reaches its maximum value. Studies have found that over 4% strain can cause microscopic damage during the sliding of collagen fibrils (Thompson et al., 2017). The failure region of the stress-strain curve demonstrates macroscopic tears associated with strain values over 8–10% (Butler et al., 2000; Thompson et al., 2017).

Viscoelastic materials demonstrate different mechanical properties depending on the rate of loading (Woo et al., 2000; Robi et al., 2013). One characteristic of viscoelastic materials such as tendons is creep, the deformation of a material in response to constant load (Jaiswal et al., 2020). *Creep test* or "fatigue" test is

used to demonstrate response of tendon to continuous or repetitive loading (Wang et al., 2018a). Creep testing helps explain the relation between time and strain under constant load (Wren et al., 2003). Upon exposure to initial load, the deformation of tendon tissue is temporary, but as the load is sustained, damage accumulates, and the subsequent strength and stiffness of the damaged tendon tissue decreases (Wang et al., 1995). It is also worth noting that the mechanical properties of different tendons varies by tendon anatomic location and function (Wang et al., 1995; Maganaris and Paul, 1999; Shani et al., 2016).

Mechanical loading, even within the range of typical of daily activities, can lead to tendon damage. *In vitro* mechanical loading studies have reported that mechanical degradation can occur within 24 h of exposure to very low levels of repetitive stress, at a level less than 5% of the ultimate tensile strength of the tissue (Parent et al., 2011). However, this observed *in vitro* degradation would likely be different *in vivo* due to the repair mechanisms of host tendon tissues and the associated supporting cells (e.g. resident connective tissue progenitor cells and immune system cells). Based on results of *in vitro* studies, Wang et al. have suggested that physiologic loading triggers tendon repair, such that the repair counteracts microscopic damage (Wang et al., 2003; Wang et al., 2015). In particular, the therapeutic effects of eccentric loading have been extensively studied in the context of treating Achilles tendinopathy (Fahlström et al., 2003). While human studies reveal that eccentric loading tends to increase the maximum force and the maximum number of repetitions tendons can sustain (Malliaras et al., 2013), the mechanism by which this form of loading has been unclear (O'Neill et al., 2015). A possible explanation can be attributed to complex muscle-tendon interactions, by which the muscle shields tendon from stress by storing energy or increasing tendon stiffness, thereby reducing damage (Sugisaki et al., 2011; Roberts and Konow, 2013; O'Neill et al., 2015). Neuromodulatory effects that facilitate adaptive or protective motor patterns may also explain therapeutic effects of eccentric loading (Rees et al., 2008; Rio et al., 2016). These interactions of the tendon with the surrounding tissue have only been captured in live patients or animal models. Therefore, effects of repair may be more significant *in vivo,* in the presence of supporting cells and chemical signals which may more readily trigger healing. This may explain the discrepancy between ruptures observed with creep testing of explanted tendon tissues and the long-term functionality of tendon tissues *in vivo* (Wang et al., 2018a).

However, some degree of mechanical stimulation is required to maintain normal tendon structural and mechanical properties. Live studies have revealed that stress shielding can cause deterioration of tendon tissue. Early studies assessing the effects of completely releasing stress in various live animal models revealed that collagen bundles were less aligned, and fibrils tended to be smaller in diameter (Muellner et al., 2001; Majima et al., 2003). Stress shielding also decreased the mechanical strength and strain-at-failure of collagen fascicles (Yamamoto et al., 1999). These studies reaffirm that some level of mechanical stimulation may be essential to optimal maintenance and repair of tendon structure *in vivo*; this suggests that complete deprivation of stress in the *in vitro* setting may cause tenocytes and tendon explants to lose tendon-like properties as well.

While tensile loads are the main mechanical stress to which tendon are exposed, other forces may contribute to physiologic or pathologic responses to applied forces. Compressive forces have been suggested as a cause of tendon damage.(Almekinders et al., 2003; Hamilton and Purdam, 2004). In addition, interfibrillar shear stress and fluid shear stress also have been described in tendon tissue (Arnoczky et al., 2002a; Lavagnino et al., 2008; Szczesny and Elliott, 2014; Szczesny et al., 2015; Lee and Elliott, 2019). Low levels of fluid shear stress resulted in lower levels of collagenase mRNA inhibition, indicating that this form of mechanical stimulation plays a significant role in the preservation of collagen matrix integrity. (Lavagnino et al., 2008). Sliding and rotational behaviors in the fibers of tendon samples have also been observed; studies investigating the transference of applied force to cells also found that applied levels of strain were significantly attenuated at the fiber level, suggesting that these sliding forces may play a role in attenuating forces experienced by tendon. (Cheng and Screen, 2007; Lee and Elliott, 2019). In energy-storing tendons such as flexor tendons, fascicular sliding and interfascicular matrix (IFM) elasticity facilitated these tendons' ability to resist and recover from higher loads (Thorpe et al., 2015). Thus, sliding forces may play an important role in tendon behavior at multiple levels of organization and moderate the level of strain exerted at the cellular level.

TENDON CELL RESPONSE TO MECHANICAL LOAD

Mechanical stimulation is essential for tendon development, maturation, and repair, but the underlying mechanisms of tendon mechanoresponse elements remain poorly understood. Tendon cell and progenitor cell biology are known to be influenced by mechanical factors, (Engler et al., 2006), the response to which is mediated by the ECM itself, mechanosensors, and effector molecules (Banes et al., 1999). Matrix stiffness, discussed later in 2D model studies, has been shown to strongly influence stem cell differentiation, as demonstrated by changes in cell morphology as well as gene expression and protein production. In addition to general mechanoresponse pathways *via* membrane proteins and signalling cascades, studies have added to a growing body of knowledge of tendon-specific pathways.

Tendon-specific pathways for mechanoresponse have recently been described. (Fang et al., 2020; Passini et al., 2021). At the enthesis, cilia transduce biophysical activity *via* hedgehog (Hh) signaling to facilitate adaptation to load in an inverse relationship (Fang et al., 2020). Mechanical stimulation caused cilia disassembly, a process disrupted with the loss of Hh signaling. Deletion of ciliary genes in mice resulted in weakened entheses and decreased enthesis mineralization, suggesting that cilia may play a role in the enthesis mechanoresponse mechanisms and may also be influenced to affect pathology resulting from

overloading. In late 2021, Passini et al. published their findings that intracellular calcium signaling occurs among explanted rat tendon fascicles in response to stretch (Passini et al., 2021). At low strain rates (0.1% strain/second), tenocytes in their *ex vivo* model exhibited multiple intracellular Ca2+ signals over a longer duration, while at high strain rates (1.0% strain/second), tenocytes displayed a single shorter duration intracellular Ca2+ response. They also noted that, as strain rate increased, higher tissue stretch was required to elicit a response among 50% of the cells in their model. Passini et al. also demonstrated that tenocytes, which reside between collagen fibers and are thus exposed to mechanical shear during tissue stretching, are able to detected these shear-stress forces *via* the mechanosensitive ion channel PIEZO1. The authors proposed that the Ca2+ signals observed in their experiments may in turn activate enzymatic cross linking of collagen, contributing to increased tendon stiffness and strength and, ultimately, affecting physical performance This pathway suggests a mechanism by which tendon mechanoresponses to shearing and stretching forces are optimized in order to maintain tendon morphology and biomechanical properties.

More generally, cells, including those in tendon, may detect mechanical stimulation *via* transmembrane proteins that are integrated with cytoskeletal elements and non-receptor signaling molecules. Though studied in other mesenchymal cell populations and not unique to tendon, these pathways nevertheless play an important role in guiding the cellular response to mechanical stimulation. These mechanosensing cellular structures and surface molecules include integrins, cadherins, and connexins. (Chrzanowska-Wodnicka and Burridge, 1996; Lavagnino et al., 2011; Leckband et al., 2011; Schiele et al., 2013). For example, forces on ECM-integrin-cytoskeletal linkages may initiate signal pathways by altering protein folding or binding affinity. For example, studies have shown that stretching forces can expose binding sites on fibronectin promoting self-assembly into fibrils. (Morla and Ruoslahti, 1992; Zhong et al., 1998). Cytoskeleton deformation by mechanical stimulation can also alter transcriptional activities within the cell.(Wang et al., 2009; Tajik et al., 2016). Integrins can sense forces to which a cell is exposed and then propagate that forces to the actin cytoskeleton, nuclear laminins and eventually chromatin, which causes stretching and access to target genes for transcription.(Tajik et al., 2016). Pathways for stem cell differentiation may also be activated in this manner where actin filaments rapidly polymerize and depolymerize in response to mechanical loading, which in turn leads to translocation of MKL1 (megakaryoblastic leukemia 1) into the nucleus. MKL1 protein is shown to interact with the beta catenin (Wnt) and Smads (TGF-beta) pathways, which can further guide cellular differentiation, migration, and cell cycle regulation.(Scharenberg et al., 2014). Increased MKL1-actin activity reduces chromatin access, leading to reduction of cell pluripotency.(Hu et al., 2019).

The YAP/TAZ pathway may be another non-specific pathway that may be activated in response to tendon mechanical stimulation. YAP (Yes-associated protein) and TAZ (transcriptional co-activator with PDZ-binding motif) effector proteins in the Hippo pathway have been found to be influenced by ECM stiffness and cytoskeleton organization. (Dupont et al., 2011). YAP/TAZ play a key role in regulating the quiescence, proliferation, and differentiation of adult progenitor cells in multiple tissues including tendon. (Heng et al., 2020). In an environment with a stiff ECM or cellular attachment substrate, increased integrin clustering and focal adhesion formation increases F-actin polymerization, which in turn induces cell spreading. This then promotes translocation of YAP/TAZ into the nucleus, which consequently increases osteogenesis *via* upregulation of *RUNX2* and downregulation of *PPAR-γ*. On soft substrates, cells retain a rounder shape due to less focal adhesion formation and actin polymerization, which sequesters YAP/TAZ to the cytosol. This sequestration consequently downregulates *RUNX2* (runt-related transcription factor 2) and upregulates *PPAR-γ* (peroxisome proliferator-activated receptor gamma), driving adipogenesis. In particular, TAZ activation has been consistently reported to play a role in osteogenesis, while the role of YAP remains controversial.(Heng et al., 2020). However, Yeung et al. have reported upregulation of YAP/TAZ target genes during tendon development, possibly reflecting the concurrent deposition of ECM components. (Yeung et al., 2015).

IN VITRO TENDON CELL LOADING MODELS

Numerous loading models have been developed to study the mechanobiology of tendon. The scope of this review is limited to *in vitro* loading models, which can be grossly separated into explant, 2-dimensional (2D), or 3-dimensional (3D) loading models. The ideal *in vitro* model and loading conditions for tendon tissue engineering recapitulates the various mechanical forces transmitted through the ECM *in vivo* to native tendon cells while also maintaining cell viability. Desirable characteristics of optimal tendon tissue models include the generation of a well-aligned cellular morphology, the differentiation of progenitor cells towards a tendon-like phenotype, and the production of ECM proteins commonly observed among tendon tissues.(Butler et al., 2000; Brennan et al., 2018). These models must also have the capacity to tolerate the application of physiologically-relevant forces. Tendon tissues *in vivo* are usually subjected to uniaxial loading at a level of approximately 4–6% strain, (Screen et al., 2004), though higher and lower amounts of uniaxial loads may be utilized to replicate pathologic states. Tendon-derived stem cells (TDSCs) are endogenous progenitor cells within tendon tissues and have been isolated from both animal and human sources (Rui et al., 2010; Lui and Chan, 2011). While TDSCs may be the most relevant MSC population for tendon regeneration research, studies have found that bone marrow or adipose derived MSCs are robust alternatives.(Yin et al., 2016; Youngstrom et al., 2016). The following two sections summarize the main categories of *in vitro* tenogenic mechanical loading models as well as key principles and findings associated with the use of these models.

TABLE 1 | Overview of outcomes of applied mechanical strain to tendon explants and fascicles.

Level of strain	General outcomes
1–4%	Preservation of tendon and matrix genes including *SCX, TNMD*, *Ctgf* Wunderli et al. (2018), Tohidnezhad et al. (2020)
	Downregulation of decorin Maeda et al. (2009)
	Enhanced collagen production Maeda et al. (2007)
	Matrix deterioration at 3% strain Wang et al. (2013)
	Reduced maximum stress and energy density, increased cell death and collagenase activity; increased glycosaminoglycan content, increased PGE2 Devkota et al. (2007)
	Increased *MMP3*, *MMP13*, *MMP9* (Maeda et al. (2009); Tohidnezhad et al. (2020)
5–8%	Retention of structural integrity, cellular function Wang et al. (2013)
	Increased collagen production Wang et al. (2015)
	Rescue of unloaded tendon samples from pathologic changes Wang et al. (2015)
	Increased collagen synthesis Screen et al. (2005)
9%+	Increased *COL1A1*, *IL-6*Legerlotz et al. (2013)
	Massive collagen bundle rupture, fiber kinking and denaturationWang et al.(2013);Szczesny et al. (2018)
	Induced stretch overload injury with increased apoptosis and abnormal nuclear morphologyScott et al. (2005)

Ex vivo Tendon Loading Models

Tendon explants as an *ex vivo* loading model provide useful insight into the mechanical behavior of isolated tendons. Native cell-cell and cell-matrix interactions are preserved and may thus be investigated, providing information not otherwise available through 2D and 3D models. 2D and 3D models also currently lack the heterogeneity in cell population found in native tendon.(Viganò et al., 2017). These mechanical studies produced some of the earliest knowledge about cell-cell interactions, intrinsic tendon mechanical properties, cell viability and growth, and gene expression.

Strain levels used in *ex vivo* studies range from 1 to 9%, though strains of 20–30% have been applied to model tendon injury.(Scott et al., 2005; Legerlotz et al., 2013). A general summary of the outcomes of different levels of applied strain is given in **Table 1**, and loading parameters used in individual studies are given in **Supplementary Table S1**. Cyclic strain from 1 to 3% on tendon fascicles and whole-tendon samples have been sufficient to preserve tenocyte-like morphology and tendon specific gene expression, (Maeda et al., 2009; Wang et al., 2013; Wunderli et al., 2018; Tohidnezhad et al., 2020), but matrix deterioration and reduced maximum stress and energy density were also noted at these levels of strain.(Devkota et al., 2007; Wang et al., 2013). Physiologic loads of 5–6% also yielded increased collagen production and can rescue unloaded tendon samples from pathologic changes.(Wang et al., 2015). Overloading of explants revealed degenerative changes in ECM and increased apoptosis and inflammatory markers.(Legerlotz et al., 2013; Wang et al., 2013). Failure-loaded samples were notable for collagen fiber kinking and denaturation.(Szczesny et al., 2018). Interestingly, the lack of change in tissue modulus suggests that changes in tissue architecture initiate the first changes in tenocyte phenotype and cell viability during injury. This hypothesis has been supported by Freedman et al.'s work which found that macroscale damage and matrix disorganization caused by fatigue loading propagates down to cellular level; damaged matrix may transmit forces differently than uninjured matrix, thus spurring differential cellular responses.(Freedman et al., 2018). In summary, low to physiologic loading preserved and sometimes rescued tenogenic genes and ECM production in explants, while high strains more consistently caused structural damage, which consequently affects cellular responses due to changes in detected mechanical strain.

Because researchers can avoid the challenges in finetuning scaffold properties in *ex vivo* studies, important findings have been produced from comparing different loads. Interestingly, *ex vivo* studies of tendon explants from various species have revealed that healthy tendons can demonstrate auxetic behavior when placed under biaxial strain—that is, the tendons become thicker, rather than thinner, when stretched.(Gatt et al., 2015). Furthermore, this auxetic behavior was highly influenced by tendon microstructure, which may be compromised by damage due to excessive loads or altered tendon biology. A 3D hydrogel scaffold with auxetic properties was developed to aid in future tendon-to-muscle regeneration (Warner et al., 2017), but beyond cell viability studies, there remains little information about the effects of this scaffold with regard to guiding tenogenic differentiation among mesenchymal progenitor cells.

Two-Dimensional (2D) Loading Models

Two-dimensional loading models study the effects of mechanical stimulation, with or without additional dynamic loading, on cells grown in monolayer. In the case of dynamic loading, cells adhere to a flexible material to which mechanical strain can be applied. The stiffness of the substrate on which cells are plated has also been shown to affect tenogenic gene expression among progenitor cells.(Sharma and Snedeker, 2010). Most other models, including commercially available units such as those made by Flexcell®, use the cyclical application of negative pressure (via a vacuum device) to homogenously apply mechanical strain to the flexible material and the attached cells. This provides customizable loading conditions for experiments. 2D models mainly investigate the effects of deforming cellular cytoskeletons and nuclei, providing an approach to evaluate certain cell differentiation and migration pathways. Depending on the cell population seeded, the aim of the study may be to study mechanical stimulation's effects on the preservation of tendon-specific genes or morphology in tendon cells or the

differentiation of progenitor cells towards a tenogenic fate. However, 2D models lack a substantial ECM component and thus are not well-suited to replicate cell-ECM interactions, which is a major limitation of these techniques.

2D Mechanical Stimulation

Static mechanical stimulation of cells in monolayer may be achieved via specialized plates with defined mechanical properties. Culture plates composed of materials with different degrees of mechanical stiffness, functionalized with type I collagen or fibronectin cellular adhesion molecules, have been reported to guide the fate of bone marrow stem cells (BMSCs) towards tendon or bone phenotypes. Snedeker et al. plated BMSCs onto gel strips with stiffnesses ranging from 10 kPa to 100 kPa and found that increased *RUNX2* expression was associated with increased stiffness of a fibronectin-coated substrate. (Sharma and Snedeker, 2010). Gene expression of scleraxis (*SCX*), tenascin-C (*TNC*), tenomodulin (*TNMD*), and collagen III (*COL3*) have been noted to be increased among cells plated on collagen substrates within a more narrow range of stiffness (approximately 30–50 kPa), even in the absence of additional dynamic mechanical load.(Sharma and Snedeker, 2010, 2012). The authors hypothesize that since *SCX* expression can be affected by MAP kinase activity, and MAP kinase can be influenced by mechanical stimulation, it is possible that stiffer substrates stimulate a level of MAP kinase activity that does not permit tenogenesis, while softer substrates may provide insufficient mechanical stimulation. Islam et al. found a similar upregulation of tenogenic markers in mesenchymal stem cells (MSCs) plated on type-1 collagen sheets of varying stiffness. Higher levels of *SCX* were seen in cells on sheets with a modulus of 100 MPa compared to 0.1 MPa.(Islam et al., 2017). In addition, architectural organization of the substrate influenced tenogenesis and ECM formation. 10 MPa collagen sheets with highly aligned fibers demonstrated comparable increases in type-III collagen gene expression and cartilage oligomeric matrix protein (COMP, a protein involved in tendon load resistance) (Smith et al., 1997) as an unaligned 100 MPa sheet.(Islam et al., 2017). Finally, *RUNX2* gene expression was significantly increased after 21 days in cells seeded on the 100 MPa sheet, suggesting that the same conditions for stiffness that promote tenogenesis also promote osteogenesis over time.(Islam et al., 2017). Researchers should be aware of the time-dependent and substrate-dependent nature of tenogenic differentiation to achieve optimal conditions for tendon or tendon-like tissue formation.

2D Dynamic Mechanical Loading

Studies of biaxial or uniaxial dynamic loading have also been studied on 2D models. Biaxial loading generates a multidirectional strain (e.g. radial strain exerted on monolayer of cells adherent to a flexible substrate). Although this strain model does not typically replicate typical physiologic tendon loading, cells undergoing cyclic biaxial strain have shown increased proliferation, collagen production, and cell morphology changes similar to those observed among tenocytes.(Zeichen et al., 2000; Goodman et al., 2004; Deniz et al., 2020). Uniaxial strain more closely replicates loads experienced by native tendon cells, and thus the majority of mechanical loading research has focused on the effects of uniaxial strain on tendon and stem cells. Similar to cyclic biaxial strain, cyclic uniaxial strain has also increased collagen I production, cell proliferation, and cell alignment.(Yang et al., 2004; Riboh et al., 2008). As with static loading, duration of application of strain appear to influence cell behavior; for example, Jun N-terminal kinase 1 (JNK) pathway-mediated apoptosis was noted to be elevated over brief applications of cyclic uniaxial strain, however, after long-term exposure to strain, no differences in levels of tenocyte apoptosis were found. This implies that tenocytes may have the capacity to develop stress tolerance during prolonged periods of mechanical loading and this phenomenon may be evolutionarily and functionally beneficial *in vivo*.(Skutek et al., 2003). Although few studies have directly compared the effects of biaxial versus uniaxial strain on cell behavior, Wall et al. found that biaxial substrate strain induces lower levels of cellular strain compared to uniaxial substrate strain.(Wall et al., 2007). Wang et al. found that while uniaxial strain consistently increased expression of *SCX*, Mohawk (*MKX*), and *TNMD*, biaxial loading actually inhibited expression of those markers.(Wang et al., 2018b).

Customizable mechanical loads have afforded observation of the effects of different levels of strain on tenogenic differentiation and morphology. Though low and high strain generally model tendon behavior seen in pathological conditions, results from these studies have been varied (**Tables 2**, **3**). Loading parameters of studies discussed are included in **Supplementary Table S2**. Low magnitude loads of 2–4% have increased early gene expression of inflammatory factors and ECM degradation enzymes, (Tsuzaki et al., 2003), and tendon-derived stem cells under low strain have also demonstrated upregulated osteogenic and chondrogenic markers, including bone morphogenic protein (*BMP-2*) expression. (Chen et al., 2008; Rui et al., 2011). Conversely, low strain loading also increased tenogenic gene expression, including *MKX*, *TNMD*, and collagen, type 1, alpha 1 and 2 (*COL1A1*, *COL1A2*).(Zhang and Wang, 2010; Kayama et al., 2016). Of note, Kayama et al. did not find an increase in *SCX* expression with 2% cell strain.(Kayama et al., 2016). It is possible that 2% strain, or the duration of 2% strain used in the study, is insufficient to increase expression of that specific marker.

Moderate-to-high physiologic loads of approximately 4–8% increased ECM and tenogenic gene expression, (Chen et al., 2007; Nam et al., 2019), though some studies also noted a concomitant increase in osteogenic, adipogenic, and chondrogenic markers.(Zhang and Wang, 2013; Nie et al., 2021). This may be due to cell types used in the study. Zhang and Wang found that tendon-derived stem cells stimulated by 8% strain expressed higher levels of non-tendon genes, including transcription factor *SOX-9* and *RUNX2*, while tenocytes did not.(Zhang and Wang, 2013). Upregulation of inflammatory cytokine genes including COX-2 and PGE2 have also been noted at 8% strain by Yang et al., (Yang et al., 2005), suggesting that moderate levels of strain can spur some degree of inflammation and tendon

TABLE 2 | Overview of outcomes of applied mechanical strain to 2D loading studies using human cells (stem cells and tendon fibroblasts).

Level of strain	General outcomes
1–4%	Increased collagen type I, TGF- β Yang et al. (2004)
	Decreased COX-2, MMP-1, PGE2 gene expression Yang et al. (2005)
	Increased COX-2, IL-1 β, MMP-3 gene expression Tsuzaki et al. (2003), Wang et al. (2003)
	Transient increases in *ALP*, *RUNX2*, *OCN* gene expression Chen et al. (2008), Nam et al. (2019)
5–8%	Increased SCX, *TNMD*, *TNC* gene expression Nam et al. (2019)
	Increased TGF- β Yang et al. (2004)
	Increased collagen I, collagen III, fibronectin, N-cadherin Yang et al.(2004); Nam et al. (2019)
	Increased COX-2, MMP-1, PGE2 expression Yang et al. (2005)
	Increased JNK activation and apoptosis of tendon fibroblasts Skutek et al. (2003)
9%+	Increased *TNC*, *SCX*, *TNMD* gene expression in BMSCs Chen et al. (2008); Nam et al. (2019)
	Increased collagen type I, collagen type III, fibronectin, N-cadherin Chen et al. (2008); Nam et al. (2019)
	Increased PGE2, COX-1, COX-2 Wang et al. (2003)
	Transiently increased *ANGPTL4,* FGF-2*, COX-2, SPHK1*, TGF-alpha*, VEGF-A* and *VEGF-C* Mousavizadeh et al. (2013)

TABLE 3 | Overview of outcomes of applied mechanical strain to 2D loading studies using animal cells (stem cells and tendon fibroblasts).

Level of strain	General outcomes
1–4%	Increased *MKX*, *TNMD*, *COL1A1*, *COL1A2* gene expression in tenocytes Kayama et al. (2016)
	Increased total collagen production Riboh et al. (2008), Zhang and Wang, (2010)
	Increased BMP-2 production Rui et al. (2011)
5–8%	Increased *SCX, MKX, TNMD, COL1A2* Wang et al. (2018b)
	Increased *SOX9, RUNX2* in TDSCs but not tenocytes Zhang and Wang, (2010); Zhang and Wang, (2013)
	Increased collagen I, decorin Chen et al. (2007)
	Increased BMP-2 production Rui et al. (2011)
9%+	Increased *TNC* Zhang et al. (2008)
	Increased collagen I, collagen III Zhang et al. (2008)

matrix breakdown; conversely, the same study found that 4% strain lowered levels of COX-2, matrix metalloproteinase 1 (MMP-1), and prostaglandin E2 (PGE2).

Studies of effects of higher levels of strain from 9 to 12% begin to demonstrate inflammation and cell death thought to be involved in tendinopathy. Cyclic 10% stretching of mesenchymal stem cells resulted in higher gene expression of collagen I and III and tenascin C after 24 h, (Zhang et al., 2008), but tendon cells also transiently upregulated gene expression of angiogenic factors under 10% biaxial strain, suggesting that the development of tendinopathy may involve angiogenesis driven by tenocyte mechanoresponses. (Mousavizadeh et al., 2013). Higher mechanical loads also increased tenocyte apoptosis, inflammatory markers, and pain modulators commonly seen in tendinopathy.(Arnoczky et al., 2002b; Wang et al., 2003). To highlight the complex interactions between tendon biology, ultrastructure and biomechanical properties, interestingly, it has been noted that fatigue loading of tendon explants which is known to cause immediate changes in collagen organization and molecular denaturation is not associated with immediate changes in local tissue modulus suggesting that despite ultrastructural changes there is no immediate effect on tissue mechanical properties.(Szczesny et al., 2018).

In summary, moderate levels of static mechanical stimulation *and* dynamic load on 2D models may promote tenogenic differentiation of progenitor cells and maintain a tenocyte-like phenotype. Both low and high levels of strain induce inflammatory changes or osteogenic marker upregulation, demonstrating one way tendon may respond to pathological loads with compensatory cellular changes. However, these findings are not consistently reported across all studies, emphasizing the importance of considering other experiment factors. Both the strain level and the duration for which the strain is applied can influence cell behavior. Furthermore, the type of substrate in the extracellular environment can greatly influence study results as the materials composing the substrate may transmit applied forces differently, possibly even attenuating the magnitude of applied forces. As Han et al. have discussed, significant strain attenuation occurs due to the tendon matrix structure, and the direct application of strain to cells on 2D substrates above 4% may be supraphysiologic (Han et al., 2013). The overapplication of strain as a result may explain variable findings in the studies that have explored higher levels of mechanical loading.

Three-Dimensional (3D) *in vitro* Loading Models

Although 2D models laid the foundation for the study of tendon mechanobiology, the simplicity of the designs limits our understanding of how tendon cells are affected by the surrounding ECM. Compared to 2D models of the same material and growth factors, stem cells seeded in 3D scaffolds more consistently expressed higher levels of tenogenic gene

TABLE 4 | Overview of outcomes of applied mechanical strain to 3D loading studies using human cells (stem cells and tendon fibroblasts).

Level of strain	General outcomes
1–4%	Increased cell alignmentKuo and Tuan, (2008)
	Increased *SCX*, *MKX*, *TNMD*, *TNC*, *COL3A1* gene productionKuo and Tuan, (2008);Wu et al. (2017);Herchenhan et al. (2020)
	Increased type I collagen, type III collagenKuo and Tuan, (2008)
	Decreased type XII collagen, type XIV collagen, elastinKuo and Tuan, (2008)
9%+	Increased *COL1A1, COL3A1, DCN, SCX, TNC* gene expressionGovoni et al. (2017)
	Increased *EGR1, EGR2, FOS, COX-2* gene expressionHerchenhan et al. (2020)

TABLE 5 | Overview of outcomes of applied mechanical strain to 3D loading studies using animal cells (stem cells and tendon fibroblasts).

Level of strain	General outcomes
1–4%	Increased *TNC*, *SCX*, *COL1A1*, matrix genes (aggrecan, fibronectin, prolyl hydroxylase)Garvin et al. (2003); Scott et al. (2011)
	Increased *RUNX2*, *ALP*, *OCN* gene productionWang et al. (2021)
	Increased type I collagen, type III collagen, type XII collagenBaker et al. (2011)
	Increased heterotropic ossification and decreased biomechanical strengthWang et al. (2021)

expression, suggesting that the additional cell-matrix interactions play a significant role in guiding cells down a more tenogenic fate (Kuo and Tuan, 2008; James et al., 2011). Wang et al. have also found that the osteogenic and adipogenic differentiation noted in MSCs on a 2D model was inhibited in cells on a 3D scaffold (Wang et al., 2018b). Generally, 3D models contain cells homogenously seeded in a 3D material; scaffolds can be designed such that their architecture promotes cell alignment. Researchers may also apply additional strain by placing the cell-seeded scaffolds in a bioreactor.

Effects of Differential Loading Parameters on 3D Models

Similar to 2D model studies, cells seeded in 3D scaffolds have responded differently to varying levels of strain. Available loading conditions are summarized in **Supplementary Table S3**. Effects of loading parameters are complicated by the inherent stiffnesses of different scaffolds, but tenogenic markers have generally been upregulated in stem cells at strains of 2.5–10% (**Tables 4**, **5**).(Kuo and Tuan, 2008; Scott et al., 2011) Patel et al. reported increased gene expression of matrix metalloproteinases when tenocytes seeded in a polyethylene glycol dimethacylate (PEGDM) fiber-gel scaffold were placed under 5% strain (Patel et al., 2017). Interestingly, the same authors later found that scaffold modulus and stiffness played a more significant role in influencing gene expression than strain; cells seeded in softer fiber scaffolds with lower moduli had increased interleukin six and matrix metalloproteinase 3 compared to those in stiffer fibers (Patel et al., 2018). Increased osteogenic gene expression was also seen with extended underloading (3% strain) of tenocytes (Wang et al., 2021). Conversely, underloading 3D models also offered insight into tendon injury healing processes; a "tenostruct" created from a combination of tendon explant, tendon progenitor cells, and bone-derived macrophages in hydrogels revealed increased macrophage recruitment and progenitor cell recruitment to the underloaded explant (Stauber et al., 2021). Future research may further examine the interactions of different cell populations in 3D loading models.

Substrate Material and Architecture of 3D Scaffolds

While the finding that moderate physiologic levels of mechanical loading generally spurs tenogenesis or maintenance is not unique to 3D models, these models have allowed for further study of matrix-cell interactions. Scaffold materials and architecture can significantly affect the amount and type of force applied to cells and are thus a main focus in the design of 3D models. Innovation in this respect of bioreactor design, as a result, is considerably higher than seen in the design of 2D loading experiments. Anisotropic materials such as fibrous scaffolds may transfer force heterogeneously to cells, while isotropic materials like hydrogels transfers force more homogenously. However, there are useful applications for both types of materials, and current mechanobiology research is focused on combining the properties of both anisotropic and isotropic materials to capture the complexity of native tendon environment. The following section summarizes findings from studies using 3D loading models.

Hydrogel 3D Models

Hydrogels are a popular 3D *in vitro* loading model used in tendon engineering studies. Their ability to transfer mechanical strain uniformly to all cells offers a more controlled environment of study. Hydrogel biomaterials range from collagen I to fibrin and even decellularized plant tissue (Garvin et al., 2003; Feng et al., 2006; Contessi Negrini et al., 2020; Herchenhan et al., 2020). Decellularized tendon samples have also yielded an ECM scaffold suitable for cell culture, possibly allowing for future researchers to

conduct studies with a model that closely resembles native tendon in both architecture and composition.(Youngstrom et al., 2013; Youngstrom and Barrett, 2016). Synthetic hydrogels (e.g., polyethylene glycol, methacrylated gelatin) provide higher control of the gels' physical properties, but fibrous architecture is lacking in these substrates without additional processing.(Hiraki et al., 2021). Seeding in hydrogels induced longitudinal arrangement of cells, increased tenogenic gene expression, and increased ECM production, with and without additional growth factors.(Awad et al., 2000; Farhat et al., 2012; Govoni et al., 2017; Herchenhan et al., 2020). Of note, compared to static loading, cyclic application of mechanical strain was found to upregulate tenogenic gene markers in multipotent stem cells, particularly *SCX*.(Scott et al., 2011). Aspect ratio and cell seeding density were also found to play important roles in guiding cell phenotype, with longer MSC-collagen gels resulting in more organized collagen fiber arrangement and higher seeding densities yielding more aligned cells (Awad et al., 2000; Nirmalanandhan et al., 2007). In addition to cell-mediated matrix remodeling, various methods have been developed to align matrix fibers within hydrogels. One such method includes embedding magnetic particles to provide cells with aligned contact points (Guo and Kaufman, 2007; Hiraki et al., 2021; Xu et al., 2021, 2021).

Further development of 3D printing techniques later allowed for printing of multilayered scaffolds that improve upon the mechanical strength of hydrogels and support greater matrix organization (Rinoldi et al., 2019; Ciardulli et al., 2020). In addition, studies using gels made from extracellular matrix directly derived from tendon and muscle have also offered new insights into the role of tendon-muscle junction proteins in tendon healing. Gaffney et al. found that compared to collagen gels, ECM gels promoted higher expression of paxillin, an intracellular protein linked to focal adhesion turnover; this suggests that collagen gels may lack a component or architecture that affords key cell-matrix interactions involved in tendon healing (Gaffney et al., 2021).

3D Fibrous Scaffolds

Advancements in chemical and biological engineering have brought forth the development of fibrous scaffolds, which have led to new 3D loading scaffolds for tendon regeneration. Fibrous scaffolds provide higher levels of matrix alignment and model the shearing forces created by the sliding and stretching of collagen fibers found in the native tendon (Wu et al., 2018). Today, multiple researchers have used electrospinning methods to create sophisticated, tunable knitted structures of nanofibers whose knitted architecture and flexibility closely mimic the environment created by the native extracellular matrix (Sahoo et al., 2010; Baker et al., 2011). Highly aligned biocompatible fibers could be generated from high-speed spinning of polymer solutions, and the resulting scaffolds also possess greater tensile strength than 2D scaffolds of the same polymers (Bosworth et al., 2013). A nanofiber scaffold facilitated proliferation of bone marrow MSCs, upregulated tendon specific gene expression, and increased collagen 1 and tenascin-C production; moreover, a fibrous scaffold generated tendon tissue of higher strength, improved collagen structure, and greater cell density and alignment (Sahoo et al., 2010; Wang et al., 2016; Tu et al., 2020). Schoenenberger et al. found that a fibrous topography alone was sufficient to promote upregulation of genes for inflammatory markers (e.g., interleukin 1 beta (*IL1B*), tumor necrosis factor (*TNF*)) in macrophages and tendon cells, suggesting that nanofiber scaffolds may also be useful in modulating biological responses in tendon healing (Schoenenberger et al., 2020).

To address the nanofiber model's weak tensile strength, heterogenous fiber architecture, and insufficient mechanical support for clinical translation, later models combined multiple fiber substrates, embedded fibers in a hydrogel, or created microfiber/nanofiber yarns using novel spinning techniques (Liu et al., 2017; Wu et al., 2017; Patel et al., 2018; Lin et al., 2019; Cai et al., 2020). Patel et al. embedded PEGDM fibers in a hydrogel matrix, allowing researchers to replicate the low-shear, high-tension strain experienced by collagen fibers in the native tissue and producing similar findings to collagen based 3D models (Patel et al., 2018). A self-assembling nanofiber hydrogel made of RADA peptides has also been developed and has been shown to promote alignment and growth of tendon progenitor cells (Yin et al., 2020). A polycaprolactone/Poly (L-lactide-co-ε-caprolactone) nanofiber "yarn" developed by Cai et al. promoted tenogenic differentiation of bone marrow MSCs and retained cytocompatibility and biomechanical strength in *in vivo* rabbit studies (Cai et al., 2020). The nanofiber scaffold thus shows promise as a clinically applicable model for tendon tissue engineering. Further study of the effects of dynamic loading conditions applied to electrospun scaffolds may reveal additional findings about the biomechanical properties of tendon.

3D loading models have afforded researchers greater control over the "matrix" architecture in which they are seeding their cells for study. Consistent with 2D models, moderate levels of loading yielded results indicating tenogenic differentiation or tenocyte maintenance, but the sophistication of the scaffold designs offers a deeper understanding of the effects of the elastic moduli of the substrate itself and the additional forces experienced by native tendon, such as shearing or sliding forces.

CONSIDERATIONS AND FUTURE DIRECTIONS

The study of tendon mechanobiology using mechanical stimulation models has evolved substantially as researchers develop new techniques to more closely model the native tendon environment. The range of loading parameters, cell types, and substrates used in these studies demonstrates the complexity with which researchers must contend. As mechanical loading models grow more sophisticated, researchers must consider several issues when designing studies and translating these approaches from *in vitro* to *in vivo* investigations.

As seen above, studies have employed a wide variety of cell types, substrates, and loading parameters. Variability in

loading protocols for both 2D and 3D loading models may make it more difficult for future researchers to reproduce results from loading studies. Certain loading parameters that may drive tenogenic differentiation in one study may not elicit significant changes in another. Moderate levels of strain from 4 to 10% more often yielded tenogenic gene expression, but it was not consistently reported in studies whether other effects, such as upregulation of inflammatory markers or osteogenic genes, increased as well. Differences in results may be attributed to cell types or substrates used in the experiments, though there was no consistent trend in what genes each study tested, making comparison between cell types at the same levels of strain difficult. Responses may even vary by tendon type, which has been shown to have variations on mechanical properties and responses to loading (Zuskov et al., 2020). In addition, many bioreactors used in these studies are custom-designed, and the parameters of the reactor design may also influence cellular response. Future bioreactor studies may explore the unique properties of different tendon types, though it is unclear whether the properties seen in explant studies can be replicated in vitro models. Finally, although certain gene expression levels and protein markers are commonly used to confirm tenogenesis, studies often differ in which markers they analyze. For example, examination of ECM gene expression and protein levels may be a useful but incomplete measure of tendon differentiation, as these genes may also be upregulated in chondrogenesis or osteogenesis.

Experimental designs are also increasing in complexity in order to more closely recapitulate the biomechanical environment of native tendon, but the ability to fully capture the complexity of native biomechanical properties remains limited. Tensile strain has proven sufficient to spur some degree of tenogenic differentiation. However, as recent explant studies have revealed, there are still forces at the fascicular level of tendon structure, such as shear stress or sliding, that have not been deeply examined *in vitro* for their role in governing cellular behavior (Thorpe et al., 2015; Lee and Elliott, 2019). Non-explant *in vitro* models have yet to reach the point where they can be used to study macroscale responses to mechanical strain. While tensile strain has been shown to sufficiently drive tenogenic differentiation or preserve tendon-specific genes in a cell population, further research is required before constructs generated from bioreactors are comparable to the gold standard of autograft and/or allograft tissues used clinically for tendon repair procedures today.

Current research continues to fill in gaps in our understanding of the cellular properties of tendon as well. For example, we are now learning that cellular populations found in tendon may be more diverse and heterogeneous than previously thought, (De Micheli et al., 2020), and lineage tracing has revealed variation in cell populations seen at different severities, stages of tendon injury, and even age may play a significant role in tendon healing as well. (Dyment et al., 2014; Howell et al., 2017; Moser et al., 2018; Nichols et al., 2019). Also noteworthy are interactions within the musculotendinous unit and bone, which may moderate tendon morphology and thus function at the organ level. (O'Neill et al., 2015). *In vitro* studies have yet to incorporate this level of cellular and structural complexity into experimental design, but these may be worthwhile to explore in future research as there remains much to be understood about how the cell-level responses seen in vitro studies may be modulated by higher level interactions. Tendons are ultimately composed of hierarchical structures, and certain mechanical properties may only manifest at higher levels of organization which are not yet achieved through current bioreactor models.

In summary, *in vitro* mechanical loading models of tenogenic cell phenotypes have advanced our understanding of tendon mechanobiology and have equipped investigators with valuable tools to further explore tendon intracellular machinery, its interactions with extracellular matrix and signaling molecules. As discussed in this review, described models are widely varied, offering researchers a diverse range of bioreactors and loading parameters to reference for future research. Each model and loading scheme are associated with unique advantages and disadvantages that can be tailored to address the desired research questions of interest. Moving forward, more sophisticated mechanical loading models that better recapitulate physiologic loading will allow further exploration of the complex interactions between surrounding tissues (bone, muscle, neurovasculature, etc.) and tendon itself. Ultimately, this may deepen our understanding of the relevant molecular mechanisms associated with tendon development and pathogenesis and may provide the foundation for future tendon tissue healing and regeneration approaches.

AUTHOR CONTRIBUTIONS

SW contributed to writing of the manuscript and composing the tables. WK contributed to writing of the manuscript. TK conceived the topic and contributed to writing of the manuscript.

FUNDING

Research support for TK, Jr is provided by US Department of Veterans Affairs project # 2020-000059.

SUPPLEMENTARY MATERIAL

The Supplementary Material for this article can be found online at: https://www.frontiersin.org/articles/10.3389/fbioe.2022.826748/full#supplementary-material

REFERENCES

Almekinders, L. C., Weinhold, P. S., and Maffulli, N. (2003). Compression Etiology in Tendinopathy. *Clin. Sports Med.* 22, 703–710. doi:10.1016/s0278-5919(03)00067-x

Arnoczky, S. P., Lavagnino, M., Whallon, J. H., and Hoonjan, A. (2002a). *In Situ* cell Nucleus Deformation in Tendons under Tensile Load; a Morphological Analysis Using Confocal Laser Microscopy. *J. Orthop. Res.* 20, 29–35. doi:10.1016/s0736-0266(01)00080-8

Arnoczky, S. P., Tian, T., Lavagnino, M., Gardner, K., Schuler, P., and Morse, P. (2002b). Activation of Stress-Activated Protein Kinases (SAPK) in Tendon Cells Following Cyclic Strain: the Effects of Strain Frequency, Strain Magnitude, and Cytosolic Calcium. *J. Orthop. Res.* 20, 947–952. doi:10.1016/s0736-0266(02)00038-4

Awad, H. A., Butler, D. L., Harris, M. T., Ibrahim, R. E., Wu, Y., Young, R. G., et al. (2000). *In Vitro* characterization of Mesenchymal Stem Cell-Seeded Collagen Scaffolds for Tendon Repair: Effects of Initial Seeding Density on Contraction Kinetics. *J. Biomed. Mater. Res.* 51, 233–240. doi:10.1002/(sici)1097-4636(200008)51:2<233:aid-jbm12>3.0.co;2-b

Baker, B. M., Shah, R. P., Huang, A. H., and Mauck, R. L. (2011). Dynamic Tensile Loading Improves the Functional Properties of Mesenchymal Stem Cell-Laden Nanofiber-Based Fibrocartilage. *Tissue Eng. A* 17, 1445–1455. doi:10.1089/ten.tea.2010.0535

Banes, A. J., Horesovsky, G., Larson, C., Tsuzaki, M., Judex, S., Archambault, J., et al. (1999). Mechanical Load Stimulates Expression of Novel Genesin Vivoandin Vitroin Avian Flexor Tendon Cells. *Osteoarthritis and Cartilage* 7, 141–153. doi:10.1053/joca.1998.0169

Bosworth, L. A., Alam, N., Wong, J. K., and Downes, S. (2013). Investigation of 2D and 3D Electrospun Scaffolds Intended for Tendon Repair. *J. Mater. Sci. Mater. Med.* 24, 1605–1614. doi:10.1007/s10856-013-4911-8

Brennan, D. A., Conte, A. A., Kanski, G., Turkula, S., Hu, X., Kleiner, M. T., et al. (2018). Mechanical Considerations for Electrospun Nanofibers in Tendon and Ligament Repair. *Adv. Healthc. Mater.* 7, 1701277. doi:10.1002/adhm.201701277

Butler, D. L., Goldstein, S. A., and Guilak, F. (2000). Functional Tissue Engineering: the Role of Biomechanics. *J. Biomech. Eng.* 122, 570–575. doi:10.1115/1.1318906

Cai, J., Xie, X., Li, D., Wang, L., Jiang, J., Mo, X., et al. (2020). A Novel Knitted Scaffold Made of Microfiber/nanofiber Core-Sheath Yarns for Tendon Tissue Engineering. *Biomater. Sci.* 8, 4413–4425. doi:10.1039/d0bm00816h

Chen, C.-H., Marymont, J. V., Huang, M.-H., Geyer, M., Luo, Z.-P., and Liu, X. (2007). Mechanical Strain Promotes Fibroblast Gene Expression in Presence of Corticosteroid. *Connect. Tissue Res.* 48, 65–69. doi:10.1080/03008200601090824

Chen, Y.-J., Huang, C.-H., Lee, I.-C., Lee, Y.-T., Chen, M.-H., and Young, T.-H. (2008). Effects of Cyclic Mechanical Stretching on the mRNA Expression of Tendon/Ligament-Related and Osteoblast-specific Genes in Human Mesenchymal Stem Cells. *Connect. Tissue Res.* 49, 7–14. doi:10.1080/03008200701818561

Cheng, V. W. T., and Screen, H. R. C. (2007). The Micro-structural Strain Response of Tendon. *J. Mater. Sci.* 42, 8957–8965. doi:10.1007/s10853-007-1653-3

Chrzanowska-Wodnicka, M., and Burridge, K. (1996). Rho-stimulated Contractility Drives the Formation of Stress Fibers and Focal Adhesions. *J. Cel Biol.* 133, 1403–1415. doi:10.1083/jcb.133.6.1403

Ciardulli, M. C., Marino, L., Lovecchio, J., Giordano, E., Forsyth, N. R., Selleri, C., et al. (2020). Tendon and Cytokine Marker Expression by Human Bone Marrow Mesenchymal Stem Cells in a Hyaluronate/poly-Lactic-Co-Glycolic Acid (PLGA)/fibrin Three-Dimensional (3D) Scaffold. *Cells* 9, 1268. doi:10.3390/cells9051268

Contessi Negrini, N., Toffoletto, N., Farè, S., and Altomare, L. (2020). Plant Tissues as 3D Natural Scaffolds for Adipose, Bone and Tendon Tissue Regeneration. *Front. Bioeng. Biotechnol.* 8, 723. doi:10.3389/fbioe.2020.00723

De Micheli, A. J., Swanson, J. B., Disser, N. P., Martinez, L. M., Walker, N. R., Oliver, D. J., et al. (2020). Single-cell Transcriptomic Analysis Identifies Extensive Heterogeneity in the Cellular Composition of Mouse Achilles Tendons. *Am. J. Physiology-Cell Physiol.* 319, C885–C894. doi:10.1152/ajpcell.00372.2020

Deniz, P., Guler, S., Çelik, E., Hosseinian, P., and Aydin, H. M. (2020). Use of Cyclic Strain Bioreactor for the Upregulation of Key Tenocyte Gene Expression on Poly(glycerol-Sebacate) (PGS) Sheets. *Mater. Sci. Eng. C* 106, 110293. doi:10.1016/j.msec.2019.110293

Devkota, A. C., Tsuzaki, M., Almekinders, L. C., Banes, A. J., and Weinhold, P. S. (2007). Distributing a Fixed Amount of Cyclic Loading to Tendon Explants over Longer Periods Induces Greater Cellular and Mechanical Responses. *J. Orthop. Res.* 25, 1078–1086. doi:10.1002/jor.20389

Docheva, D., Müller, S. A., Majewski, M., and Evans, C. H. (2015). Biologics for Tendon Repair. *Adv. Drug Deliv. Rev.* 84, 222–239. doi:10.1016/j.addr.2014.11.015

Dupont, S., Morsut, L., Aragona, M., Enzo, E., Giulitti, S., Cordenonsi, M., et al. (2011). Role of YAP/TAZ in Mechanotransduction. *Nature* 474, 179–183. doi:10.1038/nature10137

Dyment, N. A., Hagiwara, Y., Matthews, B. G., Li, Y., Kalajzic, I., and Rowe, D. W. (2014). Lineage Tracing of Resident Tendon Progenitor Cells during Growth and Natural Healing. *PLoS One* 9, e96113. doi:10.1371/journal.pone.0096113

Engler, A. J., Sen, S., Sweeney, H. L., and Discher, D. E. (2006). Matrix Elasticity Directs Stem Cell Lineage Specification. *Cell* 126, 677–689. doi:10.1016/j.cell.2006.06.044

Ezura, Y., Chakravarti, S., Oldberg, A., Chervoneva, I., and Birk, D. E. (2000). Differential Expression of Lumican and Fibromodulin Regulate Collagen Fibrillogenesis in Developing Mouse Tendons. *J. Cel Biol.* 151, 779–788. doi:10.1083/jcb.151.4.779

Fahlstrom, M., Jonsson, P., Lorentzon, R., and Alfredson, H. k. (2003). Chronic Achilles Tendon Pain Treated with Eccentric Calf-Muscle Training. *Knee Surg. Sports Traumatol. Arthrosc.* 11, 327–333. doi:10.1007/s00167-003-0418-z

Fang, F., Schwartz, A. G., Moore, E. R., Sup, M. E., and Thomopoulos, S. (2020). Primary Cilia as the Nexus of Biophysical and Hedgehog Signaling at the Tendon Enthesis. *Sci. Adv.* 6, eabc1799. doi:10.1126/sciadv.abc1799

Farhat, Y. M., Al-Maliki, A. A., Chen, T., Juneja, S. C., Schwarz, E. M., O'Keefe, R. J., et al. (2012). Gene Expression Analysis of the Pleiotropic Effects of TGF-B1 in an *In Vitro* Model of Flexor Tendon Healing. *PLoS One* 7, e51411. doi:10.1371/journal.pone.0051411

Feng, Z., Tateishi, Y., Nomura, Y., Kitajima, T., and Nakamura, T. (2006). Construction of Fibroblast-Collagen Gels with Orientated Fibrils Induced by Static or Dynamic Stress: toward the Fabrication of Small Tendon Grafts. *J. Artif. Organs* 9, 220–225. doi:10.1007/s10047-006-0354-z

Fratzl, P., Misof, K., Zizak, I., Rapp, G., Amenitsch, H., and Bernstorff, S. (1998). Fibrillar Structure and Mechanical Properties of Collagen. *J. Struct. Biol.* 122, 119–122. doi:10.1006/jsbi.1998.3966

Freedman, B. R., Rodriguez, A. B., Leiphart, R. J., Newton, J. B., Ban, E., Sarver, J. J., et al. (2018). Dynamic Loading and Tendon Healing Affect Multiscale Tendon Properties and ECM Stress Transmission. *Sci. Rep.* 8, 10854. doi:10.1038/s41598-018-29060-y

Gaffney, L. S., Davis, Z. G., Mora-Navarro, C., Fisher, M. B., and Freytes, D. O. (2021). Extracellular Matrix Hydrogels Promote Expression of Muscle-Tendon Junction Proteins. *Tissue Eng. Part A*. Online ahead of print. doi:10.1089/ten.TEA.2021.0070

Garvin, J., Qi, J., Maloney, M., and Banes, A. J. (2003). Novel System for Engineering Bioartificial Tendons and Application of Mechanical Load. *Tissue Eng.* 9, 967–979. doi:10.1089/107632703322495619

Gatt, R., Vella Wood, M., Gatt, A., Zarb, F., Formosa, C., Azzopardi, K. M., et al. (2015). Negative Poisson's Ratios in Tendons: An Unexpected Mechanical Response. *Acta Biomater.* 24, 201–208. doi:10.1016/j.actbio.2015.06.018

Goodman, S. A., May, S. A., Heinegård, D., and Smith, R. K. (2004). Tenocyte Response to Cyclical Strain and Transforming Growth Factor Beta Is Dependent upon Age and Site of Origin. *Biorheology* 41, 613–628.

Govoni, M., Berardi, A. C., Muscari, C., Campardelli, R., Bonafè, F., Guarnieri, C., et al. (2017). An Engineered Multiphase Three-Dimensional Microenvironment to Ensure the Controlled Delivery of Cyclic Strain and Human Growth Differentiation Factor 5 for the Tenogenic Commitment of Human Bone Marrow Mesenchymal Stem Cells. *Tissue Eng. Part A* 23, 811–822. doi:10.1089/ten.tea.2016.0407

Guo, C., and Kaufman, L. J. (2007). Flow and Magnetic Field Induced Collagen Alignment. *Biomaterials* 28, 1105–1114. doi:10.1016/j.biomaterials.2006.10.010

Hamilton, B., and Purdam, C. (2004). Patellar Tendinosis as an Adaptive Process: a New Hypothesis. *Br. J. Sports Med.* 38, 758–761. doi:10.1136/bjsm.2003.005157

Han, W. M., Heo, S.-J., Driscoll, T. P., Smith, L. J., Mauck, R. L., and Elliott, D. M. (2013). Macro- to Microscale Strain Transfer in Fibrous Tissues Is Heterogeneous and Tissue-specific. *Biophysical J.* 105, 807–817. doi:10.1016/j.bpj.2013.06.023

Heng, B. C., Zhang, X., Aubel, D., Bai, Y., Li, X., Wei, Y., et al. (2020). Role of YAP/TAZ in Cell Lineage Fate Determination and Related Signaling Pathways. *Front. Cel Dev. Biol.* 8, 735. doi:10.3389/fcell.2020.00735

Herchenhan, A., Dietrich-Zagonel, F., Schjerling, P., Kjær, M., and Eliasson, P. (2020). Early Growth Response Genes Increases Rapidly after Mechanical Overloading and Unloading in Tendon Constructs. *J. Orthop. Res.* 38, 173–181. doi:10.1002/jor.24513

Hiraki, H. L., Matera, D. L., Rose, M. J., Kent, R. N., Todd, C. W., Stout, M. E., et al. (2021). Magnetic Alignment of Electrospun Fiber Segments within a Hydrogel Composite Guides Cell Spreading and Migration Phenotype Switching. *Front. Bioeng. Biotechnol.* 9, 679165. doi:10.3389/fbioe.2021.679165

Holmes, D. F., Graham, H. K., and Kadler, K. E. (1998). Collagen Fibrils Forming in Developing Tendon Show an Early and Abrupt Limitation in Diameter at the Growing Tips. *J. Mol. Biol.* 283, 1049–1058. doi:10.1006/jmbi.1998.2153

Hooley, C. J., McCrum, N. G., and Cohen, R. E. (1980). The Viscoelastic Deformation of Tendon. *J. Biomech.* 13, 521–528. doi:10.1016/0021-9290(80)90345-0

Howell, K., Chien, C., Bell, R., Laudier, D., Tufa, S. F., Keene, D. R., et al. (2017). Novel Model of Tendon Regeneration Reveals Distinct Cell Mechanisms Underlying Regenerative and Fibrotic Tendon Healing. *Sci. Rep.* 7, 45238. doi:10.1038/srep45238

Hu, X., Liu, Z. Z., Chen, X., Schulz, V. P., Kumar, A., Hartman, A. A., et al. (2019). MKL1-actin Pathway Restricts Chromatin Accessibility and Prevents Mature Pluripotency Activation. *Nat. Commun.* 10, 1695. doi:10.1038/s41467-019-09636-6

Humphrey, J. D., Dufresne, E. R., and Schwartz, M. A. (2014). Mechanotransduction and Extracellular Matrix Homeostasis. *Nat. Rev. Mol. Cel Biol.* 15, 802–812. doi:10.1038/nrm3896

Islam, A., Mbimba, T., Younesi, M., and Akkus, O. (2017). Effects of Substrate Stiffness on the Tenoinduction of Human Mesenchymal Stem Cells. *Acta Biomater.* 58, 244–253. doi:10.1016/j.actbio.2017.05.058

Jaiswal, D., Yousman, L., Neary, M., Fernschild, E., Zolnoski, B., Katebifar, S., et al. (2020). Tendon Tissue Engineering: Biomechanical Considerations. *Biomed. Mater.* 15, 052001. doi:10.1088/1748-605x/ab852f

James, R., Kumbar, S. G., Laurencin, C. T., Balian, G., and Chhabra, A. B. (2011). Tendon Tissue Engineering: Adipose-Derived Stem Cell and GDF-5 Mediated Regeneration Using Electrospun Matrix Systems. *Biomed. Mater.* 6, 025011. doi:10.1088/1748-6041/6/2/025011

Jozsa, L., Lehto, M., Kannus, P., Kvist, M., Reffy, A., Vieno, T., et al. (1989). Fibronectin and Laminin in Achilles Tendon. *Acta Orthopaedica Scand.* 60, 469–471. doi:10.3109/17453678909149322

Kalson, N. S., Lu, Y., Taylor, S. H., Starborg, T., Holmes, D. F., and Kadler, K. E. (2015). A Structure-Based Extracellular Matrix Expansion Mechanism of Fibrous Tissue Growth. *Elife* 4, e05958. doi:10.7554/eLife.05958

Kannus, P. (2000). Structure of the Tendon Connective Tissue. *Scand. J. Med. Sci. Sports* 10, 312–320. doi:10.1034/j.1600-0838.2000.010006312.x

Kayama, T., Mori, M., Ito, Y., Matsushima, T., Nakamichi, R., Suzuki, H., et al. (2016). Gtf2ird1 -Dependent Mohawk Expression Regulates Mechanosensing Properties of the Tendon. *Mol. Cel. Biol.* 36, 1297–1309. doi:10.1128/mcb.00950-15

Kirkendall, D. T., and Garrett, W. E. (1997). Function and Biomechanics of Tendons. *Scand. J. Med. Sci. Sports* 7, 62–66. doi:10.1111/j.1600-0838.1997.tb00120.x

Kohrs, R. T., Zhao, C., Sun, Y.-L., Jay, G. D., Zhang, L., Warman, M. L., et al. (2011). Tendon Fascicle Gliding in Wild Type, Heterozygous, and Lubricin Knockout Mice. *J. Orthop. Res.* 29, 384–389. doi:10.1002/jor.21247

Kuo, C. K., and Tuan, R. S. (2008). Mechanoactive Tenogenic Differentiation of Human Mesenchymal Stem Cells. *Tissue Eng. Part A* 14, 1615–1627. doi:10.1089/ten.tea.2006.0415

Lavagnino, M., Arnoczky, S. P., and Gardner, K. (2011). *In Situ* deflection of Tendon Cell-Cilia in Response to Tensile Loading: an *In Vitro* Study. *J. Orthop. Res.* 29, 925–930. doi:10.1002/jor.21337

Lavagnino, M., Arnoczky, S. P., Kepich, E., Caballero, O., and Haut, R. C. (2008). A Finite Element Model Predicts the Mechanotransduction Response of Tendon Cells to Cyclic Tensile Loading. *Biomech. Model. Mechanobiol.* 7, 405–416. doi:10.1007/s10237-007-0104-z

Leckband, D. E., le Duc, Q., Wang, N., and de Rooij, J. (2011). Mechanotransduction at Cadherin-Mediated Adhesions. *Curr. Opin. Cel Biol.* 23, 523–530. doi:10.1016/j.ceb.2011.08.003

Lee, A. H., and Elliott, D. M. (2019). Multi-Scale Loading and Damage Mechanisms of Plantaris and Rat Tail Tendons. *J. Orthop. Res.* 37, 1827–1837. doi:10.1002/jor.24309

Legerlotz, K., Jones, G. C., Screen, H. R. C., and Riley, G. P. (2013). Cyclic Loading of Tendon Fascicles Using a Novel Fatigue Loading System Increases Interleukin-6 Expression by Tenocytes. *Scand. J. Med. Sci. Sports* 23, 31–37. doi:10.1111/j.1600-0838.2011.01410.x

Lieber, R. L., Leonard, M. E., Brown, C. G., and Trestik, C. L. (1991). Frog Semitendinosis Tendon Load-Strain and Stress-Strain Properties during Passive Loading. *Am. J. Physiology-Cell Physiol.* 261, C86–C92. doi:10.1152/ajpcell.1991.261.1.c86

Lim, W. L., Liau, L. L., Ng, M. H., Chowdhury, S. R., and Law, J. X. (2019). Current Progress in Tendon and Ligament Tissue Engineering. *Tissue Eng. Regen. Med.* 16, 549–571. doi:10.1007/s13770-019-00196-w

Lin, Y., Zhang, L., Liu, N. Q., Yao, Q., Van Handel, B., Xu, Y., et al. (2019). *In Vitro* behavior of Tendon Stem/progenitor Cells on Bioactive Electrospun Nanofiber Membranes for Tendon-Bone Tissue Engineering Applications. *Ijn* Vol. 14, 5831–5848. doi:10.2147/ijn.s210509

Liu, R., Patel, D., Screen, H. R. C., and Becer, C. R. (2017). A2B-miktoarm Glycopolymer Fibers and Their Interactions with Tenocytes. *Bioconjug. Chem.* 28, 1955–1964. doi:10.1021/acs.bioconjchem.7b00279

Liu, S. H., Yang, R. S., Al-Shaikh, R., and Lane, J. M. (1995). Collagen in Tendon, Ligament, and Bone Healing. A Current Review. *Clin. Orthop. Relat. Res.* 265–278.

Lui, P. P. Y., and Chan, K. M. (2011). Tendon-derived Stem Cells (TDSCs): from Basic Science to Potential Roles in Tendon Pathology and Tissue Engineering Applications. *Stem Cel Rev Rep* 7, 883–897. doi:10.1007/s12015-011-9276-0

Maeda, E., Shelton, J. C., Bader, D. L., and Lee, D. A. (2009). Differential Regulation of Gene Expression in Isolated Tendon Fascicles Exposed to Cyclic Tensile Strain *In Vitro*. *J. Appl. Physiol.* 106, 506–512. doi:10.1152/japplphysiol.90981.2008

Maeda, E., Shelton, J. C., Bader, D. L., and Lee, D. A. (2007). Time Dependence of Cyclic Tensile Strain on Collagen Production in Tendon Fascicles. *Biochem. Biophysical Res. Commun.* 362, 399–404. doi:10.1016/j.bbrc.2007.08.029

Maganaris, C. N., and Paul, J. P. (1999). Vivo Human Tendon Mechanical Properties. *J. Physiol.* 521 (1), 307–313. doi:10.1111/j.1469-7793.1999.00307.x

Majima, T., Yasuda, K., Tsuchida, T., Tanaka, K., Miyakawa, K., Minami, A., et al. (2003). Stress Shielding of Patellar Tendon: Effect on Small-Diameter Collagenfibrils in a Rabbit Model. *J. Orthopaedic Sci.* 8, 836–841. doi:10.1007/s00776-003-0707-x

Malliaras, P., Kamal, B., Nowell, A., Farley, T., Dhamu, H., Simpson, V., et al. (2013). Patellar Tendon Adaptation in Relation to Load-Intensity and Contraction Type. *J. Biomech.* 46, 1893–1899. doi:10.1016/j.jbiomech.2013.04.022

Martin, J. A., Mehr, D., Pardubsky, P. D., and Buckwalter, J. A. (2003). The Role of Tenascin-C in Adaptation of Tendons to Compressive Loading. *Biorheology* 40, 321–329. Available at: https://pubmed.ncbi.nlm.nih.gov/12454422/

Morla, A., and Ruoslahti, E. (1992). A Fibronectin Self-Assembly Site Involved in Fibronectin Matrix Assembly: Reconstruction in a Synthetic Peptide. *J. Cel Biol.* 118, 421–429. doi:10.1083/jcb.118.2.421

Moser, H. L., Doe, A. P., Meier, K., Garnier, S., Laudier, D., Akiyama, H., et al. (2018). Genetic Lineage Tracing of Targeted Cell Populations during Enthesis Healing. *J. Orthop. Res.* 36, 3275–3284. doi:10.1002/jor.24122

Mousavizadeh, R., Duronio, V., McCormack, B., Khosravi, S., and Scott, A. (2013). MECHANICAL LOADING MODULATES ANGIOGENIC FACTORS IN TENDON CELLS. *Br. J. Sports Med.* 47, 4–e2. doi:10.1136/bjsports-2013-092459.12

Muellner, T., Kwasny, O., Loehnert, V., Mallinger, R., Unfried, G., Schabus, R., et al. (2001). Light and Electron Microscopic Study of Stress-Shielding Effects on Rat Patellar Tendon. *Arch. Orthopaedic Trauma Surg.* 121, 561–565. doi:10.1007/s004020100281

Nam, H. Y., Pingguan-Murphy, B., Abbas, A. A., Merican, A. M., and Kamarul, T. (2019). Uniaxial Cyclic Tensile Stretching at 8% Strain Exclusively Promotes Tenogenic Differentiation of Human Bone Marrow-Derived Mesenchymal Stromal Cells. *Stem Cell Int* 2019, 1–16. doi:10.1155/2019/9723025

Nichols, A. E. C., Best, K. T., and Loiselle, A. E. (2019). The Cellular Basis of Fibrotic Tendon Healing: Challenges and Opportunities. *Translational Res.* 209, 156–168. doi:10.1016/j.trsl.2019.02.002

Nie, D., Zhou, Y., Wang, W., Zhang, J., and Wang, J. H.-C. (2021). Mechanical Overloading Induced-Activation of mTOR Signaling in Tendon Stem/Progenitor Cells Contributes to Tendinopathy Development. *Front. Cel Dev. Biol.* 9, 687856. doi:10.3389/fcell.2021.687856

Nirmalanandhan, V. S., Rao, M., Sacks, M. S., Haridas, B., and Butler, D. L. (2007). Effect of Length of the Engineered Tendon Construct on its Structure-Function Relationships in Culture. *J. Biomech.* 40, 2523–2529. doi:10.1016/j.jbiomech.2006.11.016

O'Neill, S., Watson, P. J., and Barry, S. (2015). WHY ARE ECCENTRIC EXERCISES EFFECTIVE FOR ACHILLES TENDINOPATHY? *Int. J. Sports Phys. Ther.* 10, 552–562.

Ottani, V., Martini, D., Franchi, M., Ruggeri, A., and Raspanti, M. (2002). Hierarchical Structures in Fibrillar Collagens. *Micron* 33, 587–596. doi:10.1016/S0968-4328(02)00033-1

Parent, G., Huppé, N., and Langelier, E. (2011). Low Stress Tendon Fatigue Is a Relatively Rapid Process in the Context of Overuse Injuries. *Ann. Biomed. Eng.* 39, 1535–1545. doi:10.1007/s10439-011-0254-0

Passini, F. S., Jaeger, P. K., Saab, A. S., Hanlon, S., Chittim, N. A., Arlt, M. J., et al. (2021). Shear-stress Sensing by PIEZO1 Regulates Tendon Stiffness in Rodents and Influences Jumping Performance in Humans. *Nat. Biomed. Eng.* 5, 1457–1471. doi:10.1038/s41551-021-00716-x

Patel, D., Sharma, S., Bryant, S. J., and Screen, H. R. C. (2017). Recapitulating the Micromechanical Behavior of Tension and Shear in a Biomimetic Hydrogel for Controlling Tenocyte Response. *Adv. Healthc. Mater.* 6, 1601095. doi:10.1002/adhm.201601095

Patel, D., Sharma, S., Screen, H. R. C., and Bryant, S. J. (2018). Effects of Cell Adhesion Motif, Fiber Stiffness, and Cyclic Strain on Tenocyte Gene Expression in a Tendon Mimetic Fiber Composite Hydrogel. *Biochem. Biophysical Res. Commun.* 499, 642–647. doi:10.1016/j.bbrc.2018.03.203

Rees, J. D., Lichtwark, G. A., Wolman, R. L., and Wilson, A. M. (2008). The Mechanism for Efficacy of Eccentric Loading in Achilles Tendon Injury; an *In Vivo* Study in Humans. *Rheumatology* 47, 1493–1497. doi:10.1093/rheumatology/ken262

Riboh, J., Chong, A. K. S., Pham, H., Longaker, M., Jacobs, C., and Chang, J. (2008). Optimization of Flexor Tendon Tissue Engineering with a Cyclic Strain Bioreactor. *J. Hand Surg.* 33, 1388–1396. doi:10.1016/j.jhsa.2008.04.019

Rinoldi, C., Fallahi, A., Yazdi, I. K., Campos Paras, J., Kijeńska-Gawrońska, E., Trujillo-de Santiago, G., et al. (2019). Mechanical and Biochemical Stimulation of 3D Multilayered Scaffolds for Tendon Tissue Engineering. *ACS Biomater. Sci. Eng.* 5, 2953–2964. doi:10.1021/acsbiomaterials.8b01647

Rio, E., Kidgell, D., Moseley, G. L., Gaida, J., Docking, S., Purdam, C., et al. (2016). Tendon Neuroplastic Training: Changing the Way We Think about Tendon Rehabilitation: a Narrative Review. *Br. J. Sports Med.* 50, 209–215. doi:10.1136/bjsports-2015-095215

Robbins, J. R., Evanko, S. P., and Vogel, K. G. (1997). Mechanical Loading and TGF-β Regulate Proteoglycan Synthesis in Tendon. *Arch. Biochem. Biophys.* 342, 203–211. doi:10.1006/abbi.1997.0102

Roberts, T. J., and Konow, N. (2013). How Tendons Buffer Energy Dissipation by Muscle. *Exerc. Sport Sci. Rev.* 41, 186–193. doi:10.1097/JES.0b013e3182a4e6d5

Robi, K., Jakob, N., Matevz, K., and Matjaz, V. (2013). The Physiology of Sports Injuries and Repair Processes. *Curr. Issues Sports Exerc. Med.*, 43–86. doi:10.5772/54234

Robi, K., Jakob, N., Matevz, K., and Matjaz, V. (2013). The Physiology of Sports Injuries and Repair Processes. *Curr. Issues Sports Exerc. Med.*, 43–86. doi:10.5772/54234

Rui, Y.-F., Lui, P. P. Y., Li, G., Fu, S. C., Lee, Y. W., and Chan, K. M. (2010). Isolation and Characterization of Multipotent Rat Tendon-Derived Stem Cells. *Tissue Eng. Part A* 16, 1549–1558. doi:10.1089/ten.tea.2009.0529

Rui, Y. F., Lui, P. P. Y., Ni, M., Chan, L. S., Lee, Y. W., and Chan, K. M. (2011). Mechanical Loading Increased BMP-2 Expression Which Promoted Osteogenic Differentiation of Tendon-Derived Stem Cells. *J. Orthop. Res.* 29, 390–396. doi:10.1002/jor.21218

Sahoo, S., Ang, L. T., Goh, J. C., and Toh, S. L. (2010). Growth Factor Delivery through Electrospun Nanofibers in Scaffolds for Tissue Engineering Applications. *J. Biomed. Mater. Res. A.* 93, 1539–1550. doi:10.1002/jbm.a.32645

Scharenberg, M. A., Pippenger, B. E., Sack, R., Zingg, D., Ferralli, J., Schenk, S., et al. (2014). TGF-β-induced Differentiation into Myofibroblasts Involves Specific Regulation of Two MKL1 Isoforms. *J. Cel Sci.* 127, 1079–1091. doi:10.1242/jcs.142075

Schiele, N. R., Marturano, J. E., and Kuo, C. K. (2013). Mechanical Factors in Embryonic Tendon Development: Potential Cues for Stem Cell Tenogenesis. *Curr. Opin. Biotechnol.* 24, 834–840. doi:10.1016/j.copbio.2013.07.003

Schoenenberger, A. D., Tempfer, H., Lehner, C., Egloff, J., Mauracher, M., Bird, A., et al. (2020). Macromechanics and Polycaprolactone Fiber Organization Drive Macrophage Polarization and Regulate Inflammatory Activation of Tendon *In Vitro* and *In Vivo*. *Biomaterials* 249, 120034. doi:10.1016/j.biomaterials.2020.120034

Scott, A., Danielson, P., Abraham, T., Fong, G., Sampaio, A. V., and Underhill, T. M. (2011). Mechanical Force Modulates Scleraxis Expression in Bioartificial Tendons. *J. Musculoskelet. Neuronal Interact.* 11, 124–132.

Scott, A., Khan, K., Heer, J., Cook, J., Lian, O., and Duronio, V. (2005). High Strain Mechanical Loading Rapidly Induces Tendon Apoptosis: an *Ex Vivo* Rat Tibialis Anterior Model. *Br. J. Sports Med.* 39, e25. doi:10.1136/bjsm.2004.015164

Screen, H. R. C., Lee, D. A., Bader, D. L., and Shelton, J. C. (2004). An Investigation into the Effects of the Hierarchical Structure of Tendon Fascicles on Micromechanical Properties. *Proc. Inst. Mech. Eng. H* 218, 109–119. doi:10.1243/095441104322984004

Screen, H. R. C., Shelton, J. C., Bader, D. L., and Lee, D. A. (2005). Cyclic Tensile Strain Upregulates Collagen Synthesis in Isolated Tendon Fascicles. *Biochem. Biophysical Res. Commun.* 336, 424–429. doi:10.1016/j.bbrc.2005.08.102

Shani, R. H., Umpierez, E., Nasert, M., Hiza, E. A., and Xerogeanes, J. (2016). Biomechanical Comparison of Quadriceps and Patellar Tendon Grafts in Anterior Cruciate Ligament Reconstruction. *Arthrosc. J. Arthroscopic Relat. Surg.* 32, 71–75. doi:10.1016/j.arthro.2015.06.051

Sharma, R. I., and Snedeker, J. G. (2010). Biochemical and Biomechanical Gradients for Directed Bone Marrow Stromal Cell Differentiation toward Tendon and Bone. *Biomaterials* 31, 7695–7704. doi:10.1016/j.biomaterials.2010.06.046

Sharma, R. I., and Snedeker, J. G. (2012). Paracrine Interactions between Mesenchymal Stem Cells Affect Substrate Driven Differentiation toward Tendon and Bone Phenotypes. *PLoS One* 7, e31504. doi:10.1371/journal.pone.0031504

Skutek, M., van Griensven, M., Zeichen, J., Brauer, N., and Bosch, U. (2003). Cyclic Mechanical Stretching of Human Patellar Tendon Fibroblasts: Activation of JNK and Modulation of Apoptosis. *Knee Surg. Sports Traumatol. Arthrosc.* 11, 122–129. doi:10.1007/s00167-002-0322-y

Smith, R. K. W., Zunino, L., Webbon, P. M., and Heinegård, D. (1997). The Distribution of Cartilage Oligomeric Matrix Protein (COMP) in Tendon and its Variation with Tendon Site, Age and Load. *Matrix Biol.* 16, 255–271. doi:10.1016/s0945-053x(97)90014-7

Stauber, T., Wolleb, M., Duss, A., Jaeger, P. K., Heggli, I., Hussien, A. A., et al. (2021). Extrinsic Macrophages Protect while Tendon Progenitors Degrade: Insights from a Tissue Engineered Model of Tendon Compartmental Crosstalk. *Adv. Healthc. Mater.* 10, 2100741. doi:10.1002/adhm.202100741

Sugisaki, N., Kawakami, Y., Kanehisa, H., and Fukunaga, T. (2011). Effect of Muscle Contraction Levels on the Force-Length Relationship of the Human Achilles Tendon during Lengthening of the Triceps Surae Muscle-Tendon Unit. *J. Biomech.* 44, 2168–2171. doi:10.1016/j.jbiomech.2011.05.015

Szczesny, S. E., Caplan, J. L., Pedersen, P., and Elliott, D. M. (2015). Quantification of Interfibrillar Shear Stress in Aligned Soft Collagenous Tissues via Notch Tension Testing. *Sci. Rep.* 5, 14649–9. doi:10.1038/srep14649

Szczesny, S. E., Aeppli, C., David, A., and Mauck, R. L. (2018). Fatigue Loading of Tendon Results in Collagen Kinking and Denaturation but Does Not Change Local Tissue Mechanics. *J. Biomech.* 71, 251–256. doi:10.1016/j.jbiomech.2018.02.014

Szczesny, S. E., and Elliott, D. M. (2014). Interfibrillar Shear Stress Is the Loading Mechanism of Collagen Fibrils in Tendon. *Acta Biomater.* 10, 2582–2590. doi:10.1016/j.actbio.2014.01.032

Tajik, A., Zhang, Y., Wei, F., Sun, J., Jia, Q., Zhou, W., et al. (2016). Transcription Upregulation via Force-Induced Direct Stretching of Chromatin. *Nat. Mater* 15, 1287–1296. doi:10.1038/nmat4729

Thompson, M. S., Bajuri, M. N., Khayyeri, H., and Isaksson, H. (2017). Mechanobiological Modelling of Tendons: Review and Future Opportunities. *Proc. Inst. Mech. Eng. H* 231, 369–377. doi:10.1177/0954411917692010

Thorpe, C. T., Godinho, M. S. C., Riley, G. P., Birch, H. L., Clegg, P. D., and Screen, H. R. C. (2015). The Interfascicular Matrix Enables Fascicle Sliding and Recovery in Tendon, and Behaves More Elastically in Energy Storing Tendons. *J. Mech. Behav. Biomed. Mater.* 52, 85–94. doi:10.1016/j.jmbbm.2015.04.009

Thorpe, C. T., and Screen, H. R. C. (2016). "Tendon Structure and Composition," in *"Tendon Structure and Composition," in* Metabolic Influences On Risk For Tendon Disorders. Editors P. W. Ackermann and D. A. Hart (Cham: Springer International Publishing), 3–10.

Tohidnezhad, M., Zander, J., Slowik, A., Kubo, Y., Dursun, G., Willenberg, W., et al. (2020). Impact of Uniaxial Stretching on Both Gliding and Traction Areas of Tendon Explants in a Novel Bioreactor. *Ijms* 21, 2925. doi:10.3390/ijms21082925

Trelstad, R. L., and Hayashi, K. (1979). Tendon Collagen Fibrillogenesis: Intracellular Subassemblies and Cell Surface Changes Associated with Fibril Growth. *Develop. Biol.* 71, 228–242. doi:10.1016/0012-1606(79)90166-0

Tsuzaki, M., Bynum, D., Almekinders, L., Yang, X., Faber, J., and Banes, A. J. (2003). ATP Modulates Load-Inducible IL-1?, COX 2, and MMP-3 Gene Expression in Human Tendon Cells. *J. Cel. Biochem.* 89, 556–562. doi:10.1002/jcb.10534

Tu, T., Shen, Y., Wang, X., Zhang, W., Zhou, G., Zhang, Y., et al. (2020). Tendon ECM Modified Bioactive Electrospun Fibers Promote MSC Tenogenic Differentiation and Tendon Regeneration. *Appl. Mater. Today* 18, 100495. doi:10.1016/j.apmt.2019.100495

Viganò, M., Perucca Orfei, C., Colombini, A., Stanco, D., Randelli, P., Sansone, V., et al. (2017). Different Culture Conditions Affect the Growth of Human Tendon Stem/progenitor Cells (TSPCs) within a Mixed Tendon Cells (TCs) Population. *J. Exp. Orthop.* 4, 8–9. doi:10.1186/s40634-017-0082-8

Vogel, K. G. (2004). What Happens when Tendons bend and Twist? Proteoglycans. *J. Musculoskelet. Neuronal Interact.* 4, 202–203. Available at: https://europepmc.org/article/med/15615127

Wall, M. E., Weinhold, P. S., Siu, T., Brown, T. D., and Banes, A. J. (2007). Comparison of Cellular Strain with Applied Substrate Strain *In Vitro*. *J. Biomech.* 40, 173–181. doi:10.1016/j.jbiomech.2005.10.032

Wang, J. H.-C. (2006). Mechanobiology of Tendon. *J. Biomech.* 39, 1563–1582. doi:10.1016/j.jbiomech.2005.05.011

Wang, J., Jia, F., Yang, G., Yang, S., Campbell, B., Stone, D., et al. (2003). Cyclic Mechanical Stretching of Human Tendon Fibroblasts Increases the Production of Prostaglandin E 2 and Levels of Cyclooxygenase Expression: A Novel *In Vitro* Model Study. *Connect. Tissue Res.* 44, 128–133. doi:10.1080/713713684

Wang, N., Tytell, J. D., and Ingber, D. E. (2009). Mechanotransduction at a Distance: Mechanically Coupling the Extracellular Matrix with the Nucleus. *Nat. Rev. Mol. Cel Biol.* 10, 75–82. doi:10.1038/nrm2594

Wang, T., Chen, P., Zheng, M., Wang, A., Lloyd, D., Leys, T., et al. (2018a). *In Vitro* loading Models for Tendon Mechanobiology. *J. Orthop. Res.* 36, 566–575. doi:10.1002/jor.23752

Wang, T., Chen, P., Chen, L., Zhou, Y., Wang, A., Zheng, Q., et al. (2021). Reduction of Mechanical Loading in Tendons Induces Heterotopic Ossification and Activation of the β-catenin Signaling Pathway. *J. Orthopaedic Translation* 29, 42–50. doi:10.1016/j.jot.2021.03.004

Wang, T., Lin, Z., Day, R. E., Gardiner, B., Landao-Bassonga, E., Rubenson, J., et al. (2013). Programmable Mechanical Stimulation Influences Tendon Homeostasis in a Bioreactor System. *Biotechnol. Bioeng.* 110, 1495–1507. doi:10.1002/bit.24809

Wang, T., Lin, Z., Ni, M., Thien, C., Day, R. E., Gardiner, B., et al. (2015). Cyclic Mechanical Stimulation Rescues Achilles Tendon from Degeneration in a Bioreactor System. *J. Orthop. Res.* 33, 1888–1896. doi:10.1002/jor.22960

Wang, T., Thien, C., Wang, C., Ni, M., Gao, J., Wang, A., et al. (2018b). 3D Uniaxial Mechanical Stimulation Induces Tenogenic Differentiation of Tendon-derived Stem Cells through a PI3K/AKT Signaling Pathway. *FASEB j.* 32, 4804–4814. doi:10.1096/fj.201701384r

Wang, W., He, J., Feng, B., Zhang, Z., Zhang, W., Zhou, G., et al. (2016). Aligned Nanofibers Direct Human Dermal Fibroblasts to Tenogenic Phenotype *In Vitro* and Enhance Tendon Regeneration *In Vivo*. *Nanomedicine* 11, 1055–1072. doi:10.2217/nnm.16.24

Wang, X. T., Ker, R. F., and Alexander, R. M. (1995). Fatigue Rupture of Wallaby Tail Tendons. *J. Exp. Biol.* 198, 847–852. doi:10.1242/jeb.198.3.847

Warner, J. J., Gillies, A. R., Hwang, H. H., Zhang, H., Lieber, R. L., and Chen, S. (2017). 3D-printed Biomaterials with Regional Auxetic Properties. *J. Mech. Behav. Biomed. Mater.* 76, 145–152. doi:10.1016/j.jmbbm.2017.05.016

Woo, S. L.-Y., Debski, R. E., Zeminski, J., Abramowitch, S. D., Chan Saw, Ms, S. S., Fenwick, J. A., et al. (2000). Injury and Repair of Ligaments and Tendons. *Annu. Rev. Biomed. Eng.* 2, 83–118. doi:10.1146/annurev.bioeng.2.1.83

Wren, T. A. L., Lindsey, D. P., Beaupré, G. S., and Carter, D. R. (2003). Effects of Creep and Cyclic Loading on the Mechanical Properties and Failure of Human Achilles Tendons. *Ann. Biomed. Eng.* 31, 710–717. doi:10.1114/1.1569267

Wu, S., Wang, Y., Streubel, P. N., and Duan, B. (2017). Living Nanofiber Yarn-Based Woven Biotextiles for Tendon Tissue Engineering Using Cell Tri-culture and Mechanical Stimulation. *Acta Biomater.* 62, 102–115. doi:10.1016/j.actbio.2017.08.043

Wu, Y., Han, Y., Wong, Y. S., and Fuh, J. Y. H. (2018). Fibre-based Scaffolding Techniques for Tendon Tissue Engineering. *J. Tissue Eng. Regen. Med.* 12, 1798–1821. doi:10.1002/term.2701

Wunderli, S. L., Blache, U., and Snedeker, J. G. (2020). Tendon Explant Models for Physiologically Relevant *In Vitro* Study of Tissue Biology - a Perspective. *Connect. Tissue Res.* 61, 262–277. doi:10.1080/03008207.2019.1700962

Wunderli, S. L., Widmer, J., Amrein, N., Foolen, J., Silvan, U., Leupin, O., et al. (2018). Minimal Mechanical Load and Tissue Culture Conditions Preserve Native Cell Phenotype and Morphology in Tendon-A Novel *Ex Vivo* Mouse Explant Model. *J. Orthop. Res.* 36, 1383–1390. doi:10.1002/jor.23769

Xu, Y., Yin, H., Chu, J., Eglin, D., Serra, T., and Docheva, D. (2021). An Anisotropic Nanocomposite Hydrogel Guides Aligned Orientation and Enhances Tenogenesis of Human Tendon Stem/progenitor Cells. *Biomater. Sci.* 9, 1237–1245. doi:10.1039/d0bm01127d

Yamamoto, E., Hayashi, K., and Yamamoto, N. (1999). Mechanical Properties of Collagen Fascicles from Stress-Shielded Patellar Tendons in the Rabbit. *Clin. Biomech.* 14, 418–425. doi:10.1016/S0268-0033(99)00006-6

Yang, G., Crawford, R. C., and Wang, J. H.-C. (2004). Proliferation and Collagen Production of Human Patellar Tendon Fibroblasts in Response to Cyclic Uniaxial Stretching in Serum-free Conditions. *J. Biomech.* 37, 1543–1550. doi:10.1016/j.jbiomech.2004.01.005

Yang, G., Im, H.-J., and Wang, J. H.-C. (2005). Repetitive Mechanical Stretching Modulates IL-1β Induced COX-2, MMP-1 Expression, and PGE2 Production in Human Patellar Tendon Fibroblasts. *Gene* 363, 166–172. doi:10.1016/j.gene.2005.08.006

Yeung, C.-Y. C., Zeef, L. A. H., Lallyett, C., Lu, Y., Canty-Laird, E. G., and Kadler, K. E. (2015). Chick Tendon Fibroblast Transcriptome and Shape Depend on whether the Cell Has Made its Own Collagen Matrix. *Sci. Rep.* 5, 13555. doi:10.1038/srep13555

Yin, H., Strunz, F., Yan, Z., Lu, J., Brochhausen, C., Kiderlen, S., et al. (2020). Three-dimensional Self-Assembling Nanofiber Matrix Rejuvenates Aged/degenerative Human Tendon Stem/progenitor Cells. *Biomaterials* 236, 119802. doi:10.1016/j.biomaterials.2020.119802

Yin, Z., Guo, J., Wu, T.-y., Chen, X., Xu, L.-l., Lin, S.-e., et al. (2016). Stepwise Differentiation of Mesenchymal Stem Cells Augments Tendon-like Tissue Formation and Defect Repair *In Vivo*. *Stem Cell Transl. Med.* 5, 1106–1116. doi:10.5966/sctm.2015-0215

Youngstrom, D. W., Barrett, J. G., Jose, R. R., and Kaplan, D. L. (2013). Functional Characterization of Detergent-Decellularized Equine Tendon Extracellular Matrix for Tissue Engineering Applications. *PLoS One* 8, e64151. doi:10.1371/journal.pone.0064151

Youngstrom, D. W., and Barrett, J. G. (2016). Tendon Differentiation on Decellularized Extracellular Matrix under Cyclic Loading. *Methods Mol. Biol.* 1502, 195–202. doi:10.1007/7651_2016_332

Youngstrom, D. W., LaDow, J. E., and Barrett, J. G. (2016). Tenogenesis of Bone Marrow-, Adipose-, and Tendon-Derived Stem Cells in a Dynamic Bioreactor. *Connect. Tissue Res.* 57, 454–465. doi:10.3109/03008207.2015.1117458

Zeichen, J., van Griensven, M., and Bosch, U. (2000). The Proliferative Response of Isolated Human Tendon Fibroblasts to Cyclic Biaxial Mechanical Strain. *Am. J. Sports Med.* 28, 888–892. doi:10.1177/03635465000280061901

Zhang, G., Chen, S., Goldoni, S., Calder, B. W., Simpson, H. C., Owens, R. T., et al. (2009). Genetic Evidence for the Coordinated Regulation of Collagen Fibrillogenesis in the Cornea by Decorin and Biglycan. *J. Biol. Chem.* 284, 8888–8897. doi:10.1074/jbc.m806590200

Zhang, J., and Wang, J. H.-C. (2010). Mechanobiological Response of Tendon Stem Cells: Implications of Tendon Homeostasis and Pathogenesis of Tendinopathy. *J. Orthop. Res.* 28, 639–643. doi:10.1002/jor.21046

Zhang, J., and Wang, J. H.-C. (2013). The Effects of Mechanical Loading on Tendons - an *In Vivo* and *In Vitro* Model Study. *PLoS One* 8, e71740. doi:10.1371/journal.pone.0071740

Zhang, L., Kahn, C. J. F., Chen, H.-Q., Tran, N., and Wang, X. (2008). Effect of Uniaxial Stretching on Rat Bone Mesenchymal Stem Cell: Orientation and Expressions of Collagen Types I and III and Tenascin-C. *Cel Biol. Int.* 32, 344–352. doi:10.1016/j.cellbi.2007.12.018

Zhong, C., Chrzanowska-Wodnicka, M., Brown, J., Shaub, A., Belkin, A. M., and Burridge, K. (1998). Rho-mediated Contractility Exposes a Cryptic Site in Fibronectin and Induces Fibronectin Matrix Assembly. *J. Cel Biol.* 141, 539–551. doi:10.1083/jcb.141.2.539

Zuskov, A., Freedman, B. R., Gordon, J. A., Sarver, J. J., Buckley, M. R., and Soslowsky, L. J. (2020). Tendon Biomechanics and Crimp Properties Following Fatigue Loading Are Influenced by Tendon Type and Age in Mice. *J. Orthop. Res.* 38, 36–42. doi:10.1002/jor.24407

Conflict of Interest: The authors declare that the research was conducted in the absence of any commercial or financial relationships that could be construed as a potential conflict of interest.

Publisher's Note: All claims expressed in this article are solely those of the authors and do not necessarily represent those of their affiliated organizations, or those of the publisher, the editors and the reviewers. Any product that may be evaluated in this article, or claim that may be made by its manufacturer, is not guaranteed or endorsed by the publisher.

Copyright © 2022 Wu, Kim and Kremen. This is an open-access article distributed under the terms of the Creative Commons Attribution License (CC BY). The use, distribution or reproduction in other forums is permitted, provided the original author(s) and the copyright owner(s) are credited and that the original publication in this journal is cited, in accordance with accepted academic practice. No use, distribution or reproduction is permitted which does not comply with these terms.

frontiers in Bioengineering and Biotechnology

ORIGINAL RESEARCH
published: 21 February 2022
doi: 10.3389/fbioe.2022.825046

Toward Development of a Diabetic Synovium Culture Model

*Neeraj Sakhrani[1], Andy J. Lee[1], Lance A. Murphy[1], Hagar M. Kenawy[1], Christopher J. Visco[2], Gerard A. Ateshian[1,3], Roshan P. Shah[4] and Clark T. Hung[1,4]**

[1]Department of Biomedical Engineering, Columbia University, New York, NY, United States, [2]Department of Rehabilitation and Regenerative Medicine, Columbia University, New York, NY, United States, [3]Department of Mechanical Engineering, Columbia University, New York, NY, United States, [4]Department of Orthopedic Surgery, Columbia University, New York, NY, United States

Osteoarthritis (OA) is a degenerative joint disease characterized by articular cartilage degradation and inflammation of synovium, the specialized connective tissue that envelops the diarthrodial joint. Type 2 diabetes mellitus (DM) is often found in OA patients, with nearly double the incidence of arthritis reported in patients with diabetes (52%) than those without it (27%). The correlation between OA and DM has been attributed to similar risk factors, namely increasing age and joint loading due to obesity. However, a potential causative link is not well understood due to comorbidities involved with treating diabetic patients, such as high infection rates and poor healing response caused by hyperglycemia and insulin resistance. The purpose of this study was to investigate the effect of hyperglycemic and insulin culture conditions on synovium properties. It was hypothesized that modeling hyperglycemia-induced insulin resistance in synovium would provide novel insights of OA pathogenesis in DM patients. To simulate DM in the synovial joint, healthy synovium was preconditioned in either euglycemic (EG) or hyperglycemic (HG) glucose concentrations with insulin in order to induce the biological response of the diseased phenotype. Synovium biochemical composition was evaluated to determine ECM remodeling under hyperglycemic culture conditions. Concurrent changes in AKT phosphorylation, a signaling pathway implicated in insulin resistance, were measured along with gene expression data for insulin receptors, glucose transporters, and specific glycolysis markers involved in glucose regulation. Since fluid shear stress arising during joint articulation is a relevant upstream stimulus for fibroblast-like synoviocytes (FLS), the predominant cell type in synovium, FLS mechanotransduction was evaluated via intracellular calcium ($[Ca^{2+}]_i$). Incidence and length of primary cilia, a critical effector of cell mechanosensing, were measured as potential mechanisms to support differences in $[Ca^{2+}]_i$ responses. Hyperglycemic culture conditions decreased collagen and GAG content compared to EG groups, while insulin recovered ECM constituents. FLS mechanosensitivity was significantly greater in EG and insulin conditions compared to HG and non-insulin treated groups. Hyperglycemic treatment led to decreased incidence and length of primary cilia and decreased AKT phosphorylation, providing possible links to the mechanosensing response and suggesting a potential correlation between glycemic culture conditions, diabetic insulin resistance, and OA development.

Keywords: synovium, type 2 diabetes, insulin resistance, hyperglycemia, osteoarthritis, calcium signaling, shear stress, primary cilia

OPEN ACCESS

Edited by:
Andrea Vernengo,
AO Research Institute, Switzerland

Reviewed by:
Xiao-Feng Li,
Anhui Medical University, China
X. Lucas Lu,
University of Delaware, United States

****Correspondence:***
Clark T. Hung
cth6@columbia.edu

Specialty section:
This article was submitted to Tissue Engineering and Regenerative Medicine, a section of the journal Frontiers in Bioengineering and Biotechnology

Received: *29 November 2021*
Accepted: *24 January 2022*
Published: *21 February 2022*

Citation:
Sakhrani N, Lee AJ, Murphy LA, Kenawy HM, Visco CJ, Ateshian GA, Shah RP and Hung CT (2022) Toward Development of a Diabetic Synovium Culture Model. Front. Bioeng. Biotechnol. 10:825046. doi: 10.3389/fbioe.2022.825046

INTRODUCTION

Osteoarthritis (OA), the most common musculoskeletal disorder, is a degenerative condition that affects an estimated 250 million people worldwide (Rosa et al., 2009; Hamada et al., 2016; Stefani et al., 2019). OA is characterized by articular cartilage degradation, altered subchondral and peri-cartilaginous bone, and synovial inflammation (King and Rosenthal, 2015; Silverstein, 2017). The prevalence of comorbidities among patients with OA is high, contributing to gastrointestinal, neurological, cardiovascular, and endocrine complications (Swain et al., 2020). Type 2 diabetes mellitus (DM) is a common comorbidity in OA patients, contributing to high infection rates and poor healing (King and Rosenthal, 2015; Swain et al., 2020). DM is characterized by chronic hyperglycemia caused by a combination of insulin resistance and a deficiency of insulin secretion or action (Hamada et al., 2016; Röder et al., 2016; Galicia-Garcia et al., 2020).

The association between OA and DM is well supported. More than 90% of patients diagnosed with DM are obese (Bramante et al., 2017). Joint loading due to obesity has been linked to articular cartilage damage in the development and progression of OA (Bramante et al., 2017; Silverstein et al., 2017; Sun et al., 2021). Increasing age is another known cause for the development of both diseases as adults above the age of 65 are more than twice as likely to develop either condition (Piva et al., 2015; Veronese et al., 2019). While the separate incidences of both OA and DM are significant, overlap between the two diseases are also common. DM is often found in OA patients, with higher occurrence of arthritis reported in patients with diabetes (52%) than those without it (27%) (Piva et al., 2015). Conversely, patients diagnosed with OA have a 61% greater risk of developing DM compared to people without arthritis (Dong et al., 2017).

While the connection between OA and DM has historically been attributed to similar risk factors including increasing age and joint loading due to obesity, the effects of hyperglycemia and insulin resistance on synovium and their contribution to OA pathogenesis have not been thoroughly investigated due to the associated comorbidity involved with treating this patient population (Hamada et al., 2016). The synovium is a specialized connective tissue that envelops arthrodial joints and is comprised mainly of fibroblast-like synoviocytes (FLS) (Estell et al., 2017). The tissue maintains the synovial fluid-filled region that delivers a lubricating environment for the articulating cartilage surfaces and serves as a semi-permeable membrane that facilities solute transport across the joint (Blewis et al., 2010; Tamer, 2013; Estell et al., 2017). To this end, this research, comprised of four complementary studies, investigated the effect of hyperglycemic treatment and insulin culture conditions on synovium properties toward the development of an *in vitro* diabetic synovium model for basic science and translational research applications.

Insulin production and release has been shown to play a protective role in regulating synovial inflammation and catabolism in patients with DM (Griffin and Huffman, 2016; Song et al., 2021). While limited studies have directly investigated the role of insulin on synovium, the anabolic effects of insulin have been thoroughly investigated in a variety of other musculoskeletal tissues including bone, cartilage, and tendon where insulin serves as a vehicle that stimulates cell differentiation, proliferation, and extracellular matrix (ECM) production (Weiss and Reddi, 1980; Maor et al., 1993; Griffin and Huffman, 2016; Wu et al., 2017; Frost et al., 2018; Durgam et al., 2019; Cipriani et al., 2020). However, insulin signaling and metabolic function are impaired under diabetic conditions. This decrease in the protective role of insulin contributes to high infection rates, joint inflammation, and a poor healing response, characteristic of the arthritic disease state (Bustamante et al., 2017). Since glucose and insulin treatments have been implicated in ECM remodeling, study 1 investigated the effect of hyperglycemic and insulin culture conditions on tissue biochemical composition by looking at DNA, glycosaminoglycan (GAG), and collagen content of healthy and OA human synovium explants (Williams et al., 2015). Histological characterization of GAG and collagen distribution was assessed along with expression of glucose transporter 1 (GLUT1), as a specific marker of glucose transport in explants exposed to hyperglycemic culture conditions (Rosa et al., 2009; Li et al., 2021).

Patients with DM can suffer compromised synovium function, as the development of synovial insulin resistance under hyperglycemic conditions reduces the ability of insulin to regulate glucose levels and suppress the production of inflammatory mediators known to stimulate the progression of OA (King and Rosenthal, 2015; Griffin and Huffman, 2016). In DM, the AKT signaling pathway is involved in the regulation of insulin and glucose uptake in adipose tissue (Hamada et al., 2016; Hatting et al., 2018). The AKT signaling cascade begins with the binding of insulin to surface protein receptors. Insulin stimulates the phosphorylation of AKT, causing the translocation of glucose transporters (GLUT) to the cell membrane, which facilitates glucose uptake into the cell (**Figure 1**) (Mackenzie and Elliott, 2014; Tchetina et al., 2020). Toward efforts to better understand markers of insulin resistance or compromised insulin response in synovium exposed to hyperglycemic and insulin culture conditions, study 2 characterized concurrent changes in AKT phosphorylation and specific gene expression markers implicated in glucose activity and insulin resistance for healthy and non-diabetic OA synovial explants.

While the AKT pathway is a downstream marker of DM and OA, it is regulated by upstream calcium influxes (Danciu et al., 2003; Nicholson-Fish et al., 2016). Calcium, a ubiquitous second messenger, is one of the earliest cell signaling events activated by applied physical and chemical stimuli (Yellowley et al., 1999; Estell et al., 2017). In diabetic patients, insulin resistance contributes to a decreased cellular response to external stimuli (Wilcox, 2005; Petersen and Shulman., 2018). However, synoviocytes respond to these mechanical cues to support joint health and modulate inflammation (D'Andrea et al., 1998; Sun et al., 2003; Yanagida-Suekawa et al., 2013, Estell et al., 2017; Falconer et al., 2021). Study 3 monitored intracellular calcium response ($[Ca^{2+}]_i$) to fluid-induced shear stress of healthy and non-diabetic OA FLS that are cultured in hyperglycemic and insulin conditions.

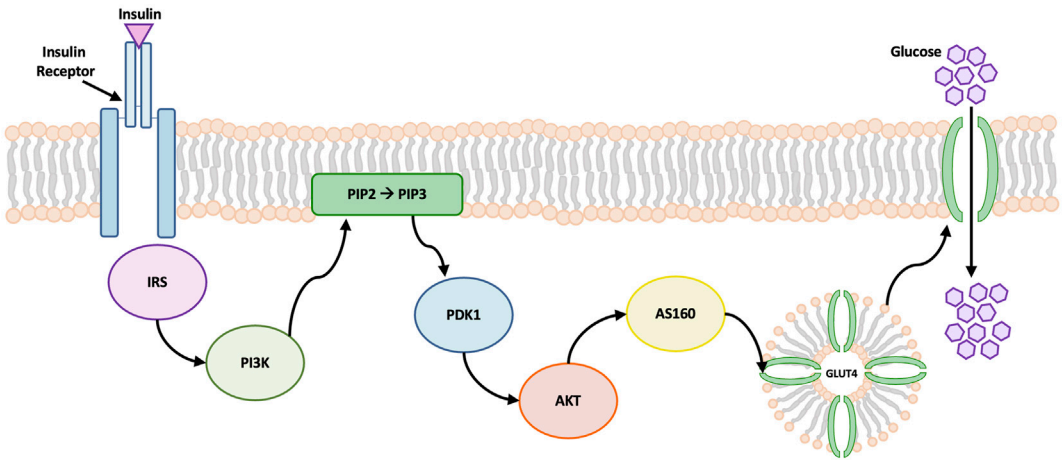

FIGURE 1 | Schematic of AKT signaling pathway. Insulin binding to cell surface receptors initiates the signal transduction cascade. Insulin promotes the phosphorylation of AKT which leads to glucose transporter 4 (GLUT4) translocation to the cell membrane. GLUT4 contains specialized vesicles that permit fusion with the cell membrane, allowing glucose uptake into the cell (Wang et al., 2020). Abbreviations: insulin receptor substrates (IRS), phosphatidylinositol 3-kinase (PI3K), 3-phosphoinositide-dependent kinase 1 (PDK1), phosphatidylinositol-4, 5-bisphosphate (PIP2), phosphatidylinositol-3, 4, 5-triphosphate (PIP3).

To further explore potential mechanisms for intracellular calcium response to shear stress between the hyperglycemic and insulin treated FLS groups, the effect of glucose on the incidence and length of primary cilia was investigated. Primary cilia are non-motile, microtubule-based organelles that emanate from the cell surface in a variety of vertebrate cells including synoviocytes, and are essential structures implicated in cell mechanotrandsuction (Malone et al., 2007; Lu et al., 2008; Ou et al., 2009; Besschetnova et al., 2010; Rattner et al., 2010; Hoey et al., 2012; Estell et al., 2017; Wheway et al., 2018). A decrease in the incidence of primary cilia has been shown to cause less mechanotransduction, contributing to decreased percentage of cells that respond to fluid shear (Estell et al., 2017). Furthermore, increased glucose concentrations lower the number of ciliated cells (Gerdes et al., 2014; Takahashi et al., 2018). Therefore, study 3 also characterized the incidence and length of primary cilia for healthy and OA FLS in order to determine the effect of hyperglycemia and insulin exposure on cilia properties, providing a potential link between FLS mechanosensitivity and fluid shear.

For healthy and non-diabetic OA synovium, upstream markers of cellular activity *via* intracellular calcium response and primary cilia properties were linked with downstream markers of compromised glucose activity and insulin resistance via characterization of AKT phosphorylation under hyperglycemic culture conditions. This model of preconditioning with hyperglycemic and insulin treated media can be optimized to confer the diabetic phenotype. Study 4 investigated the effect of hyperglycemic culture conditions and insulin exposure on AKT phosphorylation and upstream markers of cellular activity using diabetic OA synovium. We anticipate that the results from explants containing both comorbidities can be used to further develop an *in vitro* model of diabetic insulin resistance. By optimizing culture conditions, the diseased phenotype can be conferred from healthy tissue in order to overcome variability associated with age or disease state of patients undergoing total knee arthroplasty.

TABLE 1 | Human donor information. Phenotypes: **(A–C)** diabetic OA, **(D–F)** non-diabetic OA, **(G–I)** healthy. Bold values denote average age and standard deviation of each donor phenotype; Diabetic OA Human (Mean ± SD) denote donors A–C. OA Human (Mean ± SD) denote donors D–F. Healthy Human (Mean ± SD) denote donors G–I.

Donor ID	Gender	OA grade	Age	Diabetes
A	M	4	80	✓
B	F	4	69	✓
C	F	4	66	✓
D	F	4	60	×
E	F	4	63	×
F	F	4	71	×
G	M	-	19	×
H	M	-	21	×
I	M	-	22	×
Diabetic OA Human (Mean ± SD)			**72 ± 7**	
OA Human (Mean ± SD)			**65 ± 6**	
Healthy Human (Mean ± SD)			**21 ± 2**	

MATERIALS AND METHODS

Synovium Explant Harvest and Preparation

Human OA synovium explants were harvested (IRB #AAAQ2703) from the region of the joint capsule adjacent to the medial and lateral femoral condyle of three diabetic and non-diabetic subjects each (age 72 ± 7 and 65 ± 6 years old, respectively) during total knee arthroplasty (**Table 1**) (Stefani et al., 2019). Human synovium from three healthy donors (age 21 ± 2 years old) was obtained from the Musculoskeletal Transplant Foundation (Edison, NJ). Explants were trimmed of excess adipose and outer capsule tissue prior to digestion and cell isolation (Stefani et al., 2019). Human synovium samples were kept separate by donor for experiments.

Synovial explants were individually cultured for 7 days in varying glucose and insulin treated groups (n = 3 donors per

group, 2 explants/donor). Explants were treated in serum-free Dulbecco's Modified Eagle's Medium (DMEM; Gibco) and separated into two groups supplemented with different glucose concentrations: euglycemic (EG; 5.56 mM D-glucose) and hyperglycemic (HG; 12.5 mM D-glucose). Physiologic levels of human recombinant insulin (6.25 μg/ml) were added to both EG and HG groups (EGI and HGI, respectively). Individual explant specimens were cultured in 5 ml media, with media changes three times per week. Synovium explants were collected at day 0 (initial harvest, start of treatment) and day 7 (end of glycemic, insulin treatment).

Biochemistry

Human healthy and OA explants were frozen at −20°C and lyophilized overnight. Samples were weighed and solubilized by incubating for 16 h at 56°C in 0.5 mg/ml Proteinase K (Cat. No. 193504; MP Biomedicals) and Proteinase K buffer containing 50 mM Tris saline, 1 mM EDTA, 1 mM iodoacetamide (Cat. No. 12227-1000; Acros), and 10 mg/ml Pepstatin A (Cat. No. BP2671100; Fisher) (Riesle et al., 1998). DNA content was analyzed using Picogreen (Cat. No. P11496; ThermoFisher), while collagen content was analyzed using an orthohydroxyproline (OHP) assay with a 1:7.64 OHP-to-collagen mass ratio (Stegemann and Stalder, 1967). GAG content was analyzed using the 1,9-dimethylmethylene blue dye-binding assay (Product No. 341088; Sigma-Aldrich).

Media Analysis

Media samples from the synovial explants treated with glucose and insulin were collected during each media change. Day 7 media samples were assayed using Griess Reagent Kit for nitric oxide (NO) determination (Cat. No. G7921; ThermoFisher). Media samples were also assayed for GAG content. To account for temporal variations in the biochemical properties of the specimens, NO and GAG values were normalized to day 0 values.

Histological Characterization

Synovium samples were fixed in 4% paraformaldehyde (PFA), embedded in paraffin wax, and sectioned into 8 μm slices. Sections were stained with hematoxylin and eosin (H&E) to determine cell and matrix distribution, Safranin O for GAG content, and Picrosirius Red to determine collagen distribution. Samples were immunohistochemically stained for GLUT1 (1:250; rabbit monoclonal; Cat. No. ab115730; Abcam) using a 3,3′Diaminobenzidine (DAB) rabbit substrate kit (Cat. No. ab64261; Abcam) following heat-mediated epitope retrieval for 10 min at 95°C in citrate buffer (pH 6.0). The sections were counterstained with Mayer's hematoxylin (Cat. No. ab220365, Abcam).

AKT Phosphorylation

Following the glucose (EG, HG) and insulin preconditioning period, explants were weighed and placed in lysis buffer containing protease and phosphatase inhibitor cocktail (Product No. PPC1010; Sigma-Aldrich). The tissue was homogenized via bead beating using polypropylene tubes pre-filled with 1.4 mm ceramic beads (Product No. 19-627D; Omni). Relative levels of phospho- and pan-AKT were determined for each glycemic and insulin treated group using an ELISA (Cat. No. PEL-AKT-S473-T; RayBiotech) after day 7 treatment according to the manufacturer's instructions.

qPCR Preparation

FLS were isolated from healthy and OA synovial explants via type II collagenase (Cat. No. NC9522060; Fisher) digestion and expanded in αMEM containing 10% fetal bovine serum (FBS), 1% PSAM and 5 ng/ml fibroblast growth factor-2 (FGF2) (Cat. No. PHG0021; Fisher) for two passages to obtain a pure population of FLS. For gene expression analysis, healthy and OA FLS were preconditioned in EG and HG medias for 7 days. Cells were collected on days 1, 3, and 7, respectively, and resuspended in RNAlater (Cat. No. AM7020; ThermoFisher). RNA precipitation was performed using Qiagen miRNeasy columns (Cat. No. 74106; QIAGEN). cDNA was synthesized from RNA using the iScript cDNA Synthesis Kit (Product No. 1708891; Bio-Rad) and diluted to 1 ng/μl concentration for PCR. Gene specific master mixes were prepared using the designed primers, and iTaq Universal SYBR Green Supermix (Product No. 1725122; Bio-Rad). RT-qPCR was run on a QuantStudio™ six Flex Real-Time PCR System (Applied Biosystems™). The following primers (Integrated DNA Technologies IDT) were chosen: glucose transporter type 1 (GLUT1), glucose transporter type 4 (GLUT4), hexokinase II (HK2), glucose-6-phosphatase (G6PD), insulin-like growth factor 1 receptor (IGF1R), insulin receptor (INSR), and AKT Serine/Threonine Kinase 1 (AKT1) (**Table 2**). GAPDH was used as the housekeeping gene, and all samples were normalized to EG controls for each respective timepoint using the $2^{-\Delta\Delta Ct}$ method.

Fluid Shear and Calcium Imaging

FLS were plated in silicone isolators (Grace Bio-Labs) on 5 μg/cm^2 collagen type 1 coated glass slides at a cell density of 5.3×10^4 cells/cm^2 to obtain a semi-confluent layer (Estell et al., 2017). Cells were pre-conditioned in the same glucose and insulin treated groups for an additional 24 h prior to imaging, with parallel untreated controls. An osmotic control was included, consisting of EG media supplemented with sucrose (EGS).

Changes in intracellular calcium ($[Ca^{2+}]_i$) were tracked via Fura Red-AM (Cat. No. F3020; Life Technologies). FLS were stained using 5 μM Fura Red and incubated for 40 min at 37°C (Estell et al., 2017). Fluid flow-induced shear stress was applied in a parallel plate flow chamber at 0.1 Pa fluid shear stress (**Figure 2**). Chambers were secured on the microscope stage at room temperature, and unidirectional flow experiments were performed using Hank's Buffered Salt Solution (HBSS) supplemented with 0.1% fetal bovine serum. Flow studies were composed of a 6-min time lapse with the following stages: a 2-min "baseline" to observe the cells at equilibrium, followed by a "stimulation" with continuous unidirectional flow at 0.1 Pa fluid shear, then 2 min of post-flow relaxation to starting baseline levels (**Figure 2**). Images of the time lapse were acquired at a rate of 3 s per frame.

TABLE 2 | qPCR Primer Sequences for glucose metabolism genes. GLUT1: Glucose transporter type 1, GLUT4: Glucose transporter type 4, HK2: Hexokinase, G6PD: glucose-6-phosphate-dehydrogenase, IGF1R: Insulin-like growth factor 1 receptor, INSR: Insulin receptor, AKT1: AKT Serine/Threonine Kinase 1, GAPDH (housekeeping gene).

Gene	FWD primer sequence	REV primer sequence
GAPDH	CAA GAG CAC AAG AGG AAG AGA G	CTA CAT GGC AAC TGT GAG GAG
GLUT1	GGT CAG GCT CCA TTA GGA TTT	CCC AAC TGG TCT CAG GTA AAG
GLUT4	CCA GGA TCG GTT CTT TCA TCT T	CAT CTT CGG AGC CTA TCT GTT G
HK2	TGT GAG GTC CAC TCC AGA T	GAG CCC ATT GTC CGT TAC TT
G6PD	TAG GCA GCC TCT CTG CTA TAA	TGG GCT GTT TGC GGA TTT A
IGF1R	TTC TCC CTT TCT CTC TCC TCT C	GAC AGC CAC TTC CTC AAA CT
INSR	CAT GCG GAG TTG ATG CTT TG	GCA CAG TCT CCC AGT CAA TAA
AKT1	CTA CAA CCA GGA CCA TGA GAA G	TCT TGA GCA GCC CTG AAA G

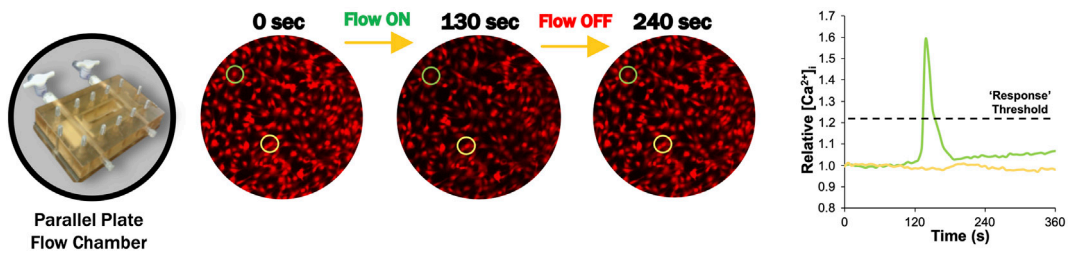

FIGURE 2 | Representative FLS calcium transient to fluid-induced shear stress (Estell et al., 2017). Prior to flow (0 s), intracellular calcium response is at equilibrium. $[Ca^{2+}]_i$ increased after flow was initiated to a maximum value at 130 s after slight delay (Estell et al., 2017). $[Ca^{2+}]_i$ returned to starting equilibrium values when flow is turned off after 240 s.

All fluid shear data were collected for 100 cells per slide, pooled across six slides per group. Fluorescence intensity was tracked for individual cells by collecting intensity versus time measurements for a circular region within the cell body, where increasing $[Ca^{2+}]_i$ resulted in decreased fluorescence (Estell et al., 2017). Fluorescence intensity was normalized to the average intensity during baseline and inverted to represent relative $[Ca^{2+}]_i$ (Estell et al., 2017). A custom Matlab (Mathworks) code was developed to calculate the percent of responding cells. Cells were considered responders if relative $[Ca^{2+}]_i$ increased 20% above baseline equilibrium measurements, which was found to be sufficient to exclude any false responses due to natural variations in equilibrium levels (**Figure 2**) (Estell et al., 2017).

Primary Cilia Incidence and Length Measurements

FLS were preconditioned in glycemic and insulin treated groups (EG, EGI, HG, HGI) for 24 h prior to fixation in 4% PFA and immunocytochemical staining with 2 mg/ml Alexa-488-tagged alpha-acetylated tubulin (Cat. No. sc-23950; Santa Cruz Biotechnology) for primary cilia visualization (Estell et al., 2017). FLS were counterstained with DAPI (Cat. No. 62248; Life Technologies) for nuclear visualization. Primary cilia were counted using Zen Blue software (Zeiss), and cilia lengths were measured using ImageJ (National Institutes of Health).

Statistical Analysis

GraphPad Prism version 9.2.0 (for Windows, GraphPad Software, San Diego, California, United States) was used for statistical analysis. Healthy, diabetic, and non-diabetic OA donor groups were analyzed separately using two-way ANOVA ($\alpha = 0.05$) with Tukey's post-hoc test to correct for multiple comparisons and determine significant differences between glucose and insulin treatment on biochemical composition, AKT phosphorylation, percent responding cells, and primary cilia measurements. Non-parametric data (e.g., gene expression) were analyzed via Fisher's Exact Test with Holm-Sidak correction for multiple comparisons. For all hyperglycemic and insulin treated media groups, replicates were combined to generate an average value across all phenotypes, glycemic conditions, and insulin treatment. Statistical significance was determined at $p < .05$.

RESULTS

Study 1. Biochemical Composition of Healthy and Non-Diabetic OA Synovium Under Hyperglycemic and Insulin Culture Conditions

In healthy synovium explants, HG treatment decreased DNA levels compared to EG groups for both control and insulin treated conditions ($p = .0215$ and $p = .0009$, respectively) (**Figure 3A**). No

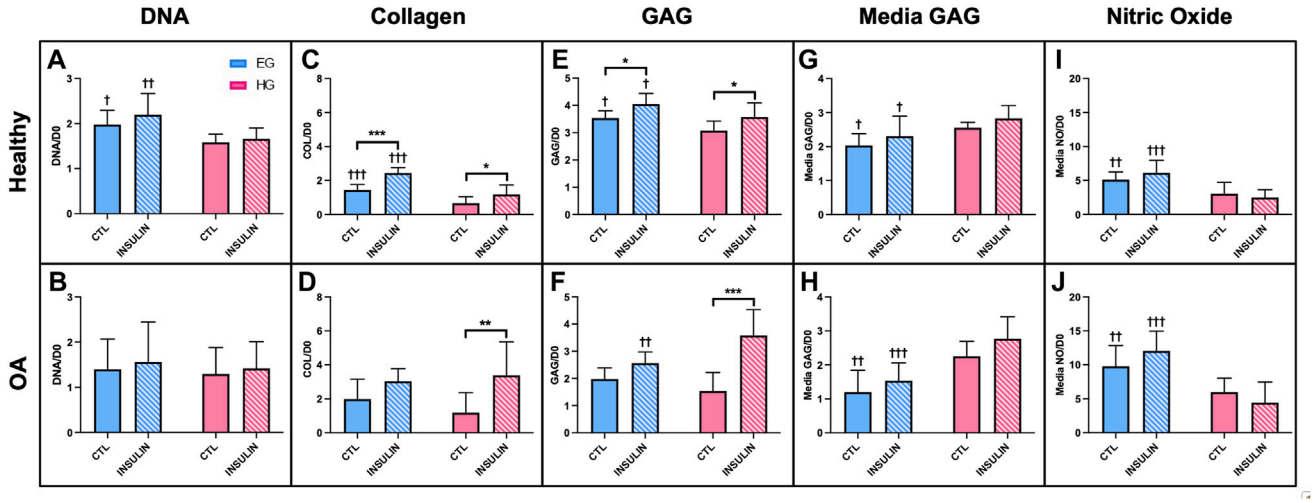

FIGURE 3 | Normalized **(A,B)** DNA, **(C,D)** collagen, **(E,F)** GAG to respective day 0 value for healthy and non-diabetic OA synovium. Release of **(G,H)** GAG and **(I,J)** NO in media from glucose and insulin treated human synovium explants. †$p < .05$, ††$p < .01$, †††$p < .0001$ (EG vs. HG). *$p < .05$, **$p < .01$, ***$p < .0001$ (control vs. insulin).

significant changes in DNA content were observed in either glucose or insulin treated OA specimens (**Figure 3B**). Healthy synovium explants exhibited decreased collagen content between EG and HG controls as well as between the parallel insulin treated groups (**Figure 3C**; $p < .0001$). No significant changes in collagen content were observed across both glycemic and insulin treated groups in OA synovium (**Figure 3D**). Comparing media groups separately, insulin treatment significantly increased collagen levels in EGI groups compared to EG in healthy explants ($p < .0001$). Compared to HG groups, HGI treatment significantly increased levels of collagen across both healthy and OA phenotypes ($p = .0162$ and $p = .0012$, respectively). HG conditions exhibited decreased GAG content compared to EG groups in healthy synovium under both control and insulin treatment ($p = .0296$ and $p = .0242$, respectively) (**Figure 3E**). In OA explants, insulin treatment increased GAG levels in HGI treated groups compared to EGI ($p = .0025$), but no significant changes were observed between the non-insulin treated groups (**Figure 3F**). Insulin treatment also significantly increased GAG content for HGI groups compared to HG controls for both healthy and diseased phenotypes ($p = .0156$ and $p < .0001$, respectively). In the healthy synovium, EGI groups also exhibited increased GAG content compared to non-insulin EG treatment ($p = .0126$).

In healthy synovium, HG treatment led to increased media GAG compared to EG for both control and insulin groups (**Figure 3G**; $p = .0135$ and $p = .0129$, respectively). The increase in media GAG for the HG and HGI groups were more profound in the OA explants compared to healthy synovium (**Figure 3H**; $p = .0003$ for control and $p < .0001$ for insulin). HG treatment decreased the release of NO in media compared to the control EG group in both the healthy and non-diabetic OA cells (**Figures 3I,J**; $p = .0073$ and $p = .0092$, respectively). With insulin exposure, explants also exhibited decreased NO release for HGI groups compared to EGI across both phenotypes ($p < .0001$). Comparing between phenotypes, NO release from OA explants was significantly higher (~48% increase across all four media conditions) compared to healthy synovium.

Histological staining of healthy synovium yielded comparable results. Similarities in synovial structural morphology under hyperglycemic and insulin culture conditions were visualized with H&E (**Figures 4A,D**). Higher intensity Picrosirius Red staining was observed in insulin treated groups (**Figures 4F,H**) compared to control EG and HG explants (**Figures 4E,G**). Slightly deeper staining of Safranin O was also evident in both EGI and HGI groups (**Figures 4J,L**), with lower intensity staining across non-insulin treated synovium (**Figures 4I,K**). GLUT1 staining was more pronounced in both HG and HGI treated groups (**Figures 4O,P**) with minimal staining in EG treated specimens (**Figures 4M,N**).

Study 2: Markers of Compromised Glucose Transport and Insulin Resistance in Healthy and OA Synovium Exposed to Hyperglycemic Culture Conditions and Insulin Treatment

Gene expression of hyperglycemic and insulin treated FLS showed significant differences between culture conditions, phenotype, and treatment timepoints. GLUT1 was upregulated under HG conditions compared to EG across all three timepoints and both phenotypes (**Figures 5A,B**; $p < .0001$). No significant differences in GLUT1 expression were observed between insulin and control groups. For healthy and OA FLS, GLUT4 was downregulated under HG conditions compared to EG across

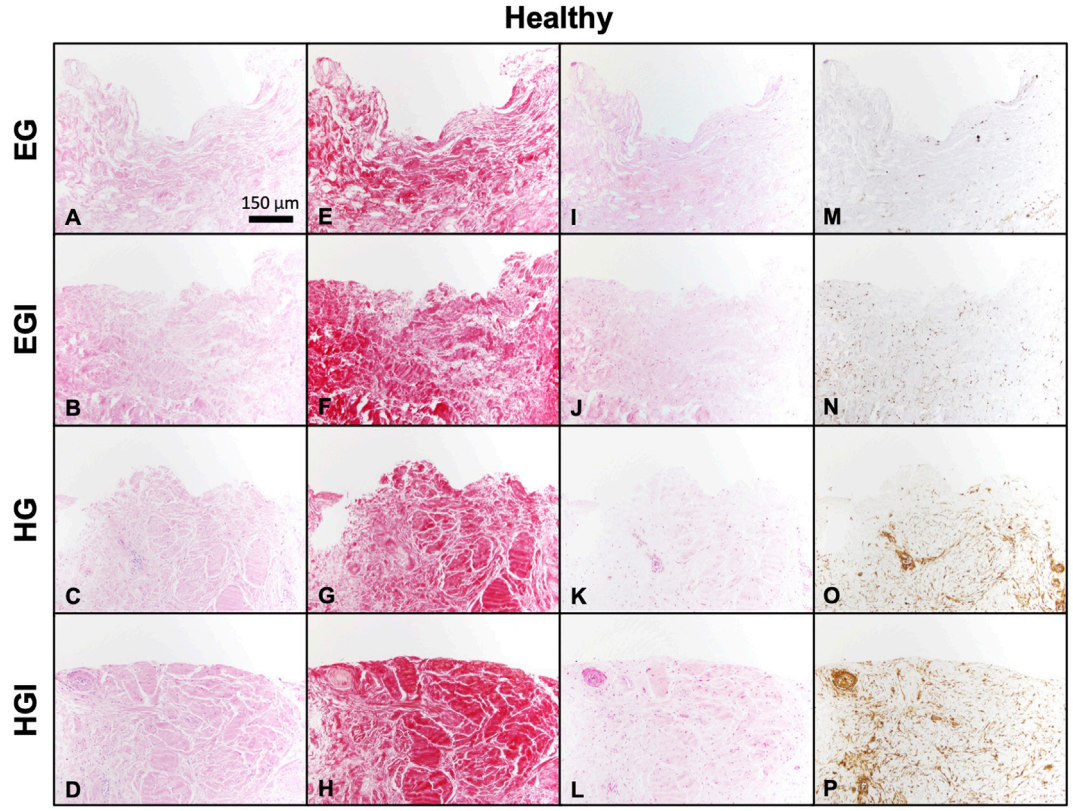

FIGURE 4 | Histology of glucose and insulin treated healthy synovium explants. **(A–D)** H&E, **(E–H)** Picrosirius Red, **(I–L)** Safranin O, and **(M–P)** GLUT1.

all timepoints (**Figures 5C,D**; $p < .0001$). Insulin treated groups exhibited elevated GLUT4 expression compared to control across most timepoints. At day 1, GLUT4 expression was significantly upregulated for EGI treated FLS compared to EG for both phenotypes ($p < .0001$), but this difference was less profound between HG and HGI groups ($p = .0002$ for healthy and $p = .0171$ for OA). At day 3, GLUT4 remained elevated for EGI groups compared to control for both healthy and OA cells ($p = .0007$ and $p = .0311$, respectively). Insulin treatment increased GLUT4 expression for HG treated healthy FLS ($p = .0170$), but no significant changes were observed in the OA phenotype. By day 7, GLUT4 levels were attenuated for all insulin treated groups with a significant difference only observed in EGI treated healthy FLS compared to control ($p = .0160$).

Expression of additional genes involved in cellular glucose regulation *via* glycolysis also yielded significant differences between EG and HG culture conditions. The following genes were mostly downregulated in FLS HG culture: HK2, G6PD, IGF1R, and INSR (**Figures 6A–H**). HK2 expression was significantly downregulated on day 7 for both phenotypes under HG culture media (**Figures 6A,B**; $p = .0030$ for healthy and $p < .0001$ for OA). G6PD expression remained consistent at day 1, but was significantly downregulated in HG treated FLS by day 3 (**Figures 6C,D**; $p = .0199$ for healthy and $p = .0012$ for OA). Day 7 G6PD expression showed more profound decreases in HG groups compared to EG for both healthy and OA cells ($p = .0017$ and $p < .0001$ respectively). IGF1R expression was downregulated only in HG treated OA FLS at days 3 and 7 (**Figure 6F**; $p = .0122$ and $p = .0014$). Across all timepoints, no significant changes in IGF1R expression between EG and HG groups were observed in healthy FLS (**Figure 6E**). INSR expression in OA FLS was also downregulated for HG samples compared to EG at day 3 and 7 (**Figure 6H**; $p = .0139$ and $p = .0020$, respectively), while no significant changes in INSR levels were observed in the healthy group (**Figure 6G**).

AKT1 expression of healthy and OA FLS was significantly downregulated under HG culture conditions. In healthy cells, HG groups exhibited attenuated AKT1 levels compared to EG across all three timepoints (**Figure 7A**, $p = .002$ for day 1, $p < .0001$ for day 3, $p = .003$ for day 7). AKT1 expression was lower in HG treated OA FLS with significant differences observed of days 1 and 3 (**Figure 7B**, $p = .0067$ and $p = .0141$, respectively). Insulin exposure mostly increased AKT1 levels compared to control EG and HG groups for both phenotypes. In OA FLS, AKT1 expression in EGI groups was significantly higher than EG across all timepoints ($p = .0016$ for day 1, $p = .0115$ for day 3, $p = .0086$ for day 7). AKT1 levels were also elevated in EGI groups of healthy cells at days 1 and 7 ($p = .0111$ and $p = .0013$, respectively). HGI treated FLS only exhibited increased AKT1 expression compared to control HG groups on day 1 for both

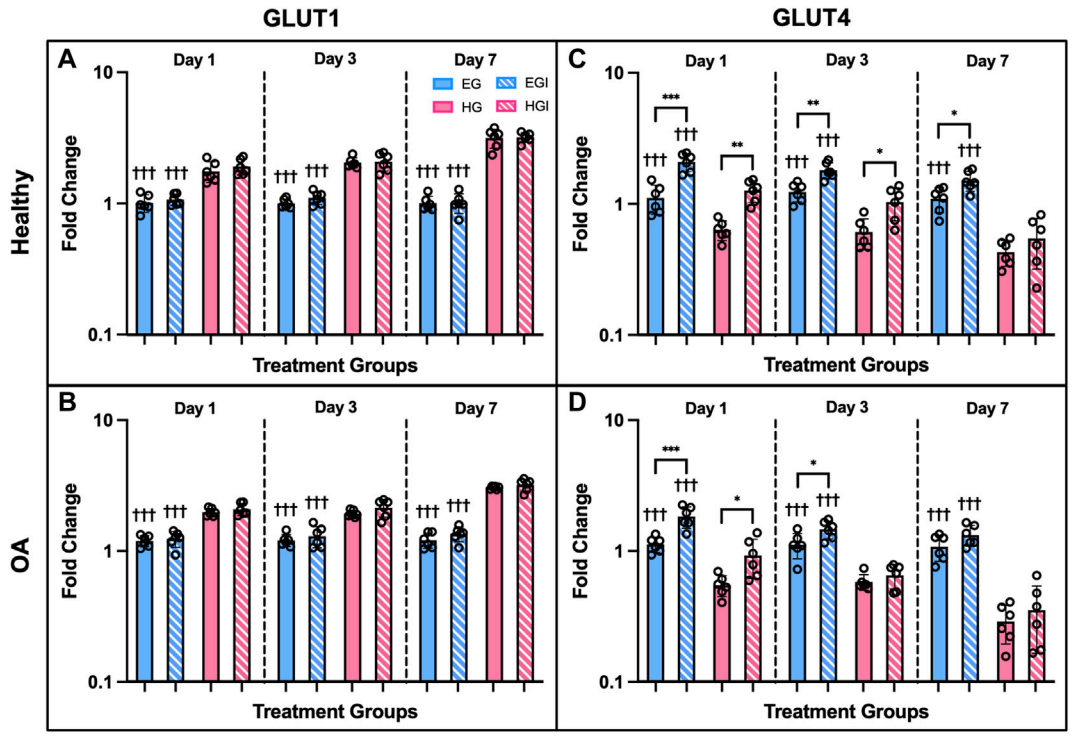

FIGURE 5 | Gene expression of healthy and OA FLS 1, 3 and 7 days after EG, EGI, HG, HGI treatment ($n = 6$), **(A,B)** GLUT1, **(C,D)** GLUT4. †$p < .05$, ††$p < .01$, †††$p < .0001$ (EG vs. HG). *$p < .05$, **$p < .01$, ***$p < .0001$ (control vs. insulin).

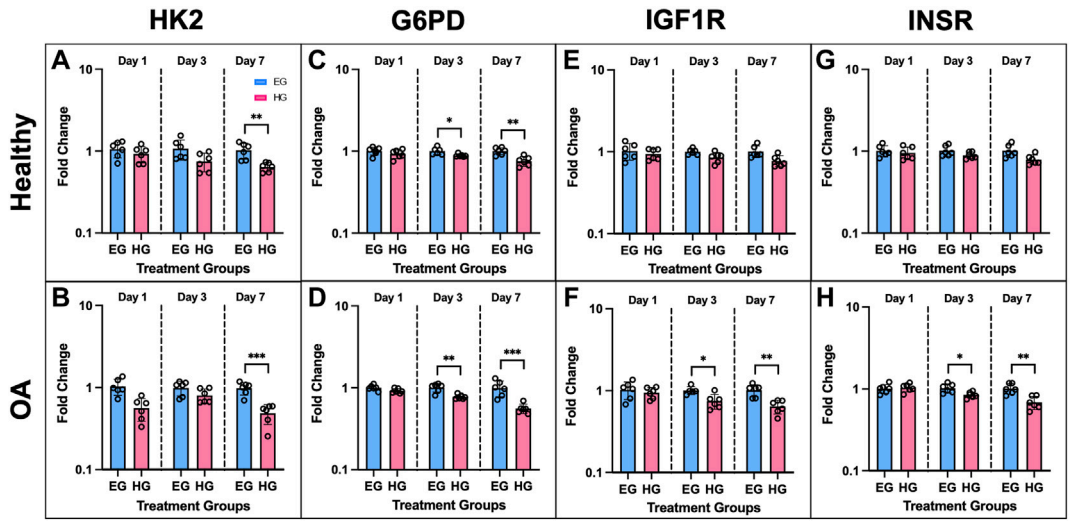

FIGURE 6 | Gene expression of healthy and OA FLS 1, 3 and 7 days after EG and HG treatment ($n = 6$), **(A,B)** HK2, **(C,D)** G6PD, **(E,F)** IGF1R, **(G,H)** INSR. *$p < .05$, **$p < .01$, ***$p < .0001$ (EG vs. HG).

healthy and OA cells ($p = .0092$ and $p = .0085$, respectively), while no significant changes were observed at later timepoints.

AKT levels were also confirmed using healthy and OA explants cultured in hyperglycemic and insulin treated media with an ELISA. Relative phospho-AKT was significantly elevated in EG compared to HG groups ($p < .0001$) for both healthy and OA explants (**Figures 7C,D**) after 7 days of glycemic and insulin treatment. Comparing between control EG groups across

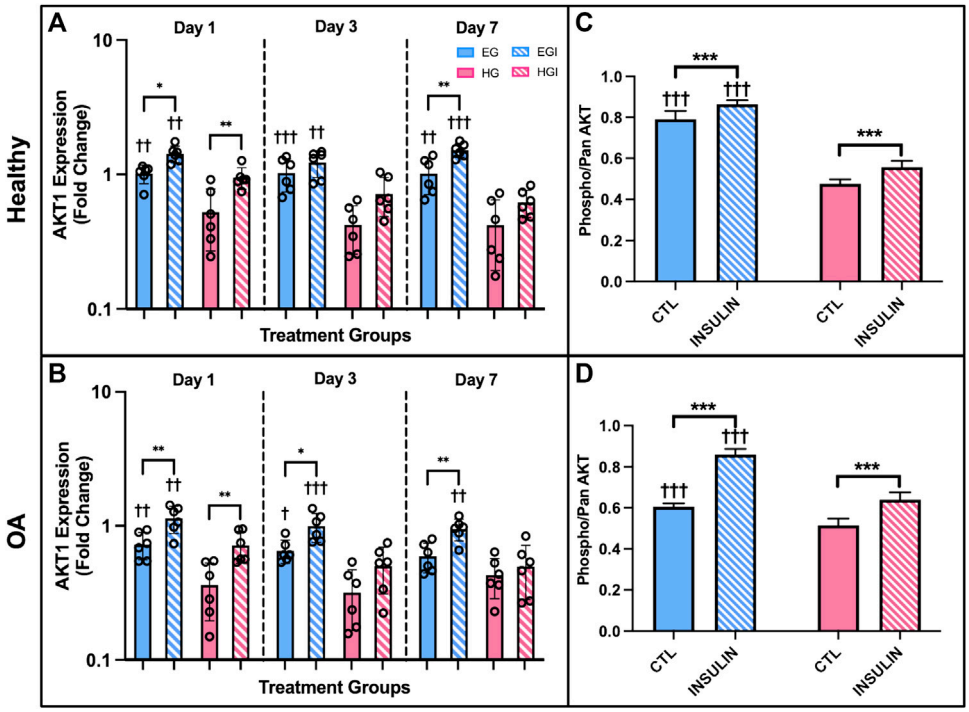

FIGURE 7 | (A,B) PCR results of AKT1 gene expression of healthy and OA FLS 1, 3 and 7 days after EG, HG, and insulin treatment. **(C,D)** ELISA results of relative phospho-AKT levels of healthy and OA synovial explants in response to hyperglycemic culture conditions and insulin treatment. †$p < .05$, ††$p < .01$, †††$p < .0001$ (EG vs. HG). *$p < .05$, **$p < .01$, ***$p < .0001$ (control vs. insulin).

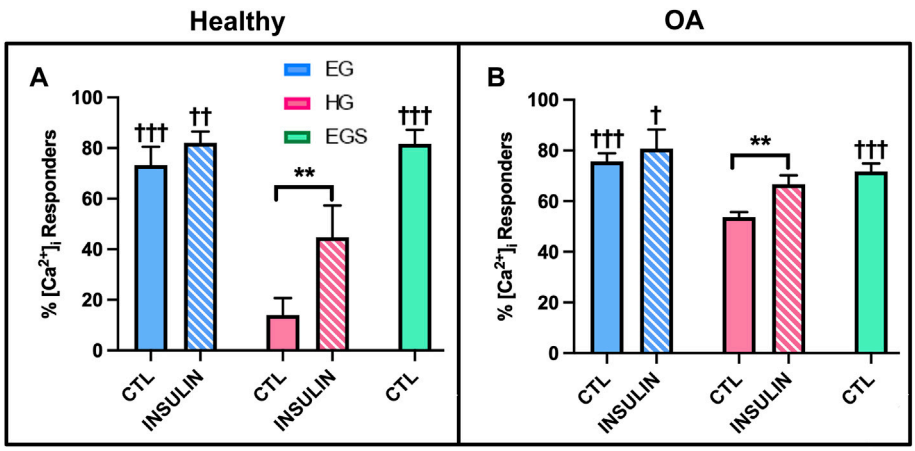

FIGURE 8 | Shear-induced $[Ca^{2+}]_i$ response with glucose, sucrose, and insulin treatment for **(A)** healthy and **(B)** non-diabetic OA FLS. †$p < .05$, ††$p < .01$, †††$p < .0001$ (EG vs. EGS vs. HG and EGI vs. HGI). *$p < .05$, **$p < .01$, ***$p < .0001$ (control vs. insulin).

phenotypes, phospho-AKT levels were elevated in the healthy explants and slightly attenuated in OA specimens (~19% decrease). Insulin treatment significantly increased levels of AKT phosphorylation compared to the respective non-insulin treated groups across both EG and HG conditions for OA synovium ($p < .0001$). In the healthy explants, relative phospho-AKT was also elevated for EGI and HGI groups compared to controls ($p < .0001$ and $p = .0005$, respectively).

Study 3: Intracellular Calcium Response ($[Ca^{2+}]_i$) to Fluid-Induced Shear Stress and Primary Cilia Properties of Healthy and Non-Diabetic OA FLS Cultured in Hyperglycemic and Insulin Media

FLS demonstrated a robust calcium signaling response to fluid shear (Hamada et al., 2016). The $[Ca^{2+}]_i$ response for healthy FLS

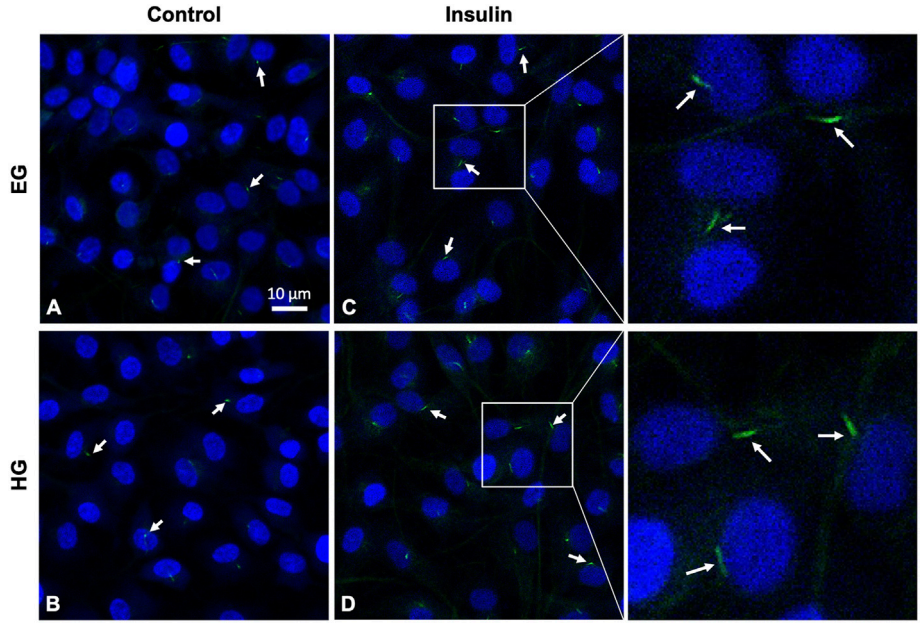

FIGURE 9 | Representative healthy FLS primary cilia (arrows), with DAPI nuclear counterstaining for visualization under **(A,C)** euglycemic and **(B,D)** hyperglycemic culture conditions ± insulin exposure.

was significantly elevated in the control EG group compared to HG treated cells (73.3 ± 7.3% responders vs. 14.0 ± 6.7%, $p <$ .0001, **Figure 8A**). While the OA FLS response to shear was elevated in the EG treated cells compared to HG ($p <$ .0001), the hyperglycemic group had a greater response to shear with 53.6 ± 4.1% responders compared to healthy FLS (**Figure 8B**). The percent response of the osmotic control consisting of EG media supplemented with sucrose (EGS) yielded similar results to EG treatment across both phenotypes, confirming no osmolarity effects. FLS response to insulin treatment was significantly greater in the EGI compared to the HGI groups for both the healthy and diseased cells (p = .0002 and p = .0103, respectively). Compared to non-insulin treated FLS, insulin exposure significantly increased percentile response for HGI treated groups for healthy and OA cells (p = .0007 and p = .0073, respectively). Specifically, the HGI group for the healthy FLS exhibited a significant increase in response that yielded similar results to those of native OA cells, with 44.7 ± 12.7% responders for the heathy HGI group vs. 53.6 ± 4.1% for the OA HG group.

HG treatment led to decreased incidence of primary cilia compared to EG groups across both phenotypes (**Figures 9A,B**, **10A,B**; p = .0210 for healthy and $p <$ .0001 for OA). Insulin treatment significantly increased cilia incidence in EG treated cells for both healthy and diseased FLS (**Figures 9C**, **10A,B**; $p <$ .0001). HGI groups also exhibited increased cilia incidence compared to HG in both healthy and OA cells (**Figures 9D**, **10A,B**; p = .0084 and p = .0052, respectively), but this difference compared to control HG groups was not as profound as EG and EGI treatment. In addition, HG treatment significantly decreased average cilia length for both phenotypes (**Figures 10C,D**; $p <$ .0001). Insulin treatment significantly increased cilia length for HGI groups compared to control HG groups for both the healthy and OA FLS (p = .0053 and p = .0062, respectively).

Study 4: AKT Phosphorylation and Upstream Markers of Cellular Activity Under Hyperglycemic and Insulin Culture Conditions for Diabetic OA Synovium

AKT phosphorylation levels, calcium response to shear stress, and cilia properties were investigated for diabetic OA synovium under the same glucose and insulin treatment conditions as the previous studies. Similar to the healthy and non-diabetic OA samples, relative phospho-AKT was significantly reduced in HG treatment compared to control EG groups ($p <$ .0001) for the diabetic OA explants (**Figure 11A**). Comparing EG and HG groups across all three phenotypes, the diabetic OA explants exhibited the greatest decrease in phospho-AKT levels between both glycemic conditions (~43% decrease between control EG and HG groups). While insulin exposure increased AKT phosphorylation in EGI groups compared to the control EG treatment (p = .0040) in the diabetic phenotype, no significant changes in AKT phosphorylation were observed between the insulin and non-insulin treated HG groups.

The $[Ca^{2+}]_i$ response to fluid shear of diabetic OA FLS was significantly elevated under EG culture conditions compared to HG treatment with 88.3 ± 4.9% vs. 34.0 ± 12.5% responders, respectively (**Figure 11B**; $p <$ .0001). Insulin treated HGI groups also exhibited decreased $[Ca^{2+}]_i$ response to shear compared to EGI (p = .0004). The response of EGS and EG groups suggest no

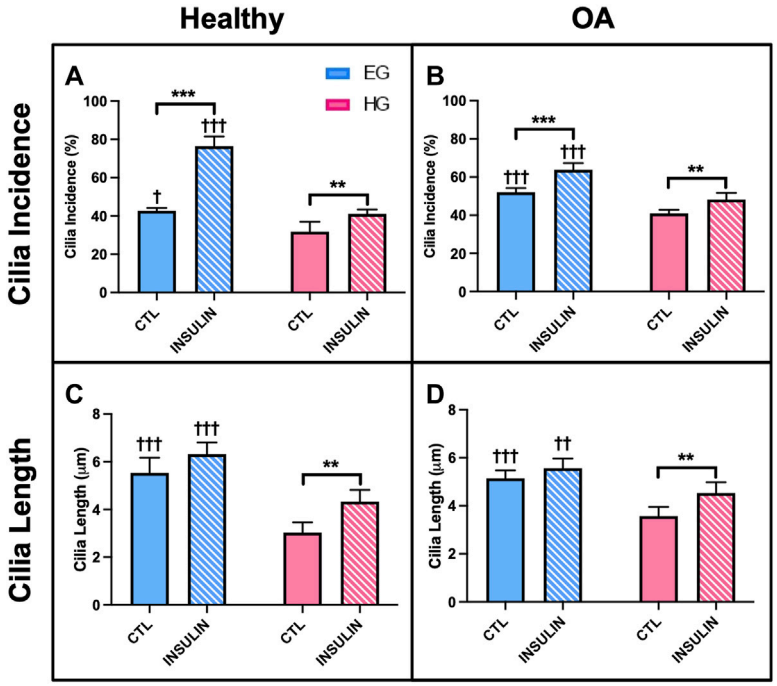

FIGURE 10 | Healthy and non-diabetic OA FLS **(A,B)** incidence and **(C,D)** length of primary cilia detected under glucose and insulin culture conditions. Cilia measurements were pooled across triplicate slides per group †p < .05, ††p < .01, †††p < .0001 (EG vs. HG). *p < .05, **p < .01, ***p < .0001 (control vs. insulin).

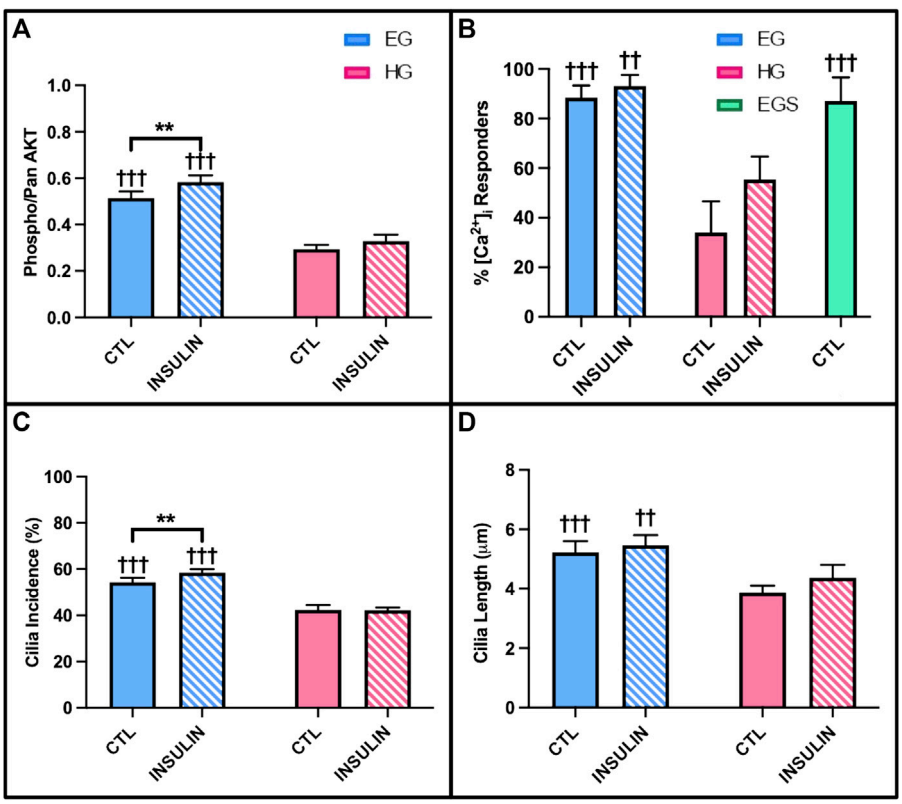

FIGURE 11 | Diabetic OA synovial explants **(A)** relative phospho- AKT levels in response to hyperglycemic culture conditions and insulin treatment. Diabetic OA FLS **(B)** shear-induced $[Ca^{2+}]_i$ response with glucose, sucrose, and insulin exposure and **(C)** incidence and **(D)** length of primary cilia. †p < .05, ††p < .01, †††p < .0001 (EG vs. HG). *p < .05, **p < .01, ***p < .0001 (control vs. insulin).

osmolarity effects. While insulin increased FLS response under HG culture conditions in the healthy and non-diabetic OA FLS (**Figures 8A,B**), no significant changes were observed between insulin treated cells and non-insulin groups in the diabetic OA phenotype (p = .9961).

Hyperglycemic and insulin treatment of diabetic OA FLS yielded similar trends in cilia incidence and length compared to healthy and OA cells from study 3. Across both glycemic culture conditions, HG treatment decreased primary cilia incidence compared to EG groups for the diabetic OA FLS (**Figure 11C**; p < .0001). Insulin exposure in the HGI groups also exhibited attenuated cilia incidence compared to EGI treated cells (p < .0001). However, insulin treatment did increase cilia incidence in the EGI groups compared to control EG (p = .0083). Unlike the healthy and OA FLS (**Figures 10A,B**), no significant changes in cilia incidence were observed between insulin and non-insulin treated HG groups (p = .9980) for the diabetic OA phenotype. For cilia length measurements, HG treatment significantly decreased cilia length in the diabetic OA cells (**Figure 11D**; p < .0001). While insulin increased average cilia length for HGI groups compared to HG groups in both healthy and non-diabetic OA cells (**Figures 10C,D**), no significant changes in cilia length were observed between the insulin and non-insulin treated EG and HG groups for the diabetic OA FLS.

DISCUSSION

Synovial fibroblasts are significant contributors to the articular cartilage environment by producing molecules important for lubrication, ECM remodeling, and regulating solute transport in and out of the joint (Hung et al., 1995; Denko et al., 1996; Harsha and Joyce, 2011; Hoey et al., 2012; Stefani, 2020). However, synovium function is compromised in patients with DM (Griffin and Huffman, 2016). It is known that the development of DM promotes synovial inflammation and insulin resistance in progression of the OA disease state (Griffin and Huffman, 2016; Li et al., 2021). In FLS isolated from non-diabetic patients with OA, it has been shown that insulin inhibits the production of inflammatory cytokines (de Luca and Olefsky, 2009; Griffin and Huffman, 2016). However, in diabetic OA patients, synovial insulin signaling is further compromised, indicative that the anti-inflammatory and anti-catabolic function of insulin is suppressed in the presence of both comorbidities (Griffin and Huffman, 2016; Veronese et al., 2019; Tchetina et al., 2020). In the current study, we sought to further the understanding of this correlation between hyperglycemia and insulin resistance that results from the coexistence of both OA and DM.

In healthy specimens, HG treatment decreased DNA levels compared to EG groups (**Figure 3A**), potentially indicative of greater cell damage, characteristic of the diabetic disease state (Brownlee, 2005). Collagen and GAG content of both healthy and OA explants were also affected by HG treatment and insulin exposure (**Figures 3C–F**), suggesting glycemic environments may affect cell sensitivity and metabolism (Hayden et al., 2005; Nagy et al., 2019). While lower levels of GAG and collagen have been shown to be characteristic features of the diabetic disease state, insulin treatment recovered these matrix constituents across all HG groups for both healthy and OA explants, indicative of its pro-anabolic effect (Stultz and Edelman, 2003; Gowd et al., 2016). Media analysis also confirmed that increased GAG in HG treated tissue contributed to ECM remodeling across both phenotypes (**Figures 3G,H**). Furthermore, HG treatment has also been associated with lower NO release in media under insulin resistant conditions, characteristic of DM (**Figures 3I,J**) (Hoshiyama et al., 2004). Insulin treatment did not have a significant effect on both media GAG and NO release, suggesting the inability of insulin to restore the effect of HG culture conditions to baseline levels exhibited under EG treatment. Histological analysis confirmed the differences observed in GAG and collagen levels under HG media conditions. The high intensity staining of GLUT1 was also observed in the HG groups (**Figures 4O,P**), suggesting that high glucose environments may alter glucose regulation and insulin activity in healthy and diseased synovium.

In the current study, reciprocal expression of the glucose transport proteins GLUT1 and GLUT4 was observed under EG and HG culture conditions in both healthy and OA FLS (Ebeling et al., 1998). Under HG culture conditions, GLUT1 expression was upregulated, while GLUT4 levels were significantly attenuated (**Figures 5A–D**). GLUT1 is expressed ubiquitously and operates independent of insulin activity, while GLUT4 is activated through translocation to cell membranes under insulin dependent mechanisms (Ebeling et al., 1998; Bryant et al., 2002, Gallagher et al., 2020). Insulin exposure had no effect on GLUT1 expression across all timepoints and both media conditions, potentially indicative of the insulin independent effect of hyperglycemia on GLUT1 levels. However, insulin significantly increased GLUT4 expression at day 1, but this difference was reduced across each subsequent timepoint. By day 7, no significant differences were observed in GLUT4 levels between insulin and non-insulin treated HG groups, supporting the reduced protective role of insulin in counteracting the elevated glucose levels and potentially indicative of insulin resistance. Overall, OA FLS exhibited lower GLUT4 levels for HG treated samples compared to healthy cells, suggesting a link between OA and diabetic insulin resistance. The lower GLUT4 expression under HG treatment supports the decreased levels of AKT phosphorylation observed in the HG treated synovial explants. Further in the glycolysis pathway, glucose that enters the cell via GLUT proteins is phosphorylated by hexokinase to G6PD (Ebeling et al., 1998; Tchetina et al., 2020). The expression of both HK2 and G6PD in HG treated FLS were significantly lower compared to control EG across both healthy and OA cells (**Figures 6A–D**), potentially indicative of the diabetic disease state (Esteves et al., 2018). The expression of IGF1R and INSR was also lower in HG treated FLS (**Figures 6E–H**), suggesting the diminished effect of insulin in regulating glucose uptake under diabetic and possible insulin resistant conditions.

The AKT phosphorylation cascade is a specific signaling pathway that connects glycolysis markers implicated in cellular glucose uptake and insulin activity (Garcia-Carbonell et al., 2016). AKT is involved in several complex signaling networks that regulate various cellular functions including cell metabolism, proliferation, motility, and apoptosis (Jazirehi et al., 2012; Du et al., 2019). It has also been

implicated in numerous comorbidities including diabetes, cardiovascular, and neurodegenerative diseases (Zarneshan et al., 2020). In DM, the AKT signaling pathway is a mediator of insulin activity and plays a crucial role in disease pathogenesis (Hamada et al., 2016; Huang et al., 2018; Gabbouj et al., 2019). It promotes the metabolic effects of insulin and facilitates glucose transport, lipid synthesis, gluconeogenesis, and glycogen synthesis (Boucher et al., 2014; Huang et al., 2018). AKT is specifically involved in insulin signaling as the activation of insulin receptors triggers a phosphorylation cascade, which is initiated by receptor autophosphorylation and the activation of insulin receptor substrate proteins (Boucher et al., 2014). The activation of insulin receptors drives the phosphorylation of AKT, thus contributing to the translocation of GLUT4 to the plasma membrane (Boucher et al., 2014; Beg et al., 2017; Nitulescu et al., 2018). Therefore, AKT is expressed in insulin-responsive tissues, including synovium, and functions to regulate glucose metabolism (Nitulescu et al., 2018). Studies have shown that AKT deletion in knockout mice has been correlated with insulin resistance, hyperinsulinemia, and glucose intolerance (Cho et al., 2001; Nitulescu et al., 2018). In addition, defects in AKT signaling have also been correlated with diabetic insulin resistance in humans (Nitulescu et al., 2018). The results of the current study support the effect of hyperglycemic culture conditions on AKT signaling and phosphorylation in a model of diabetic insulin resistance. Both healthy and diseased synovial explants demonstrated that hyperglycemia led to decreased phospho-AKT levels compared to the respective control EG groups (**Figures 7C,D**, **11A**). PCR analysis yielded consistent results with lower AKT1 expression in HG treated FLS compared to EG across all timepoints and both phenotypes (**Figures 7A,B**). Previous studies have shown that the attenuation of AKT phosphorylation levels is indicative of more insulin resistant environments (Tonks et al., 2013). Therefore, the greater decrease in AKT phosphorylation under HG culture conditions for the diabetic explants may suggest a more insulin resistant phenotype compared to healthy and non-diabetic OA tissue. For the insulin treated groups, relative phospho-AKT was elevated in the EGI and HGI groups for both healthy and non-diabetic explants. However, the difference in AKT phosphorylation between the insulin and non-insulin treated groups for the diabetic OA synovium did not show significant differences under HG culture conditions, potentially indicative of greater insulin resistance.

Since the AKT signaling pathway and markers of glycolysis have been shown to be controlled by upstream calcium influxes, intracellular calcium transients in response to fluid-induced shear were investigated in study 3 (Nicholson-Fish et al., 2016). Hyperglycemic culture conditions have been correlated with abnormal calcium signal transduction, which may be linked to reduced insulin responsiveness (Boldizsár et al., 2002; Lebeche et al., 2008) We observed that HG treated FLS exhibited fewer percent responders compared to EG groups, potentially indicative that high glucose environments decrease cellular responses and possibly affect cell function. For healthy and non-diabetic OA FLS, insulin treatment increased $[Ca^{2+}]_i$ response for HGI treated groups (**Figures 8A,B**), suggesting that insulin recovers the cell response of HG treated FLS to levels closer to the control EG groups. However, insulin exposure did not affect the number of cells that responded to shear stress for the native diabetic OA phenotype (**Figure 11B**), indicative of lower insulin responsiveness and potentially diabetic insulin resistance.

The incidence and length of primary cilia provides a potential mechanism to support changes in fluid shear-induced $[Ca^{2+}]_i$ responses among the different glucose and insulin treated FLS groups. Dysfunctional primary cilia due to hyperglycemia have been shown to inhibit mechanotransduction and cellular responses to external stimuli (Estell et al., 2017; Ritter et al., 2018; Kluth et al., 2019; Stefani et al., 2019). In study 3, HG treatment decreased cilia incidence and length across healthy and OA FLS (**Figures 10A–D**), consistent with the decrease in $[Ca^{2+}]_i$ response of FLS under hyperglycemic conditions for both phenotypes. However, insulin exposure increased cilia incidence and length for HGI groups compared to control HG treatment for both healthy and non-diabetic OA FLS, further supporting the difference in insulin responders between the two phenotypes. Interestingly, the diabetic OA FLS displayed no significant changes in primary cilia length and incidence between insulin and non-insulin treated HG groups (**Figures 11C,D**), potentially indicative of decreased insulin responsiveness in recovering the effects of the high glucose environment.

Overall, the current study demonstrated that hyperglycemic treatment and insulin exposure affects synovium ECM properties. Hyperglycemic culture conditions also alter the expression of cell insulin receptors, glucose transporters, and specific glycolysis markers implicated in glucose uptake and breakdown. A correlation appears to exist between relative levels of AKT phosphorylation, percent responders to fluid shear, and cilia incidence and length. Specifically, it is known that OA environments increase synoviocyte sensitivity to fluid shear by altering intercellular communication, which may affect downstream functions such as decreased AKT phosphorylation and altered glycolysis markers, implicated in compromised insulin activity that contribute to progression of the diabetic disease state (Wilcox, 2005; Boucher et al., 2014).

Potential limitations associated with this research include a control, healthy synovium group that was significantly younger and all male, compared to the diseased tissue groups (OA ± DM). The latter reflects the inherent challenges of procuring normal tissues of any age for such studies and higher female incidence of OA. While the current study using healthy tissue exposed to HG conditions revealed that normal synovium is very sensitive to changes in glucose and insulin levels compared to OA-diseased tissue, similar trends across all three phenotypes were observed. The latter is even more remarkable in that the findings were observed using tissue from donor ages spanning 4 decades (19–80 years old) and despite sex-composition differences between the groups. In this context, these findings are supportive of our contention that healthy synovium with a high glucose culture-induced diabetic phenotype can serve as a model of diabetic insulin resistance.

To better understand the connection between OA and DM, future work will continue to explore strategies to induce the diabetic phenotype from healthy tissue. Preconditioning media with various hyperglycemic concentrations will be optimized to

confer the diabetic phenotype and overcome confounding factors associated with age or the disease state of patients undergoing total knee arthroplasty. With superposition of pro-inflammatory cytokines (Stefani et al., 2019), this tissue platform would permit simulated study of DM with the comorbidity of OA, as well as the evaluation of therapeutic strategies aimed at their mitigation. Using the *in vitro* diabetic insulin resistance model system reported here, the action of peroxisome proliferators activated receptors (PPAR), involved in regulating joint inflammation and glucose homeostasis, and other biochemical cascades can be investigated in future studies (Li et al., 2017).

DATA AVAILABILITY STATEMENT

The original contributions presented in the study are included in the article/Supplementary Files, further inquiries can be directed to the corresponding author.

ETHICS STATEMENT

Ethical review and approval was not required for the study on human participants in accordance with the local legislation and institutional requirements. Written informed consent for participation was not required for this study in accordance with the national legislation and the institutional requirements.

AUTHOR CONTRIBUTIONS

All authors contributed significantly to the studies reported in this manuscript. NS and CH designed the experiments. NS, AL, LM, and HK performed the experiments and collected the data. CV, GA, RS, and CH supervised and advised the work. NS and CH wrote the paper. All authors have read and approved the final submitted manuscript.

FUNDING

This study was supported by Orthopaedic Science and Research Foundation (OSRF), National Institutes of Health (NIH), and National Science Foundation Graduate Research Fellowship Program (NSF GRFP; NS).

ACKNOWLEDGMENTS

The authors thank Eric Semler from the Musculoskeletal Transplant Foundation (Edison, NJ) for generously providing the healthy synovium for the study. Special thanks to the Carroll Laboratories for Orthopedic Surgery for allowing us to use their facility to conduct the PCR analysis and to the histology services at the Molecular Pathology Shared Resource (MPSR) located at the Columbia University Irving Medical Center (CUIMC).

REFERENCES

Beg, M., Abdullah, N., Thowfeik, F. S., Altorki, N. K., and McGraw, T. E. (2017). Distinct Akt Phosphorylation States Are Required for Insulin Regulated Glut4 and Glut1-Mediated Glucose Uptake. *ELife* 6, e26896. doi:10.7554/eLife.26896

Besschetnova, T. Y., Kolpakova-Hart, E., Guan, Y., Zhou, J., Olsen, B. R., and Shah, J. V. (2010). Identification of Signaling Pathways Regulating Primary Cilium Length and Flow-Mediated Adaptation. *Curr. Biol.* 20 (2), 182–187. doi:10.1016/j.cub.2009.11.072

Blewis, M. E., Lao, B. J., Jadin, K. D., McCarty, W. J., Bugbee, W. D., Firestein, G. S., et al. (2010). Semi-Permeable Membrane Retention of Synovial Fluid Lubricants Hyaluronan and Proteoglycan 4 for a Biomimetic Bioreactor. *Biotechnol. Bioeng.* 106 (1),149–160. doi:10.1002/bit.22645

Boldizsár, F., Berki, T., Miseta, A., and Németh, P. (2002). Effect of Hyperglycemia on the Basal Cytosolic Free Calcium Level, Calcium Signal and Tyrosine-Phosphorylation in Human T-Cells. *Immunol. Lett.* 82 (1–2), 159–164. doi:10.1016/S0165-2478(02)00032-9

Boucher, J., Kleinridders, A., and Kahn, C. R. (2014). Insulin Receptor Signaling in Normal and Insulin-Resistant States. *Cold Spring Harbor Perspect. Biol.* 6 (1), a009191. doi:10.1101/cshperspect.a009191

Bramante, C. T., Lee, C. J., and Gudzune, K. A. (2017). Treatment of Obesity in Patients with Diabetes. *Diabetes Spectr.* 30 (4), 237–243. doi:10.2337/ds17-0030

Brownlee, M. (2005). The Pathobiology of Diabetic Complications. *Diabetes* 54 (6), 1615–1625. doi:10.2337/diabetes.54.6.1615

Bryant, N. J., Govers, R., and James, D. E. (2002). Regulated Transport of the Glucose Transporter GLUT4. *Nat. Rev. Mol. Cel Biol* 3 (4), 267–277. doi:10.1038/nrm782

Bustamante, M. F., Garcia-Carbonell, R., Whisenant, K. D., and Guma, M. (2017). Fibroblast-like Synoviocyte Metabolism in the Pathogenesis of Rheumatoid Arthritis. *Arthritis Res. Ther.* 19 (1), 110. doi:10.1186/s13075-017-1303-3

Cho, H., Mu, J., Kim, J. K., Thorvaldsen, J. L., Chu, Q., Crenshaw, E. B., III, et al. (2001). Insulin Resistance and a Diabetes Mellitus-like Syndrome in Mice Lacking the Protein Kinase Akt2 (PKBβ). *Science* 292, 1728–1731. doi:10.1126/science.292.5522.1728

Cipriani, C., Colangelo, L., Santori, R., Renella, M., Mastrantonio, M., Minisola, S., et al. (2020). The Interplay between Bone and Glucose Metabolism. *Front. Endocrinol.* 11, 122. doi:10.3389/fendo.2020.00122

D'Andrea, P., Calabrese, A., and Grandolfo, M. (1998). Intercellular Calcium Signalling between Chondrocytes and Synovial Cells in Co-culture. *Biochem. J.* 329 (3), 681–687. doi:10.1042/bj3290681

Danciu, T. E., Adam, R. M., Naruse, K., Freeman, M. R., and Hauschka, P. V. (2003). Calcium Regulates the PI3K-Akt Pathway in Stretched Osteoblasts. *FEBS Lett.* 536 (1–3), 193–197. doi:10.1016/S0014-5793(03)00055-3

de Luca, C., and Olefsky, J. M. (2009). Inflammation and Insulin Resistance. *FEBS Lett.* 582 (1), 97–105. doi:10.1016/j.febslet.2007.11.057

Denko, C. W., Boja, B., and Moskowitz, R. W. (1996). Growth Factors, Insulin-like Growth Factor-1 and Growth Hormone, in Synovial Fluid and Serum of Patients with Rheumatic Disorders. *Osteoarthritis and Cartilage* 4 (4), 245–249. doi:10.1016/S1063-4584(05)80102-5

Dong, Q., Liu, H., Yang, D., and Zhang, Y. (2017). Diabetes Mellitus and Arthritis. *Medicine* 96 (18), e6627. doi:10.1097/MD.0000000000006627

Du, H., Zhang, X., Zeng, Y., Huang, X., Chen, H., Wang, S., et al. (2019). A Novel Phytochemical, DIM, Inhibits Proliferation, Migration, Invasion and TNF-α Induced Inflammatory Cytokine Production of Synovial Fibroblasts from Rheumatoid Arthritis Patients by Targeting MAPK and AKT/mTOR Signal Pathway. *Front. Immunol.* 10, 1620. doi:10.3389/fimmu.2019.01620

Durgam, S. S., Altmann, N. N., Coughlin, H. E., Rollins, A., and Hostnik, L. D. (2019). Insulin Enhances the *In Vitro* Osteogenic Capacity of Flexor Tendon-Derived Progenitor Cells. *Stem Cell Int.* 2019, 1–10. doi:10.1155/2019/1602751

Ebeling, P., Koistinen, H. A., and Koivisto, V. A. (1998). Insulin-Independent Glucose Transport Regulates Insulin Sensitivity. *FEBS Lett.* 436 (3), 301–303. doi:10.1016/S0014-5793(98)01149-1

Estell, E. G., Murphy, L. A., Silverstein, A. M., Tan, A. R., Shah, R. P., Ateshian, G. A., et al. (2017). Fibroblast-like Synoviocyte Mechanosensitivity to Fluid Shear Is Modulated by Interleukin-1α. *J. Biomech.* 60, 91–99. doi:10.1016/j.jbiomech.2017.06.011

Esteves, J. V., Yonamine, C. Y., Pinto-Junior, D. C., Gerlinger-Romero, F., Enguita, F. J., and Machado, U. F. (2018). Diabetes Modulates MicroRNAs 29b-3p, 29c-3p, 199a-5p and 532-3p Expression in Muscle: Possible Role in GLUT4 and HK2 Repression. *Front. Endocrinol.* 9, 536. doi:10.3389/fendo.2018.00536

Falconer, J., Pucino, V., Clayton, S. A., Marshall, J. L., Raizada, S., Adams, H., et al. (2021). Spontaneously Resolving Joint Inflammation Is Characterised by Metabolic Agility of Fibroblast-like Synoviocytes. *Front. Immunol.* 12. doi:10.3389/fimmu.2021.725641

Frost, M., Balkau, B., Hatunic, M., Konrad, T., Mingrone, G., and Højlund, K. (2018). The Relationship between Bone Turnover and Insulin Sensitivity and Secretion: Cross-Sectional and Prospective Data from the RISC Cohort Study. *Bone* 108, 98–105. doi:10.1016/j.bone.2017.12.029

Gabbouj, S., Ryhänen, S., Marttinen, M., Wittrahm, R., Takalo, M., Kemppainen, S., et al. (2019). Altered Insulin Signaling in Alzheimer's Disease Brain - Special Emphasis on PI3K-Akt Pathway. *Front. Neurosci.* 13, 629. doi:10.3389/fnins.2019.00629

Galicia-Garcia, U., Benito-Vicente, A., Jebari, S., Larrea-Sebal, A., Siddiqi, H., Uribe, K. B., et al. (2020). Pathophysiology of Type 2 Diabetes Mellitus. *Ijms* 21 (17), 6275. doi:10.3390/ijms21176275

Gallagher, L., Cregan, S., Biniecka, M., Cunningham, C., Veale, D. J., Kane, D. J., et al. (2020). Insulin-Resistant Pathways Are Associated with Disease Activity in Rheumatoid Arthritis and Are Subject to Disease Modification through Metabolic Reprogramming: A Potential Novel Therapeutic Approach. *Arthritis Rheumatol.* 72 (6), 896–902. doi:10.1002/art.41190

Garcia-Carbonell, R., Divakaruni, A. S., Lodi, A., Vicente-Suarez, I., Saha, A., Cheroutre, H., et al. (2016). Critical Role of Glucose Metabolism in Rheumatoid Arthritis Fibroblast-like Synoviocytes. *Arthritis Rheumatol.* 68 (7), 1614–1626. doi:10.1002/art.39608

Gerdes, J. M., Christou-Savina, S., Xiong, Y., Moede, T., Moruzzi, N., Karlsson-Edlund, P., et al. (2014). Ciliary Dysfunction Impairs Beta-Cell Insulin Secretion and Promotes Development of Type 2 Diabetes in Rodents. *Nat. Commun.* 5 (1), 5308. doi:10.1038/ncomms6308

Gowd, V., Gurukar, A., and Chilkunda, N. D. (2016). Glycosaminoglycan Remodeling during Diabetes and the Role of Dietary Factors in Their Modulation. *Wjd* 7 (4), 67. doi:10.4239/wjd.v7.i4.67

Griffin, T. M., and Huffman, K. M. (2016). Editorial: Insulin Resistance: Releasing the Brakes on Synovial Inflammation and Osteoarthritis? *Arthritis Rheumatol.* 68 (6), 1330–1333. doi:10.1002/art.39586

Hamada, D., Maynard, R., Schott, E., Drinkwater, C. J., Ketz, J. P., Kates, S. L., et al. (2016). Suppressive Effects of Insulin on Tumor Necrosis Factor-Dependent Early Osteoarthritic Changes Associated with Obesity and Type 2 Diabetes Mellitus. *Arthritis Rheumatol.* 68 (6), 1392–1402. doi:10.1002/art.39561

Harsha, A. P., and Joyce, T. J. (2011). Challenges Associated with Using Bovine Serum in Wear Testing Orthopaedic Biopolymers. *Proc. Inst. Mech. Eng. H* 225 (10), 948–958. doi:10.1177/0954411911416047

Hatting, M., Tavares, C. D. J., Sharabi, K., Rines, A. K., and Puigserver, P. (2018). Insulin Regulation of Gluconeogenesis. *Ann. N.Y. Acad. Sci.* 1411 (1), 21–35. doi:10.1111/nyas.13435

Hayden, M. R., Tyagi, S. C., Kolb, L., Sowers, J. R., and Khanna, R. (2005). Vascular Ossification - Calcification in Metabolic Syndrome, Type 2 Diabetes Mellitus, Chronic Kidney Disease, and Calciphylaxis - Calcific Uremic Arteriolopathy: The Emerging Role of Sodium Thiosulfate. *Cardiovasc. Diabetol.* 4 (1), 4. doi:10.1186/1475-2840-4-4

Hoey, D. A., Downs, M. E., and Jacobs, C. R. (2012). The Mechanics of the Primary Cilium: An Intricate Structure with Complex Function. *J. Biomech.* 45 (1), 17–26. doi:10.1016/j.jbiomech.2011.08.008

Hoshiyama, M., Li, B., Yao, J., Harada, T., Morioka, T., and Oite, T. (2004). Effect of High Glucose on Nitric Oxide Production and Endothelial Nitric Oxide Synthase Protein Expression in Human Glomerular Endothelial Cells. *Nephron Exp. Nephrol.* 95 (2), e62–e68. doi:10.1159/000073673

Huang, X., Liu, G., Guo, J., and Su, Z. (2018). The PI3K/AKT Pathway in Obesity and Type 2 Diabetes. *Int. J. Biol. Sci.* 14 (11), 1483–1496. doi:10.7150/ijbs.27173

Hung, C. T., Pollack, S. R., Reilly, T. M., and Brighton, C. T. (1995). Real-time Calcium Response of Cultured Bone Cells to Fluid Flow. *Clin. Orthop. Relat. Res.* 313, 256–269.

Jazirehi, A. R., Wenn, P. B., and Damavand., M. (2012). Therapeutic Implications of Targeting the PI3Kinase/AKT/mTOR Signaling Module in Melanoma Therapy. *Am. J. Cancer Res.* 2 (2), 178–191.

King, K. B., and Rosenthal, A. K. (2015). The Adverse Effects of Diabetes on Osteoarthritis: Update on Clinical Evidence and Molecular Mechanisms. *Osteoarthritis and Cartilage* 23 (6), 841–850. doi:10.1016/j.joca.2015.03.031

Kluth, O., Stadion, M., Gottmann, P., Aga, H., Jähnert, M., Scherneck, S., et al. (2019). Decreased Expression of Cilia Genes in Pancreatic Islets as a Risk Factor for Type 2 Diabetes in Mice and Humans. *Cel Rep.* 26 (11), 3027–3036. doi:10.1016/j.celrep.2019.02.056

Lebeche, D., Davidoff, A. J., and Hajjar, R. J. (2008). Interplay between Impaired Calcium Regulation and Insulin Signaling Abnormalities in Diabetic Cardiomyopathy. *Nat. Rev. Cardiol.* 5 (11), 715–724. doi:10.1038/ncpcardio1347

Li, Q., Wen, Y., Wang, L., Chen, B., Chen, J., Wang, H., et al. (2021). Hyperglycemia-Induced Accumulation of Advanced Glycosylation End Products in Fibroblast-like Synoviocytes Promotes Knee Osteoarthritis. *Exp. Mol. Med.* 53, 1735–1747. doi:10.1038/s12276-021-00697-6

Li, X.-F., Sun, Y.-Y., Bao, J., Chen, X., Li, Y.-H., Yang, Y., et al. (2017). Functional Role of PPAR-γ on the Proliferation and Migration of Fibroblast-like Synoviocytes in Rheumatoid Arthritis. *Sci. Rep.* 7, 12671. doi:10.1038/s41598-017-12570-6

Lu, C. J., Du, H., Wu, J., Jansen, D. A., Jordan, K. L., Xu, N., et al. (2008). Non-Random Distribution and Sensory Functions of Primary Cilia in Vascular Smooth Muscle Cells. *Kidney Blood Press. Res.* 31 (3), 171–184. doi:10.1159/000132462

Mackenzie, R., and Elliott, B. (2014). Akt/PKB Activation and Insulin Signaling: A Novel Insulin Signaling Pathway in the Treatment of Type 2 Diabetes. *Dmso* 7, 55–64. doi:10.2147/DMSO.S48260

Malone, A. M. D., Anderson, C. T., Tummala, P., Kwon, R. Y., Johnston, T. R., Stearns, T., et al. (2007). Primary Cilia Mediate Mechanosensing in Bone Cells by a Calcium-independent Mechanism. *Proc. Natl. Acad. Sci.* 104 (33), 13325–13330. doi:10.1073/pnas.0700636104

Maor, G., Silbermann, M., von der Mark, K., Heingard, D., and Laron, Z. (1993). Insulin Enhances the Growth of Cartilage in Organ and Tissue Cultures of Mouse Neonatal Mandibular Condyle. *Calcif Tissue Int.* 52 (4), 291–299. doi:10.1007/BF00296654

Nagy, T., Fisi, V., Frank, D., Kátai, E., Nagy, Z., and Miseta, A. (2019). Hyperglycemia-Induced Aberrant Cell Proliferation; A Metabolic Challenge Mediated by Protein O-GlcNAc Modification. *Cells* 8 (9), 999. doi:10.3390/cells8090999

Nicholson-Fish, J. C., Cousin, M. A., and Smillie, K. J. (2016). Phosphatidylinositol 3-Kinase Couples Localised Calcium Influx to Activation of Akt in Central Nerve Terminals. *Neurochem. Res.* 41 (3), 534–543. doi:10.1007/s11064-015-1663-5

Nitulescu, G., Van De Venter, M., Nitulescu, G., Ungurianu, A., Juzenas, P., Peng, Q., et al. (2018). The Akt Pathway in Oncology Therapy and beyond (Review). *Int. J. Oncol.* 53(6), 2319–2331. doi:10.3892/ijo.2018.4597

Ou, Y., Ruan, Y., Cheng, M., Moser, J. J., Rattner, J. B., and van der Hoorn, F. A. (2009). Adenylate Cyclase Regulates Elongation of Mammalian Primary Cilia. *Exp. Cel Res.* 315 (16), 2802–2817. doi:10.1016/j.yexcr.2009.06.028

Petersen, M. C., and Shulman., G. I. (2018). Mechanisms of Insulin Action and Insulin Resistance. *Physiol. Rev.* 98 (4), 2133–2223. doi:10.1152/physrev.00063.2017

Piva, S. R., Susko, A. M., Khoja, S. S., Josbeno, D. A., Fitzgerald, G. K., and Toledo, F. G. S. (2015). Links between Osteoarthritis and Diabetes. *Clin. Geriatr. Med.* 31 (1), 67–87. doi:10.1016/j.cger.2014.08.019

Rattner, J. B., Paul, S., Ou, Y., van der Hoorn, F. A., and Lo, I. K. Y. (2010). Primary Cilia in Fibroblast-like Type B Synoviocytes Lie within a Cilium Pit: A Site of Endocytosis. *Histology and Histopathology* 25 (7), 865–875. doi:10.14670/HH-25.865

Riesle, J., Hollander, A. P., Langer, R., Freed, L. E., and Vunjak-Novakovic, G. (1998). Collagen in Tissue-Engineered Cartilage: Types, Structure, and Crosslinks. *J. Cel. Biochem.* 71 (3), 313–327. doi:10.1002/(sici)1097-4644(19981201)71:3<313:aid-jcb1>3.0.co;2-c

Ritter, A., Friemel, A., Kreis, N.-N., Hoock, S. C., Roth, S., Kielland-Kaisen, U., et al. (2018). Primary Cilia Are Dysfunctional in Obese Adipose-Derived Mesenchymal Stem Cells. *Stem Cel Rep.* 10 (2), 583–599. doi:10.1016/j.stemcr.2017.12.022

Röder, P. V., Wu, B., Liu, Y., and Han, W. (2016). Pancreatic Regulation of Glucose Homeostasis. *Exp. Mol. Med.* 48 (3), e219. doi:10.1038/emm.2016.6

Rosa, S. C., Gonçalves, J., Judas, F., Mobasheri, A., Lopes, C., and Mendes, A. F. (2009). Impaired Glucose Transporter-1 Degradation and Increased Glucose Transport and Oxidative Stress in Response to High Glucose in Chondrocytes from Osteoarthritic versus Normal Human Cartilage. *Arthritis Res. Ther.* 11(3), R80. doi:10.1186/ar2713

Silverstein, A. M. (2017). *Development of Biofidelic Culture Models of Osteoarthritis*. New York: Columbia University. doi:10.7916/D8HX1R48

Silverstein, A. M., Stefani, R. M., Sobczak, E., Tong, E. L., Attur, M. G., Shah, R. P., et al. (2017). Toward Understanding the Role of Cartilage Particulates in Synovial Inflammation. *Osteoarthritis and Cartilage* 25 (8), 1353–1361. doi:10.1016/j.joca.2017.03.015

Song, P., Hwang, J. S., Park, H. C., Kim, K. K., Son, H.-J., Kim, Y.-J., et al. (2021). Therapeutic Applications of Type 2 Diabetes Mellitus Drug Metformin in Patients with Osteoarthritis. *Pharmaceuticals* 14 (2), 152. doi:10.3390/ph14020152

Stefani, R. M. (2020). *Role of the Synovial Membrane in Osteoarthritis Pathogenesis and Cartilage Repair*. New York: Columbia University. doi:10.7916/d8-zwn3-5k85

Stefani, R. M., Halder, S. S., Estell, E. G., Lee, A. J., Silverstein, A. M., Sobczak, E., et al. (2019). A Functional Tissue-Engineered Synovium Model to Study Osteoarthritis Progression and Treatment. *Tissue Eng. A* 25 (7–8), 538–553. doi:10.1089/ten.tea.2018.0142

Stegemann, H., and Stalder, K. (1967). Determination of Hydroxyproline. *Clinica Chim. Acta* 18 (2), 267–273. doi:10.1016/0009-8981(67)90167-2

Stultz, C. M., and Edelman, E. R. (2003). A Structural Model that Explains the Effects of Hyperglycemia on Collagenolysis. *Biophysical J.* 85 (4), 2198–2204. doi:10.1016/S0006-3495(03)74645-1

Sun, A. R., Udduttula, A., Li, J., Liu, Y., Ren, P.-G., and Zhang, P. (2021). Cartilage Tissue Engineering for Obesity-Induced Osteoarthritis: Physiology, Challenges, and Future Prospects. *J. Orthopaedic Translation* 26, 3–15. doi:10.1016/j.jot.2020.07.004

Sun, H. B., Nalim, R., and Yokota, H. (2003). Expression and Activities of Matrix Metalloproteinases under Oscillatory Shear in IL-1-Stimulated Synovial Cells. *Connect. Tissue Res.* 44 (1), 42–49. doi:10.1080/03008200390151954

Swain, S., Sarmanova, A., Coupland, C., Doherty, M., and Zhang, W. (2020). Comorbidities in Osteoarthritis: A Systematic Review and Meta-Analysis of Observational Studies. *Arthritis Care Res.* 72 (7), 991–1000. doi:10.1002/acr.24008

Takahashi, K., Nagai, T., Chiba, S., Nakayama, K., and Mizuno, K. (2018). Glucose Deprivation Induces Primary Cilium Formation through MTORC1 Inactivation. *J. Cel Sci.* 131 (1), jcs208769. doi:10.1242/jcs.208769

Tamer, T. M. (2013). Hyaluronan and Synovial Joint: Function, Distribution and Healing. *Interdiscip. Toxicol.* 6 (3), 111–125. doi:10.2478/intox-2013-0019

Tchetina, E. V., Markova, G. A., and Sharapova, E. P. (2020). Insulin Resistance in Osteoarthritis: Similar Mechanisms to Type 2 Diabetes Mellitus. *J. Nutr. Metab.* 2020, 1–16. doi:10.1155/2020/4143802

Tonks, K. T., Ng, Y., Miller, S., Coster, A. C. F., Samocha-Bonet, D., Iseli, T. J., et al. (2013). Impaired Akt Phosphorylation in Insulin-Resistant Human Muscle Is Accompanied by Selective and Heterogeneous Downstream Defects. *Diabetologia* 56 (4), 875–885. doi:10.1007/s00125-012-2811-y

Veronese, N., Cooper, C., Reginster, J.-Y., Hochberg, M., Branco, J., Bruyère, O., et al. (2019). Type 2 Diabetes Mellitus and Osteoarthritis. *Semin. Arthritis Rheum.* 49 (1), 9–19. doi:10.1016/j.semarthrit.2019.01.005

Wang, T., Wang, J., Hu, X., Huang, X., and Chen, G.-X. (2020). Current Understanding of Glucose Transporter 4 Expression and Functional Mechanisms. *Wjbc* 11 (3), 76–98. doi:10.4331/wjbc.v11.i3.76

Weiss, R. E., and Reddi, A. H. (1980). Influence of Experimental Diabetes and Insulin on Matrix-Induced Cartilage and Bone Differentiation. *Am. J. Physiology-Endocrinology Metab.* 238 (3), E200–E207. doi:10.1152/ajpendo.1980.238.3.E200

Wheway, G., Nazlamova, L., and Hancock, J. T. (2018). Signaling through the Primary Cilium. *Front. Cel Dev. Biol.* 6, 8. doi:10.3389/fcell.2018.00008

Wilcox, G. (2005). Insulin and Insulin Resistance. *Clin. Biochem. Rev.* 26, 19–39.

Williams, A. S., Kang, L., and Wasserman, D. H. (2015). The Extracellular Matrix and Insulin Resistance. *Trends Endocrinol. Metab.* 26 (7), 357–366. doi:10.1016/j.tem.2015.05.006

Wu, Y.-F., Wang, H.-K., Chang, H.-W., Sun, J., Sun, J.-S., and Chao, Y.-H. (2017). High Glucose Alters Tendon Homeostasis through Downregulation of the AMPK/Egr1 Pathway. *Sci. Rep.* 7 (1), 44199. doi:10.1038/srep44199

Yanagida-Suekawa, T., Tanimoto, K., Tanne, Y., Mitsuyoshi, T., Hirose, N., Su, S., et al. (2013). Synthesis of Hyaluronan and Superficial Zone Protein in Synovial Membrane Cells Modulated by Fluid Flow. *Eur. J. Oral Sci.* 121 (6), 566–572. doi:10.1111/eos.12082

Yellowley, C. E., Jacobs, C. R., and Donahue, H. J. (1999). Mechanisms Contributing to Fluid-Flow-Induced Ca2+ Mobilization in Articular Chondrocytes. *J. Cel. Physiol.* 180 (3), 402–408. doi:10.1002/(sici)1097-4652(199909)180:3<402:aid-jcp11>3.0.co;2-4

Zarneshan, S. N., Fakhri, S., Farzaei, M. H., Khan, H., and Saso, L. (2020). Astaxanthin Targets PI3K/Akt Signaling Pathway toward Potential Therapeutic Applications. *Food Chem. Toxicol.* 145, 111714. doi:10.1016/j.fct.2020.111714

Conflict of Interest: The authors declare that the research was conducted in the absence of any commercial or financial relationships that could be construed as a potential conflict of interest.

Publisher's Note: All claims expressed in this article are solely those of the authors and do not necessarily represent those of their affiliated organizations, or those of the publisher, the editors, and the reviewers. Any product that may be evaluated in this article, or claim that may be made by its manufacturer, is not guaranteed or endorsed by the publisher.

Copyright © 2022 Sakhrani, Lee, Murphy, Kenawy, Visco, Ateshian, Shah and Hung. This is an open-access article distributed under the terms of the Creative Commons Attribution License (CC BY). The use, distribution or reproduction in other forums is permitted, provided the original author(s) and the copyright owner(s) are credited and that the original publication in this journal is cited, in accordance with accepted academic practice. No use, distribution or reproduction is permitted which does not comply with these terms.

frontiers in Bioengineering and Biotechnology

ORIGINAL RESEARCH
published: 08 March 2022
doi: 10.3389/fbioe.2022.823933

Disulfiram Suppressed Peritendinous Fibrosis Through Inhibiting Macrophage Accumulation and Its Pro-inflammatory Properties in Tendon Bone Healing

Qi Zhou[1,2], *Wei Wang*[1], *Fujun Yang*[2,3], *Hao Wang*[4], *Xiaodong Zhao*[5], *Yiqin Zhou*[2]*, *Peiliang Fu*[2]* *and Yaozeng Xu*[1]*

[1]Department of Orthopedics, the First Affiliated Hospital of Soochow University, Suzhou, China, [2]Department of Orthopedics, Shanghai Changzheng Hospital, Naval Medical University, Shanghai, China, [3]The Fifth People's Hospital of Zunyi, Zunyi, China, [4]Department of Orthopaedics, Shanghai Public Health Clinical Center, Fudan University, Shanghai, China, [5]Department of Orthopaedics, Weifang Traditional Chinese Hospital, Weifang, China

OPEN ACCESS

Edited by:
Dmitriy Sheyn,
Board of Governors Regenerative Medicine Institute, United States

Reviewed by:
Jess Snedeker,
University of Zurich, Switzerland
Wen Shi,
University of Nebraska Medical Center, United States

***Correspondence:**
Yiqin Zhou
drzhouyiqin@163.com
Peiliang Fu
fupeiliang@163.com
Yaozeng Xu
xuyaozeng@163.com

Specialty section:
This article was submitted to Biomaterials, a section of the journal Frontiers in Bioengineering and Biotechnology

Received: 28 November 2021
Accepted: 27 January 2022
Published: 08 March 2022

Citation:
Zhou Q, Wang W, Yang F, Wang H, Zhao X, Zhou Y, Fu P and Xu Y (2022) Disulfiram Suppressed Peritendinous Fibrosis Through Inhibiting Macrophage Accumulation and Its Pro-inflammatory Properties in Tendon Bone Healing. Front. Bioeng. Biotechnol. 10:823933. doi: 10.3389/fbioe.2022.823933

The communication between macrophages and tendon cells plays a critical role in regulating the tendon-healing process. However, the potential mechanisms through which macrophages can control peritendinous fibrosis are unknown. Our data showed a strong pro-inflammatory phenotype of macrophages after a mouse tendon–bone injury. Moreover, by using a small-molecule compound library, we identified an aldehyde dehydrogenase inhibitor, disulfiram (DSF), which can significantly promote the transition of macrophage from M1 to M2 phenotype and decrease macrophage pro-inflammatory phenotype. Mechanistically, DSF targets gasdermin D (GSDMD) to attenuate macrophage cell pyroptosis, interleukin-1β, and high mobility group box 1 protein release. These pro-inflammatory cytokines and damage-associated molecular patterns are essential for regulating tenocyte and fibroblast proliferation, migration, and fibrotic activity. Deficiency or inhibition of GSDMD significantly suppressed peritendinous fibrosis formation around the injured tendon and was accompanied by increased regenerated bone and fibrocartilage compared with the wild-type littermates. Collectively, these findings reveal a novel pathway of GSDMD-dependent macrophage cell pyroptosis in remodeling fibrogenesis in tendon–bone injury. Thus, GSDMD may represent a potential therapeutic target in tendon–bone healing.

Keywords: macrophage, tendon–bone injury, disulfiram, gasdermin D, fibrosis

INTRODUCTION

Peritendinous fibrosis is a critical complication arising after tendon injury (TI), which is primarily identified as excessive extracellular matrix (ECM) deposition and fibroblast cell activation (Manske, 2005; Juneja et al., 2013). Presently, the imbalance between ECM synthesis and degradation has been established as the leading cause of impaired tendon function and increased risk of repair after clinical surgery (Zheng et al., 2019). The transdifferentiation and proliferation of fibroblasts are the major source of ECM and can be regulated by a series of differential cytokine release in adhesive tendon tissues, including that of transforming growth factor (TGF)-β, fibroblast growth factor-2, connective

tissue growth factor, and vascular endothelial growth factor (Darby et al., 2016). In addition, while the resident tissue fibroblasts have been identified as sensitive to intrinsic mechanical and biophysical cues in tendon–bone injury (Zheng et al., 2017; Yao et al., 2019), the initiation of immune response in this process remains poorly understood.

The earliest cellular response following the surgical implantation of a tendon graft in a bone tunnel is accumulation of the various inflammatory cells (Kawamura et al., 2005). In general, the main effector myeloid cells, including monocytes and macrophages, are the first cells that are activated in response to the TI. M1 macrophages can produce different pro-inflammatory cytokines such as interleukin-1β (IL-1β) and tumor necrosis factor-α (TNF-α) during immune activation. These pro-inflammatory cytokines not only have an increased level in the early process of TI but also modulate tendon–bone response after magnetic stimulation. A number of previous studies have indicated that macrophages can negatively affect the process as macrophage depletion can significantly improve both the morphological and biomechanical properties at the healing tendon–bone interface (Cui et al., 2019). Moreover, during the successful tissue–biomaterial integration, M1 macrophages can effectively polarize into M2 macrophages (Klopfleisch, 2016), which express different genes and attain distinct functional states. M2 macrophages are anti-inflammatory, are antiparasitic, and can promote tissue repair. However, the precise mechanisms that can regulate M2 macrophage polarization and function in the tendon–bone injury are unknown.

Drug repurposing has been recently identified as a cost-effective approach to bring approved drugs rapidly in clinical treatment (Alvarez et al., 2021). In prior investigation on repurposed drugs, such as aspirin, they have been demonstrated to promote tenogenic differentiation of the tendon stem cells and to facilitate tendinopathy healing (Wang et al., 2020). Disulfiram (DSF) is an old alcohol-abuse drug that was approved by the US Food and Drug Administration (FDA) in 1949 (Bista et al., 2017). Except for its role as an acetaldehyde dehydrogenase, recent studies have revealed its role in various diseases, including antitumor activity and resistance to sepsis and obesity (Skrott et al., 2017; Bernier et al., 2020; Klimiankou and Skokowa, 2021). However, the role of DSF on macrophage is unknown. In TI, the functional phenotype change of M1 and M2 exhibits a phagocytic and pro-inflammatory function, which plays an important role in the healing process (Chamberlain et al., 2021; Yu et al., 2021). Furthermore, the reduced macrophage-mediated inflammation in the injured tendon through M1-to-M2 transmission significantly inhibits adhesion formation during tendon healing (Dong et al., 2021). Consequently, it is desirable to explore the effect of DSF on the immunoregulatory potential of macrophage in tendon–bone injury.

In the present study, we have identified a small molecular compound, DSF, which can significantly promote the transition of macrophage from the M1 to M2 phenotype. We further uncover a novel mechanism through which DSF can target gasdermin D (GSDMD) to inhibit macrophage cell pyroptosis in the tendon bone injury and a newly identified GSDMD-dependent cell interaction between immune cells and resident tendon cells. We have also explored the therapeutic potential of targeting this pathway in the context of TI.

MATERIALS AND METHODS

Reagents and Antibodies

The cell culture medium including Dulbecco's Modified Eagle's Medium (DMEM; Cat#: 10-013-CVR, Corning, New York, NY, United States) and supplements including penicillin and streptomycin (Cat#: 15140-122, Gibco, Waltham, MA, United States) were purchased from Life Science Technologies (Rockville, MD, United States). Antibodies to GSDMD (ab219800), fibronectin (FN) (ab2413), collagen I (ab34710), α-smooth muscle actin (α-SMA) (55135-1-AP), IL-1β (ab9722), high mobility group box 1 (HMGB1) (ab18256) were obtained from Abcam (Cambridge, MA, United States). Anti-caspase-11 (17D9, C1354) was from Sigma-Aldrich (Burlington, MA, United States). Anti-caspase-1 (AC-20B-00420-C100) was from AdipoGen (San Diego, CA, United States). β-Actin antibody (3700S) was purchased from Cell Signaling Technology (Danvers, MA, United States). Anti-IL-1α (sc-12741) was purchased from Santa Cruz (TX, United States). Fetal bovine serum (FBS) (Cat#: 26140-079, Gibco, NY, United States) was purchased from Life Science Technologies and heat-inactivated before utilization. M-CSF was obtained from Miltenyi Biotec (130-094-129, Westphalia, Germany). Recombinant mouse INF-γ (C600059) and IL-4 (C600050) were purchased from Sangon Biotech (Shanghai, China). Fifty-four drug libraries were directly obtained from Topscience (L2130, Shanghai, China). LPS (L2630) and DSF (PHR-1690) were purchased from Sigma-Aldrich (Sigma, Merck, Darmstadt, Germany).

Animals

All animal experiments in this study were approved by the Navy Medical University Animal Care and Use Committee. Pain and discomfort are minimized based on standard animal care guidelines. Male mice (6 weeks, SLRC Laboratory, Shanghai, China) were anesthetized by an initial intraperitoneal injection of Avertin (100 mg kg^{-1}). The Achilles tendon of the left leg was then exposed and released from the calcaneum. Thereafter, the tendon was cut at its insertion on the bone. The enthesis was destroyed by a burr. An 18G sterile needle was used to make two tunnels through the calcaneum, and a nonabsorbable suture was used to attach the tendon back to the bone. Then the wound was closed, and the mice were allowed to recover. Mice were sacrificed 30 days after surgery. For flexor tendon surgery, mice underwent complete transection and repair of the flexor digitorum longus (FDL) tendon in the right hind paw as previously reported (Loiselle et al., 2009).

Histological Evaluation

The excess soft tissues were isolated from the mice and kept the repair site complete. The specimens were fixed in 4% paraformaldehyde (PFA) for 24 h and then decalcified in Plank-Rychlo decalcifying fluid at room temperature for 16 days. The specimens were embedded in paraffin, and

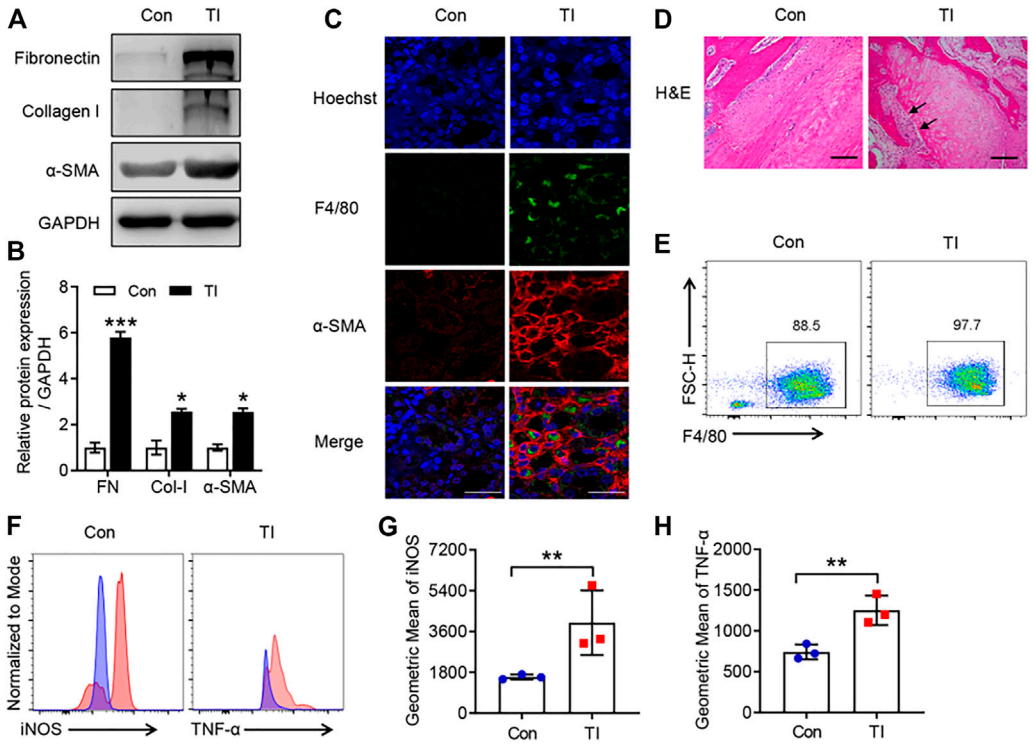

FIGURE 1 | The increased peritendinous fibrosis and macrophage infiltration in TI. **(A)** Western blot analysis of FN, Col-I, and α-SMA in tendon from control (Con) and TI mice. **(B)** Quantitative analysis of FN, Col-I, and α-SMA in **A**. **(C)** Confocal analysis of F4/80 and α-SMA in the tendon section from Con and TI mice. Scale bar = 20 μm. **(D)** H&E staining in the tendon section from Con and TI mice. Scale bar = 200 μm. **(E)** Flow cytometric analysis (FACS) of M-CSF-induced macrophages ($F4/80^+$) from Con and TI groups. **(F)** FACS representative analysis of iNOS and TNF-α. **(G,H)** Quantitative analysis of geometric mean of iNOS and TNF-α in E. Data are presented as the mean ± SEM ($n = 3$) **(B,G,H)**. $^*p < 0.05$, $^{**}p < 0.01$, $^{***}p < 0.001$.

thereafter, the slices were cut and stained with hematoxylin and eosin (H&E). The histological evaluation was performed according to the histological scoring system (Jiang et al., 2014).

Exosome Purification

Exosome purification was performed as previously described (Cui et al., 2019). Briefly, the bone-marrow-derived macrophages (BMDMs) were cultured for 72 h. The debris and dead cells in the cultured medium were removed by centrifugation at 1,000 × *g* for 10 min at 4°C. After filtration through a 2-μm filter, the medium was subjected to ultracentrifugation at 100,000 × *g* for 6 h at 4°C. The pellets were washed with PBS and then centrifuged at 100,000 × *g* for 20 min at 4°C. An exosome-containing pellet was collected and resuspended in PBS. The particle size and concentration of exosome were determined using network address translation (NTA) with ZetaView PMX 120 (Particle Metrix).

Confocal Immunofluorescent Imaging

The tendon sections from the frozen optimum cutting temperature compound (OCT)-embedded tissues were fixed with 1:1 acetone/methanol and stained with H&E. The cells were fixed in 2% PFA for 15 min at 4°C. Thereafter, the cells were washed with PBS only once and permeabilized in 0.1% Triton X-100 at 4°C for 10 min. The cells were then blocked with 3% goat serum plus 3% FBS at 4°C for 1 h. F4/80 and α-SMA were added overnight at 4°C. The cells were washed with PBS only once; the cells were then incubated with the secondary antibody for 1 h at 4°C and gently washed three times with PBS before imaging. Imaging was performed on a custom modified Olympus FV3000 laser scanning microscope equipped with a ×60 oil immersion lens.

Flow Cytometry Analysis

For the surface and cytokine staining, 100 μl of blood was harvested and blocked with an Fc blocker (BioLegend) for 30 min at 4°C. The cells were then resuspended in a 50 μl fluorescence activating cell sorter (FACS) buffer (1× PBS with 0.5% FBS, 2 mM ethylenediaminetetraacetic acid) with diluted CD86 and CD206. iNOS and TNF-α antibody were added by Foxp3/Transcription Factor Staining Buffer Set (eBioscience) according to manufacturer's protocol. For cell cycle analysis, the cells were collected and suspended in pre-cold absolute ethanol for overnight at 4°C. Thereafter, the cells were stained with propidium iodide (PI) for 30 min at dark condition. The data were acquired on a BD LSRFortessa X-20 cell analyzer (BD Biosciences) and analyzed using the FlowJo software (Tree Star, Inc.).

Cell Cultures

NIH/3T3 cell lines were purchased from the Cell Bank of Type Culture Collection, Chinese Academy of Sciences (CAS, Shanghai, China), and were cultured in DMEM

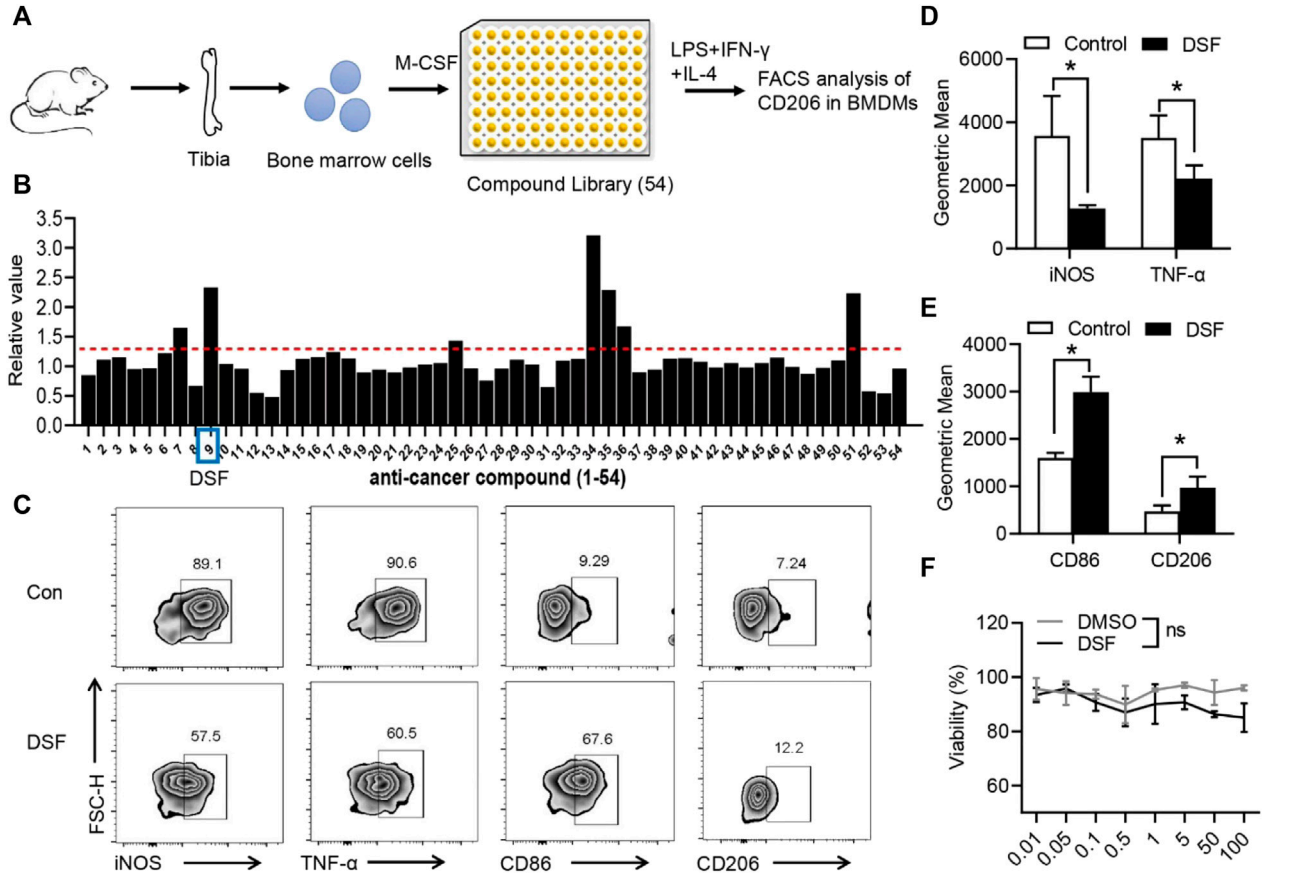

FIGURE 2 | DSF significantly promotes pro-inflammatory macrophages into the M2-type phenotype. **(A)** The diagram of screening assay. Bone marrow cells were isolated from the tibia of wild-type mice. BMDMs were induced by M-CSF (50 ng/ml). Then the cells were treated with LPS (100 ng/ml), IFN-γ (20 ng/ml), and IL-4 (20 ng/ml) for 6 h and underwent FACS analysis of CD206 expression. **(B)** Quantitative analysis of the candidates in screening assay. **(C)** BMDMs were pretreated with DSF (5 μM) or DMSO (0.01%). Then the cells were treated with LPS (100 ng/ml), IFN-γ (20 ng/ml), and IL-4 (20 ng/ml) for 6 h. FACS analysis of iNOS, TNF-α, CD86, and CD206. **(D,E)** Quantitative analysis of geometric mean of iNOS **(D)** TNF-α **(D)**, CD86 **(E)** and CD206 **(E)**. **(F)** CCK-8 analysis of BMDMs after treatment with DSF at different dosages. Data are presented as the mean ± SEM (n = 3) **(D**,**E**,**F)**. *p < 0.05.

supplemented with 10% FBS. For BMDMs, the mice were sacrificed by cervical vertebra dissection, followed by soaking in 75% alcohol for 3 min. The femur and tibia were separated on a sterile bench. The lumen was rinsed with PBS solution containing 3% FBS, and bone fragments and meat scraps were removed with a 70-μm filter. The cells were then centrifuged at $400 \times g$ of 4°C for 10 min. Thereafter, the red blood cells were subjected to lysis by red blood cell lysis buffer. The cells were suspended in 1640 medium with 10% FBS. A total of 1×10^7 cells were cultured in a T25 flask overnight, and any contaminating cells such as monocytes and fibroblasts were removed. After centrifugation at $400 \times g$ for 5 min, cells were resuspended in 1640 medium (containing 10% FBS and penicillin streptomycin). The cells were then treated with the macrophage-stimulating factor (M-CSF) at 10 ng/ml and transferred in a new T25 culture flask. The incubation was continued, and the medium was changed every 3 days, but the M-CSF concentration was kept constant. On the seventh day, the cells were collected and tested for purity.

Western Blotting

The tendons or cells were lysed in cell lysis buffer (Cell Signaling Technology, #9803) and supplemented with proteinase inhibitor at a dilution of 1:25. The protein concentrations were determined by using a BCA protein assay kit. For western blot analysis, equal amounts of protein were heat-denatured in the presence of a reducing agent and separated on 10% SDS-PAGE and transferred to PVDF membranes (Millipore, IPVH00010). The various antibodies used for western blot have been mentioned in the figure legend. The bands were detected using ECL Plus (Tanon, 180-5001) using the ChemiDoc Imaging System (AI600). The data were analyzed by ImageJ and normalized with control (as mentioned in the figure legend).

Cell Proliferation Assay

NIH/3T3 fibroblasts were seeded at a density of 2×10^3 per well into 96-well plates and were then treated with BMDM exosomes or pretreated with DSF (5 μM). The cell proliferation was assessed using the BeyoClick™ 5-ethynyl-2′-deoxyuridine (EdU) cell proliferation kit with TMB (Beyotime Biotechnology, Jiangsu,

China). This method is based on EdU acting as a novel alternative for 5-bromo-2′-deoxyuridine (BrdU) assay to directly measure the DNA synthesis or S-phase synthesis of a cell cycle *via* the reaction with fluorescent azide. The absorbance was measured at 630 OD. The experiment was performed in triplicate.

Wound Healing

NIH/3T3 fibroblasts were cultured and marked a line at the bottom. After the cells were found to cover the bottom of the plate, a 1 ml pipette tip was used to make cell scratches perpendicular to the well plate, and it was ensured that the width of each scratch remained the same. The cell culture medium was aspirated, and the well plate was rinsed three times with PBS to wash away the cell debris generated by the scratch. Thereafter, a serum-free medium was added, and pictures were taken and recorded. The culture plate was placed into the incubator for culture and was taken out every 4–6 h to capture the pictures. The experimental results were analyzed according to the collected picture data.

Morphological Analysis of Macrophages

BMDMs were isolated from the mice, seeded in the six-well plate (Life Technologies), and the cells were allowed to adhere overnight at 37°C. The cells were stimulated with LPS (100 ng/ml) for 12 h after serum starvation. For inhibitor analysis, the cells were preincubated with DSF (4 μM) or DMSO (0.01%) for 1 h. The confocal images were obtained using an FV3000 confocal system (Olympus), and the data were analyzed with ImageJ (NIH, V2.0.0).

Statistical Analyses

The results have been expressed as mean ± SEM. Unpaired Student's *t*-tests were used to compare the means of the two different groups. One-way analysis of variance (Tukey test) was applied to compare the means of three or more groups. The Wilcoxon (Gehan) statistical test was used to analyze the survival rate.

RESULTS

An Increase in Pro-inflammatory Phenotype of Macrophages and Peritendinous Fibrosis Was Observed in Mouse TI

Persistent immune cell activation, as well as upregulation of pro-fibrotic cytokines and ECM proteins, has been reported to be involved in fibrotic diseases (Chen et al., 2017; Pakshir and Hinz, 2018). We investigated the potential role of macrophage and ECM proteins in TI. There was a significantly increased expression of pro-fibrotic markers in the TI group compared with the control (**Figure 1**). The flexor tendons and surrounding tissues showed F4/80-positive staining and displayed an increased an α-SMA immunofluorescence signal in the TI group compared with the control (**Figure 1C**). The results of H&E also showed increased cells and cell nuclear staining in flexor tendons and surrounding tissues (**Figure 1D**). We then isolated BMDMs from control and TI mice. Interestingly, we found that BMDMs from the TI group showed increased expression of F4/80 compared with BMDMs from the control group (**Figure 1E**). The intrinsic gene expression of macrophages can effectively change and polarize into two distinct types, M1-type macrophages and M2-type macrophages (Wang et al., 2021). The intensity of iNOS and TNF-α in BMDMs was significantly increased from the TI group as compared with the control (**Figure 1**), thereby indicating the phenotype of M1-type macrophage in BMDM from TI mice. Collectively, these results suggested that pro-inflammatory macrophage and fibrosis were significantly activated in TI mice.

DSF Decreased Macrophage Pro-inflammatory Phenotype and Can Promote the Transition of Macrophage From M1 to M2 Phenotype

It has been established that the different tissue microenvironment and pathological conditions can facilitate the polarization of macrophages into the M2 type, which can then secrete the various anti-inflammatory cytokines and promote fibrocartilage regeneration, thus promoting the healing of TI (Dong et al., 2021). To identify whether the macrophage pro-inflammatory phenotype could be modulated by a pharmacological agent, we performed a screen of 54 natural small-molecular compounds to analyze their effects on CD106, a critical marker of the M2 phenotype (**Figure 2A**). BMDMs were isolated from the tibia of C57BL mice and pre-incubated with small-molecular compounds in a 96-well plate. BMDMs were induced by M-CSF, and cells were then treated with LPS, IFN-γ, and IL-4 for 6 h. The flow cytometry analysis showed that the ninth compound, marketed as DSF, significantly promoted the expression of CD206 (**Figure 2B**). We further investigated the markers of M1- and M2-type macrophages. The percentage and geometric mean of both iNOS and TNF-α were substantially suppressed by DSF (**Figure 2**), while the expression levels of CD86 and CD206 were increased after treatment with DSF (**Figure 2**). We also detected the cell viability of BMDMs by using the CCK-8 assay, and the results showed no significant differences between DMSO and DSF treatments. These findings indicated that DSF could significantly promote the M2-type macrophage transformation of BMDMs after LPS, IFN-γ, and IL-4 treatments.

DSF Suppressed Peritendinous Fibrosis in TI

To assess the possible role of DSF in peritendinous fibrosis following TI, mice were treated with DSF through oral administration after tendon surgery. Mice were randomly assigned to the following three groups: sham operation, TI with acetylcellulose, and TI with DSF (**Figure 3A**). The histological analysis showed significantly reduced adhesion formation and inflammatory cell infiltration and fibroblasts accumulating in the tendon–bone interface in TI mice after DSF treatment (**Figure 3B**). The immunohistochemical staining for collagen I was also robust in TI mice and significantly suppressed after DSF treatment (**Figure 3B**). Consistent with these results, the histological adhesion score was markedly higher in the TI than in the TI-with-DSF treatment group, thus indicating decreased fibrogenesis in the latter (**Figure 3C**). We also measured the metatarsophalangeal (MTP) joint flexion range of motion (ROM) in mice that underwent

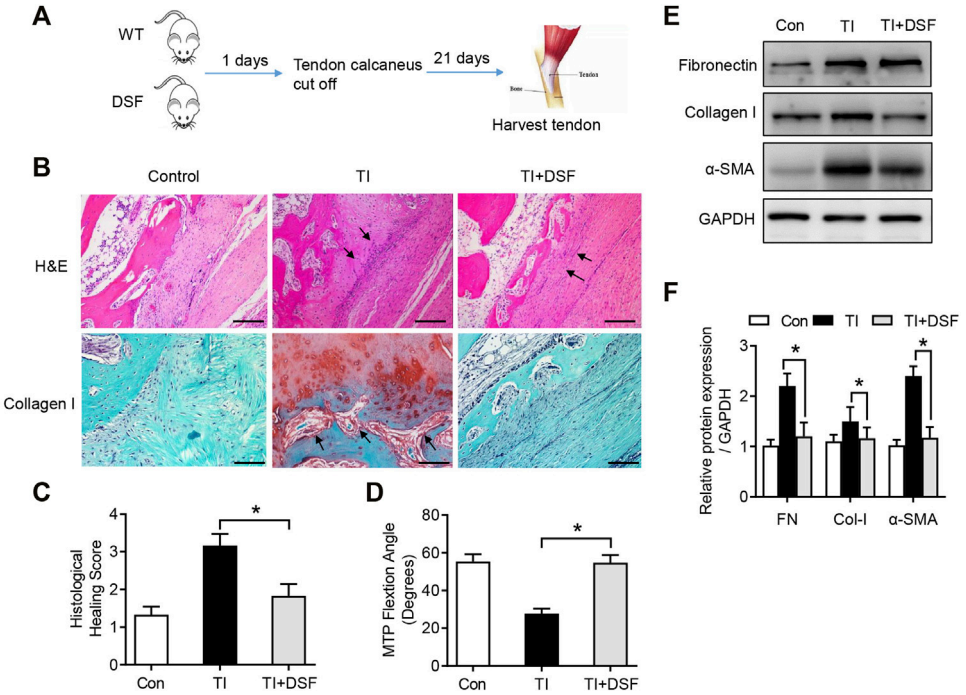

FIGURE 3 | DSF rescued peritendinous fibrosis in TI. **(A)** The diagram of mouse model conduction. **(B)** H&E and immunohistological staining of Col-I in the control, TI, and TI oral with DSF (50 mg/kg) mouse groups. Scale bar = 200 μm. **(C)** Histological adhesion score and histological healing score from the indicated groups (n = 6 per group). **(D)** MTP joint flexion ROM of the indicated groups (n = 6 per group). **(E)** Western blot analysis of FN, Col-I, and α-SMA in tendon (n = 6 per group). Data are presented as the mean ± SEM (n = 6) **(C,D)**. *p < 0.05.

flexor tendon surgery. There was a significant decrease of the MTP joint ROM in TI mice, which was substantially reduced after DSF treatment (**Figure 3D**). As peritendinous fibrosis is manifested by the excessive production of ECM proteins FN, collagen type I (Col-I), and α-SMA in TI (Harvey et al., 2019; Liu et al., 2021), we next assessed the expression of these pro-fibrotic markers in tendons by western blot analysis. The results showed increased levels of FN, Col-I, and α-SMA in TI mice compared with the control. However, the increased pro-fibrotic markers were significantly suppressed in TI mice after DSF treatment (**Figure 3E**). Overall, these results suggested that DSF suppressed peritendinous fibrosis and can serve as a potential therapeutic agent in TI mice.

DSF Inhibited Pro-inflammatory Cytokine Production and Macrophage Polarization

DSF has recently been identified as a potent inhibitor of GSDMD-mediated pyroptosis and inflammatory cytokine release (Hu et al., 2020). We next investigated the pro-inflammatory cytokine production and GSDMD pathway in the repaired tendons. The levels of IL-1β, IL-1α, and HMGB1 were significantly increased in TI mice. DSF markedly suppressed the expression of these pro-inflammatory cytokines (**Figure 4A**). In addition, we observed an increased expression of GSDMD and a detected band of GSDMD-N terminal in TI mice (**Figure 4**). GSDMD activation has been reported to be mediated by the pyroptotic caspase-1, caspase-4, and caspase-5 in humans and caspase-1 and caspase-11 in mice (Kesavardhana et al., 2020). We then investigated the expression of caspase-1 and caspase-11. Western blot showed that the expression levels of caspase-1 and caspase-11 proteins were increased in TI mice. The cleaved GSDMD-N was significantly suppressed after DSF treatment. However, the expression levels of caspase-1 and caspase-11 proteins were not suppressed by DSF (**Figure 4**). We also induced BMDMs from the control, TI, and TI + DSF mice. The results indicated that the population of F4/80 in BMDM was suppressed in TI mice after DSF treatment (**Figure 4E**). To further explore the potential role of DSF on M2 macrophages, we observed altered morphology in *ex vivo* cultured BMDMs after LPS treatment. LPS induced lamellipodia-like structures while DSF-treated macrophages showed filopodia-like structures (**Figure 4F**). Collectively, these results suggested that DSF significantly suppressed pro-inflammatory cytokine production and M1-type macrophage population in TI mice.

DSF Suppressed Fibroblast Activation and Proliferation After BMDM Exosome Treatment

Excessive fibroblast proliferation is an important pathological characteristic of peritendinous fibrosis after TI (Zheng et al., 2017). A number of recent studies have indicated that macrophage-derived exosomes can promote proliferation, migration, and fibrotic activity of fibroblast (Cui et al., 2019). To determine whether DSF was required for fibroblast proliferation and

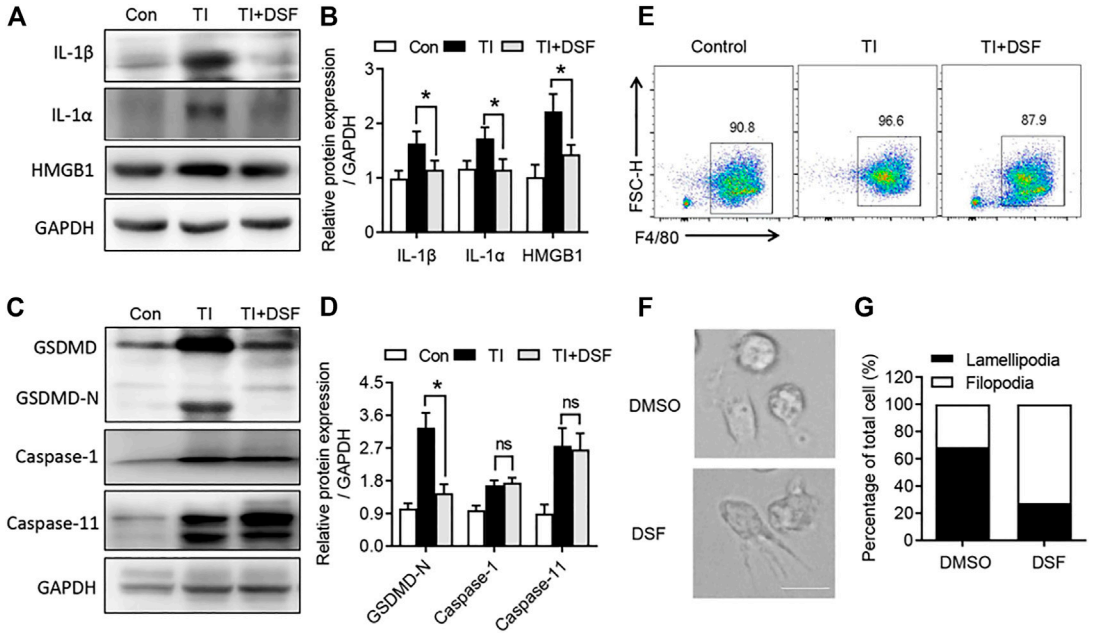

FIGURE 4 | DSF inhibited GSDMD-dependent cell pyroptosis and inflammatory cytokine release. **(A)** Western blot analysis of IL-1β, IL-1α, and HMGB1 in tendon from control, TI, and TI oral with DSF mouse groups. **(B)** Quantitative analysis of IL-1β, IL-1α, and HMGB1 in **A**. **(C)** Western blot analysis of GSDMD, GSDMD-N, caspase-1, and caspase-11 in tendon from the indicated groups. **(D)** Quantitative analysis of GSDMD-N, caspase-1, and caspase-11 in **C**. **(E)** FACS of M-CSF-induced macrophages (F4/80$^+$) from control, TI, and TI oral with DSF mouse groups. **(F,G)** BMDMs were pretreated with DMSO or DSF (5 μM) for 2 h. Then the cells were treated with LPS (100 ng/ml), IFN-γ (20 ng/ml), and IL-4 (20 ng/ml) for 6 h. The morphology of macrophages was observed by differential interference-contrast microscopy **(F)** and ratios of lamellipodial to filopodial macrophages **(G)**. Data are presented as the mean ± SEM (n = 6) **(B, D)**. *p < 0.05.

activity after BMDM exosome treatment, NIH/3T3 fibroblasts were cultured and treated with macrophage-derived exosomes. Western blot analysis showed increased FN, Col-I, and α-SMA expression in the cultured fibroblast with BMDM exosome treatment, while DSF significantly suppressed the expression of these pro-fibrotic markers (**Figure 5**). Subsequent analysis of proliferation revealed a significant upregulation of EdU in the fibroblast after BMDM exosome treatment (**Figure 5C**), which was attenuated after DSF treatment. Moreover, the increased phase of G2/M plus S after BMDM exosome treatment was significantly suppressed by DSF (**Figure 5**). We further detected the migration capacity of fibroblast by crystal violet staining (**Figure 5**) and scratch test (**Figure 5**). The increased upregulation of migration capacity of fibroblast after BMDM exosome treatment was found to be significantly suppressed by DSF. These *in vitro* data support evidence for a pro-fibrogenic role of BMDM exosomes in fibroblast, and DSF can be an effective therapeutic agent for modulating BMDM exosome-induced fibroblast proliferation and migration.

DISCUSSION

The communication between macrophages and peritendinous fibroblast plays an essential role in the tendon-healing process. Presently, there is considerable interest in tendon–bone injury that can specifically target macrophage activity, such as macrophage-derived miRNA, exosomes, or chemokines (Gelberman et al., 2017; Cui et al., 2019; Lehner et al., 2019). In this study, we have revealed a critical role of DSF in macrophage polarization and peritendinous fibrosis. In addition, a significant reduction in the levels of various pro-inflammatory cytokines such as IL-1β, TNF-α, and HMGB1 in TI mice was noted after DSF treatment. We also found that DSF significantly suppressed fibroblast activation and proliferation after BMDM exosome treatment. Furthermore, we detected the cleaved GSDMD-N and pro-inflammatory cytokines in the healing tendon of TI mice. These findings reveal the possible involvement of a novel pathway of GSDMD-dependent macrophage cell pyroptosis in remodeling fibrogenesis in tendon–bone injury. GSDMD inhibitor DSF may thus function as potential therapeutic agent in tendon–bone injury.

Infiltration of macrophages to cause tendon–bone damage has recently been increasingly associated with peritendinous adhesion (Cai et al., 2021). In an *in vitro* study, M-CSF-induced BMDMs displayed an increased F4/80 staining in the TI mice than in the control. Through systematically screening a compound library, we found that DSF significantly suppressed pro-inflammatory-type macrophages and facilitated the transformation of M2-type macrophages as indicated by increased expression levels of CD86 and CD206. The results suggested that DSF can be a therapeutic target of immune cells in remodeling tendon–bone injury. It has been established that the initiation of tendon pathology depends upon immune cell infiltration and pro-inflammatory cytokine production, such as

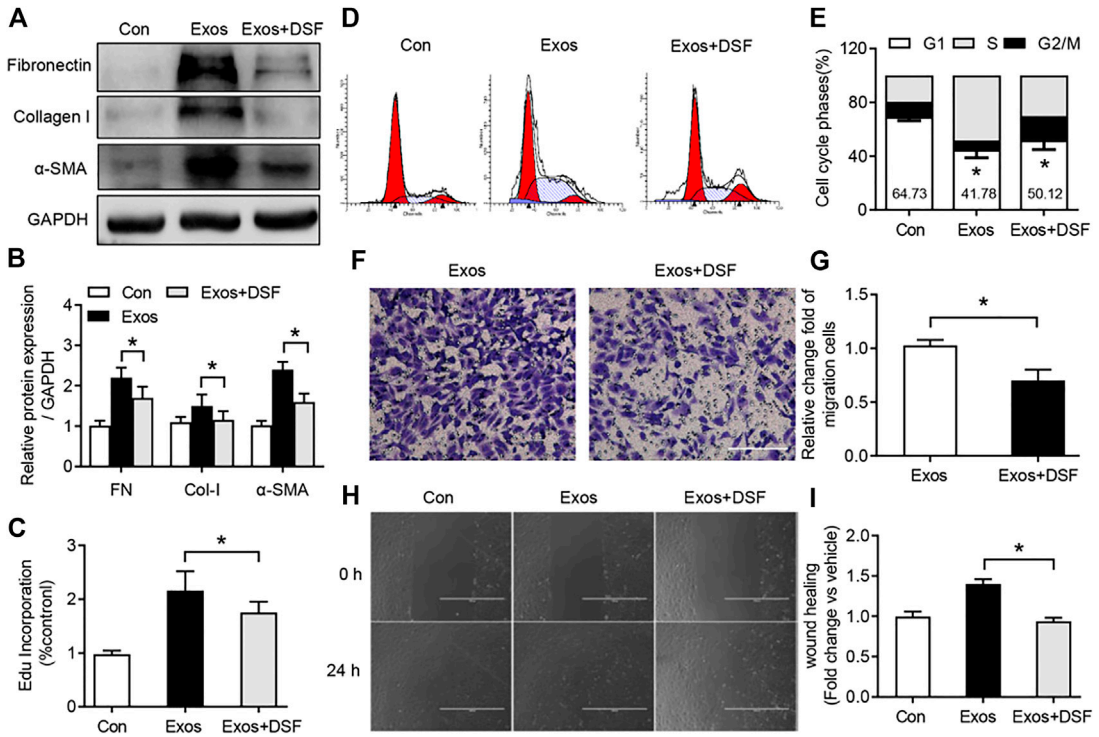

FIGURE 5 | DSF significantly reduced fibroblast activation and proliferation after BMDM exosome treatment. NIH/3T3 fibroblasts were cultured and treated with macrophage-derived exosomes. Cells were pretreated with DSF (5 μM) or DMSO (0.01%) for 2 h. **(A,B)** Western blot **(A)** and quantitative **(B)** analyses of FN, Col-I, and α-SMA in fibroblast from control, exosomes, and exosomes in the presence of DSF. **(C)** Quantitative analysis of EdU incorporation in fibroblast from control, exosomes, and exosomes in the presence of DSF. **(D,E)** FACS **(D)** and quantitative **(E)** analysis of cell cycle in fibroblast from control, exosomes, and exosomes in the presence of DSF. **(F,G)** The picture **(F)** and quantitative analysis **(G)** of the cell migration in fibroblast from control, exosomes, and exosomes in the presence of DSF. Scale bar = 20 μm. **(H,I)** The picture **(H)** and quantitative analysis **(I)** of the cell wound scratch assay in fibroblast from control, exosomes, and exosomes in the presence of DSF. Scale bar = 20 μm. Data are presented as the mean ± SEM (n = 3) **(B,C,E,G,I)**. *$p < 0.05$.

IL-6 and TNF-α (Kawamura et al., 2005; Stauber et al., 2021). In addition, TI can elicit an increase in macrophage accumulation from 1 to 28 days in Achilles TI (Marsolais et al., 2001). Furthermore, it has been reported that there was an increased infiltration of macrophages in torn supraspinatus tendon from human tendinopathy (Millar et al., 2010), and the NF-κB pathway was found to be upregulated in fibrous tissue formed around the tendon in both human and rat samples (Chen et al., 2017). Moreover, although macrophages can regulate the TI through releasing several pro-inflammatory cytokines, growth factors, or exosomes, whether there are any small-molecular compounds that can potentially mediate the crosstalk between macrophage and peritendinous fibroblast is not fully understood.

For an *in vivo* study, we have used a mouse model wherein mice underwent transection and repair of the FDL tendon in the right hind paw. This mouse model has a peritendinous fibrosis formation around the injured tendon (Ackerman and Loiselle, 2016; Lin et al., 2020). The results of our study also showed increased F4/80-positive stained cells around α-SMA cells, which clearly indicated the mutual activation of both macrophage and fibroblast. A number of previous studies have identified that macrophages are necessary for peritendinous fibrosis in this mouse model by facilitating macrophage depletion with clodronate liposomes (Cui et al., 2019). This enabled us to investigate whether inflammatory cytokines or damage-associated molecular patterns (DAMPs) that are released from macrophages might play an essential role in TI mice. The data showed that the levels of macrophage-derived IL-1β, IL-1α, or HMGB1 were significantly increased in healing tendon. The significant abundance of IL-1β, IL-1α, or HMGB1 in healing tendon may be attributed to enhanced inflammatory response, which can increase the accumulation of macrophage to the injured site (Gelberman et al., 2017; Li et al., 2021). Our immunofluorescence data also indicated increased macrophage infiltration, accompanied with peritendinous fibroblast activation in tendon bone injury, thereby suggesting that BMDM can serve as important mediators of the peritendinous fibrosis. The regulation of the pro-inflammatory phenotype macrophage transformation may act as an important messenger in mediating intercellular crosstalk between immune cells and resident tenocyte or fibroblast.

Although DSF has been used as an FDA-approved drug for treating alcohol addiction, recent studies have revealed its novel biological effects including antitumor and antimetabolic activities in diverse models (Author Anonymous, 2018; Bernier et al., 2020). In our *in vivo* study, we demonstrated that DSF alleviated peritendinous tissue fibrosis lesions after the TI. It

has been suggested that the application of DSF may be limited *in vivo* due to low water solubility, poor stability, and rapid metabolism. In live animals, orally administered DSF can be metabolized into dithiocarbamate (DTC) or DSF/Cu complex (Zhou et al., 2018; Wu et al., 2019), and it has been identified that the DSF/Cu complex can directly bind to nuclear protein localization 4 (NPL4) and promote cell apoptosis (Skrott et al., 2017). So further studies are needed to identify whether DTC or DSF/Cu complex can act as important mediators in TI. Our *in vitro* data showed that DSF exhibited a potent antifibrotic effect by, modulating the expression of various fibrotic markers such as FN, Col-I, and α-SAM in fibroblasts after BMDM exosome treatment. BMDM exosomes have previously been shown to promote fibrosis in tendon–bone injury (Cui et al., 2019). Our studies also demonstrated that DSF can significantly reduce the cell proliferation and migration after BMDM exosome treatment. These results indicated that there might be distinct effects of DSF on both the macrophages and fibroblasts. Since DSF dysregulated the p97-NPL4-ubiquitin fusion degradation protein 1 (UFD1) pathway, the effect of DSF on fibroblast proliferation and migration may be primarily dependent on the erroneous protein accumulation and cell death. Further studies are required to investigate the precise mechanism of action of DSF on fibroblasts.

GSDMD has been recently identified as a pyroptotic executioner, which can participate in the numerous diseases, such as acute kidney injury, alcoholic hepatitis, or neuroinflammation (Khanova et al., 2018; Li et al., 2019; Miao et al., 2019). Our results showed that the cleaved N-terminal of GSDMD was predominantly detected in tendon–bone injury, and the level of IL-1β was significantly suppressed after DSF treatment. In recent years, expression and activation of GSDMD have been reported in macrophages, and GSDMD-dependent pore formation can act as a conduit for IL-1β secretion (Heilig et al., 2018). GSDMD contains the N-terminal GSDMD-N domain and the C-terminal GSDMD-C domain, which are linked together by a long loop (Shi et al., 2017). The cleaved GSDMD-N thus oligomerizes in the membranes, causes lytic cells, and stimulates IL-1β release. GSDMD is widely expressed in the different tissues and cell types, with high levels of expression in the macrophages and gastrointestinal epithelia (Saeki et al., 2000). Since the whole protein in western blot contains tenocytes, fibroblasts, and macrophages, further investigations are needed to identify whether GSDMD can also be expressed in tenocyte cells and whether tenocyte cells can undergo pyroptosis during the TI.

In conclusion, the data generated in the present study highlighted an important role of DSF-mediated macrophage polarization as a potential driver of TI mice. We found that TI can trigger the upregulation of different pro-inflammatory cytokines. Our results also suggest an essential role of DSF for peritendinous fibrosis. Moreover, the FDA-approved drug DSF, which is used to treat alcohol addiction, has been recently shown to inhibit GSDMD pore formation. We found that DSF was able to effectively inhibit pyroptosis and IL-1β release from M1-type macrophages. Given the significant unmet clinical needs of TI patients, the therapeutic potential of the repurposing of this drug as a means of treating TI warrants further studies.

DATA AVAILABILITY STATEMENT

The raw data supporting the conclusion of this article will be made available by the authors, without undue reservation.

ETHICS STATEMENT

The animal study was reviewed and approved by the Navy Medical University Animal Care and Use Committee.

AUTHOR CONTRIBUTIONS

QZ performed the experiments and wrote the manuscript, YX designed the experiments, and YZ and PF analyzed the data and interpreted the results. WW, FY, HW, and XZ helped with the experiments. YX, YZ, and PF supervised the study and wrote the manuscript.

FUNDING

This work was supported by grants from the National Natural Science Foundation of China (81702209).

SUPPLEMENTARY MATERIAL

The Supplementary Material for this article can be found online at: https://www.frontiersin.org/articles/10.3389/fbioe.2022.823933/full#supplementary-material

REFERENCES

Ackerman, J. E., and Loiselle, A. E. (2016). Murine Flexor Tendon Injury and Repair Surgery. *J. Vis. Exp.* (115), 54433. doi:10.3791/54433

Alvarez, P. B., Laskaris, A., Goyeneche, A. A., Chen, Y., Telleria, C. M., and Burnier, J. V. (2021). Anticancer Effects of Mifepristone on Human Uveal Melanoma Cells. *Cancer Cel Int* 21, 607. doi:10.1186/s12935-021-02306-y

Author Anonymous (2018). The Alcohol-Abuse Drug Disulfiram Targets NPL4 to Exert Antitumor Effects. *Cancer Discov.* 8, OF7. doi:10.1158/2159-8290.CD-RW2017-235

Bernier, M., Mitchell, S. J., Wahl, D., Diaz, A., Singh, A., Seo, W., et al. (2020). Disulfiram Treatment Normalizes Body Weight in Obese Mice. *Cel Metab.* 32, 203–214. doi:10.1016/j.cmet.2020.04.019

Bista, R., Lee, D. W., Pepper, O. B., Azorsa, D. O., Arceci, R. J., and Aleem, E. (2017). Disulfiram Overcomes Bortezomib and Cytarabine Resistance in Down-Syndrome-Associated Acute Myeloid Leukemia Cells. *J. Exp. Clin. Cancer Res.* 36, 22. doi:10.1186/s13046-017-0493-5

Cai, C., Zhang, X., Li, Y., Liu, X., Wang, S., Lu, M., et al. (2021). Self-healing Hydrogel Embodied with Macrophage-Regulation and Responsive-Gene-Silencing Properties for Synergistic Prevention of Peritendinous Adhesion. *Adv. Mater.* 34 (5), e2106564. doi:10.1002/adma.202106564

Chamberlain, C. S., Kink, J. A., Wildenauer, L. A., McCaughey, M., Henry, K., Spiker, A. M., et al. (2021). Exosome-Educated Macrophages and Exosomes Differentially Improve Ligament Healing. *Stem Cells* 39, 55–61. doi:10.1002/stem.3291

Chen, S., Jiang, S., Zheng, W., Tu, B., Liu, S., Ruan, H., et al. (2017). RelA/p65 Inhibition Prevents Tendon Adhesion by Modulating Inflammation, Cell Proliferation, and Apoptosis. *Cell Death Dis* 8, e2710. doi:10.1038/cddis.2017.135

Cui, H., He, Y., Chen, S., Zhang, D., Yu, Y., and Fan, C. (2019). Macrophage-Derived miRNA-Containing Exosomes Induce Peritendinous Fibrosis after Tendon Injury through the miR-21-5p/Smad7 Pathway. *Mol. Ther. - Nucleic Acids* 14, 114–130. doi:10.1016/j.omtn.2018.11.006

Darby, I. A., Zakuan, N., Billet, F., and Desmoulière, A. (2016). The Myofibroblast, a Key Cell in normal and Pathological Tissue Repair. *Cell. Mol. Life Sci.* 73, 1145–1157. doi:10.1007/s00018-015-2110-0

Dong, L., Li, L., Song, Y., Fang, Y., Liu, J., Chen, P., et al. (2021). MSC-Derived Immunomodulatory Extracellular Matrix Functionalized Electrospun Fibers for Mitigating Foreign-Body Reaction and Tendon Adhesion. *Acta Biomater.* 133, 280–296. doi:10.1016/j.actbio.2021.04.035

Gelberman, R. H., Linderman, S. W., Jayaram, R., Dikina, A. D., Sakiyama-Elbert, S., Alsberg, E., et al. (2017). Combined Administration of ASCs and BMP-12 Promotes an M2 Macrophage Phenotype and Enhances Tendon Healing. *Clin. Orthop. Relat. Res.* 475, 2318–2331. doi:10.1007/s11999-017-5369-7

Harvey, T., Flamenco, S., and Fan, C.-M. (2019). A Tppp3+Pdgfra+ Tendon Stem Cell Population Contributes to Regeneration and Reveals a Shared Role for PDGF Signalling in Regeneration and Fibrosis. *Nat. Cel Biol* 21, 1490–1503. doi:10.1038/s41556-019-0417-z

Heilig, R., Dick, M. S., Sborgi, L., Meunier, E., Hiller, S., and Broz, P. (2018). The Gasdermin-D Pore Acts as a Conduit for IL-1β Secretion in Mice. *Eur. J. Immunol.* 48, 584–592. doi:10.1002/eji.201747404

Hu, J. J., Liu, X., Xia, S., Zhang, Z., Zhang, Y., Zhao, J., et al. (2020). FDA-Approved Disulfiram Inhibits Pyroptosis by Blocking Gasdermin D Pore Formation. *Nat. Immunol.* 21, 736–745. doi:10.1038/s41590-020-0669-6

Jiang, S., Zhao, X., Chen, S., Pan, G., Song, J., He, N., et al. (2014). Down-Regulating ERK1/2 and SMAD2/3 Phosphorylation by Physical Barrier of Celecoxib-Loaded Electrospun Fibrous Membranes Prevents Tendon Adhesions. *Biomaterials* 35, 9920–9929. doi:10.1016/j.biomaterials.2014.08.028

Juneja, S. C., Schwarz, E. M., O'Keefe, R. J., and Awad, H. A. (2013). Cellular and Molecular Factors in Flexor Tendon Repair and Adhesions: a Histological and Gene Expression Analysis. *Connect. Tissue Res.* 54, 218–226. doi:10.3109/03008207.2013.787418

Kawamura, S., Ying, L., Kim, H.-J., Dynybil, C., and Rodeo, S. A. (2005). Macrophages Accumulate in the Early Phase of Tendon-Bone Healing. *J. Orthop. Res.* 23, 1425–1432. doi:10.1016/j.orthres.2005.01.014.1100230627

Kesavardhana, S., Malireddi, R. K. S., and Kanneganti, T. D. (2020). Caspases in Cell Death, Inflammation, and Gasdermin-Induced Pyroptosis. *Annu. Rev. Immunol.* 38, 567–595. doi:10.1146/annurev-immunol-073119-095439

Khanova, E., Wu, R., Wang, W., Yan, R., Chen, Y., French, S. W., et al. (2018). Pyroptosis by Caspase11/4-Gasdermin-D Pathway in Alcoholic Hepatitis in Mice and Patients. *Hepatology* 67, 1737–1753. doi:10.1002/hep.29645

Klimiankou, M., and Skokowa, J. (2021). Old Drug Revisited: Disulfiram, NETs, and Sepsis. *Blood* 138, 2604–2605. doi:10.1182/blood.2021013438

Klopfleisch, R. (2016). Macrophage Reaction against Biomaterials in the Mouse Model - Phenotypes, Functions and Markers. *Acta Biomater.* 43, 3–13. doi:10.1016/j.actbio.2016.07.003

Lehner, C., Spitzer, G., Gehwolf, R., Wagner, A., Weissenbacher, N., Deininger, C., et al. (2019). Tenophages: A Novel Macrophage-Like Tendon Cell Population Expressing CX3CL1 and CX3CR1. *Dis. Model. Mech.* 12 (12), dmm041384. doi:10.1242/dmm.041384

Li, S., Xu, Z., Wang, Z., Xiang, J., Zhang, T., and Lu, H. (2021). Acceleration of Bone-Tendon Interface Healing by Low-Intensity Pulsed Ultrasound Is Mediated by Macrophages. *Phys. Ther.* 101 (7), pzab055. doi:10.1093/ptj/pzab055

Li, S., Wu, Y., Yang, D., Wu, C., Ma, C., Liu, X., et al. (2019). Gasdermin D in Peripheral Myeloid Cells Drives Neuroinflammation in Experimental Autoimmune Encephalomyelitis. *J. Exp. Med.* 216, 2562–2581. doi:10.1084/jem.20190377

Lin, A. H., Allan, A. N., Zitnay, J. L., Kessler, J. L., Yu, S. M., and Weiss, J. A. (2020). Collagen Denaturation Is Initiated upon Tissue Yield in Both Positional and Energy-Storing Tendons. *Acta Biomater.* 118, 153–160. doi:10.1016/j.actbio.2020.09.056

Liu, Q., Zhu, Y., Zhu, W., Zhang, G., Yang, Y. P., and Zhao, C. (2021). The Role of MicroRNAs in Tendon Injury, Repair, and Related Tissue Engineering. *Biomaterials* 277, 121083. doi:10.1016/j.biomaterials.2021.121083

Loiselle, A. E., Bragdon, G. A., Jacobson, J. A., Hasslund, S., Cortes, Z. E., Schwarz, E. M., et al. (2009). Remodeling of Murine Intrasynovial Tendon Adhesions Following Injury: MMP and Neotendon Gene Expression. *J. Orthop. Res.* 27, 833–840. doi:10.1002/jor.20769

Manske, P. R. (2005). History of Flexor Tendon Repair. *Hand Clin.* 21, 123–127. doi:10.1016/j.hcl.2004.03.004

Marsolais, D., Cote, C. H., and Frenette, J. M. (2001). Neutrophils and Macrophages Accumulate Sequentially Following Achilles Tendon Injury. *J. Orthop. Res.* 19, 1203–1209. doi:10.1016/s0736-0266(01)00031-6

Miao, N., Yin, F., Xie, H., Wang, Y., Xu, Y., Shen, Y., et al. (2019). The Cleavage of Gasdermin D by Caspase-11 Promotes Tubular Epithelial Cell Pyroptosis and Urinary IL-18 Excretion in Acute Kidney Injury. *Kidney Int.* 96, 1105–1120. doi:10.1016/j.kint.2019.04.035

Millar, N. L., Hueber, A. J., Reilly, J. H., Xu, Y., Fazzi, U. G., Murrell, G. A. C., et al. (2010). Inflammation Is Present in Early Human Tendinopathy. *Am. J. Sports Med.* 38, 2085–2091. doi:10.1177/0363546510372613

Pakshir, P., and Hinz, B. (2018). The Big Five in Fibrosis: Macrophages, Myofibroblasts, Matrix, Mechanics, and Miscommunication. *Matrix Biol.* 68-69, 81–93. doi:10.1016/j.matbio.2018.01.019

Saeki, N., Kuwahara, Y., Sasaki, H., Satoh, H., and Shiroishi, T. (2000). Gasdermin (Gsdm) Localizing to Mouse Chromosome 11 Is Predominantly Expressed in Upper Gastrointestinal Tract but Significantly Suppressed in Human Gastric Cancer Cells. *Mamm. Genome* 11, 718–724. doi:10.1007/s003350010138

Shi, J., Gao, W., and Shao, F. (2017). Pyroptosis: Gasdermin-Mediated Programmed Necrotic Cell Death. *Trends Biochemical Sciences* 42, 245–254. doi:10.1016/j.tibs.2016.10.004

Skrott, Z., Mistrik, M., Andersen, K. K., Friis, S., Majera, D., Gursky, J., et al. (2017). Alcohol-Abuse Drug Disulfiram Targets Cancer via P97 Segregase Adaptor NPL4. *Nature* 552, 194–199. doi:10.1038/nature25016

Stauber, T., Wolleb, M., Duss, A., Jaeger, P. K., Heggli, I., Hussien, A. A., et al. (2021). Extrinsic Macrophages Protect while Tendon Progenitors Degrade: Insights from a Tissue Engineered Model of Tendon Compartmental Crosstalk. *Adv. Healthc. Mater.* 10, e2100741. doi:10.1002/adhm.202100741

Wang, C., Zhang, Y., Zhang, G., Yu, W., and He, Y. (2021). Adipose Stem Cell-Derived Exosomes Ameliorate Chronic Rotator Cuff Tendinopathy by Regulating Macrophage Polarization: From a Mouse Model to a Study in Human Tissue. *Am. J. Sports Med.* 49, 2321–2331. doi:10.1177/03635465211020010

Wang, Y., He, G., Tang, H., Shi, Y., Zhu, M., Kang, X., et al. (2020). Aspirin Promotes Tenogenic Differentiation of Tendon Stem Cells and Facilitates Tendinopathy Healing through Regulating the GDF7/Smad1/5 Signaling Pathway. *J. Cel Physiol* 235, 4778–4789. doi:10.1002/jcp.29355

Wu, W., Yu, L., Jiang, Q., Huo, M., Lin, H., Wang, L., et al. (2019). Enhanced Tumor-specific Disulfiram Chemotherapy by *In Situ* Cu2+ Chelation-Initiated Nontoxicity-To-Toxicity Transition. *J. Am. Chem. Soc.* 141, 11531–11539. doi:10.1021/jacs.9b03503

Yao, Z., Wang, W., Ning, J., Zhang, X., Zheng, W., Qian, Y., et al. (2019). Hydroxycamptothecin Inhibits Peritendinous Adhesion via the Endoplasmic Reticulum Stress-dependent Apoptosis. *Front. Pharmacol.* 10, 967. doi:10.3389/fphar.2019.00967

Yu, Y., Sun, B., Wang, Z., Yang, M., Cui, Z., Lin, S., et al. (2021). Exosomes from M2 Macrophage Promote Peritendinous Fibrosis Posterior Tendon Injury via the MiR-15b-5p/FGF-1/7/9 Pathway by Delivery of circRNA-Ep400. *Front. Cel Dev. Biol.* 9, 595911. doi:10.3389/fcell.2021.595911

Zheng, W., Chen, C., Chen, S., Fan, C., and Ruan, H. (2019). Integrated Analysis of Long Non-Coding RNAs and mRNAs Associated with Peritendinous Fibrosis. *J. Adv. Res.* 15, 49–58. doi:10.1016/j.jare.2018.08.001

Zheng, W., Song, J., Zhang, Y., Chen, S., Ruan, H., and Fan, C. (2017). Metformin Prevents Peritendinous Fibrosis by Inhibiting Transforming Growth Factor-β Signaling. *Oncotarget* 8, 101784–101794. doi:10.18632/oncotarget.21695

Zhou, L., Yang, L., Yang, C., Liu, Y., Chen, Q., Pan, W., et al. (2018). Membrane Loaded Copper Oleate PEGylated Liposome Combined with Disulfiram for Improving Synergistic Antitumor Effect *In Vivo*. *Pharm. Res.* 35, 147. doi:10.1007/s11095-018-2414-5

Conflict of Interest: The authors declare that the research was conducted in the absence of any commercial or financial relationships that could be construed as a potential conflict of interest.

Publisher's Note: All claims expressed in this article are solely those of the authors and do not necessarily represent those of their affiliated organizations, or those of the publisher, the editors, and the reviewers. Any product that may be evaluated in this article, or claim that may be made by its manufacturer, is not guaranteed or endorsed by the publisher.

Copyright © 2022 Zhou, Wang, Yang, Wang, Zhao, Zhou, Fu and Xu. This is an open-access article distributed under the terms of the Creative Commons Attribution License (CC BY). The use, distribution or reproduction in other forums is permitted, provided the original author(s) and the copyright owner(s) are credited and that the original publication in this journal is cited, in accordance with accepted academic practice. No use, distribution or reproduction is permitted which does not comply with these terms.

frontiers in Bioengineering and Biotechnology

REVIEW
published: 14 March 2022
doi: 10.3389/fbioe.2022.846230

Human Organ-on-a-Chip Microphysiological Systems to Model Musculoskeletal Pathologies and Accelerate Therapeutic Discovery

*Raquel E. Ajalik[1,2], Rahul G. Alenchery[1,2], John S. Cognetti[2], Victor Z. Zhang[1,2], James L. McGrath[2], Benjamin L. Miller[2,3] and Hani A. Awad[1,2]**

[1]*Center for Musculoskeletal Research, University of Rochester, Rochester, NY, United States,* [2]*Department of Biomedical Engineering, University of Rochester, Rochester, NY, United States,* [3]*Department of Dermatology, University of Rochester, Rochester, NY, United States*

OPEN ACCESS

Edited by:
Dmitriy Sheyn, Cedars Sinai Medical Center, United States

Reviewed by:
Gadi Pelled, Cedars Sinai Medical Center, United States
Mario Rothbauer, Medical University of Vienna, Austria

***Correspondence:**
Hani A. Awad
hani_awad@urmc.rochester.edu

Specialty section:
This article was submitted to Tissue Engineering and Regenerative Medicine, a section of the journal Frontiers in Bioengineering and Biotechnology

Received: *30 December 2021*
Accepted: *21 February 2022*
Published: *14 March 2022*

Citation:
Ajalik RE, Alenchery RG, Cognetti JS, Zhang VZ, McGrath JL, Miller BL and Awad HA (2022) Human Organ-on-a-Chip Microphysiological Systems to Model Musculoskeletal Pathologies and Accelerate Therapeutic Discovery. Front. Bioeng. Biotechnol. 10:846230. doi: 10.3389/fbioe.2022.846230

Human Microphysiological Systems (hMPS), otherwise known as organ- and tissue-on-a-chip models, are an emerging technology with the potential to replace *in vivo* animal studies with *in vitro* models that emulate human physiology at basic levels. hMPS platforms are designed to overcome limitations of two-dimensional (2D) cell culture systems by mimicking 3D tissue organization and microenvironmental cues that are physiologically and clinically relevant. Unlike animal studies, hMPS models can be configured for high content or high throughput screening in preclinical drug development. Applications in modeling acute and chronic injuries in the musculoskeletal system are slowly developing. However, the complexity and load bearing nature of musculoskeletal tissues and joints present unique challenges related to our limited understanding of disease mechanisms and the lack of consensus biomarkers to guide biological therapy development. With emphasis on examples of modeling musculoskeletal tissues, joints on chips, and organoids, this review highlights current trends of microphysiological systems technology. The review surveys state-of-the-art design and fabrication considerations inspired by lessons from bioreactors and biological variables emphasizing the role of induced pluripotent stem cells and genetic engineering in creating isogenic, patient-specific multicellular hMPS. The major challenges in modeling musculoskeletal tissues using hMPS chips are identified, including incorporating biological barriers, simulating joint compartments and heterogenous tissue interfaces, simulating immune interactions and inflammatory factors, simulating effects of *in vivo* loading, recording nociceptors responses as surrogates for pain outcomes, modeling the dynamic injury and healing responses by monitoring secreted proteins in real time, and creating arrayed formats for robotic high throughput screens. Overcoming these barriers will revolutionize musculoskeletal research by enabling physiologically relevant, predictive models of human tissues and joint diseases to accelerate and de-risk therapeutic discovery and translation to the clinic.

Keywords: organ-on-chip, tissue-on-chip, microphysiologic systems, musculoskeletal, muscle, bone, cartilage, tendon and ligament

1 INTRODUCTION

Musculoskeletal conditions encompass a wide spectrum of pain or damage associated with muscle, bone, cartilage, tendon, ligament, joints, and nerves. Injuries to musculoskeletal tissues are the leading cause of disability worldwide and often limit mobility and restrict the patients' ability to work or participate in recreational activities. As the mean age of the population increases, it is expected that the prevalence of musculoskeletal conditions and the associated socioeconomic burden will increase drastically in the coming decades (Sebbag et al., 2019). The most frequently reported musculoskeletal conditions in the US include arthritis, chronic joint pain, and back pain. Treatments typically prioritize pain-relief, including benzodiazepines, muscle relaxants, serotonin-norepinephrine reuptake inhibitors (SNRIs), non-steroidal anti-inflammatory drugs (NSAIDs), or combinations of those and other pain-relieving drugs (Hsu et al., 2019). While effective as palliative treatments, these are not disease-modifying or reparative drugs that address the molecular basis of the pathology. Therefore, there is a critical need for an improved understanding of the mechanisms of musculoskeletal pathologies to guide the development of drugs that resolve the underlying causes.

The process for drug and therapeutic discovery, development, and approval is arduous and costly. Discovery typically starts in academic or pharmaceutical laboratories. Unfortunately, many discoveries in academic laboratories fail to be reproducible or scaled up in pharmaceutical research and development laboratories. Leading drug candidates may be abandoned in the developmental "valley of death" because they are too slow or too costly to develop. And even well-funded efforts can fail in clinical trials despite promising preclinical findings. As a result, only ~10% of the therapeutic development pipelines entering phase I clinical trials typically proceed to FDA approval. Without a technological breakthrough that reduces risk and front-end investments required for drug development, these significant barriers will continue to hamper development and translation efforts (Hay et al., 2014).

Less than 8% of active interventional clinical trials of musculoskeletal diseases in the United States involve disease-modifying biological therapies, including stem cell therapy, growth factors and platelet-rich-plasma trials. The shortage of biological therapies for musculoskeletal conditions, excluding arthritis, highlights several issues for the field to recognize and tackle. The American Academy of Orthopedic Surgeons (AAOS) Symposium in 2015 identified the root cause as the incomplete knowledge of musculoskeletal disease mechanisms and a lack of reliable biomarkers to inform clinical trials (LaPrade et al., 2016). In addition to frequent findings of poor efficacy, late-stage clinical trials fail from flawed study designs, inappropriate statistical endpoints, drug safety, or underpowered clinical trials resulting from patient dropouts and insufficient enrollment (Fogel, 2018). Although not all these factors can be controlled, there is an opportunity to address efficacy and safety assessment of therapeutic candidates earlier in the preclinical stages with better models of human musculoskeletal disease.

The level of evidence obtained from preclinical studies using animal models and *in vitro* culture systems is constrained by the limitations of these models. Animal models have been the cornerstone of translatable biomedical research over the past century. Despite their undeniable value in biomedical research, animal models have numerous limitations that unfortunately have contributed to the arduous and costly new therapy development process. Animal studies are intrinsically low throughput and do not accurately predict the drug's effects and bioavailability in humans due to differences in pharmacokinetic and pharmacodynamic (PK/PD) responses. In addition, animal models used for biomedical studies are almost always inbred for research purposes and thus lack the genetic diversity of the human population. Lastly, studies of experimentally-induced acute or chronic musculoskeletal conditions do not use consensus models to allow uniformity in outcomes and valid interpretations of different experiments. Current *in vitro* culture models represent artificial, non-physiological conditions, mostly consisting of a single cell type or at best co-cultures of two cell types, to simulate the paracrine signaling between immune cells (e.g., macrophages) and mesenchymal cells (e.g., myocytes, fibroblasts, osteoblasts, osteocytes, and chondrocytes). Three dimensional (3D) scaffolds such as collagen are often used, but they are typically monocellular and not readily amenable to modeling the heterogeneity in a tissue. These systems are, therefore, inadequate to faithfully model treatment effects on acute or chronic musculoskeletal conditions or predict clinical outcomes.

Biomedical innovations such as induced pluripotent stem cells (iPSCs) from adult somatic cells (Takahashi and Yamanaka, 2006), CRISPR/CAS for gene editing (Jinek et al., 2012), and organ-on-a-chip (OoaC), also known as microphysiological systems (MPS), are ushering in an era where *in vitro* systems provide relevant, accessible, and flexible models of tissues and organs. MPS typically use microfluidic channels or compartments that model micro-scale units of multicellular tissues or organs (Bhatia and Ingber, 2014), tissue interfaces (Griep et al., 2013), and multi-organ systems (Sung et al., 2013). Ideally, MPS are allometrically scaled models of human tissues in their anatomical and physiological contexts. These technologies have various applications including disease modeling, drug discovery, toxicology screening, and personalized medicine (Esch et al., 2015). The integration of major tissues and organs in the human body in a single chip or connected chips to predict safety, efficacy and PK/PD of drug candidates in humans is one of the most exciting recent advances in the biomedical sciences (**Figure 1**). Therefore, MPS are a disruptive technology platform for evaluating safety and efficacy during the early stages of drug and therapeutic development and informing the planning and execution of clinical trials. This was recently demonstrated by a breakthrough study that used MPS of vascularized human kidney spheroids with integrated tissue-embedded microsensors for oxygen, glucose, lactate, and glutamine to provide real-time assessment of nephrotoxicity of immunosuppressive (cyclosporine) and anticancer (cisplatin) drugs. Importantly, the kidney-on-a-chip uncovered a previously unknown mechanism of injury involving glucose transport and predicted the protective effects of sodium-glucose cotransporter-2 (SGLT2) inhibitor (empagliflozin)

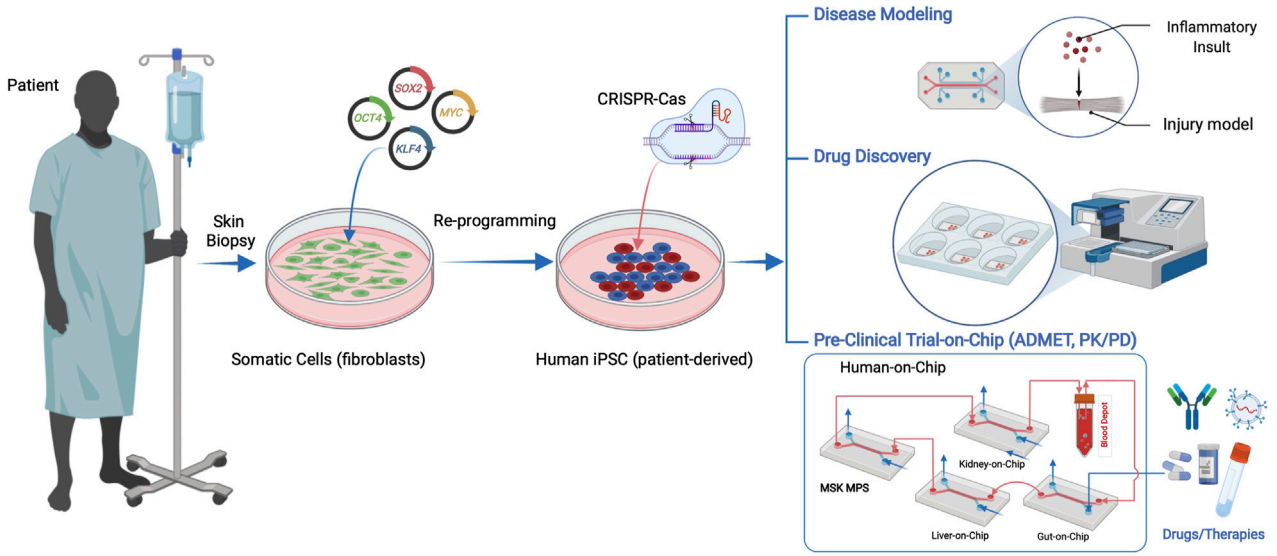

FIGURE 1 | Human iPSCs can be derived from patient somatic cells procured through a minimally invasive tissue biopsy and reprogramming using pluripotency factors. hiPSC applications in microphysiological systems include disease models, drug discovery, and human preclinical trials on a chip, including ADMET (absorbance, distribution, metabolism, excretion, and toxicity) and pharmacokinetics and pharmacodynamics (PK/PD) studies.

against the nephrotoxicity induced by the immunosuppressive and anticancer drugs. The sensor-enabled kidney-on-a-chip prediction of safety and efficacy of the combination therapy was validated through retrospective analysis of a clinical study involving 247 patients receiving cyclosporine or cisplatin alone or in combination with the SGLT2 inhibitor empagliflozin (Cohen et al., 2021). Such works are paving the way for MPS technology to transform drug development and patient healthcare.

Despite the proliferation of these sophisticated chips to model various tissue and organ systems, scientists in the musculoskeletal field have been slow to develop and adopt them. For example, there has been significant progress in developing and validating MPS for major diseases associated with high mortality rates such as the heart (Marsano et al., 2016), lung (Huh et al., 2010), intestines (Bein et al., 2018), and liver (Raasch et al., 2019). Many of these systems are reported in the Microphysiology Systems Database (MPS-Db) developed by the University of Pittsburgh Drug Discovery Institute to aggregate and manage data from different laboratories and to provide reference and clinical data to evaluate and validate experimental MPS results (Gough et al., 2016). Currently, musculoskeletal models of bone, joint, and skeletal muscle account for <10% of the entries in the MPS-Db. Arguably, the slow adoption of MPS in studies of musculoskeletal diseases can be attributed to conceptual and practical challenges in modeling cell and extracellular matrix (ECM) interactions in the dynamic injury and healing processes, *in vivo* mechanical loading, incorporating vascularization and innervation, and recreating joints and sophisticated soft-to-hard tissue interfaces.

Therefore, this review outlines current tools and trends in the MPS field, citing examples of early applications to model musculoskeletal diseases. In addition to providing an overview of critical issues in MPS, the review discusses specific challenges that should be prioritized in future MPS models of musculoskeletal diseases to accelerate their adoption into the drug and therapeutic discovery pipeline and in virtual clinical trials.

2 FROM BIOREACTORS TO MICROPHYSIOLOGICAL SYSTEMS

Bioreactors are closed cell and tissue culture systems in which the biochemical and biophysical environments of the culture are tightly regulated and monitored (**Figure 2A**). Traditionally bioreactors have been used as cell expansion systems for cell therapy, 3D engineered tissue training and maturation systems, and extracorporeal organ support devices (Ellis et al., 2005). MPS adopt many of the traditional bioreactor design principles, including perfusion, shear stimulation, or mechanical actuation (stretch or compression) on a much smaller scale with most applications focused on human disease research and drug screening (**Figure 2B**). Bioreactors and MPS manufacturing approaches are typically decoupled, where the tissue constructs and device components are manufactured separately and then assembled. This approach offers high flexibility in design through simulations and iterative prototypes before final manufacturing. For example, the design of a scaffold-free and perfused bioreactor can be optimized using computational fluid dynamic (CFD) simulations, allowing for tissue-specific designs to be optimized in silico. When tissue constructs with built-in microchannels are cultured in CFD-optimized bioreactors, effective nutrient perfusion and tissue maturation could be achieved over weeks of culture (Sego et al., 2020). This

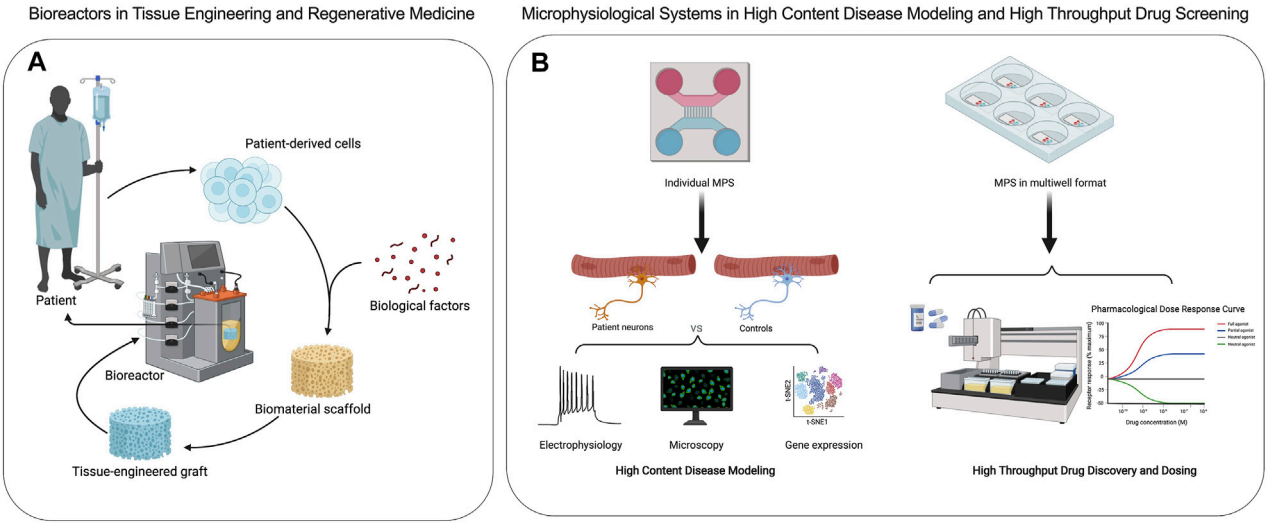

FIGURE 2 | Applications of bioreactors and microphysiological systems are distinct. **(A)** Bioreactors are used to create engineered transplantable tissue grafts in tissue engineering and regenerative medicine. **(B)** Microphysiological systems are used in high content disease modeling and high throughput drug discovery and screening of efficacy and toxicity.

approach was utilized in the fabrication of autologous cartilage-bone grafts engineered for temporomandibular joint regeneration (TMJ). Both patient-specific geometry and scale were utilized to produce dual-perfusion bioreactors to match the patient's geometry and cultivate mature constructs seeded with chondrogenic and osteogenic progenitors for weeks *in vitro* before demonstrating efficacy in TMJ reconstruction studies in large animals (Chen et al., 2020). The combination of computational simulation and experimental validation is commonplace in studies involving MPS as well (Aleman et al., 2019). In addition, bioreactors are commonly instrumented with sensors to monitor oxygen, glucose, lactate, and glutamine to provide real-time cell metabolism. The recent study from Cohen et al. (2021) suggested that tissue-embedded microsensors for oxygen, glucose, lactate, and glutamine in a kidney-on-a-chip MPS provide real-time assessment of cellular metabolism that led to the discovery of glucose transport as a nephrotoxicity mechanism associated with immunosuppressants and anti-cancer drugs (Cohen et al., 2021). Therefore, bioreactor design principles and technologies can be quite useful in informing design criteria and scaling down integrated sensors for MPS towards the goals of disease modeling and drug testing in clinically relevant contexts.

3 FROM ORGANOIDS TO ORGAN-ON-A-CHIP

Organoids are defined as 3D multicellular *in vitro* tissue constructs that mimic corresponding *in vivo* organs, such that they can be used to study aspects of that organ in the tissue culture system (De Souza, 2018). In general, they lack preconceived structure and architecture provided through intentional design of the micro tissue. Despite this, organoids can acquire the native organ's 3D complexity and functionality *in vivo* based on cell-cell communication, spatial cues and gradients (Rossi et al., 2018). Organoids can be used in MPS applications involving disease models, drug discovery and testing, and regenerative medicine. For example, human iPSCs derived from ALS patients were used to create functional sensorimotor organoids (neuromuscular junctions (NMJs)) to probe how distinct ALS variants may impair skeletal muscles and motor neurons at the level of the NMJ (**Figures 3A–E**) (Pereira et al., 2021). Other examples include trabecular bone organoids, formed by seeding primary osteoblasts and osteoclasts onto femoral head micro-trabeculae, which are then encapsulated in fibrin spheroids and cultured to model a pathological bone mass loss due to simulated microgravity (**Figures 3F–J**) (Iordachescu et al., 2021). Additional examples of organoid based MPS of musculoskeletal tissues are listed in **Table 1**. These examples provide a strong case for organoid-based microphysiological disease models for therapeutic screening. Advantages of using organoids as MPS include the close mimicry to embryonic cell assembly and tissue growth *in vivo* and the small size of spherical organoids that represent fully functioning microphysiological units. Disadvantages include the high variability in self-assembling cell clusters and difficulty in controlling the culture conditions, including those required for reproducible differentiation.

MPS are most commonly synonymous with organ-on-a-chip (OoaC), microdevices engineered to contain patterned cells and ECM to model tissue and organ structure and function at the micro-scale. The defining characteristics of OoaC include recreating the 3D arrangement of tissues on the platform, patterning multiple organotypic cells in a physiologically relevant context, and simulating biochemical (signals) and biophysical (forces) cues relevant to the modeled tissue or organ. For example, the effectiveness of co-culturing 3D human skeletal muscle fiber tissues with human iPSC-derived motor neurons to study the NMJ depends on whether the model

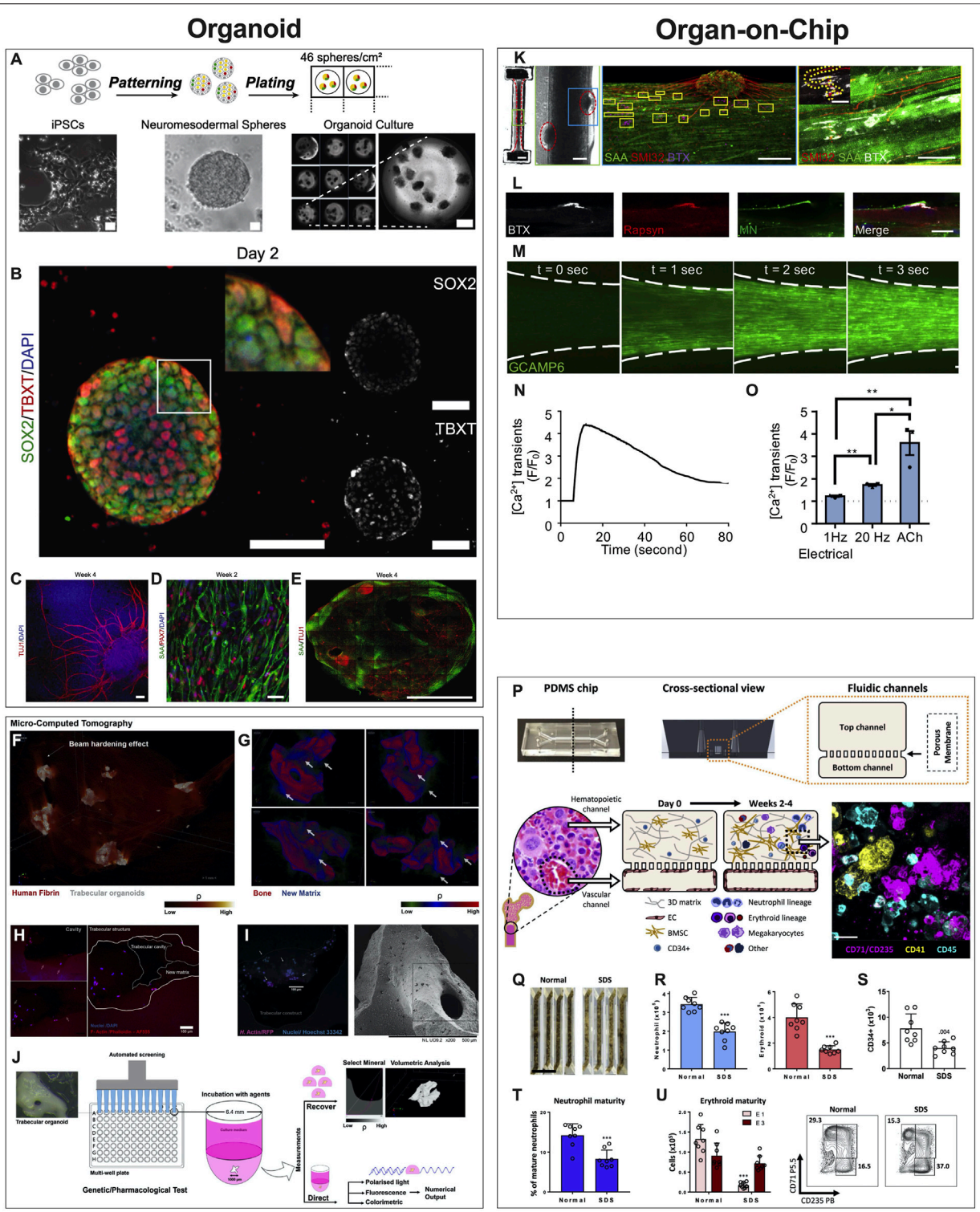

FIGURE 3 | Examples of Organoids and Organ-on-a-Chip Microphysiological Systems. **(A–E)** Human sensorimotor organoid model uses iPSCs cultured in suspension and allowed to self-assemble into organoids and mature in culture over several weeks **(A)**, with immunostaining for neuronal stem cell (TUJ1), myogenic (TBXT, PAX7), neuromesodermal (SOX2/TBXT), and neurogenic (SOX2) transcription factors and the sarcomeric α-actinin (SAA) **(B–E)**. The platform was used to test several ALS traits and their effect on the NMJ, elucidating key events and attributes of motor neuron diseases. [Reproduced from (Pereira et al., 2021) with permission]. **(F–J)** Trabecular bone in fibrin gel organoids **(F)** demonstrating bone remodeling *in vitro* **(G)** via the coupled activities of osteoblasts **(H)** and osteoclasts **(I)**. This human trabecular bone organoid allows for detailed morphologic and resorption events to be studied and chemically characterized **(J)**, including investigating the

(*Continued*)

FIGURE 3 | effects of microgravity on bone loss. [Reproduced from (Iordachescu et al., 2021) with permission]. **(K–O)** 3D neuromuscular co-culture in an organ-on-a-chip augments AChR signaling. A representative 3D skeletal muscle-motor neuron (MN) co-culture at 2 weeks **(K)**. Neuromuscular tissue outlined with red dashed line in left panel. Representative confocal image of a 2-week old neuromuscular co-culture immunostained for sarcomeric α-actinin (SAA; green), α-bungarotoxin (BTX; magenta), and neurofilament heavy SMI-32 (red). A neuromuscular co-culture immunostained on Day 10 of differentiation for Rapsyn (red), bungarotoxin (BTX, white), and counter stained with Hoechst 33342 (blue). **(L)** Epifluorescence images of a GCaMP6-labeled transduced 3D muscle tissue to visualize muscle fiber calcium transients at time-points before (t = 0 s) and after (t = 1, 2, and 3 s) ACh stimulation. **(M)** Time course of GCaMP6 reporter fluorescence following ACh-induced stimulation of a representative 3D muscle tissue. **(N)** Quantification of GCaMP6 signal after 3D skeletal muscle tissue low (1 Hz) or high (20 Hz) electrical stimulation, or ACh biochemical stimulation, and relative to phosphate buffered saline treated control tissues (dotted line). **(O)** [Reproduced from (Afshar Bakooshli et al., 2019) with permission]. **(P–U)** The design of the human bone marrow on chip recapitulates human bone marrow histology through a vascular layer in contact with bone marrow derived mesenchymal stromal cells embedded in an extracellular matrix with immune cell progenitors over 2–4 weeks. **(P)** BM Chips seeded with $CD34^+$ cells from normal donors versus SDS patients at 2 weeks of culture. **(Q)** Neutrophil [**(R)**, left)], erythroid [**(R)**, right], and $CD34^+$ **(S)** cell numbers were quantified by flow cytometry. Percentages of neutrophils with a mature CD16hi surface phenotype in control versus SDS BM Chips were quantified by flow cytometry **(T)**. Number of erythroid cells at different maturation states (left) and representative flow plots (right) depicting the percentages of the erythroid subpopulations (E1: immature, E3: mature), as quantified by flow cytometry **(U)**. (Reproduced from (Chou et al., 2020) with permission).

TABLE 1 | Examples of organoid models of musculoskeletal tissues and organs.

Organ/tissue represented	Disease/disorder or application	Treatment tested	Cell type used	References
Skeletal cartilage	Pharmacological and environmental toxicity and Shwachman-diamond syndrome (SDS)		Adult human bone marrow-derived mesenchymal progenitor cells (hBM-MPCs)	Pirosa et al. 2019
Cartilage and bone	Osteoarthritis	Scaffold-mediated lentiviral gene delivery of dox-inducible cytokine inhibitors and growth factors	Human MSCs	Rowland et al. 2018
Trabecular Bone	Degenerative effects induced by low-shear mechanical stimulation	—	Primary human osteoblasts and Primary human osteoclast precursors	Iordachescu et al. 2021
Trabecular Bone	Regulation of bone remodeling	—	Murine osteogenic cells	Park et al. 2021
Neuromuscular Junction	Amyotropic lateral sclerosis (ALS)	—	iPSCs and ALS mutated isogenic iPSC lines	Pereira et al. 2021
Neuromuscular Trunk	Neuromuscular degenerative diseases	—	Human pluripotent stem cells and iPSCs	Faustino Martins et al. 2020

is 2D or 3D. When 3D NMJ-on-chip models were compared to 2D culture conditions, they demonstrated functional superiority in fiber maturation and Acetylcholine receptors (AChR) clustering that affected the electrophysiological responses, strongly suggesting that 3D NMJ-on-chip is a powerful model to study adult human sensorimotor synaptogenesis and NMJ disease *in vitro* (**Figures 3K–O**) (Afshar Bakooshli et al., 2019).

In addition, the periarterial, perisinusoidal, mesenchymal, and osteoblastic hematopoietic niches in the bone marrow (BM) *in vivo* have been modeled in a two-channel vascularized BM-on-chip platform. The BM channel was simulated using a fibrin hydrogel in which $CD34^+$ cells and marrow-derived stromal cells were co-cultured, whereas the vascular channel, separated from the channel using a porous elastic membrane, was lined with endothelial cells cultured under media flow (**Figures 3P–U**). The BM-on-chip device reproduced key features in the BM hematopoietic stem cell niche and simulated expected pathologies in hematopoiesis when constructed using cells from SDS (Shwachman–Diamond syndrome) patients (Chou et al., 2020). Additional examples of OoaCs based MPS of musculoskeletal tissues are listed in **Table 2**. These examples demonstrate the advantages of OoaC microdevices, which provide physiologically relevant, human-specific alternatives to animal testing for the study of disease pathophysiology, and the ability to recapitulate clinically relevant disease states by engineering features of organ architecture and physiology at the microscale. Disadvantages include the simplistic nature of these disease models. Regardless, the common aphorism stating that "*all models are wrong, but some are useful*" applies here. The level of complexity needed in creating these models must balance a real value that otherwise could not be attained from a simpler model.

4 CONSIDERATIONS FOR BUILDING MUSCULOSKELETAL MICROPHYSIOLOGICAL SYSTEMS

4.1 Cell Sources

There are various cell sources for MPS, which include primary cells, cell lines, stem cells, and iPSCs. Each source has advantages and disadvantages, which must be factored in their utilization in MPS applications. Arguably, these cells must be derived from human sources for the MPS to have their highest impact.

TABLE 2 | Examples of tissue-on-a-chip models of musculoskeletal tissues and organs.

Organ/tissue represented	Disease/disorder or application	Treatment tested	Cell type used	References
Neuromuscular Junction	Motor neuron disease (MND)	—	Human embryonic stem cells (hESC), human iPSC-derived MNs (ESCs and iPSCs as healthy control), or human iPSC-derived MNs from patients with NMD, in combination with human iPSC derived skeletal muscle cells	Osaki et al. 2020
Neuromuscular Junction	Myasthenia gravis	—	Human primary fibroblasts, human PSC motor neurons	Afshar Bakooshli et al. 2019
Muscle	Acute oxidative injury and cancer cahexia	—	Human MSCs (Lonza), human skeletal myoblasts (hSKMB; Lonza) A549 lung adenocarcinoma spheroids, human lung fibroblasts, THP-1-derived macrophages	Mondrinos et al. 2021
Skeletal muscle	Oxygen deficits in skeletal muscle during exercise	—	Primary human myoblasts	Davis et al. 2019
Skeletal muscle	Hypertrophy	—	Primary human myoblasts	Khodabukus et al. 2019
Skeletal and smooth muscle	Duchenne muscular dystrophy (DMD)	—	Healthy & DMD derived human muscle myoblasts	Nesmith et al. 2016
Skeletal muscle	—	Biohybrid valveless pump-bot powered by "living" engineered skeletal muscle	C2C12 mouse skeletal myoblasts	Li et al. 2019
Skeletal muscle	Screening platform and *in vitro* muscle injury model	Cardiotoxin	C2C12 mouse murine myoblast cell line	Agrawal et al. 2017
Cartilage and bone junction	Osteoarthritis	Celecoxib	iPSC-derived mesenchymal progenitor cells (iMPCs)	Lin et al. 2019
Articular cartilage	Osteoarthritis	Triamcinolone steroid treatment	Primary equine chondrocytes	Rosser et al. 2019
Articular cartilage	Osteoarthritis	Interleukin-1 receptor antagonist (IL-1Ra) and rapamycin	Primary human articular chondrocytes (hACs)	Occhetta et al. 2019
Articular joint	Osteoarthritis	RS-504393 (CCR2 antagonist) and Cenicriviroc (CCR2/CCR5 antagonist)	Primary synovial fibroblasts, articular chondrocytes, GFP-HUVECs, PBMC derived monocytes, patient synovial fluid	Mondadori et al. 2021
Bone marrow niche	Interaction of infused HSPC, lymphoma and leukemic cells	—	Bone marrow mononuclear cells (BMNC), Stro-1+ MSC	Aleman et al. 2019
Hematopoietic microenvironment	—	—	HUVECs, Stromal fibroblast cell lines (HS5-GFP & HS27a-GFP), Peripheral blood mononuclear cells (PBMCs), Mesenchymal stem cells (MSCs)	Kotha et al. 2018
Bone perivascular niche	Breast cancer cell colonization into bone		Endothelial cells, bone marrow MSCs and MDA-MB-231/GFP or MDA-MB-231/Luc cells	Marturano-Kruik et al. 2018
Bone marrow	Model of hematopoietic response to drug exposure, ionizing radiation, and genetic mutation	—	Human CD34 cells, patient derived Bone marrow stromal cells, primary human-derived bone marrow mononuclear cells	Chou et al. 2020
Bone	Breast cancer	—	Murine calvaria preosteoblasts (MC3T3-E1) and human breast cancer cell lines MDA-MB-231^{GFP} and its metastatic suppressed variant MDA-MB-231 ^{GFP}	Hao et al. 2018

4.1.1 Primary Cells

Primary or somatic cells are directly isolated from living tissue and ideally suited to model the tissue from which they are extracted. In many tissues, primary cell isolation retrieves heterogeneous populations, including tissue-resident stem cells (Alberts et al., 2002). This necessitates protocols to purify and enrich the desired cell type based on a variety of sorting criteria and technologies. Furthermore, dissociating the different subpopulations of cells from the tissue results in a loss of important spatial cues and gradients, leading to

dedifferentiation (Shoshani and Zipori, 2015). To maintain the differentiated cell phenotype, specific culture media, culture conditions, and matrix requirements must be empirically optimized. Despite their obvious advantages in performing their differentiated functions and secreting tissue-specific molecules, primary cells have limitations. Primary cells experience stress-induced senescence after multiple passages and endure replicative aging and contact inhibition that limit their proliferation *in vitro* (Sherr and DePinho, 2000). Although commonly seen in aging tissues, replicative senescence *in vitro* poses significant challenges in modeling diseases, especially when senescence is not a feature of the disease. Furthermore, the availability of primary cells is limited because their harvest is typically invasive and can result in significant donor site morbidities. This is a serious limitation in modeling or integrating different types of patient-specific cells in MPS.

4.1.2 Immortalized Cell Lines

Human primary cells undergo a limited number of cell divisions (40–60) in culture before they reach senescence and lose their ability to divide. This loss of proliferative ability is attributed to reduced telomerase activity at high passage numbers (Hayflick and Moorhead, 1961). Therefore, immortalized cell lines, created using techniques such as human telomerase reverse transcriptase (hTERT), can overcome the Hayflick limit of primary cells. Cell lines can undergo unlimited divisions in culture at low cost, making them readily available from several commercial vendors and widely used across numerous laboratories worldwide. These properties afford them desirable consistency and reproducibility, making them a popular choice for basic research to study the molecular mechanisms of human disease in academic laboratories. They are also used in industrial production of recombinant proteins and vaccines and for drug cytotoxicity testing. Unfortunately, these cell types exhibit significant chromosomal and genetic abnormalities, which limit their ability to reproduce normal cell behavior *in vitro* (Lorsch et al., 2014). These drawbacks do not always outweigh the simplicity of using immortalized cell lines, particularly during MPS development where design iteration and testing does not require physiologically accurate cells. Cell lines should be replaced by more representative cells however, in the translational application of MPS models.

4.1.3 Stem Cells

Stem cells are perhaps the single most important discovery in regenerative medicine. They possess properties that can theoretically correct pathological changes caused by disease or injury. However, stem cells and their progenies can also be used as primary components of personalized (patient specific) MPS models of human disease. By definition, stem cells are characterized by the ability to self-renew indefinitely by symmetric or asymmetric cell division while maintaining an undifferentiated state and the ability to differentiate into the various fates of specialized cell types under the right chemical and biological cues. This latter property refers to the regenerative potency of stem cells. While the nomenclature is generally not uniformly used, pluripotent stem cells can differentiate into cells from any of the three embryonic germ layers: the ectoderm, the mesoderm, and the endoderm. First successfully isolated from the inner cell mass of the blastocyst by James Thompson in 1998 (Thomson et al., 1998), human embryonic stem cells (hESC) are demonstrably pluripotent, making them promising therapies in regenerative medicine and indispensable tools for basic research, drug discovery and testing. Therefore, they represent an important cell source for MPS models of human disease. However, the use of hESC is contentious due to ethical concerns related to their embryonic source, which restricted federal funding for continued generation of new hESC colonies. Moreover, early colonies of hESC have been generated using murine fibroblast feeder layers and animal sera, making them potentially unsuitable for clinical applications of regenerative medicine. As so, the derivation of differentiated cells from high passage hESC, some of which are now greater than 20 years-old, should be carefully assessed to ensure the cells have not accumulated abnormal traits. Alternative sourcing of hESC can be achieved through somatic cell nuclear transfer (SCNT or cloning) but this also raises ethical concerns about the unhinged use of this technology to clone human fetuses. In addition, the empirical protocols to generate and maintain hESC in their undifferentiated state are inefficient and could lead to spontaneous uncontrolled differentiation events that must be monitored and eliminated carefully.

Alternative sources of stem cells include extraembryonic fetal tissues such as the placenta and the umbilical cord (Wharton's jelly). In addition, stem cells have been identified in specialized compartments or niches in numerous tissues that retain a moderate level of regenerative abilities throughout postnatal and adult life. These adult stem cells are multipotent, such that they can differentiate into different cell types that make the tissue or related tissues from the same embryonic germ layers. As with primary cells, the invasive isolation of human adult stem cells is associated with tissue injury and donor site morbidity that constrain their applications in MPS models.

However, bone marrow, which harbors hematopoietic stem cells (HSC) and mesenchymal stromal (also called stem) cells (MSC), is a replenishable, readily accessible source of adult stem cells with minimal morbidity. HSC give rise to myeloid and lymphoid progenies of blood and immune cells through well-characterized steps of differentiation, which can be replicated *in vitro* (Orkin and Zon, 2008). As such, marrow-derived HSC represent an important source of cells for MPS models incorporating interactions with immune cells. Marrow-derived mesenchymal cells were first identified by Friedenstein due to their clonogenic (colony forming) replicative properties and their propensity for osteogenic differentiation *in vitro* and ectopic bone formation *in vivo* (Friedenstein et al., 1987). Caplan later coined the term mesenchymal stem cells and significantly advanced the concept of mesengenesis, the differentiation of musculoskeletal progenies from MSC (Caplan, 1994). Protocols for isolating and characterizing human MSC and demonstrating the multilineage potential of MSC were later developed (Pittenger et al., 1999). Numerous studies have since demonstrated the ability of MSC to differentiate into musculoskeletal cells to be used in cell therapy and tissue engineering, including osteoblasts, chondrocytes,

myocytes, tenocytes, adipocytes, and endothelial cells [reviewed in (Andrzejewska et al., 2019)]. Stem cells were also isolated from other tissues such as adipose-derived stem cells (ASC), which display comparable multilineage differentiation potential to marrow-derived MSC. Both MSC and ASC, as well as other tissue-derived adult stem cells, are now believed to be pericytes in vascular niches of these tissues (Crisan et al., 2008). And while the current paradigm in regenerative medicine has now shifted to emphasize the immunomodulatory and trophic phenotypes of adult stem cells with respect to their therapeutic potential (Caplan, 2017), their utility in MPS models of musculoskeletal diseases still requires efficient and reproducible multilineage differentiation protocols. Therefore, human marrow-derived HSC and MSC can potentially be useful tools in constructing isogenic vascularized tissue MPS models of musculoskeletal diseases.

4.1.4 Induced Pluripotent Stem Cells

The Noble prize discovery that somatic cells can be reprogrammed to turn back the clock and induce a pluripotent stem cell-like state opens limitless possibilities for applications in MPS models. iPSCs were originally derived from murine embryonic and adult fibroblasts through viral transfection with *Oct3/4*, *Klf4*, *Sox2*, and *c-Myc* pluripotency factors (Takahashi and Yamanaka, 2006). This discovery was later translated to generate human iPSCs through transfection of hESC–derived somatic cells, primary fetal tissues (lung, skin), and neonatal and adult dermal fibroblasts with the same or similar factors (*OCT4*, *SOX2*, *NANOG*, *LIN28, or KLF4, MYC*) (Yu et al., 2007). Today, numerous well characterized human iPSCs can be purchased from commercial vendors and cell banks or generated on demand from adult fibroblasts in academic laboratories and through commercial services. Numerous studies indicate human iPSCs bear a remarkably comparable pluripotency to hESCs. Therefore, hiPSCs hold great potential in cell and gene therapy to address genetic and degenerative diseases. Techniques such as *ex vivo* gene therapy or CRISPR/Cas9 can correct genetic mutations associated with various diseases in patient-derived iPSC progenies, which can then be used in autologous cell and gene therapies. Personalized, autologous iPSC-based therapies circumvent triggering an immune response and subsequent graft rejection. Additionally, human iPSCs hold great potential in MPS-based disease models for drug discovery and toxicity testing (Bellin et al., 2012).

In particular, the use of human iPSC-derived cells from an autologous donor overcomes the previously intractable problem of creating interconnected, isogenic MPS models of multiple tissues or organ, paving the way towards clinically relevant human-on-chip models (**Figure 1**). Therefore, human iPSC technology is highly valuable in MPS models of musculoskeletal conditions, especially for composite tissues that require incorporating different cell types such as muscle-tendon (myotendinous junctions) and tendon/ligament-bone interface (entheses), osteochondral tissues, vascularized and innervated muscle and bone tissues or composites thereof.

Despite their undeniable potential for MPS applications, the use of human iPSC in modeling human diseases has limitations. The relationship between the genome and epigenome has broadened the understanding of the types of molecular events that cause human disease. Current strategies for iPSC generation/regeneration of isogenic tissues eliminates this epigenetic memory from donor cells while maintaining the patient's intact genome. Although human iPSC are effective for modeling purely genetic disease (e.g., Amyotrophic Lateral Sclerosis or Duchenne muscular dystrophy), they have limitations in modeling diseases stemming from both genetic and epigenetic factors. They also have other challenges in modeling important biological variables that maybe systemic rather than purely cellular, including sex and age.

As with stem cells, the utility of human iPSCs in MPS models of musculoskeletal diseases requires efficient and reproducible multilineage differentiation protocols. Strategies to generate human iPSC musculoskeletal derivatives have been described in numerous publications, including osteoblasts (Zujur et al., 2020), tenocytes (Nakajima et al., 2021), chondrocytes (Wu et al., 2021), skeletal muscle (Rao et al., 2018), motor neurons (Bianchi et al., 2018), endothelial cells and vascular smooth muscle cells (Patsch et al., 2015), and monocytes and their progenies (macrophages and dendritic cells) (Cao et al., 2019), depicted as examples of recent protocols in **Figure 4**.

4.2 Extracellular Matrix Biomaterials

Polymeric hydrogels are widely used in MPS platforms as they resemble the macromolecular ECM of many tissues and organs, providing proper cellular architecture, support, and function. The three main categories of hydrogels include natural, synthetic, and hybrid materials. Animal sourced natural hydrogels such as collagen and fibrin are biocompatible and provide native cell-binding ligands and biochemical properties present in native tissues. On the other hand, the process of deriving natural hydrogels from animals results in limited mechanical strengths, long-term storage instabilities, and batch differences, reviewed in (Terrell et al., 2020). Alternatively, synthetic hydrogels provide more control over mechanical strength and batch differences as they are chemically synthesized from precursor molecules. However, synthetic hydrogels often require additional chemical modifications to promote cell adherence and viability (Cruz-Acuña and García, 2017). Often, hybrid hydrogels are synthesized from biological macromolecules such as hyaluronic acid, which can be combined with synthetic hydrogels or chemically modified using acrylation reactions to enable photo crosslinking upon the addition of photo initiators and exposure to light (Jiang et al., 2020).

Aside from hydrogels, ECM derived biomaterials also include decellularized scaffolds which provide a native environment for tissue engineering, electrospun fibrous scaffolds providing nano-microscale fibrous structures with interconnecting pores, and 3D-printed materials fabricated to fit the desired geometry. Materials for these approaches can be native (tissue-derived), synthetic, or hybrid. The primary advantages of these approaches are the controlled architecture acquired through scaffolding and high-definition fabrication techniques achieved with electrospinning and 3D-printing. Limitations of these approaches include the difficulty in recreating cell-ECM interactions *in vivo* and biomechanically matching the tissue of interest with a biomaterial scaffold.

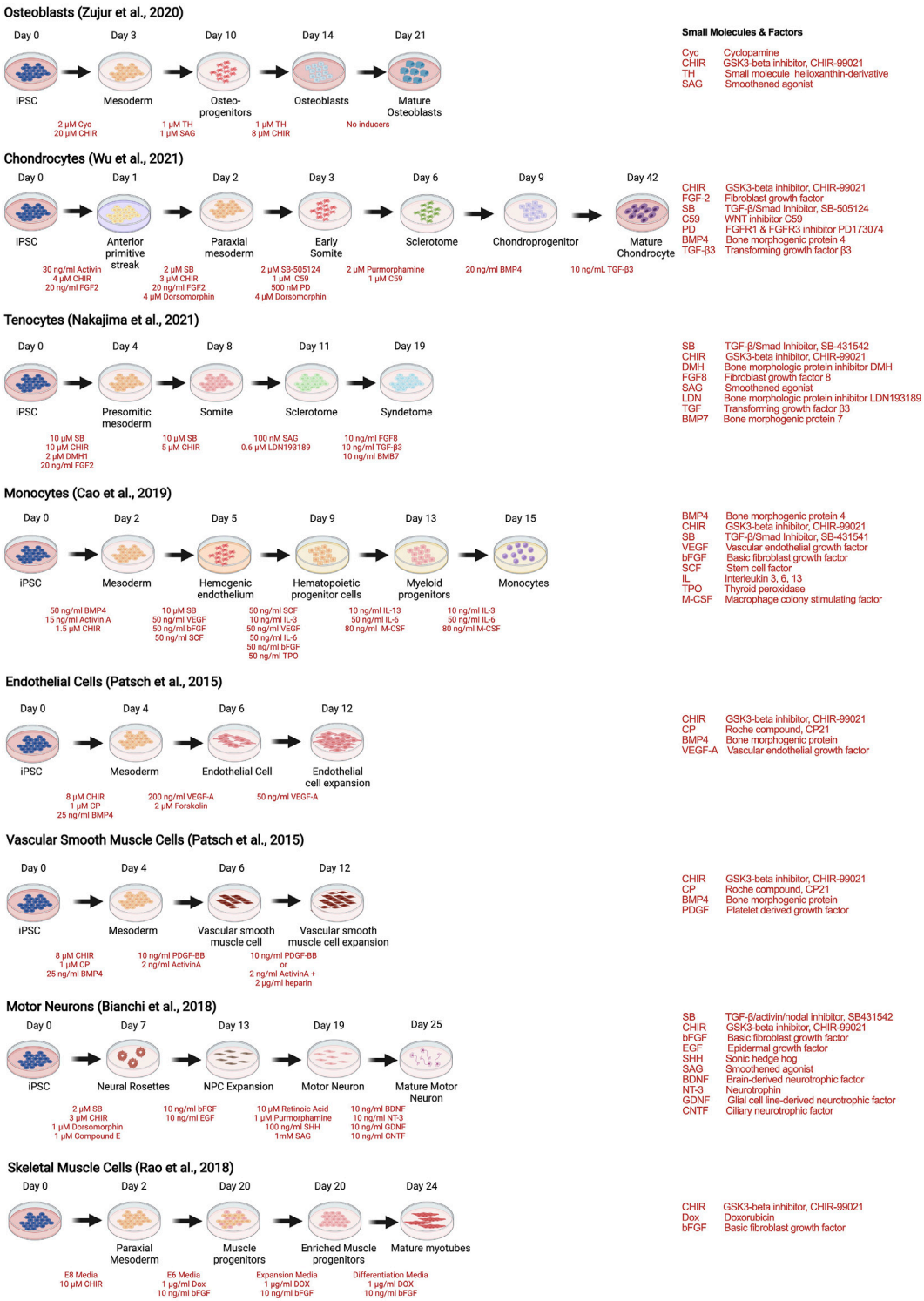

FIGURE 4 | Strategies to derive musculoskeletal cells from human iPSCs through stepwise differentiation.

Although not thoroughly covered here, others have extensively reviewed the biomaterials and fabrication methods which are key components in successful representation of musculoskeletal disease models (Cunniffe et al., 2019; Li et al., 2021).

4.3 Fabrication Materials in MPS Devices

Beyond the conceptual design of the MPS, practical considerations influence the choice of materials used in device fabrication. The most commonly used fabrication materials for

MPS devices are elastomers and rigid polymers. The choice of the fabrication materials affects manufacturability, assembly flexibility, maintaining sterility, incorporating precise physical stimuli (e.g., stretch and flow-induced shear), molecular adsorption and absorption, and longitudinal monitoring of outcomes through live microscopy or integrated sensors.

4.3.1 Elastomers

Elastomers are cross-linked polymers with weakly entangled chains. Due to their low elastic moduli and weak intermolecular forces, they easily deform (stretch or compress) and experience high strains without failure when an external force is exerted but return to their undeformed state when the force is withdrawn. Polydimethylsiloxane (PDMS) is an elastomer that has been widely adopted in the microfluidics community for its versatility, biocompatibility, permeability, and low cost. PDMS has been crucial in the early work of MPS and remains a prodigious material, with most devices still utilizing PDMS as their primary structural component. Despite its popularity, some limitations of PDMS include incompatibility with inorganic solvents, absorption of small hydrophobic molecules, adsorption of biomolecules, and gas permeability that lead to changes in concentrations of solutions over time (Ren et al., 2013). The multilayer soft lithographic fabrication method of PDMS is widely implemented in the MPS field yet is inadequate for industrial and high-throughput applications, both of which will be necessary if MPS are to be adopted into the drug development workflows. As an alternative, thermoplastic elastomers (TPE) offer thermoforming processing while maintaining low cost, optical transparency, biocompatibility, and flexibility comparable to PDMS. Flexible elastomers such as tetrafluoroethylene-propylene (FEPM), poly (polyol sebacate), and poly (esteramide) have been developed as PDMS alternatives. For example, Sano et al. (2019) modeled the endothelial-epithelial interface in a MPS by combining two FEPM microchannels separated by a collagen membrane that permits fluid flow through the channels and mechanical strain through vacuum chambers (Sano et al., 2019). Such innovations are highly practical as many MPS currently prototyped with PDMS can be re-designed with such materials. Reducing absorption of small hydrophobic drugs signified the potential of FEPM as an alternative to PDMS for drug discovery, with other materials offering similar performance such as poly [octamethylene maleate (anhydride) citrate) (POMaC) (Zhao et al., 2019]. Nonetheless, these alternative elastomers do not fully eliminate small molecule absorption in MPS and research into novel nonabsorbent elastomers with optical transparency, flexibility, and ease of fabrication continues. For the musculoskeletal field, elastomers have the highest impact as many of the tissues require bulk-tissue actuation (i.e., tendon stretching, cartilage compression) that can be hard to achieve without flexible materials.

4.3.2 Rigid Polymers

Rigid thermoplastic polymers such as Polystyrene (PS), Poly (methyl methacrylate) (PMMA), Polyurethane, Teflon, and PEGDA are high strength, relatively inflexible, low cost, light weight, optically transparent, and biocompatible (low monomer leaching) materials widely used in fabricating MPS devices. These rigid thermoplastics can be reshaped multiple times by reheating, which is advantageous for molding and bonding. These materials can be fabricated through silicon master molds, reactive ion etching (REI), injection molding and hot embossing. Therefore, thermoplastic components of MPS devices can have high upfront production and development costs not feasible for prototyping but suitable for large batch manufacturing. As an alternative, rapid prototyping methods include CNC micromilling techniques and 3D printing to allow for quick, low-cost fabrication at the benchtop.

Generally, rigid polymers show improved solvent compatibility compared to PDMS including some resistance to alcohols. However, they are incompatible with organic solvents such as ketones and hydrocarbons. Their low gas permeability makes them unsuitable for long-term and static cell studies in sealed microchannels and microchambers. These environments limit gas permeance which can be lethal to cells, particularly in incubators where CO_2 exchange is necessary for buffering the cell media and can accumulate in impermeable, static platforms. Yet, it can be optimal when using media with premixed gases to monitor dissolved oxygen consumption and pH levels in the MPS environment for example (Müller et al., 2021). The advantages of impermeability were observed in two studies where PMMA and PS were compared to PDMS devices and demonstrated more reliable results in drug toxicity and effectiveness screening. In both cases, the rigid thermoplastic polymer MPS results resembled *in vivo* findings with respect to cytotoxicity and drug effectiveness compared to the PDMS MPS, which likely experienced dosage changes overtime due to protein absorption by the PDMS surfaces (Nguyen et al., 2019). Although optimal for microscopy and PK/PD studies, the rigidity of these materials makes it difficult for actuation to be incorporated. Therefore, hybrid MPS devices are common to take advantage of elastomeric and rigid polymer properties.

5 CHALLENGES FOR MUSCULOSKELETAL MPS

The implementation of intentional design strategy is key to successful MPS application. This requires that MPS platforms are designed to: 1) model the disease within the context of the tissue's physiological and functional parameters, 2) enable longitudinal and endpoint assays, and 3) accommodate the skills, resources, and objectives of the end user. Physiological and functional parameters include gradients, heterogenous interfaces, biological barriers, mechanical or electrical stimulation, fluid flow, and interconnectivity with different tissue or organ chips. Longitudinal assays include brightfield and fluorescent microscopy, multiplex sensing of secreted proteins, while destructive endpoint assays include histology, immunohistochemistry, and q-PCR. End users could be trainees in academic laboratories pursuing high content data to uncover mechanisms of disease, drug discovery scientists in

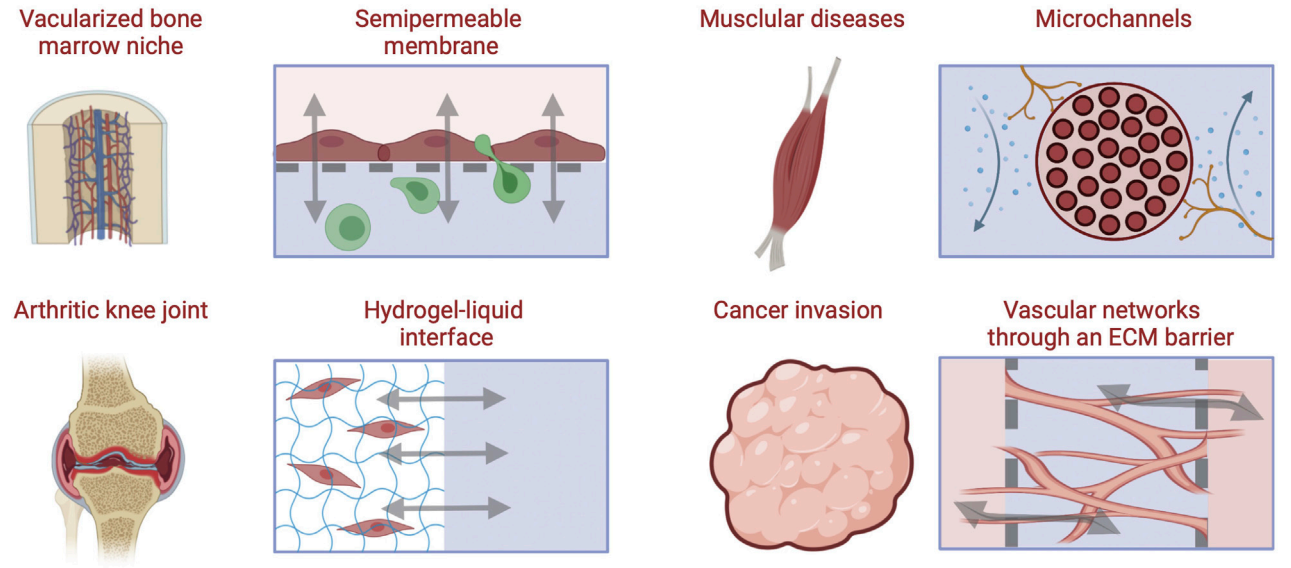

FIGURE 5 | Approaches for engineering barriers and interfaces in musculoskeletal tissues, including porous membrane-based vascular barriers, microchannels, hydrogel-liquid interface, and perfusable microvascular channels network within through an ECM hydrogel barrier [Inspired from (Yeste et al., 2018)].

a pharmaceutical R&D facility pursuing high throughput data to identify hits that could be developed as drugs or biologics, or clinical trial technicians seeking proof of safety or efficacy of a drug candidate.

In addition to the challenges of creating clinically-faithful disease models with biomarkers that capture the dynamic nature of acute or chronic pathologies, tissues and joints in the musculoskeletal system, there are various specialized features that require engineering innovations to model them on MPS. For example, the migration of innate and adaptive immune cells from the bone marrow into the vasculature, the infiltration of platelets, neutrophils, macrophages, and various immune cells to sites of tissue injury, and cancer metastases growth underscore the importance of engineering permeable vascular barriers. Biological interfaces and ECM gradients, such as the myotendinous junction and the enthesis are critical not only for mechanical function but also for cellular functions and signaling, and there are several engineering approaches to engineer gradients that would need to be scaled down for MPS. Directed motor neuron terminal attachment to highly organized muscle fibers is another example of the intricate microarchitectural engineering that would be required to model innervated tissues (Rodríguez Cruz et al., 2020). Furthermore, sophisticated joint-on-chip designs must create closed compartments of joint cartilage and the underlying subchondral bone, synovial fluid, and vascularized synovial capsular tissues with articular motion to simulate nutrient transport, lubrication, *in vivo* loading, and inflammation. Importantly, engineering outcomes of pain indicators in MPS is critical to designing clinical trials-on-chip since pain is one of the most significant patient-reported outcomes in the clinic.

The following sections discuss seven challenges that should be prioritized in future musculoskeletal MPS platforms to increase the predictive power of these models in disease research and drug discovery areas. These challenges include engineering biological barriers, engineering heterogenous tissue interfaces, incorporation of immune cells and inflammatory factors, biomechanical actuation and loading, incorporating surrogate measurements for pain, integrating inline sensors for real-time monitoring of dynamic processes, and creating arrayed formats for high throughput screening.

5.1 Engineered Biological Barriers

The following section describes compartmentalized approaches used to engineer biological and vascular barriers in MPS with application examples in musculoskeletal disease models (**Figure 5**).

5.1.1 Semipermeable Membranes

Early strategies to polarize apical and basal epithelial or endothelial cell surfaces were accomplished with permeable substrates. Membrane filters were used to culture epithelial cells and form polarized monolayers with transport and permeability qualities of *in vivo* transporting epithelium (Cereijido et al., 1978). These models served as experimental platforms still in use today to elucidate epithelial and endothelial disease mechanisms in different organs (Boccellato et al., 2019). Semipermeable membranes separate chambers into two compartments allowing molecular and cellular transport only through nano- to micro-sized pores, respectively. These can be of particular importance in musculoskeletal tissues as fluid flow is incorporated to simulate vasculature, synovial fluid, or interstitial flow and cell cultures are required to be in suspension or direct contact with other cells or tissues. Semipermeable membranes permit exact compartmentalization, often difficult to achieve with

ECM scaffold approaches, while allowing for cell-cell signaling Thermoplastics, elastomers, and inorganic materials have been used to fabricate porous membranes. The advantages of permeable membranes in MPS are their biocompatibility, optical transparency, and flexibility. Nevertheless, there are other variables to consider when implementing porous membranes including pore size, mechanical properties (stiffness), and thinness which have been extensively reviewed by Chung et al. (Chung et al., 2018). Compartmentalizing MPS using membranes allows for permeability assays to be performed as supernatants can be collected from both apical and basolateral compartments, delineating biological cues specific to luminal and basal cell surfaces. Additionally, the inclusion of micron-scale pores allows for cell transmigration studies between compartments, while strictly nanoporous membranes (pores < 100 nm) limit communication between tissues to paracrine signaling.

As an example, a recently published joint-on-chip model includes vascularized synovium and articular cartilage PDMS compartments separated by lined trapezoidal posts 90 μm apart creating micropores for cellular transmigration (Mondadori et al., 2021). Monocytes were introduced into the vascularized channel ± TNF-α and shear stress activation and monitored their transmigration into the osteoarthritic (OA) synovial fluid and cartilage compartments, identifying higher transmigration in the presence of OA synovial fluid compared to control medium alone. When monocytes were incubated with CCR2 and CCR5 receptor antagonists a significant reduction of extravasation was observed comparable to the control group where no OA synovial fluid was present. Such models serve as tools to study mechanisms responsible for abnormal macrophage infiltration and can be expanded to other leukocytes to study inflammatory musculoskeletal diseases. One limitation of many of the microfabricated membranes lies in their supraphysiologic thickness which slows the exchange of soluble factors between compartments but can negatively impact longitudinal microscopic imaging. Therefore, technologies to fabricate ultrathin porous membranes, which would mimic the *in vivo* barriers is a priority in MPS fabrication research.

5.1.2 Hydrogel-Liquid Interface

Hydrogels physically support cells in MPS while enabling direct interaction with surrounding fluid and/or other tissues. When incorporating hydrogels into MPS, a vital property to consider in addition to cytocompatibility and mechanical properties are molecular diffusion rates. Liquid interfaces with optimized hydrogels are powerful instruments to mimic native joints, simulate local inflammation, and administer therapeutics for drug screening assays. Additionally, such hydrogels can be patterned, and 3D printed to create musculoskeletal models with precisely controlled architectures. As an example, an osteochondral-tissue chip using human iPSCs was developed to model the pathology of OA by embedding induced mesenchymal progenitor cells (iMPC) in a methacrylated gelatin hydrogel. The cell-laden construct was placed in a bioreactor with two separated fluidic channels accessing the top and bottom of the construct respectively. A chondrogenic medium was perfused in the top channel and an osteogenic medium was supplied through the bottom conduit over 28 days to induce chondrogenic/osteogenic differentiation of the iMPCs. The construct was shown to effectively model OA in the cartilage compartment through the introduction of IL-1β, and responds by reducing inflammatory cytokines when treated with Celecoxib, a COX-2 inhibitor commonly used as a first-line treatment for OA (Lin et al., 2019).

5.1.3 Microchannels

Directly patterning microchannels into the MPS substrate is an effective approach to control the cellular architecture and organization. Microchannels link two adjacent chambers and can be lined with monolayer forming cells such as endothelial or epithelial cells to completely cover the inner surfaces or they can be used to guide axonal growth. Microchannels have been used to model the human neuromuscular junction (NMJ) transmission upon exposure to inhibitors, where motoneurons (MNs) can communicate with skeletal muscle cells in two separate compartments connected by microchannels embedded in a PDMS BioMEM construct. Physiological behavior was evidenced in the system as high frequency excitation of the MNs drove the myotubes to contract into tetanus while pharmacological NMJ inhibitors added to the muscle compartment demonstrated that MN-induced muscle contraction could be attenuated (Santhanam et al., 2018). Such a strategy can be pivotal in studies of neuromuscular degenerative diseases or injury states.

5.1.4 Vascular Networks Embedded in ECM

Perfusable channels are often designed to be embedded in hydrogel constructs within MPS, usually to form vascular networks. Vascular networks are critical to many diseases such as metastatic cancer, inflammation, and fibrosis. Incorporating vasculature into musculoskeletal MPS also permits immune cell components to be introduced and drug studies to be tested through vascularized models which can provide estimates of PK/PD. Vascular networks for MPS have been successfully incorporated into various tissues and organs and showed improved outcomes for disease modeling and physiological function (Jeon et al., 2015; Chen et al., 2017; Ewald et al., 2021). Vascularization in MPS can be achieved by physically patterning hollow channels through hydrogels and then infusing vascular cells to adhere to the tunnel walls forming vasculature with a perfusable lumen. Additionally, 3D printing techniques can be used to form more complex constructs such as larger blood vessels (Dellaquila et al., 2021). Nonetheless, these architectures can be difficult to achieve in MPS dimensions and often do not recapitulate the isotropic architecture of *in vivo* vasculature, such as in the bone marrow, a substantial challenge in musculoskeletal tissues that must be overcome to develop physiologically relevant MPS models.

Another approach to address this challenge is the self-assembled formation of vasculature from endothelial lined microchannels through a gel-liquid interface with angiogenic gradients driving vascular growth in the hydrogel (Kim et al., 2013). These mature networks have been shown to form

impermeable vascular barriers allowing for perfusion of immune cells, biochemical signaling, and treatments between connected compartments (Ewald et al., 2021). For example, MPS were developed to model 3D vascularized muscle fibers using a sequential molding technique using optogenetic, Channelrhodopsin-2 expressing muscle fiber bundles and 3D vessels (600 μm diameter) in a collagen gel (Osaki et al., 2018). The interaction between the muscle fibers and the endothelial cells was modulated through secreted angiopoietin-1 and optical stimulation of muscle tissue contraction, which induced angiogenic sprouting. On the other hand, myogenesis and improved muscle contraction were regulated by interactions with the endothelial cells through angiopoetin-1/neuregulin-1 signaling, demonstrating the feasibility of embedding vascular networks in hydrogel models of musculoskeletal tissue, and the importance of accounting for signaling between endothelial cells and myocytes in the formation of functional muscle models.

5.2 Engineered Heterogenous Tissue Interfaces

In musculoskeletal tissues, the integration of soft-to-hard interfaces *in vitro* such as the cartilage-bone junction, neuromuscular junctions, myotendinous (muscle-to-bone) junction, and entheses (tendon-to-bone junction) into MPS are significant unmet needs. Modeling injury to biological junctions in a humanized model requires the integration of multiple tissues and phases into one MPS. This can be a particularly challenging process *in vitro* where cell matrix needs differ widely. Rowland et al. (2018) developed an anatomically shaped cartilage derived matrix construct to spatially organize chondrogenic and osteogenic differentiation of a bone marrow-derived mesenchymal stem cell population by controlling the site-specific expression of transcription and growth factors (Rowland et al., 2018). This model relies on the antagonistic effects of chondrogenic and osteogenic growth factors in a co-culture organoid model, which was designed to investigate aberrant inflammation in joints (Rowland et al., 2018). The cellular and structural complexity at interface regions connecting muscle to tendon (myotendinous junction or MTJ) or tendon/ligament to bone (enthesis) represent important functional adaptations and are commons sites of acute and chronic injuries. The largely extracellular tendon aspect of the MTJ develops ridge-like protrusions, which interdigitate with finger-like myofibrils in the muscle to increase contact surface area and enhance the MTJ strength (Knudsen et al., 2015). The engineering feat of recreating the interdigitating interface between muscle fibers and the mostly acellular ECM of tendon remains unmet, although recent scaffold-free approaches are showing promise (De Pieri et al., 2021). The enthesis is a common feature of both tendon and ligament insertion into bone. Recent evidence revealed continuous, spatially graded mineralization of the collagenous tendon as it inserts into the bone (Patel et al., 2018). The discovery of the graded composition inspired novel approaches for interface tissue engineering via biomimetic gradation of mineralization in nanofibrous-scaffolds (Li et al., 2009). The engineering of these heterogenous tissue interfaces remains an unmet need and a challenge for MPS models of MTJ or enthesis injury, but several strategies have been described in the literature (Phillips et al., 2008; Li et al., 2009; Manfrin et al., 2019). Although not specific to soft-to-hard interfaces, modeling heterogenous tissues requires the optimization of co-culture conditions for the several cell types involved. This presents unique hurdles which could potentially be overcome by incorporating gradient generators within the chips control the spatial concentrations of differentiating factors (**Figure 6A**) (Manfrin et al., 2019). Alternatively, scaffold-mediated spatially graded gene delivery strategy implemented to create a spatial gradient of Runx2 retrovirus within 3D matrices has been implemented as a tissue engineering approach for the enthesis (**Figure 6B**), which could be translated in MPS (Phillips et al., 2008). Additionally, mimicking the enthesis using a spatially graded coating of calcium phosphate on electrospun nanofibers can be a viable strategy for modeling the enthesis in a MPS (**Figure 6C**) (Li et al., 2009). Furthermore, substrate interactions such as stiffness, topography and pore density, which can affect cell differentiation must also be factored in.

5.3 Incorporation of Immune Cells and Inflammatory Factors

Inflammation represents the body's response to cell and tissue damage from harmful agents or injury. The initiation, progression, and resolution phases of inflammation in musculoskeletal tissues and disease are important considerations in developing effective treatments. Acute injury to musculoskeletal tissues initiates the recruitment of inflammatory cells (neutrophils, monocytes, lymphocytes, and mast cells) to the injury site. Neutrophils, the first phagosomes recruited, set the stage to the activation of monocytes and lymphocytes to attack and eliminate foreign organisms and agents. The functional consequences of activation of circulating monocytes to macrophages, which represent the innate immune response, depend on their polarization, with M1 macrophages effecting phagocytosis and proinflammatory cytokines secretion and M2 macrophages typically credited with anti-inflammatory cytokine and growth factor secretion to initiate tissue repair (Sunwoo et al., 2020). Lymphocytes represent the body's adaptive immune system and complement the innate immune responses. Among these are T and B cells, which are varied with complex effector functions both promoting and attenuating inflammatory responses (Murphy and Weaver, 2016).

The need to incorporate immune system function on MPS is not unique to those interested in musculoskeletal research. However, efforts to create "immune-system-on-a-chip" and similar platforms have largely been limited to three types of systems. These include systems with immune cells in tumors, systems investigating the interaction between endothelium and immune cells, and systems modeling the inflammatory process as a whole (Polini et al., 2019). While these models are not specific to musculoskeletal diseases, they provide valuable insights. An example of this is the three organ "body-on-a-chip" model used to study monocyte activation using an MPS model to recapitulate

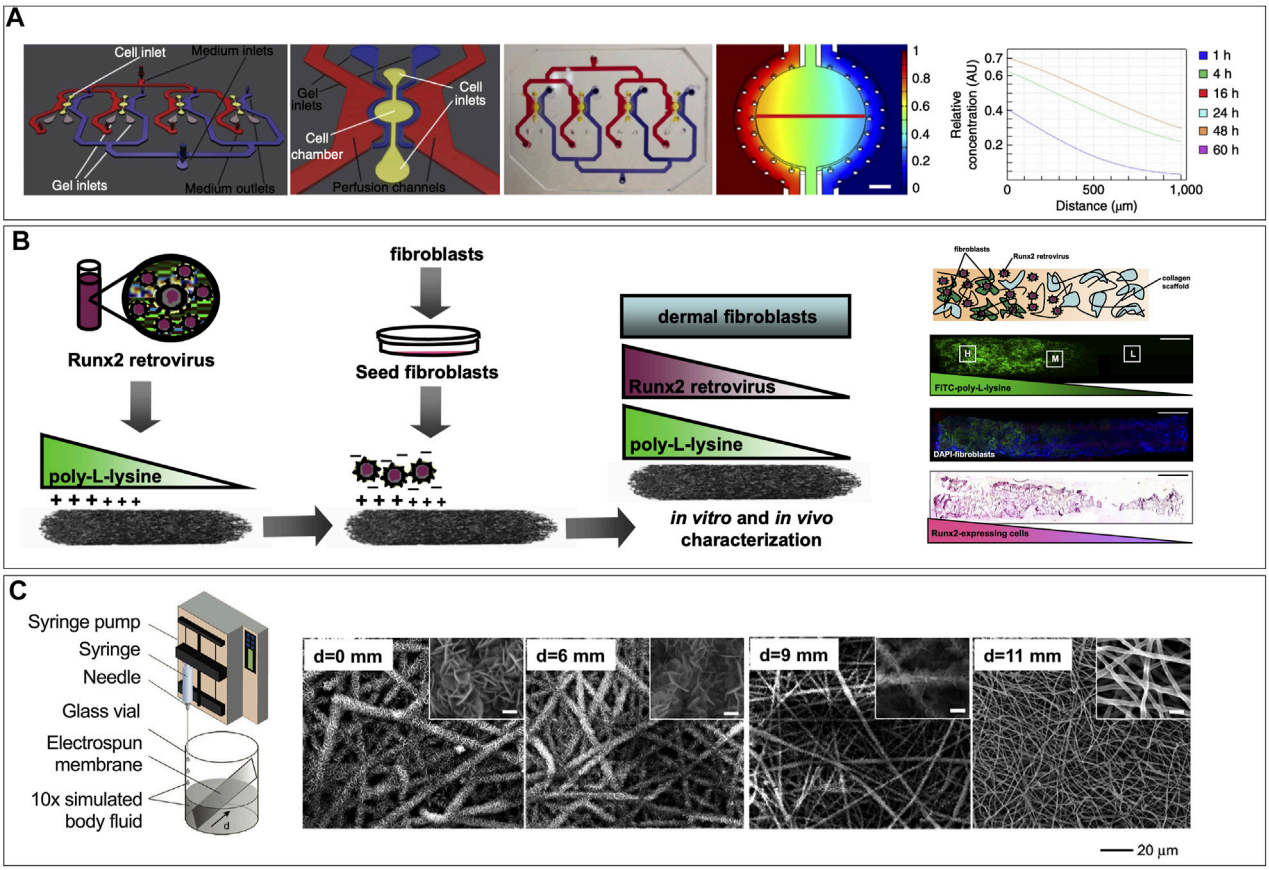

FIGURE 6 | Strategies for creating gradients that could be implemented in microphysiological systems. **(A)** Engineered signaling centers for the spatially controlled patterning of human pluripotent stem cells, showing schematic of the microfluidic device a single unit of the device, a picture of the PDMS microfluidic device filled with colored ink in the distinct compartments, and computational simulation of the diffusion of a reference molecule from the source side of the cell chamber after 48 h of perfusion. [Reproduced from (Manfrin et al., 2019) with permission]. **(B)** Schematic representation of scaffold-mediated spatially graded gene delivery strategy implemented to create a spatial distribution of Runx2 retrovirus within 3D matrices. The proximal portion of collagen scaffolds was coated with PLL before incubation in retroviral supernatant and fibroblast seeding. Representation of a fibroblast-seeded construct containing spatial patterns of noncovalently immobilized retrovirus, showing distribution of Runx2 retrovirus (R2RV) created by partially coating the proximal portion (left side) of collagen scaffolds with PLL at a dipping speed of 170 μm/s before incubation in retroviral supernatant and cell seeding. Confocal microscopy images demonstrating a graded distribution of FITC-labeled PLL (green) **(B)** and FITC-labeled PLL gradient colocalized with uniformly distributed cell nuclei (DAPI, blue), and immunohistochemical staining for eGFP (pink) counterstained with hematoxylin (blue) revealed elevated eGFP expression on the proximal scaffold portion coated with PLL-R2RV. [Reproduced from (Phillips et al., 2008. Copyright (2008) National Academy of Sciences, United States) with permission]. **(C)** Nanofiber scaffolds with gradations in mineral content for mimicking the enthesis using a graded coating of calcium phosphate on a nonwoven mat of electrospun nanofibers by submerging in 10× concentrated simulated body fluid added at a constant rate to linearly reduce the deposition time from the bottom to the top end of the substrate (d refers to the distance from the bottom edge of the substrate) (Left). SEM images of graded calcium phosphate coatings on the PLGA nanofibers from different regions, with d = 0 mm representing the longest exposure to SBF and d = 11 mm representing the shortest exposure to SBF [Reproduced from (Li et al., 2009) with permission].

the complex responses of the immune system to various stimuli (Sasserath et al., 2020). As described earlier, the activation of monocytes to macrophages is a key component of many musculoskeletal diseases. Consequently, macrophage plasticity makes it difficult to study macrophages and their niches *in vivo*. For example, the intrinsic vs. extrinsic factors affecting the fate, heterogeneity and plasticity of synovial macrophages is still largely unknown, yet breakthroughs in this area can dramatically improve joint treatments (Culemann et al., 2019; Hannemann et al., 2021). Therefore, information gained from these types of models will be valuable in informing future musculoskeletal therapies. Targeted musculoskeletal MPS systems that also incorporate immune and inflammatory components are emerging. As discussed earlier, a microfluidic model of the articular joint has been used to study monocyte extravasation in osteoarthritis (Mondadori et al., 2021). Another example is the bone-marrow-on-a-chip which allows for the study of hematopoietic physiology and effect of toxicity on immune cells in different disease models (Chou et al., 2020). These examples and others serve to highlight the potential for musculoskeletal MPS models to incorporate immune system components and the continued motivation for prioritizing this research.

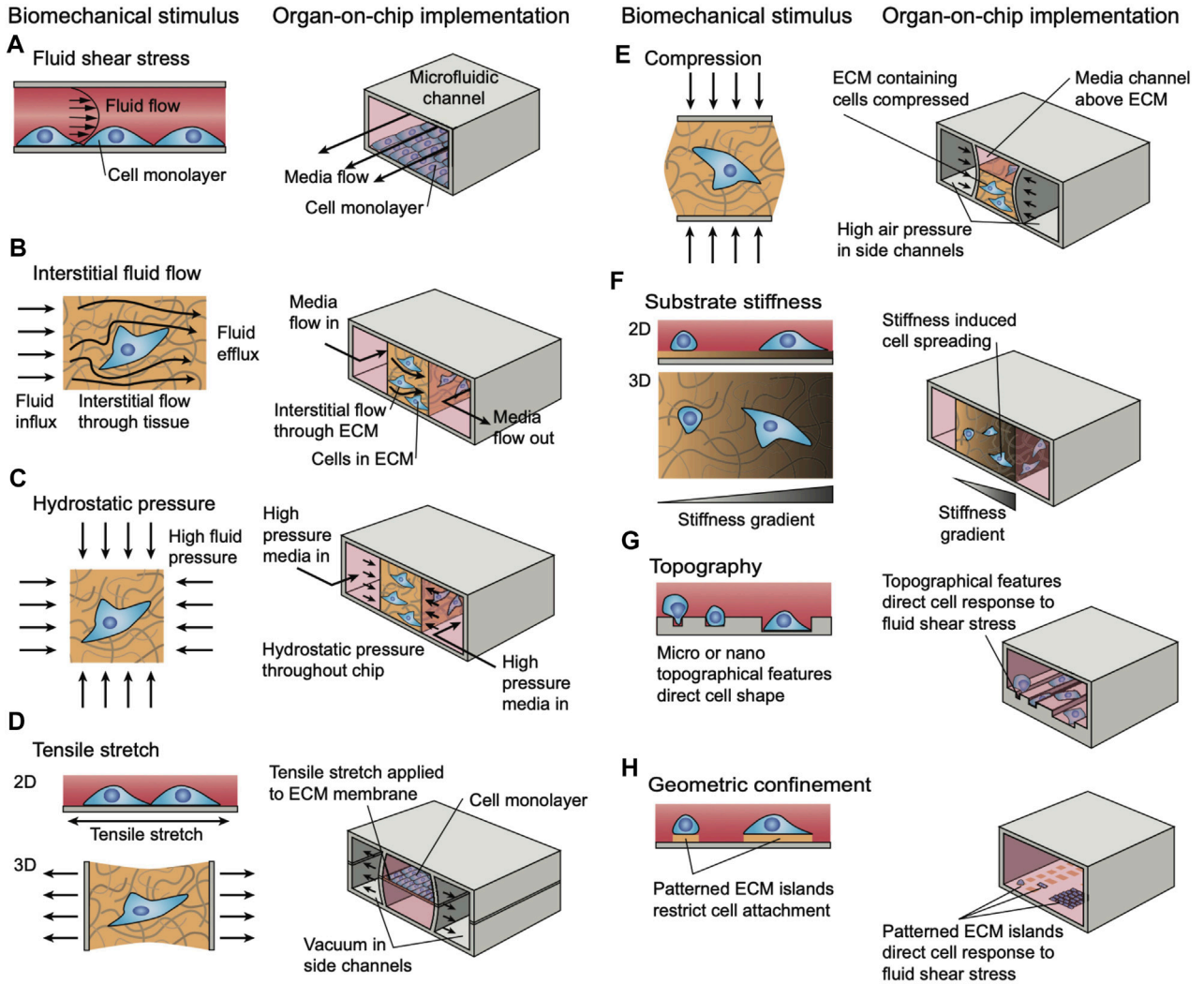

FIGURE 7 | Strategies for simulating different modalities of biomechanical loading and stimuli in microphysiological systems. Reproduced from (Thompson et al., 2020) under the Creative Commons Attribution License (CC BY).

5.4 Biomechanical Actuation and Loading

When considering the application of MPS to the musculoskeletal system, much of the utility of MPS relies on the ability to integrate mechanical stimulation through various actuation strategies. The functions of mechanical stimulation during development are well established, including in the musculoskeletal system (Mammoto et al., 2013). In development, forces exerted by muscles on neighboring tissues are important regulators of proper formation of mature musculoskeletal tissues. These effects are diverse and include controlling the 3-dimensional geometry of bones, developing strong muscle-tendon junctions, and many others. Even beyond development, mechanical forces have been shown to contribute to the health and function of mature tissues as well as aging ones. One example that has been studied extensively is the potential compensation of age-related bone loss by mechanical stimulation (Shwartz et al., 2013). Additionally, preclinical and clinical studies have demonstrated the effectiveness of physical therapy (mechanical loading) as a component of treatment protocol after musculoskeletal injuries. Therefore, it is imperative that musculoskeletal MPS incorporate mechanical stimuli that are native to the tissue.

There are numerous strategies of mechanical actuation applied in tissue-on-a-chip research platforms. However, implementation in musculoskeletal MPS models is still in development. One of the most common ways to mechanically stimulate MPS models is to deform the substrate upon which cells or tissues are cultured. Often, this is accomplished through the use of vacuum chambers to stretch a flexible PDMS membrane, as has been reported in a model alveolar-capillary membrane (Huh et al., 2010). A similar technique has been implemented in a muscle model of muscular dystrophy in an MPS (Michielin et al., 2015) to stretch microtissues made of fibroblast-laden collagen hydrogels (Walker et al., 2018). In these cases, the substrate actuates 2D monolayers through membrane deflection, to

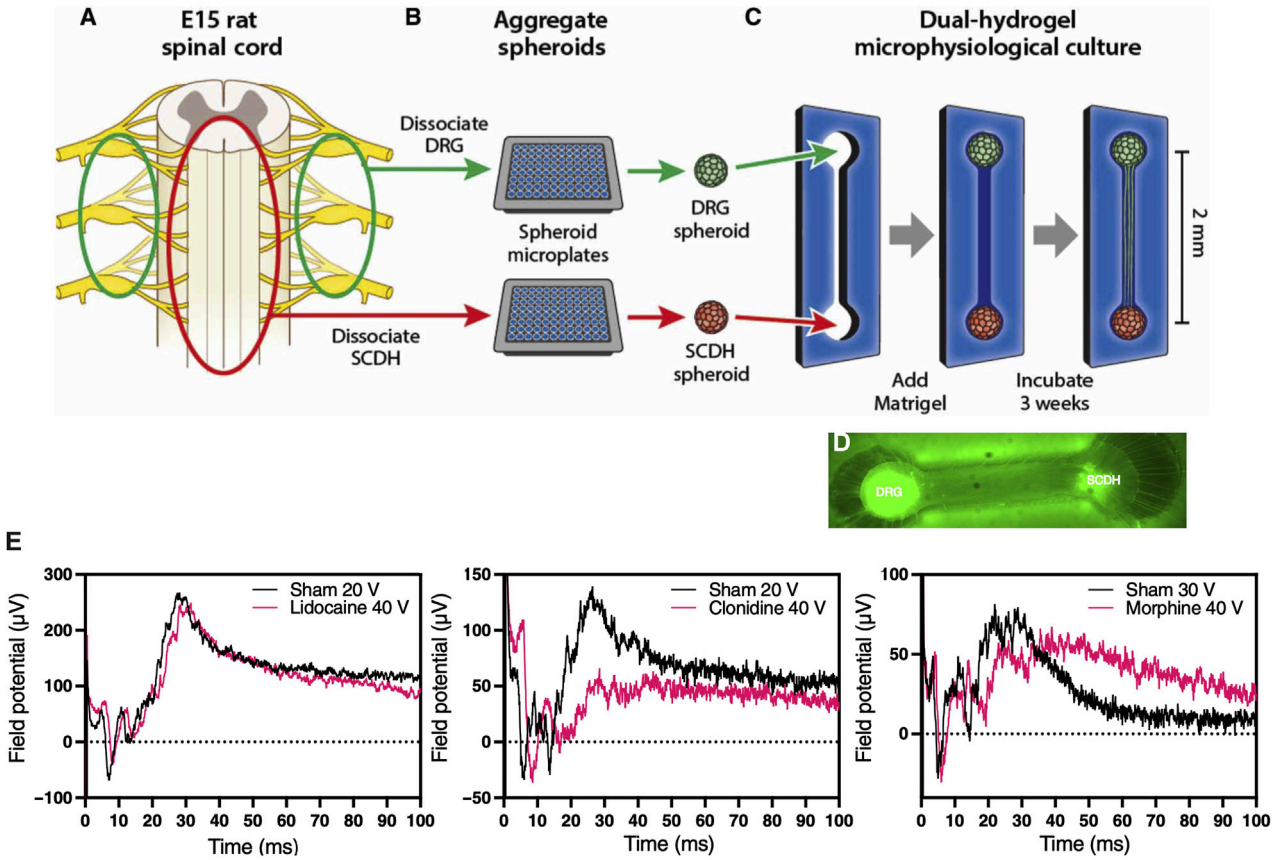

FIGURE 8 | Morphine-sensitive synaptic transmission in a microphysiological model of afferent nociceptive signaling. **(A)** Dorsal root ganglion (DRG) (green) and spinal cord dorsal horn (SCDH) (red) nerve tissues are harvested from E15 rat embryos. **(B)** Tissue is pooled by type, dissociated into a single-cell suspension, and aggregated in spheroid microplates to generate a batch of spheroids identical in size and composition. **(C)** A growth-restrictive outer-gel polyethylene glycol mold is fabricated to shape the cultures; spheroids are seeded in the mold, and the mold is filled with growth-permissive Matrigel. Over 3 weeks of culture, microphysiological tissue emerges **(D)** from which system-level functional data are obtained. **(E)** Differential desensitization of the afferent DRG input through treatments with lidocaine (left), clonidine (middle), and morphine (right) traces. [Reproduced from (Pollard et al., 2021) with permission].

simulate peristalsis or breathing motions, and 3D tissues which typically actuate multi-axially throughout the volume. These principles have been applied to MPS of cartilage-on-a-chip to introduce gradients of compression (Lee et al., 2018; Paggi et al., 2020) to simulate movements of joints. Other techniques involve using mechanical actuators to physically manipulate a substrate or device (Kamble et al., 2016) are frequently used for multi-axial actuation, however these techniques will often require larger experimental set-ups outside of the microfluidic device to provide the necessary actuation. These techniques may also be adapted to provide compressive loads on cells and tissues, for example to study osteogenesis from several stem cell sources (Park et al., 2012). Other, more passive, techniques for incorporating mechanical stimuli in MPS models through direct device manipulation include constraining cells in specially designed compartments and patterned substrates that illicit phenotypic changes (Männik et al., 2021). In general, these techniques are used in elastomeric PDMS-based microfluidic devices (**Figure 7**) (Thompson et al., 2020).

As most MPS models rely heavily on microfluidics for proper function, many have utilized controlled fluid flow to provide mechanical stimulation in their devices (Ergir et al., 2018). Typically, the stimulation by fluid flow is used to study the effects of shear stress in biological systems. This has been extensively utilized in recent research including in several bone models (Middleton et al., 2017). Still, fluidic-based actuation is most reasonable for systems modeling environments with fluid flow, such as blood vessels.

Beyond these two main categories of modeling *in vivo* forces and deformations, other, less common, techniques are also described in the literature (Ergir et al., 2018). These include acoustic based actuator, electromechanical and electromagnetic, and optical techniques. Electromechanical and electromagnetic techniques may involve electrical stimulation of cells in the

device or utilizing the electromagnetic properties of biomolecules or magnetic beads. Optical techniques may include the use of optical tweezers to provide small-scale stimulation of MPS models. Many of these techniques are not common presently as research in the field is still rapidly progressing.

5.5 Afferent Nociceptive Signaling (Pain) Outcomes

Peripheral sensory neurons known as nociceptors are responsible for relaying pain perception to specialized centers in the brain. Many acute and chronic musculoskeletal pathologies are painful. In fact, pain is often times linked to musculoskeletal functional impairments, and as such represents a key patient reported outcome in clinical trials, which is very challenging to replicate in MPS-based virtual clinical trials. Several MPS are being developed to model efferent nociceptive signaling in an effort to screen experimental compounds for analgesic effect that could alleviate the need for using opioids. A recent study modeled spinal cord dorsal horn, a common target for analgesic intervention, by coculturing peripheral and dorsal spinal cord nerve cells in a MPS, which led to autonomous emergence of native nerve tissue macrostructure and distinct synaptic transmission in response to different analgesics, including morphine, lidocaine, and clonidine (**Figure 8**) (Pollard et al., 2021). This demonstrates the potential to incorporate nociceptors in MPS to record surrogate signals for pain. To that end, Moy et al. (2021) incorporated sensory neurons into an established microJoint MPS to monitor the interplay between the peripheral nervous system and joint tissues (Moy et al., 2021). This could be accomplished by incorporating microchannels to enable sensory neuron innervation of joint tissues, where the neural activity is assessed with micro electrode arrays (MEAs) and fura2-based calcium imaging. Using a 3D printed PDMS system, the sensory dorsal root ganglion (DRG) neurons were allowed to extend in the microchannels and exposed to conditioned media from OA-modeled microJoint. This led to an increase in calcium flux in the sensory neuron microchannels. While the work is preliminary, it indicates the feasibility to incorporate sensory neurons in MPS to study OA pain via recording the electrical activity of the neurons or a surrogate calcium signal, which could be extended to other musculoskeletal pathologies.

5.6 Integration of Sensors

In addition to close recapitulation of tissue physiology and disease biomarkers *in vitro*, it is highly desirable for tissue chip models to be able to sense various parameters of the system to understand the dynamics of healthy tissue physiology, as well as in disease or injury states. Current MPS employ numerous sensing modalities, including fluorescence microscopy (Zahavi et al., 2015; Sheyn et al., 2019), electrical resistance of tissue barriers (Henry et al., 2017), microelectrode arrays for electrically active tissue (Jeong et al., 2018) and electrochemical signaling (Ezra et al., 2015), pH and dissolved gases (Bavli et al., 2016; Mousavi Shaegh et al., 2016; Prill et al., 2016), and stress/pressure sensors for muscle contractility (Aung et al., 2016), among others. These have revealed a great deal of information for physical and structural parameters of well-controlled MPS.

In addition, protein secretion by damaged or otherwise stimulated cells is an important aspect of musculoskeletal disease and injury. While the sensing mechanisms mentioned above are effective at yielding information about many different physical parameters of the system, the ability to sense proteins secreted by altered cells in real time would increase the value of the information obtained from such a model considerably. Current tissue chip models utilize sensors of primarily imaging outcomes or off-chip measurements of secreted proteins via standard assays. This leaves a great need in the field of musculoskeletal research for tissue chip models that incorporate sensitive, real-time protein sensors for the elucidation of disease and injury mechanisms. Some models include immunosensing modules for secreted analytes (Zhang et al., 2017); however, such models lack sensitivity and are downstream of the MPS, resulting in diluted analytes and loss of temporal resolution. To our knowledge, no MPS features real-time sensing of secreted analytes on the same chip as the cells being studied.

Real-time sensing for specific proteins secreted by an MPS will require integrating sensors able to achieve the sensitivity threshold required to observe relevant quantities of analytes secreted in musculoskeletal injury and disease. Current research indicates the detection of cytokines, as well as other proteins, at levels as low as pg/mL in serum or in macroscale *in vitro* models. However, some microfluidic *in vitro* models have shown single-cell secretion of cytokines from T-cells at levels in the ng/mL range at close proximity to the cells (Li et al., 2018). Thus, serum levels of secreted analytes might not accurately reflect levels in close proximity to their cellular source, due to downstream dilution. By relying on downstream sensor modules, analytes of interest become diluted, and the temporal information about their release may be lost. This further motivates sensor integration and highlights that tissue chip models incorporating label-free biosensing will need significant dynamic range as well as high sensitivity to detect and quantify important analytes.

To improve the quality of information obtained from *in vitro* tissue models, it is important to consider certain design parameters as the field progresses. Disease and injury sequelae can occur on short timescales, including in musculoskeletal injuries. Therefore, it is critical that *in vitro* models of these conditions are able to measure tissue responses in real time and should preferably incorporate inline antibody-functionalized sensors in close physical proximity to the tissue construct. Another important consideration is sensor regeneration, or the restoration of saturated antibody-functionalized surfaces. Many antibody regeneration protocols exist, usually consisting of harsh chemical treatments (Goode et al., 2015). If regeneration is required during experimental timeframes, the microfluidics of the system must be organized so that regeneration solutions do not come into contact with tissue components, since most regeneration formulae are toxic to cells.

5.7 Arrayed Formats for High Throughput Screening

While MPS enable gathering high content biochemical, functional, and histological data from each device, their value can be increased when the platform is composed of an array of chips that can be

assayed quickly and accurately for high throughput screens. Multiplexing has become common practice for researchers to analyze multiple factors at once, improving data consistency by allowing multiple targets to be investigated within the environment. The physical footprint of MPS must be amenable to high-throughput tests including access to culture media and tissues, visualization of tissue cultures, and simple assembly and operation. For example, a 96-well plate platform for bulk production of human muscle microtissues (hMMTs) for phenotypic drug testing has been developed (Afshar et al., 2020). The fabrication of the tissue plate is a simple one-stage casting step of a 96-well plate, which requires uncomplicated workflows with low number of cells used. Purified $CD56^+$ myogenic progenitor cells were differentiated into the skeletal muscle model, which was used to predict structural and functional treatment responses of Dexamethasone, Cerivastatin, and IGF-1, in addition to predicting effects of the chemotherapeutics Gemcitabine and Ironotecan (Afshar et al., 2020). Such models would be simple to integrate into drug screening and toxicity workflows as they can provide large data sets with minimal variability as tissue constructs can be differentiated identically *in situ*. Significant advancements have also been made in the functional genomics screening field where Caft-ID, a CRISPR-based microRaft array technology, followed by gRNA identification, was developed to couple the power of image-based phenotyping of stress granules with easy-to-use pooled CRISPR screening workflows on microRaft arrays. Stress granules are protein-RNA cytoplasmic foci that form transiently during cellular perturbations including oxidative stress, heat shock and immune activation and have been linked to degenerative diseases and even cancer. The Craft-ID platform expands on the power of CRISPR-screening to high-content imaging and machine learning to allow the interrogation of genetic modulators of subcellular and cell-morphological phenotypes which, previously were inaccessible with bulk infection models (Wheeler et al., 2020). This trend towards more automated, miniaturized MPS increases throughput and content of platforms, which has clear advantages for the early stages of drug discovery and screening in terms of improving rigor and reproducibility.

6 CONCLUSION

The poor translation from preclinical animal studies to human clinical applications and incomplete understanding of the mechanisms of action and the lack of biomarkers to define biological efficacy represent significant barriers that impede the development of disease modifying therapies for musculoskeletal conditions. The emerging technology of hMPS might offer transformative opportunities to cost-effectively address the aforementioned barriers. MPS is a wide-encompassing term for sophisticated *in vitro* human models, also known as tissue- and organ-on-a-chip, carefully designed to offer standardized predictive models by mimicking physiologically relevant aspects of living tissues and organ systems. Applications in modeling musculoskeletal acute and chronic injury are slowly developing. Keys to translational implementation MPS models of musculoskeletal pathologies include developing strategies to: engineer vascular and biological barriers and heterogenous tissue interfaces; incorporate immune cells and inflammatory factors; enable biomechanical actuation to simulate *in vivo* loading; incorporate sensory neurons (nociceptors) to record surrogate measurements for pain; integrate inline sensors for real-time monitoring of secreted proteins critical to modulating these dynamic processes; and develop arrayed formats for high throughput screening. Furthermore, issues of scalability, reproducibility, and validation, which are not discussed in this review, are also of paramount importance and have been addressed in other reviews (Hargrove-Grimes et al., 2021).

AUTHOR CONTRIBUTIONS

REA drafted the article. REA and HA prepared the figures. RGA, VZ, JC, BM, JM, HA made substantial, direct and intellectual contribution to the work, and got involved in the process of preparation, correction, and modification of the manuscript. All of them approved it for publication.

FUNDING

This manuscript was supported by the National Center for Advancing Translational Sciences (NCATS) and the National Institute of Arthritis and Musculoskeletal and Skin Diseases (NIAMS) of the National Institutes of Health under award number UG3TR003281. REA is funded by a Graduate Research Fellwoship Award from the National Science Foundation. RGA is funded by NIAMS training award T32AR076950. VZZ is funded by the National Institute of General Medical Sciences (NIGMS) training award T32GM007356. The content is solely the responsibility of the authors and does not necessarily represent the official views of the National Institutes of Health or the National Science Foundation.

ACKNOWLEDGMENTS

Graphics included in **Figures 1**, **2**, **4**, **5** were created with BioRender.com.

REFERENCES

Afshar Bakooshli, M., Lippmann, E. S., Mulcahy, B., Iyer, N., Nguyen, C. T., Tung, K., et al. (2019). A 3D Culture Model of Innervated Human Skeletal Muscle Enables Studies of the Adult Neuromuscular junction. *Elife* 8, e44530. doi:10.7554/eLife.44530

Afshar, M. E., Abraha, H. Y., Bakooshli, M. A., Davoudi, S., Thavandiran, N., Tung, K., et al. (2020). A 96-well Culture Platform Enables Longitudinal Analyses of Engineered Human Skeletal Muscle Microtissue Strength. *Sci. Rep.* 10, 6918. doi:10.1038/s41598-020-62837-8

Agrawal, G., Aung, A., and Varghese, S. (2017). Skeletal Muscle-On-A-Chip: An *In Vitro* Model to Evaluate Tissue Formation and Injury. *Lab. Chip* 17, 3447–3461. doi:10.1039/c7lc00512a

Alberts, B., Johnson, A., and Lewis, J. (2002). *Molecular Biology of the Cell*. 4th ed. New York: Garlan Science.

Aleman, J., George, S. K., Herberg, S., Devarasetty, M., Porada, C. D., Skardal, A., et al. (2019). Deconstructed Microfluidic Bone Marrow On-A-Chip to Study Normal and Malignant Hemopoietic Cell-Niche Interactions. *Small* 15, e1902971. doi:10.1002/smll.201902971

Andrzejewska, A., Lukomska, B., and Janowski, M. (2019). Concise Review: Mesenchymal Stem Cells: From Roots to Boost. *Stem Cells* 37, 855–864. doi:10.1002/stem.3016

Aung, A., Bhullar, I. S., Theprungsirikul, J., Davey, S. K., Lim, H. L., Chiu, Y.-J., et al. (2016). 3D Cardiac μtissues within a Microfluidic Device with Real-Time Contractile Stress Readout. *Lab. Chip* 16, 153–162. doi:10.1039/c5lc00820d

Bavli, D., Prill, S., Ezra, E., Levy, G., Cohen, M., Vinken, M., et al. (2016). Real-time Monitoring of Metabolic Function in Liver-On-Chip Microdevices Tracks the Dynamics of Mitochondrial Dysfunction. *Proc. Natl. Acad. Sci. USA* 113, E2231–E2240. doi:10.1073/pnas.1522556113

Bein, A., Shin, W., Jalili-Firoozinezhad, S., Park, M. H., Sontheimer-Phelps, A., Tovaglieri, A., et al. (2018). Microfluidic Organ-On-A-Chip Models of Human Intestine. *Cell Mol. Gastroenterol. Hepatol.* 5, 659–668. doi:10.1016/j.jcmgh.2017.12.010

Bellin, M., Marchetto, M. C., Gage, F. H., and Mummery, C. L. (2012). Induced Pluripotent Stem Cells: the New Patient? *Nat. Rev. Mol. Cel. Biol.* 13, 713–726. doi:10.1038/nrm3448

Bhatia, S. N., and Ingber, D. E. (2014). Microfluidic Organs-On-Chips. *Nat. Biotechnol.* 32, 760–772. doi:10.1038/nbt.2989

Bianchi, F., Malboubi, M., Li, Y., George, J. H., Jerusalem, A., Szele, F., et al. (2018). Rapid and Efficient Differentiation of Functional Motor Neurons from Human iPSC for Neural Injury Modelling. *Stem Cel Res.* 32, 126–134. doi:10.1016/j.scr.2018.09.006

Boccellato, F., Woelffling, S., Imai-Matsushima, A., Sanchez, G., Goosmann, C., Schmid, M., et al. (2019). Polarised Epithelial Monolayers of the Gastric Mucosa Reveal Insights into Mucosal Homeostasis and Defence against Infection. *Gut* 68, 400–413. doi:10.1136/gutjnl-2017-314540

Cao, X., Yakala, G. K., Van Den Hil, F. E., Cochrane, A., Mummery, C. L., and Orlova, V. V. (2019). Differentiation and Functional Comparison of Monocytes and Macrophages from hiPSCs with Peripheral Blood Derivatives. *Stem Cel Rep.* 12, 1282–1297. doi:10.1016/j.stemcr.2019.05.003

Caplan, A. I. (1994). The Mesengenic Process. *Clin. Plast. Surg.* 21, 429–435. doi:10.1016/s0094-1298(20)31020-8

Caplan, A. I. (2017). New MSC: MSCs as Pericytes Are Sentinels and Gatekeepers. *J. Orthop. Res.* 35, 1151–1159. doi:10.1002/jor.23560

Cereijido, M., Robbins, E., Dolan, W., Rotunno, C., and Sabatini, D. (1978). Polarized Monolayers Formed by Epithelial Cells on a Permeable and Translucent Support. *J. Cel. Biol.* 77, 853–880. doi:10.1083/jcb.77.3.853

Chen, M. B., Whisler, J. A., Fröse, J., Yu, C., Shin, Y., and Kamm, R. D. (2017). On-chip Human Microvasculature Assay for Visualization and Quantification of Tumor Cell Extravasation Dynamics. *Nat. Protoc.* 12, 865–880. doi:10.1038/nprot.2017.018

Chen, D., Wu, J. Y., Kennedy, K. M., Yeager, K., Bernhard, J. C., Ng, J. J., et al. (2020). Tissue Engineered Autologous Cartilage-Bone Grafts for Temporomandibular Joint Regeneration. *Sci. Transl. Med.* 12 (565), eabb6683. doi:10.1126/scitranslmed.abb6683

Chou, D. B., Frismantas, V., Milton, Y., David, R., Pop-Damkov, P., Ferguson, D., et al. (2020). On-chip Recapitulation of Clinical Bone Marrow Toxicities and Patient-specific Pathophysiology. *Nat. Biomed. Eng.* 4, 394–406. doi:10.1038/s41551-019-0495-z

Chung, H. H., Mireles, M., Kwarta, B. J., and Gaborski, T. R. (2018). Use of Porous Membranes in Tissue Barrier and Co-Culture Models. *Lab. Chip* 18, 1671–1689. doi:10.1039/c7lc01248a

Cohen, A., Ioannidis, K., Ehrlich, A., Regenbaum, S., Cohen, M., Ayyash, M., et al. (2021). Mechanism and Reversal of Drug-Induced Nephrotoxicity on a Chip. *Sci. Transl. Med.* 13, eabd6299. doi:10.1126/scitranslmed.abd6299

Crisan, M., Yap, S., Casteilla, L., Chen, C.-W., Corselli, M., Park, T. S., et al. (2008). A Perivascular Origin for Mesenchymal Stem Cells in Multiple Human Organs. *Cell Stem Cell* 3, 301–313. doi:10.1016/j.stem.2008.07.003

Cruz-Acuña, R., and García, A. J. (2017). Synthetic Hydrogels Mimicking Basement Membrane Matrices to Promote Cell-Matrix Interactions. *Matrix Biol.* 57-58, 324–333. doi:10.1016/j.matbio.2016.06.002

Culemann, S., Grüneboom, A., Nicolás-Ávila, J. Á., Weidner, D., Lämmle, K. F., Rothe, T., et al. (2019). Locally Renewing Resident Synovial Macrophages Provide a Protective Barrier for the Joint. *Nature* 572, 670–675. doi:10.1038/s41586-019-1471-1

Cunniffe, G. M., Díaz-Payno, P. J., Sheehy, E. J., Critchley, S. E., Almeida, H. V., Pitacco, P., et al. (2019). Tissue-specific Extracellular Matrix Scaffolds for the Regeneration of Spatially Complex Musculoskeletal Tissues. *Biomaterials* 188, 63–73. doi:10.1016/j.biomaterials.2018.09.044

Davis, B. N., Yen, R., Prasad, V., and Truskey, G. A. (2019). Oxygen Consumption in Human, Tissue-Engineered Myobundles during Basal and Electrical Stimulation Conditions. *APL Bioeng.* 3, 026103. doi:10.1063/1.5093417

De Pieri, A., Rochev, Y., and Zeugolis, D. I. (2021). Scaffold-free Cell-Based Tissue Engineering Therapies: Advances, Shortfalls and Forecast. *Npj Regen. Med.* 6, 18. doi:10.1038/s41536-021-00133-3

De Souza, N. (2018). Organoids. *Nat. Methods* 15, 23. doi:10.1038/nmeth.4576

Dellaquila, A., Le Bao, C., Letourneur, D., and Simon-Yarza, T. (2021). Vitro Strategies to Vascularize 3D Physiologically Relevant Models. *Adv. Sci. (Weinheim, Baden-Wurttemberg, Germany)* 8, e2100798. doi:10.1002/advs.202100798

Ellis, M., Jarman-Smith, M., and Chaudhuri, J. B. (2005). "Bioreactor Systems for Tissue Engineering: A Four-Dimensional Challenge," in *Bioreactors for Tissue Engineering: Principles, Design and Operation*. Editors J. Chaudhuri and M. Al-Rubeai (Dordrecht: Springer Netherlands), 1–18.

Ergir, E., Bachmann, B., Redl, H., Forte, G., and Ertl, P. (2018). Small Force, Big Impact: Next Generation Organ-On-A-Chip Systems Incorporating Biomechanical Cues. *Front. Physiol.* 9, 1417. doi:10.3389/fphys.2018.01417

Esch, E. W., Bahinski, A., and Huh, D. (2015). Organs-on-chips at the Frontiers of Drug Discovery. *Nat. Rev. Drug Discov.* 14, 248–260. doi:10.1038/nrd4539

Ewald, M. L., Chen, Y.-H., Lee, A. P., and Hughes, C. C. W. (2021). The Vascular Niche in Next Generation Microphysiological Systems. *Lab. Chip* 21, 3244–3262. doi:10.1039/d1lc00530h

Ezra, E., Maor, I., Bavli, D., Shalom, I., Levy, G., Prill, S., et al. (2015). Microprocessor-based Integration of Microfluidic Control for the Implementation of Automated Sensor Monitoring and Multithreaded Optimization Algorithms. *Biomed. Microdevices* 17, 82. doi:10.1007/s10544-015-9989-y

Faustino Martins, J.-M., Fischer, C., Urzi, A., Vidal, R., Kunz, S., Ruffault, P.-L., et al. (2020). Self-Organizing 3D Human Trunk Neuromuscular Organoids. *Cell Stem Cell* 26, 172–186.e6. doi:10.1016/j.stem.2019.12.007

Fogel, D. B. (2018). Factors Associated with Clinical Trials that Fail and Opportunities for Improving the Likelihood of success: A Review. *Contemp. Clin. trials Commun.* 11, 156–164. doi:10.1016/j.conctc.2018.08.001

Friedenstein, A. J., Chailakhyan, R. K., and Gerasimov, U. V. (1987). Bone Marrow Osteogenic Stem Cells: *In Vitro* Cultivation and Transplantation in Diffusion chambers. *Cell Prolif.* 20, 263–272. doi:10.1111/j.1365-2184.1987.tb01309.x

Goode, J. A., Rushworth, J. V. H., and Millner, P. A. (2015). Biosensor Regeneration: A Review of Common Techniques and Outcomes. *Langmuir* 31, 6267–6276. doi:10.1021/la503533g

Gough, A., Vernetti, L., Bergenthal, L., Shun, T. Y., and Taylor, D. L. (2016). The Microphysiology Systems Database for Analyzing and Modeling Compound Interactions with Human and Animal Organ Models. *Appl. Vitro Toxicol.* 2, 103–117. doi:10.1089/aivt.2016.0011

Griep, L. M., Wolbers, F., De Wagenaar, B., Ter Braak, P. M., Weksler, B. B., Romero, I. A., et al. (2013). BBB on Chip: Microfluidic Platform to

Mechanically and Biochemically Modulate Blood-Brain Barrier Function. *Biomed. Microdevices* 15, 145–150. doi:10.1007/s10544-012-9699-7

Hannemann, N., Apparailly, F., and Courties, G. (2021). Synovial Macrophages: from Ordinary Eaters to Extraordinary Multitaskers. *Trends Immunol.* 42, 368–371. doi:10.1016/j.it.2021.03.002

Hao, S., Ha, L., Cheng, G., Wan, Y., Xia, Y., Sosnoski, D. M., et al. (2018). A Spontaneous 3D Bone-On-A-Chip for Bone Metastasis Study of Breast Cancer Cells. *Small* 14, e1702787. doi:10.1002/smll.201702787

Hargrove-Grimes, P., Low, L. A., and Tagle, D. A. (2021). Microphysiological Systems: What it Takes for Community Adoption. *Exp. Biol. Med. (Maywood)* 246, 1435–1446. doi:10.1177/15353702211008872

Hay, M., Thomas, D. W., Craighead, J. L., Economides, C., and Rosenthal, J. (2014). Clinical Development success Rates for Investigational Drugs. *Nat. Biotechnol.* 32, 40–51. doi:10.1038/nbt.2786

Hayflick, L., and Moorhead, P. S. (1961). The Serial Cultivation of Human Diploid Cell Strains. *Exp. Cel. Res.* 25, 585–621. doi:10.1016/0014-4827(61)90192-6

Henry, O. Y. F., Villenave, R., Cronce, M. J., Leineweber, W. D., Benz, M. A., and Ingber, D. E. (2017). Organs-on-Chips with Integrated Electrodes for Trans-epithelial Electrical Resistance (TEER) Measurements of Human Epithelial Barrier Function. *Lab. Chip* 17, 2264–2271. doi:10.1039/c7lc00155j

Hsu, J. R., Mir, H., Wally, M. K., and Seymour, R. B. (2019). Clinical Practice Guidelines for Pain Management in Acute Musculoskeletal Injury. *J. Orthop. Trauma* 33, e158–e182. doi:10.1097/bot.0000000000001430

Huh, D., Matthews, B. D., Mammoto, A., Montoya-Zavala, M., Hsin, H. Y., and Ingber, D. E. (2010). Reconstituting Organ-Level Lung Functions on a Chip. *Science* 328, 1662–1668. doi:10.1126/science.1188302

Iordachescu, A., Hughes, E. A. B., Joseph, S., Hill, E. J., Grover, L. M., and Metcalfe, A. D. (2021). Trabecular Bone Organoids: a Micron-Scale 'humanised' Prototype Designed to Study the Effects of Microgravity and Degeneration. *NPJ Microgravity* 7, 17. doi:10.1038/s41526-021-00146-8

Jeon, J. S., Bersini, S., Gilardi, M., Dubini, G., Charest, J. L., Moretti, M., et al. (2015). Human 3D Vascularized Organotypic Microfluidic Assays to Study Breast Cancer Cell Extravasation. *Proc. Natl. Acad. Sci. USA* 112, 214–219. doi:10.1073/pnas.1417115112

Jeong, S., Kim, S., Buonocore, J., Park, J., Welsh, C. J., Li, J., et al. (2018). A Three-Dimensional Arrayed Microfluidic Blood-Brain Barrier Model with Integrated Electrical Sensor Array. *IEEE Trans. Biomed. Eng.* 65, 431–439. doi:10.1109/tbme.2017.2773463

Jiang, Y., Yang, Y., Zheng, X., Yi, Y., Chen, X., Li, Y., et al. (2020). Multifunctional Load-Bearing Hybrid Hydrogel with Combined Drug Release and Photothermal Conversion Functions. *NPG Asia Mater.* 12, 18. doi:10.1038/s41427-020-0199-6

Jinek, M., Chylinski, K., Fonfara, I., Hauer, M., Doudna, J. A., and Charpentier, E. (2012). A Programmable Dual-RNA-Guided DNA Endonuclease in Adaptive Bacterial Immunity. *Science* 337, 816–821. doi:10.1126/science.1225829

Kamble, H., Barton, M. J., Jun, M., Park, S., and Nguyen, N.-T. (2016). Cell Stretching Devices as Research Tools: Engineering and Biological Considerations. *Lab. Chip* 16, 3193–3203. doi:10.1039/c6lc00607h

Khodabukus, A., Madden, L., Prabhu, N. K., Koves, T. R., Jackman, C. P., Muoio, D. M., et al. (2019). Electrical Stimulation Increases Hypertrophy and Metabolic Flux in Tissue-Engineered Human Skeletal Muscle. *Biomaterials* 198, 259–269. doi:10.1016/j.biomaterials.2018.08.058

Kim, S., Lee, H., Chung, M., and Jeon, N. L. (2013). Engineering of Functional, Perfusable 3D Microvascular Networks on a Chip. *Lab. Chip* 13, 1489–1500. doi:10.1039/c3lc41320a

Knudsen, A. B., Larsen, M., Mackey, A. L., Hjort, M., Hansen, K. K., Qvortrup, K., et al. (2015). The Human Myotendinous junction: an Ultrastructural and 3D Analysis Study. *Scand. J. Med. Sci. Sports* 25, e116–e123. doi:10.1111/sms.12221

Kotha, S. S., Hayes, B. J., Phong, K. T., Redd, M. A., Bomsztyk, K., Ramakrishnan, A., et al. (2018). Engineering a Multicellular Vascular Niche to Model Hematopoietic Cell Trafficking. *Stem Cel. Res. Ther.* 9, 77–14. doi:10.1186/s13287-018-0808-2

LaPrade, R. F., Dragoo, J. L., Koh, J. L., Murray, I. R., Geeslin, A. G., and Chu, C. R. (2016). AAOS Research Symposium Updates and Consensus: Biologic Treatment of Orthopaedic Injuries. *J. Am. Acad. Orthop. Surg.* 24, e62–e78. doi:10.5435/jaaos-d-16-00086

Lee, D., Erickson, A., You, T., Dudley, A. T., and Ryu, S. (2018). Pneumatic Microfluidic Cell Compression Device for High-Throughput Study of Chondrocyte Mechanobiology. *Lab. Chip* 18, 2077–2086. doi:10.1039/c8lc00320c

Li, X., Xie, J., Lipner, J., Yuan, X., Thomopoulos, S., and Xia, Y. (2009). Nanofiber Scaffolds with Gradations in mineral Content for Mimicking the Tendon-To-Bone Insertion Site. *Nano Lett.* 9, 2763–2768. doi:10.1021/nl901582f

Li, X., Soler, M., Szydzik, C., Khoshmanesh, K., Schmidt, J., Coukos, G., et al. (2018). Label-Free Optofluidic Nanobiosensor Enables Real-Time Analysis of Single-Cell Cytokine Secretion. *Small* 14, e1800698. doi:10.1002/smll.201800698

Li, Z., Seo, Y., Aydin, O., Elhebeary, M., Kamm, R. D., Kong, H., et al. (2019). Biohybrid Valveless Pump-Bot Powered by Engineered Skeletal Muscle. *Proc. Natl. Acad. Sci. USA* 116, 1543–1548. doi:10.1073/pnas.1817682116

Li, Z., Xiang, S., Li, E. N., Fritch, M. R., Alexander, P. G., Lin, H., et al. (2021). Tissue Engineering for Musculoskeletal Regeneration and Disease Modeling. *Handbook Exp. Pharmacol.* 265, 235–268. doi:10.1007/164_2020_377

Lin, Z., Li, Z., Li, E. N., Li, X., Del Duke, C. J., Shen, H., et al. (2019). Osteochondral Tissue Chip Derived from iPSCs: Modeling OA Pathologies and Testing Drugs. *Front. Bioeng. Biotechnol.* 7, 411. doi:10.3389/fbioe.2019.00411

Lorsch, J. R., Collins, F. S., and Lippincott-Schwartz, J. (2014). Fixing Problems with Cell Lines. *Science* 346, 1452–1453. doi:10.1126/science.1259110

Männik, J., Teshima, T. F., Wolfrum, B., and Yang, D. (2021). Lab-on-a-chip Based Mechanical Actuators and Sensors for Single-Cell and Organoid Culture Studies. *J. Appl. Phys.* 129, 210905. doi:10.1063/5.0051875

Mammoto, T., Mammoto, A., and Ingber, D. E. (2013). Mechanobiology and Developmental Control. *Annu. Rev. Cel Dev. Biol.* 29, 27–61. doi:10.1146/annurev-cellbio-101512-122340

Manfrin, A., Tabata, Y., Paquet, E. R., Vuaridel, A. R., Rivest, F. R., Naef, F., et al. (2019). Engineered Signaling Centers for the Spatially Controlled Patterning of Human Pluripotent Stem Cells. *Nat. Methods* 16, 640–648. doi:10.1038/s41592-019-0455-2

Marsano, A., Conficconi, C., Lemme, M., Occhetta, P., Gaudiello, E., Votta, E., et al. (2016). Beating Heart on a Chip: a Novel Microfluidic Platform to Generate Functional 3D Cardiac Microtissues. *Lab. Chip* 16, 599–610. doi:10.1039/c5lc01356a

Marturano-Kruik, A., Nava, M. M., Yeager, K., Chramiec, A., Hao, L., Robinson, S., et al. (2018). Human Bone Perivascular Niche-On-A-Chip for Studying Metastatic Colonization. *Proc. Natl. Acad. Sci. USA* 115, 1256–1261. doi:10.1073/pnas.1714282115

Michielin, F., Serena, E., Pavan, P., and Elvassore, N. (2015). Microfluidic-assisted Cyclic Mechanical Stimulation Affects Cellular Membrane Integrity in a Human Muscular Dystrophy *In Vitro* Model. *RSC Adv.* 5, 98429–98439. doi:10.1039/c5ra16957g

Middleton, K., Al-Dujaili, S., Mei, X., Günther, A., and You, L. (2017). Microfluidic Co-culture Platform for Investigating Osteocyte-Osteoclast Signalling during Fluid Shear Stress Mechanostimulation. *J. Biomech.* 59, 35–42. doi:10.1016/j.jbiomech.2017.05.012

Mondadori, C., Palombella, S., Salehi, S., Talò, G., Visone, R., Rasponi, M., et al. (2021). Recapitulating Monocyte Extravasation to the Synovium in an Organotypic Microfluidic Model of the Articular Joint. *Biofabrication* 13, 045001. doi:10.1088/1758-5090/ac0c5e

Mondrinos, M. J., Alisafaei, F., Yi, A. Y., Ahmadzadeh, H., Lee, I., Blundell, C., et al. (2021). Surface-directed Engineering of Tissue Anisotropy in Microphysiological Models of Musculoskeletal Tissue. *Sci. Adv.* 7, eabe9446. doi:10.1126/sciadv.abe9446

Mousavi Shaegh, S. A., De Ferrari, F., Zhang, Y. S., Nabavinia, M., Binth Mohammad, N., Ryan, J., et al. (2016). A Microfluidic Optical Platform for Real-Time Monitoring of pH and Oxygen in Microfluidic Bioreactors and Organ-On-Chip Devices. *Biomicrofluidics* 10, 044111. doi:10.1063/1.4955155

Moy, J., Li, Z., Liu, F.-W., Loeza-Alcocer, E., Hartung, J., Nagarajan, V., et al. (2021). Modeling Joint Pain on a Chip: Integrating Sensory Neurons in the microJoint to Model Osteoarthritis. *The J. Pain* 22, 583. doi:10.1016/j.jpain.2021.03.025

Müller, B., Sulzer, P., Walch, M., Zirath, H., Buryška, T., Rothbauer, M., et al. (2021). Measurement of Respiration and Acidification Rates of Mammalian Cells in Thermoplastic Microfluidic Devices. *Sensors Actuators B: Chem.* 334, 129664. doi:10.1016/j.snb.2021.129664

Murphy, K. M., and Weaver, C. (2016). *Janeway's Immunobiology: Ninth International Student Edition*. (Florida, NY: Garland Science, Taylor & Francis Group, LLC).

Nakajima, T., Nakahata, A., Yamada, N., Yoshizawa, K., Kato, T. M., Iwasaki, M., et al. (2021). Grafting of iPS Cell-Derived Tenocytes Promotes Motor Function Recovery after Achilles Tendon Rupture. *Nat. Commun.* 12, 5012. doi:10.1038/s41467-021-25328-6

Nesmith, A. P., Wagner, M. A., Pasqualini, F. S., O'Connor, B. B., Pincus, M. J., August, P. R., et al. (2016). A Human *In Vitro* Model of Duchenne Muscular Dystrophy Muscle Formation and Contractility. *J. Cel. Biol.* 215, 47–56. doi:10.1083/jcb.201603111

Nguyen, T., Jung, S. H., Lee, M. S., Park, T.-E., Ahn, S.-K., and Kang, J. H. (2019). Robust Chemical Bonding of PMMA Microfluidic Devices to Porous PETE Membranes for Reliable Cytotoxicity Testing of Drugs. *Lab. Chip* 19, 3706–3713. doi:10.1039/c9lc00338j

Occhetta, P., Mainardi, A., Votta, E., Vallmajo-Martin, Q., Ehrbar, M., Martin, I., et al. (2019). Hyperphysiological Compression of Articular Cartilage Induces an Osteoarthritic Phenotype in a Cartilage-On-A-Chip Model. *Nat. Biomed. Eng.* 3, 545–557. doi:10.1038/s41551-019-0406-3

Orkin, S. H., and Zon, L. I. (2008). Hematopoiesis: An Evolving Paradigm for Stem Cell Biology. *Cell* 132, 631–644. doi:10.1016/j.cell.2008.01.025

Osaki, T., Sivathanu, V., and Kamm, R. D. (2018). Crosstalk between Developing Vasculature and Optogenetically Engineered Skeletal Muscle Improves Muscle Contraction and Angiogenesis. *Biomaterials* 156, 65–76. doi:10.1016/j.biomaterials.2017.11.041

Osaki, T., Uzel, S. G. M., and Kamm, R. D. (2020). On-chip 3D Neuromuscular Model for Drug Screening and Precision Medicine in Neuromuscular Disease. *Nat. Protoc.* 15, 421–449. doi:10.1038/s41596-019-0248-1

Paggi, C. A., Venzac, B., Karperien, M., Leijten, J. C. H., and Le Gac, S. (2020). Monolithic Microfluidic Platform for Exerting Gradients of Compression on Cell-Laden Hydrogels, and Application to a Model of the Articular Cartilage. *Sens. Actuators B: Chem.* 315, 127917. doi:10.1016/j.snb.2020.127917

Park, S.-H., Sim, W. Y., Min, B.-H., Yang, S. S., Khademhosseini, A., and Kaplan, D. L. (2012). Chip-Based Comparison of the Osteogenesis of Human Bone Marrow- and Adipose Tissue-Derived Mesenchymal Stem Cells under Mechanical Stimulation. *PLoS ONE* 7, e46689. doi:10.1371/journal.pone.0046689

Park, Y., Cheong, E., Kwak, J.-G., Carpenter, R., Shim, J.-H., and Lee, J. (2021). Trabecular Bone Organoid Model for Studying the Regulation of Localized Bone Remodeling. *Sci. Adv.* 7, eabd6495. doi:10.1126/sciadv.abd6495

Patel, S., Caldwell, J. M., Doty, S. B., Levine, W. N., Rodeo, S., Soslowsky, L. J., et al. (2018). Integrating Soft and Hard Tissues via Interface Tissue Engineering. *J. Orthop. Res.* 36, 1069–1077. doi:10.1002/jor.23810

Patsch, C., Challet-Meylan, L., Thoma, E. C., Urich, E., Heckel, T., O'Sullivan, J. F., et al. (2015). Generation of Vascular Endothelial and Smooth Muscle Cells from Human Pluripotent Stem Cells. *Nat. Cel Biol* 17, 994–1003. doi:10.1038/ncb3205

Pereira, J. D., Dubreuil, D. M., Devlin, A.-C., Held, A., Sapir, Y., Berezovski, E., et al. (2021). Human Sensorimotor Organoids Derived from Healthy and Amyotrophic Lateral Sclerosis Stem Cells Form Neuromuscular Junctions. *Nat. Commun.* 12, 4744. doi:10.1038/s41467-021-24776-4

Phillips, J. E., Burns, K. L., Le Doux, J. M., Guldberg, R. E., and Garcia, A. J. (2008). Engineering Graded Tissue Interfaces. *Proc. Natl. Acad. Sci.* 105, 12170–12175. doi:10.1073/pnas.0801988105

Pirosa, A., Clark, K. L., Tan, J., Yu, S., Yang, Y., Tuan, R. S., et al. (2019). Modeling Appendicular Skeletal Cartilage Development with Modified High-Density Micromass Cultures of Adult Human Bone Marrow-Derived Mesenchymal Progenitor Cells. *Stem Cel. Res. Ther.* 10, 388. doi:10.1186/s13287-019-1505-5

Pittenger, M. F., Mackay, A. M., Beck, S. C., Jaiswal, R. K., Douglas, R., Mosca, J. D., et al. (1999). Multilineage Potential of Adult Human Mesenchymal Stem Cells. *Science* 284, 143–147. doi:10.1126/science.284.5411.143

Polini, A., Del Mercato, L. L., Barra, A., Zhang, Y. S., Calabi, F., and Gigli, G. (2019). Towards the Development of Human Immune-System-On-A-Chip Platforms. *Drug Discov. Today* 24, 517–525. doi:10.1016/j.drudis.2018.10.003

Pollard, K. J., Bowser, D. A., Anderson, W. A., Meselhe, M., and Moore, M. J. (2021). Morphine-sensitive Synaptic Transmission Emerges in Embryonic Rat Microphysiological Model of Lower Afferent Nociceptive Signaling. *Sci. Adv.* 7, eabj2899. doi:10.1126/sciadv.abj2899

Prill, S., Bavli, D., Levy, G., Ezra, E., Schmälzlin, E., Jaeger, M. S., et al. (2016). Real-time Monitoring of Oxygen Uptake in Hepatic Bioreactor Shows CYP450-independent Mitochondrial Toxicity of Acetaminophen and Amiodarone. *Arch. Toxicol.* 90, 1181–1191. doi:10.1007/s00204-015-1537-2

Raasch, M., Fritsche, E., Kurtz, A., Bauer, M., and Mosig, A. S. (2019). Microphysiological Systems Meet hiPSC Technology - New Tools for Disease Modeling of Liver Infections in Basic Research and Drug Development. *Adv. Drug Deliv. Rev.* 140, 51–67. doi:10.1016/j.addr.2018.06.008

Rao, L., Qian, Y., Khodabukus, A., Ribar, T., and Bursac, N. (2018). Engineering Human Pluripotent Stem Cells into a Functional Skeletal Muscle Tissue. *Nat. Commun.* 9, 126. doi:10.1038/s41467-017-02636-4

Ren, K., Zhou, J., and Wu, H. (2013). Materials for Microfluidic Chip Fabrication. *Acc. Chem. Res.* 46, 2396–2406. doi:10.1021/ar300314s

Rodríguez Cruz, P. M., Cossins, J., Beeson, D., and Vincent, A. (2020). The Neuromuscular Junction in Health and Disease: Molecular Mechanisms Governing Synaptic Formation and Homeostasis. *Front. Mol. Neurosci.* 13, 610964. doi:10.3389/fnmol.2020.610964

Rosser, J., Bachmann, B., Jordan, C., Ribitsch, I., Haltmayer, E., Gueltekin, S., et al. (2019). Microfluidic Nutrient Gradient-Based Three-Dimensional Chondrocyte Culture-On-A-Chip as an *In Vitro* Equine Arthritis Model. *Mater. Today Bio* 4, 100023. doi:10.1016/j.mtbio.2019.100023

Rossi, G., Manfrin, A., and Lutolf, M. P. (2018). Progress and Potential in Organoid Research. *Nat. Rev. Genet.* 19, 671–687. doi:10.1038/s41576-018-0051-9

Rowland, C. R., Glass, K. A., Ettyreddy, A. R., Gloss, C. C., Matthews, J. R. L., Huynh, N. P. T., et al. (2018). Regulation of Decellularized Tissue Remodeling via Scaffold-Mediated Lentiviral Delivery in Anatomically-Shaped Osteochondral Constructs. *Biomaterials* 177, 161–175. doi:10.1016/j.biomaterials.2018.04.049

Sano, E., Mori, C., Matsuoka, N., Ozaki, Y., Yagi, K., Wada, A., et al. (2019). Tetrafluoroethylene-Propylene Elastomer for Fabrication of Microfluidic Organs-On-Chips Resistant to Drug Absorption. *Micromachines* 10, 793. doi:10.3390/mi10110793

Santhanam, N., Kumanchik, L., Guo, X., Sommerhage, F., Cai, Y., Jackson, M., et al. (2018). Stem Cell Derived Phenotypic Human Neuromuscular junction Model for Dose Response Evaluation of Therapeutics. *Biomaterials* 166, 64–78. doi:10.1016/j.biomaterials.2018.02.047

Sasserath, T., Rumsey, J. W., Mcaleer, C. W., Bridges, L. R., Long, C. J., Elbrecht, D., et al. (2020). Differential Monocyte Actuation in a Three-Organ Functional Innate Immune System-on-a-Chip. *Adv. Sci.* 7, 2000323. doi:10.1002/advs.202000323

Sebbag, E., Felten, R., Sagez, F., Sibilia, J., Devilliers, H., and Arnaud, L. (2019). The World-wide burden of Musculoskeletal Diseases: a Systematic Analysis of the World Health Organization Burden of Diseases Database. *Ann. Rheum. Dis.* 78, 844–848. doi:10.1136/annrheumdis-2019-215142

Sego, T. J., Prideaux, M., Sterner, J., Mccarthy, B. P., Li, P., Bonewald, L. F., et al. (2020). Computational Fluid Dynamic Analysis of Bioprinted Self-supporting Perfused Tissue Models. *Biotechnol. Bioeng.* 117, 798–815. doi:10.1002/bit.27238

Sherr, C. J., and DePinho, R. A. (2000). Cellular Senescence: Minireview Mitotic Clock or Culture Shock? *Cell* 102, 407–410. doi:10.1016/s0092-8674(00)00046-5

Sheyn, D., Cohn-Yakubovich, D., Ben-David, S., De Mel, S., Chan, V., Hinojosa, C., et al. (2019). Bone-chip System to Monitor Osteogenic Differentiation Using Optical Imaging. *Microfluid Nanofluidics* 23, 99. doi:10.1007/s10404-019-2261-7

Shoshani, O., and Zipori, D. (2015). Stress as a Fundamental Theme in Cell Plasticity. *Biochim. Biophys. Acta (Bba) - Gene Regul. Mech.* 1849, 371–377. doi:10.1016/j.bbagrm.2014.07.006

Shwartz, Y., Blitz, E., and Zelzer, E. (2013). One Load to Rule Them All: Mechanical Control of the Musculoskeletal System in Development and Aging. *Differentiation* 86, 104–111. doi:10.1016/j.diff.2013.07.003

Sung, J. H., Esch, M. B., Prot, J.-M., Long, C. J., Smith, A., Hickman, J. J., et al. (2013). Microfabricated Mammalian Organ Systems and Their Integration into Models of Whole Animals and Humans. *Lab. Chip* 13, 1201–1212. doi:10.1039/c3lc41017j

Sunwoo, J. Y., Eliasberg, C. D., Carballo, C. B., and Rodeo, S. A. (2020). The Role of the Macrophage in Tendinopathy and Tendon Healing. *J. Orthop. Res.* 38, 1666–1675. doi:10.1002/jor.24667

Takahashi, K., and Yamanaka, S. (2006). Induction of Pluripotent Stem Cells from Mouse Embryonic and Adult Fibroblast Cultures by Defined Factors. *Cell* 126, 663–676. doi:10.1016/j.cell.2006.07.024

Terrell, J. A., Jones, C. G., Kabandana, G. K. M., and Chen, C. (2020). From Cells-On-A-Chip to Organs-On-A-Chip: Scaffolding Materials for 3D Cell Culture in Microfluidics. *J. Mater. Chem. B* 8, 6667–6685. doi:10.1039/d0tb00718h

Thompson, C. L., Fu, S., Knight, M. M., Thorpe, S. D., and Thorpe, S. D. (2020). Mechanical Stimulation: A Crucial Element of Organ-On-Chip Models. *Front. Bioeng. Biotechnol.* 8, 602646. doi:10.3389/fbioe.2020.602646

Thomson, J. A., Itskovitz-Eldor, J., Shapiro, S. S., Waknitz, M. A., Swiergiel, J. J., Marshall, V. S., et al. (1998). Embryonic Stem Cell Lines Derived from Human Blastocysts. *Science* 282, 1145–1147. doi:10.1126/science.282.5391.1145

Walker, M., Godin, M., and Pelling, A. E. (2018). A Vacuum-Actuated Microtissue Stretcher for Long-Term Exposure to Oscillatory Strain within a 3D Matrix. *Biomed. Microdevices* 20, 43. doi:10.1007/s10544-018-0286-4

Wheeler, E. C., Vu, A. Q., Einstein, J. M., Disalvo, M., Ahmed, N., Van Nostrand, E. L., et al. (2020). Pooled CRISPR Screens with Imaging on Microraft Arrays Reveals Stress Granule-Regulatory Factors. *Nat. Methods* 17, 636–642. doi:10.1038/s41592-020-0826-8

Wu, C.-L., Dicks, A., Steward, N., Tang, R., Katz, D. B., Choi, Y.-R., et al. (2021). Single Cell Transcriptomic Analysis of Human Pluripotent Stem Cell Chondrogenesis. *Nat. Commun.* 12, 362. doi:10.1038/s41467-020-20598-y

Yeste, J., Illa, X., Alvarez, M., and Villa, R. (2018). Engineering and Monitoring Cellular Barrier Models. *J. Biol. Eng.* 12, 18. doi:10.1186/s13036-018-0108-5

Yu, J., Vodyanik, M. A., Smuga-Otto, K., Antosiewicz-Bourget, J., Frane, J. L., Tian, S., et al. (2007). Induced Pluripotent Stem Cell Lines Derived from Human Somatic Cells. *Science* 318, 1917–1920. doi:10.1126/science.1151526

Zahavi, E. E., Ionescu, A., Gluska, S., Gradus, T., Ben-Yaakov, K., and Perlson, E. (2015). A Compartmentalized Microfluidic Neuromuscular Co-culture System Reveals Spatial Aspects of GDNF Functions. *J. Cel. Sci.* 128, 1241–1252. doi:10.1242/jcs.167544

Zhang, Y. S., Aleman, J., Shin, S. R., Kilic, T., Kim, D., Mousavi Shaegh, S. A., et al. (2017). Multisensor-integrated Organs-On-Chips Platform for Automated and Continual *In Situ* Monitoring of Organoid Behaviors. *Proc. Natl. Acad. Sci. USA* 114, E2293–E2302. doi:10.1073/pnas.1612906114

Zhao, Y., Rafatian, N., Feric, N. T., Cox, B. J., Aschar-Sobbi, R., Wang, E. Y., et al. (2019). A Platform for Generation of Chamber-Specific Cardiac Tissues and Disease Modeling. *Cell* 176, 913–927.e18. doi:10.1016/j.cell.2018.11.042

Zujur, D., Kanke, K., Onodera, S., Tani, S., Lai, J., Azuma, T., et al. (2020). Stepwise Strategy for Generating Osteoblasts from Human Pluripotent Stem Cells under Fully Defined Xeno-free Conditions with Small-Molecule Inducers. *Regener. Ther.* 14, 19–31. doi:10.1016/j.reth.2019.12.010

Conflict of Interest: The authors declare that the research was conducted in the absence of any commercial or financial relationships that could be construed as a potential conflict of interest.

The reviewer GP declared a past co-authorship with one of the authors HA to the handling Editor.

Publisher's Note: All claims expressed in this article are solely those of the authors and do not necessarily represent those of their affiliated organizations, or those of the publisher, the editors and the reviewers. Any product that may be evaluated in this article, or claim that may be made by its manufacturer, is not guaranteed or endorsed by the publisher.

Copyright © 2022 Ajalik, Alenchery, Cognetti, Zhang, McGrath, Miller and Awad. This is an open-access article distributed under the terms of the Creative Commons Attribution License (CC BY). The use, distribution or reproduction in other forums is permitted, provided the original author(s) and the copyright owner(s) are credited and that the original publication in this journal is cited, in accordance with accepted academic practice. No use, distribution or reproduction is permitted which does not comply with these terms.

frontiers | Frontiers in Bioengineering and Biotechnology

BRIEF RESEARCH REPORT
published: 01 April 2022
doi: 10.3389/fbioe.2022.817300

Three-Dimensional Modeling and *In Silico* Kinematic Evaluation of Interspinous Ligament Desmotomy in Horses

Adam Henry Biedrzycki and George Louis Elane*

University of Florida, Gainesville, United States

Background: Interspinous ligament desmotomy (ISLD) has been shown to improve the comfort of horses diagnosed with overriding dorsal spinous processes (DSP), but its effects on spine mobility are unknown.

Objective: To objectively quantify the change in mobility of thoracic vertebrae following ISLD using CT and medical modeling software.

Study design: Prospective cadaveric manipulation of seven equine thoracolumbar spines collected from T11-L1.

Methods: Spines were collected from T11-L1 with the musculature intact. Flexion and extension phases were achieved with a ratchet device calibrated to 2000N. Bone volume CT scans were performed in resting, flexion, and extension phase preoperatively. Interspinous ligament desmotomy was performed at each intervertebral space (n = 8), and bone volume CT imaging was repeated for each phase. The spinal sections were individually segmented and imported into medical software for kinematic evaluation. T11 of each phase were superimposed, the distance between each dorsal spinous process, the total length of the spine, and the maximal excursion of the first lumbar vertebra along with angular rotational information were recorded.

Results: The mean distance between each dorsal spinous process increased by 5.6 ± 4.9 mm, representing a 24 ± 21% increase in mobility following ISLD. L1 dorsoventral excursion increased by 15.3 ± 11.9 mm, craniocaudal motion increased by 6.9 ± 6.5 mm representing a 47 ± 36.5% and 14.5 ± 13.7% increase, respectively. The rotation of L1 about the mediolateral axis increased by 6.5° post-ISLD.

Conclusion and Clinical Relevance: ISLD increases dorsoventral, craniocaudal, and rotational motion of the equine spine. The computer modeling methodology used here could be used to evaluate multiplanar spinal kinematics between treatments.

Keywords: horse, spine, overriding, interspinous, desmotomy, kinematics, *in silico*

Abbreviations: CT, computed tomography; DICOM, digital imaging and communications in medicine; ISL, interspinous ligament; ISLD, interspinous ligament desmotomy; DSP, dorsal spinous process; ORDSP, overriding dorsal spinous processes; ROM, range of motion.

OPEN ACCESS

Edited by:
Mark Buckley,
University of Rochester, United States

Reviewed by:
Kara Brown,
University of Pennsylvania, United States
Rahul Gawri,
McGill University, Canada

****Correspondence:***
Adam Henry Biedrzycki
dradam@ufl.edu

Specialty section:
This article was submitted to Biomaterials, a section of the journal Frontiers in Bioengineering and Biotechnology

Received: *17 November 2021*
Accepted: *28 February 2022*
Published: *01 April 2022*

Citation:
Biedrzycki AH and Elane GL (2022) Three-Dimensional Modeling and In Silico Kinematic Evaluation of Interspinous Ligament Desmotomy in Horses. Front. Bioeng. Biotechnol. 10:817300. doi: 10.3389/fbioe.2022.817300

INTRODUCTION

Impingement or overriding of the equine dorsal spinous processes (ORDSP), otherwise known as "kissing spines", represents the most common source of thoracolumbar and back pain in horses (Jeffcott, 1980). Thoracolumbar vertebrae T10-18 are the most commonly affected, though the cranial lumbar vertebrae can occasionally be affected (Denoix and Dyson, 2011; Zimmerman et al., 2012). Presenting complaints of horses affected by back pain typically include a history of poor performance, pain on thoracolumbar palpation, and epaxial muscle atrophy in advanced cases. The assessment of pain on palpation of back musculature is subjective due to individual interpretation and techniques; pressure algometry is a more objective determination (Trager et al., 2020). Furthermore, the role and importance of musculature in horses with back pain are further highlighted when considering that postural changes to limit the dorsoventral range of motion (ROM) of the spine can occur by horses' contraction of the epaxial muscles (Trager et al., 2020). Diagnosis of ORDSP can be challenging due to the low correlation of diagnostic imaging with clinical disease but is frequently characterized by an increase in radiopacity of the dorsal spinous processes (DSPs) on radiographs (Erichsen et al., 2004; Zimmerman et al., 2012; Trager et al., 2020). Diagnostic information can also be complemented by observing increased radiopharmaceutical uptake on nuclear scintigraphy (Erichsen et al., 2003). Additional diagnostics via ultrasonographic identification of fiber disruption of the ISL in horses with ORDSP is supported by a histological evaluation that reported loss of ISL integrity and fiber disruption in horses with ORDSP, although clinical correlation is not always apparent (Ehrle et al., 2019). Initial medical management typically consists of corticosteroid injection, muscle relaxants, and other analgesics, aimed at improving the comfort during the physical rehabilitation period. The available surgical treatments include surgical resection of the DSPs under general anesthesia, and subtotal ostectomy in the standing horse; however, these can result in poor cosmetic outcome and postoperative complications (Roberts, 1968; Perkins et al., 2005; de Souza et al., 2021). The strong supraspinous ligament runs along the length of the spinal column and must be elevated from the DSPs along with the mutifidis dorsi, spinalis thoracic, and longissimus dorsi muscles in order to permit the removal of a portion of the DSP (Rubio-Martinez et al., 2021). The ISL occupies the space between the DSPs and interspinous ligament desmotomy (ISLD) has been shown to ameliorate back pain (Coomer et al., 2012) but its effects on increasing mobility of the spine are unknown. Several studies have shown a clinical improvement in horses suffering from poor performance post-ISLD (Prisk and García-López, 2019; Brown et al., 2020), however, others have mentioned long-term complications such as unilateral neurogenic atrophy of epaxial musculature (Derham et al., 2021). The main effects of ISLD appear to be due to reduced tension on the afferent nociceptive receptors located at the ligament insertion, which abolish the pain response (Coomer et al., 2012). An increase in nerve fibers within the ISL itself has also been identified histologically, transection of which may contribute to a change in pain level (Ehrle et al., 2019).

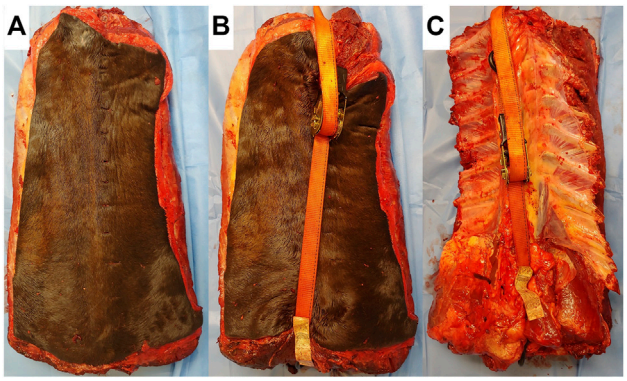

FIGURE 1 | Images of spine sections prior to CT scanning. **(A)** Resting phase. **(B)** Flexion, ratchet strap calibrated to 2000N is placed on the dorsal aspect, compressing the dorsal spinous processes together. **(C)** Extension, ratchet strap is placed in the ventral aspect of the section, separating the dorsal spinous processes, and placing the interspinous ligament under tension.

Radiographically, an enlargement of the interspinous space was observed after ISLD, although this was not quantified (Coomer et al., 2012). Furthermore, we do not know if the effect of ISLD has beneficial mobility changes or deleterious secondary biomechanical consequences; further studies are required to address these effects. Few studies have objectively evaluated the kinematics of the equine spine at the individual vertebral level, although more generalized kinematic studies have been performed (Townsend et al., 1983) and more recently kinematics between straight-line motion and circle in trot and with a rider have been evaluated (Martin et al., 2017; Byström et al., 2021). These studies utilized motion capture cameras and skin markers, which have certain limitations when applied (Pourcelot et al., 1998). This study aimed to quantify the postoperative change in the mobility of thoracic vertebrae using a combination of CT and medical modeling software using postmortem spine specimens from T11 to L1. The objectives were to explore and quantify post-ISLD changes in mobility in the following ways: 1) investigate DSP distance and length of spine sections, 2) investigate the mobility of each vertebral segment, and 3) investigate the vertical (dorsoventral) excursion of the first lumbar vertebrae. We hypothesized that 1) the distance between each DSP and overall length of the spine would be increased following ISLD, thereby signifying an increase in length or mobility in a craniocaudal distance and 2) the mobility between each DSP would increase post-ISLD and 3) the vertical excursion of the first lumbar vertebra (relative to T11) would be increased postoperatively, signifying an increase in mobility in the dorsoventral direction post-ISLD.

MATERIALS AND METHODS

Study Design

Spines of seven skeletally mature horses with a body mass between 400 and 550 kg euthanatized for reasons unrelated to

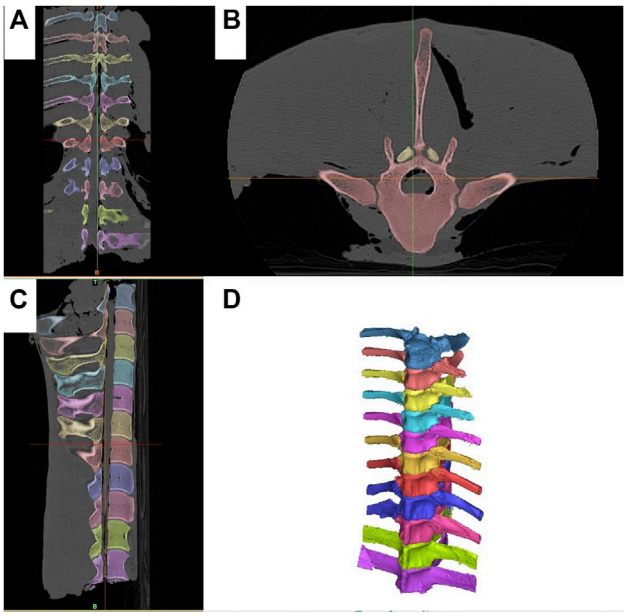

FIGURE 2 | Segmentation of the T11-L1 spine segments. Each vertebra is segmented separately and denoted in a different color. **(A)** Dorsal CT scan view. **(B)** Axial CT scan view, **(C)** Sagittal CT scan view. **(D)** 3D reconstruction of each individual spinous process.

lameness or back pain were collected *en bloc* from T11-L1 with the skin, ventral and epaxial, and hypaxial musculature intact and the ribs severed at least eight inches from the spinal column (**Figure 1**). The spines were imaged and surgery was performed within 4 h of euthanasia, prior to the onset of rigor mortis. For CT evaluation (160 Slice Toshiba Aquillion CT Scanner, Cannon Medical Systems, Tustin, CA, United States) helical volume data (slice thickness of 0.5 and 0.3 mm slice overlap) was acquired. The bone reconstruction algorithm was used for all CT-based 3D reconstructions and analyses. The images were acquired in resting, extension, and flexion phases using a ratchet device before and after ISLD (**Figure 1**). The ratchet device was inserted into the spinal canal of the T11 vertebrae and the L1 Vertebrae and placed either on the dorsal or ventral aspect. The ratchet had a maximum strength of 2000N, verified with an inline force transducer and thus, the spine was loaded in each direction with 2000N. Based on CT imaging, the spines were screened for any preexisting ORDSP, inter DSP narrowing, or increased radio-opacity on the cranial and caudal margins of the DSPs and excluded if CT signs of these conditions were evident. ISLD was performed as previously described (Coomer et al., 2012). Briefly, 1 3.5" spinal needle was used to identify the interspinous space between each vertebra. Then, a 1 cm paramedian skin incision was made approximately 3 cm off midline using a #10 blade. Curved 7" Mayo scissors were inserted to bluntly penetrate the interspinous space and passed axially to transect the ligament, taking care not to damage the supraspinous ligament. This was repeated at each interspinous space n=8. The CT images in each position, both pre and post-ISLD were exported as DICOM files. The imaging data in DICOM files were imported into Materialise Mimics™ and 3-Matic™ (Materialise Medical Imaging Software Suite, Materialise NV, Leuven, Belgium) computer software for segmentation and 3D modeling of anatomic structures. In the software, each spinous process was individually segmented; the ribs were excluded (**Figure 2**). The initial process consisted of creating renderings, referred to as masks, using the Hounsfield Unit (HU) density range; for the spinous processes, an HU range of +700 to +3000 was used. Following the creation of the masks, 3D parts of each individual spinous section were created. These 3D renderings were then checked for imperfections and corrected with wrap and smooth algorithms. The parts were then imported into the spatial manipulation software program and the 11th thoracic vertebra of each phase was superimposed, maintaining the spatial relationship between them and each successive vertebra. Based on this data, the individual distance between the cranial-most aspect of each DSP (denoted by the most craniodorsal point), and the total spine length was measured and recorded in mm for each of the three phases (extension, flexion, and resting) at both the pre and post-ISLD time points (**Figure 3**). This provided information about the individual spinal motion. Finally, to gain an understanding regarding the global motion of the spine segments (T11-L1), the L1 in the extension and flexion phases were then superimposed over L1 in the resting position. This was achieved via a global registration algorithm, which aligns the features of different phase T11 sections within each horse resulting in a near-perfect alignment. The remainder of the spinal column segments within each phase move concurrently with respect to the parent T11 vertebrae, thus preserving the alignments. Following this, the translation and angular rotation of each phase (resting, flexion, and extension) was exported as a transformation matrix and Hausdorff distances of L1, the furthest vertebrae away from T11, were measured to demonstrate maximal changes between different phases (**Figure 4**) (Biedrzycki et al., 2021).

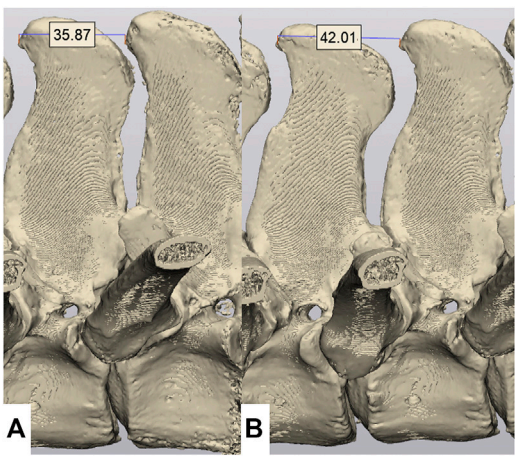

FIGURE 3 | Measurement of the inter DSP distance. Measurements are made from the cranial aspect of one DSP to the cranial aspect of the adjacent DSP. **(A)** Flexion phase, demonstrating an inter DSP distance of 35.87 mm. **(B)** Resting phase, demonstrating a inter DSP distance of 42.01 mm.

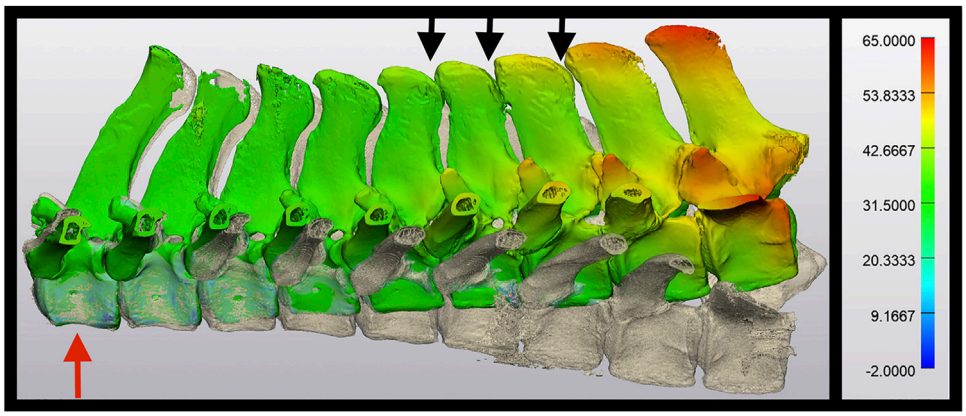

FIGURE 4 | Use of Hausdorff distance to demonstrate dorsoventral excursion. In this image, T11vertebra (red arrow) have been superimposed over each other. The spine curving toward the top of the image represents a spine in extension, and the spine curving toward the bottom of the image represents the same spine in flexion. The color overlay represents the translation in mm between the two phases, peaking at 65.0 mm in this post-ISLD section. Note the close proximity of each DSP and narrowing of the interspinous space (black arrows) during the flexion phase.

Statistical Analyses

A test for normality was performed using Shapiro-Wilk. Data evaluating the interspinous distances were evaluated using a paired samples *t*-test. To determine the effects between pre and post-ISLD on each individual vertebra, a repeated measure 2-way analysis of variance with spinal section number and surgical condition (pre or post) as factors with a post-hoc Tukey's test. Data were reported as mean ± standard deviation. Where data were not normally distributed, a Wilcoxon signed-rank test was performed, and data were reported as median (range). The significance was set at $p \leq 0.05$. Statistics were performed with MedCalc software (Ver 19.1) and post-hoc power analysis was performed using G*Power.

RESULTS

Horses

The spines from four Quarter horses, and one Thoroughbred, Warmblood, and Spotted Saddle Horse each were included in the study. The sexes comprised of four mares and three geldings with an age of 16.3 ± 3.3 years and weight of 461 ± 46.6 kg. All spines were included in the study and were considered normal; none met the criteria for exclusion.

Resting Phase

There was no significant difference between the interspinous distance in the resting phase between each vertebra in the pre-surgical spine (39.89 ± 2.84 mm) and the post-surgical (39.90 ± 2.84 mm, $p = 0.98$). However, the power of this test was only 5%. To have sufficient power (80%) to detect a difference among the spinous process at rest given our effect size (0.003), a sample size approaching 2,000,000 sections would be required. Although 2,000,000 + sections are required to have sufficient power at a 20-micron difference, our study was sufficiently powered at 80% to determine that the true difference between the resting phases of the specimens we examined is less than 2.2 mm. Furthermore, we also identified a significant effect of vertebral space in our model ($p < 0.01$), indicating that the inter DSP distance is not homogenous among the vertebrae. However, even though we were unable to detect a difference at the interspinous level, there was a significant difference at the global level (T11-L1 range). After ISLD, the total distance between the cranial aspects of T11 to L1 is significantly increased ($p = 0.03$) from 310.0 ± 13.9 mm pre-surgery to 313.9 ± 11.8 post-surgery. The effect of ISLD on the total spinal length from T11 to L1 increases the length by 3.8 ± 3.1 mm. This 3.8 mm increase represents a 1.2 ± 1.0% change in the total length of the spine.

Range of Motion—Individual Spine Segments

There was no significant difference in the inter DSP distance measured from the cranial aspect of one vertebra to the cranial aspect of the next vertebrae during extension between pre-surgical spines (27.4 ± 19.1 mm) and the post-ISLD spines (33.9 ± 9.0 mm, $p = 0.32$, **Figure 3**). However, for flexion, a significant increase in the inter DSP distance between pre-surgical (34.3 ± 17.4 mm) and the post-ISLD (44.4 ± 10.6 mm, $p = 0.046$) was identified. Combining these extension and flexion values to generate a total dorsoventral range of motion (ROM) for each individual space, we demonstrate that preoperatively, this ROM is 17.9 ± 3.0 mm. The effect of ISLD is to significantly increase this ROM to 23.5 ± 4.0 mm ($p = 0.02$). Thus the effect of ISLD at a single vertebral site was to increase the ROM between two adjacent vertebrae by 5.6 ± 4.9 mm. This distance represents a 24 ± 21% increase in maximal ROM post-ISLD.

Global Spine Movement

L1 has significantly more total translation (excursion) in the dorsoventral direction between the pre-surgical (32.6 ± 10.8 mm) and the post-ISLD spine (48.0 ± 14.0 mm, $p = 0.01$). This

represents an increase of 15.3 ± 11.9 mm of travel or an increase of 47.0 ± 36.5% in dorsoventral excursion. Extrapolating this figure, which represents the effects of 8 ISLDs, to a single ISLD at a single site provides an estimated effect of approximately 5.9% increase in dorsoventral excursion per ISLD site. L1 also has significantly more translation in the craniocaudal direction between the pre-surgical (22.9 ± 10.8 mm) and the post-ISLD spine (29.8 ± 10.9 mm, $p = 0.03$). This represents an increase of 6.9 ± 6.5 mm of travel or an increase of 30.1 ± 28.4% in craniocaudal translation. Extrapolating this figure to a single ISLD at a single site provides an estimated effect of approximately 3.8% increase in craniocaudal excursion per ISLD site. The angle of rotation of L1 between flexion and extension significantly increases from 12.0° (7.9–35.6°) pre-surgery to 21.8° (14.7–55.6°) degrees post-ISLD ($p = 0.01$). This represents an increase in the angular rotation of L1 of 6.5° (2.1–20.8°).

DISCUSSION

We successfully achieved our objectives, and this study represents the first *in silico* quantification of the change in mobility of thoracic vertebrae following ISLD using CT and medical modeling software. The lack of significant difference between individual spines in the preoperative and postoperative "resting" phases in this study suggests that this formed an adequate baseline for comparison of the flexion and extension phases. Despite this, we identified that there are differences in the interspinous distances between different vertebrae, although we did not have sufficient power to further determine where these differences exist during flexion and extension in this study. Furthermore, we also identified that the resting total length of the spine section we were studying (T11-L1) significantly increased by 3.8 mm, supporting our first hypothesis. However, this increase is approximately 1.2% of the total length of the spinal section analyzed and could be explained by thermal variations in the muscles and soft tissues over time and the initial flexion and extension phases, since the pre-surgical imaging was always performed prior to the surgical intervention.

The caudal thoracic and the lumbar spine is the least mobile region of the equine back (Townsend et al., 1983). However, this is the region at most risk for kissing spines and where surgical intervention is required. During the study, the determination of which specific desmotomy sites would be the most efficacious in increasing the overall mobility was considered. Although increasing mobility is not necessarily the clinical goal of the ISLD procedure, for the purposes of this study into the investigation of mobility we wanted to choose sites which would have most impact. However, a power calculation indicated that 1,309 spines would be required in order to make this determination, and the consideration was abandoned. Thus, in order to achieve a maximum global effect given the previously identified lack of mobility in this region, it was elected to perform ISLD at each intervertebral site (for a total of eight sites) in the current study, as opposed to the original description of the procedure, which had a mean of five surgical sites (Coomer et al., 2012). This approach was chosen in order to determine the maximum change in vertebral excursion following ISLD by increasing the number of desmotomy sites. Furthermore, we chose to measure our inter DSP distance from the cranial aspect of one vertebra to the cranial aspect of the next vertebrae rather than the distance between each DSP. This was performed due to issues selecting the optimal caudal marker, which was not reliably determined and varied based on the different computer views. To remove excessive variation, we elected to use only one point per spine, the most cranial and repeatable prominence on each DSP.

We identified that increased motion between the spinous processes occurs in the flexion phase in comparison to the extension phase during spinal motion in normal spines. Furthermore, there was no significant effect of ISLD on increasing the amount of motion in the extension phase; ISLD only had a significant effect on increasing the degree of motion in flexion. A limit of 2000N was used as a maximum value due to DSP fracture identified in preliminary studies if forces greater than 2000N were used in the extension phase. Although it is conceivable that forces greater than 2000N could have been applied in flexion, the authors decided to keep the forces consistent for direct comparisons between the two modes. This appears to make sense since, with transection of the ligament, one would not expect an increased motion when spines are compressed together (extension) but rather when they are placed in tension and forced apart (flexion). Thus, we found evidence to support our second hypothesis that the range of motion between each DSP would increase post-ISLD. Since our results demonstrate the effects on normal spine segments, horses with kissing spines exhibiting close proximity (similar to a type of "extension" phase) are likely to have greater effects of ISLD on mobility in the flexion direction than presented here, thus our results are likely to underestimate the clinical scenario. The constriction of the interspinous ligament on the mobility of the DSPs was first recognized by Coomer et al. who developed the ISLD technique (Coomer et al., 2012). Following ISLD, there was an increase in interspinous space observed on postoperative radiographs. They theorized that tension of the interspinous ligament alone was holding the DSPs in close proximity to each other, although the quantification of this change was not determined at that time. This ancillary finding of increased mobility is further supported by our study.

In terms of global spinal motion between T11-L1, we found evidence to support our third hypothesis. It stands to reason that the increase in dorsoventral excursion of the first lumbar vertebra by 15.3 mm following ISLD likely represents a cumulative increase in range of motion by severing the interspinous ligament between each preceding thoracic vertebra, thereby allowing the lumbar vertebra more freedom to move further in the dorsoventral direction. Similarly, the 6.9 mm increase in craniocaudal motion was statistically significant following ISLD and suggests that the interspinous ligament may constrict craniocaudal motion in addition to dorsoventral motion (Coomer et al., 2012). As demonstrated by this study, severing this ligament increased rotation of the lumbar vertebra by 6.5° supporting the notion that the ISLD increases the ability of the

affected vertebrae to rotate further increasing overall spine mobility.

Histopathology of the interspinous ligament of horses affected by ISLD had revealed disruption of normal anatomy and fibrocartilaginous metaplasia in one report (Ehrle et al., 2019). The upregulation of fibrocartilage in affected horses may indicate a decrease in mobility, which predisposes to enthesiophyte formation and the osseous radiographic changes typically seen in horses with ORDSP. Furthermore, the number of nerves within the interspinous ligament was increased in horses with ORDSP in the same report (Ehrle et al., 2019). It is likely that nociception may play a part in decreasing mobility of the spine, and that severing these nerves consequently increases analgesia and allows the horse to engage in rehabilitative physiotherapy following ISLD.

The effect of ISLD is to enhance the mobility and rotation of the spine by approximately 24% per spinous segment in terms of total, maximal ROM in flexion and extension. Furthermore, the maximal excursion of the spine in a dorsoventral direction can increase by 5.9% at each ISLD site. It should be noted that these are maximal or extreme ranges of motion; at rest or physiological conditions, these changes represent a difference of only 1.6% in total spinal length and underscore the necessity of appropriate rehabilitation therapy in clinical cases (Prisk and García-López, 2019). The original description of the ISLD technique emphasized the need for postoperative physical training to encourage epaxial muscle strength and core stability. The core strengthening exercises, after resolution of back pain, may increase the cross-sectional area of the spinal stabilizing musculature. If the spine is hypermobile post-ISLD as our study suggests, then a post-rehabilitation increase in support or spinal stabilization may be beneficial.

This study has several limitations. Many of our results have large SD values, which are only slightly smaller than the mean value itself. For example, the effect of ISLD on the total spinal length from T11 to L1 increases the length by 3.8 ± 3.1 mm. This 3.8 mm increase represents a 1.2 ± 1.0% change in the total length of the spine. However, the data are still significantly different, although there is a less than 3% chance of type I error. Although the data are significant and we have evidence to support our hypotheses, the authors have concern that there are systemic type I errors with our data; that the null hypothesis has been incorrectly rejected. This level of caution should be applied to interpretation of all of our data.

While the spine segments collected included the most commonly affected sites for ORDSP, these segments do not represent the entire vertebral column and therefore the inclusion of more vertebrae may change the results. Anchor points to the appendicular skeleton at the sacrum and in proximity to the scapula may also affect the results. Important muscles attachments at the ribs both cranially and caudally may also affect our results. Furthermore, there was no muscle tone in our postmortem specimens. It is believed that horses with ORDSP or back pain tend to have increased tone in the epaxial musculature and as such, drugs such as methocarbamol are often prescribed. This variation in muscle tone between our sections (no muscle tone), normal live horses (normal tone), and clinically affected horses (exaggerated muscle tone), may therefore have a significant role in the true motion of the spine in the clinically affected live horse. As such, we believe our results are maybe an overestimation of the true motion that occurs. In addition, our sections included the anticlinal vertebrae (T16) and thus there may be differences in extension and flexion from the vertebrae cranial and caudal to this maker, as spinous processes in humans with the S-shaped normal human spine have different sections undergoing extension and flexion concurrently. Furthermore, during these extension and flexion phases, the spinal segments undergo translation, axial rotation, and lateral flexion which, although not evaluated in the present study, could be easily investigated with the techniques utilized in this investigation. The specimens were collected from clinically normal horses, and translation and rotation results may change in horses clinically affected by ORDSP. In addition, the study was underpowered for detecting individual changes in vertebral motion, the ISLD procedure was performed at each interspinous site for 8 sites total and supraphysiological forces were exerted on the spine. This was to allow for global changes in mobility of the spine but may not directly correlate with changes seen in clinical practice, where typically fewer total sites of ISLD are performed and lower forces are exerted. The assumptions that global spine motion can be equally divided amongst individual vertebrae may be incorrect, as there are small alterations in the plane of motion of each facet joint of the spinal vertebrae. We feel that the contribution of facet joint alignment is likely to be minimal, however, given this uncertainty we urge caution in interpretation of these findings as they may not be true approximations of individual vertebral motion. In addition, changes in individual spine mobility are unlikely to be the primary reason for clinical improvement in horses after ISLD.

Despite these limitations, this is a powerful modeling technique that would allow for further evaluations of spinal motion in a virtual setting. One of the limiting factors currently is that it is not possible to CT the thoracolumbar spine of horses *in vivo* and furthermore, one would require dynamic flexion and extension positioning in the CT to acquire meaningful ROM data. Nevertheless, the information, once acquired, could be used in a variety of virtual modeling scenarios.

In conclusion, this study demonstrated that ISLD of 8 interspinous segments increases spinal mobility. It is uncertain if this change in mobility is beneficial or if there may be secondary biomechanical consequences, such as thoracolumbar facet disease, which are beyond the scope of this study. However, the techniques utilized in this study can be valuable for evaluating spinal kinematics in three dimensions both locally (individual vertebra) and globally (effects over the entire spinal segment).

DATA AVAILABILITY STATEMENT

The raw data supporting the conclusion of this article will be made available by the authors without undue reservation.

ETHICS STATEMENT

The study was reviewed and approved by the University of Florida Institutional Animal Care and Use Committee. Written informed consent was obtained from the owners for the participation of their animals in this study.

AUTHOR CONTRIBUTIONS

GE: acquisition of data, analysis, and interpretation of the data, drafting the article, revising the article for intellectual content, and final approval of the completed article. AB: conception, design, acquisition of data, analysis and interpretation of the data, drafting the article, revising the article for intellectual content, and final approval of the completed article.

FUNDING

This study was funded by the University of Florida Surgical Translational and 3D Printing Research Lab.

REFERENCES

Biedrzycki, A. H., Kistler, H. C., Perez-Jimenez, E. E., and Morton, A. J. (2021). Use of Hausdorff Distance and Computer Modelling to Evaluate Virtual Surgical Plans with Three-Dimensional Printed Guides against Freehand Techniques for Navicular Bone Repair in Equine Orthopaedics. *Vet. Comp. Orthop. Traumatol.* 34 (01), 009–016. doi:10.1055/s-0040-1721846

Brown, K. A., Davidson, E. J., Ortved, K., Ross, M. W., Stefanovski, D., Wulster, K. B., et al. (2020). Long-term Outcome and Effect of Diagnostic Analgesia in Horses Undergoing Interspinous Ligament Desmotomy for Overriding Dorsal Spinous Processes. *Vet. Surg.* 49 (3), 590–599. doi:10.1111/vsu.13377

Byström, A., Hardeman, A. M., Bragança, F. S., Roepstorff, L., Swagemakers, J. H., van Weeren, P. R., et al. (2021). Differences in Equine Spinal Kinematics between Straight Line and circle in Trot. *Sci. Rep.* 11 (1), 1–3. doi:10.1038/s41598-021-92272-2

Coomer, R. P. C., McKane, S. A., Smith, N., and Vandeweerd, J.-M. E. (2012). A Controlled Study Evaluating a Novel Surgical Treatment for Kissing Spines in Standing Sedated Horses. *Vet. Surg.* 41, 890–897. doi:10.1111/j.1532-950x.2012.01013.x

de Souza, T. C., Crowe, O. M., Bowles, D., Poore, L. A., and Suthers, J. M. (2021). Minimally Invasive Cranial Ostectomy for the Treatment of Impinging Dorsal Spinous Processes in 102 Standing Horses. *Vet. Surg.*. doi:10.1111/vsu.13736

Denoix, J.-M., and Dyson, S. J. (2011). "Thoracolumbar Spine," in *Diagnosis and Management of Lameness in the Horse*. 2nd ed. (St Louis, MO: Elsevier), 592–605. doi:10.1016/b978-1-4160-6069-7.00052-3

Derham, A. M., Schumacher, J., O' Leary, J. M., Kelly, G., and Hahn, C. N. (2021). Implications of the Neuroanatomy of the Equine Thoracolumbar Vertebral Column with Regional Anaesthesia and Complications Following Desmotomy of the Interspinous Ligament. *Equine Vet. J.* 53 (4), 649–655. doi:10.1111/evj.13402

Ehrle, A., Ressel, L., Ricci, E., Merle, R., and Singer, E. R. (2019). Histological Examination of the Interspinous Ligament in Horses with Overriding Spinous Processes. *Vet. J.* 244, 69–74. doi:10.1016/j.tvjl.2018.12.012

Erichsen, C., Eksell, P., Holm, K. R., Lord, P., and Johnston, C. (2004). Relationship between Scintigraphic and Radiographic Evaluations of Spinous Processes in the Thoracolumbar Spine in Riding Horses without Clinical Signs of Back Problems. *Equine Vet. J.* 36 (6), 458–465. doi:10.2746/0425164044877341

Erichsen, C., Eksell, P., Widstrom, C., Roethlisberger Holm, K., Johnston, C., and Lord, P. (2003). Scintigraphic Evaluation of the Thoracic Spine in the Asymptomatic Riding Horse. *Vet. Radiol. Ultrasound* 44 (3), 330–338. doi:10.1111/j.1740-8261.2003.tb00465.x

Jeffcott, L. B. (1980). Disorders of the Thoracolumbar Spine of the Horse - a Survey of 443 Cases. *Equine Vet. J.* 12 (4), 197–210. doi:10.1111/j.2042-3306.1980.tb03427.x

Martin, P., Cheze, L., Pourcelot, P., Desquilbet, L., Duray, L., and Chateau, H. (2017). Effects of the Rider on the Kinematics of the Equine Spine under the Saddle during the Trot Using Inertial Measurement Units: Methodological Study and Preliminary Results. *Vet. J.* 221, 6–10. doi:10.1016/j.tvjl.2016.12.018

Perkins, J. D., Schumacher, J., Kelly, G., Pollock, P., and Harty, M. (2005). Subtotal Ostectomy of Dorsal Spinous Processes Performed in Nine Standing Horses. *Vet. Surg.* 34, 625–629. doi:10.1111/j.1532-950x.2005.00097.x

Pourcelot, P., Audigié, F., Degueurce, C., Denoix, J. M., and Geiger, D. (1998). Kinematics of the Equine Back: a Method to Study the Thoracolumbar Flexion-Extension Movements at the Trot. *Vet. Res.* 29 (6), 519–525.

Prisk, A. J., and García-López, J. M. (2019). Long-term Prognosis for Return to Athletic Function after Interspinous Ligament Desmotomy for Treatment of Impinging and Overriding Dorsal Spinous Processes in Horses: 71 Cases (2012-2017). *Vet. Surg.* 48, 1278–1286. doi:10.1111/vsu.13298

Roberts, E. J. (1968). Resection of Thoracic or Lumbar Spinous Processes for the Relief of Pain Responsible for Lameness and Some Other Locomotor Disorders in Horses. *Proc. Am. Assoc. Equine Practnrs* 14, 13–30.

Rubio-Martinez, L. M. (2021). "Complications of Surgery for Impingement of Dorsal Spinous Processes," in *Complications in Equine Surgery*. Editors L. M. Rubio-Martinez and D. A. Hendrickson (Hoboken, New Jersey, United States: John Wiley & Sons), 833–842.

Townsend, H. G. G., Leach, D. H., and Fretz, P. B. (1983). Kinematics of the Equine Thoracolumbar Spine. *Eq Vet. J.* 15 (2), 117–122. doi:10.1111/j.2042-3306.1983.tb01732.x

Trager, L. R., Funk, R. A., Clapp, K. S., Dahlgren, L. A., Werre, S. R., Hodgson, D. R., et al. (2020). Extracorporeal Shockwave Therapy Raises Mechanical Nociceptive Threshold in Horses with Thoracolumbar Pain. *Equine Vet. J.* 52 (2), 250–257. doi:10.1111/evj.13159

Zimmerman, M., Dyson, S., and Murray, R. (2012). Close, Impinging and Overriding Spinous Processes in the Thoracolumbar Spine: The Relationship between Radiological and Scintigraphic Findings and Clinical Signs. *Equine Vet. J.* 44 (2), 178–184. doi:10.1111/j.2042-3306.2011.00373.x

Conflict of Interest: The authors declare that the research was conducted in the absence of any commercial or financial relationships that could be construed as a potential conflict of interest.

Publisher's Note: All claims expressed in this article are solely those of the authors and do not necessarily represent those of their affiliated organizations, or those of the publisher, the editors, and the reviewers. Any product that may be evaluated in this article, or claim that may be made by its manufacturer, is not guaranteed or endorsed by the publisher.

Copyright © 2022 Biedrzycki and Elane. This is an open-access article distributed under the terms of the Creative Commons Attribution License (CC BY). The use, distribution or reproduction in other forums is permitted, provided the original author(s) and the copyright owner(s) are credited and that the original publication in this journal is cited, in accordance with accepted academic practice. No use, distribution or reproduction is permitted which does not comply with these terms.

frontiers | Frontiers in Bioengineering and Biotechnology

REVIEW
published: 11 April 2022
doi: 10.3389/fbioe.2022.824156

3D Bioprinted Scaffolds for Bone Tissue Engineering: State-Of-The-Art and Emerging Technologies

Zahra Yazdanpanah[1]*, *James D. Johnston*[1,2], *David M. L. Cooper*[3] *and Xiongbiao Chen*[1,2]

[1]Division of Biomedical Engineering, College of Engineering, University of Saskatchewan, Saskatoon, SK, Canada, [2]Department of Mechanical Engineering, College of Engineering, University of Saskatchewan, Saskatoon, SK, Canada, [3]Department of Anatomy Physiology and Pharmacology, College of Medicine, University of Saskatchewan, Saskatoon, SK, Canada

Treating large bone defects, known as critical-sized defects (CSDs), is challenging because they are not spontaneously healed by the patient's body. Due to the limitations associated with conventional bone grafts, bone tissue engineering (BTE), based on three-dimensional (3D) bioprinted scaffolds, has emerged as a promising approach for bone reconstitution and treatment. Bioprinting technology allows for incorporation of living cells and/or growth factors into scaffolds aiming to mimic the structure and properties of the native bone. To date, a wide range of biomaterials (either natural or synthetic polymers), as well as various cells and growth factors, have been explored for use in scaffold bioprinting. However, a key challenge that remains is the fabrication of scaffolds that meet structure, mechanical, and osteoconductive requirements of native bone and support vascularization. In this review, we briefly present the latest developments and discoveries of CSD treatment by means of bioprinted scaffolds, with a focus on the biomaterials, cells, and growth factors for formulating bioinks and their bioprinting techniques. Promising state-of-the-art pathways or strategies recently developed for bioprinting bone scaffolds are highlighted, including the incorporation of bioactive ceramics to create composite scaffolds, the use of advanced bioprinting technologies (*e.g.*, core/shell bioprinting) to form hybrid scaffolds or systems, as well as the rigorous design of scaffolds by taking into account of the influence of such parameters as scaffold pore geometry and porosity. We also review *in-vitro* assays and *in-vivo* models to track bone regeneration, followed by a discussion of current limitations associated with 3D bioprinting technologies for BTE. We conclude this review with emerging approaches in this field, including the development of gradient scaffolds, four-dimensional (4D) printing technology via smart materials, organoids, and cell aggregates/spheroids along with future avenues for related BTE.

Keywords: bioprinting, 3D printing, bone tissue engineering, scaffold, critical-sized defect

OPEN ACCESS

Edited by:
Andrea Vernengo,
AO Research Institute, Switzerland

Reviewed by:
Francesco Baino,
Politecnico di Torino, Italy
Silvia Fare',
Politecnico di Milano, Italy

***Correspondence:**
Zahra Yazdanpanah
zay413@mail.usask.ca

Specialty section:
This article was submitted to Biomaterials, a section of the journal Frontiers in Bioengineering and Biotechnology

Received: *29 November 2021*
Accepted: *03 March 2022*
Published: *11 April 2022*

Citation:
Yazdanpanah Z, Johnston JD, Cooper DML and Chen X (2022) 3D Bioprinted Scaffolds for Bone Tissue Engineering: State-Of-The-Art and Emerging Technologies. Front. Bioeng. Biotechnol. 10:824156. doi: 10.3389/fbioe.2022.824156

INTRODUCTION

Bone is a resilient tissue with self-healing capacity. However, a large bone defect, referred to as a critical-sized defect (CSD), cannot be healed by the patient's body (Schroeder and Mosheiff, 2011; Park et al., 2015). The size of CSDs can vary by the skeletal region involved and the state of soft tissue surrounding it (Nauth et al., 2011; Schemitsch, 2017). For example, a 3-cm diameter defect is

regarded as a CSD for the radius and ulna, while a 5-cm diameter defect is classified as a CSD for the femur and tibia (Calori et al., 2011; Stewart et al., 2015). In these cases, surgical interventions such as bone grafts are needed to restore the function of the bone (Ashammakhi et al., 2019). Traditional therapeutic approaches such as autografts, allografts, and xenografts have been restricted due to associated drawbacks such as limited donor supply and donor sites, additional surgery, the potential risk of disease transmission, and immune response after implantation. Bone tissue engineering (BTE) has drawn significant attention to the creation of novel constructs to restore, maintain and/or improve bone function (Guarino et al., 2007; Wang and Yeung, 2017; Turnbull et al., 2018).

Scaffolds, cells, and cytokines are key components in BTE. Scaffolds are 3D structures providing a temporary environment for extracellular matrix (ECM) formation and cellular activity as well as diffusion of oxygen, nutrient delivery, and waste removal. These 3D structures must also provide mechanical support to resist external forces and gradually remodel over time as new bone tissue is formed (Seol et al., 2013).

Conventional fabrication methods such as solvent-casting (Kim et al., 2008; Aboudzadeh et al., 2010), particulate-leaching (Guarino et al., 2008; Verma et al., 2019), and freeze drying (Zhang and Ma, 1999; Niu et al., 2009; Aboudzadeh et al., 2010; Zhu et al., 2011; Cholas et al., 2016) have had limited capacity to control pore size, pore geometry, pore interconnectivity, and the spatial distribution of pores in scaffolds. Conversely, 3D printing, an advanced fabrication technique, is considered the most promising technique for creating biomedical scaffolds, artificial tissues, and organs due to its enhanced ability to control scaffold structure (Gu et al., 2016; Chen, 2018). Recent developments in 3D printing technology have also enabled the incorporation of living cells and growth factors into scaffolds during the fabrication process, an approach known as bioprinting, which subsequently creates biomimetic tissue (Bose et al., 2013; Zhu and Chen, 2013; Gu et al., 2016).

Here, we first provide a summary of concepts about bone structure and bone defects. We next consider different types of biomaterials, cells, and growth factors commonly used in bioprinting for BTE. We also review bioprinting techniques used in BTE, printability, as well as mechanical and osteoconductive properties of 3D printed bone scaffolds. In addition, we discuss *in-vitro* assays and *in-vivo* models to track bone regeneration using bone scaffolds. We then conclude with challenges in current studies and recommendations for future research.

BONE STRUCTURE AND DEFECTS

Living bone is a heterogeneous composite material consisting mineral, collagen (type I), and water (Guarino et al., 2007; Wu et al., 2014). Moreover, there are small quantities of other organic materials such as polysaccharides, proteins, proteoglycans, sialoproteins, and lipids in this dynamic/vascularized tissue. Hydroxyapatite (HAp), which is the major component of bone mineral, is responsible for proper provision of structural support (Wu et al., 2014; Yazdanpanah et al., 2015). In addition, bone has a cellular phase made of four main types of cells including osteoblasts (form bone tissue), osteoclasts (resorb bone tissue), osteocytes (maintain bone tissue), and bone lining cells (Hadjidakis and Androulakis, 2006; Guarino et al., 2007; Florencio-Silva et al., 2015).

General categories of bones include long bones (*e.g.*, femur and tibia), short bones (*e.g.*, carpal and tarsal bones), flat bones (*e.g.*, skull), and irregular bones (*e.g.*, spinal elements). Long bones possess a hollow diaphysis, cone-shaped metaphyses, and rounded epiphyses (Clarke, 2008). **Figure 1** illustrates the overall structure of long bone. At the macro-scale, a typical long bone includes cortical bone (compact bone), trabecular bone (cancellous or spongy bone), a periosteum, an endosteum, osteons (micro scale), collagen fibers (nanoscale), and collagen molecules (sub-nano scale). Cortical bone is dense, and is primarily responsible for providing mechanical support as well as protection. Conversely, trabecular bone, which has an open honeycomb-like structure, constitutes about 20% of skeleton mass and is typically located within the metaphyses/epiphyses at the ends of long-bones (Wu et al., 2014). Trabecular bone is less compact, more deformable, and, due to having a high surface area, more metabolically active than cortical bone (Hadjidakis and Androulakis, 2006). As it is a deformable structure, trabecular bone also plays a role in helping reduce dynamic forces associated with physiological loading (Downey and Siegel, 2006). Differences in mechanical properties between cortical and trabecular bone result from architectural differences, with cortical bone offering high resistance to axial, bending and torsional loading with a high compressive elastic modulus ($E \approx 7.0–30$ GPa) (Hutmacher et al., 2007; Chatzistavrou et al., 2011) and compressive strength ($S_c \approx 100–230$ MPa) (Hutmacher et al., 2007; Chatzistavrou et al., 2011) compared to that of trabecular bone ($E \approx 0.1–5$ GPa, $S_c \approx 2–12$ MPa) (Wu et al., 2014). The periosteum is a fibrous membrane of connective tissue observed on the bone surface, and the endosteum is a thin layer of lining cells found on the medullary cavity surface (Downey and Siegel, 2006; Wu et al., 2014). Osteons are vascular tunnels of cylindrical shape in which blood vessels and nerves are surrounded by concentric layers of bone called lamella (Guarino et al., 2007; Härle and Boudrieau, 2012; Olson and Carlson, 2017). What differentiates primary vs secondary osteons, also known as Haversian systems, is the way they are formed. Primary osteons are relatively small, less mineralized structures, formed in early life in locations where bone did not previously exist. During postnatal growth, resorption of existing bone occurs, and larger secondary osteons are deposited. These secondary osteons, which are the main structural unit of cortical bone, are constantly resorbed/renewed during life through the process of remodeling (Patterson-Kane and Firth, 2014). In trabecular bone, remodeling produces hemi-osteons, also known as trabecular packets, which have a similar layout to that of cortical bone osteon but are crescent-shaped (Parfitt, 1994; Dahl and Thompson, 2011; Patterson-Kane and Firth, 2014).

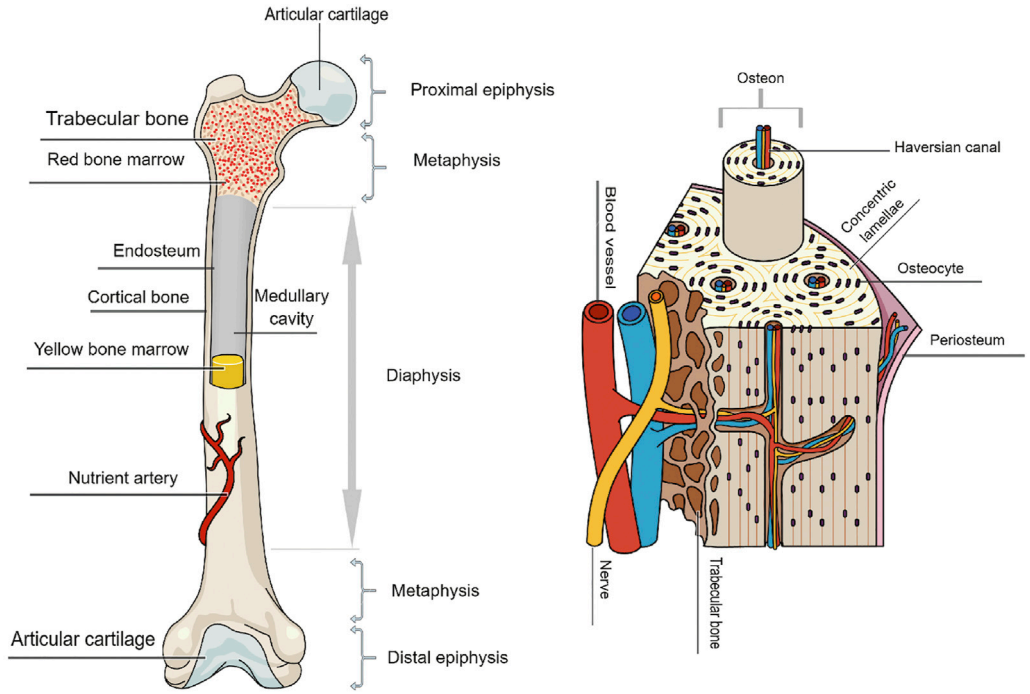

FIGURE 1 | An overall schematic representation of long bone structure.

Bone is continuously renewed throughout life by remodeling, a cyclical process by which existing bone is replaced by new bone to maintain structural, biochemical, and biomechanical properties (Hadjidakis and Androulakis, 2006; Zhou et al., 2010). Remodeling, which is conducted by individual basic multicellular units (BMUs), is performed in three main stages, including: 1) bone resorption by osteoclasts; 2) reversal, which is a transition phase from resorption to formation; and 3) bone formation by osteoblasts (Hadjidakis and Androulakis, 2006; Kenkre and Bassett, 2018). Within the BMU, bone resorption is coupled with bone formation so that old bone is replaced by an equivalent amount of new bone to maintain skeletal balance (Martin and Rodan, 2008).

Bone defects can be caused by congenital abnormalities, trauma (*e.g.*, fractures and non-unions), bone disease (*e.g.*, osteoporosis, osteosarcoma, osteonecrosis), or surgery (*e.g.*, tumor removal, spinal fusion) (Gao et al., 2014; Loi et al., 2016; Ma et al., 2018; Ashammakhi et al., 2019) and have clinical as well as socioeconomic importance (Pneumaticos et al., 2010; Loi et al., 2016). Based on the American Academy of Orthopedic Surgeons (Stevens et al., 2008), 6.3 million fractures happen each year in the United States and half a million surgical procedures were performed in 2005 using autografts or allografts to repair bone defects, which cost approximately $2.5 billion USD. In 2011 (Loi et al., 2016), 465,070 spinal fusion treatments were performed using bone grafts in the United States. It has been reported that costs for treatment of bone fractures will reach $25 billion USD by 2025 (Loi et al., 2016).

Management of large bone defects, known as CSDs, is of great importance given they have negative effects on the patient's quality of life due to prolonged hospitalizations and consecutive re-operations (Pneumaticos et al., 2010; Roseti et al., 2017). Despite the importance, no standard definition for a CSD has been reported in literature and the lack of consistency around its definition has led to conflicting opinions on their management (Schemitsch, 2017). General guidelines consider a defect size length greater than 1–2 cm and greater than 50% loss of the bone circumference as a CSD (Schemitsch, 2017). In addition, the classical definition of a CSD pertains to the smallest size intra-osseous wound in a particular bone and species of animal which is unable to heal during the lifetime of an animal (Pneumaticos et al., 2010; Spicer et al., 2012). Some others have also suggested that a defect is defined as a critical size when the length of deficiency is more than 2 or 3 times its diameter, or when a defect demonstrates less than 10% bone regeneration during the lifetime of the animal (Pneumaticos et al., 2010). The location and depth of the defect is also a consideration. Defects in the cortical diaphysis exhibit efficient regeneration of compact bone (Monfoulet et al., 2010). Defects though in distal and proximal epimetaphyses (which include both cortical and trabecular bone) exhibit efficient regeneration of trabecular bone but thin cortices, attributed to different bone-specific remodeling processes. The difference in healing process of various zones may come from the availability of endosteal, bone marrow, or bone lining cells (Monfoulet et al., 2010). A BTE study also found more bone formation in trabecular defect of a metaphyseal bone, which was implanted by bone scaffold with growth factor but a delayed

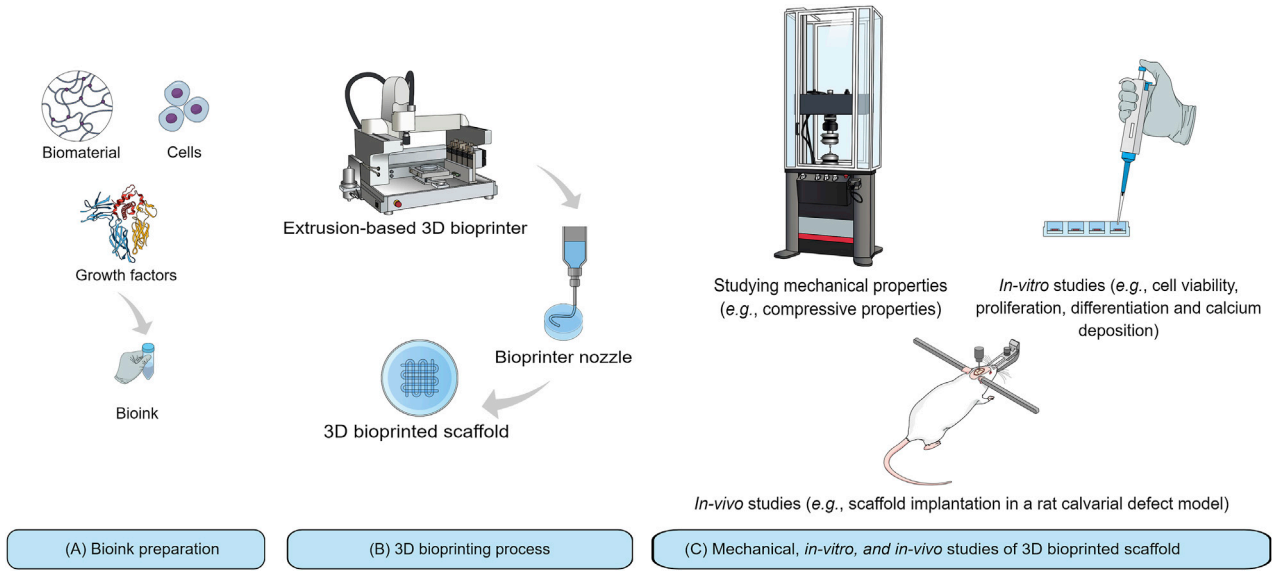

FIGURE 2 | Schematic representation of 3D bioprinting technique and its application for BTE: **(A)** Bioink preparation from three components including biomaterial, growth factor, and cells; **(B)** Bioprinting process with an extrusion-based 3D bioprinter; and **(C)** Mechanical, *in-vitro*, and *in-vivo* studies.

cortical healing (Raina et al., 2019). To guide cortical regeneration, sealing the cortical defect endosteally with a collagen membrane loaded with growth factor was found promising (Raina et al., 2019).

Bioink for Bioprinting

Bioink (**Figure 2A**) is defined as a formulation of cells which may, but do not have to, contain biomaterials and biological components such as growth factors (Groll et al., 2018). A bioink should generally meet the biological and mechanical requirements of the bioprinting process. The biomaterial used in bioink must possess appropriate biocompatibility, bioactivity, and biodegradability (Salgado et al., 2004; Murphy and Atala, 2014; Mandrycky et al., 2016; Turnbull et al., 2018; Zimmerling et al., 2021). The biomaterial must also have proper viscosity for 3D printing process (**Figure 2B**), and have appropriate mechanical properties to provide sufficient load-carrying capacity as well as stiffness to maintain integrity of the bioprinted scaffold (Murphy and Atala, 2014; Munaz et al., 2016; Zhang et al., 2017). With regards to scaffold evaluations for BTE, it is necessary to study bioprinted scaffold in terms of mechanical properties followed by evaluating cell function and osteoconductive properties by *in-vitro* studies. Scaffold implantation into a bone defect in an animal model, *in-vivo* (**Figure 2C**), has also been a complementary approach to track the capability of a bone-like scaffold to regenerate new bone within a CSD.

Biomaterials

Given that biomaterial properties determine scaffold properties, biomaterial selection is a crucial step towards fabrication of bone-engineered constructs. To date, a wide variety of both natural and synthetic biomaterials have been used for producing bone scaffolds; however, not all provide a suitable matrix to embed cells (Salgado et al., 2004; Zhang et al., 2017). Accordingly, only a limited number of biomaterials are currently available for effective cell encapsulation.

In bioprinting, hydrogels are widely used as a matrix to encapsulate cells due to their biocompatibility, biodegradability, resemblance to the native ECM, and provision of a hydrated environment, which facilitate diffusion of nutrients, oxygen, and waste removal for cell growth (Huang et al., 2016; Bishop et al., 2017; Naghieh and Chen, 2021). A hydrogel for bioprinting must possess several characteristics (Du et al., 2015; Huang et al., 2016): 1) exhibit adequate rheological properties contributing to strands with good integrity, 2) maintain its shape during 3D printing and the pores should not collapse, and 3) non-toxic to cells and allow encapsulated cells to proliferate and differentiate.

Various natural hydrogels including alginate, gelatin, chitosan, collagen, hyaluronic acid (HA) have been commonly utilized for bioprinting (Huang et al., 2016). A summary of benefits and potential limitations of the above-mentioned natural hydrogels, specifically for the purposes of bioprinting bone scaffolds, is given in **Table 1**. Among natural hydrogels, alginate has been most commonly used in bioprinting of bone scaffolds due to its controllable degradation rate and the useful property of undergoing crosslinking, which allows it to be formulated into various shapes including microspheres and fibers (Loozen et al., 2013; Perez et al., 2014; Kim Y. B. and Kim G. H., 2015; Kim Y. B. et al., 2016; Raja and Yun, 2016). However, quick loss of mechanical strength of alginate during *in-vitro* culture and poor controllability over its internal microstructure (because of its excessive hydrophilic nature) are problematic for BTE (Kim Y. B. and Kim G. H., 2015). It has been found that alginate loses its mechanical strength by about 40% after 9 days of *in-vitro* culture (Shoichet et al., 1996). In addition, alginate has limited bioactivity due to lack of cell-binding sites, which are crucial for cell

TABLE 1 | Benefits and potential limitations of natural hydrogels commonly used in bioprinted bone scaffolds.

Hydrogel	Benefits	Potential limitations	References
Alginate	• Low price • Easy to fabricate 3D structures • Good biocompatibility • Easy gelation • High biodegradability and low immunological stimulation • Retains cell viability and osmolar requirements of cells • A suitable material for 3D printing due to crosslinkable features • Shear-thinning behavior	• Bioinert • Limited long-term stability • Rapid loss of mechanical properties during *in-vitro* culture • Limited 3D shape-ability	(Neufurth et al., 2014; Chimene et al., 2016; Narayanan et al., 2016; You et al., 2016; Luo et al., 2017; Park et al., 2017; Aldaadaa et al., 2018; Di Giuseppe et al., 2018; Milazzo et al., 2019)
Gelatin	• Accelerates gelation time • Capable of reversible thermal gelation • Biocompatible • Biodegradable	• Poor mechanical properties • High degradation rate	(Luo et al., 2015, 2018)
Chitosan	• Ingredients resemble ECM components of native tissue • Non-toxic by-products • Induces cell adhesion proliferation, differentiation, and viability	• Slow gelation rate • Poor mechanical properties • Can conflict with printing of cells and pH-sensitive molecules	(Suh and Matthew, 2000; Muzzarelli et al., 2012; Demirtaş et al., 2017)
Collagen	• Low immunogenicity • Good biocompatibility • Biodegradability • Regulates cell adhesion and differentiation	• Poor mechanical properties • Loses shape and consistency • Low viscosity and slow gelation	(Rhee et al., 2016; Mohseni et al., 2018; Turnbull et al., 2018)
Hyaluronic acid	• Good biocompatibility • Non-toxic degradation by-products • Visco-elastic properties • Highly hydrophilic • Anti-microbial properties	• Poor mechanical strength	(Kim et al., 2007; Zhu et al., 2017; Ashammakhi et al., 2019; Zhai et al., 2020)

adhesion. This poor bioactivity of alginate has led researchers to modify it with cell-adhesive ligands or combine it with other biomaterials to promote cell responses in bone scaffolds (Di Giuseppe et al., 2018; Luo et al., 2018; Sarker et al., 2019). Bioactivity of alginate has been improved by modifying its surface using arginine-glycine-aspartate peptide coating (Genes et al., 2004). In addition, combining alginate with other hydrogels such as chitosan and gelatin has also created an suitable environment for bioprinting of bone-marrow derived mesenchymal stem cells (BMSCs) (Huang et al., 2016) and mesenchymal dental pulp derived stem cells (DPSCs) (Park et al., 2015). Further, alginate combined with Matrigel, which is a gelatinous protein mixture, has been used for encapsulation of endothelial progenitor cells (EPCs) (Poldervaart et al., 2014).

Gelatin is another candidate for supporting cellular functions, including cell attachment, proliferation, and differentiation given that it has cell-ligand motifs (Luo et al., 2015; Milazzo et al., 2019). In addition, the thermoresponsive behavior of gelatin has made it a popular polymer for bioinks (Milazzo et al., 2019). However, gelatin has a high degradation rate and poor mechanical strength, which can be problematic for BTE (Gautam et al., 2014). Therefore, gelatin in combination with other biomaterials, such as chitosan, alginate, fibrinogen, HA, and silk fibroin, has been used as a cell carrier in bioprinting systems for BTE applications (Das et al., 2015; Huang et al., 2016; Kang et al., 2016). Methacrylamide gelatin (MG), a modified form of gelatin, has also exhibited excellent potential for cell printing with high cell viability (>97%) (Billiet et al., 2014), indicating MG can be a good synthetic hydrogel for BTE. Additionally, MG has been used as a suitable matrix for bioprinting BMSCs and the growth factor bone morphogenetic protein-2 (BMP-2) (Du et al., 2015). Coating titanium implants using gelatin methacryloyl (GelMA), another modified form of gelatin, has also improved the osteointegration of titanium implants (McBeth et al., 2017), indicating that GelMA is a good bioink candidate for BTE as well. Crosslinking strategies has also been implemented to stabilize and improve the mechanical properties of gelatin. In this regard, chemicals such as 1-ethyl-3-(3-dimethylaminopropyl) carbodiimide (EDC) (Huh et al., 2018), glutaraldehyde (Martínez-Vázquez et al., 2015), or genipin (Akkineni et al., 2016) have been applied.

Chitosan is also a favorable biomaterial for biomedical applications. This cationic polymer has a hydrophilic surface improving cell adhesion, proliferation, differentiation, and viability. The high charge density of chitosan in solution helps chitosan form insoluble ionic complexes with water-soluble anionic polymers such as alginate (Suh and Matthew, 2000; Zhu et al., 2011; Muzzarelli et al., 2012; Bakhsheshi-Rad et al., 2019). Chitosan has shown good potential as a carrier for rabbit BMSCs and the growth factor BMP-2 in hybrid polycaprolactone (PCL)/chitosan scaffolds. This combination has made a biomimetic micro-environment with

improved cell retention, growth, and distribution (Dong et al., 2017).

Collagen provides excellent characteristics such as low immunogenicity, permeability, good biocompatibility and biodegradability, and has potential to regulate the morphology, adhesion, migration, and differentiation of cells (Mohseni et al., 2018; Turnbull et al., 2018). Collagen type I is the most commonly used form of collagen in bioprinted bone scaffolds (Semba et al., 2020). Collagen type I incorporation provided sufficient adhesion ligands in alginate-polyvinyl alcohol (PVA)-HAp for attachment and proliferation of pre-osteoblast cells (MC3T3-E1) (Bendtsen et al., 2017). Coating of scaffolds with collagen has also improved adhesion, proliferation, and osteogenic differentiation of osteoblast-like cells (MG63) (Vandrovcová et al., 2011) and osteogenic differentiation of human adipose-derived stem cells (hADSCs) (Linh et al., 2020). Collagen type I is not highly favorable for bioprinting bone scaffolds due to its slow gelation kinetics and low viscosity (Ashammakhi et al., 2019). A bioprintable form of collagen type I, however, has been made by adding agarose to its matrix, resulting in printed mesenchymal stem cells (MSCs) (Duarte Campos et al., 2016). Also, combining collagen type I with HA has resulted in osteochondral scaffolds with a well-suited ECM for osteoblasts (Park et al., 2014).

HA is a hydrophilic natural polymer which is well-known to be a major component of ECM in connective tissues of all mammals (Bae et al., 2011). HA has potential to be used in biomedical applications due to its biocompatibility, non-toxic degradation by-products, visco-elastic properties, and capability to retain water which keeps tissues hydrated (Bae et al., 2011; Zhu et al., 2017; Ashammakhi et al., 2019). Further, anti-microbial properties of HA makes it a good candidate for implantation in bone defects (Zhai et al., 2020). However, the natural form of HA hydrogel is easily degraded in water due to its weak mechanical strength. To overcome this limitation, a modified form of the HA network, such as acrylated HA followed by ultraviolet (UV) light crosslinking, has been used to make a suitable matrix with tunable mechanical and degradation properties for cell and growth factor encapsulation in BTE (Kim et al., 2007). Photo-crosslinked methacrylated hyaluronic acid (MeHA), another chemically-modified form of HA, also appears to be a good matrix for bioprinting in BTE as *in-vitro* research indicated good levels of cell viability (64.4%) and osteogenic differentiation (Poldervaart et al., 2017). Also, HA in combination with methylcellulose has also exhibited good capability for bioprinting of MSCs (Law et al., 2018).

The majority of natural hydrogels share a common drawback related to insufficient mechanical properties which do not mimic native bone (Baino et al., 2015). To address this limitation, enhanced mechanical performance of bioprinted scaffolds has been pursued using synthetic polymers (Gao et al., 2014). For instance, bioprinted bone scaffolds made of poly (ethylene glycol) dimethacrylate (PEGDMA) and HAp exhibited an elastic modulus of ~359 kPa, which did not meet that of natural bone but was higher relative to natural polymers (less than 5 kPa) (Gao et al., 2014). Poly (lactic-co-glycolic acid) (PLGA) and poly (ethylene glycol) (PEG) blend has been another successful synthetic polymer for bioprinting of mechanically strong constructs (E~57 MPa) (Sawkins et al., 2015) consisting of immortalized human mesenchymal stem cells (hMSCs) for bone repair.

Cells

Cells selected for BTE applications should mimic the physiological state of native cells and be able to maintain their function *in-vivo*. Also, cell proliferation under both *in-vitro* and *in-vivo* conditions must occur in a controlled manner. An implanted scaffold may fail because of too little proliferation. On the other hand, excessive proliferation may cause a lack of enough oxygen and nutrient delivery to all cells and consequently, cell apoptosis occurs. Further, the timing of cell proliferation is also of great importance such that an initial high cell proliferation be desirable but it must be sustained at a specific rate (Murphy and Atala, 2014).

Various types of cells, including stem cells and cell lines, have been utilized in bioprinting of bone scaffolds. Osteoblast cell lines are used for bone repair and regeneration in clinical applications because they are bone-forming cells engaged in formation and mineralization of bone matrix. Restricted *in-vitro* proliferation is the major drawback which is associated with usage of fully differentiated osteoblasts (Kargozar et al., 2019). The most common cell line encapsulated in bone scaffolds by means of bioprinting has been MC3T3-E1 pre-osteoblast cells which have shown the promising ability to differentiate into mature osteoblasts (Raja and Yun, 2016; Bendtsen et al., 2017; Demirtaş et al., 2017). In addition, the MG63 cell line has been utilized in 3D scaffold-based osteosarcoma models to improve tumor therapy outcomes (Bassi et al., 2020) and in 3D printed scaffolds to study bone regeneration (McBeth et al., 2017). Related to bioprinted bone scaffolds, MG63 cells were also successfully laden into 3D printed scaffolds of PCL/alginate and the *in-vitro* osteogenic activity of cell-laden scaffolds was found to be superior compared to non cell-laden scaffolds (Kim Y. B. et al., 2016). Human osteogenic sarcoma cells (SaOS-2) are another category of bone-related cells that have been employed in bioprinted bone scaffolds (Neufurth et al., 2014).

Undifferentiated stem cells (*e.g.*, MSCs), which can be isolated from a number of tissues including bone marrow and adipose tissue, have also been extensively used in biomedical applications (Su et al., 2012; Qi et al., 2016) (it is important to note that undifferentiated stem cells and cell lines need to be cultured in a medium which is supplemented with ascorbic acid, dexamethasone, and -glycerophosphate for osteogenic activity (Kargozar et al., 2019)). Stem cells have been introduced as a suitable cell source in BTE owing to their distinct characteristics, including self-renewal and good capability to differentiate into various cell lineages (Kargozar et al., 2019). MSCs are easily expanded *in-vitro* and can proliferate and differentiate into cell lineages such as osteoblasts, chondrocytes, and adipocytes. Stem cells such as BMSCs harvested from Sprague-Dawley rats (Du et al., 2015; Huang et al., 2016) and humans (Gao et al., 2014; Poldervaart et al., 2017), hADSCs (Murphy et al., 2017), as well as human amniotic fluid-derived stem cells (hAFSCs), have been used in bioprinting of bone scaffolds. The main reasons for using ASCs in bioprinted bone scaffolds are ease of availability and great proliferation rate (Kargozar et al., 2019). Although the number of cells harvested from 1 g of adipose tissue is about 500 times greater than that harvested from the same amount of bone marrow

(Kargozar et al., 2019), ASCs have been found to have lower osteogenic activity compared to BMSCs (Kargozar et al., 2019). The main disadvantages of BMSCs, however, are related to the culturing process and isolation, both of which are time-consuming (Kargozar et al., 2019). DPSCs are another type of stem cells that have been successfully encapsulated in bone scaffolds by bioprinting. Compared to MSCs derived from bone marrow, DPSCs have greater potential for osteogenic differentiation and induction of vasculature (Park et al., 2015). Human nasal inferior turbinate tissue-derived mesenchymal stromal cells (hTMSCs) are also another promising source of cells that have been used in bioprinted bone scaffolds (Das et al., 2015). The hTMSCs express a proliferation rate five times higher than that of BMSCs and display approximately 30 times higher yield than that of ADSCs (Das et al., 2015). Also, parameters such as the passage number and donor age do not significantly impact the differentiation characteristics of hTMSCs (Pati et al., 2015). Muscle-derived stem/stromal cells, which are a population of self-renewing cells, has been another source of cells used in bioprinted bone scaffolds (Phillippi et al., 2008). Human umbilical vein endothelial cells (HUVECs) have also been used in bioprinting of bone scaffolds given they contribute to osteogenesis via secretion of regulatory molecules such as growth factors (Chen et al., 2018).

Taken together, this review indicates that there is no simple process for identifying one type of cell best suited for BTE. The selection criteria for cell type depends on factors such as availability, ease of isolation and culturing as well as cost of treatment (Kumar et al., 2019). Parameters such as the type of biomaterial and bioprinting technique also need to be considered regarding cell type selection.

Growth Factors

For treating large bone defects, vascularization still remains a challenge for BTE. One strategy used to enhance vascularization in bioprinted bone scaffolds has been usage of growth factors (Shahabipour et al., 2020). Biological aids, such as growth factors, play an important role in providing signals at damaged sites, which enable cells to migrate and stimulate the healing process (Salgado et al., 2004; Bishop et al., 2017). Accordingly, new bone formation is regulated by a range of growth factors and biomolecules, which can be included as a component of the bioink or added to the printed scaffold (Mouriño and Boccaccini, 2009; Turnbull et al., 2018).

The most common growth factor used in BTE has been the osteoinductive BMP-2 (Phillippi et al., 2008; Danhier et al., 2012; Jun et al., 2013; Poldervaart et al., 2013; Du et al., 2015). BMPs recruit MSCs to the healing location and differentiate them into the osteogenic lineage. The mechanism by which they do this is not fully understood; however, it is known that BMP-2 is the most effective inducer of osteoblastic differentiation (Salgado et al., 2004; Bai et al., 2013; Wang and Yeung, 2017). To stimulate osteogenesis, the concentration of BMP-2 has been found to be important and is dependent on the animal model. It has been reported that 0.2–0.4 mg/ml of BMP-2 is favorably osteoinductive in rats while higher concentrations of 0.43 mg/ml and 0.75–1.5 mg/ml are required for sheep and primates, respectively. However, concentrations above 1.5 mg/ml for BMP-2 have been found to cause toxic side effects (Bao et al., 2017).

Vascular endothelial growth factor (VEGF), which is found in a variety of vascularized tissues including bone, is commonly used in bone scaffolds due to its role to induce angiogenesis. VEGF regulates vascularization by recruitment of endothelial cells and play an important role to improve bone healing through both intramembranous and endochondral ossification (Salgado et al., 2004; Bai et al., 2013; Park et al., 2015; Stegen et al., 2015; Fahimipour et al., 2017; Shahabipour et al., 2020). Like BMP-2, the dosage of VEGF used in a bone scaffold should be taken into consideration. High concentrations of VEGF may cause toxicity, as well as non-functional vasculature (Dreyer et al., 2020). A concentration of 2.6 μg/animal has been found to be the highest allowable dosage of VEGF (Dreyer et al., 2020).

Compared to the effect of structures containing either BMP-2 or VEGF alone, dual delivery better promotes bone regeneration (Patel et al., 2008; Park et al., 2015). For example, dual delivery of BMP-2 and VEGF in bioprinted scaffolds of gelatin/alginate resulted in enhanced vascularization, which, in turn, promoted bone formation (Park et al., 2015). Most importantly, the specific ratio of BMP-2 and VEGF has been found to affect the synergistic effect of their combined use (Bao et al., 2017). Inappropriate proportions of BMP-2 to VEGF can have a negative influence on repair of a CSD. The ratio of 1 BMP-2 to 4 VEGF causes inhibition on bone formation; however, the ratio of 5 to 4 and above contributes to enhancing bone formation (Bao et al., 2017).

Due to restrictions, including the rapid degradation of growth factors and deactivation by enzymes *in-vivo*, polymeric delivery systems have been widely used as carriers to maintain biological functionality as well as the sustained and controlled delivery of growth factors (Yu et al., 2008; Jun et al., 2013; Izadifar et al., 2014). PLGA is one of the most successfully used biodegradable polymers in delivery systems because its hydrolysis contributes to metabolite monomers, lactic acid and glycolic acid, which are easily metabolized by the body via the Krebs cycle. Minimal systemic toxicity is also found with PLGA for biomedical applications (Danhier et al., 2012; Izadifar M. et al., 2015). Biodegradable PLGA has been investigated in various forms including microparticles and nanoparticles for BMP-2 and VEGF delivery (Kempen et al., 2009; Yilgor et al., 2009; Lee et al., 2011; Sawkins et al., 2015; Fahimipour et al., 2017).

Gelatin microparticles have also been used as delivery systems for growth factors, both *in-vitro* and *in-vivo*, due to their biodegradability and non-toxicity characteristics (Poldervaart et al., 2013; Poldervaart et al., 2014). Gelatin microparticles act as a suitable carrier for VEGF in bioprinted alginate/Matrigel scaffolds (Poldervaart et al., 2014). Controlled release of VEGF from gelatin microparticles led to a marked increase in vascularization, *in-vivo,* when compared to scaffolds with no VEGF or VEGF-loaded scaffolds with no gelatin microparticles (fast release) (Poldervaart et al., 2014).

Also, injectable thermoresponsive hydrogels have provided suitable matrices for delivery of BMP and VEGF. Such hydrogel systems are at a solution state at room temperature and convert to a gel state at body temperature. This characteristic enables delicate substances such as cells and growth factors to be readily encapsulated into the solution by

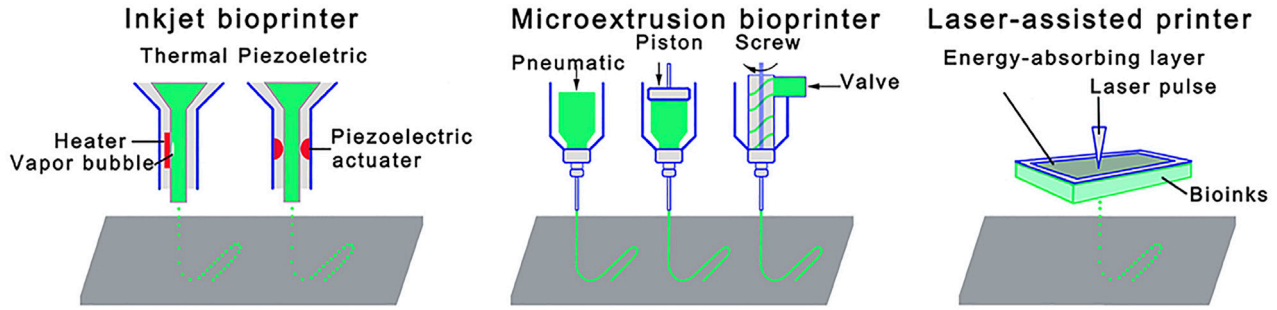

FIGURE 3 | Schematic illustrations of 3D bioprinting techniques: Inkjet bioprinter; microextrusion bioprinter; and laser-assisted bioprinter. Reprinted from Li et al., (2021). Copyright 2021, Front. Bioeng. Biotechnol (Li et al., 2021).

TABLE 2 | Bioprinted bone scaffolds fabricated with various bioprinting techniques.

Bioink	Bioprinting technique	Cell	Ref
Alginate+HAp+PVA+Collagen	Microextrusion (The HyRel System 30 3D printer with a modified EMO-25 extruder)	MC3T3-E1	Bendtsen and Wei, (2017)
Alginate+HAp+PVA	Microextrusion (The HyRel System 30 3D printer with a modified EMO-25 extruder)	MC3T3-E1	Bendtsen et al. (2017)
Alginate, chitosan, Alginate+HAp, Chitosan+HAp	Microextrusion (The Fab@Home™)	MC3T3-E1	Demirtaş et al. (2017)
Alginate	Microextrusion (pneumatic-based)	MC3T3-E1	Raja and Yun, (2016)
Alginate+gelatin+carboxymethyl chitosan	Microextrusion (pneumatic-based)	BMSCs	Huang et al. (2016)
MG hydrogel	Microextrusion (screw-based)	BMSCs	Du et al. (2015)
Matrigel+alginate	Microextrusion (pneumatic-based)	EPCs	Poldervaart et al. (2014)
Matrigel	Microextrusion (pneumatic-based)	ASCs	Murphy et al. (2017)
Gelatin, silk fibroin	Microextrusion (pneumatic-based)	hTMSCs	Das et al. (2015)
Alginate	Microextrusion (pneumatic-based)	MG63	Kim et al. (2016b)
Alginate+gelatin, collagen	Microextrusion (pneumatic-based)	DPSCs	Park et al. (2015)
Alginate	Microextrusion (pneumatic-based)	MC3T3-E1	Ahn et al. (2013)
Alginate/gelatin, MSCs	Microextrusion (pneumatic-based) used for HUVEC-laden alginate/gelatin, a piezoelectric nozzle used for MSCs	HUVECs MSCs	Chen et al. (2018)
Acrylated PEG, acrylated peptide	Inkjet (thermal-based)	hMSCs	Gao et al. (2015)
PEGDMA with nHAp and BGs	Inkjet (thermal-based)	hMSCs	Gao et al. (2014)
collagen type I/agarose	Inkjet (thermal-based)	MSCs	Duarte Campos et al. (2016)
Collagen/nHAp	LAB	Mesenchymal stromal cells	Keriquel et al. (2017)
Human osteoprogenitor cells, nHAp	LAB	Human osteoprogenitors	Catros et al. (2011)
Alginate, gelatin	Microextrusion (pneumatic-based)	SaOS-2	Neufurth et al. (2014)
Alginate, gelatin	Microextrusion (pneumatic-based)	Human endothelial cells	Akkineni et al. (2016)

mixing and then injected to the target site in the body. For instance, injectable hydrogel systems composed of PLGA-PEG-PLGA showed good capability to encapsulate BMP-2 and VEGF and release in a sustained manner (Bao et al., 2017).

Bioprinting Scaffolds for Bone Tissue Engineering

Fabrication of Bioprinted Scaffolds

To date, several bioprinting techniques have been used for fabricating bioprinted scaffolds with inkjet, laser-assisted, and microextrusion techniques being the three major approaches applied (**Figure 3**) (Li et al., 2021).

With an inkjet bioprinter, thermal or piezoelectric means are used as the driving force to print small droplets of the bioink via the nozzle (Groll et al., 2018; Ashammakhi et al., 2019). The strengths of thermal inkjet bioprinting are high printing speed and low operating costs. Although it has been reported that heat and mechanical stress involved in this technique can damage cells (Ashammakhi et al., 2019; Li et al., 2021), the technique can result in high cell viability rates given that the bioink is heated for a very short time (*e.g.*, less than 2 μs) (Gao et al., 2015). For example,

hMSCs-laden peptide-conjugated PEG bone scaffolds fabricated by inkjet bioprinting showed high cell viability (~87.9%) (**Table 2**) (Gao et al., 2015). Similarly, cell viability of 86.62% was shown in hMSCs-laden scaffolds of PEGDMA consisting of bioactive glass (BG) and HAp nanoparticles (nHAp), which were bioprinted by the thermal inkjet technique (Gao et al., 2014). In another BTE study (Duarte Campos et al., 2016), the viability of MSCs in various collagen I/agarose hydrogels bioprinted by the thermal inkjet technique was around 98% after 21 days of culture. This technique has been found to be safe for delicate substances as well, such as growth factors (Phillippi et al., 2008). One research group used inkjet printing to engineer stem cell microenvironments to create spatially defined patterns of immobilized BMP-2 (Phillippi et al., 2008). Thermal inkjet bioprinters, however, lack precision regarding droplet size and shape. They have also limitations regarding usage of biomaterials that are not heat or mechanically resistant. In this regard, piezoelectric-driven inkjet bioprinters can be used to overcome the limitations associated with thermal inkjet bioprinters; however, concerns of potential cell damage at 15-25 kHZ frequencies specific to piezoelectric-driven inkjet bioprinters have been mentioned (Li et al., 2021).

Laser-assisted bioprinting (LAB), which is a nozzle-free technique, consists of three main components: 1) a laser source, 2) a ribbon coated with an absorbing layer (*e.g.*, gold or titanium), containing the bioink, and 3) a collector lying beyond the ribbon (Bishop et al., 2017). This technique starts with suspending the bioink on the bottom of the ribbon followed by evaporation induced by a laser beam, which scans over the ribbon. Afterwards, vapor bubbles propel discrete droplets onto the collector due to high pressure (Bishop et al., 2017; Li et al., 2021). LAB has advantages including printing high cell densities, high cell viability, high speed, and high degree of printing resolution (Li et al., 2021). LAB is a promising technology providing excellent control over the cell density down to the single cell level, which allows control over the functionality of cell (Keriquel et al., 2017). Successful *in-situ* bioprinting of mesenchymal stromal cells encapsulated in collagen/nHAp matrix onto a mouse calvarial bone defect has been recently performed using LAB (**Table 2**) (Keriquel et al., 2017). It has also been shown that LAB is an effective technique to fabricate bioprinted scaffolds made of nHAp and osteoblastic cells (Catros et al., 2011) with no change to the physico-chemical properties of nHAp nor the viability, proliferation, and phenotype of osteoblastic cells up to 15 days (Catros et al., 2011). Although it seems LAB is a promising technology for constructing tissues, it has been only used in a limited number of BTE studies. This could be due to shortcomings associated with this technique, such as the time-consuming process of ribbon preparation, potential metallic residuals in the final scaffold, and the high production cost (Mandrycky et al., 2016; Bishop et al., 2017).

In microextrusion, the bioink is loaded in a cartridge and extruded on a platform either by pneumatic or mechanical forces (*e.g.*, screw- or piston-based) (Ashammakhi et al., 2019; Naghieh and Chen, 2021). Microextrusion is the most widely used method to fabricate bioprinted bone scaffolds due to the benefits of being capable of printing a wide spectrum of biomaterials (*e.g.*, soft hydrogels, synthetic polymers, and polymer/ceramic composites) (Mandrycky et al., 2016) and high cell deposition densities (Bishop et al., 2017; Li et al., 2021). This technique can print biomaterials with a viscosity range from 30 mPa.s to over 6×10^7 mPa.s (Mandrycky et al., 2016). It is able to employ either multiple nozzles to print biomaterials separately (Izadifar Z. et al., 2015; Ashammakhi et al., 2019) or co-axial nozzles to print biomaterials simultaneously such as core/shell designs (Raja and Yun, 2016). Microextrusion has been widely used to bioprint hydrogels (**Table 2**) such as alginate (Ahn et al., 2013; Park et al., 2015; Kim Y. B. et al., 2016; Huang et al., 2016; Raja and Yun, 2016; Demirtaş et al., 2017), chitosan (Demirtaş et al., 2017), gelatin (Park et al., 2015; Huang et al., 2016), collagen (Park et al., 2015), carboxylmethyl chitosan (Huang et al., 2016), MG (Du et al., 2015), MeHA (Poldervaart et al., 2017), and cell-laden composite scaffolds (Bendtsen et al., 2017; Bendtsen and Wei, 2017). It has been found that a wide range of cell types such as MC3T3-E1 (Bendtsen et al., 2017; Demirtaş et al., 2017), MG-63 (Kim Y. B. et al., 2016), BMSC (Du et al., 2015), DPSC (Park et al., 2015), hAFSCs (Kang et al., 2016), and hTMSCs (Du et al., 2015) can be successfully bioprinted using this technique. Though, the resolution of microextrusion bioprinters is moderate at between 50 and 500 μm (Mandrycky et al., 2016; Ashammakhi et al., 2019). In addition, cell structure and cell viability can be affected by shear stress during the printing process. However, approaches including reducing extrusion pressure or increasing the needle size can manage the cell viability issue (Bishop et al., 2017; Li et al., 2021). A comparison between bioprinting techniques including inkjet, LAB and microextrusion is given in **Table 3**.

Printability

In 3D printing, printability is an important concept requiring the bioink to be deposited in an accurate and precise manner with high spatial and temporal control such that the printed structure replicates the virtual model (Murphy and Atala, 2014; Fu et al., 2021). Preferably, the bioink should be in liquid form before being extruded from the nozzle tip (to help avoid nozzle jamming) while after printing it should experience rapid solidification/gelation to maintain its shape (He et al., 2016).

There are several factors affecting bioink printability, most notably crosslinking (**Figure 4**) performed using either chemical or physical methods (or both) (Mandrycky et al., 2016). UV light is used as a chemical crosslinking method for GelMA hydrogel (Du et al., 2015; McBeth et al., 2017) while chemicals such as EDC/N-hydroxysuccinimide are used to crosslink collagen hydrogel chemically (Linh et al., 2020). Crosslinking can also be physical by ion gelation (*e.g.*, for alginate, chitosan, and gellan gum hydrogels) (Park et al., 2015; Akkineni et al., 2016; Kim Y. B. et al., 2016; Naghieh et al., 2018a; Sarker et al., 2018; Sadeghianmaryan et al., 2020) or by thermal gelation (*e.g.*, for collagen) (Arumugasaamy et al., 2017). When bioinks are used, crosslinker concentration must be sufficient to print structures with high printability and cell viability (Ashammakhi et al., 2019). In other words, crosslinker concentration should be sufficiently

TABLE 3 | Comparison between inkjet, laser-assisted, and microextrusion bioprinting techniques.

	Inkjet	LAB	Microextrusion	Ref
Cell viability	High (>85%)	High (>95%)	Low to moderate (40–80%)	(Gao et al., 2014, 2015; Duarte Campos et al., 2016; Mandrycky et al., 2016)
Supported viscosity	Low viscosities (3.5–12 mPa.s)	Low to moderate viscosities (1–300 mPa.s)	Wide range of viscosities (30 mPa.s to over 6×10^7 mPa.s)	(Chang et al., 2011; Mandrycky et al., 2016)
Printing resolution	High	High	Moderate	(Mandrycky et al., 2016; Ashammakhi et al., 2019)
Strengths	• Low-cost operation • High cell viability • Fast printing	• High resolution • Fast printing • High cell viability • Precise fabrication • Possibility of *in-situ* bioprinting • Given that it is a nozzle-free technique, it can avoid cell clogging	• Prints a wide spectrum of biomaterials • Prints high cell densities	(Mandrycky et al., 2016; Keriquel et al., 2017; Chen, 2018)
Limitations	• Lack of precision regarding droplet size and shape • Biomaterials that are not heat or mechanically resistant may be comprised • Cell damage at 15–25 kHz frequencies	• Time-consuming process of ribbon preparation • Metallic residuals in the final scaffold • High production cost	• Shear stress during printing affects cell viability • Low printing speed • Moderate resolution • Low to moderate cell viability	(Mandrycky et al., 2016; Fu et al., 2021; Li et al., 2021)

high to achieve structural integrity (*i.e.*, shape fidelity) and sufficiently low to be safe for cell function (Rajaram et al., 2014). Previous research indicates that crosslinking alginate with high concentration of $CaCl_2$ (>2.5 wt%) led to cell death whereas low $CaCl_2$ concentration (<2.5 wt%) contributed to a slow crosslinking rate, which in turn resulted in structures with poor shape fidelity (Raja and Yun, 2016). In another study (Kim Y. B. et al., 2016), partial crosslinking of alginate solution with a $CaCl_2$/cell-laden alginate mixing ratio of 3:7 resulted in high printability as well as high cell viability (~95%) compared to other mixing ratios (0:10, 1:9, 2:8, 4:6, 5:5).

Printability and cell viability can also be influenced by bioink concentration/formulation as well as printing temperature (**Figure 4**) (Ouyang et al., 2016; Sarker et al., 2019; Soltan et al., 2019; Naghieh et al., 2020). While bioinks with high viscosity provide better shape fidelity, less viscous bioinks provide a more suitable environment for cell viability due to reduced shear stress experienced during printing (Murphy and Atala, 2014; Ouyang et al., 2016). A recent study assessing the printability of gelatin/alginate bioink showed that the bioink relied on gelatin concentration. Printing the bioink with a ratio of 5% gelatin to 1% alginate at 27.5°C and 30°C resulted in fusion of subsequent layers and formation of circular interconnected channels. In contrast, printing the bioink with a ratio of 7.5% gelatin to 1% alginate at 30°C led to constructs with (preferable) distinguished layers, smooth surfaces, and square interconnected channels with regular edges. Further, printing the bioink with a ratio of 10% gelatin to 1% alginate at 25°C made constructs with irregular strands and interconnected channels. Also, high viability of embryonic stem cells was observed with gelatin/alginate bioinks printed using lower gelatin concentrations and high printing temperatures. As a result, the recommended optimized concentration and temperature for high printability and cell viability was a ratio of 7.5% gelatin to 1% alginate and 30°C, respectively (Ouyang et al., 2016). Bioink concentration/formulation also affected shape fidelity of scaffolds consisting of agarose and collagen type I (Duarte Campos et al., 2016). Here pure collagen type I was unable to form hollow structures with proper shape as complete gelation was not achieved. Increasing the agarose content in the collagen type I matrix enhanced the viscosity, gelation temperature, and consequently the accuracy of printability. Also, 98% of cell viability in various agarose/collagen type I hydrogels was observed, indicating effectiveness various hydrogel formulations and bioprinting processes for cell functionality. Further research (Raja and Yun, 2016) has shown that increasing alginate concentration from 6 wt% to 9 wt% in α-tricalcium phosphate (TCP) core/cell-laden alginate shell scaffolds resulted in high printability without detrimental effects on the viability of MC3T3-E1 cells. Another group also introduced PVA/HAp suspension into alginate formulation to improve printability without toxic effects on the viability of MC3T3-E1 cells (Bendtsen et al., 2017).

Printability can also be affected by printing pressure, nozzle speed, printing angles, and the distance between strands (**Figure 4**) (He et al., 2016). Overly high pressure results in quick extrusion or jetting while low pressure results in nozzle clogging. Pressure, which directly affects the flow rate, must be properly tuned to overcome the resistance of flow in the nozzle for proper extrudability (He et al., 2016; Naghieh and Chen, 2021). An overly slow or fast (translating) nozzle speed, relative to the extrusion rate, can also affect printability. Here, strands larger than the needle diameter have been created when the extrusion rate is greater than the nozzle speed, and vice versa (He et al., 2016; Gerdes et al., 2020; Fu et al., 2021). The angle of printing is also of importance as acute angles less than 90° offer poor

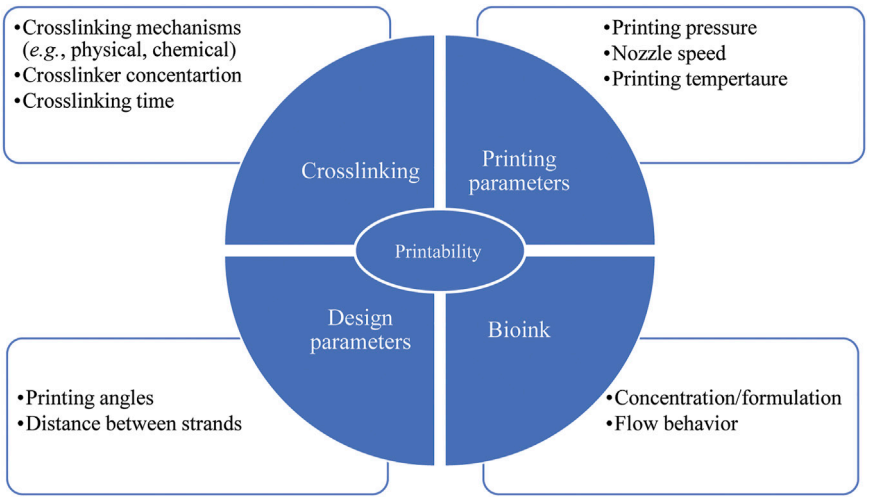

FIGURE 4 | Parameters affecting scaffold printability; factors related to crosslinking, bioink and printing parameters have to be taken into consideration to achieve both favorable printability and cell viability.

printability relative to 90° right angles and obtuse angles greater than 90° (He et al., 2016). Specifically, an acute printing angle leads to an overlap problem where the extrusion of hydrogel was doubled. Strand fusion is another issue arising if the distance between strands is too small (He et al., 2016). Fusion between successive layers also affects printability since it changes scaffold height, which can be problematic if a specific size is needed (He et al., 2016).

Additionally, the flow behavior of bioink has a critical influence on printability (**Figure 4**). From rheological point of view, a bioink should exhibit non-Newtonian shear thinning behaviour during printing with rapid viscosity recovery afterwards. With such properties viscosity is directly proportional to the applied stress, thereby allowing the bioink to be easily extruded from a nozzle tip under low pressure (Kyle et al., 2017). Such properties are also a benefit for encapsulated cells (Wu et al., 2018). Recent research (Wu et al., 2018) found excellent shear thinning and immediate viscosity recovery of bioinks composed of gellan gum and poly (ethylene glycol) diacrylate (PEGDA), which enabled constructs to print with high shape fidelity. Further, high cell viability (above 87%) over a prolonged cell culture (21 days) was found, indicating that a gellan gum/PEGDA can be an appropriate bioink for fabricating biomimetic bone.

Mechanical and Osteoconductive Properties

Influence of Structural Features

Structure plays a crucial role on the mechanical and osteoconductive properties of scaffolds as well as cell functions. An adequate structure will allow flow of nutrients and oxygen into the scaffold and removal of cell waste products, thereby promoting cell survival and tissue regeneration. The degree of porosity and pore size also affects the rate of degradation (Perez and Mestres, 2016). For instance, cell proliferation was found to be 14% higher in 3D bioprinted gelatin scaffolds with pores larger than 580 µm when compared to scaffolds with a 435-µm pore size (Choi et al., 2018). Viability and proliferation of hMSCs were also higher in 3D printed PCL scaffolds with large pores due to large surface area for cells to adhere and proliferate (Domingos et al., 2013). A balance though exists between pores being sufficiently large to accommodate cells, facilitate diffusion of oxygen and nutrients, as well as facilitate waste removal without negatively affecting the scaffolds ability to bear load (Loh and Choong, 2013; Perez and Mestres, 2016). For instance, when increasing pore size from 245 to 433 µm, the compressive modulus and maximum allowable stress before failure of PCL scaffolds decreased by approximately 50 and 75%, respectively (Domingos et al., 2013). Scaffolds with small pore size possess greater load carrying capacity while scaffolds with large pore sizes contain less material, making scaffolds easier to deform (Domingos et al., 2013; Rotbaum et al., 2019). Many studies have been performed to identify the optimum pore size range for *in-vitro* cell research and *in-vivo* bone regeneration studies. Pore sizes larger than 300 µm appear to be beneficial for new bone and capillary formation; conversely, pore sizes smaller than 100 µm may not be promising for mass transport and cell migration (Roosa et al., 2010). However, there is no consensus on the optimal pore size for a bone scaffold. For example, MC3T3-E1 cells exhibited higher proliferation rates *in-vitro* with polypropylene-based scaffolds with a pore size of 350 vs. 500 µm, with the latter size found to be too large for adhesion and proliferation of cells (Lee et al., 2010). High cellular activities with small pores is thought to be due to strands being close to one other within the same layer, resulting in a high number of contact points and consequently high cell function (Domingos et al., 2013). In contrast, a pore size of 500 µm (vs. 250 µm) was found to be more effective for osteointegration and bone formation *in-vivo* with polydopamine-laced HAp/collagen/calcium silicate

scaffold (Lee et al., 2019). In another study (Lee et al., 2016), *in-vivo* evaluations of PCL/HAp scaffolds exhibited higher bone regeneration with larger pores (600 and 1000 μm) when compared to scaffolds with smaller pores (200 μm). Inconsistent findings need to be interpreted with caution as other factors, including the type of biomaterials, specific material preparation technique, scaffold fabrication method as well as the type of cells, all potentially affect the specific pore size range for a bone scaffold (Roosa et al., 2010). Accordingly, more research is needed to identify optimal structures and pore sizes for scaffolds prior to its use as a bone substitute.

Internal geometry of scaffolds (*i.e.,* the arrangement of strands throughout the scaffold) has also been found to affect cell function. For example, low cell-seeding efficiency results from poor interactions between cells and scaffold material, which can be adjusted via internal geometry (Sobral et al., 2011). Cell-seeding efficiency is lower in scaffolds with homogeneous internal geometry as the culture medium has a direct path to travel within the scaffold; conversely, cell-seeding efficiency is higher in scaffolds with gradient pore sizing (Sobral et al., 2011). This improvement is attributed to an offset between scaffold layers, which affects the flow rate of the cell medium within the scaffold, thereby contributing to higher interaction between cells (Sobral et al., 2011; Yeo et al., 2012). Specifically, offset strands result in a higher number of anchorage points, thereby providing a larger surface area for cell attachment. The result is decreased cell loss and improved seeding efficiency, differentiation, and proliferation (Park et al., 2011; Perez and Mestres, 2016). For example, interlayer strand diameter offset values of 50 and 100% in PCL/β-TCP scaffolds resulted in higher seeding efficiency of MG63 cells, cell viability, alkaline phosphatase (ALP) activity, and calcium deposition when compared to scaffolds without an offset (Yeo et al., 2012). Similarly, higher MSC proliferation was observed in PCL scaffolds with an interlayer offset compared to scaffolds without interlayer offset (Yilgor et al., 2008). While an interlayer offset appears to have a beneficial influence on cell function, this could vary depending upon the cell type and biomaterials employed. For example, no difference in proliferation of MC3T3-E1 cells on PCL/PLGA scaffolds (with or without interlayer offset) was found (Lee et al., 2012). Conflicting findings have also been reported regarding the influence of internal geometry on compressive properties of scaffolds. PCL/β-TCP scaffolds with 50 and 100% interlayer offset values appear to possess a higher bending modulus (+7%) than scaffolds without an offset (Yeo et al., 2012). Conversely, an experimental study on PCL/HAp (40% HAp) scaffolds with an offset exhibited lower compressive elastic moduli (−50%) relative to scaffolds without an offset (Park et al., 2011) Another PCL/HAp (5% HAp) study also found a lower compressive modulus (−40%) with scaffolds having an interlayer offset (Buyuksungur et al., 2017). Rationale for lower elastic moduli was attributed to the shifted strands being unable to support overlying strands when loaded. It is worthwhile note though that other studies of PCL/HAp (Pierantozzi et al., 2020) and PCL/PLGA scaffolds (Lee et al., 2012) found no difference in the compressive moduli of scaffolds with and without an interlayer offset. Further research is needed to identify an appropriate offset which maximizes cell function while simultaneously achieving mechanical properties mimicking native bone.

The shape and geometry (*e.g.*, rectangular, triangular) of internal pores (*i.e.*, shape of embedded pores within scaffold) is also another structural property affecting cell function, osteoconductive, and mechanical properties of a bone scaffold (Sobral et al., 2011). Specifically, pore shape and geometry can be altered using specific lay-down patterns (Domingos et al., 2013). For instance, quadrangular, triangular, and complex polygonal pores have been created using 0°/90°, 0°/60°/120°, and 0°/45°/90°/135° laydown patterns, respectively. As readily apparent, increasing the number of deposition angles (*i.e.*, smaller deposition angles) in the 3D printing process creates pores with more complex geometry. Mechanical property wise, PCL scaffolds with quadrangular pores exhibited higher compressive moduli (~34.2 MPa) relative to triangular (~30.5 MPa) and polygonal pores (~19.1 MPa) (Domingos et al., 2013). Rationale was attributed to adjacent layers sliding more easily with scaffolds made using smaller deposition angles (Domingos et al., 2013). Sliding then resulted in more deformation and lower compressive moduli. Deposition angles have also affected the cell viability whereby lower viability of hMSCs was noted with small deposition angles [125]. Rationale for these findings is likely due to limited cell accessibility and colonization with smaller angles (Domingos et al., 2013). Interestingly, hexagonal-shaped pores appear to offer both high cell viability and strength. Glass-ceramic scaffolds with hexagonal-shaped pores were found to possess compressive strength (S_c~122 MPa) comparable to cortical bone and elastic moduli (E~2.4 GPa) comparable to trabecular bone (Roohani-Esfahani et al., 2016). Rationale was attributed to high contact area between strands in subsequent layers as well as the creation of a highly anisotropic structure which enhanced load transfer when compared to other patterns (*e.g.*, zigzag, curved, rectangular) (Roohani-Esfahani et al., 2016). Similar findings were reported by Van Bael et al. (2012) where Ti6Al4V bone scaffolds with hexagonal pores showed higher elastic moduli (~11.3 GPa) relative to rectangular (~2.8 GPa) and triangular pores (~2.04 GPa). In addition, hexagonal pores exhibited the highest cell growth, followed by rectangular and triangular pores. Rationale was due to high number of corners with hexagonal pores, which permitted rapid cell bridging as the distance between strands was shorter relative to other configurations (Van Bael et al., 2012).

Influence of Bioactive Ceramics

To date, bioceramics have been largely used to help repair and reconstruct diseased or damaged living tissues and organs of the body (Baino et al., 2015; Sadeghianmaryan et al., 2022). The use of bioactive ceramics in combination with polymers in BTE has gained interest as the resulting constructs possess bioactivity and high compressive strength/moduli provided by the ceramic phase while the polymeric network provides toughness, flexibility, and biodegradability (Huang et al., 2018; Kumar et al., 2019).

Mechanical properties of bioprinted scaffolds are of importance because they affect osteogenic differentiation and cell morphology (Kim et al., 2017). In cell-laden scaffolds,

enhanced mechanical and osteoconductive properties have also been made using bioceramics such as TCP and HAp (Kim et al., 2017; Ashammakhi et al., 2019). TCP contains two crystals namely α-TCP and β-TCP, where α has higher solubility than β. In an aqueous medium (*e.g.*, culturing condition in minimum essential media alpha), α-TCP shows a cementic reaction which hardens the bioceramic and subsequently forms calcium-deficient hydroxyl apatite. Although two crystals of TCP have similar chemical structure, α-TCP demonstrates more rapid bone formation *in-vivo* compared to β-TCP. Mechanically, cell-laden collagen-coated α-TCP/collagen scaffolds showed lower elastic modulus (0.55 MPa) relative to that of trabecular bone but the elastic modulus was markedly higher than pure cell-laden collagen (0.04 MPa) (Kim et al., 2017). Biological activity wise, cell-laden collagen-coated α-TCP/collagen scaffolds showed higher osteoconductive properties (ALP activity, osteopontin (OPN), and calcium deposition) compared to pure collagen (Kim et al., 2017).

HAp, in particular, has been widely explored in BTE studies due to its biocompatibility, osteoconductivity as well as close compositional and mineralogical similarities to the inorganic component of natural bone (Wiria et al., 2007; Kim et al., 2012; Serra et al., 2013; Qi et al., 2016; Bendtsen et al., 2017; Wang et al., 2017; Kumar et al., 2019). With regards to mechanics, HAp exhibits an elastic modulus of 35–120 GPa and a compressive strength of 120–900 MPa (Milazzo et al., 2019). Related higher MC3T3-E1 cell viability (~96%) was observed with an optimized formulation of bioprinted PVA/HAp/alginate, attributed to the incorporation of PVA/HAp compared to that of cell-laden alginate scaffolds (~60%) (Bendtsen et al., 2017). Various formulations of PVA/HAp/alginate scaffolds encapsulated with MC3T3-E1 cells showed an elastic modulus (~2–10 kPa) lower than that of trabecular bone, but the scaffolds remained intact over 14 days incubation in culture media. These results suggest that cell-laden PVA/HAp/alginate scaffolds could support cellular activity for 14 days *in-vitro* (Bendtsen et al., 2017). Research on hASCs-laden alginate/gelatin/nHAp also showed that incorporation of nHAp particles improved osteogenic activity and bone formation both *in-vitro* (osteogenesis-related genes) and *in-vivo* (subcutaneously implanted) when compared to pure hydrogel (Wang et al., 2016). Additionally, adding HAp into bioprinted hASCs-loaded hydrogels (gelatin methacrylate/HA) supported bone matrix mineralization, as confirmed by biomarkers (including collagen type I, ALP, and OPN), making this HAp-modified hydrogel a promising bioink for bone bioprinting (Wenz et al., 2017). Adding HAp into chitosan and alginate hydrogels also increased osteogenic gene expression and enhanced bone mineral density relative to pure hydrogels (Demirtaş et al., 2017). Taken together, prior research indicates that HAp plays an important role in adhesion, growth, proliferation, and differentiation of osteogenesis-related cells. HAp incorporation into alginate formulation also provides a suitable environment for differentiation of MC3T3-E1 cells into osteoblasts as well as calcium deposition (Bendtsen and Wei, 2017; Kumar et al., 2019).

Bioactive glasses are another category of bioceramics that have received increasing attention for fabricating bone scaffolds with 3D printing technology. BGs have the capability to bond to native bone tissue, thereby providing a stable interface needed for a range of biological functions such as angiogenesis and tissue regeneration (Baino et al., 2015). When BGs are used, rapid release of ion dissolution products leads to the formation of a nHAp layer on the BG surface, which can interface with host tissue (Baino and Vitale-Brovarone, 2014; Murphy et al., 2017; Baino and Fiume, 2020). Another advantage associated with using BGs is that their chemical composition and subsequent degradation rate can be tailored. Accordingly, scaffolds containing BGs can be designed with a degradation rate matching that of bone ingrowth and remodeling (Fu et al., 2011). For example, hybrid bioprinted scaffolds consisting of PCL/BGs, along with ASCs-loaded Matrigel, showed ~23% weight loss over 2 weeks and strong bioactivity via formation of HAp crystals (Murphy et al., 2017). However, there is limited information regarding the use of BGs in 3D bioprinted bone scaffolds, as well as its effect on vascularization and bone formation *in-vivo*.

Influence of Hybrid Systems

The mechanical and osteoconductive properties of bone scaffolds have also been adjusted through the fabrication of hybrid scaffolds. In a hybrid system, scaffolds are printed using two materials with different mechanical and biological properties (Akkineni et al., 2016; Raja and Yun, 2016). The stiffer material carries the majority of the applied load and thereby shields the (less stiff) softer material. Soft natural hydrogels (*e.g.*, collagen, gelatin, and alginate), can then be used for embedding delicate substances including cells or growth factors (Park et al., 2015; Akkineni et al., 2016; Kim Y. B. et al., 2016). Synthetic polymers, such as PCL, have been commonly used in hybrid scaffolds as the stiffer material. Cell-laden hybrid scaffolds of PCL/chitosan showed a compressive strength of ~7 MPa (comparable to trabecular bone with $S_c \approx 2–12$ MPa (Wu et al., 2014)), and much higher than that of chitosan (<1 MPa) (Dong et al., 2017). In addition, higher cell retention, proliferation, bone matrix formation, and evidence of osteogenesis (*e.g.*, via presence of collagen type I, osteocalcin (OCN), ALP) were found in cell-laden PCL/chitosan hybrid scaffolds compared to PCL scaffolds. Elastic moduli of 2–13 MPa have been observed with hybrid scaffolds containing PCL/alginate strands, with various porosities (*i.e.*, 41, 62, 66%) coated by cell-laden alginate bioink (Kim Y. B. et al., 2016). Although the resulting elastic moduli were much lower than that of native trabecular bone ($E \approx 100–5000$ MPa (Wu et al., 2014)), it was higher than that of pure cell-laden alginate ($E \approx 3.6–32.1$ kPa (Naghieh et al., 2018b)). A research including both *in-vitro* and *in-vivo* studies on hybrid PCL scaffolds loaded with bioprinted HAp-modified alginate suggested such hybrid system for osteochondral regeneration; however, no mechanical evaluation was done in this study (You et al., 2018).

Specialized arrangements, such as core/shell designs (**Figure 5**), have shown promise as new hybrid scaffolds (Perez and Kim, 2015). With such designs, the structure is made of a soft inner core surrounded by a stiff outer shell (Akkineni et al., 2016). Here the core would contain cells or growth factors (Perez et al., 2015). The

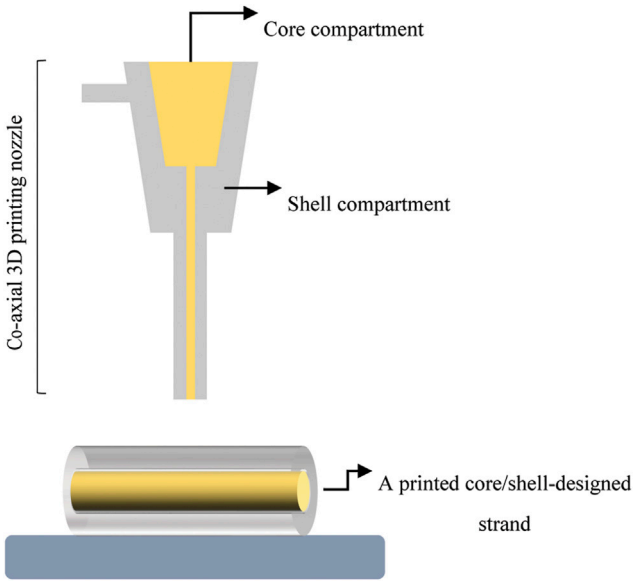

FIGURE 5 | A schematic illustrating core/shell designed strand fabricated with a co-axial 3D printing nozzle.

core has also been reinforced with a stiffer material such as PCL (Kim M. and Kim G. H., 2015), a higher hydrogel concentration (Ahn et al., 2013), and a bioactive ceramic (Raja and Yun, 2016). Core/shell scaffold designs comprised of a collagen hydrogel (0.6 wt%) as the core and high concentration alginate hydrogel (16.7 wt%) as the shell exhibited a higher elastic modulus of ~200 MPa compared to scaffolds with pure alginate strands in both the core and shell (E~1 MPa) (Akkineni et al., 2016). With this approach, hybrid core/shell scaffold designs comprised of collagen/alginate reached the lower end of elastic moduli for trabecular bone (E ≈ 100–5000 MPa (Wu et al., 2014)). Also, bioprinted scaffolds consisting of a α-TCP core and cell-laden alginate shell exhibited a compressive strength of 3.2 MPa (Raja and Yun, 2016), comparable to that of trabecular bone (S_c ≈ 2–12 MPa (Wu et al., 2014)), while the strength of pure alginate hydrogel was less than 0.5 MPa. Biologically, MC3T3-E1 cells encapsulated in the alginate shell were able to maintain their viability (>90%) for a long culture period (35 days) (Raja and Yun, 2016). In light of core/shell scaffolds, mechanical findings showed that adding HAp into the shell formulation not only led to 1.8-fold increase in elastic modulus of core (PCL)/shell (gelatin/PVA/HAp) scaffolds, but also resulted in superior ALP activity and calcium mineralization of MG-63 cells relative to HAp-free formulation (Kim et al., 2020). Hybrid scaffolds are also highly beneficial for dual release of growth factors both temporally and spatially to induce bone regeneration effectively (Park et al., 2015; Perez et al., 2015; Akkineni et al., 2016). In this regard, a novel 3D printing system printed two different hydrogels within a PCL framework: 1) a collagen hydrogel loaded with DPSC/BMP-2 in the periphery zone; and 2) an alginate/gelatin hydrogel loaded with DPSC/VEGF in center zone. This approach enables either dual release or sequential delivery of two growth factors for vascularized BTE (Park et al., 2015).

Tracking Bone Regeneration

In-Vitro

It is necessary to assess the performance of bone tissue-engineered constructs using pre-clinical *in-vitro* studies prior to evaluating therapeutic feasibility in animal studies (Salgado et al., 2004). In BTE studies, bone-specific biomarkers including enzymes (ALP) and proteins (OPN, OCN, and collagen type I) have been commonly studied to evaluate the osteogenic activity of scaffolds *in-vitro* (Li et al., 2016). ALP is an enzyme found in the bloodstream, with most of ALP produced in the liver and some within bones, intestines and kidneys (Kuo and Chen, 2017). It is an initial biomarker used to assess osteogenic differentiation and phenotype (Kim SE. et al., 2016). Additionally, OCN, which is the most abundant non-collagenous protein in bone, has been used as a biomarker of osteoblast function to assess bone formation (Kuo and Chen, 2017). OPN, which also belongs to the family of non-collagenous proteins, is secreted by several cells (such as osteoblasts and osteoclasts) and plays a crucial role in bone remodeling and biomineralization (Singh et al., 2018). Collagen type I is also the major protein component of the ECM in bone and its expression is often studied to evaluate osteogenic activity (Bao et al., 2017). Further, the expression of genes including Runt-related transcription factor-2, which is the master gene related to osteoblast differentiation, as well as osterix has also been studied with respect to pre-osteoblastic stage. The expression of these bone biomarkers is commonly identified by biochemical analysis including real time reverse transcription-polymerase chain reaction (Bao et al., 2017; Demirtaş et al., 2017; Liu et al., 2019) (Dong et al., 2017). After osteogenic differentiation stage, differentiated cells start to secrete a mineralized matrix resulting in calcium deposition, which is used as a biomarker for mature osteoblasts and is usually assessed by Alizarin Red Staining (Florencio-Silva et al., 2015; Kim Y. B. et al., 2016; Hwang and Horton, 2019; Pierantozzi et al., 2020).

Accordingly, cell viability and cell proliferation are other important parameters to be assessed. This is needed as encapsulated cells may experience high shear stress during the bioprinting process as well as excessive crosslinking (Zhang et al., 2017). The type of cells and biomaterials present may also affect the viability of cells (Ashammakhi et al., 2019). In bioprinted scaffolds, colorimetric assays including live/dead, MTT (Thiazolyl Blue Tetrazolium Bromide) or Presto Blue (PB) have been used to study cell viability and subsequently cell proliferation (Akkineni et al., 2016; Kim Y. B. et al., 2016; Demirtaş et al., 2017; Zhang et al., 2021). Recently, PB has been offered as an alternative to MTT to assess the viability and proliferation of MC3T3-E1 cells (Demirtaş et al., 2017) as well as human umbilical vein endothelial cells (Boncler et al., 2014). The major benefit of PB assay is that it is resazurin-based which is a water-soluble dye and consequently non-toxic to cells. Whereas MTT is a tetrazolium-based by which MTT converts into purple formazan compound in metabolically active cells. Formazan product must be solubilized in dimethyl sulfoxide which can cause cytotoxicity. Further, PB assay is faster due to shorter incubation time needed (10 min to 2 h) (Boncler et al., 2014)

compared to that of MTT (2–4 h) (Boncler et al., 2014; Pierantozzi et al., 2020). However, the gap observed here is that PB assay has only been used for a limited number of cells in comparison with MTT and further investigation is needed.

In-Vivo

Although *in-vitro* studies are critical stepping stones, they cannot fully reflect *in-vivo* models which are the ultimate test for testing the efficacy of bioprinted scaffolds. Consequently, pre-clinical (animal) *in-vivo* studies are needed to study integration and function of bone scaffolds (Ashammakhi et al., 2019). *In-vivo* studies, however, are cost intensive, require strict ethical considerations, and a key limitation is variation between species. Specifically, bone composition, density, and mechanical properties in commonly used *in-vivo* animal models (*e.g.*, rats, pigs) are different from those of humans, which may lead to outcomes different from what would been seen in humans (Abubakar et al., 2016; Caddeo et al., 2017; Klüter et al., 2019). The choice of an animal model is thus a crucial step towards the success of pre-clinical *in-vivo* studies.

An appropriate animal model should mimic the clinical setting such that it is biologically comparable (as much as possible) to human physiology (Salgado et al., 2004). In BTE studies, much of the research has focused on rodent models (such as mice (Chuenjitkuntaworn et al., 2010; Poldervaart et al., 2013), and rats (Blum et al., 2003; Sawyer et al., 2009; Harada et al., 2014; Perez et al., 2015; Suenaga et al., 2015; Sukul et al., 2015; Kang et al., 2016; Qi et al., 2016; Bao et al., 2017; Song et al., 2017; Liu et al., 2019)) and rabbit models (Oh et al., 2007; Kim et al., 2012, 2014; Jun et al., 2013; Pae et al., 2019) due to economic considerations, reproducibility, and throughput. Usage of bigger animal models, such as goats (Yu et al., 2008) or sheep (Ahmed and Hamad, 2020), is rare mainly due to the high cost (Salgado et al., 2004; Spicer et al., 2012).

Anatomically, the calvarium has widely served as a model site to create bone defects and subsequently track bone regeneration. The calvarium provides a relatively large and accessible surface upon which to perform a surgical operation and for handling the specimen. This defect model also permits the creation of a reproducible defect, which can be quickly generated and does not require fixation for stabilization of the skeleton (unlike femoral defects) (Salgado et al., 2004; Spicer et al., 2012). In addition, a uniform circular defect can be created, which enables a convenient means to assess bone regeneration by radiographical and histological analyses (Salgado et al., 2004). However, a calvarial defect is not an appropriate defect model when intending to track bone formation and remodeling under biomechanical loading given that this anatomical site experiences little-to-no loading compared to long bones (Spicer et al., 2012).

In terms of physical size, a defect 8 mm in diameter is regarded as an acceptable CSD in the rat calvarium (Patel et al., 2008; Kang et al., 2016). Bilateral calvarial defects have also been created in a rat calvarium using subcritical-sized defects 5 mm in diameter. This side-by-side approach allows comparisons of control and treatments groups without variation caused by other factors (*e.g.*, activity levels). Accordingly, fewer animals are needed for the study design (Sawyer et al., 2009; Sohn et al., 2010; Zhang et al., 2014; Qi et al., 2016; Liu et al., 2019). However, there is potential for interactions between the two adjacent defects, which can affect study outcomes (Spicer et al., 2012).

Calvarial defects have also been used with rabbits. A key benefit is that multiple defects can be created in a single rabbit as they have a larger cranium than that of rats (Sohn et al., 2010; Pae et al., 2019). Though, the 8 mm diameter defect used with rats is too small for rabbits (Pae et al., 2019). A study of various-sized defects in rabbits indicated that a single CSD should be larger than 15 mm in diameter but two bilateral 11 mm diameter calvarial defects could be a suitable alternative (Sohn et al., 2010).

In addition to calvarial models, other sites including the tibia and femur have been used to track bone formation and regeneration within a CSD. Compared with calvarial models, tibial and femoral bone defect models are more suited when the bone scaffold will be used as a load-bearing bone graft. To date, tibial defects 1.2 cm (Bao et al., 2017), 1.5 cm (Wu et al., 2017), and 0.7 cm (Kim SE. et al., 2016) in length have been created in rabbits and rats. Femoral bone defects (diameter 5 mm, height 2.5 mm) have been applied with rabbits (Buyuksungur et al., 2017). Another alternative to calvarial models are ectopic models (*i.e.*, subcutaneous models) (Bao et al., 2017) where rats or mice are usually used. With subcutaneous models, scaffolds are implanted in the back of animal to observe bone scaffold degradation as well as vascularization prior tracking bone regeneration using bone defects (Salgado et al., 2004; Bao et al., 2017). To assess the bone regeneration capabilities of implanted bone scaffolds within CSDs, histological analyses using hematoxylin and eosin staining as well as Masson's trichrome staining have been commonly used (Chuenjitkuntaworn et al., 2010; Liu et al., 2019). In addition, computerized imaging analysis such as micro-computed tomography (micro-CT) is a useful method to obtain information about bone, density, and structure as well as new bone integration with the host bone (Salgado et al., 2004). **Table 4** summarizes several 3D bioprinted bone scaffolds that have been studied via *in-vitro*, *in-vivo,* or both to track bone regeneration as well as cell activities such as cell viability, proliferation, and differentiation.

Challenges and Recommendations for Future Research

Although bioprinting has received considerable attention as a promising technique to produce porous biomimetic scaffolds with controllable geometries, as this review indicated, challenges remain in fabricating scaffolds to repair CSDs. The most promising emerging techniques employ vertical or horizontal gradients of bioink along with gradient structures. These techniques are only beginning to be explored; however, they appear to be a promising strategy to develop constructs mimicking the design and composition of bone. Further, although many attempts have been performed to study the influence of structural features on mechanical and biological properties of bone scaffolds, this area has not gained much attention in bioprinted scaffolds, and it needs to be

TABLE 4 | Tracking bone regeneration using bioprinted scaffolds.

Bioink	Bioprinting technique	Cell	Growth factor	Study type	Summary of findings	Ref
Matrigel, alginate, gelatin microparticles	Microextrusion (pneumatic-based)	EPCs	VEGF	*In-vitro* and *in-vivo* (subcutaneous implantation in mice)	• Controlled release of VEGF via gelatin microparticles was found. • Thanks to prolonged release of VEGF, significant increase *in-vivo* vascularization observed	Poldervaart et al. (2014)
Collagen, nHAp	LAB	Mesenchymal stromal cells	---	*In-vitro* and *in-vivo* (bilateral calvarial bone defect in mice)	• Cell-laden collagen/nHAp bioprinted in disk geometry exhibited significant increase in bone regeneration *in-vivo* compared to collagen/nHAp without cells and cell-laden collagen/nHAp printed in ring geometry. • Both bioprinted geometries showed an increase in metabolic activity from day 1 to day 8 post-printing	Keriquel et al. (2017)
Composite hydrogel (gelatin+Fibrinogen+hyaluronic acid+glycerol)	Microextrusion (pneumatic-based)	hAFSCs	---	*In-vitro* and *in-vivo* (single calvarial bone defect in rats)	• New bone was formed within the bioprinted scaffold. Whereas, fibrotic tissue ingrowth and minimal bone formation were found in the blank defect and the defect treated with cell-free scaffold, respectively. • Vascularization within the new formed bone was found in the bioprinted scaffolds. However, poor vascularization was observed in blank defect and the defect implanted with cell-free scaffold. Blood vessels in cell-free scaffolds were restricted to periphery portion. • Cell viability after bioprinting was found to be around 91%. • Osteogenic differentiation of hAFSCs in bioprinted scaffolds was confirmed via calcium deposition	Kang et al. (2016)
Alginate+gelatin, collagen	Microextrusion (pneumatic-based)	DPSCs	VEGF, BMP-2	*In-vitro* and *in-vivo* (subcutaneous implantation in mice)	• After bioprinting, cell viability rates in collagen and alginate/gelatin hydrogels were found to be 92 and 99%, respectively. • Presence of BMP-2 and VEGF in cell-laden hydrogels were effective for both vasculogenic and osteogenic differentiation. • Cell-laden hydrogels with BMP-2 showed higher calcium mineralization, ALP, and Runx-2 compared to cell-laden hydrogels without BMP-2. • Spatial and temporal release of growth factors were achieved using cell-laden hydrogels. • Bone regeneration was faster in pre-vascularized structures (cell-laden hydrogels containing both BMP-2 and VEGF) than in non-vascularized structures (cell-laden hydrogel with no growth factor, cell-laden hydrogel with BMP-2 only)	Park et al. (2015)

(Continued on following page)

TABLE 4 | (*Continued*) Tracking bone regeneration using bioprinted scaffolds.

Bioink	Bioprinting technique	Cell	Growth factor	Study type	Summary of findings	Ref
Alginate	Microextrusion (pneumatic-based)	MG63	---	*In-vitro*	• Cell survival rate was found to be around 93%, after bioprinting process. • Homogenous cell distribution was observed in bioprinted scaffolds which resulted in higher osteogenic differentiation (ALP) and calcium mineralization relative to non-bioprinted scaffolds. • Higher cell proliferation was found in cell-laden scaffolds compared to non-bioprinted scaffolds	Kim et al. (2016b)
Alginate, Chitosan, Alginate+HAp, Chitosan+HAp	Microextrusion (pneumatic-based)	MC3T3-E1	---	*In-vitro*	• The positive effect of HAp on osteogenic activity of cells in hydrogels was confirmed with bone biomarkers including ALP, OCN, collagen type I, and Runx-2. • Three and 9 days after bioprinting, average cell viabilities were found to be around 89–93% and 90–95%, respectively	Demirtaş et al. (2017)
Alginate, gelatin	Microextrusion (pneumatic-based)	SaOS-2	---	*In-vitro*	• Overlaying cell-laden hydrogel with calcium salt of polyphosphate in parallel with adding osteogenic supplements to the culture medium led to a remarkable increase in cell proliferation and calcium mineralization.	Neufurth et al. (2014)
Alginate, gelatin	Microextrusion (pneumatic-based)	Human endothelial cells	BMP-2, VEGF	*In-vitro*	• A dual delivery of BMP-2 and VEGF was achieved with core/shell bioprinting. • One day after bioprinting, human endothelial cells showed a cell viability of 66.2% and it increased to 84.5% after 21 days of culture	Akkineni et al. (2016)
Alginate, gelatin, MSCs	Microextrusion (pneumatic-based) used for HUVEC-laden alginate/gelatin, a piezoelectric nozzle used for MSCs	HUVECs MSCs	---	*In-vitro*	• Evaluation of angiogenic properties exhibited the capability of alginate/gelatin hydrogel to help form and maintain vascular network over 7 days of culture. • Findings showed that HUVEC-laden hydrogel had a positive effect on osteogenesis of MSCs as proved by bone biomarkers. • Hydrogel had a positive effect on cell proliferation throughout the bioprinted scaffold	Chen et al. (2018)
Acrylated PEG, acrylated peptide	Inkjet (thermal-based)	hMSCs	---	*In-vitro*	• Cell viability of 87.9% post-printing was found. • PEG-peptide scaffolds stimulated and increased osteogenic activity and calcium mineralization of cells for long time period (21 days)	Gao et al. (2015)

investigated. Complex-shaped pores including hexagonal, which have shown good potential to satisfy requirements of native bone mechanically and biologically, should be specifically explored in cell-laden scaffolds. Another limitation pertains to the restricted usage of BGs in bioprinting of bone scaffolds compared to other bioceramics such as HAp or TCP. More research is then needed in this regard.

Fabricating scaffolds with dynamic functionality is another challenge which has not yet been achieved with current bioprinting techniques. Four-dimensional (4D) emerging technology has created new avenues of research using smart biomaterials. Using 4D printing, self-folding tubes have been made upon immersion in cell culture media with stimuli-responsive biomaterials (Kirillova et al., 2017). The key benefit of this technique is that dynamic bioprinted scaffolds made of stimuli-responsive biomaterials will be able to change their shapes over time under different intrinsic and/or external stimuli (Wan et al., 2020). In addition, bioprinted scaffolds made of stimuli-responsive biomaterials will be able to adopt to the vascularization, which is the main obstacle in BTE, and cell behavior specific to the micro-environment of the defect area (Wan et al., 2020). Importantly, this approach avoids the need to create vascular-like networks in scaffolds to help repair bone defects. However, when optimizing a bioink made of stimuli-responsive biomaterials, printability and cell viability should also be taken into consideration which may be another challenge.

With regards to *in-vivo* studies, conventional micro-CT has been the most widely used method to track bone regeneration although the synchrotron radiation micro-CT provides benefits including images with greater quality, resolution, contrast, shorter scan time as well as non-destructive 3D visualization (Cooper et al., 2011). Synchrotron radiation micro-CT has been illustrated promising to perform *in-vivo* imaging to track tissue regeneration once scaffolds are implanted in live animals over duration of study (Izadifar et al., 2016; Duan et al., 2021). This state-of-the-art approach is missing in most BTE studies although it can provide researchers with useful information in terms of scaffold degradation rate, the way implant is integrated with the host tissue, vascularization, and bone formation over time.

Taken together, classic bone tissue engineering approaches (scaffold-based) has been unable to fabricate a bone organ model for clinical application to date. Organoid, which is an emerging technology in tissue engineering, has been introduced as a promising field of study to fabricate functional organs including human bone (Burdis and Kelly, 2021). Organoids are defined as "*in-vitro* 3D cellular clusters derived exclusively from embryonic stem cells, induced pluripotent stem cells or primary tissue, capable of self-renewal and self-organization, and exhibiting similar organ functionality as the tissue of origin" (Fatehullah et al., 2016). According to Fatehullah et al. (2016), organoid may "rely on artificial ECM to facilitate their self-organization into structures that resemble native tissue architecture". Most recently, organoids for woven bone (Akiva et al., 2021) and trabecular bone (Yongkuk et al., 2021) have been successfully developed. In addition to organoids, biofabrication of cell aggregates/spheroids (cell-based tissue engineering) has emerged as a promising approach for vascularized bone regeneration (Heo et al., 2019).

With regard to clinical applications, bioceramics, most typically calcium phosphates and BGs, have been used in the form of granules or powder as a bone filler and injectable formulations as bone cement (Baino et al., 2015). In addition, HAp-coated metal joint prostheses and hemispherical ceramic (alumina) acetabular cups have been used for hip arthroplasty (Rajaratnam et al., 2008; Baino et al., 2015). Alumina and HAp are used in clinical applications as they do not generate an immune response (Baino et al., 2015). Straumann® BioCeramic™ and Bio-Oss® are examples of commercial bone mineral substitutes (Sabetrasekh et al., 2010). It is important to note that current commercial applications employ a limited number of biomaterials (*e.g.*, bioceramics and metal grafts). Bioprinted bone scaffolds containing both cell-laden hydrogel and supportive polymers are potential future commercial products for clinical application.

CONCLUSION/SUMMARY

Although bone has the capacity for self-healing, bone grafts and substitutes are needed to repair CSDs. Due to the limitations associated with conventional therapeutic methods, considerable attention is being paid to BTE to repair bone defects and improve functionality. Biomedical scaffolds provide a temporary template for mechanical support, cell attachment, and induction of bone formation *in-vivo*. In this regard, scaffold structure is of great importance as it affects cell activities, waste removal, the transport of nutrients and molecules to the inner parts of the scaffold, as well as the mechanical integrity of the scaffold.

3D printing techniques are gaining prominence for creating scaffolds due to their capacity to create highly porous structures with interconnected pores. In addition, bioprinting allows for the creation of biomimetic scaffolds using different types of biomaterials (*e.g.*, natural, synthetic), cells (*e.g.*, cell lines and stem cells), and growth factors (*e.g.*, osteogenic and angiogenic). To date, various studies have aimed to create a scaffold with mechanical and osteoconductive properties mimicking native bone. Consensus though is lacking regarding optimal structural features of bone scaffolds, fabrication method, material preparation technique, cell type, biological aids, and implantation site. Accordingly, more research is needed.

Also, an important goal in tissue engineering applications has been the delivery of biological aids such as growth factors to the defect site in a controlled manner without loss of bioactivity, which is crucial for generation of new blood vessels (*i.e.*, vascularization). Nanoparticulate-delivery systems and microparticles have demonstrated good potential to achieve this BTE objective.

Although hydrogels provide an appropriate matrix for cell encapsulation, their mechanical properties do not match those of native bone. Therefore, a CSD cannot be treated with scaffolds made of hydrogel alone and supportive resistance, mimicking the mechanical properties of trabecular and

cortical bone, is needed. Recently, state-of-the-art printing methods have emerged to fabricate biomedical scaffolds with specific designs, such as core/shell structures which enable the protection of cells and biomolecules while simultaneously providing a suitable platform for dual delivery or sequential delivery of growth factors into the surrounding environment. To fabricate bioprinted bone scaffolds, various including inkjet, LAB, and microextrusion have been used, with microextrusion being most used.

To track bone regeneration in bone scaffolds, *in-vitro* and *in-vivo* assessments have been done as preclinical evaluations. Despite many advances in this area, there are still challenges pertaining to these assessments. Specifically, *in-vitro* studies cannot completely mimic the *in-vivo* condition. *In-vivo* studies are also cost intensive, need strict ethical considerations, and the major limitation is bone variation between species.

No functional bone organ/construct has yet been fabricated using conventional tissue engineering and 3D printing approaches. Technologies including 4D printing, organoids, and cell aggregates/spheroids have emerged to pave this path, which are still in infant stages for treating large bone defects.

AUTHOR CONTRIBUTIONS

All authors conceptualized the manuscript. ZY wrote the original manuscript and designed illustrations in **Figures 1**, **2**, **4**, **5**. JJ, DC, and XC reviewed and edited the manuscript. All authors contributed to the article and approved the submitted version.

FUNDING

This research was funded by a Collaborative Innovation Grant from the Saskatchewan Health Research Foundation, Discovery Grants from the Natural Science and Engineering Research Council of Canada (JDJ: RGPIN-2015-06420; DML: RGPIN-2020-06043; XBC: RGPIN-2019-06396), and a Devolved Scholarship from the University of Saskatchewan.

ACKNOWLEDGMENTS

The authors would like to thank Jacqueline Dolovich for assisting in the manuscript edit.

REFERENCES

Aboudzadeh, N., Imani, M., Shokrgozar, M. A., Khavandi, A., Javadpour, J., Shafieyan, Y., et al. (2010). Fabrication and Characterization of poly(D,L-lactide-co-glycolide)/hydroxyapatite Nanocomposite Scaffolds for Bone Tissue Regeneration. *J. Biomed. Mater. Res.* 94A, 137–145. doi:10.1002/jbm.a.32673

Abubakar, A. A., Noordin, M. M., Azmi, T. I., Kaka, U., and Loqman, M. Y. (2016). The Use of Rats and Mice as Animal Models in *Ex Vivo* Bone Growth and Development Studies. *Bone Jt. Res.* 5, 610–618. doi:10.1302/2046-3758.512.bjr-2016-0102.r2

Ahmed, J. M., and Hamad, S. A. (2020). *In Vitro* and *In Vivo* Evaluation of Osteoconductive Properties of Novel GelMa/Eggshell-Derived Calcium Phosphate Composite Scaffold. *Eur. J. Mol. Clin. Med.* 7, 1–19.

Ahn, S., Lee, H., and Kim, G. (2013). Functional Cell-Laden Alginate Scaffolds Consisting of Core/shell Struts for Tissue Regeneration. *Carbohydr. Polym.* 98, 936–942. doi:10.1016/j.carbpol.2013.07.008

Akiva, A., Melke, J., Ansari, S., Liv, N., Meijden, R., Erp, M., et al. (2021). An Organoid for Woven Bone. *Adv. Funct. Mater.* 31, 2010524. doi:10.1002/adfm.202010524

Akkineni, A. R., Ahlfeld, T., Lode, A., and Gelinsky, M. (2016). A Versatile Method for Combining Different Biopolymers in a Core/shell Fashion by 3D Plotting to Achieve Mechanically Robust Constructs. *Biofabrication* 8, 045001. doi:10.1088/1758-5090/8/4/045001

Aldaadaa, A., Owji, N., and Knowles, J. (2018). Three-dimensional Printing in Maxillofacial Surgery: Hype versus Reality. *J. Tissue Eng.* 9, 2041731418770909. doi:10.1177/2041731418770909

Arumugasaamy, N., Baker, H. B., Kaplan, D. S., Kim, P. C. W., and Fisher, J. P. (2017, Fabrication and Printing of Multi-Material Hydrogels). "*Fabrication and Printing of Multi-Material Hydrogels BT - 3D Printing and Biofabrication*," in, eds. A. Ovsianikov, J. Yoo, and V. Mironov (Cham: Springer International Publishing), 1–34.doi:10.1007/978-3-319-40498-1_13-1

Ashammakhi, N., Hasan, A., Kaarela, O., Byambaa, B., Sheikhi, A., Gaharwar, A. K., et al. (2019). Advancing Frontiers in Bone Bioprinting. *Adv. Healthc. Mater.* 8, 1801048. doi:10.1002/adhm.201801048

Bae, M. S., Yang, D. H., Lee, J. B., Heo, D. N., Kwon, Y.-D., Youn, I. C., et al. (2011). Photo-cured Hyaluronic Acid-Based Hydrogels Containing Simvastatin as a Bone Tissue Regeneration Scaffold. *Biomaterials* 32, 8161–8171. doi:10.1016/j.biomaterials.2011.07.045

Bai, Y., Li, P., Yin, G., Huang, Z., Liao, X., Chen, X., et al. (2013). BMP-2, VEGF and bFGF Synergistically Promote the Osteogenic Differentiation of Rat Bone Marrow-Derived Mesenchymal Stem Cells. *Biotechnol. Lett.* 35, 301–308. doi:10.1007/s10529-012-1084-3

Baino, F., Novajra, G., and Vitale-Brovarone, C. (2015). Bioceramics and Scaffolds: A Winning Combination for Tissue Engineering. *Front. Bioeng. Biotechnol.* 3, 202. doi:10.3389/fbioe.2015.00202

Baino, F., and Fiume, E. (2020). 3D Printing of Hierarchical Scaffolds Based on Mesoporous Bioactive Glasses (MBGs)-Fundamentals and Applications. *Mater.* 13. doi:10.3390/ma13071688

Baino, F., and Vitale-Brovarone, C. (2014). Mechanical Properties and Reliability of Glass-Ceramic Foam Scaffolds for Bone Repair. *Mater. Lett.* 118, 27–30. doi:10.1016/j.matlet.2013.12.037

Bakhsheshi-Rad, H. R., Chen, X., Ismail, A. F., Aziz, M., Abdolahi, E., and Mahmoodiyan, F. (2019). Improved Antibacterial Properties of an Mg-Zn-Ca alloy Coated with Chitosan Nanofibers Incorporating Silver Sulfadiazine Multiwall Carbon Nanotubes for Bone Implants. *Polym. Adv. Technol.* 30, 1333–1339.

Bao, X., Zhu, L., Huang, X., Tang, D., He, D., Shi, J., et al. (2017). 3D Biomimetic Artificial Bone Scaffolds with Dual-Cytokines Spatiotemporal Delivery for Large Weight-Bearing Bone Defect Repair. *Sci. Rep.* 7, 7814. doi:10.1038/s41598-017-08412-0

Bassi, G., Panseri, S., Dozio, S. M., Sandri, M., Campodoni, E., Dapporto, M., et al. (2020). Scaffold-Based 3D Cellular Models Mimicking the Heterogeneity of Osteosarcoma Stem Cell Niche. *Sci. Rep.* 10, 22294.

Bendtsen, S. T., Quinnell, S. P., and Wei, M. (2017). Development of a Novel Alginate-polyvinyl Alcohol-hydroxyapatite Hydrogel for 3D Bioprinting Bone Tissue Engineered Scaffolds. *J. Biomed. Mater. Res.* 105, 1457–1468. doi:10.1002/jbm.a.36036

Bendtsen, S. T., and Wei, M. (2017). *In Vitro* evaluation of 3D Bioprinted Tri-polymer Network Scaffolds for Bone Tissue Regeneration. *J. Biomed. Mater. Res.* 105, 3262–3272. doi:10.1002/jbm.a.36184

Billiet, T., Gevaert, E., De Schryver, T., Cornelissen, M., and Dubruel, P. (2014). The 3D Printing of Gelatin Methacrylamide Cell-Laden Tissue-Engineered Constructs with High Cell Viability. *Biomaterials* 35, 49–62. doi:10.1016/j.biomaterials.2013.09.078

Bishop, E. S., Mostafa, S., Pakvasa, M., Luu, H. H., Lee, M. J., Wolf, J. M., et al. (2017). 3-D Bioprinting Technologies in Tissue Engineering and Regenerative Medicine: Current and Future Trends. *Genes Dis.* 4, 185–195. doi:10.1016/j.gendis.2017.10.002

Blum, J. S., Barry, M. A., Mikos, A. G., and Jansen, J. A. (2003). *In Vivo* Evaluation of Gene Therapy Vectors in Ex Vivo-Derived Marrow Stromal Cells for Bone Regeneration in a Rat Critical-Size Calvarial Defect Model. *Hum. Gene Ther.* 14, 1689–1701. doi:10.1089/104303403322611719

Boncler, M., Różalski, M., Krajewska, U., Podsędek, A., and Watala, C. (2014). Comparison of PrestoBlue and MTT Assays of Cellular Viability in the Assessment of Anti-proliferative Effects of Plant Extracts on Human Endothelial Cells. *J. Pharmacol. Toxicol. Methods* 69, 9–16. doi:10.1016/j.vascn.2013.09.003

Bose, S., Vahabzadeh, S., and Bandyopadhyay, A. (2013). Bone Tissue Engineering Using 3D Printing. *Mater. Today* 16, 496–504. doi:10.1016/j.mattod.2013.11.017

Burdis, R., and Kelly, D. J. (2021). Biofabrication and Bioprinting Using Cellular Aggregates, Microtissues and Organoids for the Engineering of Musculoskeletal Tissues. *Acta Biomater.* 126, 1–14. doi:10.1016/j.actbio.2021.03.016

Buyuksungur, S., Endogan Tanir, T., Buyuksungur, A., Bektas, E. I., Torun Kose, G., Yucel, D., et al. (2017). 3D Printed Poly(ε-Caprolactone) Scaffolds Modified with Hydroxyapatite and Poly(propylene Fumarate) and Their Effects on the Healing of Rabbit Femur Defects. *Biomater. Sci.* 5, 2144–2158. doi:10.1039/c7bm00514h

Caddeo, S., Boffito, M., and Sartori, S. (2017). Tissue Engineering Approaches in the Design of Healthy and Pathological *In Vitro* Tissue Models. *Front. Bioeng. Biotechnol.* 5, 40. doi:10.3389/fbioe.2017.00040

Calori, G. M., Mazza, E., Colombo, M., and Ripamonti, C. (2011). The Use of Bone-Graft Substitutes in Large Bone Defects: Any Specific Needs? *Injury* 42, S56–S63. doi:10.1016/j.injury.2011.06.011

Catros, S., Fricain, J. C., Guillotin, B., Pippenger, B., Bareille, R., Remy, M., et al. (2011). Laser-assisted Bioprinting for Creating On-Demand Patterns of Human Osteoprogenitor Cells and Nano-Hydroxyapatite. *Biofabrication* 3, 025001. doi:10.1088/1758-5082/3/2/025001

Chang, C. C., Boland, E. D., Williams, S. K., and Hoying, J. B. (2011). Direct-write Bioprinting Three-Dimensional Biohybrid Systems for Future Regenerative Therapies. *J. Biomed. Mater. Res.* 98B, 160–170. doi:10.1002/jbm.b.31831

Chatzistavrou, X., Newby, P., and Boccaccini, A. R. (2011). "Bioactive Glass and Glass-Ceramic Scaffolds for Bone Tissue Engineering," in *Woodhead Publishing Series in Biomaterials*. Editor H. O. B. T.-B. G. Ylänen (Cambridge: Woodhead Publishing), 107–128. doi:10.1533/9780857093318.2.107

Chen, D. X. B. (2018). *Extrusion Bioprinting of Scaffolds for Tissue Engineering Applications*. Springer.

Chen, Y.-W., Shen, Y.-F., Ho, C.-C., Yu, J., Wu, Y.-H. A., Wang, K., et al. (2018). Osteogenic and Angiogenic Potentials of the Cell-Laden Hydrogel/mussel-Inspired Calcium Silicate Complex Hierarchical Porous Scaffold Fabricated by 3D Bioprinting. *Mater. Sci. Eng. C* 91, 679–687. doi:10.1016/j.msec.2018.06.005

Chimene, D., Lennox, K. K., Kaunas, R. R., and Gaharwar, A. K. (2016). Advanced Bioinks for 3D Printing: a Materials Science Perspective. *Ann. Biomed. Eng.* 44, 2090–2102. doi:10.1007/s10439-016-1638-y

Cholas, R., Kunjalukkal Padmanabhan, S., Gervaso, F., Udayan, G., Monaco, G., Sannino, A., et al. (2016). Scaffolds for Bone Regeneration Made of Hydroxyapatite Microspheres in a Collagen Matrix. *Mater. Sci. Eng. C* 63, 499–505. doi:10.1016/j.msec.2016.03.022

Chuenjitkuntaworn, B., Inrung, W., Damrongsri, D., Mekaapiruk, K., Supaphol, P., and Pavasant, P. (2010). Polycaprolactone/hydroxyapatite Composite Scaffolds: Preparation, Characterization, and *In Vitro* and *In Vivo* Biological Responses of Human Primary Bone Cells. *J. Biomed. Mater. Res.* 94A, 241–251. doi:10.1002/jbm.a.32657

Clarke, B. (2008). Normal Bone Anatomy and Physiology. *Cjasn* 3, S131–S139. doi:10.2215/cjn.04151206

Cooper, D. M. L., Erickson, B., Peele, A. G., Hannah, K., Thomas, C. D. L., and Clement, J. G. (2011). Visualization of 3D Osteon Morphology by Synchrotron Radiation Micro-CT. *J. Anat.* 219, 481–489. doi:10.1111/j.1469-7580.2011.01398.x

Dahl, A. C. E., and Thompson, M. S. (2011, Mechanobiology of Bone). "*5.18 - Mechanobiology of Bone*," in, ed. T.-C. B. M.B (*Second E. Moo-Young* (Burlington: Academic Press), 217–236.doi:10.1016/b978-0-08-088504-9.00419-0

Danhier, F., Ansorena, E., Silva, J. M., Coco, R., Le Breton, A., and Préat, V. (2012). PLGA-based Nanoparticles: an Overview of Biomedical Applications. *J. Controlled Release* 161, 505–522. doi:10.1016/j.jconrel.2012.01.043

Das, S., Pati, F., Choi, Y.-J., Rijal, G., Shim, J.-H., Kim, S. W., et al. (2015). Bioprintable, Cell-Laden Silk Fibroin-Gelatin Hydrogel Supporting Multilineage Differentiation of Stem Cells for Fabrication of Three-Dimensional Tissue Constructs. *Acta Biomater.* 11, 233–246. doi:10.1016/j.actbio.2014.09.023

Demirtaş, T. T., Irmak, G., and Gümüşderelioğlu, M. (2017). A Bioprintable Form of Chitosan Hydrogel for Bone Tissue Engineering. *Biofabrication* 9, 35003.

Domingos, M., Intranuovo, F., Russo, T., De Santis, R., Gloria, A., Ambrosio, L., et al. (2013). The First Systematic Analysis of 3D Rapid Prototyped Poly(ε-Caprolactone) Scaffolds Manufactured through BioCell Printing: the Effect of Pore Size and Geometry on Compressive Mechanical Behaviour and In vitro hMSC Viability. *Biofabrication* 5, 045004. doi:10.1088/1758-5082/5/4/045004

Dong, L., Wang, S.-J., Zhao, X.-R., Zhu, Y.-F., and Yu, J.-K. (2017). 3D- Printed Poly(ε-Caprolactone) Scaffold Integrated with Cell-Laden Chitosan Hydrogels for Bone Tissue Engineering. *Sci. Rep.* 7, 13412. doi:10.1038/s41598-017-13838-7

Downey, P. A., and Siegel, M. I. (2006). Bone Biology and the Clinical Implications for Osteoporosis. *Phys. Ther.* 86, 77–91. doi:10.1093/ptj/86.1.77

Dreyer, C. H., Kjaergaard, K., Ding, M., and Qin, L. (2020). Vascular Endothelial Growth Factor for *In Vivo* Bone Formation: A Systematic Review. *J. Orthopaedic Translation* 24, 46–57. doi:10.1016/j.jot.2020.05.005

Du, M., Chen, B., Meng, Q., Liu, S., Zheng, X., Zhang, C., et al. (2015). 3D Bioprinting of BMSC-Laden Methacrylamide Gelatin Scaffolds with CBD-BMP2-Collagen Microfibers. *Biofabrication* 7, 044104. doi:10.1088/1758-5090/7/4/044104

Duan, X., Li, N., Chen, X., and Zhu, N. (2021). Characterization of Tissue Scaffolds Using Synchrotron Radiation Microcomputed Tomography Imaging. *Tissue Eng. C: Methods* 27, 573–588. doi:10.1089/ten.tec.2021.0155

Duarte Campos, D. F., Blaeser, A., Buellesbach, K., Sen, K. S., Xun, W., Tillmann, W., et al. (2016). Bioprinting Organotypic Hydrogels with Improved Mesenchymal Stem Cell Remodeling and Mineralization Properties for Bone Tissue Engineering. *Adv. Healthc. Mater.* 5, 1336–1345. doi:10.1002/adhm.201501033

Fahimipour, F., Rasoulianboroujeni, M., Dashtimoghadam, E., Khoshroo, K., Tahriri, M., Bastami, F., et al. (2017). 3D Printed TCP-Based Scaffold Incorporating VEGF-Loaded PLGA Microspheres for Craniofacial Tissue Engineering. *Dental Mater.* 33, 1205–1216. doi:10.1016/j.dental.2017.06.016

Fatehullah, A., Tan, S. H., and Barker, N. (2016). Organoids as an *In Vitro* Model of Human Development and Disease. *Nat. Cel Biol.* 18, 246–254. doi:10.1038/ncb3312

Florencio-Silva, R., Sasso, G. R. da. S., Sasso-Cerri, E., Simões, M. J., and Cerri, P. S. (2015). Biology of Bone Tissue: Structure, Function, and Factors that Influence Bone Cells. *Biomed. Res. Int.* 2015. doi:10.1155/2015/421746

Francis Suh, J.-K., and Matthew, H. W. T. (2000). Application of Chitosan-Based Polysaccharide Biomaterials in Cartilage Tissue Engineering: a Review. *Biomaterials* 21, 2589–2598. doi:10.1016/s0142-9612(00)00126-5

Fu, Q., Saiz, E., and Tomsia, A. P. (2011). Direct Ink Writing of Highly Porous and strong Glass Scaffolds for Load-Bearing Bone Defects Repair and Regeneration. *Acta Biomater.* 7, 3547–3554. doi:10.1016/j.actbio.2011.06.030

Fu, Z., Naghieh, S., Xu, C., Wang, C., Sun, W., and Chen, X. (2021). Printability in Extrusion Bioprinting. *Biofabrication* 13, 33001. doi:10.1088/1758-5090/abe7ab

Gao, G., Schilling, A. F., Yonezawa, T., Wang, J., Dai, G., and Cui, X. (2014). Bioactive Nanoparticles Stimulate Bone Tissue Formation in Bioprinted Three-Dimensional Scaffold and Human Mesenchymal Stem Cells. *Biotechnol. J.* 9, 1304–1311. doi:10.1002/biot.201400305

Gao, G., Yonezawa, T., Hubbell, K., Dai, G., and Cui, X. (2015). Inkjet-bioprinted Acrylated Peptides and PEG Hydrogel with Human Mesenchymal Stem Cells Promote Robust Bone and Cartilage Formation with Minimal Printhead Clogging. *Biotechnol. J.* 10, 1568–1577. doi:10.1002/biot.201400635

Gautam, S., Chou, C.-F., Dinda, A. K., Potdar, P. D., and Mishra, N. C. (2014). Fabrication and Characterization of PCL/gelatin/chitosan Ternary Nanofibrous Composite Scaffold for Tissue Engineering Applications. *J. Mater. Sci.* 49, 1076–1089. doi:10.1007/s10853-013-7785-8

Genes, N. G., Rowley, J. A., Mooney, D. J., and Bonassar, L. J. (2004). Effect of Substrate Mechanics on Chondrocyte Adhesion to Modified Alginate Surfaces. *Arch. Biochem. Biophys.* 422, 161–167. doi:10.1016/j.abb.2003.11.023

Gerdes, S., Mostafavi, A., Ramesh, S., Memic, A., Rivero, I. V., Rao, P., et al. (2020). Process-Structure-Quality Relationships of Three-Dimensional Printed Poly(Caprolactone)-Hydroxyapatite Scaffolds. *Tissue Eng. A* 26, 279–291. doi:10.1089/ten.tea.2019.0237

Giuseppe, M. D., Law, N., Webb, B., A. Macrae, R., Liew, L. J., Sercombe, T. B., et al. (2018). Mechanical Behaviour of Alginate-Gelatin Hydrogels for 3D Bioprinting. *J. Mech. Behav. Biomed. Mater.* 79, 150–157. doi:10.1016/j.jmbbm.2017.12.018

Groll, J., Burdick, J. A., Cho, D. W., Derby, B., Gelinsky, M., Heilshorn, S. C., et al. (2018). A Definition of Bioinks and Their Distinction from Biomaterial Inks. *Biofabrication* 11, 013001. doi:10.1088/1758-5090/aaec52

Gu, B. K., Choi, D. J., Park, S. J., Kim, M. S., Kang, C. M., and Kim, C.-H. (2016). 3-dimensional Bioprinting for Tissue Engineering Applications. *Biomater. Res.* 20, 12. doi:10.1186/s40824-016-0058-2

Guarino, V., Causa, F., and Ambrosio, L. (2007). Bioactive Scaffolds for Bone and Ligament Tissue. *Expert Rev. Med. Devices* 4, 405–418. doi:10.1586/17434440.4.3.405

Guarino, V., Causa, F., Netti, P. A., Ciapetti, G., Pagani, S., Martini, D., et al. (2008). The Role of Hydroxyapatite as Solid Signal on Performance of PCL Porous Scaffolds for Bone Tissue Regeneration. *J. Biomed. Mater. Res.* 86B, 548–557. doi:10.1002/jbm.b.31055

Hadjidakis, D. J., and Androulakis, I. I. (2006). Bone Remodeling. *Ann. New York Acad. Sci.* 1092, 385–396. doi:10.1196/annals.1365.035

Harada, N., Watanabe, Y., Sato, K., Abe, S., Yamanaka, K., Sakai, Y., et al. (2014). Bone Regeneration in a Massive Rat Femur Defect through Endochondral Ossification Achieved with Chondrogenically Differentiated MSCs in a Degradable Scaffold. *Biomaterials* 35, 7800–7810. doi:10.1016/j.biomaterials.2014.05.052

Härle, F., and Boudrieau, R. J. (2012). "Chapter 2 - Maxillofacial Bone Healing," in *Oral and Maxillofacial Surgery in Dogs and Cats*. Editors F. J. M. Verstraete and M. J. Lommer (Oxford: W.B. Saunders), 7–13.

He, Y., Yang, F., Zhao, H., Gao, Q., Xia, B., and Fu, J. (2016). Research on the Printability of Hydrogels in 3D Bioprinting. *Sci. Rep.* 6, 29977. doi:10.1038/srep29977

Heo, D. N., Hospodiuk, M., and Ozbolat, I. T. (2019). Synergistic Interplay between Human MSCs and HUVECs in 3D Spheroids Laden in Collagen/fibrin Hydrogels for Bone Tissue Engineering. *Acta Biomater.* 95, 348–356. doi:10.1016/j.actbio.2019.02.046

Huang, B., Caetano, G., Vyas, C., Blaker, J. J., Diver, C., and Bártolo, P. (2018). Polymer-Ceramic Composite Scaffolds: The Effect of Hydroxyapatite and β-tri-Calcium Phosphate. *Mater.* 11, 129. doi:10.3390/ma11010129

Huang, J., Fu, H., Wang, Z., Meng, Q., Liu, S., Wang, H., et al. (2016). BMSCs-laden Gelatin/sodium Alginate/carboxymethyl Chitosan Hydrogel for 3D Bioprinting. *RSC Adv.* 6, 108423–108430. doi:10.1039/c6ra24231f

Huh, J., Lee, J., Kim, W., Yeo, M., and Kim, G. (2018). Preparation and Characterization of Gelatin/α-TCP/SF Biocomposite Scaffold for Bone Tissue Regeneration. *Int. J. Biol. Macromolecules* 110, 488–496. doi:10.1016/j.ijbiomac.2017.09.030

Hutmacher, D. W., Schantz, J. T., Lam, C. X. F., Tan, K. C., and Lim, T. C. (2007). State of the Art and Future Directions of Scaffold-Based Bone Engineering from a Biomaterials Perspective. *J. Tissue Eng. Regen. Med.* 1, 245–260. doi:10.1002/term.24

Hwang, P. W., and Horton, J. A. (2019). Variable Osteogenic Performance of MC3T3-E1 Subclones Impacts Their Utility as Models of Osteoblast Biology. *Sci. Rep.* 9, 8299. doi:10.1038/s41598-019-44575-8

Izadifar, M., Haddadi, A., Chen, X., and Kelly, M. E. (2014). Rate-programming of Nano-Particulate Delivery Systems for Smart Bioactive Scaffolds in Tissue Engineering. *Nanotechnology* 26, 012001. doi:10.1088/0957-4484/26/1/012001

Izadifar, M., Kelly, M. E., Haddadi, A., and Chen, X. (2015a). Optimization of Nanoparticles for Cardiovascular Tissue Engineering. *Nanotechnology* 26, 235301. doi:10.1088/0957-4484/26/23/235301

Izadifar, Z., Chang, T., Kulyk, W., Chen, X., and Eames, B. F. (2015b). Analyzing Biological Performance of 3D-Printed, Cell-Impregnated Hybrid Constructs for Cartilage Tissue Engineering. *Tissue Eng. Part. C Methods* 22, 173–188. doi:10.1089/ten.TEC.2015.0307

Izadifar, Z., Honaramooz, A., Wiebe, S., Belev, G., Chen, X., and Chapman, D. (2016). Low-dose Phase-Based X-ray Imaging Techniques for *In Situ* Soft Tissue Engineering Assessments. *Biomaterials* 82, 151–167. doi:10.1016/j.biomaterials.2015.11.044

Jun, S.-H., Lee, E.-J., Jang, T.-S., Kim, H.-E., Jang, J.-H., and Koh, Y.-H. (2013). Bone Morphogenic Protein-2 (BMP-2) Loaded Hybrid Coating on Porous Hydroxyapatite Scaffolds for Bone Tissue Engineering. *J. Mater. Sci. Mater. Med.* 24, 773–782. doi:10.1007/s10856-012-4822-0

Kang, H. W., Lee, S. J., Ko, I. K., Kengla, C., Yoo, J. J., and Atala, A. (2016). A 3D Bioprinting System to Produce Human-Scale Tissue Constructs with Structural Integrity. *Nat. Biotechnol.* 34, 312–319. doi:10.1038/nbt.3413

Kargozar, S., Mozafari, M., Hamzehlou, S., Brouki Milan, P., Kim, H.-W., and Baino, F. (2019). Bone Tissue Engineering Using Human Cells: a Comprehensive Review on Recent Trends, Current Prospects, and Recommendations. *Appl. Sci.* 9, 174. doi:10.3390/app9010174

Kempen, D. H. R., Lu, L., Heijink, A., Hefferan, T. E., Creemers, L. B., Maran, A., et al. (2009). Effect of Local Sequential VEGF and BMP-2 Delivery on Ectopic and Orthotopic Bone Regeneration. *Biomaterials* 30, 2816–2825. doi:10.1016/j.biomaterials.2009.01.031

Kenkre, J., and Bassett, J. (2018). The Bone Remodelling Cycle. *Ann. Clin. Biochem.* 55, 308–327. doi:10.1177/0004563218759371

Keriquel, V., Oliveira, H., Rémy, M., Ziane, S., Delmond, S., Rousseau, B., et al. (2017). *In Situ* printing of Mesenchymal Stromal Cells, by Laser-Assisted Bioprinting, for *In Vivo* Bone Regeneration Applications. *Sci. Rep.* 7, 1778. doi:10.1038/s41598-017-01914-x

Kim, B.-S., Yang, S.-S., and Lee, J. (2014). A Polycaprolactone/cuttlefish Bone-Derived Hydroxyapatite Composite Porous Scaffold for Bone Tissue Engineering. *J. Biomed. Mater. Res.* 102, 943–951. doi:10.1002/jbm.b.33075

Kim, H., Hwangbo, H., Koo, Y., and Kim, G. (2020). Fabrication of Mechanically Reinforced Gelatin/Hydroxyapatite Bio-Composite Scaffolds by Core/Shell Nozzle Printing for Bone Tissue Engineering. *Int. J. Mol. Sci.* 21. doi:10.3390/ijms21093401

Kim, J., McBride, S., Tellis, B., Alvarez-Urena, P., Song, Y. H., Dean, D. D., et al. (2012). Rapid-prototyped PLGA/β-TCP/hydroxyapatite Nanocomposite Scaffolds in a Rabbit Femoral Defect Model. *Biofabrication* 4, 025003. doi:10.1088/1758-5082/4/2/025003

Kim, J., Kim, I. S., Cho, T. H., Lee, K. B., Hwang, S. J., Tae, G., et al. (2007). Bone Regeneration Using Hyaluronic Acid-Based Hydrogel with Bone Morphogenic Protein-2 and Human Mesenchymal Stem Cells. *Biomaterials* 28, 1830–1837. doi:10.1016/j.biomaterials.2006.11.050

Kim, M., and Kim, G. H. (2015a). Electrohydrodynamic Direct Printing of PCL/collagen Fibrous Scaffolds with a Core/shell Structure for Tissue Engineering Applications. *Chem. Eng. J.* 279, 317–326. doi:10.1016/j.cej.2015.05.047

Kim, S.-H., Lim, B.-K., Sun, F., Koh, K., Ryu, S.-C., Kim, H.-S., et al. (2008). Preparation of High Flexible Composite Film of Hydroxyapatite and Chitosan. *Polym. Bull.* 62, 111–118. doi:10.1007/s00289-008-1008-5

Kim, S. E., Yun, Y. P., Shim, K. S., Kim, H. J., Park, K., and Song, H. R. (2016a). 3D Printed Alendronate-Releasing Poly(caprolactone) Porous Scaffolds Enhance Osteogenic Differentiation and Bone Formation in Rat Tibial Defects. *Biomed. Mater.* 11, 055005. doi:10.1088/1748-6041/11/5/055005

Kim, W. J., Yun, H.-S., and Kim, G. H. (2017). An Innovative Cell-Laden α-TCP/collagen Scaffold Fabricated Using a Two-step Printing Process for Potential Application in Regenerating Hard Tissues. *Sci. Rep.* 7, 3181. doi:10.1038/s41598-017-03455-9

Kim, Y. B., and Kim, G. H. (2015b). PCL/Alginate Composite Scaffolds for Hard Tissue Engineering: Fabrication, Characterization, and Cellular Activities. *ACS Comb. Sci.* 17, 87–99. doi:10.1021/co500033h

Kim, Y. B., Lee, H., Yang, G.-H., Choi, C. H., Lee, D., Hwang, H., et al. (2016b). Mechanically Reinforced Cell-Laden Scaffolds Formed Using Alginate-Based Bioink Printed onto the Surface of a PCL/alginate Mesh Structure for Regeneration of Hard Tissue. *J. Colloid Interf. Sci.* 461, 359–368. doi:10.1016/j.jcis.2015.09.044

Kirillova, A., Maxson, R., Stoychev, G., Gomillion, C. T., and Ionov, L. (2017). 4D Biofabrication Using Shape-Morphing Hydrogels. *Adv. Mater.* 29, 1703443. doi:10.1002/adma.201703443

Klüter, T., Hassan, R., Rasch, A., Naujokat, H., Wang, F., Behrendt, P., et al. (2019). An *Ex Vivo* Bone Defect Model to Evaluate Bone Substitutes and Associated Bone Regeneration Processes. *Tissue Eng. Part. C Methods* 26, 56–65. doi:10.1089/ten.TEC.2019.0274

Kumar, A., Kargozar, S., Baino, F., and Han, S. S. (2019). Additive Manufacturing Methods for Producing Hydroxyapatite and Hydroxyapatite-Based Composite Scaffolds: A Review. *Front. Mater.* 6, 313. doi:10.3389/fmats.2019.00313

Kuo, T.-R., and Chen, C.-H. (2017). Bone Biomarker for the Clinical Assessment of Osteoporosis: Recent Developments and Future Perspectives. *Biomark. Res.* 5, 18. doi:10.1186/s40364-017-0097-4

Kyle, S., Jessop, Z. M., Al-Sabah, A., and Whitaker, I. S. (2017). 'Printability' of Candidate Biomaterials for Extrusion Based 3D Printing: State-Of-The-Art. *Adv. Healthc. Mater.* 6, 1700264. doi:10.1002/adhm.201700264

Law, N., Doney, B., Glover, H., Qin, Y., Aman, Z. M., Sercombe, T. B., et al. (2018). Characterisation of Hyaluronic Acid Methylcellulose Hydrogels for 3D Bioprinting. *J. Mech. Behav. Biomed. Mater.* 77, 389–399. doi:10.1016/j.jmbbm.2017.09.031

Lee, D. J., Kwon, J., Kim, Y. I., Wang, X., Wu, T. J., Lee, Y. T., et al. (2019). Effect of Pore Size in Bone Regeneration Using Polydopamine-Laced Hydroxyapatite Collagen Calcium Silicate Scaffolds Fabricated by 3D Mould Printing Technology. *Orthod. Craniofac. Res.* 22 (Suppl. 1), 127–133. doi:10.1111/ocr.12261

Lee, J.-S., Cha, H., Jung, J. W., Kim, J. Y., and Cho, D.-W. (2012). Effect of Pore Architecture and Stacking Direction on Mechanical Properties of Solid Freeform Fabrication-Based Scaffold for Bone Tissue Engineering. *J. Biomed. Mater. Res. Part. A.* 100, 1846–1853. doi:10.1002/jbm.a.34149

Lee, J.-W., Yun, H.-S., and Nakano, T. (2016). Induction of Biological Apatite Orientation as a Bone Quality Parameter in Bone Regeneration Using Hydroxyapatite/Poly ε-Caprolactone Composite Scaffolds. *Tissue Eng. Part C: Methods* 22, 856–863. doi:10.1089/ten.tec.2016.0133

Lee, J. W., Ahn, G., Kim, J. Y., and Cho, D.-W. (2010). Evaluating Cell Proliferation Based on Internal Pore Size and 3D Scaffold Architecture Fabricated Using Solid Freeform Fabrication Technology. *J. Mater. Sci. Mater. Med.* 21, 3195–3205. doi:10.1007/s10856-010-4173-7

Lee, J. W., Kang, K. S., Lee, S. H., Kim, J.-Y., Lee, B.-K., and Cho, D.-W. (2011). Bone Regeneration Using a Microstereolithography-Produced Customized Poly(propylene Fumarate)/diethyl Fumarate Photopolymer 3D Scaffold Incorporating BMP-2 Loaded PLGA Microspheres. *Biomaterials* 32, 744–752. doi:10.1016/j.biomaterials.2010.09.035

Li, L.-J., Kim, S.-N., and Cho, S.-A. (2016). Comparison of Alkaline Phosphatase Activity of MC3T3-E1 Cells Cultured on Different Ti Surfaces: Modified Sandblasted with Large Grit and Acid-Etched (MSLA), Laser-Treated, and Laser and Acid-Treated Ti Surfaces. *J. Adv. Prosthodont.* 8, 235–240. doi:10.4047/jap.2016.8.3.235

Li, N., Guo, R., and Zhang, Z. J. (2021). Bioink Formulations for Bone Tissue Regeneration. *Front. Bioeng. Biotechnol.* 9, 44. doi:10.3389/fbioe.2021.630488

Linh, N. T. B., Abueva, C. D. G., Jang, D. W., and Lee, B. T. (2020). Collagen and Bone Morphogenetic Protein-2 Functionalized Hydroxyapatite Scaffolds Induce Osteogenic Differentiation in Human Adipose-derived Stem Cells. *J. Biomed. Mater. Res.* 108, 1363–1371. doi:10.1002/jbm.b.34485

Liu, D., Nie, W., Li, D., Wang, W., Zheng, L., Zhang, J., et al. (2019). 3D Printed PCL/SrHA Scaffold for Enhanced Bone Regeneration. *Chem. Eng. J.* 362, 269–279. doi:10.1016/j.cej.2019.01.015

Loh, Q. L., and Choong, C. (2013). Three-dimensional Scaffolds for Tissue Engineering Applications: Role of Porosity and Pore Size. *Tissue Eng. B: Rev.* 19, 485–502. doi:10.1089/ten.teb.2012.0437

Loi, F., Córdova, L. A., Pajarinen, J., Lin, T.-h., Yao, Z., and Goodman, S. B. (2016). Inflammation, Fracture and Bone Repair. *Bone* 86, 119–130. doi:10.1016/j.bone.2016.02.020

Loozen, L. D., Wegman, F., Öner, F. C., Dhert, W. J. A., and Alblas, J. (2013). Porous Bioprinted Constructs in BMP-2 Non-viral Gene Therapy for Bone Tissue Engineering. *J. Mater. Chem. B* 1, 6619–6626. doi:10.1039/c3tb21093f

Luo, Y., Li, Y., Qin, X., and Wa, Q. (2018). 3D Printing of Concentrated Alginate/gelatin Scaffolds with Homogeneous Nano Apatite Coating for Bone Tissue Engineering. *Mater. Des.* 146, 12–19. doi:10.1016/j.matdes.2018.03.002

Luo, Y., Lode, A., Akkineni, A. R., and Gelinsky, M. (2015). Concentrated Gelatin/alginate Composites for Fabrication of Predesigned Scaffolds with a Favorable Cell Response by 3D Plotting. *RSC Adv.* 5, 43480–43488. doi:10.1039/c5ra04308e

Luo, Y., Luo, G., Gelinsky, M., Huang, P., and Ruan, C. (2017). 3D Bioprinting Scaffold Using Alginate/polyvinyl Alcohol Bioinks. *Mater. Lett.* 189, 295–298. doi:10.1016/j.matlet.2016.12.009

Ma, H., Feng, C., Chang, J., and Wu, C. (2018). 3D-printed Bioceramic Scaffolds: From Bone Tissue Engineering to Tumor Therapy. *Acta Biomater.* 79, 37–59. doi:10.1016/j.actbio.2018.08.026

Mandrycky, C., Wang, Z., Kim, K., and Kim, D.-H. (2016). 3D Bioprinting for Engineering Complex Tissues. *Biotechnol. Adv.* 34, 422–434. doi:10.1016/j.biotechadv.2015.12.011

Martin, T. J., and Rodan, G. A. (2008). "Intercellular Communication during Bone Remodeling," in *CHAPTER 20 - Intercellular Communication during Bone RemodelingOsteoporosis*. Editors R. Marcus, D. Feldman, D. A. Nelson, and C. J. Rosen. Third Edition (San Diego: Academic Press), 547–560. doi:10.1016/b978-012370544-0.50022-7

Martínez-Vázquez, F. J., Cabañas, M. V., Paris, J. L., Lozano, D., and Vallet-Regí, M. (2015). Fabrication of Novel Si-Doped Hydroxyapatite/gelatine Scaffolds by Rapid Prototyping for Drug Delivery and Bone Regeneration. *Acta Biomater.* 15, 200–209.

McBeth, C., Lauer, J., Ottersbach, M., Campbell, J., Sharon, A., and Sauer-Budge, A. F. (2017). 3D Bioprinting of GelMA Scaffolds Triggers mineral Deposition by Primary Human Osteoblasts. *Biofabrication* 9, 015009. doi:10.1088/1758-5090/aa53bd

Milazzo, M., Contessi Negrini, N., Scialla, S., Marelli, B., Farè, S., Danti, S., et al. (2019). Additive Manufacturing Approaches for Hydroxyapatite-Reinforced Composites. *Adv. Funct. Mater.* 29, 1903055. doi:10.1002/adfm.201903055

Mohseni, M., Jahandideh, A., Abedi, G., Akbarzadeh, A., and Hesaraki, S. (2018). Assessment of Tricalcium Phosphate/collagen (TCP/collagene)nanocomposite Scaffold Compared with Hydroxyapatite (HA) on Healing of Segmental Femur Bone Defect in Rabbits. *Artif. Cell Nanomedicine, Biotechnol.* 46, 242–249. doi:10.1080/21691401.2017.1324463

Monfoulet, L., Rabier, B., Chassande, O., and Fricain, J.-C. (2010). Drilled Hole Defects in Mouse Femur as Models of Intramembranous Cortical and Cancellous Bone Regeneration. *Calcif. Tissue Int.* 86, 72–81. doi:10.1007/s00223-009-9314-y

Mouriño, V., and Boccaccini, A. R. (2009). Bone Tissue Engineering Therapeutics: Controlled Drug Delivery in Three-Dimensional Scaffolds. *J. R. Soc. Interf.* 7, 209–227.

Munaz, A., Vadivelu, R. K., St. John, J., Barton, M., Kamble, H., and Nguyen, N.-T. (2016). Three-dimensional Printing of Biological Matters. *J. Sci. Adv. Mater. Devices* 1, 1–17. doi:10.1016/j.jsamd.2016.04.001

Murphy, C., Kolan, K., Li, W., Semon, J., Day, D., and Leu, M. (2017). 3D Bioprinting of Stem Cells and Polymer/bioactive Glass Composite Scaffolds for Bone Tissue Engineering. *Int. J. Bioprint* 3, 005–064. doi:10.18063/IJB.2017.01.005

Murphy, S. V., and Atala, A. (2014). 3D Bioprinting of Tissues and Organs. *Nat. Biotechnol.* 32, 773–785. doi:10.1038/nbt.2958

Muzzarelli, R. A. A., Greco, F., Busilacchi, A., Sollazzo, V., and Gigante, A. (2012). Chitosan, Hyaluronan and Chondroitin Sulfate in Tissue Engineering for Cartilage Regeneration: a Review. *Carbohydr. Polym.* 89, 723–739. doi:10.1016/j.carbpol.2012.04.057

Naghieh, S., and Chen, D. (2021). Printability – a Key Issue in Extrusion-Based Bioprinting. *J. Pharm. Anal.* 11, 564–579. doi:10.1016/j.jpha.2021.02.001

Naghieh, S., Karamooz-Ravari, M. R., Sarker, M., Karki, E., and Chen, X. (2018a). Influence of Crosslinking on the Mechanical Behavior of 3D Printed Alginate Scaffolds: Experimental and Numerical Approaches. *J. Mech. Behav. Biomed. Mater.* 80, 111–118. doi:10.1016/j.jmbbm.2018.01.034

Naghieh, S., Sarker, M. D., Karamooz-Ravari, M. R., McInnes, A. D., and Chen, X. (2018b). Modeling of the Mechanical Behavior of 3D Bioplotted Scaffolds Considering the Penetration in Interlocked Strands. *Appl. Sci.* 8. doi:10.3390/app8091422

Naghieh, S., Sarker, M. D., Sharma, N. K., Barhoumi, Z., and Chen, X. (2020). Printability of 3D Printed Hydrogel Scaffolds: Influence of Hydrogel Composition and Printing Parameters. *Appl. Sci.* 10.

Narayanan, L. K., Huebner, P., Fisher, M. B., Spang, J. T., Starly, B., and Shirwaiker, R. A. (2016). 3D-Bioprinting of Polylactic Acid (PLA) Nanofiber-Alginate Hydrogel Bioink Containing Human Adipose-Derived Stem Cells. *ACS Biomater. Sci. Eng.* 2, 1732–1742. doi:10.1021/acsbiomaterials.6b00196

Nauth, A., McKee, M. D., Einhorn, T. A., Watson, J. T., Li, R., and Schemitsch, E. H. (2011). Managing Bone Defects. *J. Orthop. Trauma* 25, 462–466. doi:10.1097/BOT.0b013e318224caf0

Neufurth, M., Wang, X., Schröder, H. C., Feng, Q., Diehl-Seifert, B., Ziebart, T., et al. (2014). Engineering a Morphogenetically Active Hydrogel for Bioprinting

of Bioartificial Tissue Derived from Human Osteoblast-like SaOS-2 Cells. *Biomaterials* 35, 8810–8819. doi:10.1016/j.biomaterials.2014.07.002

Niu, X., Feng, Q., Wang, M., Guo, X., and Zheng, Q. (2009). Porous Nano-HA/collagen/PLLA Scaffold Containing Chitosan Microspheres for Controlled Delivery of Synthetic Peptide Derived from BMP-2. *J. Controlled Release* 134, 111–117. doi:10.1016/j.jconrel.2008.11.020

Oh, S. H., Park, I. K., Kim, J. M., and Lee, J. H. (2007). *In Vitro* and *In Vivo* Characteristics of PCL Scaffolds with Pore Size Gradient Fabricated by a Centrifugation Method. *Biomaterials* 28, 1664–1671. doi:10.1016/j.biomaterials.2006.11.024

Olson, E. J., and Carlson, C. S. (2017). "Bones, Joints, Tendons, and Ligaments," in *Pathologic Basis of Veterinary Disease*. Editor J. F. Zachary. Sixth Edition (Mosby), 954–1008. doi:10.1016/b978-0-323-35775-3.00016-3

Ouyang, L., Yao, R., Zhao, Y., and Sun, W. (2016). Effect of Bioink Properties on Printability and Cell Viability for 3D Bioplotting of Embryonic Stem Cells. *Biofabrication* 8, 035020. doi:10.1088/1758-5090/8/3/035020

Pae, H. C., Kang, J. H., Cha, J. K., Lee, J. S., Paik, J. W., Jung, U. W., et al. (2019). 3D-printed Polycaprolactone Scaffold Mixed with β-tricalcium Phosphate as a Bone Regenerative Material in Rabbit Calvarial Defects. *J. Biomed. Mater. Res.* 107, 1254–1263. doi:10.1002/jbm.b.34218

Parfitt, A. M. (1994). Osteonal and Hemi-Osteonal Remodeling: The Spatial and Temporal Framework for Signal Traffic in Adult Human Bone. *J. Cel. Biochem.* 55, 273–286. doi:10.1002/jcb.240550303

Park, J., Lee, S. J., Chung, S., Lee, J. H., Kim, W. D., Lee, J. Y., et al. (2017). Cell-laden 3D Bioprinting Hydrogel Matrix Depending on Different Compositions for Soft Tissue Engineering: Characterization and Evaluation. *Mater. Sci. Eng. C* 71, 678–684. doi:10.1016/j.msec.2016.10.069

Park, J. Y., Choi, J. C., Shim, J. H., Lee, J. S., Park, H., Kim, S. W., et al. (2014). A Comparative Study on Collagen Type I and Hyaluronic Acid Dependent Cell Behavior for Osteochondral Tissue Bioprinting. *Biofabrication* 6, 035004. doi:10.1088/1758-5082/6/3/035004

Park, J. Y., Shim, J.-H., Choi, S.-A., Jang, J., Kim, M., Lee, S. H., et al. (2015). 3D Printing Technology to Control BMP-2 and VEGF Delivery Spatially and Temporally to Promote Large-Volume Bone Regeneration. *J. Mater. Chem. B* 3, 5415–5425. doi:10.1039/c5tb00637f

Park, S. A., Lee, S. H., and Kim, W. D. (2011). Fabrication of Porous Polycaprolactone/hydroxyapatite (PCL/HA) Blend Scaffolds Using a 3D Plotting System for Bone Tissue Engineering. *Bioproc. Biosyst Eng* 34, 505–513. doi:10.1007/s00449-010-0499-2

Patel, Z. S., Young, S., Tabata, Y., Jansen, J. A., Wong, M. E. K., and Mikos, A. G. (2008). Dual Delivery of an Angiogenic and an Osteogenic Growth Factor for Bone Regeneration in a Critical Size Defect Model. *Bone* 43, 931–940. doi:10.1016/j.bone.2008.06.019

Pati, F., Song, T.-H., Rijal, G., Jang, J., Kim, S. W., and Cho, D.-W. (2015). Ornamenting 3D Printed Scaffolds with Cell-Laid Extracellular Matrix for Bone Tissue Regeneration. *Biomaterials* 37, 230–241. doi:10.1016/j.biomaterials.2014.10.012

Patterson-Kane, J. C., and Firth, E. C. (2014). "Tendon, Ligament, Bone, and Cartilage: Anatomy, Physiology, and Adaptations to Exercise and Training," in *The Athletic Horse*. Editors D. R. Hodgson, K. H. McKeever, and C. M. McGowan. Second Edition (W.B. Saunders), 202–242. doi:10.1016/b978-0-7216-0075-8.00022-8

Perez, R. A., and Kim, H.-W. (2015). Core-shell Designed Scaffolds for Drug Delivery and Tissue Engineering. *Acta Biomater.* 21, 2–19. doi:10.1016/j.actbio.2015.03.013

Perez, R. A., Kim, J.-H., Buitrago, J. O., Wall, I. B., and Kim, H.-W. (2015). Novel Therapeutic Core-Shell Hydrogel Scaffolds with Sequential Delivery of Cobalt and Bone Morphogenetic Protein-2 for Synergistic Bone Regeneration. *Acta Biomater.* 23, 295–308. doi:10.1016/j.actbio.2015.06.002

Perez, R. A., Kim, M., Kim, T.-H., Kim, J.-H., Lee, J. H., Park, J.-H., et al. (2014). Utilizing Core-Shell Fibrous Collagen-Alginate Hydrogel Cell Delivery System for Bone Tissue Engineering. *Tissue Eng. Part A* 20, 103–114. doi:10.1089/ten.tea.2013.0198

Perez, R. A., and Mestres, G. (2016). Role of Pore Size and Morphology in Musculo-Skeletal Tissue Regeneration. *Mater. Sci. Eng. C* 61, 922–939. doi:10.1016/j.msec.2015.12.087

Phillippi, J. A., Miller, E., Weiss, L., Huard, J., Waggoner, A., and Campbell, P. (2008). Microenvironments Engineered by Inkjet Bioprinting Spatially Direct Adult Stem Cells toward Muscle- and Bone-like Subpopulations. *Stem Cells* 26, 127–134. doi:10.1634/stemcells.2007-0520

Pierantozzi, D., Scalzone, A., Jindal, S., Stīpniece, L., Šalma-Ancāne, K., Dalgarno, K., et al. (2020). 3D Printed Sr-Containing Composite Scaffolds: Effect of Structural Design and Material Formulation towards New Strategies for Bone Tissue Engineering. *Composites Sci. Technology* 191, 108069. doi:10.1016/j.compscitech.2020.108069

Pneumaticos, S. G., Triantafyllopoulos, G. K., Basdra, E. K., and Papavassiliou, A. G. (2010). Segmental Bone Defects: from Cellular and Molecular Pathways to the Development of Novel Biological Treatments. *J. Cel. Mol. Med.* 14, 2561–2569. doi:10.1111/j.1582-4934.2010.01062.x

Poldervaart, M. T., Goversen, B., de Ruijter, M., Abbadessa, A., Melchels, F. P. W., Öner, F. C., et al. (2017). 3D Bioprinting of Methacrylated Hyaluronic Acid (MeHA) Hydrogel with Intrinsic Osteogenicity. *PLoS One* 12, e0177628. doi:10.1371/journal.pone.0177628

Poldervaart, M. T., Gremmels, H., van Deventer, K., Fledderus, J. O., Öner, F. C., Verhaar, M. C., et al. (2014). Prolonged Presence of VEGF Promotes Vascularization in 3D Bioprinted Scaffolds with Defined Architecture. *J. Controlled Release* 184, 58–66. doi:10.1016/j.jconrel.2014.04.007

Poldervaart, M. T., Wang, H., van der Stok, J., Weinans, H., Leeuwenburgh, S. C. G., Öner, F. C., et al. (2013). Sustained Release of BMP-2 in Bioprinted Alginate for Osteogenicity in Mice and Rats. *PLoS One* 8, e72610. doi:10.1371/journal.pone.0072610

Qi, X., Huang, Y., Han, D., Zhang, J., Cao, J., Jin, X., et al. (2016). Three-dimensional Poly (ε-Caprolactone)/hydroxyapatite/collagen Scaffolds Incorporating Bone Marrow Mesenchymal Stem Cells for the Repair of Bone Defects. *Biomed. Mater.* 11, 025005. doi:10.1088/1748-6041/11/2/025005

Raina, D. B., Qayoom, I., Larsson, D., Zheng, M. H., Kumar, A., Isaksson, H., et al. (2019). Guided Tissue Engineering for Healing of Cancellous and Cortical Bone Using a Combination of Biomaterial Based Scaffolding and Local Bone Active Molecule Delivery. *Biomaterials* 188, 38–49. doi:10.1016/j.biomaterials.2018.10.004

Raja, N., and Yun, H.-s. (2016). A Simultaneous 3D Printing Process for the Fabrication of Bioceramic and Cell-Laden Hydrogel Core/shell Scaffolds with Potential Application in Bone Tissue Regeneration. *J. Mater. Chem. B* 4, 4707–4716. doi:10.1039/c6tb00849f

Rajaram, A., Schreyer, D., and Chen, D. (2014). Bioplotting Alginate/Hyaluronic Acid Hydrogel Scaffolds with Structural Integrity and Preserved Schwann Cell Viability. *3D Printing and Additive Manufacturing* 1, 194–203. doi:10.1089/3dp.2014.0006

Rajaratnam, S. S., Jack, C., Tavakkolizadeh, A., George, M. D., Fletcher, R. J., Hankins, M., et al. (2008). Long-term Results of a Hydroxyapatite-Coated Femoral Component in Total Hip Replacement. *The J. Bone Jt. Surg. Br. volume* 90-B, 27–30. doi:10.1302/0301-620x.90b1.19731

Rhee, S., Puetzer, J. L., Mason, B. N., Reinhart-King, C. A., and Bonassar, L. J. (2016). 3D Bioprinting of Spatially Heterogeneous Collagen Constructs for Cartilage Tissue Engineering. *ACS Biomater. Sci. Eng.* 2, 1800–1805. doi:10.1021/acsbiomaterials.6b00288

Roohani-Esfahani, S. I., Newman, P., and Zreiqat, H. (2016). Design and Fabrication of 3D Printed Scaffolds with a Mechanical Strength Comparable to Cortical Bone to Repair Large Bone Defects. *Sci. Rep.* 6, 19468–8. doi:10.1038/srep19468

Roosa, S. M. M., Kemppainen, J. M., Moffitt, E. N., Krebsbach, P. H., and Hollister, S. J. (2010). The Pore Size of Polycaprolactone Scaffolds Has Limited Influence on Bone Regeneration in Anin Vivomodel. *J. Biomed. Mater. Res.* 92A, 359–368. doi:10.1002/jbm.a.32381

Roseti, L., Parisi, V., Petretta, M., Cavallo, C., Desando, G., Bartolotti, I., et al. (2017). Scaffolds for Bone Tissue Engineering: State of the Art and New Perspectives. *Mater. Sci. Eng. C* 78, 1246–1262. doi:10.1016/j.msec.2017.05.017

Rotbaum, Y., Puiu, C., Rittel, D., and Domingos, M. (2019). Quasi-static and Dynamic *In Vitro* Mechanical Response of 3D Printed Scaffolds with Tailored Pore Size and Architectures. *Mater. Sci. Eng. C* 96, 176–182. doi:10.1016/j.msec.2018.11.019

Sabetrasekh, R., Tiainen, H., Lyngstadaas, S. P., Reseland, J., and Haugen, H. (2010). A Novel Ultra-porous Titanium Dioxide Ceramic with Excellent Biocompatibility. *J. Biomater. Appl.* 25, 559–580. doi:10.1177/0885328209354925

Sadeghianmaryan, A., Naghieh, S., Alizadeh Sardroud, H., Yazdanpanah, Z., Afzal Soltani, Y., Sernaglia, J., et al. (2020). Extrusion-based Printing of Chitosan Scaffolds and Their *In Vitro* Characterization for Cartilage Tissue Engineering. *Int. J. Biol. Macromolecules* 164, 3179–3192. doi:10.1016/j.ijbiomac.2020.08.180

Sadeghianmaryan, A., Naghieh, S., Yazdanpanah, Z., Sardroud, H. A., Sharma, N. K., Wilson, L. D., et al. (2022). Fabrication of Chitosan/alginate/hydroxyapatite Hybrid Scaffolds Using 3D Printing and Impregnating Techniques for Potential Cartilage Regeneration. *Int. J. Biol. Macromol.* doi:10.1016/j.ijbiomac.2022.01.201

Salgado, A. J., Coutinho, O. P., and Reis, R. L. (2004). Bone Tissue Engineering: State of the Art and Future Trends. *Macromol. Biosci.* 4, 743–765. doi:10.1002/mabi.200400026

Sarker, M. D., Naghieh, S., McInnes, A. D., Ning, L., Schreyer, D. J., and Chen, X. (2019). Bio-fabrication of Peptide-Modified Alginate Scaffolds: Printability, Mechanical Stability and Neurite Outgrowth Assessments. *Bioprinting* 14, e00045. doi:10.1016/j.bprint.2019.e00045

Sarker, M., Izadifar, M., Schreyer, D., and Chen, X. (2018). Influence of Ionic Crosslinkers (Ca2+/Ba2+/Zn2+) on the Mechanical and Biological Properties of 3D Bioplotted Hydrogel Scaffolds. *J. Biomater. Sci. Polym. Edition* 29, 1126–1154. doi:10.1080/09205063.2018.1433420

Sawkins, M. J., Mistry, P., Brown, B. N., Shakesheff, K. M., Bonassar, L. J., and Yang, J. (2015). Cell and Protein Compatible 3D Bioprinting of Mechanically strong Constructs for Bone Repair. *Biofabrication* 7, 035004. doi:10.1088/1758-5090/7/3/035004

Sawyer, A. A., Song, S. J., Susanto, E., Chuan, P., Lam, C. X. F., Woodruff, M. A., et al. (2009). The Stimulation of Healing within a Rat Calvarial Defect by mPCL-TCP/collagen Scaffolds Loaded with rhBMP-2. *Biomaterials* 30, 2479–2488. doi:10.1016/j.biomaterials.2008.12.055

Schemitsch, E. H. (2017). Size Matters: Defining Critical in Bone Defect Size! *J. Orthop. Trauma* 31, S20. doi:10.1097/BOT.0000000000000978

Semba, J. A., Mieloch, A. A., and Rybka, J. D. (2020). Introduction to the State-Of-The-Art 3D Bioprinting Methods, Design, and Applications in Orthopedics. *Bioprinting* 18, e00070. doi:10.1016/j.bprint.2019.e00070

Seol, Y.-J., Park, D. Y., Park, J. Y., Kim, S. W., Park, S. J., and Cho, D.-W. (2013). A New Method of Fabricating Robust Freeform 3D Ceramic Scaffolds for Bone Tissue Regeneration. *Biotechnol. Bioeng.* 110, 1444–1455. doi:10.1002/bit.24794

Serra, T., Planell, J. A., and Navarro, M. (2013). High-resolution PLA-Based Composite Scaffolds via 3-D Printing Technology. *Acta Biomater.* 9, 5521–5530. doi:10.1016/j.actbio.2012.10.041

Shahabipour, F., Ashammakhi, N., Oskuee, R. K., Bonakdar, S., Hoffman, T., Shokrgozar, M. A., et al. (2020). Key Components of Engineering Vascularized 3-dimensional Bioprinted Bone Constructs. *Translational Res.* 216, 57–76. doi:10.1016/j.trsl.2019.08.010

Shoichet, M. S., Li, R. H., White, M. L., and Winn, S. R. (1996). Stability of Hydrogels Used in Cell Encapsulation: An *In Vitro* Comparison of Alginate and Agarose. *Biotechnol. Bioeng.* 50, 374–381. doi:10.1002/(sici)1097-0290(19960520)50:4<374::aid-bit4>3.0.co;2-i

Singh, A., Gill, G., Kaur, H., Amhmed, M., and Jakhu, H. (2018). Role of Osteopontin in Bone Remodeling and Orthodontic Tooth Movement: a Review. *Prog. Orthod.* 19, 18. doi:10.1186/s40510-018-0216-2

Sobral, J. M., Caridade, S. G., Sousa, R. A., Mano, J. F., and Reis, R. L. (2011). Three-dimensional Plotted Scaffolds with Controlled Pore Size Gradients: Effect of Scaffold Geometry on Mechanical Performance and Cell Seeding Efficiency. *Acta Biomater.* 7, 1009–1018. doi:10.1016/j.actbio.2010.11.003

Sohn, J.-Y., Park, J.-C., Um, Y.-J., Jung, U.-W., Kim, C.-S., Cho, K.-S., et al. (2010). Spontaneous Healing Capacity of Rabbit Cranial Defects of Various Sizes. *J. Periodontal Implant Sci.* 40, 180–187. doi:10.5051/jpis.2010.40.4.180

Soltan, N., Ning, L., Mohabatpour, F., Papagerakis, P., and Chen, X. (2019). Printability and Cell Viability in Bioprinting Alginate Dialdehyde-Gelatin Scaffolds. *ACS Biomater. Sci. Eng.* 5, 2976–2987. doi:10.1021/acsbiomaterials.9b00167

Song, J. E., Tripathy, N., Shin, J. H., Lee, D. H., Cha, J. G., Park, C. H., et al. (2017). *In Vivo* bone Regeneration Evaluation of Duck's Feet Collagen/PLGA Scaffolds in Rat Calvarial Defect. *Macromol. Res.* 25, 994–999. doi:10.1007/s13233-017-5134-5

Spicer, P. P., Kretlow, J. D., Young, S., Jansen, J. A., Kasper, F. K., and Mikos, A. G. (2012). Evaluation of Bone Regeneration Using the Rat Critical Size Calvarial Defect. *Nat. Protoc.* 7, 1918–1929. doi:10.1038/nprot.2012.113

Stegen, S., van Gastel, N., and Carmeliet, G. (2015). Bringing New Life to Damaged Bone: the Importance of Angiogenesis in Bone Repair and Regeneration. *Bone* 70, 19–27. doi:10.1016/j.bone.2014.09.017

Stevens, B., Yang, Y., Mohandas, A., Stucker, B., and Nguyen, K. T. (2008). A Review of Materials, Fabrication Methods, and Strategies Used to Enhance Bone Regeneration in Engineered Bone Tissues. *J. Biomed. Mater. Res.* 85B, 573–582. doi:10.1002/jbm.b.30962

Stewart, S., Bryant, S. J., Ahn, J., and Hankenson, K. D. (2015). "Bone Regeneration," in *Translational Regenerative Medicine*. Editors A. Atala and J. G. Allickson (Boston: Academic Press), 313–333. doi:10.1016/b978-0-12-410396-2.00024-4

Suenaga, H., Furukawa, K. S., Suzuki, Y., Takato, T., and Ushida, T. (2015). Bone Regeneration in Calvarial Defects in a Rat Model by Implantation of Human Bone Marrow-Derived Mesenchymal Stromal Cell Spheroids. *J. Mater. Sci. Mater. Med.* 26, 254. doi:10.1007/s10856-015-5591-3

Sukul, M., Min, Y.-K., Lee, S.-Y., and Lee, B.-T. (2015). Osteogenic Potential of Simvastatin Loaded Gelatin-Nanofibrillar Cellulose-β Tricalcium Phosphate Hydrogel Scaffold in Critical-Sized Rat Calvarial Defect. *Eur. Polym. J.* 73, 308–323. doi:10.1016/j.eurpolymj.2015.10.022

Turnbull, G., Clarke, J., Picard, F., Riches, P., Jia, L., Han, F., et al. (2018). 3D Bioactive Composite Scaffolds for Bone Tissue Engineering. *Bioactive Mater.* 3, 278–314. doi:10.1016/j.bioactmat.2017.10.001

Van Bael, S., Chai, Y. C., Truscello, S., Moesen, M., Kerckhofs, G., Van Oosterwyck, H., et al. (2012). The Effect of Pore Geometry on the *In Vitro* Biological Behavior of Human Periosteum-Derived Cells Seeded on Selective Laser-Melted Ti6Al4V Bone Scaffolds. *Acta Biomater.* 8, 2824–2834. doi:10.1016/j.actbio.2012.04.001

Vandrovcová, M., Douglas, T., Hauk, D., Grössner-Schreiber, B., Wiltfang, J., Bacakova, L., et al. (2011). Influence of Collagen and Chondroitin Sulfate (CS) Coatings on poly-(lactide-co-glycolide)(PLGA) on MG 63 Osteoblast-like Cells. *Physiol. Res.* 60, 797.

Verma, N., Zafar, S., and Talha, M. (2019). Influence of Nano-Hydroxyapatite on Mechanical Behavior of Microwave Processed Polycaprolactone Composite Foams. *Mater. Res. Express* 6, 85336. doi:10.1088/2053-1591/ab260d

Wan, Z., Zhang, P., Liu, Y., Lv, L., and Zhou, Y. (2020). Four-dimensional Bioprinting: Current Developments and Applications in Bone Tissue Engineering. *Acta Biomater.* 101, 26–42. doi:10.1016/j.actbio.2019.10.038

Wang, W., and Yeung, K. W. K. (2017). Bone Grafts and Biomaterials Substitutes for Bone Defect Repair: A Review. *Bioactive Mater.* 2, 224–247. doi:10.1016/j.bioactmat.2017.05.007

Wang, X.-F., Lu, P.-J., Song, Y., Sun, Y.-C., Wang, Y.-G., and Wang, Y. (2016). Nano Hydroxyapatite Particles Promote Osteogenesis in a Three-Dimensional Bio-Printing Construct Consisting of alginate/gelatin/hASCs. *RSC Adv.* 6, 6832–6842. doi:10.1039/c5ra21527g

Wang, X., Jiang, M., Zhou, Z., Gou, J., and Hui, D. (2017). 3D Printing of Polymer Matrix Composites: A Review and Prospective. *Composites B: Eng.* 110, 442–458. doi:10.1016/j.compositesb.2016.11.034

Wenz, A., Borchers, K., Tovar, G. E. M., and Kluger, P. J. (2017). Bone Matrix Production in Hydroxyapatite-Modified Hydrogels Suitable for Bone Bioprinting. *Biofabrication* 9, 044103. doi:10.1088/1758-5090/aa91ec

Wiria, F. E., Leong, K. F., Chua, C. K., and Liu, Y. (2007). Poly-ε-caprolactone/hydroxyapatite for Tissue Engineering Scaffold Fabrication via Selective Laser Sintering. *Acta Biomater.* 3, 1–12. doi:10.1016/j.actbio.2006.07.008

Wu, D., Yu, Y., Tan, J., Huang, L., Luo, B., Lu, L., et al. (2018). 3D Bioprinting of Gellan Gum and Poly (Ethylene Glycol) Diacrylate Based Hydrogels to Produce Human-Scale Constructs with High-Fidelity. *Mater. Des.* 160, 486–495. doi:10.1016/j.matdes.2018.09.040

Wu, H., Lei, P., Liu, G., Shrike Zhang, Y., Yang, J., Zhang, L., et al. (2017). Reconstruction of Large-Scale Defects with a Novel Hybrid Scaffold Made from Poly(L-Lactic acid)/Nanohydroxyapatite/Alendronate-Loaded Chitosan Microsphere: *In Vitro* and *In Vivo* Studies. *Sci. Rep.* 7, 359. doi:10.1038/s41598-017-00506-z

Wu, S., Liu, X., Yeung, K. W. K., Liu, C., and Yang, X. (2014). Biomimetic Porous Scaffolds for Bone Tissue Engineering. *Mater. Sci. Eng. R: Rep.* 80, 1–36. doi:10.1016/j.mser.2014.04.001

Yazdanpanah, Z., Bahrololoom, M. E., and Hashemi, B. (2015). Evaluating Morphology and Mechanical Properties of Glass-Reinforced Natural Hydroxyapatite Composites. *J. Mech. Behav. Biomed. Mater.* 41, 36–42. doi:10.1016/j.jmbbm.2014.09.021

Yeo, M., Simon, C. G., and Kim, G. (2012). Effects of Offset Values of Solid Freeform Fabricated PCL-β-TCP Scaffolds on Mechanical Properties and

Cellular Activities in Bone Tissue Regeneration. *J. Mater. Chem.* 22, 21636–21646. doi:10.1039/c2jm31165h

Yilgor, P., Sousa, R. A., Reis, R. L., Hasirci, N., and Hasirci, V. (2008). 3D Plotted PCL Scaffolds for Stem Cell Based Bone Tissue Engineering. *Macromol. Symp.* 269, 92–99. doi:10.1002/masy.200850911

Yilgor, P., Tuzlakoglu, K., Reis, R. L., Hasirci, N., and Hasirci, V. (2009). Incorporation of a Sequential BMP-2/BMP-7 Delivery System into Chitosan-Based Scaffolds for Bone Tissue Engineering. *Biomaterials* 30, 3551–3559. doi:10.1016/j.biomaterials.2009.03.024

Yongkuk, P., Eugene, C., Jun-Goo, K., Ryan, C., Jae-Hyuck, S., and Jungwoo, L. (2021). Trabecular Bone Organoid Model for Studying the Regulation of Localized Bone Remodeling. *Sci. Adv.* 7, eabd6495.

You, F., Chen, X., Cooper, D. M. L., Chang, T., and Eames, B. F. (2018). Homogeneous Hydroxyapatite/alginate Composite Hydrogel Promotes Calcified Cartilage Matrix Deposition with Potential for Three-Dimensional Bioprinting. *Biofabrication* 11, 015015. doi:10.1088/1758-5090/aaf44a

You, F., Wu, X., Zhu, N., Lei, M., Eames, B. F., and Chen, X. (2016). 3D Printing of Porous Cell-Laden Hydrogel Constructs for Potential Applications in Cartilage Tissue Engineering. *ACS Biomater. Sci. Eng.* 2, 1200–1210. doi:10.1021/acsbiomaterials.6b00258

Yu, D., Li, Q., Mu, X., Chang, T., and Xiong, Z. (2008). Bone Regeneration of Critical Calvarial Defect in Goat Model by PLGA/TCP/rhBMP-2 Scaffolds Prepared by Low-Temperature Rapid-Prototyping Technology. *Int. J. Oral Maxillofacial Surg.* 37, 929–934. doi:10.1016/j.ijom.2008.07.012

Zhai, P., Peng, X., Li, B., Liu, Y., Sun, H., and Li, X. (2020). The Application of Hyaluronic Acid in Bone Regeneration. *Int. J. Biol. Macromolecules* 151, 1224–1239. doi:10.1016/j.ijbiomac.2019.10.169

Zhang, J., Eyisoylu, H., Qin, X.-H., Rubert, M., and Müller, R. (2021). 3D Bioprinting of Graphene Oxide-Incorporated Cell-Laden Bone Mimicking Scaffolds for Promoting Scaffold Fidelity, Osteogenic Differentiation and Mineralization. *Acta Biomater.* 121, 637–652. doi:10.1016/j.actbio.2020.12.026

Zhang, R., and Ma, P. X. (1999). Poly(?-hydroxyl Acids)/hydroxyapatite Porous Composites for Bone-Tissue Engineering. I. Preparation and Morphology. *J. Biomed. Mater. Res.* 44, 446–455. doi:10.1002/(sici)1097-4636(19990315)44:4<446::aid-jbm11>3.0.co;2-f

Zhang, W., Zhu, C., Ye, D., Xu, L., Zhang, X., Wu, Q., et al. (2014). Porous Silk Scaffolds for Delivery of Growth Factors and Stem Cells to Enhance Bone Regeneration. *PLoS One* 9, e102371. doi:10.1371/journal.pone.0102371

Zhang, Y. S., Yue, K., Aleman, J., Mollazadeh-Moghaddam, K., Bakht, S. M., Yang, J., et al. (2017). 3D Bioprinting for Tissue and Organ Fabrication. *Ann. Biomed. Eng.* 45, 148–163. doi:10.1007/s10439-016-1612-8

Zhou, H., Lu, S. S., and Dempster, D. W. (2010). "Bone Remodeling," in *Osteoporosis in Men*. Editors E. S. Orwoll, J. P. Bilezikian, and D. Vanderschueren. Second Edition (San Diego: Academic Press), 15–24. doi:10.1016/b978-0-12-374602-3.00002-x

Zhu, N., Li, M. G., Cooper, D., and Chen, X. B. (2011). Development of Novel Hybrid poly(L-Lactide)/chitosan Scaffolds Using the Rapid Freeze Prototyping Technique. *Biofabrication* 3, 034105. doi:10.1088/1758-5082/3/3/034105

Zhu, N., and Chen, X. (2013). Biofabrication of Tissue Scaffolds. *Adv. Biomater. Sci. Biomed. Appl.*, 315–328. doi:10.5772/54125

Zhu, Z., Wang, Y.-M., Yang, J., and Luo, X.-S. (2017). Hyaluronic Acid: a Versatile Biomaterial in Tissue Engineering. *Plast. Aesthet. Res.* 4. doi:10.20517/2347-9264.2017.71

Zimmerling, A., Yazdanpanah, Z., Cooper, D. M. L., Johnston, J. D., and Chen, X. (2021). 3D Printing PCL/nHA Bone Scaffolds: Exploring the Influence of Material Synthesis Techniques. *Biomater. Res.* 25, 3. doi:10.1186/s40824-021-00204-y

Conflict of Interest: The authors declare that the research was conducted in the absence of any commercial or financial relationships that could be construed as a potential conflict of interest.

Publisher's Note: All claims expressed in this article are solely those of the authors and do not necessarily represent those of their affiliated organizations, or those of the publisher, the editors and the reviewers. Any product that may be evaluated in this article, or claim that may be made by its manufacturer, is not guaranteed or endorsed by the publisher.

Copyright © 2022 Yazdanpanah, Johnston, Cooper and Chen. This is an open-access article distributed under the terms of the Creative Commons Attribution License (CC BY). The use, distribution or reproduction in other forums is permitted, provided the original author(s) and the copyright owner(s) are credited and that the original publication in this journal is cited, in accordance with accepted academic practice. No use, distribution or reproduction is permitted which does not comply with these terms.

frontiers | Frontiers in Bioengineering and Biotechnology

REVIEW
published: 12 April 2022
doi: 10.3389/fbioe.2022.866627

Research Progress of Exosomes in Bone Diseases: Mechanism, Diagnosis and Therapy

Fanying Meng[1†], Xu Xue[1†], Zhifeng Yin[2†], Fei Gao[1], Xiuhui Wang[1*] and Zhen Geng[1*]*

[1]*Institute of Translational Medicine, Shanghai University, Shanghai, China,* [2]*Department of Orthopedics, Shanghai Zhongye Hospital, Shanghai, China*

With the global escalation of the aging process, the number of patients with bone diseases is increasing year by year. Currently, there are limited effective treatments for bone diseases. Exosome, as a vital medium in cell-cell communication, can mediate tissue metabolism through the paracrine transmission of various cargos (proteins, nucleic acids, lipids, etc.) carried by itself. Recently, an increasing number of researchers have proven that exosomes play essential roles in the formation, metabolism, and pathological changes of bone and cartilage. Because exosomes have the advantages of small size, rich sources, and low immunogenicity, they can be used not only as substitutes for the traditional treatment of bone diseases, but also as biomarkers for the diagnosis of bone diseases. This paper reviews the research progress of several kinds of cells derived-exosomes in bone diseases and provides a theoretical basis for further research and clinical application of exosomes in bone diseases in the future.

Keywords: exosomes, bone diseases, micro-RNA, biomaterials, bone regeneration

OPEN ACCESS

Edited by:
Andrea Vernengo,
AO Research Institute, Switzerland

Reviewed by:
Wei Seong Toh,
National University of Singapore, Singapore
Xingming Shi,
Augusta University, United States

***Correspondence:**
Fei Gao
flyhightly@shu.edu.cn
Xiuhui Wang
blackrabbit@shu.edu.cn
Zhen Geng
nanboshan1987@163.com

[†]These authors have contributed equally to this work

Specialty section:
This article was submitted to Tissue Engineering and Regenerative Medicine, a section of the journal Frontiers in Bioengineering and Biotechnology

Received: *31 January 2022*
Accepted: *15 March 2022*
Published: *12 April 2022*

Citation:
Meng F, Xue X, Yin Z, Gao F, Wang X and Geng Z (2022) Research Progress of Exosomes in Bone Diseases: Mechanism, Diagnosis and Therapy. Front. Bioeng. Biotechnol. 10:866627. doi: 10.3389/fbioe.2022.866627

INTRODUCTION

With the intensification of global aging, the number of patients with bone-related diseases (including osteoarthritis (OA), osteoporosis (OP), bone defect) has increased sharply (Zhao H. et al., 2018; Mei et al., 2020; Ren et al., 2021). These diseases not only bring physical and psychological pain to patients, but also result in enormous financial burdens to society (Hernlund et al., 2013; Hu et al., 2021a; Xue et al., 2021b). For OA, it was estimated that nearly 250 million OA patients worldwide, and the incidence was anticipated to increase further (Hunter and Bierma-Zeinstra, 2019). A statistical report pointed out that in some developed countries, the cost of treating OA could reach 1–2.5% of gross domestic product (Hunter et al., 2014). At present, the main ways to treat OA include drug treatment and surgical intervention (Zhou et al., 2020; Jin et al., 2021). However, painkillers and anti-inflammatory drugs commonly used in drug treatment could only relieve pain, not completely cure it. In addition, although advanced OA could be surgically intervened, it might be accompanied by many complications. In short, there is still no effective treatment to reverse the progression of OA (Glyn-Jones et al., 2015; Hu et al., 2019; Fang et al., 2021; Yajun et al., 2021). For OP, estimates showed that more than 200 million people worldwide suffered from OP (Ensrud and Crandall, 2017). Statistically, OP-related fractures cost approximately $17.9 and 4 pounds billion per year in the United States and United Kingdom, respectively (Clynes et al., 2020). Additionally, among hip fractures caused by OP, 21–30% of patients died within 1 year (Force et al., 2018). Unfortunately, OP usually takes a long period and even requires lifelong treatment with many side effects (Compston et al., 2019; Chen J. et al., 2021). For bone defects, although autogenous and allogeneic bone grafts

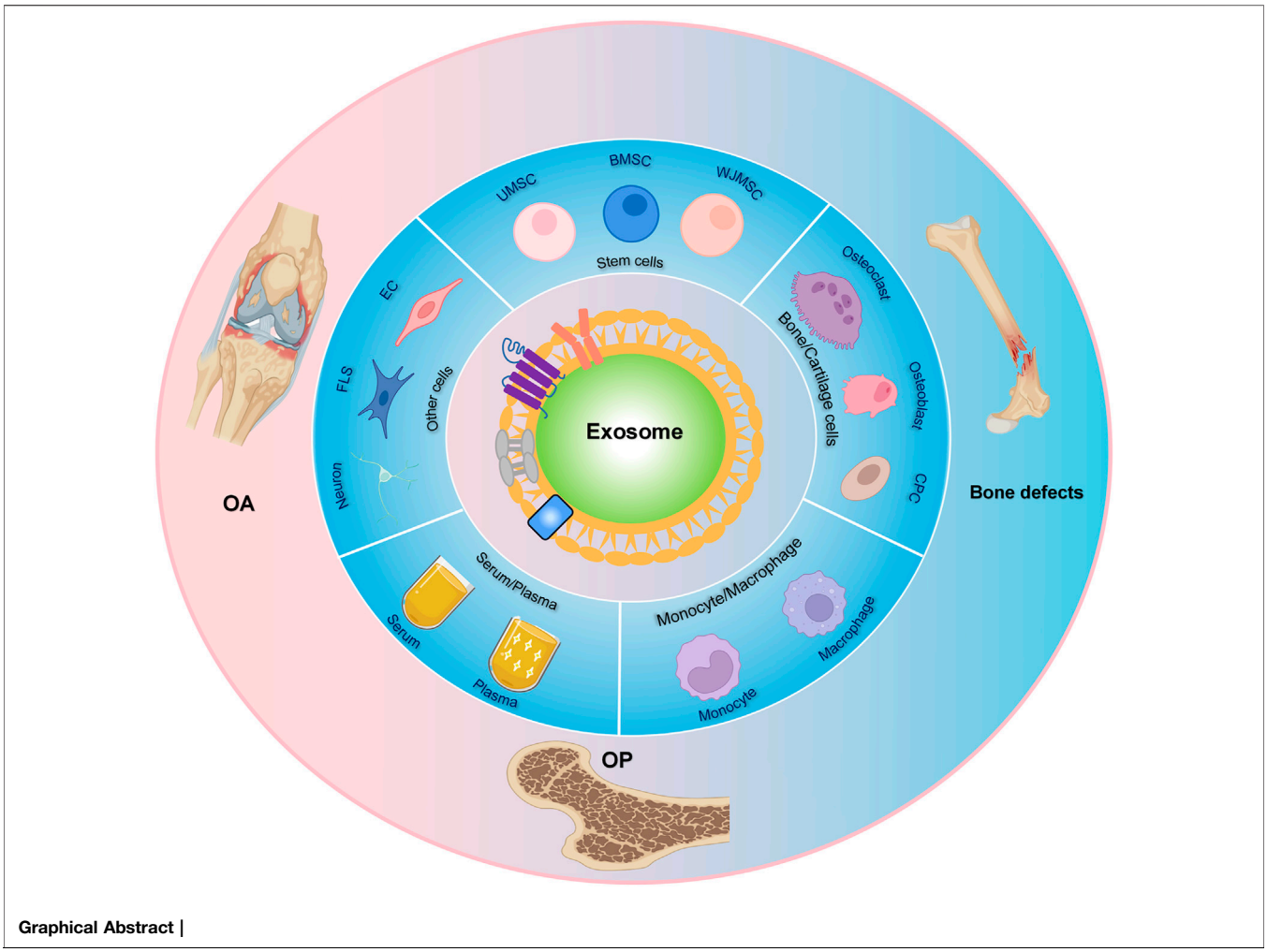

Graphical Abstract |

have been widely used for repairing bone defects, there are still some limitations in these two treatments, such as inflammation, limited autogenous bone, and immune rejection (Lee and Goodman, 2015; Qin et al., 2016; Xue et al., 2021a; Chen W. et al., 2021). In recent years, stem cell treatment has been located at the forefront of the field of bone regenerative medicine (Hao et al., 2016; Debnath et al., 2018). However, its molecular mechanism is not precise, and there are still some limitations, such as high cost, limited donors, and so on. Therefore, alternative and novel treatment strategies are imperatively needed to meet the clinical requirements of bone diseases.

It is generally considered that bone is a complex organ containing various cells, such as osteoblasts, osteoclasts, macrophages, endothelial cells, stem cells, and other cells (Wang L. et al., 2021). These cells surrounding the bone microenvironment communicate with each other and participate in bone metabolism together. Extracellular vesicles (EVs) have attracted extensive attention as an important medium of cell-cell communication (van der Pol et al., 2012). EVs can be further divided into exosomes, ectosomes (microparticles/microvesicles), apoptotic bodies, oncosomes and some other EVs subtypes (Thery et al., 2018; Ni et al., 2020). Among these different subtypes of EVs, exosome is one of the most widely studied subtypes as evidenced by an exponentially increasing number of exosome-related researches in recent years (Lawson et al., 2016). Exosome has a phospholipid bilayer structure with a diameter of 30–150 nm and can be secreted by various cells through the endosomal pathway (**Figure 1**) (Thery et al., 2002; Klumperman and Raposo, 2014). The history of exosomes could be traced back to 1983. It was firstly found by Harding et al. (1983), Pan and Johnstone (1983) in rat and sheep animal models, respectively. They found that a nano-vesicle containing transferrin was released during the maturation of reticulocytes into erythrocytes. According to its endosomal origin, this nano-vesicle was officially named "exosome" by Johnstone in 1987 (Johnstone et al., 1987). Over a long period of time, exosomes were considered to be cellular waste used by cells to transport metabolic products and little attention was paid to them. In recent years, accumulating evidence indicated that exosome was a natural endogenous nano-carrier that played an essential role in cell-cell communication (Mathieu et al., 2019; Cheng et al., 2021). This was mainly due to the fact that exosomes could involve in cell signaling and intercellular communication by carrying various bioactive substances (including proteins, nucleic acids, lipids, etc.) to the target cells (Yang D. et al., 2020; Norouzi-Barough et al., 2021). Moreover, they could exist stably in body fluids (such as

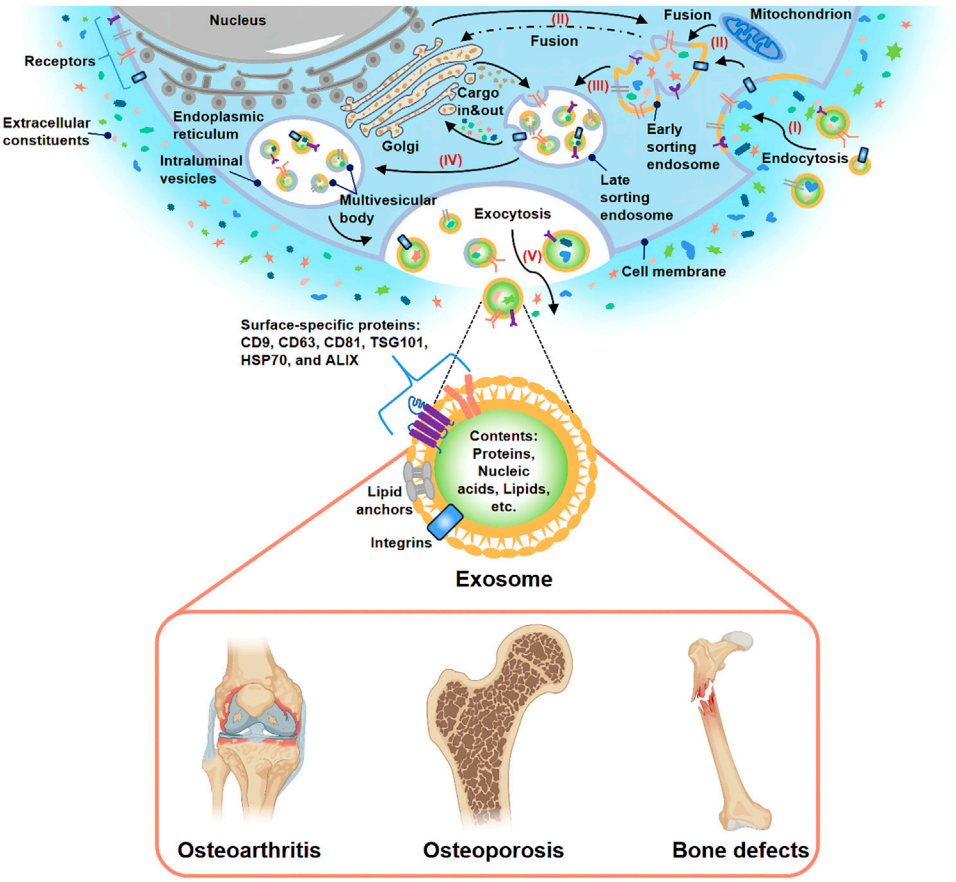

FIGURE 1 | Biogenesis, secretion, and potential application of exosome. (I) Extracellular constituents and cell surface proteins entered cells through endocytosis. (II) The formation of the cell membrane budded in the luminal side. The fusion of the bud with the compositions of the endoplasmic reticulum, Golgi, and mitochondria gave rise to early sorting endosome formation. (III) Then, early sorting endosome led to late sorting endosome. (IV) The secondary invagination was modified with cargos, giving rise to the generation of various intraluminal vesicles and the formation of the multivesicular body. (V) At last, the exocytosis of the multivesicular body released intraluminal vesicles to the outside of cells in the form of exosomes. Many studies have demonstrated that exosome-based treatment was effective for OA, OP, and bone defects.

blood, urine and breast milk, etc.) and conditioned medium for cell culture (Han et al., 2016; Cobelli et al., 2017). Because of the above characteristics, Masaoutis et al. proposed that exosomes could act as an important signaling mediator in bone remodeling (Li Q. et al., 2018; Masaoutis and Theocharis, 2019). Nowadays, a large number of growth studies have demonstrated that exosomes could be used in cell-free therapy to effectively improve bone disease and solve the problems (immune rejection, insufficient bone mass, and poor stability) caused by traditional bone implants and stem cell therapy (Bjorge et al., 2017; Huang J. et al., 2021).

At present, the research field of EVs is not mature and still faces many challenges. Due to the problems of overlapping size, similar composition and lack of standardized surface markers, the existing EVs isolation methods (ultracentrifugation method, kit-based method, etc.) and purification methods could not prepare purified EVs specific subtypes. Therefore, the current EVs preparations obtained are highly heterogeneous. In order to further accelerate the regulation and development of this field, the International Society for Extracellular Vesicles (ISEV) issued the Minimal Information for Studies of EVs in 2018 (MISEV 2018) (Thery et al., 2018). MISEV2018 recommended naming different subtypes of EVs according to physical characteristics, biochemical composition, or cell of origin unless the pathway can be demonstrated by live imaging techniques. For the purposes of this review, "exosomes" are described as EVs with a diameter of 30–200 nm whose surface markers meet the basic requirements of MISEV2018 and regardless of their purity and origin. Based on the current knowledge, this article reviews the investigation status of exosomes in the domain of bone diseases and aims to bring novel approaches for bone diseases treatment in the clinic (**Figure 1**).

EXOSOMES AND BONE DISEASES

Stem Cell-Derived Exosomes

Stem cells are cells with a very high differentiation potential, which have been confirmed to play critical roles in the growth of bone (Jiang et al., 2020). Currently, stem cell therapy has been used in the clinic as an alternative strategy for allogeneic and

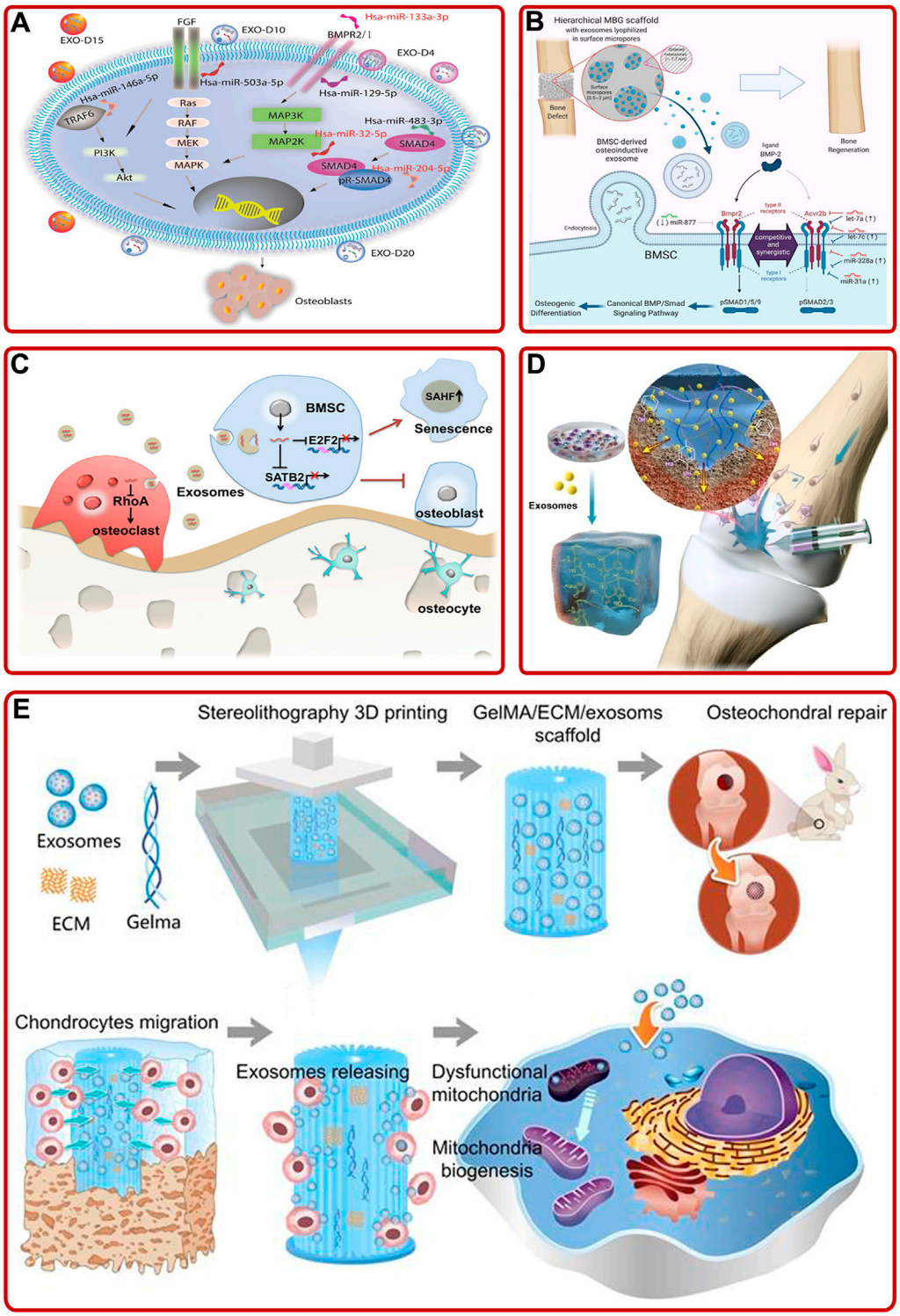

FIGURE 2 | (A) BMSC-derived exosomes induced osteogenic differentiation of hMSCs through mediating the PI3K/Akt and MAPK signaling pathways by upregulating/downregulating osteogenic and anti-osteogenic miRNAs (Zhai et al., 2020). **(B)** Schematic of the mechanism BMSC-derived osteoinductive exosomes functionalized hierarchical MBG scaffold promoted bone regeneration (Liu A. et al., 2021). **(C)** Aged BMSC- derived exosomal miR-31a-5p inhibited BMSCs functions in cellular aging and osteogenesis *via* the E2F2 and SATB2 signaling pathways and promoted osteoclastic differentiation via the RhoA signaling pathway (Xu et al., 2018). **(D)** Schematic described that superficial cartilage could be regenerated by injecting BMSC-derived exosomes containing hydrogels (Zhang F.-X. et al., 2021). **(E)** 3D printed ECM/Gelma/BMSC-derived exosomes scaffold enhanced chondrocyte mitochondrial biogenesis and promoted osteochondral regeneration in rabbit models (Chen et al., 2019).

allogeneic bone transplantation (Perez et al., 2018). Recent researches pointed out that the function of stem cells in promoting bone repair is mainly attributed to their paracrine secretion (Tao et al., 2018). Exosome had been proved to be an essential medium involved in paracrine. In this way, exosome, which could bypass immune rejection caused by stem cell therapy and bone deficiency in traditional surgical techniques, was regarded as a good candidate for cell-free therapy (Furuta et al., 2016; Hu et al., 2021b). In the last decades, stem cell-derived exosomes were demonstrated better therapeutic potential in OA, OP, and bone defects (Liu S. et al., 2020). The following paragraphs and **Supplementary Table S1** introduce the effects of several stem cells-derived exosomes in bone diseases.

Bone Marrow Mesenchymal Stem Cell-Derived Exosomes

Bone marrow mesenchymal stem cells (BMSCs) mainly differentiate into osteoblasts and chondrocytes, so they have great effects on bone/cartilage formation (Fan et al., 2017; Gao et al., 2021). During this process of differentiation, exosomes activated and participated in different intracellular pathways to facilitate osteogenesis/chondrogenesis by transporting their cargos (Metavarayuth et al., 2019; Wong et al., 2020). For example, Zhang L. et al. (2020) elucidated that BMSC-derived exosomes improved fracture healing by promoting osteogenesis and angiogenesis via the BMP-2/Smad1/RUNX2 signaling pathway. Furthermore, the impacts of BMSC-derived exosomes on angiogenesis could be further enhanced by low-dose dimethyloxalylglycine (Liang et al., 2019). In addition, Zhao P. et al. (2018) indicated that BMSC-derived exosomes could proliferate osteoblasts and relieve OP through the MAPK signaling pathway. Among various cargos carried by exosomes, small RNA (sRNA), especially micro-RNA (miRNA), has been proved to be the primary medium involved in cell-cell communication (Pegtel et al., 2010). For instance, Zhai et al. (2020) concluded that human BMSC (hBMSC)-derived exosomes could facilitate bone formation by upregulating osteogenic miRNAs (Hsa-miR-146a-5p, Hsa-miR-503-5p, Hsa-miR-483-3p, and Hsa-miR-129-5p) or downregulating anti-osteogenic miRNAs (Hsa-miR-32-5p, Hsa-miR-133a-3p, and Hsa-miR-204-5p) to activate PI3K/Akt and MAPK signaling pathways (**Figure 2A**). Moreover, Fan et al. (2020) found that downregulation of miR-29a could inhibit the expression of natural bone morphogenetic protein (BMP) antagonist noggin, activate BMP/Smad signaling pathway, and enhance the osteogenic characteristics of BMSCs-derived exosomes. Additionally, Liu A. et al. (2021) optimized BMSC-derived exosomes immobilized in hierarchical mesoporous bioactive glass (MBG) scaffold via lyophilization. Then they found that BMSC-derived exosomal let-7a-5p, let-7c-5p, miR-328a-5p, and miR-31a-5p could activate the phosphorylation of Smad1/5/9 and activate BMP/Smad signaling pathway by targeting Acvr2b to mediate osteogenic differentiation and repair bone defects (**Figure 2B**). Besides, other BMSC-derived exosomal miRNAs, such as miR-122-5p (Liao et al., 2019), miR-15b (Li Y. et al., 2020), miR-206 (Huang et al., 2021d), miR-19b (Huang et al., 2021c), miR-146a (Liu L. et al., 2021), miR-877 (Liang et al., 2021), miR-218 (Hassan et al., 2012), and miR-128-3p (Xu et al., 2020) also played significant roles in stimulating osteogenesis and angiogenesis. Briefly, BMSCs-derived exosomal miRNAs could participate in various pathways to promote bone formation, suggesting BMSC may be a key cell in maintaining bone metabolism.

It is worth noting that not all BMSC-derived exosomes play an active role in promoting osteogenesis. A rat model of OP with alveolar bone degeneration study showed that BMSC-derived exosomes accelerated osteoclasts formation (Xu and Wang, 2017). In addition, serval studies have pointed out the effect of age on exosomes. Xu et al. (2018) demonstrated that overexpression of aged BMSC-derived exosomal miR-31a-5p could not only inhibit osteogenesis *via* the E2F2 and SATB2 signaling pathways, respectively, but also promote osteoclastic differentiation through the RhoA pathway, resulting in bone loss (**Figure 2C**). Meanwhile, Jia et al. (2020) provided convincing evidence that BMSC-derived exosomes from young rats could upregulate the expression of osteogenesis-related genes, promote BMSCs proliferation, and accelerate bone establishment in aged rats. The above studies suggested that special attentions should be paid to the effects of pathology, age and other internal or external factors when using exosomes to treat bone diseases in the future.

BMSC-derived exosomes also played crucial roles in promoting cartilage repair and relieving OA. On the one hand, BMSC derived-exosomes promoted cartilage repair by directly acting on chondrocytes or indirectly participating in cartilage-related signaling pathways. For example, Hingert et al. (2020) proposed that BMSC-derived exosomes could improve the activity of chondrocytes and accelerate chondrocytes proliferation. Further mechanism studies pointed out that BMSC-derived exosomal miR-136-5p facilitated chondrocyte migration and proliferation through targeting ELF3 and downregulating ELF3 expression in a traumatic OA mouse model (Chen et al., 2020e). In addition, BMSC-derived exosomal circular RNA (circRNA_0001236) could also facilitate cartilage repair through miR-3677-3p/Sox9 signaling axis (Mao et al., 2021). Interestingly, Liu et al. obtained an exosome *via* pretreating BMSC-derived exosome by a new small molecular compound Kartogenin. Then, they found that the obtained exosome could promote chondrogenesis through upregulating COL2A1, Prg4, and SOX-9 (Liu C. et al., 2020). On the other hand, OA could lead to changes in the extracellular matrix of cartilage and aggravate the injury due to inflammation. BMSC-derived exosomes maintained the stability of cartilage extracellular matrix and alleviate OA by inhibiting inflammatory factors or inflammation-related signaling pathways (Jin et al., 2020). For instance, He et al. (2020b) confirmed that BMSC-derived exosomes could promote cartilage formation by weakening the inhibitory effects of pro-inflammatory cytokines on chondrocyte proliferation and migration. Moreover, Vonk et al. (2018) found that BMSC-derived exosomes could affect the cartilage homeostasis, stimulate the production of polysaccharides and collagen, and inhibit the upregulation of pro-inflammatory interleukin. Additionally, BMSC-derived exosomes reduced cartilage injury via converting the M1 phenotype of macrophages to the M2

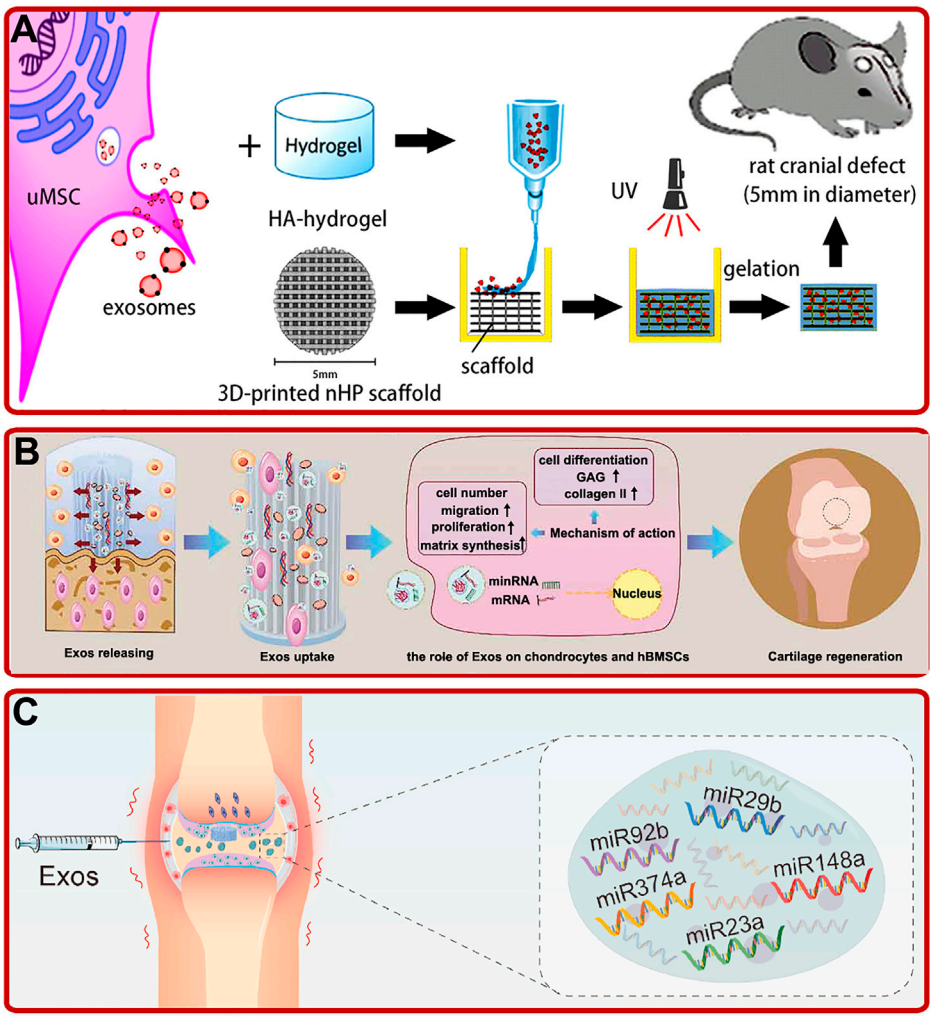

FIGURE 3 | (A) UMSC-derived exosomes combined with the HA-hydrogel and the 3D-printed nHP scaffold for cranial defect repair (Zhang Y. et al., 2021). **(B)** Exosomes (exos) released from hydrogel improved the migration, proliferation, and chondrogenic differentiation of hBMSCs and enhanced the formation of glycosaminoglycan (GAG), ECM, and collagen II, and thus promoted cartilage regeneration (Hu H. et al., 2020). **(C)** Schematic of WJMSC-derived exosomal miRNAs facilitated osteochondral regeneration (Jiang et al., 2021).

phenotype, decreasing the release of inflammatory factors (Zhang J. et al., 2020). Further research proved that mouse BMSC-derived exosomes overexpressing miRNA-210 could protect chondrocytes from injury by inhibiting the inflammation-related NF-κB signaling pathway (He et al., 2020a). Meanwhile, the treatment of rat OA models proved that low-intensity pulsed ultrasound could enhance this process (Liao et al., 2021).

Exosomes are often combined with technologies or biomaterials to achieve ideal functions, such as specific bone targeting, better osteogenic properties, and bone healing ability. For instance, Luo et al. (2019) fabricated an engineered exosome through coupling exosomes with BMSC-specific aptamers *via* high-affinity recognition. The engineered exosomes had a specific bone targeting ability and could significantly induce bone regeneration. In addition, Huang et al. (2020) prepared a functional exosome (BMP2 overexpression) via gene-editing technology. The exosome not only promoted the expression of BMP2, RUNX2, Osterix, and BMP9 *in vitro*, but also accelerated the healing of skull defects *in vivo*. In addition, other data indicated that exosomes and materials had a synergistic role in tissue healing. For example, Zhang F.-X. et al. (2021) found that BMSC-derived exosomes and adhesive hydrogel had a synergistic role in promoting BMSCs migration, proliferation, and differentiation, and repairing the osteochondral defects (**Figure 2D**). As well, Chen et al. (2019) demonstrated that chondrocyte extracellular matrix (ECM)/methacrylic acid gelatin (Gelma)/BMSC-derived exosomes scaffold fabricated by 3D printing technology could repair the mitochondrial dysfunction of chondrocytes, promote chondrocytes migration, and facilitate cartilage regeneration in rabbit models (**Figure 2E**). In addition, other studies suggested that BMSC-derived exosomes modified biomaterials, such as TiO2 nanotubes and hydrogel, exhibited superior properties on BMSCs proliferation and

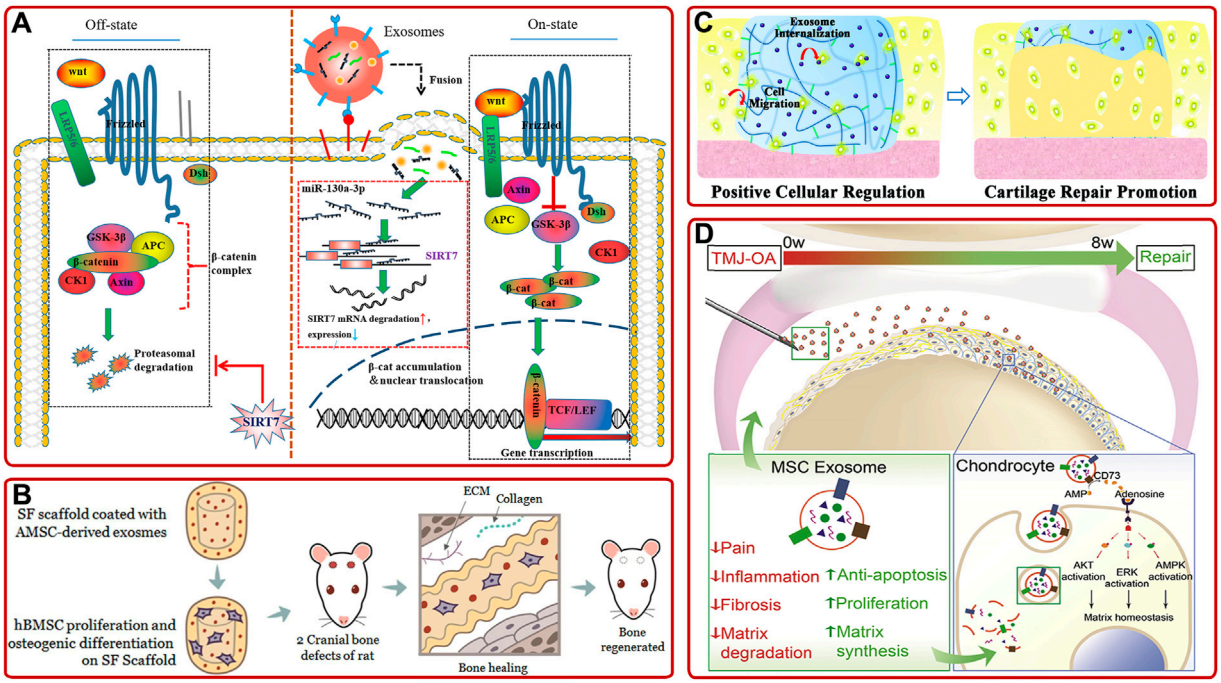

FIGURE 4 | (A) Schematic diagram of the mechanism that AMSC-derived exosomal miR-130a-3p enhanced osteogenic differentiation of AMSCs via the SIRT7/Wnt/β-catenin signaling axis (Yang S. et al., 2020). **(B)** AMSC-derived exosomes-coated silk fibroin 3D-scaffold implants facilitated bone healing in the calvarial bone defects of SD rats (Kyung Kim et al., 2021). **(C)** IPSC-derived exosomes internalized hydrogel glue positively facilitated cells to promote cartilage repair (Liu et al., 2017). **(D)** Schematic of the proposed mechanisms of MSC-derived exosome in repairing and regenerating TMJ-OA (Zhang S. et al., 2019).

differentiation, inflammation regulation, and bone healing (Huang C.-C. et al., 2021; Zhang B. et al., 2021; Zhao et al., 2021). In brief, the addition of exosomes or engineered exosomes could prepare better biomaterials for the treatment of bone diseases, which pointed out a novel research direction.

Umbilical Cord Mesenchymal Stem Cell and Wharton's Jelly of Umbilical Cord Mesenchymal Stem Cell-Derived Exosomes

Compared with other stem cells-derived exosomes, human umbilical cord mesenchymal stem cell (hUCMSC) and Wharton's jelly of umbilical cord mesenchymal stem cell (WJMSC)-derived exosomes have the characteristics of clean source, strong proliferation and high immunity. Several studies showed that hUCMSC-derived exosomes could promote OP and bone fracture healing by boosting BMSCs proliferation, migration, osteogenic differentiation and angiogenesis *via* Wnt and miR-1263/Mob1/Hippo signaling pathways (Zhang Y. et al., 2019; Zhou et al., 2019; Liu W. et al., 2020; Yang B.-c. et al., 2020). Based on these characteristics, by injecting hUCMSC-derived exosomes intravenously into a mouse OP model, Hu Y. et al. (2020) revealed that hUCMSC-derived exosomes could prevent the decrease of bone mass and maintain bone strength by promoting bone formation, reducing bone resorption and fat accumulation. In addition, hUCMSC-derived exosomes-modified hydrogels also showed excellent osteogenic and chondrogenic effects. For instance, by fabricating a hUMSC-derived exosomes modified Gel/hyaluronic acid (nHP) scaffold, Zhang et al. found that the addition of hUMSC-derived exosomes promoted rat cranial defects healing through activating the miR-21/NOTCH1/DLL4 signaling pathway (**Figure 3A**) (Zhang Y. et al., 2021). In addition, studies by Wang L. et al. (2020) revealed that hUCMSC-derived exosomes could enhance the reparative effect of coralline hydroxyapatite/silk fibroin/glycol chitosan/difunctionalized polyethylene glycol self-healing hydrogel in SD rats with induced femoral condyle defect. Moreover, Hu H. et al. (2020) prepared a hUCMSC-derived exosomes modified Gelma/nanoclay hydrogel. The modified hydrogel could effectively boost the chondrocytes migration, proliferation, and differentiation and promote cartilage regeneration (**Figure 3B**).

Wharton's jelly of umbilical cord mesenchymal stem cell (WJMSC), which has a strong ability of proliferation and differentiation, is a kind of MSCs extracted from the umbilical cord (Li et al., 2015). Recently, studies indicated that WJMSC-derived exosomes could also play important roles in bone reconstruction. For example, Jiang et al. (2021) confirmed that human WJMSC-derived exosomes could promote the proliferation of BMSCs and chondrocytes, facilitate the polarization of macrophages to M2 phenotype, reduce the inflammatory response, and regenerate bone and cartilage (**Figure 3C**). In addition, Kuang et al. (2019) found that human WJMSC-derived exosomes could inhibit osteocyte apoptosis through miR-21/PTEN/AKT signaling pathway *via* TUNEL and high-throughput RNA sequencing methods.

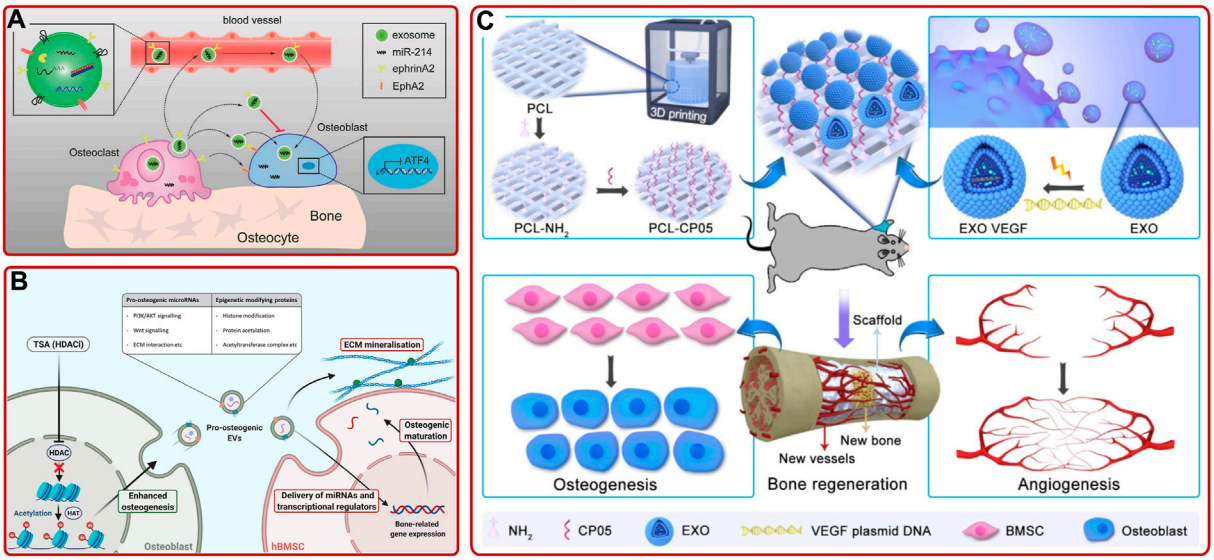

FIGURE 5 | (A) MiR-214-containing exosomes from osteoclasts inhibited osteoblast function *via* ephrinA2/EphA2 recognition and can also be secreted into the blood as a biomarker for bone loss (Sun et al., 2016). **(B)** Schematic illustration of the mechanism that osteoblast-derived EVs pretreated with TSA enhanced the osteogenic differentiation of hBMSCs and osteoblast mineralization (Man et al., 2021). **(C)** 3D-printed porous PCL scaffold functionalized with VEGF@CPC-derived exosomes exhibited better osteogenic and angiogenic ability (Zha et al., 2021).

Other Stem Cells-Derived Exosomes

In addition to the widely studied stem cell exosomes mentioned above, other stem cells (including adipose-derived mesenchymal stem cell (AMSC), induced pluripotent stem cell (iPSC), etc.)-derived exosomes also have potential therapeutic applications in the field of bone diseases.

AMSC-derived exosomes. Previous studies showed that AMSC-derived exosomes could inhibit the activation of NLRP3 inflammasome in osteoclasts and reduce the apoptosis of osteoblasts to relieve OP (Ren et al., 2019; Wang S. et al., 2021; Zhang L. et al., 2021). Furthermore, Yang S. et al. (2020) demonstrated that miR-130a-3p played a vital role in determining the osteogenic differentiation of AMSCs-derived exosomes. They further proved that the overexpression of miR-130a-3p could downregulate the expression of SIRT7 and upregulate the expression of Wnt signaling pathway-associated protein (**Figure 4A**). Moreover, recent studies confirmed that AMSC-derived exosomes pretreated with TNF-α or osteogenic medium have better osteogenic ability than non-pretreated ones (Lu et al., 2017; Zhu et al., 2021). As well, AMSC-derived exosomes combined with biomaterials have been proved to promote osteogenic differentiation and bone regeneration cooperatively (Li W. et al., 2018; Li S. et al., 2021). For example, Kyung Kim et al. (2021) demonstrated AMSCs-derived exosomes modified silk fibroin 3D-scaffold showed better bone healing ability than non-modified scaffold in a calvarial bone defects SD rat model (**Figure 4B**).

iPSC-derived exosomes. IPSC can be induced from patients' autologous stem cells and have no ethical problems, so they have attracted much attention. Meanwhile, emerging investigations have shown that iPSC-derived exosomes could provide a promising option in treating bone diseases. For example, Qi et al. (2016) found that exosomes secreted by MSCs derived from human induced pluripotent stem cells (hiPSC-MSC-Exos) could promote vascular and bone regeneration in ovariectomized (OVX) rat models. They also proved tricalcium phosphate modified with hiPSC-MSC-Exos could accelerate bone repair through activating PI3K/Akt signaling pathway (Zhang J. et al., 2016). In addition, other investigations showed that hiPSC-MSC-Exos had a stronger effect on facilitating chondrocytes migration and proliferation and ameliorating OA than synovial cells-derived exosomes (Zhu et al., 2017). This result opened up a way for IPSC-derived exosomes in cartilage repair, but the specific mechanism remained to be further studied. Based on this, Liu et al. (2017) developed a hydrogel glue with the incorporation of hiPSC-MSC-Exos by *in-situ* method (**Figure 4C**). Then, they found that the incorporation of hiPSC-MSC-Exos could significantly increase articular cartilage regeneration in a rabbit articular cartilage defect model.

Moreover, there are some other stem cells-derived exosomes, such as human embryonic stem cell-derived exosomes (Zhang S. et al., 2016; Zhang S. et al., 2018; Zhang S. et al., 2019), human gingival mesenchymal stem cell-derived exosomes (Diomede et al., 2018), human dental pulp stem cell-derived exosomes (Swanson et al., 2020; Xie et al., 2020), periodontal ligament stem cell-derived exosomes (Yu et al., 2021), human perivascular stem cell-derived exosomes (Xu et al., 2019), amniotic fluid stem cell-derived exosomes (Zavatti et al., 2020), and synovial mesenchymal stem cell-derived exosomes (Duan et al., 2021), has

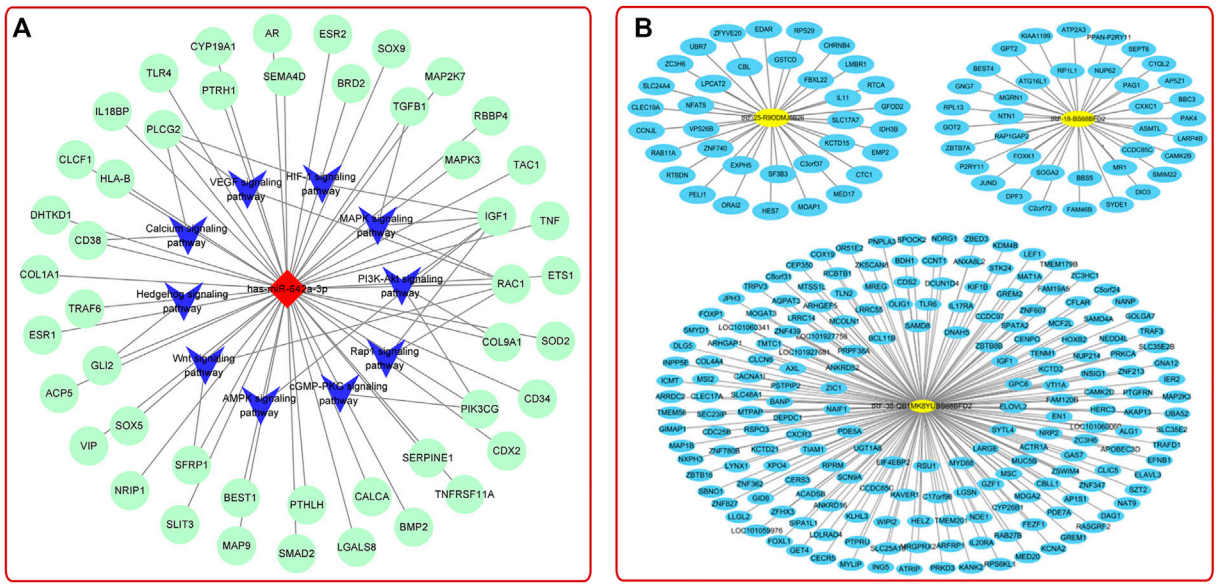

FIGURE 6 | (A) MiRNA-mRNA-KEGG interaction network analysis showed the top 10 OP-related pathways (Kong et al., 2021). **(B)** TRF-25, tRF-38, and tRF-18 were potential targets to OP treatment (Zhang Y. et al., 2018).

also been demonstrated to promote osteogenic differentiation, bone repair and cartilage repair. To be more specific, Zhang S. et al. (2019) found intravenous injection of hESC-MSCs-Exos could control pain and repair cartilage in temporomandibular joint OA (TMJ-OA). (**Figure 4D**). Especially, as the only known mammalian organ that can be regenerated annually, the deer antler is an ideal organ to overcome the insufficiency of stem cells. Lei et al. (2021) proved that the deer antler stem cell-derived exosomes could reduce inflammation, delay cell senescence, and promote bone and cartilage regeneration.

Bone/Cartilage Cell-Derived Exosomes

Osteoblasts and osteoclasts are the two most dominant cells that responsible for bone formation and resorption in the skeletal system, respectively (Yuan et al., 2016; Chen H. et al., 2020; Chen et al., 2020f). Osteoblast-osteoclast communication plays a key role in maintaining skeletal metabolism (Yuan et al., 2018). They coordinate with each other to maintain the homeostasis of the bone microenvironment (Deng et al., 2015; Chen et al., 2018a; Chen et al., 2018b; Li X. et al., 2020). Therefore, exploring the osteoblast-osteoclast communication will help understand the mechanism of bone homeostasis and provide a potential therapy for bone diseases treatment. Some studies suggested that exosomal miRNA took a crucial effect in osteoblast-osteoclast communication (Yin et al., 2017; Teotia et al., 2021). Sun et al. (2016) found that osteoclast-derived miR-214-containing exosomes could be secreted into the blood and inhibit the function of osteoblasts through interacting with ephrinA2 and EphA2 (**Figure 5A**). As well, Li et al. (2016) confirmed that osteoclast-targeted miR-214-3p inhibition augmented bone formation in aging OVX mice. On the contrary, osteoblast-derived exosomes could downregulate the heparanase gene and inhibit the differentiation of osteoclasts by increasing the expression of miR-503-3p during bone mineralization (Wang Q. et al., 2021). In addition, Ge et al. provided convincing evidence that osteoblast-derived exosomes contained osteogenesis-related proteins and could increase the number of bone trabeculae and bone volume in OVX rabbits (Ge et al., 2015; Ge et al., 2017; Sadat-Ali et al., 2021). Moreover, by transferring miRNA to activate the Wnt signaling pathway, osteoblast-derived exosomes could enhance the osteogenic differentiation of BMSCs (Cui et al., 2016). Additionally, osteoblast-derived EVs pretreated with histone deacetylase inhibitor trichostatin A (TSA) could significantly promote the osteogenic differentiation of hBMSCs and osteoblast mineralization (**Figure 5B**) (Man et al., 2021). These studies provided theoretical foundations for the clinical application of osteoblast-derived exosomes in the future. Surprisingly, Niedermair et al. (2020) showed that osteoblast-derived exosomes from patients with hip arthritis (CA), OP, and CA/OP could decrease BMSCs viability and alkaline phosphatase gene expression. This result suggested that the microenvironment of osteoblast-derived exosomal donor cells should be considered to avoid the opposite therapeutic effect.

Chondrogenic progenitor cell (CPC) is vital to maintain cartilage homeostasis and has received widespread attention in cartilage therapy (Kim et al., 2019). Currently, researchers have illustrated that CPC-derived exosomes play an essential part in MSC-chondrocyte communication and cartilage regeneration (Koelling et al., 2009; Yao and Wang, 2013). For example, Wang R. et al. (2020) discovered that CPC-derived exosomes not only enhanced chondrocytes proliferation and migration *in vitro*, but also promoted articular cartilage repair *in vivo*. In addition, several studies have shown that CPC-derived exosomes could also take effect in the therapy of bone defects. For instance, Zha et al. (2021) fabricated a VEGF@CPC-derived exosomes

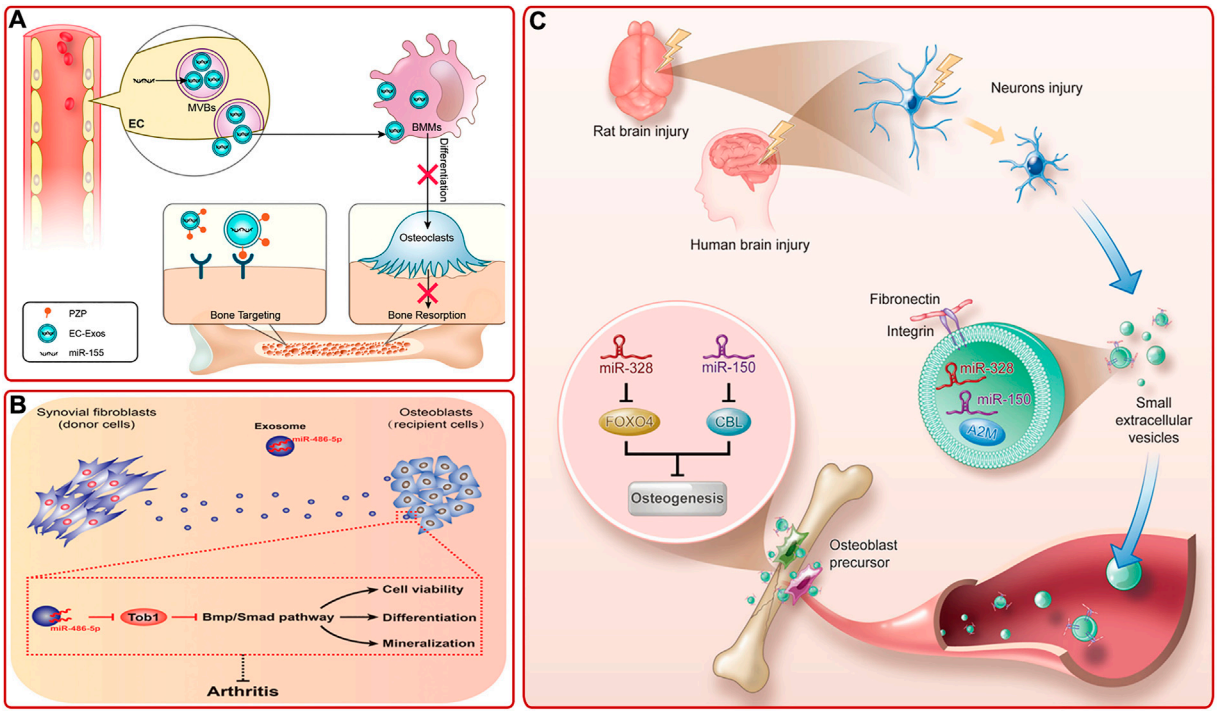

FIGURE 7 | (A) Diagram of bone targeting and functional EC-exos (Song et al., 2019). **(B)** FLSs-exos carrying miR-486-5p inhibited Tob1 to activate the BMP/Smad signaling pathway, thus enhancing osteoblast proliferation, mineralization, and differentiation, then alleviating RA (Chen J. et al., 2020). **(C)** Schematic mechanism of bone healing accelerated by the damaged brain. Damaged neurons released exosomes, which were rich in miR-328a-3p and miR-150-5p. They could target FOXO4 and CBL and thus promoted osteogenesis (Xia et al., 2021).

functionalized 3D-printed porous polycaprolactone (PCL) scaffold and verified that the functionalized scaffolds could induce osteogenic differentiation and promote angiogenesis and bone regeneration (**Figure 5C**). In contrast, current study showed that chondrocyte-derived exosomes could promote CPC proliferation, increase chondrogenesis markers' expression, and inhibit angiogenesis (Chen Y. et al., 2018). The multiple effects of bone/cartilage cell-derived exosomes in bone diseases had been listed in **Supplementary Table S2**.

Macrophage-Derived Exosomes

Macrophage-MSC communication plays a significant role in maintaining bone homeostasis and promoting bone establishment (Pieters et al., 2019; Chen K. et al., 2020; Kang et al., 2020; Wang D. et al., 2021). Previous studies have confirmed that macrophages communicate with MSC and affect its osteogenic differentiation through exosomes (Ekstrom et al., 2013). Moreover, recent studies demonstrated that exosomes derived from M0, M1, and M2 macrophages exerted distinct influences on the proliferation and differentiation of MSCs (Xia et al., 2020). For instance, researchers proved that M2 polarized macrophage-derived exosomes could inhibit the adipogenesis of BMSCs and promote its osteogenesis by mediating the miR-690/IRS-1/TAZ signaling axis (Li Z. et al., 2021). In another pathway, M2 polarized macrophage-derived exosomes could directly target salt-inducible kinase 2 and 3 genes to induce MSCs osteogenic differentiation (Xiong et al., 2020). In the clinic, it is universally acknowledged that diabetic patients often have a high incidence of fracture and prolonged healing time. A recent study illustrated that diabetic bone marrow macrophage-derived exosomes could inhibit the osteogenic differentiation of BMSCs and bone healing (Zhang D. et al., 2021). This inhibitory effect could be counteracted by inhibiting the expression of the miR-144-5p gene, which provided a new target for treating diabetic patients. Meanwhile, Bai et al. (2020) illuminated that macrophage-derived exosomes also have an influence on the growth of chondrocytes. Macrophage (pretreated with anti-inflammatory factor IL-4 or IL-13 *in vitro*) derived-exosomes, which containing Sox9 mRNA and protein, were beneficial to chondrocyte differentiation.

Based on the above functions of macrophage-derived exosomes, many studies combined them with biomaterials to improve osteogenic activity. For instance, Zhang T. et al. (2021) indicated that macrophage-derived exosomes modified titanium fostered osteoblast differentiation and mineralization, and osseointegration (Wei et al., 2019). Also, Liu et al. found that mineralized collagen pretreated with macrophage-derived exosomes could significantly facilitate MSC osteogenesis and bone regeneration (Liu A. et al., 2020). All these studies develop a novel way in the field of bone disease treatment. **Supplementary Table S3** summarized some recent studies on macrophage-derived exosomes in bone diseases.

Serum and Plasma-Derived Exosomes

There are a large number of exosomes in serum/plasma, and increasing studies pointed out that serum/plasma-derived exosomes have a great application prospect in early detection, diagnosis, and later treatment of bone diseases (Xie et al., 2018; Yang et al., 2021) (**Supplementary Table S4**). It is generally recognized that postmenopausal women often miss the best time for treating OP. In order to solve this problem, the researchers detected the plasma-derived exosomes of early postmenopausal women by small RNA sequencing method and concluded that exosomal miR-642a-3p might contribute to the prediction and diagnosis of early postmenopausal OP (**Figure 6A**) (Kong et al., 2021). Furthermore, Chen et al. found that plasma-derived exosomal TRF-25, TRF-38, and TRF-18 were closely related to OP (**Figure 6B**) (Zhang Y. et al., 2018). These studies use cutting-edge bioinformatics, and the results obtained by big data's analysis were provided references for further exploration of the pathological mechanism of OP. In addition, other studies have shown that plasma-derived exosomal surface protein markers (PSMB9, AARS, PCBP2, and VSIR) (Chen M. et al., 2020), serum-derived exosomal hsa_circ_0006859 (Zhi et al., 2021), and long non-coding RNAs (LncRNA) (Teng et al., 2020) could also be used as new markers for the diagnosis of OP. Recently, studies found that the serum-derived exosomal miRNAs varied with age, external stimulation, and other factors. For example, serum-derived exosomes in young mice with high expression of miRNA-19b-3p could boost the BMSCs osteogenic differentiation in fatigue aged osteoporotic mice, suggesting that the osteogenic capacity of serum-derived exosomes was related to the age of the donor (Xun et al., 2021). In addition, Du et al. found that radiation could affect bone metabolism and regeneration by regulating the expression of plasma-derived exosomal miRNAs (Du et al., 2021). This study provided a novel method for the treatment of radiation-induced bone diseases.

Other Exosomes

Studies on other exosomes also provided multiple strategies for bone diseases treatment (**Supplementary Table S5**). For example, Sun et al. (2019) pointed out that sinus mucosa-derived cell-derived exosomes and periosteum-derived cell-derived exosomes could mediate paracrine effects to promote osteogenesis. The endothelial cell (EC) is a kind of highly active cells located in the inner layer of blood vessels, which can secrete a variety of substances and is essential for organogenesis (Seton-Rogers, 2014). Song et al. (2019) provided evidence that EC-derived exosomes (EC-exos) contained miR-155 and could reduce the activity of osteoclasts and promote bone targeting (**Figure 7A**). Recently, studies proved that endothelial progenitor cells (EPCs), which are precursors of ECs, could also indirectly promote bone formation *via* secreting exosomes. EPC-derived exosomes could facilitate bone formation by stimulating angiogenesis or by promoting the recruitment and differentiation of osteoclast precursors *via* LncRNA-MALAT1 (Cui et al., 2019; Jia et al., 2019). Fibroblast-like synoviocytes (FLSs) are the most important cells at the pannus-cartilage junction (Bustamante et al., 2017). Recent studies showed that FLSs-derived exosomes could also stimulate bone growth (Tan et al., 2020). For instance, Chen J. et al. (2020) found that FLSs-derived exosomes (FLSs-exos) could be swallowed by osteoblasts in the mouse model of collagen-induced rheumatoid arthritis (RA) and activate osteogenesis-related signaling pathways by upregulating miR-486-5p and targeting Tob1 to promote osteogenic differentiation (**Figure 7B**). Clinically, there was an interesting phenomenon that concomitant traumatic brain injury could accelerate bone formation. To explore the underlying mechanism, Xia et al. (2021) revealed that damaged neurons released exosomes (rich in miR-328a-3p and miR-150-5p) could facilitate osteogenesis by targeting the 3′UTR of FOXO4 and CBL (**Figure 7C**).

CONCLUSION AND OUTLOOKS

Collectively, exosome is a natural nano-carrier containing various active cargos (miRNA, proteins, lipids, etc.) and plays a vital role in regulating bone metabolism. Based on their small size, wide source, and low immunogenicity, exosomes will have promising study and application prospects in the field of early diagnosis and therapy of bone diseases.

However, this field is still in the immature stage of basic research and preclinical exploration. The contents of exosomes are complex, which hinders the further exploration of their action mechanisms. It is worth mentioning that with the continuous development of proteomics and bioinformatics technology, several studies have been carried out more in-depth. For example, Chen M. et al. (2020) found four proteins closely related to OP (PSMB9, PCBP2, VSIR, and AARS) by quantitative proteomics and bioinformatics. This contributes to understanding the mechanism of bone disease. As the contents of exosomes are also related to different pathological conditions, external and internal factors, it is necessary to pay attention to the changes of conditions when studying the effects of different contents. In addition, a standardized separation and purification scheme is needed to further promote the clinical development of therapeutic exosomes. Consistent separation schemes and purification indexes are the premises of large-scale mass production for clinical application. The existing methods for the separation of exosomes include ultracentrifugation, commercial kit, size exclusion chromatography (SEC), tangential flow filtration (TFF), etc. Ultracentrifugation is the earliest and most widely used method. However, this method takes a long time and is difficult to meet the requirements of purity and yield. The commercial kit-based method takes less time than the ultracentrifugation method, but the specific principles and ingredients of most products have not been clarified. Recently, SEC and TFF based on size separation have been recognized by increasing researchers. Because it can obtain higher purity exosomes more easily. However, it is necessary to remove serum from the conditioned medium, which may change the activity of donor cells. In order to establish a perfect preparation system, Lim et al. proposed a set of relatively optimal manufacturing processes for researchers' reference (Reiner et al., 2017). For instance, the system should have

the characteristics of high capacity (unless the product is high potency), high yield, and reproducible purity. Meanwhile, the system should be a closed system with clear reaction principles and disposable components, and accord with serum-free culture. In addition, the manufacturing process should follow the Good Manufacturing Practice, which requires scientists to work together to establish a standard manufacturing process. Currently, another challenge for the clinical promotion of therapeutic exosomes is that they have not been strictly tested for clinical potency. In order to solve this problem, Lim et al. proposed a series of potentially quantifiable indicators to reach a consensus on the potency of different preparations (Witwer et al., 2019). Additionally, they proposed that different indicators should be evaluated by different independent laboratories and then analyzed and discussed together to ensure their credibility. In order to accelerate the application of exosomes, the cooperation of different teams is necessary. Furthermore, researchers can detect specific components that play vital roles in different diseases. Lim et al. proposed that under the guidance of major regulators, exosomes could be detected by a specific component to ensure that the potency of exosomes in the clinical treatment process is consistent (Gimona et al., 2021). In addition, the mode of exosomes' administration (systemic or local) needs to be considered. Previously, most studies used systemic injections. Recent studies combined exosomes with biomaterials to locally administer drugs to animals. These results showed excellent effects of promoting bone and cartilage formation. However, the difference between systemic administration and local administration in the treatment of bone diseases needs to be further studied. In particular, due to the above limitations, few studies have compared the effects of different sources-derived exosomes in bone diseases treatment. Personalized treatment for different diseases is gaining importance. It is hoped that after standardizing therapeutic exosomes, there will be increasing studies to analyze the therapeutic effects of different exosomes. Briefly, it will be a trend to study exosomes in the future, which will help to broaden our cognitive field of exosomes and provide more strategies for the treatment of bone diseases.

AUTHOR CONTRIBUTIONS

Writing-original draft preparation, FM, XX, and ZY; writing-review and editing, supervision and funding acquisition, FG, XW, and ZG. All authors listed have made a substantial, direct, and intellectual contribution to the work and approved it for publication.

FUNDING

The authors acknowledge the financial support from National Key R&D Program of China (2018YFC2001500); National Natural Science Foundation of China (91749204, 82172098, 81771491, 32101084). All funds received for open access publication fees from our institution.

SUPPLEMENTARY MATERIAL

The Supplementary Material for this article can be found online at: https://www.frontiersin.org/articles/10.3389/fbioe.2022.866627/full#supplementary-material

REFERENCES

Bai, J., Zhang, Y., Zheng, X., Huang, M., Cheng, W., Shan, H., et al. (2020). LncRNA MM2P-Induced, Exosome-Mediated Transfer of Sox9 from Monocyte-Derived Cells Modulates Primary Chondrocytes. *Cell Death Dis.* 11 (9), 763. doi:10.1038/s41419-020-02945-5

Bjørge, I. M., Kim, S. Y., Mano, J. F., Kalionis, B., and Chrzanowski, W. (2017). Extracellular Vesicles, Exosomes and Shedding Vesicles in Regenerative Medicine - a New Paradigm for Tissue Repair. *Biomater. Sci.* 6 (1), 60–78. doi:10.1039/c7bm00479f

Bustamante, M. F., Garcia-Carbonell, R., Whisenant, K. D., and Guma, M. (2017). Fibroblast-like Synoviocyte Metabolism in the Pathogenesis of Rheumatoid Arthritis. *Arthritis Res. Ther.* 19 (1), 110. doi:10.1186/s13075-017-1303-3

Chen, H., Fang, C., Zhi, X., Song, S., Gu, Y., Chen, X., et al. (2020a). Neobavaisoflavone Inhibits Osteoclastogenesis through Blocking RANKL Signalling-mediated TRAF6 and c-Src Recruitment and NF-κB, MAPK and Akt Pathways. *J. Cel Mol Med* 24 (16), 9067–9084. doi:10.1111/jcmm.15543

Chen, J., Liu, M., Luo, X., Peng, L., Zhao, Z., He, C., et al. (2020b). Exosomal miRNA-486-5p Derived from Rheumatoid Arthritis Fibroblast-like Synoviocytes Induces Osteoblast Differentiation through the Tob1/BMP/Smad Pathway. *Biomater. Sci.* 8 (12), 3430–3442. doi:10.1039/c9bm01761e

Chen, J., Zhang, H., Wu, X., Wang, F., Wang, Y., Gao, Q., et al. (2021a). PTHG2 Reduces Bone Loss in Ovariectomized Mice by Directing Bone Marrow Mesenchymal Stem Cell Fate. *Stem Cell Int.* 2021, 1–13. doi:10.1155/2021/8546739

Chen, K., Jiao, Y., Liu, L., Huang, M., He, C., He, W., et al. (2020c). Communications between Bone Marrow Macrophages and Bone Cells in Bone Remodeling. *Front. Cel Dev. Biol.* 8, 598263. doi:10.3389/fcell.2020.598263

Chen, M., Li, Y., Lv, H., Yin, P., Zhang, L., and Tang, P. (2020d). Quantitative Proteomics and Reverse Engineer Analysis Identified Plasma Exosome Derived Protein Markers Related to Osteoporosis. *J. Proteomics* 228, 103940. doi:10.1016/j.jprot.2020.103940

Chen, P., Zheng, L., Wang, Y., Tao, M., Xie, Z., Xia, C., et al. (2019). Desktop-stereolithography 3D Printing of a Radially Oriented Extracellular Matrix/mesenchymal Stem Cell Exosome Bioink for Osteochondral Defect Regeneration. *Theranostics* 9 (9), 2439–2459. doi:10.7150/thno.31017

Chen, W., Zhou, Z., Chen, D., Li, Y., Zhang, Q., and Su, J. (2021b). Bone Regeneration Using MMP-Cleavable Peptides-Based Hydrogels. *Gels* 7 (4), 199. doi:10.3390/gels7040199

Chen, X., Shi, Y., Xue, P., Ma, X., Li, J., and Zhang, J. (2020e). Mesenchymal Stem Cell-Derived Exosomal microRNA-136-5p Inhibits Chondrocyte Degeneration in Traumatic Osteoarthritis by Targeting ELF3. *Arthritis Res. Ther.* 22 (1), 256. doi:10.1186/s13075-020-02325-6

Chen, X., Zhang, Z., Hu, Y., Cui, J., Zhi, X., Li, X., et al. (2020f). Lactulose Suppresses Osteoclastogenesis and Ameliorates Estrogen Deficiency-Induced Bone Loss in Mice. *Aging Dis.* 11 (3), 629–641. doi:10.14336/AD.2019.0613

Chen, X., Zhi, X., Wang, J., and Su, J. (2018a). RANKL Signaling in Bone Marrow Mesenchymal Stem Cells Negatively Regulates Osteoblastic Bone Formation. *Bone Res.* 6, 34. doi:10.1038/s41413-018-0035-6

Chen, X., Zhi, X., Yin, Z., Li, X., Qin, L., Qiu, Z., et al. (2018b). 18β-Glycyrrhetinic Acid Inhibits Osteoclastogenesis *In Vivo* and *In Vitro* by Blocking RANKL-Mediated RANK-TRAF6 Interactions and NF-Kb and MAPK Signaling Pathways. *Front. Pharmacol.* 9, 647. doi:10.3389/fphar.2018.00647

Chen, Y., Xue, K., Zhang, X., Zheng, Z., and Liu, K. (2018c). Exosomes Derived from Mature Chondrocytes Facilitate Subcutaneous Stable Ectopic Chondrogenesis of Cartilage Progenitor Cells. *Stem Cel Res Ther.* 9 (1), 318. doi:10.1186/s13287-018-1047-2

Cheng, Q., Dai, Z., Shi, X., Duan, X., Wang, Y., Hou, T., et al. (2021). Expanding the Toolbox of Exosome-Based Modulators of Cell Functions. *Biomaterials* 277, 121129. doi:10.1016/j.biomaterials.2021.121129

Clynes, M. A., Harvey, N. C., Curtis, E. M., Fuggle, N. R., Dennison, E. M., and Cooper, C. (2020). The Epidemiology of Osteoporosis. *Br. Med. Bull.* 133 (1), 105–117. doi:10.1093/bmb/ldaa005

Cobelli, N. J., Leong, D. J., and Sun, H. B. (2017). Exosomes: Biology, Therapeutic Potential, and Emerging Role in Musculoskeletal Repair and Regeneration. *Ann. N.Y. Acad. Sci.* 1410 (1), 57–67. doi:10.1111/nyas.13469

Compston, J. E., McClung, M. R., and Leslie, W. D. (2019). Osteoporosis. *The Lancet* 393 (10169), 364–376. doi:10.1016/s0140-6736(18)32112-3

Cui, Y., Fu, S., Sun, D., Xing, J., Hou, T., and Wu, X. (2019). EPC-derived Exosomes Promote Osteoclastogenesis through LncRNA-MALAT1. *J. Cel Mol Med* 23 (6), 3843–3854. doi:10.1111/jcmm.14228

Cui, Y., Luan, J., Li, H., Zhou, X., and Han, J. (2016). Exosomes Derived from Mineralizing Osteoblasts Promote ST2 Cell Osteogenic Differentiation by Alteration of microRNA Expression. *FEBS Lett.* 590 (1), 185–192. doi:10.1002/1873-3468.12024

Debnath, S., Yallowitz, A. R., McCormick, J., Lalani, S., Zhang, T., Xu, R., et al. (2018). Discovery of a Periosteal Stem Cell Mediating Intramembranous Bone Formation. *Nature* 562 (7725), 133–139. doi:10.1038/s41586-018-0554-8

Deng, L., Wang, Y., Peng, Y., Wu, Y., Ding, Y., Jiang, Y., et al. (2015). Osteoblast-derived Microvesicles: A Novel Mechanism for Communication between Osteoblasts and Osteoclasts. *Bone* 79, 37–42. doi:10.1016/j.bone.2015.05.022

Diomede, F., Gugliandolo, A., Cardelli, P., Merciaro, I., Ettorre, V., Traini, T., et al. (2018). Three-dimensional Printed PLA Scaffold and Human Gingival Stem Cell-Derived Extracellular Vesicles: a New Tool for Bone Defect Repair. *Stem Cel Res Ther.* 9 (1), 104. doi:10.1186/s13287-018-0850-0

Du, Y., Tang, H., Gu, X., Shi, Y., Gong, P., and Yao, Y. (2021). Radiation Can Regulate the Expression of miRNAs Associated with Osteogenesis and Oxidation in Exosomes from Peripheral Blood Plasma. *Oxidative Med. Cell Longevity* 2021, 1–10. doi:10.1155/2021/6646323

Duan, A., Shen, K., Li, B., Li, C., Zhou, H., Kong, R., et al. (2021). Extracellular Vesicles Derived from LPS-Preconditioned Human Synovial Mesenchymal Stem Cells Inhibit Extracellular Matrix Degradation and Prevent Osteoarthritis of the Knee in a Mouse Model. *Stem Cel Res Ther.* 12 (1), 427. doi:10.1186/s13287-021-02507-2

Ekström, K., Omar, O., Granéli, C., Wang, X., Vazirisani, F., and Thomsen, P. (2013). Monocyte Exosomes Stimulate the Osteogenic Gene Expression of Mesenchymal Stem Cells. *PLoS One* 8 (9), e75227. doi:10.1371/journal.pone.0075227

Ensrud, K. E., and Crandall, C. J. (2017). Osteoporosis. *Ann. Intern. Med.* 167 (3), ITC17–ITC32. doi:10.7326/AITC201708010

Fan, J., Lee, C.-S., Kim, S., Chen, C., Aghaloo, T., and Lee, M. (2020). Generation of Small RNA-Modulated Exosome Mimetics for Bone Regeneration. *ACS Nano* 14 (9), 11973–11984. doi:10.1021/acsnano.0c05122

Fan, Y., Hanai, J.-i., Le, P. T., Bi, R., Maridas, D., DeMambro, V., et al. (2017). Parathyroid Hormone Directs Bone Marrow Mesenchymal Cell Fate. *Cel Metab.* 25 (3), 661–672. doi:10.1016/j.cmet.2017.01.001

Fang, C., Guo, J.-w., Wang, Y.-j., Li, X.-q., Zhang, H., Cui, J., et al. (2021). Diterbutyl Phthalate Attenuates Osteoarthritis in ACLT Mice via Suppressing ERK/c-fos/NFATc1 Pathway, and Subsequently Inhibiting Subchondral Osteoclast Fusion. *Acta Pharmacol. Sin* 2021, 543. doi:10.1038/s41401-021-00747-9

Force, U. S. P. S. T., Curry, S. J., Krist, A. H., Owens, D. K., Barry, M. J., Caughey, A. B., et al. (2018). Screening for Osteoporosis to Prevent Fractures. *JAMA* 319 (24), 2521–2531. doi:10.1001/jama.2018.7498

Furuta, T., Miyaki, S., Ishitobi, H., Ogura, T., Kato, Y., Kamei, N., et al. (2016). Mesenchymal Stem Cell-Derived Exosomes Promote Fracture Healing in a Mouse Model. *Stem Cell Transl Med* 5 (12), 1620–1630. doi:10.5966/sctm.2015-0285

Gao, Q., Wang, L., Wang, S., Huang, B., Jing, Y., and Su, J. (2021). Bone Marrow Mesenchymal Stromal Cells: Identification, Classification, and Differentiation. *Front. Cel Dev. Biol.* 9, 787118. doi:10.3389/fcell.2021.787118

Ge, M., Ke, R., Cai, T., Yang, J., and Mu, X. (2015). Identification and Proteomic Analysis of Osteoblast-Derived Exosomes. *Biochem. Biophysical Res. Commun.* 467 (1), 27–32. doi:10.1016/j.bbrc.2015.09.135

Ge, M., Wu, Y., Ke, R., Cai, T., Yang, J., and Mu, X. (2017). Value of Osteoblast-Derived Exosomes in Bone Diseases. *J. Craniofac. Surg.* 28 (4), 866–870. doi:10.1097/SCS.0000000000003463

Gimona, M., Brizzi, M. F., Choo, A. B. H., Dominici, M., Davidson, S. M., Grillari, J., et al. (2021). Critical Considerations for the Development of Potency Tests for Therapeutic Applications of Mesenchymal Stromal Cell-Derived Small Extracellular Vesicles. *Cytotherapy* 23 (5), 373–380. doi:10.1016/j.jcyt.2021.01.001

Glyn-Jones, S., Palmer, A. J. R., Agricola, R., Price, A. J., Vincent, T. L., Weinans, H., et al. (2015). Osteoarthritis. *The Lancet* 386 (9991), 376–387. doi:10.1016/s0140-6736(14)60802-3

Han, C., Sun, X., Liu, L., Jiang, H., Shen, Y., Xu, X., et al. (2016). Exosomes and Their Therapeutic Potentials of Stem Cells. *Stem Cell Int.* 2016, 1–11. doi:10.1155/2016/7653489

Hao, Z.-C., Wang, S.-Z., Zhang, X.-J., and Lu, J. (2016). Stem Cell Therapy: a Promising Biological Strategy for Tendon-Bone Healing after Anterior Cruciate Ligament Reconstruction. *Cell Prolif.* 49 (2), 154–162. doi:10.1111/cpr.12242

Harding, C., Heuser, J., and Stahl, P. (1983). Receptor-mediated Endocytosis of Transferrin and Recycling of the Transferrin Receptor in Rat Reticulocytes. *J. Cel Biol.* 97, 329–339. doi:10.1083/jcb.97.2.329

Hassan, M. Q., Maeda, Y., Taipaleenmaki, H., Zhang, W., Jafferji, M., Gordon, J. A. R., et al. (2012). miR-218 Directs a Wnt Signaling Circuit to Promote Differentiation of Osteoblasts and Osteomimicry of Metastatic Cancer Cells. *J. Biol. Chem.* 287 (50), 42084–42092. doi:10.1074/jbc.M112.377515

He, L., Chen, Y., Ke, Z., Pang, M., Yang, B., Feng, F., et al. (2020a). Exosomes Derived from miRNA-210 Overexpressing Bone Marrow Mesenchymal Stem Cells Protect Lipopolysaccharide Induced Chondrocytes Injury via the NF-Kb Pathway. *Gene* 751, 144764. doi:10.1016/j.gene.2020.144764

He, L., He, T., Xing, J., Zhou, Q., Fan, L., Liu, C., et al. (2020b). Bone Marrow Mesenchymal Stem Cell-Derived Exosomes Protect Cartilage Damage and Relieve Knee Osteoarthritis Pain in a Rat Model of Osteoarthritis. *Stem Cel Res Ther.* 11 (1), 276. doi:10.1186/s13287-020-01781-w

Hernlund, E., Svedbom, A., Ivergård, M., Compston, J., Cooper, C., Stenmark, J., et al. (2013). Osteoporosis in the European Union: Medical Management, Epidemiology and Economic burden. *Arch. Osteoporos.* 8, 136. doi:10.1007/s11657-013-0136-1

Hingert, D., Ekström, K., Aldridge, J., Crescitelli, R., and Brisby, H. (2020). Extracellular Vesicles from Human Mesenchymal Stem Cells Expedite Chondrogenesis in 3D Human Degenerative Disc Cell Cultures. *Stem Cel Res Ther.* 11 (1), 323. doi:10.1186/s13287-020-01832-2

Hu, C., Ashok, D., Nisbet, D. R., and Gautam, V. (2019). Bioinspired Surface Modification of Orthopedic Implants for Bone Tissue Engineering. *Biomaterials* 219, 119366. doi:10.1016/j.biomaterials.2019.119366

Hu, H., Dong, L., Bu, Z., Shen, Y., Luo, J., Zhang, H., et al. (2020a). miR-23a-3p-abundant Small Extracellular Vesicles Released from Gelma/nanoclay Hydrogel for Cartilage Regeneration. *J. Extracellular Vesicles* 9 (1), 1778883. doi:10.1080/20013078.2020.1778883

Hu, Y., Chen, X., Wang, S., Jing, Y., and Su, J. (2021a). Subchondral Bone Microenvironment in Osteoarthritis and Pain. *Bone Res.* 9 (1), 20. doi:10.1038/s41413-021-00147-z

Hu, Y., Li, X., Zhang, Q., Gu, Z., Luo, Y., Guo, J., et al. (2021b). Exosome-guided Bone Targeted Delivery of Antagomir-188 as an Anabolic Therapy for Bone Loss. *Bioactive Mater.* 6 (9), 2905–2913. doi:10.1016/j.bioactmat.2021.02.014

Hu, Y., Zhang, Y., Ni, C.-Y., Chen, C.-Y., Rao, S.-S., Yin, H., et al. (2020b). Human Umbilical Cord Mesenchymal Stromal Cells-Derived Extracellular Vesicles Exert Potent Bone Protective Effects by CLEC11A-Mediated Regulation of Bone Metabolism. *Theranostics* 10 (5), 2293–2308. doi:10.7150/thno.39238

Huang, C.-C., Kang, M., Lu, Y., Shirazi, S., Diaz, J. I., Cooper, L. F., et al. (2020). Functionally Engineered Extracellular Vesicles Improve Bone Regeneration. *Acta Biomater.* 109, 182–194. doi:10.1016/j.actbio.2020.04.017

Huang, C.-C., Kang, M., Shirazi, S., Lu, Y., Cooper, L. F., Gajendrareddy, P., et al. (2021a). 3D Encapsulation and Tethering of Functionally Engineered Extracellular Vesicles to Hydrogels. *Acta Biomater.* 126, 199–210. doi:10.1016/j.actbio.2021.03.030

Huang, J., Xiong, J., Yang, L., Zhang, J., Sun, S., and Liang, Y. (2021b). Cell-free Exosome-Laden Scaffolds for Tissue Repair. *Nanoscale* 13 (19), 8740–8750. doi:10.1039/d1nr01314a

Huang, Y., Xu, Y., Feng, S., He, P., Sheng, B., and Ni, J. (2021c). miR-19b Enhances Osteogenic Differentiation of Mesenchymal Stem Cells and Promotes Fracture Healing through the WWP1/Smurf2-Mediated KLF5/β-Catenin Signaling Pathway. *Exp. Mol. Med.* 53 (5), 973–985. doi:10.1038/s12276-021-00631-w

Huang, Y., Zhang, X., Zhan, J., Yan, Z., Chen, D., Xue, X., et al. (2021d). Bone Marrow Mesenchymal Stem Cell-Derived Exosomal miR-206 Promotes Osteoblast Proliferation and Differentiation in Osteoarthritis by Reducing Elf3. *J. Cel Mol Med* 25 (16), 7734–7745. doi:10.1111/jcmm.16654

Hunter, D. J., and Bierma-Zeinstra, S. (2019). Osteoarthritis. *The Lancet* 393 (10182), 1745–1759. doi:10.1016/s0140-6736(19)30417-9

Hunter, D. J., Schofield, D., and Callander, E. (2014). The Individual and Socioeconomic Impact of Osteoarthritis. *Nat. Rev. Rheumatol.* 10 (7), 437–441. doi:10.1038/nrrheum.2014.44

Jia, Y., Qiu, S., Xu, J., Kang, Q., and Chai, Y. (2020). Exosomes Secreted by Young Mesenchymal Stem Cells Promote New Bone Formation during Distraction Osteogenesis in Older Rats. *Calcif Tissue Int.* 106 (5), 509–517. doi:10.1007/s00223-019-00656-4

Jia, Y., Zhu, Y., Qiu, S., Xu, J., and Chai, Y. (2019). Exosomes Secreted by Endothelial Progenitor Cells Accelerate Bone Regeneration during Distraction Osteogenesis by Stimulating Angiogenesis. *Stem Cel Res Ther* 10 (1), 12. doi:10.1186/s13287-018-1115-7

Jiang, F., Zhang, W., Zhou, M., Zhou, Z., Shen, M., Chen, N., et al. (2020). Human Amniotic Mesenchymal Stromal Cells Promote Bone Regeneration via Activating Endogenous Regeneration. *Theranostics* 10 (14), 6216–6230. doi:10.7150/thno.45249

Jiang, S., Tian, G., Yang, Z., Gao, X., Wang, F., Li, J., et al. (2021). Enhancement of Acellular Cartilage Matrix Scaffold by Wharton's Jelly Mesenchymal Stem Cell-Derived Exosomes to Promote Osteochondral Regeneration. *Bioactive Mater.* 6 (9), 2711–2728. doi:10.1016/j.bioactmat.2021.01.031

Jin, Y., Xu, M., Zhu, H., Dong, C., Ji, J., Liu, Y., et al. (2021). Therapeutic Effects of Bone Marrow Mesenchymal Stem Cells-derived Exosomes on Osteoarthritis. *J. Cel Mol Med* 25 (19), 9281–9294. doi:10.1111/jcmm.16860

Jin, Z., Ren, J., and Qi, S. (2020). Human Bone Mesenchymal Stem Cells-Derived Exosomes Overexpressing microRNA-26a-5p Alleviate Osteoarthritis via Down-Regulation of PTGS2. *Int. Immunopharmacology* 78, 105946. doi:10.1016/j.intimp.2019.105946

Johnstone, R. M., Adam, M., Hammond, J. R., Orr, L., and Turbide, C. (1987). Vesicle Formation during Reticulocyte Maturation. Association of Plasma Membrane Activities with Released Vesicles (Exosomes). *J. Biol. Chem.* 262 (19), 9412–9420. doi:10.1016/s0021-9258(18)48095-7

Kang, M., Huang, C.-C., Lu, Y., Shirazi, S., Gajendrareddy, P., Ravindran, S., et al. (2020). Bone Regeneration Is Mediated by Macrophage Extracellular Vesicles. *Bone* 141, 115627. doi:10.1016/j.bone.2020.115627

Kim, Y. G., Park, U., Park, B. J., and Kim, K. (2019). Exosome-mediated Bidirectional Signaling between Mesenchymal Stem Cells and Chondrocytes for Enhanced Chondrogenesis. *Biotechnol. Bioproc. E* 24 (5), 734–744. doi:10.1007/s12257-019-0332-y

Klumperman, J., and Raposo, G. (2014). The Complex Ultrastructure of the Endolysosomal System. *Cold Spring Harbor Perspect. Biol.* 6, a016857. doi:10.1101/cshperspect.a016857

Koelling, S., Kruegel, J., Irmer, M., Path, J. R., Sadowski, B., Miro, X., et al. (2009). Migratory Chondrogenic Progenitor Cells from Repair Tissue during the Later Stages of Human Osteoarthritis. *Cell Stem Cell* 4 (4), 324–335. doi:10.1016/j.stem.2009.01.015

Kong, D., Chen, T., Zheng, X., Yang, T., Zhang, Y., and Shao, J. (2021). Comparative Profile of Exosomal microRNAs in Postmenopausal Women with Various Bone mineral Densities by Small RNA Sequencing. *Genomics* 113 (3), 1514–1521. doi:10.1016/j.ygeno.2021.03.028

Kuang, M.-j., Huang, Y., Zhao, X.-g., Zhang, R., Ma, J.-x., Wang, D.-c., et al. (2019). Exosomes Derived from Wharton's Jelly of Human Umbilical Cord Mesenchymal Stem Cells Reduce Osteocyte Apoptosis in Glucocorticoid-Induced Osteonecrosis of the Femoral Head in Rats via the miR-21-PTEN-AKT Signalling Pathway. *Int. J. Biol. Sci.* 15 (9), 1861–1871. doi:10.7150/ijbs.32262

Kyung Kim, D., Lee, S., Kim, M., Jeong, Y., and Lee, S. (2021). Exosome-coated Silk Fibroin 3D-Scaffold for Inducing Osteogenic Differentiation of Bone Marrow Derived Mesenchymal Stem Cells. *Chem. Eng. J.* 406, 127080. doi:10.1016/j.cej.2020.127080

Lawson, C., Vicencio, J. M., Yellon, D. M., and Davidson, S. M. (2016). Microvesicles and Exosomes: New Players in Metabolic and Cardiovascular Disease. *J. Endocrinol.* 228 (2), R57–R71. doi:10.1530/JOE-15-0201

Lee, K.-J., and Goodman, S. B. (2015). Identification of Periprosthetic Joint Infection after Total Hip Arthroplasty. *J. Orthopaedic Translation* 3 (1), 21–25. doi:10.1016/j.jot.2014.10.001

Lei, J., Jiang, X., Li, W., Ren, J., Wang, D., Ji, Z., et al. (2021). Exosomes from Antler Stem Cells Alleviate Mesenchymal Stem Cell Senescence and Osteoarthritis. *Protein Cell* 13, 220–226. doi:10.1007/s13238-021-00860-9

Li, D., Liu, J., Guo, B., Liang, C., Dang, L., Lu, C., et al. (2016). Osteoclast-derived Exosomal miR-214-3p Inhibits Osteoblastic Bone Formation. *Nat. Commun.* 7, 10872. doi:10.1038/ncomms10872

Li, Q., Huang, Q.-P., Wang, Y.-L., and Huang, Q.-S. (2018a). Extracellular Vesicle-Mediated Bone Metabolism in the Bone Microenvironment. *J. Bone Miner Metab.* 36 (1), 1–11. doi:10.1007/s00774-017-0860-5

Li, S., Liu, J., Liu, S., Jiao, W., and Wang, X. (2021a). Chitosan Oligosaccharides Packaged into Rat Adipose Mesenchymal Stem Cells-Derived Extracellular Vesicles Facilitating Cartilage Injury Repair and Alleviating Osteoarthritis. *J. Nanobiotechnol* 19 (1), 343. doi:10.1186/s12951-021-01086-x

Li, T., Xia, M., Gao, Y., Chen, Y., and Xu, Y. (2015). Human Umbilical Cord Mesenchymal Stem Cells: an Overview of Their Potential in Cell-Based Therapy. *Expert Opin. Biol. Ther.* 15, 1293–1306. doi:10.1517/14712598.2015.1051528

Li, W., Liu, Y., Zhang, P., Tang, Y., Zhou, M., Jiang, W., et al. (2018b). Tissue-Engineered Bone Immobilized with Human Adipose Stem Cells-Derived Exosomes Promotes Bone Regeneration. *ACS Appl. Mater. Inter.* 10 (6), 5240–5254. doi:10.1021/acsami.7b17620

Li, X., Wang, L., Huang, B., Gu, Y., Luo, Y., Zhi, X., et al. (2020a). Targeting Actin-Bundling Protein L-Plastin as an Anabolic Therapy for Bone Loss. *Sci. Adv.* 6. doi:10.1126/sciadv.abb7135

Li, Y., Wang, J., Ma, Y., Du, W., Feng, H., Feng, K., et al. (2020b). MicroRNA-15b Shuttled by Bone Marrow Mesenchymal Stem Cell-Derived Extracellular Vesicles Binds to WWP1 and Promotes Osteogenic Differentiation. *Arthritis Res. Ther.* 22 (1), 269. doi:10.1186/s13075-020-02316-7

Li, Z., Wang, Y., Li, S., and Li, Y. (2021b). Exosomes Derived from M2 Macrophages Facilitate Osteogenesis and Reduce Adipogenesis of BMSCs. *Front. Endocrinol.* 12, 680328. doi:10.3389/fendo.2021.680328

Liang, B., Liang, J.-M., Ding, J.-N., Xu, J., Xu, J.-G., and Chai, Y.-M. (2019). Dimethyloxaloylglycine-stimulated Human Bone Marrow Mesenchymal Stem Cell-Derived Exosomes Enhance Bone Regeneration through Angiogenesis by Targeting the AKT/mTOR Pathway. *Stem Cel Res Ther* 10 (1), 335. doi:10.1186/s13287-019-1410-y

Liang, Z., Yang, L., and Lv, Y. (2021). Exosome Derived from Mesenchymal Stem Cells Mediates Hypoxia-specific BMP2 Gene Delivery and Enhances Bone Regeneration. *Chem. Eng. J.* 422, 130084. doi:10.1016/j.cej.2021.130084

Liao, Q., Li, B. J., Li, Y., Xiao, Y., Zeng, H., Liu, J. M., et al. (2021). Low-intensity Pulsed Ultrasound Promotes Osteoarthritic Cartilage Regeneration by BMSC-Derived Exosomes via Modulating the NF-Kb Signaling Pathway. *Int. Immunopharmacology* 97, 107824. doi:10.1016/j.intimp.2021.107824

Liao, W., Ning, Y., Xu, H.-J., Zou, W.-Z., Hu, J., Liu, X.-Z., et al. (2019). BMSC-derived Exosomes Carrying microRNA-122-5p Promote Proliferation of Osteoblasts in Osteonecrosis of the Femoral Head. *Clin. Sci. (Lond)* 133 (18), 1955–1975. doi:10.1042/CS20181064

Liu, A., Jin, S., Fu, C., Cui, S., Zhang, T., Zhu, L., et al. (2020a). Macrophage-derived Small Extracellular Vesicles Promote Biomimetic Mineralized Collagen-

Mediated Endogenous Bone Regeneration. *Int. J. Oral Sci.* 12 (1), 33. doi:10.1038/s41368-020-00100-6

Liu, A., Lin, D., Zhao, H., Chen, L., Cai, B., Lin, K., et al. (2021a). Optimized BMSC-Derived Osteoinductive Exosomes Immobilized in Hierarchical Scaffold via Lyophilization for Bone Repair through Bmpr2/Acvr2b Competitive Receptor-Activated Smad Pathway. *Biomaterials* 272, 120718. doi:10.1016/j.biomaterials.2021.120718

Liu, C., Li, Y., Yang, Z., Zhou, Z., Lou, Z., and Zhang, Q. (2020b). Kartogenin Enhances the Therapeutic Effect of Bone Marrow Mesenchymal Stem Cells Derived Exosomes in Cartilage Repair. *Nanomedicine* 15, 273–288. doi:10.2217/nnm-2019-0208

Liu, L., Yu, F., Li, L., Zhou, L., Zhou, T., Xu, Y., et al. (2021b). Bone Marrow Stromal Cells Stimulated by Strontium-Substituted Calcium Silicate Ceramics: Release of Exosomal miR-146a Regulates Osteogenesis and Angiogenesis. *Acta Biomater.* 119, 444–457. doi:10.1016/j.actbio.2020.10.038

Liu, S., Xu, X., Liang, S., Chen, Z., Zhang, Y., Qian, A., et al. (2020c). The Application of MSCs-Derived Extracellular Vesicles in Bone Disorders: Novel Cell-free Therapeutic Strategy. *Front. Cel Dev. Biol.* 8, 619. doi:10.3389/fcell.2020.00619

Liu, W., Li, L., Rong, Y., Qian, D., Chen, J., Zhou, Z., et al. (2020d). Hypoxic Mesenchymal Stem Cell-Derived Exosomes Promote Bone Fracture Healing by the Transfer of miR-126. *Acta Biomater.* 103, 196–212. doi:10.1016/j.actbio.2019.12.020

Liu, X., Yang, Y., Li, Y., Niu, X., Zhao, B., Wang, Y., et al. (2017). Integration of Stem Cell-Derived Exosomes with *In Situ* Hydrogel Glue as a Promising Tissue Patch for Articular Cartilage Regeneration. *Nanoscale* 9 (13), 4430–4438. doi:10.1039/c7nr00352h

Lu, Z., Chen, Y., Dunstan, C., Roohani-Esfahani, S., and Zreiqat, H. (2017). Priming Adipose Stem Cells with Tumor Necrosis Factor-Alpha Preconditioning Potentiates Their Exosome Efficacy for Bone Regeneration. *Tissue Eng. A* 23 (21-22), 1212–1220. doi:10.1089/ten.tea.2016.0548

Luo, Z.-W., Li, F.-X. -Z., Liu, Y.-W., Rao, S.-S., Yin, H., Huang, J., et al. (2019). Aptamer-functionalized Exosomes from Bone Marrow Stromal Cells Target Bone to Promote Bone Regeneration. *Nanoscale* 11 (43), 20884–20892. doi:10.1039/c9nr02791b

Man, K., Brunet, M. Y., Fernandez-Rhodes, M., Williams, S., Heaney, L. M., Gethings, L. A., et al. (2021). Epigenetic Reprogramming Enhances the Therapeutic Efficacy of Osteoblast-derived Extracellular Vesicles to Promote Human Bone Marrow Stem Cell Osteogenic Differentiation. *J. Extracellular Vesicles* 10 (9), e12118. doi:10.1002/jev2.12118

Mao, G., Xu, Y., Long, D., Sun, H., Li, H., Xin, R., et al. (2021). Exosome-transported circRNA_0001236 Enhances Chondrogenesis and Suppress Cartilage Degradation via the miR-3677-3p/Sox9 axis. *Stem Cel Res Ther* 12 (1), 389. doi:10.1186/s13287-021-02431-5

Masaoutis, C., and Theocharis, S. (2019). The Role of Exosomes in Bone Remodeling: Implications for Bone Physiology and Disease. *Dis. Markers* 2019, 1–12. doi:10.1155/2019/9417914

Mathieu, M., Martin-Jaular, L., Lavieu, G., and Théry, C. (2019). Specificities of Secretion and Uptake of Exosomes and Other Extracellular Vesicles for Cell-To-Cell Communication. *Nat. Cel Biol* 21 (1), 9–17. doi:10.1038/s41556-018-0250-9

Mei, Z., Dong, X., Qian, Y., Hong, D., Xie, Z., Yao, G., et al. (2020). Association between the Metabolome and Bone mineral Density in a Chinese Population. *EBioMedicine* 62, 103111. doi:10.1016/j.ebiom.2020.103111

Metavarayuth, K., Maturavongsadit, P., Chen, X., Sitasuwan, P., Lu, L., Su, J., et al. (2019). Nanotopographical Cues Mediate Osteogenesis of Stem Cells on Virus Substrates through BMP-2 Intermediate. *Nano Lett.* 19 (12), 8372–8380. doi:10.1021/acs.nanolett.9b02001

Ni, Z., Zhou, S., Li, S., Kuang, L., Chen, H., Luo, X., et al. (2020). Exosomes: Roles and Therapeutic Potential in Osteoarthritis. *Bone Res.* 8, 25. doi:10.1038/s41413-020-0100-9

Niedermair, T., Lukas, C., Li, S., Stöckl, S., Craiovan, B., Brochhausen, C., et al. (2020). Influence of Extracellular Vesicles Isolated from Osteoblasts of Patients with Cox-Arthrosis And/or Osteoporosis on Metabolism and Osteogenic Differentiation of BMSCs. *Front. Bioeng. Biotechnol.* 8, 615520. doi:10.3389/fbioe.2020.615520

Norouzi-Barough, L., Shirian, S., Gorji, A., and Sadeghi, M. (2021). Therapeutic Potential of Mesenchymal Stem Cell-Derived Exosomes as a Cell-free Therapy Approach for the Treatment of Skin, Bone, and Cartilage Defects. *Connect. Tissue Res.* 63, 83–96. doi:10.1080/03008207.2021.1887855

Pan, B.-T., and Johnstone, R. M. (1983). Fate of the Transferrin Receptor during Maturation of Sheep Reticulocytes *In Vitro*: Selective Externalization of the Receptor. *Cell* 33, 967–978. doi:10.1016/0092-8674(83)90040-5

Pegtel, D. M., Cosmopoulos, K., Thorley-Lawson, D. A., van Eijndhoven, M. A. J., Hopmans, E. S., Lindenberg, J. L., et al. (2010). Functional Delivery of Viral miRNAs via Exosomes. *Proc. Natl. Acad. Sci. U.S.A.* 107 (14), 6328–6333. doi:10.1073/pnas.0914843107

Perez, J. R., Kouroupis, D., Li, D. J., Best, T. M., Kaplan, L., and Correa, D. (2018). Tissue Engineering and Cell-Based Therapies for Fractures and Bone Defects. *Front. Bioeng. Biotechnol.* 6, 105. doi:10.3389/fbioe.2018.00105

Pieters, B. C. H., Cappariello, A., van den Bosch, M. H. J., van Lent, P. L. E. M., Teti, A., and van de Loo, F. A. J. (2019). Macrophage-Derived Extracellular Vesicles as Carriers of Alarmins and Their Potential Involvement in Bone Homeostasis. *Front. Immunol.* 10, 1901. doi:10.3389/fimmu.2019.01901

Qi, X., Zhang, J., Yuan, H., Xu, Z., Li, Q., Niu, X., et al. (2016). Exosomes Secreted by Human-Induced Pluripotent Stem Cell-Derived Mesenchymal Stem Cells Repair Critical-Sized Bone Defects through Enhanced Angiogenesis and Osteogenesis in Osteoporotic Rats. *Int. J. Biol. Sci.* 12 (7), 836–849. doi:10.7150/ijbs.14809

Qin, Y., Sun, R., Wu, C., Wang, L., and Zhang, C. (2016). Exosome: A Novel Approach to Stimulate Bone Regeneration through Regulation of Osteogenesis and Angiogenesis. *Ijms* 17 (5), 712. doi:10.3390/ijms17050712

Reiner, A. T., Witwer, K. W., van Balkom, B. W. M., de Beer, J., Brodie, C., Corteling, R. L., et al. (2017). Concise Review: Developing Best-Practice Models for the Therapeutic Use of Extracellular Vesicles. *Stem Cell Transl Med* 6 (8), 1730–1739. doi:10.1002/sctm.17-0055

Ren, L., Song, Z.-j., Cai, Q.-w., Chen, R.-x., Zou, Y., Fu, Q., et al. (2019). Adipose Mesenchymal Stem Cell-Derived Exosomes Ameliorate Hypoxia/serum Deprivation-Induced Osteocyte Apoptosis and Osteocyte-Mediated Osteoclastogenesis *In Vitro*. *Biochem. Biophysical Res. Commun.* 508 (1), 138–144. doi:10.1016/j.bbrc.2018.11.109

Ren, X., Liu, H., Wu, X., Weng, W., Wang, X., and Su, J. (2021). Reactive Oxygen Species (ROS)-Responsive Biomaterials for the Treatment of Bone-Related Diseases. *Front. Bioeng. Biotechnol.* 9, 820468. doi:10.3389/fbioe.2021.820468

Sadat-Ali, M., Al-Dakheel, D. A., Al-Turki, H. A., and Acharya, S. (2021). Efficacy of Autologous Bone Marrow Derived Mesenchymal Stem Cells (MSCs), Osteoblasts and Osteoblasts Derived Exosome in the Reversal of Ovariectomy (OVX) Induced Osteoporosis in Rabbit Model. *AM. J. Transl Res.* 13, 6175–6181.

Seton-Rogers, S. (2014). Endothelial Cells Create a Niche. *Nat. Rev. Cancer* 14 (5), 298. doi:10.1038/nrc3730

Song, H., Li, X., Zhao, Z., Qian, J., Wang, Y., Cui, J., et al. (2019). Reversal of Osteoporotic Activity by Endothelial Cell-Secreted Bone Targeting and Biocompatible Exosomes. *Nano Lett.* 19 (5), 3040–3048. doi:10.1021/acs.nanolett.9b00287

Sun, R., Xu, S., and Wang, Z. (2019). Rat Sinus Mucosa- and Periosteum-derived Exosomes Accelerate Osteogenesis. *J. Cell Physiol.* 234 (12), 21947–21961. doi:10.1002/jcp.28758

Sun, W., Zhao, C., Li, Y., Wang, L., Nie, G., Peng, J., et al. (2016). Osteoclast-derived microRNA-Containing Exosomes Selectively Inhibit Osteoblast Activity. *Cell Discov* 2, 16015. doi:10.1038/celldisc.2016.15

Swanson, W. B., Zhang, Z., Xiu, K., Gong, T., Eberle, M., Wang, Z., et al. (2020). Scaffolds with Controlled Release of Pro-mineralization Exosomes to Promote Craniofacial Bone Healing without Cell Transplantation. *Acta Biomater.* 118, 215–232. doi:10.1016/j.actbio.2020.09.052

Tan, F., Wang, D., and Yuan, Z. (2020). The Fibroblast-like Synoviocyte Derived Exosomal Long Non-coding RNA H19 Alleviates Osteoarthritis Progression through the miR-106b-5p/TIMP2 Axis. *Inflammation* 43 (4), 1498–1509. doi:10.1007/s10753-020-01227-8

Tao, S.-C., Guo, S.-C., and Zhang, C.-Q. (2018). Modularized Extracellular Vesicles: The Dawn of Prospective Personalized and Precision Medicine. *Adv. Sci.* 5 (2), 1700449. doi:10.1002/advs.201700449

Teng, Z., Zhu, Y., Zhang, X., Teng, Y., and Lu, S. (2020). Osteoporosis Is Characterized by Altered Expression of Exosomal Long Non-coding RNAs. *Front. Genet.* 11, 566959. doi:10.3389/fgene.2020.566959

Teotia, A. K., Qayoom, I., Singh, P., Mishra, A., Jaiman, D., Seppälä, J., et al. (2021). Exosome-Functionalized Ceramic Bone Substitute Promotes Critical-Sized Bone Defect Repair in Rats. *ACS Appl. Bio Mater.* 4 (4), 3716–3726. doi:10.1021/acsabm.1c00311

Théry, C., Witwer, K. W., Aikawa, E., Alcaraz, M. J., Anderson, J. D., Andriantsitohaina, R., et al. (2018). Minimal Information for Studies of Extracellular Vesicles 2018 (MISEV2018): a Position Statement of the International Society for Extracellular Vesicles and Update of the MISEV2014 Guidelines. *J. Extracell Vesicles* 7 (1), 1535750. doi:10.1080/20013078.2018.1535750

Théry, C., Zitvogel, L., and Amigorena, S. (2002). Exosomes: Composition, Biogenesis and Function. *Nat. Rev. Immunol.* 2 (8), 569–579. doi:10.1038/nri855

van der Pol, E., Böing, A. N., Harrison, P., Sturk, A., and Nieuwland, R. (2012). Classification, Functions, and Clinical Relevance of Extracellular Vesicles. *Pharmacol. Rev.* 64 (3), 676–705. doi:10.1124/pr.112.005983

Vonk, L. A., van Dooremalen, S. F. J., Liv, N., Klumperman, J., Coffer, P. J., Saris, D. B. F., et al. (2018). Mesenchymal Stromal/stem Cell-Derived Extracellular Vesicles Promote Human Cartilage Regeneration *In Vitro*. *Theranostics* 8 (4), 906–920. doi:10.7150/thno.20746

Wang, D., Wang, J., Zhou, J., and Zheng, X. (2021a). The Role of Adenosine Receptor A2A in the Regulation of Macrophage Exosomes and Vascular Endothelial Cells during Bone Healing. *Jir* 14, 4001–4017. doi:10.2147/JIR.S324232

Wang, L., Wang, J., Zhou, X., Sun, J., Zhu, B., Duan, C., et al. (2020a). A New Self-Healing Hydrogel Containing hucMSC-Derived Exosomes Promotes Bone Regeneration. *Front. Bioeng. Biotechnol.* 8, 564731. doi:10.3389/fbioe.2020.564731

Wang, L., Zhang, H., Wang, S., Chen, X., and Su, J. (2021b). Bone Marrow Adipocytes: A Critical Player in the Bone Marrow Microenvironment. *Front. Cel Dev. Biol.* 9, 770705. doi:10.3389/fcell.2021.770705

Wang, Q., Shen, X., Chen, Y., Chen, J., and Li, Y. (2021c). Osteoblasts-derived Exosomes Regulate Osteoclast Differentiation through miR-503-3p/Hpse axis. *Acta Histochem.* 123 (7), 151790. doi:10.1016/j.acthis.2021.151790

Wang, R., Jiang, W., Zhang, L., Xie, S., Zhang, S., Yuan, S., et al. (2020b). Intra-articular Delivery of Extracellular Vesicles Secreted by Chondrogenic Progenitor Cells from MRL/MpJ Superhealer Mice Enhances Articular Cartilage Repair in a Mouse Injury Model. *Stem Cel Res Ther* 11 (1), 93. doi:10.1186/s13287-020-01594-x

Wang, S., Jia, J., and Chen, C.-h. (2021d). LncRNA-KCNQ1OT1: A Potential Target in Exosomes Derived from ADSCs for the Treatment of Osteoporosis. *Stem Cell Int* 2021, 7690006. doi:10.21203/rs.3.rs-576971/v1

Wei, F., Li, M., Crawford, R., Zhou, Y., and Xiao, Y. (2019). Exosome-integrated Titanium Oxide Nanotubes for Targeted Bone Regeneration. *Acta Biomater.* 86, 480–492. doi:10.1016/j.actbio.2019.01.006

Witwer, K. W., Van Balkom, B. W. M., Bruno, S., Choo, A., Dominici, M., Gimona, M., et al. (2019). Defining Mesenchymal Stromal Cell (MSC)-derived Small Extracellular Vesicles for Therapeutic Applications. *J. Extracellular Vesicles* 8 (1), 1609206. doi:10.1080/20013078.2019.1609206

Wong, K. L., Zhang, S., Wang, M., Ren, X., Afizah, H., Lai, R. C., et al. (2020). Intra-Articular Injections of Mesenchymal Stem Cell Exosomes and Hyaluronic Acid Improve Structural and Mechanical Properties of Repaired Cartilage in a Rabbit Model. *Arthrosc. J. Arthroscopic Relat. Surg.* 36 (8), 2215–2228. e2212. doi:10.1016/j.arthro.2020.03.031

Xia, W., Xie, J., Cai, Z., Liu, X., Wen, J., Cui, Z.-K., et al. (2021). Damaged Brain Accelerates Bone Healing by Releasing Small Extracellular Vesicles that Target Osteoprogenitors. *Nat. Commun.* 12 (1), 6043. doi:10.1038/s41467-021-26302-y

Xia, Y., He, X.-T., Xu, X.-Y., Tian, B.-M., An, Y., and Chen, F.-M. (2020). Exosomes Derived from M0, M1 and M2 Macrophages Exert Distinct Influences on the Proliferation and Differentiation of Mesenchymal Stem Cells. *PeerJ* 8, e8970. doi:10.7717/peerj.8970

Xie, L., Guan, Z., Zhang, M., Lyu, S., Thuaksuban, N., Kamolmattayakul, S., et al. (2020). Exosomal circLPAR1 Promoted Osteogenic Differentiation of Homotypic Dental Pulp Stem Cells by Competitively Binding to Hsa-miR-31. *Biomed. Res. Int.* 2020, 1–13. doi:10.1155/2020/6319395

Xie, Y., Gao, Y., Zhang, L., Chen, Y., Ge, W., and Tang, P. (2018). Involvement of Serum-Derived Exosomes of Elderly Patients with Bone Loss in Failure of Bone Remodeling via Alteration of Exosomal Bone-Related Proteins. *Aging Cell* 17 (3), e12758. doi:10.1111/acel.12758

Xiong, Y., Chen, L., Yan, C., Zhou, W., Yu, T., Sun, Y., et al. (2020). M2 Macrophagy-Derived Exosomal miRNA-5106 Induces Bone Mesenchymal Stem Cells towards Osteoblastic Fate by Targeting Salt-Inducible Kinase 2 and 3. *J. Nanobiotechnol* 18 (1), 66. doi:10.1186/s12951-020-00622-5

Xu, J., Wang, Y., Hsu, C.-Y., Gao, Y., Meyers, C. A., Chang, L., et al. (2019). Human Perivascular Stem Cell-Derived Extracellular Vesicles Mediate Bone Repair. *Elife* 8. doi:10.7554/eLife.48191

Xu, R., Shen, X., Si, Y., Fu, Y., Zhu, W., Xiao, T., et al. (2018). MicroRNA-31a-5p from Aging BMSCs Links Bone Formation and Resorption in the Aged Bone Marrow Microenvironment. *Aging Cell* 17 (4), e12794. doi:10.1111/acel.12794

Xu, S., and Wang, Z. (2017). Bone Marrow Mesenchymal Stem Cell-Derived Exosomes Enhance Osteoclastogenesis during Alveolar Bone Deterioration in Rats. *RSC Adv.* 7 (34), 21153–21163. doi:10.1039/c6ra27931g

Xu, T., Luo, Y., Wang, J., Zhang, N., Gu, C., Li, L., et al. (2020). Exosomal miRNA-128-3p from Mesenchymal Stem Cells of Aged Rats Regulates Osteogenesis and Bone Fracture Healing by Targeting Smad5. *J. Nanobiotechnol* 18 (1), 47. doi:10.1186/s12951-020-00601-w

Xue, X., Hu, Y., Deng, Y., and Su, J. (2021a). Recent Advances in Design of Functional Biocompatible Hydrogels for Bone Tissue Engineering. *Adv. Funct. Mater.* 31 (19), 2009432. doi:10.1002/adfm.202009432

Xue, X., Hu, Y., Wang, S., Chen, X., Jiang, Y., and Su, J. (2022b). Fabrication of Physical and Chemical Crosslinked Hydrogels for Bone Tissue Engineering. *Bioactive Mater.* 12, 327–339. doi:10.1016/j.bioactmat.2021.10.029

Xun, J., Li, C., Liu, M., Mei, Y., Zhou, Q., Wu, B., et al. (2021). Serum Exosomes from Young Rats Improve the Reduced Osteogenic Differentiation of BMSCs in Aged Rats with Osteoporosis after Fatigue Loading *In Vivo*. *Stem Cel Res Ther* 12 (1), 424. doi:10.1186/s13287-021-02449-9

Yajun, W., Jin, C., Zhengrong, G., Chao, F., Yan, H., Weizong, W., et al. (2021). Betaine Attenuates Osteoarthritis by Inhibiting Osteoclastogenesis and Angiogenesis in Subchondral Bone. *Front. Pharmacol.* 12, 723988. doi:10.3389/fphar.2021.723988

Yang, B.-c., Kuang, M.-j., Kang, J.-y., Zhao, J., Ma, J.-x., and Ma, X.-l. (2020a). Human Umbilical Cord Mesenchymal Stem Cell-Derived Exosomes Act via the miR-1263/Mob1/Hippo Signaling Pathway to Prevent Apoptosis in Disuse Osteoporosis. *Biochem. Biophysical Res. Commun.* 524 (4), 883–889. doi:10.1016/j.bbrc.2020.02.001

Yang, C., Gao, C., Liu, N., Zhu, Y., Zhu, X., Su, X., et al. (2021). The Effect of Traumatic Brain Injury on Bone Healing from a Novel Exosome Centered Perspective in a Mice Model. *J. Orthopaedic Translation* 30, 70–81. doi:10.1016/j.jot.2021.09.003

Yang, D., Zhang, W., Zhang, H., Zhang, F., Chen, L., Ma, L., et al. (2020b). Progress, Opportunity, and Perspective on Exosome Isolation - Efforts for Efficient Exosome-Based Theranostics. *Theranostics* 10 (8), 3684–3707. doi:10.7150/thno.41580

Yang, S., Guo, S., Tong, S., and Sun, X. (2020c). Exosomal miR-130a-3p Regulates Osteogenic Differentiation of Human Adipose-Derived Stem Cells through Mediating SIRT7/Wnt/β-catenin axis. *Cel Prolif.* 53 (10), e12890. doi:10.1111/cpr.12890

Yao, Y., and Wang, Y. (2013). ATDC5: an Excellent *In Vitro* Model Cell Line for Skeletal Development. *J. Cel. Biochem.* 114 (6), 1223–1229. doi:10.1002/jcb.24467

Yin, P., Lv, H., Li, Y., Deng, Y., Zhang, L., and Tang, P. (2017). Exosome-Mediated Genetic Information Transfer, a Missing Piece of Osteoblast-Osteoclast Communication Puzzle. *Front. Endocrinol.* 8, 336. doi:10.3389/fendo.2017.00336

Yu, W., Su, X., Li, M., Wan, W., Li, A., Zhou, H., et al. (2021). Three-dimensional Mechanical Microenvironment Enhanced Osteogenic Activity of Mesenchymal Stem Cells-Derived Exosomes. *Chem. Eng. J.* 417, 128040. doi:10.1016/j.cej.2020.128040

Yuan, F.-L., Wu, Q.-y., Miao, Z.-N., Xu, M.-H., Xu, R.-S., Jiang, D.-L., et al. (2018). Osteoclast-Derived Extracellular Vesicles: Novel Regulators of Osteoclastogenesis and Osteoclast-Osteoblasts Communication in Bone Remodeling. *Front. Physiol.* 9, 628. doi:10.3389/fphys.2018.00628

Yuan, F.-L., Xu, M.-H., Li, X., Xinlong, H., Fang, W., and Dong, J. (2016). The Roles of Acidosis in Osteoclast Biology. *Front. Physiol.* 7, 222. doi:10.3389/fphys.2016.00222

Zavatti, M., Beretti, F., Casciaro, F., Bertucci, E., and Maraldi, T. (2020). Comparison of the Therapeutic Effect of Amniotic Fluid Stem Cells and Their Exosomes on Monoiodoacetate-induced Animal Model of Osteoarthritis. *Biofactors* 46 (1), 106–117. doi:10.1002/biof.1576

Zha, Y., Li, Y., Lin, T., Chen, J., Zhang, S., and Wang, J. (2021). Progenitor Cell-Derived Exosomes Endowed with VEGF Plasmids Enhance Osteogenic Induction and Vascular Remodeling in Large Segmental Bone Defects. *Theranostics* 11 (1), 397–409. doi:10.7150/thno.50741

Zhai, M., Zhu, Y., Yang, M., and Mao, C. (2020). Human Mesenchymal Stem Cell Derived Exosomes Enhance Cell-Free Bone Regeneration by Altering Their miRNAs Profiles. *Adv. Sci.* 7 (19), 2001334. doi:10.1002/advs.202001334

Zhang, B., Huang, J., Liu, J., Lin, F., Ding, Z., and Xu, J. (2021a). Injectable Composite Hydrogel Promotes Osteogenesis and Angiogenesis in Spinal Fusion by Optimizing the Bone Marrow Mesenchymal Stem Cell Microenvironment and Exosomes Secretion. *Mater. Sci. Eng. C* 123, 111782. doi:10.1016/j.msec.2020.111782

Zhang, D., Wu, Y., Li, Z., Chen, H., Huang, S., Jian, C., et al. (2021b). MiR-144-5p, an Exosomal miRNA from Bone Marrow-Derived Macrophage in Type 2 Diabetes, Impairs Bone Fracture Healing via Targeting Smad1. *J. Nanobiotechnol* 19 (1), 226. doi:10.1186/s12951-021-00964-8

Zhang, F.-X., Liu, P., Ding, W., Meng, Q.-B., Su, D.-H., Zhang, Q.-C., et al. (2021c). Injectable Mussel-Inspired Highly Adhesive Hydrogel with Exosomes for Endogenous Cell Recruitment and Cartilage Defect Regeneration. *Biomaterials* 278, 121169. doi:10.1016/j.biomaterials.2021.121169

Zhang, J., Liu, X., Li, H., Chen, C., Hu, B., Niu, X., et al. (2016a). Exosomes/tricalcium Phosphate Combination Scaffolds Can Enhance Bone Regeneration by Activating the PI3K/Akt Signaling Pathway. *Stem Cel Res Ther* 7 (1), 136. doi:10.1186/s13287-016-0391-3

Zhang, J., Rong, Y., Luo, C., and Cui, W. (2020a). Bone Marrow Mesenchymal Stem Cell-Derived Exosomes Prevent Osteoarthritis by Regulating Synovial Macrophage Polarization. *Aging* 12, 25138–25152. doi:10.18632/aging.104110

Zhang, L., Jiao, G., Ren, S., Zhang, X., Li, C., Wu, W., et al. (2020b). Exosomes from Bone Marrow Mesenchymal Stem Cells Enhance Fracture Healing through the Promotion of Osteogenesis and Angiogenesis in a Rat Model of Nonunion. *Stem Cel Res Ther* 11 (1), 38. doi:10.1186/s13287-020-1562-9

Zhang, L., Wang, Q., Su, H., and Cheng, J. (2021d). Exosomes from Adipose Derived Mesenchymal Stem Cells Alleviate Diabetic Osteoporosis in Rats through Suppressing NLRP3 Inflammasome Activation in Osteoclasts. *J. Biosci. Bioeng.* 131 (6), 671–678. doi:10.1016/j.jbiosc.2021.02.007

Zhang, S., Chu, W. C., Lai, R. C., Lim, S. K., Hui, J. H. P., and Toh, W. S. (2016b). Exosomes Derived from Human Embryonic Mesenchymal Stem Cells Promote Osteochondral Regeneration. *Osteoarthritis and Cartilage* 24 (12), 2135–2140. doi:10.1016/j.joca.2016.06.022

Zhang, S., Chuah, S. J., Lai, R. C., Hui, J. H. P., Lim, S. K., and Toh, W. S. (2018a). MSC Exosomes Mediate Cartilage Repair by Enhancing Proliferation, Attenuating Apoptosis and Modulating Immune Reactivity. *Biomaterials* 156, 16–27. doi:10.1016/j.biomaterials.2017.11.028

Zhang, S., Teo, K. Y. W., Chuah, S. J., Lai, R. C., Lim, S. K., and Toh, W. S. (2019a). MSC Exosomes Alleviate Temporomandibular Joint Osteoarthritis by Attenuating Inflammation and Restoring Matrix Homeostasis. *Biomaterials* 200, 35–47. doi:10.1016/j.biomaterials.2019.02.006

Zhang, T., Jiang, M., Yin, X., Yao, P., and Sun, H. (2021e). Mechanism of Exosomes Involved in Osteoimmunity Promoting Osseointegration Around Titanium Implants with Small-Scale Topography. *Front. Bioeng. Biotechnol.* 9, 682384. doi:10.3389/fbioe.2021.682384

Zhang, Y., Cai, F., Liu, J., Chang, H., Liu, L., Yang, A., et al. (2018b). Transfer RNA-Derived Fragments as Potential Exosome tRNA-Derived Fragment Biomarkers for Osteoporosis. *Int. J. Rheum. Dis.* 21 (9), 1659–1669. doi:10.1111/1756-185X.13346

Zhang, Y., Hao, Z., Wang, P., Xia, Y., Wu, J., Xia, D., et al. (2019b). Exosomes from Human Umbilical Cord Mesenchymal Stem Cells Enhance Fracture Healing through HIF-1α-mediated Promotion of Angiogenesis in a Rat Model of Stabilized Fracture. *Cell Prolif* 52 (2), e12570. doi:10.1111/cpr.12570

Zhang, Y., Xie, Y., Hao, Z., Zhou, P., Wang, P., Fang, S., et al. (2021f). Umbilical Mesenchymal Stem Cell-Derived Exosome-Encapsulated Hydrogels Accelerate Bone Repair by Enhancing Angiogenesis. *ACS Appl. Mater. Inter.* 13 (16), 18472–18487. doi:10.1021/acsami.0c22671

Zhao, H., Li, X., Zhang, D., Chen, H., Chao, Y., Wu, K., et al. (2018a). Integrative Bone Metabolomics-Lipidomics Strategy for Pathological Mechanism of Postmenopausal Osteoporosis Mouse Model. *Sci. Rep.* 8 (1), 16456. doi:10.1038/s41598-018-34574-6

Zhao, P., Xiao, L., Peng, J., Qian, Y. Q., and Huang, C. C. (2018b). Exosomes Derived from Bone Marrow Mesenchymal Stem Cells Improve Osteoporosis through Promoting Osteoblast Proliferation via MAPK Pathway. *Eur. Rev. Med. Pharmacol. Sci.* 22, 3962–3970. doi:10.26355/eurrev-201806-1528010.26355/eurrev_201806_15280

Zhao, Q., Zhang, Y., Xiao, L., Lu, H., Ma, Y., Liu, Q., et al. (2021). Surface Engineering of Titania Nanotubes Incorporated with Double-Layered Extracellular Vesicles to Modulate Inflammation and Osteogenesis. *Regen. Biomater.* 8 (3), rbab010. doi:10.1093/rb/rbab010

Zhi, F., Ding, Y., Wang, R., Yang, Y., Luo, K., and Hua, F. (2021). Exosomal Hsa_circ_0006859 Is a Potential Biomarker for Postmenopausal Osteoporosis and Enhances Adipogenic versus Osteogenic Differentiation in Human Bone Marrow Mesenchymal Stem Cells by Sponging miR-431-5p. *Stem Cel Res Ther* 12 (1), 157. doi:10.1186/s13287-021-02214-y

Zhou, J., Liu, H. X., Li, S. H., Gong, Y. S., Zhou, M. W., Zhang, J. H., et al. (2019). Effects of Human Umbilical Cord Mesenchymal Stem Cells-Derived Exosomes on Fracture Healing in Rats through the Wnt Signaling Pathway. *Eur. Rev. Med. Pharmacol. Sci.* 23, 4954–4960. doi:10.26355/eurrev_201906_18086

Zhou, Q., Cai, Y., Jiang, Y., and Lin, X. (2020). Exosomes in Osteoarthritis and Cartilage Injury: Advanced Development and Potential Therapeutic Strategies. *Int. J. Biol. Sci.* 16 (11), 1811–1820. doi:10.7150/ijbs.41637

Zhu, M., Liu, Y., Qin, H., Tong, S., Sun, Q., Wang, T., et al. (2021). Osteogenically-induced Exosomes Stimulate Osteogenesis of Human Adipose-Derived Stem Cells. *Cell Tissue Bank* 22 (1), 77–91. doi:10.1007/s10561-020-09867-8

Zhu, Y., Wang, Y., Zhao, B., Niu, X., Hu, B., Li, Q., et al. (2017). Comparison of Exosomes Secreted by Induced Pluripotent Stem Cell-Derived Mesenchymal Stem Cells and Synovial Membrane-Derived Mesenchymal Stem Cells for the Treatment of Osteoarthritis. *Stem Cel Res Ther* 8 (1), 64. doi:10.1186/s13287-017-0510-9

Conflict of Interest: The authors declare that the research was conducted in the absence of any commercial or financial relationships that could be construed as a potential conflict of interest.

Publisher's Note: All claims expressed in this article are solely those of the authors and do not necessarily represent those of their affiliated organizations or those of the publisher, the editors, and the reviewers. Any product that may be evaluated in this article, or claim that may be made by its manufacturer, is not guaranteed or endorsed by the publisher.

Copyright © 2022 Meng, Xue, Yin, Gao, Wang and Geng. This is an open-access article distributed under the terms of the Creative Commons Attribution License (CC BY). The use, distribution or reproduction in other forums is permitted, provided the original author(s) and the copyright owner(s) are credited and that the original publication in this journal is cited, in accordance with accepted academic practice. No use, distribution or reproduction is permitted which does not comply with these terms.

frontiers | Frontiers in Bioengineering and Biotechnology

ORIGINAL RESEARCH
published: 05 May 2022
doi: 10.3389/fbioe.2022.851904

Cryogel Scaffold-Mediated Delivery of Adipose-Derived Stem Cells Promotes Healing in Murine Model of Atrophic Non-Union

Katherine R. Hixon[1,2]*, *Dakota B. Katz*[1,3,4,5], *Jennifer A. McKenzie*[1], *Anna N. Miller*[1], *Farshid Guilak*[1,3,4,5] and *Matthew J. Silva*[1,3,4]

[1]Department of Orthopaedic Surgery, Musculoskeletal Research Center, Washington University, St. Louis, MO, United States, [2]Thayer School of Engineering, Dartmouth College, Hanover, NH, United States, [3]Department of Biomedical Engineering, Washington University, St. Louis, MO, United States, [4]Center of Regenerative Medicine, Washington University, St. Louis, MO, United States, [5]Shriners Hospitals for Children—St. Louis, St. Louis, MO, United States

Non-union is defined as the permanent failure of a bone to heal and occurs clinically in 5% of fractures. Atrophic non-unions, characterized by absent/minimal callus formation, are poorly understood and difficult to treat. We recently demonstrated a novel murine model of atrophic non-union in the 3.6Col1A1-tk (Col1-tk) mouse, wherein dosing with the nucleoside analog ganciclovir (GCV) was used to deplete proliferating osteoprogenitor cells, leading to a radiographic and biomechanical non-union after the mid-shaft femur fracture. Using this Col1-tk atrophic non-union model, we hypothesized that the scaffold-mediated lentiviral delivery of doxycycline-inducible BMP-2 transgenes would induce osteogenesis at the fracture site. Cryogel scaffolds were used as a vehicle for GFP+ and BMP-2+ cell delivery to the site of non-union. Cryogel scaffolds were biofabricated through the cross-linking of a chitosan–gelatin polymer solution at subzero temperatures, which results in a macroporous, spongy structure that may be advantageous for a bone regeneration application. Murine adipose-derived stem cells were seeded onto the cryogel scaffolds, where they underwent lentiviral transduction. Following the establishment of atrophic non-unions in the femurs of Col1-tk mice (4 weeks post-fracture), transduced, seeded scaffolds were surgically placed around the site of non-union, and the animals were given doxycycline water to induce BMP-2 production. Controls included GFP+ cells on the cryogel scaffolds, acellular scaffolds, and sham (no scaffold). Weekly radiographs were taken, and endpoint analysis included micro-CT and histological staining. After 2 weeks of implantation, the BMP-2+ scaffolds were infiltrated with cartilage and woven bone at the non-union site, while GFP+ scaffolds had woven bone formation. Later, timepoints of 8 weeks had woven bone and vessel formation within the BMP-2+ and GFP + scaffolds with cortical bridging of the original fracture site in both groups. Overall, the cell-seeded cryogels promoted osseous healing. However, while the addition of BMP-2 promoted the endochondral ossification, it may provide a slower route to healing. This proof-of-concept study demonstrates the potential for cellularized cryogel scaffolds to enhance the healing of non-unions.

Keywords: animal models, fracture healing, tissue engineering, cryogels, BMP-2

OPEN ACCESS

Edited by:
Dmitriy Sheyn,
Board of Governors Regenerative Medicine Institute, United States

Reviewed by:
Martin James Stoddart,
AO Research Institute, Switzerland
Galina Shapiro,
Hebrew University of Jerusalem, Israel

****Correspondence:***
Katherine R. Hixon
katherine.r.hixon@dartmouth.edu

Specialty section:
This article was submitted to Tissue Engineering and Regenerative Medicine, a section of the journal Frontiers in Bioengineering and Biotechnology

Received: *10 January 2022*
Accepted: *23 March 2022*
Published: *05 May 2022*

Citation:
Hixon KR, Katz DB, McKenzie JA, Miller AN, Guilak F and Silva MJ (2022) Cryogel Scaffold-Mediated Delivery of Adipose-Derived Stem Cells Promotes Healing in Murine Model of Atrophic Non-Union. Front. Bioeng. Biotechnol. 10:851904. doi: 10.3389/fbioe.2022.851904

INTRODUCTION

Non-union is defined as the permanent failure of a bone to heal and occurs clinically in approximately 5% of all fractures (Einhorn, 1995; Choi et al., 2004). With increased risk due to factors such as sex, smoking, and diabetes, currently available invasive surgical treatments result in major physical and financial burdens on individuals (Zura et al., 2016; Mills et al., 2017; Dailey et al., 2018; Ekegren et al., 2018). Among the several types of non-unions, atrophic non-unions, characterized by absent/minimal osteochondral callus formation, are poorly understood and difficult to treat (Mills and Simpson, 2012; Thomas and Kehoe, 2021). Furthermore, in atrophic non-unions, bone healing has become stagnant, and surgical intervention with the addition of a biological agent, such as a bone graft, is often necessary to induce regeneration (Moghaddam et al., 2016; Sun et al., 2019). While autografts remain the gold standard for treatment, there are inherent disadvantages including potential for infection, donor site morbidity, and limited availability (Roberts and Rosenbaum, 2012; Sohn and Oh, 2019).

Animal models of atrophic non-unions have been described in mice (Choi et al., 2004; Lu et al., 2007; Garcia et al., 2008; Garcia et al., 2011; Wang et al., 2019), rats (Cullinane et al., 2002; Harrison et al., 2003; Kokubu et al., 2003; Reed et al., 2003; Schmidhammer et al., 2006; Kaspar et al., 2008; Tawonsawatruk et al., 2014; Roberto-Rodrigues et al., 2015), and rabbits (Oni, 1995; Brownlow and Simpson, 2000; Park et al., 2002). Most available models target fracture healing by disrupting the tissues needed for repair through invasive methods such as osteotomy, periosteal stripping, and/or devascularization (Mills and Simpson, 2012; Gómez-Barrena et al., 2015; Panteli et al., 2015). While such methods do yield an atrophic non-union, they do not model some clinical atrophic non-unions, which occur without extensive tissue damage and are attributed to "failure of biology." We recently developed a novel murine model of atrophic non-union in the 3.6Col1A1-tk (Col1-tk) mouse, where dosing with the nucleoside analog ganciclovir (GCV) is used to deplete replicating osteoblast lineage cells (Hixon et al., 2021). Briefly, in proliferating cells that express the thymidine kinase (tk) "suicide gene," GCV is converted to a toxic nucleotide, which is then incorporated into the DNA. This results in targeted death of dividing tk + cells, which prevents the proliferative expansion needed to form a callus, leading to callus formation failure after the fracture and thus radiographic and biomechanical non-union. Notably, because non-dividing cells are spared, the fracture site is still populated by viable cells including, presumably, skeletal progenitors. Once GCV is withdrawn, there is potential for these resident cells to proliferate and contribute to fracture healing, although our prior work showed that this does not happen spontaneously (Hixon et al., 2021). This biologically relevant model allows for the testing of novel intervention techniques that might reactivate the quiescent native cells to rescue an atrophic non-union.

Tissue engineering scaffolds provide a promising alternative to currently used bone grafts due to their tailorable properties to modify porosity, mechanical integrity, and degradation rate. Cryogels are hydrogel-based scaffolds that have enhanced porosity and mechanical properties due to the addition of a freezing process during fabrication (Henderson et al., 2013; Hixon et al., 2017a; Bakhshpour et al., 2019). Briefly, following the cross-linking of a polymer solution, the mixture is immediately frozen, resulting in the formation of ice crystals throughout the solution. Upon thawing and melting of these ice crystals, the resulting polymer structure is macroporous, sponge-like, and mechanically durable (Henderson et al., 2013; Okay, 2014). Previous studies have demonstrated that cryogels are suitable for the treatment of complex bone defects including critical size defects in both long bones and craniofacial applications (Dumas et al., 2012; Mishra et al., 2014; Hixon et al., 2017b). However, their application to enhance the repair of atrophic non-unions has not been previously investigated. While tissue engineering approaches have an excellent capability to promote both tissue repair and regeneration of bone injury, further modification can improve their applicability in treating more complex bone defects (e.g., atrophic non-unions, where biological healing has been disrupted) through the ability to deliver specific cell types and/or growth factors. Previous studies have developed woven polymer scaffolds capable of mediating stem cell differentiation and cartilaginous extracellular matrix (ECM) formation using a lentivirus-based method (Brunger et al., 2014; Glass et al., 2014). Subsequent work developed scaffold-mediated lentiviral gene delivery of bone morphogenetic protein-2 (BMP-2), a potent osteogenic factor (Rowland et al., 2018). While woven fiber scaffolds are favorable for tissue-engineered cartilage applications, cryogel scaffolds offer a promising alternative for *in situ* bone regeneration due to their macroporous structure and high pore interconnectivity, which allows fluid flow, cell mobility, and angiogenesis (Hixon et al., 2016; Bakhshpour et al., 2019). Specifically, chitosan–gelatin cryogels are composed of natural materials and have been extensively characterized with pore diameters ranging from 30 to 100 μm conducive to cell infiltration (Kathuria et al., 2009). The combination of cryogel scaffolds with a lentivirus-based method holds the potential to induce bone formation and healing (Rodrigues et al., 2013; Liao et al., 2016; Kemençe and Bölgen, 2017). We focused on the local delivery of BMP-2, long recognized as a potent osteoinductive growth factor capable of improving healing of non-unions, fractures, spinal fusions, and dental implants (Lo et al., 2012; Krishnakumar et al., 2017). Previous studies have shown that following the stabilization of a fracture, exogenous BMP-2 induces cartilage formation and can promote endochondral ossification. Furthermore, the periosteum has been shown to be a target of exogenous BMP-2 (Yu et al., 2010). Notably, previous studies have focused on cellular engineering approaches, including the engineering of mesenchymal stem cells (MSCs) to express BMP-2 in combination with vascular endothelial growth factor (VEGF) or mineral-coated microparticles (Kumar et al., 2010; Orth et al., 2017). Such approaches have demonstrated osseous bridging and increased bone formation. Despite this, the treatment of atrophic non-union can be challenging where the tunable delivery of a biological agent, along with a scaffold matrix, is necessary for appropriate, localized treatment to encourage cell

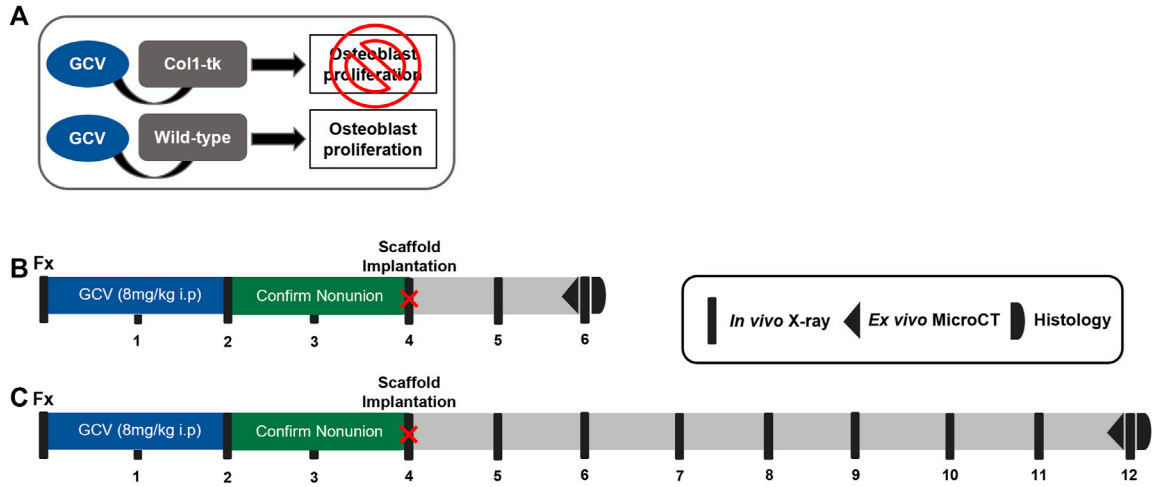

FIGURE 1 | Schematic of the establishment of a non-union and scaffold implantation in Col1-tk mice. **(A)** While receiving the GCV drug, any Col1-tk + cells within the mouse that are proliferating will selectively die. Non-proliferating osteoblasts will remain alive. Once the drug is removed, any proliferating osteoblasts will not die. **(B, C)** Col1-tk mice at 12 weeks of age were subjected to a femur fracture, followed by daily GCV administration for 2 weeks to blunt the healing response. The mice were monitored from week 1–4 by X-ray to confirm minimal callus formation. At 4 weeks post-fracture, an additional surgery was performed, and the scaffolds were implanted. The mice were monitored by X-ray for 2–8 weeks post-scaffold implantation until sacrifice. The outcomes included micro-CT and histology.

infiltration and initiate healing. Additionally, the exclusively uncontrolled delivery of growth factors such as BMP-2, as well as delivery methods without tunability, can have deleterious results such as excessive heterotopic ossification or increased cancer risk (Shi et al., 2013; Skovrlj et al., 2015; Shi et al., 2017). Thus, we used a doxycycline-inducible BMP-2 lentivirus for the tunable and inducible delivery of BMP-2 in an adipose stem cell-seeded scaffold to the non-union site. The viral vector has been shown to have a high transduction efficiency and result in an inducible production of BMP-2 when exposed to doxycycline (Glass et al., 2014; Rowland et al., 2018). In combination with the biologically relevant Col1-tk mouse model of atrophic non-union, this treatment method allows for the testing of a novel intervention technique to rescue fracture non-union. We hypothesize that the tissue-engineered scaffold-mediated gene delivery of a cell population overexpressing the osteogenic transgene BMP-2 will induce osteogenesis at the site of non-union. Previous work has demonstrated that scaffold-mediated gene delivery can induce sustained transgene expression and ECM formation by MSCs (Kokubu et al., 2003; Hixon et al., 2016; Hixon et al., 2017a; de Lageneste et al., 2018), and we anticipate that using this approach with BMP-2 will provide the osteoinductive environment necessary to drive periosteal healing.

MATERIALS AND METHODS

Scaffold Fabrication

Cryogel scaffolds (n = 4/group/timepoint) were fabricated based on a previously established protocol (Kathuria et al., 2009). Briefly, 80 mg of low-viscosity chitosan (MP Biomedicals) was dissolved in 8 ml of 1% acetic acid solution (Fisher Scientific). Following dissolution, 320 mg of gelatin (from cold water fish skin; Sigma) was added to the solution and mixed for 1 h. In a separate scintillation vial, 1% glutaraldehyde solution was prepared using 2 ml of 1% acetic acid solution for cross-linking. All the solutions were cooled at 4°C for 1 h. The solutions were mixed by decanting and then immediately poured into precooled 12-well plates (Sigma), such that a thickness of 3–4 mm was achieved, and frozen at −20°C for 18 h. At this time, the plates were thawed at room temperature (RT) water and trimmed into rectangular sheets (6 mm × 12 mm × 1.5 mm). The scaffolds were sterilized in 1% peracetic acid (PAA; Sigma) for 90 min and then rinsed with sterile 1X phosphate-buffered saline (PBS) three times for 10 min (Yoganarasimha et al., 2014; Costa et al., 2015). Following sterilization, all the scaffolds were placed at −80°C for 1 h and subsequently lyophilized (Sentry 2.0 VirTis BenchTop Pro Freeze Dryer; SP Scientific) for 24 h to ensure complete drying. The resulting cryogel scaffolds were macroporous (pore diameters of 30–100 μm) and sponge-like in structure, allowing them to undergo compression without the crack propagation (Brunger et al., 2014; Gómez-Barrena et al., 2015). Additionally, the cryogels were fabricated from the natural materials that render them compatible with cells and supportive of angiogenesis (Glass et al., 2014).

Lentivirus Production

The doxycycline-inducible lentiviral vector was generated by cloning *BMP2* into the modified TMPrtTA vector (provided by Danos Lab) as previously described (Rowland et al., 2018). To produce the lentivirus, HEK293T cells were co-transfected with either the dox-*BMP2* vector or a constitutive GFP lentiviral vector with a second-generation packaging plasmid psPAX2 (Addgene, No. 12260) and an envelope plasmid pMD2.G (Addgene, No. 12259) by calcium phosphate precipitation

(Salmon and Trono, 2007). The lentivirus was stored at −80°C until further use. The functional titer of each virus was determined *via* qRT-PCR to ascertain the number of lentiviral DNA copies integrated into the genome of the transduced HeLa cells (Salmon and Trono, 2007). On the day of transduction, the lentivirus was thawed and concentrated ~100-fold using Amicon Ultra 100 kDa MWCO filters (Millipore, UFC9100).

Scaffold-Mediated Lentiviral Transduction

To immobilize the lentivirus on the scaffolds, cryogels (n = 4/group/timepoint) were incubated overnight with 0.002% poly-L-lysine (Sigma), washed with PBS, and then incubated with enough concentrated lentivirus to transduce 500,000 or 1 million cells for 1.5 h at 37°C. The scaffolds were rinsed again with PBS, moved to a new low-attachment 24-well plate (Corning), and seeded with 500,000 cells for *in vitro* experiments and 1 million cells for implanted scaffolds. The expansion medium was added to each sample for 1 h after the cell seeding. All mediums were changed 24 h later. The scaffolds were cultured in the expansion medium for six days to facilitate cell infiltration. A subset of scaffolds were then fixed in a neutral-buffered formalin (NBF) for 24 h, placed in a 30% sucrose solution for an additional 24 h, and embedded in an optimal cutting temperature (OCT) compound. Once frozen, the cryogels were cryosectioned at 20 μm and stained with 4′,6-diamidino-2-phenylindole (DAPI) to visualize the cellular infiltration. All other scaffolds remained in culture.

In Vitro BMP-2 Analysis

After 6 days of culture in the expansion medium, the medium was changed to osteogenic medium containing DMEM-HG (Gibco), 10% lot selected FBS, 1% penicillin–streptomycin (Gibco), 50 μg/ml L-ascorbic acid 2-phosphate (Sigma), 10 nM dexamethasone (Sigma), and 10 mM β-glycerophosphate (Sigma). Doxycycline (dox) groups were supplemented with either 0.1 or 1 μg/ml dox (Sigma). Half medium changes were performed every other day for 28 days, and medium samples were collected on days 0, 2, 6, 10, 16, 22, and 28 of the osteogenic culture. The concentration of BMP-2 in the medium (n = 4/group/timepoint) was measured by ELISA (R&D).

Scaffold Micro-CT Analysis

Following 28 days of osteogenic culture, the scaffolds (n = 4/group/timepoint) were scanned using the Bruker SkyScan 1176 micro-CT at 40 V, 600 μA. Micro-CT datasets were reconstructed with NRecon software using a dynamic range of 0.1, ring artifact correction of 11, and beam hardening correction of 20%. Mineralization was quantified *via* calibration against hydroxyapatite phantoms using CT-Analyzer software. Acellular scaffolds soaked in the medium for 28 days served as a control.

Mouse Lines

A total of 62 male and female mice at 12 weeks of age were used in one of the four experimental groups: sham, scaffold only, GFP cells + scaffold, and BMP-2 cells + scaffold. Experimental procedures were approved by the Institutional Animal Care and Use Committee (IACUC) at Washington University in St. Louis in accordance with the Animal Welfare Act and PHS Policy on Humane Care and Use of Laboratory Animals. Atrophic non-unions were established in transgenic 3.6Col1A1-tk (Col1-tk) mice (rederived from the frozen embryos provided by Drs. Robert Jilka and Charles O'Brien) by targeting the replicating osteoblast progenitors (Jilka et al., 2009). As these mice express the herpes simplex virus thymidine kinase gene (HSV-tk, or "tk"), driven by the 3.6-kb rat Col1A1 promoter which is active in the osteoblast lineage cells; the addition of the nucleoside analog ganciclovir (GCV) targets replicating osteoblast progenitors (**Figure 1A**). This process occurs through the conversion of GCV to a toxic version of the nucleotide which is incorporated into the DNA, resulting in strands breaking and cell apoptosis (Jilka et al., 2009). To generate Col1-tk mice, male C57BL6/J (The Jackson Laboratory, #000664) mice were bred with female mice, heterozygous for the tk transgene (tk-positive). This resulted in the heterozygous tk-positive (Col1-tk) and tk-negative (wild-type, WT) mice. Only one allelic copy of the tk transgene is necessary to achieve the tk-positive and the male Col1-tk mice are sterile. All genotyping procedures were completed by Transnetyx (Cordova, TN) from toe biopsies taken from the mice for the real-time PCR (probe: puro). Additional breeding was used in the littermates (tk-positive females and tk-negative males). Prior to and during the experimental procedures, all the mice were group-housed (up to five mice/cage) under standard 12-h light/dark cycles with full access to food and water. Note that breeders were given high-fat chow, but following weaning, the experimental mice were given normal chow. All the mice were dosed with ganciclovir (GCV, 8 mg/kg i.p., McKesson) once daily starting at the fracture (12 weeks of age) for 2 weeks. The mice were euthanized by CO_2 asphyxiation at designated endpoints from 6 to 12 weeks after the fracture.

Establishment of the Non-Union

We recently demonstrated a model of atrophic non-union in Col1-tk mice dosed with GCV (Hixon et al., 2021). Briefly, a previously established protocol was employed to create a full fracture in the right femur of 12-week-old mice (Gardner et al., 2011). All mice were given buprenorphine SR (1 mg/kg, s.c.) for analgesia 1 h before surgery. The fracture was created by applying a transverse force across the right femoral mid-diaphysis using a custom 3-pt bending setup (DynaMight 8841; Instron). The femur was then stabilized using a 24-gauge metal pin (MicroGroup), and the incision was closed using 3-0 nylon sutures (Ethicon). We confirmed proper fixation by radiography (Faxitron Ultrafocus 100; Faxitron Bioptics) immediately following the fracture surgery. Note that in the WT mice, this model closely mirrors the classic fracture injury and healing response (Einhorn, 1998; Bonnarens and Einhorn, 1984), displaying both endochondral and intramembranous healing within the fracture gap and around the periphery, respectively (Liu et al., 2017; McKenzie et al., 2019). To establish the atrophic non-union, Col1-tk mice were dosed with GCV at the time of bone injury for 2 weeks, at which time the drug was withdrawn. All the animals were then

monitored by weekly radiography (Faxitron) for an additional 2 weeks to confirm a lack of bone formation and healing response, consistent with a non-union (4 weeks following fracture surgery; **Figures 1B**,C). Dosing, withdrawal, and revision surgery timepoints were based on the previous work in this mouse line and cover the established bridging window in the control mice (Garcia et al., 2013; Liu et al., 2017; Hixon et al., 2021).

Adipose-Derived Stem Cell Isolation

In the preparation for scaffold implantation, the subcutaneous adipose tissue was dissected from 12-week-old WT mice immediately following euthanasia (CO_2 asphyxiation). The dissected tissue was minced and placed in a digestion solution (0.1% collagenase and 1% penicillin/streptomycin in Dulbecco's Modified Eagle's Medium (DMEM)) at 37°C for 1 h. The samples underwent gentle inversion every 10 min. Following incubation, the tissue was transferred to a 10 cm culture dish, mechanically shredded with forceps, and then placed in an incubator for 30 min (37°C and 5% CO_2). At this time, the cell suspension was passed through a 70-μm sterile filter and centrifuged at 1300 rpm for 10 min at 4°C. The supernatant was removed and the cell pellet was resuspended in the growth medium (10% fetal bovine serum (FBS) and 1% penicillin/streptomycin in DMEM). All the cells were expanded to passage four which has previously been demonstrated to exhibit greater than 90% homogeneity for the MSC markers (CD13, CD29, CD44, CD73, and CD90) (Mitchell et al., 2006; Baer and Geiger, 2012; Dunham et al., 2020). All the adipose-derived stem cells (ADSCs) were immediately seeded onto the cryogel scaffolds at passage four for the *in vivo* implantation.

Scaffold Preparation for Implantation

The cryogel scaffolds were fabricated as described previously in the *Scaffold Fabrication*. Three scaffold groups were prepared for implantation: scaffold only (acellular; no lentivirus), scaffold + ADSCs transduced to express GFP, and scaffold + ADSCs transduced to express BMP-2 (n = 5–7/group/timepoint). In the preparation for implantation, all the scaffolds were seeded with ADSCs (± lentiviral transduction). Briefly, for the lentiviral transduction, BMP-2 or GFP lentiviruses were immobilized on the scaffold and 1 million cells were seeded and transduced, as described previously in *Scaffold Mediated Lentiviral Transduction*. All samples were cultured for 6 days to allow for cell infiltration and proliferation to occur throughout the cryogels.

Scaffold Implantation

At 4 weeks following the fracture, the achievement of an atrophic non-union in Col1-tk mice was confirmed *via* the radiograph. All the mice were given buprenorphine SR (1 mg/kg, s. c.) for analgesia 1 h before the surgery. An 8- to 10-mm incision was created along the previously fractured femur and the muscle was gently separated from the non-union site, exposing 7 mm of the femur. The assigned scaffold type (n = 5–7/group/timepoint) was placed under the femur and wrapped around the non-union such that the surrounding muscle held the scaffold in place. The muscle was closed with 4.0 vicryl suture, then the incision was closed using the running subcuticular 6-0 PDS sutures (Ethicon). Immediately following the surgery, radiographs were used to confirm that the non-union site remained. Note that the controls included a sham group where the surgery was completed, but no scaffold was implanted. All the animals received dox water (1 μg/ml in 5% sugar water; Sigma) for the duration of the study, changed weekly. The animals were monitored radiographically for 2 or 8 weeks after the surgery, chosen from the previous studies (Douglas et al., 2012; Hao et al., 2016; Orth et al., 2017), to observe the potential rescue of the non-union site. Following euthanasia, both the right and left femurs were dissected for micro-CT and processed for the histological evaluation (**Figures 1B**,C).

Radiographic Evaluation

Lateral radiographs were taken weekly following the full fracture until euthanasia (×3 magnification, Faxitron UltraFocus100; n = 5–7/group/timepoint). All the radiographs were blindly scored for the degree of healing using a modified RUST scoring system with both the sides of the fracture scored individually and a max score of 6 total: score = 1 designates only the fracture line is present, score = 2 is visible callus and fracture line, and score = 3 is completely bridged with no fracture visible (Cunningham et al., 2017; Fiset et al., 2018; Thomas and Kehoe, 2021). The mice were excluded from the study if there was a loss of fixation during healing or an atrophic non-union was not achieved by week 4 post-fracture (5 mice total).

Micro-Computed Tomography

Following euthanasia, the right and left femurs (n = 5–7/group/timepoint) were dissected and immediately fixed in 10% NBF for 24 h. After fixation, all the pins were removed from the bone and *ex vivo* scans were completed using micro-CT on the right and left femurs (VivaCT 40, Scanco Medical AG, Switzerland; 10.5 μm voxel size, 55 kV, 145 μA, 300 ms integration time). For the right fractured femurs, a 600 slice (6.3 mm length and diameter) ROI cylinder was centered at the fracture midpoint and thresholds of 180 and 250 per mile was used for 2 and 8 weeks timepoints, respectively, to segment the total bone (callus + cortical). A high-density threshold of 460 per mile was then used to segment out the original cortical bone of all the right (fractured) femurs. The cortical bone volume was subtracted from the total bone volume of each sample to determine the volume of new callus bone formed. In some samples, the fracture lines were no longer visible due to healing, so the point of fracture was found from the radiographic images at 0–2 weeks post-fracture (femoral head to fracture midpoint distance). For the left (intact) femurs, a 100 slice (1.05 mm) ROI was analyzed to compare the systemic changes due to the surgery or BMP-2 production. Following scanning, all the femurs were decalcified and processed for histology.

Histological Staining and Analysis

Following micro-CT, the samples were decalcified in 14% EDTA (pH 7.0) for 2 weeks (n = 5–7/group/timepoint). Standard paraffin processing was completed where all the fractured femurs were sectioned longitudinally at 5 μm thickness. Slides

from all the samples were stained with picrosirius red/alcian blue to visualize the different tissues (mineralized callus, cartilage, and fibrous tissue/other) at the fracture site. Immunohistochemistry (IHC) was also used to localize the endomucin expression to evaluate the presence of vasculature throughout the scaffold, as well as the HSV-tk and GFP expression to identify the role of the tk+ and GFP+ cells in healing, respectively. To accomplish this, the paraffin slides were first deparaffinized in xylene and rehydrated in graded ethanol. Next, incubation with 3% H_20_2 for 5 min blocked the endogenous peroxidases. Note that proteinase K was used for the antigen retrieval for endomucin slides prior to blocking (5 min, 23°C). HSV-tk and GFP endogenous epitopes were blocked with 10% goat serum (abcam—ab7481) in PBS at RT for 1 h. The sections were then incubated with rabbit polyclonal anti-HSV tk (1:100; gift from William Summers, Yale) and rabbit-anti-GFP (1:500; Life Technologies A11122) overnight at 4°C, followed by a secondary polymer-HRP anti-rabbit antibody incubation for 1 h (1:200 Dako P0448). The endomucin staining followed the manufacturer's instructions (Vectastain Elite ABC kit, Rat IgG PK-6104) and used the primary antibodies for endomucin (1:400, eBioV.7C7 #14–5851–85). All the IHC samples were incubated with DAB chromagen (brown; Vector DAB, SK-4105, 30–45 s) and counterstained with modified Mayer's hematoxylin (Vector Hematoxylin QS, H-3404). Images were obtained on a NanoZoomer slide scanner (20x; Hamamatsu Photonics). Picrosirius Red/alcian blue, HSV-tk, and endomucin images were blinded and qualitatively assessed for the callus and scaffold composition.

Statistics

Prior to the experiments, sample sizes for the study were calculated using a power analysis with α = 0.05 and β= 0.20 (https://www.stat.ubc.ca/~rollin/stats/ssize/n2.html). The estimates of sample variance and effect size were based on the previous data and biological importance (McKenzie et al., 2019). One-way ANOVA with the Tukey *post hoc* test was used for *in vitro* bone volume and bone mineral density analysis. A chi-square test was used to assess the fracture union based on the RUST radiographic scoring at 2 and 8 weeks post-scaffold implantation. Two-way ANOVA with the Tukey *post hoc* test was used to correct for multiple comparisons for *ex vivo* micro-CT. Significance was considered at p-values < 0.05, with trends noted at $p < 0.10$. All the data analysis was performed using Prism (version 9; GraphPad Software, La Jolla, CA, USA).

RESULTS

In Vitro Analysis Confirms Cellular Infiltration and BMP-2 Production

The ADSCs were seeded onto the cryogel scaffolds were cultured for 6 days and then cryosectioned to visualize cell adhesion and infiltration (**Figure 2A**). As shown by DAPI stain (blue), the ADSCs were able to infiltrate the matrix of all the cryogel scaffolds in the short window of culture, consistent with prior results with other cell types (Hixon et al., 2016; Hixon et al., 2017a). To verify the BMP-2 production, following an initial 6 days of culture, the cells were given osteogenic medium ± the addition of doxycycline (dox; **Figure 2B**). The non-transduced and transduced cells that did not receive dox (no dox) had negligible BMP-2 production over 28 days of culture. Similarly, a low dose of 0.1 μg/ml of dox was not sufficient to initiate the detectable BMP-2 production. However, when the transduced cells were exposed to 1 μg/ml of dox, a significantly higher production of BMP-2 was noted in all the samples which lasted over 28 days. It should be noted that while there was some variability in the BMP-2 secretion, these are the biological replicates. Thus, the seeded constructs may have been of slightly different sizes, seeded with slightly different numbers of cells, or received slightly different amounts of virus. Following the culture, micro-CT was used to quantify the mineralized volume and density (**Figures 2C**,D). The transduced cells given 1 μg/ml of dox and thus, producing BMP-2, had significantly more mineralized volume than the non-transduced cells and significantly higher bone mineral density than the acellular scaffolds ($p < 0.05$). Additionally, the transduced cells either left untreated or supplemented with 0.1 μg/ml of dox also had significantly higher bone mineral density than the acellular scaffolds ($p < 0.05$). Note that due to the presence of osteogenic medium, some mineralized volume and bone mineral density levels, when the cells are present, are not unexpected. These results indicate that cryogel scaffolds support mineralization by the ADSCs *in vitro*, and that the mineralized volume is enhanced by the dox-inducible cellular production of BMP-2.

Radiographic Healing Was Improved by the Presence of Cells

Blinded scoring of the radiographs was completed weekly until sacrifice at 2 or 8 weeks post-scaffold implantation (6 or 12 weeks post-fracture; **Figure 3**). Less than 50% of the animals treated with either scaffold only or with a sham implantation procedure showed complete bridging of both the cortices at the fracture site at 12 weeks. As both the groups consisted of Col1-tk animals treated with GCV, they were not expected to heal. In comparison, the scaffolds seeded with GFP+ cells and the scaffolds seeded with cells producing BMP-2 were the only groups that reached the complete bridging in all the animals by 12 weeks. Specifically, the fractures in all the animals treated with GFP+ scaffolds had complete bridging (RUST score = 6) after 6 weeks, while over 70% of the BMP-2+ scaffolds were bridged by week 8 and 100% by week 12. Notably, in all the animals treated with the BMP-2+ scaffolds, mineralization was observed radiographically by week 5–7 (1–3 weeks following implantation) throughout the implanted scaffold surrounding the fracture site. In comparison, the GFP+ groups only exhibited mineral within the scaffold in 2 of the 14 samples at varying timepoints. There was no significant difference between the radiograph scores of any groups at 6 weeks. However, the radiograph scores of both the scaffold and sham groups were significantly different than the radiograph scores of both the GFP and BMP-2 groups at 12 weeks. Note that there was no significance between

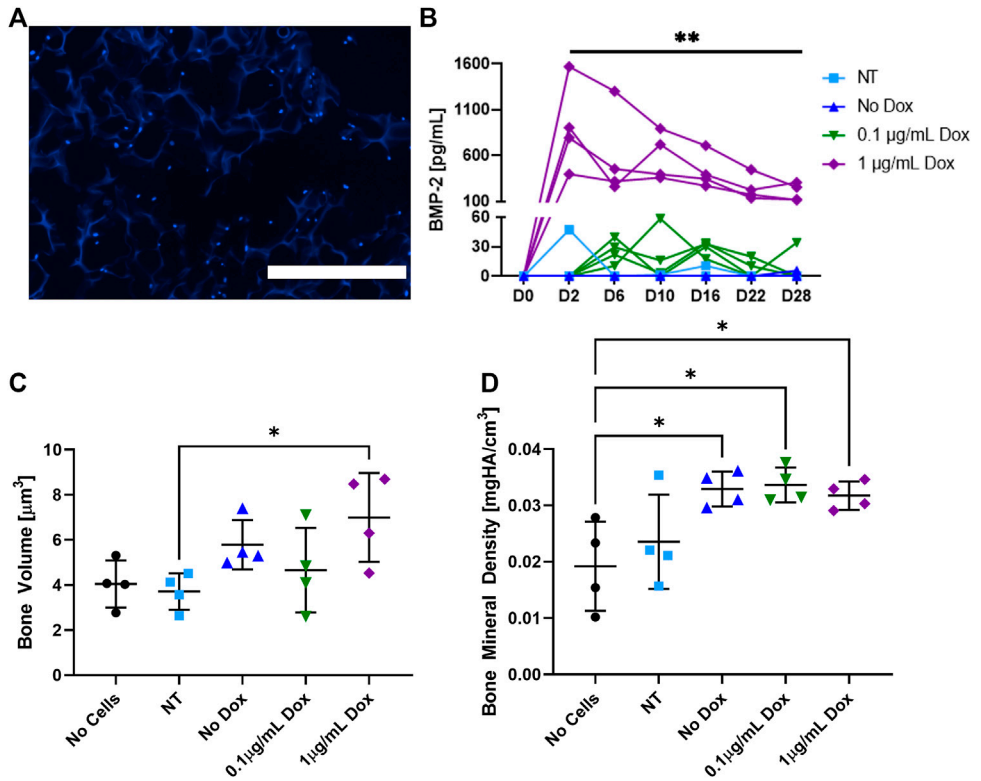

FIGURE 2 | *In vitro* analysis of the cell-seeded cryogel scaffolds. **(A)** Representative DAPI (blue) staining demonstrates the ADSCs infiltrated throughout the cryogel scaffold after 6 days of culture. **(B)** Measured by an ELISA, BMP-2 production was induced in transduced cells treated with 1 µg/ml of dox over 28 days, whereas non-transduced (NT) cells, transduced cells that did not receive dox, and transduced cells that only received 0.1 µg/ml of dox had statistically lower ($p < 0.01$) BMP-2 production. In transduced cells treated with 1 µg/ml of dox, **(C)** mineralized volume and **(D)** bone mineral density were significantly higher than those of non-transduced cells and acellular scaffolds, respectively ($p < 0.05$). The white scale bar denotes 400 µm.

the sham and scaffold groups or the GFP and BMP-2 groups at this timepoint ($\chi 2$, $p < 0.05$). In summary, the cellularized scaffolds promoted the radiographic healing, and the addition of BMP-2 stimulated the scaffold mineral formation.

Non-Unions Treated With BMP-2+ Cellularized Scaffolds Had Higher Mineral Content

Following the treatment with scaffolds for 2 or 8 weeks, the animals were sacrificed for micro-CT and histological evaluation. *Ex vivo* micro-CT analysis determined the callus bone volume at both 2 and 8 weeks for all the groups (**Figure 4**). Note that the 2 and 8 weeks timepoints had a threshold at 180 and 250 per mile, respectively, to isolate the scaffold mineral and thus, cannot be directly compared. At 2 weeks, the BMP-2+ cellularized scaffolds had significantly more bone volume than the acellular scaffold group ($p < 0.05$) and also trended higher compared to the sham control ($p < 0.0668$; **Figure 4A**). Three-dimensional reconstructions further demonstrate this, with the mineral formation around the non-union site and infiltrating into the surrounding scaffold. At 8 weeks, the BMP-2+ cellularized scaffolds had significantly more bone volume than all the other groups ($p < 0.001$; **Figure 4B**). Three-dimensional reconstructions at this timepoint also demonstrate mineral formation around the non-union site within the surrounding scaffold. Additionally, while the fracture line remains apparent between 2 and 8 weeks in the majority of the scaffold only and sham groups, the GFP+ and BMP-2+ cellularized scaffolds exhibited a higher ratio of bridging and remodeling of the cortical bone between 2 and 8 weeks. We assessed the skeletal phenotype of the left (intact) femora using micro-CT and found no significance between any groups ($p < 0.05$; **Supplementary Table S1**), indicating no systemic differences between the treatments. In summary, the cellularized scaffolds promoted bridging at the fracture site, but only BMP-2+ scaffolds produced a significant new bone surrounding the fracture site.

Histology Demonstrated Vessels Throughout the Surrounding Scaffold and Complete Cortical Bridging With the Addition of Cellularized Scaffolds

Following the micro-CT analysis of 2-8 weeks samples, histological evaluation was completed using picrosirius red/alcian blue stain (**Figure 5**). At 2 weeks post-sham surgery (6 weeks post-fracture), the sham control group displayed

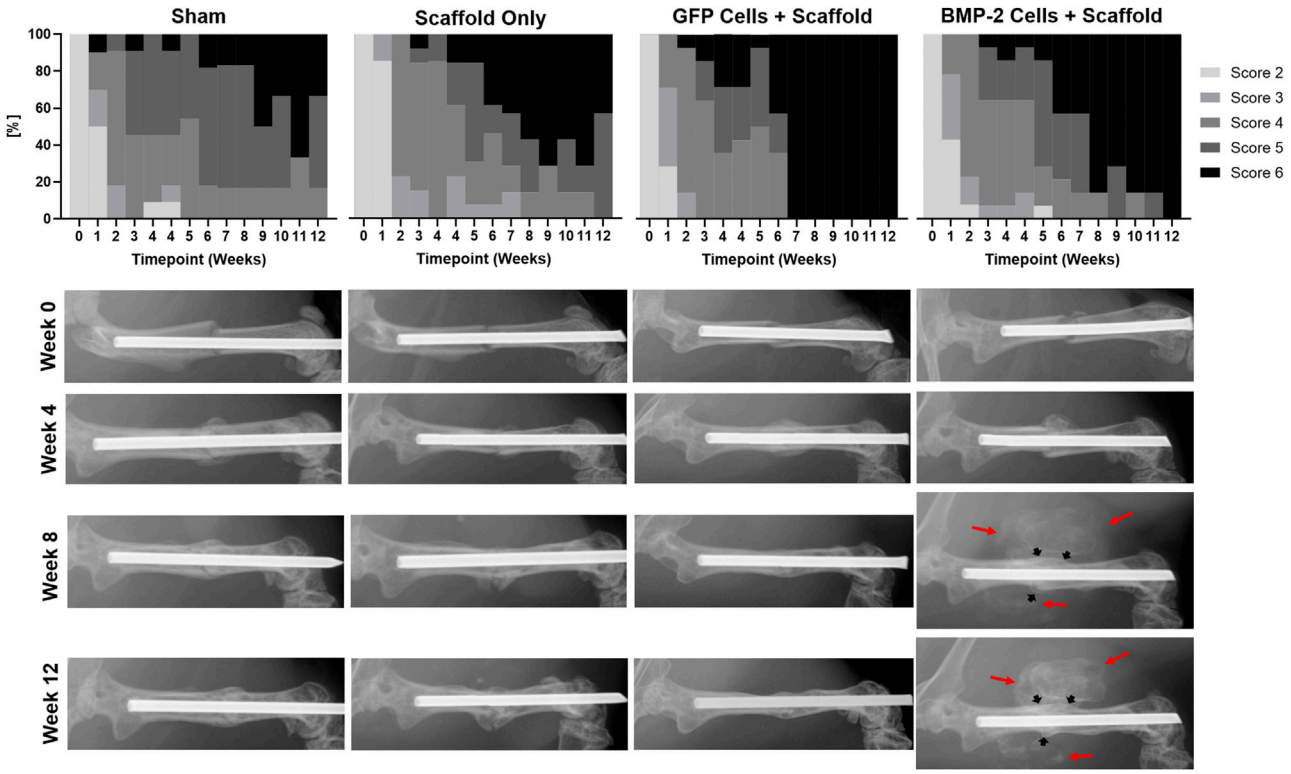

FIGURE 3 | Radiographic scoring of atrophic non-unions treated with sham (no scaffold or cells) control, cryogel (acellular) scaffold only, scaffolds seeded with GFP+ cells, and scaffolds seeded with cells expressing BMP-2. Due to the treatment with GCV and insufficient rescue, less than 50% of the Col1-tk scaffold only or sham groups had complete bridging at 12 weeks. Comparatively, the GFP+ and BMP-2+ cells were the only groups to achieve full bridging by week 12, with GFP+ cells displaying a score of 6 by week 6. Scoring of the radiographs demonstrated no significant difference between any groups at 6 weeks. However, there were significant differences between both the sham and scaffold groups as compared to both the GFP and BMP-2 groups at 12 weeks (χ^2, $p < 0.05$). Representative radiographs are shown from the time of fracture (Week 0) and at 4, 8, and 12 weeks. The BMP-2+ cellularized scaffolds possessed visually mineralized scaffolds surrounding the non-union site beginning 1–3 weeks following implantation (red arrows) in addition to the endogenous fracture callus (black arrows).

minimal woven bone formation and high levels of fibrous tissue. After 8 weeks, incomplete healing was still noted in 5 of the 6 samples, despite woven bone formation and some cortical bridging at all of the fracture sites. Similarly, the scaffold only treatment displayed some calcified areas with almost no cartilage present and minimal infiltration into the surrounding scaffold, showing incomplete endochondral bone formation. After 8 weeks, full bridging (denoted by continuous cortical bone) had visually occurred in 3 of the 7 samples, with the remaining samples possessing fibrous tissue and minimal cartilage. In the animals treated with the GFP+ cellularized scaffolds, new bone was formed at 2 weeks with the presence of minimal cartilage and fibrous tissue. By 8 weeks postimplantation, full bridging was achieved in 7 of the 7 samples, with the new bone infiltrated into the surrounding scaffold and no fibrous tissue or cartilage. When the cryogel scaffolds seeded with the BMP-2-expressing cells were implanted, cartilage was visualized surrounding the non-union site and within the surrounding scaffold in 6 of the 7 samples at 2 weeks. After 8 weeks, bridging was visually achieved in all the samples with the mineral infiltrating any surrounding scaffold still present; no fibrous or cartilage callus tissue was observed. In summary, the majority of samples in the sham and scaffold only groups displayed remnants of the original fragmented cortical bone with visible fracture surfaces and lacked complete bridging, whereas the GFP+ and BMP-2+ groups displayed continuous cortical surfaces such that the fracture line was no longer visible in most samples.

The sections were also stained for endomucin to identify the presence of vasculature, HSV-tk to localize the tk + cells, and GFP to discern the role of GFP+ cells in both the endogenous callus at the non-union site, as well as within the scaffold (**Figure 6**, **Supplementary Figures S1, S2**). Overall, all the groups possessed a large number of vessels directly at the fracture site and closely associated with the woven bone formation at 2 weeks (**Figure 6A**). After 8 weeks, the vasculature at this site was greatly reduced with little to no endomucin staining in all the groups. When the surrounding scaffolds were examined (**Figure 6B**), the vessels were visible both within the scaffold matrix and accompanying the new bone formation at 2 and 8 weeks in all the groups treated with a scaffold ± cells. The new bone was typically formed on the edges of the scaffold, both proximal and distal to the fracture site. With respect to the HSV-tk staining, the positively stained osteoblasts and osteocytes were

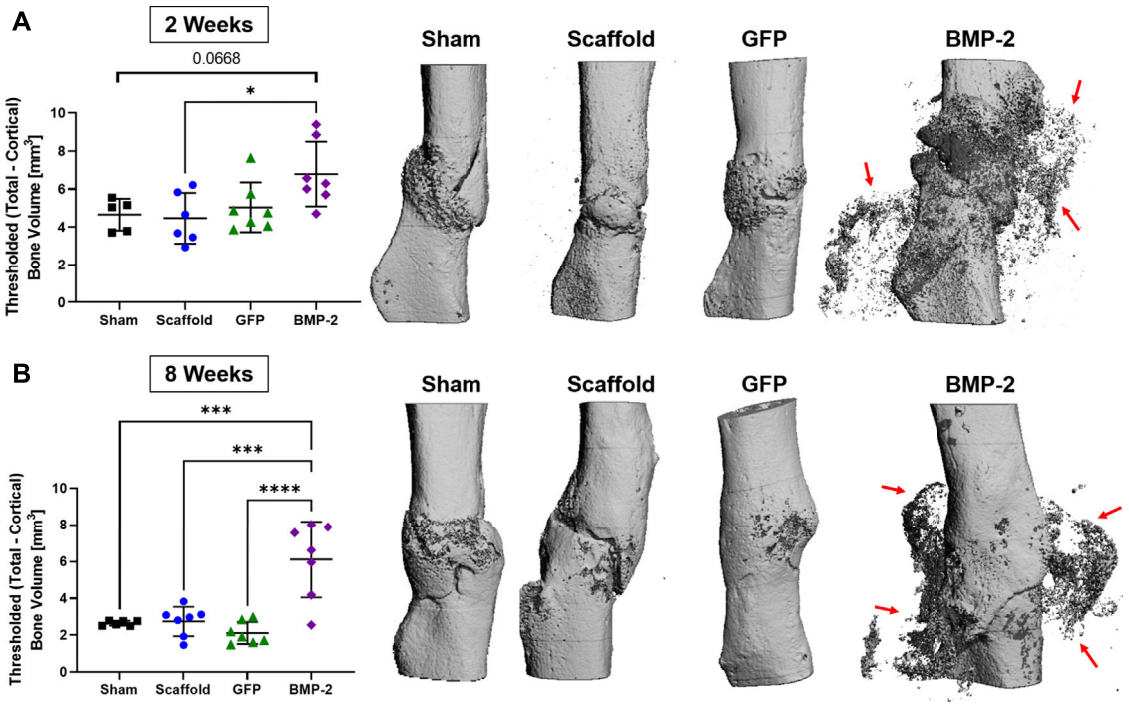

FIGURE 4 | *Ex vivo* micro-CT analysis of non-unions treated with sham control, scaffold only, GFP+ cellularized scaffolds, and BMP-2+ cellularized scaffolds at **(A)** 2 and **(B)** 8 weeks after repair. The callus bone volume is the threshold total bone—cortical bone. At 2 weeks, the BMP-2+ scaffolds had significantly more callus bone volume than (acellular) the scaffold only ($p < 0.05$) and trended higher than the sham control ($p < 0.0668$). At 8 weeks, the BMP-2+ scaffolds had significantly more callus bone volume than all the other groups ($p < 0.001$). Three-dimensional reconstructions demonstrate that fracture lines are still present in the sham and scaffold groups at both 2 and 8 weeks, whereas the GFP and BMP-2 groups exhibited increased bridging and remodeling after 8 weeks. Finally, both timepoints exhibited a high mineral content surrounding the non-union site of the BMP-2+ groups (red arrows).

detected within the bone tissue in some samples from every group at both 2 and 8 weeks (**Supplementary Figure S1**). After 8 weeks, all the BMP-2+ scaffolds also possessed HSV-tk + cells (red arrows) localized to the new bone formed within the scaffold, indicating the invasion of host cells. Finally, GFP+ staining was found within the scaffold around the fracture site at 2 weeks in all the samples treated with scaffolds seeded with GFP+ cells (**Supplementary Figure S2**). However, after 8 weeks, there was no GFP+ staining in 5 of the 7 samples, with very little staining in the remaining 2 samples, demonstrating that the GFP+ cells were no longer present at 8 weeks in the majority of samples.

DISCUSSION

We hypothesized that a bioactive cryogel-mediated, doxycycline-inducible lentiviral gene delivery system of BMP-2 would induce osteogenesis at the atrophic non-union defect site. This approach was based on the previous studies which demonstrated that scaffold-mediated gene delivery can induce the sustained transgene expression and protein synthesis by MSCs (Brunger et al., 2014; Glass et al., 2014; Moutos et al., 2016; Huynh et al., 2018; Rowland et al., 2018). Overall, the *in vitro* data demonstrated the feasibility of the cryogel-mediated lentiviral delivery of BMP-2 with adhesion and infiltration of cells, as well as the sustained BMP-2 production over 28 days. *In vivo*, following implantation at 4 weeks, 50% or less of the animals treated with either scaffold only or the sham control had a complete radiographic bridging at 12 weeks. This blunted healing response was consistent with our previous study that established the Col1-tk atrophic non-union model (Hixon et al., 2021). Comparatively, the radiograph analysis showed that the scaffolds seeded with GFP + cells and the scaffolds seeded with cells producing BMP-2 were the only groups that reached complete bridging in all the animals by the end of 12 weeks. Mineralization was also noted radiographically throughout the implanted scaffold surrounding the fracture site in all the animals treated with the BMP-2+ cells. Histologically, it was observed that the GFP+ and BMP-2+ scaffolds both had woven bone formation as early as 2 weeks after the implantation, with BMP-2+ scaffolds displaying both cartilage and woven bone directly at the non-union site, as well as infiltrated into the surrounding scaffold. At 8 weeks after the GFP+ and BMP-2+ scaffold implantation, the woven bone was noted within the scaffold and the non-union site had undergone complete bridging as noted by the continuous cortical bone. Furthermore, the overall addition of a scaffold ± cells resulted in blood vessel formation, as well as HSV-tk + cells in the BMP-2 samples, localized to new bone within the scaffold matrix at 8 weeks. Importantly, in the GFP+ cell group, while the GFP+ cells were noted histologically at 2 weeks, the majority of

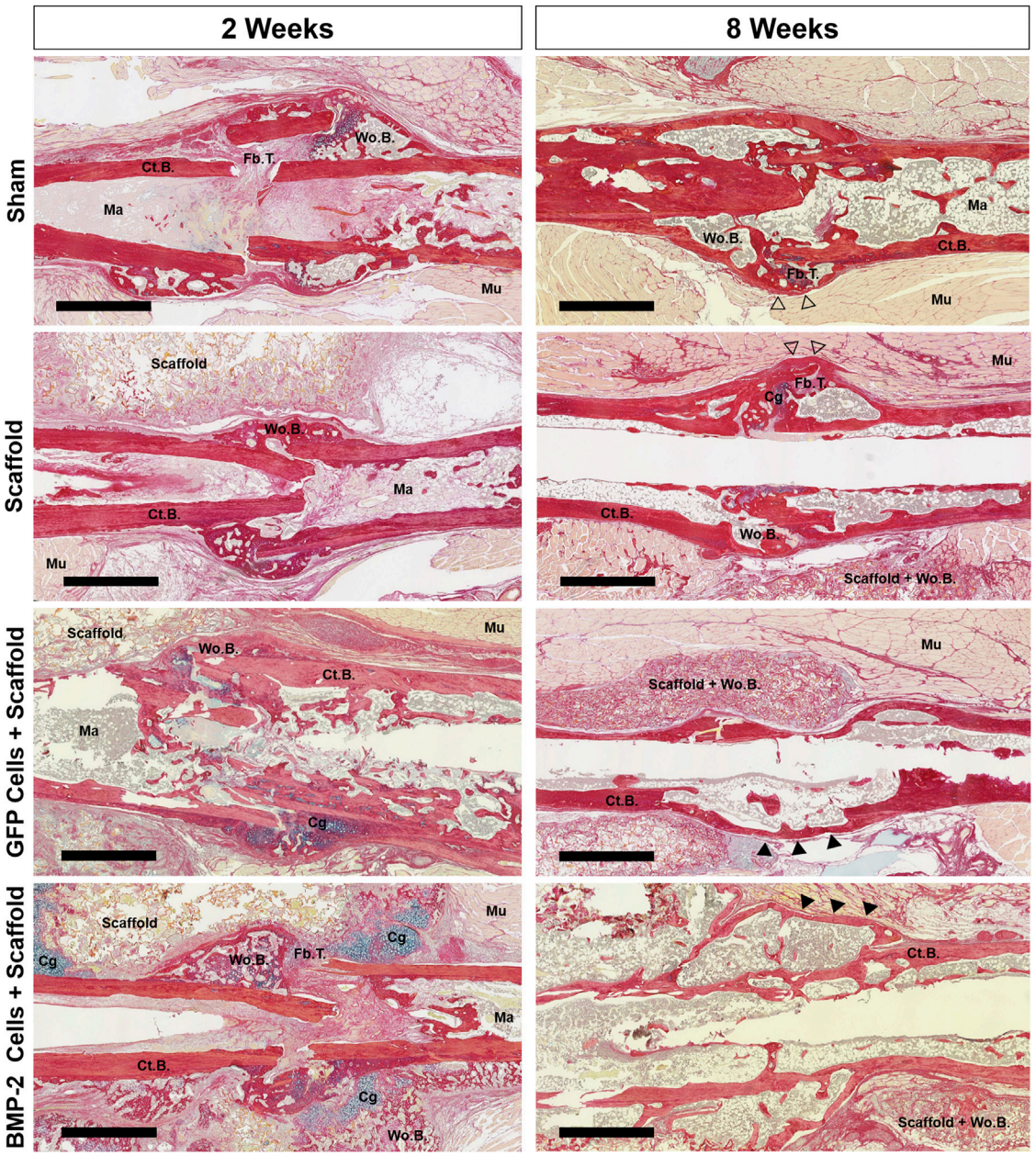

FIGURE 5 | Representative picrosirius red/alcian blue staining of the nonunion site of all groups at 2 and 8 weeks postimplantation. Both the scaffold only and sham groups displayed early woven bone and fibrous tissue, followed by additional bridging and bone formation between 2 and 8 weeks. At 8 weeks, the callus had some pockets of woven bone at a still visible fracture site (open arrowheads). While the GFP+ group had some cartilage, it was minimal and resulted in bridging in all animals by 8 weeks. At 2 weeks, 6 of the 7 BMP-2+ groups displayed the cartilage both surrounding the nonunion site and within the surrounding scaffold. After 8 weeks, bridging was visually achieved in all BMP-2 samples with mineral infiltration into the surrounding scaffolds. Cortical bridging was denoted by filled arrowheads. Scale bars denote 1 mm. Cg, cartilage; Ct.B, cortical bone; Fb.T, fibrous tissue/other; Ma, marrow; Mu, muscle; Wo.B, woven bone.

samples had no GFP+ cells within the scaffold or around the fracture site at 8 weeks. This observation indicates that the native cells were responsible for bone formation seen at 8 weeks, and we infer that the native cells that were not targeted during the 2 weeks of GCV dosing were activated by the implantation of the cellularized scaffolds. Overall, the cell-seeded cryogels resulted in osseous healing and while the addition of BMP-2 promoted endochondral ossification, this appeared to delay healing contrary to our initial hypothesis. It is possible that the promotion of endochondral ossification may produce a better functional result in the long term as it mimics normal fracture healing. However, this should be further investigated

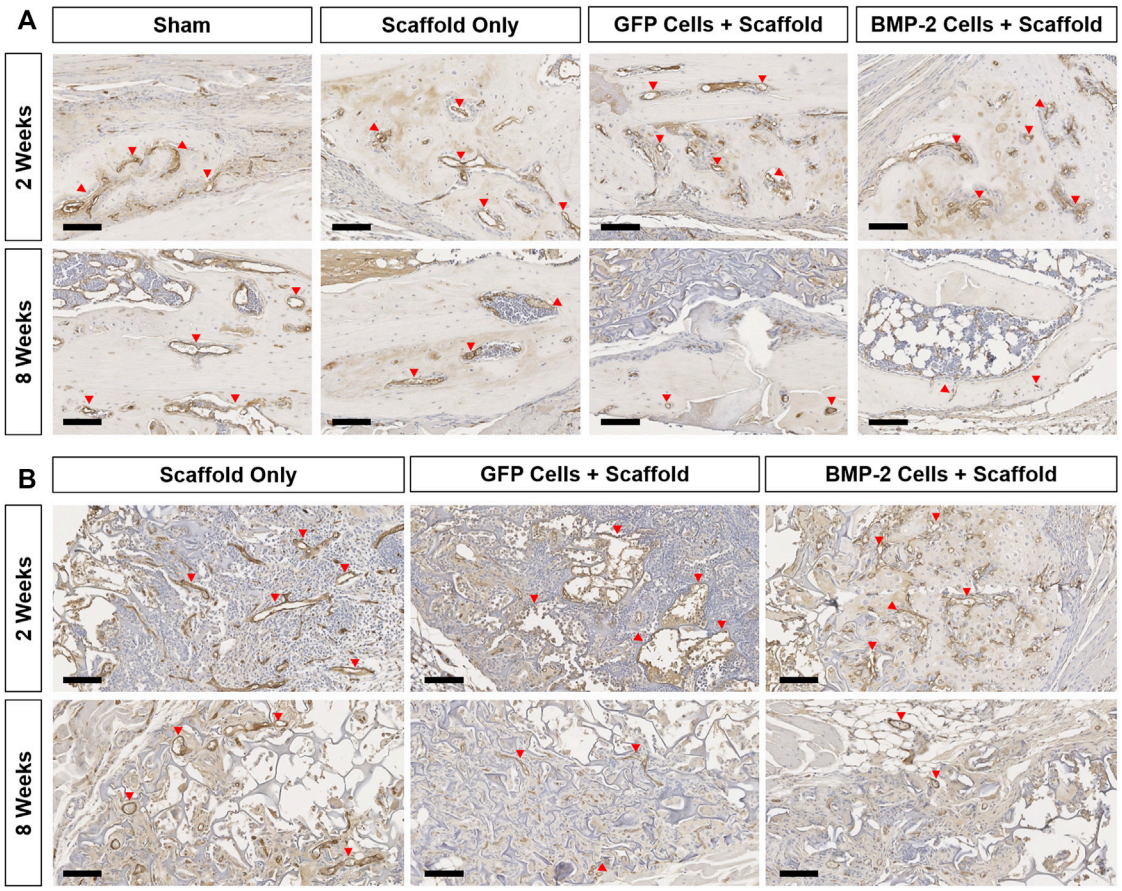

FIGURE 6 | Representative endomucin (brown) staining of the vasculature within the non-union and scaffold sites of all the groups at 2 and 8 weeks postimplantation. **(A)** 10x images of the woven bone at 2 weeks show extensive vessel staining in all the groups (red arrows). Comparatively, at 8 weeks, vessel staining was greatly reduced in all groups. **(B)** Endomucin staining within the scaffold showed vasculature associated with new bone formation at both the timepoints in all groups treated with a scaffold ± cells. Scale bars denote 100 μm.

with future biomechanical testing. Our findings support further investigation and development of a cell-seeded tissue engineering cryogel (±BMP-2) to target specific timepoints in the clinical non-union healing process.

Endochondral ossification plays a critical role in fracture repairing and remodeling. This process occurs between the two fractured ends where the cartilage contributes to a soft callus to initially stabilize the fracture site. In combination with intramembranous ossification and the formation of a hard callus, full bridging occurs with the continuous cortical bone (Marsell and Einhorn, 2011). BMP-2 has been previously shown to induce chondrogenic differentiation, osteogenic differentiation, and endochondral ossification within the same system (Zhou et al., 2016). Thus, the expression of BMP-2 not only encouraged bone formation within the implanted scaffolds surrounding the fracture site, but also appeared to promote endochondral ossification and bridging at the fracture site. Notably, cellularized scaffolds without the BMP-2 transfection also appeared to improve healing at the fracture site, and thus we are not able to fully attribute the improved healing to the effects of local BMP-2 production based on this initial study. Future work should examine shorter timepoints to identify the windows of healing as guided by the addition of the scaffold-mediated lentiviral delivery of BMP-2. This would allow for targeted healing within an atrophic non-union. Additionally, the scaffold-mediated lentiviral transduction technique could be applied to an acellular scaffold to deliver BMP-2 to the non-union site, encouraging a similar endochondral ossification response without using implanted cells.

The use of the Col1-tk mouse as a model of atrophic non-union, as well as our scaffold fabrication and implantation techniques, has several limitations. Our previous study has demonstrated that 2 weeks of GCV dosing in Col1-tk mice blunted callus formation and led to a functional non-union at 12 weeks (Hixon et al., 2021). We also observed that *via* radiography, *in vivo* micro-CT, and histology that the fracture healing response did not change after the first 4 weeks in Col1-tk mice, that is, once the non-union was established, it did not recover on its own. Thus, we selected the 4-weeks timepoint for the intervention in the current study. Unexpectedly, we noted that in some sham and scaffold only samples, there was radiographic and histological evidence of cortical bridging. It

is possible that the surgical intervention increased blood flow at the injury site or otherwise created an environment that reactivated periosteal cells that were dormant. In addition, the previous work has demonstrated that muscle-derived stem cells can differentiate into the cartilage and bone and directly participate in fracture healing (Liu et al., 2010; Shah et al., 2013). A short period of GCV dosing following the scaffold implantation surgery may block the healing due solely to surgical intervention, providing a more challenging environment to test the interventions. Regarding the cryogel scaffolds, these were designed for the ease of handling and cell seeding *in vitro,* as well as for the feasibility of surgical implantation. Yet, the thickness of the scaffolds was large relative to the femur dimensions, and they showed some tendency to "unwrap" after the implantation. This resulted in a diffuse region of mineralization in the BMP-2+ scaffold group. Additionally, the thick scaffold layer may have hindered the cellular and vascular infiltration of the scaffold, as well as integration of the scaffold bone with the native callus at the bone surface. Despite this, 5 of the 7 BMP-2 group had mineralized scaffold directly integrated with the fully bridged cortical bone. In the remaining 2 samples, the mineralized scaffold rested against the bridged fracture site. However, the cortical bone was continuous with no apparent fracture sites, demonstrating the overall contribution to healing by the BMP-2+ scaffolds as compared to scaffold only. Future studies will further optimize the scaffold size and overall placement to minimize disruption and physical scaffold movement following implantation. Finally, this study served as a proof-of-concept, and overall, BMP-2 delivery was not controlled or localized appropriately. Future work should reconfigure the release to be more localized to the fracture site and target the BMP-2-induced endochondral ossification, which could be advantageous to bone healing. In addition to this, it was demonstrated that the dox-inducible BMP-2 expression can promote endochondral ossification in the cryogel itself which could be optimized spatially and temporally.

The current clinical practice of non-union often involves surgical intervention and the use of autologous bone graft. While the autologous graft is effective in promoting healing, it requires a second-site surgery and has other limitations/contraindications including potential infection, donor site morbidity, and limited availability (Roberts and Rosenbaum, 2012; Sohn and Oh, 2019). Therefore, we selected a tissue engineering approach that does not use the autologous bone graft, but does require a surgical intervention, as a first step toward an alternative to current practices. Of interest was the finding that the cell-seeded scaffolds may enhance the healing in atrophic non-unions. Notably, the sham group histologically closely mirrored the delayed bone bridging and blunted callus formation as previously shown in our Col1-tk mouse model of atrophic non-union where no intervention had been employed (Hixon et al., 2021). In contrast, both the GFP+ and BMP-2+ cellularized cryogel scaffolds resulted in the radiographic bridging at the site of the non-union. The GFP+ scaffolds appeared to result in faster healing than the BMP-2+ scaffolds. This could be attributed to the initial high cartilage response in the BMP-2+ scaffolds, which may have delayed the overall healing of the non-union. One of the major downfalls in treating complex bone defects is a lack of structure and stability to guide healing. To combat this, tissue engineering scaffolds provide a unique template that can be tailored to target an appropriate structure. Combining the tunable delivery of a biological agent with a scaffold may further enhance healing in complex atrophic non-unions. In this study, the addition of cells in combination with the cryogel scaffolds resulted in cortical bridging, suggesting that cryogels seeded with the ADSCs (with or without the addition of BMP-2) is a promising experimental approach to promote the rescue of the non-union. Future work should include mechanical testing to directly compare BMP-2+ and GFP+ cellularized scaffolds to define the functionality of this rescue technique. Additionally, as this is a tunable/inducible system, the BMP-2 delivery window should be further explored to identify if it is advantageous to include BMP-2 or if solely providing the cells is sufficient to induce regeneration.

In conclusion, we demonstrated that a cryogel scaffold seeded with cells enhances fracture healing at a non-union site as radiographic and histological bridging was achieved in all animals treated with cell-seeded scaffolds (±BMP-2). Furthermore, the addition of BMP-2 resulted in cartilage formation at early timepoints, stimulating the process of endochondral ossification, but slightly delayed overall healing. Overall, the cryogel scaffolds provided a supportive, porous matrix for bone ingrowth and new tissue formation. This research is significant as it utilizes a clinically relevant model of atrophic non-union to evaluate a novel rescue technique to induce bone formation and promote healing at the non-union site. These promising initial findings support the continued refinement and the study of cellularized cryogels for treating the non-healing fractures.

DATA AVAILABILITY STATEMENT

The raw data supporting the conclusion of this article will be made available by the authors, without undue reservation.

ETHICS STATEMENT

Experimental procedures were approved by the Institutional Animal Care and Use Committee (IACUC) at Washington University in St. Louis in accordance with the Animal Welfare Act and PHS Policy on Humane Care and Use of Laboratory Animals.

AUTHOR CONTRIBUTIONS

Study design: KH, DK, JM, FG, and MS. Study conduct: KH, DK, JM, and AM. Data collection: KH, DK, JM, and AM. Data analysis: KH, DK, and JM. Data interpretation: KH, DK, JM, and MS. Drafting the manuscript: KH. Revising the manuscript:

KH, DK, JM, AM, FG, and MS. Approving the final version of the manuscript: KH, DK, JM, AM, FG, and MS.

FUNDING

This work was supported by funding from NIAMS (R01 AR050211, P30 AR074992, P30 AR073752, R01 AG15768, R01 AG46927, R01 AR07299, R21 AR076636, T32 AR060719, and F32 AR076191) and Dept. of Defense W81XWH-20-PRMRP-IIRA. Paraffin histological images were taken with the Nanozoomer at Alafi Neuroimaging Core (S10 RR027552).

ACKNOWLEDGMENTS

We would like to thank the Washington University in St. Louis Musculoskeletal Research Center (MRC) Cores and staff for assistance. Specifically, thanks to both Crystal Idleburg and Samantha Coleman for histological processing and sectioning of all specimens. We also would like to thank Sara Oswald for scaffold micro-CT assistance and Drs. Gretchen Meyer and Chelsey Dunham for training with ADSC isolation. 3.6Col1a1-tk mice were kindly provided by the laboratories of Drs. Robert Jilka and Charles O'Brien (University of Arkansas for Medical Sciences, Little Rock, AR, USA). Finally, we acknowledge Dr. Scott Sell at Saint Louis University for providing lyophilization resources for scaffold fabrication.

SUPPLEMENTARY MATERIAL

The Supplementary Material for this article can be found online at: https://www.frontiersin.org/articles/10.3389/fbioe.2022.851904/full#supplementary-material

REFERENCES

Baer, P. C., and Geiger, H. (2012). Adipose-derived Mesenchymal Stromal/stem Cells: Tissue Localization, Characterization, and Heterogeneity. *Stem Cell Int* 2012, 812693. doi:10.1155/2012/812693

Bakhshpour, M., Idil, N., Perçin, I., and Denizli, A. (2019). Biomedical Applications of Polymeric Cryogels. *Appl. Sci.* 9 (3), 553. doi:10.3390/app9030553

Bonnarens, F., and Einhorn, T. A. (1984). Production of a Standard Closed Fracture in Laboratory Animal Bone. *J. Orthop. Res.* 2 (1), 97–101. doi:10.1002/jor.1100020115

Brownlow, H. C., and Simpson, A. H. R. W. (2000). Metabolic Activity of a New Atrophic Nonunion Model in Rabbits. *J. Orthop. Res.* 18 (3), 438–442. doi:10.1002/jor.1100180316

Brunger, J. M., Huynh, N. P., Guenther, C. M., Perez-Pinera, P., Moutos, F. T., Sanchez-Adams, J., et al. (2014). Scaffold-mediated Lentiviral Transduction for Functional Tissue Engineering of Cartilage. *Proc. Natl. Acad. Sci. U S A.* 111 (9), E798–E806. doi:10.1073/pnas.1321744111

Choi, P., Ogilvie, C., Thompson, Z., Miclau, T., and Helms, J. A. (2004). Cellular and Molecular Characterization of a Murine Non-union Model. *J. Orthop. Res.* 22 (5), 1100–1107. doi:10.1016/j.orthres.2004.03.008

Costa, S. A., Paula, O. F., Silva, C. R., Leão, M. V., and Santos, S. S. (2015). Stability of Antimicrobial Activity of Peracetic Acid Solutions Used in the Final Disinfection Process. *Braz. Oral Res.* 29, S1806. doi:10.1590/1807-3107BOR-2015.vol29.0038

Cullinane, D. M., Fredrick, A., Eisenberg, S. R., Pacicca, D., Elman, M. V., Lee, C., et al. (2002). Induction of a Neoarthrosis by Precisely Controlled Motion in an Experimental Mid-femoral Defect. *J. Orthop. Res.* 20 (3), 579–586. doi:10.1016/s0736-0266(01)00131-0

Cunningham, B. P., Brazina, S., Morshed, S., and Miclau, T. (2017). Fracture Healing: A Review of Clinical, Imaging and Laboratory Diagnostic Options. *Injury* 48 (Suppl. 1), S69–s75. doi:10.1016/j.injury.2017.04.020

Dailey, H. L., Wu, K. A., Wu, P.-S., McQueen, M. M., and Court-Brown, C. M. (2018). Tibial Fracture Nonunion and Time to Healing after Reamed Intramedullary Nailing: Risk Factors Based on a Single-Center Review of 1003 Patients. *J. Orthop. Trauma* 32 (7), e263–e269. doi:10.1097/bot.0000000000001173

de Lageneste, O. D., Julien, A., Abou-Khalil, R., Frangi, G., Carvalho, C., Cagnard, N., et al. (2018). Periosteum Contains Skeletal Stem Cells with High Bone Regenerative Potential Controlled by Periostin. *Nat. Commun.* 9 (1), 773. doi:10.1038/s41467-018-03124-z

Douglas, T. E. L., Messersmith, P. B., Chasan, S., Mikos, A. G., de Mulder, E. L. W., Dickson, G., et al. (2012). Enzymatic Mineralization of Hydrogels for Bone Tissue Engineering by Incorporation of Alkaline Phosphatase. *Macromol. Biosci.* 12 (8), 1077–1089. doi:10.1002/mabi.201100501

Dumas, J. E., BrownBaer, P. B., Prieto, E. M., Guda, T., Hale, R. G., Wenke, J. C., et al. (2012). Injectable Reactive Biocomposites for Bone Healing in Critical-Size Rabbit Calvarial Defects. *Biomed. Mater.* 7 (2), 024112. doi:10.1088/1748-6041/7/2/024112

Dunham, C., Havlioglu, N., Chamberlain, A., Lake, S., and Meyer, G. (2020). Adipose Stem Cells Exhibit Mechanical Memory and Reduce Fibrotic Contracture in a Rat Elbow Injury Model. *FASEB j.* 34 (9), 12976–12990. doi:10.1096/fj.202001274r

Einhorn, T. A. (1998). The Cell and Molecular Biology of Fracture Healing. *Clin. Orthop. Relat. Res.* 355, S7–S21. doi:10.1097/00003086-199810001-00003

Einhorn, T. A. (1995). Enhancement of Fracture-Healing. *J. Bone Jt. Surg.* 77 (6), 940–956. doi:10.2106/00004623-199506000-00016

Ekegren, C., Edwards, E., de Steiger, R., and Gabbe, B. (2018). Incidence, Costs and Predictors of Non-Union, Delayed Union and Mal-Union Following Long Bone Fracture. *Ijerph* 15 (12), 2845. doi:10.3390/ijerph15122845

Fiset, S., Godbout, C., Crookshank, M. C., Zdero, R., Nauth, A., and Schemitsch, E. H. (2018). Experimental Validation of the Radiographic Union Score for Tibial Fractures (RUST) Using Micro-computed Tomography Scanning and Biomechanical Testing in an Iin-Vivo Rat Model. *J. Bone Jt. Surg Am* 100 (21), 1871–1878. doi:10.2106/JBJS.18.00035

Garcia, P., au, fnm., Histing, T., Holstein, J., Klein, W., Laschke, M., et al. (2013). Rodent Animal Models of Delayed Bone Healing and Non-union Formation: a Comprehensive Review. *eCM* 26, 1–14. discussion 12-4. doi:10.22203/ecm.v026a01

Garcia, P., Herwerth, S., Matthys, R., Holstein, J. H., Histing, T., Menger, M. D., et al. (2011). The LockingMouseNail-A New Implant for Standardized Stable Osteosynthesis in Mice. *J. Surg. Res.* 169 (2), 220–226. doi:10.1016/j.jss.2009.11.713

Garcia, P., Holstein, J. H., Maier, S., Schaumlöffel, H., Al-Marrawi, F., Hannig, M., et al. (2008). Development of a Reliable Non-union Model in Mice. *J. Surg. Res.* 147 (1), 84–91. doi:10.1016/j.jss.2007.09.013

Gardner, M. J., Putnam, S. M., Wong, A., Streubel, P. N., Kotiya, A., and Silva, M. J. (2011). Differential Fracture Healing Resulting from Fixation Stiffness Variability: a Mouse Model. *J. Orthopaedic Sci.* 16 (3), 298–303. doi:10.1007/s00776-011-0051-5

Glass, K. A., Link, J. M., Brunger, J. M., Moutos, F. T., Gersbach, C. A., and Guilak, F. (2014). Tissue-engineered Cartilage with Inducible and Tunable Immunomodulatory Properties. *Biomaterials* 35 (22), 5921–5931. doi:10.1016/j.biomaterials.2014.03.073

Gómez-Barrena, E., Rosset, Philippe., Lozano, Daniel., Stanovici, Julien., Ermthaller, Christian., and Gerbhard, Florian. (2015). Bone Fracture Healing: Cell Therapy in Delayed Unions and Nonunions. *Bone* 70, 93–101. doi:10.1016/j.bone.2014.07.033

Hao, C., Wang, Y., Shao, L., Liu, J., Chen, L., and Zhao, Z. (2016). Local Injection of Bone Mesenchymal Stem Cells and Fibrin Glue Promotes the Repair of Bone

Atrophic Nonunion *In Vivo*. *Adv. Ther.* 33 (5), 824–833. doi:10.1007/s12325-016-0329-2

Harrison, L. J., Cunningham, J. L., Strömberg, L., and Goodship, A. E. (2003). Controlled Induction of a Pseudarthrosis: a Study Using a Rodent Model. *J. Orthopaedic Trauma* 17 (1), 11–21. doi:10.1097/00005131-200301000-00003

Henderson, T. M. A., Ladewig, K., Haylock, D. N., McLean, K. M., and O'Connor, A. J. (2013). Cryogels for Biomedical Applications. *J. Mater. Chem. B* 1 (21), 2682–2695. doi:10.1039/c3tb20280a

Hixon, K. R., McKenzie, J. A., Sykes, D. A. W., Yoneda, S., Hensley, A., Buettmann, E. G., et al. (2021). Ablation of Proliferating Osteoblast Lineage Cells after Fracture Leads to Atrophic Nonunion in a Mouse Model. *J. Bone Miner Res.* 36 (11), 2243–2257. doi:10.1002/jbmr.4424

Hixon, K. R., Melvin, A. M., Lin, A. Y., Hall, A. F., and Sell, S. A. (2017). Cryogel Scaffolds from Patient-specific 3D-Printed Molds for Personalized Tissue-Engineered Bone Regeneration in Pediatric Cleft-Craniofacial Defects. *J. Biomater. Appl.* 32, 598–611. doi:10.1177/0885328217734824

Hixon, K. R., Eberlin, C. T., Kadakia, P. U., McBride-Gagyi, S. H., Jain, E., and Sell, S. A. (2016). A Comparison of Cryogel Scaffolds to Identify an Appropriate Structure for Promoting Bone Regeneration. *Biomed. Phys. Eng. Express* 2 (3), 035014. doi:10.1088/2057-1976/2/3/035014

Hixon, K. R., Lu, T., and Sell, S. A. (2017). A Comprehensive Review of Cryogels and Their Roles in Tissue Engineering Applications. *Acta Biomater.* 62 (Suppl. C), 29–41. doi:10.1016/j.actbio.2017.08.033

Huynh, N. P. T., Brunger, J. M., Gloss, C. C., Moutos, F. T., Gersbach, C. A., and Guilak, F. (2018). Genetic Engineering of Mesenchymal Stem Cells for Differential Matrix Deposition on 3D Woven Scaffolds. *Tissue Eng. Part. A.* 24 (19-20), 1531–1544. doi:10.1089/ten.TEA.2017.0510

Jilka, R. L., O'Brien, C. A., Ali, A. A., Roberson, P. K., Weinstein, R. S., and Manolagas, S. C. (2009). Intermittent PTH Stimulates Periosteal Bone Formation by Actions on post-mitotic Preosteoblasts. *Bone* 44 (2), 275–286. doi:10.1016/j.bone.2008.10.037

Kaspar, K., Matziolis, G., Strube, P., Sentürk, U., Dormann, S., Bail, H. J., et al. (2008). A New Animal Model for Bone Atrophic Nonunion: Fixation by External Fixator. *J. Orthop. Res.* 26 (12), 1649–1655. doi:10.1002/jor.20651

Kathuria, N., Tripathi, A., Kar, K., and Kumar, A. (2009). Synthesis and Characterization of Elastic and Macroporous Chitosan-Gelatin Cryogels for Tissue Engineering. *Acta Biomater.* 5 (1), 406–418. doi:10.1016/j.actbio.2008.07.009

Kemençe, N., and Bölgen, N. (2017). Gelatin- and Hydroxyapatite-Based Cryogels for Bone Tissue Engineering: Synthesis, Characterization,in Vitroandin Vivobiocompatibility. *J. Tissue Eng. Regen. Med.* 11 (1), 20–33. doi:10.1002/term.1813

Kokubu, T., Hak, D. J., Hazelwood, S. J., and Reddi, A. H. (2003). Development of an Atrophic Nonunion Model and Comparison to a Closed Healing Fracture in Rat Femur. *J. Orthop. Res.* 21 (3), 503–510. doi:10.1016/s0736-0266(02)00209-7

Krishnakumar, G. S., Roffi, A., Reale, D., Kon, E., and Filardo, G. (2017). Clinical Application of Bone Morphogenetic Proteins for Bone Healing: a Systematic Review. *Int. Orthopaedics (Sicot)* 41 (6), 1073–1083. doi:10.1007/s00264-017-3471-9

Kumar, S., Wan, C., Ramaswamy, G., Clemens, T. L., and Ponnazhagan, S. (2010). Mesenchymal Stem Cells Expressing Osteogenic and Angiogenic Factors Synergistically Enhance Bone Formation in a Mouse Model of Segmental Bone Defect. *Mol. Ther.* 18 (5), 1026–1034. doi:10.1038/mt.2009.315

Liao, H.-T., Shalumon, K. T., Chang, K.-H., Sheu, C., and Chen, J.-P. (2016). Investigation of Synergistic Effects of Inductive and Conductive Factors in Gelatin-Based Cryogels for Bone Tissue Engineering. *J. Mater. Chem. B* 4 (10), 1827–1841. doi:10.1039/c5tb02496j

Liu, R., Schindeler, A., and Little, D. G. (2010). The Potential Role of Muscle in Bone Repair. *J. Musculoskelet. Neuronal Interact* 10 (1), 71–76.

Liu, X., McKenzie, J. A., Maschhoff, C. W., Gardner, M. J., and Silva, M. J. (2017). Exogenous Hedgehog Antagonist Delays but Does Not Prevent Fracture Healing in Young Mice. *Bone* 103, 241–251. doi:10.1016/j.bone.2017.07.017

Lo, K. W.-H., Ulery, B. D., Ashe, K. M., and Laurencin, C. T. (2012). Studies of Bone Morphogenetic Protein-Based Surgical Repair. *Adv. Drug Deliv. Rev.* 64 (12), 1277–1291. doi:10.1016/j.addr.2012.03.014

Lu, C., Miclau, T., Hu, D., and Marcucio, R. S. (2007). Ischemia Leads to Delayed union during Fracture Healing: a Mouse Model. *J. Orthop. Res.* 25 (1), 51–61. doi:10.1002/jor.20264

Marsell, R., and Einhorn, T. A. (2011). The Biology of Fracture Healing. *Injury* 42 (6), 551–555. doi:10.1016/j.injury.2011.03.031

McKenzie, J. A., Maschhoff, C., Liu, X., Migotsky, N., Silva, M. J., and Gardner, M. J. (2019). Activation of Hedgehog Signaling by Systemic Agonist Improves Fracture Healing in Aged Mice. *J. Orthop. Res.* 37 (1), 51–59. doi:10.1002/jor.24017

Mills, L. A., Aitken, S. A., and Simpson, A. H. R. W. (2017). The Risk of Non-union Per Fracture: Current Myths and Revised Figures from a Population of over 4 Million Adults. *Acta Orthopaedica* 88 (4), 434–439. doi:10.1080/17453674.2017.1321351

Mills, L. A., and Simpson, A. H. R. W. (2012). In Vivomodels of Bone Repair. *The J. Bone Jt. Surg. Br. volume* 94-B (7), 865–874. doi:10.1302/0301-620x.94b7.27370

Mishra, R., Goel, S. K., Gupta, K. C., and Kumar, A. (2014). Biocomposite Cryogels as Tissue-Engineered Biomaterials for Regeneration of Critical-Sized Cranial Bone Defects. *Tissue Eng. Part. A.* 20 (3-4), 751–762. doi:10.1089/ten.TEA.2013.0072

Mitchell, J. B., McIntosh, K., Zvonic, S., Garrett, S., Floyd, Z. E., Kloster, A., et al. (2006). Immunophenotype of Human Adipose-Derived Cells: Temporal Changes in Stromal-Associated and Stem Cell-Associated Markers. *Stem Cells* 24 (2), 376–385. doi:10.1634/stemcells.2005-0234

Moghaddam, A., Thaler, B., Bruckner, T., Tanner, M., and Schmidmaier, G. (2016). Treatment of Atrophic Femoral Non-unions According to the diamond Concept: Results of One- and Two-step Surgical Procedure. *J. Orthop.* 14 (1), 123–133. doi:10.1016/j.jor.2016.10.003

Moutos, F. T., Glass, K. A., Compton, S. A., Ross, A. K., Gersbach, C. A., Guilak, F., et al. (2016). Anatomically Shaped Tissue-Engineered Cartilage with Tunable and Inducible Anticytokine Delivery for Biological Joint Resurfacing. *Proc. Natl. Acad. Sci. U S A.* 113 (31), E4513–E4522. doi:10.1073/pnas.1601639113

Oni, O. O. A. (1995). A Non-union Model of the Rabbit Tibial Diaphysis. *Injury* 26 (9), 619–622. doi:10.1016/0020-1383(95)00132-s

O. Okay (Editor) (2014). *Polymeric Cryogels: Macroporous Gels with Remarkable Properties* (Cham: Springer International Publishing).

Orth, M., au, fnm., Kruse, N., Braun, B., Scheuer, C., Holstein, J., et al. (2017). BMP-2-coated mineral Coated Microparticles Improve Bone Repair in Atrophic Non-unions. *eCM* 33, 1–12. doi:10.22203/ecm.v033a01

Panteli, M., Pountos, I., Jones, E., and Giannoudis, P. V. (2015). Biological and Molecular Profile of Fracture Non-union Tissue: Current Insights. *J. Cel. Mol. Med.* 19 (4), 685–713. doi:10.1111/jcmm.12532

Park, S.-H., Silva, M., Bahk, W.-J., McKellop, H., and Lieberman, J. R. (2002). Effect of Repeated Irrigation and Debridement on Fracture Healing in an Animal Model. *J. Orthop. Res.* 20 (6), 1197–1204. doi:10.1016/s0736-0266(02)00072-4

Reed, A. A. C., Joyner, C. J., Isefuku, S., Brownlow, H. C., and Simpson, A. H. R. W. (2003). Vascularity in a New Model of Atrophic Nonunion. *J. Bone Jt. Surg. Br. volume* 85-B (4), 604–610. doi:10.1302/0301-620x.85b4.12944

Roberto-Rodrigues, M., Fernandes, R. M. P., Senos, R., Scoralick, A. C. D., Bastos, A. L., Santos, T. M. P., et al (2015). Novel Rat Model of Nonunion Fracture with Vascular Deficit. *Injury* 46 (4), 649–654. doi:10.1016/j.injury.2015.01.033

Roberts, T. T., and Rosenbaum, A. J. (2012). Bone Grafts, Bone Substitutes and Orthobiologics: the Bridge between Basic Science and Clinical Advancements in Fracture Healing. *Organogenesis* 8 (4), 114–124. doi:10.4161/org.23306

Rodrigues, S. C., Salgado, C. L., Sahu, A., Garcia, M. P., Fernandes, M. H., and Monteiro, F. J. (2013). Preparation and Characterization of Collagen-Nanohydroxyapatite Biocomposite Scaffolds by Cryogelation Method for Bone Tissue Engineering Applications. *J. Biomed. Mater. Res.* 101A (4), 1080–1094. doi:10.1002/jbm.a.34394

Rowland, C. R., Glass, K. A., Ettyreddy, A. R., Gloss, C. C., Matthews, J. R. L., Huynh, N. P. T., et al. (2018). Regulation of Decellularized Tissue Remodeling via Scaffold-Mediated Lentiviral Delivery in Anatomically-Shaped Osteochondral Constructs. *Biomaterials* 177, 161–175. doi:10.1016/j.biomaterials.2018.04.049

Salmon, P., and Trono, D. (2007). Production and Titration of Lentiviral Vectors. *Curr. Protoc. Hum. Genet.* Chapter 12, Unit 12.10. doi:10.1002/0471142905.hg1210s54

Schmidhammer, R., Zandieh, S., Mittermayr, R., Pelinka, L. E., Leixnering, M., Hopf, R., et al. (2006). Assessment of Bone union/nonunion in an Experimental Model Using Microcomputed Technology. *J. Trauma Inj. Infect. Crit. Care* 61 (1), 199–205. doi:10.1097/01.ta.0000195987.57939.7e

Shah, K., Majeed, Z., Jonason, J., and O'Keefe, R. J. (2013). The Role of Muscle in Bone Repair: the Cells, Signals, and Tissue Responses to Injury. *Curr. Osteoporos. Rep.* 11 (2), 130–135. doi:10.1007/s11914-013-0146-3

Shi, L., Sun, W., Gao, F., Cheng, L., and Li, Z. (2017). Heterotopic Ossification Related to the Use of Recombinant Human BMP-2 in Osteonecrosis of Femoral Head. *Medicine (Baltimore)* 96 (27), e7413. doi:10.1097/md.0000000000007413

Shi, S., de Gorter, D. J. J., Hoogaars, W. M. H., 't Hoen, P. A. C., and ten Dijke, P. (2013). Overactive Bone Morphogenetic Protein Signaling in Heterotopic Ossification and Duchenne Muscular Dystrophy. *Cell. Mol. Life Sci.* 70 (3), 407–423. doi:10.1007/s00018-012-1054-x

Skovrlj, B., Koehler, S. M., Anderson, P. A., Qureshi, S. A., Hecht, A. C., Iatridis, J. C., et al. (2015). Association between BMP-2 and Carcinogenicity. *Spine (Phila Pa. 1976* 40 (23), 1862–1871. doi:10.1097/BRS.0000000000001126

Sohn, H.-S., and Oh, J.-K. (2019). Review of Bone Graft and Bone Substitutes with an Emphasis on Fracture Surgeries. *Biomater. Res.* 23 (1), 9. doi:10.1186/s40824-019-0157-y

Sun, L., Li, Z., Ma, T., Xue, H.-Z., Wang, Q., Lu, D.-G., et al. (2019). Treatment of Atrophic Nonunion via Autogenous Ilium Grafting Assisted by Vertical Fixation of Double Plates: A Case Series of Patients. *J. Int. Med. Res.* 47 (5), 1998–2010. doi:10.1177/0300060518814607

Tawonsawatruk, T., Kelly, M., and Simpson, H. (2014). Evaluation of Native Mesenchymal Stem Cells from Bone Marrow and Local Tissue in an Atrophic Nonunion Model. *Tissue Eng. C: Methods* 20 (6), 524–532. doi:10.1089/ten.tec.2013.0465

Thomas, J. D., and Kehoe, J. L. (2021). *Bone Nonunion, in StatPearls*. Treasure Island (FL): StatPearls Publishing; Copyright © 2021, StatPearls Publishing LLC.

Wang, L., Tower, R. J., Chandra, A., Yao, L., Tong, W., Xiong, Z., et al. (2019). Periosteal Mesenchymal Progenitor Dysfunction and Extraskeletally-Derived Fibrosis Contribute to Atrophic Fracture Nonunion. *J. Bone Miner Res.* 34 (3), 520–532. doi:10.1002/jbmr.3626

Yoganarasimha, S., Trahan, W. R., Best, A. M., Bowlin, G. L., Kitten, T. O., Moon, P. C., et al. (2014). Peracetic Acid: A Practical Agent for Sterilizing Heat-Labile Polymeric Tissue-Engineering Scaffolds. *Tissue Eng. Part C: Methods* 20 (9), 714–723. doi:10.1089/ten.tec.2013.0624

Yu, Y. Y., Lieu, S., Lu, C., and Colnot, C. (2010). Bone Morphogenetic Protein 2 Stimulates Endochondral Ossification by Regulating Periosteal Cell Fate during Bone Repair. *Bone* 47 (1), 65–73. doi:10.1016/j.bone.2010.03.012

Zhou, N., Li, Q., Lin, X., Hu, N., Liao, J.-Y., Lin, L.-B., et al. (2016). BMP2 Induces Chondrogenic Differentiation, Osteogenic Differentiation and Endochondral Ossification in Stem Cells. *Cell Tissue Res* 366 (1), 101–111. doi:10.1007/s00441-016-2403-0

Zura, R., Xiong, Z., Einhorn, T., Watson, J. T., Ostrum, R. F., Prayson, M. J., et al. (2016). Epidemiology of Fracture Nonunion in 18 Human Bones. *JAMA Surg.* 151 (11), e162775. doi:10.1001/jamasurg.2016.2775

Conflict of Interest: The authors declare that the research was conducted in the absence of any commercial or financial relationships that could be construed as a potential conflict of interest.

Publisher's Note: All claims expressed in this article are solely those of the authors and do not necessarily represent those of their affiliated organizations, or those of the publisher, the editors, and the reviewers. Any product that may be evaluated in this article, or claim that may be made by its manufacturer, is not guaranteed or endorsed by the publisher.

Copyright © 2022 Hixon, Katz, McKenzie, Miller, Guilak and Silva. This is an open-access article distributed under the terms of the Creative Commons Attribution License (CC BY). The use, distribution or reproduction in other forums is permitted, provided the original author(s) and the copyright owner(s) are credited and that the original publication in this journal is cited, in accordance with accepted academic practice. No use, distribution or reproduction is permitted which does not comply with these terms.

frontiers | Frontiers in Bioengineering and Biotechnology

ORIGINAL RESEARCH
published: 24 May 2022
doi: 10.3389/fbioe.2022.825005

Synoviocyte-Derived Extracellular Matrix and bFGF Speed Human Chondrocyte Proliferation While Maintaining Differentiation Potential

Rachel D. Truong[1], *Megan A. Bernier*[1], *James E. Dennis*[2] *and Thomas J. Kean*[1,2,3]*

[1]College of Medicine, University of Central Florida, Orlando, FL, United States, [2]Department of Orthopedic Surgery, Baylor College of Medicine, Houston, TX, United States, [3]Biionix Cluster, Internal Medicine, College of Medicine, University of Central Florida, Orlando, FL, United States

Improving the ability of human chondrocytes to proliferate, while maintaining their differentiation potential, has presented a great challenge in cartilage tissue engineering. In this study, human chondrocytes were cultured under four unique growth conditions at physiologic oxygen tension: tissue culture plastic (TCP) only, synoviocyte matrix (SCM)–coated flasks only, SCM-coated flasks with bFGF media supplement, and TCP with bFGF media supplement. The results indicated that, compared to standard TCP, all test conditions showed significantly increased cell expansion rates and an increase in both glycosaminoglycan (GAG) and collagen content during redifferentiation culture. Specifically, the combined SCM + bFGF growth condition showed an additive effect, with an increase of approximately 36% more cells per passage (5–7 days) when compared to the SCM alone. In conclusion, the results of this study demonstrate that bFGF and SCM can be used as supplements to enhance the growth of human chondrocytes both as individual enhancers and as a combined additive.

Keywords: synoviocyte matrix, human chondrocyte, human chondrogenesis, chondrocyte expansion, cartilage tissue engineering, fibroblast growth factor, arthritis, osteoarthritis

OPEN ACCESS

Edited by:
Dmitriy Sheyn,
Cedars Sinai Medical Center,
United States

Reviewed by:
Guus van den Akker,
Maastricht University, Netherlands
Lucienne A. Vonk,
CO.DON AG, Germany

***Correspondence:**
Thomas J. Kean
Thomas.kean@ucf.edu

Specialty section:
This article was submitted to Tissue Engineering and Regenerative Medicine, a section of the journal Frontiers in Bioengineering and Biotechnology

Received: *29 November 2021*
Accepted: *15 April 2022*
Published: *24 May 2022*

Citation:
Truong RD, Bernier MA, Dennis JE and Kean TJ (2022) Synoviocyte-Derived Extracellular Matrix and bFGF Speed Human Chondrocyte Proliferation While Maintaining Differentiation Potential. Front. Bioeng. Biotechnol. 10:825005. doi: 10.3389/fbioe.2022.825005

INTRODUCTION

Osteoarthritis (OA) is characterized as a chronic degenerative joint disease that increases in prevalence with age, afflicting the majority of patients over age 65 as displayed by radiographic evidence (Oliveria et al., 1995). Treatment modalities are aimed first at addressing symptoms through nonpharmacologic methods such as weight management, braces and then pharmacologically through pain relievers such as nonsteroidal anti-inflammatory drugs and steroid injections (Bennell et al., 2012). If both non-pharmacologic and pharmacologic methods fail, joint replacement surgery can be performed, a technique for which OA is the leading indication (Robertsson et al., 2010). A randomized controlled trial performed by Skou et al. (2015) has shown that total knee replacement followed by nonsurgical treatment proved to be more effective at reducing pain and improving function at a 12-month follow-up than nonsurgical treatment alone. However, it was also noted in the same trial that patients who were assigned total knee replacement reported a higher number of serious adverse events. It, therefore, becomes imperative to find a treatment that is just as effective as total joint replacement but reduces the risk of adverse events and overcomes the procedure's limited lifetime of 15–20 years. This limited lifetime is especially

concerning for patients aged <65 years as there is a distinct possibility that their total joint replacement could fail and require further invasive procedures before they die.

One such avenue of treatment is to use human articular chondrocytes (HACs) to repair the tissue in the diseased joint. Autologous chondrocyte implantation (ACI) and matrix-assisted autologous chondrocyte implantation (MACI) are both generally accepted techniques that have shown promise in the treatment of symptomatic chondral defects of the knee (Bartlett et al., 2005). However, human chondrocytes used in these techniques are known to de-differentiate quickly, losing their ability to form the hyaline-like cartilage tissue necessary to help treat large OA lesions (Giovannini et al., 2010). This leads to a decrease in hyaline cartilage production with time, implying that, while ACI and MACI are commonly used to delay total joint replacement, these methods may not be able to completely obviate the eventual need for total joint replacement.

Maintaining cell potency, therefore, becomes a vital goal for the purposes of tissue engineering. A synoviocyte-derived extracellular matrix has previously been shown to create an environment ideal for the proliferation of human chondrocytes without the loss of the re-differentiation potential (Kean and Dennis, 2015). Similarly, media supplemented with bFGF have been shown to cause both human mesenchymal stem cells and rabbit chondrocytes isolated from both auricular and articular sources to proliferate more rapidly than when exposed to control conditions (Solchaga et al., 2005; Mounts et al., 2012). Sieber et al. (2020) noted that, because of its avascular nature, the articular cartilage is supplied oxygen *via* diffusion from the surrounding synovial fluid, leading to oxygen tension of the tissue varying from 2–9%. Multiple groups have also previously shown that oxygen tension in the articular cartilage ranges from 2–5% (Grant and Smith, 1963; Lund-Olesen, 1970; Brighton and Heppenstall, 1971; Pattappa et al., 2019). Zhou et al. (2004) have also previously demonstrated *via* a modeling approach that the rate of oxygen consumption in the articular cartilage fell in an oxygen tension–dependent manner once the tissue oxygen tension fell below 5%. The use of oxygen tension at 5% has been shown by multiple groups, including our own, to be beneficial for chondrocyte culture (Lafont et al., 2008; Das et al., 2010; Kean and Dennis, 2015; Anderson et al., 2018; Dennis et al., 2020). Oxygen tension of 5% was, therefore, chosen because of this decreased level within the range of oxygen tensions reported as physiological.

This study examines the potential of promoting HAC growth under physiological environmental conditions (5% oxygen tension) with varying combinations of bFGF and the synoviocyte matrix (SCM). It also aims to investigate the possibility of maintaining HAC differentiation potential while undergoing growth under such conditions. The results of this study will indicate if a growth environment enhanced with the SCM and bFGF will lead to increased human chondrocyte proliferation while maintaining differentiation potential. Success in such a growth environment demonstrates the potential for the use of the SCM + bFGF in engineering cartilage lesion treatment modalities, addressing the fibrocartilage seen in ACI and MACI techniques.

MATERIALS AND METHODS

Ethics Statement

Human chondrocytes were obtained from total joint replacement surgery discarded tissue with written informed consent under IRB-approved protocols from Case Western Reserve University and Baylor College of Medicine: IRB # IRB08-00104 and H-36374, respectively.

Human Chondrocyte Isolation

The discarded surgical tissue of patients who had undergone total knee replacement was collected ($n = 5$). Macroscopically normal cartilage tissue was dissected from the joint under sterile conditions and minced into pieces measuring <1 mm^3. These pieces were then sequentially digested, first with hyaluronidase (30 min, 660 U/ml in DMEM; Sigma) and then with collagenase (overnight; 583 U/ml in DMEM with 10% FBS; Worthington Biochemical). This resulted in a cell slurry which was washed through a 70-μm filter with DMEM, centrifuged (600 RCF, 5 min) and plated (6000 cells/cm^2) into tissue culture flasks in growth media (DMEM supplemented with 10% FBS 1% pen/strep) from which the primary cell culture (p0) cell stocks were produced. Once the tissue culture flasks reached 90% confluence, they were trypsinized and cryogenically stored (95% FBS, 5% DMSO).

Synoviocyte Matrix Production

Synoviocyte matrix–coated flasks were prepared as previously described (Kean and Dennis, 2015). Briefly, porcine synoviocytes were thawed from frozen stocks and cultured in a growth medium (DMEM-LG supplemented with 10% fetal bovine serum (FBS) and 1% penicillin/streptomycin) until 80%–90% confluent. The growth medium was then switched to DMEM-LG with FBS and ascorbate-2-phosphate (50 μM) for 5–7 days. Ascorbate-2-phosphate was included to increase ECM production, as previously carried out by Pei and He (2012), although it is understood that this can impact other aspects of the cell culture. After this period, the flask was washed with PBS and then frozen in a dry ice 100% ethanol bath. Dry ice–cooled ethanol was then used to devitalize the cell layer by pipetting into the flask; after 1 min, ethanol was removed and the flask was inverted to dry. The synoviocyte matrix was then stored at 4°C until ready for use in HAC growth.

Chondrocyte Expansion and Aggregate Production

Chondrocytes were thawed from frozen stocks and seeded (6000 cells/cm^2) into four separate flasks with unique growth conditions: 1) tissue culture plastic (TCP) only, 2) SCM-coated flasks only, 3) SCM-coated flasks with bFGF (10 ng/ml) media supplement, and 4) TCP with bFGF (10 ng/ml) media

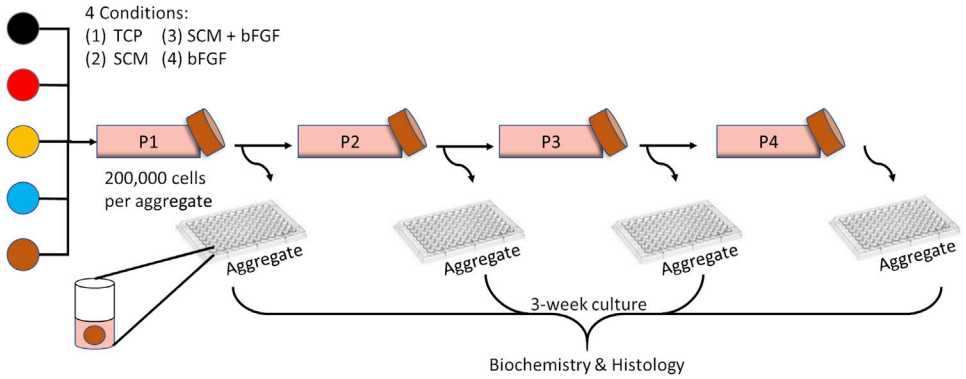

FIGURE 1 | Experimental overview. Human chondrocytes from five donors (each color represents a donor) were expanded for four passages on tissue culture plastic (TCP), synoviocyte-derived extracellular matrix (SCM), on synoviocyte matrix with bFGF (SCM + bFGF), or on tissue culture plastic with bFGF (bFGF). At the end of each expansion period, the chondrocytes were trypsinized and seeded as aggregates and passaged to a new flask of the same type.

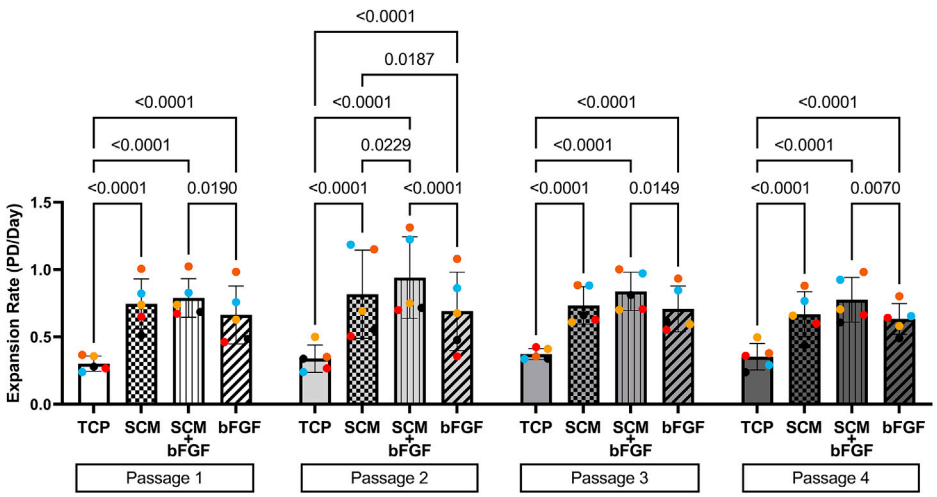

FIGURE 2 | Expansion of human chondrocytes. Human chondrocytes from five donors (each color represents a donor) for four passages on tissue culture plastic (TCP), synoviocyte-derived extracellular matrix (SCM), on synoviocyte matrix with bFGF (SCM + bFGF), or on tissue culture plastic with bFGF (FGF). $p < 0.05$ are shown, two-way ANOVA.

supplement (**Figure 1**). The bFGF concentration was chosen based on a previous study (Solchaga et al., 2005). All samples were cultured at a physiologic oxygen tension of 5% and in a growth medium of DMEM-LG with 10% FBS and 1% penicillin/streptomycin. Once the cell population in the fastest growth environment reached 85–99% confluence, all flasks were trypsinized and passaged (0.25% trypsin/EDTA; Gibco). The cells were counted with a hemocytometer, and population doublings were calculated using the formula PD = [log10 (harvested cell count)—log10 (seeded cell count)] x 3.32, and sequential passages were summed to give cumulative population doublings (Kean and Dennis, 2015). Cartilage aggregates were formed in addition to passaging a subset of these cells into new flasks of the same type (6000 cells/cm^2). This process was repeated three more times for a total of four passages (**Figure 1**). Cartilage aggregates were formed as previously described (Kean and Dennis, 2015). Briefly, 200,000 cells per well in sterile nonadherent 96-well plates were condensed into aggregates by centrifugation (600 RCF, 5 min). Cell aggregates were cultured in defined chondrogenic media (DMEM-HG (Hyclone) supplemented with 1% ITS + premix (BD Biosciences), 1 % glutamax (Gibco), 1% pyruvate (Gibco), 1% nonessential amino acids (Gibco), 1% penicillin/streptomycin (Gibco), 0.5% fungizone (Gibco), dexamethasone (100 nM, Sigma), ascorbate-2-phosphate (130 μM, Wako Chemicals), and TGFβ1 (10 ng/ml) for 21 days with the medium changed every other day.

Biochemical Assays

At the end of the 21-day culture period, cartilage aggregates were assessed for wet weight, DNA, and glycosaminoglycan and hydroxyproline content as previously described (Dennis et al., 2020). Briefly, the aggregates were digested with papain, and then the digests were split between DNA/glycosaminoglycan (GAG)

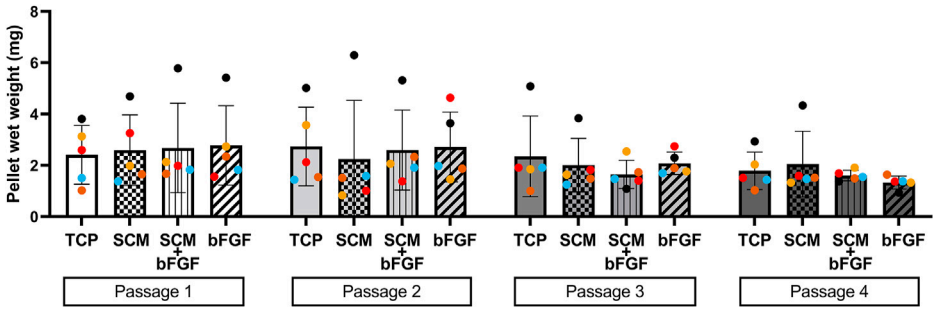

FIGURE 3 | Human cartilage aggregate wet weight. Cartilage aggregates from five donors (average aggregate weight, ≥three aggregates per donor, each color represents a donor) for four passages on tissue culture plastic (TCP), synoviocyte-derived extracellular matrix (SCM), on synoviocyte matrix with bFGF (SCM + bFGF), or on tissue culture plastic with bFGF (bFGF). $p < 0.05$ are shown, two-way ANOVA (no significant differences found).

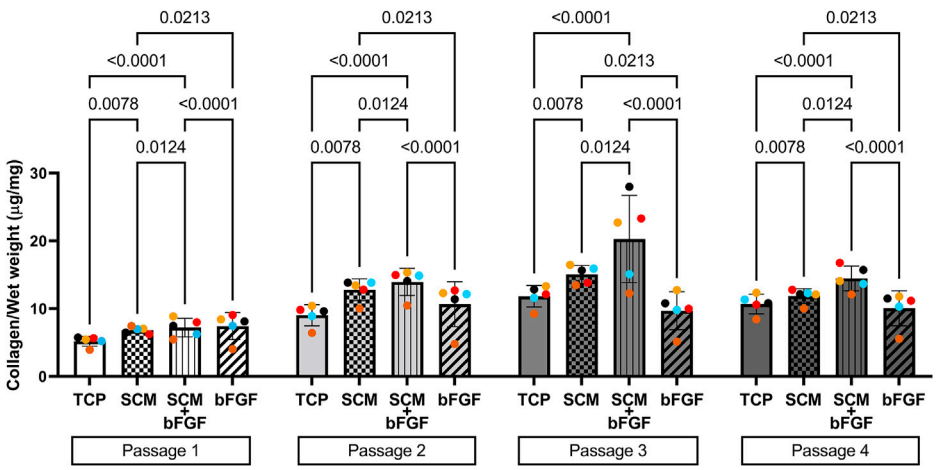

FIGURE 4 | Collagen content of human cartilage aggregates. Cartilage aggregates from five donors (average aggregate collagen content per mg wet weight, ≥two aggregates per donor, each color represents a donor) for four passages on tissue culture plastic (TCP), synoviocyte-derived extracellular matrix (SCM), on synoviocyte matrix with bFGF (SCM + bFGF), or on tissue culture plastic with bFGF (bFGF). $p < 0.05$ are shown, two-way ANOVA.

assay and hydroxyproline (HDP) assays. DNA was determined from the digest using Hoechst solution (0.667 µg/ml in 0.2 M pH 8.0 phosphate buffer; 33258; Sigma Aldrich). GAG was determined using a dot blot assay and binding/extraction of safranin-O. HDP was determined from the acid-hydrolyzed digest using Ehrlich's reagent. The collagen content was estimated from the HDP concentration by a conversion factor of 7.6 (Venn and Maroudas, 1977).

Histology

Aggregates were formalin-fixed overnight and then transferred to 70% ethanol, dehydrated through graded ethanol and xylene to paraffin, and then paraffin-embedded. The paraffin sections (8 µm) were deparaffinized and hydrated before staining with safranin-O (Sigma Aldrich) for GAG with a Fast Green (AA16520-06, Alfa Aesar) counterstain.

Immunohistochemistry: Paraffin sections were deparaffinized and hydrated and then incubated with pronase (1 mg/ml, 10 min, room temp, Sigma). The sections were rinsed in PBS and then blocked with BSA (3%, 15 min, RT, BSA Fraction V, Omnipur). The sections were incubated overnight at 4°C with primary antibodies: type I collagen (Clone II-4CII, MP Biomedical 631703), type II collagen (DSHB II-II6B3), and type X collagen (kind gift of Gary Gibson, Henry Ford Hospital, Detroit, MI). After overnight incubation, the sections were rinsed with PBS, blocked with 3% BSA (15 min, RT), and then incubated with a secondary antibody (1 h, RT, biotinylated horse anti-mouse; Vector labs; BA2000). The slides were then rinsed with PBS and incubated with streptavidin-HRP (30 min, RT, Invitrogen SNN1004). Then, the slides were rinsed with PBS and incubated with Vector VIP Peroxidase (10 min, RT, Vector labs) before counterstaining in Fast Green and xylene mounting.

Statistics

Each donor was expanded and multiple aggregates were formed at the end of each passage (3–8 aggregates per donor/passage).

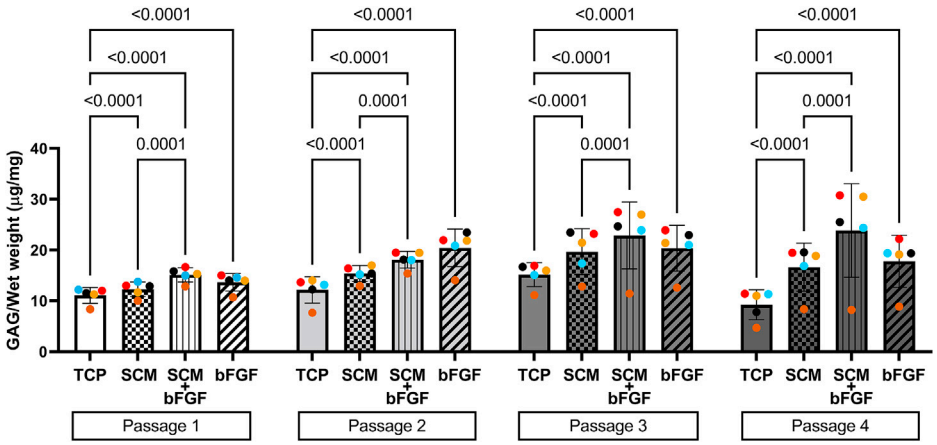

FIGURE 5 | Glycosaminoglycan (GAG) content of human cartilage aggregates. Cartilage aggregates from five donors (average aggregate GAG content per mg wet weight, ≥two aggregates per donor, each color represents a donor) for four passages on tissue culture plastic (TCP), synoviocyte-derived extracellular matrix (SCM), on synoviocyte matrix with bFGF (SCM + bFGF), or on tissue culture plastic with bFGF (bFGF). $p < 0.05$ are shown, two-way ANOVA.

The mean value for each donor is represented by a colored symbol in figures, with the overall mean from all donors and standard deviation shown. Two-way repeated measures ANOVA was performed with matching across the passage and surface type (GraphPad Prism). Post-hoc analysis of ANOVA was corrected for multiple comparisons using Tukey's method (GraphPad Prism).

RESULTS

Human articular chondrocytes from five donors were grown in each of the four culture conditions described: TCP, SCM, SCM + FGF, and FGF (**Figure 1**). To determine how proliferation was impacted by these culture conditions, the expansion rate was measured over four passages. The cells expanded significantly quicker in all test conditions across all four passages versus the TCP control (**Figure 2**). SCM + bFGF stimulated proliferation the most in all passages, surpassing that by both SCM and bFGF alone. The addition of FGF or SCM alone significantly increased the expansion rate vs. TCP at all four passages.

The cell aggregates were formed after passaging cells from each condition independently. These aggregates were tested for wet weight (**Figure 3**), collagen content (**Figure 4**), and GAG content (**Figure 5**). Additional replicates were also used for histological assessment (**Figure 6** and **Supplementary Figures S2–S13**). The aggregate wet weight was similar across all conditions but showed some donor dependence with one donor being consistently higher than the mean +S.D. (**Figure 3**). The aggregate wet weight negatively correlated with the passage, with a trend showing decreasing wet weight (**Figure 3** and **Supplementary Figure S1**).

To determine if the growth conditions tested impacted the collagen content of the cell aggregates, the hydroxyproline concentration was measured and used to estimate the collagen content. In passage 1, SCM + bFGF and bFGF alone had the highest levels of collagen (**Figure 4**). However, in the subsequent passages, the SCM and SCM + bFGF groups are the highest. SCM + bFGF has significantly higher collagen content only in passages 3 and 4 than all other groups (**Figure 4**). TCP alone has significantly lower collagen content in all passages except in passage 3 where no significant difference was observed other than that of bFGF (**Figure 4**). Overall, the collagen content tended to increase in all groups as the passage number increases.

The other critical component of the cartilage, GAG, was also quantified from cell aggregates formed at each passage. Overall, the GAG concentration increased in all groups in passages 1 through 3, with a slight decrease in passage 4 by all groups except SCM + bFGF, which remained consistent (**Figure 5**). TCP alone had significantly lower GAG content than all other groups in all four passages (**Figure 5**). In passage 1, SCM + bFGF and bFGF have a similar level of GAG, but in passage 2, FGF has a slight increase. However, in passages 3 and 4, SCM + bFGF has the highest level of GAG expression.

To assess aggregate cellularity, DNA content per milligram wet weight of aggregates was also assessed (**Figure 6**). In general, the DNA content increased with the passage across all conditions, signifying decreased production of the extracellular matrix per cell. There was a significant effect of the passage as a source of variability ($p = 0.0007$) and an interaction between the culture conditions and passages ($p = 0.0002$), but there was no significant effect of the culture condition on the aggregate DNA content (two-way ANOVA).

Cell aggregates were also used for the histological assessment of GAG by safranin-O/Fast Green staining. The same trends observed in the quantification of GAG content are seen in the histology staining. TCP alone has lighter staining at three of the four passages (**Figure 7**). The SCM alone has the darkest staining at passage 3 but is darker overall than TCP. SCM + bFGF has slightly darker staining at passage 3 versus other passages (**Figure 7**). The SCM, SCM + bFGF, and bFGF show slightly darker staining in passage 1 than TCP. While both the SCM and SCM + bFGF seem to have darker staining as the passages increase, TCP and bFGF seem to have lighter staining (**Figure 7**). There were apparent differences between donors,

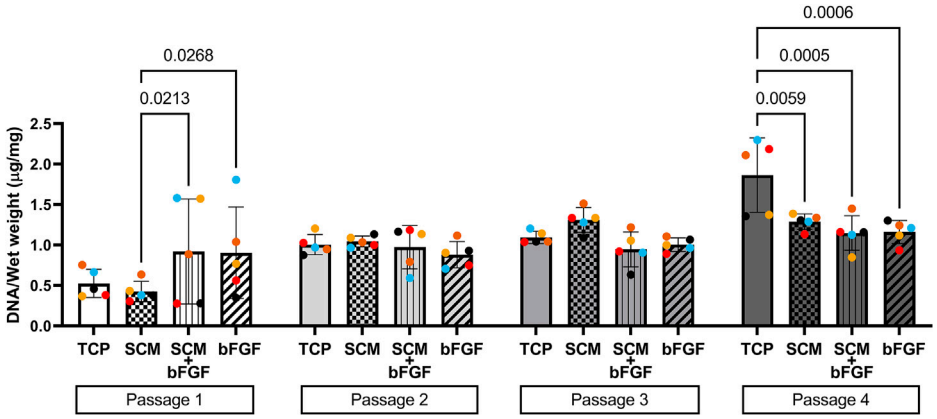

FIGURE 6 | DNA content of aggregates. DNA was extracted from cartilage aggregates and normalized to wet weight (five donors, ≥2 aggregates per donor, each color represents a donor) at each of four passages on tissue culture plastic (TCP), synoviocyte-derived extracellular matrix (SCM), on synoviocyte matrix with bFGF (SCM + bFGF), or on tissue culture plastic with bFGF (bFGF). $p < 0.05$ are shown, two-way ANOVA.

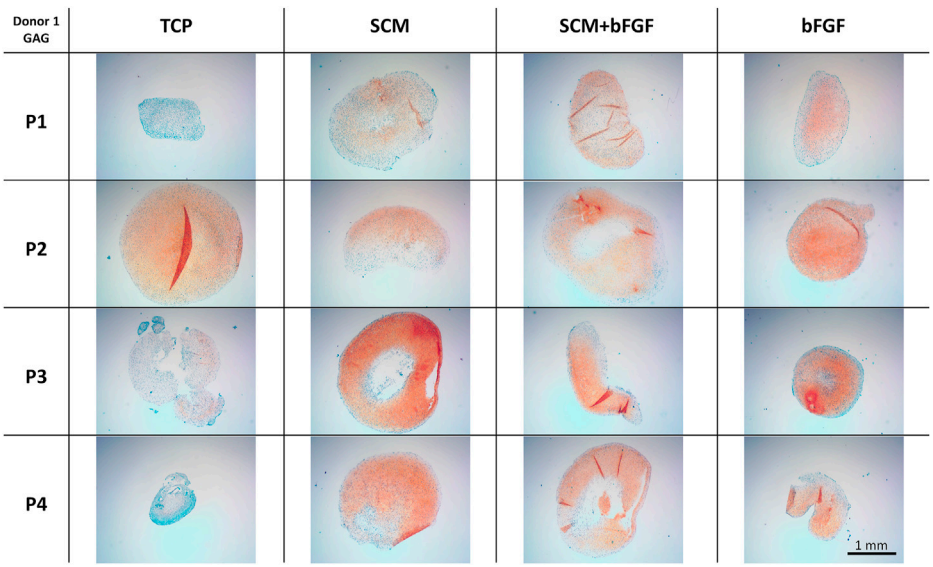

FIGURE 7 | Cartilage aggregate images showing glycosaminoglycan (GAG) staining. Sections of cartilage aggregates from a single donor over the four passages on each surface are shown here stained with safranin-O/Fast Green. All at the same scale, scale bar 1 mm. See **Supplementary Figures S2–S4** for other donors.

with donor 5 exhibiting much less GAG staining (**Supplementary Figure S4**). Across donors and conditions, the lag in GAG expression at P1 is most evident in TCP-derived chondrocytes but is present in all conditions (**Figure 7** and **Supplementary Figures S2–S4**). The differences between donor, passage, and condition are less evident with donors 1–3 on the SCM, SCM + bFGF, and bFGF, respectively, with all three donors having GAG staining at passage 4 under those conditions (**Figure 7** and **Supplementary Figures S2–S4**).

To further investigate the extracellular matrix deposited by the chondrocytes during aggregate culture, immunohistochemistry was performed. Staining was observed for type II collagen across all conditions at all passages (**Figure 8**). Slightly weaker staining at passage 4 is evident in aggregates made from cells cultured with bFGF. Across the donors, donor 5 again shows relatively weak staining in all conditions (**Supplementary Figure S7**). The SCM and SCM + bFGF appear to have the most intense staining across all passages and donors (**Figure 8** and **Supplementary Figures S5–S7**). A similar donor- and passage-dependent extracellular matrix expression as was seen in the GAG images is evident (**Figure 8** and **Supplementary Figures S5–S7**).

Fibrous tissue formation, assessed by type I collagen staining, was also performed (**Figure 9**). Again, in all conditions tested, there was significant deposition of type I collagen. This was relatively stronger in the TCP group versus the other conditions. When looking across donors, there was a

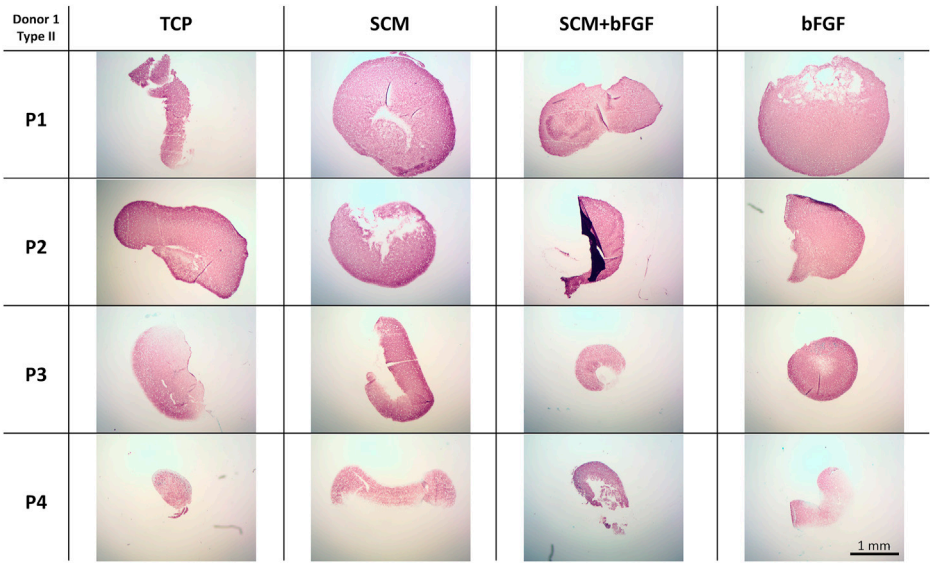

FIGURE 8 | Cartilage aggregate images showing type II collagen staining. Sections of cartilage aggregates from a single donor over the four passages in each condition are shown here stained for type II collagen. All at the same scale, scale bar 1 mm. See **Supplementary Figures S5–S7** for other donors.

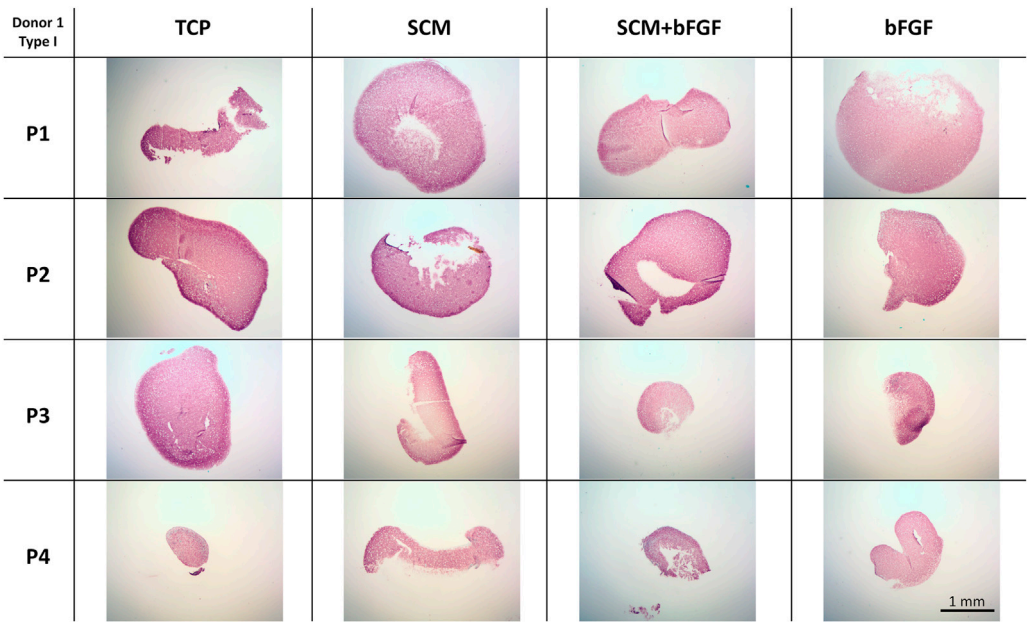

FIGURE 9 | Cartilage aggregate images showing type I collagen staining. Sections of cartilage aggregates from a single donor over the four passages in each condition are shown here stained for type I collagen. All at the same scale, scale bar 1 mm. See **Supplementary Figures S8–S10** for other donors.

significant lack of staining in donor 5 (**Supplementary Figure S10**). In general, there was a trend to more intense staining as passages increased across all donors (**Figure 9** and **Supplementary Figures S8–S10**).

Hypertrophic tissue formation, indicated by type X collagen, was also assessed (**Figure 10**). Type X collagen staining was more pronounced in TCP at P1 than in the other three conditions. The SCM had the least intense staining across all four passages. SCM + bFGF and bFGF had relatively strong staining at passage 2, with bFGF also having relatively strong staining at passage 3 (**Figure 10**). Staining in Donor 5 was quite weak overall with some stronger staining in TCP at P3 and P4; SCM at P1, P2, and P3; and FGF at P1 (**Supplementary Figure S13**). Across all

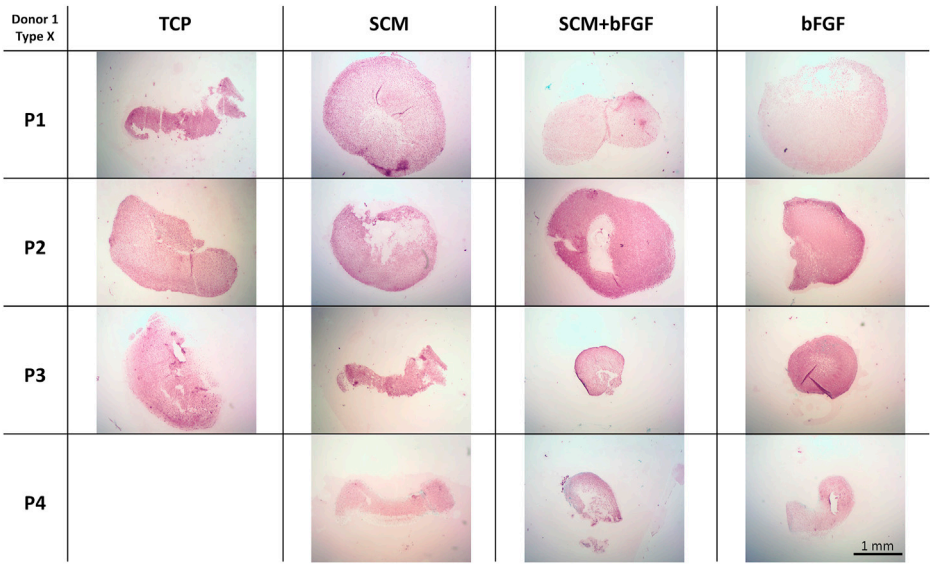

FIGURE 10 | Cartilage aggregate images showing type X collagen staining. Sections of cartilage aggregates from a single donor over the four passages in each condition are shown here stained for type X collagen. All at the same scale, scale bar 1 mm. See **Supplementary Figures S11–S13** for other donors.

donors, a general pattern of more intense staining in TCP was evident (**Figure 10** and **Supplementary Figures S11–S13**).

DISCUSSION

In the field of human tissue engineering, bFGF has already been shown to lead to the expansion of human neural stem cells and has demonstrated an important role in the regulation of stem cell proliferation (Flax et al., 1998; Amit et al., 2000; Zhang et al., 2001). A previous study examined the effects of bFGF on the proliferation and phenotypic differentiation of human neural stem cells, both alone and in combination with the epidermal growth factor (EGF) and leukemia inhibitory factor (LIF), with results indicating that while bFGF did lead to increased cell proliferation, the combination of bFGF, EGF, and LIF led to a more efficient proliferation of human neural stem cells than any other growth environment (Tarasenko et al., 2004). bFGF has also been shown to lead to increased proliferation of human corneal cells, leading to accelerated wound healing. In particular, when added to the platelet-derived growth factor BB-isoform (PDGF-BB), the combination leads to faster wound closure than with bFGF or PDGF-BB individually (Gallego-Muñoz et al., 2017). Based on the aforementioned studies, bFGF in combination with other substances that promote tissue growth leads to an additive effect of cellular expansion than if bFGF was added alone to the growth environment, a notion that was reinforced by the findings of this study.

This study showed a significant improvement in human chondrocyte expansion and an increase in both GAG and collagen content in cartilage aggregates with all three test conditions compared with standard TC plates. The results show a significantly increased cell expansion rate between all three test conditions (SCM, SCM + bFGF, bFGF) and the control (TCP) ($p < 0.0001$), sustained throughout the four passages. This is consistent with our previous work that has shown enhanced growth of chondrocytes with the use of SCM compared to TCP (Kean et al., 2019; Dennis et al., 2020). In addition, chondrocytes cultured in SCM + bFGF showed a significantly higher expansion rate than in bFGF alone in all four passages, indicating that there is some additional benefit to including both components. The combination of SCM + bFGF resulted in approximately 36% more cells per passage (5–7 days) than in SCM alone. The SCM contains both the growth factors and provides an almost 3D surface for growth. The increased surface area along with additional growth factors could further stimulate proliferation more than that achieved with either SCM or bFGF alone. With the GAG and collagen content serving as positive correlative markers for cartilage production, these results imply an improved ability of chondrocytes to retain their differentiation potential, addressing a major obstacle in prior studies.

Another challenge encountered in tissue-engineered cartilage is that it is typically found to be deficient in type II collagen specifically, which provides tensile strength to the cartilage tissue and resistance against compression (Phull et al., 2016; Whitney et al., 2018). In our study, it was found that the growth environment containing SCM + bFGF had significantly greater collagen content in passages 3 and 4 than in all other conditions. This increase in collagen content was indicated in the hydroxyproline assay, which shows the amount of total collagen in the matrix. It is, therefore, possible that we could be observing an increase in the fibrous collagen content, specifically type I collagen, and a decrease in type II collagen. This was not evident in the immunohistochemistry data which

had only minor correlations with the increased staining and passage. This increase in types I and X collagen and a decrease in type II were most apparent in the TCP group. In a previous work, it was observed that the type I collagen in our tissue-engineered cartilage reduced with increased culture time to 2 months, something we did not investigate here (Dennis et al., 2020).

It should also be noted that the GAG concentration increased over passages 1 to 3 in all conditions, which is contrary to most present literature (Schmal et al., 2007). For this phenomenon, we have three possible explanations: improved isolation of the chondrocyte tissue, improved cryopreservation and recovery of the tissue, and culturing in physiologic oxygen tension from day 0. In this study, we collected and incubated the tissue at room temperature in defined chondrogenic media, rather than in PBS on ice (Cook et al., 2014). In addition, we chose to sequentially digest the tissue first in hyaluronidase and then collagenase rather than hyaluronidase, trypsin, and collagenase as we had found trypsin/EDTA to have negative effects on the cell yield (data not shown). We also found that we could preserve the cells just as well, if not better, in 5% DMSO versus 10% (data not shown). Finally, as was shown in several previous studies, culturing the cells and tissues in physiologic oxygen tension led to increased extracellular matrix deposition and increased mechanical properties of the tissue-engineered cartilage. The cells and tissues were, therefore, cultured in physioxia from day 0 of the study which could have greatly contributed to an advantageous environment for chondrocyte cell growth. This seems to be particular to the articular cartilage as we found a negative effect of 5% oxygen in auricular chondrocytes (Kean et al., 2016; Dennis et al., 2018). All of the aforementioned minor modifications have previously been shown to be potentially advantageous for chondrocyte culture growth, and considering the results of this study, they certainly seem to be of benefit.

As previously mentioned, preserving the ability of the chondrocytes to differentiate is one of the greatest challenges of cartilage tissue engineering. Treatment of OA lesions has proven to be challenging, considering that ACI and MACI have both been developed as excellent treatment strategies that do not require total joint replacement surgery but that tissue created from these methods often fails to maintain the differentiation ability of chondrocytes producing fibrous tissue (Giovannini et al., 2010). This loss of differentiation ability leads to an eventual decline in hyaline cartilage production, thus leading to a delay of, rather than the prevention of, total joint replacement surgery. However, this study has shown that sustained chondrocyte growth is, indeed, possible through the use of SCM + bFGF growth media. It, therefore, supports the idea that such an environment is conducive and advantageous for maintaining chondrocyte differentiation ability, marking an important advancement in the field of joint regeneration. Although adding bFGF to the healing process may raise safety concerns, several studies have shown that the addition of growth factors, including bFGF, IFG-I, and TGF-β1, to the treatment of bone fractures enhanced the healing process while having an excellent safety profile (Schmidmaier et al., 2004; Kawaguchi et al., 2007).

Several previous studies have examined the effects of other FGFs, including FGF-18 and a sequence of FGF-2, 9, and 18 on the growth and differentiation of MSCs and chondrocytes. Shimoaka et al. (2002) found that compared with FGF-2, FGF-18 had similar stimulatory action on osteoclast bone resorption and mitogenic activation of osteoblasts and chondrocytes as FGF-2, indicating that FGF-18 could compensate for the roles FGF-2 plays in normal physiology. Future directions of this study could include the use of other FGFs, such as FGF-18, in combination with the SCM to examine if another FGF could potentially outperform bFGF in terms of enhancing chondrocyte proliferation potential. The results of this study can eventually lead to major improvements in the lifespan of ACI and MACI, thus allowing for a decrease in the need for eventual total joint replacement. Larger or even total joint resurfacing *via* ACI, MACI, or 3D bioprinting could also become distinct possibilities. Other directions of the study include the potential for the creation of a larger cell reservoir to treat multiple cartilage tissue lesions from a single, potentially smaller, biopsy and possible pre-implantation testing for chondrogenicity.

CONCLUSION

Human articular chondrocyte tissues cultured in environments enhanced with bFGF, SCM, and a combination of the two have shown significant improvement in expansion potential when compared to tissue cultured on typical culture plastic alone. In particular, bFGF + SCM was shown to perform the best overall, with 36% more cells per passage than with the SCM alone. An observed increase in the GAG and collagen content in all the growth mediums is also indicative of the improved ability of cultured chondrocytes to maintain their differentiation ability and therefore marks an important step forward in the field of tissue engineering.

DATA AVAILABILITY STATEMENT

The original contributions presented in the study are included in the article/**Supplementary Material**, further inquiries can be directed to the corresponding author.

ETHICS STATEMENT

The studies involving human participants were reviewed and approved by the Case Western Reserve University (IRB# IRB08-00104) and Baylor College of Medicine (H-36374). The patients/participants provided their written informed consent to participate in this study.

AUTHOR CONTRIBUTIONS

TK and JD contributed to the conception, design, and data collection of the study. RT, MB, and TK wrote sections and contributed to the drafting of the manuscript. All authors contributed to the reading, revision, and approval of the submitted version of the manuscript.

FUNDING

We gratefully acknowledge the NIH (JED, AR053622, DE015322), Rolanette and Berdon Lawrence 323 Bone Disease Program of Texas and the University of Central Florida (TJK) for funding. Article processing charges were provided in part by the UCF College of Graduate Studies Open Access Publishing Fund.

ACKNOWLEDGMENTS

The monoclonal antibody developed by by Linsenmayer, T.F. (DSHB Hybridoma Product II-II6B3) was obtained from the Developmental Studies Hybridoma Bank, created by the NICHD of the NIH and maintained at The University of Iowa, Department of Biology, Iowa City, IA 52242. We also acknowledge the kind gift of type X collagen antibody from Gary Gibson, Henry Ford Hospital, Detroit, MI.

SUPPLEMENTARY MATERIAL

The Supplementary Material for this article can be found online at: https://www.frontiersin.org/articles/10.3389/fbioe.2022.825005/full#supplementary-material

Supplementary Figure S1 | Correlation of the decreased aggregate wet weight with increased population doublings. There was a negative correlation of the aggregate wet weight with increased population doublings **(A)** TCP, **(B)** SCM, **(C)** SCM+bFGF, and **(D)** bFGF.

Supplementary Figure S2 | Cartilage aggregate images of donor 2 showing glycosaminoglycan (GAG) staining. The sections of cartilage aggregates from donor 2 over the four passages on each surface are shown here stained with safranin-O/Fast Green. All at the same scale, scale bar 1 mm. See **Supplementary Figures S2–S4** for other donors.

Supplementary Figure S3 | Cartilage aggregate images of donor 3 showing glycosaminoglycan (GAG) staining. Sections of cartilage aggregates from donor 3 over the four passages on each surface are shown here stained with safranin-O/Fast Green. All at the same scale, scale bar 1 mm. See **Supplementary Figures S2–S4** for other donors.

Supplementary Figure S4 | Cartilage aggregate images of donor 5 showing glycosaminoglycan (GAG) staining. Sections of cartilage aggregates from donor 5 over the four passages on each surface are shown here stained with safranin-O/Fast Green. All at the same scale, scale bar 1 mm. See **Supplementary Figures S2–S4** for other donors.

Supplementary Figure S5 | Cartilage aggregate images of donor 2 showing type II collagen staining. Sections of cartilage aggregates from donor 2 over the four passages in each condition are shown here stained for type II collagen. All at the same scale, scale bar 1 mm. See **Supplementary Figures S5–S7** for other donors.

Supplementary Figure S6 | Cartilage aggregate images of donor 3 showing type II collagen staining. Sections of cartilage aggregates from donor 3 over the four passages in each condition are shown here stained for type II collagen. All at the same scale, scale bar 1 mm. See **Supplementary Figures S5–S7** for other donors.

Supplementary Figure S7 | Cartilage aggregate images of donor 5 showing type II collagen staining. Sections of cartilage aggregates from donor 5 over the four passages in each condition are shown here stained for type II collagen. All at the same scale, scale bar 1 mm. See **Supplementary Figures S5–S7** for other donors.

Supplementary Figure S8 | Cartilage aggregate images of donor 2 showing type I collagen staining. Sections of cartilage aggregates from donor 2 over the four passages in each condition are shown here stained for type I collagen. All at the same scale, scale bar 1 mm. See **Supplementary Figures S8–S10** for other donors.

Supplementary Figure S9 | Cartilage aggregate images of donor 3 showing type I collagen staining. Sections of cartilage aggregates from donor 3 over the four passages in each condition are shown here stained for type I collagen. All at the same scale, scale bar 1 mm. See **Supplementary Figures S8–S10** for other donors.

Supplementary Figure S10 | Cartilage aggregate images of donor 5 showing type I collagen staining. Sections of cartilage aggregates from donor 5 over the four passages in each condition are shown here stained for type I collagen. All at the same scale, scale bar 1 mm. See **Supplementary Figures S8–S10** for other donors.

Supplementary Figure S11 | Cartilage aggregate images of donor 2 showing type X collagen staining. Sections of cartilage aggregates from donor 2 over the four passages in each condition are shown here stained for type X collagen. All at the same scale, scale bar 1 mm. See **Supplementary Figures S11–S13** for other donors.

Supplementary Figure S12 | Cartilage aggregate images of donor 3 showing type X collagen staining. Sections of cartilage aggregates from donor 3 over the four passages in each condition are shown here stained for type X collagen. All at the same scale, scale bar 1 mm. See **Supplementary Figures S11–S13** for other donors.

Supplementary Figure S13 | Cartilage aggregate images of donor 5 showing type X collagen staining. Sections of cartilage aggregates from donor 5 over the four passages in each condition are shown here stained for type X collagen. All at the same scale, scale bar 1 mm. See **Supplementary Figures S11–S13** for other donors.

REFERENCES

Amit, M., Carpenter, M. K., Inokuma, M. S., Chiu, C.-P., Harris, C. P., Waknitz, M. A., et al. (2000). Clonally Derived Human Embryonic Stem Cell Lines Maintain Pluripotency and Proliferative Potential for Prolonged Periods of Culture. *Dev. Biol.* 227, 271–278. doi:10.1006/dbio.2000.9912

Anderson, D. E., Markway, B. D., Weekes, K. J., McCarthy, H. E., and Johnstone, B. (2018). Physioxia Promotes the Articular Chondrocyte-like Phenotype in Human Chondroprogenitor-Derived Self-Organized Tissue. *Tissue Eng. Part A* 24, 264–274. doi:10.1089/ten.TEA.2016.0510

Bartlett, W., Skinner, J. A., Gooding, C. R., Carrington, R. W. J., Flanagan, A. M., Briggs, T. W. R., et al. (2005). Autologous Chondrocyte Implantation versus Matrix-Induced Autologous Chondrocyte Implantation for Osteochondral Defects of the Knee. *J. Bone Jt. Surg. Br.* 87-B, 640–645. doi:10.1302/0301-620X.87B5.15905

Bennell, K. L., Hunter, D. J., and Hinman, R. S. (2012). Management of Osteoarthritis of the Knee. *BMJ* 345, e4934. doi:10.1136/bmj.e4934

Brighton, C. T., and Heppenstall, R. B. (1971). Oxygen Tension in Zones of the Epiphyseal Plate, the Metaphysis and Diaphysis. *J. Bone Jt. Surg.* 53, 719–728. doi:10.2106/00004623-197153040-00011

Cook, J. L., Stoker, A. M., Stannard, J. P., Kuroki, K., Cook, C. R., Pfeiffer, F. M., et al. (2014). A Novel System Improves Preservation of Osteochondral Allografts. *Clin. Orthop.* 472, 3404–3414. doi:10.1007/s11999-014-3773-9

Das, R. H. J., van Osch, G. J. V. M., Kreukniet, M., Oostra, J., Weinans, H., and Jahr, H. (2010). Effects of Individual Control of pH and Hypoxia in Chondrocyte Culture. *J. Orthop. Res.* 28, 537–545. doi:10.1002/jor.20994

Dennis, J. E., Bernardi, K. G., Kean, T. J., Liou, N. E., and Meyer, T. K. (2018). Tissue Engineering of a Composite Trachea Construct Using Autologous Rabbit Chondrocytes. *J. Tissue Eng. Regen. Med.* 12, e1383–e1391. doi:10.1002/term.2523

Dennis, J. E., Whitney, G. A., Rai, J., Fernandes, R. J., and Kean, T. J. (2020). Physioxia Stimulates Extracellular Matrix Deposition and Increases Mechanical Properties of Human Chondrocyte-Derived Tissue-Engineered Cartilage. *Front. Bioeng. Biotechnol.* 8, 1281. doi:10.3389/fbioe.2020.590743

Flax, J. D., Aurora, S., Yang, C., Simonin, C., Wills, A. M., Billinghurst, L. L., et al. (1998). Engraftable Human Neural Stem Cells Respond to Development Cues, Replace Neurons, and Express Foreign Genes. *Nat. Biotechnol.* 16, 1033–1039. doi:10.1038/3473

Gallego-Muñoz, P., Ibares-Frías, L., Valsero-Blanco, M. C., Cantalapiedra-Rodriguez, R., Merayo-Lloves, J., and Martínez-García, M. C. (2017). Effects of TGFβ1, PDGF-BB, and bFGF, on Human Corneal Fibroblasts Proliferation and Differentiation during Stromal Repair. *Cytokine* 96, 94–101. doi:10.1016/j.cyto.2017.03.011

Giovannini, S., Diaz-Romero, J., Aigner, T., Mainil-Varlet, P., and Nesic, D. (2010). Population Doublings and Percentage of S100-Positive Cells as Predictors of *In Vitro* Chondrogenicity of Expanded Human Articular Chondrocytes. *J. Cell. Physiol.* 222, 411–420. doi:10.1002/jcp.21965

Grant, J. L., and Smith, B. (1963). Bone Marrow Gas Tensions, Bone Marrow Blood Flow, and Erythropoiesis in Man. *Ann. Intern. Med.* 58, 801–809. doi:10.7326/0003-4819-58-5-801

Kawaguchi, H., Jingushi, S., Izumi, T., Fukunaga, M., Matsushita, T., Nakamura, T., et al. (2007). Local Application of Recombinant Human Fibroblast Growth Factor-2 on Bone Repair: A Dose-Escalation Prospective Trial on Patients with Osteotomy. *J. Orthop. Res.* 25, 480–487. doi:10.1002/jor.20315

Kean, T. J., and Dennis, J. E. (2015). Synoviocyte Derived-Extracellular Matrix Enhances Human Articular Chondrocyte Proliferation and Maintains Re-differentiation Capacity at Both Low and Atmospheric Oxygen Tensions. *PloS One* 10, e0129961. doi:10.1371/journal.pone.0129961

Kean, T. J., Mera, H., Whitney, G. A., MacKay, D. L., Awadallah, A., Fernandes, R. J., et al. (2016). Disparate Response of Articular- and Auricular-Derived Chondrocytes to Oxygen Tension. *Connect. Tissue Res.* 57, 319–333. doi:10.1080/03008207.2016.1182996

Kean, T., Ge, Z., Li, Y., Chen, R., and Dennis, J. (2019). Transcriptome-Wide Analysis of Human Chondrocyte Expansion on Synoviocyte Matrix. *Cells* 8, 85. doi:10.3390/cells8020085

Lafont, J. E., Talma, S., Hopfgarten, C., and Murphy, C. L. (2008). Hypoxia Promotes the Differentiated Human Articular Chondrocyte Phenotype through SOX9-dependent and -independent Pathways. *J. Biol. Chem.* 283, 4778–4786. doi:10.1074/jbc.M707229200

Lund-Olesen, K. (1970). Oxygen Tension in Synovial Fluids. *Arthritis Rheum.* 13, 769–776. doi:10.1002/art.1780130606

Mounts, T., Ginley, N., Schluchter, M., and Dennis, J. E. (2012). Optimization of the Expansion and Differentiation of Rabbit Chondrocytes *In Vitro*. *Cartilage* 3, 181–187. doi:10.1177/1947603511420999

Oliveria, S. A., Felson, D. T., Reed, J. I., Cirillo, P. A., and Walker, A. M. (1995). Incidence of Symptomatic Hand, Hip, and Knee Osteoarthritis Among Patients in a Health Maintenance Organization. *Arthritis Rheum.* 38, 1134–1141. doi:10.1002/art.1780380817

Pattappa, G., Johnstone, B., Zellner, J., Docheva, D., and Angele, P. (2019). The Importance of Physioxia in Mesenchymal Stem Cell Chondrogenesis and the Mechanisms Controlling its Response. *Int. J. Mol. Sci.* 20, 484. doi:10.3390/ijms20030484

Pei, M., and He, F. (2012). Extracellular Matrix Deposited by Synovium-Derived Stem Cells Delays Replicative Senescent Chondrocyte Dedifferentiation and Enhances Redifferentiation.. *J. Cell Physiol.* 227 (5), 2163–2174. doi:10.3390/ijms20030484

Phull, A.-R., Eo, S.-H., Abbas, Q., Ahmed, M., and Kim, S. J. (2016). Applications of Chondrocyte-Based Cartilage Engineering: An Overview. *Biomed. Res. Int.* 2016, 1879837. doi:10.1155/2016/1879837

Robertsson, O., Bizjajeva, S., Fenstad, A. M., Furnes, O., Lidgren, L., Mehnert, F., et al. (2010). Knee Arthroplasty in Denmark, Norway and Sweden. A Pilot Study from the Nordic Arthroplasty Register Association. *Acta Orthop.* 81, 82–89. doi:10.3109/17453671003685442

Schmal, H., Zwingmann, J., Fehrenbach, M., Finkenzeller, G., Stark, G. B., Südkamp, N. P., et al. (2007). bFGF Influences Human Articular Chondrocyte Differentiation. *Cytotherapy* 9, 184–193. doi:10.1080/14653240601182846

Schmidmaier, G., Wildemann, B., Ostapowicz, D., Kandziora, F., Stange, R., Haas, N. P., et al. (2004). Long-term Effects of Local Growth Factor (IGF-I and TGF-β1) Treatment on Fracture Healing: A Safety Study for Using Growth Factors. *J. Orthop. Res.* 22, 514–519. doi:10.1016/j.orthres.2003.09.009

Shimoaka, T., Ogasawara, T., Yonamine, A., Chikazu, D., Kawano, H., Nakamura, K., et al. (2002). Regulation of Osteoblast, Chondrocyte, and Osteoclast Functions by Fibroblast Growth Factor (FGF)-18 in Comparison with FGF-2 and FGF-10. *J. Biol. Chem.* 277, 7493–7500. doi:10.1074/jbc.M108653200

Sieber, S., Michaelis, M., Gühring, H., Lindemann, S., and Gigout, A. (2020). Importance of Osmolarity and Oxygen Tension for Cartilage Tissue Engineering. *BioRes. Open Access* 9, 106–115. doi:10.1089/biores.2020.0009

Skou, S. T., Roos, E. M., Laursen, M. B., Rathleff, M. S., Arendt-Nielsen, L., Simonsen, O., et al. (2015). A Randomized, Controlled Trial of Total Knee Replacement. *N. Engl. J. Med.* 373, 1597–1606. doi:10.1056/NEJMoa1505467

Solchaga, L. A., Penick, K., Porter, J. D., Goldberg, V. M., Caplan, A. I., and Welter, J. F. (2005). FGF-2 Enhances the Mitotic and Chondrogenic Potentials of Human Adult Bone Marrow-Derived Mesenchymal Stem Cells. *J. Cell. Physiol.* 203, 398–409. doi:10.1002/jcp.20238

Tarasenko, Y. I., Yu, Y., Jordan, P. M., Bottenstein, J., and Wu, P. (2004). Effect of Growth Factors on Proliferation and Phenotypic Differentiation of Human Fetal Neural Stem Cells. *J. Neurosci. Res.* 78, 625–636. doi:10.1002/jnr.20316

Venn, M., and Maroudas, A. (1977). Chemical Composition and Swelling of Normal and Osteoarthrotic Femoral Head Cartilage. I. Chemical Composition. *Ann. Rheumatic Dis.* 36, 121–129. doi:10.1136/ard.36.2.121

Whitney, G. A., Kean, T. J., Fernandes, R. J., Waldman, S., Tse, M. Y., Pang, S. C., et al. (2018). Thyroxine Increases Collagen Type II Expression and Accumulation in Scaffold-free Tissue-Engineered Articular Cartilage. *Tissue Eng. Part A* 24, 369–381. doi:10.1089/ten.TEA.2016.0533

Zhang, S.-C., Wernig, M., Duncan, I. D., Brüstle, O., and Thomson, J. A. (2001). *In Vitro* differentiation of Transplantable Neural Precursors from Human Embryonic Stem Cells. *Nat. Biotechnol.* 19, 1129–1133. doi:10.1038/nbt1201-1129

Zhou, S., Cui, Z., and Urban, J. P. G. (2004). Factors Influencing the Oxygen Concentration Gradient from the Synovial Surface of Articular Cartilage to the Cartilage-Bone Interface: A Modeling Study. *Arthritis Rheum.* 50, 3915–3924. doi:10.1002/art.20675

Conflict of Interest: The authors declare that the research was conducted in the absence of any commercial or financial relationships that could be construed as a potential conflict of interest.

Publisher's Note: All claims expressed in this article are solely those of the authors and do not necessarily represent those of their affiliated organizations, or those of the publisher, the editors, and the reviewers. Any product that may be evaluated in this article, or claim that may be made by its manufacturer, is not guaranteed or endorsed by the publisher.

Copyright © 2022 Truong, Bernier, Dennis and Kean. This is an open-access article distributed under the terms of the Creative Commons Attribution License (CC BY). The use, distribution or reproduction in other forums is permitted, provided the original author(s) and the copyright owner(s) are credited and that the original publication in this journal is cited, in accordance with accepted academic practice. No use, distribution or reproduction is permitted which does not comply with these terms.

frontiers | Frontiers in Bioengineering and Biotechnology

REVIEW
published: 02 June 2022
doi: 10.3389/fbioe.2022.879187

Electrical Stimulation of Acute Fractures: A Narrative Review of Stimulation Protocols and Device Specifications

*Peter J. Nicksic[1], D'Andrea T. Donnelly[1], Nishant Verma[2,3], Allison J. Setiz[1], Andrew J. Shoffstall[4,5], Kip A. Ludwig[2,3,6], Aaron M. Dingle[1] and Samuel O. Poore[1]**

[1]Division of Plastic Surgery, University of Wisconsin School of Medicine and Public Health, Madison, WI, United States, [2]Department of Biomedical Engineering, University of Wisconsin—Madison, Madison, WI, United States, [3]Wisconsin Institute for Translational Neuroengineering (WITNe), University of Wisconsin—Madison, Madison, WI, United States, [4]Department of Biomedical Engineering, Case Western Reserve University, Cleveland, OH, United States, [5]APT Center, Louis Stokes Cleveland VA Medical Center, Cleveland, OH, United States, [6]Department of Neurological Surgery, University of Wisconsin—Madison, Madison, WI, United States

OPEN ACCESS

Edited by:
Andrea Vernengo,
AO Research Institute, Switzerland

Reviewed by:
Ben-Yi Liau,
Hungkuang University, Taiwan
Lohitash Karumbaiah,
University of Georgia, United States

***Correspondence:**
Samuel O. Poore
poore@surgery.wisc.edu

Specialty section:
This article was submitted to Tissue Engineering and Regenerative Medicine, a section of the journal Frontiers in Bioengineering and Biotechnology

Received: 19 February 2022
Accepted: 26 April 2022
Published: 02 June 2022

Citation:
Nicksic PJ, Donnelly DT, Verma N, Setiz AJ, Shoffstall AJ, Ludwig KA, Dingle AM and Poore SO (2022) Electrical Stimulation of Acute Fractures: A Narrative Review of Stimulation Protocols and Device Specifications. Front. Bioeng. Biotechnol. 10:879187. doi: 10.3389/fbioe.2022.879187

Orthopedic fractures have a significant impact on patients in the form of economic loss and functional impairment. Beyond the standard methods of reduction and fixation, one adjunct that has been explored since the late 1970s is electrical stimulation. Despite robust evidence for efficacy in the preclinical arena, human trials have mixed results, and this technology is not widely accepted. The purpose of this review is to examine the body of literature supporting electrical stimulation for the purpose of fracture healing in humans with an emphasis on device specifications and stimulation protocols and delineate a minimum reporting checklist for future studies of this type. We have isolated 12 studies that pertain to the administration of electrical stimulation for the purpose of augmenting fracture healing in humans. Of these, one was a direct current electrical stimulation study. Six studies utilized pulsed electromagnetic field therapy and five used capacitive coupling. When examining these studies, the device specifications were heterogenous and often incomplete in what they reported, which rendered studies unrepeatable. The stimulation protocols also varied greatly study to study. To demonstrate efficacy of electrical stimulation for fractures, the authors recommend isolating a fracture type that is prone to nonunion to maximize the electrical stimulation effect, a homogenous study population so as to not dilute the effect of electrical stimulation, and increasing scientific rigor in the form of pre-registration, blinding, and sham controls. Finally, we introduce the critical components of minimum device specification reporting for repeatability of studies of this type.

Keywords: electrical stimulation, fracture, human, direct current, pulsed electromagnetic field, capacitive coupling

1 INTRODUCTION

Traumatic fractures are estimated to incur $265.4 billion dollars per year of economic loss due to cost of healthcare and time away from work in the United States alone (Yelin et al., 2016). Additionally, delays in fracture healing are associated with increased pain, functional limitations, and a decreased quality of life for patients (Cook et al., 2015). For these reasons, many efforts have been made to

augment and expedite the process of fracture healing. These types of adjunct therapies include electrical stimulation (ES) and low-intensity pulsed ultrasound therapy (LIPUS). A recent meta-analysis aggregated 13 randomized controlled trials examining the effect of LIPUS (10) and pulsed electromagnetic field (PEMF) therapy (3) on acute fracture healing (Hannemann et al., 2014a). While there was no significant effect for time to radiographic union overall, subgroup analysis found that these treatments decreased time radiographic union for subgroups of upper extremity fractures (mean difference = −20.23 days, 95% CI −32.68– −7.77, p = 0.001, I^2 = 67%) and non-operative fractures (mean difference = −26.65 days, 95% CI = −50.38– −2.91, p = 0.03, I^2 = 98%) (Hannemann et al., 2014a). While LIPUS and other adjuncts may show promise in improving outcomes in specific subtypes of acute fractures, there is large body of literature in support of ES for the purpose of bone healing. Electrical stimulation and its relationship to bone formation was first described by Fukada and Yasuda (1957). In their seminal paper, they described the piezoelectric quality of bone—that is, that bone generates endogenous electrical fields when put under mechanical stress. Since then, researchers have attempted to harness exogenous ES to heal a variety of osseous insults in both animals and humans.

There are three modalities of ES currently in use: direct current electrical stimulation (DCES), capacitive coupling (CC), and inductive coupling. Direct current electrical stimulation (DCES) is an invasive method in which the cathode is placed percutaneously directly into the site of osseous injury and electron flow is unidirectional from the anode, which is placed in nearby subcutaneous tissue. Capacitive coupling is most commonly noninvasive and involves electrodes which are placed on the skin on either side of osseous injury. The alternating current generates an electrical field between the electrodes. Inductive coupling, most commonly in the form of PEMF, utilizes two solenoids oriented parallel to the skin surface on opposite sides of the osseous injury. Current is pulsed through the solenoids, and a magnetic field is generated, which induces a perpendicular electrical field.

There is a robust body of evidence in support of ES for fracture non-unions, spinal fusions, and acute fractures in small animal models (Guizzardi et al., 1994; France et al., 2001; Atalay et al., 2015; Liu et al., 2021; Nicksic et al., 2022). There has also been a resurgence in interest in the field of ES for the purpose of bone healing in *in vitro* studies (Li et al., 2019; Portan et al., 2019; Escobar et al., 2020; Stephan et al., 2020). However, when translating these stimulation protocols and device specifications to large animals and humans, there has been varying levels of success (Paterson et al., 1977a; Paterson et al., 1977b; Miller et al., 1984; Law et al., 1985; Muttini et al., 2014).

The reason there has been mixed success in the translation of ES for bone healing from *in vitro* and small animal studies to large animal studies and clinical trials is likely multifactorial. One issue likely lies in getting stimulation to the fracture site in larger limbs. For the more popular noninvasive stimulation modalities, computer modeling data demonstrates that changing the thickness of skin, subcutaneous fat, muscle, and cortical bone all have significant effects on the energy transmitted to the fracture site (Lunt, 1985; Plonsey and Barr, 1995). This is supported by the fact that large animal studies using DCES—where stimulation can be administered reliably regardless of scale—are largely more successful in inducing osteogenesis than noninvasive treatments (Nicksic et al., 2022).

A recent meta-analysis of randomized, sham-controlled clinical trials demonstrated that electrical bone growth stimulators (EGBS) are only effective at reducing the 12 months non-union rate in the spinal fusion subgroup (p = 0.002, 95% CI = 0.45–0.84), and the effect for acute fractures, non-union, delayed union, and osteotomy subgroups was not significant (Aleem et al., 2016). One indication for the use of ES is the treatment of acute (fresh) fractures—fractures expected to heal within the normal time course for the injury once promptly and adequately reduced and fixated—which are the most common osseous injury (Yelin et al., 2016). Returning to the literature to examine the methodologies of human studies for acute fractures may shed light on why ES is not a widely accepted therapy.

Given the abundance of evidence in preclinical studies and mixed results from clinical trials, this review aims to 1) summarize the data of key studies for the treatment of acute fractures with ES stratified by ES modality, 2) examine the methodologies of these studies with attention to ES device specifications and stimulation protocols, and 3) draw conclusions about what is necessary to conduct a future study of this type so that the methodology may be applied to other fracture types. To do this, we queried the MEDLINE database for relevant search terms including combinations of "electrical stimulation," "bone healing," "fracture," "direct current," "PEMF," and "capacitive coupling," searching for human studies pertaining to the treatment of acute fractures with electrical stimulation. *In vitro* and animal studies, case reports, and studies not available in the English language were excluded. Our query yielded one DCES study, six PEMF studies, and five CC studies (**Table 1**).

2 FACTORS AFFECTING FRACTURE HEALING

When evaluating orthopedic fractures, there are many factors intrinsic to the injury pattern that can give the clinician an estimate of the healing potential and level of intervention required. One important factor affecting fracture healing is fracture location. Generally, time to radiographic union (when the bone is considered healed on radiographs or computed tomography) and/or clinical union (when the patient can resume normal function without pain or limitation) is inversely proportional to the vascular supply of the bone. For example, the mid-diaphysis of the femur has a robust vascular supply from the surrounding muscle, and typically heals relatively quickly and reliably. By contrast, the femoral neck and mid-diaphyseal tibia have minimal surrounding vascularized tissue, and fractures of these locations are often treated more aggressively as the healing potential is lower (Zura et al., 2016b). A similar concept holds true for "short bones"—the carpal and tarsal bones. These bones have a tenuous vascular

TABLE 1 | This table presents the pre-registration, randomization, sham-control, and blinding status of the studies included in our review, organized in chronological order. This is followed by number of participants, details of the study population, type of fracture, stimulation protocol, device specifications, and outcomes of the studies. Green fill denotes significant results. Red fill denotes nonsignificant results. Gray fill denotes that the study results are not applicable.

Author(s)	Year	Pre-Registration	Randomized	Sham-Controlled	Blinding	N	Study Population	Fracture type	Fixation	ES Modality	ES Protocol	ES Specs	Outcome
Jorgenson	1977	NR	Yes	No	None	71	General	Closed tibial fractures	External fixation	DCES	Continuous until clinical union	Constant voltage, 1Hz, 0.7-1.3V, 40μA	ES group with 30% reduction in time to clinical union ($P < 0.001$)
Wahlstrom et al.	1984	NR	Yes	Yes	None	30	Women, 50-70 years	Extra-articular distal radius fractures, <10 degrees dorsal angulation	Dorsal-blocking splint	PEMF	Continuous for 4 weeks	4G, 1-1000Hz	Decreased time (5 days) to radiographic union in the ES group ($P < 0.05$)
Benazzo et al.	1995	No	No	No	None	25	Athletes	Lower Extremity stress fractures	None	CC	Continuous until clinical union	Constant voltage, 3.0-6.3V, 60kHz, 5-10mA	88% of fractures healed, no control group for comparison
Fourie and Bowerbank	1997	No	Yes	No	Yes	227	Isolated tibial fractures with less than 2 closed reduction efforts without osteopenia	Tibial shaft fractures	Casting	CC	30 minutes per day for 10 days	100mA, 60V peak maximum, 4.0-4.25kHz	No significant effect for time to radiographic union
Beck et al.	2008	NR	Yes	Yes	NR	44	General	Tibial stress fractures	None	CC	15 hours per day until clinical union	Constant voltage, 3.0-6.0V, 60kHz, 5-10mA	No significant difference in time to clinical union between the active and sham groups
Itoh et al.	2008	No	Yes	No	NR	43	Heavily comminuted distal radius fractures	Distal radius fractures	External fixation	CC	Continuous while the external fixator was in place	2Hz, 30μA, 0-60kΩ loading resistance	Decrease in radial collapse in the stimulation group ($P < 0.01$)
Faldini et al.	2010	NR	Yes	Yes	NR	77	General	Femoral neck fractures	Cannulated screw ORIF	PEMF	8 hours per day for 90 days, starting POD7	2mT, 75Hz, 1.2msec pulse	Active compliant group demonstrated higher radiographic union rates at 30-, 60-, 90-day timepoints ($P < 0.05$)
Adie et al.	2011	Yes	Yes	Yes	Double	218	General	Midshaft tibial fractures	All types	PEMF	10 hours per day for 12 weeks, starting 2 weeks post injury	None disclosed	No significant difference between groups for time to radiographic union significant difference between groups for revision surgery rates, radiographic union at 6 months, or patient reported outcomes
Hannemann et al.	2012	NR	Yes	Yes	Double	53	General	Non-operative scaphoid fractures	Thumb spica cast	PEMF	Continuously for 12 weeks from fixation	15Hz, 50mV, 5ms pulse width	ES group with greater radiographic union scores at 6 weeks ($P < 0.001$)
Hannemann et al.	2014	NR	Yes	Yes	Double	102	No pre-existing wrist pathology	Non-operative scaphoid fractures	Thumb spica cast	PEMF	Continuously for 12 weeks from fixation	15Hz, 50mV, 5ms pulse width	No significant difference between groups for time to radiographic union
Martinez-Rondanelli et al.	2014	NR	Yes	Yes	Double	63	18-60 years old	Diaphyseal femoral fractures	Open reduction internal fixation	PEMF	1 hour per day for 8 weeks, starting 6 weeks post operatively	0.5-2.0mT, 5-10Hz	No significant difference between groups for time to radiographic union
Piazolla et al.	2015	No	Yes	Yes	None	24	General	Acute vertebral compression fractures	Open reduction internal fixation	CC	50% duty cycle, continuous until radiographic union	25μA, 12.5Hz	Stimulation group with higher radiographic union scores at the 30, 60, and 90 day timepoints ($P < 0.0001$ for all)

N, number of participants; ES Specs, electrical stimulation specifications.

supply and are prone to nonunion (Zura et al., 2016b). One other important intrinsic factor that affects fracture healing capacity is the level of comminution. Highly comminuted fractures—or fractures with multiple small fragments—typically are associated with higher energy injuries or lower bone quality. Speaking broadly, a fracture with a higher level of comminution is more likely to proceed to malunion (a fracture that heals in an extra-anatomic position) or nonunion. For example, a minimally comminuted distal radius fracture may be treated with a thumb spica cast, whereas a more comminuted distal radius fracture might require open reduction, possibly bone grafting, and plating to heal (Ring et al., 2005).

In addition to factors intrinsic to the injury itself, there are patient-related factors that can greatly affect fracture healing. A recent meta-analysis aggregated all patient factors associated with nonunion (Zura et al., 2016a). In this study, they demonstrated that advanced patient age, smoking history, alcoholism, osteoporosis, obesity, and diabetes were all associated with increased rates of nonunion for various fracture locations (Zura et al., 2016a). Between male and female sex, the nonunion rate has been shown to be higher in women after the age of 45–54 years. However, younger women have a lower rate of operative nonunions than men (Mills et al., 2017). All of these factors are important to consider when analyzing results from studies utilizing ES to augment fracture healing.

3 DIRECT CURRENT ELECTRICAL STIMULATION

Direct current electrical stimulation involves percutaneous wire leads placed into the area of osseous injury (**Figure 1**). The cathode placed at the site of osseous injury results in electrochemical reduction of molecular oxygen, which is believed to create an alkaline, low-oxygen microenvironment (Brighton and Friedenberg, 1974; Haddad et al., 2007). This state favors osteoblast differentiation and stimulates osteoclasts to produce vascular endothelial growth factor, which induces vasculogensis (Bushinsky, 1996; Kaysinger and Ramp, 1998). Because lead placement requires an operation and carries risk of infection or device malfunction, DCES is not an optimal modality for treatment of acute fractures. As such, DCES is typically reserved for occasional use in operative, acute fractures with high-risk of delayed union or non-union, as many surgeons would prefer the standard methods of reduction and fixation first before accepting the infection risk associated with lead placement and removal. Another shortcoming of DCES is that, because the flow electrons is unidirectional, the cathode accumulates a negative charge at higher currents, leading to the deleterious concentrations of faradic salts (Zengo et al., 1976). Therefore, there is a limit to the current density and charge that can applied safely (Brighton et al., 1981).

3.1 DCES May Be Effective for Fracture Healing but With a Significant Infection Risk

However, one randomized study was performed that examined DCES treatment in 71 patients with closed, acute tibial fractures treated with an external fixator (Jorgensen, 1977). There was no mention of pre-registration in the manuscript. Of these, 12 were excluded for lead-site infections. There were no other inclusion or exclusion criteria for fracture morphology or injury type defined. Insulated screws proximal and distal to the fracture acted as the cathode, but the screw material was not stated. Additionally, the screws were not insulated from the skin or muscle, and no current measurement at the level of the bone was performed. The experimental group was treated with a voltage-controlled constant stimulation of 1 Hz, and 0.7–1.3 V with a measured current of 40 μA until the fractures met criteria for clinical union, as defined by lack of fracture mobility on clinical exam and pain-free ambulation. Participants underwent monthly radiographs and mechanical testing until the fracture attained a set degree of stiffness. The experimental group showed an accelerated time to clinical union by 30% (2.4 months) when compared to controls (3.6 months) ($p < 0.001$).

4 PULSED ELECTROMAGNETIC FIELD

Pulsed electromagnetic field therapy is a more attractive modality to augment acute fracture healing, because it can be administered non-invasively and, therefore, does not carry risks of infection or additional operations (**Figure 2**). Pulsed electromagnetic field therapy is believed to increase cytoplasmic calcium by activating voltage-gated calcium channels intracellularly and is associated with upregulation of multiple key growth factors (insulin-like growth factor 2, bone morphogenic proteins [BMPs] 2 and 4, and transforming growth factor -beta {TGF-β}) inducing osteoblast differentiation, proliferation, and extracellular matrix deposition (Haddad et al., 2007; Khalifeh et al., 2018).

4.1 PEMF Demonstrates Mixed Results for Long Bone Fracture Healing With Compliance Issues

Studies have examined the effect of PEMF therapy on healing of long bone fractures prone to delayed or nonunion. Wahlström (1984) published an unblinded, randomized, sham-controlled study evaluating the effect of PEMF on 30 women between the ages of 50–70 years with acute, non-operative, extra-articular distal radius fractures with apex dorsal angulation less than 10 degrees. No mention of pre-registration was made. Post-injury day one, participants were fixed with a dorsal-blocking plaster cast with an imbedded copper solenoid and current generator, producing a magnetic field of 4 Gauss (G) within the range of 1–1000 Hz for 4 weeks. No solenoid geometry was reported. The apparatus was checked weekly with a gaussmeter to ensure continued functioning, but no calculations or measurements were offered to estimate the magnetic field at the level of the fracture. Bone scintigraphy and radiographs were completed at 1, 2, 4 and 8 weeks to evaluate for fracture displacement and radiographic union. Radionucleotide uptake ratio—the intensity of the callus on bone scintigraphy referenced to a non-healing control

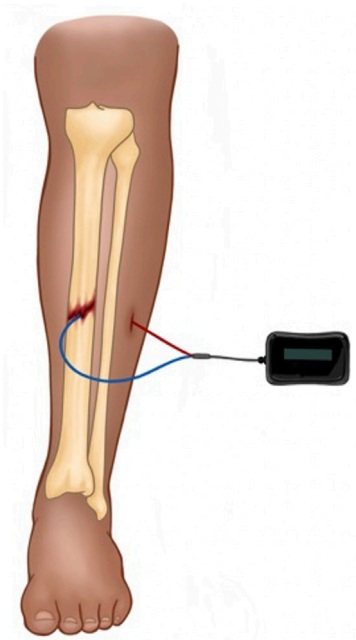

FIGURE 1 | Depicted is a schematic for DCES in the treatment of a midshaft tibial fracture. The device is comprised of a power source (which is typically placed subcutaneously) and the cathode (blue lead) and anode (red lead). The cathode is placed at the fracture site, and the anode is placed in nearby soft tissue.

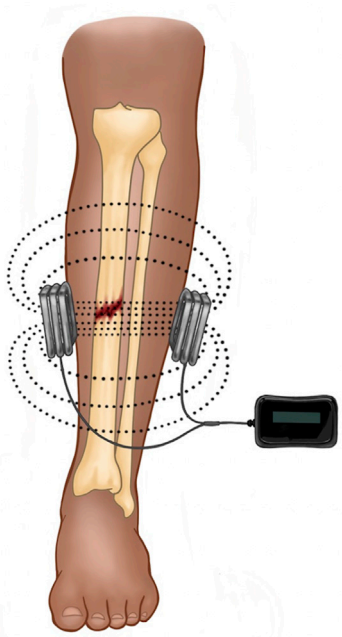

FIGURE 2 | Depicted is a schematic for PEMF in the treatment of a midshaft tibial fracture. The device is completely external and comprised of a power source and two solenoids oriented parallel to the skin surface. Current is pulsed through the solenoids and a magnetic field is produced (dotted lines), which induces a perpendicular electrical field (not depicted).

bone—was significantly higher in the stimulation group at week 1 and 2 ($p < 0.05$, $p < 0.01$ respectively). There was no significant difference at 4 and 8 weeks. Time to radiographic union, defined as when the intensity of radionucleotide uptake started to decrease, was significantly reduced in the stimulation group at 18 days versus 23 days in the control group ($p < 0.05$). Of note, the rate of re-displacement of fractures was nonsignificant between the treatment and control groups and was instead correlated to original displacement and stability of reduction.

Faldini et al. (2010) investigated the use of PEMF on operative fractures of the femoral neck in 77 patients, randomized to either sham or active stimulation. No mention of pre-registration was made. The fractures were fixed percutaneously with cannulated screws within 3 days post-injury, and stimulation with sham versus active PEMF devices began on post-operative day 7. The PEMF device used was the Biostim (Igea, Carpi, Italy), and the stimulation protocol consisted of 2 mT peak magnetic field, 75 Hz, and 1.2 msec pulse duration for 8 h per day for 90 days. Specific coil dimensions were not reported. Compliance was monitored with a timer inside the device that recorded device activity. Radiographs were completed at regular intervals to 2 years following surgery. Radiographic union was defined as a minimum of 70% of the fracture being bridged with trabeculae. The level of compliance was heterogenous in both the active and control groups, so data analysis was performed in subgroups of compliant (greater than 6 h per day of device use) and noncompliant (less than 6 h per day of device use). Patients in the active compliant group demonstrated a higher rate of radiographic union at the 30-, 60-, and 90-days timepoints when compared to the active noncompliant and placebo groups ($p < 0.05$). Of note, the active compliant group was significantly younger than the active noncompliant group (67.1 ± 6.0 years, 71.6 ± 3.1 years, respectively, $p < 0.05$).

Martinez-Rondanelli et al. (2014) examined the effect of PEMF on closed, diaphyseal femoral fractures in a double-blind, randomized, sham-controlled study of 63 patients, 18–60 years of age. No mention of pre-registration was made. Custom stimulation devices delivering 5–10 Hz and 0.5–2.0 mT were applied 6 weeks after operative fixation of the fractures, 1 hour per day for 8 weeks. Depending upon the patients' thigh diameter, the coil diameters could be adjusted, but no calculations were offered as to how this was performed, and no coil geometry was described. Radiographs were performed at 12, 18, and 24 weeks post-operatively and were classified by a radiologist as non-union, partial union, or complete union. There was no significant difference in rate of radiographic union between groups.

Adie et al. (2011) performed a pre-registered, randomized, double-blind, sham-controlled trial for PEMF on 218 tibial diaphyseal fractures. All midshaft tibial fractures were included, regardless of means of fixation. This study used the commercially available Biomet® Bone Healing System (Zimmer Biomet, Indiana, IN, United States) PEMF device, and the device specifications were not disclosed. The device was applied over the plaster or fiberglass cast for 10 h per day for 12 weeks, 2 weeks

following injury and initial fixation. Compliance was measured by the device's internal timer, which clocked hours of use. Outcomes measures included rate of secondary surgery for nonunion at 1-year post-injury, radiographic union at 6 months, and patient reported outcomes at 1 year. In this study, there were no significant effects of PEMF for revision surgery rates, radiographic union at 6 months, or patient reported functional outcomes.

4.2 Little Efficacy Demonstrated With PEMF for Healing Short Bone Fractures

In addition to long bone fractures, there have been PEMF studies on fractures of short bones prone to nonunion and delayed union. Hannemann et al. (2012) conducted a double-blind, sham-controlled study in which the effect of PEMF was examined in 53 nonoperative scaphoid fractures. No mention of pre-registration was made. All patients had thumb spica cast-implanted PEMF stimulators (Ossatec, Uden, Netherlands) with only the treatment group being active. The device specifications were 15 Hz, 50 mV, and a pulse width of 5 μs and burst width of 5 ms. No coil geometry or magnetic field strength was reported. Stimulation was applied continuously until complete union or 12 weeks post-injury. Radiographic union was blindly assessed by two surgeons and a radiologist and categorized into three groups: nonunion, possible union, and complete union. Tenderness at the anatomic snuffbox was assessed with longitudinal compression of the scaphoid. Clinical exams and radiographs were obtained at regular intervals to 1-year post-injury. The treatment group demonstrated a reduction in snuffbox tenderness ($p = 0.003$) and increased radiographic union scores ($p < 0.001$) at the 6-week timepoint only.

Hannemann et al. (2014b) performed a similar study evaluating PEMF for nonoperative scaphoid fractures in 102 patients using computed tomography (CT) imaging instead of plain radiographs. There was no mention of pre-registration. Patients were excluded if their fractures were displaced, if they had proximal pole scaphoid fractures, fracture dislocations, additional fractures, or pre-existing wrist impairments. Patients received continuous stimulation with the same device (Ossatec, Uden, Netherlands) incorporated into a plaster cast placed above the fracture site with the same specifications as the previous study (Hannemann et al., 2012). Clinical and CT examinations were performed at regular intervals up to 1 year. There was no significant difference in time to radiographic union between groups.

5 CAPACITIVE COUPLING

Capacitive coupling is typically a non-invasive method of ES in which electrodes are placed on the skin, and an alternating current generates an electrical field between the electrodes (**Figure 3**). Similar to PEMF, CC induces an increase in cytoplasmic calcium by activating voltage-gated calcium channels, which initiates the calmodulin-mediated pathway of osteogenesis (Crocker et al., 1988; Brighton et al., 2001). Capacitive coupling therapy is also associated with upregulation of BMP 2 and 4 and TGF-β1 in osteoblasts (Zhuang et al., 1997; Wang et al., 2006). With alternating current, there is no risk of accumulation of faradic salts at the electrode/electrolyte interface, because the electrochemical reactions are persistently being reversed. This allows for much higher charge densities than would be possible with direct current. Due to poor penetrance of the electrical field into soft tissue (Plonsey and Barr, 1995), CC is only practical for superficial bones (e.g., distal radius or tibia).

5.1 CC may be Useful in the Treatment of Lower Extremity Stress Fractures

Benazzo et al.(1995) performed an open case-series (therefore, no control group) of tarsal, metatarsal, fibular and tibial stress fractures of 25 athletes treated with CC. The device provided a voltage-controlled sinusoidal waveform from 3.0 to 6.3 V, and 60 kHz. The current was estimated to be between 5 and 10 mA. No electrode geometry or spacing was provided to calculate charge density. Stimulation was continuous until the fracture demonstrated radiographic evidence of healing or until 3 weeks passed with no reported change. Participants underwent bi-weekly radiographic evaluation. Fractures were determined to be healed if the radiographs showed incomplete healing with a marked decrease of pain. Final radiological assessment found that 88% of fractures healed, 8% improved and 4% did not heal. Beck et al. (2008) also examined the effect of CC on 44 patients with tibial stress fractures in a randomized, sham-controlled study. No mention of pre-registration was made. Constant voltage stimulation of 3.0–6.0 V, 60 kHz with a measured 5–10 mA was applied for 15 h a day until the fractures reached clinical union. No electrode geometry or spacing was provided to calculate charge density. Clinical union was determined by the absence of reported pain after hopping 10 cm for 30 s. There was no significant difference in time to clinical union between the active and sham groups, however superior treatment compliance was associated with reduced healing time in the experimental group ($p = 0.003$).

5.2 CC With Mixed Results for Long and Short Bone Fracture Healing at a Wide Range of Stimulation Parameters

Fourie and Bowerbank applied CC to acute tibial fractures of 227 patients in an unregistered, blinded, randomized study without sham controls (Fourie and Bowerbank, 1997). Patients were excluded if they had additional fractures, associated medical comorbidities, or if they received two or more closed reduction efforts. All mechanisms of injury, fracture morphologies, and fracture locations within the tibia were included. Electrodes were placed in windows of a plaster cast with the guidance of radiographs, delivering constant voltage stimulation with an estimated 100 mA and a 60 V peak maximum. One subgroup received 4.0 kHz, while another subgroup received 4.10–4.25 kHz. No electrode geometry or spacing was provided to calculate charge density, and no measurements of electric field were offered. The fractures

FIGURE 3 | Depicted is a schematic for CC in the treatment of a midshaft tibial fracture. The device is completely external and comprised of a power source and two skin surface electrodes. The alternating current generates an electrical field between the electrodes (dotted lines) with significant falloff into tissue (dissipation of dotted lines).

were stimulated 30 min per day for 10 days. Radiographic union was assessed by a single-blinded radiologist, and the fractures were categorized into non-union, partial union, and nonunion. There were no significant differences in time to radiographic union between groups. However, there was a significant effect of time to radiographic union when fractures from both stimulation and control groups were analyzed by mechanism of injury (p = 0.0005), type of fracture (p = 0.015), the presence of a fractured fibula (p = 0.026), and degree of displacement (p = 0.0005) for time to radiographic union.

Itoh et al. (2008) investigated CC on heavily comminuted, intra-articular fractures of the distal radius in 43 patients in a randomized study without sham controls. No mention of blinding was made. The pins of an external fixator acted as the electrodes and provided a 2 Hz sinusoidal wave of constant current stimulation at 30 μA with 0–60 kΩ of loading resistance. No electrode geometry or spacing was provided to calculate charge density, and no measurements of electric field were offered. A control group received an external fixator with no electrical stimulation. The fractures were considered healed when radiographs showed the presence of bridging trabeculae, and no remaining radiolucent lines between fracture fragments. Radiographs completed weekly demonstrated a significant decrease in radial collapse in the stimulation group ($p < 0.01$). Results of this study must be guarded, however, because the external fixators were left in place for an average of 39.0 ± 4.2 and 48.9 ± 7.2 weeks for the control and stimulation groups, respectively, which is significantly longer than what is considered standard of care for duration of external fixator placement.

In 2015, Piazzolla et al. (2015) evaluated the efficacy of CC on 24 acute vertebral compression fractures in an unregistered, randomized, sham-controlled study. The electrodes placed on the skin delivered constant current stimulation at 25 μA at 12.5 Hz with a duty cycle of 50%. No electric field measurements or electrode geometry or spacing were reported. Magnetic resonance imaging (MRI) was completed at 0, 30, 60 and 90 days. An unblinded neuroradiologist and two orthopedists analyzed the MRIs to determine healing scores. The stimulation group demonstrated higher radiographic healing scores at the 30-, 60- and 90-day timepoints ($p < 0.0002$, $p < 0.0001$, and $p < 0.0001$, respectively). There was an improvement in pain scores and patient reported outcomes as determined by the Visual Analog Scale, and Oswestry Low Back Disability Index (p = 0.007, p = 0.002, respectively). Complete healing measured by MRI was found only at the 90-day timepoint in the stimulation group (p = 0.0001).

6 DISCUSSION

6.1 Optimizing Outcomes in EGBS Studies for Acute Fractures

This extensive examination of the body of literature of ES on osseous healing has revealed several important trends. The first issue presents itself in selecting the study population. Ideally, the study population should be a group of patients who would benefit most from EGBS therapy. The fracture location should be an area with a high rate of nonunion (e.g., middle tibia or scaphoid) (Zura et al., 2016b) and strict inclusion and exclusion criteria should be applied so that the effect of ES is not diluted. This includes controlling for multiple variables like fracture morphology, mechanisms of injury, patient comorbidities, smoking status, sexes, and ages for a given fracture location. For example, Fourie and Bowerbank (1997) examined the effect of CC on tibial fractures and found no effect based on ES but did find significant correlations for mechanism of injury, fracture morphology, degree of displacement, and presence of fibular fractures. If the study population, for example, consisted of osteopenic females aged 54–70 years with minimally displaced distal radius fractures from a fall from standing, the chances of a significant effect for ES may be larger.

Another common issue is the lack of consistency in reporting of device specifications. Many studies devise custom stimulators and do not offer any calculation or measurement of the strength of stimulation. As such, the study is not replicable, and any results of the study cannot be applied to other fracture locations or patient populations. For DCES studies, we would recommend reporting the current density (measured or calculated), frequency, and cathode material, as these variables have all been shown to affect osteogenesis in animal studies (Spadaro and Becker, 1979; Spadaro, 1982). For CC studies, we would recommend reporting electrical field strength (measured) or enough information (electrode geometry and distance between

them) to calculate charge density, frequency, and distance between electrodes. For PEMF studies, the magnetic field strength (measured or calculated), frequency, and coil geometry (number of turns and size and shape of the solenoid) are necessary to replicate results.

Finally, we recommend National Institute of Health pre-registration of future EGBS studies with an overall increase in methodological rigor. Ideally, studies would be double-blinded and sham-controlled with statistical power analysis performed based on anticipated effect size. The stimulation protocol – hours of stimulation per day and weeks of therapy duration – would be derived from past studies and be justified with data. Currently, stimulation protocols are heterogenous for any given modality. For example, PEMF studies range from 1 hour per day for 8 weeks to constantly for 12 weeks (Hannemann et al., 2012; Hannemann et al., 2014b; Martinez-Rondanelli et al., 2014). These studies should also define strict criteria or a quantifiable metric for endpoints like radiographic or clinical union. Standardizing these variables and outcome measures would provide meaningful and replicative data that would potentially move ES into the clinical arena should positive results be found.

6.2 The Optimal ES Modality for Treatment of Acute Fractures

When determining what the most promising ES modality is for the treatment of acute fractures, each of the available modalities – DCES, CC, and PEMF – have significant advantages and weaknesses. The ideal EGBS would possess qualities of each of these modalities. Direct current electrical stimulation can be delivered directly to the fracture site, bypassing intervening soft tissue and offering a predictable amount of current to treat the fracture (**Figure 1**). When examining the large animal literature, DCES studies are typical more successful in inducing osteogenesis than the noninvasive modalities (Nerubay et al., 1986; Chakkalakal et al., 1990; Cook et al., 2004). These studies applied a wide range of stimulation currents and were successful in inducing osteogenesis within a range of 20–100 μA, and lower stimulation currents (13 μA) were not successful (Nerubay et al., 1986; Chakkalakal et al., 1990; Toth et al., 2000). These results are problematic for translation into humans, however, because these studies used custom-built stimulators and did not report cathode material, lead geometry, or measures of current density in all cases (Nicksic et al., 2022). Direct current electrical stimulation remains largely unstudied in humans as it is impractical, requiring operations for lead placement and removal and presenting an unacceptable infection risk (Jorgensen, 1977).

Capacitive Coupling is noninvasive which eliminates the constraints of operative placement of the device and the risk of infection. However, the fall off of the electrical field in tissue of high resistivity like skin and subcutaneous fat – $\sim 1/r^2$ where r is the distance from the signal source – is prohibitive for treatment of many long bone fractures (Plonsey and Barr, 1995). This is reflected in the large animal literature utilizing CC to induce osteogenesis. One study demonstrated no effect with 5–10 mA at 60 kHz in a canine tibial distraction osteogenesis model (Pepper et al., 1996). However, a more recent study showed benefit at 1.5 mA, 12.5 Hz for sheep tibial delayed union by quantitative histomorphometry ($p < 0.0001$) and quantitative radiodensity analysis ($p < 0.0043$) (Muttini et al., 2014). An important note is that in this study, the electrodes were implanted in bone proximal and distal to the fracture and, for this reason, did not have to overcome the resistivity of skin and subcutaneous adipose tissue. Therefore, CC is not applicable to treatment of fractures outside of the spine, middle tibia, wrist, and ankle. Of the CC studies included, three studies (Benazzo et al., 1995; Beck et al., 2008; Piazzolla et al., 2015) describe administering currents transcutaneously that are orders of magnitude lower than the extremum of the dose-response curve modeled for CC. In a rat sciatic denervation osteoporosis model, Brighton et al. found that with constant voltage stimulation of 0.66 V (estimated current of 584.6 ± 21.2 μA) the dry weight of osteoporotic tibia was closest to the contralateral control (ratio of 0.922, $p < 0.05$) (Brighton et al., 1988). Scaling this dose-response curve to humans with thicker skin and significantly more interposing soft tissue between the skin and target bone, it is unlikely that administering 5 mA of stimulation would penetrate the skin, much less have any effect on bone.

Finally, PEMF appears to be an attractive option for treatment of acute fractures as it is both noninvasive, and the induced electrical field can more easily penetrate soft tissue. However, there are significant patient compliance issues with these devices that make them less practical. Many protocols required lengthy durations of treatment, resulting in low levels of patient compliance (Faldini et al., 2010). Other variables also significantly affect the induced electrical field. For example, the thickness of tissue planes (fat, muscle, and bone) and their relative difference in resistivity, as well as even small changes in the placement of the PEMF device with relationship to the fracture, dramatically change the intensity of the electrical field at the fracture site (Lunt, 1985). By contrast to *in vitro* and small animal studies, large animal studies have largely been unsuccessful in inducing osteogenesis with PEMF therapy (Nicksic et al., 2022). Studies to date have included a range of indications in both canine and sheep models (Miller et al., 1984; Law et al., 1985), but the single study that was able to demonstrate benefit for PEMF therapy applied 0.2 mT, 1.5 Hz stimulation to a canine mid-diaphyseal tibial 2 mm gap osteotomy model (Inoue et al., 2002). This stimulation was applied for 4 weeks for 1 h per day, beginning at 4 weeks post-injury. More work is required to determine the dose-response curve for PEMF therapy in large animals and humans.

In human studies, these issues are not completely addressed by cast-implanted PEMF devices, as this strategy adds new variables including the thickness and resistivity of the cast material and air between the cast and the skin. Unless the PEMF devices are calibrated on a patient-by-patient basis and compliance issues are addressed, the results of cast-implanted PEMF studies will remain unpredictable.

Based on the available literature, several patterns emerge that could potentially lead to an ideal EGBS. It should possess qualities of all the available modalities for ES (**Figure 4**). First, like DCES, the strength of stimulation should be predictable at the level of the fracture, regardless of thickness of intervening soft tissue or patient position. Second, similar to CC and PEMF, it should also be semi- or noninvasive so that there is negligible risk of

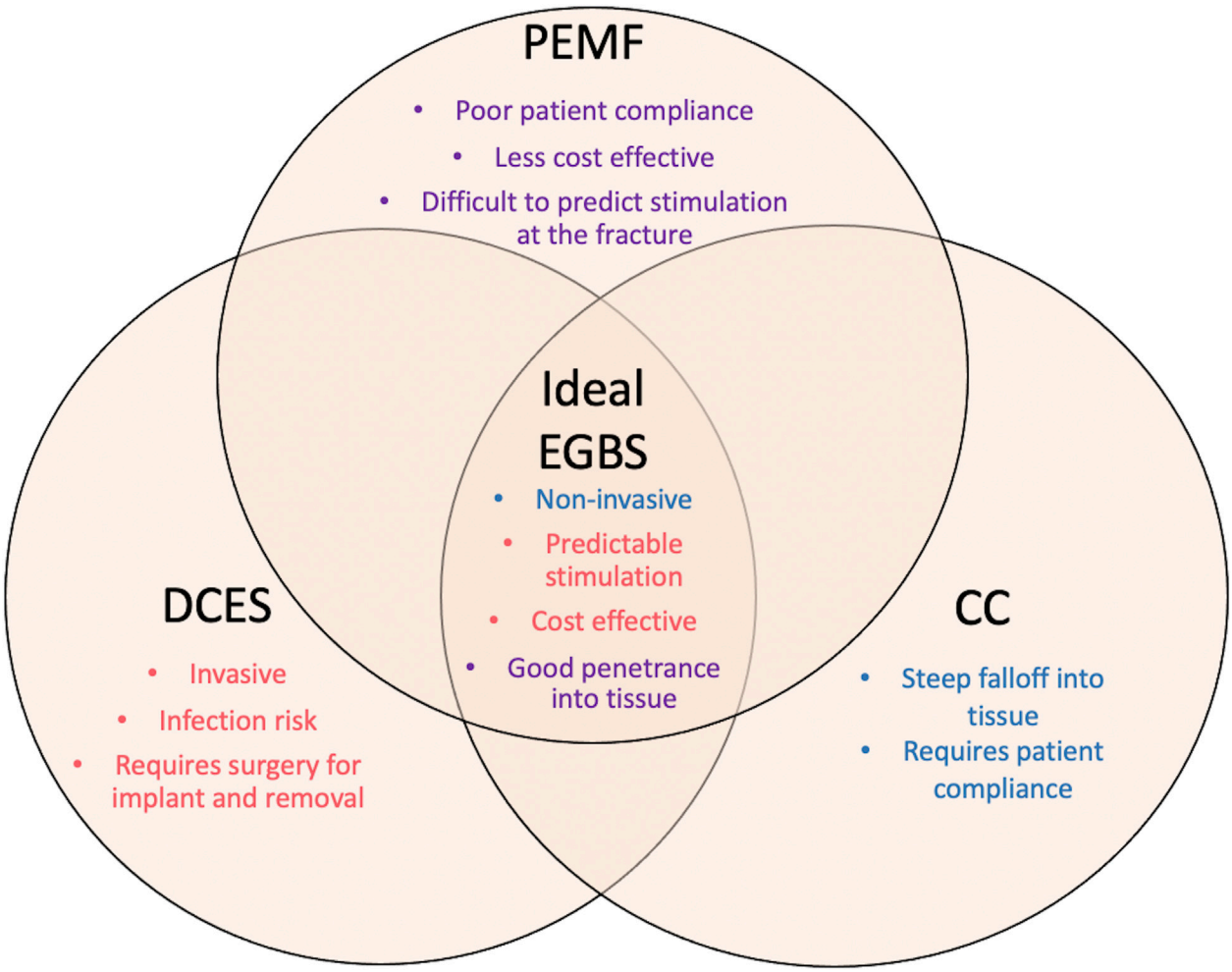

FIGURE 4 | This diagram represents the qualities of the ideal electronic bone growth stimulator. The characteristics of the different modalities of ES are listed under each type. The weaknesses of each type of ES are listed on the periphery of the figure. The strengths of each type of modality that should comprise the ideal EGBS are listed centrally. Purple text denotes qualities of PEMF. Red text denotes qualities of DCES. Blue text denotes qualities of CC. This figure is meant to emphasize the need for innovation in the field of bone growth stimulation, as the ideal EGBS does not yet exist.

infection, and the device can be administered non-operatively. Lastly, it should be cost effective so that it can be used widely. Further innovation beyond what is currently available, perhaps in the field of conductive microparticles, could potentially offer a viable and clinically relevant methodology of electrical stimulation for bone healing.

6.3 Future Directions for Electrical Stimulation

Outside of the indication for augmentation of acute fracture healing, there is a robust body of literature to demonstrate that ES can be used to improve peripheral nerve regeneration, neuroplasticity, and soft tissue wound healing (Zuo et al., 2020; Luo et al., 2021; Sousa et al., 2022). One key component of the literature for these fields is that the dose-response curve and optimal duration of therapy is well described. To date, these important elements are missing from the bone stimulation literature. For other osseous indications, treatment of osteoporosis has been largely unsuccessful in preclinical studies with ES therapy likely for reasons previously stated (i.e., electromagnetic fields are not uniform through space and efficacy of treatment is heavily dependent on stimulator placement) (van der Jagt et al., 2012). Before attempting to address systemic bone diseases, delineation of a clear dose-response curve and optimal duration of therapy should be achieved for focal osseous injuries.

7 CONCLUSION

Electrical bone growth stimulators have shown promise in treating acute fractures in preclinical studies. To date, there is

no agreement as to their efficacy in humans. The next steps to studying ES for the purpose of healing acute fractures in humans are to select the appropriate study population, report replicable data for device specifications, and develop sound methodologies to minimize bias. In the same vein, development of a more practical and reliable modality of ES is needed to maximize outcomes.

AUTHOR CONTRIBUTIONS

PJN—manuscript drafting, editing, study design. DTD—manuscript drafting. NV—manuscript editing. AJSe—figure drafting. AJSh—manuscript editing. KAL—manuscript editing. AMD—manuscript editing. SOP—manuscript editing, study design.

REFERENCES

Adie, S., Harris, I. A., Naylor, J. M., Rae, H., Dao, A., Yong, S., et al. (2011). Pulsed Electromagnetic Field Stimulation for Acute Tibial Shaft Fractures. *JBJS* 93 (17), 1569–1576. doi:10.2106/jbjs.j.00869

Aleem, I. S., Aleem, I., Evaniew, N., Busse, J. W., Yaszemski, M., Agarwal, A., et al. (2016). Efficacy of Electrical Stimulators for Bone Healing: a Meta-Analysis of Randomized Sham-Controlled Trials. *Sci. Rep.* 6 (1), 31724–31810. doi:10.1038/srep31724

Atalay, Y., Güneş, N., Güner, M. D., Akpolat, V., Çelik, M. S., and Güner, R. (2015). Pentoxifylline and Electromagnetic Field Improved Bone Fracture Healing in Rats. *Dddt* 9, 5195. doi:10.2147/dddt.s89669

Beck, B. R., Matheson, G. O., Bergman, G., Norling, T., Fredericson, M., Hoffman, A. R., et al. (2008). Do Capacitively Coupled Electric Fields Accelerate Tibial Stress Fracture Healing? *Am. J. Sports Med.* 36 (3), 545–553. doi:10.1177/0363546507310076

Benazzo, F., Mosconi, M., Beccarisi, G., and Galli, U. (1995). Use of Capacitive Coupled Electric Fields in Stress Fractures in Athletes. *Clin. Orthop. Relat. Res.* 310 (310), 145–149. doi:10.1097/00003086-199501000-00023

Brighton, C. T., Friedenberg, Z. B., Black, J., Esterhai, J. L., Jr, Mitchell, J. E., and Montique, F., Jr (1981). Electrically Induced Osteogenesis: Relationship between Charge, Current Density, and the Amount of Bone Formed: Introduction of a New Cathode Concept. *Clin. Orthop. Relat. Res.* 161 (161), 122–132. doi:10.1097/00003086-198111000-00015

Brighton, C. T., and Friedenberg, Z. B. (1974). Electrical Stimulation and Oxygen Tension. *Ann. N. Y. Acad. Sci.* 238 (1), 314–320. doi:10.1111/j.1749-6632.1974.tb26800.x

Brighton, C. T., Tadduni, G. T., Goll, S. R., and Pollack, S. R. (1988). Treatment of Denervation/disuse Osteoporosis in the Rat with a Capacitively Coupled Electrical Signal: Effects on Bone Formation and Bone Resorption. *J. Orthop. Res.* 6 (5), 676–684. doi:10.1002/jor.1100060509

Brighton, C. T., Wang, W., Seldes, R., Zhang, G., and Pollack, S. R. (2001). Signal Transduction in Electrically Stimulated Bone Cells. *J. Bone Jt. Sur.-Am.* 83 (10), 1514–1523. doi:10.2106/00004623-200110000-00009

Bushinsky, D. A. (1996). Metabolic Alkalosis Decreases Bone Calcium Efflux by Suppressing Osteoclasts and Stimulating Osteoblasts. *Am. J. Physiology-Renal Physiology* 271 (1), F216–F222. doi:10.1152/ajprenal.1996.271.1.f216

Chakkalakal, D. A., Lippiello, L., Shindell, R. L., and Connolly, J. F. (1990). Electrophysiology of Direct Current Stimulation of Fracture Healing in Canine Radius. *IEEE Trans. Biomed. Eng.* 37 (11), 1048–1058. doi:10.1109/10.61030

Cook, J. J., Summers, N. J., and Cook, E. A. (2015). Healing in the New Millennium: Bone Stimulators. *Clin. podiatric Med. Surg.* 32 (1), 45–59. doi:10.1016/j.cpm.2014.09.003

Cook, S. D., Patron, L. P., Christakis, P. M., Bailey, K. J., Banta, C., and Glazer, P. A. (2004). Direct Current Stimulation of Titanium Interbody Fusion Devices in Primates. *Spine J.* 4 (3), 300–311. doi:10.1016/j.spinee.2003.11.005

Crocker, G., Dawson, R. A., Barton, C. H., and MacNeil, S. (1988). An Extracellular Role for Calmodulin-like Activity in Cell Proliferation. *Biochem. J.* 253 (3), 877–884. doi:10.1042/bj2530877

Escobar, J. F., Vaca-González, J. J., Guevara, J. M., Vega, J. F., Hata, Y. A., and Garzón-Alvarado, D. A. (2020). *In Vitro* evaluation of the Effect of Stimulation with Magnetic Fields on Chondrocytes. *Bioelectromagnetics* 41 (1), 41–51. doi:10.1002/bem.22231

Faldini, C., Cadossi, M., Luciani, D., Betti, E., Chiarello, E., and Giannini, S. (2010). Electromagnetic Bone Growth Stimulation in Patients with Femoral Neck Fractures Treated with Screws: Prospective Randomized Double-Blind Study. *Curr. Orthop. Pract.* 21 (3), 282–287. doi:10.1097/bco.0b013e3181d4880f

Fourie, J. A., and Bowerbank, P. (1997). Stimulation of Bone Healing in New Fractures of the Tibial Shaft Using Interferential Currents. *Physiother. Res. Int.* 2 (4), 255–268. doi:10.1002/pri.110

France, J. C., Norman, T. L., Santrock, R. D., McGrath, B., and Simon, B. J. (2001). The Efficacy of Direct Current Stimulation for Lumbar Intertransverse Process Fusions in an Animal Model. *Spine* 26 (9), 1002–1007. doi:10.1097/00007632-200105010-00003

Fukada, E., and Yasuda, I. (1957). On the Piezoelectric Effect of Bone. *J. Phys. Soc. Jpn.* 12 (10), 1158–1162. doi:10.1143/JPSJ.12.1158

Guizzardi, S., Di Silvestre, M., Govoni, P., and Scandroglio, R. (1994). Pulsed Electromagnetic Field Stimulation on Posterior Spinal Fusions. *J. spinal Disord.* 7 (1), 36–40. doi:10.1097/00002517-199407010-00005

Haddad, J. B., Obolensky, A. G., and Shinnick, P. (2007). The Biologic Effects and the Therapeutic Mechanism of Action of Electric and Electromagnetic Field Stimulation on Bone and Cartilage: New Findings and a Review of Earlier Work. *J. Altern. Complementary Med.* 13 (5), 485–490. doi:10.1089/acm.2007.5270

Hannemann, P. F. W., Göttgens, K. W. A., van Wely, B. J., Kolkman, K. A., Werre, A. J., Poeze, M., et al. (2012). The Clinical and Radiological Outcome of Pulsed Electromagnetic Field Treatment for Acute Scaphoid Fractures. *J. bone Jt. Surg. Br.* 94-B (10), 1403–1408. doi:10.1302/0301-620x.94b10.28844

Hannemann, P. F. W., Mommers, E. H. H., Schots, J. P. M., Brink, P. R. G., and Poeze, M. (2014a). The Effects of Low-Intensity Pulsed Ultrasound and Pulsed Electromagnetic Fields Bone Growth Stimulation in Acute Fractures: a Systematic Review and Meta-Analysis of Randomized Controlled Trials. *Arch. Orthop. Trauma Surg.* 134 (8), 1093–1106. doi:10.1007/s00402-014-2014-8

Hannemann, P. F. W., Van Wezenbeek, M. R., Kolkman, K. A., Twiss, E. L. L., Berghmans, C. H. J., Dirven, P. A. M. G. M., et al. (2014b). CT Scan-Evaluated Outcome of Pulsed Electromagnetic Fields in the Treatment of Acute Scaphoid Fractures. *bone & Jt. J.* 96-B (8), 1070–1076. doi:10.1302/0301-620x.96b8.33767

Inoue, N., Ohnishi, I., Chen, D., Deitz, L. W., Schwardt, J. D., and Chao, E. Y. S. (2002). Effect of Pulsed Electromagnetic Fields (PEMF) on Late-phase Osteotomy Gap Healing in a Canine Tibial Model. *J. Orthop. Res.* 20 (5), 1106–1114. doi:10.1016/s0736-0266(02)00031-1

Itoh, S., Ohta, T., Sekino, Y., Yukawa, Y., and Shinomiya, K. (2008). Treatment of Distal Radius Fractures with a Wrist-Bridging External Fixation: The Value of Alternating Electric Current Stimulation. *J. Hand Surg. Eur. Vol.* 33 (5), 605–608. doi:10.1177/1753193408092253

Jorgensen, T. E. (1977). Electrical Stimulation of Human Fracture Healing by Means of a Slow Pulsating, Asymmetrical Direct Current. *Clin. Orthop. Relat. Res.* 124 (124), 124–127. doi:10.1097/00003086-197705000-00016

Kaysinger, K. K., and Ramp, W. K. (1998). Extracellular pH Modulates the Activity of Cultured Human Osteoblasts. *J. Cell. Biochem.* 68 (1), 83–89. doi:10.1002/(sici)1097-4644(19980101)68:1<83::aid-jcb8>3.0.co;2-s

Khalifeh, J. M., Zohny, Z., MacEwan, M., Stephen, M., Johnston, W., Gamble, P., et al. (2018). Electrical Stimulation and Bone Healing: a Review of Current Technology and Clinical Applications. *IEEE Rev. Biomed. Eng.* 11, 217–232. doi:10.1109/rbme.2018.2799189

Law, H., Annan, I., McCarthy, I., Hughes, S., Stead, A., Camburn, M., et al. (1985). The Effect of Induced Electric Currents on Bone after Experimental Osteotomy in Sheep. *J. Bone Jt. Surg. Br.* 67-B (3), 463–469. doi:10.1302/0301-620x.67b3.3873459

Li, S., Lu, D., Tang, J., Min, J., Hu, M., Li, Y., et al. (2019). Electrical Stimulation Activates Fibroblasts through the Elevation of Intracellular Free Ca2+: Potential

Mechanism of Pelvic Electrical Stimulation Therapy. *BioMed Res. Int.* 2019, 7387803. doi:10.1155/2019/7387803

Liu, Y., Hao, L., Jiang, L., and Li, H. (2021). Therapeutic Effect of Pulsed Electromagnetic Field on Bone Wound Healing in Rats. *Electromagn. Biol. Med.* 40 (1), 26–32. doi:10.1080/15368378.2020.1851252

Lunt, M. J. (1985). Theoretical Model for Investigating the Magnetic and Electric Fields Produced during Pulsed Magnetic Field Therapy for Nonunion of the Tibia. *Med. Biol. Eng. Comput.* 23 (4), 293–300. doi:10.1007/bf02441581

Luo, R., Dai, J., Zhang, J., and Li, Z. (2021). Accelerated Skin Wound Healing by Electrical Stimulation. *Adv. Healthc. Mat.* 10 (16), 2100557. doi:10.1002/adhm.202100557

Martinez Rondanelli, A., Martinez, J. P., Moncada, M. E., Manzi, E., Pinedo, C. R., and Cadavid, H. (2014). Electromagnetic Stimulation as Coadjuvant in the Healing of Diaphyseal Femoral Fractures: a Randomized Controlled Trial. *Colomb. Médica* 45 (2), 67–71. doi:10.25100/cm.v45i2.1479

Miller, G. J., Burchardt, H., Enneking, W. F., and Tylkowski, C. M. (1984). Electromagnetic Stimulation of Canine Bone Grafts. *J. Bone & Jt. Surg.* 66 (5), 693–698. doi:10.2106/00004623-198466050-00007

Mills, L. A., Aitken, S. A., and Simpson, A. H. R. W. (2017). The Risk of Non-union Per Fracture: Current Myths and Revised Figures from a Population of over 4 Million Adults. *Acta Orthop.* 88 (4), 434–439. doi:10.1080/17453674.2017.1321351

Muttini, A., Abate, M., Bernabò, N., Cavani, F., Mingozzi, R., Tosi, U., et al. (2014). Effect of Electric Current Stimulation in Combination with External Fixator on Bone Healing in a Sheep Fracture Model. *Vet. Ital.* 50 (4), 249–257. doi:10.12834/VetIt.271.963.2

Nerubay, J., Marganit, B., Bubis, J. J., Tadmor, A., and Katznelson, A. (1986). Stimulation of Bone Formation by Electrical Current on Spinal Fusion. *Spine* 11 (2), 167–169. doi:10.1097/00007632-198603000-00014

Nicksic, P. J., Donnelly, D. A., Hesse, M., Bedi, S., Verma, N., Seitz, A., et al. (2022). Electronic Bone Growth Stimulators for Augmentation of Osteogenesis in *In Vitro* and *In Vivo* Models: A Narrative Review of Electrical Stimulation Mechanisms and Device Specifications. *Front. Bioeng. Biotechnol.* 91. doi:10.3389/fbioe.2022.793945

Paterson, D. C., Carter, R. F., Maxwell, G. M., Hillier, T. M., Ludbrook, J., and Savage, J. P. (1977a). Electrical Bone-Growth Stimulation in an Experimental Model of Delayed Union. *Lancet* 309 (8025), 1278–1281. doi:10.1016/s0140-6736(77)91318-6

Paterson, D. C., Hillier, T. M., Carter, R. F., Ludbrook, J., Maxwell, G. M., and Savage, J. P. (1977b). Experimental Delayed Union of the Dog Tibia and its Use in Assessing the Effect of an Electrical Bone Growth Stimulator. *Clin. Orthop. Relat. Res.* 128 (128), 340–350. doi:10.1097/00003086-197710000-00046

Pepper, J. R., Herbert, M. A., Anderson, J. R., and Bobechko, W. P. (1996). Effect of Capacitive Coupled Electrical Stimulation on Regenerate Bone. *J. Orthop. Res.* 14 (2), 296–302. doi:10.1002/jor.1100140219

Piazzolla, A., Solarino, G., Bizzoca, D., Garofalo, N., Dicuonzo, F., Setti, S., et al. (2015). CAPACITIVE COUPLING ELECTRIC FIELDS IN THE TREATMENT OF VERTEBRAL COMPRESSION FRACTURES. *J. Biol. Regul. Homeost. Agents* 29 (3), 637–646.

Plonsey, R., and Barr, R. C. (1995). Electric Field Stimulation of Excitable Tissue. *IEEE Trans. Biomed. Eng.* 42 (4), 329–336. doi:10.1109/10.376126

Portan, D. V., Deligianni, D. D., Papanicolaou, G. C., Kostopoulos, V., Psarras, G. C., and Tyllianakis, M. (2019). Combined Optimized Effect of a Highly Self-Organized Nanosubstrate and an Electric Field on Osteoblast Bone Cells Activity. *BioMed Res. Int* 2019. doi:10.1155/2019/7574635

Ring, D., Rhim, R., Carpenter, C., and Jupiter, J. B. (2005). Comminuted Diaphyseal Fractures of the Radius and Ulna: Does Bone Grafting Affect Nonunion Rate? *J. Trauma Inj. Infect. Crit. Care* 59 (2), 436–440. doi:10.1097/01.ta.0000174839.23348.43

Sousa, A. S. P., Moreira, J., Silva, C., Mesquita, I., Macedo, R., Silva, A., et al. (2022). Usability of Functional Electrical Stimulation in Upper Limb Rehabilitation in Post-Stroke Patients: A Narrative Review. *Sensors* 22 (4), 1409. doi:10.3390/s22041409

Spadaro, J. A., and Becker, R. O. (1979). Function of Implanted Cathodes in Electrode-Induced Bone Growth. *Med. Biol. Eng. Comput.* 17 (6), 769–775. doi:10.1007/bf02441560

Spadaro, J. A. (1982). Electrically Enhanced Osteogenesis at Various Metal Cathodes. *J. Biomed. Mat. Res.* 16 (6), 861–873. doi:10.1002/jbm.820160611

Stephan, M., Zimmermann, J., Klinder, A., Sahm, F., van Rienen, U., Kämmerer, P. W., et al. (2020). Establishment and Evaluation of an *In Vitro* System for Biophysical Stimulation of Human Osteoblasts. *Cells* 9 (9), 1995. doi:10.3390/cells9091995

Toth, J. M., Seim, H. B., III, Schwardt, J. D., Humphrey, W. B., Wallskog, J. A., and Turner, A. S. (2000). Direct Current Electrical Stimulation Increases the Fusion Rate of Spinal Fusion Cages. *Spine* 25 (20), 2580–2587. doi:10.1097/00007632-200010150-00007

van der Jagt, O. P., van der Linden, J. C., Waarsing, J. H., Verhaar, J. A. N., and Weinans, H. (2012). Systemic Treatment with Pulsed Electromagnetic Fields Do Not Affect Bone Microarchitecture in Osteoporotic Rats. *Int. Orthop. (SICOT)* 36 (7), 1501–1506. doi:10.1007/s00264-011-1471-8

Wahlström, O. (1984). Stimulation of Fracture Healing with Electromagnetic Fields of Extremely Low Frequency (EMF of ELF). *Clin. Orthop. Relat. Res.* 186 (186), 293–301.

Wang, Z., Clark, C. C., and Brighton, C. T. (2006). Up-regulation of Bone Morphogenetic Proteins in Cultured Murine Bone Cells with Use of Specific Electric Fields. *J. Bone & Jt. Surg.* 88 (5), 1053–1065. doi:10.2106/jbjs.e.00443

Yelin, E., Weinstein, S., and King, T. (2016). The Burden of Musculoskeletal Diseases in the United States. *Semin. Arthritis. Rheum.* 46 (3), 259–260. doi:10.1016/j.semarthrit.2016.07.013()

Zengo, A. N., Bassett, C. A. L., Prountzos, G., Pawluk, R. J., and Pilla, A. (1976). *In Vivo* effects of Direct Current in the Mandible. *J. Dent. Res.* 55 (3), 383–390. doi:10.1177/00220345760550031601

Zhuang, H., Wang, W., Seldes, R. M., Tahernia, A. D., Fan, H., and Brighton, C. T. (1997). Electrical Stimulation Induces the Level of TGF-β1 mRNA in Osteoblastic Cells by a Mechanism Involving Calcium/Calmodulin Pathway. *Biochem. biophysical Res. Commun.* 237 (2), 225–229. doi:10.1006/bbrc.1997.7118

Zuo, K. J., Gordon, T., Chan, K. M., and Borschel, G. H. (2020). Electrical Stimulation to Enhance Peripheral Nerve Regeneration: Update in Molecular Investigations and Clinical Translation. *Exp. Neurol.* 332, 113397. doi:10.1016/j.expneurol.2020.113397

Zura, R., Mehta, S., Della Rocca, G. J., and Steen, R. G. (2016a). Biological Risk Factors for Nonunion of Bone Fracture. *JBJS Rev.* 4 (1), e5. doi:10.2106/jbjs.Rvw.O.00008

Zura, R., Xiong, Z., Einhorn, T., Watson, J. T., Ostrum, R. F., Prayson, M. J., et al. (2016b). Epidemiology of Fracture Nonunion in 18 Human Bones. *JAMA Surg.* 151 (11), e162775. doi:10.1001/jamasurg.2016.2775

Conflict of Interest: The authors declare that the research was conducted in the absence of any commercial or financial relationships that could be construed as a potential conflict of interest.

Publisher's Note: All claims expressed in this article are solely those of the authors and do not necessarily represent those of their affiliated organizations, or those of the publisher, the editors and the reviewers. Any product that may be evaluated in this article, or claim that may be made by its manufacturer, is not guaranteed or endorsed by the publisher.

Copyright © 2022 Nicksic, Donnelly, Verma, Setiz, Shoffstall, Ludwig, Dingle and Poore. This is an open-access article distributed under the terms of the Creative Commons Attribution License (CC BY). The use, distribution or reproduction in other forums is permitted, provided the original author(s) and the copyright owner(s) are credited and that the original publication in this journal is cited, in accordance with accepted academic practice. No use, distribution or reproduction is permitted which does not comply with these terms.

frontiers | Frontiers in Bioengineering and Biotechnology

METHODS
published: 20 June 2022
doi: 10.3389/fbioe.2022.855777

Bone Marrow Microenvironment-On-Chip for Culture of Functional Hematopoietic Stem Cells

Azmeer Sharipol[1,2], *Maggie L. Lesch*[3], *Celia A. Soto*[2,4] *and Benjamin J. Frisch*[1,2,4,5]*

[1]Department of Biomedical Engineering, University of Rochester, Rochester, NY, United States, [2]Center for Musculoskeletal Research, University of Rochester Medical Center, Rochester, NY, United States, [3]Department of Microbiology and Immunology, University of Rochester Medical Center, Rochester, NY, United States, [4]Department of Pathology and Laboratory Medicine, University of Rochester Medical Center, Rochester, NY, United States, [5]Wilmot Cancer Institute, University of Rochester Medical Center, Rochester, NY, United States

Hematopoiesis takes place in the bone marrow and is supported by a complex cellular and molecular network in the bone marrow microenvironment. Commonly used models of the human bone marrow microenvironment include murine models and two-dimensional and three-dimensional tissue cultures. While these model systems have led to critical advances in the field, they fail to recapitulate many aspects of the human bone marrow. This has limited our understanding of human bone marrow pathophysiology and has led to deficiencies in therapy for many bone marrow pathologies such as bone marrow failure syndromes and leukemias. Therefore, we have developed a modular murine bone marrow microenvironment-on-chip using a commercially available microfluidic platform. This model includes a vascular channel separated from the bone marrow channel by a semi-porous membrane and incorporates critical components of the bone marrow microenvironment, including osteoblasts, endothelial cells, mesenchymal stem cells, and hematopoietic stem and progenitor cells. This system is capable of maintaining functional hematopoietic stem cells *in vitro* for at least 14 days at frequencies similar to what is found in the primary bone marrow. The modular nature of this system and its accessibility will allow for acceleration of our understanding of the bone marrow.

Keywords: bone marrow, hematopoietic stem cell, bone marrow microenvironment, bone marrow on a chip, tissue engineering, 3D chip, osteoblast, mesenchymal stem cell

OPEN ACCESS

Edited by:
Andrea Vernengo,
AO Research Institute, Switzerland

Reviewed by:
Borhane Guezguez,
German Cancer Research Center (DKFZ), Germany
Philippe Bourin,
Independent Researcher, Toulouse, France

***Correspondence:**
Benjamin J. Frisch
benjamin_frisch2@urmc.rochester.edu

Specialty section:
This article was submitted to Tissue Engineering and Regenerative Medicine, a section of the journal Frontiers in Bioengineering and Biotechnology

Received: *15 January 2022*
Accepted: *26 April 2022*
Published: *20 June 2022*

Citation:
Sharipol A, Lesch ML, Soto CA and Frisch BJ (2022) Bone Marrow Microenvironment-On-Chip for Culture of Functional Hematopoietic Stem Cells. Front. Bioeng. Biotechnol. 10:855777. doi: 10.3389/fbioe.2022.855777

INTRODUCTION

The adult hematopoietic system arises from the hematopoietic stem cell (HSC) that resides in and is supported by the HSC niche within the bone marrow. The HSC niche is a complex, interconnected network of cellular and molecular components within the bone marrow microenvironment (BMME) (Frisch, 2019). A major challenge that hampers progress in the field of the BMME is the lack of a reliable model system that can recapitulate the human bone marrow. Murine models have been used extensively because they allow for *in vivo* studies and powerful genetic tools. However, mouse models often fail to recapitulate the human environment. Conventional 2D cultures are another common approach used to investigate the human BMME for the study of normal hematopoiesis and

hematopoietic malignancies (Congrains et al., 2021). However, 2D cultures lack the ability to completely elucidate bone marrow pathophysiology and are typically limited to 2–3 different cell types. Overall, the inadequacies of conventional preclinical models contribute to a relatively poor understanding of the human BMME and the large attrition rates of Phase II and III of clinical trials (Arrowsmith and Miller, 2013).

In recent years, *in vitro* 3D models of various organ systems have been developed to facilitate basic biology research and drug development and screening. The development of these preclinical disease models is beneficial in understanding complex microenvironmental interactions with the potential implications of discovering novel treatment strategies (Duarte et al., 2018). The three-dimensional culture strategy is advantageous as it can provide an avenue to recapitulate the complex tissue microstructures while reducing the exhaustive requirements of animal models (Huh et al., 2011; Low and Tagle, 2017a; Low and Tagle, 2017b; Osaki et al., 2018; Kelm et al., 2019; Low et al., 2020). Therefore, a 3D microphysiological system will advance the field of BMME research by providing a viable platform for applications in mechanistic studies and drug discovery.

Several groups have shown the use of fibrin-based hydrogels in microfluidics platforms and the incorporation of a dynamic vasculature component were able to sustain HSCs *in vitro* (Chou et al., 2020; Nelson et al., 2021). Synthetically derived scaffolds such as PEG crosslinked with MMP-degradable peptide or tethered with adhesive ligands show promising evidence of HSC sensitivity towards culture dimension and flow conditions (Bray et al., 2017; Rödling et al., 2017). Although these developments provide valuable insights into establishing niche incorporated models, the outcomes of these models are limited to studying myelotoxicity towards drugs and radiation rather than insights into the mechanisms of HSC/niche interactions. Most of the current models lack major BMME components such as osteoblastic cells. Osteoblasts are important in establishing the endosteal HSC niche compartment, regulating bone remodeling and promoting the survival of lymphoid progenitors (Duarte et al., 2018). Our group and others have shown that leukemic cell interactions with the BMME, specifically through osteoblastic crosstalk, can drive leukemic progression and development (Frisch et al., 2012; Staversky et al., 2018; Ackun-Farmmer et al., 2021). Therefore, it is crucial to incorporate the osteoblastic components in addition to the vascular niche to generate a reliable 3D model of the BMME.

In this study, we generated a 3D model of the murine BMME with functional osteoblastic, endothelial, and stromal cell compartments to recapitulate the endosteal niche that is favorable for HSC survival. We used a commercially available microfluidics system, the Human Emulation System from Emulate Bio, and fibrin hydrogel scaffolding to culture HSC and performed competitive transplant assays to evaluate the self-renewal property of BMME-on-chip grown HSCs. The development of this preclinical model is valuable for the study of BMME pathologies, BMME-hematopoietic cells crosstalk, and identifying novel therapeutic targets.

MURINE BMME-ON-CHIP

Our goal was to generate a BMME-on-chip with niche components that are reliable, cost-effective, and easily adopted across research laboratories (**Figure 1**). The development of in-house microfluidics models is beneficial in generating complex architecture for *in vitro* systems; however, it can be time-consuming and limited to a specific laboratory. In this study, we utilized Emulate Chip S-1™ to provide the geometry and mechanical support to culture cells. The chip contains two channels separated by a semi-porous membrane which allows for the physical separation of cellular compartments. The chip is assembled with a housing system, Pod™, that contains input and output reservoirs for both channels and is connected to a module that automatically regulates fluid flow in each channel. The validated setup allows for efficient culturing of cells without the need for frequent media changes, troubleshooting flow modules, or optimizing microfluidics architecture.

We have cultured bone marrow stromal cells (BMSC) isolated from wild type C57BL/6 J mice into the apical channel of Chip S-1 to create a supportive osteoblastic layer (**Figure 2**)**.** Upon 14 days of culture under a continuous flow rate of 30 μL/h with osteoblast differentiation media, robust differentiation and mineralization were observed in chips, as shown by positive alkaline phosphatase and Von Kossa staining and quantification (**Figure 2B**). On D14, we introduced mouse endothelial C166 cells on the basal surface of the membrane to generate a supportive vascular endothelial monolayer (**Figure 1C**). C166 cells completely occupied the membrane of the channel at D2 and surrounded the walls of the channel by D7, as indicated by positive nuclei staining (DAPI, **Figure 2D**). On D7, we found robust endothelium formation as shown by cobblestone morphology and tight junction protein expression, zonula occludens-1 (ZO-1) (**Figure 2E**). On D14, a cell-laden fibrin hydrogel was introduced in the apical compartment containing BMSC and whole bone marrow cells. The chip was then subjected to a culture regime of supplemented endothelial media in the basal channel at 30 ul/hr. The chip was grown for 7 days before harvesting on D21 for analysis (**Figure 1B**).

We expect that the BMME-on-chip can provide a conducive environment for marrow cell culture due to the multifaceted culture system. In particular, we are interested in investigating the fate of hematopoietic stem cell and progenitor cells (HSPC) within the marrow compartment after 7 days of chip culture. Therefore, on D21, we harvested cells from BMME-on-chip and control mice BM and stained them for lineage (Gr1, CD3e, B220, and Ter119) and HSPC (Sca1 and cKit) markers[7] (**Figure 3A**). HSPC (LSK, Lin−Sca+cKit+) population was preserved in healthy BMME-on-chip after 7 days of culture at ~0.3% of total cells. This is two-fold greater than levels to *in vivo* of ~0.15% (**Figure 3B**). The data strongly suggest that BMME-on-chip is a reliable surrogate for HSPC maintenance *in vitro*.

HSPC are self-renewing and multipotent cells able to reconstitute the BM and differentiate into mature blood cells. Therefore, the standard functional analysis of HSPC is *via* a mouse BM transplantation model, whereby experimental HSPC are transplanted into myeloablated mice with the addition of

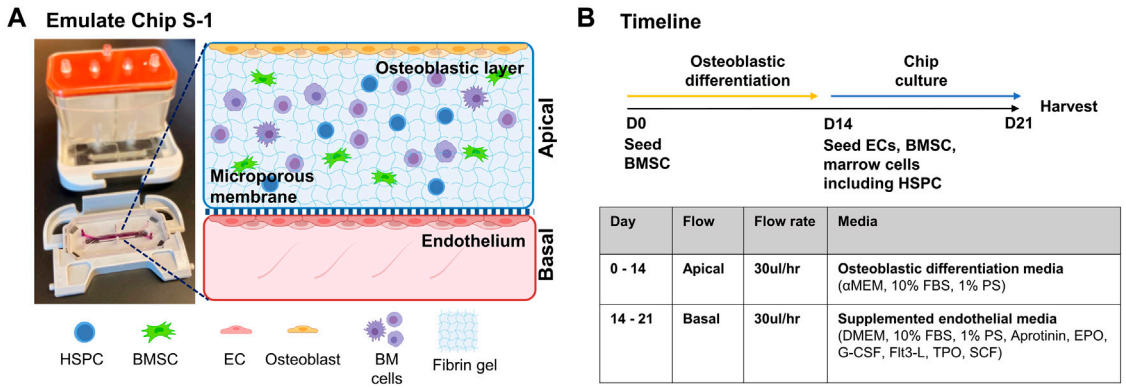

Day	Flow	Flow rate	Media
0 - 14	Apical	30ul/hr	**Osteoblastic differentiation media** (αMEM, 10% FBS, 1% PS)
14 - 21	Basal	30ul/hr	**Supplemented endothelial media** (DMEM, 10% FBS, 1% PS, Aprotinin, EPO, G-CSF, Flt3-L, TPO, SCF)

FIGURE 1 | BMME-on-chip with osteoblastic, endothelium layer and whole bone marrow cells. **(A)** Diagram of BMME-on-chip and **(B)** culture timeline. Illustrated using Biorender.com.

competitor cells as an internal control (**Figure 4**). Sorted LSK cells from C57BL/6 J mice (CD45.2+) were grown in chips with CD45.2+ BMSCs for 14 days (**Figure 4A**). The whole content of each chip was mixed with whole BM cells from CD45.1+ PepBoy B6 mouse as a competitor and transplanted into a lethally irradiated CD45.1+ PepBoy B6 mice (**Figures 4B–C**). Equal numbers of CD45.2+ freshly isolated bone marrow cells were also mixed with CD45.1+ BM cells and transplanted into lethally irradiated CD45.1+ recipients as controls. We analyzed peripheral blood (PB) cells *via* flow cytometry at multiple timepoints after the transplant. We found that CD45.2+ chip LSK were able to successfully engraft in recipient mice at similar levels compared to control HSPC from whole bone marrow (**Figure 5**). In particular, chip LSK gave rise to ~40–60% of total PB cells, which include myeloid populations, B lymphocytes, and T lymphocytes (**Figure 5B**). To confirm multilineage differentiation capacity, we compared the frequency of myeloid and lymphoid cells that were derived from CD45.2+ cells in primary recipients. CD45.2+ cells harvested from the BMME-on-chip generated myeloid cells at similar frequencies compared to cells harvested from freshly isolated bone marrow (C). At 28-weeks post-transplant, myeloid frequencies were at ~20% in peripheral blood of both chip and mouse recipients (D), while lymphoid populations were at ~80% (D-E). Thus, our findings suggest that chip-derived cells have the equivalent potential for generating myeloid and lymphoid cells to the mouse control group.

Bone marrow engraftment was analyzed by detecting chimerism of CD45+ HSPC populations at a very late timepoint, 28-weeks post-transplant. Flow cytometry was used to quantify chimerism in LSK population and lineage-committed myeloid progenitors (Lin−cKit+) and lymphoid precursors (Lin−Sca1+) (**Figures 6A–E**). Chimerism was observed in all three populations in the majority of the mice transplanted with HSPC from bone marrow and chip (**Figures 6H–J**). In particular, CD45.2+ donor cells were observed at a high percentage in LSK populations of control recipients M1, M4, and M5 and in chip recipients C1, C4, and C5 (**Figure 6H**). All of the five control recipients showed engraftment of CD45.2+ donor cells, with M2 and M3 having a majority of the repopulated LSK derived from donor cells. On the other hand, two out of the five chip recipients showed low to no repopulation of LSK by donor cells. Myeloid and lymphoid committed cells also showed chimerism as indicated by CD45.2+ cells in control and chip recipients (**Figures 6I and J**).

HSPC subpopulations were further analyzed within the LSK cells in recipient mice with high chimerism (M1, M4, M5, C1, C4, and C5) (**Figure 7**). Our findings showed CD45.2+ repopulation of myeloid-biased (MPP2 and MPP3) and lymphoid-biased (MPP4) multipotent progenitor populations in chip recipients at similar levels to control recipients (**Figures 7B–D and G–I**). In addition, CD45.2+ short-term and long-term repopulating HSC (ST-HSC) and (LT-HSC) were also observed at high levels, 40% for both groups, in chip recipients. Overall, the majority of mice transplanted with HSPCs obtained from BMME-on-chip cultures maintained similar distribution of HSPC subpopulations even through this very long-term engraftment.

To investigate long-term HSPC function, a secondary transplant assay was performed by injecting bone marrow cells isolated from primary recipient mice into myeloablated secondary recipients (**Figure 8A**). PB was analyzed at 4- and 8-weeks post-transplant. Consistent with engraftment data in the bone marrow, only C1, C4, and C5 samples from the chip group showed engraftment of CD45.2+ cells at 4- and 8-weeks (**Figures 8B and C**). Overall, CD45.2+ chip-derived cells comprised approximately 20% of total live cells at 4- and 8-weeks post-transplant (**Figure 8D**). Although the mouse group showed higher trends of engraftment, the comparison showed no statistical significance between the groups. Importantly, long-term differentiation of HSPC into mature blood populations was maintained as indicated by monocyte and lymphocyte populations that were CD45.2+ post-transplant (**Figures 8E and F**).

Our findings currently showed that chip grown HSPC are self-renewing and capable of regenerating the hematopoietic system,

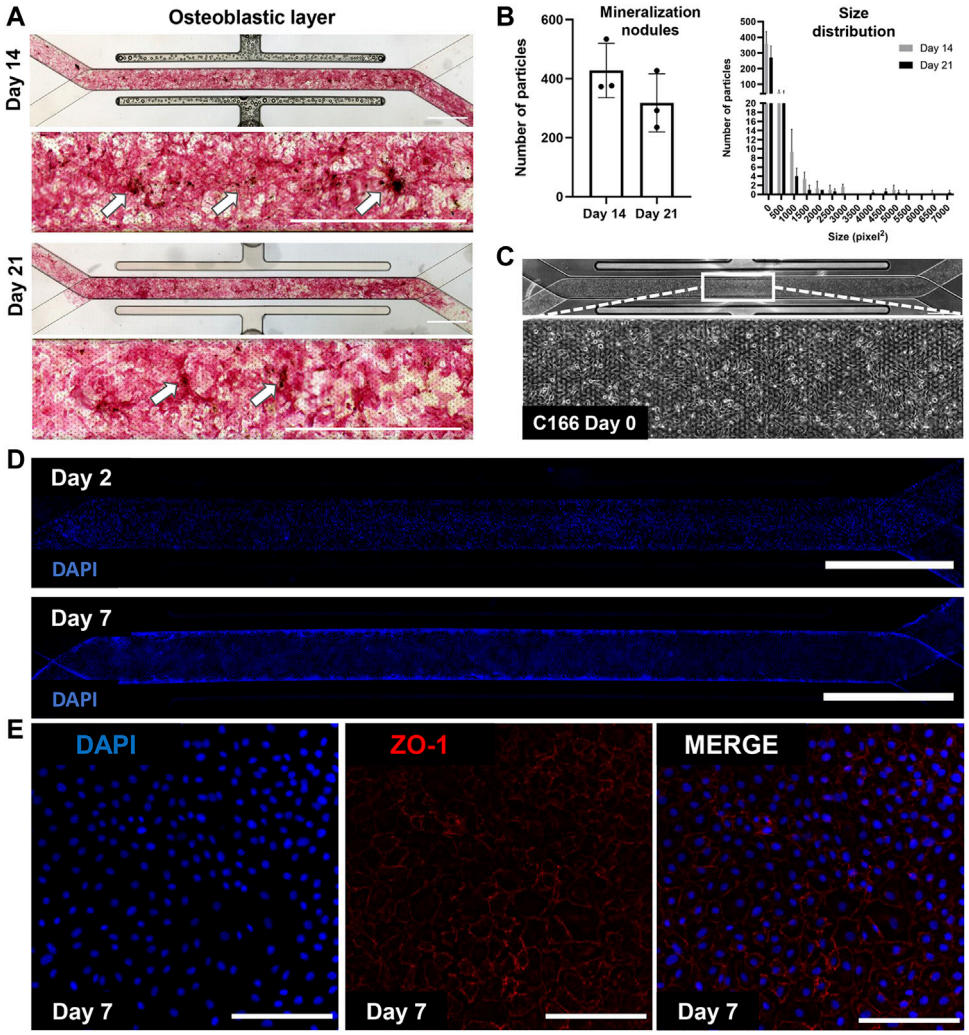

FIGURE 2 | Mineralized osteoblastic layer and C166 endothelium formation with tight junction expression. **(A)** Representative images of positive mineralization by alkaline phosphatase and Von Koss staining on D14 and D21. Arrows indicate calcium nodules and scale bar = 2 mm. **(B)** Quantification of mineralization using particle analysis *via* ImageJ of D14 and D21 mineralized chips. **(C)** Representative image of C166 monolayer on the chip on D0 post-seeding. **(D)** Representative fluorescent images of C166 cells (nuclei, DAPI) on Day 2 and Day 7. Scale bar = 2 mm. **(E)** C166 endothelium formed cobblestone morphology and expressed tight junction protein, ZO-1 (red). Scale bar = 100 μm).

which current 3D systems have not been able to demonstrate. This reliability of the chip to provide a permissive microenvironment for HSC maintenance makes it a valuable platform for future work in studying HSPC interactions with the BMME and BM pathologies. Here, we present step by step methodologies to generate BMME-on-chip, including protocols for Emulate Chip preparation, cell culture, MSC isolation, chip characterization, and competitive transplant assay.

MATERIALS

Reagents

αMEM (1x) (Gibco, Cat #A10490-01).
DMEM (1x) (Corning, Cat #10-013-CV).
FBS (Gibco, Cat #26140-079).
PBS 1X (Corning, Cat# 21-040-CV).
0.25% Trypsin-EDTA (1x) (Gibco, Cat #25200-056).
Pen–Strep (Penicillin–Streptomycin, Sigma-Aldrich, Cat #P4).
L-ascorbic acid (Krackeler, 45-A4544).
Glycerol 2-phosphate disodium salt hydrate (Krackeler, G9422).
Recombinant mouse EPO (Fisher, 587602).
Recombinant murine G-CSF, murine (PeproTech, Cat# 50-813-314.
Recombinant murine FLT3-ligand (PeproTech, Cat# 250-31L).
Recombinant murine TPO (PeproTech, Cat# 50-813-680).
Recombinant murine SCF (PeproTech, Cat#250-03).

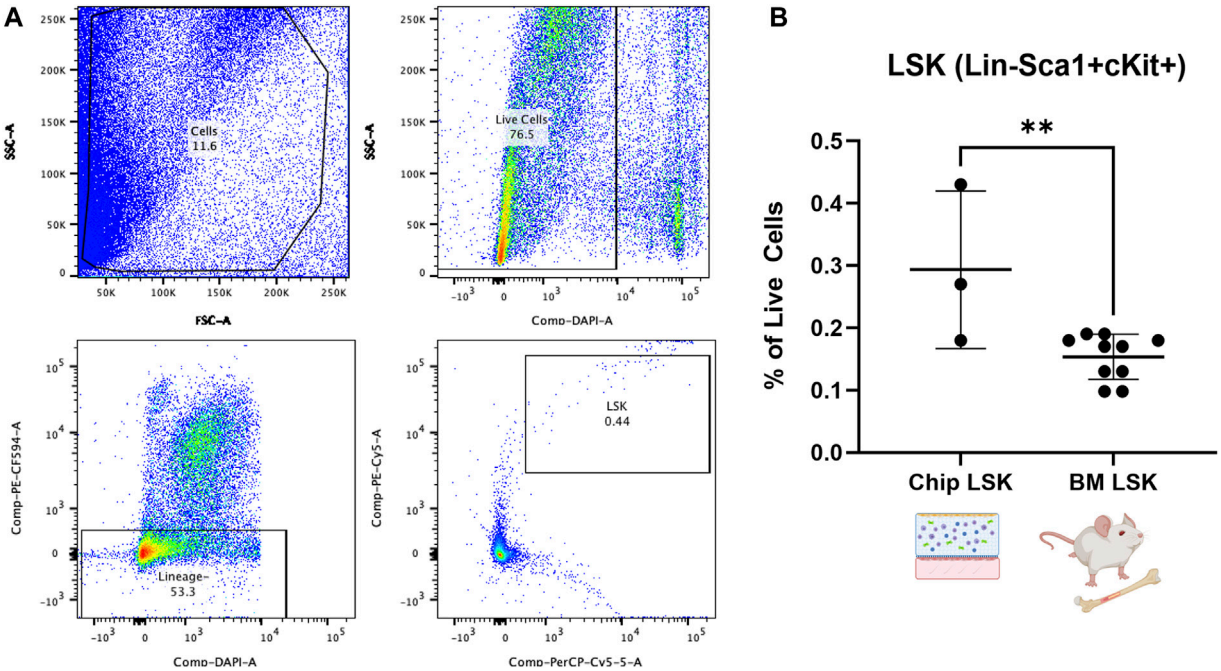

FIGURE 3 | Flow cytometric analysis of HSPC cells (LSK: Lineage-, Sca1+, cKit+) from whole bone marrow cells in BMME-on-Chip. **(A)** Gating strategy for analysis of LSK cells using FlowJo v10. **(B)** Percent of LSK in live cells population in the chip on D21 and control C57Bl/6J BM at 6–8 weeks of age (Mean, SD). Statistical analysis was performed using an unpaired *t*-test. **: $p \leq 0.01$. BM: Bone marrow.

Recombinant murine IL3 (PeproTech, Cat# 213-13).
Recombinant murine IL6 (PeproTech, Cat# 216-16).
Fibrinogen, lyophilized (Sigma, Cat# 341578).
Thrombin, lyophilized (Sigma, Cat# 605195).
Aprotinin, lyophilized (Sigma, Cat# A3426).
Matrigel® (Corning, Cat# 354234) - for Chip S-1 activation.
Collagen type I solution, 8–11 mg/mL (Corning, Cat# 354249) - for Chip S-1 activation.
Nattokinase (Pure Formulas, Cat# PE 1801).
Collagenase type 1 (Gibco, Cat#17-018–029).
HEPES (Fisher BioReagents, BP299100).
10% Neutral buffered formalin (VWR, Cat# 89370-094).
Silver nitrate solution, $AgNO_3$, 99.9+% (AlfaAesar, Cat#11414).
Fast Red Violet LB salt (Sigma, Cat# F3381).
Tris-HCl at 0.2M, pH 8.3 (Roche, Cat# 10812846001).
N,N-Dimethylformamide (DMF) (AlfaAesar, Cat#A13547).
Naphthol AS-MX phosphate, (Sigma, Cat# N4875).
UltraComp Beads (Invitrogen, Cat# 501129040).
Distilled water.
Ammonium chloride (NH4Cl) (Krackeler, Cat# 45-213330).
Ethylenediaminetetraacetic acid (EDTA) (Sigma, Cat# E4884).
Sodium bicarbonate (NaHCO3) (Sigma, Cat#S6014).

Plastics

500 mL Vacuum filtration flask 0.22 µm (LPS CellPro, Cat# V50022).
250 mL Vacuum filtration flask 0.22 µm (LPS CellPro, Cat# V25022).
50 mL Sterile-HV sterile centrifuge tube PVDF membrane, 0.45 µm, top filter unit (Milipore, Cat# SE1M003M00).
Eppendorf tubes 1.5 mL (FisherSci, 02-682-002).
40 µm cell strainer (Fisher, 08-771-1).
6-well cell culture plate (Nest, Cat# 703001).
Cell culture dish, 150 mm × 25 mm (Nest, Cat# 715001).
17 × 75 mm culture tubes with closures (VWR, 60818-496).

Mice

All mice and protocols used in the experiments were approved by the Institutional Animal Care and Use Committee, the University Committee on Animal Resources at the University of Rochester School of Medicine Dentistry (URMC). Animals were housed in the Vivarium facility at URMC.

C57BL/6 J mice, males, 8–12 weeks of age (Jackson Laboratories, Strain# 000664).

B6 CD45.1+ mice, males, 8–12 weeks of age (B6.SJL-*Ptprc*^{a} *Pepc*^{c}/BoyJ) (Jackson Laboratories, Strain# 002014).

Cells

C166 cell line (ATCC Cat# CRL-2581).

Emulate Human Emulation System

Chip S-1™
Pod™ Portable Module.
Zoë™ Culture Module.
Orb™ Hub Module.

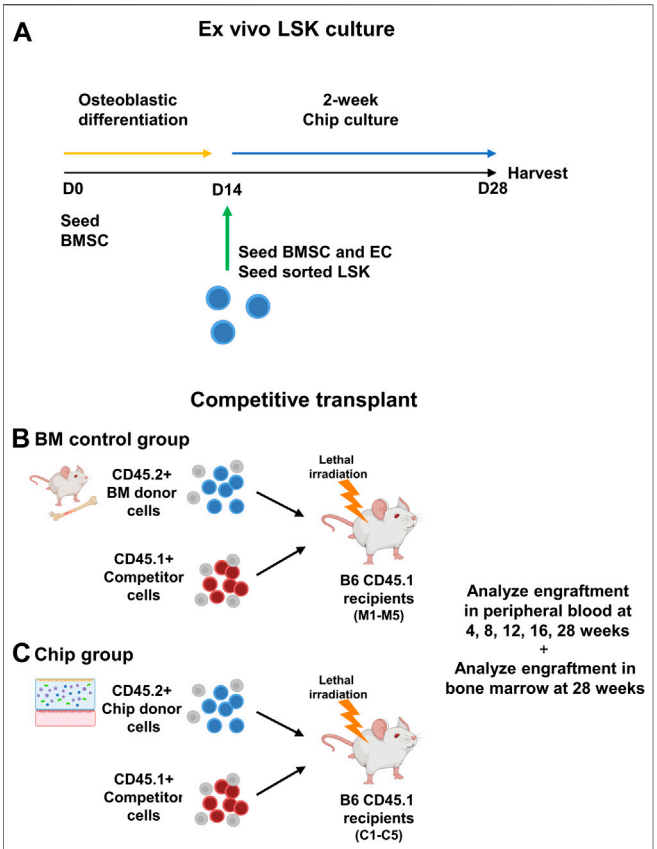

FIGURE 4 | Diagram of *ex vivo* culture of sorted LSK cells in BMME-on-chip and competitive transplant. **(A)** CD45.2+ LSK cells were sorted using flow cytometry and cultured with BMSC in hydrogel for 14 days in BMME-on-chip. **(B)** Functional analysis using competitive transplant assay of bone marrow and chip grown LSK CD45.2+ donor into recipient B6 CD45.1 **(C)** with CD45.1+ competitor cells. Illustrated using Biorender.com.

Equipment

Cell culture incubator set to 37°C. 5% CO_2, 95% humidity.
Water bath set to 37°C.
Cytation 5 Imaging System.
^{137}Cs radiation source (GAMMACELL- 40).

Reagent Setup

FBS Heat Inactivation

1) Thaw frozen FBS overnight at 4°C.
2) Once thawed, bring serum to room temperature.
3) Place serum in a 56°C water bath for 30 min and swirl the bottle every 5 min.
4) Make aliquots of heat-inactivated serum and store at −20°C until use.

Complete media (10% FBS + 1% PS)

1) Thaw 5 mL Pen–Strep in a 37°C water bath.
2) For 500 mL of complete media, combine 5 mL Pen–Strep, 50 mL of heat-inactivated FBS, and 445 mL of αMEM.
3) Vacuum filter complete media using a 500 mL vacuum filtration flask.
4) Make 50 mL aliquots of media in conical tubes.
5) Warm up to 37°C prior to use or store in a fridge for short term use or in a freezer for long term use.

Osteoblast Differentiation Media

1) Make 1M stock solution of glycerol 2-phosphate disodium salt hydrate in sterile water. Store stock in smaller aliquots in a −20°C freezer.
2) For 200 mL of differentiation media, combine 10 mg of L-ascorbic acid, 2 mL of 1M thawed glycerol solution, and 200 mL of complete media.
3) Filter media using a 250 mL vacuum filtration system. Warm media to 37°C before use or store in a freezer or fridge. The media will have a final concentration of 50 µg/mL of L-ascorbic acid and 10 mM of glycerol 2-phosphate disodium salt hydrate.
3) Gas equilibrate with 0.45 µm Steriflip-HV and warm up media for at least 1 h at 37°C prior to use with chips.

Endothelial Media (10% FBS + 1% PS) for C166 Culture

1) For 500 mL of complete endothelial media, combine thawed 5 mL Pen–Strep, 50 mL of heat-inactivated FBS, and 445 mL of DMEM.
2) Warm up to 37°C prior to use or store at 4°C for short term use.

Supplemented DMEM Media

1) For 50 mL of media combine complete endothelial media (10% FBS +1% PS) with the following concentration of cytokines: EPO 20 ng/mL, G-CSF 1 ng/mL, FLT3L 100 ng/mL, TPO 100 ng/mL, SCF 50 ng/mL, IL-3 10 ng/mL, and IL-6 10 ng/mL.
2) Warm up to 37°C prior to use or store in a fridge for short term use or in a freezer for long term use.
3) Gas equilibrate with 0.45 µm Steriflip-HV and warm up media for at least 1 h at 37°C prior to use with chips.

Fibrin Gel Components

1) Fibrinogen: resuspend at 25 mg/mL in sterile water and make aliquots of 100 µL or 200 µL. Store in a −20°C freezer.
2) Aprotinin: resuspend at 1 mg/mL in sterile water and make aliquots of 12.5 µL or 25 µL. Store in a −20°C freezer.
3) Thrombin: resuspend at 1 U/µL in sterile water and make aliquots of 1 µL. Store in a −20°C freezer.
4) Collagen Type I solution: make aliquots of 10–25 µL. Store in a fridge at 4°C.

Chip Digestion Solution

1) Warm up complete DMEM in a 37°C water bath for at least an hour.
2) Prepare 5 mL of digestion solution with final concentrations of 1 mg/mL nattokinase, 25 mM HEPES, and 1 mg/mL collagenase type 1.

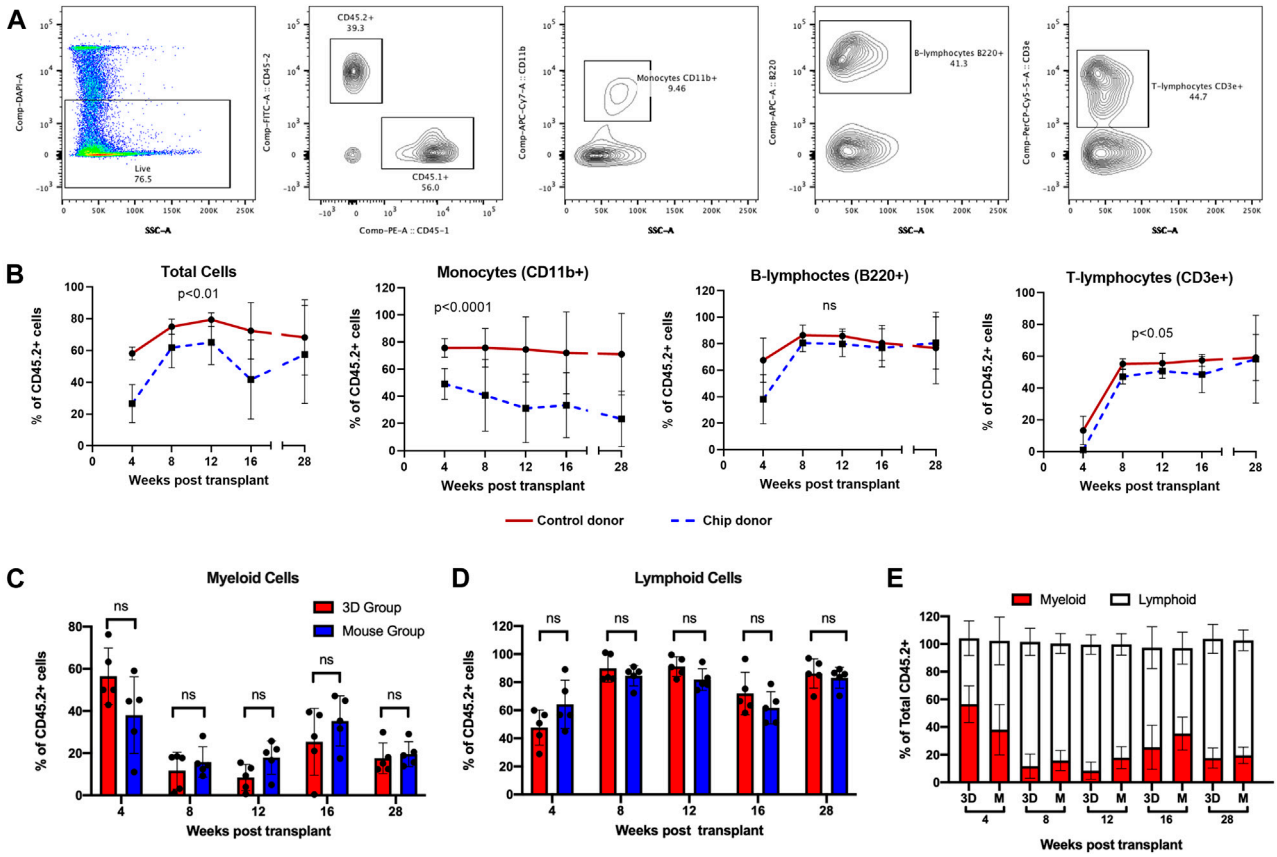

FIGURE 5 | Differentiation of LSK transplanted into mature peripheral blood phenotypes over time. **(A)** Gating strategy for flow cytometry analysis at 4, 8, 12, 16, and 27-weeks post-transplantation. CD11b+, B220+, and CD3e+ were gated from CD45.2+ live cells. **(B)** Quantification of CD45.2+ donor cells in total cell, CD11b+ monocyte, B220+ B-lymphocyte, and CD3e+ T-lymphocyte populations. **(C)** Chip grown CD45.2+ cells gave rise to myeloid cells at a similar frequency to mouse control. Quantification was performed by gating CD11b+ cells within CD45.2+ populations. **(D)** Chip CD45.2+ cells engrafted into mature lymphoid populations similar to the mouse control group. Data are shown as combined percentage of B220+ and CD3e+ cells in CD45.2+ cells. The gating strategy for **(C** and **D)** is provided in **Supplementary Figure S4**. **(E)** Graph showing the percentage of myeloid and lymphoid cells in total CD45.2+ peripheral blood cells. All flow analysis was performed using FlowJo v10. Statistical analysis for **(B)** was performed using restricted maximum likelihood (REML). N = 5 per group. Statistical analysis for **(C,D)** was performed using multiple Mann–Whitney tests.

Flow Cytometry Staining Buffer (2% FACS Buffer)

1) Prepare 2% FACS buffer by combining thawed 10 mL of heat-inactivated FBS with 500 µL of 1X PBS.
2) Store in a fridge at 4°C. Use cold buffer for staining and bone marrow dissociation.

Alkaline Phosphatase and VonKossa Staining

1) Prepare fresh alkaline phosphatase staining substrate by dissolving 0.005 g of Napthol AS MX with 200 µL of DMF in an Eppendorf tube. Combine 25 mL of Tris HCL pH 8.3, 0.2 M with 25 mL of distilled water. Combine all reagents together with 0.03 g of red violet LB salt.
2) Prepare 2.5% silver nitrate Von Kossa staining solution by dissolving 2.5 g of silver nitrate with 100 mL of distilled water.

Red Blood Cell Lysis Buffer

1) Prepare a solution of 156 mmol/L NH4Cl, 127 µmol/L EDTA, and 12 mmol/L NaHCO3.

METHODS AND PROTOCOLS

BMME-On-Chip Preparation

Day-14: (I) Primary Bone Marrow Cell Isolation

1) Obtain marrow cells from long bones of the hind limbs of mice and flush out marrow using a 25-gauge needle and FACS buffer.
2) Dissociate marrow with a 16-gauge needle and filter with a 40 µm cell strainer. Collect in a 50 mL conical tube.
3) Fill the conical tube to 25 mL with FACS buffer and centrifuge the cell solution at 1000rpm for 5 min. Remove the supernatant and resuspend the cells in 10 mL of FACS buffer.
4) Count the cells using trypan blue and hemacytometer.

Day-14: (II) Primary BMSC Cell Culture

1) Warm up complete media to 37°C in a water bath.
2) Isolate primary bone marrow cells and count the cells.

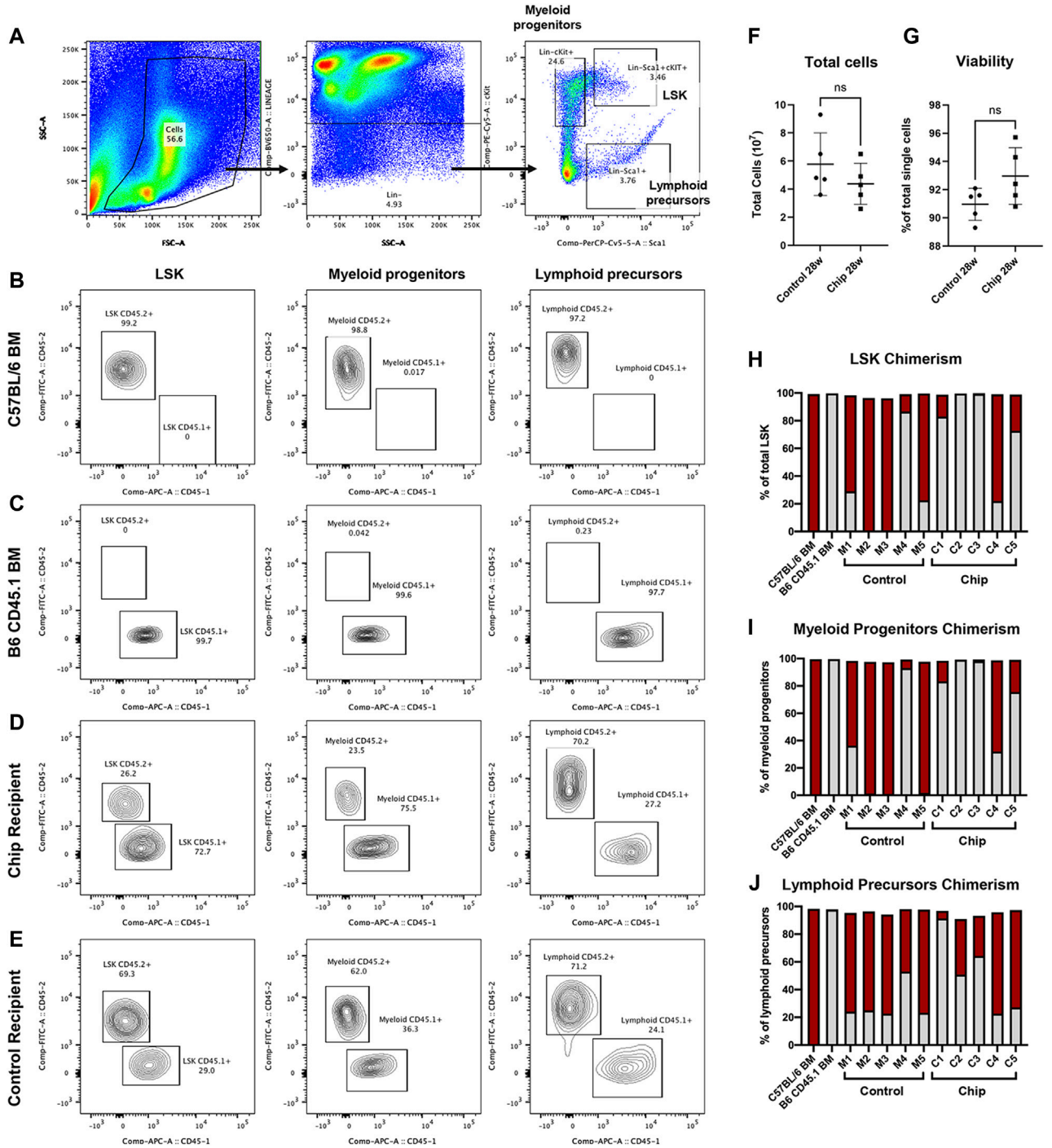

FIGURE 6 | Engraftment and repopulation of HSPC, myeloid progenitor, and lymphoid precursor populations in bone marrow by BMME-on-chip grown LSK cells. **(A)** Bone marrow of recipient mice was isolated and analyzed using flow cytometry for lineage markers, stem cell markers Sca1+ and cKit+. **(B–E)** Representative contour plots of CD45.1+ and CD45.2+ in LSK (Lin-cKit + Sca1+), myeloid (lin-cKit+), and lymphoid (lin-Sca1+) cells in bone marrow of **(B)** CD45.2+ C5BL/6J, **(C)** B6 CD45.1+, **(D)** chip transplant recipient, and **(E)** mouse marrow control recipient. **(F)** Quantification of total bone marrow cells after isolation. **(G)** Viability isolated bone marrow cells using flow cytometry (negative DAPI staining). Statistical analysis for F and G was performed using an unpaired *t*-test. ns = no significance, error bar = SD. **(H–J)** Chimerism of LSK **(H)**, myeloid **(I)**, and lymphoid **(J)** cells indicating repopulation of CD45.2+ donor cells and competitor CD45.1+ cells in recipient mice. Data show the percent of total cells analyzed using flow cytometry of bone marrow from each recipient mouse. In particular, control recipients M1, M4, and M5, and chip recipients C1, C4, and C5 show chimerism in LSK populations.

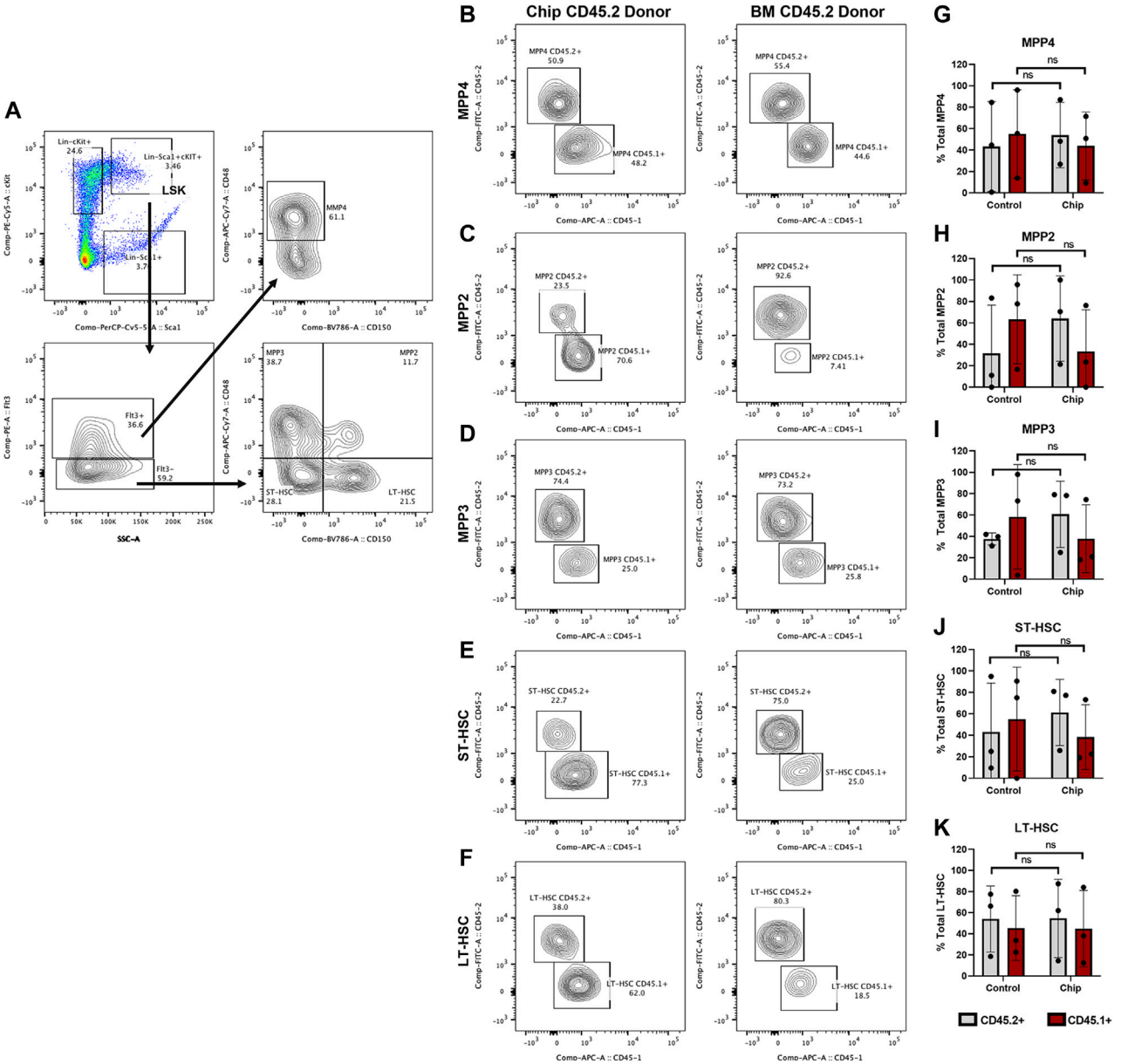

FIGURE 7 | Repopulation of myeloid-biased MPP2+ and MPP3+, lymphoid-biased MPP4+ multipotent progenitor and HSC populations by BMME-on-chip donor cells. Subpopulations of specific progenitor cells and short-term and long-term repopulating HSC (ST-HSC and LT-HSC) within the LSK populations were analyzed for mice recipients with CD45.2+ and CD45.1+ chimerism (M1, M4, M5, C1, C4, and C5). **(A)** Flow cytometry gating of LSK subpopulations. **(B–K)** Representative contour plots and quantification of donor and competitor cells in LSK subpopulations. Statistical analysis was performed using multiple Whitney–Mann tests. *N* = 3 per group. Error bars = standard deviation, ns = non-significant.

3) Centrifuge and resuspend the cells in complete media to obtain a cell concentration of 2×10^6 cells/ml.
4) Seed 3 ml of cell solution in each well of a tissue culture treated 6-well plates to obtain a seeding concentration of 6×10^6cells/well or 6.25×10^5cells/cm^2.
5) Grow cells for four days untouched in a cell incubator at 37°C, 5% CO_2, and 95% humidity to let the BMSCs adhere.
6) On day 4, replace media with warm complete media to remove non-adhered cells, dead cells, and debris.
7) Expand BMSCs for another 7–10 days before using use. Replace media every 2–3 days.

Day-1: Reagent Preparation and Emulate Chip S-1 Chip Activation

1) Prepare chip activation and extracellular matrix solution according to the manufacturer's instruction (Basic Organ-Chip Culture Protocol, Emulate EP177 v1.0, April 30, 2019, https://emulatebio.com/wp-content/uploads/2021/06/EP177_v1.0_Basic_Organ-Chip_Culture_Protocol.pdf).

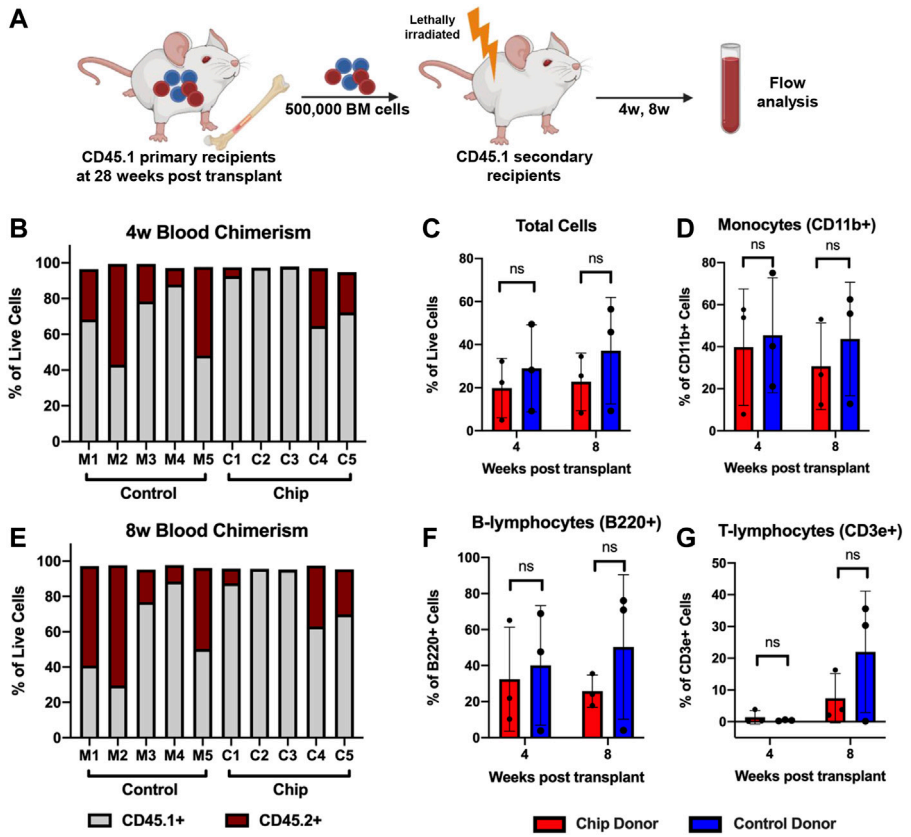

FIGURE 8 | Repopulation of peripheral blood population in secondary transplant recipients shows maintenance of long-term HSPC function after BMME-on-chip culture. **(A)** Diagram of secondary transplant of lethally irradiated mice with bone marrow cells from primary recipients at 28 weeks post-transplant. Peripheral blood was analyzed using flow cytometry at 4w and 8w post-secondary transplant. **(B,C)** Flow cytometry data showing chimerism of CD45.2+ donor cells in total live cells in peripheral blood at 4w and 8w. Consistent with bone marrow engraftment data, C2 and C3 do not have CD45.2+ engraftment. **(D–F)** Flow analysis of total cells, monocytes, and lymphocytes from chip recipients with CD45.2+ engraftment (C1, C4, and C5) compared to mouse recipients (C1, C4, and C5). Flow analyses were performed using FlowJo V10. Statistical analysis for **(D–F)** was performed using an unpaired *t*-test. *N* = 3. ns = non-significant.

2) Once activated, each cell compartment is added in a sequential manner according to the workflow timeline in **Figure 1B**.

Day 0: (I) BMSC Cell Seeding and Osteoblastic Cell Differentiation

1) Trypsinize BMSC cells in T-75 flasks using 5 mL of 0.25% Trypsin-EDTA for 3 min in a cell culture incubator.
2) Neutralize the trypsin by adding 20 mL of gas equilibrated osteoblastic differentiation media. Gently pipette the solution to release the cells and centrifuge the cells at 500 g.
3) Repeat trypsinization if there are still adhered BMSC on the culture flask.
4) Resuspend the cells in 10 mL of the same media for cell counting. Centrifuge the cells and remove the supernatant.
5) Resuspend the BMSCs in an appropriate volume of media to obtain a density of 2×10^6 cells/mL.
6) Prepare Chip S-1 by flushing both the apical and basal channels with 100 µL of gas equilibrated media.
7) Remove the content of the apical channel using an aspirator and immediately pipette 45 µL of the cell solution to obtain a seeding density of 6×10^4 cells/chip.
8) Invert the chips and place them in a sterile cell culture dish (150 mm × 25 mm) to allow BMSC to adhere on the top surface of the apical channel. Add 1 mL of sterile water in a 15 mL conical tube cap in the culture dish to maintain humidity.
9) Leave the chips in the cell culture incubator for 2 h.
10) After 2 h, check on BMSC adherence on the top surface of the apical channel under a light microscope to ensure 70–90% confluent seeding. Reseed the chips with BMSC if the seeding density is low.
11) Remove unadhered cells by pipetting about 200 ul of media at the inlet of the apical channel while simultaneously aspirating the outflow at the outlet channel. Do not fully aspirate the content of the channels. Repeat washing with the basal channel.
12) Prepare Emulate Pod™ by placing 3 ml of gas equilibrated osteoblastic differentiation media into the inlet reservoir of

the apical channel. Fill the apical outlet, basal inlet, and outlet reservoirs with 300 µL of media.
13) Assemble the chip with the Pod™ and connect the system to the Zoe™ Culture Module according to the manufacturer's instructions (Basic Organ-Chip Culture Protocol, Emulate EP177 v1.0, April 30, 2019—refer to Day 2: Chips to Pods and Pods to Zoe section).
14) Set the flow settings to 30 µL/h in the apical channel and no flow in the basal channel.
15) Differentiate cells for 14 days while checking for air bubbles in the channels every 2–3 days. Clear any air bubbles with gas equilibrated media.
16) Add gas equilibrated media into the apical channel inlet reservoirs every 2–3 days and remove the content of the outlet reservoir. Replace 300 µL of media into the reservoir to avoid drying out.

Day 0: (II) BMSC Culture Preparation

Isolate and culture bone marrow cells from C57BL/6 J to obtain BMSC on Day 14 for cell encapsulation. Follow protocols for primary bone marrow cell isolation and BMSC culture.

Day 10: C166 Cell Line Culture

1) Warm up complete endothelial media to 37°C in a water bath.
2) Thaw a vial of frozen C166 appropriately according to the manufacturer's protocol. (https://www.atcc.org/products/crl-2581).
3) Resuspend cells in 10 mL of complete endothelial media and seed the cells in a T-75 culture flask.
4) Incubate cells for 2–3 days until reaching 70–80% confluency before use.
5) Cells can be passaged at a 1:5 or 1:10 ratio and stored appropriately in liquid nitrogen before use. Use C166 at passage 1-5.

Day 14: (I) Endothelial Cell Seeding

1) Trypsinize C166 endothelial cells in T-75 flasks using 5 mL of 0.25% Trypsin-EDTA for 3 min in a cell culture incubator.
2) Neutralize the trypsin by adding 20 mL of gas equilibrated complete endothelial media. Gently pipette the solution to release the cells and centrifuge the cells at 1000 rpm or 500 g. Resuspend the cells in 10 mL of media and count the cells.
3) Seed 25 µL of 2×10^6cells/mL C166 cell solution into the basal channel of the chips similarly according to the BMSC seeding protocol.
4) Invert the chips to allow cells to adhere onto the membrane surface of the basal channel (**Figure 1A**). Leave the cells to adhere in the incubator for two hours.

Day 14: (II) Hydrogel Seeding and Coculture

1) Isolate bone marrow cells from 1 C57BL/6 J mouse according to the primary bone marrow cell isolation protocol. Count the cells and resuspend them in gas equilibrated supplemented DMEM media.
2) Trypsinize and collect the BMSC grown for 14 days. Count the cells and resuspend them in gas equilibrated supplemented DMEM media.
3) Thaw fibrin hydrogel components. Calculate the volume of each component needed for the number of chips to be seeded. Each chip will obtain 45 µL of fibrin gel solution containing whole bone marrow cells and BMSC in the apical channel. The final gel solution will have 5 mg/mL of fibrinogen, 25 µg/mL aprotinin, 0.2 mg/mL collagen type 1, and 0.5 U/mL thrombin.
4) To prevent premature crosslinking, prepare the gel solution in two separate mixes. Combine fibrinogen and aprotinin in tube A and collagen type 1 and thrombin in tube B.
5) Combine 6×10^4 BMSC and 6×10^4 bone marrow cells per chip and resuspend in the amount of media required to bring up the total volume to the desired final volume. Mix the cell solution with tube B.
6) For each chip, separately aliquot the desired volume tube A and tube B containing media with cells and immediately seed into the apical channel of Chip S-1. Check for bubbles. Reseed the apical channel in the presence of air bubbles.
7) Leave the chips in the cell incubator for 30 min to 1 h in a humidified cell culture dish for the gel to fully polymerize.
8) Remove the contents of the inlet and outlet reservoirs of the Pod™ and fill up 3 mL of gas equilibrated supplemented endothelial media in the basal channel inlet reservoirs. Add about 300 µL of media to the remaining reservoirs.
9) After the gel is polymerized, connect Chip S-1 to Pod™ and Zoë™. Setup flow at 30 µL/h in the basal channel where the endothelial cell monolayer is present.
10) Culture chip for another 7 days. Check for bubbles and replace the media every 2–3 days.

Day 21: Harvesting Cells

1) Prepare chip digestion solution.
2) Disconnect Chip S-1 from the Zoë™ and plug the outlet ports of the apical and basal channels with a 200 µL pipette tip.
3) Add 100 µL digestion solution to the apical channel and 50 µL digestion solution to the basal channel. Leave pipette tips in the inlet port.
4) Incubate the chips for 1 h in the incubator.
5) After 1 h, collect the contents of the apical and basal channel into a microcentrifuge tube.
6) Trypsinize the channels with 0.25% Trypsin-EDTA for 5 min at 37°C to collect the remaining cells on the membrane surfaces. Check for detachment under a light microscope.
7) Collect trypsin digest into the same collection tubes and add 1 mL of media to neutralize the trypsin.
8) Centrifuge the cell suspension to remove the digest media.
9) Resuspend cells in 1 mL of media and count the cells.
10) The cells are now ready for appropriate analysis steps.

Flow Cytometry

1) C57BL/6 J marrow cell control. Isolate cells from each mouse using the previous cell isolation protocol. Cells can be stored in liquid nitrogen.
2) Resuspend the cells in a 5 mL 1 × RBC lysis buffer for 5 min at room temperature.
3) Wash with 5 mL FACS buffer. Centrifuge the cells and decant the supernatant.
4) Resuspend the cells in FACS buffer and set aside 1×10^6 of isolated C57BL/6 J cells for DAPI and unstained compensation controls.
5) Prepare the primary lineage staining solution with the appropriate antibodies (**Supplementary Table S1**). Prepare the desired volume of master mix for 1 µL of each antibody solution per sample.
6) Centrifuge the harvested cells and controls in FACS tubes. Remove the supernatant.
7) Add 100 µL of lineage-biotin staining solution to each sample and leave the cells at 4°C for 25 min. In the meantime, prepare fluorophore-conjugated antibodies staining solution **Supplementary Table S1**.
8) Wash with staining solution by topping off the FACS tube with FACS buffer. Centrifuge the cells and decant the supernatant.
9) Repeat the staining process with fluorophore-conjugate antibodies solution. Leave the cells at 4°C for 25 min.
10) In the meantime, prepare flow cytometry compensation control for each fluorophore by combining 1 µL of conjugated antibody, 2 drops of UltraComp beads, and 200 µL of FACS buffer in a FACS tube. For lineage compensation, combine all four biotin-labelled lineage antibodies with fluorescently labelled streptavidin antibodies. For DAPI staining control, resuspend prepared C57BL6J cells with 200 µL of DAPI solution. Prepare unstained cells in 200 µL FACS buffer.
11) After staining is completed, wash the staining solution appropriately. Resuspend the cells in 200 µL of DAPI solution.
12) The cells are ready for flow cytometry analysis using the appropriate cell analyzer system. For the abovementioned experiments, cells were analyzed using BD LSRFortessa™ and BD FACS diva software. Gating analysis was performed using FlowJo v10.7. LSK sorting and *Ex-vivo* culture in BMME-on-chip

Ex Vivo LSK Culture and Competitive Transplant

Day 0—Day 14(I): BMME-On-Chip Preparation

Generate chips with osteoblastic layer and endothelium layer according to BMME-on-chip preparation protocol: Day 14 to Day 14 (I).

Day 14: (II) Donor LSK Cells Sorting

1) Euthanize 4 C57BL/6 J CD45.2+ mice and isolate bone marrow cells appropriately.
2) Lyse RBCs as previously described for flow cytometric analysis.
3) Count the cells and prepare the desired volume of staining solutions (**Supplementary Table S2**). Set aside 1×10^6 cells each for non-magnetically depleted control, unstained cells, and DAPI.
4) Stain the cells with magnetically-labelled lineage antibodies at 1:100 (**Supplementary Table S2**) for 25 min at 4°C.
5) Wash the cells with 2 mL of FACS buffer.
6) Resuspend in streptavidin-conjugated magnetic particles using volume corresponding to 50 µL per 1×10^7 cells. Incubate the cells for 20 min at 4°C.
7) Add FACS buffer to the top of the volume of the tubes to 1 mL. Magnetically deplete the cells by placing the samples on a magnet for 4 min. Remove lineage negative supernatant into intermediate flow tube.
8) Resuspend magnetically labelled cells with 1 mL of FACS buffer again and repeat depletion.
9) Perform depletion one more time and transfer the supernatant to the final tubes.
10) Stain the depleted cells with fluorophore-conjugated antibodies for 25 min at 4°C (**Supplementary Table S2**). Prepare the compensation controls.
11) After staining, add 250 µL of FACS buffer to each sample tube. The samples are ready for flow sorting. Sort for HSPC (Lin-Sca1+cKit+). For the experiments above, cells were sorted using a FACSAria cell sorter (BD Biosciences).

Day 14: (III) LSK and BMSC Gel Seeding

1) Prepare gel solution as described in the BMME-on-chip preparation: Day 14(II).
2) Seed LSK cells at 3×10^4cells and BMSC 6×10^4 in fibrin hydrogel appropriately in the apical channel of prepared Chip S-1.
3) Culture cells under a continuous flow condition at 30 µL/h with supplemented DMEM media in the basal channel for another 14 days. Check for air bubbles and replace the media every 2–3 days.

Day 29: Primary Irradiation of Recipient Mice

1) Irradiate 10 B6 CD45.1+ mice with 5Gy of irradiation. Five mice will receive bone marrow cells from CD45.2+ mouse donors, and five mice will receive bone marrow cells from CD45.2+ chip cells (**Figures 3B and C**).

Day 28: (I) Harvesting Cells

1) Harvest the content of each cell according to the described protocol, Day 21: harvesting cells. The cell is ready for competitive transplant assay into B6 CD45.1+ recipients.
2) Isolate bone marrow cells from 1 B6 CD45.1+ mouse. These cells will be used as the competitor.
3) Isolate bone marrow cells from 1 C57BL/6 J mouse. These cells will be used as the control bone marrow donor.

Day 28: (II) Competitive Transplant

1) Prepare cell solution for competitive transplant with the following setup:

Chip Group: Each recipient will receive the total contents of 1 chip (CD45.2+ donor) and 1×10^5 CD45.1+ competitor cells.

Control Group: Each recipient will receive a number of C57BL/6 J bone marrow cells (CD45.2+ donor) equivalent to the average number of cells obtained from the chips and 1×10^5 CD45.1+ competitor cells.

Each mouse will receive a cell solution of 100 μL in FACS buffer.

2) Perform secondary irradiation of the ten recipient mice with 5Gy irradiation. Perform competitive transplant *via* tail-vein injection.
3) Collect 2–3 drops (~200 μL) of peripheral blood at 4, 8, 12, 16, and 28-weeks post-transplant using submandibular bleeding technique. Analyze CD45.2+ donor engraftment using flow cytometry to detect CD3e+ T-lymphocytes, B220+ B-lymphocytes, and CD11b+ myeloid cells that are differentiated from CD45.1+ competitor cells (**Supplementary Table S3**).
4) Isolate bone marrow at 28-weeks post-transplantation (or earlier at 16-weeks) to analyze for CD45.2+ donor engraftment in HSPC population using flow cytometry (**Supplementary Table S4**).

Alkaline Phosphatase and Von Kossa Staining

1) To analyze mineralization for osteoblastic differentiation on chips, fix chips by adding 10% neutral formalin buffer into the inlet of the apical (50 μL) and basal channels (20 μL). Fix cells at room temperature for 30 min.
2) Wash the cells with 1x distilled water for 5 min. Repeat 2–3 times.
3) Add prepared alkaline phosphatase staining solution into the apical and basal channel of each chip. Incubate for 45 min at room temperature.
4) Rinse in distilled water 3–4 times and leave in distilled water for 1 h.
5) Stain with 2.5% silver nitrate solution of 30 min.
6) Aspirate the solution and rinse with distilled water 3 times.
7) Image cells under a microscope or store them at 4°C. For the abovementioned experiments, images were taken using Biotek Cytation 5 Cell Imagine Multimode Reader at 10 × magnification with color brightfield. Mosaic imaging and stitching were automated using Biotek Gen5 imaging and analysis software.

Image Analysis Using ImageJ

Image analysis of the alkaline phosphatase and Von Kossa stained chips was performed using ImageJ software, as described in **Supplementary Figure S1.** Immunofluorescent staining and imaging were performed as described in **Supplementary Figure S2**. Image analysis of ZO-1 and DAPI staining was performed in ImageJ, as described in **Supplementary Figure S3**.

Statistical Analysis

All statistical analyses were performed using GraphPad Prism 9 statistical analysis software. For all quantitative results, groups are reported as mean ± standard deviation (SD). For comparisons between two groups, statistical analysis was performed using student's unpaired two-tailed *t*-test for normally distributed. Otherwise, unpaired and non-parametric multiple *t*-tests were performed with Mann–Whitney post-test. For comparisons between two groups across timepoints (**Figure 5**), statistical analysis was performed using restricted maximum likelihood (REML).

ANTICIPATED RESULTS

We anticipate that the modular nature of this BMME-on-chip will allow for rigorous analysis of individual cellular components of the bone marrow microenvironment in a model that more closely recapitulates the *in situ* HSC niche. The modular nature of this model and the ability to use different cell populations from unique sources and genetic backgrounds is a powerful tool. We anticipate that this system will be used to clarify the roles of individual cell populations of the BMME during hematopoietic homeostasis, as well as during aging, and in pathological states such as leukemia and multiple bone marrow failure syndromes.

LIMITATIONS

The described murine BMME-on-chip provides validation that an *in vitro* system is capable of maintaining multi-potent and self-renewing HSCs for at least 14 days. Competitive transplantation of HSCs into an immune competent recipient is the gold standard for quantifying HSC function. As this analysis is not possible with the use of human cells, this represents a strength of the murine system in validation prior to the use of a fully human BMME-on-chip. However, it also represents a limitation as mouse models do not always recapitulate the human environment. Previously published BMME-on-chip devices that use human tissue have demonstrated the ability to maintain phenotypic HSPCs (Chou et al., 2020). Therefore, it is likely that the functional ability to self-renew and repopulate the hematopoietic system of a myeloablated recipient that we report here in the murine model is translatable to a human environment.

While our murine BMME-on-chip includes multiple key components of the bone marrow HSC niche, it is not fully representative of the physiologic bone marrow. For example, osteoclastic bone resorption is an ongoing process *in vivo* and is a component not included in our system. In addition, osteocytes embedded in bone are the most abundant bone cell *in vivo* and are not present in our BMME-on-chip (Frisch, 2019). The relative importance of these cells and

processes for the regulation of HSCs are not well-established, and thus the implication of their absence in our system is not known (Soto et al., 2021). However, the ability of our BMME-on-chip to maintain a fully functional HSC population suggests that they are not required for HSC maintenance.

CONCLUSION

In leukemia such as acute myeloid leukemia (AML) and chronic myeloid leukemia (CML), leukemic cells can interact with the surrounding stroma to create a favorable environment for leukemia stem cell LSC maintenance and expansion of leukemic cells (Frisch et al., 2012; Shafat et al., 2017; Behrmann et al., 2018; Staversky et al., 2018; Xu et al., 2021). The BMME is made up of cellular and noncellular components such as BMSC, endothelial cells, osteoblasts, osteoclasts, fibroblasts, adipocytes, macrophages, and extracellular matrix that provide crucial signals for the homeostatic regulation of hematopoietic systems. Leukemia has been shown to interact with the BM niche by modulating endothelial activation, establishing crosstalk with fibroblasts, and inhibiting osteoblasts (Ryningen et al., 2005; Frisch et al., 2012; Pezeshkian et al., 2013; Krevvata et al., 2014; Shafat et al., 2017; Staversky et al., 2018). In particular, our group and others have shown that leukemic cell interaction with osteoblasts is an important component in sustaining leukemic burden. However, the interactions of the HSC niche with bone marrow pathologies are poorly understood (Soto et al., 2021). AML is the most common form of leukemia that arises in the bone marrow (Soto et al., 2021). The standard therapy for AML of combined daunorubicin and cytarabine administration, termed 7 + 3 induction therapy, which was first employed in the 1970s, is still the predominant upfront therapy for most AML patients and gives rise to poor outcomes with an overall 5-years survival rate of <30% (Roussel et al., 2020; Kantarjian et al., 2021). Therefore, a better understanding of the role of the BMME in AML is critical for the improvement in therapy and patient outcomes.

The use of a BMME-on-chip that recapitulates many of the cellular interactions that occur in the BMME *in vivo* will allow for rigorous analysis of the BMME during hematologic malignancies. A murine environment, like the one in the BMME-on-chip described herein, will validate that phenotypes identified *in vivo* murine leukemic models can be recreated in an *in vitro* environment, and suggest that the *in vitro* environment of a similar human BMME-on-chip will recreate human bone marrow phenotypes that are not possible to directly observe *in vivo*. Therefore, this BMME-on-chip microphysiological platform will serve as a critical pre-clinical model for the identification of novel therapeutic targets.

DATA AVAILABILITY STATEMENT

The raw data supporting the conclusion of this article will be made available by the authors, without undue reservation.

ETHICS STATEMENT

The animal study was reviewed and approved by the University Committee on Animal Resources, University of Rochester.

AUTHOR CONTRIBUTIONS

AS performed experiments and wrote the manuscript. ML performed experiments. CS performed experiments. BF oversaw all experiments and wrote and edited the manuscript.

FUNDING

The experiments described were funded by the Department of Laboratory Medicine and the Wilmot Cancer Institute at the University of Rochester Medical Center.

ACKNOWLEDGMENTS

The authors thank Dr. Danielle S. W. Benoit for guidance throughout the preparation of the manuscript and access to Biorender.com. The author also thank Dr. Catherine E. Ovitt for providing antibodies and guidance for immunofluorescent staining.

SUPPLEMENTARY MATERIAL

The Supplementary Material for this article can be found online at: https://www.frontiersin.org/articles/10.3389/fbioe.2022.855777/full#supplementary-material

REFERENCES

Ackun-Farmmer, M. A., Soto, C. A., Lesch, M. L., Byun, D., Yang, L., Calvi, L. M., et al. (2021). Reduction of Leukemic Burden *via* Bone-Targeted Nanoparticle Delivery of an Inhibitor of C-Chemokine (C-C Motif) Ligand 3 (CCL3) Signaling. *FASEB J.* 35 (4), e21402. doi:10.1096/fj.202000938RR

Arrowsmith, J., and Miller, P. (2013). Phase II and Phase III Attrition Rates 2011-2012. *Nat. Rev. Drug Discov.* 12 (8), 569. doi:10.1038/nrd4090

Behrmann, L., Wellbrock, J., and Fiedler, W. (2018). Acute Myeloid Leukemia and the Bone Marrow Niche-Take a Closer Look. *Front. Oncol.* 8, 444. doi:10.3389/fonc.2018.00444

Bray, L. J., Binner, M., Körner, Y., von Bonin, M., Bornhäuser, M., and Werner, C. (2017). A Three-Dimensional *Ex Vivo* Tri-Culture Model Mimics Cell-Cell Interactions Between Acute Myeloid Leukemia and the Vascular Niche. *Haematologica* 102 (7), 1215–1226. doi:10.3324/haematol.2016.157883

Chou, D. B., Frismantas, V., Milton, Y., David, R., Pop-Damkov, P., Ferguson, D., et al. (2020). On-Chip Recapitulation of Clinical Bone Marrow Toxicities and

Patient-Specific Pathophysiology. *Nat. Biomed. Eng.* 4 (4), 394–406. doi:10.1038/s41551-019-0495-z

Congrains, A., Bianco, J., Rosa, R. G., Mancuso, R. I., and Saad, S. T. O. (2021). 3D Scaffolds to Model the Hematopoietic Stem Cell Niche: Applications and Perspectives. *Mater. (Basel)* 14 (3). doi:10.3390/ma14030569

Duarte, D., Hawkins, E. D., and Lo, C. (2018). The Interplay of Leukemia Cells and the Bone Marrow Microenvironment. *Blood* 131 (14), 1507–1511. doi:10.1182/blood-2017-12-784132

Frisch, B. J., Ashton, J. M., Xing, L., Becker, M. W., Jordan, C. T., and Calvi, L. M. (2012). Functional Inhibition of Osteoblastic Cells in an *In Vivo* Mouse Model of Myeloid Leukemia. *Blood* 119 (2), 540–550. doi:10.1182/blood-2011-04-348151

Frisch, B. J. (2019). The Hematopoietic Stem Cell Niche: What's So Special About Bone? *Bone* 119, 8–12. doi:10.1016/j.bone.2018.05.017

Huh, D., Hamilton, G. A., and Ingber, D. E. (2011). From 3D Cell Culture to Organs-On-Chips. *Trends Cell. Biol.* 21 (12), 745–754. doi:10.1016/j.tcb.2011.09.005

Kantarjian, H., Kadia, T., DiNardo, C., Daver, N., Borthakur, G., Jabbour, E., et al. (2021). Acute Myeloid Leukemia: Current Progress and Future Directions. *Blood Cancer J.* 11 (2), 41. doi:10.1038/s41408-021-00425-3

Kelm, J. M., Lal-Nag, M., Sittampalam, G. S., and Ferrer, M. (2019). Translational *In Vitro* Research: Integrating 3D Drug Discovery and Development Processes into the Drug Development Pipeline. *Drug Discov. Today* 24 (1), 26–30. doi:10.1016/j.drudis.2018.07.007

Krevvata, M., Silva, B. C., Manavalan, J. S., Galan-Diez, M., Kode, A., Matthews, B. G., et al. (2014). Inhibition of Leukemia Cell Engraftment and Disease Progression in Mice by Osteoblasts. *Blood, J. Am. Soc. Hematol.* 124 (18), 2834–2846. doi:10.1182/blood-2013-07-517219

Low, L. A., Sutherland, M., Lumelsky, N., Selimovic, S., Lundberg, M. S., and Tagle, D. A. (2020). Organs-On-A-Chip. *Adv. Exp. Med. Biol.* 1230, 27–42. doi:10.1007/978-3-030-36588-2_3

Low, L. A., and Tagle, D. A. (2017). Microphysiological Systems (Tissue Chips) and Their Utility for Rare Disease Research. *Adv. Exp. Med. Biol.* 1031, 405–415. doi:10.1007/978-3-319-67144-4_23

Low, L. A., and Tagle, D. A. (2017). Tissue Chips - Innovative Tools for Drug Development and Disease Modeling. *Lab. Chip* 17 (18), 3026–3036. doi:10.1039/c7lc00462a

Nelson, M. R., Ghoshal, D., Mejías, J. C., Rubio, D. F., Keith, E., and Roy, K. (2021). A Multi-Niche Microvascularized Human Bone Marrow (hBM) On-A-Chip Elucidates Key Roles of the Endosteal Niche in hBM Physiology. *Biomaterials* 270, 120683. doi:10.1016/j.biomaterials.2021.120683

Osaki, T., Sivathanu, V., and Kamm, R. D. (2018). Vascularized Microfluidic Organ-Chips for Drug Screening, Disease Models and Tissue Engineering. *Curr. Opin. Biotechnol.* 52, 116–123. doi:10.1016/j.copbio.2018.03.011

Pezeshkian, B., Donnelly, C., Tamburo, K., Geddes, T., and Madlambayan, G. J. (2013). Leukemia Mediated Endothelial Cell Activation Modulates Leukemia Cell Susceptibility to Chemotherapy Through a Positive Feedback Loop Mechanism. *PloS One* 8 (4), e60823. doi:10.1371/journal.pone.0060823

Rödling, L., Ivo, S., Saskia, K., Karen, B., Jan, H., Cornelia, L. T., et al. (2017). 3D Models of the Hematopoietic Stem Cell Niche Under Steady-State and Active Conditions. *Sci. Rep.* 7 (1), 4625. doi:10.1038/s41598-017-04808-0

Roussel, X., Daguindau, E., Berceanu, A., Desbrosses, Y., Warda, W., Neto da Rocha, M., et al. (2020). Acute Myeloid Leukemia: From Biology to Clinical Practices Through Development and Pre-Clinical Therapeutics. *Front. Oncol.* 10, 599933. doi:10.3389/fonc.2020.599933

Ryningen, A., Wergeland, L., Glenjen, N., Gjertsen, B. T., and Bruserud, Ø. (2005). *In Vitro* Crosstalk Between Fibroblasts and Native Human Acute Myelogenous Leukemia (AML) Blasts *via* Local Cytokine Networks Results in Increased Proliferation and Decreased Apoptosis of AML Cells as Well as Increased Levels of Proangiogenic Interleukin 8. *Leukemia Res.* 29 (2), 185–196. doi:10.1016/j.leukres.2004.06.008

Shafat, M. S., Gnaneswaran, B., Bowles, K. M., and Rushworth, S. A. (2017). The Bone Marrow Microenvironment - Home of the Leukemic Blasts. *Blood Rev.* 31 (5), 277–286. doi:10.1016/j.blre.2017.03.004

Soto, C. A., Lo Celso, C., Purton, L. E., and Frisch, B. J. (2021). From the Niche to Malignant Hematopoiesis and Back: Reciprocal Interactions Between Leukemia and the Bone Marrow Microenvironment. *JBMR Plus* 5 (10), e10516. doi:10.1002/jbm4.10516

Staversky, R. J., Byun, D. K., Georger, M. A., Zaffuto, B. J., Goodman, A., Becker, M. W., et al. (2018). The Chemokine CCL3 Regulates Myeloid Differentiation and Hematopoietic Stem Cell Numbers. *Sci. Rep.* 8 (1), 14691. doi:10.1038/s41598-018-32978-y

Xu, B., Hu, R., Liang, Z., Chen, T., Chen, J., Hu, Y., et al. (2021). Metabolic Regulation of the Bone Marrow Microenvironment in Leukemia. *Blood Rev.* 48, 100786. doi:10.1016/j.blre.2020.100786

Conflict of Interest: The authors declare that the research was conducted in the absence of any commercial or financial relationships that could be construed as a potential conflict of interest.

Publisher's Note: All claims expressed in this article are solely those of the authors and do not necessarily represent those of their affiliated organizations, or those of the publisher, the editors, and the reviewers. Any product that may be evaluated in this article, or claim that may be made by its manufacturer, is not guaranteed or endorsed by the publisher.

Copyright © 2022 Sharipol, Lesch, Soto and Frisch. This is an open-access article distributed under the terms of the Creative Commons Attribution License (CC BY). The use, distribution or reproduction in other forums is permitted, provided the original author(s) and the copyright owner(s) are credited and that the original publication in this journal is cited, in accordance with accepted academic practice. No use, distribution or reproduction is permitted which does not comply with these terms.

frontiers | Frontiers in Bioengineering and Biotechnology

TYPE Original Research
PUBLISHED 05 August 2022
DOI 10.3389/fbioe.2022.945639

Check for updates

OPEN ACCESS

EDITED BY
Dmitriy Sheyn,
Board of Governors Regenerative Medicine Institute, United States

REVIEWED BY
Spencer Szczesny,
The Pennsylvania State University, United States
Brianne Connizzo,
Boston University, United States

*CORRESPONDENCE
Catherine K. Kuo,
ckk@umd.edu

SPECIALTY SECTION
This article was submitted to Tissue Engineering and Regenerative Medicine, a section of the journal Frontiers in Bioengineering and Biotechnology

RECEIVED 16 May 2022
ACCEPTED 12 July 2022
PUBLISHED 05 August 2022

CITATION
Nguyen PK, Jana A, Huang C, Grafton A, Holt I, Giacomelli M and Kuo CK (2022), Tendon mechanical properties are enhanced via recombinant lysyl oxidase treatment.
Front. Bioeng. Biotechnol. 10:945639.
doi: 10.3389/fbioe.2022.945639

COPYRIGHT
© 2022 Nguyen, Jana, Huang, Grafton, Holt, Giacomelli and Kuo. This is an open-access article distributed under the terms of the Creative Commons Attribution License (CC BY). The use, distribution or reproduction in other forums is permitted, provided the original author(s) and the copyright owner(s) are credited and that the original publication in this journal is cited, in accordance with accepted academic practice. No use, distribution or reproduction is permitted which does not comply with these terms.

Tendon mechanical properties are enhanced *via* recombinant lysyl oxidase treatment

Phong K. Nguyen[1,2], Aniket Jana[3], Chi Huang[1], Alison Grafton[3], Iverson Holt[3], Michael Giacomelli[1] and Catherine K. Kuo[1,2,3,4,5]*

[1]Department of Biomedical Engineering, University of Rochester, Rochester, NY, United States, [2]Center for Musculoskeletal Research, University of Rochester Medical Center, Rochester, NY, United States, [3]Fischell Department of Bioengineering, University of Maryland, College Park, MD, United States, [4]Department of Orthopaedics, University of Rochester Medical Center, Rochester, NY, United States, [5]Department of Orthopaedics, University of Maryland School of Medicine, Baltimore, MD, United States

Tendon mechanical properties are significantly compromised in adult tendon injuries, tendon-related birth defects, and connective tissue disorders. Unfortunately, there currently is no effective treatment to restore native tendon mechanical properties after postnatal tendon injury or abnormal fetal development. Approaches to promote crosslinking of extracellular matrix components in tendon have been proposed to enhance insufficient mechanical properties of fibrotic tendon after healing. However, these crosslinking agents, which are not naturally present in the body, are associated with toxicity and significant reductions in metabolic activity at concentrations that enhance tendon mechanical properties. In contrast, we propose that an effective method to restore tendon mechanical properties would be to promote lysyl oxidase (LOX)-mediated collagen crosslinking in tendon during adult tissue healing or fetal tissue development. LOX is naturally occurring in the body, and we previously demonstrated LOX-mediated collagen crosslinking to be a critical regulator of tendon mechanical properties during new tissue formation. In this study, we examined the effects of recombinant LOX treatment on tendon at different stages of development. We found that recombinant LOX treatment significantly enhanced tensile and nanoscale tendon mechanical properties without affecting cell viability or collagen content, density, and maturity. Interestingly, both tendon elastic modulus and LOX-mediated collagen crosslink density plateaued at higher recombinant LOX concentrations, which may have been due to limited availability of adjacent lysine residues that are near enough to be crosslinked together. The plateau in crosslink density at higher concentrations of recombinant LOX treatments may have implications for preventing over-stiffening of tendon, though this requires further investigation. These findings demonstrate the exciting potential for a LOX-based therapeutic to enhance tendon mechanical properties *via* a naturally occurring crosslinking mechanism, which could have tremendous implications for an estimated 32 million acute and chronic tendon and ligament injuries each year in the U.S.

KEYWORDS

tendon, collagen crosslinking, lysyl oxidase, tendon healing, mechanical properties, birth deformity, orthopaedic, musculoskeletal

Introduction

Tendon is a highly collagenous connective tissue that transmits forces from muscle to bone to enable movement. Unfortunately, tendon injuries are highly prevalent throughout the body. For example, flexor tendon injuries affect 33 per 100,000 persons each year (de Jong et al., 2014). Achilles tendon injuries account for up to 50% of all sports-related injuries (Järvinen et al., 2005; Raikin et al., 2013). Rotator cuff injuries affect 30% of people over the age of 60, leading to over 600,000 repairs each year in the U.S. (Vitale et al., 2007; Dang and Davies, 2018). Despite their critical musculoskeletal functions, tendons lack the ability to regenerate when injured (Arya and Kulig, 2010; Helland et al., 2013; Derwin and Thomopoulos, 2020; Sarmiento and Little, 2021). Tendons are also commonly associated with heritable connective tissue disorders and birth abnormalities, including Ehlers-Danlos syndrome (EDS) and clubfoot (Browne, 1931; Windisch et al., 2007; Gazit et al., 2016). It has been estimated that tendon-related birth defects affect up to 1 in 100 live births each year (Kowalczyk and Feluś, 2016). Unfortunately, there are currently no effective treatment strategies to restore native mechanical properties to tendons in any of these scenarios. Thus, there is a critical need for therapeutics to promote tendon mechanical properties.

Lysyl oxidase (LOX) is a critical regulator of tendon mechanical properties during new tissue formation. LOX catalyzes the formation of crosslinks between collagen molecules, including trivalent hydroxylysyl pyridinoline (HP) and lysyl pyridinoline (LP), the two most prevalent LOX-mediated collagen crosslinks in tendon (Eyre et al., 1984; Eyre et al., 2008). We previously discovered that inhibition of LOX activity during tendon development blocks formation of new HP and LP crosslinks between collagen molecules, and that this inhibition of collagen crosslinking prevents increases in tendon elastic modulus (Marturano et al., 2013; Marturano et al., 2014). Furthermore, inhibition of increases in elastic modulus due to inhibition of LOX crosslinking occurred without affecting collagen content and organization (Marturano et al., 2013; Marturano et al., 2014). Our studies also revealed that tendon elastic modulus correlates strongly with crosslink density (r^2 = 0.8, $p < 0.0001$) as well as LOX activity levels (r^2 = 0.8, $p < 0.05$) during normal development and also when LOX activity is inhibited (Marturano et al., 2014; Pan et al., 2018). Taken together, LOX plays an important role in regulating tendon mechanical properties by modulating collagen crosslinking.

LOX-mediated collagen crosslink density correlates significantly with elastic modulus in healthy adult tendons in human, goat, and horse (Eyre et al., 1984; Ng et al., 1996; Thorpe et al., 2010). Unfortunately, adult tendons post-healing are associated with abnormal and typically inferior mechanical properties (Beredjiklian et al., 2003; Arya and Kulig, 2010; Helland et al., 2013; Sereysky et al., 2013; Theodossiou and Schiele, 2019; Arvind and Huang, 2021). Higher HP and LP crosslink density levels have been reported during the early stages of healing of injured human supraspinatus tendons compared to healthy tendons, but the study only examined one timepoint and it was hypothesized that these increases were temporary (Bank et al., 1999). Indeed, rabbit medial collateral ligaments have been reported to possess lower elastic modulus and pyridinoline crosslink density after complete healing at 40 weeks post-injury compared to non-injured controls (Frank et al., 1995). In addition, it has been shown in skin and liver that crosslink density increases significantly during the early remodeling phase but eventually decreases and remains at lower levels compared to healthy controls (Bailey et al., 1975; Bailey and Light, 1985; Ricard-Blum et al., 1992). Taken together, enhancement of LOX-mediated collagen crosslinking may be necessary to restore normal tendon mechanical properties and function.

Crosslinking has been studied as a potential treatment to enhance tendon mechanical properties with limited degrees of success (Caliari et al., 2011; Fessel and Snedeker, 2011; Fessel et al., 2012; Fessel et al., 2014; Green et al., 2017). In particular, crosslinkers such as 1-ethyl-3-(3-dimethylaminopropyl) carbodiimide, glutaraldehyde, and genipin have been tested to enhance the mechanical properties of tendon explants and engineered tendon tissue (Caliari et al., 2011; Fessel and Snedeker, 2011; Fessel et al., 2012; Green et al., 2017). However, these crosslinkers do not occur naturally in human and are associated with cytotoxicity at levels that improve tendon mechanical properties (Fessel et al., 2014). In contrast, LOX-mediated crosslinking of collagen occurs naturally during development and correlates directly with mechanical properties of homeostatic adult tendons (Eyre et al., 1984; Ng et al., 1996; Thorpe et al., 2010). A therapeutic treatment that promotes naturally occurring crosslinking to enhance tendon mechanical properties would have significant clinical implications.

In addition to poor tendon healing, abnormal LOX-mediated collagen crosslinking has been implicated in heritable connective tissue disorders and birth abnormalities that affect tendon, including EDS, clubfoot, and Menkes disease (Di Ferrante et al., 1975; Kuivaniemi et al., 1985; Royce and Steinmann, 1990; Knitlova et al., 2021; Novotny et al., 2022). For example, EDS is associated with lower LOX enzyme levels and compromised tendon mechanical properties compared to healthy counterparts (Kuivaniemi et al., 1985; Nielsen et al., 2014). In clubfoot patients, LOX protein and LOX-mediated crosslink density levels are both higher in the contracted tendons

as compared to the non-contracted tendons (Knitlova et al., 2021; Novotny et al., 2022). Although clubfoot is treatable postnatally *via* an extensive 5-year bracing process called the Ponseti method, the treated clubfoot tendons possess lower elastic modulus compared to age-match healthy children and recurrence of clubfoot after the 5-year process is as high as 37% (Richards et al., 2008; Bor et al., 2009; Masala et al., 2012; Sætersdal et al., 2012; Zhao et al., 2014). These examples indicate a need for more effective treatments that can restore native mechanical properties of tendon that are involved in connective tissue disorders and musculoskeletal birth defects. Based on these findings, future therapeutics could target LOX-mediated collagen crosslinking to enhance mechanical properties of abnormally weak tendons during treatment of connective tissue disorders and musculoskeletal abnormalities in childhood years.

There is a critical need to effectively enhance tendon mechanical properties of abnormally weak tendons that are associated with connective tissue disorders and birth abnormalities and adult tendon injuries. Because tendon-related birth defects develop at different stages during pregnancy and injured adult tendons undergo various stages of new tissue formation during healing, we aimed to examine the effects of recombinant LOX (rLOX) treatment on embryonic tendons at different developmental stages. We treated chick embryo tendons from two developmental stages with rLOX and measured LOX-mediated collagen crosslink density, tendon mechanical properties, cell number and viability, and collagen content, organization, and maturation. We hypothesized that 1) rLOX treatment would enhance LOX-mediated collagen crosslink density and tendon mechanical properties at different developmental stages, 2) LOX-mediated collagen crosslink density and tendon elastic modulus would plateau at higher rLOX concentrations, and 3) cell viability and collagen content, organization, and maturation would not be affected by rLOX treatment. Our findings here establish the feasibility of therapeutic treatment strategies to enhance tendon mechanical properties by promoting LOX-mediated collagen crosslinking, a naturally occurring mechanism.

Materials and methods

Experimental overview

Chick embryo calcaneal tendons from two developmental stages Hamburger-Hamilton stage (HH) HH40 (embryonic day 14) and HH43 (embryonic day 17), were used for *in ovo* and *ex ovo* experiments. HH40 and HH43 were chosen based on our previous findings that significant collagen deposition, organization, and crosslinking, as well as elaboration of tendon mechanical properties, are rapidly increasing through HH40 and HH43 (the embryo hatches after HH45) (Kuo et al., 2008; Marturano et al., 2013; Marturano et al., 2014). For *in ovo* experiments, recombinant (r) LOX or vehicle (Ctrl) was injected *in vivo* between the calcaneal tendon and the underlying tibia bone. Embryos were sacrificed and tendons were dissected for tensile testing after 48 h. For *ex ovo* experiments, tendon explants were cultured in medium supplemented with rLOX or vehicle. Tendon explants were harvested after 72 h culture for atomic force microscopy, histological staining, and two-photon imaging. The number of biological replicates in all experiments was determined by power analysis, where each sample was from a different chick embryo.

In ovo culture

Fertilized white leghorn chick embryos (University of Connecticut Poultry Farm, CT) were cultured in humidified rocking incubators at 37.5°C. At HH20, a small window was created in the eggshell, as we previously described (Stein et al., 2019). Transparent tape was placed on top of the window and the windowed eggs were subsequently incubated in humidified non-rocking incubators at 37.5°C. At HH38 and HH41, embryos were each injected with 3 μg of rLOX (Origene, MD) dissolved in 30 μl vehicle (25 mM Tris HCl, pH 7.3, 100 mM glycine, 10% glycerol) between the calcaneal tendon and the underlying tibia bone at 0 h and 24 h. The contralateral control limb was injected with 30 μl vehicle. The window was re-sealed with tape and embryos were returned to the incubators. After 48 h, embryos were sacrificed at HH40 and HH43, and the calcaneal tendons were dissected for tensile mechanical testing.

Tensile mechanical testing and data analysis

Tendons treated *in vivo* with either vehicle or rLOX were harvested and tensile tested as previously described (Navarro et al., 2022). Briefly, tendons were gripped at each end and stretched uniaxially at 1% strain per second until failure. Elastic modulus was calculated based on the slope of the linear region of the stress-strain curve. Peak stress was calculated by normalizing the maximum load recorded during testing to the cross-sectional area. Peak strain was determined by the strain value at peak stress.

Ex ovo explant culture

Calcaneal tendons of HH40 and HH43 chick embryos were dissected out of the limb, using our previously established protocol to ensure muscle and fibrocartilage were excluded (Navarro et al., 2022). After the tendon was separated from the limb, tendon bundles separated easily from each other during

gentle extraction using fine tweezers. Tendon bundles range from 1.55 to 3.41 mm in length and from 200 to 400 μm in diameter. Each experiment required $N = 5$ biological replicates, with a different embryo as the source of each biological replicate (N). Bundles from a tendon of the same embryo were divided across treatment groups: Ctrl, 1X, 2X, and 5X rLOX. This process was implemented for $N = 5$ different embryos. Tendon bundle explants were cultured for 72 h in complete medium consisting of Dulbecco's modified Eagle's medium (Life Technologies, CA), 10% fetal bovine serum (Atlanta Biologicals, GA), and 1% antimycotic-antibiotic (Gibco, CA). Culture medium was replenished and supplemented with either 0 (vehicle), 1.5, 3, or 7.5 μg/ml rLOX (corresponding to 1X, 2X, or 5X rLOX) at 0 h, 24 h, and 48 h. Studies have shown LOX remains active up to 120 h *in vitro* (Trackman et al., 1981; Kagan and Li, 2003). Tendon explants were harvested for assays at 72 h.

Cryopreservation and cryosectioning

Tendons were cryopreserved and cryosectioned as previously described (Marturano et al., 2013). Briefly, tendons were immersed in 10% (v/v) dimethyl sulfoxide (Sigma, MO) HBSS solution for 15 min at room temperature, with tissue-to-solution volume ratio of at least 1:10. Tendons were then incubated in optimal cutting temperature (OCT) medium (Sakura Finetek, CA) for 30 min at room temperature, slowly frozen at −1°C/min to −80°C in an isopropanol bath, and then stored in a −80°C freezer. Frozen blocks were cryosectioned at 20 μm thickness for assays described below. At the start of as well as during sectioning, the frozen tissue block was adjusted as needed to ensure collagen fibers were oriented in the longitudinal direction, parallel to the sectioning plane.

Force volume-atomic force microscopy

AFM was performed on 20 μm-thick sections following our previously established methods (Marturano et al., 2013). Briefly, tendon cryosections were immersed in PBS at room temperature for 5 min to remove the OCT and DMSO. Samples were then immersed in fresh PBS during AFM testing. To ensure the location of AFM testing was consistent from one sample to the next, we visualized the entire bundle length using brightfield imaging. The mid-point of tendon bundles along the longitudinal length was determined using the x-y coordinates provided by the imaging software and chosen as the location for AFM probing. Pyramidal Si_3N_4 probes with an approximately 20 nm tip radius and a spring constant of 0.06 N/m (Bruker, MA) were used on an MFP-3D AFM machine (Asylum Research, CA). Tissue was indented by the nanoscale probe at 6 μm/s rate. For each measurement, the probe was descended onto the tissue until 40 nm deflection in the cantilever was detected. Force maps were recorded within a 10 μm × 10 μm area with a 64 × 64 force curve array. Individual elastic moduli were calculated by fitting individual force-displacement curves to the Hertzian equation, also as described in our previous study (Marturano et al., 2013). For each tendon sample, median elastic modulus was calculated from 4,096 data points per force map. Median, rather than mean, was reported for each sample because of non-symmetrical increases in moduli across the 4,096 data points per force map.

Hematoxylin and eosin staining and image analysis

Tendon sections were stained with H&E and imaged under brightfield microscopy (20X objective, ZEISS Axio Scan, Germany). For each biological replicate (N), cells were counted per 120 × 120 μm^2 area manually using the Cell Counter plug-in in ImageJ (NIH, MD) by three independent reviewers. The cell number per area was calculated as total cells divided by area.

TdT-mediated dUTP nick end labeling (TUNEL) staining and image analysis

Apoptotic cells were detected in TUNEL-stained tendon sections using the *In Situ* Cell Death Detection Kit, TMR red (Roche, Germany). Counter-staining with Hoechst 33342 (Thermo Fisher, MA) was used to visualize all cell nuclei. Stained sections were imaged using a FLUOVIEW FV3000 laser scanning confocal system (Olympus, PA). TUNEL-positive cells and Hoescht 33342-positive cells fluoresced red and blue, respectively. To enhance visualization in figures, Hoescht 33342-positive cells were pseudo-colored green. To measure cell viability based on TUNEL staining, images were converted to 16-bit (grey scale) and a universal threshold was applied to all images to identify individual cells. Total cell number based on Hoeschst staining (N_{total}) and TUNEL-positive cells (N_a) were counted using the Analyze Particle function in ImageJ (NIH, MD). The percentage of viable cells was calculated as $[(N_{total}–N_a)/N_{total}\ ]$ x 100%.

Picrosirius red staining and image analysis

Tendon sections were stained with PSR and imaged using brightfield and polarized light microscopy (20X objective, ZEISS Axio Scan, Germany). Light source angle was kept consistent between all samples as it is non-adjustable on the ZEISS Axio Scan. Collagen content was assessed by analyzing brightfield

images of PSR-stained sections. Brightfield images were converted into 8-bit format and thresholded to identify PSR-positive staining areas. PSR-positive staining area fraction of each image was quantified to determine collagen content per unit area. Collagen maturity was assessed by analyzing polarized images of the same PSR-stained sections used in the analysis above. It has previously been shown that polarization color shifts from the shorter wavelength color green to higher wavelength colors yellow and then red as collagen fibers increase in diameter and packing density, as typically occurs during maturation (Junqueira et al., 1982; Dayan et al., 1989). Accordingly, the percentages of green, yellow, and red collagen fibers have been used to evaluate collagen maturity in polarized microscopy images of tissues (Wolman and Kasten, 1986; Monaghan et al., 2017; Patel et al., 2018). Here, we characterized green fibers as immature fibers, yellow fibers as intermediate fibers, and red fibers as mature fibers, using the following method. Polarized images were converted into 8-bit format. In order to set the appropriate threshold levels that classify red, yellow, and green pixels, we evaluated the intensity ratio of red to green signal (I_R/I_G) for at least 20 visibly red and green regions within tendon per embryonic stage. The selection of lower to higher intensity red and green regions was performed by 3 independent reviewers. A pixel was classified as red if $I_R/I_G \geq 1.8$, green if $I_R/I_G \leq 1.1$, and yellow if $1.1 < I_R/I_G < 1.8$. The ranges of I_R/I_G ratio for each color were entered into a MATLAB code. To ensure there was no human bias, the same code was applied to every image to quantify the percentage of red (mature), yellow (intermediate), and green (immature) fibers.

Two-photon microscopy and image analysis

Tendon sections were imaged using an Olympus FVMPE-RS microscope system with an Olympus 25X water immersion objective (Olympus, Japan). Fibrillar collagen was visualized based on forward second harmonic generation (F-SHG) signal (780/370–410 nm). Image segmentation was performed by generating a binary mask using intensity thresholding with a custom MATLAB code (Mathworks, CA). Average pixel intensity of each image was quantified to determine collagen content per unit area. The Directionality plugin in FIJI (NIH, MD) was used to quantify the angle of collagen fiber orientation (JY, 2010; Sensini et al., 2018; Bah et al., 2020). First, SHG images were imported and converted into 8-bit format. Fourier spectrum analysis was then performed to create a histogram of orientation angle of collagen fibers within the images. The histogram peak represented the predominant orientation angle, and the histogram width represented the dispersion of collagen fiber orientation angles. Lower dispersion value indicated more aligned collagen fibers.

High performance liquid chromatography

Tendon samples were flash frozen in liquid nitrogen and ground with pestle and mortar. Samples were then transferred into 1.5 ml Eppendorf tubes for long-term storage at −80°C or immediately processed for HPLC. Frozen tendon samples were lyophilized and reduced with 10 mg/ml sodium borohydride ($NaBH_4$) in 1 mM sodium hydroxide (NaOH) for 2 h at room temperature. Acetic acid was added until pH = 3 was achieved to stop the reaction. Samples were hydrolyzed with 6 M hydrochloric acid at 110°C for 20 h. Samples were lyophilized until completely dried, weighed, and then reconstituted in 50 µl of 1% heptafluorobutyric acid (HFBA) HPLC-grade water. Samples were injected into a 4.6 mm × 150 mm C18 reverse phase column (Shimadzu, Japan) and analyzed for pyridinoline content (HP and LP) based on fluorescence signal (297/395 nm) (Bank et al., 1997). Crosslink density was calculated as the ratio of HP and LP content to dry mass of each sample.

Statistical analyses

Power analysis was performed with G*Power software based on preliminary data with power = 0.9 and significance level $\alpha = 0.05$ using 1 sample, 2-sided equality, and 2-sample equivalence scenarios (Faul et al., 2007). Power analysis determined $N = 5$ per embryonic stage and condition was needed for tensile testing, AFM, H&E staining and image analysis, PSR staining and image analysis, and SHG imaging and image analysis, and $N = 3$ per embryonic stage and condition was needed for HPLC. Student *t*-test was used to analyze statistical differences between rLOX and vehicle control (Ctrl) treatments for tensile and nanoscale elastic moduli, cell number and viability, and collagen content, alignment, and maturity. 1-way ANOVA followed by Tukey's post-hoc analysis was used to analyze statistical differences in nanoscale elastic modulus and crosslink density between Ctrl, 1X, 2X, and 5X rLOX treatments. Exponential plateau fit analysis was used to examine the plateaus in elastic modulus and crosslink density with increasing rLOX concentrations. Linear regression analysis was used to examine the correlation between elastic modulus and crosslink density. All statistical analyses were performed using Graphpad Prism v8 (CA, United States).

Results

Tensile testing revealed tendon elastic modulus and peak stress increased significantly with rLOX treatment whereas peak strain was not affected for both HH40 and HH43 tendons (Figures 1A–F).

AFM maps revealed more regions with higher elastic modulus values in both HH40 and HH43 tendons when treated with rLOX (Figures 2A,B). Relative frequency

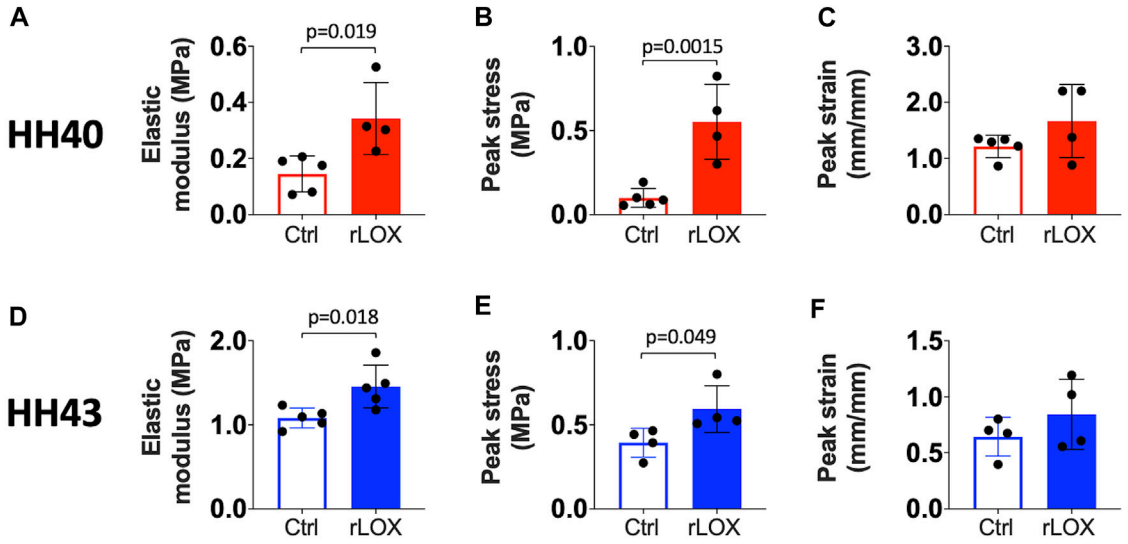

FIGURE 1
Tensile mechanical properties of HH40 and HH43 tendons were significantly enhanced by rLOX treatment of the tendon during development *in vivo*. Elastic modulus **(A)** and peak stress **(B)** of HH40 tendons increased significantly with rLOX as compared to Ctrl treatment. Peak strain **(C)** of HH40 tendons was unchanged with rLOX treatment. Elastic modulus **(D)** and peak stress **(E)** of HH43 tendons increased significantly with rLOX treatment. Peak strain **(F)** of HH43 tendons was unchanged with rLOX treatment. Statistically significant differences were determined by Student *t*-test with $p < 0.05$. $n = 5$ per stage and treatment group.

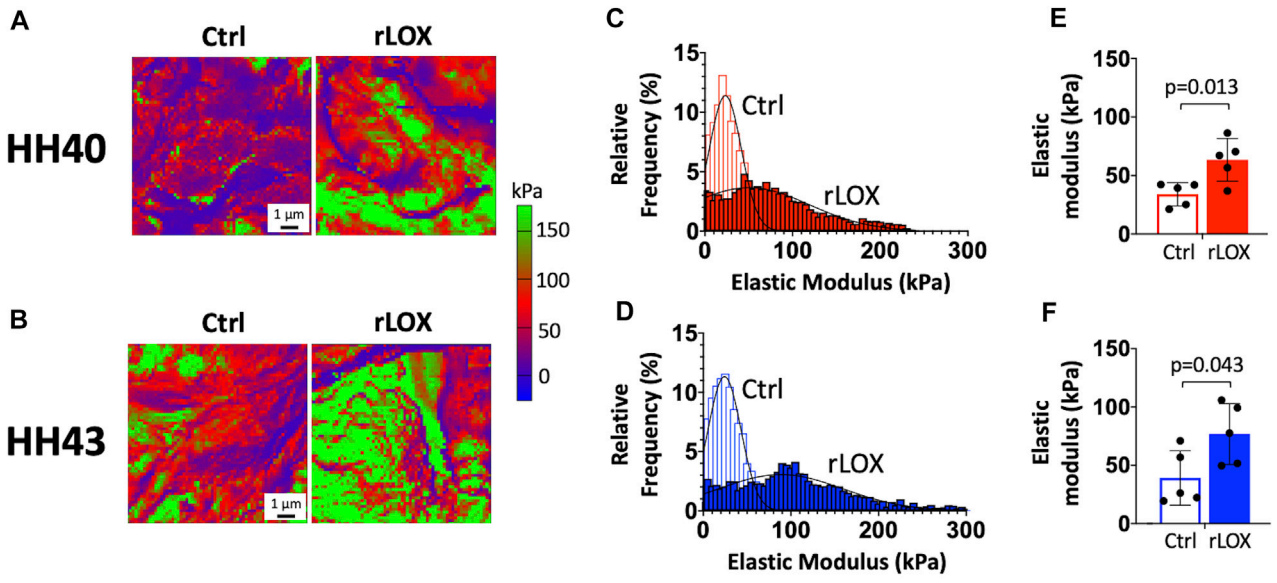

FIGURE 2
Nanoscale elastic moduli of HH40 and HH43 tendon explants were significantly increased with rLOX treatment *ex ovo*. **(A,B)** Representative elastic modulus maps showed HH40 **(A)** and HH43 tendons **(B)** possess more regions of higher elastic modulus after rLOX treatment compared to Ctrl treatment. **(C,D)** Representative histograms showed increasing frequency of higher elastic moduli in HH40 **(C)** and HH43 tendons **(D)** after rLOX treatment compared to Ctrl treatment. Additionally, treatment with rLOX led to wider distribution of elastic modulus values for tendon explants of both stages. **(E,F)** Median elastic moduli of HH40 **(E)** and HH43 tendons **(F)** were significantly increased with rLOX treatment. Statistically significant differences were determined by Student *t*-test with $p < 0.05$. $n = 5$ per stage and treatment group.

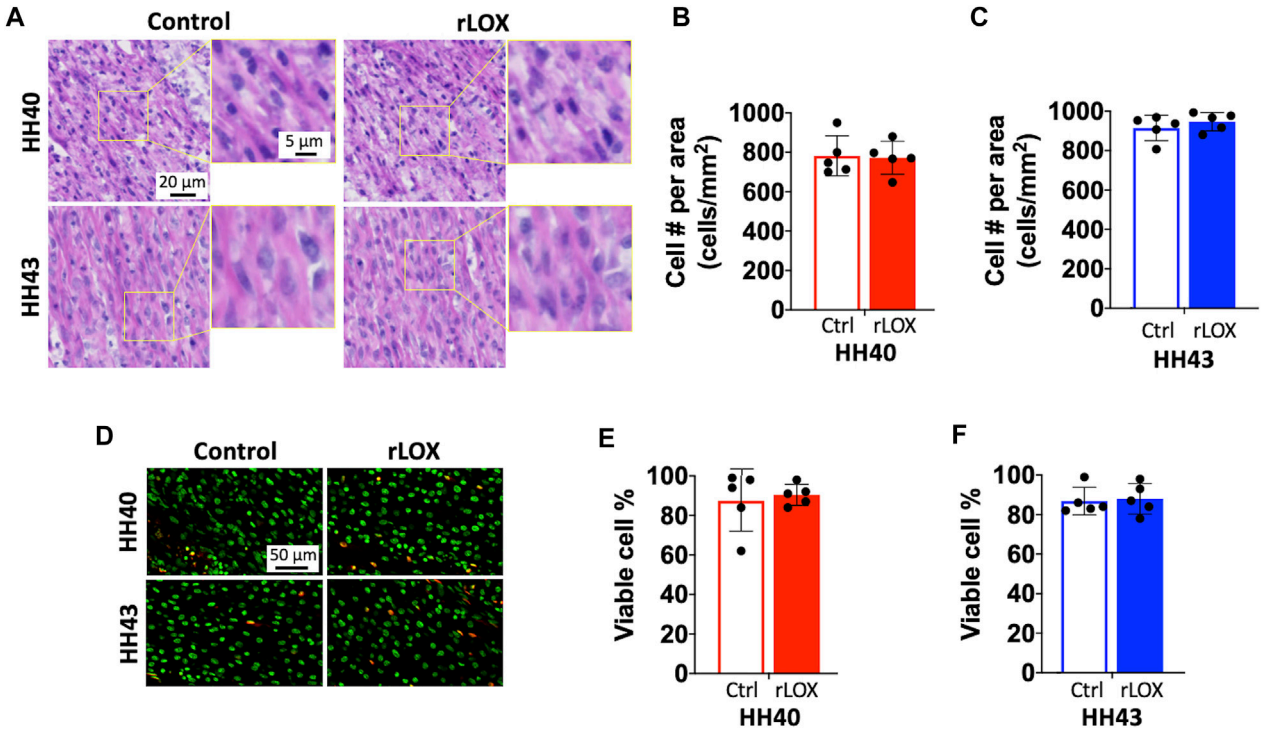

FIGURE 3
Cell number and viability of HH40 and HH43 tendon explants were similar between rLOX and Ctrl treatments. **(A)** Representative images of H&E-stained HH40 and HH43 tendons after rLOX and Ctrl treatments. High magnification images showed intact cell nuclei and lack of cell debris. **(B,C)** Cell density was not affected by rLOX treatment in both HH40 **(B)** and HH43 **(C)** tendons. **(D)** Representative images of TUNEL- and Hoescht 33342-stained HH40 and HH43 tendons after rLOX and Ctrl treatments. TUNEL-positive cells were red and Hoescht 33342-positive cells were pseudo-colored green. **(E,F)** Percentages of viable cells in both HH40 and HH43 tendons were similar between rLOX and Ctrl treatments. Statistically significant differences were determined by Student *t*-test with $p < 0.05$. $n = 5$ per stage and treatment group.

histograms showed rLOX treatment led to wider distributions of elastic moduli with higher elastic modulus values (Figures 2C,D). Median nanoscale elastic moduli of HH40 and HH43 tendons both increased significantly with rLOX treatment over those with Ctrl treatment (Figures 2E,F).

H&E staining showed intact nuclei and no cell debris in both HH40 and HH43 tendons, with no apparent differences between rLOX and Ctrl treatments (Figure 3A). Cell density remained constant between rLOX and Ctrl treatments for HH40 and HH43 tendons, quantified based on image analysis of H&E stains (Figures 3B,C). TUNEL and Hoechst 33342 staining revealed mostly viable cells with few TUNEL-positive cells in HH40 and HH43 tendons, with no apparent differences between rLOX and Ctrl treatments (Figure 3D). Percentages of apoptotic cells were similar between rLOX and Ctrl treatments, quantified based on image analysis of TUNEL-positive cells (Figures 3E,F).

SHG images of fibrillar collagen appeared similar between rLOX and Ctrl treatments for HH40 and HH43 tendons (Figures 4A,B). Images were then analyzed to quantify collagen content, density, and dispersion angle. Quantification of total SHG signal intensity showed fibrillar collagen content was not affected by rLOX treatment in both HH40 and HH43 tendons (Figures 4C,D). Quantification of SHG signal density per unit area showed fibrillar collagen density was not affected by rLOX treatment in both HH40 and HH43 tendons (Figures 4E,F). Quantification of dispersion angle showed fibrillar collagen alignment was not affected by rLOX treatment in HH40 tendons (Figure 4G). However, lower dispersion angle with rLOX treatment indicated higher levels of collagen alignment with rLOX treatment in HH43 tendons (Figure 4H).

Brightfield and polarized microscopy images of PSR-stained HH40 and HH43 tendon sections appeared similar between rLOX and Ctrl treatments (Figures 5A,B). Collagen content of both HH40 and HH43 tendons were not affected by rLOX treatment (Figures 5C,D), which agreed with our analyses of SHG images (Figures 4C,D). The percentages of immature, intermediate, and mature fibers in both HH40 and HH43 tendons also were not affected by rLOX treatments (Figures 5E–J).

AFM maps of HH43 tendons showed increasing regions of higher elastic modulus values with increasing rLOX

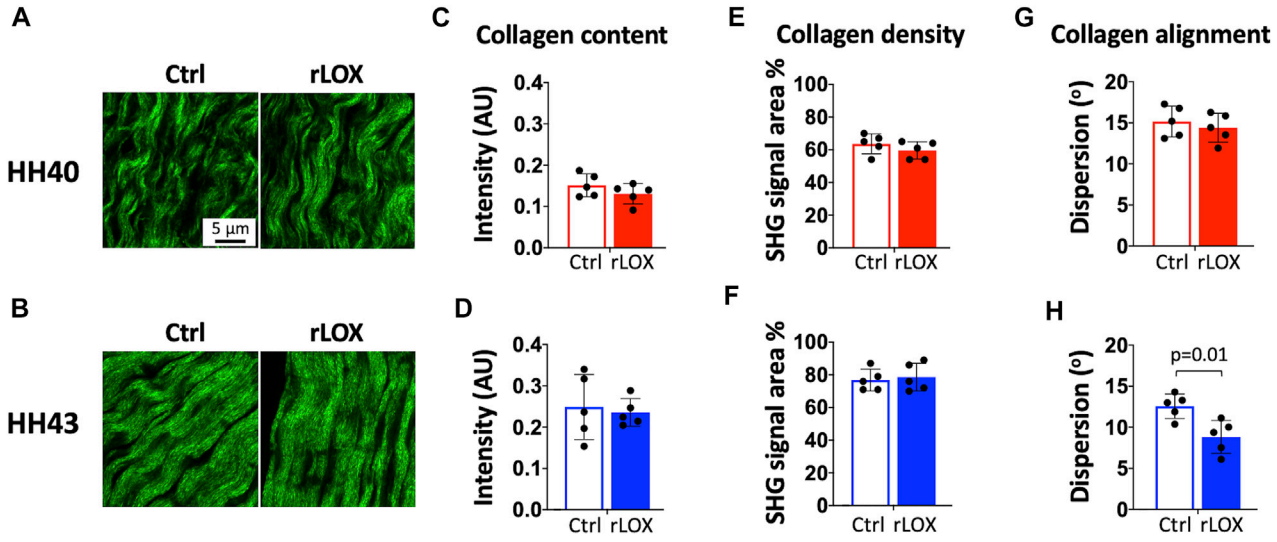

FIGURE 4
SHG imaging and image analysis of HH40 and HH43 tendon explants after rLOX and vehicle control treatments. **(A,B)** Representative SHG images of HH40 **(A)** and HH43 **(B)** tendons after rLOX and Ctrl treatments. **(C,D)** Collagen content was not affected by rLOX treatment in both HH40 **(C)** and HH43 **(D)** tendons. **(E,F)** Collagen density was not affected by rLOX treatment in both HH40 **(E)** and HH43 **(F)** tendons. **(G)** Collagen alignment, based on dispersion angle, was not affected by rLOX treatment in HH40 tendons. **(H)** Collagen alignment in HH43 tendons increased significantly with rLOX treatment, indicated by significantly lower dispersion angle in HH43 tendons after rLOX treatment. Statistically significant differences were determined by Student *t*-test with $p < 0.05$. $n = 5$ per stage and treatment group.

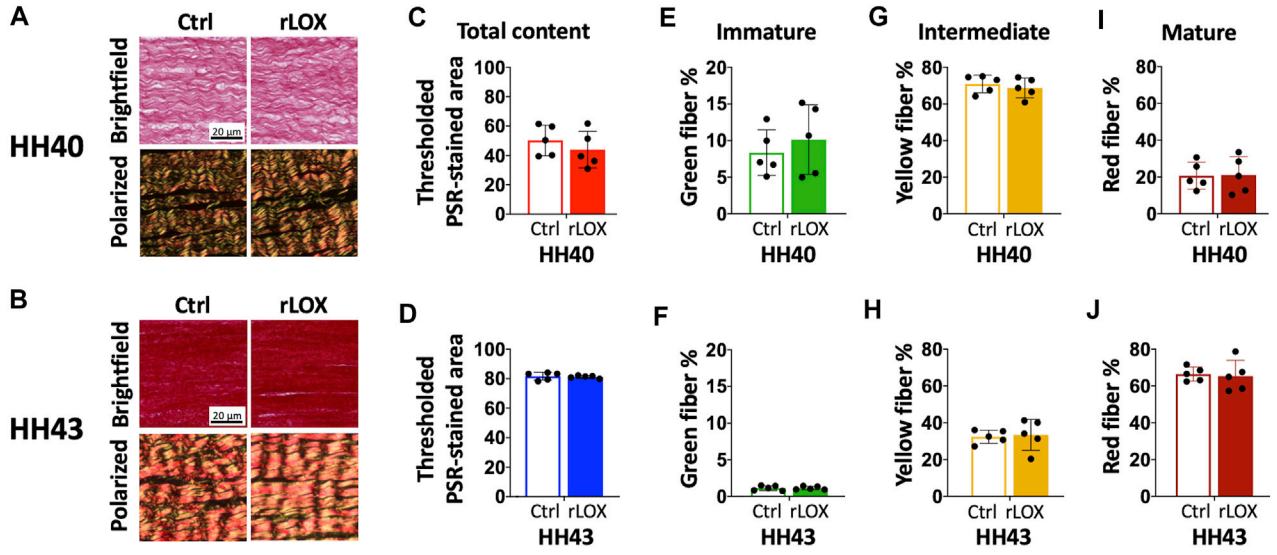

FIGURE 5
Collagen maturity of HH40 and HH43 tendon explants was not affected by rLOX treatment. **(A,B)** Representative brightfield and polarized microscopy images of PSR-stained HH40 **(A)** and HH43 **(B)** tendons that were treated with rLOX and Ctrl treatments. **(C,D)** Collagen content did not change with rLOX treatments in both HH40 **(C)** and HH43 **(D)** tendons. **(E–J)** Percentages of immature (green), intermediate (yellow), and mature (red) collagen did not change with rLOX treatments. **(E,F)** The percentage of immature collagen was not affected by rLOX treatments in both HH40 **(E)** and HH43 **(F)** tendons. **(G,H)** The percentage of intermediate collagen was not affected by rLOX treatments in both HH40 **(G)** and HH43 **(H)** tendons. **(I,J)** The percentage of mature collagen was not affected by rLOX treatments in both HH40 **(I)** and HH43 **(J)** tendons. Statistically significant differences were determined by Student *t*-test with $p < 0.05$. $n = 5$ per stage and treatment group.

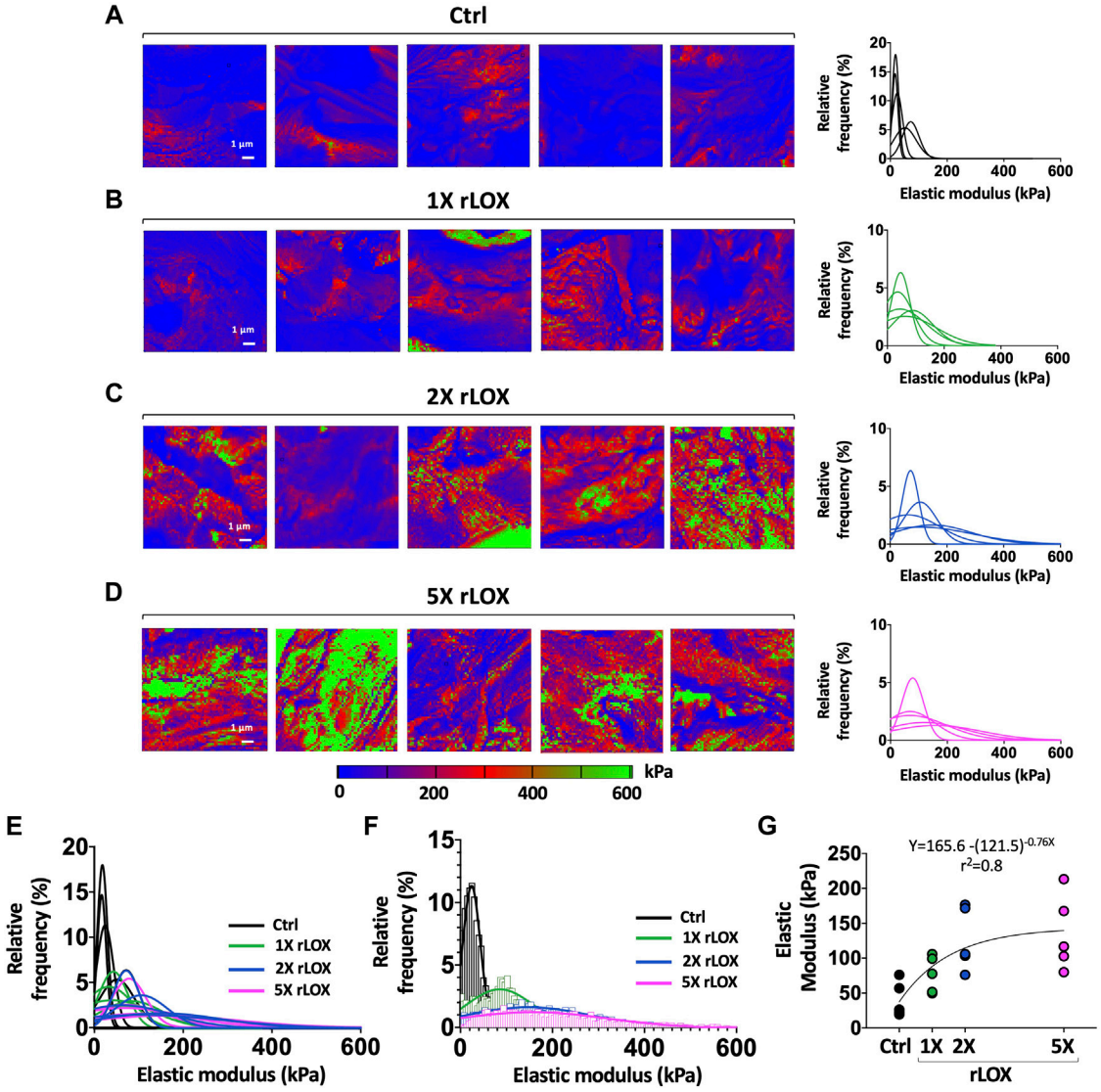

FIGURE 6
Plateau in elastic moduli of HH43 tendon explants was observed at higher rLOX concentration. **(A–D)** Elastic modulus maps and relative frequency histograms showed the shifts to higher elastic moduli between Ctrl (0X) **(A)** and 1X **(B)**, 2X **(C)**, and 5X **(D)** rLOX treatments. Treatment of 1X, 2X, and 5X rLOX led to wider distribution in the elastic modulus relative frequency histograms compared to Ctrl treatment. Relative frequency distribution of tendon elastic moduli almost overlapped between 2X and 5X rLOX treatments. The color scale of the elastic modulus maps was adjusted to capture the full range of maximum and minimum modulus values for all treatment groups. **(E)** All relative frequency distribution of tendon elastic moduli from 5 biological replicates from each treatment: Ctrl, 1X, 2X, and 5X rLOX. **(F)** Relative frequency distribution of tendon elastic moduli of one representative biological replicate from each treatment: Ctrl, 1X, 2X, and 5X rLOX. **(G)** Median tendon elastic moduli calculated from 4,096 data points per map increased significantly with rLOX treatments compared to Ctrl treatment. Tendon elastic modulus plateaued at higher rLOX concentration (exponential plateau fit, $r^2 = 0.8$). $n = 5$ per stage and treatment group. Note that the intensity bar for the heat map of elastic modulus in Panel has a different scale than in Panel 2 to capture the increases in elastic modulus with rLOX concentration.

concentrations (Figures 6A–D). Relative frequency histograms of the elastic moduli in these maps showed that elastic modulus distribution broadened and shifted to include higher elastic modulus values when treated with increasing rLOX concentrations (Figures 6A–F). Histograms of elastic moduli differed between tendons treated with 0X (Ctrl), 1X, and 2X rLOX (Figures 6A–C). In contrast, elastic modulus histograms appeared similar and overlapping for tendons treated with 2X and 5X rLOX, suggesting 2X and 5X rLOX had similar effects on elastic modulus (Figures 6C,D). Correspondingly, median elastic moduli of rLOX-treated tendons increased from 0X to 2X rLOX, but then appeared to plateau between 2X and 5X rLOX

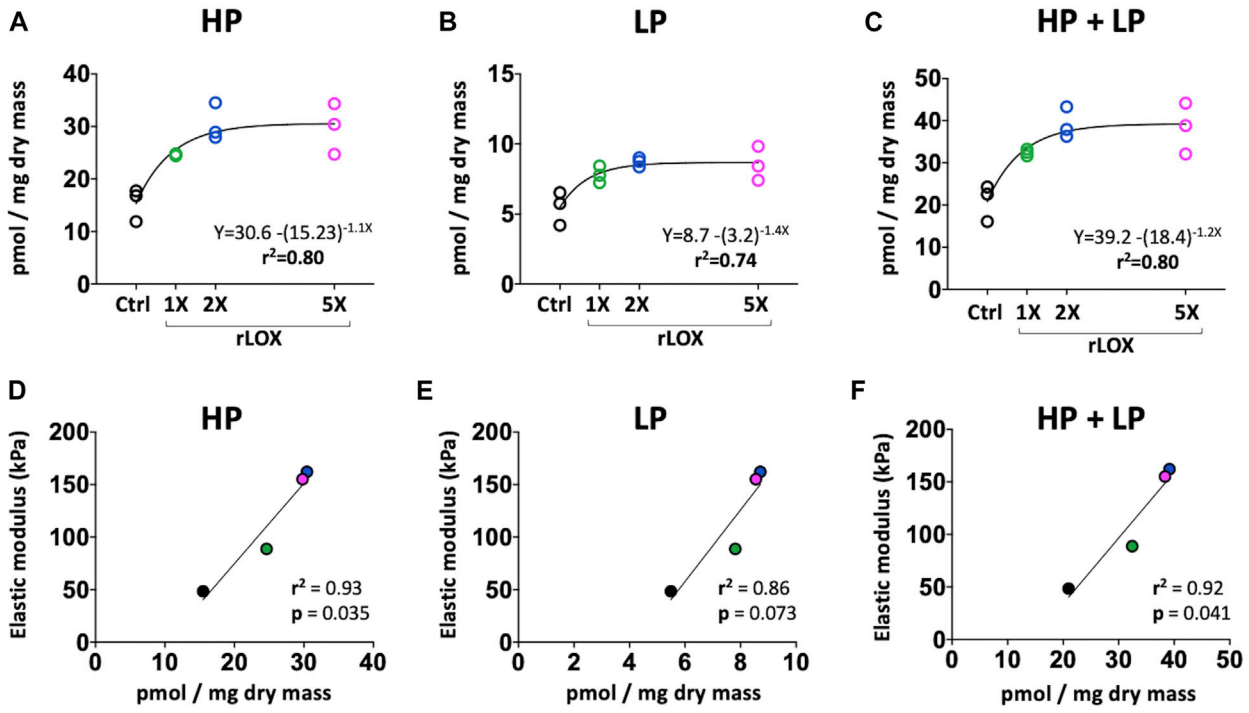

FIGURE 7
HP and LP crosslink density (normalized to dry mass). **(A–C)** HP **(A)**, LP **(B)**, and total HP and LP **(C)** crosslink density plateaued at higher rLOX concentrations (exponential plateau fit, r^2 = 0.7-0.8). **(D–F)** Correlation between LOX-mediated crosslink density and tendon elastic modulus. **(D)** HP crosslink density were highly and significantly correlated with tendon elastic modulus (r^2 = 0.93 and p = 0.035). **(E)** LP crosslink density showed high correlation with elastic modulus (r^2 = 0.86, p = 0.073). **(F)** Total HP and LP crosslink density were highly and significantly correlated with tendon elastic modulus (r^2 = 0.92 and p = 0.041). Statistically significant differences were determined by Pearson correlation and linear regression with $p < 0.05$. N = 3 per stage and treatment group.

concentrations, reflected by a plateau curve fit with r^2 = 0.8 (Figure 6G).

HP, LP, and total HP and LP crosslink densities of HH43 tendons treated with 0X (Ctrl), 1X, 2X, and 5X rLOX were measured using HPLC. Similar to elastic moduli, crosslink densities increased from 0X to 2X rLOX, and then plateaued between 2X and 5X rLOX (Figures 7A–C). With and without rLOX treatment, HP crosslink densities were at least 4 to 5 times higher than LP densities, which was consistent with previous reports (Marturano et al., 2014). Notably, HP and total HP and LP crosslink densities correlated highly and significantly with tendon elastic modulus (r^2 = 0.93, p = 0.035; r^2 = 0.92, p = 0.041; respectively) (Figures 7D–F).

Discussion

In this study, we demonstrated rLOX treatment can be used to controllably enhance the mechanical properties of developing tendons at different stages of functional tissue formation. Our exciting proof-of-concept data motivates the idea that a LOX-based therapeutic could be used throughout different phases of adult tendon healing to improve outcomes. As another application, a LOX-based intervention could potentially restore the mechanical properties of abnormally developing tendons during fetal development *in utero*. In this study, rLOX treatment increased tensile elastic modulus and peak strength in both HH40 and HH43 tendons. Nanoscale elastic modulus also increased significantly with rLOX treatment in both stage tendons. These changes in mechanical properties corresponded with changes in LOX-mediated crosslink density, whereas cell viability and collagen content and collagen fiber maturity did not change with rLOX treatment for either developmental stage. Interestingly, collagen fiber alignment in HH43 tendons was significantly enhanced by rLOX treatment. A particularly exciting finding was that crosslink density and tendon elastic modulus both plateaued at higher rLOX concentrations. The overlapping plateaus and the high correlation between elastic modulus and crosslink density (r^2 = 0.92; p = 0.041) may have been due to limited availability of neighboring lysine residues within the tendon. It is exciting to consider the possibility that this mechanism could prevent the tendon from over-stiffening by preventing over-crosslinking of collagen, though this requires further investigation. Our studies

demonstrate the potential for LOX-based therapeutic approaches to enhance tendon mechanical properties *via* LOX-mediated crosslinking which occurs naturally in the body. These novel findings have significant implications for strategies to treat adult tendon injuries, connective tissue disorders, and tendon-related birth abnormalities.

Tensile mechanical properties of tendon were significantly enhanced with rLOX treatment *in vivo*. Previously, we demonstrated LOX-mediated crosslinking of collagen is a key regulator of developing tendon mechanical properties. In particular, inhibition of LOX activity during tendon development inhibited the formation of LOX-mediated crosslinks (HP, LP) during development, which in turn prevented increases in elastic modulus (Marturano et al., 2013; Marturano et al., 2014). Our current study now demonstrates rLOX treatment can induce additional collagen crosslinking and lead to increases in tendon elastic modulus and peak stress without affecting peak strain (Figure 1). This enables the tendon to sustain greater mechanical load without requiring a change in length. A LOX-based therapeutic would be attractive, as LOX-mediated crosslinking is a natural regulator of tendon mechanical properties in human and other species (Eyre et al., 1984; Ng et al., 1996; Thorpe et al., 2010). In contrast, other studies have explored strategies to enhance tendon mechanical properties using crosslinkers that do not naturally occur within the human body, including genipin, 1-ethyl-3-(3-dimethylaminopropyl) carbodiimide, glutaraldehyde, and ultraviolet light (Caliari et al., 2011; Fessel and Snedeker, 2011; Fessel et al., 2014; Green et al., 2017). Unfortunately, these crosslinkers are associated with significant limitations, including cytotoxicity and significant reductions in metabolic activity at concentrations needed to enhance tendon mechanical properties (Caliari et al., 2011; Fessel and Snedeker, 2011; Fessel et al., 2014; Green et al., 2017). As an alternative to these efforts, our data suggest a LOX-based therapeutic would have significant clinical implications as it could enhance tissue mechanical properties *via* a crosslinking mechanism that occurs naturally in human without affecting cell viability.

Tensile elastic moduli of tendons at different stages of development were significantly enhanced with rLOX treatment *in vivo* (Figure 1). These data suggest that rLOX treatment could be effective when delivered at different phases of new tendon formation. The ability to enhance tendon mechanical properties *via* rLOX treatment at both an earlier and later phase of new tissue formation could be beneficial for adult tendon healing strategies as well as interventions for abnormal development. In particular, rLOX treatments could be administered at varying phases of new tissue formation after injury to adult tendon, presenting the possibility of accelerating tendon healing and return to function. It was exciting to observe that even with less organized collagen ECM, HH40 tendons increased in elastic modulus and peak stress with rLOX treatment, suggesting less organized ECM during adult tendon healing could also benefit from rLOX treatment. While it may be advantageous to administer interventions for tendon-related birth abnormalities as early as possible, this would be dependent on the timing of detection, which varies widely depending on the syndrome. *In utero*, congenital hand anomalies in which tendons are underdeveloped, are detected as early as the end of the first trimester. However, other tendon-related syndromes, such as clubfoot, are typically detected later in the second and third trimesters (Browne, 1937; Quintero et al., 1999; Lee et al., 2002; Krakow et al., 2009; Kowalczyk and Felus, 2016; Bogers et al., 2019; Bekiou and Gourounti, 2020). Thus, the ability to treat tendon abnormalities at varying stages of tissue development is important. However, it is also important to note that rLOX treatment would likely need to be tailored to the phase of tissue formation. In response to rLOX treatment at the same concentration, tensile elastic modulus of HH40 tendons increased 136% whereas that of HH43 tendons increased 35% compared to control treatments (Figure 1). During normal development, collagen content increases rapidly from HH38 through the latest embryonic stages (Marturano et al., 2013; Marturano et al., 2014). Considering HH40 tendons possess 2.8-fold lower crosslink-to-collagen ratio compared to HH43 tendons (Marturano et al., 2014), HH40 tendons appear to possess more available collagen sites for crosslinking than HH43 tendons. In this case, rLOX treatment would catalyze more collagen crosslinking in HH40 than HH43 tendons, leading to a higher fold increase in elastic modulus of HH40 than HH43 tendons compared to their respective controls. Future studies would be needed to optimize rLOX effects at different phases of tissue formation in adult and embryonic systems. It would be beneficial to develop a LOX-based therapeutic that can be effective at more than one stage of tendon tissue formation during adult tendon healing as well as during tendon development *in utero*.

Our previous work showed tensile modulus and nanoscale modulus both increase as a function of developmental stage (Marturano et al., 2013; Navarro et al., 2022). Here, we treated tendon explants with rLOX and used AFM to measure changes in the values and spatial distribution of nanoscale moduli. Similar to tensile moduli, median nanoscale elastic moduli of both HH40 and HH43 tendons increased significantly with rLOX treatment (Figures 2E,F). Firstly, these results suggest the enhancements in tendon mechanical properties measured with tensile testing and AFM were due to rLOX-induced crosslinking rather than unknown systemic effects induced by rLOX. Secondly, AFM maps revealed rLOX treatment shifted the spatial distribution of nanoscale moduli toward both higher values as well as greater heterogeneity within a tissue (Figures 2A–D, 6A–F). The AFM probe is sensitive to small-scale components in the tissue, including cells, fibrillar collagen, and other ECM components (Marturano et al., 2013). Previous AFM measurements of embryonic tendon also revealed that increases in nanoscale moduli are spatially

heterogeneous, highlighting collagen-rich regions that could be crosslinked by LOX and collagen-poor regions that would be minimally affected by LOX (Marturano et al., 2013). Consistent with this, the spatial heterogeneity of moduli across the tendon appeared to decrease when LOX activity was inhibited to block the formation of new crosslinks during development (Marturano et al., 2013). Taken together, rLOX treatment in this current study likely induced formation of new crosslinks in the regions that contain fibrillar collagen, and had little effect on regions that lacked available sites for collagen crosslinking. Consequently, elastic modulus would have increased in collagen-rich regions and been less affected in collagen-poor regions of the tendon. This heterogeneity was likely the source of the variabilities observed in AFM measurements both within a sample as well as between samples of the same stage and condition (Figures 2, 6).

The rLOX-induced increases in tensile modulus and nanoscale modulus demonstrate the potential for a therapeutic that promotes LOX-mediated crosslinking to promote tendon mechanical properties during new tissue formation, perhaps during adult tendon healing or fetal tendon development. A concern, however, is that a LOX-based therapeutic could lead to too many collagen crosslinks and consequently over-stiffen the tendon. To test this possibility, we treated explant tendons with increasing concentrations of rLOX (up to 5 times higher (5X rLOX) than the initial rLOX concentration tested) and used HPLC to characterize changes in crosslink density and AFM to characterize changes in mechanical properties. It was exciting to discover that increases in both crosslink density and median nanoscale modulus plateaued at higher rLOX concentrations, and that crosslink density and elastic modulus correlated linearly (Figures 7D–F). These findings suggest the plateau in elastic modulus at higher rLOX concentrations was due to the plateau in LOX-mediated collagen crosslink density. LOX catalyzes the conversion of lysine and hydroxylysine residues to reactive aldehydes within the telopeptide regions of collagen (Eyre et al., 1984; Kagan and Li, 2003). Crosslinking occurs when these reactive aldehydes are near enough to other aldehydes or lysine residues to spontaneously form covalent bonds. Thus, not only do lysine and hydroxylysine residues need to be available and accessible, but they also need to be in close physical proximity to other residues on adjacent collagen molecules, fibrils, or fibers for LOX-mediated collagen crosslinking to occur. It is possible that higher rLOX concentrations did not lead to additional crosslinks because there were no more available and accessible crosslinking sites in physical proximity. In the absence of additional crosslink formation, modulus also would not increase at the higher rLOX concentrations, which is what we observed (Figures 6, 7). It is intriguing to consider that this plateau may have occurred before the tendon could become overly stiff. In particular, 2X and 5X rLOX treatment of HH43 tendons led to an elastic modulus that was 280% higher than with control treatment (Figure 6). For comparison, normally developing tendon increases its elastic modulus 300% from HH43 to HH45 (the chick embryo hatches after HH45) (Navarro et al., 2022). It is also possible that rLOX induced cell behaviors that regulated, partially or wholly, the increases and plateau in tendon mechanical properties. Future studies will need to examine how the mechanical properties at plateau after rLOX treatment compare with the mechanical properties of non-treated healthy tendons, as the ability for tendon to intrinsically prevent over-crosslinking by LOX would be an enormous advantage for a therapeutic that promotes LOX-mediated crosslinking.

There was a smaller difference between AFM-determined elastic moduli of HH40 and HH43 tendons (Figure 2) compared to our previous study (Marturano et al., 2013). Here, we used AFM to probe sections of tendon bundles after *in vitro* culture with rLOX or vehicle for 3 days, whereas our previous work used tensile testing and AFM to characterize the mechanical properties of whole tendon (Marturano et al., 2013). It is possible that when freed from the larger tendon structure and sheath, the tendon bundle exhibited a lower elastic modulus, as detected by AFM indentation testing, because it was in a less constrained state. Additionally, it is possible that after 3 days of culture, there was a small but significant enough amount of water penetration to reduce the elastic modulus of the tendon bundle. These factors may have contributed to the smaller difference in AFM-determined elastic moduli of HH40 and HH43 tendons in the current study.

Collagen content and maturity for both HH40 and HH43 tendons were not affected by rLOX treatment (Figures 4, 5). Interestingly, rLOX treatment increased collagen alignment in HH43 but not HH40 tendons. Fibrillar collagen density was relatively low in HH40 tendons, with visible space between fibers in SHG images (Figures 4A,B). In contrast, HH43 tendons possessed higher fibrillar collagen density, with tighter packing and greater alignment in SHG images (Figures 4A,B). With more space to move around, collagen in HH40 tendons may have been less organized when crosslinked by exogenous rLOX. In this case, disorganized collagen matrix would persist in HH40 tendons. In HH43 tendons, however, collagen was already in more densely packed arrangements when exogenous rLOX was added. With little room to move around, new collagen may have incorporated into the highly organized network and further promoted alignment as density increased. Crosslinking by exogenous rLOX would further stabilize this collagen organization. Additional studies would be needed to test this hypothesis for the stage-dependent effect of rLOX treatment on collagen organization.

This study establishes the potential for a LOX-based therapeutic to enhance mechanical properties of tendon. However, to develop treatments for tendon healing, future studies should examine the effects of rLOX treatment on crosslink density and mechanical properties of adult tendons, both healthy and after acute or chronic injury. Future studies should also explore delivery strategies to target whole tendon and specific regions within tendon. We previously discovered elastin is not detected in embryonic tendons (Marturano et al., 2013), but future studies with adult tendon should consider how LOX-induced crosslinking of elastin may also affect tendon mechanical properties. It would also be important for future studies to examine how higher concentrations and longer durations of rLOX treatment time may affect tensile mechanical properties, crosslinking rate, and cell behavior. Here, we hypothesized that rLOX directly mediated new collagen crosslink formation, reflected by the significant increases in HP and LP crosslink density in both HH40 and HH43 tendons (Figure 7). However, it is also possible that rLOX induced cells to synthesize more LOX, which could also lead to increases in collagen crosslinking. Thus, it could be interesting to examine the effects of rLOX treatment on mechanical properties of acellular tissues. Based on our findings, a LOX-based therapeutic could be applied at different stages during fetal development to enhance elastic modulus of abnormally weak tendons associated with musculoskeletal disorders. Similarly, treatment could be applied at various phases of new tissue formation during adult tendon healing. However, in both cases, a LOX-based treatment to enhance tendon mechanical properties at different phases of tissue formation would require optimization, and also need investigation of sustainability and longer term effects. Taken together, the exciting data presented here demonstrate the potential to develop a therapeutic strategy based on naturally occurring LOX-mediated collagen crosslinking to restore mechanical properties and function after postnatal tendon injury and abnormal fetal tendon development.

Data availability statement

The original contributions presented in the study are included in the article/Supplementary Material, further inquiries can be directed to the corresponding author.

Ethics statement

All chick embryo experiments complied with Institutional Animal Care and Use Committee requirements at the University of Rochester and the University of Maryland.

Author contributions

PN designed and performed experiments and assays. AJ wrote the MATLAB code that was used to assess collagen maturity that contributed to Figure 5. CH and MG helped with the multiphoton imaging and the collagen content data analyses that contributed to Figure 4. AG and IH helped with cell counting that contributed to Figures 3B,C. PN and CK designed experiments, performed data analyses, interpreted the data, and wrote the manuscript. CK conceived the project. All authors have read and approved the submitted manuscript.

Funding

This study was supported in part by the National Institutes of Health under grant number NIAMS /NIH R01AR072886 (to CK).

Conflict of interest

The authors declare that the research was conducted in the absence of any commercial or financial relationships that could be construed as a potential conflict of interest.

Publisher's note

All claims expressed in this article are solely those of the authors and do not necessarily represent those of their affiliated organizations, or those of the publisher, the editors and the reviewers. Any product that may be evaluated in this article, or claim that may be made by its manufacturer, is not guaranteed or endorsed by the publisher.

References

Arvind, V., and Huang, A. H. (2021). Reparative and maladaptive inflammation in tendon healing. *Front. Bioeng. Biotechnol.* 9, 719047. doi:10.3389/fbioe.2021.719047

Arya, S., and Kulig, K. (2010). Tendinopathy alters mechanical and material properties of the Achilles tendon. *J. Appl. Physiol.* 108 (3), 670–675. doi:10.1152/japplphysiol.00259.2009

Bah, I., Fernandes, N. R. J., Chimenti, R. L., Ketz, J., Flemister, A. S., Buckley, M. R., et al. (2020). Tensile mechanical changes in the Achilles tendon due to Insertional Achilles tendinopathy. *J. Mech. Behav. Biomed. Mat.* 112, 104031. doi:10.1016/j.jmbbm.2020.104031

Bailey, A. J., Bazin, S., Sims, T. J., Le Lous, M., Nicoletis, C., Delaunay, A., et al. (1975). Characterization of the collagen of human hypertrophic and normal scars. *Biochimica Biophysica Acta - Protein Struct.* 405 (2), 412–421. doi:10.1016/0005-2795(75)90106-3

Bailey, A. J., and Light, N. D. (1985). Intermolecular cross-linking in fibrotic collagen. *Ciba Found. Symp.* 114, 80–96. doi:10.1002/9780470720950.ch6

Bank, R. A., Beekman, B., Verzijl, N., de Roos, J. A. D. M., Nico Sakkee, A., TeKoppele, J. M., et al. (1997). Sensitive fluorimetric quantitation of pyridinium and pentosidine crosslinks in biological samples in a single high-performance liquid chromatographic run. *J. Chromatogr. B Biomed. Sci. Appl.* 703 (1), 37–44. doi:10.1016/S0378-4347(97)00391-5

Bank, R. A., TeKoppele, J. M., Oostingh, G., Hazleman, B. L., and Riley, G. P. (1999). Lysylhydroxylation and non-reducible crosslinking of human supraspinatus tendon collagen: Changes with age and in chronic rotator cuff tendinitis. *Ann. Rheum. Dis.* 58 (1), 35–41. doi:10.1136/ard.58.1.35

Bekiou, A., and Gourounti, K. (2020). Reduced fetal movements and perinatal mortality. *Mat. Sociomed.* 32 (3), 227. doi:10.5455/msm.2020.32.227-234

Beredjiklian, P. K., Favata, M., Cartmell, J. S., Flanagan, C. L., Crombleholme, T. M., Soslowsky, L. J., et al. (2003). Regenerative versus reparative healing in tendon: A study of biomechanical and histological properties in fetal sheep. *Ann. Biomed. Eng.* 31 (10), 1143–1152. doi:10.1114/1.1616931

Bogers, H., Rifouna, M. S., Cohen-Overbeek, T. E., Koning, A. H. J., Willemsen, S. P., van der Spek, P. J., et al. (2019). First trimester physiological development of the fetal foot position using three-dimensional ultrasound in virtual reality. *J. Obstet. Gynaecol. Res.* 45 (2), 280–288. doi:10.1111/jog.13862

Bor, N., Coplan, J. A., and Herzenberg, J. E. (2009). Ponseti treatment for idiopathic clubfoot: Minimum 5-year followup. *Clin. Orthop. Relat. Res.* 467 (5), 1263–1270. doi:10.1007/s11999-008-0683-8

Browne, D. (1931). Congenital talipes equino-varus. *Br. Med. J.* 2 (3693), 696–699. doi:10.1136/bmj.2.3693.696

Browne, D. (1937). Talipes equino varus. *Postgrad. Med. J.* 13 (144), 349–362. doi:10.1136/pgmj.13.144.349

Caliari, S. R., Ramirez, M. A., and Harley, B. A. (2011). The development of collagen-GAG scaffold-membrane composites for tendon tissue engineering. *Biomaterials* 32 (34), 8990–8998. doi:10.1016/j.biomaterials.2011.08.035

Dang, A., and Davies, M. (2018). Rotator cuff disease: Treatment options and considerations. *Sports Med. Arthrosc. Rev.* 26 (3), 129–133. doi:10.1097/jsa.0000000000000207

Dayan, D., Hiss, Y., Hirshberg, A., Bubis, J. J., and Wolman, M. (1989). Are the polarization colors of picrosirius red-stained collagen determined only by the diameter of the fibers? *Histochemistry* 93 (1), 27–29. doi:10.1007/bf00266843

de Jong, J. P., Nguyen, J. T., Sonnema, A. J., Nguyen, E. C., Amadio, P. C., Moran, S. L., et al. (2014). The incidence of acute traumatic tendon injuries in the hand and wrist: A 10-year population-based study. *Clin. Orthop. Surg.* 6 (2), 196. doi:10.4055/cios.2014.6.2.196

Derwin, K. A., and Thomopoulos, S. (2020). Discovery to delivery in tendon research. *J. Orthop. Res.* 38 (1), 5–6. doi:10.1002/jor.24549

Di Ferrante, N., Leachman, R. D., Angelini, P., Donnelly, P. V., Francis, G., and Almazan, A. (1975). Lysyl oxidase deficiency in Ehlers-Danlos syndrome type V. *Connect. Tissue Res.* 3 (1), 49–53. doi:10.3109/03008207509152341

Eyre, D. R., Paz, M. A., and Gallop, P. M. (1984). Cross-linking in collagen and elastin. *Annu. Rev. Biochem.* 53, 717–748. doi:10.1146/annurev.bi.53.070184.003441

Eyre, D. R., Weis, M. A., and Wu, J. J. (2008). Advances in collagen cross-link analysis. *Methods* 45 (1), 65–74. doi:10.1016/j.ymeth.2008.01.002

Faul, F., Erdfelder, E., Lang, A.-G., and Buchner, A. (2007). G*Power 3: A flexible statistical power analysis program for the social, behavioral, and biomedical sciences. *Behav. Res. Methods* 39 (2), 175–191. doi:10.3758/BF03193146

Fessel, G., Cadby, J., Wunderli, S., van Weeren, R., and Snedeker, J. G. (2014). Dose- and time-dependent effects of genipin crosslinking on cell viability and tissue mechanics - toward clinical application for tendon repair. *Acta Biomater.* 10 (5), 1897–1906. doi:10.1016/j.actbio.2013.12.048

Fessel, G., and Snedeker, J. G. (2011). Equivalent stiffness after glycosaminoglycan depletion in tendon--an ultra-structural finite element model and corresponding experiments. *J. Theor. Biol.* 268 (1), 77–83. doi:10.1016/j.jtbi.2010.10.007

Fessel, G., Wernli, J., Li, Y., Gerber, C., and Snedeker, J. G. (2012). Exogenous collagen cross-linking recovers tendon functional integrity in an experimental model of partial tear. *J. Orthop. Res.* 30 (6), 973–981. doi:10.1002/jor.22014

Frank, C., McDonald, D., Wilson, J., Eyre, D., and Shrive, N. (1995). Rabbit medial collateral ligament scar weakness is associated with decreased collagen pyridinoline crosslink density. *J. Orthop. Res.* 13 (2), 157–165. doi:10.1002/jor.1100130203

Gazit, Y., Jacob, G., and Grahame, R. (2016). Ehlers-danlos syndrome-hypermobility type: A much neglected multisystemic disorder. *Rambam Maimonides Med. J.* 7 (4), e0034. doi:10.5041/rmmj.10261

Green, E. C., Zhang, Y., Li, H., and Minus, M. L. (2017). Gel-spinning of mimetic collagen and collagen/nano-carbon fibers: Understanding multi-scale influences on molecular ordering and fibril alignment. *J. Mech. Behav. Biomed. Mat.* 65, 552–564. doi:10.1016/j.jmbbm.2016.08.022

Helland, C., Bojsen-Møller, J., Raastad, T., Seynnes, O. R., Moltubakk, M. M., Jakobsen, V., et al. (2013). Mechanical properties of the patellar tendon in elite volleyball players with and without patellar tendinopathy. *Br. J. Sports Med.* 47 (13), 862–868. doi:10.1136/bjsports-2013-092275

Järvinen, T. A., Kannus, P., Maffulli, N., and Khan, K. M. (2005). Achilles tendon disorders: Etiology and epidemiology. *Foot Ankle Clin.* 10 (2), 255–266. doi:10.1016/j.fcl.2005.01.013

Junqueira, L. C., Montes, G. S., and Sanchez, E. M. (1982). The influence of tissue section thickness on the study of collagen by the Picrosirius-polarization method. *Histochemistry* 74 (1), 153–156. doi:10.1007/bf00495061

Jy, T. (2010). Directionality plugin for ImageJ [online]. Available at: https://imagej.net/plugins/directionality.

Kagan, H. M., and Li, W. (2003). Lysyl oxidase: Properties, specificity, and biological roles inside and outside of the cell. *J. Cell. Biochem.* 88 (4), 660–672. doi:10.1002/jcb.10413

Knitlova, J., Doubkova, M., Eckhardt, A., Ostadal, M., Musilkova, J., Bacakova, L., et al. (2021). Increased collagen crosslinking in stiff clubfoot tissue: Implications for the improvement of therapeutic strategies. *Int. J. Mol. Sci.* 22 (21), 11903. doi:10.3390/ijms222111903

Kowalczyk, B., and Felus, J. (2016). Arthrogryposis: An update on clinical aspects, etiology, and treatment strategies. *Arch. Med. Sci.* 12 (1), 10–24. doi:10.5114/aoms.2016.57578

Krakow, D., Lachman, R. S., and Rimoin, D. L. (2009). Guidelines for the prenatal diagnosis of fetal skeletal dysplasias. *Genet. Med.* 11 (2), 127–133. doi:10.1097/GIM.0b013e3181971ccb

Kuivaniemi, H., Peltonen, L., and Kivirikko, K. I. (1985). Type IX ehlers-danlos syndrome and Menkes syndrome: The decrease in lysyl oxidase activity is associated with a corresponding deficiency in the enzyme protein. *Am. J. Hum. Genet.* 37 (4), 798–808.

Kuo, C. K., Petersen, B. C., and Tuan, R. S. (2008). Spatiotemporal protein distribution of TGF-βs, their receptors, and extracellular matrix molecules during embryonic tendon development. *Dev. Dyn.* 237 (5), 1477–1489. doi:10.1002/dvdy.21547

Lee, S. H., Cho, J. Y., Song, M. J., Min, J. Y., Han, B. H., Lee, Y. H., et al. (2002). Fetal musculoskeletal malformations with a poor outcome: Ultrasonographic, pathologic, and radiographic findings. *Korean J. Radiol.* 3 (2), 113. doi:10.3348/kjr.2002.3.2.113

Marturano, J. E., Arena, J. D., Schiller, Z. A., Georgakoudi, I., and Kuo, C. K. (2013). Characterization of mechanical and biochemical properties of developing embryonic tendon. *Proc. Natl. Acad. Sci. U. S. A.* 110 (16), 6370–6375. doi:10.1073/pnas.1300135110

Marturano, J. E., Xylas, J. F., Sridharan, G. V., Georgakoudi, I., and Kuo, C. K. (2014). Lysyl oxidase-mediated collagen crosslinks may be assessed as markers of functional properties of tendon tissue formation. *Acta Biomater.* 10 (3), 1370–1379. doi:10.1016/j.actbio.2013.11.024

Masala, S., Manenti, G., Antonicoli, M., Morosetti, D., Claroni, G., Simonetti, G., et al. (2012). Real time evaluation of monolateral clubfoot with sonoelastography. Preliminary results. *Muscles Ligaments Tendons J.* 2 (1), 49–52.

Monaghan, M. G., Holeiter, M., Brauchle, E., Layland, S., Lu, Y., Deb, A., et al. (2017). Exogenous miR-29B delivery through a hyaluronan-based injectable system yields functional maintenance of the infarcted myocardium. *Tissue Eng. Part A* 24, 57–67. doi:10.1089/ten.TEA.2016.0527

Navarro, J., Korcari, A., Nguyen, P., Bah, I., AlKhalifa, A., Fink, S., et al. (2022). Method development and characterization of chick embryo tendon mechanical properties. *J. Biomech.* 133, 110970. doi:10.1016/j.jbiomech.2022.110970

Ng, G. Y., Oakes, B. W., Deacon, O. W., McLean, I. D., and Eyre, D. R. (1996). Long-term study of the biochemistry and biomechanics of anterior cruciate ligament-patellar tendon autografts in goats. *J. Orthop. Res.* 14 (6), 851–856. doi:10.1002/jor.1100140602

Nielsen, R. H., Couppé, C., Jensen, J. K., Olsen, M. R., Heinemeier, K. M., Malfait, F., et al. (2014). Low tendon stiffness and abnormal ultrastructure distinguish classic Ehlers-Danlos syndrome from benign joint hypermobility syndrome in patients. *FASEB J.* 28 (11), 4668–4676. doi:10.1096/fj.14-249656

Novotny, T., Eckhardt, A., Doubkova, M., Knitlova, J., Vondrasek, D., Vanaskova, E., et al. (2022). The possible role of hypoxia in the affected tissue of relapsed clubfoot. *Sci. Rep.* 12 (1), 4462. doi:10.1038/s41598-022-08519-z

Pan, X., Li, J. W., Brown, E. B., and Kuo, C. K. (2018). *Embryo movements regulate tendon mechanical property elaboration during development*. London: Philosophical Transactions of the Royal Society B: Mechanics of Development. doi:10.1098/rstb.2017.0325

Patel, B., Xu, Z., Pinnock, C. B., Kabbani, L. S., and Lam, M. T. (2018). Self-assembled collagen-fibrin hydrogel reinforces tissue engineered adventitia vessels seeded with human fibroblasts. *Sci. Rep.* 8 (1), 3294. doi:10.1038/s41598-018-21681-7

Quintero, R. A., Johnson, M. P., Mendoza, G., and Evans, M. I. (1999). Ontogeny of clenched-hand development in trisomy 18 fetuses: A serial transabdominal fetoscopic observation. *Fetal diagn. Ther.* 14 (2), 68–70. doi:10.1159/000020892

Raikin, S. M., Garras, D. N., and Krapchev, P. V. (2013). Achilles tendon injuries in a United States population. *Foot Ankle Int.* 34 (4), 475–480. doi:10.1177/1071100713477621

Ricard-Blum, S., Bresson-Hadni, S., Vuitton, D. A., Ville, G., and Grimaud, J. A. (1992). Hydroxypyridinium collagen cross-links in human liver fibrosis: Study of alveolar echinococcosis. *Hepatology* 15 (4), 599–602. doi:10.1002/hep.1840150408

Richards, B. S., Faulks, S., Rathjen, K. E., Karol, L. A., Johnston, C. E., Jones, S. A., et al. (2008). A comparison of two nonoperative methods of idiopathic clubfoot correction: The Ponseti method and the French functional (physiotherapy) method. *J. Bone Jt. Surgery-American Volume* 90 (11), 2313–2321. doi:10.2106/jbjs.G.01621

Royce, P. M., and Steinmann, B. (1990). Markedly reduced activity of lysyl oxidase in skin and aorta from a patient with Menkes' disease showing unusually severe connective tissue manifestations. *Pediatr. Res.* 28 (2), 137–141. doi:10.1203/00006450-199008000-00012

Sarmiento, P., and Little, D. (2021). Tendon and multiomics: Advantages, advances, and opportunities. *npj Regen. Med.* 6 (1), 61. doi:10.1038/s41536-021-00168-6

Sætersdal, C., Fevang, J. M., Fosse, L., and Engesæter, L. B. (2012). Good results with the Ponseti method: A multicenter study of 162 clubfeet followed for 2-5 years. *Acta Orthop.* 83 (3), 288–293. doi:10.3109/17453674.2012.693015

Sensini, A., Gualandi, C., Zucchelli, A., Boyle, L. A., Kao, A. P., Reilly, G. C., et al. (2018). Tendon fascicle-inspired nanofibrous scaffold of polylactic acid/collagen with enhanced 3D-structure and biomechanical properties. *Sci. Rep.* 8 (1), 17167. doi:10.1038/s41598-018-35536-8

Sereysky, J. B., Flatow, E. L., and Andarawis-Puri, N. (2013). Musculoskeletal regeneration and its implications for the treatment of tendinopathy. *Int. J. Exp. Pathol.* 94 (4), 293–303. doi:10.1111/iep.12031

Stein, M. J., Buckley, M. R., Manuele, D., Gutierrez, A., Loor, J. S., Nguyen, P. K., et al. (2019). Design of a bioreactor to assess the effect of passive joint loading in a live chick embryo in ovo. *Tissue Eng. Part C. Methods* 25 (11), 655–661. doi:10.1089/ten.TEC.2019.0114

Theodossiou, S. K., and Schiele, N. R. (2019). Models of tendon development and injury. *BMC Biomed. Eng.* 1, 32. doi:10.1186/s42490-019-0029-5

Thorpe, C. T., Stark, R. J., Goodship, A. E., and Birch, H. L. (2010). Mechanical properties of the equine superficial digital flexor tendon relate to specific collagen cross-link levels. *Equine Vet. J.* Suppl (38), 538–543. doi:10.1111/j.2042-3306.2010.00175.x

Trackman, P. C., Zoski, C. G., and Kagan, H. M. (1981). Development of a peroxidase-coupled fluorometric assay for lysyl oxidase. *Anal. Biochem.* 113 (2), 336–342. doi:10.1016/0003-2697(81)90086-5

Vitale, M. A., Vitale, M. G., Zivin, J. G., Braman, J. P., Bigliani, L. U., Flatow, E. L., et al. (2007). Rotator cuff repair: An analysis of utility scores and cost-effectiveness. *J. Shoulder Elb. Surg.* 16 (2), 181–187. doi:10.1016/j.jse.2006.06.013

Windisch, G., Anderhuber, F., Haldi-Brändle, V., and Exner, G. U. (2007). Anatomical study for an updated comprehension of clubfoot. Part II: Ligaments, tendons and muscles. *J. Children's. Orthop.* 1 (1), 79–85. doi:10.1007/s11832-006-0004-2

Wolman, M., and Kasten, F. H. (1986). Polarized light microscopy in the study of the molecular structure of collagen and reticulin. *Histochemistry* 85 (1), 41–49. doi:10.1007/bf00508652

Zhao, D., Liu, J., Zhao, L., and Wu, Z. (2014). Relapse of clubfoot after treatment with the Ponseti method and the function of the foot abduction orthosis. *Clin. Orthop. Surg.* 6 (3), 245. doi:10.4055/cios.2014.6.3.245

frontiers | Frontiers in Bioengineering and Biotechnology

TYPE Original Research
PUBLISHED 11 August 2022
DOI 10.3389/fbioe.2022.959210

Check for updates

OPEN ACCESS

EDITED BY
Rahul Gawri,
McGill University, Canada

REVIEWED BY
Francesco Travascio,
University of Miami, United States
Vicky Varghese,
Medical College of Wisconsin,
United States

*CORRESPONDENCE
Cheng-Kung Cheng,
ckcheng2020@sjtu.edu.cn
Zhi-Cai Shi,
zhicaishi@vip.sina.com
Ning-Fang Mao,
maonf@163.com

†These authors have contributed equally to this work and share first authorship

SPECIALTY SECTION
This article was submitted to Biomaterials,
a section of the journal
Frontiers in Bioengineering and Biotechnology

RECEIVED 01 June 2022
ACCEPTED 18 July 2022
PUBLISHED 11 August 2022

CITATION
Huang Z-B, Nie M-D, Zhang N-Z, Liu S, Yuan J-B, Lin X-M, Cheng C-K, Shi Z-C and Mao N-F (2022), Biomechanical evaluation of a short-rod technique for lumbar fixation surgery.
Front. Bioeng. Biotechnol. 10:959210.
doi: 10.3389/fbioe.2022.959210

COPYRIGHT
© 2022 Huang, Nie, Zhang, Liu, Yuan, Lin, Cheng, Shi and Mao. This is an open-access article distributed under the terms of the Creative Commons Attribution License (CC BY). The use, distribution or reproduction in other forums is permitted, provided the original author(s) and the copyright owner(s) are credited and that the original publication in this journal is cited, in accordance with accepted academic practice. No use, distribution or reproduction is permitted which does not comply with these terms.

Biomechanical evaluation of a short-rod technique for lumbar fixation surgery

Ze-Bin Huang[1†], Mao-Dan Nie[2†], Ning-Ze Zhang[3], Shu Liu[1], Jia-Bin Yuan[1], Xu-Miao Lin[1], Cheng-Kung Cheng[2*], Zhi-Cai Shi[1*] and Ning-Fang Mao[1*]

[1]Department of Spine Surgery, First Affiliated Hospital of Naval Medical University, Shanghai, China, [2]School of Biomedical Engineering, Shanghai Jiao Tong University, Shanghai, China, [3]Key Laboratory of Biomechanics and Mechanobiology, Ministry of Education, Beijing Advanced Innovation Center for Biomedical Engineering, School of Biological Science and Medical Engineering, Beihang University, Beijing, China

Objective: The purpose of this study was to analyze the stability and instrument-related complications associated with fixation of the lumbar spine using the Short-Rod (SR) technique.

Methods: Using finite element analysis, this study assessed the stability of a bilateral lumbar fixation system when inserting the pedicle screws at angles of 10°, 15°, and 20° to the endplate in the sagittal plane. Using the most stable construct with a screw angle, the model was then assessed with different rod lengths of 25, 30, 35, and 45 mm. The optimal screw inclination angle and rod length were incorporated into the SR model and compared against traditional parallel screw insertion (pedicle screws in parallel to the endplate, PPS) in terms of the stability and risk of instrument-related complications. The following parameters were evaluated using the validated L4–L5 lumbar finite element model: axial stiffness, range of motion (ROM), stress on the endplate and facet joint, von-Mises stress on the contact surface between the screw and rod (CSSR), and screw displacement.

Results: The results showed that the SR model with a 15° screw inclination angle and 35 mm rod length was superior in terms of construct stability and risk of complications. Compared to the PPS model, the SR model had lower stiffness, lower ROM, less screw displacement, and lower stress on the facet cartilage, the CSSR, and screws. However, the SR model also suffered more stress on the endplate in flexion and lateral bending.

Conclusion: The SR technique with a 15° screw inclination and 35 mm rod length offers good lumbar stability with a low risk of instrument-related complications.

KEYWORDS

implantation technique, short-rod technique, pedicle screw, screw inclination angle, rod length, biomechanical evaluation

Introduction

The function of the spine is to provide flexibility, support the upper body, and protect the spinal cord and nerve roots. Some idiopathic diseases and severe external loads may cause nerve compression and destabilize the spine (Bogduk, 2016). Pedicle screw fixation is considered the gold standard for stabilization of degenerative disk disease (Shih et al., 2012; Chu et al., 2019), and the most common practice is to insert pedicle screws in parallel to the endplate (PPS) and connect them with rods. The effectiveness of the PPS technique in providing primary stability to the lumbar spine is widely recognized (Fang et al., (2022). However, the PPS technique requires extensive tissue dissection to implant the internal fixation device, often resulting in muscle atrophy, back pain, and symptoms of failed back surgery (Fu et al., 2020).

Nonparallel screws can increase the biomechanical stability of the device by converging in the sagittal plane. Farshad et al. (2014) found that sagittal nonparallel screws have at least equal initial fixation strength compared to PPS. Pang et al. (2015) reported that proper angular inclination of the screw can significantly improve the stability of the screw. However, the screws in these studies were oriented in the same oblique orientation. In a clinical study, we noticed that changing the angle for ipsilateral screws to be inserted obliquely with different orientations into the vertebrae in the sagittal plane can tightly connect the tails of the screws so that a shorter rod is required, which allows for implantation through a smaller incision. We named this novel technique as the Short-Rod (SR) technique. Patients with small incisions experience less blood loss during surgery, a quicker return to daily activities, lower cost, and less postoperative chronic back pain and iatrogenic injury (Bresnahan et al., 2017; Momin and Steinmetz, 2020). However, despite the obvious advantages of the SR technique, there is no clear guidance on choosing a suitable screw inclination angle or rod length. In addition, screw fixation alters the biomechanical behavior of spinal structures, and complications associated with this technique have been frequently reported. Previous studies evaluated specific properties of the nonparallel screws, such as the screw pull-out strength (Farshad et al., 2014), but a comprehensive analysis of the biomechanical function and risk of the SR technique has not been considered.

Symptoms of degenerative disc disease are mostly due to instability of the lumbar spine (Bogduk, 2016). Assessing the stability of the lumbar spine, such as ROM and axial stiffness (Christine et al., 2019), is the most important indicator of the effectiveness of surgery. Postoperative complications are a major cause of re-operation and reduced patient quality of life, with endplate fracture, facet joint degeneration, screw loosening, and breakage being the most commonly reported (DieeN et al., 1999; Chang et al., 2017; Nie et al., 2019; Xi et al., 2021). The biomechanical evaluation of screw fixation systems by experimental methods is time-consuming, labor-intensive, and expensive. Finite element model (FEM) analysis can parametrically alter one input factor such as the force or moment and assess its impact on different screw insertion techniques (Kim et al., 2012). It is widely used for the mechanical analysis of lumbar internal fixation systems due to its reproducibility and repeatability (Dreischarf et al., 2014).

This study proposes to use the FEM to investigate the impact on the biomechanics of different screw inclinations and rod lengths using the SR technique, with the aim of defining appropriate parameters for stable fixation. Then, the biomechanical characteristics of the SR technique and PPS technique will be compared under different loading modes. The hypothesis of this study is that the SR technique offers better stability and a lower risk of instrument-related complications than the PPS technique.

Materials and methods

Development of an intact lumbar finite element model

A 3-dimensional lumbar model consisting of an L4–L5 functional spinal unit was reconstructed from CT scans (SOMATOM Definition AS+, Siemens, Germany) of a 30-year-old healthy female in Mimics 10.01 (Materialise Technologies, Belgium). The CT images were taken with a slice thickness of 0.625 mm. The solid model was built by reverse engineering in Geomagic Studio 10.0 (Geomagic Inc., United States) and Solidworks 2021 (SolidWorks Corp., MA, United States). The solid model mesh was then converted to a meshed model in Hypermesh 17.0 (Altair Engineering Corp., United States). Figure 1 shows the lumbar spine model, which contains the cortical bone, cancellous bone, posterior structure, endplate, nucleus pulposus, annulus fibrosus, and annulus fiber substance. The intervertebral disc height of the model in this study is 9.90 mm, the vertebral body height of L4 is 31.06 mm, and the vertebral body height of L5 is 28.56 mm, all of which are within the range reported in literature (Campbell-Kyureghyan et al., 2005), indicating that the model geometry is universal. Mesh convergence testing of the intact lumbar model was performed in Abaqus 2021 (Dassault Systemes Simulia Inc., France) using stress distribution. The element size was reduced until there was a negligible change in the *in situ* force in the disc. The resulting model consisted of 604,487 elements of 1 mm in size.

The properties of all components in the lumbar spine model are shown in Table 1. Collagen fibers were simulated using tension-only truss elements (T3D2) and embedded in the ground substance of the intervertebral disc with an average angle of ±30° to the endplates to form the annulus fibrosus. The ground substance was composed of eight layers 1.0 mm thick (Zhang et al., 2022). The volume ratio of the annulus fibrosus and

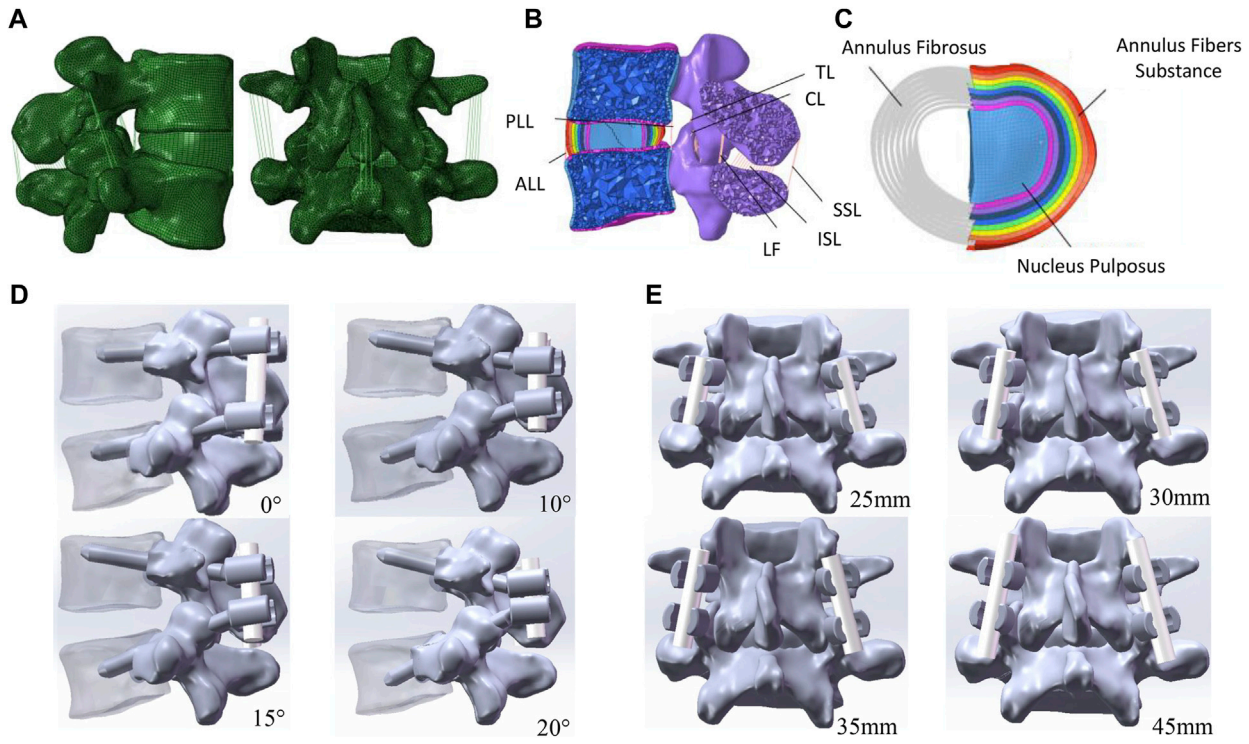

FIGURE 1
Finite element model of the lumbar spine. **(A)** L4–L5 functional spinal unit. **(B)** Transverse section of L4–L5 spine. **(C)** Intervertebral disc model. **(D)** Instrumented vertebra and pedicle screw model showing different screw angles. **(E)** Instrumented vertebra and pedicle screw model showing different rob lengths.

TABLE 1 Properties of different components in the lumbar spine model (Zhang et al., 2022).

Components	Young's modulus (MPa)	Poisson's ratio	Cross-sectional area (mm)
Cortical bone	12000	0.3	
Cancellous bone	100	0.2	
Posterior bone	3500	0.25	
Endplate	500	0.3	
Nucleus pulposus	1	0.49	
Annulus fibrosus	4.2	0.45	
Annulus fiber layers	360–550	—	0.76
ALL	15.6–20	0.3	63.7
PLL	10–20	0.3	18
LF	13–19.5	0.3	40
CL	7.5–33	0.3	32
ITL	12.0–58.7	0.3	1.8
ISL	8.8–15	0.3	25.2
SSL	9.8–12	0.3	35.1
Screw-rod system	110000	0.3	

nucleus pulposus was 3:7 (Goto et al., 2002). The cortical bone was 1 mm thick, and the endplates on the upper and lower surface of the vertebrae simulated the connection between the vertebrae and the intervertebral disc (Song et al., 2021). The thickness of the cartilage layer of the facet joint was assumed to be 0.2 mm (Kim et al., 2015). All ligaments were modeled using truss elements (T3D2) placed under tension only without compression, which included the anterior longitudinal ligament (ALL), posterior longitudinal ligament (PLL), interspinous ligament (ISL), supraspinous ligament (SSL), ligamentum flavum (LF), ligament intertransversarii (ITL), and capsular ligament (CL). The insertion locations of ligaments were referenced from the anatomical attachment points (Thompson, 2015). Node sharing was set between each ligament and its attachment point to the bone and between each vertebra and disc to increase the efficiency of modeling.

Validation of the intact lumbar finite element model

To validate the FE model, the L4–L5 intervertebral disc was subjected to pure compressive forces of 150, 400, and 1000 N, and the resulting stresses were compared with *in vitro* experimental data (Brinckmann and Grootenboer, 1991; Dreischarf et al., 2014). Considering the limitations on exercise postoperatively, the model was also placed under a 300 N axial (Song et al., 2021) and three different moments (3.0, 7.5, and 10 Nm) to simulate flexion, extension, lateral bending, and axial rotation. The resulting range of motion (ROM) of L4–L5 was compared with *in vivo* experimental results (Goel et al., 1985; Yamamoto et al., 1989; Karahalios et al., 2010). To validate the PPS model, the L4–L5 intervertebral disc was subjected to a 300 N axial and 7.5 Nm, and the resulting von-Mises stresses and ROM were compared with those in previous studies (Liu et al., 2020; Zhang et al., 2021).

Development of the surgical lumbar finite element model

The L4–L5 spinal segment was secured by bilateral fixation with polyaxial screws (Ø6.0 mm × 45 mm) and rods (Ø3.5). The pedicle screws were titanium alloy (Ti_6Al_4V). The coefficient of friction for the contact interfaces between the screws and vertebrae was set as 0.1 (Xu et al., 2013).

In the PPS model, the screws were placed horizontal to the endplate, while in the SR model, the screws were angled at 10° (SR-10°), 15° (SR-15°), and 20° (SR-20°) to the endplate plane (Figure 1D) (Farshad et al., 2014; Pang et al., 2015). The same insertion point was used regardless of screw inclination, and both techniques had the same projection angle on the horizontal plane. All screws were inserted under the instruction of an experienced surgeon.

Few studies discuss the effect of rod length on the screw-rod fixation system, but rod length is related to wound size and should be considered in terms of surgical approach and postoperative recovery. The rod lengths in this study were determined based on the author's clinical experience; 25 mm (SR-25 mm, tangent to screw head), 30 mm (SR-30 mm, 2.5 mm protrusion from screw head), 35 mm (SR-35 mm, 5 mm protrusion from screw head), and 45 mm (SR-45 mm, 10 mm protrusion from screw head) (Figure 1E).

Spinal stability was analyzed by measuring the range of motion (ROM) and compressive stiffness around the neutral zone of the spinal segment (Chen et al., 1990; Christine et al., 2019). Common instrument-related complications were also assessed, including the risk of endplate fracture, degeneration of facet joints, and screw loosening and breakage (DieeN et al., 1999; Nie et al., 2019; Xi et al., 2021). These risks were assessed using the stress distribution and displacement of the model (Chen et al., 2001).

The lower surface of L5 was fixed in all directions, and a reference point was established on the upper surface of L4 as the point of the force application. The properties were the same as those of the intact lumbar model. The axial compressive stiffness of each model under a 300 N load was determined from the load–displacement curves. Then, a 7.5-Nm moment was added to the surface of the model to simulate flexion, extension, lateral bending, and axial rotation. The ROM, stress on the endplate and facet cartilage, von-Mises stress on the screws and contact surface between the screw and rod (CSSR), and the screw displacement were calculated.

Results

Validation of the intact lumbar finite element model and pedicle screws in parallel to the endplate model

The mean intervertebral disc pressure at the L4–L5 segment was 0.147, 0.419, and 1.049 MPa under compressive forces of 150, 400, and 1000 N, respectively, which were within the range of experimental data (Brinckmann and Grootenboer, 1991; Dreischarf et al., 2014). The segmental ROM under a 300 N axial load and moments of 3, 7.5, and 10 Nm was comparable to experimental results from literature (Figure 2) (Goel et al., 1985; Yamamoto et al., 1989; Karahalios et al., 2010). These results confirm the reliability of the intact FE model.

In addition, the results of the PPS model were similar to those reported in other studies. Results from Liu et al. (2020) and this study show that the ROM of the PPS model, in comparison to the intact model, was reduced by approximately 70% in flexion, extension, and lateral bending and by approximately 50% in rotation. The maximum von-Mises stress on the screws in this

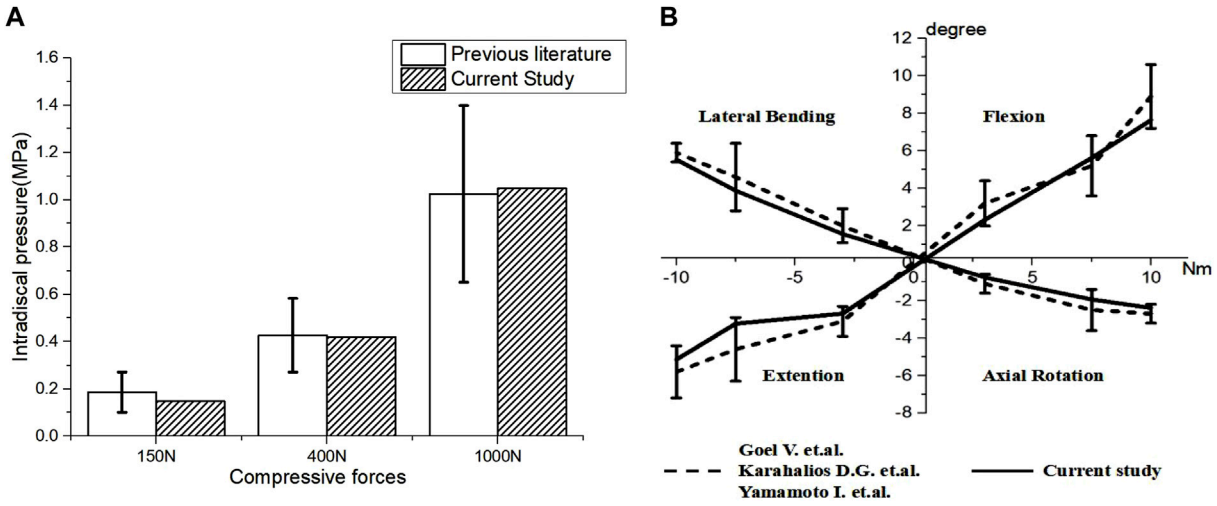

FIGURE 2
Validation of the L4–L5 spinal finite element model. **(A)** Comparison of intervertebral disc stress at the L4–L5 level and the *in vitro* experimental data from Dreischarf et al. (2014) and Brinckmann and Grootenboer, 1991, **(B)** ROM of L4–L5 lumbar spine.

study was similar to findings reported by Zhang et al. (2021). This supports the validity of the PPS model in this study.

Influence of screw inclination

As shown in Figure 3, implantation of the bilateral supports caused a significant increase in the axial compressive stiffness of the lumbar segment under a 300 N axial compressive force. Under the same load, the SR-15° model had the greatest stiffness, increasing by 19.9% over the intact spine, while the SR-20° model was 15.74% stiffer than the intact model. Correspondingly, the SR-15° model had the smallest ROM, and the SR-20° model had the largest. These results indicate that the SR-15° implantation method provided the greatest stability to the lumbar spine.

Of all models and motion patterns simulated, the mean stress on the endplate was smallest in the SR-15° model, and SR-10° was the largest in flexion, extension, lateral bending, and axial rotation (Figure 4). The SR-15° model had the smallest facet cartilage stress, and SR-10° had the greatest. This demonstrated that the risk of endplate fracture and facet joint degeneration was considerably lower in SR-15° than in SR-10°. The maximum von-Mises stress on the screw increased as the angle of inclination increased, and the stress values were more evenly distributed than in other models. The SR-20° model showed the greatest stress on the screws (Figure 5). Greater screw displacement increases the risk of screw loosening. The maximum screw displacement in the three models was in flexion, and the SR-15° model had the smallest screw displacement. The SR-15° model had the lowest von-Mises stress at the CSSR increased as the angle of inclination increased, and the maximum stress for all models was located to the right of L5, shown in Figure 5.

Influence of rod length

Based on the abovementioned results, it is recommended to angle the pedicle screws at 15° to the endplate plane (SR-15°). As shown in Figure 6, under a 300 N axial load, the SR-35 mm model had the largest axial stiffness and the SR-25 mm had the smallest. There was little variation in the ROM when using different rod lengths, but SR-35 mm had the smallest ROM. These results indicate that the SR-35 mm model could offer the best restraint to the lumbar spine. The SR-30 mm model had higher stress on facet cartilage with different rod lengths. The SR-35 mm model had the lowest von-Mises stress on the endplate (Figure 7). However, the stress on the screws was smallest in extension and lateral bending for SR-30 mm, and the screw displacement was relatively large (Figure 8). The von-Mises stress at the CSSR was smallest in the SR-35 mm model and was evenly distributed.

Feasibility of the short rod technique

Due to the excellent performance of the bilateral fixation system with 15° screw inclination and 35 mm rod, these parameters were used incorporated into the Short-rod (SR) technique to analyze the stability of the fixation and risk of complications. As shown in Figure 9, after implantation, the axial stiffness of the models increased, while there was a reduction in the ROM, endplate stress, and facet cartilage stress. The axial

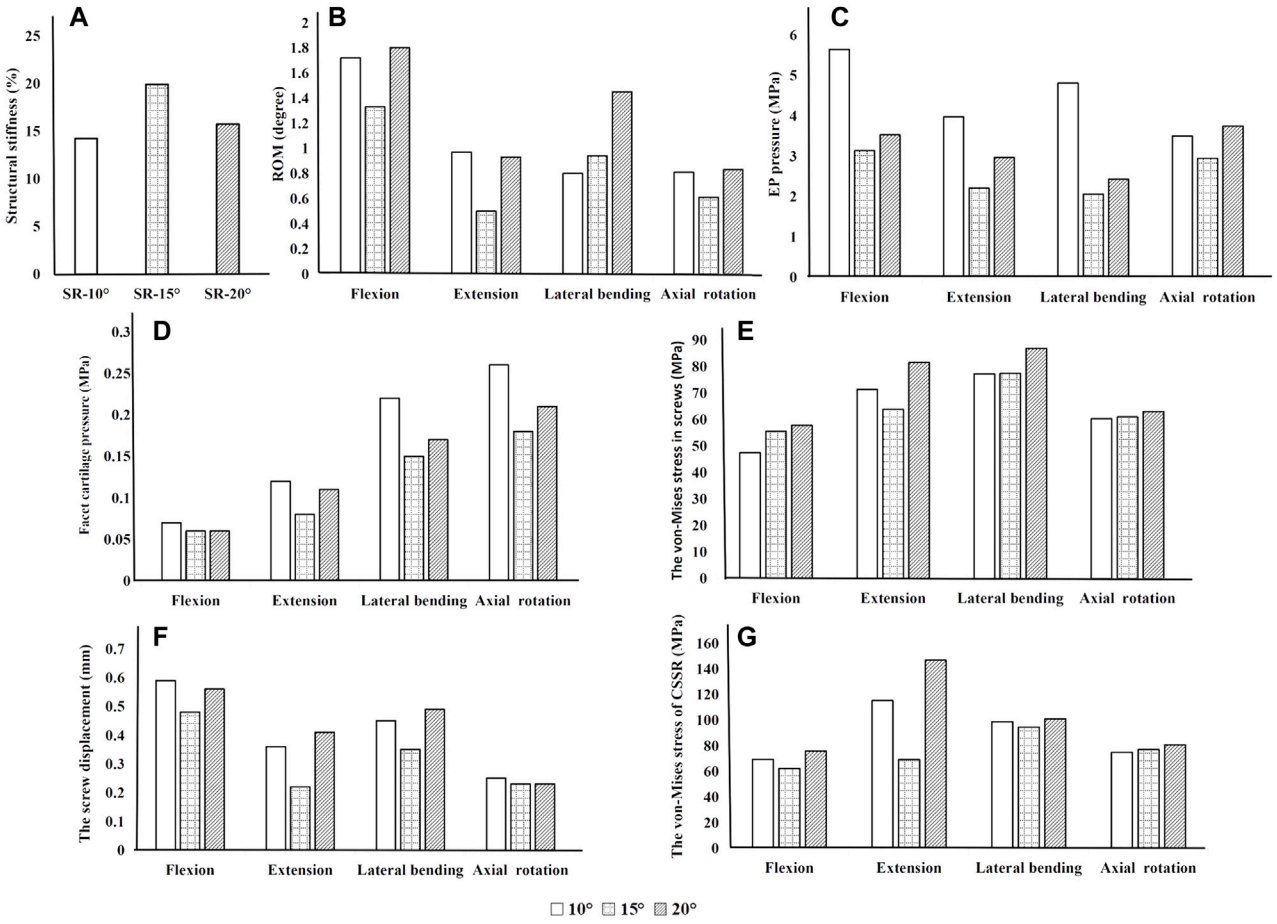

FIGURE 3
Parameters of the models for different screw inclination angles when placed under flexion, extension, lateral bending, and axial rotation. **(A)** Axial stiffness, **(B)** segmental ROM, **(C)** von-Mises stress on the endplate, **(D)** von-Mises stress on facet cartilage, **(E)** von-Mises stress on screws, **(F)** displacement of pedicle screws, and **(G)** von-Mises stress of CSSR.

stiffness of the SR model was slightly higher than that of the PPS model. The SR model had a smaller ROM and was more restricted than the PPS model. The endplate stress in the SR model was slightly lower than in the PPS model in extension and axial rotation (Figure 10). Similarly, the SR model showed lower stress on the facet cartilage than the PPS model.

The SR model had lower screw stress than the PPS model (Figure 11). The SR model also produced smaller screw displacement in all motions. The stress at the CSSR of the SR model was lower, and the maximum von-Mises stress occurred to the right of L5, implying a higher risk of fracture.

Discussion

This study aimed to assess lumbar stability when using the Short-rod (SR) technique at the L4–L5 level in a validated finite element model (FEM). The SR method allows for a smaller incision because of the angled screw insertion and shorter rod required for fixation. In this study, the setup with a 15° screw angle and a rod with 5 mm protrusion from the screw head offered the greatest lumbar stability and lowest risk of complications and thus is recommended for clinical use. The results show that the SR technique is more stable than the traditional PPS technique and carries less risk of facet joint degeneration, but this method also has a higher risk of endplate fracture in flexion and lateral bending.

The placement of screws in the vertebrae should be carefully considered when planning surgery because incorrect or unsuitable placement can have a major impact on clinical outcomes and patient mobility. Inappropriate placement may also compromise the structural stability of the lumbar spine, increasing the risk of fracture and screw loosening. This study assessed the stability of the lumbar spine and risk of

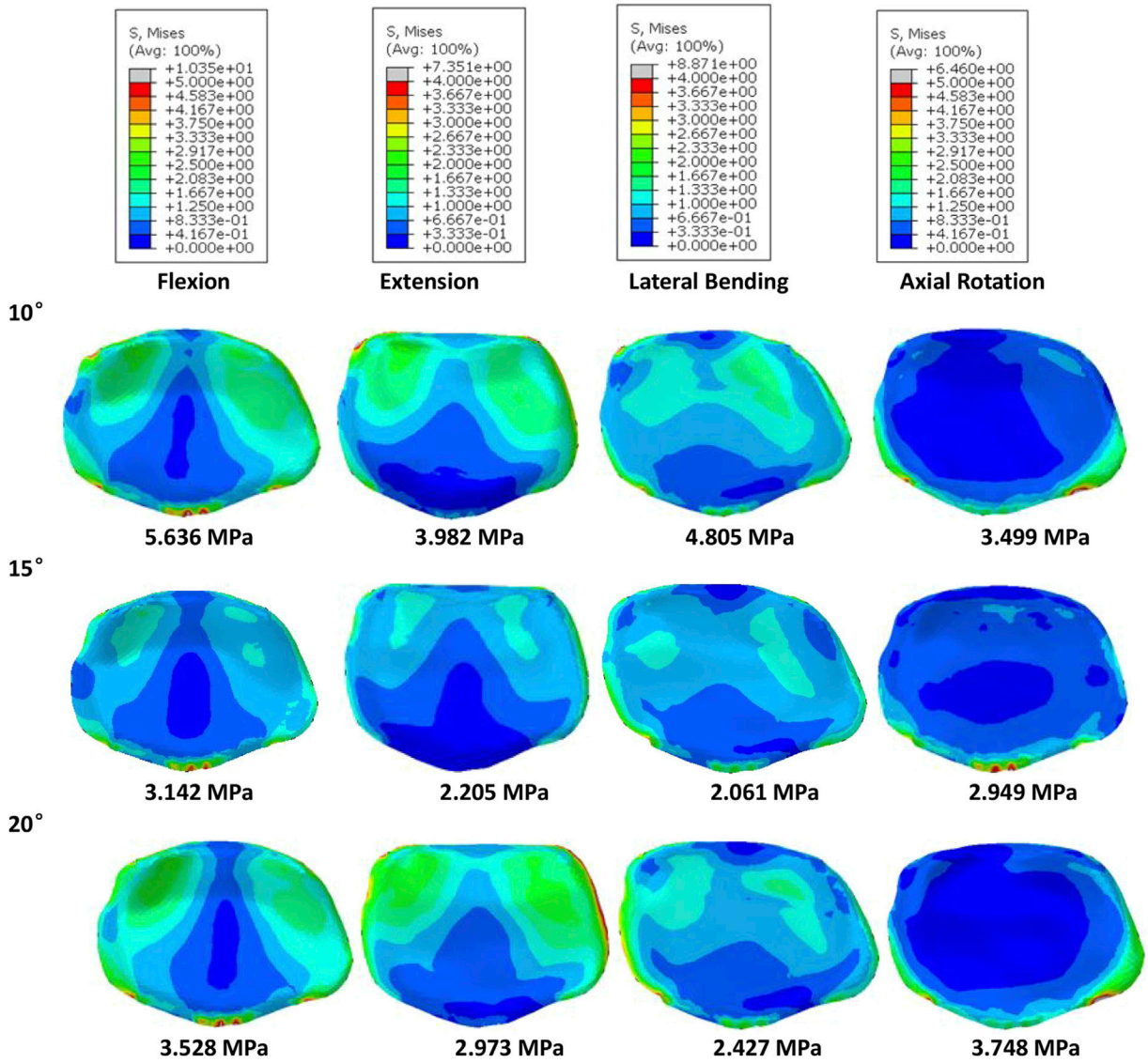

FIGURE 4
Von-Mises stress on the L4 endplate of the models for different screw inclination angles when placed under flexion, extension, lateral bending, and axial rotation, with the mean stress noted beneath each image.

complications when screws were inserted at 10° (SR-10°), 15° (SR-15°), and 20° (SR-20°) relative to the vertebral endplate. The SR-15° model has the greatest stiffness and the smallest ROM, indicating a more stable spine. Once the screw type is selected, the major factors affecting the holding power of pedicle screws are bone density and insertion angle (Varghese et al., 2017; Varghese et al., 2018). Pull-out strength predicts the initial stability of the fusion constructs post operation. Poorer bone quality with lower pull-out strength has been reported in many pieces of literature (Varghese et al., 2017). However, the effect of insertion angle is still controversial. Varghese et al. reported the pull-out force decreases with an increase in insertion in synthetic cancellous bone (Varghese et al., 2017), but (Farshad et al., 2014) reported that increasing the angle of the screws can enhance the pull-out strength with animal bone. Different materials may lead to completely different conclusions. Tilting the screws was found to increase the compressive stiffness and reduce the ROM in this study by a validated human lumbar spine model. The result seems to support Farshad's conclusion more, perhaps because of the more similar material properties. However, the SR-15° model was significantly more stable than SR-20°. This may be due to the shorter projection length of screws in the sagittal plane of the SR-20° model, which would reduce contact with the anterior column of the vertebral body. An

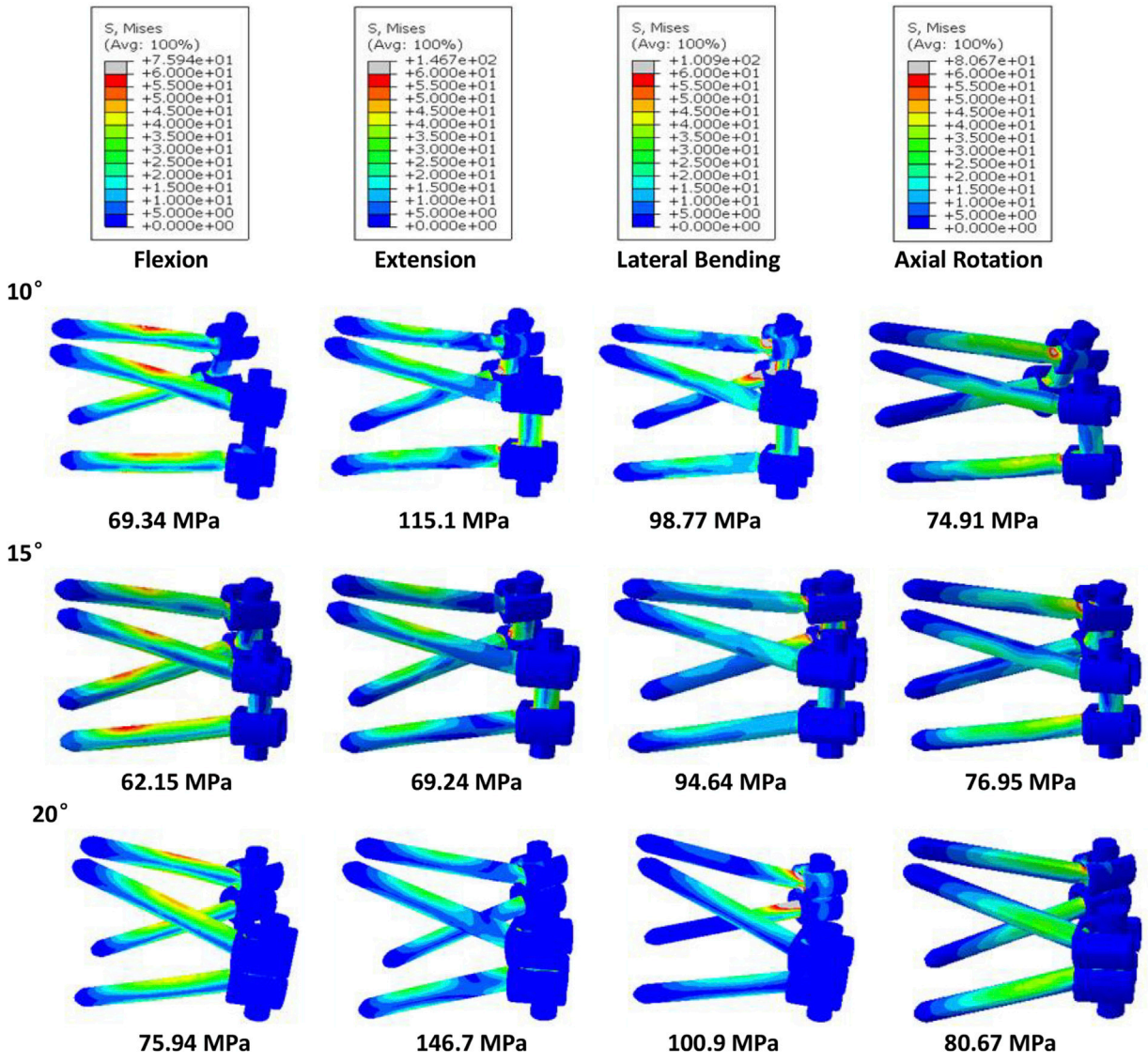

FIGURE 5
Von-Mises stress on the screws of the models for different screw inclination angles when placed under flexion, extension, lateral bending, and axial rotation, with the peak stress noted beneath each image.

assessment of potential instrument-related complications showed that SR-15° had the lowest stress on the vertebral endplate and facet cartilage, which is expected to reduce the risk of fracture and degeneration. A high number of cases of lower back pain in the general population are associated with endplate fracture in daily life (DieeN et al., 1999), while the SR-15° approach may reduce the incidence of back pain due to the lower risk of endplate fracture, but it still needs to be further assessed through a clinical study. High stress concentrations can lead to breakage of the fixation system (Newcomb et al., 2017), so the high stress observed on the CSSR to the right of L5 is of particular concern. As the screw angle increases, so does the risk of screw breakage. SR-15° was observed with moderate stress levels on the screws, more uniform stress distribution, and smaller screw displacement than both SR-10° and SR-20°, which can effectively reduce the risk of complications related to screw fixation. Krag et al. (1988) found that screw displacements over 0.7 mm could lead to trabecular bone damage, and all models in this study recorded a screw displacement less than 0.59 mm with little risk of screw loosening. Although we did not perform pull-out experiments, we predict that SR-15° has better pull-out strength based on the higher lumbar stiffness and less screw displacement. In addition, when placing the screw, this study found that a 20° inclination

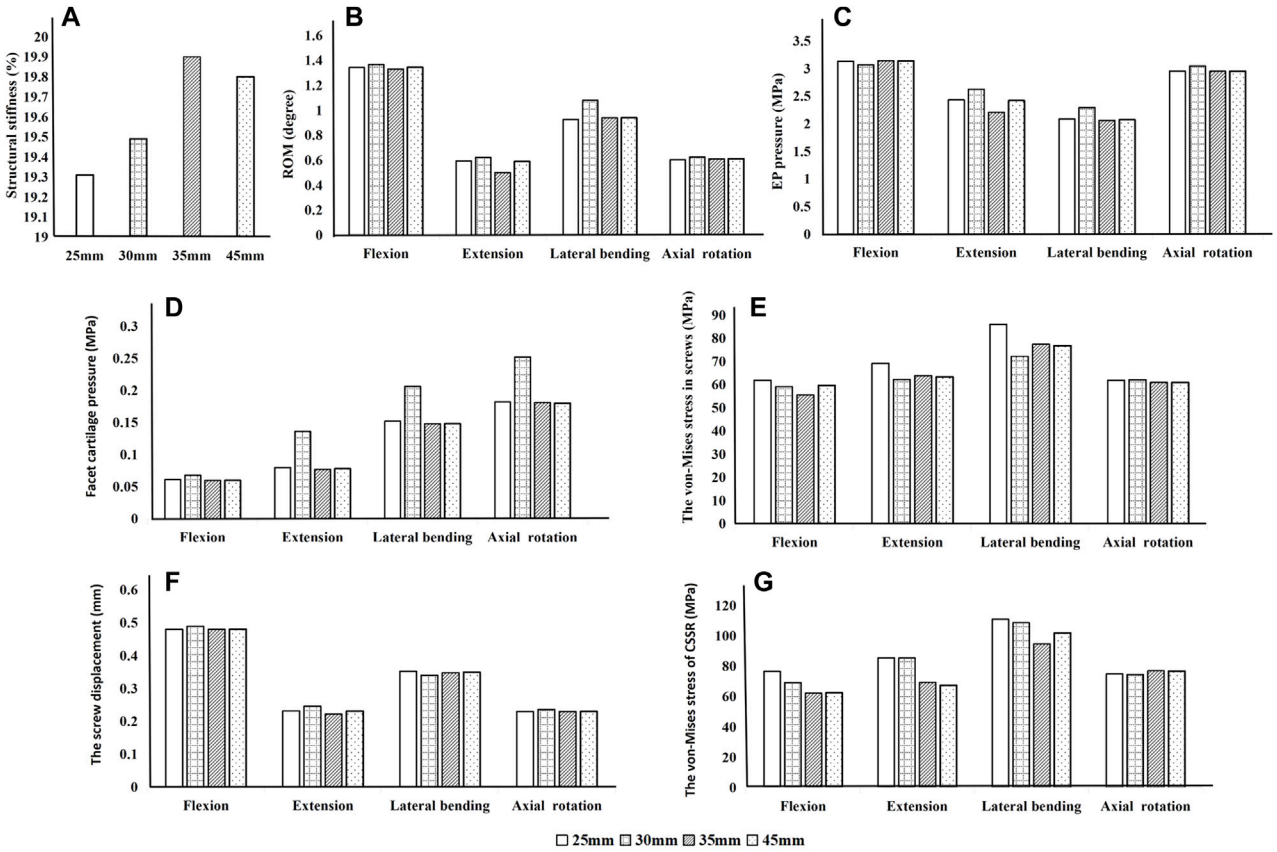

FIGURE 6
Parameters of the models for different rod lengths when placed under flexion, extension, lateral bending, and axial rotation. **(A)** Axial stiffness, **(B)** ROM, **(C)** von-Mises stress on endplates, **(D)** von-Mises stress on facet cartilage, **(E)** von-Mises stress on pedicle screws, **(F)** displacement of pedicle screws, and **(G)** von-Mises stress at the contact surface between the screw and rod (CSSR).

may cause the tail of the screw to collide and increase the risk of intraoperative penetrating the vertebral endplate or damaging the pedicle because the lumbar spine is physiologically lordotic (Yang et al., 2019), which greatly increases the difficulty of the operation.

This study also compared the biomechanical characteristics of different rod lengths. With the SR method, the screw on the ipsilateral side is at an acute angle. Using a uniaxial screw will result in greater screw reduction force and more axial slip and is more prone to axial slip than uniplanar and polyaxial screws (Serhan et al., 2010). Therefore, polyaxial screws were used in this study, which also allowed the screw head to be angled to accommodate the rod to improve seating and reduce axial slip. To assess the effect of rod length on stability, we compared stiffness and ROM across the four groups. The results show that SR-25 mm had lower stiffness than the other three groups, indicating a poor overall resistance to deformation. This may be due to the shorter rods that do not extend beyond the distal screw heads, causing inadequate engagement with the screw head (Serhan et al., 2010). In contrast, the longer rods that extended past the screw head could provide a buffer for rod slippage. The SR-35 mm and SR-45 mm constructs had a lower ROM. This study also assessed the relationship between rod length and risk of complications. The results showed that SR-35 mm had the smallest screw displacement and screw stress, while SR-25 mm had high screw stress, suggesting that the longer rod length may decrease the force on the screw. However, SR-35 mm and SR-45 mm had little difference on the stress on the endplates, facet cartilage, or CSSR, while SR-45 mm requires a larger incision for implantation. Although there was no significant difference in results between groups with different rod lengths, this study recommends using the SR-35 mm setup based on the numerical superiority of the results.

Based on the assessment of biomechanical characteristics of the lumbar spine when using different screw inclinations and rod lengths, we recommend a 15° screw inclination and a rod length of 35 mm for the SR technique.

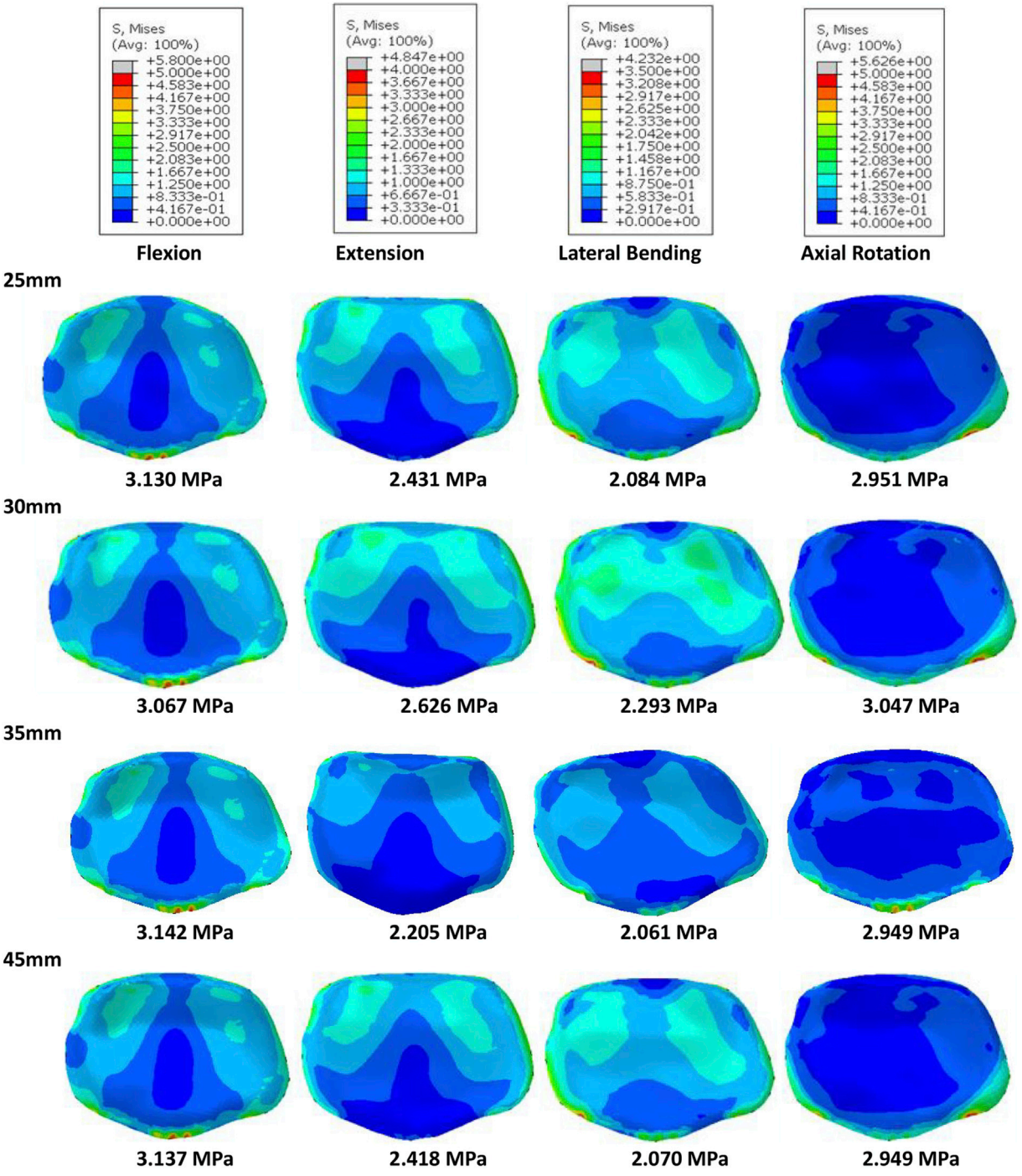

FIGURE 7
Von-Mises stress on the L5 endplate of the models for different rod lengths when placed under flexion, extension, lateral bending, and axial rotation, with the mean stress noted beneath each image.

This study evaluated the stability of the SR technique by comparing the axial stiffness and ROM against the PPS technique. The results showed that the SR technique has greater stiffness and a smaller ROM, which can provide better stability to the vertebrae. The pedicle is the strongest part of the vertebra due to the surrounding hard cortical bone, and the inclination of the screws increases the contact area with the cortical bone (Xi et al., 2021), which may enhance the

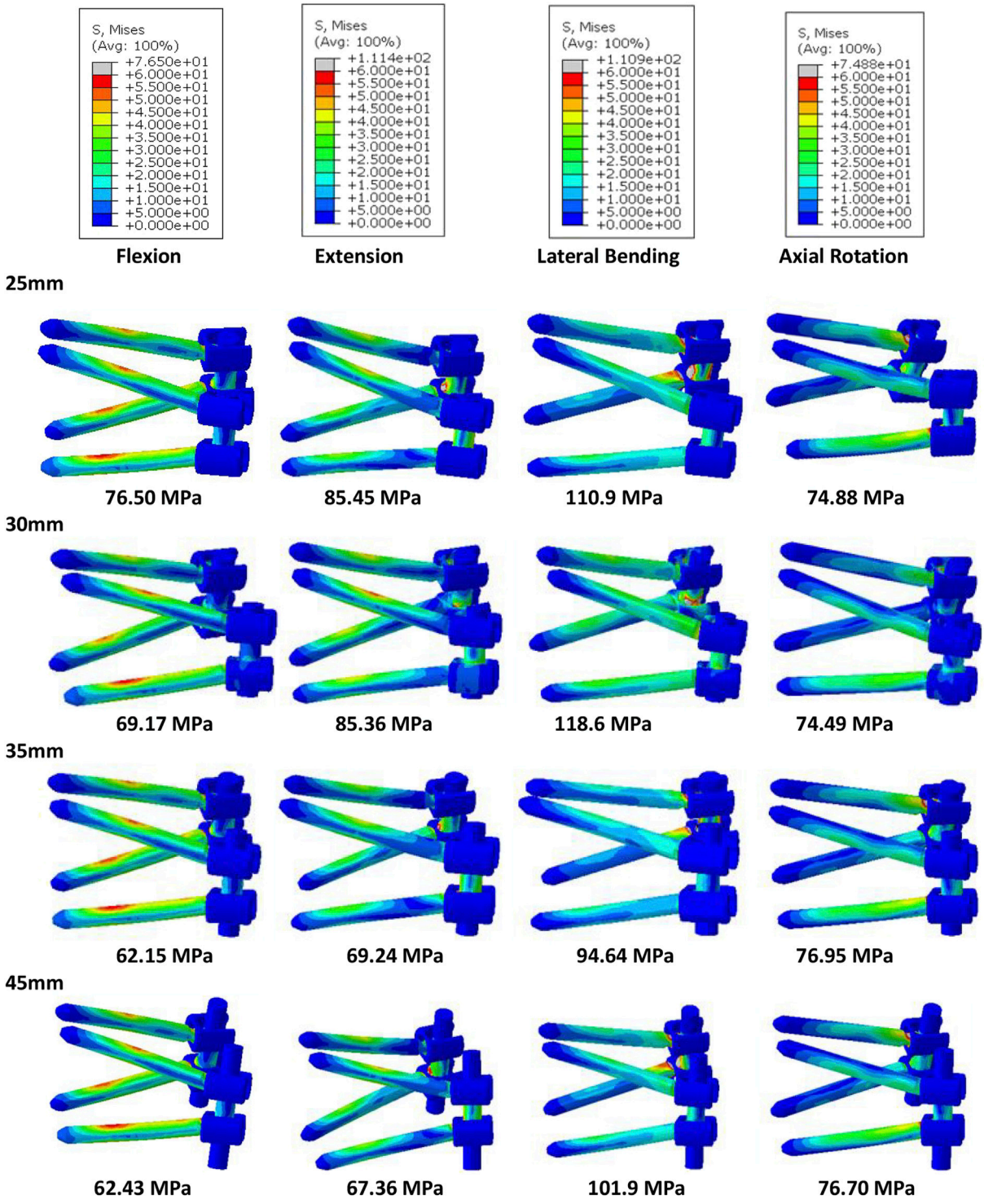

FIGURE 8
Von-Mises stress on the screws of the models for different rod lengths when placed under flexion, extension, lateral bending, and axial rotation, with the peak stress noted beneath each image.

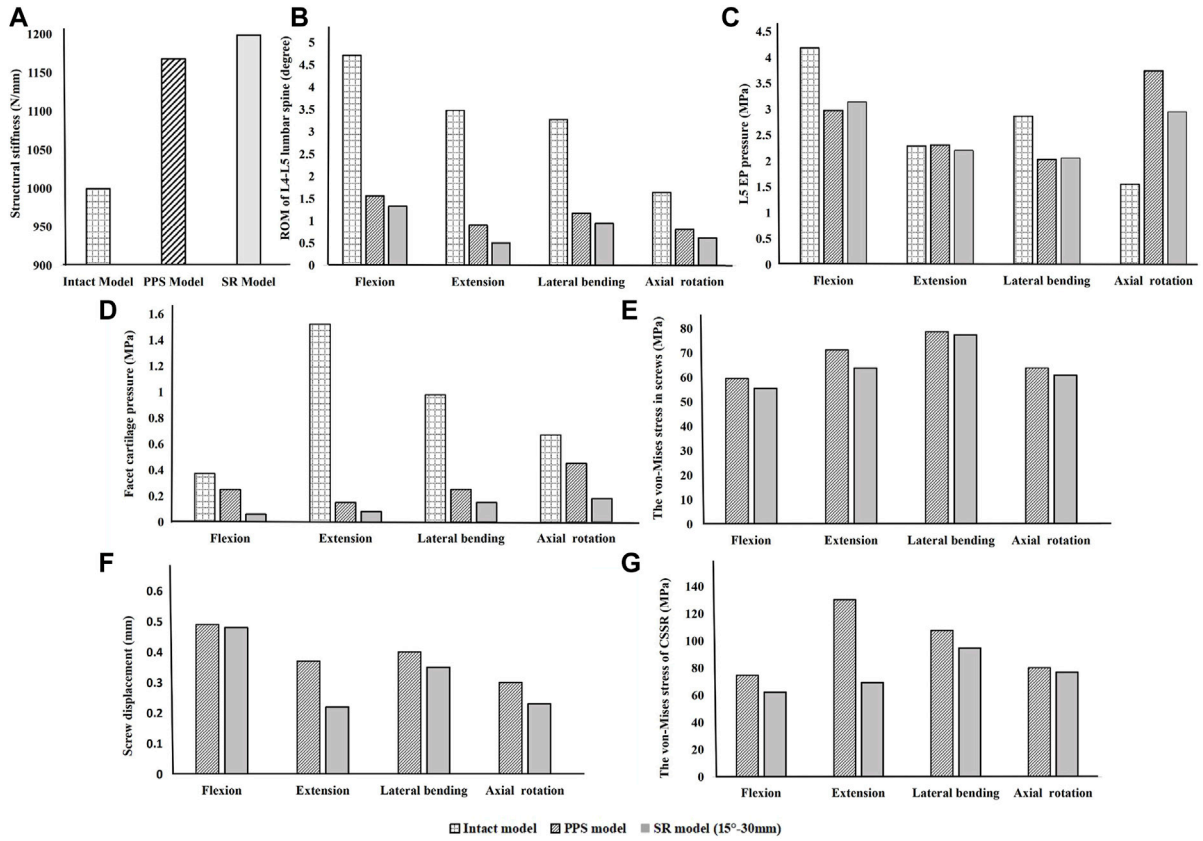

FIGURE 9
Comparison of the intact model, PPS model, and SR model. **(A)** Axial stiffness, **(B)** ROM, **(C)** endplate pressure, **(D)** von-Mises stress on facet cartilage, **(E)** von-Mises stress in screws, **(F)** displacement of pedicle screws, and **(G)** von-Mises stress at CSSR under flexion, extension, lateral bending, and axial rotation.

biomechanical stability of the SR technique. İnceoğlu et al. (2011) also found that increasing the contact area between the screw and cortical bone can increase the screw pullout resistance. Additionally, the SR technique requires a smaller incision than the PPS method, resulting in less disruption of the lumbar musculature. Since the lumbar musculature plays an important role in stability (Panjabi, 2003), it is possible that the SR technique will result in a more stable spine post-operatively and bring shorter fusion times.

Securing a segment of the lumbar spine will result in a stress differential between fixed and non-fixed segments, which is accepted as the main factor in the development of adjacent segment degeneration (ASD) (Hikata et al., 2014; Park et al., 2018). The excellent stability and stiffness of SR constructs can reduce the risk of ASD and improve the long-term clinical outcome. In addition, the entry point of screws with the PPS method is close to the facet joint of the adjacent segment, and there is a risk of damage to the articular facet, which can lead to further degeneration of ASD (Wang et al., 2022).

While playing an important role in the physiological function of the lumbar spine, facet joints also carry 6%–30% of the axial compressive load (Yin et al., 2020). This loading may also accelerate the degeneration of the facet joint, especially in people over 60 years of age (Yin et al., 2020). Such degeneration usually begins with changes in the articular cartilage and eventually leads to destruction of the entire joint and tissues. This study found that the SR method resulted in less facet cartilage stress than PPS in the surgery segment, which could reduce degeneration of the facet joint.

The fracture of the endplate is one of the common complications after lumbar fusion surgery, reported with a rate of 2.2%–14.6% (Inoue et al., 2021), and osteoporotic spines and older females are recognized as being at heightened risk (Nakahashi et al., 2019). This study found that stress on the endplate was significantly reduced and the stress was more evenly distributed under the action of the screw than in the intact model. Lower endplate stress and fewer stress concentrations would reduce the incidence of endplate fracture. The SR technique allows for lower endplate stress in extension

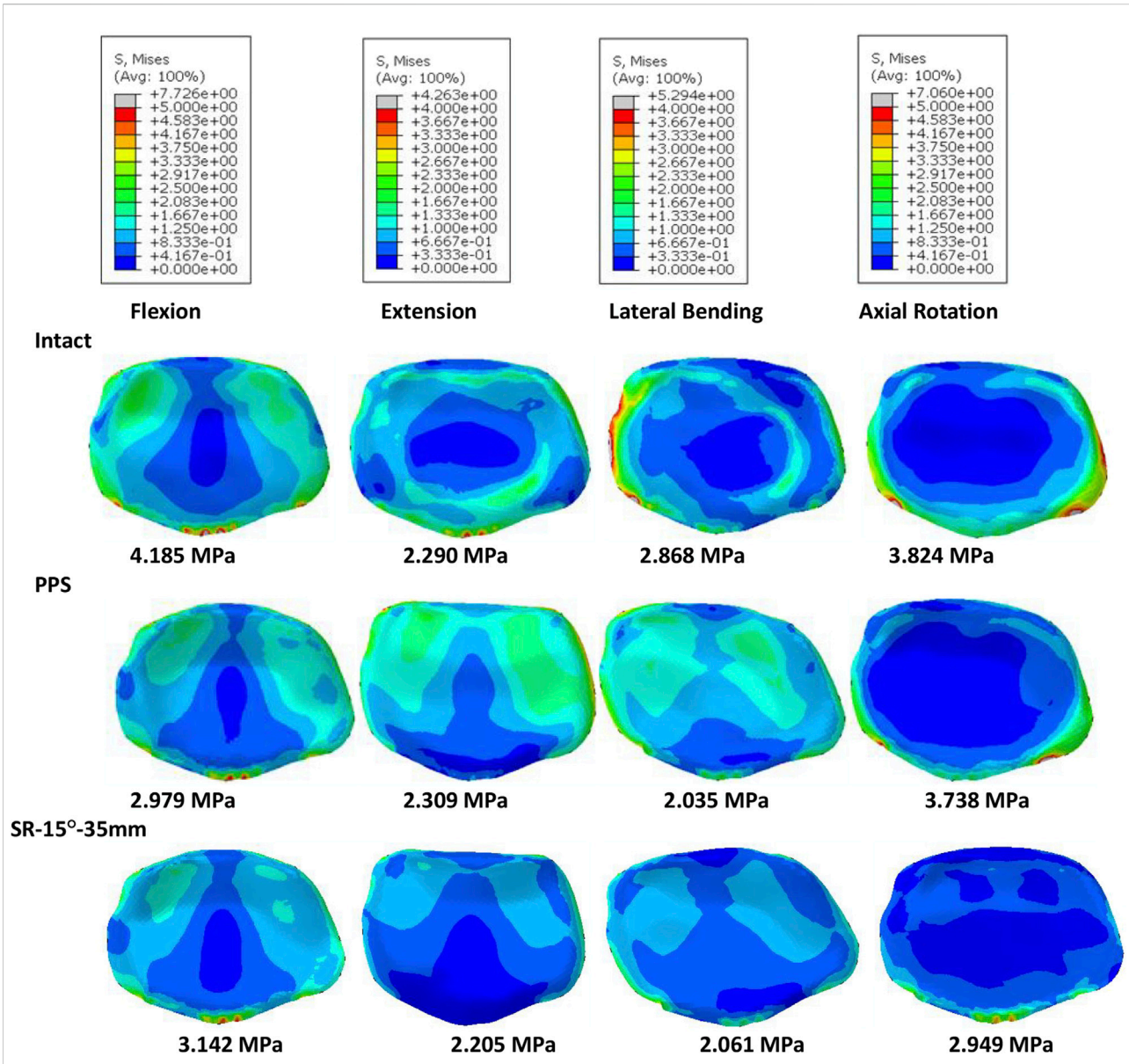

FIGURE 10
Von-Mises stress on the L4 endplate of the intact model, PPS model, and SR model, with the mean stress noted beneath each image.

and axial rotation but higher in flexion and lateral bending, meaning that the SR technique should be used cautiously in people prone to fracture, such as in osteoporotic patients.

Screw loosening and breakage are also common complications associated with pedicle screws, occurring in 0.8%–27% of cases, and may exceed 50% in patients with osteoporosis (Xi et al., 2021). Newcomb et al. (2017) found that using a larger insertion angle for pedicle screws may reduce the risk of screw loosening and breakage. Our study found that stresses were concentrated on the tail of the screw in the SR model, which may lead to fatigue failure around this region. However, the maximum von-Mises stress on the screws in the SR model was smaller than in the PPS model, meaning it was at a lower risk of screw fracture. The results of this study showed lower CSSR stresses with the SR method, which may also decrease the risk of screw breakage. Fragmentation of the CSSR region has been reported in the literature. A screw-rod system like the "crane" force structure determines the stress concentration at the center of rotation, where the screw and rod come into contact (Song et al., 2021). In addition to the stress on the pedicle screw, the insertion method and stability of the screw fixation system can also have a considerable effect on the healing capacity of the injured vertebra. Repeated displacement not only limits the growth of new trabecular

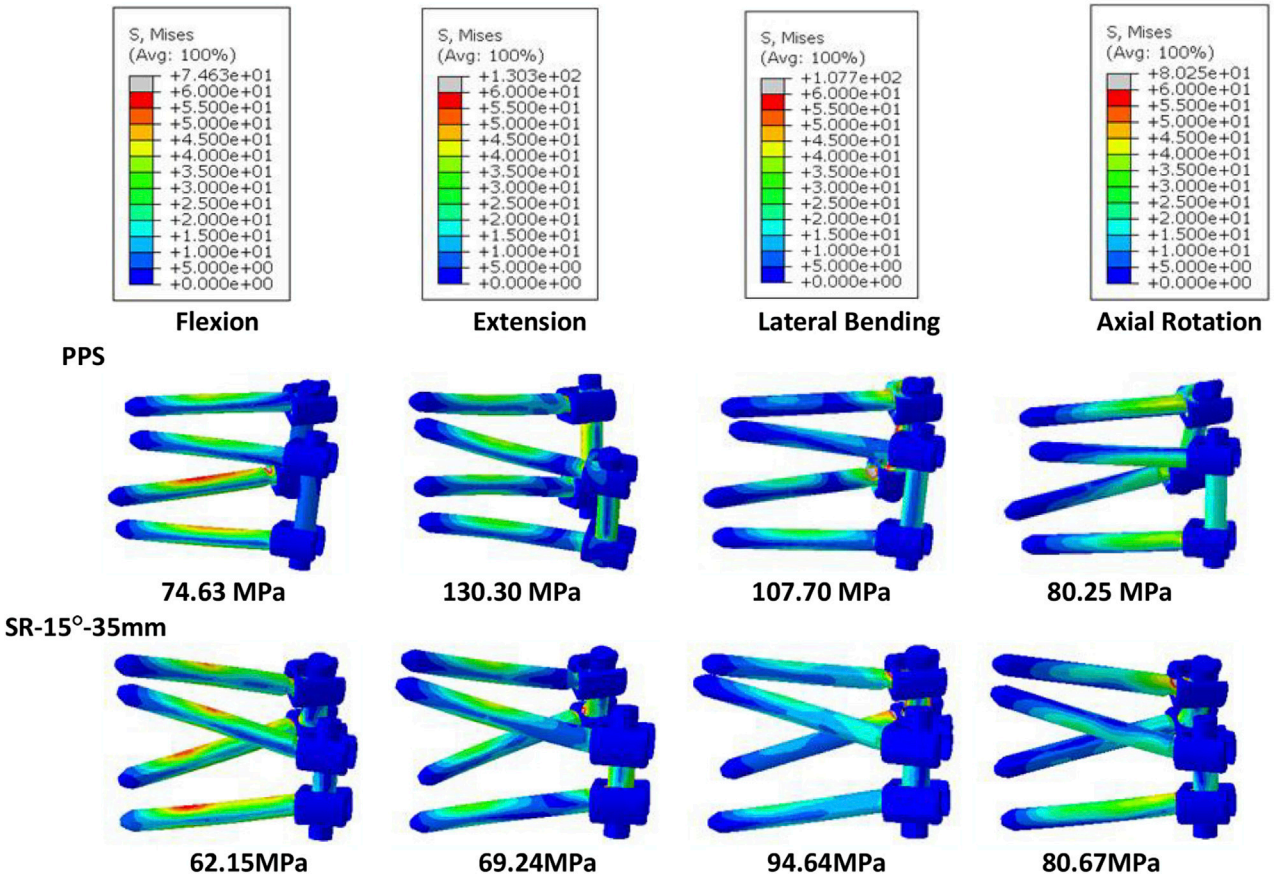

FIGURE 11
Von-Mises stress on screws of the PPS model and SR model, with the peak stress noted beneath each image.

bone but also causes resorption of grafted bone (Zhou et al., 2020). This study found that the SR technique suffered lower screw displacement than the PPS technique, suggesting this technique may carry a lower risk of screw loosening, although the difference between the two groups was not significant. The maximum screw displacement in the SR model was 0.48 mm, which was significantly less than the 0.7 mm reported by Krag et al. (1988), which could lead to trabecular bone damage and screw loosening. Future studies may also consider including longer screws for assessment, which have been reported to better constrain the fixation system (Cunningham et al., 2010).

The SR technique can provide better initial stability and lower the risk of facet joint degeneration. Also, because of the minimally invasive approach, SR can reduce iatrogenic complications caused by extensive iatrogenic paraspinal muscle injury. However, long-term screw-related complications cannot be ignored and may be improved by removing the internal fixation after fusion Tsuang et al., (2019).

There are some limitations to this study. First, the lumbar models did not consider musculature, which may affect the stability and flexibility of the spine. Second, this study did not consider the effect of rod curvature. However, since the SR technique uses a shorter rod length, the amount of bending would be negligible. Third, this study did not consider the effect of bone mineral density on stress pattern behavior. Methods to discuss the effects of internal fixation using non-osteoporotic models are widely used. In order to specifically discuss the effect of screw inclination angle and rod length on fixation, the fixation effect with different bone mineral densities will be discussed in future studies. Fourth, this study only considered screw angle and rod length and did not consider parameters such as screw length, diameter, and thread that are equally important for the stability of the fixation system. This study was to determine how the SR technique operates and evaluate the biomechanics of the SR technique. The geometric parameters of the screw can be considered in future studies to optimize the SR technique. Finally, the FEM did not directly assess the impact of SR technology on the adjacent vertebral segment, but instead used the axial stiffness of the fixed vertebrae to predict the risk of adjacent vertebral disease.

Conclusion

This study used finite element analysis to evaluate the effects of screw inclination angle and rod length with the SR technique on the lumbar spine. The biomechanical function of the lumbar spine was compared among the intact model, PPS model, and SR model. Compared to the PPS technique, the SR technique with a 15° screw inclination to the endplates in the sagittal plane and 35 mm rod length was more stable, required a smaller incision, and presented a lower risk of facet joint degeneration, screw breakage, and screw loosening. However, the SR technique is also at a slightly higher risk of endplate fracture than the PPS technique. The results of this study support that the use of the SR technique can offer good lumbar stability with a low risk of instrument-related complication.

Data availability statement

The raw data supporting the conclusion of this article will be made available by the authors, without undue reservation.

Ethics statement

Ethical review and approval were not required for the study on human participants in accordance with the local legislation and institutional requirements. Written informed consent for participation was not required for this study in accordance with the national legislation and the institutional requirements.

Author contributions

N-FM, Z-CS, and C-KC conceived and designed the study and the interpretation of data, supervised the research, and assisted in reviewing and editing the manuscript. Z-BH and M-DN conducted the experiment, completed the analysis and interpretation of data from the FEM models, and wrote the initial draft of the article. SL and N-ZZ completed the acquisition of data and the analysis and interpretation of data. J-BY and X-ML provided clinical guidance and analyzed data. All authors participated in revising the article and agreed to be personally accountable for their own contributions and ensure that questions related to the accuracy and integrity of any part of the work have been appropriately investigated and resolved with reference to literature when needed. All authors have read and agreed to the published version of the manuscript.

Acknowledgments

Colin McClean is acknowledged for his assistance with editing this manuscript.

Conflict of interest

The authors declare that the research was conducted in the absence of any commercial or financial relationships that could be construed as a potential conflict of interest.

Publisher's note

All claims expressed in this article are solely those of the authors and do not necessarily represent those of their affiliated organizations, or those of the publisher, the editors, and the reviewers. Any product that may be evaluated in this article, or claim that may be made by its manufacturer, is not guaranteed or endorsed by the publisher.

References

Bogduk, N. (2016). Functional anatomy of the spine. *Handb. Clin. Neurol.* 136, 675–688. doi:10.1016/B978-0-444-53486-6.00032-6

Bresnahan, L. E., Smith, J. S., Ogden, A. T., Quinn, S., Cybulski, G. R., Simonian, N., et al. (2017). Assessment of paraspinal muscle cross-sectional area after lumbar decompression: Minimally invasive versus open approaches. *Clin. spine Surg.* 30 (3), E162–E168. doi:10.1097/BSD.0000000000000038

Brinckmann, P., and Grootenboer, H. (1991). Change of disc height, radial disc bulge, and intradiscal pressure from discectomy. An *in vitro* investigation on human lumbar discs. *Spine* 16 (6), 641–646. doi:10.1097/00007632-199106000-00008

Campbell-Kyureghyan, N., Jorgensen, M., Burr, D., and Marras, W. (2005). The prediction of lumbar spine geometry: Method development and validation. *Clin. Biomech.* 20 (5), 455–464. doi:10.1016/j.clinbiomech.2005.01.006

Chang, C.-M., Lai, Y.-S., and Cheng, C.-K. (2017). Effect of different inner core diameters on structural strength of cannulated pedicle screws under various lumbar spine movements. *Biomed. Eng. OnLine* 16 (1), 105. doi:10.1186/s12938-017-0392-1

Chen, C.-S., Cheng, C.-K., Liu, C.-L., and Lo, W.-H. (2001). Stress analysis of the disc adjacent to interbody fusion in lumbar spine. *Med. Eng. Phys.* 23 (7), 485–493. doi:10.1016/S1350-4533(01)00076-5

Chen, P.-Q., Shih, C.-M., Cheng, C.-K., Jan, W.-T., and Wu, C.-M. (1990). Biomechanical studies of posterior spinal instrumentation system for scoliosis-an intact porcine spine model. *J. Orthop. Surg. Taiwan* 7 (1), 1–12.

Christine, Rustenburg, Sayf, Faraj, Roderick, M. H, Kingma, I., van Royen, B. J., Stadhouder, A., et al. (2019). The biomechanical effect of single-level laminectomy and posterior instrumentation on spinal stability in degenerative lumbar scoliosis: A human cadaveric study. *Neurosurg. Focus* 46 (5), E15. doi:10.3171/2019.2.FOCUS1911

Chu, Y.-L., Chen, C.-H., Tsuang, F.-Y., Chiang, C.-J., Wu, Y., Kuo, Y.-J., et al. (2019). Incomplete insertion of pedicle screws in a standard construct reduces the fatigue life: A biomechanical analysis. *Plos one* 14 (11), e0224699. doi:10.1371/journal.pone.0224699

Cunningham, B., Sefter, J., Hu, N., Kim, S., Bridwell, K., McAfee, P., et al. (2010). Biomechanical comparison of iliac screws versus interbody femoral ring allograft on lumbosacral kinematics and sacral screw strain. *Spine* 35 (6), E198–E205. doi:10.1097/BRS.0b013e3181c142bf

DieeN, J. H. V., Weinans, H., and Toussaint, H. M. (1999). Fractures of the lumbar vertebral endplate in the etiology of low back pain: A hypothesis on the causative role of spinal compression in aspecific low back pain. *Med. Hypotheses* 53 (3), 246–252. doi:10.1054/mehy.1998.0754

Dreischarf, M., Zander, T., Shirazi-Adl, A., Puttlitz, C., Adam, C., Chen, C., et al. (2014). Comparison of eight published static finite element models of the intact lumbar spine: Predictive power of models improves when combined together. *J. biomechanics* 47 (8), 1757–1766. doi:10.1016/j.jbiomech.2014.04.002

Fang, G., Chen, S., Zhuang, W., Huang, W., Sang, H., Kenfack, Y. J., et al. (2022). Pancreatic cancer metastasis to the spine: A systematic review of management strategies and outcomes with case illustration. *World Neurosurg.* 160, 94–101.e4. doi:10.1016/j.wneu.2022.01.016

Farshad, M., Farshad-Amacker, N. A., Bachmann, E., Snedeker, J. G., and Schmid, S. L. (2014). Biomechanical comparison of sagittal-parallel versus non-parallel pedicle screw placement. *Acta Neurochir. (Wien).* 156 (11), 2147–2151. doi:10.1007/s00701-014-2244-0

Fu, C.-J., Chen, W.-C., Lu, M.-L., Cheng, C.-H., and Niu, C.-C. (2020). Comparison of paraspinal muscle degeneration and decompression effect between conventional open and minimal invasive approaches for posterior lumbar spine surgery. *Sci. Rep.* 10 (1), 14635. doi:10.1038/s41598-020-71515-8

Goel, V., Goyal, S., Clark, C., Nishiyama, K., and Nye, T. (1985). Kinematics of the whole lumbar spine. Effect of discectomy. *Spine* 10 (6), 543–554. doi:10.1097/00007632-198507000-00008

Goto, K., Tajima, N., Chosa, E., Totoribe, K., Kuroki, H., Arizumi, Y., et al. (2002). Mechanical analysis of the lumbar vertebrae in a three-dimensional finite element method model in which intradiscal pressure in the nucleus pulposus was used to establish the model. *J. Orthop. Sci.* 7 (2), 243–246. doi:10.1007/s007760200040

Hikata, T., Kamata, M., and Furukawa, M. (2014). Risk factors for adjacent segment disease after posterior lumbar interbody fusion and efficacy of simultaneous decompression surgery for symptomatic adjacent segment disease. *J. Spinal Disord. Tech.* 27 (2), 70–75. doi:10.1097/BSD.0b013e31824e5292

Inceoğlu, S., Montgomery, W. H., Clair, S. S., and Mclain, R. F. (2011). Pedicle screw insertion angle and pullout strength: Comparison of 2 proposed strategies. *J. Neurosurg. Spine* 14 (5), 670–676. doi:10.3171/2010.11.SPINE09886

Inoue, G., Saito, W., Miyagi, M., Imura, T., Shirasawa, E., Ikeda, S., et al. (2021). Prevalence and location of endplate fracture and subsidence after oblique lumbar interbody fusion for adult spinal deformity. *BMC Musculoskelet. Disord.* 22 (1), 880. doi:10.1186/s12891-021-04769-6

Karahalios, D. G., Kaibara, T., Porter, R. W., Kakarla, U. K., Reyes, P. M., Baaj, A. A., et al. (2010). Biomechanics of a lumbar interspinous anchor with anterior lumbar interbody fusion. *J. Neurosurg. Spine* 12 (4), 372–380. doi:10.3171/2009.10.SPINE09305

Kim, H.-J., Chun, H.-J., Kang, K.-T., Moon, S.-H., Kim, H.-S., Park, J.-O., et al. (2012). The biomechanical effect of pedicle screws' insertion angle and position on the superior adjacent segment in 1 segment lumbar fusion. *Spine* 37 (19), 1637–1644. doi:10.1097/BRS.0b013e31823f2115

Kim, H.-J., Kang, K.-T., Son, J., Lee, C.-K., Chang, B.-S., Yeom, J. S., et al. (2015). The influence of facet joint orientation and tropism on the stress at the adjacent segment after lumbar fusion surgery: A biomechanical analysis. *Spine J.* 15 (8), 1841–1847. doi:10.1016/j.spinee.2015.03.038

Krag, M., Beynnon, B., Pope, M., and DeCoster, T. (1988). Depth of insertion of transpedicular vertebral screws into human vertebrae: Effect upon screw-vertebra interface strength. *J. spinal Disord.* 1 (4), 287–294. doi:10.1097/00002517-198800140-00002

Liu, C.-W., Wang, L.-L., Xu, Y.-K., Chen, C.-M., Wang, J.-C., Tsai, W.-T., et al. (2020). Traditional and cortical trajectory screws of static and dynamic lumbar fixation-a finite element study. *BMC Musculoskelet. Disord.* 21 (1), 463. doi:10.1186/s12891-020-03437-5

Momin, A. A., and Steinmetz, M. P. (2020). Evolution of minimally invasive lumbar spine surgery. *World Neurosurg.* 140, 622–626. doi:10.1016/j.wneu.2020.05.071

Nakahashi, M., Uei, H., Tokuhashi, Y., Maseda, M., Sawada, H., Soma, H., et al. (2019). Vertebral fracture in elderly female patients after posterior fusion with pedicle screw fixation for degenerative lumbar pathology: A retrospective cohort study. *BMC Musculoskelet. Disord.* 20 (1), 259. doi:10.1186/s12891-019-2534-z

Newcomb, A. G., Baek, S., Kelly, B. P., and Crawford, N. R. (2017). Effect of screw position on load transfer in lumbar pedicle screws: A non-idealized finite element analysis. *Comput. methods biomechanics Biomed. Eng.* 20 (2), 182–192. doi:10.1080/10255842.2016.1209187

Nie, T., Chen, D.-j., Tang, B., Song, Q., Liu, X., Zhang, B., et al. (2019). *In vivo* dynamic motion characteristics of the lower lumbar spine: L4–5 lumbar degenerative disc diseases undergoing unilateral or bilateral pedicle screw fixation combined with TLIF. *J. Orthop. Surg. Res.* 14 (1), 171. doi:10.1186/s13018-019-1198-6

Pang, Z. H., Miao, L., Zhang, Y. B., Yao, Y. F., Pei, S. K., and Orthopedics, D. O. (2015). Effect of different angles of implanted screws on the stability of pedicle screw. *Chin. J. Tissue Eng. Res.* 19 (48), 7765–7769. doi:10.3969/j.issn.2095-4344.2015.48.010

Panjabi, M. M. (2003). Clinical spinal instability and low back pain. *J. Electromyogr. Kinesiol.* 13 (4), 371–379. doi:10.1016/S1050-6411(03)00044-0

Park, J.-S., Shim, K.-D., Song, Y.-S., and Park, Y.-S. (2018). Risk factor analysis of adjacent segment disease requiring surgery after short lumbar fusion: The influence of rheumatoid arthritis. *Spine J.* 18 (9), 1578–1583. doi:10.1016/j.spinee.2018.02.005

Serhan, H., Hammerberg, K., O'Neil, M., Sturm, P., Mardjetko, S., Crawford, A., et al. (2010). Intraoperative techniques to reduce the potential of set-screw loosening in long spinal constructs: A static and fatigue biomechanical investigation. *J. Spinal Disord. Tech.* 23 (7), e31–36. doi:10.1097/BSD.0b013e3181c982a1

Shih, S.-L., Chen, C.-S., Lin, H.-M., Huang, L.-Y., Liu, C.-L., Huang, C.-H., et al. (2012). Effect of spacer diameter of the dynesys dynamic stabilization system on the biomechanics of the lumbar spine: A finite element analysis. *J. Spinal Disord. Tech.* 25 (5), E140–E149. doi:10.1097/BSD.0b013e31824e5e10

Song, M., Sun, K., Li, Z., Zong, J., Tian, X., Ma, K., et al. (2021). Stress distribution of different lumbar posterior pedicle screw insertion techniques: A combination study of finite element analysis and biomechanical test. *Sci. Rep.* 11 (1), 12968. doi:10.1038/s41598-021-90686-6

Thompson, J. C. (2015). *Netter's concise orthopaedic anatomy E-book*. Amsterdam, Netherlands: Elsevier Health Sciences.

Tsuang, F. Y., Tsai, J. C., and Lai, D. M. (2019). Effect of lordosis on adjacent levels after lumbar interbody fusion, before and after removal of the spinal fixator: A finite element analysis. *BMC Musculoskelet. Disord.* 20, 470. doi:10.1186/s12891-019-2886-4

Varghese, V., Krishnan, V., and Kumar, G. S. (2018). Evaluating pedicle-screw instrumentation using decision-tree analysis based on pullout strength. *Asian Spine J.* 12 (4), 611–621. doi:10.31616/asj.2018.12.4.611

Varghese, V., Kumar, G. S., and Krishnan, V. (2017). Effect of various factors on pull out strength of pedicle screw in normal and osteoporotic cancellous bone models. *Med. Eng. Phys.* 40, 28–38. doi:10.1016/j.medengphy.2016.11.012

Wang, P., Zhang, J., Liu, T., Yang, J., and Hao, D. (2022). Multivariate analysis of pedicle screw invasion of the proximal facet joint after lumbar surgery. *BMC Musculoskelet. Disord.* 23 (1), 39. doi:10.1186/s12891-021-04975-2

Xi, X., Zeng, Z., Li, F., Wang, C., Ma, B., Xie, N., et al. (2021). Caudad insertion of pedicle screws facilitates interbody distraction during spondylolisthetic vertebrae restoration: A retrospective study. *Pain Ther.* 10 (2), 1537–1550. doi:10.1007/s40122-021-00315-3

Xu, H., Tang, H., Guan, X., Jiang, F., Xu, N., Ju, W., et al. (2013). Biomechanical comparison of posterior lumbar interbody fusion and transforaminal lumbar interbody fusion by finite element analysis. *Neurosurgery* 72 (1), ons21–26. doi:10.1227/NEU.0b013e3182742a69

Yamamoto, I., Panjabi, M. M., Crisco, T., and Oxland, T. (1989). Three-dimensional movements of the whole lumbar spine and lumbosacral joint. *Spine* 14 (11), 1256–1260. doi:10.1097/00007632-198911000-00020

Yang, J.-S., He, B., Tian, F., Liu, T.-J., Liu, P., Zhang, J.-N., et al. (2019). Accuracy of robot-assisted percutaneous pedicle screw placement for treatment of lumbar spondylolisthesis: A comparative cohort study. *Med. Sci. Monit.* 25, 2479–2487. doi:10.12659/MSM.913124

Yin, J., Liu, Z., Li, C., Luo, S., Lai, Q., Wang, S., et al. (2020). Effect of facet-joint degeneration on the *in vivo* motion of the lower lumbar spine. *J. Orthop. Surg. Res.* 15 (1), 340. doi:10.1186/s13018-020-01826-z

Zhang, L., Li, H.-M., Zhang, R., Zhang, H., and Shen, C.-L. (2021). Biomechanical changes of adjacent and fixed segments through cortical bone trajectory screw fixation versus traditional trajectory screw fixation in the lumbar spine: A finite element analysis. *World Neurosurg.* 151, e447–e456. doi:10.1016/j.wneu.2021.04.061

Zhang, N.-Z., Xiong, Q.-S., Yao, J., Liu, B.-L., Zhang, M., Cheng, C.-K., et al. (2022). Biomechanical changes at the adjacent segments induced by a lordotic porous interbody fusion cage. *Comput. Biol. Med.* 143, 105320. doi:10.1016/j.compbiomed.2022.105320

Zhou, F., Yang, S., Liu, J., Lu, J., Shang, D., Chen, C., et al. (2020). Finite element analysis comparing short-segment instrumentation with conventional pedicle screws and the Schanz pedicle screw in lumbar 1 fractures. *Neurosurg. Rev.* 43 (1), 301–312. doi:10.1007/s10143-019-01146-9

frontiers | Frontiers in Bioengineering and Biotechnology

TYPE Original Research
PUBLISHED 19 August 2022
DOI 10.3389/fbioe.2022.870193

Check for updates

OPEN ACCESS

EDITED BY
Mark Buckley,
University of Rochester, United States

REVIEWED BY
Roman Eliseev,
University of Rochester, United States
Eng Kuan Moo,
University of Calgary, Canada

*CORRESPONDENCE
Michelle L. Delco,
mld12@cornell.edu

SPECIALTY SECTION
This article was submitted to Tissue Engineering and Regenerative Medicine, a section of the journal Frontiers in Bioengineering and Biotechnology

RECEIVED 06 February 2022
ACCEPTED 29 June 2022
PUBLISHED 19 August 2022

CITATION
Thomas MA, Fahey MJ, Pugliese BR, Irwin RM, Antonyak MA and Delco ML (2022), Human mesenchymal stromal cells release functional mitochondria in extracellular vesicles.
Front. Bioeng. Biotechnol. 10:870193.
doi: 10.3389/fbioe.2022.870193

COPYRIGHT
© 2022 Thomas, Fahey, Pugliese, Irwin, Antonyak and Delco. This is an open-access article distributed under the terms of the Creative Commons Attribution License (CC BY). The use, distribution or reproduction in other forums is permitted, provided the original author(s) and the copyright owner(s) are credited and that the original publication in this journal is cited, in accordance with accepted academic practice. No use, distribution or reproduction is permitted which does not comply with these terms.

Human mesenchymal stromal cells release functional mitochondria in extracellular vesicles

Matthew A. Thomas[1], Megan J. Fahey[1], Brenna R. Pugliese[1], Rebecca M. Irwin[1], Marc A. Antonyak[2] and Michelle L. Delco[1]*

[1]Cornell University College of Veterinary Medicine, Department of Clinical Sciences, Ithaca, NY, United States, [2]Cornell University College of Veterinary Medicine, Department of Molecular Medicine, Ithaca, NY, United States

Cartilage and other skeletal soft tissues heal poorly after injury, in part due to their lack of vascularity and low metabolic rate. No pharmacologic approaches have proven effective in preventing chronic degenerative disease after joint injury. Mesenchymal stromal cells (MSCs) have been investigated for their ability to treat pain associated with osteoarthritis (OA) and preserve articular cartilage. Limitations of MSCs include variability in cell phenotype, low engraftment and retention rates, and inconsistent clinical outcomes. Therefore, acellular biologic therapies such as extracellular vesicles (EVs) are currently being investigated. MSC-derived EVs have been found to replicate many of the therapeutic effects of their cells of origin, but the mechanisms driving this remain unclear. Recent evidence in non-orthopedic tissues suggests MSCs can rescue injured cells by donating mitochondria, restoring mitochondrial function in recipient cells, preserving cell viability, and promoting tissue repair. Our group hypothesized that MSCs package mitochondria for export into EVs, and that these so-called "mitoEVs" could provide a delivery strategy for cell-free mitochondria-targeted therapy. Therefore, the goals of this study were to: 1) characterize the vesicle fractions of the MSCs secretome with respect to mitochondrial cargoes, 2) determine if MSC-EVs contain functional mitochondria, and 3) determine if chondrocytes can take up MSC-derived mitoEVs. We isolated exosome, microvesicle, and vesicle-free fractions from MSC-conditioned media. Using a combination of dynamic light scattering and nanoparticle tracking, we determined that MSC-EV populations fall within the three size categories typically used to classify EVs (exosomes, microvesicles, apoptotic bodies). Fluorescent nanoparticle tracking, immunoblotting, and flow cytometry revealed that mitochondrial cargoes are abundant across all EV size populations, and mitoEVs are nearly ubiquitous among the largest EVs. Polarization staining indicated a subset of mitoEVs contain functional mitochondria. Finally, flow cytometry and fluorescent imaging confirmed uptake of mitoEVs by chondrocytes undergoing rotenone/antimycin-induced mitochondrial dysfunction. These data indicate that MSCs package intact, functional mitochondria into EVs, which can be transferred to chondrocytes in the absence of direct cell-cell interactions. This work suggests intercellular transfer of healthy MT to chondrocytes could

represent a new, acellular approach to augment mitochondrial content and function in poorly-healing avascular skeletal soft tissues.

KEYWORDS

MSCs, mitoEVs, secretome, mitochondria, mitochondrial transfer, regenerative orthobiologic

1 Introduction

Cartilage is responsible for dissipating mechanical forces and providing a near frictionless articular surface for locomotion (Sophia Fox et al., 2009). Injury to the articular surface leads to chondrocyte death and cartilage matrix degradation. This cellular and structural damage initiates cycles of inflammation and irreversible tissue degeneration, culminating in end-stage osteoarthritis (OA) (Madry et al., 2011), a leading cause of chronic pain and disability worldwide (Lawrence et al., 2008). Cartilage and other skeletal soft tissues such as meniscus, ligament and intervertebral disc have a low metabolic rate, poor vascularization and as such, possess limited healing capacity (Bianchi and Sinigaglia, 2012). Further, no current therapeutics can slow progression of OA after joint injury (Sarzi-Puttini et al., 2005).

Recent studies have shown that mitochondrial dysfunction is one of the earliest responses of chondrocytes to mechanical injury, implicating mitochondria (MT) as an important mediator of injury-induced OA (Blanco et al., 2011; Goetz et al., 2017; Delco et al., 2018a; Bonnevie et al., 2018; Liu et al., 2019). We have found that the mitoprotective peptide SS-31 can improve MT function, preserve chondrocyte viability, and prevent tissue loss following cartilage injury (Delco et al., 2018b; Bartell et al., 2020). These findings support the concept of protecting MT function after acute injury to prevent cartilage loss, however MT-targeted strategies to improve healing of degenerated articular cartilage have not been investigated.

Tissue healing is an energy intensive process, and MT dysfunction mediates many degenerative diseases, including Parkinson's (Winklhofer and Haass, 2010), cardiomyopathy (Pacak et al., 2015), and pulmonary fibrosis (Watson et al., 2016). MT dysfunction has been less well studied in cartilage, in part because chondrocytes are largely glycolytic and do not heavily rely on MT for energy production during homeostasis (Bianchi and Sinigaglia, 2012). However, MT also act as signaling hubs in cellular processes such as apoptosis and autophagy, and are critical organelles for maintenance of cartilage homeostasis (Loeser, 2011). Inflammation that occurs in OA is associated with a shift towards glycolysis for energy production in chondrocytes (Zheng et al., 2021). This metabolic shift may represent an attempt to restore energy capacity after MT dysfunction reduces an already limited supply (Mobasheri et al., 2017). Therefore, replacing dysfunctional MT that have been lost to injury and/or disease may promote healing in avascular, metabolically quiescent tissues such as articular cartilage.

Intercellular MT transfer, a process whereby injured and dysfunctional cells recruit MSCs to donate functional MT, has been shown to restore MT function in energy-expensive tissues such as neurons (Berridge et al., 2016), cardiomyocytes (Pacak et al., 2015) and renal tubular epithelia (Konari et al., 2019), as well as more quiescent, poorly vascularized tissues such as the corneal epithelia (Jiang et al., 2016). *In vivo* murine models of acute lung injury revealed that MSC-mediated MT transfer protects against tissue degeneration after pulmonary injury (Islam et al., 2012; Jackson et al., 2016). Though the mechanisms mediating intercellular MT transfer have not been fully elucidated, evidence from a variety of cell and tissue types implicate processes requiring direct cell-cell contact, including filapodial extensions, tunneling nanotubules, gap junction formation, and cell-cell fusion events (Chinnery et al., 2008; Larsson et al., 2008; Murray and Krasnodembskaya, 2019).

In addition to direct cell-cell MT transfer, our group and others have documented apparent non-contact MT transfer via extracellular vesicles (EVs). EVs are small, membrane bound structures released by all cell types. EVs serve as vehicles for cell-cell signaling and orchestrate many biologic processes including inflammation, immunomodulation, homeostasis, metastasis, and tissue repair (Lai et al., 2010; Luwig and Giebel, 2012; Yuana et al., 2013; Kogure et al., 2020). While EV populations are heterogenous and remain largely uncharacterized, they are most commonly classified into three categories based on size and mode of biogenesis: exosomes, microvesicles (MVs), and apoptotic bodies (Gould and Raposo, 2013). Recent work has identified mitochondria-specific cargoes, including DNA, RNA, and proteins in EVs originating from many cell types, including fibroblasts (Sansone et al., 2017), neurons (Peruzzotti-Jametti et al., 2021), and MSCs (Phinney et al., 2015). Furthermore, intact MT have been identified in larger vesicles derived from adipocytes (Crewe et al., 2021) and MSCs (Phinney et al., 2015; Morrison et al., 2017). In one study, at least 60% of human plasma-derived EVs contained MT, and MT cargoes were ubiquitous in the very largest vesicles (Zhang et al., 2020). Further, EV-mediated MT transfer has been documented between MSCs and professional phagocytic cells; *in vitro,* macrophages were found to take up MSC-derived EVs containing MT and incorporate them into their mitochondrial networks (Phinney et al., 2015; Morrison et al., 2017). This process of stem cell to phage mitoEV-mediated transfer has

also been documented from neural stem cells (NSCs) to mononuclear phagocytes, with transfer restoring ATP capacity, upregulating oxidative phosphorylation, and reducing inflammation (Peruzzotti-Jametti et al., 2021). However, MSC-derived mitoEV transfer has not been demonstrated to chondrocytes. Intriguingly, our group has reported MSC-chondrocyte MT transfer in direct coculture and observed MSCs apparently shedding MT into the extracellular space during co-culture with injured chondrocytes (Bennett et al., 2019; Fahey et al., 2022). However, it was unclear if these MT were packaged within EVs (mitoEVs). Therefore, the goals of this study were to characterize EVs produced by murine and human bone marrow derived-MSCs (including mitochondrial cargoes), determine if MSC-mitoEVs contain functional mitochondria, and investigate whether chondrocytes are capable of taking up MSC-derived mitoEVs. While live MSCs have shown promise as an orthobiologic therapy (Kingery et al., 2019), the therapeutic use of live cells presents significant clinical challenges (Musiał-Wysocka et al., 2019). Harvesting autologous MSCs from sources such as bone marrow or cartilage requires painful and/or invasive procedures, while the use of non-autologous cells raises concerns of immunogenicity and tumorigenesis (Hall and Watt, 1989; Charron, 2013). Additionally, culturing, expanding, transporting, and storing live MSCs requires a large investment of time, resources, and expertise (Asghar et al., 2014). These obstacles, alongside the high regulatory burden associated with the clinical use of MSCs, have greatly limited their widespread use and caused clinicians to seek more practical and readily available orthobiologics.

2 Materials and methods

2.1 Cell sources and culture

Bone marrow-derived MSCs were isolated from 5 week old PHaM mitoDendra2 (Jax stock 018385) mice, as previously described (Huang et al., 2015). Chondrocytes were isolated from 5 day old UBC mCherry mice (Jax stock 017614), as previously reported (Gosset et al., 2008). Cells were cryopreserved in liquid nitrogen then thawed and cultured for use as needed. Protocols were approved by the Institutional Animal Care and Use Committee at Cornell University. Murine cells expressing endogenous fluorophores were used for characterizing the size of the whole EV population using dynamic light scattering (DLS), and for assessing mitoEV uptake by chondrocytes with confocal imaging and flow cytometry. Human bone marrow-derived MSCs were purchased at passage two (Millipore Sigma: SCC034) and used for nanoparticle tracking, western blot, and identification of mitoEVs with flow cytometry. For all experiments using human MSCs, cells were passaged no more than 3 times, cultured to 85% confluence, rinsed thrice with PBS and serum starved for 24 h before EV isolation.

2.2 Extracellular vesicle isolation

For all experiments, cell-conditioned media was removed and placed on ice immediately following 24-h serum starvation. To characterize the size range of the entire MSC-derived EV population using (DLS), murine MSC cell-conditioned media (CCM) was centrifuged at 3,000 x g for 15 min. The supernatant was then processed using the Exoquick-TC ULTRA kit (System Bio: EQULTRA-20TC-1), according to manufacturer's instructions. For nanoparticle tracking, western blot, flow cytometry, and confocal imaging studies, a validated filtration-ultracentrifugation technique was used to isolate EV fractions of specific size ranges, as previously described (Wang et al., 2021). These fractions consisted of vesicle free media, (VFM, no EVs) exosomes, (EX, 30–100 nm) and microvesicles (MVs, 100–1000 nm). Briefly, following CCM collection, adhered MSCs were lysed and placed on ice. The CCM was clarified of cellular debris with two consecutive centrifugation steps (1,000 x g for 5 min). To isolate MVs, CCM was vacuum filtered through a Steriflip filter (0.22 µm; Millipore: SE1M179M6). MVs were collected on top of the filter and were immediately placed on ice or lysed for protein analysis. The filtrate was subjected to 100,000 x g centrifugation at 4°C for 4 h in a Beckman Coulter Optima XE Ultracentrifuge. The supernatant (vesicle-free media; VFM) was removed and concentrated using an Amicon centrifugal concentrator with a 10kDa pore size. The pellet (EX fraction) was lysed and immediately placed on ice. Total whole cell lysate (WCL), MV, EX, and VFM protein content was quantified by Bradford Assay. Validation of EV isolation was performed by western blot for EV-specific markers and calcein staining/flow cytometry (Gray et al., 2015).

2.3 EV size characterization

The relative size distribution of EVs from MT stressed and MT protected cells was characterized by DLS (Malvern Nano ZS Zetasizer). Murine MSCs were passaged 2–3 times, cultured to 85% confluence in standard growth media at 21% O_2 and 5% CO_2; then rinsed thrice with phosphate buffered saline (PBS) and stimulated with the mitochondrial inhibitor rotenone/antimycin (Sigma: R8875, 0.5 µM/Sigma: A8674, 0.5 µM), treated with the mitoprotective peptide SS-31 (1 uM), or left untreated during a 24-h serum starvation prior to EV isolation. Three measurements were obtained per sample at 25°C, a detection angle of 173°, and a refractive index of 1.334 (PBS), then averaged. The experiment was repeated twice, for an $n = 3$. Percent area under the curve, maximum intensity, and mean particle size were calculated for major peaks. To obtain a more accurate quantification of sub-

micron sized EVs, human MSCs were cultured as described above, then isolated using filtration/ultracentrifugation. Nanoparticle tracking was performed using a Malvern NanoSight NS300 configured with a 488 nm laser and 565 nm long pass filter for fluorescent detection. Five, 60 s videos were taken, individual particles were tracked, and hydrodynamic size was calculated via the Stokes-Einstein equation. To validate our isolation technique EX, MV, vesicle-free media, and PBS (control) were analyzed to confirm that each fraction fell within the expected size range based on previous work (Zhang et al., 2020). Samples were diluted in double filtered (.22 um) PBS to a concentration between 10^7–10^9 per mL and analyzed at room temperature. Size distribution of EVs in each fraction was measured using the 488 nm laser. The size distribution of mitoEVs specifically was determined by staining microvesicle fractions with the mitochondrial probe Mitotracker Red (100 nM; Thermofisher: M22425) and using the 565 nm, long pass filter. Unstained and vesicle-free samples served as negative controls.

2.4 Characterization of MSC secretome fractions by western blot

A total of 25 μg protein from human MSC-EV fractions isolated by filtration/ultracentrifugation was resolved by SDS-PAGE under reducing conditions (4–20%; Invitrogen Novex Wedge Well, 1.0 mM; Tris-Glycine, Mini Protein Gel, 10-well; XCell SureLock Mini). The gel was transferred to a polyvinylidene difluoride membrane (0.45 μm; 10 × 10 cm, Thermofisher), which was blocked in tris-buffered saline with 5% bovine serum albumin, then cut based on molecular weight. Sections were incubated with respective primary antibodies overnight: HSP90 (Cell Signaling: 4877S) was used as a positive loading control; Flotillin (Cell Signaling: 3436S) was used as a positive EV marker expected to be detected in all lysates (WCL, MV, EX); IκBα (Cell Signaling: 4814S) was used as cellular marker to screen for cellular contaminants in conditioned media fractions; ATP5A1 (Thermofisher:459240) and COXIV (Cell Signaling: 4850S) were used to probe for mitochondrial proteins. The membrane sections were rinsed three times with tris-buffered saline and incubated with horseradish peroxidase-conjugated secondary antibody for 1 h at room temperature with gentle rocking. All primary and secondary antibodies were used at 1:1,000 dilutions. Proteins were detected using enhanced chemiluminescence reagents and a chemiluminescent imaging device (Bio-Rad Chemidoc XRS).

2.5 MitoEV identification and size characterization by flow cytometry

To investigate the presence of mitoEVs, human MSC-MVs were cultured and isolated as described above, then stained with Calcein AM (10 uM; Thermofisher: C3099) to identify intact vesicles (Gray et al., 2015), and MitoTracker Deep Red (100 nM; Thermofisher: M22426) to label intact mitochondria. MVs were resuspended in double filtered PBS and immediately analyzed by flow cytometry (FACSAria Fusion, BD Biosciences). Unstained controls and EV fractions stained with individual fluorophores were prepared for each trial and used to set positive fluorescence thresholds within each experiment to account for variations in fluorescent intensitiy and instrument settings between experiments. Events positive for both Calcein and MitoTracker were considered mitoEVs. Events positive for Calcein only were considered EVs lacking whole mitochondria cargoes. Events positive for Mitotracker alone were considered free mitochondria (i.e., not contained within EVs). Data analysis was conducted using FlowJo (version 10.8; FlowJo LLC) software. To investigate the relative size distribution of mitoEVs within the isolated MV population, the backgating tool in FlowJo was used. MitoEV events were plotted based on vesicle size (FSC-H vs. FSC-A). Gates were created to encompass progressively larger size percentiles (1^{st}, 50^{th}, 80^{th}, 90^{th}, 95^{th}) so that, for example, events falling within the 95^{th} percentile represented the largest 5% of all EVs. The fraction of mitoEVs within each size percentile was recorded.

2.6 MitoEV polarity assessment

In order to investigate the presence of functional (polarized) mitochondrial cargos, human MSC-MVs were stained with calcein AM and tetramethylrhodamine, methyl ester (TMRM; 200nM; Thermofisher: 2,668), which fluoresces red-orange only when taken up across a polarized mitochondrial membrane. Single color and unstained controls were used to set thresholds for each fluorophore, as above. Events double positive for calcein and TMRM were considered mitoEVs containing functional mitochondria.

2.7 MitoEV uptake by articular chondrocytes

2.7.1 Flow cytometry of chondrocytes cultured with MSC-MVs

To gather quantitative data on rates of mitoEV-mediated mitochondrial transfer, PHaM mitoDendra2 MSCs were cultured to 85% confluence, rinsed thrice with PBS, and serum starved for 12 h. MSC- microvesicles were isolated via filtration as described above. Murine articular chondrocytes were harvested from 5 to 6 day old pups, as previously described (Gosset et al., 2008). Passage two to three chondrocytes were cultured to 80% confluence and incubated for 12 h in serum free media with or without murine MSC-derived MVs. Cells were then fixed and analyzed using an Attune NxT cytometer. Single

cells were gated for using forward and side scatter. A negative control fluorescent threshold for dendra2 was set using non-MV treated chondrocytes. Chondrocytes fluorescing above dendra2 threshold were considered to have taken up mitoEVs.

2.7.2 Confocal imaging of chondrocytes cultured with MSC-MVs

PHaM mitoDendra2 MSCs were cultured, rinsed thrice with PBS and serum starved for 24 h. Murine chondrocytes were cultured to 80% confluence on a chamber slide system (Lab-Tek: 177429), then stained with Mitotracker Red (100 nM; Thermofisher: M7512) and incubated with MSC-derived MVs for 12 h under serum starvation. Chondrocytes were then fixed on the chambered slide with 4% PFA, coverslipped with fluoromount containing DAPI nuclear stain. Chondrocyte cultures were imaged on a Zeiss LSM880 inverted i880 multiphoton microscope with a ×63 oil immersion objective using sequential, 3-channel scans; 359/457 nm (DAPI), 490/507 nm (Dendra2) 581/644 nm (Mitotracker red) excitation/emission, respectively. Z stacks were performed (14–20 slices at a step size of .38 µm) on a subset of co-fluorescent cells to investigate if MSC-derived fluorescent mitochondria were localized to the MT networks within recipient chondrocytes.

2.8 Statistical analysis

For DLS parameters (percent area under the curve, maximum intensity, and mean particle size), a one-way ANOVA was used, followed by Dunnett's multiple comparison's test to assess differences between groups (NS, RA, SS31) at each peak. To validate mitoEV quantification and mitochondrial polarity data, one-way ANOVA followed by Dunnett's multiple comparisons tests were used to assess differences between the experimental groups (MitoTracker + calcein and TMRM + calcein, respectively), single color controls (MitoTracker, calcein, and MitoTracker, TMRM, respectively), and unstained controls. Polarity data was log transformed for statistical analysis. To assess differences between MV-treated (+MV) and non-treated (-MV) chondrocytes, data was log transformed and an unpaired t-test was used to compare groups. All statistical analyses were performed using Graphpad Prism version 8.3, with significance set at $p \leq 0.05$.

3 Results

3.1 MSC-EV isolation validation and basic characterization

To characterize the entire MSC-EV population, a size distribution was obtained by DLS. Similar to previous reports (Zhang et al., 2020), EVs clustered into three size ranges: small vesicles (5–10 nm in diameter), medium (100–1,000 nm), and a subgroup of much larger vesicles (5000–10000 nm) (Figure 1A) likely representing exosomes, microvesicles (MVs), and apoptotic bodes, respectively. The non-stimulated group had a significantly higher percent area in the first size peak than either the rotenone/antimycin or the SS-31 stimulated group. Both stimulated groups showed a significantly higher percent area in the second (medium) peak than the non-stimulated group ($p < 0.05$). Since DLS is not well suited to quantifying heterogenous populations of particles, we also performed nanoparticle tracking analysis (NTA) of EV fractions. NTA data validated our isolation protocol; particles clustered in size ranges consistent with exosomes (10–150 nm) and MVs (100–1,000 nm). The negative control diluent (double filtered PBS) was negative for EV-sized particles (Figure 1B). Next, we used Western Blot to qualitatively characterize our separated MV, EX, and vesicle free media (VFM) fractions. To confirm that the fractions were devoid of cells and cellular debris, we probed for the cellular marker, IκBα, which was detected in our whole cell lysate (WCL) but not MV or EX. The ubiquitous marker for cells and conditioned media, HSP90, was detected in WCL, EX, and VFM, as expected. Flotillin, an EV marker, was detected in WCL, MV, and EX but not VFM. Mitochondrial proteins were detected in WCL (ATP5A1, COXIV) and MV (COXIV) (Figure 1C), indicating the presence of mitochondrial cargoes in the microvesicle fraction of the MSC secretome.

3.2 Characterization of mitoEVs

Quantification of mitoEVs was performed on flow cytometry. Events exceeding the fluorescence thresholds for both MitoTracker Deep Red and calcein (i.e. red-green double-positive) were considered mitoEVs (Figure 2A). An average of 71% (range 58.6–97%) of intact EVs contained MT (Figure 2B). The double stained group contained ~7-fold higher percentage of double positive events compared to controls, indicating that the mitoEV signal was not a result of autofluorescence or artifact (Figure 2B). Backgating analysis revealed that mitoEVs were present throughout the entire size distribution of particles, however EVs lacking MT tended to be below the 50th percentile for size (Figure 2C). Further, the vast majority (~90%) of the largest EVs (95th size percentile) contained MT. (Figure 2D). Because size data gathered from backgating analysis is qualitative rather than quantitative, we also performed fluorescent nanoparticle tracking analysis on MVs stained with and without MitoTracker Deep Red (Figure 2E). Fluorescent nanoparticle tracking supported our flow cytometry data; mitoEVs were found to be distributed throughout the EV

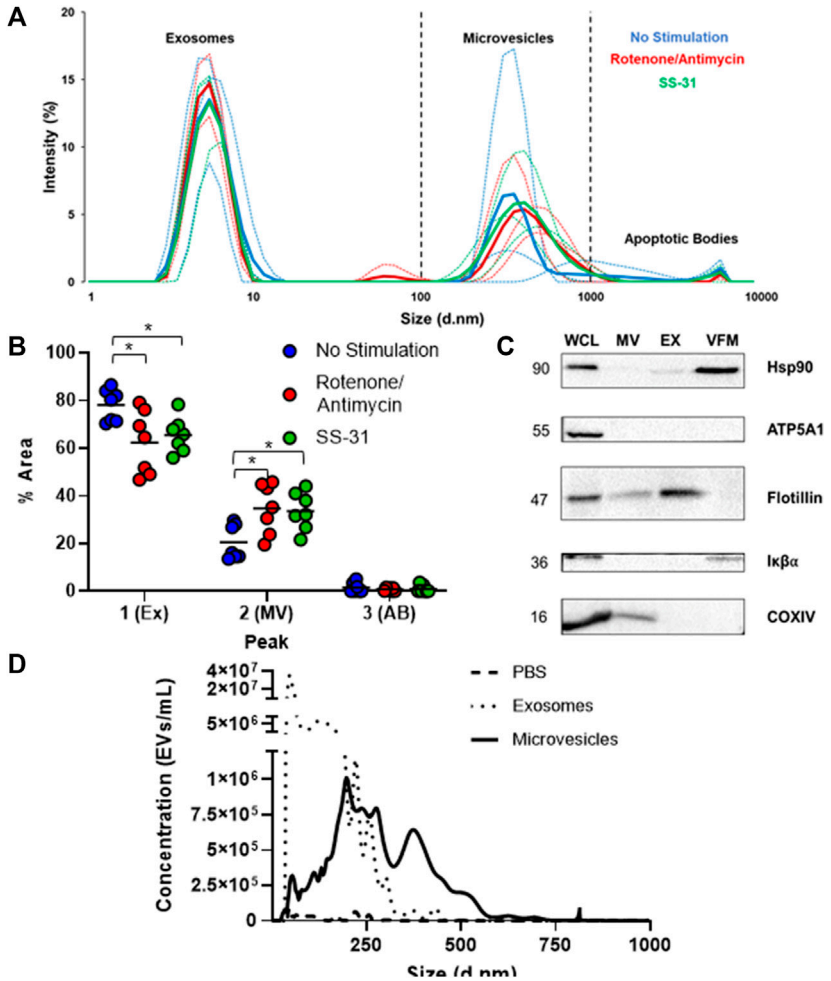

FIGURE 1
Basic characterization of human MSC-derived extracellular vesicles. **(A)** Dynamic Light Scattering (DLS) of cell-conditioned media (CCM) from murine MSCs revealed three sub-populations of EVs based on size: small, (~5–10 nm) medium, (~100–1000 nm) and large (5,000–10,000 nm), which likely represent exosomes, microvesicles, and apoptotic bodies, respectively. Thin lines represent individual trials (n = 3), thick lines represent averaged curves. **(B)** Analysis by one way ANOVA of average percent area under the curve on DLS data revealed a significantly smaller 1st (exosome) peak and a significantly larger 2nd (microvesicle) peak for both stimulated groups (* = $p \leq 0.05$). **(C)** Immunoblotting of whole cell lysate (WCL) and microvesicle (MV), exosome (EX), and vesicle free media (VFM) fractions of CCM. Ubiquitous marker HSP90 is present in WCL, EX, and VFM fractions. The EV marker flotillin is present in all fractions except VFM, and the cellular marker IκBα is absent from exosome (EX) and microvesicle (MV) fractions, as expected. MT protein ATP5A1 was found only in WCL, but COXIV (MT) was found in WCL and MVs. **(D)** Nanoparticle tracking analysis (NTA) of PBS (negative control), EX, and MV fractions indicates that EXs outnumber MVs by several orders of magnitude amongst particles less than 1μm, the maximum detection size of NTA.

size spectrum but tended to be larger than the general population. Further, this more sensitive analysis revealed that mitoEVs clustered around 3–400 nm, 600 nm, and 1 μm, suggesting the presence of distinct sub-populations of mitoEVs (Figure 2E). Unstained samples were undetectable when analyzed using the 565 nm fluorescent laser, and groups stained with MitoTracker, but analyzed with brightfield tracking did not show a shift in size distribution, validating our method for detecting mitoEVs (Figure 2E).

3.3 A subset of mitoEVs contain functional mitochondria

To characterize the functionality of mitochondrial cargoes within MSC-derived mitoEVs, we analyzed MT polarity via TMRM staining on flow cytometry, with events staining above threshold for calcein and TMR considered mitoEVs containing polarized MT (Figure 3A). An average of 31% (range 5.38–69.16%) of EVs contained functional MT, suggesting that

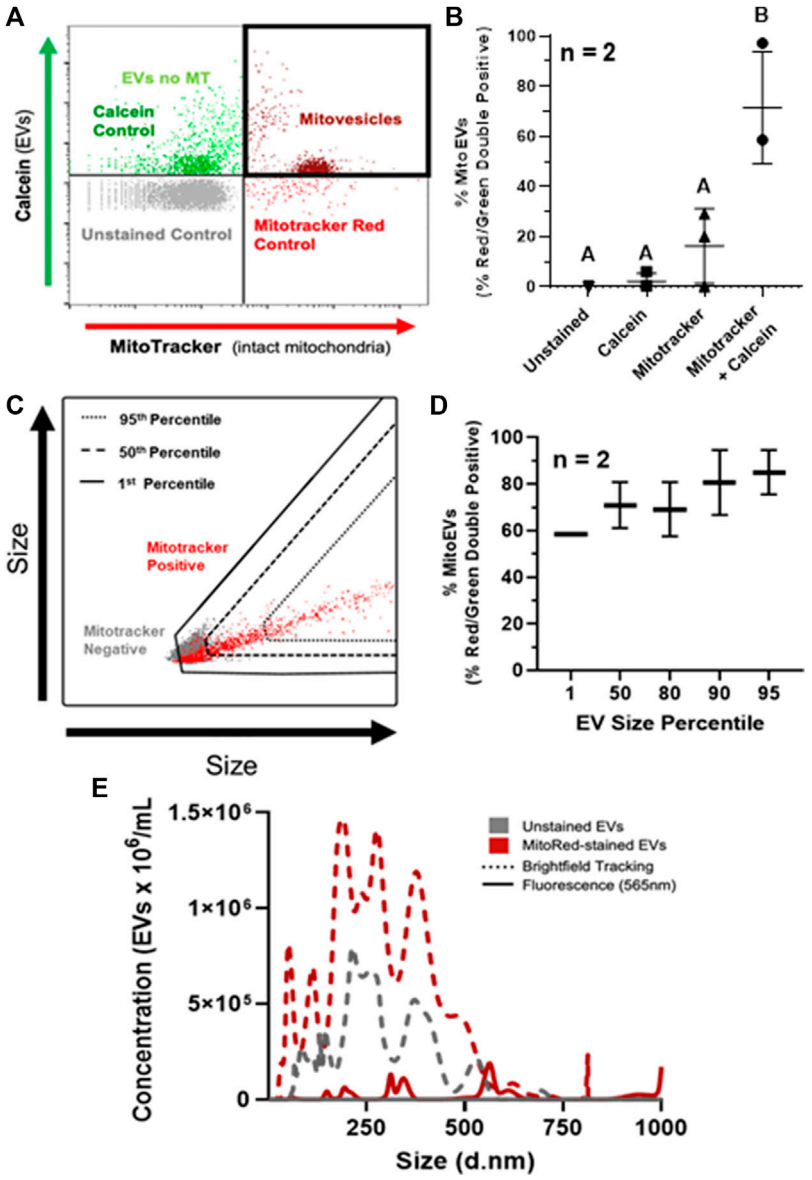

FIGURE 2
MSC-derived EVs contain mitochondria (MT). **(A)** Events fluorescing above control thresholds for Calcein AM (Green) and Mitotracker (Red) on flow cytometry were classified as EVs containing intact MT (i.e., mitoEVs; dark red). **(B)** Quantification of mitoEVs (red-green double positive events) and three control groups; Mitotracker only (▲), calcein only (■), and unstained control (▼), compared to EVs stained with calcein + Mitotracker (●). **(C)** Representative flow plot depicting backgating strategy for assessing relative sizes of mitoEVs (red) and MT-negative EVs (gray). **(D)** Backgating revealed that EVs of all sizes contain MT, but EVs lacking MT are generally small, and the majority of the largest EVs contain MT. **(E)** Fluorescent NTA revealed mitoEVs (solid red line) trend larger than the general EV population (dotted lines) and cluster into distinct sub-groups. Groups that do not share letters (Panel B) are significantly different ($p \leq 0.05$) by one way ANOVA.

MT polarity in mitoEVs is highly variable (Figure 3B). The double-stained experimental group contained significantly more double-positive events than unstained and calcein control groups. Although the experimental group contained a mean of 6-fold more double-positive events than the TMRM control, the difference did not reach statistical significance ($p = 0.0735$) due to high variability in the experimental group between trials ($n = 3$).

3.4 MitoEVs are taken up by chondrocytes and incorporated into chondrocyte mitochondrial networks

To interrogate whether articular chondrocytes are capable of taking up MSC-derived mitoEVs from the extracellular environment, we stained murine chondrocytes with MitoTracker Red to label the MT networks, tthen incubated

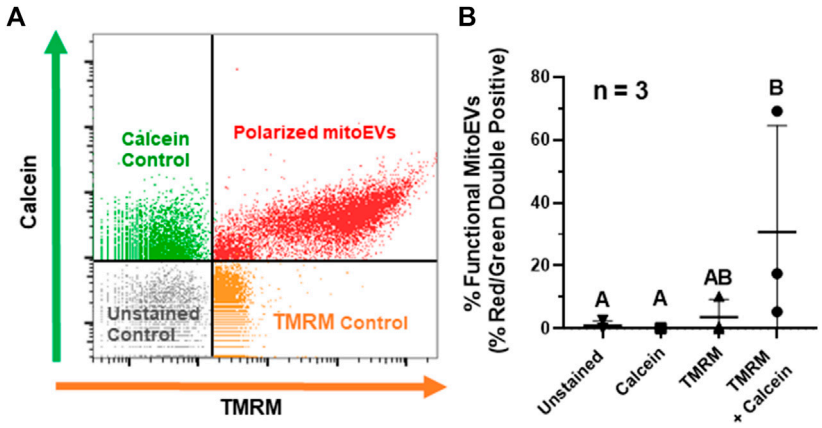

FIGURE 3
A subset of MitoEVs contain functional mitochondria. **(A)** Representative flow plot identifying polarized mitoEVs; events fluorescing above control thresholds for calcein AM (green) and TMRM (orange) were classified as mitoEVs containing functional MT (red). **(B)**. Quantification of functional mitoEVs (red-green double positive events) and three control groups; TMRM only (▲), calcein only (■), and unstained control (▼), compared to EVs stained with calcein + TMRM (●). Data is expressed as the fraction of double-positive events in each group. of percent red/green double positive showed statistically significant differences between the double stained experimental group and single color/unstained controls Groups that do not share a letter are significantly different (n = 3, $p \leq 0.05$) by one-way ANOVA.

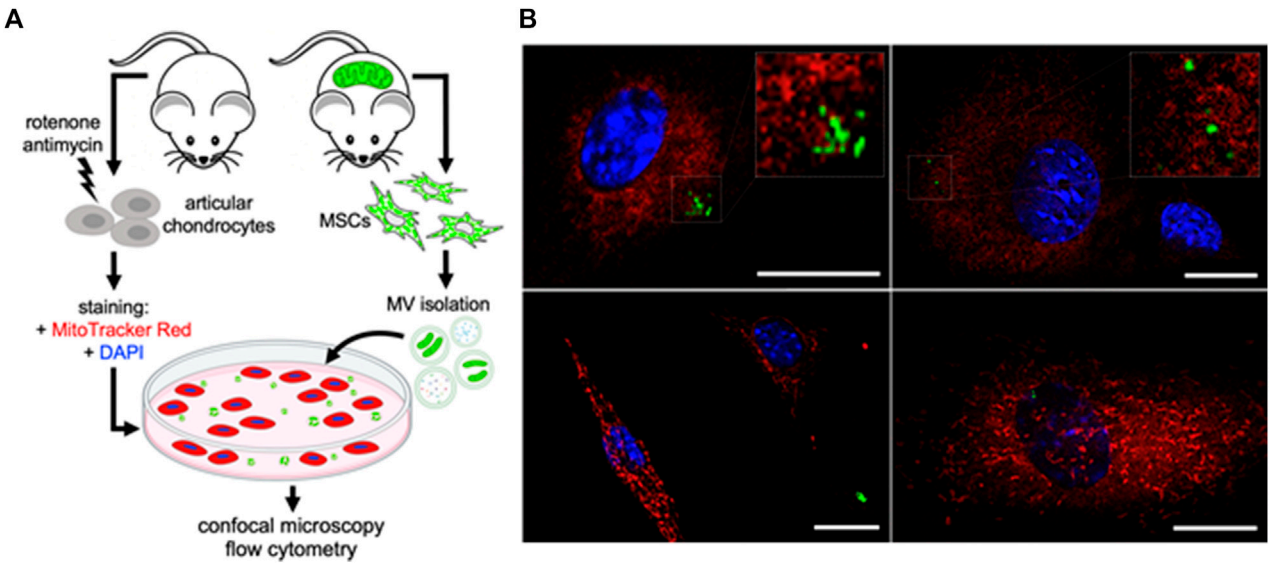

FIGURE 4
Murine Chondrocytes take up MT from MSC-derived Microvesicles **(A)** Schematic depicting experimental method for imaging non-contact intercellular MT transfer **(B)** Confocal images of MSC-MitoEVs and mitoEV mediated MT transfer. MT Transfer demonstrated with mitoEVs (green) incorporated into chondrocyte MT networks (red). Chondrocytes were co-cultured with MSC-microvesicles for 12 h, then fixed and imaged.

them with MVs isolated from MSCs expressing endogenous, MT-specific green fluorescence (Figure 4A). Confocal imaging revealed mitoEVs located in both the extracellular space and within chondrocytes (Figure 4B). Z-stacked imaging confirmed that MSC-derived MT localized to the MT networks within chondrocytes (see Supplemental Materials for representative 3D reconstructions). To confirm the phenomenon could be replicated, imaging experiments were performed twice on two separate days. As an orthogonal approach, we also cultured unstained chondrocytes with MSC-derived MVs, and

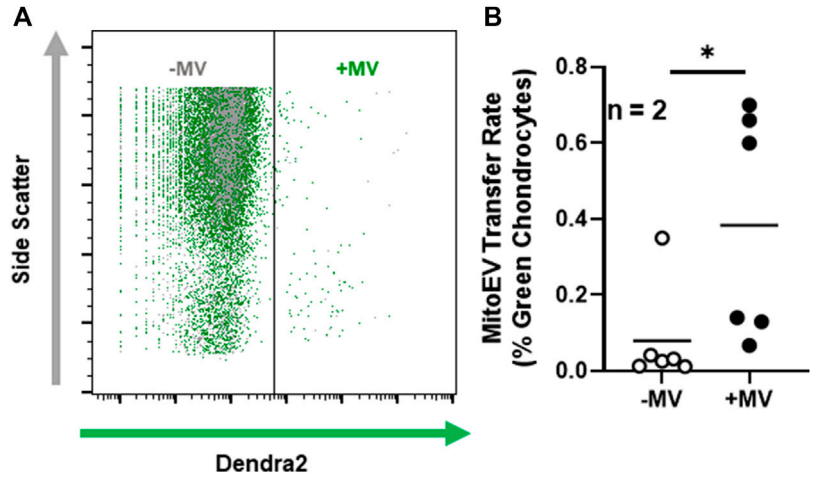

FIGURE 5
Chondrocytes take up MSC-derived MT following incubation with MitoEVs **(A)** Representative flow cytometry plots of chondrocytes incubated with (+MV) and without (-MV) microvesicles isolated from MSCs expressing endogenous, MT-specific dendra2 fluorescence. Dendra2 (green) threshold was set using control chondrocytes. Events fluorescing above threshold were considered chondrocytes having taken up mitoEVs. **(B)** Quantification of mitoEV uptake by chondrocytes in culture ($n = 2$) reveals the +MV group had a higher rate of transfer events than -MV. Data are expressed as the fraction of chondrocytes above threshold for green fluorescence. * = $p \leq 0.05$, by one-way ANOVA.

performed flow cytometry (Figure 5A). This method provided quantitative data on the rate of mitoEV-mediated MT transfer; an average of 0.4% of chondrocytes took up mitoEVs in culture (Figure 5B). Although the rate of mitoEV uptake was low and variable in our experimental system, there was a significant difference between MV-treated and untreated groups (Figure 5B, $p < 0.05$).

4 Discussion

This study demonstrated that human MSCs release intact, functional MT in EVs. To the best of our knowledge, this work represents the first evidence of MSC to chondrocyte, EV-mediated MT transfer. Further, we confirmed that MSC-derived mitoEVs can serve as a vehicle for MT transfer in the absence of direct cell-cell interactions between MSCs and chondrocytes. Our findings are consistent with previous reports, where Phinney et al. found that MSCs undergoing oxidative stress produced vesicles containing dysfunctional, partially depolarized MT to outsource mitophagy. Macrophages engulfed these vesicles and repurposed functional components, improving bioenergetics for both the MSC and macrophage (Phinney et al., 2015). Morrison et al. used mitochondrial organelle staining of MSC-derived EVs and flow cytometry to show that mitoEVs released by MSCs can be incorporated by macrophages into their MT networks. MitoEV uptake by macrophages enhanced phagocytosis by promoting oxidative phosphorylation, and improved their ability to treat lipopolysaccharide-induced lung injury *in vivo* (Morrison et al., 2017). Consistent with our findings, evidence that cells release both functional and non-functional MT in EVs suggests mitoEV transfer is a dynamic, context-driven process, likely involving crosstalk (i.e., bidirectional mitoEV transfer) between donor and recipient cells (Morris and Hollenbeck, 1993; Plotnikov et al., 2008). Studies of contact intercellular MT transfer, involving direct interactions between donor and recipient cells in other tissues indicate that calcium signaling and gap junction proteins play an important role (Islam et al., 2012; Hayakawa et al., 2016). However, the mechanisms of EV-mediated MT transfer are unclear, and further investigation is warranted. In our proof-of-concept experimental design, we found a low rate of mitoEV uptake by chondrocytes *in vitro*. However, it should be noted that several factors, including culture time and MV numbers were not optimized for these experiments. In similar work, where chondrocytes and MSCs were directly co-cultured, the frequency of MT transfer was higher than reported here for mitoEV-mediated transfer; between 1–15% depending on experimental parameters, including culture time, cell ratios, and environmental conditions (Bennett et al., 2019; Fahey et al., 2022). Therefore, we anticipate that future work to optimize experimental parameters and identify mechanisms mediating MSC-chondrocyte mitoEV transfer will allow us to manipulate the rate of mitoEV release by MSCs and uptake by chondrocytes.

To investigate functionality of MT packaged into mitoEVs we used TMRM staining, where fluorescent intensity is directly

proportional to the inner MT membrane potential (Brand and Nicholls, 2011). Using this technique, we found that a subset (at least 5%, up to 70%) of mitoEVs contain functional MT, meaning that they have a competent electron transport chain and are capable of producing ATP. We suspect that the high variability in TMRM-staining between experiments is reflective of the exquisite sensitivity of mitochondria to depolarization, and subtle differences in MT stress induced by EV isolation and analysis techniques, especially flow cytometry, although further studies would be required to confirm this. Our preliminary experience suggests that while fluorescence activated cell sorting (FACS) of mitoEV subpopulations is possible, this approach is damaging to mitoEV polarity, and too time, effort, and cost-intensive to be practical at this time (Kormelink et al., 2016). However, our data suggest the possibility of more scalable, size-dependent methods of mitoEV isolation; We found that more than 70% of MSC-MVs are mitoEVs, a higher percentage than previously reported (Morrison et al., 2017). This is likely due to several experimental differences, such as cell of origin, EV isolation technique, and EV identification method. However, further size analysis of our mitoEV population indicated that nearly all of the MVs >500 nm contain mitochondria. Further studies to investigate methods of isolating mitoEVs based on a size will be necessary to investigate the functional impact of mitoEV uptake on injured chondrocytes. Based on work suggesting MSC donation of functional MT to injured cells can rescue cell viability and promote tissue healing, optimizing functionality of mitoEVs during isolation would be an important consideration for the investigation of mitoEVs as a regenerative orthobiologic therapy (Pacak et al., 2015; Berridge et al., 2016; Jiang et al., 2016; Konari et al., 2019).

Our data suggest mitoEVs themselves are not a homogenous population, but rather a diverse collection of vesicles containing distinct mitochondrial cargoes, with a range of functionality. Distinct mitoEV sub-populations may play biologically distinct roles, including cellular rescue through intercellular mitochondrial transfer, outsourcing of mitophagy and diverse signaling functions (Phinney et al., 2015; Morrison et al., 2017; Sansone et al., 2017; Zhang et al., 2020; Peruzzotti-Jametti et al., 2021). DLS size data further supports this. We found that agents known to affect mitochondrial dynamics and function shift the size profile of EV subgroups released by MSCs; When MSCs were stimulated with either a mitoprotective peptide or a MT specific stressor, we observed a significant shift towards a larger 100–1,000 nm, “medium” peak, presumably MVs. Although our current experimental methods did not allow us to determine why both groups responded similarly, these data suggest mitoEV release is responsive to changes in cellular MT function. It is possible that following rotenone/antimycin-induced MT stress, MSCs increased packaging of dysfunctional MT into MVs, consistent with the previous work demonstrating stressed MSCs release unhealthy MT into EVs to outsource mitophagy (Phinney et al., 2015). Following mitoprotective treatment with SS-31, MSCs may similarly increase export of healthy, functional MT in mitoEVs. Further research into the origin, mechanisms of release, and function of mitoEV sub-populations is necessary to elucidate how MSC MT function is related to mitoEV biogenesis.

Measurement of particles smaller than 200 nm (i.e., exosomes) was limited to size and protein analysis. Neither of the MT proteins we probed for (COXIV an outer MT membrane protein and ATP5A1, an enzyme that catalyzes synthesis of ATP) was present in the exosome fraction. This may be due to the specific proteins we chose to investigate, rather than an indicator that MSC-exosomes do not transport MT components. Previous analysis has shown that exosomes may be more likely to contain miRNA and mtDNA, as opposed to the MT membrane proteins and intact MT seen in larger vesicles such as MVs (Phinney et al., 2015; Torralba et al., 2018; D’Acunzo et al., 2021). As techniques improve and high resolution, microparticle optimized flow cytometers become more widely available, characterization of individual mitoEV sub-populations will become more straightforward.

Anunderlying goal of this study was to characterize MSC-derived mitoEVs and investigate their potential suitability as vehicles for non-contact, acellular MT delivery in therapeutic applications. The properties that make EVs effective in long range endogenous communication, also make them excellent candidates for regenerative therapy. EV lipid bilayers are durable enough to retain structural integrity after freeze-thawing and remain intact following intraarticular injection (Li et al., 2019). EVs are non-replicating and have low levels of major histocompatibility complex proteins, posing minimal risk of immunogenicity or tumorigenicity (Yeo et al., 2013; Zhu et al., 2017; Tsiapalis and O’Driscoll, 2020). We confirmed the presence of functional MT in MSC-MVs, identified evidence of distinct sub-populations of mitoEVs, and found that, although MT are present in MVs of all sizes, large MVs are much more likely to contain MT. Further, we observed evidence that stressed chondrocytes will take up MT packaged in mitoEVs in the absence of physical interactions with the parent MSCs. The methods developed in this study will allow investigation into the effects of these mitoEVs after uptake and the mechanisms underlying this phenomenon, as well as those behind why distinct sub-populations such as functional and dysfunctional mitoEVs are released.

Data availability statement

The original contributions presented in the study are included in the article/Supplementary Material, further inquiries can be directed to the corresponding author.

Ethics statement

The animal study was reviewed and approved by Institutional Animal Care and Use Committee at Cornell University" Catherine.

Author contributions

MT, MD, and MA contributed to the conception and design of the study. MT conducted cell culture and dynamic light scattering. MT and BP performed flow cytometry and nanoparticle tracking experiments. MF ran western blot experiments. RI and MT took confocal images. MT, MF, and MD wrote and edited sections of the manuscript. MT ran statistical analysis.

Funding

This study was funded by NIH NIAMS grants K08AR068470 and R03AR075929 and the Harry M. Zweig Fund for Equine Research. This work was performed in part at the Cornell NanoScale Facility, a member of the National Nanotechnology Coordinated Infrastructure (NNCI), which is supported by the National Science Foundation (Grant NNCI-2025233). Methods schematic created with BioRender.com.

Conflict of interest

The authors declare that the research was conducted in the absence of any commercial or financial relationships that could be construed as a potential conflict of interest.

Publisher's note

All claims expressed in this article are solely those of the authors and do not necessarily represent those of their affiliated organizations, or those of the publisher, the editors and the reviewers. Any product that may be evaluated in this article, or claim that may be made by its manufacturer, is not guaranteed or endorsed by the publisher.

Supplementary material

The Supplementary Material for this article can be found online at: https://www.frontiersin.org/articles/10.3389/fbioe.2022.870193/full#supplementary-material

References

Asghar, W., El Assal, R., Shafiee, H., Anchan, R. M., and Demirci, U. (2014). Preserving human cells for regenerative, reproductive, and transfusion medicine. *Biotechnol. J.* 9, 895–903. doi:10.1002/biot.201300074

Bartell, L. R., Fortier, L. A., Bonassar, L. J., Szeto, H. H., Cohen, I., Delco, M. L., et al. (2020). Mitoprotective therapy prevents rapid, strain-dependent mitochondrial dysfunction after articular cartilage injury. *J. Orthop. Res.* 38, 1257–1267. doi:10.1002/jor.24567

Bennett, M. P., Vivancos-Koopman, I., Seewald, L., Wells, K., Robinette, T., Delco, M. L., et al. (2019). Intercellular mitochondrial transfer from mesenchymal stem cells to stressed chondrocytes. *Osteoarthr. Cartil.* 27, S51–S52. doi:10.1016/j.joca.2019.02.074

Berridge, M. V., Schneider, R. T., and McConnell, M. J. (2016). Mitochondrial transfer from astrocytes to neurons following ischemic insult: Guilt by association? *Cell. Metab.* 24, 376–378. doi:10.1016/j.cmet.2016.08.023

Bianchi, G., and Sinigaglia, L. (20122012). Chondrogenesis, joint formation, and cartilage metabolism. *Arthritis Res. Ther.* 142, A5. doi:10.1186/AR3712

Blanco, F. J., Rego, I., and Ruiz-Romero, C. (20112011). The role of mitochondria in osteoarthritis. *Nat. Rev. Rheumatol.* 73 (7), 161–169. doi:10.1038/nrrheum.2010.213

Bonnevie, E. D., Delco, M. L., Bartell, L. R., Jasty, N., Cohen, I., Fortier, L. A., et al. (2018). Microscale frictional strains determine chondrocyte fate in loaded cartilage. *J. Biomech.* 74, 72–78. doi:10.1016/j.jbiomech.2018.04.020

Brand, M. D., and Nicholls, D. G. (2011). Assessing mitochondrial dysfunction in cells. *Biochem. J.* 435, 297–312. doi:10.1042/BJ20110162

Charron, D. (2013). Allogenicity & immunogenicity in regenerative stem cell therapy. *Indian J. Med. Res.* 138, 749–754.

Chinnery, H. R., Pearlman, E., and McMenamin, P. G. (2008). Cutting edge: Membrane nanotubes *in vivo*: A feature of mhc class II + cells in the mouse cornea. *J. Immunol.* 180, 5779–5783. doi:10.4049/jimmunol.180.9.5779

Crewe, C., Funcke, J. B., Li, S., Joffin, N., Gliniak, C. M., Ghaben, A. L., et al. (2021). Extracellular vesicle-based interorgan transport of mitochondria from energetically stressed adipocytes. *Cell. Metab.* 33, 1853–1868. doi:10.1016/J.CMET.2021.08.002

D'Acunzo, P., Pérez-González, R., Kim, Y., Hargash, T., Miller, C., Alldred, M. J., et al. (2021). Mitovesicles are a novel population of extracellular vesicles of mitochondrial origin altered in down syndrome. *Sci. Adv.* 7, 5085–5097. doi:10.1126/SCIADV.ABE5085/SUPPL_FILE/ABE5085_SM.PDF

Delco, M. L., Bonnevie, E. D., Szeto, F. S., Bonassar, L. W., and Fortier, L. A. (2018b). Mitoprotective therapy preserves chondrocyte viability and prevents cartilage degeneration in an *ex vivo* model of posttraumatic osteoarthritis. *J. Orthop. Res.* 36, 2147–2156. doi:10.1002/JOR.23882

Delco, M. L., Bonnevie, E. D., Bonassar, L. J., and Fortier, L. A. (2018a). Mitochondrial dysfunction is an acute response of articular chondrocytes to mechanical injury. *J. Orthop. Res.* 36, 739–750. doi:10.1002/jor.23651

Fahey, M. J., Bennett, M. P., Thomas, M. A., Vivancos-Koopman, I., Browning, L., Bonassar, L. J., et al. (2022). Mesenchymal stromal cells donate mitochondria to articular chondrocytes exposed to mitochondrial, environmental, and mechanical stress. *BioRxiv*. doi:10.1101/2022.05.12.491696

Goetz, J. E., Coleman, M. C., Fredericks, D. C., Petersen, E., Martin, J. A., McKinley, T. O., et al. (2017). Time-dependent loss of mitochondrial function precedes progressive histologic cartilage degeneration in a rabbit meniscal destabilization model. *J. Orthop. Res.* 35, 590–599. doi:10.1002/jor.23327

Gosset, M., Berenbaum, F., Thirion, S., and Jacques, C. (2008). Primary culture and phenotyping of murine chondrocytes. *Nat. Protoc.* 3, 1253–1260. doi:10.1038/nprot.2008.95

Gould, S. J., and Raposo, G. (2013). As we wait: Coping with an imperfect nomenclature for extracellular vesicles. *J. Extracell. Vesicles* 2, 20389. doi:10.3402/JEV.V2I0.20389

Gray, W. D., Mitchell, A. J., and Searles, C. D. (2015). An accurate, precise method for general labeling of extracellular vesicles. *MethodsX* 2, 360–367. doi:10.1016/j.mex.2015.08.002

Hall, P. A., and Watt, F. M. (1989). *Stem cells: The generation and maintenance of cellular diversity*, 106, 619–633. doi:10.1242/dev.106.4.619*Development*

Hayakawa, K., Esposito, E., Wang, X., Terasaki, Y., Liu, Y., Xing, C., et al. (2016). Transfer of mitochondria from astrocytes to neurons after stroke. *Nature* 535, 551–555. doi:10.1038/nature18928

Huang, S., Xu, L., Sun, Y., Wu, T., Wang, K., Li, G., et al. (2015). An improved protocol for isolation and culture of mesenchymal stem cells from mouse bone marrow. *J. Orthop. Transl.* 3, 26–33. doi:10.1016/j.jot.2014.07.005

Islam, M. N., Das, S. R., Emin, M. T., Wei, M., Sun, L., Westphalen, K., et al. (2012). Mitochondrial transfer from bone-marrow-derived stromal cells to pulmonary alveoli protects against acute lung injury. *Nat. Med.* 18, 759–765. doi:10.1038/nm.2736

Jackson, M. V., Morrison, T. J., Doherty, D. F., McAuley, D. F., Matthay, M. A., Kissenpfennig, A., et al. (2016). Mitochondrial transfer via tunneling nanotubes is an important mechanism by which mesenchymal stem cells enhance macrophage phagocytosis in the *in vitro* and *in vivo* models of ARDS. *Stem Cells* 34, 2210–2223. doi:10.1002/stem.2372

Jiang, D., Gao, F., Zhang, Y., Wong, D. S. H., Li, Q., Tse, H. F., et al. (2016). Mitochondrial transfer of mesenchymal stem cells effectively protects corneal epithelial cells from mitochondrial damage. *Cell. Death Dis.* 7, e2467. doi:10.1038/cddis.2016.358

Kingery, M. T., Manjunath, A. K., Anil, U., and Strauss, E. J. (2019). Bone marrow mesenchymal stem cell therapy and related bone marrow-derived orthobiologic therapeutics. *Curr. Rev. Musculoskelet. Med.* 12, 451–459. doi:10.1007/s12178-019-09583-1

Kogure, A., Yoshioka, Y., and Ochiya, T. (2020). Extracellular vesicles in cancer metastasis: Potential as therapeutic targets and materials. *Int. J. Mol. Sci.* 21, 4463. doi:10.3390/ijms21124463

Konari, N., Nagaishi, K., Kikuchi, S., and Fujimiya, M. (2019). Mitochondria transfer from mesenchymal stem cells structurally and functionally repairs renal proximal tubular epithelial cells in diabetic nephropathy *in vivo*. *Sci. Rep.* 9, 5184. doi:10.1038/s41598-019-40163-y

Kormelink, T. G., Arkesteijn, G. J. A., Nauwelaers, F. A., van den Engh, G., Nolte-'t Hoen, E. N. M., Wauben, M. H. M., et al. (2016). Prerequisites for the analysis and sorting of extracellular vesicle subpopulations by high-resolution flow cytometry. *Cytom. A* 89, 135–147. doi:10.1002/cyto.a.22644

Lai, R. C., Arslan, F., Lee, M. M., Sze, N. S. K., Choo, A., Chen, T. S., et al. (2010). Exosome secreted by MSC reduces myocardial ischemia/reperfusion injury. *Stem Cell. Res.* 4, 214–222. doi:10.1016/j.scr.2009.12.003

Larsson, L. I., Bjerregaard, B., and Talts, J. F. (2008). Cell fusions in mammals. *Histochem. Cell. Biol.* 129, 551–561. doi:10.1007/s00418-008-0411-1

Lawrence, R. C., Felson, D. T., Helmick, C. G., Arnold, M. L., Deyo, R. A., Gabriel, S., et al. (2008). Estimates of the prevalence of arthritis and other rheumatic conditions in the United States. Part II. *Arthritis Rheum.* 58, 26–35. doi:10.1002/ART.23176

Li, J. J., Hosseini-Beheshti, E., Grau, G. E., Zreiqat, H., and Little, C. B. (2019). Stem cell-derived extracellular vesicles for treating joint injury and osteoarthritis. *Nanomaterials* 9, 261. doi:10.3390/NANO9020261

Liu, H., Li, Z., Cao, Y., Cui, Y., Yang, X., Meng, Z., et al. (2019). Effect of chondrocyte mitochondrial dysfunction on cartilage degeneration: A possible pathway for osteoarthritis pathology at the subcellular level. *Mol. Med. Rep.* 20, 3308–3316. doi:10.3892/mmr.2019.10559

Loeser, R. F. (2011). Aging and osteoarthritis. *Curr. Opin. Rheumatol.* 23, 492–496. doi:10.1097/BOR.0B013E3283494005

Ludwig, A. K., and Giebel, B. (2012). Exosomes: Small vesicles participating in intercellular communication. *Int. J. Biochem. Cell. Biol.* 44, 11–15. doi:10.1016/J.BIOCEL.2011.10.005

Madry, H., Luyten, F. P., and Facchini, A. (20112011). Biological aspects of early osteoarthritis. *Knee Surg. Sports Traumatol. Arthrosc.* 20, 407–422. doi:10.1007/S00167-011-1705-8

Mobasheri, A., Rayman, M. P., Gualillo, O., Sellam, J., Van Der Kraan, P., Fearon, U., et al. (2017). The role of metabolism in the pathogenesis of osteoarthritis. *Nat. Rev. Rheumatol.* 13, 302–311. doi:10.1038/nrrheum.2017.50

Morris, R. L., and Hollenbeck, P. J. (1993). The regulation of bidirectional mitochondrial transport is coordinated with axonal outgrowth. *J. Cell. Sci.* 104, 917–927. doi:10.1242/jcs.104.3.917

Morrison, T. J., Jackson, M. V., Cunningham, E. K., Kissenpfennig, A., McAuley, D. F., O'Kane, C. M., et al. (2017). Mesenchymal stromal cells modulate macrophages in clinically relevant lung injury models by extracellular vesicle mitochondrial transfer. *Am. J. Respir. Crit. Care Med.* 196, 1275–1286. doi:10.1164/RCCM.201701-0170OC

Murray, L. M. A., and Krasnodembskaya, A. D. (2019). Concise review: Intercellular communication via organelle transfer in the biology and therapeutic applications of stem cells. *Stem Cells* 37, 14–25. doi:10.1002/stem.2922

Musiał-Wysocka, A., Kot, M., and Majka, M. (2019). The pros and cons of mesenchymal stem cell-based therapies. *Cell. Transpl.* 28, 801–812. doi:10.1177/0963689719837897

Pacak, C. A., Preble, J. M., Kondo, H., Seibel, P., Levitsky, S., Del Nido, P. J., et al. (2015). Actin-dependent mitochondrial internalization in cardiomyocytes: Evidence for rescue of mitochondrial function. *Biol. Open* 4, 622–626. doi:10.1242/bio.201511478

Peruzzotti-Jametti, L., Bernstock, J. D., Willis, C. M., Manferrari, G., Rogall, R., Fernandez-Vizarra, E., et al. (2021). Neural stem cells traffic functional mitochondria via extracellular vesicles. *PLoS Biol.* 19, e3001166. doi:10.1371/JOURNAL.PBIO.3001166

Phinney, D. G., Di Giuseppe, M., Njah, J., Sala, E., Shiva, S., St Croix, C. M., et al. (2015). Mesenchymal stem cells use extracellular vesicles to outsource mitophagy and shuttle microRNAs. *Nat. Commun.* 6, 8472. doi:10.1038/ncomms9472

Plotnikov, E. Y., Khryapenkova, T. G., Vasileva, A. K., Marey, M. V., Galkina, S. I., Isaev, N. K., et al. (2008). Cell-to-cell cross-talk between mesenchymal stem cells and cardiomyocytes in co-culture. *J. Cell. Mol. Med.* 12, 1622–1631. doi:10.1111/j.1582-4934.2007.00205.x

Sansone, P., Savini, C., Kurelac, I., Chang, Q., Amato, L. B., Strillacci, A., et al. (2017). Packaging and transfer of mitochondrial DNA via exosomes regulate escape from dormancy in hormonal therapy-resistant breast cancer. *Proc. Natl. Acad. Sci. U. S. A.* 114, E9066–E9075. doi:10.1073/PNAS.1704862114

Sarzi-Puttini, P., Cimmino, M. A., Scarpa, R., Caporali, R., Parazzini, F., Zaninelli, A., et al. (2005). Osteoarthritis: An overview of the disease and its treatment strategies. *Semin. Arthritis Rheum.* 35, 1–10. doi:10.1016/J.SEMARTHRIT.2005.01.013

Sophia Fox, A. J., Bedi, A., and Rodeo, S. A. (2009). The basic science of articular cartilage: Structure, composition, and function. *Sports Health.* 1, 461–468. doi:10.1177/1941738109350438

Torralba, D., Baixauli, F., Villarroya-Beltri, C., Fernández-Delgado, I., Latorre-Pellicer, A., Acín-Pérez, R., et al. (20182018). Priming of dendritic cells by DNA-containing extracellular vesicles from activated T cells through antigen-driven contacts. *Nat. Commun.* 9, 2658. doi:10.1038/s41467-018-05077-9

Tsiapalis, D., and O'Driscoll, L. (2020). Mesenchymal stem cell derived extracellular vesicles for tissue engineering and regenerative medicine applications. *Cells* 9, 991. doi:10.3390/CELLS9040991

Wang, F., Cerione, R. A., and Antonyak, M. A. (2021). Isolation and characterization of extracellular vesicles produced by cell lines. *Star. Protoc.* 2, 100295. doi:10.1016/j.xpro.2021.100295

Watson, W. H., Ritzenthaler, J. D., and Roman, J. (2016). Lung extracellular matrix and redox regulation. *Redox Biol.* 8, 305–315. doi:10.1016/J.REDOX.2016.02.005

Winklhofer, K. F., and Haass, C. (20101802). Mitochondrial dysfunction in Parkinson's disease. *Biochimica Biophysica Acta - Mol. Basis Dis.* 24, 29–44. doi:10.1016/J.BBADIS.2009.08.013

Yuana, Y., Sturk, A., and Nieuwland, R. (2013). Extracellular vesicles in physiological and pathological conditions. *Blood Rev.* 27, 31–39. doi:10.1016/J.BLRE.2012.12.002

Yeo, R. W. Y., Lai, R. C., Tan, K. H., and Lim, S. K. (2013). Exosome: A novel and safer therapeutic refinement of mesenchymal stem cell. *J. Circulating Biomarkers.* doi:10.5772/57460

Zhang, X., Hubal, M. J., and Kraus, V. B. (2020). Immune cell extracellular vesicles and their mitochondrial content decline with ageing. *Immun. Ageing* 17, 1. doi:10.1186/s12979-019-0172-9

Zheng, L., Zhang, Z., Sheng, P., and Mobasheri, A. (2021). The role of metabolism in chondrocyte dysfunction and the progression of osteoarthritis. *Ageing Res. Rev.* 66, 101249. doi:10.1016/J.ARR.2020.101249

Zhu, X., Badawi, M., Pomeroy, S., Sutaria, D. S., Xie, Z., Baek, A., et al. (2017). Comprehensive toxicity and immunogenicity studies reveal minimal effects in mice following sustained dosing of extracellular vesicles derived from HEK293T cells. *J. Extracell. Vesicles* 6, 1324730. doi:10.1080/20013078.2017.1324730

frontiers | Frontiers in Bioengineering and Biotechnology

ORIGINAL RESEARCH
published: 23 August 2022
doi: 10.3389/fbioe.2022.885369

In Situ Assessment of Porcine Osteochondral Repair Tissue in the Visible–Near Infrared Spectral Region

*Shital Kandel[1], William Querido[1], Jessica M. Falcon[1], Hannah M. Zlotnick[2], Ryan C. Locke[2], Brendan Stoeckl[2], Jay M. Patel[2,3], Chetan A. Patil[1], Robert L. Mauck[2] and Nancy Pleshko[1]**

[1]Department of Bioengineering, Temple University, Philadelphia, PA, United States, [2]Department of Bioengineering, University of Pennsylvania, Philadelphia, PA, United States, [3]Department of Orthopedics, Emory University, Atlanta, GA, United States

Standard assessment of cartilage repair progression by visual arthroscopy can be subjective and may result in suboptimal evaluation. Visible–near infrared (Vis-NIR) fiber optic spectroscopy of joint tissues, including articular cartilage and subchondral bone, provides an objective approach for quantitative assessment of tissue composition. Here, we applied this technique in the 350–2,500 nm spectral region to identify spectral markers of osteochondral tissue during repair with the overarching goal of developing a new approach to monitor repair of cartilage defects *in vivo*. Full thickness chondral defects were created in Yucatan minipigs using a 5-mm biopsy punch, and microfracture (MFx) was performed as a standard technique to facilitate repair. Tissues were evaluated at 1 month (in adult pigs) and 3 months (in juvenile pigs) post-surgery by spectroscopy and histology. After euthanasia, Vis-NIR spectra were collected *in situ* from the defect region. Additional spectroscopy experiments were carried out *in vitro* to aid in spectral interpretation. Osteochondral tissues were dissected from the joint and evaluated using the conventional International Cartilage Repair Society (ICRS) II histological scoring system, which showed lower scores for the 1-month than the 3-month repair tissues. In the visible spectral region, hemoglobin absorbances at 540 and 570 nm were significantly higher in spectra from 1-month repair tissue than 3-month repair tissue, indicating a reduction of blood in the more mature repair tissue. In the NIR region, we observed qualitative differences between the two groups in spectra taken from the defect, but differences did not reach significance. Furthermore, spectral data also indicated that the hydrated environment of the joint tissue may interfere with evaluation of tissue water absorbances in the NIR region. Together, these data provide support for further investigation of the visible spectral region for assessment of longitudinal repair of cartilage defects, which would enable assessment during routine arthroscopy, particularly in a hydrated environment.

Keywords: visible–near infrared (Vis-NIR), fiber optic spectroscopy, cartilage repair, microfracture, *in situ* optical spectroscopy

OPEN ACCESS

Edited by:
Dmitriy Sheyn,
Cedars Sinai Medical Center,
United States

Reviewed by:
Ryan Michael Porter,
University of Arkansas for Medical Sciences, United States
Diane Wagner,
Indiana University, Purdue University Indianapolis, United States

****Correspondence:***
Nancy Pleshko
npleshko@temple.edu

Specialty section:
This article was submitted to Tissue Engineering and Regenerative Medicine, a section of the journal Frontiers in Bioengineering and Biotechnology

Received: *28 February 2022*
Accepted: *13 June 2022*
Published: *23 August 2022*

Citation:
Kandel S, Querido W, Falcon JM, Zlotnick HM, Locke RC, Stoeckl B, Patel JM, Patil CA, Mauck RL and Pleshko N (2022) In Situ Assessment of Porcine Osteochondral Repair Tissue in the Visible–Near Infrared Spectral Region. Front. Bioeng. Biotechnol. 10:885369. doi: 10.3389/fbioe.2022.885369

INTRODUCTION

Articular cartilage, a connective tissue present at the end of long bones in diarthrodial joints, provides a smooth and lubricated surface for bone articulation without friction. It is composed of approximately 80 wt% water and 20% extracellular matrix, which consists of proteins including collagen type II and proteoglycans (Sophia Fox et al., 2009; Gao et al., 2014). Chondrocytes are the

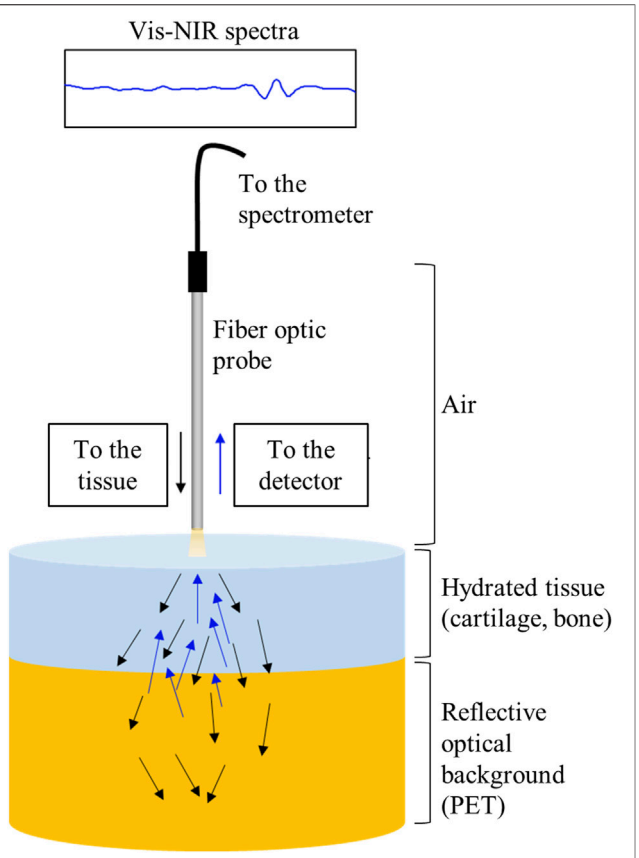

FIGURE 1 | Schematic of light scattering through cartilage tissue and a semi-infinite reflecting surface.

primary cells in this tissue that represent about 2% of the total volume of healthy adult cartilage. This tissue is also characterized by a lack of blood vessels, nerves, and lymphatics; thus, when an injury occurs, the tissue healing is very limited (Suh et al., 1995; Poole et al., 2001). Ultimately, progression of an injury or degradation of this tissue can result in the debilitating disease osteoarthritis (OA).

Osteoarthritis causes painful movement and discomfort and must be treated early for the best chance of success (Braun and Gold, 2012). Microfracture treatments are widely used for repair of chondral defects associated with OA, in particular for small defects less than ~2 cm^2 (Mithoefer et al., 2009). In this approach, a defect is repaired using a sharp tool (awl) to puncture holes in the subchondral plate, which allows blood and mesenchymal stem cells that reside in the bone marrow to migrate to the defect site and initiate repair (Steadman et al., 2010; Fisher et al., 2015). The repair process, however, frequently results in formation of undesirable fibrocartilage rich in collagen type I (Steadman et al., 2010; Kim et al., 2015; Vega et al., 2017).

Current gold-standard techniques for repair assessment include the use of the ICRS II scoring system, developed by the International Society of Cartilage Repair (ICRS) (Mainil-Varlet et al., 2010). This is a destructive approach based on the histology scoring of the repair tissue, and since this is an end-point test, longitudinal repair of the tissue cannot be assessed. Furthermore, second-look biopsies of repairing joint tissues are not the standard of care in the US or Europe (Brun et al., 2008). Similarly, another approach for assessment of tissue repair utilizes the Oswestry Arthroscopy Score. This scoring technique includes a visual and tactile assessment of repair tissue and can be performed arthroscopically (Paatela et al., 2020). However, the scoring can be subjective and may result in suboptimal assessment of defect repair (Brismar et al., 2002).

Infrared (IR) spectroscopic analysis has been used in evaluation of cartilage and bone tissue in both the mid-IR (MIR; 4,000–400 cm^{-1} or 2,500–25,000 nm) and near-IR (NIR; 10,000–4,000 cm^{-1} or 1000–2,500 nm) spectral regions (Querido et al., 2021). The NIR region has an advantage in the analysis of thick tissues as radiation can penetrate and be detected up to several millimeters into the tissue, including in cartilage (Padalkar and Pleshko, 2015). Considering that an average human articular cartilage ranges from 1 to 3 mm thickness, information from the entire cartilage depth can be obtained with NIR spectral analysis. NIR fiber optic spectroscopy has been previously used to non-destructively monitor matrix development in tissue-engineered cartilage constructs *in situ* (Hanifi et al., 2017; Yousefi et al., 2017; Kandel et al., 2020) and to assess proteoglycan content and cartilage thickness (Sarin et al., 2019). In particular, the baseline offset of NIR raw spectra have shown to be associated with an increase in the matrix development in engineered cartilage (Kandel et al., 2020). Additionally, the absorbances at 5,800 and 5,900 cm^{-1} have also been shown to be associated with accumulation of matrix representing the development of engineered cartilage (Kandel et al., 2020). In the case of NIR spectra of healthy cartilage with underlying subchondral bone, the ratio of water absorbances at 5,200 cm^{-1} and 7,000 cm^{-1} have been shown to reflect the increase in the ratio of thickness of subchondral bone to articular cartilage (Mcgoverin et al., 2014).

In addition to spectroscopy in the NIR region, analysis in the visible spectral region (Vis; 350–700 nm) can provide important information on tissue composition. This spectral region has been used extensively for characterization of the light interaction with different biological tissues, including breast tissue, forearm muscle, abdomen, and forehead. In these studies, absorbances from tissue components such as deoxygenated and oxygenated hemoglobin, lipids, and water were monitored to yield information related to composition and/or function (Taroni et al., 2003; Jacques, 2013). In an osteochondral defect, this spectral region may provide information on hemoglobin, which would indicate the presence of a blood clot and/or neovascularization in the repairing tissue, typically present in the early stages of repair and less so at the later stages.

The overall aim of this study was to evaluate the potential of Vis-NIR fiber optic spectroscopy to assess molecular changes related to tissue repair in osteochondral tissues *in situ* in a porcine preclinical model. This was carried out by collection of spectra from tissues at the defect site, followed by experiments to facilitate spectral interpretation. The depth of detection of diffuse reflectance spectra in the Vis-NIR spectral regions was also investigated.

METHODS

Animal Study

Animal procedures were approved by the Institutional Animal Care and Use Committee (IACUC) at the University of Pennsylvania and performed in the animal facility at the University of Pennsylvania. Animals in the current study were part of larger studies at U Penn, where the mature and immature animals comprised separate studies. For the 1-month study, six skeletally mature (age 12 months at the beginning of the study) Yucatan minipigs (Sinclair Bioresources, Auxvasse, MO, United States) were used, while for the 3-month study, three juvenile (age 6 months at the beginning of the study) Yucatan minipigs (Sinclair Bioresources, Auxvasse, MO, United States) were used. In each animal, full thickness chondral defects were created bilaterally in the trochlear groove using a 5-mm biopsy punch, at proximal, middle, and distal locations of the medial and lateral sides (six defects in the right hind limb per animal, as part of a larger study). MFx treatments were randomized from joint to joint to enable consistency with regard to their load-bearing location. Awl-based microfracture procedures (diameter: 0.8 mm; depth: 2 mm) with three marrow stimulation holes were carried out. In total, there were n = 9 microfracture-treated cartilage defects in the 1-month animal study and n = 6 microfracture-treated cartilage defects in the 3-month animal study. The animals were housed and recovered under veterinary care. At the end of the study period (1 or 3 months post-surgery), all animals were euthanized, and the tissues were evaluated spectroscopically and histologically (in addition to other end-point tests related to the original studies, and not reported here).

Vis-NIR Spectra Collection

Vis-NIR spectra were collected from the microfracture-treated defect tissue and from native healthy cartilage immediately after euthanasia *in situ* in intact joints. Spectra were collected in a diffuse reflectance configuration using a fiber optic reflectance probe (Malvern Panalytical, United States) with six illumination fibers (600 microns diameter) and one collection fiber attached with a 2-mm spacer on the tip of the probe. The probe was connected to an ASD LabSpec four Standard-Res Lab Analyzer spectrometer (Malvern Panalytical, United States). The fiber optic probe tip diameter was approximately 3 mm. As the osteochondral defects were created using a 5-mm-diameter biopsy punch, we consistently collected data from the center portion of the repair tissue. These spectral data reflected average absorbances over the 3 mm diameter region, which, based on the awl diameter of 0.8 mm, would include a combination of punctured and non-punctured subchondral bone regions. From each tissue region, n = 3 spectra were collected, with 50 co-added scans and 8.5 ms of integration time over a spectral range of 350–2,500 nm. The spectra were divided into the visible region (350–750 nm) and the NIR region (1000–2,500 nm or 10,000–4,000 cm^{-1}). All the visible region spectra were presented as wavelength (nm), and the NIR region spectra were presented as frequency (wavenumber, cm^{-1}) per convention. The spectra were processed in ViewSpec Pro (Malvern Panalytical) for splice correction of detector regions. The corrected spectra were then processed in Unscrambler X (CAMO, Norway) software. The spectra were smoothed using the Savitzky–Golay (SG) filter with nine smoothing points. Second-derivative processing was used (SG filter with 15 points smoothing), and then the spectra were inverted to evaluate the positive intensity of peaks of interest. Outcomes from spectral analysis in the NIR region were absorbance peak intensities reflecting water content (peaks at 7,000 and 5,200 cm^{-1}) and matrix protein content (peaks at 5,900 and 5,800 cm^{-1}), while absorbance peaks reflecting oxygenated hemoglobin (blood) content (peaks at 540 and 570 nm) were investigated in the visible region (van Kampen and Zijlstra, 1983).

Vis-NIR Depth of Detection Into Joint Tissue

The extent of light interaction from the fiber optic probe into the tissues was of interest to aid in spectral interpretation of the repairing joint tissue spectra. This was assessed as the depth of detection in the harvested intact joint tissue and in the cartilage and bone separately and together. Harvested repair tissue from the 1-month microfracture study (primarily fibrous tissue, based on histology) was also investigated separately. Briefly, fresh stifle joints from one adult Yorkshire pig (Animal Biotech Inc. Doylestown, PA) were dissected, and multiple full osteochondral plugs were harvested using a 6-mm biopsy punch (Miltex). Vis-NIR spectra of tissues of varying thicknesses of articular cartilage (1.6–4 mm), subchondral bone (1–3 mm), and intact total joint tissue (cartilage and bone, 3–6 mm) were collected on top of 25 mm of polyethylene terephthalate (PET). PET acts as a diffusely reflective optical background with semi-infinite optical thickness and also is characterized by unique spectral absorbances (Zonios and Dimou, 2006). (**Figure 1**). The PET polymer was chosen as it has distinct peaks in the spectral regions of interest. In the NIR region, the 8,865 cm^{-1} (1,130 nm) absorbance has been previously used to characterize PET polymer (Moroni et al., 2015) and arises from the 2nd overtone of C-H stretching; the PET absorbance at 6000 cm^{-1} (1,660 nm) arises from 1st overtone of aromatic C-H stretching plus methylene stretching (Lachenal, 2006). The ability to detect these absorbances while collecting spectral data from tissues on top of PET can establish the depth of detection. Similarly, in the visible region, PET has a characteristic peak at 375 nm (Ouchi et al., 1999). The depth of detection into the tissue was determined based on the minimum thickness of tissue from which the PET signal was not detected in the spectra, similar to that previously described in Padalkar and Pleshko, (2015). A Spectralon standard underneath the tissues was used as a control for data collection.

Histology

Full depth explants of the defect repair tissue regions were fixed in 4% paraformaldehyde for 24 h. Samples were decalcified for 8 weeks by placing the samples in 50-ml conical tubes with 15–20 ml of decalcification solution (Formical-2000) with intermittent changes, followed by embedding in paraffin wax. To account for variations in subchondral histomorphology with sectioning depth into the tissue block, we obtained sections

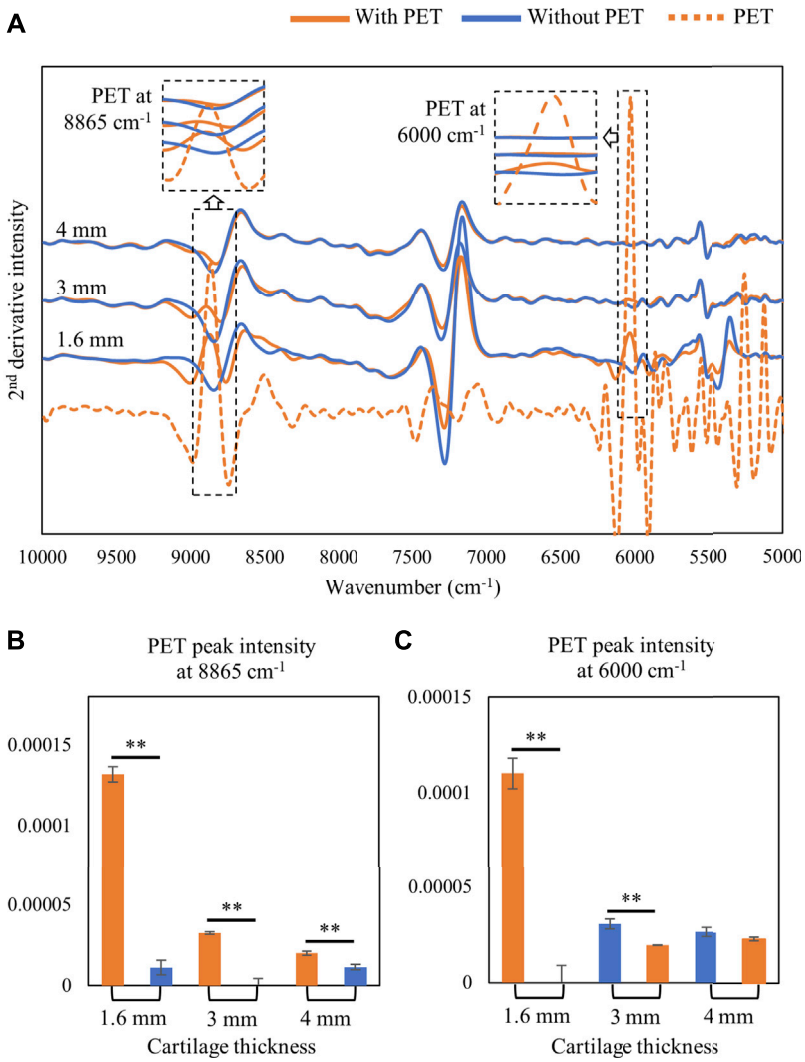

FIGURE 2 | (A) Second-derivative spectra of harvested cartilage tissue collected on top of a semi-infinite PET block or on Spectralon standard (without PET). The depth of detection of PET signal at higher and lower frequencies was monitored by assessment of the PET signal at 8865 cm^{-1} and 6000 cm^{-1}, respectively. **(B)** 8865 cm^{-1} signal intensity can be detected with a cartilage thickness of up to 4 mm. **(C)** 6000 cm^{-1} PET signal intensity can be detected with a cartilage thickness of up to 3 mm only. $**p < 0.01$.

approximately from the center of each defect region, observing the size of the defect region as guide to select the appropriate sections (larger defect, more central defect position). The embedded samples were sectioned at 8 microns thickness onto the glass slides, and for each sample, the section with the largest defect region was stained with Safranin-O (0.2%) and fast green (0.02%) and imaged under a bright field microscope. One adjacent section from each block was obtained for Fourier transform infrared (FTIR) spectral imaging, as described in the following section.

Histological ICRS II Scoring

Four blinded independent observers previously trained in ICRS scoring of tissues reviewed and scored control and defect sections using the ICRS II Histological Assessment Scale (Mainil-Varlet et al., 2010). While all parameters that comprise the ICRS II scale were scored on a scale from 0 (poor defect repair) to 100 (normal articular cartilage), only the following parameters having significant differences between the two groups were reported: overall average score, matrix staining, surface architecture, basal integration, subchondral bone abnormality, and vascularization. The four observer scores obtained for each parameter were averaged.

FTIR Spectroscopic Imaging for the Assessment of Defect Thickness

As it was challenging to assess defect thickness based on the contrast in the histology sections, FTIR imaging data were collected from unstained sections of 5 microns thickness on low-e slides (Kevley Technologies). Sections were imaged using a Spotlight 400 imaging

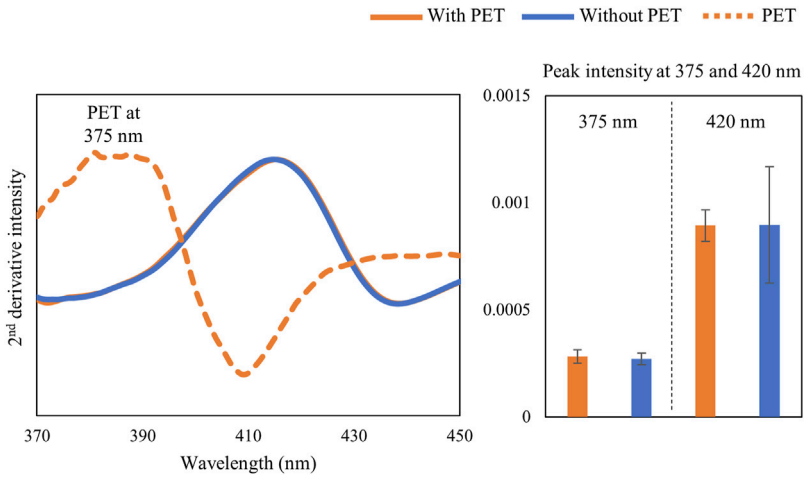

FIGURE 3 | (A) Second-derivative spectra of cartilage tissue (1.6 mm) with and without a semi-infinite PET polymer (25 mm) and the polymer alone showing the PET peak at 375 nm and cartilage peak at 420 nm. **(B)** Second-derivative peak intensity with and without PET underneath cartilage tissue.

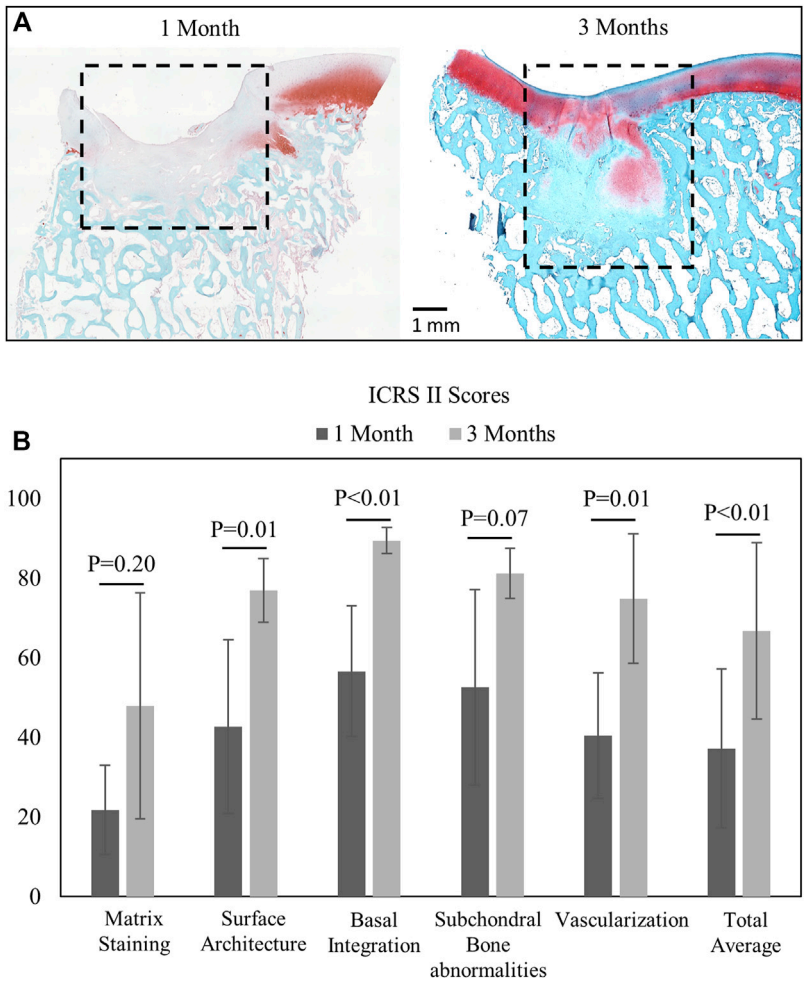

FIGURE 4 | (A) Saf-O- and fast green-stained images from 1-month ($n = 9$) and 3-month ($n = 6$) animals with the defined repair tissue region. **(B)** Mean and standard deviation of ICRS II component scores (comparisons by the Wilcoxon rank sum test, significance at $p < 05$).

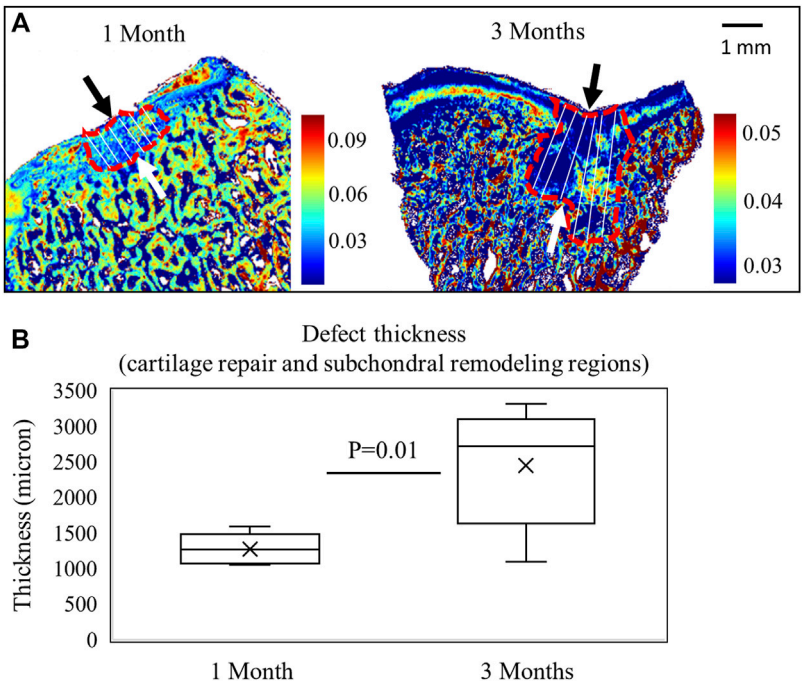

FIGURE 5 | (A) FTIR images based on the 1338 cm^{-1}/Amide II areas after 1 month of repair in a mature animal ($n = 9$) and 3 months of repair in a juvenile animal ($n = 6$). The measurement lines of defect thickness are shown, including both cartilage repair and subchondral remodeling regions. **(B)** Defect thickness is significantly greater in the 3-month animals (Student's *t*-test).

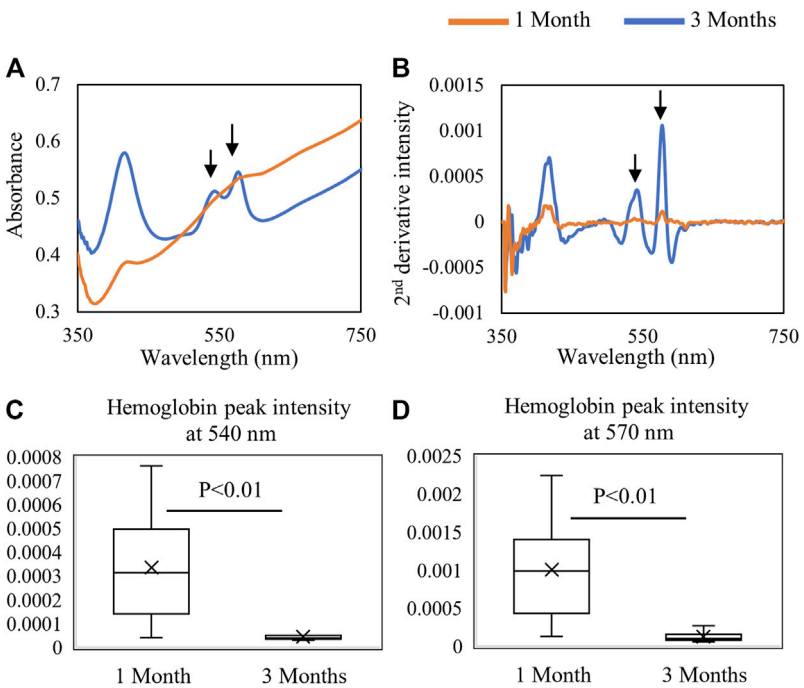

FIGURE 6 | Average **(A)** raw and **(B)** second-derivative inverted Vis-NIR spectra from 1-month ($n = 9$) and 3-month ($n = 6$) defects *in situ*. The visible spectra clearly depict the differences in hemoglobin absorbance (540 and 570 nm) between 1-month and 3-month repair. Quantified second-derivative peak intensities of hemoglobin peaks at **(C)** 540 nm and **(D)** 570 nm showing greater hemoglobin detection in the 1-month tissue (Student's *t*-test).

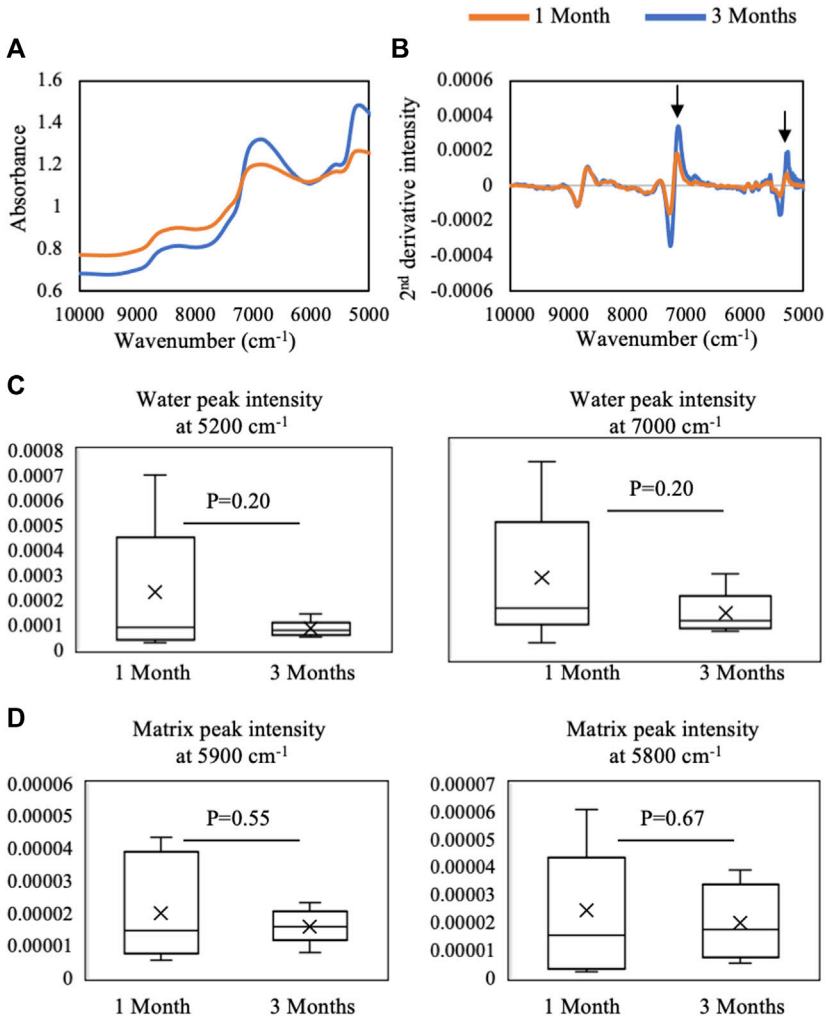

FIGURE 7 | Average **(A)** raw and **(B)** second-derivative inverted NIR spectra from 1-month (n = 9) and 3-month (n = 6) defects *in situ*. The spectra highlight qualitative differences in water absorbances at 5,200 cm^{-1} and 7,000 cm^{-1} between 1 month and 3 months of repair. Quantified second-derivative peak intensities of **(C)** water absorbances and **(D)** matrix absorbances in 1- and 3-month defects. Although trends are present, no significant differences were found in intensities between 1- and 3-month defects (Student's t-test).

spectrometer (Perkin Elmer) with a spectral resolution of 8 cm^{-1}, spatial resolution of 25 μm, and two co-added scans. Spectral images were analyzed using ISys 5.0 software (Malvern Instruments). The ratio of the integrated areas of the collagen absorbance centered at 1,338 cm^{-1} to the amide II protein absorbance (West et al., 2005) was used to define the contrast related to the defect area. For each defect, 10 measurements were taken and averaged to calculate the defect thickness in each sample.

Data Analysis

Results of measurements were reported as means and standard deviations. Comparisons of parameters between 1- and 3-month repair tissues were assessed by a Wilcoxon Rank Sum Test (ICRS II scores ad sub-scores) or Student's t-test (defect thickness and spectral parameters), considering $p < 0.05$ for significance.

RESULTS

Depth of Vis-NIR Detection Into Cartilage Tissue

The detection depth of the NIR signal into tissue was assessed by monitoring the signal intensity of PET signature peaks at 8,865 and 6,000 cm^{-1} (**Figure 2A**). The 8,865 cm^{-1} peak could be detected through 4 mm of cartilage thickness as shown in **Figure 2B**; however, in the lower frequency range, the 6000 cm^{-1} absorbance was only detected through 3 mm of cartilage (**Figure 2C**).

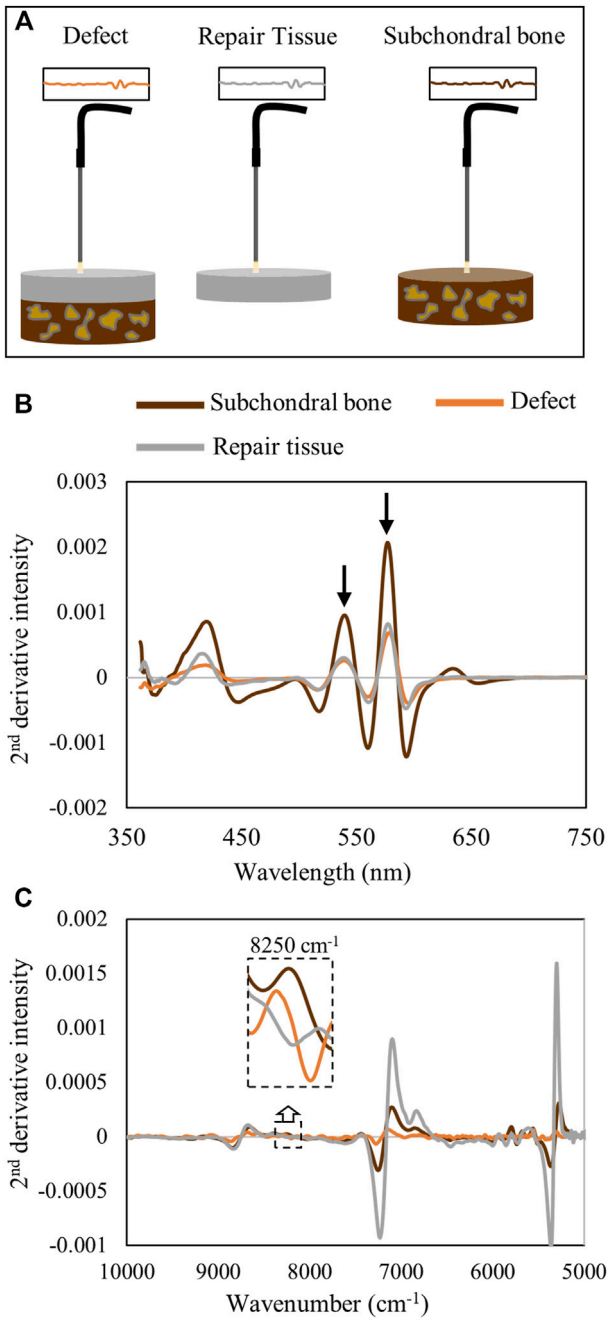

FIGURE 8 | (A) Schematic of data collection from the defect tissue (*in situ*) and individual components, repair tissue, and subchondral bone, *ex vivo*. **(B)** Second-derivative spectra from the defect *in situ* and isolated repair tissue and subchondral bone *ex vivo* in the visible range demonstrate the hemoglobin peak intensities at 540 and 570 nm in the defect tissue are more similar to those in the repair tissue than to those in subchondral bone. **(C)** Second-derivative spectra in the NIR region demonstrate the differences in the water absorbances in the repair tissue in *ex vivo* compared to *in situ* spectra. At 8250 cm^{-1}, the influence of subchondral bone on the *in situ* defect spectrum is apparent while absent in the isolated repair tissue spectrum.

It is known that light penetration into biological tissue is greatly diminished in the visible region (Ash et al., 2017). Thus, it was not surprising that the PET signal at 375 nm was not detectable even through a cartilage thickness of 1.6 mm (**Figure 3**).

Histological Scoring of Cartilage Tissue Repair

Histological staining and blinded ICRS II scoring revealed better repair after 3 months in the juvenile animals than 1 month of repair in the mature animals (**Figures 4A,B**). As expected, repair tissue at 3 months had higher combined total average score (**Figure 4B**) and better surface architecture, basal integration, and vascularization within the repair tissue than the 1-month repair tissues ($p < 0.01$).

Defect Thickness

Sample images after 1 and 3 months of repair are shown in **Figure 5A**. The defect thickness (comprising cartilage repair and subchondral remodeling regions) is significantly higher in 3-month juvenile animals than 1-month adult animals ($p < 0.05$) (**Figure 5B**). The increase in defect thickness seems to be primarily due to a more expansive subchondral remodeling seen in the juvenile animals, which is typical of juvenile osteochondral tissue healing following MFx (Pfeifer et al., 2017).

Vis-NIR Spectroscopic Analysis

Fiber optic-based Vis-NIR spectra were used to non-destructively assess the properties of the repair tissue at 1 and 3 months post-surgery. The spectra were divided into the visible region (350–750 nm) as shown in **Figure 6** and the NIR region (10,000–5,000 cm^{-1}) as shown in **Figure 7**. The raw spectra in the visible region showed differences between 1 and 3 months repair tissue based primarily on differences in hemoglobin absorbance peaks at 540 and 570 nm (**Figure 6A**). The inverted second-derivative spectra clearly showed the differences in hemoglobin absorbances (**Figure 6B**), which could be quantitatively assessed based on peak intensities (**Figures 6C,D**).

In the NIR region, the average raw spectra of 1-month repair tissue showed qualitatively more water absorbance and a slightly higher baseline offset than 3-month repair tissue (**Figure 7A**). The second-derivative processing revealed that differences between 1- and 3-month repair tissue were primarily in water absorbances at 7,000 and 5,200 cm^{-1} (**Figure 7B**), but quantification did not yield significant differences (**Figure 7C**). Similarly, quantification of NIR parameters reflecting protein content showed no significant differences ($p > 0.05$) (**Figure 7D**).

To confirm that the hemoglobin peaks were primarily arising from the soft repair tissue, and not from underlying subchondral bone, spectra of isolated repair tissue were collected and compared with those from the entire defect *in situ*, as well as with those from isolated subchondral bone (**Figure 8A**). The averaged spectra show that the hemoglobin absorbances at 540 and 570 nm from the *in situ* defect are similar to the absorbance from the isolated repair tissue (**Figure 8B**). This is in line with our previous observation of the shallow depth of detection of visible light in this spectral region (**Figure 3**). In contrast, in the NIR region, the water absorbances are much

higher in the isolated repair tissue *ex vivo* than in the defect *in situ*, and the subchondral bone spectrum more closely resembles the *in situ* defect spectrum (**Figure 8C**). The subchondral bone influence on the NIR spectra of the defect can also be observed in the 8250 cm^{-1} region, which shows the absorbance peak in both subchondral bone and in the defect, while the isolated repair tissue does not have this absorbance.

DISCUSSION

Cartilage defects and degeneration cause disability and pain in millions of people worldwide. Accurate evaluation of tissue pathology and progression of repairing cartilaginous tissues would aid in management of defect repair, potentially preventing progression to widespread tissue degeneration (Jones, 2009; Li et al., 2020). Arthroscopy is the gold standard for investigation of intra-articular pathology of the knee (Dehaven and Collins, 1975; Paatela et al., 2020). Conventionally, arthroscopic assessment of joint tissues is carried out to qualitatively assess the tissue using visual or tactile evaluation using a hook probe. Arthroscopic scoring systems such as Oswestry Arthroscopy Score (OAS) can be used to measure the quality of repair following articular cartilage surgery and can be used as a semiquantitative outcome measure (Smith et al., 2005; Paatela et al., 2020). However, the use of a tactile probe can be highly subjective and thus suboptimal (Brismar et al., 2002; Spahn et al., 2009). Vis-NIR spectroscopy using portable spectrometers and fiber optic probes offers a powerful alternative approach for the quantitative assessment of cartilage and subchondral tissue. Previously, NIR spectroscopy equipped with a fiber optic diffuse reflectance probe was used to investigate cartilage and subchondral bone properties in juvenile equines where information from the NIR first optical window (750–1,900 nm or ~13,333–5263 cm^{-1}) was found to be useful for characterizing and estimating subchondral bone properties, such as bone volume fraction, bone mineral density, and thickness and thus potentially could be adapted for arthroscopy (Sarin et al., 2018). However, those outcomes were based on artificial neural network analyses, which require very large sample sizes. Here, we highlight an expanded spectral range to include the visible region hemoglobin absorbances. This was shown to be a valuable tool for assessment of changes in *in vivo* repair tissue in a Yucatan minipig chondral defect model and potentially in other animal models and clinical scenarios.

Assessment of defects by conventional ICRS II histological scoring showed differences in many of the scored parameters between the 1- and 3-month timepoints. As expected, the repair tissue improved over time, even though there was significant bone remodeling observed at the 3-month timepoint. Such remodeling in this juvenile minipig cohort is unsurprising, as younger Yucatan minipigs undergo greater bony changes post-microfracture than adult animals (Pfeifer et al., 2017). Nonetheless, one of the most notable results from this study was the ability to detect the presence of varied amounts of blood in the repairing defects, which could be useful for longitudinal monitoring of the repair process. Although the NIR region of the *in situ* spectra did not show significant differences in spectra from 1- and 3-month repair tissue, some overall trends were apparent, which could likely be better defined with future multivariate spectral analyses, such as those carried out in other studies (Sarin et al., 2018; Prakash et al., 2019). Furthermore, it appeared that the NIR spectral features from the defect region were more similar to the subchondral bone than to the soft repair tissue. This is in line with the findings of Sarin et al. (2018), in which NIR spectral data from intact joints reflected subchondral bone properties.

The process of tissue repair in the joint environment is complex and can take months, or even years. Post-surgery defect repair occurs in three biological phases: the clot formation phase, repair cartilage formation phase, and cartilage maturation phase (Mithoefer et al., 2012). Immediately after microfracture is performed, the defect region is filled with a blood clot rich in mesenchymal stem cells from subchondral bone marrow (Steadman et al., 2010). This initial phase is also marked by increased neovascularization, with capillary blood vessels from the marrow invading the defect region (Shapiro et al., 1993). Along maturation, this blood-rich tissue is gradually replaced by cartilaginous repair tissue over time; thus, the reduction in blood content can be used as a spectral marker for the progression of cartilage repair.

The timeline for the clot phase and subsequent cartilaginous tissue repair varies depending on characteristics of the native tissue and defect. Shapiro et al. (1993), in their study of repair of full-thickness articular cartilage defects in rabbit models for over a period of 24 weeks, found that cartilage repair begins with fibrinous clot and invasion of blood vessels for few days followed by extracellular matrix synthesis as early as 10 days and fibrocartilaginous tissue with chondrocytes present by 3 weeks. From 6, 8, 10, and 12 weeks, progressive differentiation of cells into chondroblasts, chondrocytes, and osteoblasts and synthesis of cartilage and bone matrices in their appropriate locations was found with both tidemark and compact lamellar subchondral bone plate formation to occur by 24 weeks (Shapiro et al., 1993).

It is important to note, however, that this relatively quick repair progression may be related to the animal model, as rabbit cartilage has been described as having high potential for spontaneous healing (Chu et al., 2010). It is thus possible that in humans and large animals, the clot phase may persist for over weeks before progressive maturation into fibrocartilage repair tissue (Fortier et al., 2012; Guermazi et al., 2015). Here, our results indicate that the amount of blood clot and/or neovascularization in the repair tissue is greater in adult pigs after 1 month of defect creation than in juvenile animals after 3 months. The more intense neovascularization is observed by the lower ICRS II scoring (indicating more presence of blood vessels), and the greater blood content (possibly in the clot and/or within blood vessels) was detected by Vis-NIR fiber optic spectroscopy.

Understanding the resultant spectra collected from a defect comprised several tissue types is challenging due to overlapping absorbances from the multiple tissues present. During Vis-NIR spectroscopic data collection of cartilage or repair tissue, the incident light has variable penetration into the soft tissues (hyaline cartilage, fibrocartilage, and fibrous tissue) and the

underlying subchondral bone. An earlier study by Padalkar and Pleshko, (2015) showed that using the diffuse reflectance fiber optic mode of spectra collection, NIR light can penetrate into cartilage tissue and detect more than 4 mm in 7,000–9,000 cm^{-1} and up to 3 mm in 5,000–7,000 cm^{-1}. The study provided an approximation of light interaction at different thicknesses of articular cartilage. Thus, there is potential for the resultant NIR signals from joint tissue to arise from a combination of tissue types. However, it is also well known that measurement depth of the NIR diffuse reflectance depends in part on the geometry of the optical fiber probe used for illumination and detection of light from biological tissue. Arimoto et al. (2005) showed quantitatively that the measurement depth of NIR diffuse reflectance light into human skin depends on both the geometry (distance between illumination and detection fibers) and thickness of optical fibers in the probe. The determination of depth of detection by light into the defect is critical to evaluate the progression of repair in the defect. In our estimation, we have found that the repair tissue thickness increases from 1.5 mm in 1 month to ~ 3.5 mm in 3 months (**Figure 5**), and that NIR light detection into the tissue ranges from 3 mm in low-frequency regions (6,000 cm^{-1}) to more than 4 mm in high-frequency regions (8,865 cm^{-1}) (**Figure 2**). Thus, the NIR light collected through the defect repair tissues interacts with multiple features and tissues of the defect area, assessing both soft tissue and subchondral bone repair regions. This may be a confounding factor contributing to why it was not possible to detect significant changes in NIR spectra between 1- and 3-month repair tissues. This is particularly evident in a higher frequency CH-overtone peak at 8,250 cm^{-1} (Burns and Ciurczak, 2007; Mcgoverin et al., 2014) which has a greater absorbance in subchondral bone and in the defect spectra than the soft repair tissue (**Figure 8C**). Mcgoverin et al. (2014) have previously observed that this peak absorbance is more related to subchondral bone than cartilage in osteochondral tissue. In our study, we also found the influence of subchondral bone on the *in situ* defect spectra based on this peak.

Interestingly, the intensities of the water absorbance peaks at 5,200 cm^{-1} and 7,000 cm^{-1} were not significantly different in the *in situ* defect spectra from 1- to 3-month repair tissues. This was surprising, as differences in these peak intensities reflect the relative amount of bone and cartilage, respectively, as the 5,200 cm^{-1} absorbance is typically greater than the 7,000 cm^{-1} in bone. This discrepancy is likely due to the influence of free water from the joint that is confounding the spectral comparisons between the two groups. Comparison to spectra from free water supports this possibility, as the 5,200/7,000 cm^{-1} ratio observed in the *in situ* data is more similar to that in free water (<1) (Padalkar et al., 2013) than to that in bone (>1.2) or repair tissue (>1.2) in the current study. This ratio has also been found to be a determinant of healthy cartilage where the ratio is lower than 1, while in degraded cartilage it is greater than 1 (Brown et al., 2011).

Diffuse reflectance spectra in the visible region have a lower depth of detection than that in the NIR spectral region. Ash et al. (2017) found that the interaction of light in the visible range of 400–600 nm is reduced in depth by nearly 5 times compared to that of the NIR range. Thus, in the visible range, the light interaction in the defect primarily occurs within the top soft tissue layer. Nevertheless, the visible region was very useful for assessment of changes in hemoglobin related to blood clot formation and remodeling with microfracture. Ideally, this would be implemented in collection of data from individual defects over the course of a study, which would also provide better information related to spectral changes associated with repair across all spectral regions. The lack of significant differences in NIR spectral parameters between the two groups studied here can also be attributed to the inherent individual variations in the tissue repair process, in particular at early timepoints. Kim et al. (2015) highlighted the importance of longer duration studies, 1 year to 2 years, to fully investigate the repair of the cartilage defects in Yucatan minipig models.

It is important to acknowledge limitations of this study with respect to comparing repair tissue from animals of different ages. This issue can be highlighted based on the study by Pfeifer et al. (2017), which described age-dependent differences in cartilage repair in juvenile (6 months) and skeletally mature (18 months) Yucatan minipigs. Similar to the animals in the current study, they evaluated tissue repair at the stifle joints after creating full thickness defects in the trochlear groove followed by treatment with MFx. After 6 weeks post-operatively, it was noted that the juvenile pigs had more extensive subchondral bone remodeling but overall better quality of repair tissue. Here, we analyzed tissue repair after 1 month using adult animals, whereas juvenile animals were used to analyze repair after 3 months. In line with results from Pfeifer et al., our juvenile animals had better quality repair tissue (ICRS II scores) but a more extensive subchondral bone remodeling (quantified here as a greater defect thickness). It is possible that these differences arise not only from the length of time of post-operative tissue repair but also as a difference between juvenile and adult animals. This would be an important confounding factor with respect to making conclusions about the progression of MFx-based cartilage repair.

Another confounding factor relates to differences in tissue sections analyzed for ICRS scoring and for thickness measurements by IR imaging. Several sections were cut for histology, and the section from the center-most region of the defect was chosen for ICRS scoring. As a result, sections for IR imaging analysis of tissue thickness came from off-center regions. This discrepancy leads to the potential for differences in the appearance of subchondral remodeling and healing within the same defect, which is reflected in **Figures 4**, **5**. **Figure 5** shows virtually no subchondral remodeling in the 1-month tissue, while some remodeling is apparent in **Figure 4**, taken from the center region of the defect. In spite of these confounding factors, the primary contribution of this study, assessment of defect repair by Vis-NIR spectroscopy, remains the same. Differences in composition between repair tissue with better (juvenile animals, 3 months of repair) or poorer (adult animals, 1 month of repair) quality can be investigated using this modality.

CONCLUSION

Together, these data demonstrate a novel application of non-destructive fiber optic Vis-NIR spectral analysis for evaluation of chondral microfracture repair. Results from this study provide

new insights into spectral parameters to assess the composition of cartilage repair tissue *in situ*, including hemoglobin absorbances, which may be a valuable approach toward quantitative assessment of tissue repair. Furthermore, with advancements in the development of arthroscopic fiber optic probes (Spahn et al., 2007; Sarin et al., 2018; Magnus et al., 2021), this study can have a significant impact as a foundation to inform on the design of future preclinical and clinical studies for a longitudinal spectroscopic analysis of chondral and osteochondral defect healing.

DATA AVAILABILITY STATEMENT

The raw data supporting the conclusion of this article will be made available by the authors, without undue reservation.

ETHICS STATEMENT

The animal study was reviewed and approved by the Institutional Animal Care and Use Committee (IACUC) at the University of Pennsylvania.

AUTHOR CONTRIBUTIONS

Conceptualization: SK, RM, and NP; methodology: SK, WQ, HZ, CP, RM, and NP; investigation: SK, JF, WQ, JP, HZ, RL, CP, RM, and NP; funding acquisition: RM, NP, and HZ; resources: RM and NP; supervision: RM and NP.

FUNDING

This study was supported by the NIH (R01AR056145, P30AR069619, and F31AR077395). Additional funding was provided by the Department of Veteran's Affairs (IK6 RX003416) and the NSF (CMMI: 15-48571).

ACKNOWLEDGMENTS

The author would like to thank the veterinary staff at the University of Pennsylvania's University Laboratory Animal Resources (ULAR) for their help in the study. The authors are grateful for the Penn Center for Musculoskeletal Disorder (PCMD) histology core (NIH P30AR069619).

REFERENCES

Arimoto, H., Egawa, M., and Yamada, Y. (2005). Depth Profile of Diffuse Reflectance Near-Infrared Spectroscopy for Measurement of Water Content in Skin. *Skin. Res. Technol.* 11, 27–35. doi:10.1111/j.1600-0846.2005.00093.x

Ash, C., Dubec, M., Donne, K., and Bashford, T. (2017). Effect of Wavelength and Beam Width on Penetration in Light-Tissue Interaction Using Computational Methods. *Lasers Med. Sci.* 32, 1909–1918. doi:10.1007/s10103-017-2317-4

Braun, H. J., and Gold, G. E. (2012). Diagnosis of Osteoarthritis: Imaging. *Bone* 51, 278–288. doi:10.1016/j.bone.2011.11.019

Brismar, B. H., Wredmark, T., Movin, T., Leandersson, J., and Svensson, O. (2002). Observer Reliability in the Arthroscopic Classification of Osteoarthritis of the Knee. *J. Bone Jt. Surg. Br.* 84-B, 42–47. doi:10.1302/0301-620x.84b1.0840042

Brown, C. P., Jayadev, C., Glyn-Jones, S., Carr, A. J., Murray, D. W., Price, A. J., et al. (2011). Characterization of Early Stage Cartilage Degradation Using Diffuse Reflectance Near Infrared Spectroscopy. *Phys. Med. Biol.* 56, 2299–2307. doi:10.1088/0031-9155/56/7/024

Brun, P., Dickinson, S. C., Zavan, B., Cortivo, R., Hollander, A. P., and Abatangelo, G. (2008). Characteristics of Repair Tissue in Second-Look and Third-Look Biopsies from Patients Treated with Engineered Cartilage: Relationship to Symptomatology and Time after Implantation. *Arthritis Res. Ther.* 10, R132. doi:10.1186/ar2549

Burns, D. A., and Ciurczak, E. W. (2007). *Handbook of Near-Infrared Analysis*. Boca Raton, Florida, United States: CRC Press.

Chu, C. R., Szczodry, M., and Bruno, S. (2010). Animal Models for Cartilage Regeneration and Repair. *Tissue Eng. Part B Rev.* 16, 105–115. doi:10.1089/ten.teb.2009.0452

Dehaven, K. E., and Collins, H. R. (1975). Diagnosis of Internal Derangements of the Knee. The Role of Arthroscopy. *JBJS* 57, 802–810. doi:10.2106/00004623-197557060-00014

Fisher, M. B., Belkin, N. S., Milby, A. H., Henning, E. A., Bostrom, M., Kim, M., et al. (2015). Cartilage Repair and Subchondral Bone Remodeling in Response to Focal Lesions in a Mini-Pig Model: Implications for Tissue Engineering. *Tissue Eng. Part A* 21, 850–860. doi:10.1089/ten.tea.2014.0384

Fortier, L. A., Cole, B. J., and Mcilwraith, C. W. (2012). Science and Animal Models of Marrow Stimulation for Cartilage Repair. *J. Knee Surg.* 25, 3–8. doi:10.1055/s-0032-1310389

Gao, Y., Liu, S., Huang, J., Guo, W., Chen, J., Zhang, L., et al. (2014). The ECM-Cell Interaction of Cartilage Extracellular Matrix on Chondrocytes. *BioMed Res. Int.* 2014, 648459. doi:10.1155/2014/648459

Guermazi, A., Roemer, F. W., Alizai, H., Winalski, C. S., Welsch, G., Brittberg, M., et al. (2015). State of the Art: MR Imaging after Knee Cartilage Repair Surgery. *Radiology* 277, 23–43. doi:10.1148/radiol.2015141146

Hanifi, A., Palukuru, U., Mcgoverin, C., Shockley, M., Frank, E., Grodzinsky, A., et al. (2017). Near Infrared Spectroscopic Assessment of Developing Engineered Tissues: Correlations with Compositional and Mechanical Properties. *Analyst* 142, 1320–1332. doi:10.1039/c6an02167k

Jacques, S. L. (2013). Optical Properties of Biological Tissues: a Review. *Phys. Med. Biol.* 58, R37–R61. doi:10.1088/0031-9155/58/11/r37

Jones, D. G. (2009). Articular Cartilage Degeneration: Etiologic Association with Obesity. *Ochsner J.* 9, 137–139.

Kandel, S., Querido, W., Falcon, J. M., Reiners, D. J., and Pleshko, N. (2020). Approaches forIn SituMonitoring of Matrix Development in Hydrogel-Based Engineered Cartilage. *Tissue Eng. Part C. Methods* 26, 225–238. doi:10.1089/ten.tec.2020.0014

Kim, I. L., Pfeifer, C. G., Fisher, M. B., Saxena, V., Meloni, G. R., Kwon, M. Y., et al. (2015). Fibrous Scaffolds with Varied Fiber Chemistry and Growth Factor Delivery Promote Repair in a Porcine Cartilage Defect Model. *Tissue Eng. Part A* 21, 2680–2690. doi:10.1089/ten.tea.2015.0150

Lachenal, G. (1997). Characterization of Poly(Ethylene Terephthalate) Using Near and Far FTIR Spectroscopy. *Int. J. Polym. Analysis Charact.* 3, 145–158. doi:10.1080/10236669708032760

Li, Y., Liem, Y., Sullivan, N., Tucker, D., Florio, S., Martin, D., et al. (2020). Quick and Accurate Evaluation of Cartilage Histopathology on Undecalcified Osteochondral Tissue. *Osteoarthr. Cartil.* 28, S178–S179. doi:10.1016/j.joca.2020.02.289

Magnus, J., Conor, H., Juncheng, Z., Man, I. W., Tom, V., Brian, S., et al. (2021). Raman Needle Probe for Compositional and Structural Analysis of Articular Cartilage during Early Osteoarthritis. *Proc. SPIE* 2021, 11631. doi:10.1117/12.2578482

Mainil-Varlet, P., Van Damme, B., Nesic, D., Knutsen, G., Kandel, R., and Roberts, S. (2010). A New Histology Scoring System for the Assessment of the Quality of Human Cartilage Repair: ICRS II. *Am. J. Sports Med.* 38, 880–890. doi:10.1177/0363546509359068

Mcgoverin, C. M., Lewis, K., Yang, X., Bostrom, M. P. G., and Pleshko, N. (2014). The Contribution of Bone and Cartilage to the Near-Infrared Spectrum of Osteochondral Tissue. *Appl. Spectrosc.* 68, 1168–1175. doi:10.1366/13-07327

Mithoefer, K., Hambly, K., Logerstedt, D., Ricci, M., Silvers, H., and Villa, S. D. (2012). Current Concepts for Rehabilitation and Return to Sport after Knee Articular Cartilage Repair in the Athlete. *J. Orthop. Sports Phys. Ther.* 42, 254–273. doi:10.2519/jospt.2012.3665

Mithoefer, K., Mcadams, T., Williams, R. J., Kreuz, P. C., and Mandelbaum, B. R. (2009). Clinical Efficacy of the Microfracture Technique for Articular Cartilage Repair in the Knee. *Am. J. Sports Med.* 37, 2053–2063. doi:10.1177/0363546508328414

Moroni, M., Mei, A., Leonardi, A., Lupo, E., and Marca, F. (2015). PET and PVC Separation with Hyperspectral Imagery. *Sensors* 15, 2205–2227. doi:10.3390/s150102205

Ouchi, I., Miyamura, R., Sakaguchi, M., Hosaka, S., and Kitagawa, M. (1999). Excitation and Emission Spectra of Polyethylene Terephthalate and Polyethylene 2,6-naphthalate Films. *Polym. Adv. Technol.* 10, 195–198. doi:10.1002/(sici)1099-1581(199903)10:3<195::aid-pat875>3.0.co;2-0

Paatela, T., Vasara, A., Nurmi, H., Kautiainen, H., and Kiviranta, I. (2020). Assessment of Cartilage Repair Quality with the International Cartilage Repair Society Score and the Oswestry Arthroscopy Score. *J. Orthop. Res.* 38, 555–562. doi:10.1002/jor.24490

Padalkar, M. V., and Pleshko, N. (2015). Wavelength-dependent Penetration Depth of Near Infrared Radiation into Cartilage. *Analyst* 140, 2093–2100. doi:10.1039/c4an01987c

Padalkar, M. V., Spencer, R. G., and Pleshko, N. (2013). Near Infrared Spectroscopic Evaluation of Water in Hyaline Cartilage. *Ann. Biomed. Eng.* 41, 2426–2436. doi:10.1007/s10439-013-0844-0

Pfeifer, C. G., Fisher, M. B., Saxena, V., Kim, M., Henning, E. A., Steinberg, D. A., et al. (2017). Age-Dependent Subchondral Bone Remodeling and Cartilage Repair in a Minipig Defect Model. *Tissue Eng. Part C. Methods* 23, 745–753. doi:10.1089/ten.tec.2017.0109

Poole, A. R., Kojima, T., Yasuda, T., Mwale, F., Kobayashi, M., and Laverty, S. (2001). Composition and Structure of Articular Cartilage. *Clin. Orthop. Relat. Res.* 391, S26–S33. doi:10.1097/00003086-200110001-00004

Prakash, M., Joukainen, A., Torniainen, J., Honkanen, M. K. M., Rieppo, L., Afara, I. O., et al. (2019). Near-infrared Spectroscopy Enables Quantitative Evaluation of Human Cartilage Biomechanical Properties during Arthroscopy. *Osteoarthr. Cartil.* 27, 1235–1243. doi:10.1016/j.joca.2019.04.008

Querido, W., Kandel, S., and Pleshko, N. (2021). Applications of Vibrational Spectroscopy for Analysis of Connective Tissues. *Molecules* 26, 922. doi:10.3390/molecules26040922

Sarin, J. K., Nykänen, O., Tiitu, V., Mancini, I. A. D., Brommer, H., Visser, J., et al. (2019). Arthroscopic Determination of Cartilage Proteoglycan Content and Collagen Network Structure with Near-Infrared Spectroscopy. *Ann. Biomed. Eng.* 47, 1815–1826. doi:10.1007/s10439-019-02280-7

Sarin, J. K., Te Moller, N. C. R., Mancini, I. A. D., Brommer, H., Visser, J., Malda, J., et al. (2018). Arthroscopic Near Infrared Spectroscopy Enables Simultaneous Quantitative Evaluation of Articular Cartilage and Subchondral Bone *In Vivo*. *Sci. Rep.* 8, 13409. doi:10.1038/s41598-018-31670-5

Shapiro, F., Koide, S., and Glimcher, M. J. (1993). Cell Origin and Differentiation in the Repair of Full-Thickness Defects of Articular Cartilage. *J. Bone Jt. Surg. Am.* 75, 532–553. doi:10.2106/00004623-199304000-00009

Smith, G. D., Taylor, J., Almqvist, K. F., Erggelet, C., Knutsen, G., Portabella, M. G., et al. (2005). Arthroscopic Assessment of Cartilage Repair: A Validation Study of 2 Scoring Systems. *Arthrosc. J. Arthrosc. Relat. Surg.* 21, 1462–1467. doi:10.1016/j.arthro.2005.09.007

Sophia Fox, A. J., Bedi, A., and Rodeo, S. A. (2009). The Basic Science of Articular Cartilage: Structure, Composition, and Function. *Sports Health* 1, 461–468. doi:10.1177/1941738109350438

Spahn, G., Klinger, H. M., and Hofmann, G. O. (2009). How Valid Is the Arthroscopic Diagnosis of Cartilage Lesions? Results of an Opinion Survey Among Highly Experienced Arthroscopic Surgeons. *Arch. Orthop. Trauma Surg.* 129, 1117–1121. doi:10.1007/s00402-009-0868-y

Spahn, G., Plettenberg, H., Kahl, E., Klinger, H. M., Mückley, T., and Hofmann, G. O. (2007). Near-infrared (NIR) Spectroscopy. A New Method for Arthroscopic Evaluation of Low Grade Degenerated Cartilage Lesions. Results of a Pilot Study. *BMC Musculoskelet. Disord.* 8, 47. doi:10.1186/1471-2474-8-47

Steadman, J. R., Rodkey, W. G., and Briggs, K. K. (2010). Microfracture. *Cartilage* 1, 78–86. doi:10.1177/1947603510365533

Suh, J.-K., Scherping, S., Mardi, T., Richard Steadman, J., and Woo, S. L. Y. (1995). Basic Science of Articular Cartilage Injury and Repair. *Operative Tech. Sports Med.* 3, 78–86. doi:10.1016/s1060-1872(95)80033-6

Taroni, P., Pifferi, A., Torricelli, A., Comelli, D., and Cubeddu, R. (2003). *In Vivo* absorption and Scattering Spectroscopy of Biological Tissues. *Photochem. Photobiol. Sci.* 2, 124–129. doi:10.1039/b209651j

van Kampen, E. J., and Zijlstra, W. G. (1983). "Spectrophotometry of Hemoglobin and Hemoglobin Derivatives," in *Advances in Clinical Chemistry*. Editors A. L. Latner and M. K. Schwartz (Amsterdam, Netherlands: Elsevier). doi:10.1016/s0065-2423(08)60401-1

Vega, S., Kwon, M. Y., Kwon, M., and Burdick, J. (2017). Recent Advances in Hydrogels for Cartilage Tissue Engineering. *eCM* 33, 59–75. doi:10.22203/ecm.v033a05

West, P. A., Torzilli, P. A., Chen, C., Lin, P., and Camacho, N. P. (2005). Fourier Transform Infrared Imaging Spectroscopy Analysis of Collagenase-Induced Cartilage Degradation. *J. Biomed. Opt.* 10, 14015–14016. doi:10.1117/1.1854131

Yousefi, F., Kim, M., Nahri, S. Y., Mauck, R. L., and Pleshko, N. (2017). Near-Infrared Spectroscopy Predicts Compositional and Mechanical Properties of Hyaluronic Acid-Based Engineered Cartilage Constructs. *Tissue Eng. Part A* 24, 106–116. doi:10.1089/ten.TEA.2017.0035

Zonios, G., and Dimou, A. (2006). Modeling Diffuse Reflectance from Semi-infinite Turbid Media: Application to the Study of Skin Optical Properties. *Opt. Express* 14, 8661–8674. doi:10.1364/oe.14.008661

Conflict of Interest: The authors declare that the research was conducted in the absence of any commercial or financial relationships that could be construed as a potential conflict of interest.

Publisher's Note: All claims expressed in this article are solely those of the authors and do not necessarily represent those of their affiliated organizations, or those of the publisher, the editors, and the reviewers. Any product that may be evaluated in this article, or claim that may be made by its manufacturer, is not guaranteed or endorsed by the publisher.

Copyright © 2022 Kandel, Querido, Falcon, Zlotnick, Locke, Stoeckl, Patel, Patil, Mauck and Pleshko. This is an open-access article distributed under the terms of the Creative Commons Attribution License (CC BY). The use, distribution or reproduction in other forums is permitted, provided the original author(s) and the copyright owner(s) are credited and that the original publication in this journal is cited, in accordance with accepted academic practice. No use, distribution or reproduction is permitted which does not comply with these terms.

frontiers | Frontiers in Bioengineering and Biotechnology

TYPE Original Research
PUBLISHED 30 August 2022
DOI 10.3389/fbioe.2022.960694

Check for updates

OPEN ACCESS

EDITED BY
Mark Buckley,
University of Rochester, United States

REVIEWED BY
Johnson V. John,
Terasaki Institute for Biomedical Innovation, United States
Hamid Mirzadeh,
Amirkabir University of Technology, Iran

*CORRESPONDENCE
Yaobin Wu,
wuyaobin2018@smu.edu.cn
Ling Wang,
wangling0607@smu.edu.cn

SPECIALTY SECTION
This article was submitted to Biomaterials, a section of the journal Frontiers in Bioengineering and Biotechnology

RECEIVED 03 June 2022
ACCEPTED 26 July 2022
PUBLISHED 30 August 2022

CITATION
Yang Q, Li J, Su W, Yu L, Li T, Wang Y, Zhang K, Wu Y and Wang L (2022), Electrospun aligned poly(ε-caprolactone) nanofiber yarns guiding 3D organization of tendon stem/progenitor cells in tenogenic differentiation and tendon repair. *Front. Bioeng. Biotechnol.* 10:960694. doi: 10.3389/fbioe.2022.960694

COPYRIGHT
© 2022 Yang, Li, Su, Yu, Li, Wang, Zhang, Wu and Wang. This is an open-access article distributed under the terms of the Creative Commons Attribution License (CC BY). The use, distribution or reproduction in other forums is permitted, provided the original author(s) and the copyright owner(s) are credited and that the original publication in this journal is cited, in accordance with accepted academic practice. No use, distribution or reproduction is permitted which does not comply with these terms.

Electrospun aligned poly(ε-caprolactone) nanofiber yarns guiding 3D organization of tendon stem/progenitor cells in tenogenic differentiation and tendon repair

Qiao Yang[1], Jianfeng Li[1,2], Weiwei Su[3], Liu Yu[3], Ting Li[3], Yongdi Wang[2], Kairui Zhang[4], Yaobin Wu[3]* and Ling Wang[1]*

[1]Biomaterials Research Center, School of Biomedical Engineering, Southern Medical University, Guangzhou, China, [2]The First School of Clinical Medicine, Southern Medical University, Guangzhou, China, [3]Guangdong Engineering Research Center for Translation of Medical 3D Printing Application, Guangdong Provincial Key Laboratory of Medical Biomechanics, National Key Discipline of Human Anatomy, School of Basic Medical Sciences, Southern Medical University, Guangzhou, China, [4]Division of Orthopaedics and Traumatology, Department of Orthopaedics, Nanfang Hospital, Southern Medical University, Guangzhou, China

Hierarchical anisotropy structure directing 3D cellular orientation plays a crucial role in designing tendon tissue engineering scaffolds. Despite recent development of fabrication technologies for controlling cellular organization and design of scaffolds that mimic the anisotropic structure of native tendon tissue, improvement of tenogenic differentiation remains challenging. Herein, we present 3D aligned poly (ε-caprolactone) nanofiber yarns (NFYs) of varying diameter, fabricated using a dry-wet electrospinning approach, that integrate with nano- and micro-scale structure to mimic the hierarchical structure of collagen fascicles and fibers in native tendon tissue. These aligned NFYs exhibited good *in vitro* biocompatibility, and their ability to induce 3D cellular alignment and elongation of tendon stem/progenitor cells was demonstrated. Significantly, the aligned NFYs with a diameter of 50 μm were able to promote the tenogenic differentiation of tendon stem/progenitor cells due to the integration of aligned nanofibrous structure and suitable yarn diameter. Rat tendon repair results further showed that bundled NFYs encouraged tendon repair *in vivo* by inducing neo-collagen organization and orientation. These data suggest that electrospun bundled NFYs formed by aligned nanofibers can mimic the aligned hierarchical structure of native tendon tissue, highlighting their potential as a biomimetic multi-scale scaffold for tendon tissue regeneration.

KEYWORDS

electrospinning, nanofiber yarns, 3D alignment, tendon stem/progenitor cells, tenogenic differentiation, tendon repair

Introduction

Partial or complete tendon ruptures caused by accidents and sports disrupt collagen alignment, leading to loss of function and reduced mobility (Hasan et al., 2014; Nau and Teuschl, 2015). However, native tendon has a poor endogenous ability to regenerate after injury due to fewer blood vessels and nerves in the tendon tissue (Silver et al., 2003; Longo et al., 2011; Kalson et al., 2015). Alternatively, tissue engineering (TE) strategies have demonstrated potential application for tendon tissue regeneration, and biomaterial scaffolds provide a temporary extracellular matrix (ECM) for cell adhesion and proliferation, which is a key element in guiding tissue regeneration (Chen et al., 2015; Zhang, 2020). Tendon has a hierarchical organization, and the subunits of the tendon are the fascicles (diameters: 100–500 μm), which consist of highly aligned collagen fibers (diameters: 1–20 μm) (Zhang et al., 2006; Carniel and Fancello, 2019; Puetzer et al., 2021). Such hierarchical structure is easily disordered upon injury due to the chaotic arrangement of neo-collagen in scar tissue appearing at the site of the defect, thereby weakening the mechanical properties and functionality of the injured tendon (Sharma and Maffulli, 2005). This critical structure-function relationship reflects the design strategy for developing a suitable scaffold to facilitate the capacity of TE tendon to mimic the hierarchical structure of native tendon. The functional recovery of tendon tissue is a critical point in tendon TE scaffold development and is an ongoing challenge.

Recently, various fabrication technologies, such as electrospinning (Wu et al., 2016; Ma et al., 2018; Zhu et al., 2021), self-assembly (Gonzalez-Masis et al., 2020; Yin et al., 2020), and 3D bioprinting (Merceron et al., 2015; Chae et al., 2021; Zhang et al., 2021), have been developed to mimic the structure of native tendon by controlling aligned cellular organization. Among these techniques, electrospinning has been widely used in tendon TE due to its ability to prepare aligned nano- and micro-fibers efficiently and mimic the anisotropic hierarchical structure of native tendon tissue (Sensini and Cristofolini, 2018). In previous studies, continuous electrospun filaments have been made through changing the type of collectors (Dabirian et al., 2007; Bosworth, 2014; Laranjeira et al., 2017; Xie et al., 2021) to prepare a hierarchical structure for tendon tissue (Wu et al., 2017b; Sensini et al., 2019; Sensini et al., 2021). Mouthuy et al. (2015) fabricated a polydioxanone filament using a wire collector and assembled filaments into yarn to mimic the structure of native tendon, but then failed to control the diameter of the filaments. To achieve a similar effect, Sensini et al. (2019) prepared a multi-scale scaffold by rolling aligned nanofiber films to form a unit, then assembled them to make the multi-scale scaffold. Similarly, Laranjeira et al. (2017) produced braided and woven scaffolds using different textile techniques to weave together nanofiber threads into fibrils, then fibers, and, ultimately, 3D scaffolds. In addition to the morphological and mechanical features of the scaffold, it is well-established that suitable diameters and functions are extremely important for cell proliferation and differentiation. However, the effects of bundled nanofiber diameter have not been investigated.

Recently, we developed a series of aligned nanofiber yarns (NFYs) based on an advanced wet-dry electrospinning technique to induce 3D cellular alignment and differentiation. We further developed biomimetic anisotropic scaffolds based on these aligned NFYs for various TE applications, including skeletal muscle, cardiac, and nerve TE (Wang et al., 2015; Wu et al., 2017b; Wang et al., 2019). However, due to the similar structure of tendon tissue, the effect of aligned NFYs on tenogenic differentiation *in vitro* and tendon repair *in vivo* has remained unclear.

Furthermore, stem cells have been regarded as a promising cell type for tendon regeneration. Among the types of stem cells isolated from different tissue sources, tendon stem/progenitor cells (TSPCs), which were isolated from tendon sources, were thought to be especially suitable for the tendon microenvironment and highly likely to differentiate into tenocytes (Guo et al., 2016). However, a recent study showed that TSPCs tend to undergo chondrogenic/osteogenic differentiation under inflammatory conditions, which ultimately leads to ectopic calcification in tendon tissue (Chen et al., 2019). It was found that local stem/progenitor cells are induced into an erroneous differentiation in the diseased tendon (Hu et al., 2016). Therefore, promoting tenogenic differentiation of TSPCs plays a key role in tendon regeneration, yet remains a challenging prospect. Although several previous studies reported that scaffolds with aligned structures could improve the tenogenic differentiation of TSPCs (Yin et al., 2010), there are still few reports on the design of aligned scaffolds that integrate with nano-, micro- and macro-scale structures and would mimic the hierarchical structure of native tendon to promote tenogenic differentiation of TSPCs and tendon repair.

Herein, we report the development of a series of aligned bundled scaffolds based on NFYs prepared by our previously developed wet-dry electrospinning technique, which demonstrated well-defined nano/microarchitecture that mimicked the hierarchical structure of fascicles and collagen fibers in native tendon tissue (Figure 1A). TSPCs were seeded on aligned NFYs, and the effects of the nano- and micro-structure of aligned NFYs on the cellular alignment and organization of TSPCs were investigated. After culture for 7 days in differentiation medium, the effects of different NFY diameters on the tenogenic differentiation of TSPCs was also investigated. Furthermore, aligned NFY bundle scaffolds were implanted into the rat tendon defect model to investigate their ability to improve *in vivo* tendon repair. The electrospun aligned NFYs were able to guide cellular alignment and organization, thereby improving tenogenic differentiation of TSPCs *in vitro*, which suggests that these aligned NFY bundle scaffolds mimic the hierarchical structure of collagen fascicles and fibers in native tendon tissue and demonstrates great potential for tendon TE applications.

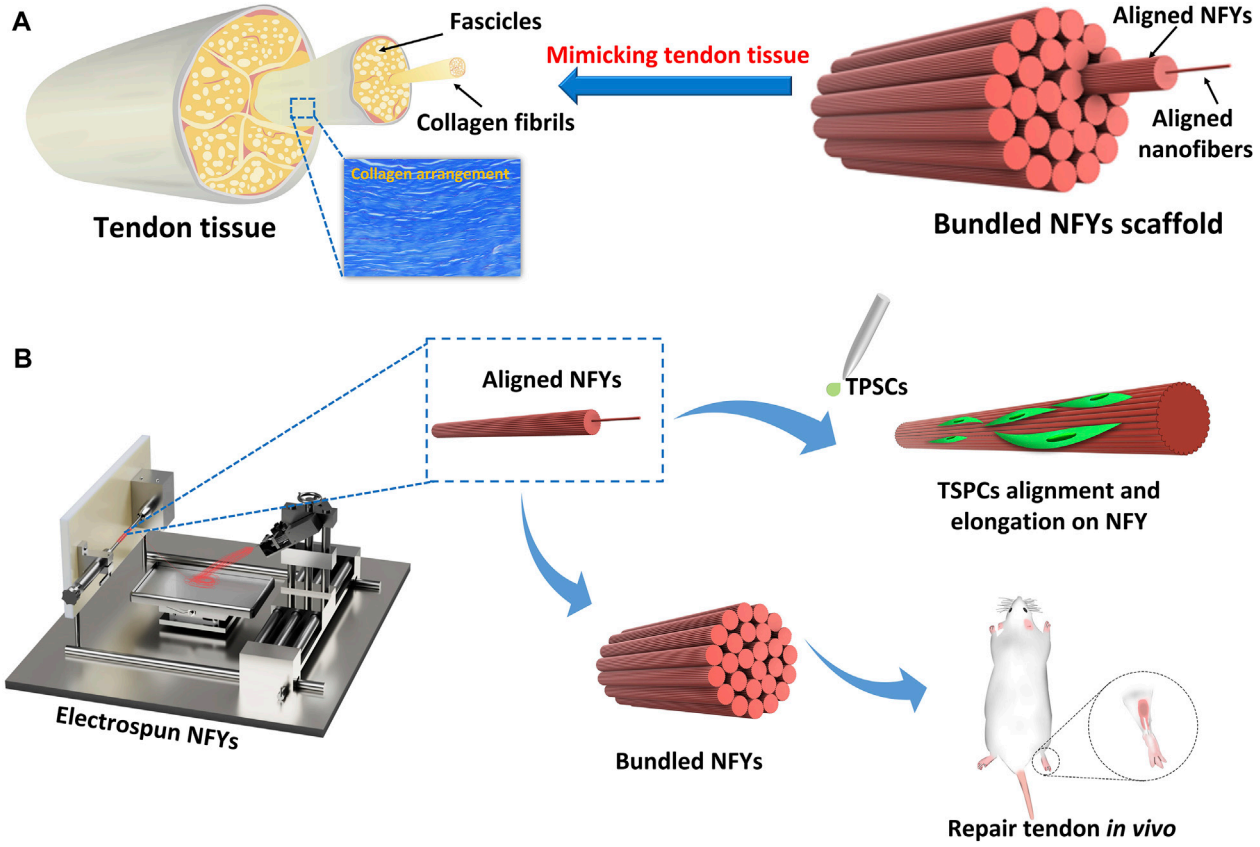

FIGURE 1
The preparation scheme of aligned PCL NFYs and their applications for tenogenic differentiation *in vitro* and tendon repair *in vivo*. **(A)** The complex hierarchical structure of native tendon tissue, consisting of aligned collagen fascicles with aligned fibers. The bundled NFY scaffold mimicked the hierarchical structure of native tendon. **(B)** Fabrication scheme based on aligned NFYs that mimic native tendon tissue to produce the hierarchical structure of scaffolds through a dry-wet electrospinning technique.

Materials and methods

Materials

Poly (ε-caprolactone) (PCL, average Mn = 80 000), collagenase type I (collagenase from *Clostridium histolyticum* for general use), Poly-L-lysine (PLL), paraformaldehyde (PFA), 2-phospho-L-ascorbic acid trisodium, bovine serum albumin (BSA), and pentobarbital were obtained by Sigma-Aldrich (Sigma-Aldrich, Saint Louis, United Kingdom). Hexafluoroisopropanol (HFIP) was purchased from Macklin (Macklin, China).

Preparation of PCL aligned nanofiber yarns

The aligned PCL NFYs were prepared via dry-wet electrospinning following our previously reported process (Wang et al., 2015; Wu et al., 2017b; Wang et al., 2019). PCL was dissolved at 100 mg/ml in hexafluoroisopropanol at room temperature for 12 h. The schematic diagram in Figure 1 illustrates the working principle of the electrospinning device (ET-2535, Ucalery, China). In brief, the PCL solution was drawn into a 5 ml syringe with a 21G needle with a length of 15 mm, an inner diameter of 0.5 mm, and an outer diameter of 0.8 mm (Ucalery, China). Injection speed was 1 ml/h using a syringe pump (ET-2535, Ucalery, China). The length of the drum was 21 cm and the diameter was 3 cm. Spinning was induced by adjusting the positive and negative pressure of the electrospinning instrument; the positive voltage was set at 18 kV and the negative voltage at 2 kV. During the electrospinning process, the random nanofibrous mat was received on the surface of a water/ethanol (V/V 8:2) mixture, and the continuous NFYs were then obtained by dragging from the surface of the solution using a rolling receptor to gain. The distance between the needle and surface of the solution was approximately 10 cm, and the distance between the liquid surface

and the receptor was approximately 15 cm. While the other conditions were fixed, aligned NFYs with different diameters could be obtained by varying the rotation speed of the receptor, ranging from 2 to 80 mm/min. The aligned NFY samples were collected from the receiver and kept at room temperature for at least 2 days before subsequent experiments.

Morphological characterization and mechanical properties of aligned NFYs

Scanning electron microscopy (SEM, Sigma HD, United States) was used at an accelerating voltage of 2 kV to analyze the microstructure surface chemistry of aligned NFYs; each sample had three groups of replicates. The diameter distribution and alignment properties of nanofibers were counted using the ImageJ software module OrientationJ; each sample type had three replicates. Mechanical testing of single aligned NFYs was performed via dynamic thermo-mechanical analysis (Q800, DMA, United States). First, both ends of the single aligned NFY were clamped on filter paper and then fixed on the upper and lower arms of the instrument. The lengths of the aligned NFYs tested were approximately 2 cm. Uniaxial tensile testing was carried out at a stretching rate of 5 mm/min until specimen failure. As for the mechanical properties of bound NFYs, we bundled 50 NFYs of each diameter, and then used a universal testing machine (a series of LS, AMETEK, United States) to test the force and strain of these bound NFYs. The lengths of aligned NFYs tested were approximately 14 cm. Uniaxial tensile testing was carried out at a stretching rate of 5 mm/min until specimen failure. More than five parallel samples were measured for each sample of different NFY diameter.

Isolation and culture of TSPCs

The Achilles tendon and patella tendon were obtained to isolate tendon stem/progenitor cells (TSPCs) from 6 to 8 week old Sprague Dawley (SD) rats, which were obtained following the approved guidelines set by the Institutional Animal Care and Use Committee, Southern Medical University. First, the peritendinous connective tissue was carefully removed, and the samples were washed three times with Dulbecco's phosphate buffered saline (DPBS, Gibco, China). The samples were then minced into 2 mm^2 pieces and digested with 3 mg/ml collagenase type I for 30 min at 37°C. Following digestion, the samples were diluted with DPBS, filtered through a 70 μm cell strainer, and then centrifuged at 1,000 rpm for 15 min. Single-cell suspensions were cultured in a cell culture incubator at 5% CO_2 and 37°C in Dulbecco's Modified Eagle's Medium (DMEM, Gibco, China) containing 20% fetal bovine serum (FBS, Gibco, Australia) and 1% penicillin/streptomycin. TSPC colonies were observed under a microscope after 5 days. A previous study has shown that TSPCs have good expression of tenomodulin (TNMD) up to passage 10 (Tan et al., 2012), so cells from passages 3-8 were used in our subsequent experiments.

Characterization of TSPCs

Expression of stem cell surface markers was analyzed by flow cytometry. TSPCs (1.0 × 106 cells) in 500 μL of 10% FBS-DMEM were incubated with the following phycoerythrin-conjugated or fluorescein-isothiocyanate-conjugated mouse anti-rat monoclonal antibodies at 4°C for 1 h: anti-CD18 (561409, BD PHARMINGEN, United States), anti-CD34 (ab187284, abcam, United States), anti-CD44 (561409, BD PHARMINGEN, United States), anti-CD45 (MCA45PE, SEROTEC, United States), and anti-CD90 (561409, BD PHARMINGEN, United States). Before being tested, the cells were washed twice with DPBS and then re-suspended in 500 μL of ice-cold 10% FBS-DMEM and 1 μL propidium iodide. FACs results were analyzed using BD FACSCanto II (BD Biosciences, United States).

TSPC culture on aligned NFYs

TSPCs were seeded and cultured on aligned NFYs of varying diameters following several steps. First, the aligned NFY samples were fixed around a 3D-printed rectangle model. Second, the aligned NFY samples were sterilized by immersion in 75% ethanol for 30 min, followed by 30 min of UV irradiation. After drying, the aligned NFYs were soaked in 1% ε-Poly-L-lysine solution for 30 min and dried overnight. Finally, the TSPC suspension (0.3 ml, 3×10^5 cells/mL) was dropped onto aligned NFYs and allowed to adhere at 37° C for 4 h. When most cells had adhered to the surface of the NFYs, the aligned NFY samples were peeled off from the PDMS mold and placed into wells of a 6-well plate for continued culture for required experiments. The cell culture medium was changed every 2 days.

Viability of TSPCs on aligned NFYs

The cellular activity of TSPCs seeded on the aligned NFYs was evaluated by Live/Dead assay (Beyotime, China) after 24 h and by Alamar Blue assay (Molecular Probes, Invitrogen, China) after 1, 5, and 7 days in culture, according to the manufacturer's instructions. After being seeded on the aligned NFYs of various diameters, cells were cultured for 24 h to allow cell spreading. Cell-laden NFYs ($n = 3$) were then transferred to a new plate and washed with DPBS to remove the non-adherent cells. Calcein AM stained living cells with green fluorescence, and propidium iodide (PI) stained dead cells with red fluorescence. Before

adding the working fluid, samples were washed with DPBS and then incubated for 30 min. Fluorescence imaging was carried out using confocal laser scanning microscopy (Nikon A1, China). Cells were incubated in 10% (v/v) Alamar Blue reagent in growth medium at 37° C for 4 h. The fluorescence of the supernatant was measured using a microplate reader (Synergy HT, Bio-Tek Instruments, United States) at an excitation wavelength of 560 nm and an emission wavelength of 590 nm.

Morphological evaluation of TSPCs on aligned NFYs

The morphology and organization of TSPCs on aligned NFYs of various diameters were analyzed via immunofluorescence imaging after 3 days in culture; each sample had three replicates. Cultured cells were gently rinsed twice with DPBS for 3 min and then fixed with 4% PFA for 15 min at room temperature. After fixation, cells were gently rinsed with DPBS three times and then treated with 0.2% Triton X-100 for 45 min. The samples were blocked using 1% BSA for 2 h and then treated with fluorescein isothiocyanate (FITC)-phalloidin (Invitrogen, China) conjugated at 4° C overnight and counterstained with 4', 6-diamidino-2-phenylindole (DAPI, Sigma, United States). Fluorescence imaging was carried out using a confocal laser microscope (Nikon A1, China). Images of F-actin fluorescence were processed using the OrientationJ module of ImageJ software and the elongation and orientation of TSPCs on these aligned NFYs were analyzed following the protocol of our previous study (Wang et al., 2015). Cell elongation was determined by measuring nuclear aspect ratios and the angle between the long axis of the cells and the direction of aligned NFYs to generate alignment histograms. Cells cultured on glass slides were the 2D control group.

Tenogenic differentiation of TSPCs on aligned NFYs

TSPCs were cultured on aligned NFYs of various diameters in differentiation medium (growth medium with 50 mg/ml 2-phospho-L-ascorbic acid trisodium) to induce tenogenic differentiation for 7 days; each sample had three replicates. After 7 days of induction, the cell-seeded NFYs were carefully rinsed twice with DPBS and then fixed with 4% PFA for 15 min at room temperature. After fixation, the cells were carefully washed twice with DPBS and then treated with 0.2% Triton X-100 for 45 min. After blocking in 1% BSA in DPBS for 2 h, the cell constructs were incubated with rabbit anti-TNMD antibody (ab203676, abcam, China) and rabbit anti-collagen I (Col1a1) antibody (CO20191-01, Invitrogen, China) at 4° C overnight. The cell constructs were then washed with DPBS, and Alexa Fluor 488 (ab150077, abcam, China) conjugated secondary antibody was added and samples were incubated for 45 min at room temperature. After incubation, the cell constructs were washed with DPBS and cell nuclei were counterstained with DAPI for 5 min. Finally, the cell-seeded NFYs were observed under a confocal laser microscope (Nikon A1, China).

Real-time qPCR

For real-time quantitative PCR (RT-qPCR) analyses, total RNA was extracted using Trizol (AG RNAex Pro Reagent, AG, China) following the manufacturer's instructions. For synthesizing cDNA, 0.2–1 μL RNA was used in a reverse transcription reagents kit protocol (Abm, Canada). Three cDNA parallel compositions were obtained. Real-time qPCR was carried out according to the protocol. Briefly, qPCR reactions were first carried out on ice, and each well contained 7.5 μL MagicSYBR Mixture, 0.15 μL ROX, 0.5 μL cDNA, 6.35 μL H_2O, and 0.6 μL mixed primers. The plates were inserted in an Applied Biosystems QuanStudio™3 Real-Time PCR (Singapore) Instrument for cycling at the following temperature profile: 95° C for 30 s, then 40 cycles of 95° C for 5 s followed by 60° C for 30 s. The primer sequences were as shown in Table 1. Each sample had three groups of replicates.

In vivo rat Achilles tendon repair model and histological evaluation

The animal experiment procedures were approved by the Institutional Animal Care and Use Committee, Southern Medical University. The SD rats (n = 6, 8-weeks-old) were treated with 1% pentobarbital sodium intraperitoneally at 40 mg/kg body weight. After anesthesia, a 6 mm length of the Achilles tendon was removed to make a defect model. Bundles of 50 yarns of NFY-50 were used to prepare the aligned NFY scaffolds to provide mechanical support for the repaired tendon. The NFY-50 scaffolds (50 yarns, length = 0.2 cm) were sutured to the residual Achilles tendon using a non-resorbable suture (5–0 nylon) via the Kessler method of tendon repair. Tendons that had been cut off directly served as the control group. The animals were allowed free movement after surgery. After 6 weeks of implantation, samples from each group were harvested and fixed in 4% PFA. Samples were then dehydrated through a series of increasing concentrations of ethanol, embedded in paraffin blocks, and sectioned at a thickness of 8μm. Sections were stained with hematoxylin-eosin (H&E), Masson's trichrome, and Picrosirius red. Finally, the stained paraffin sections were observed under an optical microscope (Nikon Nxi, China). The Masson's trichrome images were processed using the OrientationJ module of ImageJ software, with analysis of the orientation

TABLE 1 Gene primer sequences for RT-qPCR.

Genes	5′-3′	Primer Sequences (5'→3')	Production size (bp)
GAPDH	Forward	CTCTCTGCTCCTCCCTGTTC	105
	Reverse	TACGGCCAAATCCGTTCACA	
TNMD	Forward	CAATGGGTGGTCCCACAAGT	231
	Reverse	TCGACCTCCTTGGTAGCAGT	
DCN	Forward	ATCACAGAAGAGGCAACGAGC	163
	Reverse	GAGACTTGCGCCAGAAGGAA	
Col1a1	Forward	ACGCCATCAAGGTCTACTGC	159
	Reverse	ACTCGAACGGGAATCCATCG	
SCX	Forward	GAGAACACCCAGCCCAAACA	84
	Reverse	CCGTCTTTCTGTCACGGTCT	

of neo-collagen in the defect site of each rat. Each group included three replicates.

Statistical analysis

Experiments were run in triplicate for each sample and results are presented as mean ± standard deviation. Quantitative data and measurement of cell aspect ratios and orientation were obtained using ImageJ software, with results including at least 5 images of 3 independent locations within each sample (cell number >100). Statistical differences were obtained through analysis of variance followed by Tukey's significant difference post hoc test. A significance level of 0.05 was applied to indicate significant differences.

Results

Preparation and Characterization of aligned NFYs

The fabrication of aligned NFYs based on a modified electrospinning device is shown in Figure 1B, and the process of fabricating these aligned NFYs is detailed in Supplementary Video S1. Briefly, the PCL polymer solution (100 mg/ml) was extruded by the pump in a high voltage field to prepare a mat of random nanofibers on the surface of a water/ethanol mixture. Subsequently, a rolling receptor pulled the nanofibers mat from the solution's surface to form aligned NFYs. By controlling the rotation rate of the rolling receptor, a series of aligned NFYs with varying diameters were fabricated using the dry-wet electrospinning approach. The microstructure of the aligned NFYs was observed using SEM. The images showed that the aligned NFYs were loose and porous cylinders, and that the bundled NFYs had a hierarchical structure similar to native collagen fibers and fascicles of the tendon (Figure 2A; Supplementary Figure S1A). The nanofiber diameter was controlled, at 732.1 ± 167.22 nm by adjusting the parameters of electrospinning. The diameter of the aligned NFYs decreased dramatically from 100 ± 24 μm to 10 ± 2 μm when the receptor rotation rate increased from 2 to 80 mm/min, respectively (Figure 2B). The aligned NFYs with diameters of 10 ± 2 μm, 50 ± 10 μm, and 100 ± 24 μm were designated NFY-10, NFY-50, and NFY-100, respectively. NFY-10, NFY-50, and NFY-100 showed the proportion of oriented nanofibers, in the range of ±10°, to be 95.13%, 88.21%, and 85.66%, respectively (Figure 2C), suggesting that aligned NFYs have great improvement in axial orientation with increased rotation speed. The loaded-force of aligned NFYs was measured using a single fiber tensile test. The tensile analysis results showed that the force of a single NFY-100 was as high as 5.16 ± 0.04 cN, while NFY-50 was slightly decreased at 3.16 ± 0.16 cN, and NFY-10 was only 1.13 ± 0.13 cN (Figure 2D). Furthermore, the strain of aligned NFYs increased from 141 ± 41% to 486 ± 17% with the increase of NFY diameter from 10 μm to 100 μm, respectively. As shown in Figure 2E, the loaded-force of the bundled 50 yarns of NFY-10 was 0.44 ± 0.1 N with a stretching speed of 5 mm/min. Comparatively, the loaded-force of the bundled 50 yarns of NFY-100 was 3.31 ± 0.37 N. Notably, the loaded-force of the bundled 50 yarns of NFY-50 was 2.15 ± 0.09 N, which is suitable for tendon tissue with a loaded-force of 2–3 N (Table 2). These results revealed that nano- and micro-scale NFYs containing highly aligned nanofibers can be successfully prepared using the dry-wet electrospinning approach, with the mechanical properties of NFYs easily controlled by changing their diameters.

Identification and characterization of TSPCs

After 3 days of isolation, a small number of TSPCs with spindle-like morphology were observed. The cells proliferated continuously and formed colony units after 9 days. The

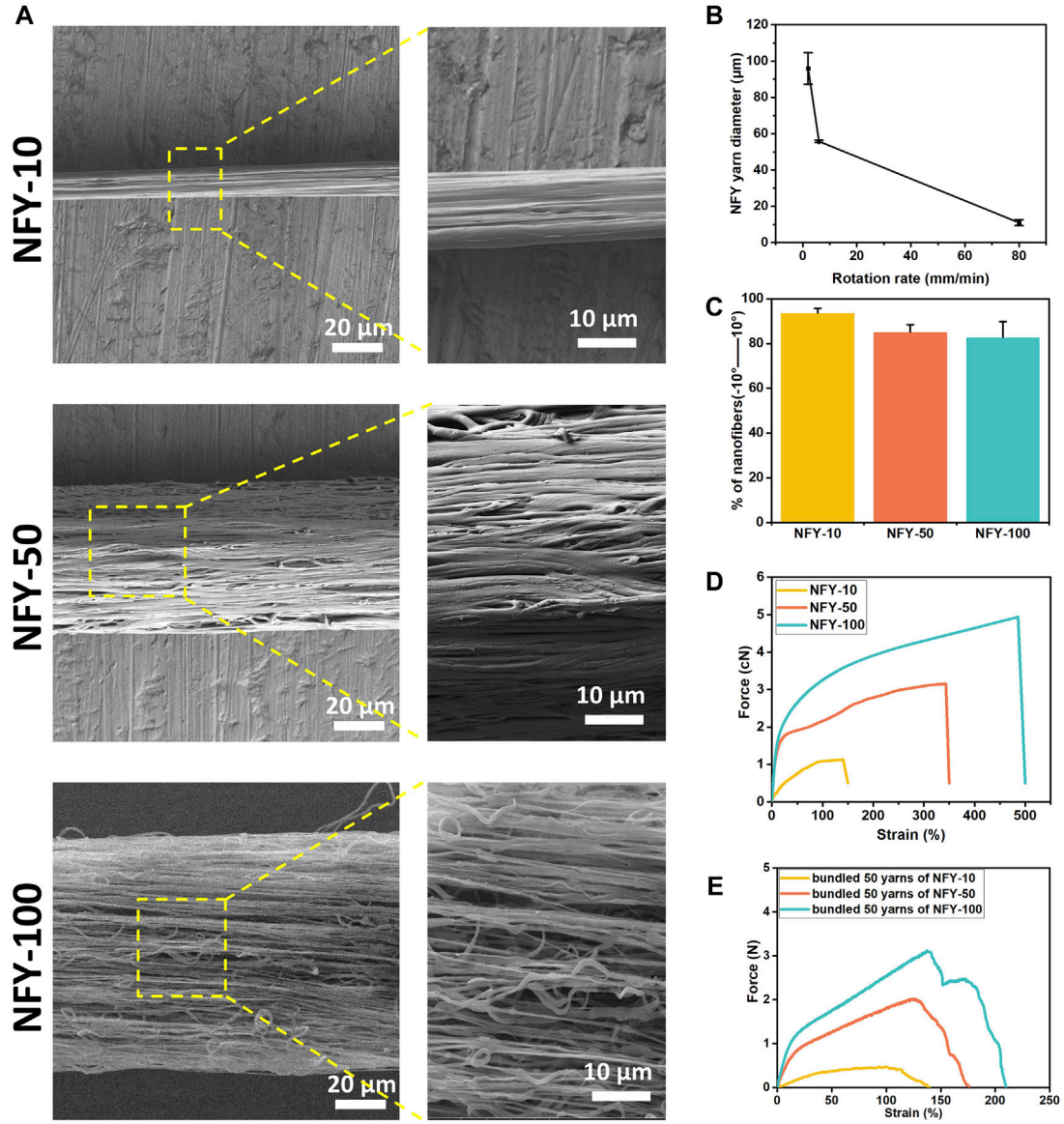

FIGURE 2
Microstructure and mechanical properties of aligned NFYs. **(A)** SEM images and their magnification images of aligned NFYs with average diameters of 10 μm, 50 μm, and 100 μm, respectively. **(B)** The relationship between and the diameter of NFYs and the rotation rate of the receptor. **(C)** Histograms of relative alignment within ±10° show uniform orientation of nanofibers in aligned NFYs. **(D)** Force-Strain curves of NFYs with different diameters via single fiber tensile test. **(E)** Force-Strain curves of 50-yarn bundles of NFYs with different diameters via tensile test.

tenogenic differentiation capacity of TSPCs was verified by testing the expression of TNMD. As shown in Figure 3B, the TSPCs had obvious expression of TNMD. Furthermore, as shown in Figure 3C, over 92% and 33% of TSPCs were positive for BMSC markers CD90 and CD44, respectively, while they were negative for CD18, which is a surface receptor present on BMSCs (Miura et al., 2005). In addition, the TSPCs did not express hematopoietic cell markers, including CD34 and CD45, which are both highly expressed in tenocytes (Li et al., 2021), further confirming that these tendon-derived cells were TSPCs.

Viability and morphology of TSPCs on aligned NFYs

TSPCs were seeded on single aligned NFYs of various diameters, cell viability was assessed using the Live/Dead assay

TABLE 2 Mechanical properties of single and 50-yarn bundles of aligned NFYs with different diameters.

Sample groups	Force	Strain
NFY-10	1.13 ± 0.13 cN	141 ± 41%
NFY-50	3.16 ± 0.16 cN	314 ± 16%
NFY-100	5.16 ± 0.04 cN	486 ± 17%
Bundled 50 yarns of NFY-10	0.44 ± 0.1 N	93 ± 18%
Bundled 50 yarns of NFY-50	2.15 ± 0.09 N	124 ± 25%
Bundled 50 yarns of NFY-100	3.31 ± 0.37 N	158 ± 26%

after for 24 h in culture, and cell proliferation was assessed using Alamar Blue reagent after 1, 5, and 7 days in culture. TSPCs cultured on aligned NFYs showed high viability, with few dead cells and excellent elongation (Figure 4A). The proliferation results showed that all aligned NFY groups had a significant increase in cell growth during the culture period. On the first day of cell culture, there were no significant differences between the aligned NFY groups ($p > 0.05$). As time in culture increased, the number of TSPCs on the aligned NFYs of various groups showed significant differences ($p < 0.05$). In particular, the NFY-100 group showed significantly higher cell numbers than the NFY-10 and NFY-50 groups on days 5 and 7 (Figure 4B). These results demonstrated that TSPC growth increases with increased NFY diameter, and the aligned NFYs, regardless of diameter, have good biocompatibility.

The cellular alignment and elongation behaviors of TSPCs on aligned NFYs with different diameters were assessed by F-actin staining after 3 days in culture. The cytoskeleton was stained green using FITC-conjugated phalloidin, and the nucleus was stained blue using DAPI. The images of F-actin staining show that TSPCs spread well on the surface of all aligned NFYs and exhibited aligned and elongated morphologies (Figures 5A–C). In contrast, cells in the 2D group showed random spindle morphology (Figure 5D). Furthermore, quantitative analysis of cell alignment was accomplished by measuring the angle between

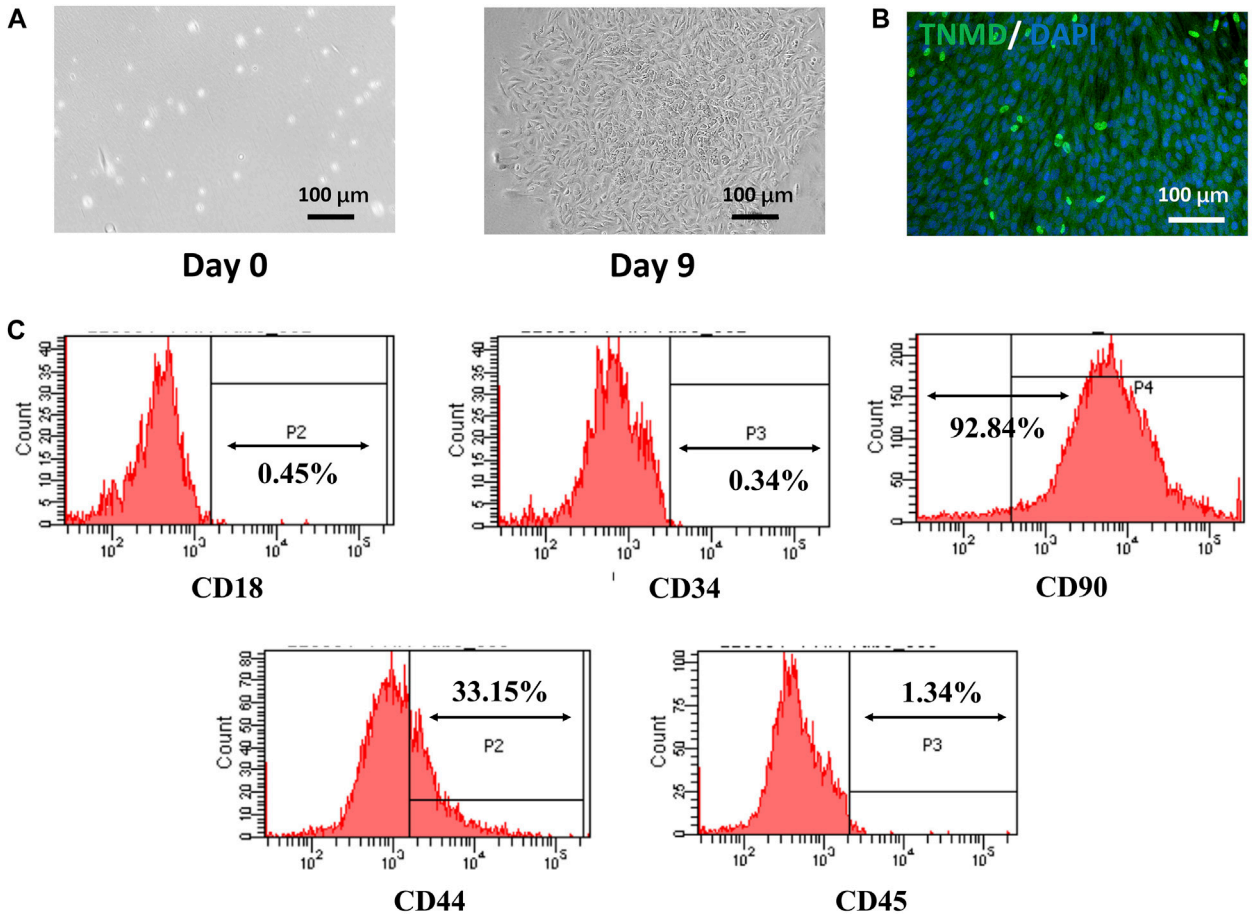

FIGURE 3
Isolation and Characterization of TSPCs. **(A)** The morphology of rat TSPCs at P0, **(B)** the tenogenic differentiation of TSPCs cultured for 7 days in differentiation medium, **(C)** Flow cytometry analysis of the expression of cell surface makers related to stem cells and hematopoietic cells.

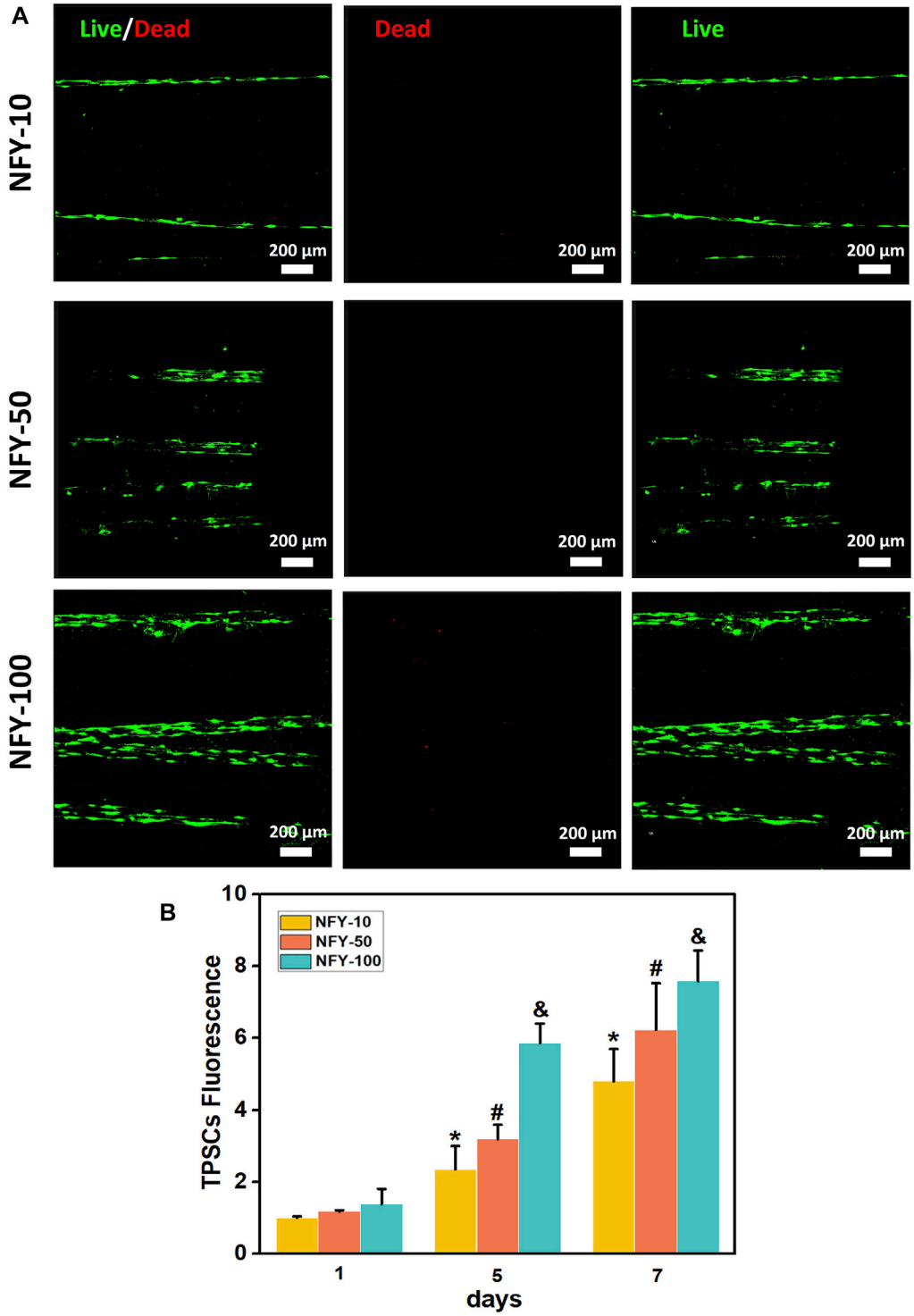

FIGURE 4
The viability of TSPCs on aligned NFYs with different diameters. **(A)** Fluorescence imaging of living (green) and dead (red) TSPCs seeded on aligned NFYs and cultured in growth medium for 24 h. **(B)** The proliferation of TSPCs on NFYs with different diameters, after 7 days, as measured using Alamar Blue. $^{*}p < 0.05$ compared with the NFY-10 group at day 1, $^{\#}p < 0.05$ compared with the NFY-50 group at day 1, and $^{\&}p < 0.05$ compared with the NFY-100 group at day 1.

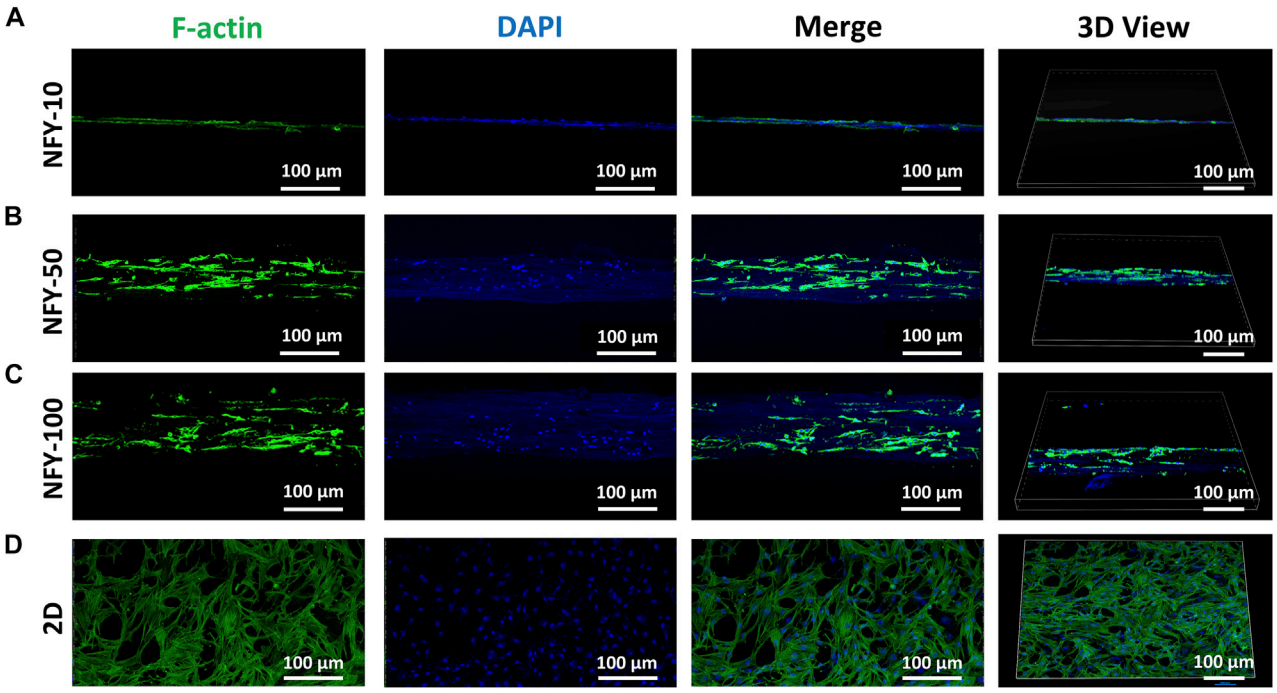

FIGURE 5
The top and 3D views of TSPCs with F-actin-stained cytoskeletons (green) and DAPI-stained nuclei (blue) after 3 days of culture on NFY-10 **(A)**, NFY-50 **(B)**, and NFY-100 **(C)**, as well as cells in the 2D group **(D)**. Scale bar = 100 μm. TSPCs cultured on single aligned NFYs with varying diameters showed aligned morphology, contrasting with the morphology of the 2D control group.

cell growth direction and the direction of aligned NFYs, including relative alignment in ±10° increments (Figure 6A). These data show that the orientation ratio of cells within ±10° on NFY-10, NFY-50, and NFY-100 were 73%, 58%, and 53%, respectively (Figures 6B–E), while the orientation ratio was only 12% in the 2D group (Figure 6F). Additionally, cell elongation behavior was estimated by assessing TSPC nuclear aspect ratios, which demonstrated a significant improvement in cellular elongation of the NFY-10 group compared to that of the 2D group (Figure 6H). Together, these data indicate that aligned NFYs are able to enhance the 3D cellular alignment and elongation of TSPCs, which mimics native collagen fibers with tenocyte alignment. Notably, TSPCs showed better alignment and elongation behaviors when cultured on aligned NFYs with smaller diameters.

Tenogenic differentiation of TSPCs on aligned NFYs

To explore the effects of aligned NFYs on tenogenic differentiation of TSPCs, cells were seeded on aligned NFYs of various diameters and then cultured in differentiation medium for 7 days. TNMD is a marker of the mature tenogenic phenotype. Type I collagen (Col1a1) is a major matrix component of native tendons that supports essential mechanical properties of tendon tissue (Goh et al., 2014). Tenogenic differentiation was examined by TNMD immunostaining. Images of TNMD and Col1a1 staining showed that the fluorescence intensity in all of the aligned NFY groups was higher than that of the 2D group, indicating that TSPCs on these aligned NFYs had higher TNMD and Col1a1 expression compared with the 2D group, and that aligned NFYs enhanced tenogenic differentiation of TSPCs, as suggested by enhanced expression of these markers (Figures 7A,B). Additionally, NFY-50 showed the highest TNMD expression, compared with NFY-10 and NFY-100, which indicates that the best tenogenic differentiation of TSPCs occurred on NFY-50.

We also investigated the effects of cell culture on aligned NFYs on the tenogenic differentiation of TSPCs maintained in growth medium for 7 days. Decorin (DCN) is the most abundant small protein-polysaccharide rich in leucine in the tendon and plays a key role in ensuring precise alignment and stability of collagen fibers related to the phenotype of the tendon. Scleraxis (SCX) is an essential transcription factor for tenogenesis (Bavin et al., 2017). RT-qPCR results showed that aligned NFYs improve the expression of tendon-related genes, including TNMD, DCN, Col1a1, and SCX (Figure 7C). Gene expression of TNMD and DCN was approximately 30 times and 20 times greater,

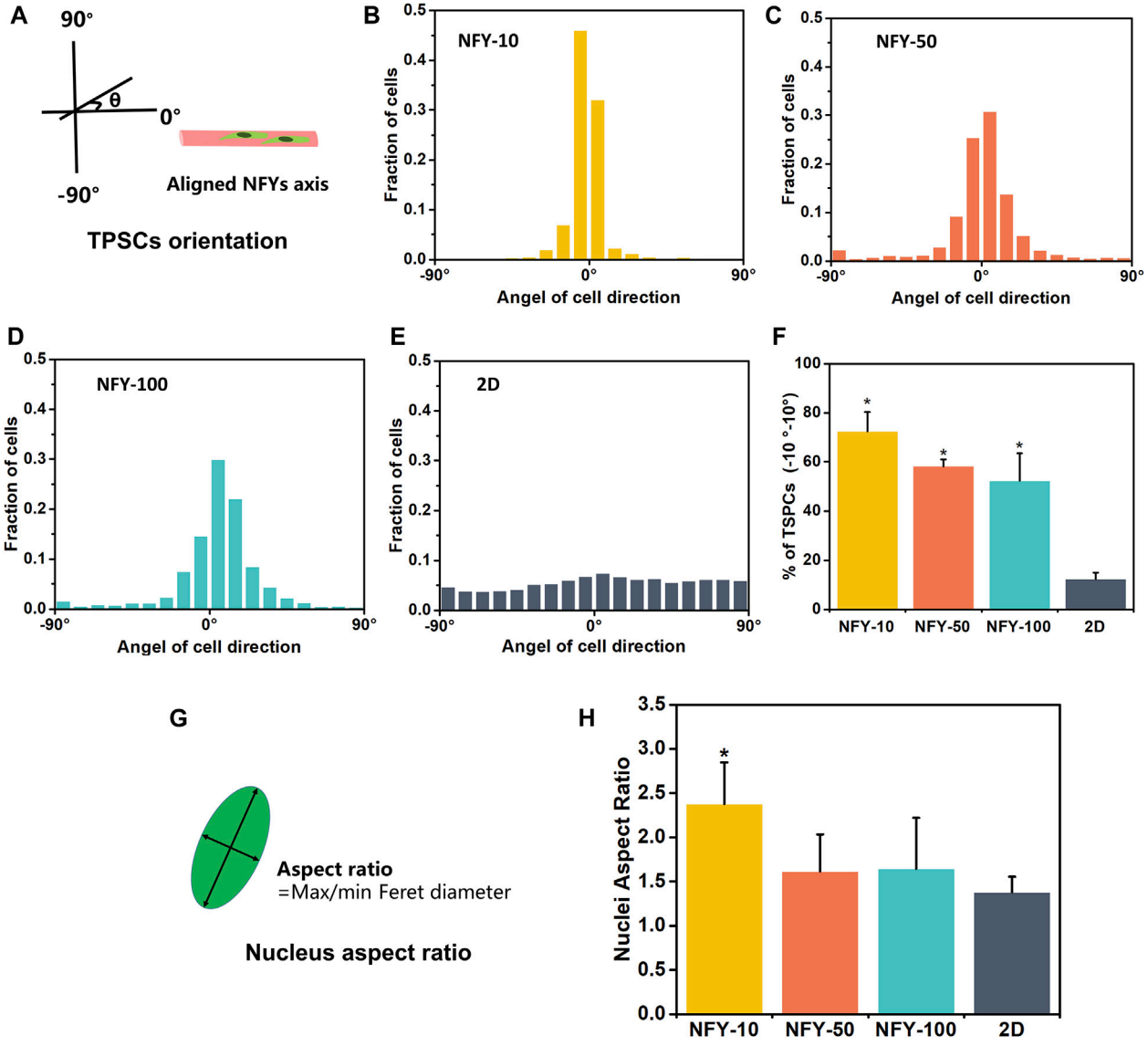

FIGURE 6
Quantitative measurement of cellular alignment and elongation of TSPCs on aligned NFYs. **(A)** Schematic diagram of cellular orientation measurement. The histograms show the cellular angles and distribution of TSPCs on NFYs with diameters of 10 μm **(B)**, 50 μm **(C)**, 10 μm **(D)**, and on a 2D tissue culture plate **(E)**. **(F)** Histograms of the relative alignment in ±10° increments demonstrate cellular alignment of TSPC on NFYs of varying diameters, in contrast to the random morphologies observed in the 2D group; *$p < 0.05$. **(G)** Schematic diagram of nuclear aspect ratios calculated from measurement of the length and width of the nucleus. **(H)** Histograms of nuclear aspect ratio of TSPCs on NFYs and TSPCs in the 2D group; *$p < 0.05$.

respectively, in cultures with NFY-50 compared with the 2D group ($p < 0.05$). These results indicate that the 3D aligned and multi-scale structure of aligned NFYs may improve the tenogenic differentiation of TSPCs. Interestingly, cells cultured with NFY-50 showed the highest expression of TNMD, DCN, and Col1a1. These results are consistent with the TNMD and Col1a1 immunofluorescence staining results, further confirming the enhanced effect of aligned NFYs on tenogenic differentiation of TSPCs.

Aligned NFYs aid in repair of rat Achilles tendon injury *in vivo*

The ability of single NFYs to improve the tenogenic differentiation of TSPCs has been verified. Therefore, to investigate the effects of NFYs on improving tendon regeneration *in vivo*, we implanted 50-yarn NFY bundles into a rat tendon injury model. The NFY-50 group showed significantly better tenogenic differentiation of TSPCs

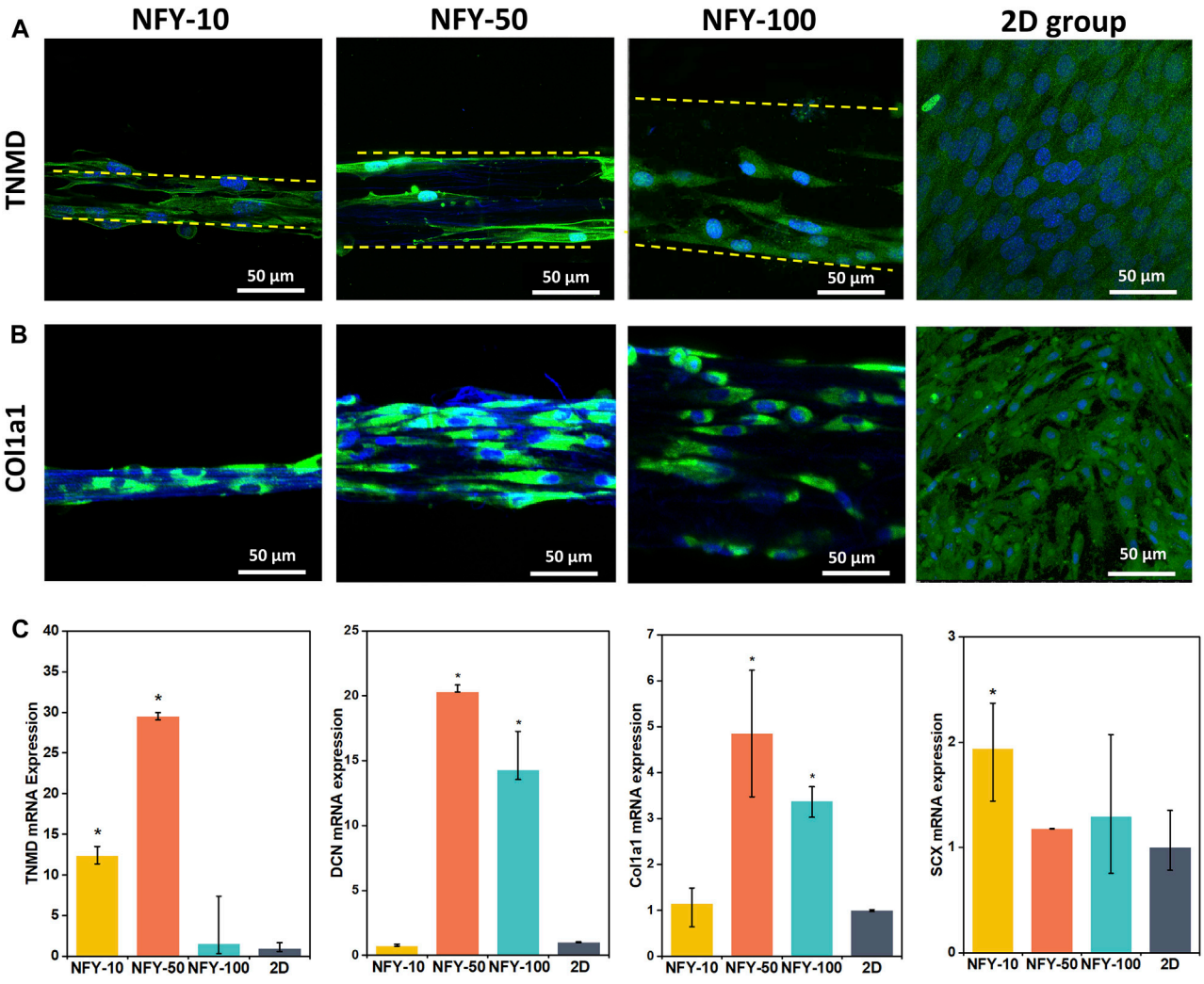

FIGURE 7
Tenogenic differentiation of TSPCs cultured on aligned NFYs of varying diameters. **(A)** Immunofluorescence images of TNMD staining of TSPCs on aligned NFYs of different diameters, and cells from the 2D control group, after 7 days in culture; green indicates TNMD, blue indicates cell nucleus. **(B)** Immunofluorescence images of Col1a1 staining of TSPCs on aligned NFYs of different diameters, and cells from the 2D control group after 7 days in culture; green indicates Col1a1, blue indicates cell nucleus. **(C)** RT-qPCR analysis of tenogenic gene expression in TSPCs cultured on aligned NFYs and cells from the 2D group. ($n = 3$; $*p < 0.05$).

compared with the other NFY groups. Therefore, we used NFY-50 to further investigate effects of NFYs on *in vivo* tendon repair. Tendon injury usually includes three sequential phases from injury onset to healing: the injured tendon initially becomes inflamed, forming granulation tissue within the injury region to serve as a provisional matrix. Then, type III collagen fibers, fibronectin, and proteoglycans are formed at the injury site and type III collagen fibers are replaced by type I collagen fibers at the proliferation stage. Finally, there is alignment of tenocytes and collagen fibers, with type I collagen fibers increasing and type III collagen fibers decreasing (Vasiliadis and Katakalos, 2020). In our study, 6 weeks after implantation, partial neo-tissue with a typical white, tendon-like appearance was observed in rats that received the bundled NFY-50 scaffold (Figure 8A). To identify the type of collagen prominent in the neo-tissue, we used Picrosirius red staining to distinguish collagen types in the tendon defect area. As shown in Figure 8C, the aligned NFY scaffold group formed more collagen I (red), with little collagen III (green) remaining; in contrast, the injury only group showed more collagen III formation, indicating that aligned NFY scaffolds improve tendon regeneration. H&E staining results (Figure 8D) showed partial formation of aligned neo-tissue around the NFY-50 scaffold. Bundled NFY-50 scaffolds surrounded by high cell nuclei density indicated that the nanofiber structure of NFY-50 had allowed immune cells and blood infiltration, which may have enhanced tissue remodeling.

10.3389/fbioe.2022.960694

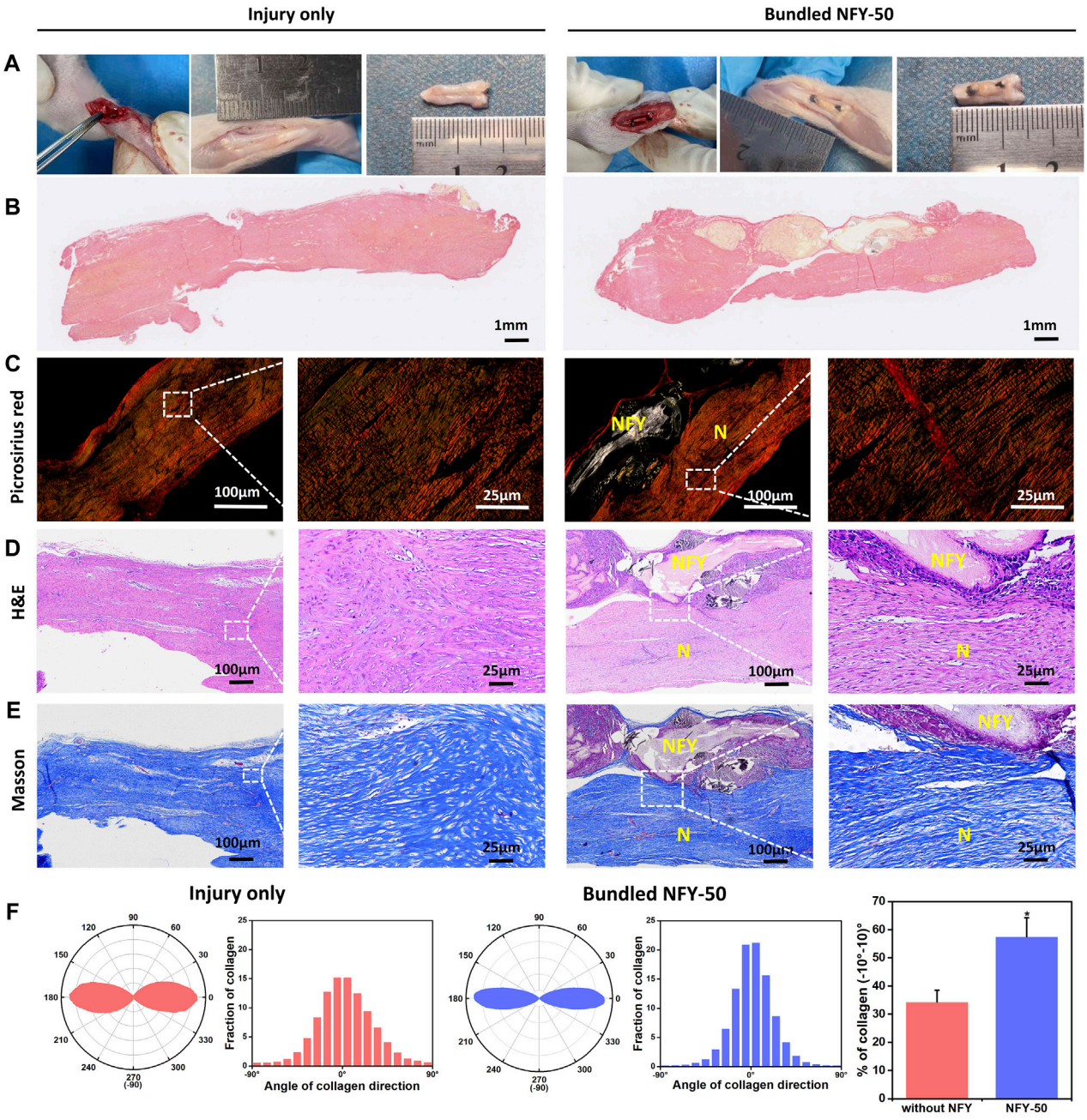

FIGURE 8
The effects of aligned NFYs on tendon repair *in vivo*. **(A)** NFY bundles were implanted into the rat Achilles tendon injury model; tendons were cut off directly in the injury only group. **(B)** Whole Picrosirius red staining with a light mirror. **(C)** Picrosirius red staining with a polariscope. **(D)** Images of H&E and **(E)** Masson's trichrome staining of the defect site 6 weeks after bundled NFY implantation or injury only treatment. For Picrosirius red staining, red indicates collagen I and green indicates collagen III. N, neo-collagen; NFY, NFY-50. **(F)** Quantitative analysis of collagen orientation and distribution and histograms showing relative alignment in ±10° increments. *$p < 0.05$.

Images taken at high magnification showed partial neo-tissue that was organized and aligned, as it was guided by the aligned micro- and macro-structure and mechanical support of the bundled NFY-50 scaffold. In contrast, the neo-tissue in the injury only group was disordered and showed typical scar tissue without aligned structure. Masson's trichrome staining (Figure 8E) results also indicated that neo-tissue formation included an abundance of collagen fibers (blue), and showed that the collagen fibers had an aligned microstructure along the direction of the NFY-50 scaffold. These quantitative data

demonstrate that the orientation ratio of collagen within ±10°in the injury only and NFY-50 groups were 34% ± 4% and 57% ± 6%, respectively. Therefore, the injury only group showed amorphous organization, indicating fibrous scar tissue formation, compared to alignment in the NFY-50 group.

Discussion

Native tendon tissues show a hierarchical structure, where highly-aligned collagen fibers form fascicles, and many fascicles are bound together to form the tendon (Goh et al., 2014). Tenocytes, in particular, lay on the longitudinally aligned collagen fascicles and fibers and exhibit cellular orientation. This hierarchical structure plays a key role in the high tensile strength of native tendon. Therefore, developing a biomimetic TE scaffold with a hierarchical structure that enhanced cellular alignment, elongation, and mechanical strength would improve tendon repair (Vasiliadis and Katakalos, 2020). In preparing the biomimetic scaffold, the first challenge is in providing suitable mechanical support for the newly synthesized ECM at the injury site during tendon tissue regeneration. In this study, we chose PCL polymer as the primary material from which to develop the electrospun NFY due to its suitable mechanical properties, good biocompatibility, and broad use in various biomedical applications (Sun et al., 2006; Hu et al., 2016).

The electrospinning technique is regarded as a promising approach to preparing aligned nanofibers. For instance, previous studies have shown that aligned nanofiber sheets promote cellular elongation and tenogenic differentiation (Watari et al., 2012; Tu et al., 2020). However, those nanofiber sheets have failed to mimic the complex hierarchical structure of native tendon tissue. In contrast, we have reported on a series of NFYs, prepared using a well-developed dry-wet electrospinning technique, that were able to guide 3D cellular alignment and elongation in soft TE applications (Wu et al., 2017b; Wang et al., 2019). Therefore, in this study, we utilized our dry-wet electrospinning system to prepare the aligned PCL NFYs with an abundance of aligned nanofibers that mimicked the hierarchical structure of alignment fascicles and collagen fibers in native tendon tissue (Figure 2; Supplementary Figure S1). The aligned NFYs with smaller diameters had better alignment structure but less robust mechanical properties (Figure 2D). The rotation rate of the NFY receptor played a key role in the diameter and orientation of NFYs. When the receptor was rotating faster, the random nanofibers would be dragged from the surface of the solution and received on the receptor faster. Therefore, the NFYs would have better alignment structure and smaller diameter with increased rotation rate of the receptor. In addition, a previous study suggested that nanofiber orientation was affected by the rate of the receptor with only one variable (Vimal et al., 2016). The mechanical properties of murine tendons showed 2–3 N according to a previous study (Kurtaliaj et al., 2019). In comparison, we found that the 50-yarn bundles of NFY-50 had suitable force with 2.15 ± 0.09 N, demonstrating suitable mechanical properties for rat tendon tissue repair compared with NFYs of other diameters.

Several types of stem cells isolated from different tissue sources, such as bone marrow, adipose tissue, and tendon, have been applied in tendon TE applications (Bi et al., 2007; Bavin et al., 2015; Wu et al., 2017a; Laranjeira et al., 2017). Among them, TSPCs, which are isolated from tendon sources and differentiate into tenocytes to regulate tendon homeostasis, would be more suitable for the tendon microenvironment (Guo et al., 2016). A previous study revealed promising results from the use of TSPCs in tendon injury repair *in vivo* (Youngstrom et al., 2016). In our study, we used TSPCs to evaluate the effects of aligned NFYs on tenogenic differentiation *in vitro*, after successful isolation of TSPCs from rat tendon tissue and confirmatory assessment of tenogenic markers using flow cytometry (Figure 3). The composition and structure of the ECM regulates the phenotype and differentiation of TSPCs and affects the regeneration of functional tendon tissue (Sheng et al., 2019). Recent studies have investigated the effects of nanofiber diameters on the behavior of tendon cells (English et al., 2015; Jenkins and Little, 2019). However, there are still few reports on investigation of scaffolds with integrated hierarchical structure that induce TSPCs behavior and phenotypes that lead to tenogenic differentiation. In our study, we successfully prepared aligned NFYs of varying diameters, allowing us to study the effects of NFY diameter on cellular response and tenogenic differentiation of TSPCs. The proliferation results showed that the TSPCs on NFY-50 and NFY-100 exhibited higher proliferation rates compared with the other groups (Figure 4). One of reasons for this phenomenon was greater contact inhibition on NFYs of smaller diameter due to reduced area available for cell growth. In a prior study, Gerard and Goldbeter (2014) created a detailed computational model to interpret contact inhibition, which suggested that the proliferation of cells would be inhibited by the Hippo/YAP pathway rather than culture conditions when cell density reached the threshold. Another reason was higher initial adhesion rate in the groups with NFYs of larger diameters, with the larger diameter providing increased adhesion area and greater area for cell growth. As observed by the results of Alamar Blue staining on day 1 in culture, there was a rising trend in the number of TSPCs on the NFYs with increasing diameters. Moreover, our previous study showed that cell adhesion would be limited by the narrower surface of the aligned NFYs of smaller diameter, which is consistent with the results of the current study. On the other hand, F-actin staining confirmed that the 3D

aligned NFYs provided a 3D microenvironment that induced TSPCs to orient in alignment with the NFYs (Figures 5, 6). More importantly, recent studies demonstrated that nanofiber scale could affect cell differentiation (Sheng et al., 2019). For instance, Bashur et al. (2009) showed that electrospun nanofibers exhibited nanoscale fiber diameters similar to those of collagen fibers in native tendon, and that the nanofibers could increase the level of TNMD gene expression. In our study, both RT-qPCR and immunofluorescence staining to assess levels of the tenogenic markers TNMD, DCN, and Col1a1 showed that use of NFYs of 50 μm diameter significantly improved the tenogenic differentiation of TSPCs compared with use of aligned NFYs of other sizes (Figure 7). These results are mainly due to the aligned structure of NFY-50 and it's diameter, which is similar to the collagen fascicles and fibers of rat tendon tissue of approximately 50–300 μm in diameter. Ultimately, aligned NFYs with 3D hierarchical structure consisting of aligned monodisperse nanofibers promoted tenogenic differentiation of TSPCs.

To further investigate the effects of the aligned NFYs on tendon repair *in vivo*, NFY-50 was chosen for implantation due its superior ability to promote TSPCs tenogenic differentiation and suitable mechanical properties. We bundled 50 yarns of NFY-50 together to prepare the aligned NFY scaffolds to mimic the macrostructure of the tendon tissue and provide mechanical support for the repaired tendon. We then made a defect in the Achilles tendon of a rat model and implanted the scaffold. Tissue was harvested 6 weeks later to obtain sections for H&E, Masson's trichrome, and Picrosirius red staining. NFY-50 scaffolds resulted in better histological structure and regeneration ability compared with the injury only group (Figure 8). Based on histological evaluation, there was obvious degradation of aligned NFYs due to the greater surface area of the nano-scale structure (Zhang et al., 2014). A previous study showed that the PCL grafts composed of nanofiber sheets had undergone significant degradation, suggesting an advanced cell response when the tendon was repaired during the 6-week period of remodeling (Bosworth, 2014). In our study, NFYs composed of numerous nanofibers showed a higher degradation rate and many macrophages gathered around the scaffold. The main reason for inflammation was the adsorption of protein on the surface of implanted NFY scaffolds due to the nanofibrous structure (Zhou and Groth, 2018). With degradation of the bundled NFY-50, neo-collagen filled in the scaffolds after 6 weeks. The complete tissue sections (Picrosirius red staining) are shown in Figure 8B, demonstrating that the bundled NFY-50 connected the fracture of the tendon as a bridge, and that neo-collagen appeared inside the degraded area of the bundled NFY-50 to wrap it externally. Upon degradation of the bundled NFY-50, i.e., the PCL materials, neo-collagen replaced the NFY scaffold to achieve repair of the tendon.

To further distinguish different types of collagen, we used polarized light microscopy (PLM) to image tissue with Picrosirius red staining, where type Ⅰ collagen fibers appeared bright red-yellow, while type Ⅲ collagen fibers appeared green (Rittié, 2017). A recent study revealed that type Ⅰ collagen fibers are associated with mechanical strength (Goh et al., 2014). The type III collagen fibers would be gradually replaced by type I collagen fibers during tendon remodeling, and type I collagen fibers begin to align along the long axis of the tendon (Deng et al., 2014). In this study, the Picrosirius red assay demonstrated that the type Ⅰ collagen fibers were stained bright red-yellow in the NFY scaffold group in contrast with the injury only group, indicating that the bundles of NFY-50 improved mechanical strength and induced neo-collagen alignment of the neo-tendon tissue. There were fewer type Ⅲ collagen fibers in the aligned NFY scaffolds than in the injury only group (Figure 7D). These results indicate that the aligned NFYs enhance regeneration of tendon tissue and, at the same time, guide the aligned formation of collagen fibers during tendon repair.

Above all, this study confirmed that PCL 3D aligned NFYs prepared by dry-wet electrospinning provide suitable mechanical support and the hierarchical structure guidance for tendon tissue regeneration, and that NFY-50 improves tenogenic differentiation of TSPCs as a biomimetic of similar diameter to collagen fascicles and fibers in native tendon. Bundled NFY scaffolds mimic the macrostructure of tendon tissue and provide mechanical support for the repaired tendon *in vivo*. There is high potential for use of aligned NFY-50 in development of additional scaffolds that require element units to produce hierarchical 3D aligned scaffolds for the construction of tissue-specific functional architecture, thus advancing regenerative therapies for soft tissue repair.

Conclusion

In this study, highly aligned NFYs of varying diameters were fabricated and characterized to investigate their effects on the behavior of TSPCs. We found that aligned NFYs could mimic the topography and mechanical properties of collagen fascicles and fibers of native tendon. Aligned NFYs induced TSPCs orientation and elongation. Moreover, aligned NFYs enhanced tenogenic gene and protein expression, including that of TNMD; NFYs of 50 μm diameter showed the greatest effect. Taken together, these data indicate that the nanofibrous structure of aligned NFYs is able to induce TSPCs orientation and elongation, and the muti-scale structure of aligned NFYs may improve tenogenic differentiation. To further investigate the effects of aligned NFYs on tendon repair *in vivo*, 50-yarn bundles of NFY-50 were implanted in rat Achilles tendon models, with the results demonstrating that the aligned hierarchical NFY scaffolds induced neo-collagen orientation

and cell alignment, and that bundled NFY-50 scaffolds enhanced tendon tissue regeneration. Overall, these results suggest that aligned NFYs of well-defined diameter mimic the complex hierarchical structure of native collagen fascicles and fibers and show excellent potential for use in tendon regeneration applications.

Data availability statement

The raw data supporting the conclusions of this article will be made available by the authors, without undue reservation.

Ethics statement

The animal study was reviewed and approved by the Institutional Animal Care and Use Committee, Southern Medical University.

Author contributions

QY and LW conceived of and designed the experiments, and wrote the manuscript. QY performed the cell culture experiments. JL contributed to the analysis. WS and KZ contributed to the animal experiment. LY and TL contributed to the 3D print models. YW contributed to the aligned NFY preparation. LW and YW revised the manuscript and supported this project. All authors discussed the results and commented on the manuscript.

Funding

This work was supported by the National Natural Science Foundation of China (31900960, 32000955), the Guangdong Basic and Applied Basic Research Foundation (2019A1515011413), and the Science and Technology Program of Guangzhou (202102020894).

Conflict of interest

The authors declare that the research was conducted in the absence of any commercial or financial relationships that could be construed as a potential conflict of interest.

Publisher's note

All claims expressed in this article are solely those of the authors and do not necessarily represent those of their affiliated organizations, or those of the publisher, the editors, or the reviewers. Any product that may be evaluated in this article, or claim that may be made by its manufacturer, is not guaranteed or endorsed by the publisher.

Supplementary material

The Supplementary Material for this article can be found online at: https://www.frontiersin.org/articles/10.3389/fbioe.2022.960694/full#supplementary-material

References

Bashur, C. A., Shaffer, R. D., Dahlgren, L. A., Guelcher, S. A., and Goldstein, A. S. (2009). Effect of fiber diameter and alignment of electrospun polyurethane meshes on mesenchymal progenitor cells. *Tissue Eng. Part A* 15, 2435–2445. doi:10.1089/ten.tea.2008.0295

Bavin, E. P., Atkinson, F., Barsby, T., and Guest, D. J. (2017). Scleraxis is essential for tendon differentiation by equine embryonic stem cells and in equine fetal tenocytes. *Stem Cells Dev.* 26, 441–450. doi:10.1089/scd.2016.0279

Bavin, E. P., Smith, O., Baird, A. E., Smith, L. C., and Guest, D. J. (2015). Equine induced pluripotent stem cells have a reduced tendon differentiation capacity compared to embryonic stem cells. *Front. Vet. Sci.* 2, 55. doi:10.3389/fvets.2015.00055

Bi, Y., Ehirchiou, D., Kilts, T. M., Inkson, C. A., Embree, M. C., Sonoyama, W., et al. (2007). Identification of tendon stem/progenitor cells and the role of the extracellular matrix in their niche. *Nat. Med.* 13, 1219–1227. doi:10.1038/nm1630

Bosworth, L. A. (2014). Travelling along the clinical roadmap: developing electrospun scaffolds for tendon repair. *Conf. Pap. Sci.* 2014, 1–6. doi:10.1155/2014/304974

Carniel, T. A., and Fancello, E. A. (2019). A numerical insight on the pericellular matrix and elastin fibers in the multiscale mechanics of tendon fascicles. *Eur. J. Mech. - A/Solids* 76, 146–154. doi:10.1016/j.euromechsol.2019.04.001

Chae, S., Sun, Y., Choi, Y. J., Ha, D. H., Jeon, I., and Cho, D. W. (2021). 3D cell-printing of tendon-bone interface using tissue-derived extracellular matrix bioinks for chronic rotator cuff repair. *Biofabrication* 13, 035005. doi:10.1088/1758-5090/abd159

Chen, J. L., Zhang, W., Liu, Z. Y., Heng, B. C., Ouyang, H. W., and Dai, X. S. (2015). Physical regulation of stem cells differentiation into teno-lineage: current strategies and future direction. *Cell Tissue Res.* 360, 195–207. doi:10.1007/s00441-014-2077-4

Chen, Y., Xie, Y., Liu, M., Hu, J., Tang, C., Huang, J., et al. (2019). Controlled-release curcumin attenuates progression of tendon ectopic calcification by regulating the differentiation of tendon stem/progenitor cells. *Mater. Sci. Eng. C* 103, 109711. doi:10.1016/j.msec.2019.04.090

Dabirian, F., Hosseini, Y., and Ravandi, S. a. H. (2007). Manipulation of the electric field of electrospinning system to produce polyacrylonitrile nanofiber yarn. *J. Text. Inst.* 98, 237–241. doi:10.1080/00405000701463979

Deng, D., Wang, W., Wang, B., Zhang, P., Zhou, G., Zhang, W. J., et al. (2014). Repair of Achilles tendon defect with autologous ASCs engineered tendon in a rabbit model. *Biomaterials* 35, 8801–8809. doi:10.1016/j.biomaterials.2014.06.058

English, A., Azeem, A., Spanoudes, K., Jones, E., Tripathi, B., Basu, N., et al. (2015). Substrate topography: a valuable *in vitro* tool, but a clinical red herring for *in vivo* tenogenesis. *Acta Biomater.* 27, 3–12. doi:10.1016/j.actbio.2015.08.035

Gerard, C., and Goldbeter, A. (2014). The balance between cell cycle arrest and cell proliferation: control by the extracellular matrix and by contact inhibition. *Interface Focus* 4, 20130075. doi:10.1098/rsfs.2013.0075

Goh, K. L., Listrat, A., and Béchet, D. (2014). Hierarchical mechanics of connective tissues: integrating insights from nano to macroscopic studies. *J. Biomed. Nanotechnol.* 10, 2464–2507. doi:10.1166/jbn.2014.1960

Gonzalez-Masis, J., Cubero-Sesin, J. M., Guerrero, S., Gonzalez-Camacho, S., Corrales-Urena, Y. R., Redondo-Gomez, C., et al. (2020). Self-assembly study of type I collagen extracted from male Wistar Hannover rat tail tendons. *Biomater. Res.* 24, 19. doi:10.1186/s40824-020-00197-0

Guo, J., Chan, K. M., Zhang, J. F., and Li, G. (2016). Tendon-derived stem cells undergo spontaneous tenogenic differentiation. *Exp. Cell Res.* 341, 1–7. doi:10.1016/j.yexcr.2016.01.007

Hasan, J., Fisher, J., and Ingham, E. (2014). Current strategies in meniscal regeneration. *J. Biomed. Mat. Res.* 102, 619–634. doi:10.1002/jbm.b.33030

Hu, J. J., Yin, Z., Shen, W. L., Xie, Y. B., Zhu, T., Lu, P., et al. (2016). Pharmacological regulation of *in situ* tissue stem cells differentiation for soft tissue calcification treatment. *Stem Cells* 34, 1083–1096. doi:10.1002/stem.2306

Jenkins, T. L., and Little, D. (2019). Synthetic scaffolds for musculoskeletal tissue engineering: cellular responses to fiber parameters. *npj Regen. Med.* 4, 15. doi:10.1038/s41536-019-0076-5

Kalson, N. S., Lu, Y., Taylor, S. H., Starborg, T., Holmes, D. F., and Kadler, K. E. (2015). Expansion mechanism of fibrous tissue A structure-based extracellular matrix expansion A structure-based extracellular matrix A structure-based extracellular matrix expansion mechanism of fibrous tissue growth. *eLife*, e60280. doi:10.7554/eLife.05958.001

Kurtaliaj, I., Golman, M., Abraham, A. C., and Thomopoulos, S. (2019). Biomechanical testing of murine tendons. *J. Vis. Exp.* 4, e05958 doi:10.3791/60280

Laranjeira, M., Domingues, R. M. A., Costa-Almeida, R., Reis, R. L., and Gomes, M. E. (2017). 3D mimicry of native-tissue-fiber architecture guides tendon-derived cells and adipose stem cells into artificial tendon constructs. *Small* 13, 1700689. doi:10.1002/smll.201700689

Li, Y., Wu, T., and Liu, S. (2021). Identification and distinction of tenocytes and tendon-derived stem cells. *Front. Cell Dev. Biol.* 9, 629515. doi:10.3389/fcell.2021.629515

Longo, U. G., Lamberti, A., Maffulli, N., and Denaro, V. (2011). Tissue engineered biological augmentation for tendon healing: a systematic review. *Br. Med. Bull.* 98, 31–59. doi:10.1093/bmb/ldq030

Ma, J., He, Y., Liu, X., Chen, W., Wang, A., Lin, C. Y., et al. (2018). A novel electrospun-aligned nanoyarn/three-dimensional porous nanofibrous hybrid scaffold for annulus fibrosus tissue engineering. *Int. J. Nanomedicine* 13, 1553–1567. doi:10.2147/IJN.S143990

Merceron, T. K., Burt, M., Seol, Y. J., Kang, H. W., Lee, S. J., Yoo, J. J., et al. (2015). A 3D bioprinted complex structure for engineering the muscle-tendon unit. *Biofabrication* 7, 035003. doi:10.1088/1758-5090/7/3/035003

Miura, Y., Miura, M., Gronthos, S., Allen, M. R., Cao, C., Uveges, T. E., et al. (2005). Defective osteogenesis of the stromal stem cells predisposes CD18-null mice to osteoporosis. *Proc. Natl. Acad. Sci. U. S. A.* 102, 14022–14027. doi:10.1073/pnas.0409397102

Mouthuy, P. A., Zargar, N., Hakimi, O., Lostis, E., and Carr, A. (2015). Fabrication of continuous electrospun filaments with potential for use as medical fibres. *Biofabrication* 7, 025006. doi:10.1088/1758-5090/7/2/025006

Nau, T., and Teuschl, A. (2015). Regeneration of the anterior cruciate ligament: current strategies in tissue engineering. *World J. Orthop.* 6, 127–136. doi:10.5312/wjo.v6.i1.127

Puetzer, J. L., Ma, T., Sallent, I., Gelmi, A., and Stevens, M. M. (2021). Driving hierarchical collagen fiber formation for functional tendon, ligament, and meniscus replacement. *Biomaterials* 269, 120527. doi:10.1016/j.biomaterials.2020.120527

Rittié, L. (2017). *Fibrosis*. United States: Springer New York.

Sensini, A., and Cristofolini, L. (2018). Biofabrication of electrospun scaffolds for the regeneration of tendons and ligaments. *Mater. (Basel)* 11, 1963. doi:10.3390/ma11101963

Sensini, A., Gualandi, C., Focarete, M. L., Belcari, J., Zucchelli, A., Boyle, L., et al. (2019). Multiscale hierarchical bioresorbable scaffolds for the regeneration of tendons and ligaments. *Biofabrication* 11, 035026. doi:10.1088/1758-5090/ab20ad

Sensini, A., Santare, M. H., Eichenlaub, E., Bloom, E., Gotti, C., Zucchelli, A., et al. (2021). Tuning the structure of nylon 6, 6 electrospun bundles to mimic the mechanical performance of tendon fascicles. *Front. Bioeng. Biotechnol.* 9, 626433. doi:10.3389/fbioe.2021.626433

Sharma, P., and Maffulli, N. (2005). Tendon injury and tendinopathy: Healing and repair. *J. Bone Jt. Surg.* 87, 187–202. doi:10.2106/jbjs.d.01850

Sheng, D., Li, J., Ai, C., Feng, S., Ying, T., Liu, X., et al. (2019). Electrospun PCL/Gel-aligned scaffolds enhance the biomechanical strength in tendon repair. *J. Mat. Chem. B* 7, 4801–4810. doi:10.1039/c9tb00837c

Silver, F. H., Freeman, J. W., and Seehra, G. P. (2003). Collagen self-assembly and the development of tendon mechanical properties. *J. Biomechanics* 36, 1529–1553. doi:10.1016/S0021-9290(03)00135-0

Sun, H., Mei, L., Song, C., Cui, X., and Wang, P. (2006). The *in vivo* degradation, absorption and excretion of PCL-based implant. *Biomaterials* 27, 1735–1740. doi:10.1016/j.biomaterials.2005.09.019

Tan, Q., Lui, P. P., and Rui, Y. F. (2012). Effect of *in vitro* passaging on the stem cell-related properties of tendon-derived stem cells-implications in tissue engineering. *Stem Cells Dev.* 21, 790–800. doi:10.1089/scd.2011.0160

Tu, T., Shen, Y., Wang, X., Zhang, W., Zhou, G., Zhang, Y., et al. (2020). Tendon ECM modified bioactive electrospun fibers promote MSC tenogenic differentiation and tendon regeneration. *Appl. Mater. Today* 18, 100495. doi:10.1016/j.apmt.2019.100495

Vasiliadis, A. V., and Katakalos, K. (2020). The role of scaffolds in tendon tissue engineering. *J. Funct. Biomater.* 11, 78. doi:10.3390/jfb11040078

Vimal, S. K., Ahamad, N., and Katti, D. S. (2016). A simple method for fabrication of electrospun fibers with controlled degree of alignment having potential for nerve regeneration applications. *Mater. Sci. Eng. C* 63, 616–627. doi:10.1016/j.msec.2016.03.008

Wang, L., Wu, Y., Guo, B., and Ma, P. X. (2015). Nanofiber yarn/hydrogel core-shell scaffolds mimicking native skeletal muscle tissue for guiding 3D myoblast alignment, elongation, and differentiation. *ACS Nano* 9, 9167–9179. doi:10.1021/acsnano.5b03644

Wang, L., Wu, Y., Hu, T., Ma, P. X., and Guo, B. (2019). Aligned conductive core-shell biomimetic scaffolds based on nanofiber yarns/hydrogel for enhanced 3D neurite outgrowth alignment and elongation. *Acta Biomater.* 96, 175–187. doi:10.1016/j.actbio.2019.06.035

Watari, S., Hayashi, K., Wood, J. A., Russell, P., Nealey, P. F., Murphy, C. J., et al. (2012). Modulation of osteogenic differentiation in hMSCs cells by submicron topographically-patterned ridges and grooves. *Biomaterials* 33, 128–136. doi:10.1016/j.biomaterials.2011.09.058

Wu, S., Duan, B., Liu, P., Zhang, C., Qin, X., and Butcher, J. T. (2016). Fabrication of aligned nanofiber polymer yarn networks for anisotropic soft tissue scaffolds. *ACS Appl. Mat. Interfaces* 8, 16950–16960. doi:10.1021/acsami.6b05199

Wu, S., Wang, Y., Streubel, P. N., and Duan, B. (2017a). Living nanofiber yarn-based woven biotextiles for tendon tissue engineering using cell tri-culture and mechanical stimulation. *Acta Biomater.* 62, 102–115. doi:10.1016/j.actbio.2017.08.043

Wu, Y., Wang, L., Guo, B., and Ma, P. X. (2017b). Interwoven aligned conductive nanofiber yarn/hydrogel composite scaffolds for engineered 3D cardiac anisotropy. *ACS Nano* 11, 5646–5659. doi:10.1021/acsnano.7b01062

Xie, X., Cai, J., Yao, Y., Chen, Y., Khan, A. U. R., Wu, J., et al. (2021). A woven scaffold with continuous mineral gradients for tendon-to-bone tissue engineering. *Compos. Part B Eng.* 212, 108679. doi:10.1016/j.compositesb.2021.108679

Yin, H., Strunz, F., Yan, Z., Lu, J., Brochhausen, C., Kiderlen, S., et al. (2020). Three-dimensional self-assembling nanofiber matrix rejuvenates aged/degenerative human tendon stem/progenitor cells. *Biomaterials* 236, 119802. doi:10.1016/j.biomaterials.2020.119802

Yin, Z., Chen, X., Chen, J. L., Shen, W. L., Hieu Nguyen, T. M., Gao, L., et al. (2010). The regulation of tendon stem cell differentiation by the alignment of nanofibers. *Biomaterials* 31, 2163–2175. doi:10.1016/j.biomaterials.2009.11.083

Youngstrom, D. W., Ladow, J. E., and Barrett, J. G. (2016). Tenogenesis of bone marrow-adipose-and tendon-derived stem cells in a dynamic bioreactor. *Connect. Tissue Res.* 57, 454–465. doi:10.3109/03008207.2015.1117458

Zhang, G., Ezura, Y., Favata, M., Soslowsky, L. J., Chakravarti, S., and Birk, D. E. (2006). Development of tendon structure and function:Regulation of collagen fibrillogenesis. *J. Musculoskelet. Neuronal Interact.* 5, 5–21.

Zhang, H., Zhou, L., and Zhang, W. (2014). Control of scaffold degradation in tissue engineering: a review. *Tissue Eng. Part B Rev.* 20, 492–502. doi:10.1089/ten.TEB.2013.0452

Zhang, Y., Lei, T., Tang, C., Chen, Y., Liao, Y., Ju, W., et al. (2021). 3D printing of chemical-empowered tendon stem/progenitor cells for functional tissue repair. *Biomaterials* 271, 120722. doi:10.1016/j.biomaterials.2021.120722

Zhang, Y. (2020). *Multi-scale extracellular matrix mechanics and mechanobiology*. Cham: Springer.

Zhou, G., and Groth, T. (2018). Host responses to biomaterials and anti-inflammatory design-a brief review. *Macromol. Biosci.* 18, e1800112. doi:10.1002/mabi.201800112

Zhu, C., Qiu, J., Thomopoulos, S., and Xia, Y. (2021). Augmenting tendon-to-bone repair with functionally graded scaffolds. *Adv. Healthc. Mat.* 10, e2002269. doi:10.1002/adhm.202002269

frontiers | Frontiers in Bioengineering and Biotechnology

TYPE Original Research
PUBLISHED 02 September 2022
DOI 10.3389/fbioe.2022.921486

Check for updates

OPEN ACCESS

EDITED BY
Rahul Gawri,
McGill University, Canada

REVIEWED BY
Amani Hassan,
McGill University, Canada
Elisabeth Ferreira,
University of Arkansas for Medical Sciences, United States

*CORRESPONDENCE
W. B. Saunders,
bsaunders@cvm.tamu.edu

SPECIALTY SECTION
This article was submitted to Tissue Engineering and Regenerative Medicine, a section of the journal Frontiers in Bioengineering and Biotechnology

RECEIVED 15 April 2022
ACCEPTED 19 July 2022
PUBLISHED 02 September 2022

CITATION
Saunders WB, Dejardin LM, Soltys-Niemann EV, Kaulfus CN, Eichelberger BM, Dobson LK, Weeks BR, Kerwin SC and Gregory CA (2022), Angle-stable interlocking nailing in a canine critical-sized femoral defect model for bone regeneration studies: In pursuit of the principle of the 3R's. *Front. Bioeng. Biotechnol.* 10:921486. doi: 10.3389/fbioe.2022.921486

COPYRIGHT
© 2022 Saunders, Dejardin, Soltys-Niemann, Kaulfus, Eichelberger, Dobson, Weeks, Kerwin and Gregory. This is an open-access article distributed under the terms of the Creative Commons Attribution License (CC BY). The use, distribution or reproduction in other forums is permitted, provided the original author(s) and the copyright owner(s) are credited and that the original publication in this journal is cited, in accordance with accepted academic practice. No use, distribution or reproduction is permitted which does not comply with these terms.

Angle-stable interlocking nailing in a canine critical-sized femoral defect model for bone regeneration studies: In pursuit of the principle of the 3R's

W. B. Saunders[1]*, L. M. Dejardin[2], E. V. Soltys-Niemann[1], C. N. Kaulfus[3], B. M. Eichelberger[4], L. K. Dobson[1], B. R. Weeks[3], S. C. Kerwin[1] and C. A. Gregory[5]

[1]Department of Small Animal Clinical Sciences, College of Veterinary Medicine and Biomedical Sciences, Texas A & M University, College Station, TX, United States, [2]Department of Small Animal Clinical Sciences, College of Veterinary Medicine, Michigan State University, East Lansing, MI, United States, [3]Department of Veterinary Pathobiology, College of Veterinary Medicine and Biomedical Sciences, Texas A & M University, College Station, TX, United States, [4]Department of Large Animal Clinical Sciences, College of Veterinary Medicine and Biomedical Sciences, Texas A & M University, College Station, TX, United States, [5]Department of Molecular and Cellular Medicine, Institute for Regenerative Medicine, School of Medicine, Texas A & M Health Science Center, College Station, TX, United States

Introduction: Critical-sized long bone defects represent a major therapeutic challenge and current treatment strategies are not without complication. Tissue engineering holds much promise for these debilitating injuries; however, these strategies often fail to successfully translate from rodent studies to the clinical setting. The dog represents a strong model for translational orthopedic studies, however such studies should be optimized in pursuit of the Principle of the 3R's of animal research (replace, reduce, refine). The objective of this study was to refine a canine critical-sized femoral defect model using an angle-stable interlocking nail (AS-ILN) and reduce total animal numbers by performing imaging, biomechanics, and histology on the same cohort of dogs.

Methods: Six skeletally mature hounds underwent a 4 cm mid-diaphyseal femoral ostectomy followed by stabilization with an AS-ILN. Dogs were assigned to autograft (n = 3) or negative control (n = 3) treatment groups. At 6, 12, and 18 weeks, healing was quantified by ordinal radiographic scoring and quantified CT. After euthanasia, femurs from the autograft group were mechanically evaluated using an established torsional loading protocol. Femurs were subsequently assessed histologically.

Results: Surgery was performed without complication and the AS-ILN provided appropriate fixation for the duration of the study. Dogs assigned to the autograft

Abbreviations: IV, intravenously; AS-ILN, angle-stabile interlocking nail; SQ, subcutaneous; 3D, three-dimensional; HU, Hounsfield units; ROI, region of interest; DR, digital radiography; PACS, picture archiving and communications system; NBF, neutral buffered formalin; PBS, phosphate buffered saline; CT, computed tomography; DICOM, digital imaging and communication in medicine.

group achieved radiographic union by 12 weeks, whereas the negative control group experienced non-union. At 18 weeks, median bone and soft tissue callus volume were 9,001 mm^3 (range: 4,939–10,061) for the autograft group and 3,469 mm^3 (range: 3,085–3,854) for the negative control group. Median torsional stiffness for the operated, autograft treatment group was 0.19 Nm/° (range: 0.19–1.67) and torque at failure was 12.0 Nm (range: 1.7–14.0). Histologically, callus formation and associated endochondral ossification were identified in the autograft treatment group, whereas fibrovascular tissue occupied the critical-sized defect in negative controls.

Conclusion: In a canine critical-sized defect model, the AS-ILN and described outcome measures allowed refinement and reduction consistent with the Principle of the 3R's of ethical animal research. This model is well-suited for future canine translational bone tissue engineering studies.

KEYWORDS

canine, large animal model, critical-sized defect, non-union, bone regeneration, interlocking nail, biomechanics, computed tomography

Introduction

Critical-sized long bone defects are most commonly caused by vehicular trauma, gunshot or blast injuries, infection, tumor resection, and developmental deformities (Roddy et al., 2017). Critical-sized defects are at least two times the diameter of the affected long bone and represent a major therapeutic challenge (Roddy et al., 2017; Schemitsch, 2017). Current treatment strategies to "bridge the gap" include mechanical stabilization followed by autologous bone grafting, distraction osteogenesis, application of BMPs, or the induced membrane technique (Roddy et al., 2017). Unfortunately, none of these treatments are uniformly effective and each is associated with its own complications. Therefore, substantial effort has been devoted to the development of tissue engineering solutions to improve clinical success (Muschler et al., 2010; Roddy et al., 2017; Manzini et al., 2021; Mohaghegh et al., 2021).

Translating promising tissue engineering solutions from *in vitro* and rodent proof of concept studies to clinical use is fraught with challenges (Reichert et al., 2010; Sastry, 2014; Zheng et al., 2017). Although laboratory animal models represent an important step in the validation pathway, rodent biology and biomechanics do not simulate the clinical scenarios encountered in clinical orthopedics. For these reasons, large animals such as the sheep, pig, dog, and goat are often used as intermediary, translational models (Arinzeh et al., 2003; Liebschner, 2004; Horner et al., 2010; Muschler et al., 2010; Hahn et al., 2011; Dozza et al., 2018; Ribitsch et al., 2020). The dog represents a strong translational model species for orthopedic tissue engineering (Arinzeh et al., 2003; Lindsey et al., 2006; Hoffman and Dow, 2016). The canine musculoskeletal system experiences similar biomechanical loads to that of humans (Egermann et al., 2005; Pearce et al., 2007). Dogs also exhibit comparable bone development and physiology, complex immune systems and genetics (Ostrander and Giniger, 1997; Ribitsch et al., 2020), and are amenable to assessment tools such as arthroscopy or gait analysis that are used in clinical trials (Neu et al., 2009; Hoffman and Dow, 2016; Feichtenschlager et al., 2018).

Interlocking nails are considered by many to be the standard of care for stabilization of critical-sized bone defects (Rhorer, 2009; Dejardin et al., 2012; Shen et al., 2016; Flagstad et al., 2021; Kang et al., 2021; Viberg et al., 2021). Intramedullary fixation is commonly used for both rodent and large animal critical gap healing models (Lindsey et al., 2006; Schoen et al., 2008; Rhorer, 2009; MSc et al., 2013; Quirk et al., 2016; Shiels et al., 2018; Ozmeric et al., 2020). Despite their widespread use, acute angular instability is an inherent component of traditional interlocking nails and in the clinical setting has been termed "slack" (Lang et al., 1995; Buehler et al., 1997; Gerber and Ganz, 1998; Dejardin et al., 2006, 2014). The result of slack is unpredictably high angular deformation under torsional loads that can lead to delayed or nonunion (Pfeil et al., 2005; Dejardin et al., 2006, 2012, 2014; Lansdowne et al., 2007). In the context of large animal translational studies, slack has the potential to create a biomechanical environment in which implant performance is somewhat variable from animal to animal. One solution for this variability is to increase animal numbers. This, however, increases study costs and raises ethical concerns.

The principles of replacement, reduction, and refinement, known as the Principle of the 3R's, has guided global ethics of animal research for over 60 years (Kirk, 2018; Angelis et al., 2019). In pursuit of this principle, work has been undertaken to refine the interlocking nail implant to eliminate construct slack by development of an angle-stable interlocking nail (AS-ILN) (Dejardin et al., 2006, 2009; Lansdowne et al., 2007; Ting et al., 2009). This AS-ILN has been used in both induced-injury and clinical canine studies (Dejardin et al., 2014; Marturello et al.,

2021). It has definitively been shown to be superior to traditional nails with accelerated healing times, greater callus volume, and improved biomechanical callus properties in a 5 mm, induced-injury, tibial ostectomy model (Dejardin et al., 2014). However, AS-ILNs have not been evaluated in critical-sized defect studies, nor have investigators further reduced animal numbers by performing longitudinal radiographic studies, biomechanics, and histology on the same cohort of animals. Implementation of these strategies would represent an important advancement in pursuit of the Principle of the 3R's (Kirk, 2018; Angelis et al., 2019).

Therefore, the objective of this study was to optimize a canine critical-sized femoral defect model using an angle-stable interlocking nail (AS-ILN). We hypothesized that: 1) an AS-ILN would provide long term construct stability in a canine femoral critical-sized defect model and 2) the placement of autograft would yield faster and more robust bone regeneration than negative control defects. Radiography, quantitative CT, torsional biomechanics, and histology provided an objective and comprehensive assessment of critical-sized defect healing in a small cohort of dogs. The implant system, surgical technique, and outcome measures described herein are well-suited for future canine translational tissue engineering studies.

Materials and methods

Surgical model

This study was performed under the supervision of the Texas A&M University Institutional Animal Care and Use Committee (IACUC) and an approved animal use protocol (AUP 2013–0056). Six, male, skeletally-mature, institutionally-owned hounds were utilized in the study. Age ranged from 2.5 to 6.5 years and body weight from 23.7 to 35.5 kg. Dogs were screened pre-operatively with a general physical exam, detailed orthopedic exam by a board-certified veterinary surgeon as well as complete blood count, serum chemistry, and urinalysis. Prior to surgery, radiographs of the right femur were obtained under sedation with dexmedetomidine (125 μg/m^2) and butorphanol (0.2 mg/kg), administered intravenously (IV). Sedation was reversed with atipamezole (1,666 μg/m^2). Dogs were randomly assigned to one of two groups: autograft or negative control. All dogs received a 4 cm mid-diaphyseal femoral ostectomy with resection of periosteum at the defect tissues followed by stabilization with an 8 mm diameter x 172 mm long AS-ILN developed specifically for veterinary use (I-Loc internal fixator, Biomedtrix, Whippany, NJ) (Dejardin et al., 2014). Defects in the autograft treatment group were treated with corticocancellous autograft (see below). Defects in the negative control group did not receive any additional treatment.

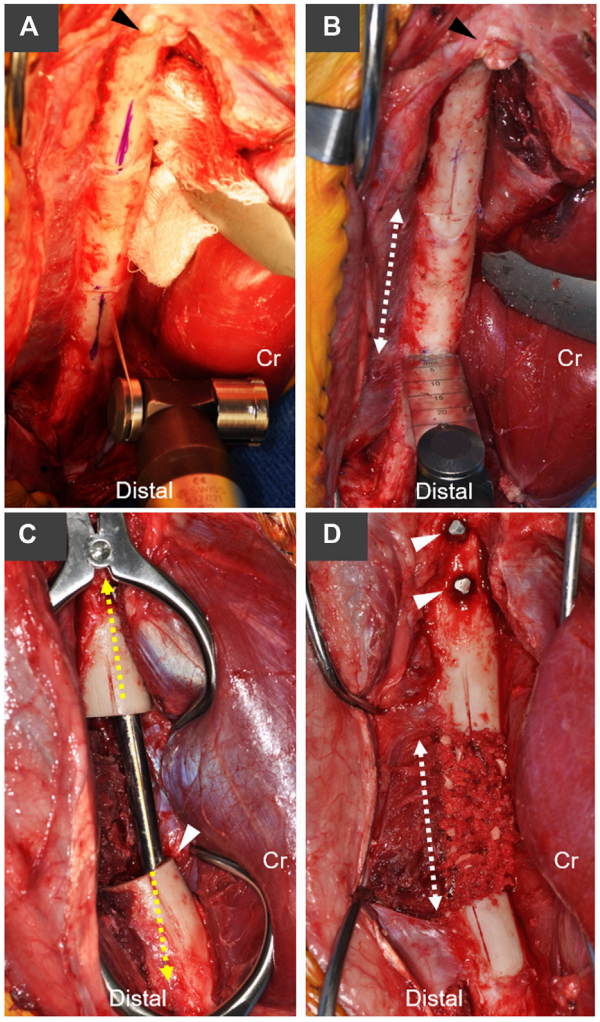

FIGURE 1
Overview of canine critical-sized femoral defect model with stabilization using an AS-ILN. **(A)** A craniolateral approach to the femur and stifle (knee) joint were performed. Longitudinal index marks were created on the lateral surface of the femur with an oscillating saw and sterile marker to maintain rotational orientation of the proximal and distal bone segments. Arrowhead denotes the base of the greater trochanter, Cr denotes cranial (anterior) position. **(B)** A 4 cm mid-diaphyseal transverse ostectomy was planned (dashed arrow). **(C)** An 8 mm × 172 mm AS-ILN was placed to stabilize the femur (see Figure 2 for specifics of AS-ILN). Dashed line denotes long axis of AS-ILN. Arrowhead denotes the intentional positioning of the cranial (anterior) cortex adjacent to the AS-ILN in order to position the nail more distally in the femoral condyle. Dogs assigned to the negative control group received no additional treatment at the ostectomy. **(D)** Dogs assigned to the autograft treatment group received a 10 cm^3 cancellous autograft which was supplemented with morselized cortical bone from the ostectomy. Dashed line denotes the extent of the ostectomy and bone graft. Arrowheads denote two proximal locking bolts placed to secure the AS-ILN to the proximal femur.

On the day of surgery, dogs were premedicated with acepromazine (0.3 mg/kg), glycopyrrolate (0.01 mg/kg), and hydromorphone (0.1 mg/kg) administered intramuscularly

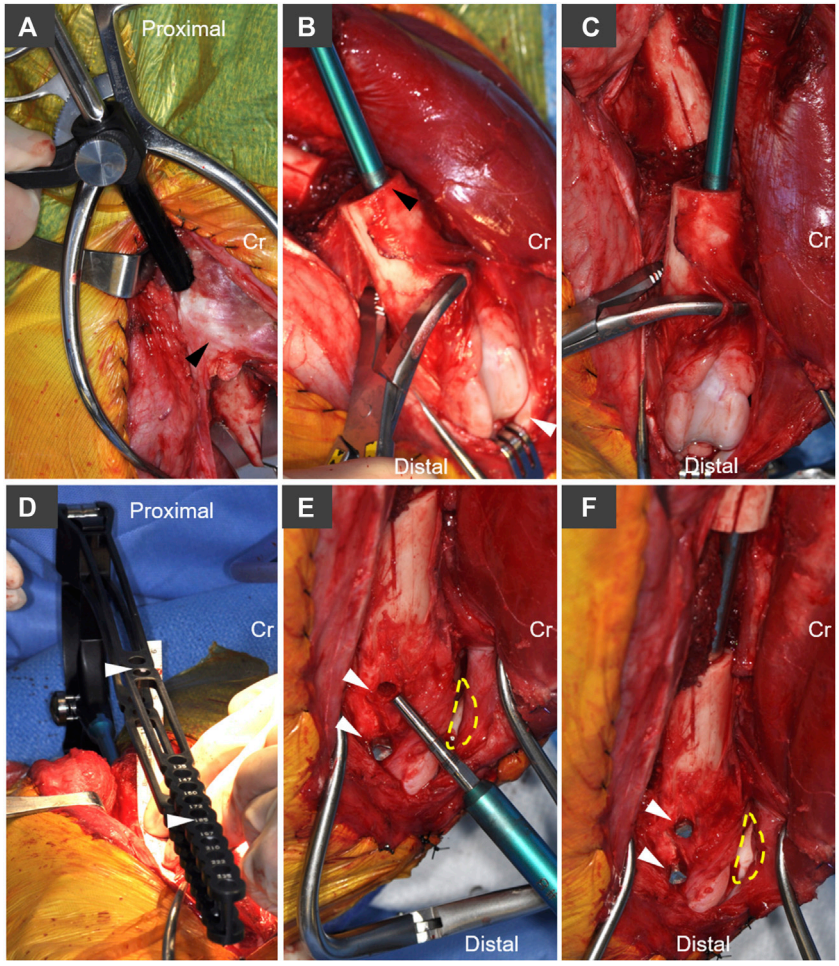

FIGURE 2
Implantation technique and system-specific instrumentation for the AS-ILN. **(A)** The intertrochanteric fossa was identified and opened with a 1/8 inch (3.2 mm) intramedullary pin. Following pin removal, a system-specific cutting tool and tissue protector were used to enlarge this opening to 8 mm. Cr denotes cranial, arrowhead denotes base of the greater trochanter. **(B)** The distal femur was stabilized with bone holding forceps placed proximal to the trochlea. A system specific cutting tool (8 mm diameter) was used to prepare the cancellous bone bed. To distalize the nail, the cutting tool was intentionally placed adjacent to the cranial (anterior) cortex in the lateral view (black arrowhead). White arrowhead denotes the patella. **(C)** From the cranial (anterior view), care was taken to ensure the cutting tool was oriented parallel to the long axis of the distal femur. **(D)** The 8 mm × 172 mm AS-ILN was attached to an extension and insertion handle and placed in normograde fashion into the femur. A system specific alignment guide (white arrowheads), with cannulations aligned to AS-ILN cannulations, was attached to the handle in order to center drilling through the AS-ILN cannulations for capture by locking bolts. **(E)** Lateral aspect of distal femoral condyle demonstrating placement of angle-stable fixation bolts in drill holes created using the alignment guide in panel **(D)**. Dashed line denotes position of patella. Arrowheads denote bolt holes. **(F)** Final bolt insertion (arrowheads) completes placement of the AS-ILN.

(IM). Anesthesia was induced with propofol (6 mg/kg maximum dose) administered IV to effect. Upon intubation, general anesthesia was maintained with isoflurane (2–4% to effect). Each dog received a morphine epidural (0.1 mg/kg, preservative-free morphine) at the L7-S1 disk space. Perioperative cefazolin (22 mg/kg IV) was administered 30 min prior to skin incision and every 90 min until skin closure. Perioperative monitoring included pulse oximetry, indirect blood pressure, end-tidal CO_2, and electrocardiography (ECG) at 5 min intervals and body temperature at 15 min intervals. All dogs were warmed with Bair Hugger Model 505 forced air warming blankets (Augustine Medical, Eden Prairie, MN) and received warm lactated ringer's solution (LRS, 10 ml/kg/h) during anesthesia. Hair was clipped from the right pelvic limb from the dorsal and ventral midlines distally to below the hock. For the dogs in the positive control group, hair was clipped in an 8 cm × 8 cm square centered over both right and left proximal greater tubercles. An initial surgical preparation was performed with three alternating scrubs of 4% chlorhexidine and 0.9% saline. Dogs were transported to the

surgical suite and positioned in left lateral recumbence. A second sterile surgical prep was performed with three alternating scrubs of 4% chlorhexidine followed by application of ChloraPrep (2% chlorhexidine, 70% isopropyl alcohol, Becton Dickinson, Franklin Lakes, NJ).

A craniolateral approach to the right femur and stifle (knee) were performed (Johnson, 2014). An oscillating saw [Small Battery Drive System, blade 532.063 (25 × 18 mm), DePuy Synthes, Raynham, MA], was used to create a longitudinal index mark on the lateral surface of the proximal and distal femur adjacent to the proposed ostectomy to ensure anatomic rotational alignment of the femur after ostectomy (Figure 1A). A 4 cm ostectomy, centered on the mid-diaphysis of the femur, was performed with the oscillating saw under continuous saline irrigation (Figure 1B). All periosteum was resected from the ostectomy site. The intertrochanteric fossa was identified and a 1/8 inch (3.2 mm) 316L stainless steel intramedullary pin (Imex Veterinary, Inc., Longview, TX) was used to open the proximal femoral metaphysis. A system-specific cutting awl and tissue protector were aligned with the long axis of the proximal femur and used enlarge this opening to 8 mm (Figure 2A). An 8 mm cutting tool was inserted through this 8 mm opening and into the ostectomy site to create the proximal path for the AS-ILN. The distal diaphysis of the femur was stabilized with clamshell bone holding forceps and the same cutting tool was again used to prepare the path for the AS-ILN into the distal femur (Figure 2B). Care was taken to ensure this path was parallel with the femur in the frontal plane (Figure 2C). In the sagittal plane, the cutting tool was intentionally tipped in a cranioproximal to caudodistal direction to ensure the distal tip of the AS-ILN was located within the caudal aspect of the femoral condyle and directed away from the femoral trochlea (Figure 1C).

A temporary extension and handle were secured to an 8 mm × 172 mm AS-ILN. The 316L surgical stainless steel nail was placed in normograde fashion proximally to distally across the ostectomy site. Nail size and length were selected using pre-operative digital templating (OrthoviewVet, Southampton, Hampshire, United Kingdom). Once in position, the excised 4 cm ring of femoral cortex and a ruler were used to ensure a precise 4 cm mid-diaphyseal defect was present for each femur (Figure 1C). The AS-ILN was secured to the femur using an alignment guide (Figure 2D) and temporary fixation posts in a 2–2 configuration (2 posts proximal, 2 posts distal). Posts were sequentially removed and conical, threaded, locking bolts were cut to length guided by a system-specific depth gauge and locked into the matching threads on the conical AS-ILN cannulations (Figures 2E,F). This coupling created an immediately angle-stable interface thus preventing construct slack (vonPfeil et al., 2005; Dejardin et al., 2006; Lansdowne et al., 2007). After AS-ILN placement, defects were copiously lavaged with saline. Dogs assigned to the autograft treatment group were treated with 10 cm^3 of autologous cancellous graft harvested from both proximal humeri. Additionally, the 4 cm cortical defect was morselized into 5–8 mm pieces with rongeurs and combined with the cancellous autograft (Figure 1D). Routine, three-layer closure was performed in an identical manner for both groups. The joint capsule was closed with size 0 polydioxanone-II (PDS®-II) (Ethicon Inc. Raritan, NJ) in a cruciate suture pattern. Fascia lata was closed with 0 PDS®-II in a simple continuous pattern. Subcutaneous tissues were closed with 2–0 poliglecaprone 25 (Monocryl®, Ethicon) in a simple continuous manner. Skin was closed with 3–0 Monocryl® in an intradermal pattern.

Post-operative radiographs were obtained (see below) and dogs were recovered from anesthesia in individual runs containing padded bedding. Upon extubation, dogs received carprofen (4 mg/kg SQ once) and hydromorphone (0.1 mg/kg q 6 h) for the first 24 h. Oral carprofen (4 mg/kg q 24 h) was continued for 5 additional days. A single injection of cefovecin sodium (8 mg/kg, Convenia®, Zoetis, Parsippany, NJ) was administered subcutaneously for post-operative antibiotic coverage. Surgical incisions and limb use were monitored daily for 5 days post-surgery, then weekly for the remainder of the study. Controlled, slow leash walking of 15-min duration (4 times daily) was initiated 1 day post-surgery. At 6 weeks, leash walks were increased to 30 min (4 times daily) for the duration of the study. At 18 weeks, dogs were humanely euthanized by administration of IV dexmedetomidine and butorphanol (see above) followed by barbiturate overdose (120 mg/kg for the initial 4.5 kg and 60 mg/kg for each additional 4.5 kg).

Radiography and computed tomography (CT)

Orthogonal femoral radiographs (craniocaudal, mediolateral) were obtained pre-operatively, immediately post-operatively, and at 6, 12, and 18 weeks using a Sound-Eklin Digital Radiography (DR) system (Sound-Eklin, Carlsbad, CA) with a Cannon digital detector plate. Images were stored on a local picture archiving and communication system (PACS) and viewed with a commercially available veterinary viewing software (eFilm 3.0, Merge Healthcare, Milwaukee, WI). At study conclusion, radiographs were exported, blinded to remove animal identity, and randomized in pairs (craniocaudal and mediolateral radiographs) for radiographic scoring by a board-certified veterinary radiologist. An ordinal scoring system was utilized to assess healing as previously described (Faria et al., 2007; Schmiedt et al., 2007). Briefly, craniocaudal and mediolateral radiographs were evaluated on a 1 – 4 scale as follows: 1: ≤1 cortex spanned by bridging callus; 2: 2 cortices with bridging callus; 3: 3 cortices with bridging callus; and 4: bridging callus present on all four cortices.

CT imaging of musculoskeletal tissues containing metal implants can be challenging due to the effects of beam hardening and metal-associated artifacts. Reduction of metal artifacts can be achieved by using specific CT parameters

(Berg et al., 2006; Lee et al., 2007). Dogs were imaged with a Siemens SOMATOM Definition AS 40-slice CT immediately post-operatively and again at 6, 12, and 18 weeks. For each scan, the femur was aligned so that the long axis of the gantry and the interlocking nail were coaxial. Sequences were acquired using high kVp (120–140), high mAs (200), low pitch (0.6–0.75), low collimation, thin slices (0.6 mm), with no overlap. For both radiographic and CT imaging, digital imaging and communications in medicine (DICOM) images were stored on a local PACS server with local and off-site image storage.

Quantitative analysis of CT

Quantitative assessment of CT images was performed using a commercially available segmentation software (Mimics V.19, Materialise NV, Leuven, Belgium). After creation of a project file, the region of interest (ROI) was identified for quantification. Using the analyze tool and the post-operative CT for each dog, two points were placed in the center of the AS-ILN, one at the proximal and one at the distal end of the ostectomy. These points were placed at the location of the first complete cortical ring adjacent to the osteotomy using transverse plane images. Using the distance measuring tool in the sagittal plane, the distance from the proximal end of the AS-ILN to the proximal point and the distance from the distal end of the AS-ILN to the distal point were determined and recorded. The distance tool was also used to confirm 4 cm (40 mm) ostectomy had been performed. These two distances (specific for each femur) were used to identify the location of the proximal and distal points on 6, 12, and 18 weeks CT scans, thus ensuring that identical regions were evaluated throughout the study.

For all scans, a cylinder (height = 40 mm, radius = 15 mm) was created using the analyze/create cylinder tool to further define the ROI. The proximal and distal extent of the cylinder were coplanar with the proximal and distal reference points. Radius of the cylinder was selected such that the ROI would contain an area 1.5x the diameter of the resected femoral diaphysis. Multiple slice editing (set in thresholding mode) was used on transverse plane images to create a new mask for either bone [700–2,000 Hounsfield units (HU)] or both bone and soft tissue (250–2,000 HU) within the ROI. Prior to creation of 3D objects, multiple slice editing (set in remove mode) was used to remove the AS-ILN and beam hardening artifact from each mask using the ellipse tool (width/height = 42). Bone and bone/soft tissue masks were transformed into 3D objects using the calculate part tool and the "optimal" setting. Volume (mm^3) and surface area (mm^2) were recorded.

Mechanical testing

After euthanasia, left and right femurs and associated soft tissues were harvested from the positive control group. Due to the lack of healing in the negative control group, these dogs were not evaluated with mechanical testing. Femurs were placed in 10% neutral buffered formalin (NBF) then stored for 4 weeks prior to analysis. Torsional analysis of non-operated, left and operated, right femurs from the autograft treatment group was performed to compare the mechanical properties of the intact and operated bones and to account for disparate properties of bones between dogs and the effects of 10% NBF fixation (Öhman et al., 2008; Wright et al., 2018). The testing protocol was performed as previously described, with minor modifications (Dejardin et al., 2014). Femurs were cut to 16 cm length, with AS-ILNs remaining in place within the three right femurs. Two divergent brass screws were placed in the ends of each femur, avoiding contact with the AS-ILN (if present) to improve stability during potting. Femurs were potted in polyester body filler ("Fiber Strand" 6371, The Martin Senour Co., Cleveland, OH) in custom designed test fixtures. An alignment guide was used to ensure that each bone was potted so that the AS-ILN was co-axial with the torsional testing axis. For femurs containing an AS-ILN, all locking bolts were removed prior to potting. This ensured that the AS-ILN would not interfere with assessment of mechanical properties during torsional loading. Potting was performed such that the distance between the innermost points of the potting and potting fixtures was identical for all specimens.

The testing protocol was performed with a 135 Nm load cell (5330–1200, Interface Inc. Scottsdale, AZ), rotary encoder (BHW16.05A72000-BP-A, Baumer Electric, Southington, CT) and sevohydraulic testing machine (1331, Instron Corp. Canton, MA) under displacement control (1°/sec) at a sampling rate of 100 Hz to a maximum displacement of 25 of internal rotation. Torsional stiffness, maximum deformation angle at failure, load at failure (Nm), and mode of failure were determined. Torsional stiffness was calculated from torque (Nm) vs angle of twist (o) graphs from 0 to 5. To limit structural damage of the specimens, tests were automatically interrupted upon detection of a 5% drop from peak (failure) torque. Following this test, the potting material and AS-ILN were carefully removed and the spiral fractures were anatomically reconstructed and stabilized with 0 polydioxanone-II suture material. Paired bones were returned to 10% NBF in preparation for histologic analysis. Removal of the AS-ILN and reconstruction of the spiral fracture allowed histologic assessment of femurs evaluated biomechanically, in pursuit of the Principle of the 3R's of animal research (Kirk, 2018; Angelis et al., 2019).

Histology

After gross evaluation and photography, the cranial surface of each femur was marked with tissue dye to maintain orientation during processing. The AS-ILNs were removed from the autograft treatment group upon completion of biomechanics (see above). Negative control specimens containing AS-ILNs

were imaged with an automated computed tomography machine (X50, North Star Imaging, Rogers, MN, United States) to locate the AS-ILN and center of the femoral defect (non-union). Proximal and distal ends of the femur were transected using a 6-inch trim saw (Hi-Tech Diamond, Westmont, IL, United States) and the AS-ILN was removed. Tissue samples were placed in a 10 to 1 ratio of decalcification solution (Formical-4™, StatLab Medical Products, McKinney, TX, United States) and were agitated for 15 days with solution exchange performed at least once weekly. Samples were removed from decalcification solution, rinsed with deionized water followed by phosphate buffered saline (PBS), and manually sectioned in the sagittal plane from cranial to caudal end. Samples were subdivided into two or three additional segments to fit within jumbo histology cassettes (7.5 × 5.2 × 1.8 cm) and returned to decalcification solution for 45 additional days. Next, samples were rinsed with deionized water and PBS, placed within pre-labelled jumbo cassettes, and processed with an automatic tissue processor (Excelsior AS, Thermo Fisher, Waltham, MA, United States) on a 30-h run with alcohol gradations of 75–100%, clearing reagents (xylenes), and vacuum-mediated paraffin wax infiltration. Samples were embedded (HistoStar Embedding and Cold Module, Thermo Fisher) using a jumbo metal mold. Blocks were sectioned at 5–6 μm onto jumbo slides with a rotary microtome (Microm HM355S, Thermo Fisher) and stained with hematoxylin and eosin (H&E) and Masson's trichrome. Slides were scanned at 10 × magnification with an Olympus VS.120 Virtual Slide System (Olympus Life Sciences, Waltham, MA, United States). Scanned images were imported into Adobe Photoshop CS6 13.0.0 (Adobe, San Jose, CA, United States), white balanced, and re-assembled to create a cohesive mosaic overview of each femur. Representative histologic mosaics (one femur from each treatment group) were selected for histologic results.

Statistics

Due to small sample size, both ordinal (radiographic scoring) and continuous (quantitative CT, biomechanics) data were reported as median and range. Descriptive statistics were performed using GraphPad Prism 6.0 (GraphPad Inc. San Diego, CA).

Results

Surgical model

Median age for dogs assigned to the autograft group was 5.5 years (range: 3.5–6.5 years) and median body weight was 25.4 kg (range: 23.7–35.8 kg). Median age for dogs assigned to the negative control group was 4.5 years (range: 2.5–6 years) and median body weight was 27.3 kg (range: 25.7–28.6 kg). Incisions healed without complication in all dogs. All dogs were toe-touching on the operated limb the day after surgery, with return to a normal limb use 7–10 days post-operatively. Limb use was maintained for all dogs through the remainder of the study.

Radiographic assessment of healing

Representative radiographs and ordinal scoring data for autograft and negative control groups are provided in Figure 3. On mediolateral (Figure 3A) and craniocaudal (Figure 3B) radiographs, bone graft is visible within the ostectomy site immediately post-operatively in the autograft group. By 6 weeks, bridging callus was visible, which increased in size and opacity at 12 and 18 weeks. This callus enhancement was captured in the ordinal scoring data (Figure 3C). In the negative control group, a small amount of callus formed at 6 weeks. However, callus formation did not progress to bridge the critical-sized defect nor was callus maturation observed. Ordinal scoring data remained at baseline. Importantly, implant complications were not identified in either treatment group.

Quantification of bone and soft tissue volume via CT

Representative bone/soft tissue reconstructions with bone volume data are provided in Figure 4. In the autograft group (green), a complete cylinder of bone and soft tissue (gray) callus was present, bridging the entirety of the critical-sized defect as shown in representative 18 weeks reconstructions (Figure 4A). Bone and soft tissue callus volume increased over time in this group. Interestingly, one of the dogs in the autograft group (age 6.5 years), exhibited a reduced healing response when compared to the other dogs within this group. In the negative control group (blue), callus formation occurred but failed to bridge the critical-sized defect as shown in representative 18 weeks reconstructions. Defects within the negative control group were primarily filled with soft tissue. Bone and soft tissue callus quantification for the negative control group remained low throughout the study.

Mechanical testing of autograft treatment group

Paired femurs from the autograft group were assessed for mechanical properties under torsional loads. The negative control group was not assessed due to the fact that none of the femurs developed bridging callus. Torsional mechanical testing results are reported in Table 1; Figure 5. Not unexpectedly, the properties of operated femurs were lower

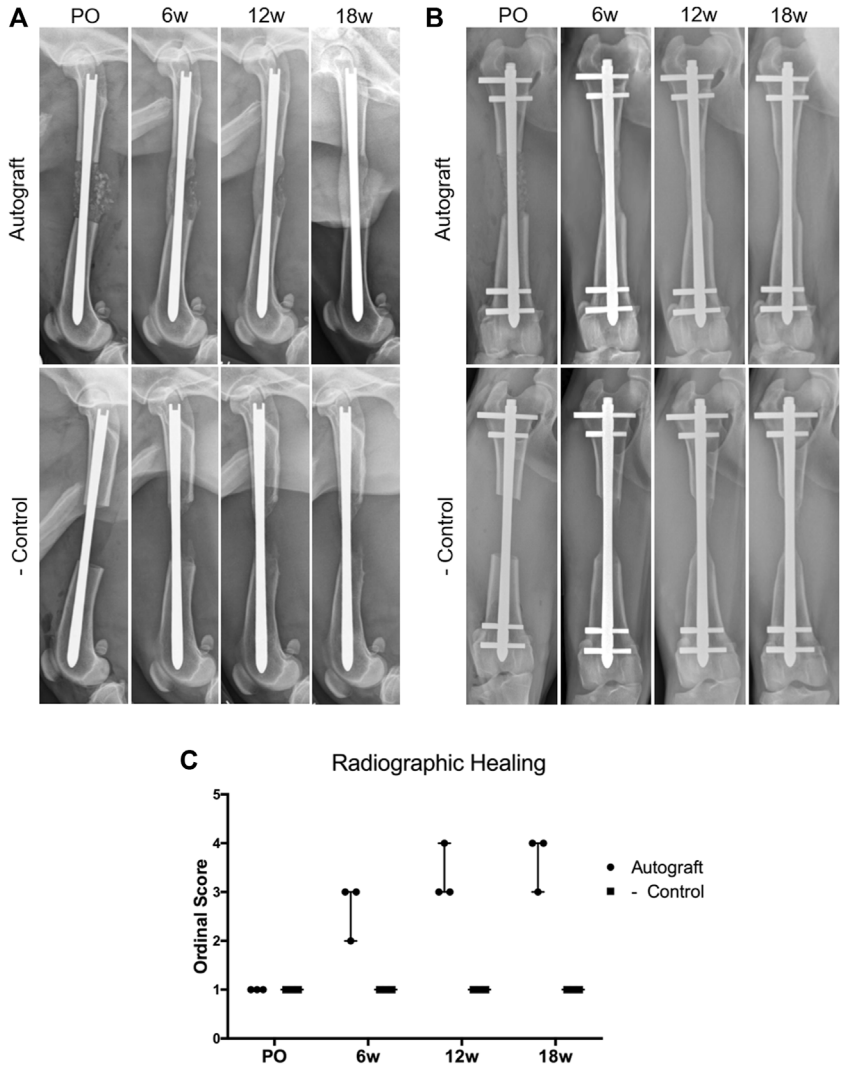

FIGURE 3
Assessment of critical-sized defect healing by ordinal radiographic scoring. Dogs were radiographed immediately post-operatively (PO) and again at 6, 12, and 18 weeks. **(A)** Representative mediolateral radiographs for the autograft and negative control groups. Note the presence of bone graft in the autograft group, which resulted in smooth, bridging callus by 18 weeks. Callus formation was present in the negative control group at 6,12, and 18 weeks; however, the callus was unable to bridge the critical-sized defect. The AS-ILN implant remained unchanged. **(B)** Representative craniocaudal (anteroposterior) radiographs. Smooth bridging callus developed in the autograft group at 6 weeks and became more substantial at 12 and 18 weeks. Minimal callus formation was identified in the negative control. The AS-ILN implant remained unchanged. **(C)** A previously described ordinal scale was used to score radiographic healing. Orthogonal radiographs from each dog were randomized and evaluated by a board-certified veterinary radiologist blinded to time point, dog, and treatment group. Data were reported using a scatter plot denoting median and range.

than that of the contralateral, non-operated femurs. A representative load-deformation curve is provided in Figure 5A, with torsional stiffness data for all bones displayed in Figure 5B. Importantly, one operated femur exhibited low torsional stiffness. This was the femur from the autograft group with the lowest amount of callus volume (Figure 4). In the operated femurs, failure occurred by spiral fracture through the callus or at the junction of the callus and distal diaphysis. In contralateral, non-operated femurs, a similar fracture pattern and location was noted, although with some degree of comminution (Figure 5C).

Histologic assessment of bone healing

Representative histology of autograft and negative control femurs are provided in Figure 6. It is important to note that for the autograft treatment group, histology was performed on the

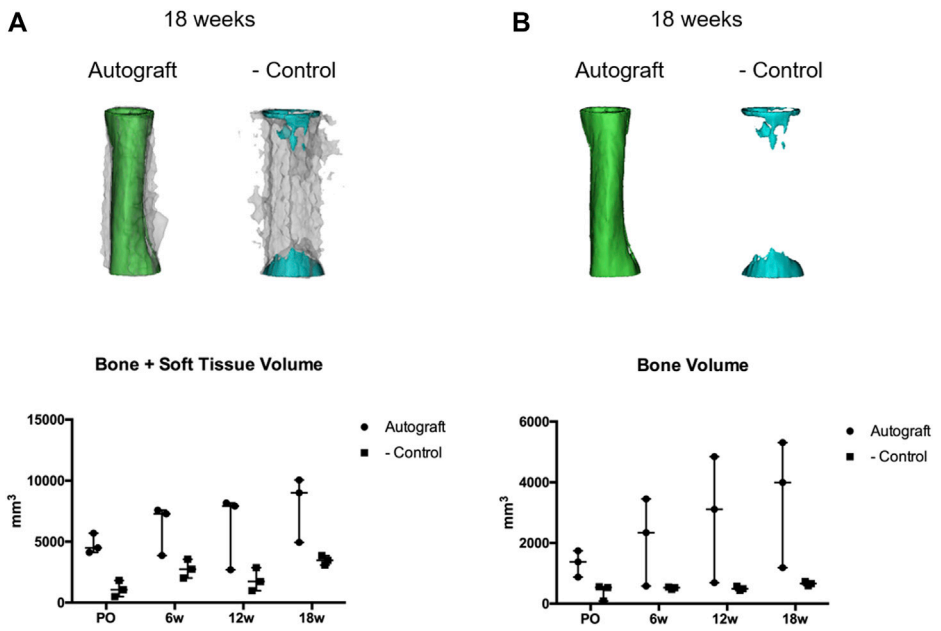

FIGURE 4
Quantitative assessment of bone and soft tissue using computed tomography (CT) and Mimics segmentation software. CT data from autograft and negative control dogs were exported to a commercially available segmentation software (Mimics 19.0, Materialise Inc., Leuven, Belgium). Segmentation of bone and soft tissues were performed to generate 3D models and quantify tissue within the critical defects. **(A)** Representative bone within autograft (green) or negative control (blue) treatment groups at 18 weeks. Soft tissue is represented by the translucent gray overlay. **(B)** Representative bone within autograft (green) and negative control (blue) treatment groups at 18 weeks. Volumetric data (mm^3) for bone + soft tissue **(A)** or bone **(B)** were reported using scatter plots denoting median and range.

TABLE 1 Biomechanical properties (torsion) of autograft treatment group.

	Stiffness (Nm/°)		Max def at failure (°)		Torque at failure (nm)		Failure mode
	Median	Range	Median	Range	Median	Range	(Number)
Autograft	0.19	0.19–1.67	7.0	7.0–14.0	12.0	1.7–14.0	Spiral fracture through callus (2) or junction of callus and distal bone (1)
Contralateral femur	3.92	3.25–4.26	12.5	11.3–12.8	42.0	34.0–54.0	Spiral fracture with comminution (3)

Table 1: At 18 weeks, three pair of femur from the autograft treatment group (n = 6 femur) were assessed for biomechanical properties in torsion. Autograft = Right femur, 4 cm defect, stabilized with AS-ILN, corticocancellous autograft. Contralateral femur = left femur, non-operated limb. Abbreviations: Nm/° = Nm per degree; Max Def at Failure (°) = Maximum angle of deformation at failure in degrees.

same group of femurs that were assessed biomechanically. In the autograft group, the mid-shaft cortical region was markedly expanded by an orderly layer of trabecular bone (Figure 6A, insets 1,2) admixed with a moderate amount of fibrovascular connective tissue and regions containing typical bone marrow. Regions of moderate endochondral ossification extended through the fibrous connective tissues and woven bone. Of note, the central medullary region in contact with the AS-ILN exhibited an orderly fibroblastic cell population within an eosinophilic matrix consistent with collagen (Figure 6A, inset 3). For the negative control, the mid-shaft cortical region was disrupted and filled with the fibrovascular connective tissue of a non-union fracture (Figure 6B, inset 2). Endochondral ossification was present within the fibrous connective tissues adjacent to the fracture (Figure 6B, inset 3) but, consistent with radiography and CT, did not bridge the critically-sized defect. Similar tissue and cell architecture was noted adjacent to the AS-ILN (Figure 6B, inset 1).

Discussion

The results of this study support both of our hypotheses. In the presence of a critical-sized canine femoral defect, the AS-ILN

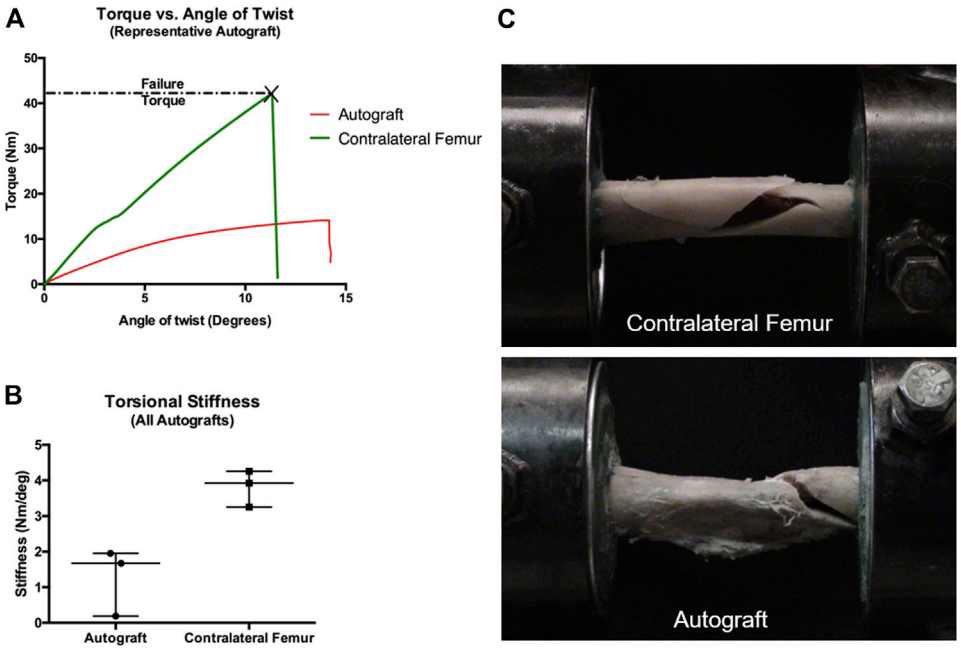

FIGURE 5
Mechanical testing of paired femurs (operated and contralateral non-operated) from autograft treatment group. For femurs containing an AS-ILN, the implant was identified within the proximal femur and a custom alignment device was used to identify the long axis of the AS-ILN and to position the AS-ILN in the center of the torsional testing axis. Prior to potting, locking bolts were removed. Specimens were potted such that the distance between innermost points of the potting was identical for all specimens. **(A)** Representative load-deformation (torque-angle of twist) graph for an autograft femur (red) and contralateral, non-operated femur (green). **(B)** Torsional stiffness values (Nm/^{0}) were determined from the load-deformation curves from 0 to 5 and reported as scatter plots denoting median and range. **(C)** Representative mode of failure images. Contralateral, non-operated femurs failed by spiral fracture with comminution. Critical-sized defect femurs treated with autograft failed by spiral fracture through the callus at the junction with the distal diaphysis.

provided sufficient and consistent construct stability for the duration of the study. There were no complications and dogs quickly began using the operated limb with subsequent resolution of visible lameness. Dogs assigned to the autograft group experienced early bridging of the critical-sized defect as early as 6 weeks, with continued bone healing to the 18 weeks end-point. Dogs assigned to the negative control group ambulated without complication despite no radiographic or CT evidence of bone healing.

Translation of promising bone tissue engineering treatments for critical-sized bone defects from conception to successful clinical application is a difficult task and has been referred to as the "valley of death" for product development (Reichert et al., 2010; Sastry, 2014; Zheng et al., 2017). Due to the regulatory classification of many tissue engineering scaffolds as medical devices (Sastry, 2014; Zheng et al., 2017), it is unknown how many tissue engineering devices have failed to translate to the clinical setting. In pharmaceutical development, it has been reported that only 11% of new drugs successfully move through Phase I-III clinical trials and not all of those proceed to market (Wong et al., 2019). It is clear that novel bone tissue engineering devices experience even lower levels of success. Despite decades of intense effort, thousands of peer-reviewed publications, and hundreds of millions of research dollars, an approved tissue engineering device for critical-sized long bone defects is currently not available (Hollister and Murphy, 2011; Amini et al., 2012).

Novel bone tissue engineering devices must be rigorously evaluated prior to initiation of clinical trials in human beings. Large animal species such as the sheep, pig, goat, and dog are often used for translational studies during product development. When used properly, large animal models are highly useful for determining scalability, developing successful workflow, obtaining preliminary safety and efficacy data, and identifying benchmarks for success during clinical trials (Liebschner, 2004; Horner et al., 2010; Muschler et al., 2010; Ribitsch et al., 2020). As detailed in our introduction, the dog represents a strong translational model for bone tissue engineering studies. Presently, only a handful of studies have described canine critical-sized or non-union defect models (Volpon, 1994; Markel et al., 1995; Arinzeh et al., 2003; Lindsey et al., 2006). These describe critical-sized defects of the canine radius, femur, and tibia and rely on diverse stabilization methods such interlocking nails, bone plates,

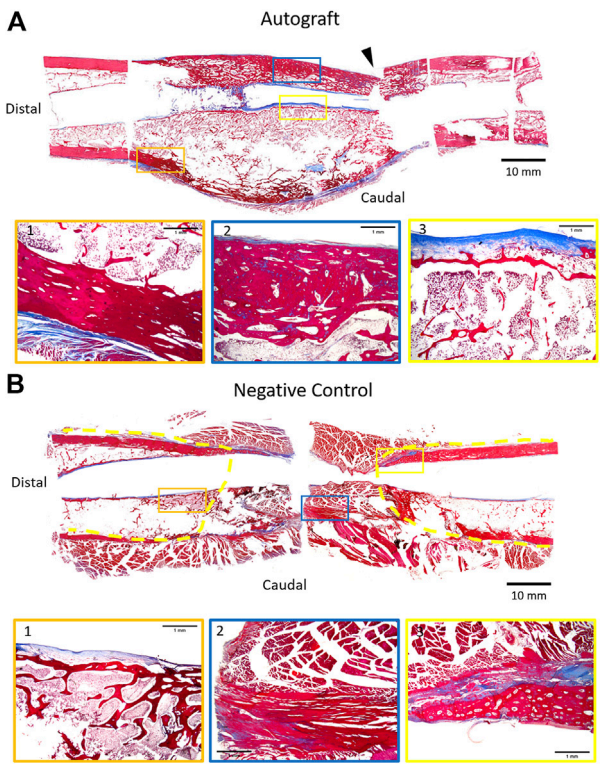

FIGURE 6
Representative histology of autograft and negative control at 18 weeks. Upon completion of mechanical testing (autograft), femurs were carefully removed from potting. AS-ILNs were removed and the fractured segments were temporarily stabilized with circumferential sutures. Samples were photographed, marked to document spatial orientation, and decalcified. To provide a comprehensive histologic image of the 4 cm defect, specimens were sub-sectioned to fit within jumbo cassettes and processed for histology. Sections were stained with Masson's Trichrome, followed by scanning and digital reconstruction to generate a low magnification digital mosaic. **(A)** Representative histology of femur treated with autograft. Arrowhead denotes location of mechanical testing failure point. The cortical region at mid-diaphysis is expanded by trabecular bone (Insets 1,2) admixed with fibrovascular connective tissue (Inset 3). **(B)** Representative histology of negative control femur. Dashed yellow lines denote extent of callus formation. In the negative control, the mid-shaft cortical region was devoid of trabecular bone and was filled by fibrovascular connective tissue (Inset 2) consistent with a non-union fracture. For low magnification montages, bar = 10 mm. For insets, bar = 1 mm.

and external fixation. Thus, there is no clear consensus on the ideal canine critical-sized defect model to evaluate bone tissue engineering devices, nor has there been much focus on refinement and reduction of the canine model in pursuit of the Principle of the 3R's (Kirk, 2018; Angelis et al., 2019). Our goal was to develop a refined canine critical-sized defect model and report detailed methods for both surgical technique and comprehensive outcome measures in pursuit of the Principles of the 3R's.

In the present study, we successfully refined a canine critical-sized femoral defect model using an AS-ILN designed to eliminate acute angular deformation (slack) and provide consistent biomechanical performance across all animals, regardless of the assigned treatment group. The AS-ILN used in the present study has been shown to reduce lameness, lead to consistent and accelerated bone healing, and produce superior callus mechanical properties when compared to a traditional interlocking nail (Dejardin et al., 2014). These advances are due to unique features of the AS-ILN system such as the conical, threaded locking mechanisms of fixation bolts and the hourglass profile of the AS-ILN (Dejardin et al., 2012). Additionally, when compared to a traditional veterinary interlocking nail in mechanical tests, the AS-ILN provided more consistent angular deformation in torsion, eliminated construct slack (Dejardin et al., 2006), responded more uniformly to bending loads (Dejardin et al., 2009), and produced similar compliance regardless of defect size (Ting et al., 2009).

The AS-ILN was implanted without complications using surgical techniques similar to those used in human beings. Due to its unique biomechanical properties and position within the medullary canal, the AS-ILN allowed for a rapid return to limb use, with all dogs ambulating normally as early as 7–10 days post-operatively. The AS-ILN provided excellent clinical function over an extended period of time, even for dogs assigned to the negative control group. This is highly relevant as many bone tissue engineering studies require a negative control group wherein the implant system must provide sufficient stability for normal ambulation in the absence of healing. Additionally, a small AS-ILN system has also been developed and is in clinical use (Marturello et al., 2020, 2021). This is highly relevant for investigators that utilize rabbit critical-sized defect models for bone tissue engineering studies. An AS-ILN system was not previously available for use in this species. The authors suggest that the small AS-ILN is well suited for rabbit femoral or tibial critical-sized defect studies.

Due to the location of the AS-ILN within the central axis of the bone, the implant system did not obstruct radiographic scoring of cortical bridging (Figure 3). The relatively small cross-sectional area of the AS-ILN, located centrally within the bone, facilitated quantification of both soft and hard callus when paired with CT scanning parameters designed to minimize metal artifact (Figure 4). Moreover, the AS-ILN served as reference point to precisely identify the region of interest (ROI) for each dog and ensured that tissue quantification was performed at identical locations and over multiple time points. The location of the AS-ILN within the central axis of the bone facilitated mechanical testing and histological assessment of callus formation. The AS-ILN was used to identify the long axis of the femur, which was positioned along the central axis of the materials testing machine for torsional testing. Upon removal of distal fixation bolts and fixation of bones in the test fixtures, the AS-ILN did not interfere with torsional testing similar to prior

work (Dejardin et al., 2014). The resulting mechanical testing data were thus representative of the fracture callus. Finally, the testing protocol was developed such that once ultimate failure occurred, loading was immediately stopped in order to allow reconstruction of the bone column for histological assessment. This testing protocol was designed to optimize objective evaluation of bone healing using various outcome measures while reducing sample size (animal numbers).

Much consideration was given to the decision to perform histology on formalin-fixed, decalcified tissues that, in the case of the autograft group, had been mechanically tested. The gold standard technique for histologic assessment of orthopedic implants and adjacent tissues involves methyl methacrylate (i.e. "plastic") embedding and non-decalcified sectioning (Maglio et al., 2020). Methacrylate embedded sections are essential for evaluation of the implant/tissue interface of orthopedic implants and bone. The AS-ILN used in the present study is composed of 316L surgical stainless steel, which is a common, biocompatible alloy for orthopedic implants (Syrett and Davis, 1979; Erdmann et al., 2010). Moreover, the objective of this study was to use an existing AS-ILN to refine and reduce animal numbers, not to perform a detailed histologic analysis or histomorphometry of a novel implant and adjacent tissues. For this reason, histology was considered complimentary to the quantified CT results. Given this reasoning, it was not justifiable to operate additional cohorts of dogs for methacrylate-embedded, non-decalcified histology. Should the techniques detailed in the present study be used in the future to evaluate novel biomaterials for bone tissue regeneration, additional cohorts of dogs might be necessary for methacrylate embedded histology to meet regulatory criteria and allow a detailed evaluation of the interactions between device and adjacent host tissues.

While limitations are expected with any study, our goal was to describe a clinically-relevant large animal translational model for future bone tissue engineering studies. First, although skeletally mature hounds were used, dog age was somewhat variable (range: 2.5–6.5 years). The oldest dog assigned to the autograft group (6.5 years) produced the lowest amount of callus (Figure 4), which correlated to low torsional stiffness and torque at failure (Figure 5; Table 1). While age is the likely explanation for the reduced healing response in this dog, it is possible (although not plausible based on prior studies) that the AS-ILN provided disparate biomechanical stability in this animal. It is well known that bone healing is more robust in younger animals (Risselada et al., 2005; Mehta et al., 2010). A study in canine clinical patients documented more rapid healing in younger dogs (Averill et al., 1999). To definitively address the issue of age on bone healing in this model, an additional canine critical-sized defect study would be necessary with closely controlled ages (young cohort versus old cohort). Interestingly, older dogs may prove useful in this model in order to more rigorously challenge autograft control groups, novel bone healing agents, or new tissue engineering devices.

Additionally, all dogs in the present study were intact males due to subject availability at the time the study was initiated. While sex has been shown to effect bone healing in rodent induced-injury models (Mehta et al., 2011; Haffner-Luntzer et al., 2021), in the canine clinical setting the AS-ILN has been successfully placed in both intact and sterilized male and female dogs and cats with no detectible effect of subject sex (Marturello et al., 2021). Future studies may be warranted to determine whether sex or sterilization status has an effect on bone healing in this canine experimentally-induced critically-sized femoral defect model.

Second, we elected to create critical-sized defects via surgical ostectomy rather than traumatic fracture. This decision was made for ethical reasons to reduce morbidity, as well as to reduce inter-animal variability and maintain small animal numbers. Third, while segmentation of CT is an accepted method for quantifying bone volume and surface area in large animal models (Dejardin et al., 2014), CT is unable to assess bone mineral density (Robertson et al., 2017; Booz et al., 2020). Dual x-ray absorptiometry (DXA) would be required to determine bone mineral density during healing in this canine critically-sized femoral defect model. Fourth, the mechanical testing protocol was limited to torsional loading on formalin-fixed bone. While determining the biomechanical properties of fracture callus in the autograft-treated femurs under both bending and torsional loads could have generated useful data, torsion has been shown to be the major loading mode of long bones (Gautier et al., 2000; Yang et al., 2014). Furthermore, the presence of the AS-ILN within the medullary cavity would have severely masked the contribution of the fracture callus to bending stiffness. Lastly, regarding the mechanical testing of formalin-fixed bone, fixation was performed to prepare specimens for routine decalcification and paraffin embedded histology. While concerns have been raised about the impact of formalin fixation on biomechanical testing of long bones, contralateral (non-operated) control femurs were tested in tandem to account for any potential effect of fixation. This concern has been recently drawn into question, it was reported that formalin fixation had no effect on the mechanical properties of human femurs, and that patient-specific associations such as age and gender were retrievable despite formalin fixation (Wright et al., 2018). Another study reported no differences in yield stress, ultimate stress, and tissue hardness for fresh bone or bone stored in 4% formalin for up to 8 weeks (Öhman et al., 2008).

In summary, critical-sized long bone defects represent a tremendous clinical challenge. Although treatments exist, none is uniformly effective. While tissue engineering devices hold much promise for these injuries, a tissue engineering solution has yet to be successfully brought to market. The dog is an excellent large animal model species for translational evaluation of encouraging tissue engineering

devices. However, a consensus on the preferred technique for inducing and assessing a canine critical-sized long bone defect model is lacking. This study describes the use of an AS-ILN with superior biomechanical properties to refine the canine critical-sized femoral defect model. Animal numbers were minimized by performing radiographic scoring, quantitative CT, torsional mechanical testing, and histology on a single cohort of dogs randomized to either autograft or negative control treatment groups. This work represents an important advancement for the canine translational model and collectively advances the field toward the Principle of the 3R's.

Data availability statement

The raw data supporting the conclusion of this article will be made available by the authors, without undue reservation.

Ethics statement

The animal study was reviewed and approved by Texas A&M University Institutional Animal Care and Use Committee (IACUC).

Author contributions

WS, first author, conception and design, collection and assembly of data, data analysis and interpretation, manuscript writing, final approval of manuscript. LD, conception and design, expertise with AS-ILN, led all mechanical testing, manuscript writing, final approval of manuscript. ES-N, responsible for collection and assembly of CT data, data analysis and interpretation, manuscript writing, final approval of manuscript. CK and BW, conception and design, led the histology efforts, assembled data, manuscript writing, final approval of manuscript. BE, led radiograph and CT imaging, collection and assembly of data, data analysis and interpretation, manuscript writing, final approval of manuscript. LD, collection and assembly of data, data analysis and interpretation, manuscript writing, final approval of manuscript. SK, collection and assembly of data, data interpretation, manuscript writing, final approval of manuscript. CG, conception and design, data analysis and interpretation, manuscript writing, final approval of manuscript. All authors read and approved the final manuscript.

Funding

This work was funded by an award from The Texas A&M Research Enhancement Fund. Funds to support histology and mechanical testing were provided by the Bone & Joint Fund, Texas A&M Foundation.

Acknowledgments

The authors wish to acknowledge Danielle M. Marturello (Michigan State University) for assistance with mechanical testing.

Conflict of interest

WS and LD are consultants for Biomedtrix (Whippany, New Jersey, United States) a subsidiary of Movora, the manufacturer of the angle-stable interlocking nail (AS-ILN) used in the present study. LD receives royalties associated with sales of the AS-ILN.

The remaining authors declare that the research was conducted in the absence of any commercial or financial relationships that could be construed as a potential conflict of interest.

Publisher's note

All claims expressed in this article are solely those of the authors and do not necessarily represent those of their affiliated organizations, or those of the publisher, the editors, and the reviewers. Any product that may be evaluated in this article, or claim that may be made by its manufacturer, is not guaranteed or endorsed by the publisher.

References

Amini, A., Ct, L., and Sp, N. (2012). Bone tissue engineering: Recent advances and challenges. *Crit. Rev. Biomed. Eng.* 40, 363–408. doi:10.1615/critrevbiomedeng.v40.i5.10

Angelis, I. D., Ricceri, L., and Vitale, A. (2019). The 3R principle: 60 years taken well. Preface. *Ann. Ist. Super. Sanita* 55, 398–399. doi:10.4415/ann_19_04_15

Arinzeh, T., Peter, S., Archambault, M., Bos, C. van den, Gordon, S., Kraus, K., et al. (2003). Allogeneic mesenchymal stem cells regenerate bone in a critical-sized canine segmental defect. *J. Bone Jt. Surg. Am.* 85, 1927–1935. doi:10.2106/00004623-200310000-00010

Averill, S. M., Johnson, A. L., Chambers, M., Smith, C. W., Kneller, S., Twardock, A. R., et al. (1999). Qualitative and quantitative scintigraphic imaging to predict fracture healing. *Vet. Comp. Orthop. Traumatol.* 12, 142–150. doi:10.1055/s-0038-1632480

Berg, B. V., Malghem, J., Maldague, B., and Lecouvet, F. (2006). Multi-detector CT imaging in the postoperative orthopedic patient with metal hardware. *Eur. J. Radiol.* 60, 470–479. doi:10.1016/j.ejrad.2006.08.008

Booz, C., Noeske, J., Albrecht, M. H., Lenga, L., Martin, S. S., Yel, I., et al. (2020). Diagnostic accuracy of quantitative dual-energy CT-based bone mineral density assessment in comparison to Hounsfield unit measurements using dual x-ray absorptiometry as standard of reference. *Eur. J. Radiol.* 132, 109321. doi:10.1016/j.ejrad.2020.109321

Buehler, K. C., Green, J., Woll, T. S., and Duwelius, P. J. (1997). A technique for intramedullary nailing of proximal third tibia fractures. *J. Orthop. Trauma* 11, 218–223. doi:10.1097/00005131-199704000-00014

Dejardin, L. M., Cabassu, J. B., Guillou, R. P., Villwock, M., Guiot, L. P., and Haut, R. C. (2014). *In vivo* biomechanical evaluation of a novel angle-stable interlocking nail design in a canine tibial fracture model. *Vet. Surg.* 43, 271–281. doi:10.1111/j.1532-950x.2014.12136.x

Dejardin, L. M., Guillou, R. P., Ting, D., Sinnott, M. T., Meyer, E., and Haut, R. C. (2009). Effect of bending direction on the mechanical behaviour of interlocking nail systems. *Vet. Comp. Orthop. Traumatol.* 22, 264–269. doi:10.3415/vcot-08-08-0075

Dejardin, L. M., Guiot, L. P., and Pfeil, D. J. F. von (2012). Interlocking nails and minimally invasive osteosynthesis. *Veterinary Clin. N. Am. Small Animal Pract.* 42, 935–962. doi:10.1016/j.cvsm.2012.07.004

Dejardin, L. M., Lansdowne, J. L., Sinnott, M. T., Sidebotham, C. G., and Haut, R. C. (2006). *In vitro* mechanical evaluation of torsional loading in simulated canine tibiae for a novel hourglass-shaped interlocking nail with a self-tapping tapered locking design. *Am. J. Veterinary Res.* 67, 678–685. doi:10.2460/ajvr.67.4.678

Dozza, B., Salamanna, F., Baleani, M., Giavaresi, G., Parrilli, A., Zani, L., et al. (2018). Nonunion fracture healing: Evaluation of effectiveness of demineralized bone matrix and mesenchymal stem cells in a novel sheep bone nonunion model. *J. Tissue Eng. Regen. Med.* 12, 1972–1985. doi:10.1002/term.2732

Egermann, M., Goldhahn, J., and Schneider, E. (2005). Animal models for fracture treatment in osteoporosis. *Osteoporos. Int.* 16, S129–S138. doi:10.1007/s00198-005-1859-7

Erdmann, N., Bondarenko, A., Hewicker-Trautwein, M., Angrisani, N., Reifenrath, J., Lucas, A., et al. (2010). Evaluation of the soft tissue biocompatibility of MgCa0.8 and surgical steel 316L *in vivo*: A comparative study in rabbits. *Biomed. Eng. Online* 9, 63. doi:10.1186/1475-925x-9-63

Faria, M., Lu, Y., Heaney, K., Uthamanthil, R., Muir, P., and Markel, M. (2007). Recombinant human bone morphogenetic protein-2 in absorbable collagen sponge enhances bone healing of tibial osteotomies in dogs. *Vet. Surg.* 36, 122–131. doi:10.1111/j.1532-950x.2007.00242.x

Feichtenschlager, C., Gerwing, M., Failing, K., Peppler, C., Kasa, A., Kramer, M., et al. (2018). Magnetic resonance imaging assessment of intra-articular structures in the canine stifle joint after implantation of a titanium tibial plateau levelling osteotomy plate. *Vet. Comp. Orthop. Traumatol.* 31, 261–272. doi:10.1055/s-0038-1647248

Flagstad, I. R., Tatman, L. M., Heare, A., Parikh, H. R., Albersheim, M., Atchison, J., et al. (2021). Single-stage versus 2-stage bilateral intramedullary nail fixation in patients with bilateral femur fractures: A multicenter retrospective review. *J. Orthop. Trauma* 35, 499–504. doi:10.1097/bot.0000000000002055

Gautier, E., Perren, S. M., and Cordey, J. (2000). Strain distribution in plated and unplated sheep tibia an *in vivo* experiment. *Injury* 31, 37–93. doi:10.1016/s0020-1383(00)80030-3

Gerber, A., and Ganz, R. (1998). Combined internal and external osteosynthesis a biological approach to the treatment of complex fractures of the proximal tibia. *Injury* 29, C22–C28. doi:10.1016/s0020-1383(98)95005-7

Haffner-Luntzer, M., Fischer, V., and Ignatius, A. (2021). Differences in fracture healing between female and male C57bl/6J mice. *Front. Physiol.* 12, 712494. doi:10.3389/fphys.2021.712494

Hahn, J. A., Witte, T. S., Arens, D., Pearce, A., and Pearce, S. (2011). Double-plating of ovine critical sized defects of the tibia: A low morbidity model enabling continuous *in vivo* monitoring of bone healing. *BMC Musculoskelet. Disord.* 12, 214–216. doi:10.1186/1471-2474-12-214

Hoffman, A. M., and Dow, S. W. (2016). Concise review: Stem cell trials using companion animal disease models. *Stem Cells* 34, 1709–1729. doi:10.1002/stem.2377

Hollister, S. J., and Murphy, W. L. (2011). Scaffold translation: Barriers between concept and clinic. *Tissue Eng. Part B Rev.* 17, 459–474. doi:10.1089/ten.teb.2011.0251

Horner, E. A., Kirkham, J., Wood, D., Curran, S., Smith, M., Thomson, B., et al. (2010). Long bone defect models for tissue engineering applications: Criteria for choice. *Tissue Eng. Part B Rev.* 16, 263–271. doi:10.1089/ten.teb.2009.0224

Johnson, K. A. (2014). "Approach to the shaft of the femur in the dog," in *Piermattei's atlas of surgical approaches to the bones and joints of the dog and cat* (St. Louis, Missouri, USA: Elsevier), 372–373.

Kang, N. W. W., Tan, W. P. J., Phua, Y. M. C., Min, A. T. G., Naidu, K., Umapathysivam, K., et al. (2021). Intramedullary nail: The past, present and the future - a review exploring where the future may lead us. *Orthop. Rev.* 13, 25546. doi:10.52965/001c.25546

Kirk, R. G. W. (2018). Recovering the principles of humane experimental technique: The 3Rs and the human essence of animal research. *Sci. Technol. Hum. Values* 43, 622–648. doi:10.1177/0162243917726579

Lang, G. J., Cohen, B. E., Bosse, M. J., and Kellam, J. F. (1995). Proximal third tibial shaft fractures. Should they be nailed? *Clin. Orthop. Relat. Res.* 315, 64–74. doi:10.1097/00003086-199506000-00008

Lansdowne, J. L., Sinnott, M. T., Dejardin, L. M., Ting, D., and Haut, R. C. (2007). *In vitro* mechanical comparison of screwed, bolted, and novel interlocking nail systems to buttress plate fixation in torsion and mediolateral bending. *Vet. Surg.* 36, 368–377. doi:10.1111/j.1532-950x.2007.00277.x

Lee, M.-J., Kim, S., Lee, S.-A., Song, H.-T., Huh, Y.-M., Kim, D.-H., et al. (2007). Overcoming artifacts from metallic orthopedic implants at high-field-strength MR imaging and multi-detector CT. *Radiographics* 27, 791–803. doi:10.1148/rg.273065087

Liebschner, M. A. K. (2004). Biomechanical considerations of animal models used in tissue engineering of bone. *Biomaterials* 25, 1697–1714. doi:10.1016/S0142-9612(03)00515-5

Lindsey, R., Gugala, Z., Milne, E., Sun, M., Gannon, F., and Latta, L. (2006). The efficacy of cylindrical titanium mesh cage for the reconstruction of a critical-size canine segmental femoral diaphyseal defect. *J. Orthop. Res.* 24, 1438–1453. doi:10.1002/jor.20154

Maglio, M., Salamanna, F., Brogini, S., Borsari, V., Pagani, S., Aldini, N. N., et al. (2020). Histological, histomorphometrical, and biomechanical studies of bone-implanted medical devices: Hard resin embedding. *BioMed Res. Int.* 2020, 1–13. doi:10.1155/2020/1804630

Manzini, B. M., Machado, L. M. R., Noritomi, P. Y., and Silva, J. V. L. da (2021). Advances in bone tissue engineering: A fundamental review. *J. Biosci.* 46, 17. doi:10.1007/s12038-020-00122-6

Markel, M. D., Bogdanske, J. J., Xiang, Z., and Klohnen, A. (1995). Atrophic nonunion can be predicted with dual energy x-ray absorptiometry in a canine ostectomy model. *J. Orthop. Res.* 13, 869–875. doi:10.1002/jor.1100130610

Marturello, D. M., Perry, K. L., and Dejardin, L. M. (2021). Clinical application of the small I-loc interlocking nail in 30 feline fractures: A prospective study. *Vet. Surg.* 50, 588–599. doi:10.1111/vsu.13594

Marturello, D. M., Pfeil, D. J. F. von, and Dejardin, L. M. (2020). Mechanical comparison of two small interlocking nails in torsion using a feline bone surrogate. *Vet. Surg.* 49, 380–389. doi:10.1111/vsu.13364

Mehta, M., Schell, H., Schwarz, C., Peters, A., Schmidt-Bleek, K., Ellinghaus, A., et al. (2011). A 5-mm femoral defect in female but not in male rats leads to a reproducible atrophic non-union. *Arch. Orthop. Trauma Surg.* 131, 121–129. doi:10.1007/s00402-010-1155-7

Mehta, M., Strube, P., Peters, A., Perka, C., Hutmacher, D., Fratzl, P., et al. (2010). Influences of age and mechanical stability on volume, microstructure, and mineralization of the fracture callus during bone healing: Is osteoclast activity the key to age-related impaired healing? *Bone* 47, 219–228. doi:10.1016/j.bone.2010.05.029

Mohaghegh, S., Hosseini, S. F., Rad, M. R., and Khojateh, A. (2021). 3D printed composite scaffolds in bone tissue engineering: A systematic review. *Curr. Stem Cell. Res. Ther.* 16, 1–62. doi:10.2174/1574888x16666210810111754

MSc, A. R. L.-G., Dc, J. L.-M., Dc, I. P.-L., Montero, A. A., MSc, G. R., PhD, F. C.-M., et al. (2013). Development of a bone nonunion in a noncritical segmental tibia defect model in sheep utilizing interlocking nail as an internal fixation system. *J. Surg. Res.* 183, 620–628. doi:10.1016/j.jss.2013.02.060

Muschler, G. F., Raut, V. P., Patterson, T. E., Wenke, J. C., and Hollinger, J. O. (2010). The design and use of animal models for translational research in bone tissue engineering and regenerative medicine. *Tissue Eng. Part B Rev.* 16, 123–145. doi:10.1089/ten.teb.2009.0658

Neu, C. P., Arastu, H. F., Curtiss, S., and Reddi, A. H. (2009). Characterization of engineered tissue construct mechanical function by magnetic resonance imaging. *J. Tissue Eng. Regen. Med.* 3, 477–485. doi:10.1002/term.188

Öhman, C., Dall'Ara, E., Baleani, M., Jan, S. V. S., and Viceconti, M. (2008). The effects of embalming using a 4% formalin solution on the compressive mechanical properties of human cortical bone. *Clin. Biomech. (Bristol, Avon.* 23, 1294–1298. doi:10.1016/j.clinbiomech.2008.07.007

Ostrander, E. A., and Giniger, E. (1997). Semper fidelis: What man's best friend can teach us about human biology and disease. *Am. J. Hum. Genet.* 61, 475–480. doi:10.1086/515522

Ozmeric, A., Tanoglu, O., Ocak, M., Celik, H. H., Firat, A., Kaymaz, F. F., et al. (2020). Intramedullary implants coated with cubic boron nitride enhance bone fracture healing in a rat model. *J. Trace Elem. Med. Biol.* 62, 126599. doi:10.1016/j.jtemb.2020.126599

Pearce, A. I., Richards, R. G., Milz, S., Schneider, E., and Pearce, S. G. (2007). Animal models for implant biomaterial research in bone: A review. *Eur. Cell. Mat.* 13, 1–10. doi:10.22203/ecm.v013a01

Pfeil, D. von, Dejardin, L., DeCamp, C., Meyer, E., Lansdowne, J., Weerts, R., et al. (2005). *In vitro* biomechanical comparison of a plate-rod combination-construct and an interlocking nail-construct for experimentally induced gap fractures in canine tibiae. *Am. J. Veterinary Res.* 66, 1536–1543. doi:10.2460/ajvr.2005.66.1536

Quirk, B. J., Sannagowdara, K., Buchmann, E. V., Jensen, E. S., Gregg, D. C., and Whelan, H. T. (2016). Effect of near-infrared light on *in vitro* cellular ATP production of osteoblasts and fibroblasts and on fracture healing with intramedullary fixation. *J. Clin. Orthop. Trauma* 7, 234–241. doi:10.1016/j.jcot.2016.02.009

Reichert, J. C., Epari, D. R., Wullschleger, M. E., Saifzadeh, S., Steck, R., Lienau, J., et al. (2010). Establishment of a preclinical ovine model for tibial segmental bone defect repair by applying bone tissue engineering strategies. *Tissue Eng. Part B Rev.* 16, 93–104. doi:10.1089/ten.teb.2009.0455

Rhorer, A. S. (2009). Percutaneous/Minimally invasive techniques in treatment of femoral shaft fractures with an intramedullary nail. *J. Orthop. Trauma* 23, S2–S5. doi:10.1097/bot.0b013e31819f2569

Ribitsch, I., Baptista, P. M., Lange-Consiglio, A., Melotti, L., Patruno, M., Jenner, F., et al. (2020). Large animal models in regenerative medicine and tissue engineering: To do or not to do. *Front. Bioeng. Biotechnol.* 8, 972. doi:10.3389/fbioe.2020.00972

Risselada, M., Kramer, M., Rooster, H. de, Taeymans, O., Verleyen, P., and Bree, H. van (2005). Ultrasonographic and radiographic assessment of uncomplicated secondary fracture healing of long bones in dogs and cats. *Vet. Surg.* 34, 99–107. doi:10.1111/j.1532-950x.2005.00017.x

Robertson, A., Godavitarne, C., and Peters, J. (2017). Bone quantification. *Orthop. Trauma* 31, 326–329. doi:10.1016/j.mporth.2017.07.009

Roddy, E., DeBaun, M. R., Daoud-Gray, A., Yang, Y. P., and Gardner, M. J. (2017). Treatment of critical-sized bone defects: Clinical and tissue engineering perspectives. *Eur. J. Orthop. Surg. Traumatol.* 28, 351–362. doi:10.1007/s00590-017-2063-0

Sastry, A. (2014). Overview of the US FDA medical device approval process. *Curr. Cardiol. Rep.* 16, 494. doi:10.1007/s11886-014-0494-3

Schemitsch, E. H. (2017). Size matters: Defining critical in bone defect size. *J. Orthop. Trauma* 31, S20–S22. doi:10.1097/bot.0000000000000978

Schmiedt, C. W., Lu, Y., Heaney, K., Muir, P., Amodie, D. M., and Markel, M. D. (2007). Comparison of two doses of recombinant human bone morphogenetic protein in absorbable collagen sponges for bone healing in dogs. *Am. J. Vet. Res.* 68, 834–840. doi:10.2460/ajvr.68.8.834

Schoen, M., Rotter, R., Schattner, S., Mittlmeier, T., Claes, L., Vollmar, B., et al. (2008). Introduction of a new interlocked intramedullary nailing device for stabilization of critically sized femoral defects in the rat: A combined biomechanical and animal experimental study. *J. Orthop. Res.* 26, 184–189. doi:10.1002/jor.20501

Shen, J., Hu, C., Yu, S., Huang, K., and Xie, Z. (2016). A meta-analysis of percutenous compression plate versus intramedullary nail for treatment of intertrochanteric HIP fractures. *Int. J. Surg.* 29, 151–158. doi:10.1016/j.ijsu.2016.03.065

Shiels, S. M., Bouchard, M., Wang, H., and Wenke, J. C. (2018). Chlorhexidine-releasing implant coating on intramedullary nail reduces infection in a rat model. *Eur. Cell. Mat.* 35, 178–194. doi:10.22203/ecm.v035a13

Syrett, B. C., and Davis, E. E. (1979). *In vivo* evaluation of a high-strength, high-ductility stainless steel for use in surgical implants. *J. Biomed. Mat. Res.* 13, 543–556. doi:10.1002/jbm.820130403

Ting, D., Cabassu, J. B., Guillou, R. P., Sinnott, M. T., Meyer, E. G., Haut, R. C., et al. (2009). *In vitro* evaluation of the effect of fracture configuration on the mechanical properties of standard and novel interlocking nail systems in bending. *Vet. Surg.* 38, 881–887. doi:10.1111/j.1532-950x.2009.00584.x

Viberg, B., Eriksen, L., Hojsager, K. D., Hojsager, F. D., Lauritsen, J., Palm, H., et al. (2021). Should pertrochanteric and subtrochanteric fractures Be treated with a short or long intramedullary nail? A multicenter cohort study. *J. Bone Jt. Surg.* 103, 2291–2298. doi:10.2106/jbjs.20.01904

Volpon, J. B. (1994). Nonunion using a canine model. *Arch. Orthop. Trauma Surg.* 113, 312–317. doi:10.1007/bf00426178

Wong, C. H., Siah, K. W., and Lo, A. W. (2019). Estimation of clinical trial success rates and related parameters. *Biostatistics* 20, 273–286. doi:10.1093/biostatistics/kxx069

Wright, B., Ragan, L., Niratisairak, S., Høiseth, A., Strømsøe, K., Steen, H., et al. (2018). High correlation between mechanical properties and bone mineral parameters in embalmed femurs after long-term storage. *Clin. Biomech. (Bristol, Avon.* 59, 136–142. doi:10.1016/j.clinbiomech.2018.09.013

Yang, P.-F., Sanno, M., Ganse, B., Koy, T., Brüggemann, G.-P., Müller, L. P., et al. (2014). Torsion and antero-posterior bending in the *in vivo* human tibia loading regimes during walking and running. *Plos One* 9, e94525. doi:10.1371/journal.pone.0094525

Zheng, S. Y., Dhruva, S. S., and Redberg, R. F. (2017). Characteristics of clinical studies used for US food and drug administration approval of high-risk medical device supplements. *JAMA* 318, 619–625. doi:10.1001/jama.2017.9414

frontiers | Frontiers in Bioengineering and Biotechnology

TYPE Original Research
PUBLISHED 15 September 2022
DOI 10.3389/fbioe.2022.985688

Check for updates

OPEN ACCESS

EDITED BY
Andrea Vernengo,
AO Research Institute, Switzerland

REVIEWED BY
Youwen Yang,
Jiangxi University of Science and Technology, China
Cijun Shuai,
Jiangxi University of Science and Technology, China

*CORRESPONDENCE
Lei Li,
changhaibai@163.com

SPECIALTY SECTION
This article was submitted to Tissue Engineering and Regenerative Medicine, a section of the journal Frontiers in Bioengineering and Biotechnology

RECEIVED 04 July 2022
ACCEPTED 19 August 2022
PUBLISHED 15 September 2022

CITATION
Lu Y, Huo Y, Yang Z, Niu Y, Zhao M, Bosiakov S and Li L (2022), Influence of the parameters of the convolutional neural network model in predicting the effective compressive modulus of porous structure.
Front. Bioeng. Biotechnol. 10:985688.
doi: 10.3389/fbioe.2022.985688

COPYRIGHT
© 2022 Lu, Huo, Yang, Niu, Zhao, Bosiakov and Li. This is an open-access article distributed under the terms of the Creative Commons Attribution License (CC BY). The use, distribution or reproduction in other forums is permitted, provided the original author(s) and the copyright owner(s) are credited and that the original publication in this journal is cited, in accordance with accepted academic practice. No use, distribution or reproduction is permitted which does not comply with these terms.

Influence of the parameters of the convolutional neural network model in predicting the effective compressive modulus of porous structure

Yongtao Lu[1,2], Yi Huo[1], Zhuoyue Yang[3], Yibiao Niu[1], Ming Zhao[1], Sergei Bosiakov[4] and Lei Li[5]*

[1]Department of Engineering Mechanics, Dalian University of Technology, Dalian, China, [2]DUT-BSU Joint Institute, Dalian University of Technology, Dalian, China, [3]Xi'an Aerospace Propulsion Institute, Xi'an, China, [4]Faculty of Mechanics and Mathematics, Belarusian State University, Minsk, Belarus, [5]Department of Vascular Surgery, The Second Affiliated Hospital of Dalian Medical University, Dalian, Liaoning, China

In recent years, the convolutional neural network (CNN) technique has emerged as an efficient new method for designing porous structure, but a CNN model generally contains a large number of parameters, each of which could influence the predictive ability of the CNN model. Furthermore, there is no consensus on the setting of each parameter in the CNN model. Therefore, the present study aimed to investigate the sensitivity of the parameters in the CNN model for the prediction of the mechanical property of porous structures. 10,500 samples of porous structure were randomly generated, and their effective compressive moduli obtained from finite element analysis were used as the ground truths to construct and train a CNN model. 8,000 of the samples were used to train the CNN model, 2000 samples were used for the cross-validation of the CNN model and the remaining 500 new structures, which did not participate in the CNN training process, were used to test the predictive power of the CNN model. The sensitivity of the number of convolutional layers, the number of convolution kernels, the number of pooling layers, the number of fully connected layers and the optimizer in the CNN model were then investigated. The results showed that the optimizer has the largest influence on the training speed, while the fully connected layer has the least impact on the training speed. Additionally, the pooling layer has the largest impact on the predictive ability while the optimizer has the least impact on the predictive ability. In conclusion, the parameters of the CNN model play an important role in the performance of the CNN model and the parameter sensitivity analysis can help optimize the CNN model to increase the computational efficiency.

KEYWORDS

convolutional neural network, bone scaffold, finite element modeling, sensitivity analysis, compressive modulus

Introduction

In recent years, the machine learning and deep learning techniques have emerged as new techniques widely used in many fields, including in the prediction of the mechanical properties of materials and the design of porous structures.

In the field of prediction of the mechanical properties of materials, Li et al. (2019) used the machine learning method to establish the implicit mapping between the effective mechanical property and the mesoscale structure of heterogeneous materials, and the results showed that the machine training model can accurately predict the elastic modulus of the structures. However, this study simplified the parameters in the CNN model through algebraic operations and the influence of parameters on the CNN model is not mentioned. Wu et al. (2019) proposed a machine learning method for predicting the effective diffusivity of two-dimensional porous structures, and the results showed that this model can accurately predict the transport properties of porous structures. Besides, one of the key issues of the research is how to select the parameters to avoid overfitting the CNN model. Graczyk and Matyka (2020) utilized CNN to predict porosity, permeability and tortuosity of porous structures, and found that the error between the predicted results of the CNN model and the theoretical value can be kept in a very small range. Besides, the parameter is reduced by 10% every 50 epochs of the training. Paul and Bhattacharjee (2018) used artificial neural network (ANN) to investigate the effects of temperature, humidity and other conditions on the properties of metal materials, and the accuracy of the ANN network prediction of fracture toughness of metal materials is close to 80%. Besides, machine learning is also widely used in some biological problems of bone tissue replacement. For example, Wu et al. (2021) proposed a new model based on machine learning techniques to predict bone ingrowth. Compared with the traditional FE model, the new prediction model of bone ingrowth based on machine learning has higher efficiency and accuracy.

In the field of the design of porous structures, Gu et al. (2018) proposed a method to design hierarchical materials using machine learning, and the results showed that tougher and stronger materials can be obtained by the method. It is worth pointing out that the study built blocks into a single unit cell to reduce the number of parameters needed in their machine learning model. Tan et al. (2020) proposed a deep learning model based on CNN for the design of microstructural materials, and found that the obtained microstructural materials with desired compliance tensor showed better mechanical properties. Besides, the proposed model reduced the number of design parameters from 4,096 to 25. Wang et al. (2018) reconstructed porous structures using the CNN model, and the results showed that the proposed method greatly improved the connectivity of the structures and exhibits better performance than conventional methods. Bessa et al. (2017) developed a new data-driven computing framework to assist in structural design, using machine learning to replace empirical constitutive models with experimental data. The results show that the mean square errors, mean relative errors, and the absolute fraction of variance values of the ANN for predicting friction factors were 1.26, 4.36×10^{-7} and 0.9993, respectively. Besides, the bone scaffold is used to replace the defected bone tissues and the machine learning has been widely used in the design of bone scaffolds, Conev et al. (2020) trained a machine learning model to predict the printing quality for a given printing configuration accurately for the material. They identified which parameters mostly affect the printing quality. Thus, the proper bone scaffolds can be designed to avoid poor print quality. Cilla et al. (2017) used machine learning techniques to optimize the bone joint replacements, which can be used in the field of the design of the bone scaffolds.

These previous studies showed that machine learning and deep learning techniques are of great significance in the fields of the prediction of mechanical properties of materials, the design of porous structures and so on. Besides, the previous study also pointed out the importance of parameter sensitivity. However, the parameter sensitivity studied in these models has not been fully understood. Therefore, it is of great importance to study the parameter sensitivity of CNN model and improve the efficiency of machine learning.

The CNN is one main branch of the deep learning techniques and the CNN networks are inspired by biological processes, in which the connectivity pattern between neurons resembles the organization and each neuron in one layer are connected to all neurons in the next layer. The CNN models consist of convolutional layers, pooling layers, and fully connected layers (Yamashita et al., 2018). The parameters of each layer of the neural network have a certain influence on the training speed and prediction ability of the entire convolutional neural network. Thus, finding the optimal parameter design is one of the important parts of the training of the convolutional neural network. However, the convolutional neural network needs to be re-trained when the parameters are adjusted. Therefore, using the optimal parameters plays a crucial role in saving computational time and increasing the model performance. However, the parameter sensitivity analysis has not been fully understood in the previous studies, which means that the prediction performance of the CNN models may be further improved and the computational efficiency can be further improved.

The present study aimed to investigate the sensitivity of the parameters in the CNN model for the prediction of the mechanical property of porous structures. A CNN model with convolutional layers, pooling layers and fully connected layers was first constructed to predict the effective compressive modulus of porous structures and then the influence of various parameters in the CNN on the training speed and prediction ability of the CNN model was investigated.

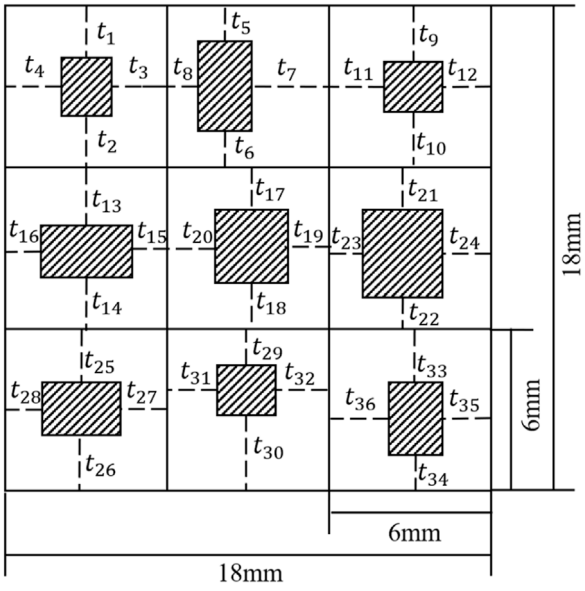

FIGURE 1
Schematic diagram of porous composite structure (The shaded areas are the pores).

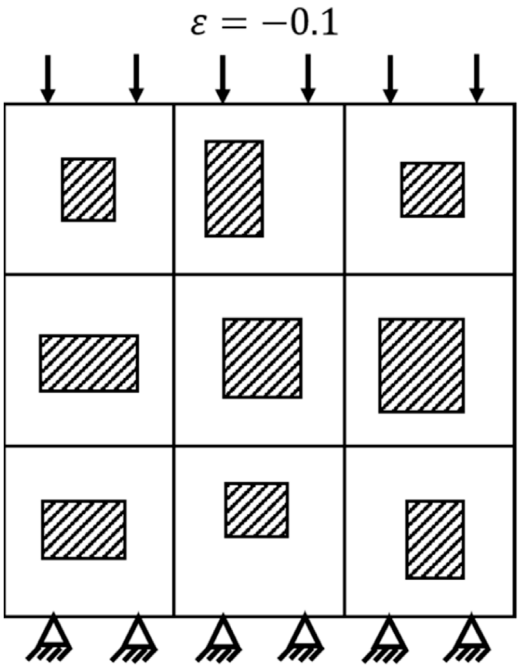

FIGURE 2
Loading and constraint defined in the finite element analysis ("ε" refers to the strain).

Materials and methods

The design setting of the 2D porous structure and the CNN model

In the present study, a two-dimensional (2D) porous structure was used as an example to investigate the parameter sensitivity of a convolutional neural network in predicting the mechanical property of the porous structure. Because the CNN model needs too many parameters, it is unrealistic to study all the parameters one by one, so 2D models are used in most of the current studies. For example, Wu et al. (2019) used 2D porous structures to simplify the parameters and it has been proved that the accuracy of the 2D model can meet the requirements. The 2D 3 × 3 porous structure was used for the demonstration in the present study (Figure 1). The dimension of the structure was set to 18.0 × 18.0 mm. In each cell of the structure, the four-dimensional parameters were set as the independent design variables. Therefore, for the entire structure, there are 36 independent design variables ($t_1 \sim t_{36}$). It is worth noting that the emergence of additive manufacturing (AM) enables the fabrication of structures with complex geometries, especially the porous structures. For example, Gu et al. (2018) used AM technique to manufacture and test the enhanced porous structures. Since in the previous studies, the fabrication of porous structures was achieved by AM technique, it is meaningful to consider the constraints of AM technique. The additive manufacturing constraint puts additional requirements for the dimension and aperture of the porous structure, i.e., the minimal thickness of the struts should be larger than the precision of the AM technique (0.2 mm in the present setting). To meet these requirements, the minimum unit for changing the dimensional variables was set to 0.2 mm. In other words, there are only three possibilities for $t_1 \sim t_{36}$, i.e., 0.2 mm, 0.4 mm and 0.6 mm.

The effective compressive moduli of the porous structures calculated from the finite element (FE) analysis were taken as the ground truths and used to train the CNN model constructed in the present study. As shown in Figure 2, the nodes on the one (down) side of the porous structures were fully constrained while the nodes on the opposite (up) side were subjected to a compressive displacement loading. The effective compressive modulus of the porous structures was calculated by the total reaction force and the displacement applied. The Ti-6Al-4V was used to make the porous structure. Therefore, in the FE model, the Young's modulus of the solid part was set to 113.8 GPa and the Poisson's ratio was set to 0.34 (Niinomi, 1998).

A CNN model was trained firstly and the procedure for the training and testing of the CNN model is presented in Figure 3. The training process of the CNN model can be briefly described as below: First, 10,000 groups of variables were randomly generated and each group of variables contained 36 independent variables ($t_1 \sim t_{36}$). Then, the corresponding

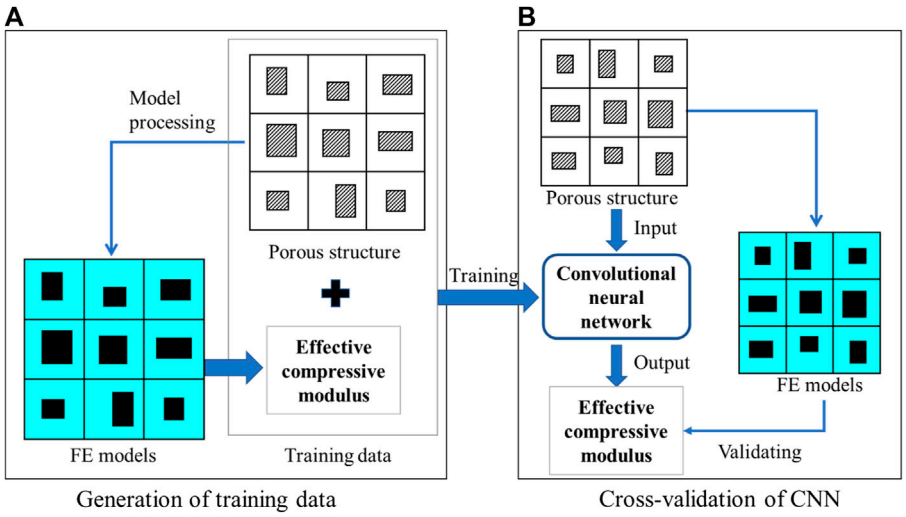

FIGURE 3
The workflow for the **(A)** training and **(B)** cross-validation of the convolutional neural network (CNN) model.

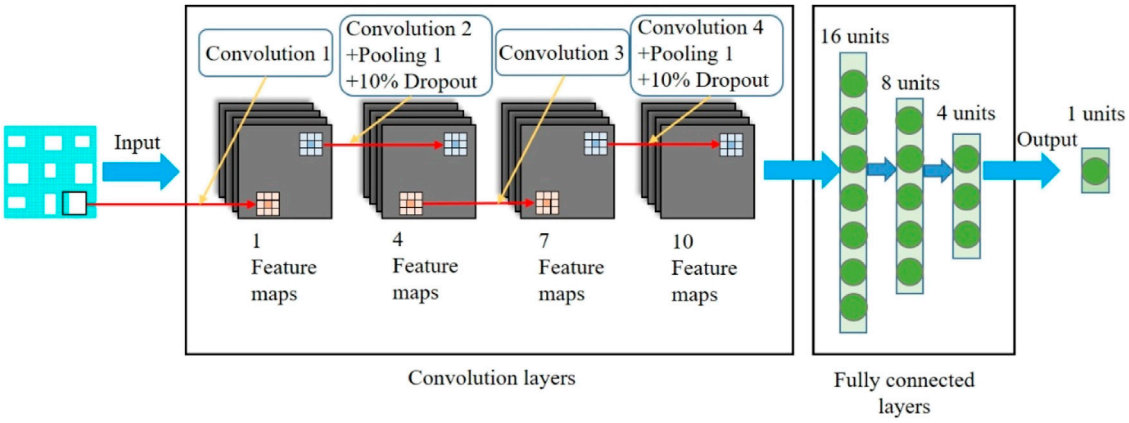

FIGURE 4
The convolutional neural network model constructed in the present study.

1000 FE models were built based on these dimensional variables. The effective compressive modulus of each sample was obtained from FE calculation and used as the ground truth for building the CNN model. Among the 10,000 samples, 8,000 were used for the training (Figure 3A), and 2,000 were used for the cross-validation (Figure 3B). It should be noted that both the 8,000 training samples and the 2000 cross-validation samples are involved in the adjustment of the parameters of the CNN model. The 2000 cross-validation samples have to be different from the 8,000 training samples. Otherwise, the CNN models constructed will have no ability to predict the elastic modulus of new porous structures.

The constructed CNN model is shown in Figure 4 and was guided by the work done by Li et al. (2019) which was created to solve a similar problem, i.e., predicting the mechanical property of porous materials using image based deep learning technique. It should be noted that there are many different types of CNN models in the literature and the CNN model in the present study is just one demonstration of the parameter sensitivity study. In the CNN model constructed (Figure 4), the input is the design of the porous structure (Figure 1) and the output is the effective compressive modulus of the input porous structure. In the CNN model constructed, four convolutional layers, two pooling layers and three fully connected layers were applied to the image. The

size of all the convolution kernels was set to 3 × 3. The maximal pooling was applied after the convolutional layers to simplify the information of the output neurons. To improve the accuracy of the CNN model, 10% dropout was used after the two pooling layers. A convolutional layer is the main building block of the CNN model, which contains a set of kernels learned throughout the training process. A pooling layer is usually incorporated between two successive convolutional layers. The pooling layer reduces the number of parameters and computational by down-sampling the representation. The fully connected layers are the last a few layers where all the inputs from the previous layer are connected to every neuron of the next layer. In the CNN model constructed in the present study, the fully connected layers compile the data extracted from the convolutional layers to form the final output. The CNN model proposed by Carneiro et al. (2017) can be seen as a typical CNN model, which contains the convolutional layers, pooling layers and fully connected layers. The convolutional layers usually contain the model parameters formed by the input weight matrices.

In the training process, because the purpose of the CNN model was to make an accurate prediction of the effective modulus of the porous structures, a loss function was defined to quantify the difference between the effective compressive modulus predicted from the CNN model and those calculated from the FE analysis, which was taken as the golden answers. Then, the kernels and biases in the convolutional layers and the weights in the fully connected layers were adjusted using the backpropagation algorithm (Rubio et al., 2011). In the present study, the mean absolute error (MAE) was set as the objective function:

$$\mathrm{MAE}[Y, f(X)] = \frac{1}{n}\sum_{i=1}^{n}\left|Y - f(X)\right| \tag{1}$$

where Y is the effective compressive modulus of the porous structures calculated from the FE analysis; $f(X)$ is the corresponding effective compressive modulus calculated from the CNN model and n is the number of samples used for the cross-validation (n = 2000 in the present study).

The CNN model was built using the Tensorflow 2.0 module in Python 3.7. The training process was conducted on a desktop computer with the setting of i7-8700 CPU, 32G RAM, and the Nvidia GTX1060. The batch size was set to 128 and the training was iterated for 50 epochs.

Parameter sensitivity analysis

The CNN model mainly consisted of convolutional layers, pooling layers, and fully connected layers, among which the pooling layers and dropout were interspersed. In the present study, the parameter sensitivity analysis was carried out by changing some parameters and maintaining other parameters unchanged in each analysis. The parameters involved are the number of convolution layers, the number of convolution kernels, the number of pooling layers, the number of the fully connected layer and the optimizer. Specifically, the number of convolutional layers was chosen from 4, 6 and 8 layers, the size of the convolution kernel in each convolutional layer was chosen from 2, 4, 6, 8, 10 and 12, the number of pooling layers was chosen from 0 to 1, the number of fully connected layers was chosen from 2, 3 and 4 and the optimizer was chosen from AdaGrad, RMSprop (Elyanow et al., 2020) and Adam (Christiansen et al., 2018). After the training, 500 new samples that did not participate in the training and cross-validation process were randomly generated (following the same procedure for generating the 10,000 samples) to assess the predictive ability of the CNN model.

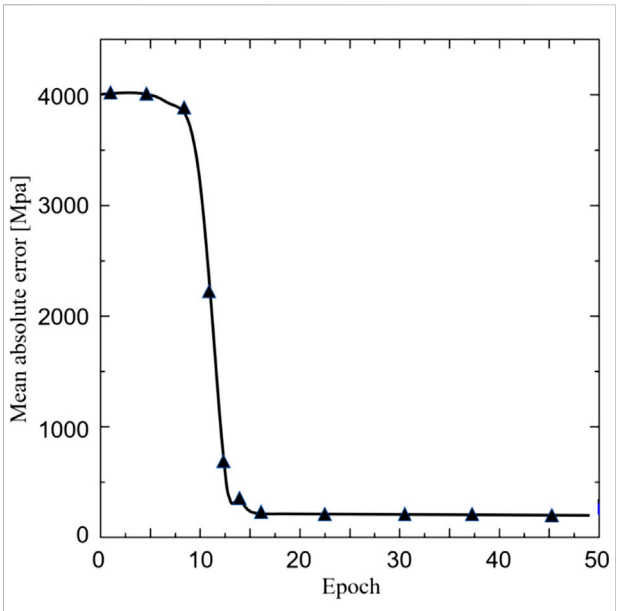

FIGURE 5
The relationship between the mean absolute error and the Epoch.

The samples of porous structures firstly passed through the convolutional layer, then through the pooling layer, and finally through the fully connected layer. Therefore, the parameter sensitivity study was divided into four stages: 1) The sensitivity of the convolutional layer, 2) the sensitivity of the pooling layer, 3) the sensitivity of the fully connected layer and 4) the sensitivity of the optimizer. The best parameter design from the previous stage was retained when entering the next stage. In the initial design, there were 4 convolutional layers, 2 the pooling layers, 3 fully connected layers and the optimizer was RMSprop.

The parameter sensitivity was investigated firstly using the speed of convergence. In the present study, the CNN model was considered convergent when the MAE is stabilized and below 200.0 MPa. It should be noted the convergence condition depends on the applications and could be different in different scenarios. The parameter sensitivity was then

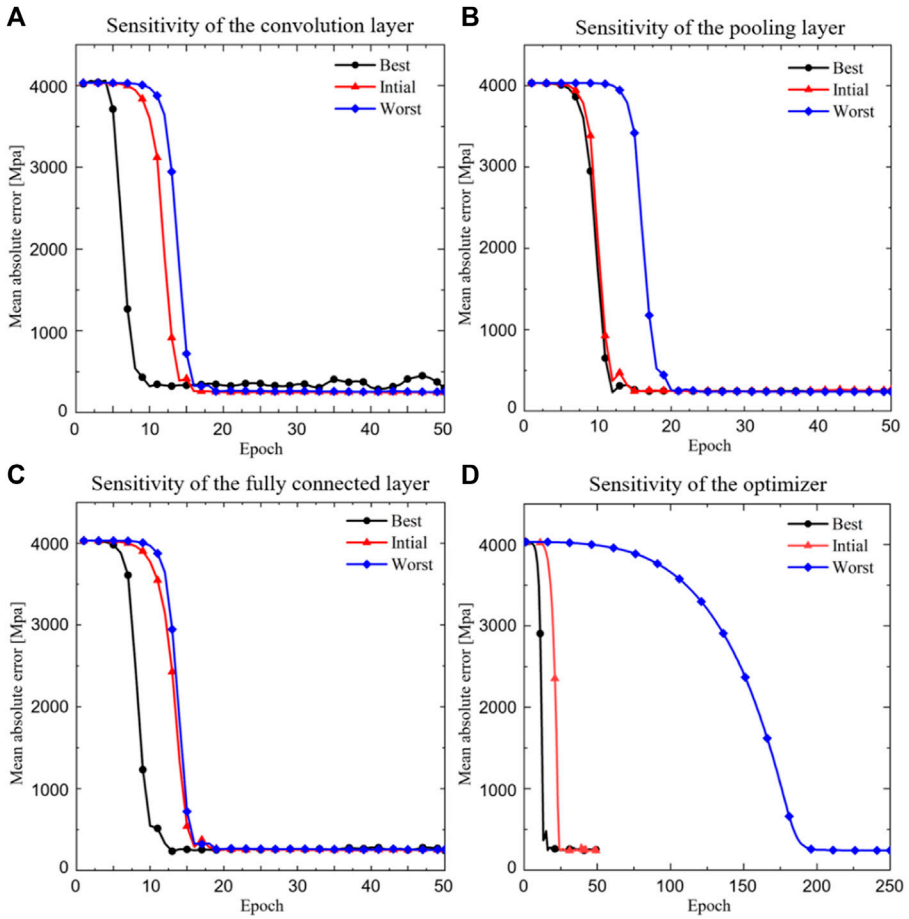

FIGURE 6
The relationship between the mean absolute error and the epoch. **(A)** Sensitivity of the convolution layer; **(B)** Sensitivity of the pooling layer; **(C)** Sensitivity of the fully connected layer and **(D)** Sensitivity of the optimizer ('Best' refers to the case with the fastest iterative convergence speed and the corresponding best parameters are listed in Table 1).

investigated using the relative prediction error (RPE), which is defined as below:

$$\mathrm{RPE} = \frac{\left|P^{\mathrm{CNN}} - P^{\mathrm{RVE}}\right|}{P^{\mathrm{RVE}}} \times 100\% \qquad (2)$$

where P^{CNN} is the effective compressive modulus calculated from the CNN model and P^{RVE} is the corresponding value calculated from the FE analysis.

Result

Training and cross-validation of the CNN model

The relation between the mean absolute error (MAE) and the training iteration is shown in Figure 5. Since the initial values of the weights and biases are randomly assigned, the MAE at the first a few iterations is high. However, after several iterations, the MAE rapidly descends. Therefore, no over-fitting is observed in the cross-validation.

Influence of parameters on the convergence speed and predictive power of CNN model

The influence of parameters in the CNN model on the convergence speed is shown in Figure 6, where the black line represents the fastest convergence speed, the red line represents the initial convergence speed and the blue line represents the slowest convergence speed. It is shown that when the convolutional layer is modified, the convergence of the CNN model can be changed from 10 epochs (the best

TABLE 1 The parameters used in the fastest convergent scenario.

	Number of convolutional layers	Number of convolutional kernels	Number of pooling layers	Number of convolutional layers	Optimizer
(a)	2	2, 4	2	3	RMSprop
(b)	2	2, 4	1	3	RMSprop
(c)	2	2, 4	1	2	RMSprop
(d)	2	2, 4	1	2	Adam

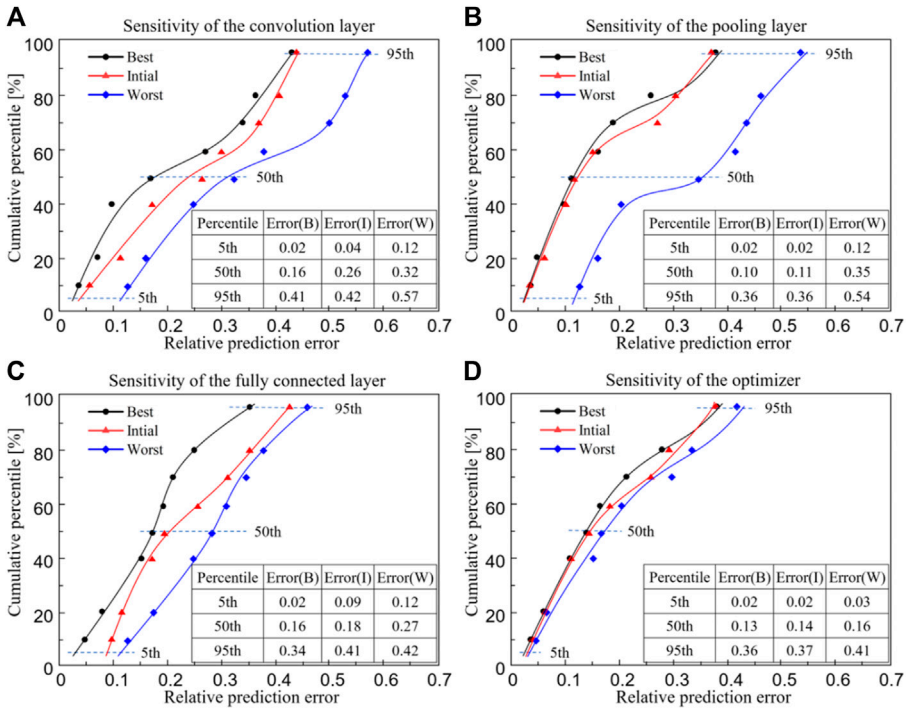

FIGURE 7
The relationship between the cumulative percentile and the relative prediction error from the convolutional neural network model. **(A)** Sensitivity of the convolution layer; **(B)** Sensitivity of the pooling layer; **(C)** Sensitivity of the fully connected layer and **(D)** Sensitivity of the optimizer ('Best' refers to the case with the lowest 95th percentile of relative prediction error and the corresponding best parameters are listed in Table 2).

scenario) to 17 epochs (the worst scenario) (Figure 6A). When the pooling layer is modified, the convergence of the CNN model can be changed from 10 epochs to 20 epochs (Figure 6B). When the fully connected layer is modified, the convergence of the CNN model can be changed from 12 epochs to 18 epochs (Figure 6C). When the optimizer is modified, the convergence of the CNN model can be changed from 10 epochs to 200 epochs (Figure 6D). The best parameters corresponding to Figures 6A–D are listed in Table 1 (a–d).

The influence of parameters in the CNN model on the predictive power is shown in Figure 7, where the black line represents the best prediction, the red line represents the initial prediction and the blue line represents the worst prediction. Since the data are not normally distributed, the 5th, 50th and 95th percentiles are reported. Regarding the 95th percentile of the relative prediction error, it is shown in Figure 7 that when the convolutional layer is modified, the error can be changed from 0.41 (the best scenario) to 0.57 (the worst scenario) (Figure 7A); when the pooling layer is modified, the error can be changed from 0.36 to 0.54 (Figure 7B); when the fully connected layer is modified, the error can be changed from 0.34 to 0.42 (Figure 7C) and when the optimizer is modified, the error can be changed from 0.36 to 0.41 (Figure 7D). The best parameters corresponding to Figures 7A–D are listed in Table 2 (a–d).

TABLE 2 The parameters with the lowest 95th percentile of relative prediction error.

	Number of convolution layers	Number of convolution kernels	Number of pooling layers	Number of convolution layers	Optimizer
(a)	4	2, 4, 6, 8	2	3	RMSprop
(b)	4	2, 4, 6, 8	0	3	RMSprop
(c)	4	2, 4, 6, 8	0	2	RMSprop
(d)	4	2, 4, 6, 8	0	2	Adam

Discussion

In the present study, a convolutional neural network (CNN) model for predicting the effective compressive modulus of the porous structures was developed and a parameter sensitivity analysis was performed to investigate the influence of parameters on the convergence speed and predictive power of the CNN model. The present study showed that the parameter sensitivity analysis is a crucial step in the development of the CNN model and can help optimize the CNN model to improve its efficiency. It should be noted that in the present study, the CNN model was chosen as one representative machine learning model to demonstrate the parameter sensitivity. Nevertheless, the conclusion made in the manuscript, i.e., it is very necessary to conduct a sensitivity analysis when a new model is constructed. Besides, the sensitivity analysis should be not only limited to the CNN model but also applicable to most machine learning and deep learning models.

In the present study, the performance of the CNN model was evaluated using both the iterative convergence speed and the relative prediction error. In terms of the convergence speed, after modifying the convolutional layer, the pooling layer, the fully connected layer and the optimizer, the differences between the best and worst numbers of iterations when CNN models are converged are 7 epochs, 10 epochs, 6 epochs and 190 epochs, respectively. It should be noted that the epochs refer to the iteration number of the CNN model. To increase the prediction accuracy of the CNN model, the CNN model will update its parameters in each iteration (epoch). Therefore, the epochs will increase the performance of the CNN model, and will indirectly affect the performance of the porous structure if the machine learning based inverse design framework is used in the design of porous structures (Wang et al., 2022). Regarding the optimizer, the results showed that the optimizer has the largest impact on the speed of the training convergence, while the fully connected layer has the least impact on the speed of the training convergence. Therefore, it is recommended to choose Adam or RMSprop instead of AdaGrad as the initial optimizer for training the CNN model in the present study. The reason why AdaGrad is slow is that Adaptive Gradient (AdaGrad) can adjust a different learning rate for each different parameter, updating important parameters with smaller steps and less important parameters with larger steps (Duchi et al., 2011). Since the CNN model constructed in the present study is a basic and simple one, the convergence speed of the AdaGrad optimizer is relatively slow. However, it is undeniable that the AdaGrad optimizer would have a good performance in other complex CNN models (Yuan et al., 2019).

Regarding the influence of the parameters in the CNN model on the predictive power of the CNN model, the results showed that the convolutional layer and pooling layer have a larger impact, while the fully connected layer has the least impact. Therefore, to improve the prediction power of the CNN model, it is preferable to adjust the pooling layer and the convolutional layer. It should be noted that the input sample used in this study is a 6×6 matrix and each feature point is equally important. Therefore, increasing the pooling layer would ignore the important feature points, which would reduce the computation time but decrease the prediction power (You et al., 2021). Consequently, the pooling layer has a great influence on the predictive ability of the CNN model in this study. For samples with insignificant feature points, adjusting the convolutional layer may have a larger influence on the predictive power of the CNN model.

It should be noted that in the present study, the 'best' refers to the case with the fastest iterative convergence speed in Figure 6, or the best prediction accuracy in Figure 7, and the 'worst' refers to the case with the slowest iterative convergence speed in Figure 6, or the worst prediction accuracy in Figure 7, and the 'initial' refers to the setting of 4 convolutional layers, 2 the pooling layers, 3 fully connected layers and the optimizer of RMSprop. The initial setting of the parameters is taken from Li et al. (2019). It should be noted that it is hard to find a set of parameters that make the CNN model possess the fastest convergence speed and the best prediction accuracy at the same time. Therefore, depending on the specific requirements, the definition of 'best' would be different in different scenarios. In the present study, the convergence speed and the prediction accuracy were set as two independent parameters in the parameter sensitivity analysis, and consequently the parameters which influence the convergence speed and the prediction accuracy were found respectively. On the other hand, it should be noted that there are two types of parameters in the CNN model. The first is the design

parameters, such as the number of convolutional layers and the pooling layers, etc. These parameters are adjusted one by one and while one parameter is changing, other parameters are maintained until the expected convergence was achieved. The second is the internal parameters of the CNN model, which are adjusted internally and automatically in the training process of the CNN model. In the present study, the Tensorflow is used and thus the changing of the internal parameters cannot be visualized, but they are adjusted by the program itself to increase the predictive ability of the CNN model.

It is shown in the present study that different parameters have different influence s on the performance of the CNN model and thus it is necessary to perform the parameter sensitivity analysis when a new CNN model is constructed and additionally the parameter sensitivity analysis can help optimize the CNN model to improve the computation efficiency. In some previous studies, the sensitivity analysis of the parameters of the sample is performed using the CNN model, but the sensitivity of the parameters of the CNN model itself is always ignored. Furthermore, it should be noted that the parameter sensitivity study of the newly constructed CNN model is always skipped in the previous studies. For example, Xiao et al. (2021) developed a CNN model to evaluate the anisotropic elastic behaviors of trabecular bone. In the study, four different dual energy x-ray absorptiometry (DXA) projections (i.e., one, three, six and nine) and seven DXA image resolutions (i.e., 0.05 mm/pixel, 0.15 mm/pixel, 0.3 mm/pixel, 0.6 mm/pixel, 1.2 mm/pixel, 2.0 mm/pixel and 3.0 mm/pixel) are used to train the CNN model. It should be noted that if the sensitivity analysis of the parameters of CNN was carried out, the prediction power of the CNN model could be further improved. Although the parameter sensitivity analysis of the CNN model is performed in some studies, it is not comprehensive. For example, to predict the mechanical properties of various soils, Ng et al. (2019) identified the important spectral wavelengths using the CNN model. In their study, the sensitivity analysis of only the convolutional layer was investigated and the sensitivity analysis showed that a high prediction power with R^2 = 0.95 can be achieved using a suitable convolutional layer. It can be seen from their study that the sensitivity analysis can help select the parameters that increase the prediction power of the CNN model. However, only the sensitivity of one parameter was investigated in their study. In comparison, in the present study, the sensitivity of most parameters in the CNN model was analyzed.

Some shortcomings in the present study should be noted. First, although the sensitivity of the parameters in the CNN model was investigated in the present study, it still did not consider all the parameters. For example, the size of padding in the convolutional layer (Khanolkar et al., 2021), the choice of the activation function (Leshno et al., 1993), the size of dropout (Srivastava et al., 2014) and other parameters are not considered. There are still many parameters in the CNN model the sensitivity of which still needs to be analyzed. In addition, the sensitivity of the parameters is also different for different input samples. Nevertheless, these do not compromise the message delivered in the present study, i.e., a parameter sensitivity analysis is required to optimize the CNN model when a new model is built. Second, there is a lack of real data support for the experiment to validate the prediction. Nevertheless, the FE modeling technique has been widely accepted as a reliable technique for predicting the effective compressive modulus of porous structure. For example, de Galarreta et al. (2020) performed FE analysis of porous structures to investigate the modulus and yield strength. Besides, the compression test was performed to verify the modulus and yield strength of the structures. The results showed that the FE simulation results were in good agreement with the experimental results, which means FE modeling technique is reliable. Despite this, it is still worthy to validate the predictions of the CNN models, especially for the post-elastic mechanical properties of the porous structure, such as ultimate strength. Third, when using different samples to train the CNN model, the influence of the parameters in the CNN model on the convergence speed and prediction power may be different. Therefore, the results of the present study may not be directly used when training a new CNN model and a new parameter sensitivity analysis is required. Nevertheless, the present study showed that it is crucial to perform a parameter sensitivity analysis when a new CNN model is built, which is always ignored or skipped in the previous studies. Last but not least, 2D analysis instead of 3D was performed in the present study. It should be noted even in the 2D analysis, a large computational complexity was involved, i.e., 10,500 samples and 36 independent design variables in each sample were involved. In the setting of the present study, the number of independent design variables will be exponentially increased for the 3D case, which will create a computational "disaster" in the machine learning study. On the other hand, the 2D-based analysis has played an important role in some applications, such as in the prediction of bone strength using the 2D DXA-based images (Lu et al., 2019). Therefore, despite the 2D analysis being performed, the aim of the present study has been successfully demonstrated, i.e., the importance of parameter sensitivity analysis in the CNN model development and model optimization. On the other hand, in the 3D application, the issues with biocompatible performance of the scaffolds should also be dealt with (Shuai et al., 2020).

Conclusion

In conclusion, it is revealed in the present study that the parameters in the CNN model have a big influence on both the convergence speed and the predictive power. Therefore, it is very necessary to conduct a sensitivity analysis when a new

CNN model is developed. Additionally, the parameter sensitivity analysis can help effectively reduce the training time of the CNN model and improve the prediction power of the CNN model. From the parameter analysis, it is theoretically possible to construct the most suitable CNN model which possesses a fast convergence speed and a high prediction power.

Data availability statement

The original contributions presented in the study are included in the article/Supplementary Material, further inquiries can be directed to the corresponding author.

Author contributions

YL, YH, YN, and ZY: Conceptualization, Methodology, Formal analysis, Investigation, Writing—Original draft. MZ, SB and LL: Resources, Writing—Review and Editing, Supervision.

Funding

This work was supported by the National Natural Science Foundation of China (12072066), the DUT-BSU grant (ICR 2103) and the Fundamental Research Funds for the Central Universities, China (DUT21LK21).

Conflict of interest

The authors declare that the research was conducted in the absence of any commercial or financial relationships that could be construed as a potential conflict of interest.

Publisher's note

All claims expressed in this article are solely those of the authors and do not necessarily represent those of their affiliated organizations, or those of the publisher, the editors and the reviewers. Any product that may be evaluated in this article, or claim that may be made by its manufacturer, is not guaranteed or endorsed by the publisher.

References

Bessa, M. A., Bostanabad, R., Liu, Z., Hu, A., Apley, D. W., Brinson, C., et al. (2017). A framework for data-driven analysis of materials under uncertainty: Countering the curse of dimensionality. *Comput. Methods Appl. Mech. Eng.* 320, 633–667. doi:10.1016/j.cma.2017.03.037

Carneiro, G., Nascimento, J., and Bradley, A. P. (2017). Deep learning models for classifying mammogram exams containing unregistered multi-view images and segmentation maps of lesions. *Deep Learn. Med. Image Analysis* 2017, 321–339.

Christiansen, E. M., Yang, S. J., Ando, D. M., Javaherian, A., Skibinski, G., Lipnick, S., et al. (2018). *In silico* labeling: Predicting fluorescent labels in unlabeled images. *Cell* 173 (3), 792–803. doi:10.1016/j.cell.2018.03.040

Cilla, M., Borgiani, E., Martinez, J., Duda, G. N., and Checa, S. (2017). Machine learning techniques for the optimization of joint replacements: Application to a short-stem hip implant. *Plos One* 12 (9), e0183755. doi:10.1371/journal.pone.0183755

Conev, A., Litsa, E., and Perez, M. (2020). Machine learning guided 3D printing of tissue engineering scaffolds. *Tissue Eng. Part A* 26 (23–24), 1359–1368. doi:10.1089/ten.tea.2020.0191

de Galarreta, S. R., Jeffers, J. R. T., and Ghouse, S. (2020). A validated finite element analysis procedure for porous structures. *Mat. Des.* 189, 108546. doi:10.1016/j.matdes.2020.108546

Duchi, J., Hazan, E., and Singer, Y. (2011). Adaptive subgradient methods for online learning and stochastic optimization. *J. Mach. Learn. Res.* 12 (61), 2121–2159.

Elyanow, R., Dumitrascu, B., Engelhardt, B. E. NetN. M. F-S. C., and Raphael, B. J. (2020). netNMF-sc: leveraging gene–gene interactions for imputation and dimensionality reduction in single-cell expression analysis. *Genome Res.* 30 (2), 195–204. doi:10.1101/gr.251603.119

Graczyk, K. M., and Matyka, M. (2020). Predicting porosity, permeability, and tortuosity of porous media from images by deep learning. *Sci. Rep.* 10 (1), 1–11. doi:10.1038/s41598-020-78415-x

Gu, G. X., Chen, C. T., Richmond, D. J., and Buehler, M. J. (2018). Bioinspired hierarchical composite design using machine learning: Simulation, additive manufacturing, and experiment. *Mat. Horiz.* 5 (5), 939–945. doi:10.1039/c8mh00653a

Khanolkar, P. M., Mccomb, C. C., and Basu, S. (2021). Predicting elastic strain fields in defective microstructures using image colorization algorithms. *Comput. Mater. Sci.* 186, 110068. doi:10.1016/j.commatsci.2020.110068

Leshno, M., Lin, V. Y., Pinkus, A., and Schocken, S. (1993). Multilayer feedforward networks with a nonpolynomial activation function can approximate any function. *Neural Netw.* 6 (6), 861–867. doi:10.1016/s0893-6080(05)80131-5

Li, X., Liu, Z., Cui, S., Luo, C., Li, C., and Zhuang, Z. (2019). Predicting the effective mechanical property of heterogeneous materials by image based modeling and deep learning. *Comput. Methods Appl. Mech. Eng.* 347, 735–753. doi:10.1016/j.cma.2019.01.005

Lu, Y., Zhu, Y., Krause, M., Huber, G., and Li, J. (2019). Evaluation of the capability of the simulated dual energy X-ray absorptiometry-based two-dimensional finite element models for predicting vertebral failure loads. *Med. Eng. Phys.* 69, 43–49. doi:10.1016/j.medengphy.2019.05.007

Ng, W., Minasny, B., Montazerolghaem, B., Padarian, J., Ferguson, R., Bailey, S., et al. (2019). Convolutional neural network for simultaneous prediction of several soil properties using visible/near-infrared, mid-infrared, and their combined spectra. *Geoderma* 352, 251–267. doi:10.1016/j.geoderma.2019.06.016

Niinomi, M. (1998). Mechanical properties of biomedical titanium alloys. *Mater. Sci. Eng. A* 243 (1-2), 231–236. doi:10.1016/s0921-5093(97)00806-x

Paul, S., and Bhattacharjee, S. (2018). Modeling and computation by artificial neural network of fracture toughness of low alloy steel to study the effect of alloy composition. *Int. J. Model. Simul. Sci. Comput.* 9 (6), 1850051. doi:10.1142/s1793962318500514

Rubio, J., Angelov, P., and Pacheco, J. (2011). Uniformly stable backpropagation algorithm to train a feedforward neural network. *IEEE Trans. Neural Netw.* 22 (3),

356–366. doi:10.1109/tnn.2010.2098481

Shuai, C., Liu, G., Yang, Y., Qi, F., Peng, S., Yang, W., et al. (2020). A strawberry-like Ag-decorated barium titanate enhances piezoelectric and antibacterial activities of polymer scaffold. *Nano Energy* 74, 104825. doi:10.1016/j.nanoen.2020.104825

Srivastava, N., Hinton, G., and Krizhevsky, A. (2014). Dropout: A simple way to prevent neural networks from overfitting. *J. Mach. Learn. Res.* 15 (1), 1929–1958.

Tan, R. K., Zhang, N. L., and Ye, W. (2020). A deep learning–based method for the design of microstructural materials. *Struct. Multidiscipl. Optim.* 61 (4), 1417–1438. doi:10.1007/s00158-019-02424-2

Wang, J., Wang, Y., and Chen, Y. (2022). Inverse design of materials by machine learning. *Materials* 15 (5), 1811. doi:10.3390/ma15051811

Wang, Y., Arns, C. H., Rahman, S. S., and Arns, J. Y. (2018). Porous structure reconstruction using convolutional neural networks. *Math. Geosci.* 50 (7), 781–799. doi:10.1007/s11004-018-9743-0

Wu, C., Entezari, A., Zheng, K., Fang, J., Zreiqat, H., Steven, G. P., et al. (2021). A machine learning-based multiscale model to predict bone formation in scaffolds. *Nat. Comput. Sci.* 1 (8), 532–541. doi:10.1038/s43588-021-00115-x

Wu, H., Fang, W. Z., Kang, Q., Tao, W. Q., and Qiao, R. (2019). Predicting effective diffusivity of porous media from images by deep learning. *Sci. Rep.* 9 (1), 1–12. doi:10.1038/s41598-019-56309-x

Xiao, P., Haque, E., Zhang, T., Dong, X. N., Huang, Y., and Wang, X. (2021). Can DXA image-based deep learning model predict the anisotropic elastic behavior of trabecular bone? *J. Mech. Behav. Biomed. Mater.* 124, 104834. doi:10.1016/j.jmbbm.2021.104834

Yamashita, R., Nishio, M., Do, R. K. G., and Togashi, K. (2018). Convolutional neural networks: An overview and application in radiology. *Insights Imaging* 9 (4), 611–629. doi:10.1007/s13244-018-0639-9

You, H., Yu, L., TianMC-Net, S., Ma, X., Xing, Y., Xin, N., et al. (2021). MC-Net: Multiple max-pooling integration module and cross multi-scale deconvolution network. *Knowledge-based Syst.* 23, 107456. doi:10.1016/j.knosys.2021.107456

Yuan, H., Kshirsagar, M., Zamparo, L., Lu, Y., and Leslie, C. S. (2019). BindSpace: Decodes transcription factor binding signals by large-scale sequence embedding. *Nat. Methods* 16 (9), 858–861. doi:10.1038/s41592-019-0511-y

frontiers | Frontiers in Bioengineering and Biotechnology

TYPE Original Research
PUBLISHED 27 September 2022
DOI 10.3389/fbioe.2022.937239

Check for updates

OPEN ACCESS

EDITED BY
Dmitriy Sheyn,
Cedars Sinai Medical Center,
United States

REVIEWED BY
Zhen Li,
AO Research Institute, Switzerland
Thomas J. Kean,
University of Central Florida,
United States
Nadeen Chahine,
Columbia University, United States

*CORRESPONDENCE
Lauren E. Flynn,
lauren.flynn@uwo.ca
Cheryle A. Séguin,
cheryle.seguin@schulich.uwo.ca

SPECIALTY SECTION
This article was submitted to Biomaterials, a section of the journal Frontiers in Bioengineering and Biotechnology

RECEIVED 06 May 2022
ACCEPTED 30 August 2022
PUBLISHED 27 September 2022

CITATION
Herrera Quijano MA, Sharma N, Morissette Martin P, Séguin CA and Flynn LE (2022), Development of 2-D and 3-D culture platforms derived from decellularized nucleus pulposus. *Front. Bioeng. Biotechnol.* 10:937239. doi: 10.3389/fbioe.2022.937239

COPYRIGHT
© 2022 Herrera Quijano, Sharma, Morissette Martin, Séguin and Flynn. This is an open-access article distributed under the terms of the Creative Commons Attribution License (CC BY). The use, distribution or reproduction in other forums is permitted, provided the original author(s) and the copyright owner(s) are credited and that the original publication in this journal is cited, in accordance with accepted academic practice. No use, distribution or reproduction is permitted which does not comply with these terms.

Development of 2-D and 3-D culture platforms derived from decellularized nucleus pulposus

Marco A. Herrera Quijano[1,2], Nadia Sharma[2,3], Pascal Morissette Martin[1], Cheryle A. Séguin[2,4]* and Lauren E. Flynn[1,2,3,5]*

[1]Department of Anatomy and Cell Biology, Schulich School of Medicine and Dentistry, The University of Western Ontario, London, ON, Canada, [2]Bone and Joint Institute, The University of Western Ontario, London, ON, Canada, [3]School of Biomedical Engineering, The University of Western Ontario, London, ON, Canada, [4]Department of Physiology and Pharmacology, Schulich School of Medicine and Dentistry, The University of Western Ontario, London, ON, Canada, [5]Department of Chemical and Biochemical Engineering, Faculty of Engineering, The University of Western Ontario, London, ON, Canada

Bioscaffolds derived from the extracellular matrix (ECM) have shown the capacity to promote regeneration by providing tissue-specific biological instructive cues that can enhance cell survival and direct lineage-specific differentiation. This study focused on the development and characterization of two-dimensional (2-D) and three-dimensional (3-D) cell culture platforms incorporating decellularized nucleus pulposus (DNP). First, a detergent-free protocol was developed for decellularizing bovine nucleus pulposus (NP) tissues that was effective at removing cellular content while preserving key ECM constituents including collagens, glycosaminoglycans, and the cell-adhesive glycoproteins laminin and fibronectin. Next, novel 2-D coatings were generated using the DNP or commercially-sourced bovine collagen type I (COL) as a non-tissue-specific control. In addition, cryo-milled DNP or COL particles were incorporated within methacrylated chondroitin sulphate (MCS) hydrogels as a 3-D cell culture platform for exploring the effects of ECM particle composition. Culture studies showed that the 2-D coatings derived from the DNP could support cell attachment and growth, but did not maintain or rescue the phenotype of primary bovine NP cells, which de-differentiated when serially passaged in monolayer culture. Similarly, while bovine NP cells remained highly viable following encapsulation and 14 days of culture within the hydrogel composites, the incorporation of DNP particles within the MCS hydrogels was insufficient to maintain or rescue changes in NP phenotype associated with extended *in vitro* culture based on gene expression patterns. Overall, DNP produced with our new decellularization protocol was successfully applied to generate both 2-D and 3-D bioscaffolds; however, further studies are required to assess if these platforms can be combined with additional components of the endogenous NP microenvironment to stimulate regeneration or lineage-specific cell differentiation.

KEYWORDS

intervertebral disc (IVD) degeneration, nucleus pulposus, decellularization, extracellar matrix, coatings, hydrogel composite, methacrylated chondroitin sulphate, cell culture models

1 Introduction

Low back pain (LBP) is the leading cause of disability worldwide (Murray et al., 2013), with a predicted lifetime prevalence of 80% (Balagué et al., 2012). While multifactorial, back pain has been associated with degeneration of the intervertebral disc (IVD) (Freemont 2009; DePalma, Ketchum, and Saullo 2011). IVD degeneration is marked by decreased IVD height, reduced nucleus pulposus (NP) hydration associated with a decrease in sulphated glycosaminoglycans (sGAGs) in the extracellular matrix (ECM), loss of the distinct NP-annulus fibrosus (AF) boundary, and fibrosis of the NP, leading to an inability of the IVD to withstand compressive loads (Roughley 2004; Inoue et al., 2012). Within the NP there is a shift towards greater ECM catabolism, cell senescence, apoptosis, inflammation, and in-growth of vasculature and nociceptive nerves (Freemont 2009).

Given the lack of disease-modifying interventions for disc degeneration, research has focused on engineering regenerative strategies targeting the NP (Yang and Li 2009; Fiordalisi et al., 2020). While cell therapies have shown promise (Schol and Sakai 2019), long-term cell survival may be impacted by the harsh microenvironment within the degenerated NP, limiting their therapeutic efficacy (Ludwinski et al., 2013). Moreover, direct IVD cell injections often result in cell leakage from the injection site (Vadalà et al., 2012). Cell encapsulation within biomaterial scaffolds offers a potential solution to support cell retention, survival and function *in vivo* by protecting the cells from the adverse inflammatory microenvironment associated with IVD degeneration (Drury and Mooney 2003; O'Halloran and Pandit 2007). Considerable research has focused on exploring the effects of various cell delivery platforms on regenerative cell populations (Drury and Mooney 2003; Gruber et al., 2004; O'Halloran and Pandit 2007; Tang et al., 2020), including studies suggesting that tissue-specific ECM can be harnessed to direct the lineage-specific differentiation of stem or progenitor cells (Lin et al., 2016; Robb et al., 2018; Zhou et al., 2018).

To fabricate ECM-derived bioscaffolds, decellularization techniques have been developed to remove immunogenic cellular components from tissues, while striving to preserve the native ultrastructure and cell-instructive biochemical composition of the ECM (Crapo et al., 2011). Various groups have reported NP decellularization protocols that can extract cellular content to obtain scaffolds enriched in structural ECM components (Wachs et al., 2017; Piening et al., 2022; Illien-Jünger et al., 2016; Mercuri, Gill, and Simionescu 2011; Fernandez et al., 2016; Xu et al., 2019; Chan et al., 2013). Despite its low cellularity, decellularization of the NP is challenging because it contains a high concentration of GAGs that are more easily extracted during processing as compared to highly crosslinked collagens (Tsuchiya et al., 2014; Peloso et al., 2016; Hanai et al., 2020). To date, the published NP decellularization protocols involve treatment with various types of detergents including Triton X-100, Triton X-200, sodium deoxycholate and sodium dodecyl sulphate (SDS). Notably, detergents can affect protein structure and have been reported to cause loss of GAGs and growth factors from a variety of tissues (Gilbert et al., 2006; Gilpin and Yang 2017). In addition, residual detergent can potentially have cytotoxic effects if not adequately cleared at the end of processing (Crapo et al., 2011). As such, our initial goal was to establish a detergent-free protocol for the decellularization of bovine NP that preserved collagens and GAGs.

Applying decellularized tissues in their intact form offers limited flexibility in terms of the scaffold properties. As such, there is great interest in the development of more customizable ECM-derived scaffold formats that incorporate the tissue-specific ECM composition within platforms that enable greater tuning of cell-cell and cell-ECM interactions. Using decellularized adipose tissue (DAT) as an ECM source, our team has previously established methods for fabricating novel ECM-derived coatings, microcarriers, foams, and hydrogel composites (Cheung et al., 2014; Kornmuller et al., 2017; Yu et al., 2017; Shridhar et al., 2019; Shridhar et al., 2020). Importantly, we demonstrated that the pro-adipogenic properties of the DAT in directing the differentiation of human adipose-derived stromal cells (ASCs) were conserved in these various platforms (Turner et al., 2012; Yu et al., 2013; Cheung et al., 2014; Shridhar et al., 2019). Supporting the potential of ECM-derived bioscaffolds in the context of IVD regeneration, Wachs et al. (2017) used pepsin digestion to generate decellularized nucleus pulposus (DNP) hydrogels capable of *in situ* gelation, which promoted human NP cell viability and GAG production. In another approach, Zhou et al. (2018) combined micronized porcine DNP with chondroitin sulphate to counteract the loss of GAGs observed following detergent-based decellularization and crosslinked the materials with genipin to create an injectable DNP-based cell delivery system. Encapsulation of human ASCs within the composite DNP-based material was reported to induce NP-like differentiation and the synthesis of aggrecan and type II collagen (Zhou et al., 2018).

Building from this foundation and using our approaches previously developed for adipose tissue, we incorporated the DNP generated with our new detergent-free decellularization protocol within 2-D coatings and 3-D methacrylated chondroitin sulphate (MCS) hydrogels. MCS was selected as it provides a cell-supportive matrix (Cheung et al., 2014; Shridhar et al., 2019) mimicking the proteoglycan-rich ECM of the native NP, in which aggrecan incorporating a high content of chondroitin sulphate side chains is the most abundant proteoglycan (Collin et al., 2017). We subsequently tested these platforms for their effects on primary bovine NP cell viability and phenotype *in vitro* in comparison to controls generated with commercially-sourced collagen type I to assess whether the tissue-specific ECM could help to maintain or restore the differentiated phenotype of the NP cells in culture.

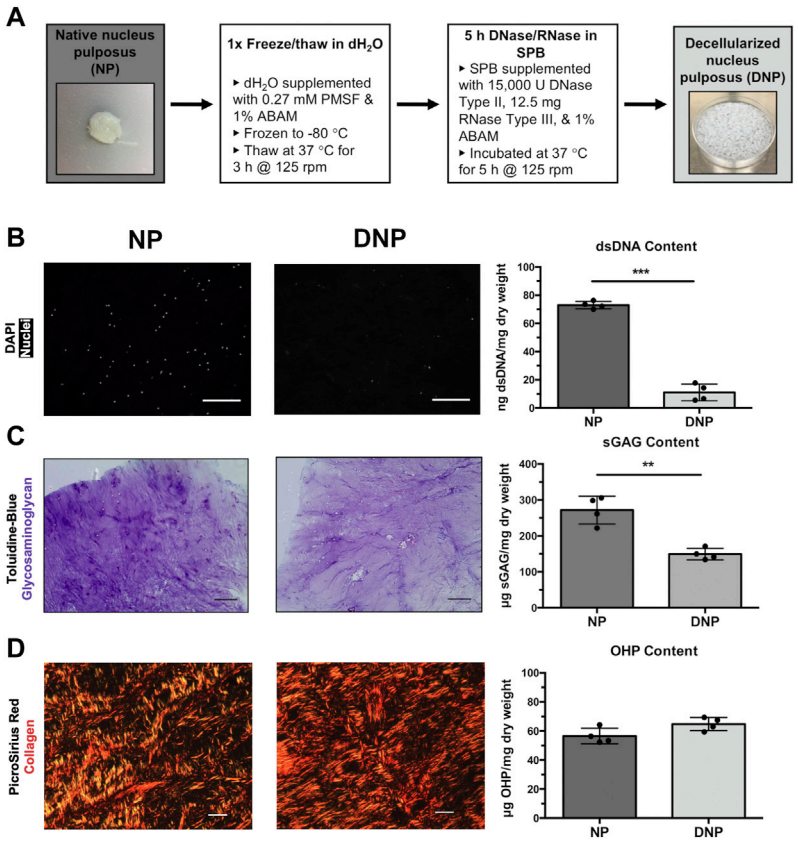

FIGURE 1
Detergent-free NP decellularization protocol effectively extracts cellular content while retaining sulphated glycosaminoglycan (sGAG) and collagen content from native NP. **(A)** Schematic of detergent-free decellularization protocol. **(B)** Representative DAPI stained sections of native nucleus pulposus tissue (NP) and decellularized NP (DNP) showed a reduction in cell nuclei (pseudo-coloured in white) following decellularization. Scale bars = 200 µm. PicoGreen quantification showed a significant reduction in dsDNA content in the DNP relative to the native NP. **(C)** Representative histological sections of NP and DNP stained with Toluidine blue detected GAGs (purple) throughout both DNP and native NP tissue sections, although staining intensity appeared to be reduced within DNP relative to NP. DMMB analysis showed ~45% retention of sGAG content within the DNP relative to the native NP. **(D)** Representative PicroSirus Red staining of NP and DNP imaged by polarized light microscopy. Staining revealed a complex network of collagen fibers, with similar patterns detected in the DNP and native NP tissues. Hydroxyproline (OHP) quantification as a measure of total collagen content showed no significant difference between DNP and native NP tissues. Scale bars = 200 µm. Data reported as mean ± SD (N = 4), $^{**}p < 0.001$, $^{***}p < 0.0001$.

2 Methods

2.1 Materials

Unless otherwise stated, all reagents were purchased from Sigma Aldrich Canada Ltd. and used as received (Oakville, Canada).

2.2 Bovine nucleus pulposus decellularization

Bovine tails were acquired from female cows (18–24 months of age) at the Mount Brydges Abattoir within 2 h post-mortem. Tails were stored at −20°C until use and then thawed overnight at 4°C prior to dissection. The musculature and soft connective tissues surrounding the vertebrae were removed under aseptic conditions. The nucleus pulposus was isolated from the IVDs of the five to six most proximal motion segments from each tail and placed in sterile 1x phosphate-buffered saline (PBS). Pooled NP tissues were minced into 2 mm^3 pieces using a scalpel and 2 mm biopsy punch.

For decellularization, 100 ml of solution was used per ~15 g starting mass of NP, with all processing steps performed at 37°C under agitation on an orbital shaker (125 rpm). All decellularization solutions were supplemented with 1% antibiotic-antimycotic (ABAM) (Gibco®, Invitrogen, Burlington, Canada) solution and 0.27 mM of the protease inhibitor phenylmethylsulfonyl fluoride (PMSF). The minced NP was frozen at −80°C in deionized water (dH_2O) overnight

and subsequently thawed at 37°C over 3 h to promote cell lysis. The tissues were then enzymatically digested for 5 h with 15,000 U DNase Type II (from bovine pancreas) and 12.5 mg RNase Type III (from bovine pancreas) in Sorensen's phosphate buffer digest solution (SPB digest) comprised of 0.17 M KH_2PO_4, 0.55 M $Na_2HPO_4{\cdot}7H_2O$, and 0.049 M $MgSO_4{\cdot}7H_2O$, (pH 7.3). The resultant decellularized nucleus pulposus (DNP) samples were washed three times for 30 min in PBS prior to freezing at −80°C in dH_2O and lyophilization for 72 h (Figure 1A). NP tissues from six tails were combined to generate a single batch of DNP for subsequent use in all studies.

2.3 Preparation of DNP/COL particles and coatings

DNP and commercially-sourced bovine type I collagen (COL) (Advanced Biomatrix, Cat # 5164-5GM, Carlsbad, United States) were cryo-milled for synthesis of DNP and COL particles using previously-established methods (Shridhar et al., 2020, 2019). In brief, cryo-milling was performed by transferring 1 g of lyophilized DNP or COL into a 25 ml milling chamber with two 10 mm stainless steel milling balls. The chamber was sealed, submerged in liquid nitrogen for 3 min, then milled for 3 min at 30 Hz (Retsch Mixer Mill MM 400 milling system). This cycle was repeated a total of three times. Cryo-milled particles were sieved through a 125 µm stainless steel mesh, and the particles that passed through the filter were collected and stored in a desiccator until further use.

To generate the ECM suspensions used to fabricate the coatings, the DNP or COL particles were added at a concentration of 25 mg/ml to 0.3% (w/w) α-amylase in 0.22 M NaH_2PO_4 (pH 5.4). The samples were digested under continuous agitation on an orbital shaker at 300 rpm for 72 h at room temperature, followed by centrifugation at 1,500 × *g* for 10 min. The digested DNP or COL pellet was rinsed twice with 10 ml of 5% (w/v) NaCl solution and once in dH_2O under agitation (300 rpm) at room temperature for 10 min, and then resuspended in 0.2 M acetic acid at a concentration of 25 mg/ml (based on the initial dry mass). The samples were incubated under agitation at 120 rpm overnight at 37°C and then homogenized using a Polytron® benchtop homogenizer (Thomas Scientific, Swedesboro, United States) to generate a uniform suspension, which was stored at 4°C until further use.

Working under aseptic conditions within a biological safety cabinet, the suspensions were applied to coat the surface of tissue culture plastic (TCP) multi-well plates (125 µl/cm^2) and left to dry overnight. Prior to culture, the coatings were decontaminated by rinsing three times in fresh 70% ethanol diluted with sterile dH_2O for 30 min, and then rehydrated by incubation for 30 min in 35% ethanol, followed by three rinses in sterile PBS and two rinses in complete NP media [DMEM supplemented with 10% fetal bovine serum (FBS) and 1% penicillin/streptomycin (P/S)] prior to cell seeding.

2.4 Preparation of composite MCS ± DNP/COL hydrogel scaffolds

Composite methacrylated chondroitin sulphate (MCS) hydrogels incorporating DNP or COL particles were synthesized using previously-established photo-polymerization methods (Cheung et al., 2014). MCS was first synthesized through the methacrylation of chondroitin sulphate (50 kDa, LKT Laboratories Inc., St. Paul, United States) with methacrylate anhydride, following previously established protocols (Shridhar et al., 2017), to obtain a final degree of methacrylation of 17%, as confirmed by ^{1}H NMR spectroscopy on an Inova 600 NMR spectrometer (Varian, United States) (Supplementary Figure 1).

MCS was added to PBS (for mechanical testing) or dH_2O (for gel content analysis) at a concentration of 20% (w/v). The sieved cryo-milled DNP or COL particles were then added to the MCS pre-polymer solution at a concentration of 5% (w/v), selected based on pilot studies that demonstrated it was the highest concentration that could be reproducibly added without interfering with hydrogel crosslinking. The MCS pre-polymer solution was left to dissolve overnight under agitation (100 rpm) at 37°C. Immediately prior to crosslinking, Irgacure 2959 photo-initiator was dissolved in PBS (5 mg/ml) for 2.5 h, sterile filtered, and incorporated into the MCS pre-polymer solution at a final concentration of 0.05% (w/v). The pre-gel solutions were then transferred into 1 ml syringe molds (ThermoFisher Scientific Inc.), and photo-crosslinked for 2 min on each side (4 min total) through exposure to long-wavelength ultraviolet light (365 nm, intensity of 12 mW/cm^2).

2.5 DNP characterization

2.5.1 Histology

To confirm decellularization and assess the presence and distribution of glycosaminoglycans (GAGs) and collagen, DNP and native NP tissue samples were fixed, paraffin-embedded, and sectioned at a thickness of 7 µm, prior to staining with either 4′,6-diamidino-2-phenylindole (DAPI), Toluidine blue (0.1%, Sigma), or Picrosirius red (1.3% picric acid and 0.1% direct red 80 (Sigma)), using previously established methods (Shridhar et al., 2019, 2020). DAPI staining was visualized using an EVOS FL fluorescence microscope (ThermoFisher Scientific Inc.), and Toluidine blue and PicroSirius Red staining were visualized using an EVOS XL Core microscope (ThermoFisher Scientific Inc., Burlington, Canada) and a Nikon Optiphot polarizing microscope (Nikon Instruments Inc., Melville, United States), respectively.

2.5.2 Immunohistochemical characterization of ECM composition

Immunohistochemical (IHC) staining was performed to assess the presence and distribution of ECM components within the minced DNP samples relative to native NP tissue controls. In brief, the samples were fixed and embedded in Tissue-Tek OCT compound (Sakura Finetek, Torrance, United States), snap frozen in liquid nitrogen, and cryo-sectioned (7 µm transverse sections). Tissue sections were fixed in acetone, blocked in 10% goat serum in Tris-buffered saline supplemented with 0.1% Tween (TBST), and incubated for 1 h at 4°C with primary antibodies diluted in TBST with 2% BSA against: collagen type I (1:100, ab34710, Abcam, Toronto, Canada), collagen type II (1:200, ab34712, Abcam), collagen type V (1:300, ab7046, Abcam), collagen type VI (1:300, ab6588, Abcam), fibronectin (1:150, ab23750, Abcam), laminin (1:200, ab11575, Abcam), or keratan sulphate (1:200, sc73518, Santa Cruz, Biotechnology). Detection was carried out with either a goat anti-rabbit IgG secondary antibody conjugated to Alexa Fluor 594 (1:200, ab150080, Abcam) or a goat anti-mouse IgG secondary antibody conjugated to Alexa Fluor 680 (1:200, ab175775, Abcam), in 2% BSA in TBST for 1 h at room temperature. Slides were mounted in fluoroshield mounting medium (Abcam). No primary antibody controls were included for all experiments. Images were acquired using a EVOS FL fluorescence microscope (Thermo Fisher Scientific Inc.).

2.5.3 Biochemical characterization of DNP and COL platforms

For biochemical analyses to quantitatively assess cell content, as well as retention of sulphated GAG (sGAG) and collagen content following decellularization, DNP and native NP samples were lyophilized and cryo-milled as described above without sieving, and then incubated in a digestion buffer comprised of 100 nM Na_2HPO_4, 5 mM EDTA, and 5 mM L-Cysteine in dH_2O (pH 6.5) supplemented with 125 µg/ml of papain at 60°C for ~18 h. dsDNA content was quantified using the Quant-iT™ PicoGreen® dsDNA kit (Invitrogen) according to the manufacturer's instructions. sGAG and collagen content were quantified using the dimethylmethylene blue (DMMB) and hydroxyproline (OHP) assays, respectively, based on published methods (Martin et al., 2019). The resulting data was normalized to the initial dry mass of each sample. In addition, the DMMB and OHP assays were performed following similar methods to quantify the sGAG and collagen content in the sieved DNP and COL particles, as well as the DNP and COL coatings.

2.5.4 SEM analysis of DNP and COL particle and coating ultrastructure

SEM analysis was used to visualize the ultrastructure of the sieved and lyophilized DNP and COL particles, as well as the DNP and COL coatings, using established protocols (Shridhar et al., 2020). To visualize their interior structure, the DNP and COL coatings were scratched using a scalpel blade and then lyophilized. Briefly, the dry samples were coated with osmium prior to imaging with a LEO 1530 microscope at an accelerating voltage of 1–2 kV and working distance of 4–6 mm.

2.5.5 DNP and COL particle size analysis

To determine their particle size distributions, cryo-milled and sieved DNP and COL particle samples were analyzed using a Malvern Mastersizer 2000 (Malvern Instruments Ltd., Worcestershire, United Kingdom). In brief, ~300 mg samples of the particles were rehydrated in dH_2O and analyzed according to manufacturer's instructions (Brown and Flynn. 2015).

2.6 Composite hydrogel characterization

Gel content analysis of the MCS ± DNP/COL hydrogels was performed to quantify the amount of the MCS pre-polymer that was incorporated into the hydrogel network and confirm that the ECM particles were not interfering with the crosslinking efficiency, following published protocols (Cheung et al., 2014).

In addition, unconfined compression testing was performed to compare the bulk compressive properties of the MCS ± DNP/COL hydrogels. To generate consistent scaffolds sized for mechanical testing, 110 µl cell-free single-phase (MCS only) and composite MCS + DNP/COL hydrogels were synthesized and photo-crosslinked individually within the syringe molds. Following photo-crosslinking, the hydrogels were equilibrated overnight in PBS at 37°C. Immediately prior to mechanical testing, the height and diameter of the hydrogels were measured using digital calipers, to confirm the samples had a height to diameter ratio of ~1.5. Unconfined compression testing was carried out using a UniVert system (CellScale Biomaterials Testing, Waterloo, Canada) fitted with a 0.5 N load cell and a PBS bath maintained at 37°C. Samples were subjected to two pre-conditioning cycles to a maximum of 10% strain at a rate of 0.05%/s. The hydrogels then underwent four cycles of cyclic compression testing with a 0.01 N preload applied at the beginning of each cycle, and a maximum strain of 10% at a rate of 0.05%/s per cycle (Shridhar et al., 2019). Young's moduli were calculated from the slope of the linear region of the nominal stress-strain curve, with the stress values at 7% and 10% strain being used as the boundary conditions.

2.7 2-D and 3-D cell culture studies

2.7.1 Primary bovine NP cell isolation and culture

Primary NP cells were isolated from bovine IVD tissues using previously published methods (Séguin et al., 2004). For each cell isolation, NP tissues were pooled from the five to six most proximal motion segments from two tails (female cows,

18–24 months of age). Isolated NP cells were seeded at an initial density of 25,000 cells/cm^2 onto TCP dishes (ThermoFisher Scientific Inc.) and maintained in complete NP media (DMEM, 10% FBS, 1% P/S) at 37°C and 5% CO_2. Cells seeded directly following isolation were designated as passage 0 (P0). Culture media was changed every 2 days and the cells were passaged at 85%–90% confluence (approximately 5 days).

2.7.2 Cell seeding/passaging on the DNP/COL coatings

Culture studies were performed using the DNP and COL coatings to assess whether culturing on the tissue-specific ECM could help to maintain the phenotype of NP cells serially passaged in monolayer culture. For these studies, NP cells (P0) were seeded at a density of 25,000 cells/cm^2 on the DNP coatings, COL coatings, or uncoated TCP controls and cultured until the TCP cells reached ~85% confluence (37°C, 5% CO_2). The NP cells cultured on the ECM coatings were passaged by digesting the DNP or COL with 0.25% collagenase A in serum-free media (DMEM supplemented with 1% P/S) for 45 min at 37°C, with pipetting every 15 min. The TCP control cells were passaged using trypsin (Gibco). The isolated cells were centrifuged at 1,200 × *g* for 5 min, washed once in complete NP media, and then resuspended in complete NP media and re-seeded on their respective coatings at 25,000 cells/cm^2. This process was repeated to generate cells from P0 to P3 for viability and gene expression analyses, described in detail below. Time in culture to target confluence was ~5 days for P0 cells and ~3 days for cells between P1 and P3.

Additional studies were performed to assess the ability of the DNP coatings to rescue the phenotype of de-differentiated NP cells. For these studies, samples of the bovine NP cells were serially passaged on TCP to passage 3 (P3) to generate the de-differentiated cells. Un-passaged (P0) or de-differentiated (P3) NP cells were seeded onto the DNP coatings, COL coatings, or uncoated TCP at a density of 25,000 cells/cm^2 and cultured for 2 or 4 days (37°C, 5% CO_2).

2.7.3 Cell encapsulation within the composite MCS hydrogels

3-D culture studies were performed to assess the effects of incorporating the tissue-specific ECM particles on the viability and phenotype of bovine NP cells encapsulated within the MCS hydrogels. Prior to cell culture, the MCS was decontaminated under UV light for 30 min and the DNP/COL particles were decontaminated in 70% ethanol overnight, followed by three successive 1 h rinses in PBS. For the studies, P0 or P3 NP cells were trypsin released, centrifuged (1,200 × *g* for 5 min) and resuspended in complete NP media at a concentration of 2 × 10^7 cells/ml. The NP cell suspension (20% v/v) was combined with the MCS pre-polymer solution (80% v/v), the samples were well mixed with an 18G needle, and crosslinking was performed as described above. The photo-crosslinked hydrogels were extruded from the syringe molds and cut into 50 µl sized scaffolds, each containing ~1 × 10^6 NP cells. The hydrogels were cultured individually within low-adherence 12-well tissue culture plates (Sarstedt, Nümbrecht, Germany) in NP media at 37°C under 5% CO_2.

2.8 LIVE/DEAD® cell viability characterization

Confocal imaging using a LIVE/DEAD® Viability/Cytotoxicity Assay (Invitrogen) was performed to assess the viability and distribution of cells on the 2-D and 3-D culture platforms, as previously reported (Shridhar et al., 2019). NP cells were imaged on the 2-D coatings or TCP controls from P0 to P3. Within the 3-D hydrogels, cells were imaged at 24 h, 72 h, 7 days, and 14 days post-encapsulation. Imaging was performed using a Zeiss LSM800 Confocal Microscope with Airyscan. Images were acquired at ×5 magnification using the tiling function and z-stack features to visualize the entire cross-section of each hydrogel at three to four depths, separated by 50 µm, starting at the surface of the gel.

2.9 RT-qPCR gene expression analysis

For the 2-D coating studies, the cells were collected in 1 ml PureZOL (Bio-Rad Laboratories, Mississauga, Canada) with the use of a cell scraper. For the DNP or COL coatings, the samples were sonicated three times using a Model 100 Sonic Dismembrator (ThermoFisher Scientific Inc.) in 3 s bursts. For the cells cultured within the MCS ± DNP/COL hydrogels for 24 h, 72 h, 7 days, or 14 days, four 50 µl hydrogels were pooled and placed into 2 ml of PureZOL (Bio-Rad). A microtube pestle was used to mechanical disrupt the hydrogels, followed by sonication ten times in 1 s bursts with the Model 100 Sonic Dismembrator.

Total RNA was extracted with the Aurum Total RNA Fatty and Fibrous Tissue kit (Bio-Rad), according to the manufacturer's instructions. RNA concentration was determined using a NanoDrop 2000 spectrophotometer (ThermoFisher Scientific Inc.). Complimentary DNA was synthesized from 300 ng of RNA for the coating experiments, and 500 ng of RNA for the 3-D hydrogel experiments, using the iScript™ cDNA synthesis kit (Bio-Rad). Gene expression was analyzed by SYBR-based real-time qPCR using a Bio-Rad CFX-384 thermocycler. PCR reactions were run in triplicate, using 312 nM of forward and reverse primers, with 2x SsoFast EvaGreen Supermix (Bio-Rad). The PCR program consisted of the following: initial 2 min enzyme activation at 95°C, 10 s denaturation at 95°C, 30 s annealing/elongation at 60°C, for total of 45 cycles. Gene expression was calculated using the ΔΔCt method, normalized to expression of the housekeeping

TABLE 1 RT-qPCR list of genes and primer sequences.

Gene	Forward (5′ → 3′)	Reverse (5′ → 3′)	Primer efficiency
COL2A1	CCTCTGCGACGACATAATCT	GGTTCTCCTTTCTGTCCCTTTG	91%
COL1A1	CCAATGGCGCTCCTGGTATT	ACCAGGTTCACCGCTGTTAC	96%
ACAN	ACCTACGATGTCTACTGCTACG	AGAGTGGCGTTTTGGGATTC	106%
SOX9	GCAAGCTCTGGAGACTGCTG	CGTTCTTCACCGACTTCCTCC	90%
KRT 8	CTCCTTCATCGACAAGGTGCG	CTATGTTGCTCCGGGCAGT	96%
KRT 19	ACCTGCGGGACCAGATTCTC	AGACGGGCATTGTCGATCTG	109%
ACTA2	GCCGAGAACTTTCAGGGACC	CATTGTCACACACCAAGGCG	98%
FSP1 (*S100A4*)	CTTCCTCTCTCTTGCTCCTGAC	GCTTGAACTTGTCACCCTCCT	102%
GAPDH	AAGGTCGGAGTGAACGGATTC	ATTGATGGCGACGATGTCAA	94%

gene glyceraldehyde 3-phosphate dehydrogenase (*GAPDH*). Stability of GAPDH gene expression was validated prior to analysis (average C_q 22.3, min C_q 21.1, max C_q 23.5). All PCR primers were validated for efficiency and specificity, and sequences are displayed in Table 1. No template controls were included for all reactions.

2.10 Statistical analyses

All numerical data are represented as mean ± standard deviation (SD), with replicate data points graphed individually. All statistical analyses were performed using GraphPad Prism 6 (GraphPad Software, San Diego, United States). A Kolmogorov-Smirnov test was done to compare the particle size distribution of the cryo-milled DNP and COL particles. The biochemical characterization data of DNP and NP was analyzed using a two-tailed unpaired Student's *t*-test, while DNP and COL particles/coatings biochemical data were analyzed by one-way ANOVA. Gene expression levels of NP cells seeded on 2-D coatings or encapsulated within the 3-D hydrogels were compared between groups using two-way ANOVA with a Tukey's post-hoc comparison of means. Differences with $p < 0.05$ were considered to be statistically significant.

3 Results

3.1 The decellularization protocol effectively extracted cells from bovine nucleus pulposus while retaining ECM components

The first aim of this study was to develop and validate a protocol for NP decellularization, with the overall goal of enhancing removal of cell content while retaining ECM components including GAGs and collagens. The initial decellularization protocol tested was based on methods established for decellularizing porcine auricular cartilage, which were adapted from the literature (Graham et al., 2016) and involved an extended 10-day process including freeze-thaw cell lysis in a hypotonic buffer, treatment with the non-ionic detergent Triton-X100, and enzymatic digestion with DNase and RNase. Although the protocol was effective at extracting cells, histological staining revealed minimal retention of GAGs at the end of processing (Supplementary Figure 2). Based on this, the protocol was systematically altered, including investigating the effects of varying buffer conditions, treatment times, and ultimately the elimination of the detergent treatment step.

In brief, the finalized two-step protocol involved treating minced bovine NP tissue with a single freeze-thaw cycle in dH_2O to lyse cells, followed by a 5 h enzymatic digestion in DNase and RNase (Figure 1A). DAPI staining showed a marked reduction in cell nuclei relative to the native tissue controls (Figure 1B). The imaging results were corroborated by the PicoGreen assay results, which demonstrated a significant reduction of ~85% in dsDNA content following decellularization (Figure 1B). Toluidine blue staining verified that GAGs were retained throughout the processed tissues, although the staining intensity was reduced in comparison to the native NP samples (Figure 1C). Consistent with these findings, quantification through the DMMB assay indicated ~45% retention of sGAG content following decellularization (Figure 1C). Picrosirius red staining revealed similar networks of interwoven collagen fibers in both the DNP and native NP samples, and the hydroxyproline assay confirmed there was no significant difference in the total collagen content between the groups (Figure 1D).

Following confirmation of decellularization, immunohistochemical staining was performed to further probe the ECM composition in the DNP relative to the native NP (Figure 2). Staining for collagen types I, II, V, and VI revealed similar staining intensities and spatial distribution patterns in the DNP compared to the native NP. Similarly, both laminin and fibronectin were

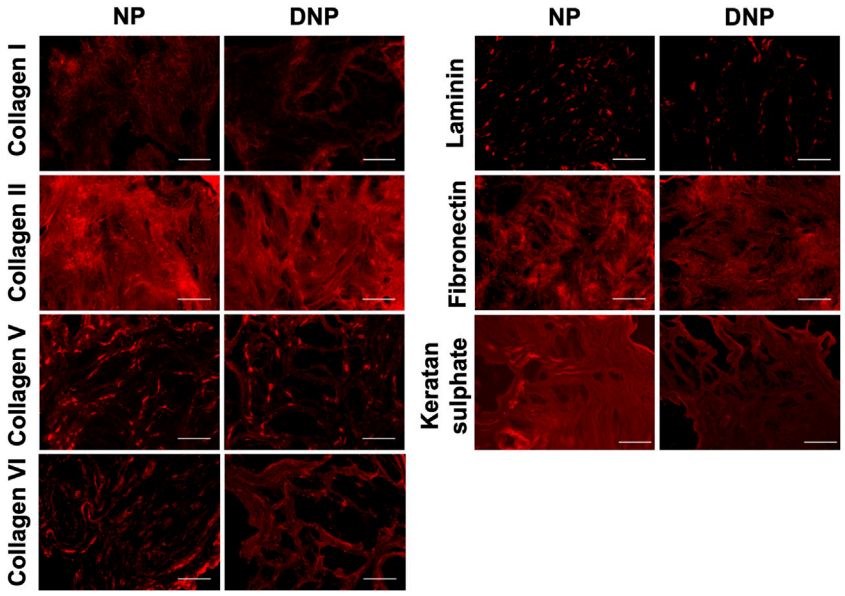

FIGURE 2
Immunofluorescence analysis confirms the maintenance of key NP ECM constituents following decellularization. Representative images showing the presence and distribution of collagen type I, collagen type II, collagen type V, collagen type VI, laminin, and fibronectin, with similar distribution patterns and staining intensities in the decellularized NP (DNP) and the native nucleus pulposus (NP). Keratan sulphate showed a similar spatial distribution pattern with qualitatively decreased staining intensity within the DNP relative to the native NP. Scale bars = 200 μm (N = 3).

qualitatively well retained following decellularization. Although the spatial distribution of keratan sulphate was similar in the DNP and native NP, a decrease in staining intensity was observed following decellularization, consistent with the reduced sGAG content in the DNP.

3.2 Particles and coatings derived from DNP or COL are structurally and compositionally distinct

Based on our findings of efficient removal of cells and general maintenance of the ECM content in the DNP generated with our detergent-free decellularization protocol, we proceeded with developing and testing 2-D and 3-D biomaterial culture platforms that could be applied to assess the effects of the DNP on the *in vitro* culture and expansion of primary bovine NP cells. Platforms were also generated using commercially-available type-I collagen sourced from bovine tendons to compare the effects of a non-tissue-specific ECM control. As a first step in fabricating both biomaterial formats, the DNP and COL were cryo-milled and sieved through a 125 μm mesh to remove larger particles. Characterization using a Mastersizer system confirmed that >80% of the DNP and COL particles were less than 125 μm (Figure 3A), with average diameters of 60.34 ± 55.44 μm for the DNP particles and 83.84 ± 54.45 μm for the COL particles. There was no significant difference in the particle size distributions between the groups based on a Kolmogorov–Smirnov nonparametric test ($p < 0.05$) (Figure 3B). To generate the coatings, applying methods previously developed by our group (Shridhar et al., 2020), the particles were subsequently digested with α-amylase and homogenized in acetic acid.

SEM analysis revealed that the DNP particles had a more open porous structure, with visible fibers observed, while the COL particles appeared more compacted with a smoother surface ultrastructure (Figure 3C). While the surface of both the DNP and COL coatings appeared smooth, imaging of the scratched region revealed that both had a multilayer internal structure, with the DNP coatings appearing to have larger gaps between the layers.

Biochemical quantification revealed a significant ~4.2-fold reduction in relative sGAG content in the DNP coatings as compared to the DNP particles, indicating that the further processing resulted in a marked loss of GAGs (Figure 3D). No sGAG was detected in either the COL particles or coatings. In contrast, the hydroxyproline assay indicated a significant ~1.4-fold increase in the relative collagen content in the DNP coatings as compared to the DNP particles, likely due to the dramatic reduction in GAG content observed (Figure 3E). Consistent with this interpretation, there was no significant difference in the hydroxyproline content between the COL particles and coatings.

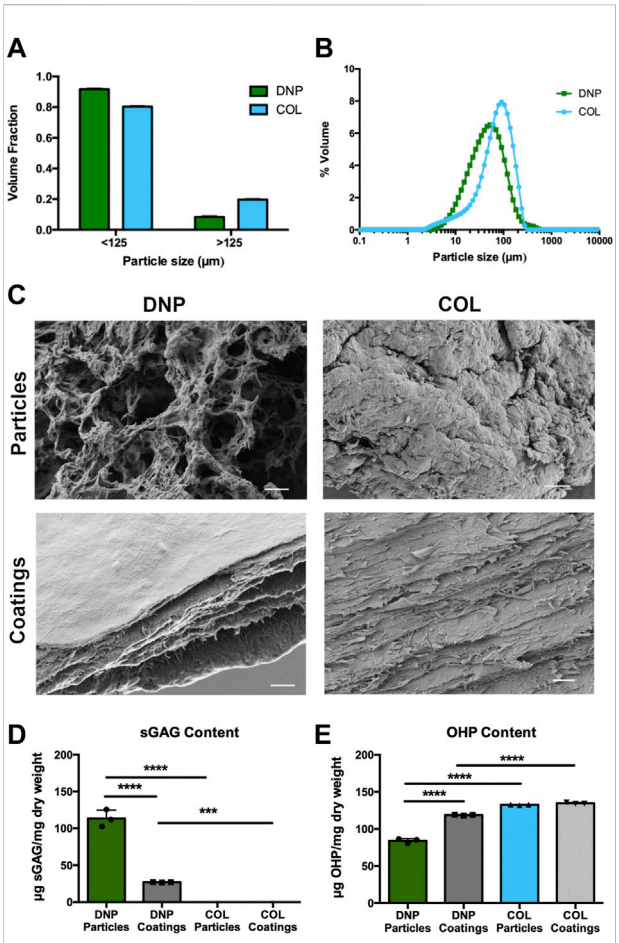

FIGURE 3
DNP particles are compositionally and structurally distinct from DNP coatings. **(A)** Volume fraction of cryomilled DNP and COL particles showed that particles were predominantly less than 125 μm (N = 3). **(B)** Particle size distribution plots based on the Mastersizer analysis. There was no significant difference between the DNP and COL groups based on the Kolmogorov-Smirnov test ($p < 0.05$). **(C)** Scanning electron microscopy (SEM) of DNP or COL particles showed a distinct extracellular matrix ultrastructure as compared to their respective coatings. Images captured at ×5,000 magnification. Scale bars = 2 μm. **(D)** DMMB analysis of sGAG content showed a significant decrease in sGAG within the DNP coatings relative to the DNP particles, while both COL particles and coatings had negligible amounts. **(E)** Collagen content as measured by the hydroxyproline (OHP) assay, showed an increase in relative collagen content within the DNP coatings as compared to the DNP particles (N = 3, ***$p < 0.001$, ****$p < 0.0001$).

3.3 DNP coatings provide a cell-supportive platform for cell expansion but do not alter the NP cell phenotype

Having generated the 2-D coating culture platform, we next assessed the effects of the ECM coatings on primary bovine NP cells over sequential passages. Since the cells on the coatings could not be visualized with brightfield microscopy, live cells were imaged using calcein-AM staining following 3 days in culture on the DNP and COL coatings, along with the TCP controls. All substrates were found to support primary NP cell attachment following serial passaging, although decreased cell density was consistently observed on the DNP and COL coatings as compared to cells cultured on TCP (Supplementary Figure 3).

To assess the effects of culture on the 2-D ECM coatings on the maintenance of the NP cell phenotype following serial passage in monolayer culture, RT-qPCR analysis was used to quantify the expression of NP-associated markers (*KRT8, KRT19, SOX9*), ECM genes (*COL2A1, COL1A1, ACAN*), and fibroblast-associated markers (*ACTA2, FSP1*). Similar to previous reports (Cui et al., 2012; Rosenzweig et al., 2017; Ashraf et al., 2020), our analysis demonstrated a robust decrease in the expression of NP-associated markers in primary cells over serial passage (P0–P3) on TCP (Figure 4, grey bars). Compared to primary (P0) NP cells cultured on TCP, primary (P0) NP cells cultured on DNP coatings showed significantly lower expression of the NP-associated markers *KRT8*, *KRT19*, and *SOX9* - a change not induced by culture of P0 NP cells on COL coatings (Figure 4A). In general, culture of NP cells on either DNP or COL coatings did not significantly alter the expression of ECM genes compared to cells cultured on TCP, with the exception of *ACAN* which was significantly increased in P0 NP cells on COL coatings compared to P0 NP cells on either TCP or DNP coatings (Figure 4B). Lastly, although a generalized loss of NP-specific gene expression was noted in primary cells following serial passaging in 2-D on all substrates, this was not associated with increased expression of either *ACTA2*, a myofibroblast marker, or FSP1, a marker of activated fibroblasts (Figure 4C). These findings suggest that *in vitro* culture of primary bovine NP cells on DNP coatings did not promote the maintenance of the NP phenotype across serial passages when compared to cells cultured on TCP.

To assess the short-term effects of the ECM coatings on primary NP cells and to determine if they could restore the phenotype of de-differentiated primary NP cells, late passage NP cells (passaged three times on TCP) or primary un-passaged (P0) NP cells were seeded onto TCP, DNP coatings or COL coatings, and gene expression was assessed after 2 or 4 days. Short term culture of P0 NP cells on 2-D coatings did not significantly alter the expression of NP-associated markers or ECM genes compared to P0 cells cultured on either TCP or COL; a significant increase in the expression of *COL1A1* was however detected following 4 days of culture of P0 NP cells on DNP compared to cells cultured on TCP or COL coatings (Figures 5A,B). In general, culture of de-differentiated NP cells on ECM coatings did not reverse the loss of expression of NP markers associated with serial passage *in vitro*. The expression of *KRT8*, *KRT19*, and *COL2A1* were significantly decreased in P3 cells at both time points compared to P0 cells, unaffected by culture on the ECM coatings. This was associated with a significant increase in the expression of *COL1A1* in P3 NP cells on all coatings at 4 days compared to P0 cells (Figure 5B). The expression of *SOX9* was significantly decreased in P3 cells cultured on both TCP and DNP at both time points

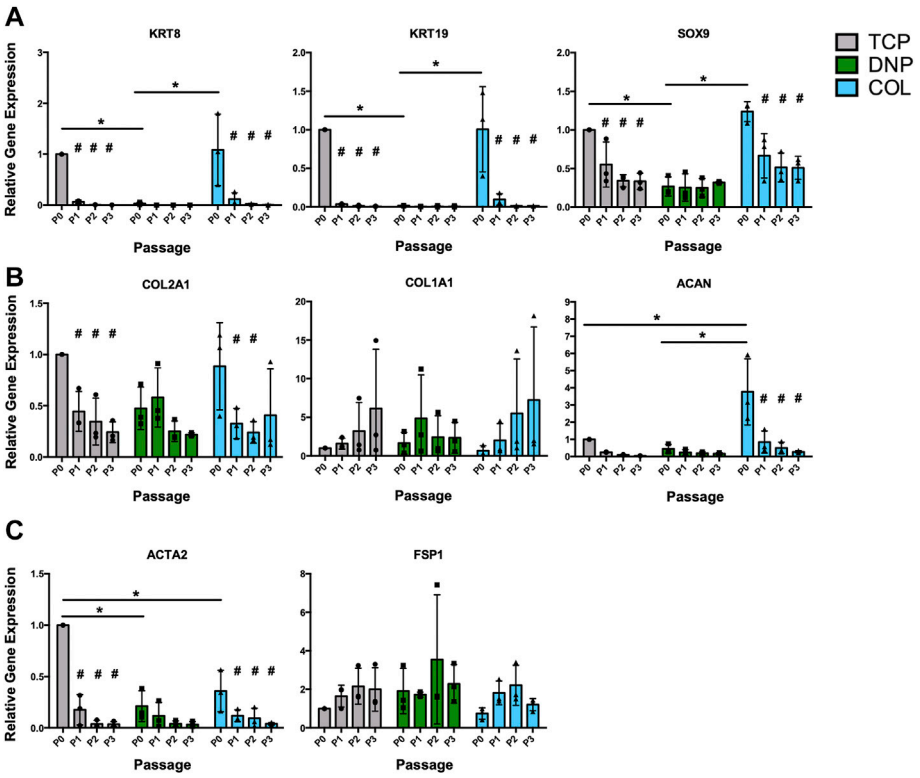

FIGURE 4
RT-qPCR gene expression analysis of serially passaged primary bovine NP cells grown in monolayer on tissue culture plastic or ECM coatings. Primary bovine NP cells (P0) were cultured in monolayer on tissue culture plastic (TCP), decellularized NP (DNP) coatings, or type I collagen (COL) coatings and serially passaged (P1-P3) on the same culture substrate. Gene expression analysis was performed to quantify expression of **(A)** NP-associated markers (*KRT8, KRT19, SOX9*), **(B)** ECM genes (*COL2A1, COL1A1, ACAN*), and **(C)** fibroblast markers (*ACTA2, FSP1*). Relative gene expression was determined using the $\Delta\Delta C_t$ method normalized to expression of the housekeeping gene *GAPDH*, and expressed relative to P0 cells on TCP. Data is presented as mean ± SD (N = 3, $p < 0.05$, * indicates significant differences between culture conditions, # indicates significant differences within each condition relative to P0 cells).

compared to P0 cells (Figure 5A). While the expression of *ACAN* was decreased in P3 NP cells on all substrates at both 2 and 4 days compared to P0 cells, a moderate but significant increase was detected in P3 NP cells cultured on COL compared to those cultured on either TCP or DNP (Figure 5B). Lastly, decreased expression of NP-related genes was not associated with increased expression of fibroblast-associated markers in NP cells on ECM coatings (Figure 5C). Taken together, these findings suggest that culture of de-differentiated NP cells on the DNP coatings alone was unable to rescue the NP-specific phenotype, but that the ECM source used to generate the coatings impacted NP gene expression.

3.4 MCS hydrogels containing DNP provide a cell supportive platform for NP cell culture but do not alter the NP cell phenotype

While culture on 2-D coatings was insufficient to maintain or rescue the phenotype of the cultured bovine NP cells, we postulated that the lack of observed bioactive effects of the DNP may be attributed to alterations in the ECM composition with the additional processing required to generate the coatings, as well as to the 2-D nature of the culture model. As such, our next step was to establish a 3-D culture platform that could be applied to encapsulate the bovine NP cells in combination with cryomilled DNP or COL particles (Supplementary Figure 4A). More specifically, we successfully fabricated composite MCS hydrogels incorporating 5% w/v ECM via UV-crosslinking that were stable in long-term culture. Gel content analysis indicated that the incorporation of the ECM did not interfere with the cross-linking process (Supplementary Figure 4B). Consistent with this interpretation, mechanical testing confirmed that there was no significant difference in the Young's moduli between the three hydrogel groups (Supplementary Figure 4C).

Primary NP cells (P0 and P3) were encapsulated within the MCS + DNP or MCS + COL composite hydrogels, or MCS alone, to assess the capacity of the 3-D culture platforms to support NP cell viability up to 14 days in culture. Following encapsulation, P0 NP

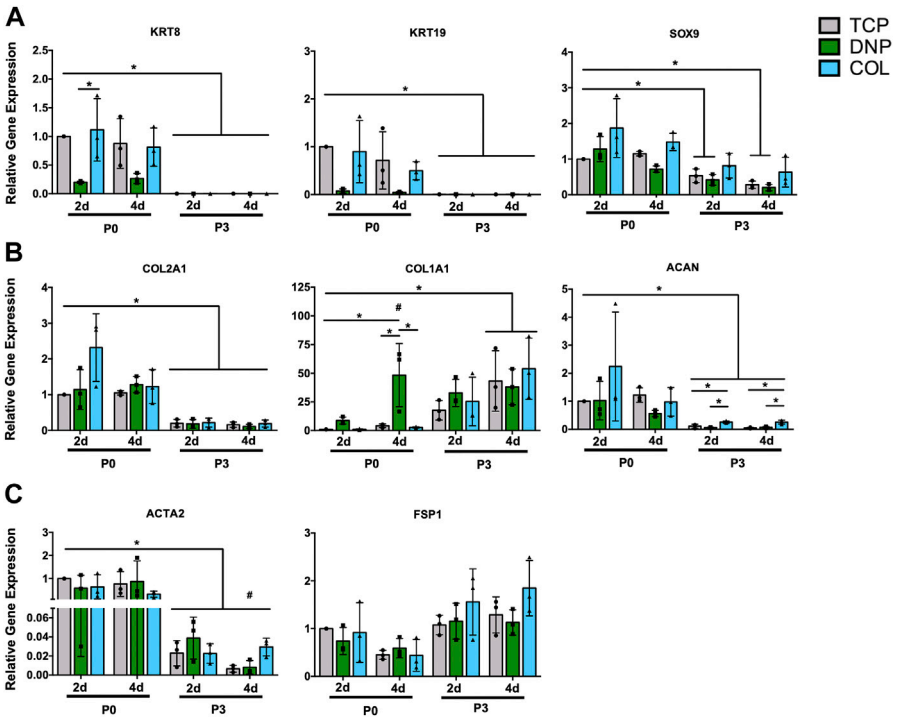

FIGURE 5
RT-qPCR gene expression analysis of primary bovine NP cells following short term culture in monolayer on tissue culture plastic or ECM coatings. Un-passaged (P0) and late passage (P3) primary bovine NP cells were seeded onto tissue culture plastic (TCP), decellularized NP (DNP) coatings, or type I collagen (COL) coatings. Cells were cultured *in vitro* for 2 days (2d) or 4 days (4d). Gene expression analysis was performed to quantify expression of **(A)** NP-associated markers (*KRT8, KRT19, SOX9*), **(B)** ECM genes (*COL2A1, COL1A1, ACAN*), and **(C)** fibroblast markers (*ACTA2, FSP1*). Relative gene expression was determined using the $\Delta\Delta C_t$ method normalized to expression of the housekeeping gene *GAPDH*, and expressed relative to P0 cells on TCP at 2 days. Data is presented as mean ± SD (N = 3, $p < 0.05$, * indicates significant difference between culture conditions, # indicates significant difference within each condition relative to 2d).

cells showed a uniform distribution throughout all hydrogels (Figure 6). In general, the MCS, MCS + DNP, and MCS + COL groups showed high cell viability across all timepoints assessed. Qualitative observations suggested a reduction in the number of viable cells present in the MCS group following 7 and 14 days of culture as compared to the MCS + DNP or MCS + COL groups. Notably, NP cell clustering was observed after 7 and 14 days in culture only within the MCS + DNP and MCS + COL hydrogels. These findings were consistent with those of P3 NP cells encapsulated within the composite hydrogels (Supplementary Figure 5), confirming that the platform supported the viability of the encapsulated bovine NP cells and suggesting that the cells were interacting with the cryomilled ECM.

The effects of culture in the 3-D DNP-containing MCS hydrogels on the expression of NP-associated markers, ECM genes, and fibroblast-associated markers were assessed in primary un-passaged (P0) bovine NP cells up to 14 days of culture (Figure 7). Overall, the incorporation of the DNP or COL particles within MCS hydrogels did not significantly alter gene expression relative to the MCS alone at any timepoint investigated. In all 3-D cultures, primary NP cells showed a general decrease in the expression of NP-associated genes over time in culture. While a significant decrease in *ACAN* expression was only detected in MCS + COL hydrogels by 14 days in culture, a significant decrease in *KRT19*, *SOX9*, and *COL2A1* expression was detected in NP cells within all three hydrogel groups by 14 days compared to baseline gene expression in MCS (24 h) (Figures 7A,B). In keeping with our findings on 2-D coatings, the expression of the fibroblast-associated markers *ACTA2* and *FSP1* remained unchanged over time in 3-D culture (Figure 7C).

Lastly, to assess whether culture within the 3-D MCS + DNP hydrogels could rescue the phenotype of de-differentiated NP cells, late passage (P3) NP cells were encapsulated within the MCS, MCS + DNP, or MCS + COL hydrogels and cultured up to 14 days. To contextualize changes in gene expression, these data were assessed relative to baseline levels of gene expression in P0 NP cells (MCS only at 24 h). Similar to P0 NP cells, the incorporation of the DNP or COL particles did not significantly alter gene expression in P3 NP cells relative to the MCS alone at all timepoints (Figure 8). No significant change in the expression of the NP-associated markers or ECM genes was detected over time in culture within any of the hydrogel groups (Figures 8A,B). Compared to P0 NP cells at baseline

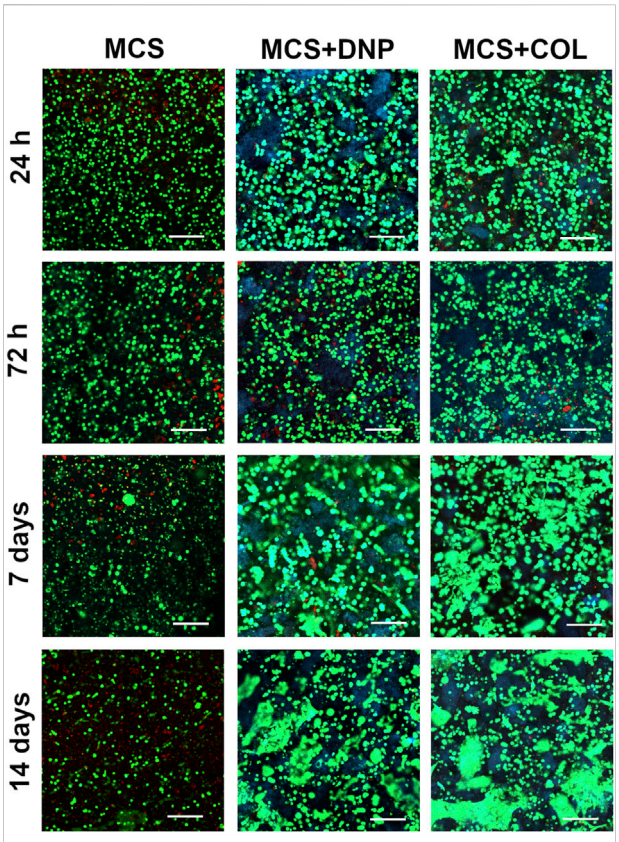

FIGURE 6
Primary bovine NP cells remain viable following encapsulation and *in vitro* culture within MCS ± DNP/COL up to 14 days. Unpassaged P0 primary bovine NP cells were encapsulated within MCS, MCS + DNP or MCS + COL hydrogels, and cultured *in vitro* for 24 h, 72 h, 7 days, or 14 days. Representative confocal microscopy images were captured at each time point showing live cells stained with calcein-AM (green), dead cells with ethidium homodimer-1 (red), and auto-fluorescence of DNP and COL particles (blue). Images were captured at depths between 75–150 μm from the surface of each hydrogel construct. Scale bars = 200 μm. Images are representative of N = 3 individual cell preparations.

(MCS only at 24 h), P3 NP cells showed a significant reduction in the expression of *KRT8*, *COL2A1*, and *ACTA2* at all time points, unaffected by hydrogel composition. Expression of the fibroblast-associated markers *ACTA2* and *FSP1* were not altered over time in any of the hydrogel groups (Figure 8C). Taken together, these findings suggest that culture of primary NP cells within composite hydrogels containing DNP particles was not sufficient to prevent the loss of or restore the NP cell phenotype following *in vitro* cell culture.

4 Discussion

Many *in vitro* studies involve the expansion of cells in 2-D on rigid tissue culture plastic substrates that are convenient for supporting cell attachment and proliferation, but substantially alter cell-cell and cell-ECM interactions as compared to the native cellular microenvironment, which can markedly affect cell function (Rubashkin, Ou, and Weaver 2014; Rosenzweig et al., 2017; Ashraf et al., 2020). Notably, monolayer culture of primary bovine NP cells on TCP results in loss of the NP phenotype with serial passaging, as measured by decreased NP-associated marker expression (Ashraf et al., 2020). Recognizing the cell-instructive capacity of the ECM, the primary goal of this study was to develop 2-D and 3-D culture platforms that mimic the complex ECM within the native nucleus pulposus. As a first step, a detergent-free decellularization protocol was established that involved subjecting minced bovine NP tissue to one freeze-thaw cycle in deionized water to promote cell lysis, followed by 5 h of digestion with DNase and RNase to remove residual nucleic acids that could cause an immunogenic response if the DNP was applied *in vivo* (Gilbert et al., 2009; Gilpin and Yang 2017). Due to the limited availability of healthy human NP tissue, previous studies have similarly validated decellularization protocols using bovine or porcine NP tissues (Mercuri et al., 2011; Fernandez et al., 2016; Illien-Jünger et al., 2016; Wachs et al., 2017). The NP from these species more closely resembles the cellular and ECM composition of the human NP as compared to other preclinical animal models such as the mouse or rabbit (Demers et al., 2004; Alini et al., 2008).

In healthy tissues, the NP ECM consists predominantly of proteoglycans [~65% of the NP ECM dry weight (Hwang et al., 2014)] including aggrecan, enmeshed within an irregular network of collagen and elastin fibers (Adams and Roughley, 2006). Chondroitin sulphate and keratan sulphate are the most abundant GAGs found within the native NP (Adams and Roughley, 2006), which contribute to a net negative charge that promotes water influx into the tissues (Roughley, 2004). The high water content of the NP [~80% of the total wet weight (Urban and Roberts, 2003; Hwang et al., 2014)] generates swelling pressure that is critical for maintaining the IVD height and proper transmission of compressive loads (Freemont 2009; Inoue et al., 2012). GAGs are also important for the bioactivity of the ECM, sequestering growth factors and bioactive molecules to increase their local concentration (Ramirez and Rifkin, 2003), as well as directly modulating numerous cell functions including proliferation, migration, and differentiation (Peloso et al., 2016).

Decellularization of the NP is challenging because the treatments required to remove cellular content often result in a marked loss of GAGs, shifting the resultant ECM to a more collagen-rich environment that could have substantially different effects on IVD cell types. In developing our detergent-free protocol, we spent a substantial amount of time exploring the effects of various treatment steps to establish a process that was reproducibly effective and that balanced removal of cellular content with preservation of GAGs. We found that protocol

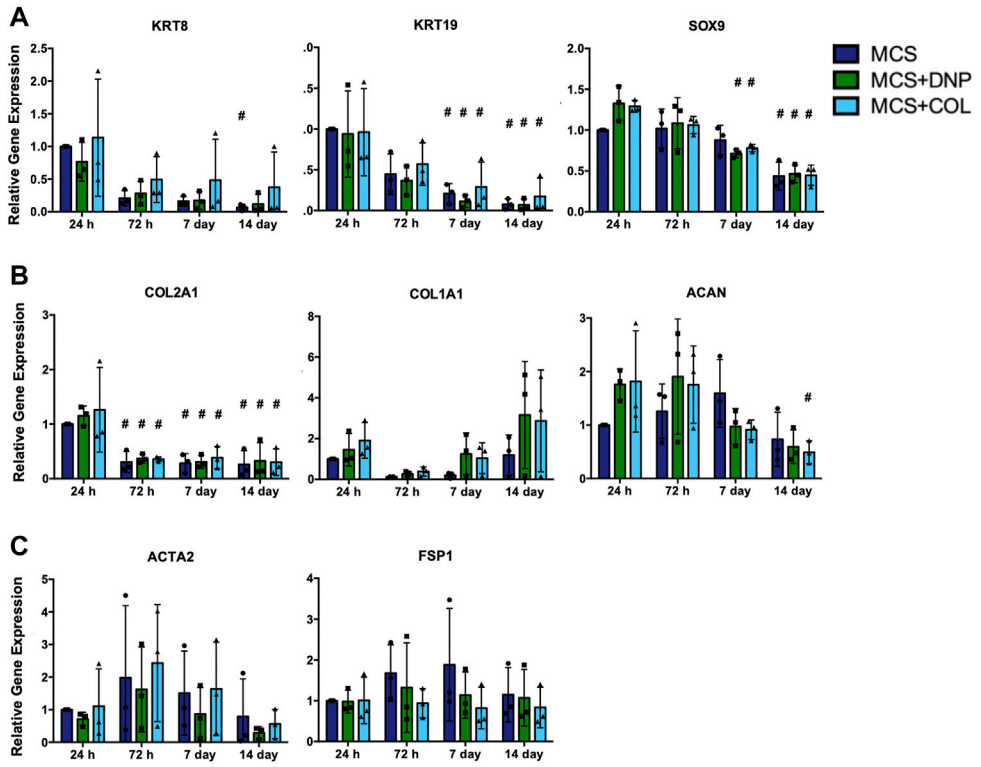

FIGURE 7
RT-qPCR gene expression analysis of primary bovine NP cells encapsulated within MCS ± DNP/COL scaffolds and cultured *in vitro* up to 14 days. Unpassaged (P0) primary bovine NP cells were encapsulated within MCS, MCS + DNP, or MCS + COL hydrogels, and cultured *in vitro* for 24 h, 72 h, 7 days, or 14 days. Gene expression analysis was performed to quantify expression of **(A)** NP-associated markers (*KRT8, KRT19, SOX9*), **(B)** ECM genes (*COL2A1, COL1A1, ACAN*), and **(C)** fibroblast markers (*ACTA2, FSP1*). Relative gene expression was determined using the $\Delta\Delta C_t$ method normalized to expression of the housekeeping gene *GAPDH*, and expressed relative to cells encapsulated within MCS at 24 h. Data is presented as mean ± SD (N = 3, $p < 0.05$, * indicates significant difference between culture conditions, # indicates significant difference within each condition relative to 24 h).

duration was an important factor in GAG retention, which has also been reported with other tissue types (Gilpin and Yang, 2017; Reginensi et al., 2020), with extended protocols including additional freeze-thaw cycles having limited benefit in further reducing cell content.

Our finalized protocol resulted in an ~85% reduction in dsDNA content, while retaining ~45% of sGAGs based on dry weight. For comparison, Illien-Jünger et al. (2016) reported an ~85% reduction in dsDNA content with ~15% retention of sGAGs with their optimized protocol for decellularizing bovine NP, which involved repeated freeze-thaw cycles, followed by tissue milling and treatment with sodium deoxycholate and DNase. Similarly, Fernandez et al. (2016) reported a ~92% reduction in dsDNA content and ~30% retained sGAG content with their most effective detergent-based protocol for bovine NP, involving treatment with Triton-X100, DNase, and RNase. Hensley et al. (2018) applied a combination of detergents, ultrasonication, freeze-thaw cycles, and digestion with DNase and RNase to decellularize intact bovine IVDs, showing an ~84% decrease in DNA content coupled with ~55% retention of sGAGs within the NP region. The enhanced preservation of GAGs may be related to their strategy of processing of the tissues with the annulus fibrosus intact, as it may have functioned as a barrier to reduce GAG loss. Further extending the whole tissue approach, Norbertczak et al. (2020) subjected bovine IVDs that included intact cartilaginous endplates to a decellularization protocol involving SDS treatment, freeze-thaw cycles, sonication, and DNase/RNase digestion. There was no significant reduction in DNA content in the decellularized NP compared to the native NP controls, indicating that NP decellularization was impeded by presence of the surrounding tissues. Safranin O staining showed a marked reduction in staining intensity in the NP following decellularization, while DMMB assay results showed greater sGAG loss in the outer regions of the IVD that were more effectively decellularized.

Importantly, our immunohistochemical characterization studies confirmed that the DNP generated with our protocol

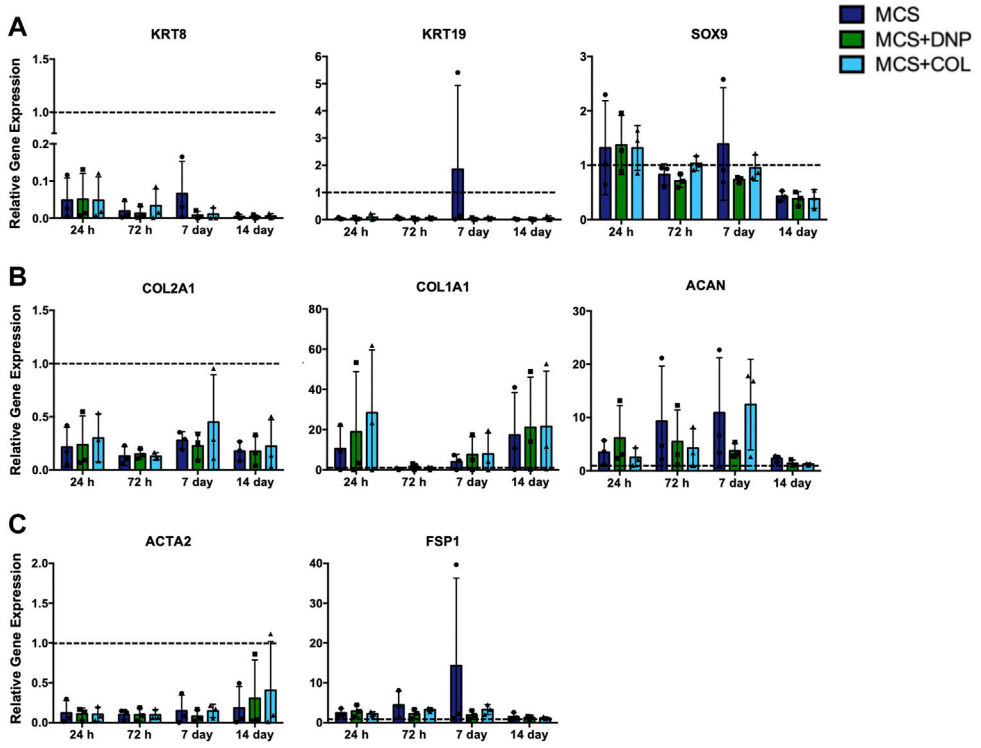

FIGURE 8
RT-qPCR gene expression analysis of late passage primary bovine NP cells encapsulated within MCS ± DNP/COL scaffolds and cultured *in vitro* up to 14 days. Late passage (P3) primary bovine NP cells were encapsulated within MCS, MCS + DNP, or MCS + COL hydrogels, and cultured *in vitro* for 24 h, 72 h, 7 days, or 14 days. Gene expression analysis was performed to quantify expression of **(A)** NP-associated markers (*KRT8, KRT19, SOX9*), **(B)** ECM genes (*COL2A1, COL1A1, ACAN*), and **(C)** fibroblast markers (*ACTA2, FSP1*). Relative gene expression was determined using the $\Delta\Delta C_t$ method normalized to expression of the housekeeping gene *GAPDH*, and expressed relative to P0 cells encapsulated within MCS at 24 h (dotted line indicated on graphs). Data is presented as mean ± SD (N = 3 $p < 0.05$).

also contained multiple collagen types as expected based on the native tissue source (Roughley, 2004), with intense staining for collagen type II, which is the most abundant collagen type within the healthy NP [~15%–20% of the NP ECM dry weight (Hwang et al., 2014)]. Moreover, the cell-adhesive glycoproteins laminin and fibronectin were retained, which may be favorable for mediating cell adhesion, viability, and other downstream responses (Francisco et al., 2013; Hwang et al., 2014). Given the well characterized structural heterogeneity of the native NP in terms of ECM fragmentation (Craddock et al., 2018), future studies will focus on assessing the integrity of the ECM within the DNP in the context of ECM integrity and biological activity.

Following the establishment of the decellularization protocol, our next objective was to apply our expertise in ECM-derived bioscaffold fabrication to integrate the DNP into customized platforms tuned for 2-D and 3-D cell culture. As a starting point, we adapted methods that we previously established using adipose-derived ECM to generate novel DNP coatings (Shridhar et al., 2020). ECM-derived coatings from a variety of tissues have previously been shown to guide cell attachment, proliferation, and lineage-specific differentiation (DeQuach et al., 2010; Rothrauff, 2017; Shridhar et al., 2020). In contrast to the common strategy of digesting the ECM with the proteolytic enzyme pepsin, our approach involves digestion with α-amylase and homogenization in acetic acid to create an ECM suspension with preserved collagen fibrils. Digestion with α-amylase cleaves carbohydrate groups in the collagen telopeptide regions and can destabilize collagen-glycoprotein complexes, enhancing dispersion of the collagen fibrils within the acetic acid and allowing for the creation of more homogeneous coatings (Shridhar et al., 2020). Our previous study comparing coatings generated with α-amylase-digested DAT versus pepsin-digested DAT showed that α-amylase digestion generated coatings that were softer, thicker and more stable, and that retained a fibrous tissue-like ultrastructure that was completely lost following pepsin digestion (Shridhar et al., 2020). A similar multi-layer fibrous ultrastructure was observed in the current study in both the DNP and collagen control coatings.

Both the DNP and COL coatings were shown to support cell attachment and growth, with serial passaging enabled through collagenase digestion. However, neither coating type was able to maintain the NP phenotype following serial passages based on

gene expression analysis. More specifically, consistent with previous findings with primary NP cells cultured on TCP (Cui et al., 2012; Rosenzweig et al., 2017; Ashraf et al., 2020), we observed a reduction in the mRNA expression levels of the NP-associated markers and type II collagen with serial passaging on TCP and COL coatings. The increased expression of *AGG* we detected in P0 NP cells cultured on COL coatings compared to TCP is consistent with previous reports of increased proteoglycan synthesis in rabbit NP cells cultured on collagen coatings (Inoue et al., 2005). Of note, the expression of the NP-associated markers *KRT8*, *KRT18*, and *SOX9* were reduced in P0 NP cells on DNP coatings compared to cells cultured on TCP and COL, demonstrating that the composition of the 2-D ECM coatings impacted cell phenotype. Additionally, the gene expression results indicated that the DNP coatings were unable to rescue the NP phenotype of de-differentiated P3 cells.

One possible limitation was that the further processing steps required for coating fabrication resulted in a significant reduction in GAG content relative to the DNP, with only ~10% retention compared to the native NP tissues, which may have impacted the bioactivity of the coatings. In addition to the direct effects associated with loss of ECM proteoglycans, the loss of GAG content would indirectly impact additional factors, including the content of matricellular proteins and growth factors that serve as important biological regulators of the NP microenvironment (Bedore et al., 2014; Guerrero et al., 2021a). Moreover, we expect that the observed changes in ECM composition of the DNP within 2-D coatings would be associated with changes in both topography and stiffness of the coatings, which would alter the cellular response. In addition, we postulated that the 2-D nature of this platform may not have been favorable for maintaining the differentiated state, based on previous reports that culture of NP cells in 3-D is more effective at retaining the NP phenotype (Yuan et al., 2011; Guerrero et al., 2021b). One postulated factor that may be influencing this response is that NP cells can retain their rounded morphology when cultured in 3-D, while 2-D culture results in a spindle-shaped morphology (Yuan et al., 2011), as was observed in the current study.

As a next-step, we decided to investigate the response of the primary bovine NP cells encapsulated within 3-D MCS hydrogels incorporating DNP particles, which had significantly higher sGAG content as compared to the DNP coatings and were expected to promote a rounded NP cell shape. We selected MCS as it mimics the native proteoglycans of the NP, and have previously shown that high viability was maintained over 14 days in culture when human ASCs were encapsulated within the hydrogels, both with and without the incorporation of DAT or decellularized trabecular bone (DTB) particles (Shridhar et al., 2019). The addition of the DNP or COL particles at 5% w/v did not alter the crosslinking efficiency or bulk compressive properties of the hydrogels, supporting the application of the platforms specifically for exploring the effects of the ECM particles on the cellular response.

All three MCS hydrogel systems supported the viability of the encapsulated bovine NP cells. The composite MCS hydrogels incorporating the DNP or COL particles qualitatively contained a higher density of viable cells compared to the MCS only hydrogels following extended culture, consistent with our previous work that showed that the incorporation of DAT particles enhanced the retention of viable human ASCs encapsulated and cultured within the MCS hydrogels (Cheung et al., 2014). Cell clustering was observed at 7 and 14 days within the MCS + DNP and MCS + COL hydrogels, which we previously observed with the ASCs in the MCS + DAT composites (Cheung et al., 2014; Brown et al., 2015), suggesting that the ECM particles may have supported cell attachment. However, culture in the DNP- or COL-containing 3-D hydrogels did not prevent the loss of NP-associated gene expression in primary P0 cells observed over time in culture, nor restore the NP phenotype in de-differentiated P3 bovine NP cells.

One potential influencing factor is that the hydrogels were much stiffer than values reported for the native human NP of ~5–25 kPa (Cloyd et al., 2007; Borrelli and Buckley 2020) and bovine NP of ~6–19 kPa (Recuerda et al., 2011; Grenier et al., 2014). Notably, Gilchrist et al. (2011) demonstrated the importance of both ECM ligands and substrate stiffness on NP phenotype, with a more native NP morphology, enhanced cell-cell interactions, and augmented proteoglycan synthesis when porcine NP cells were cultured on soft (<720 Pa) ECM substrates that contained laminin. Further emphasizing the importance of mechanical properties, Xu et al. demonstrated that encapsulating rat NP cells within gelatin hydrogels of increasing stiffness resulted in increased cell de-differentiation (Xu et al., 2021). As such, the higher stiffness of the MCS hydrogels may have counteracted any beneficial effects of the DNP. In the future, it would be interesting to explore the cellular response within hydrogels that more closely mimic the native mechanical properties of the NP. The molecular weight of the chondroitin sulphate may have been another factor that influenced the cellular response based on the work of Jeong et al. (2014), whose biochemical assay results suggested that porcine NP cells cultured on the surface of hyaluronic acid (HA)-polyethylene glycol composite hydrogels synthesized with 27 kDa HA were undergoing de-differentiation, while those cultured on hydrogels synthesized with 59 kDa HA accumulated significantly more sGAG, although the mechanisms of these effects were unclear.

Strategies to enhance cell clustering within the hydrogels may be favorable for maintaining the NP phenotype within the hydrogels, mimicking the observed benefits of micromass cultures (Séguin et al., 2004; Gawri et al., 2017; Kushioka et al., 2019). Supporting this approach, Hwang et al. (2016) demonstrated that the formation of N-cadherin positive cell clusters was critical for maintaining the morphology, phenotype, and biosynthetic activity of human and porcine NP cells. Similarly, Spillekorn et al. (2014) showed that culturing canine notochord cells in native cell clusters within alginate hydrogels was favorable for retaining their phenotype in long-term culture.

While our culture models strive to mimic the native ECM composition, it is important to recognize that there are other factors within the cellular microenvironment that are key regulators of NP phenotype and function. While the ECM alone may be insufficient to maintain the differentiated phenotype of the bovine NP cells, it is possible that it could function synergistically with these other factors to have a beneficial effect. For example, while we previously observed only low levels of expression of adipogenic genes in the human ASCs cultured on the DAT coatings in proliferation medium, adipogenic gene and protein expression, as well as intracellular lipid accumulation, were significantly enhanced when the ASCs were cultured on the α-amylase-digested DAT coatings in adipogenic differentiation medium as compared to when the cells were cultured on α-amylase-digested COL coatings, pepsin-digested DAT or COL coatings, or TCP (Shridhar et al., 2020). Similarly, while there were no observed osteoinductive effects when the DTB particles were incorporated within the MCS hydrogels on encapsulated human ASCs, our previous findings support that the DTB had bioactive effects in modulating osteogenesis when combined with soluble factors within osteogenic differentiation medium (Shridhar et al., 2019). As such, supplementation of the medium with growth factors such as BMP-2 (Gilbertson et al., 2008), BMP-7 (Kawakami et al., 2005; Masuda et al., 2006; Wei et al., 2008), FGF-2 (Tsai et al., 2007), GDF-5, TGF-β1 (Henry et al., 2017) or TGF-β3, which have been shown to enhance NP cell survival and ECM synthesis (Ashraf et al., 2020), bioactive proteins such as CCN2 which has been shown to promote ECM synthesis in NP cells (Erwin et al., 2006), or SLRPs (e.g., biglycan or decorin) associated with enhanced survival and matrix synthesis in IVD progenitor cells (Chen et al., 2017), may help to maintain the NP phenotype in combination with the DNP and as such could be the focus of subsequent studies. In addition, it could be interesting to explore the effects of hypoxia, building from previous work that has shown that porcine NP cells better maintain their differentiated phenotype when cultured under 1% O_2 as compared to atmospheric conditions (~21% O_2) (Jaworski et al., 2019). Finally, it would be interesting to explore the effects of mechanical stimulation on the phenotype of the NP cells encapsulated within our 3-D MCS hydrogels, which was also suggested by Priyadarshani et al. (2016), who similarly observed decreased expression levels of the NP-associated genes *SOX9*, *ACAN*, and *COL2A1*, coupled with increased expression of *COL1A1*, following long-term culture of human NP cells within type II collagen-HA composite hydrogels.

5 Conclusion

In the current study we successfully established a reproducible detergent-free decellularization protocol for bovine nucleus pulposus, and successfully integrated the DNP within novel 2-D and 3-D culture platforms. While the ECM alone was insufficient for maintaining the mature bovine NP phenotype based on analysis of gene expression, both platforms were shown to support cell viability in culture and further investigation of their utility is warranted to assess their potential as tissue-specific cell culture platforms for NP regenerative applications. Building from this work, it would be interesting to assess the phenotypic response at the protein level using techniques such as western blotting, ELISA, or immunohistochemistry, to see if there may be differences in matrix synthesis or secretion that were not detected at the gene expression level. Furthermore, it would be worthwhile to investigate alternative cell sources such as bone marrow-derived mesenchymal stromal cells (MSCs), adipose-derived stromal cells, or induced pluripotent stem cells (iPSCs), to see if the ECM could be harnessed within strategies to drive their lineage-specific differentiation towards an NP phenotype.

Data availability statement

The original contributions presented in the study are included in the article/Supplementary Materials, further inquiries can be directed to the corresponding authors.

Author contributions

CS and LF conceptualized and designed the study in collaboration with MQ and NS. MQ performed the experimental studies, with NS contributing to decellularization protocol development and PM performing the immunohistochemical characterization of the NP tissues. MQ performed the data analysis with guidance from CS and LF, and MQ, CS and LF interpreted the data and wrote the manuscript.

The project was supported through operating grant funding awarded to LF and CS.

Funding

Funding for this study was provided by the Ontario Institute for Regenerative Medicine (OIRM) and the Bone and Joint Institute at Western University, with infrastructure support from the Natural Sciences and Engineering Research Council of Canada (NSERC) Research Tools and Instruments Program, the Canada Foundation for Innovation (CFI) and the Ontario Research Fund (ORF). MQ and NS were supported in part by Transdisciplinary Training Awards from the Bone and Joint Institute at Western University, Canada and scholarship funding from the CONNECT! NSERC CREATE Training Program in Soft Connective Tissue Regeneration/Therapy. CS is supported by a Career Development award from the Arthritis Society.

Acknowledgments

The authors would like to acknowledge Todd Simpson and the Western Nanofabrication Facility for access to equipment and assistance with the SEM imaging. We also thank Courtney Brooks for support with training and technical assistance with the cell culture studies.

Conflict of interest

The authors declare that the research was conducted in the absence of any commercial or financial relationships that could be construed as a potential conflict of interest.

Publisher's note

All claims expressed in this article are solely those of the authors and do not necessarily represent those of their affiliated organizations, or those of the publisher, the editors and the reviewers. Any product that may be evaluated in this article, or claim that may be made by its manufacturer, is not guaranteed or endorsed by the publisher.

Supplementary material

The Supplementary Material for this article can be found online at: https://www.frontiersin.org/articles/10.3389/fbioe.2022.937239/full#supplementary-material

References

Adams, M. A., and Roughley, P. J. (2006). What is intervertebral disc degeneration, and what causes it? *Spine* 31 (18), 2151–2161. doi:10.1097/01.brs.0000231761.73859.2c

Alini, M., Eisenstein, S. M., Ito, K., Little, C., Kettler, A., Masuda, K., , et al.Hans, JW (2008). Are animal models useful for studying human disc disorders/degeneration? *Eur. Spine J.* 17 (1), 2–19. doi:10.1007/s00586-007-0414-y

Ashraf, S., Chatoor, C., Chong, J., Pilliar, R., Santerre, S., and Kandel, R. (2020). Transforming growth factor β enhances tissue formation by passaged nucleus pulposus cells *in vitro*. *J. Orthop. Res.* 38 (2), 438–449. doi:10.1002/jor.24476

Balagué, F., Mannion, A. F., Pellisé, F., and Cedraschi, C. (2012). Non-specific low back pain. *Lancet* 379 (9814), 482–491. doi:10.1016/S0140-6736(11)60610-7

Bedore, J., Leask, A., and Séguin, A. S. (2014). Targeting the extracellular matrix: Matricellular proteins regulate cell-extracellular matrix communication within distinct niches of the intervertebral disc. *Matrix Biol.* 37, 124–130. doi:10.1016/j.matbio.2014.05.005

Borrelli, C., and Buckley, C. T. (2020). Injectable disc-derived ECM hydrogel functionalised with chondroitin sulfate for intervertebral disc regeneration. *Acta Biomater.* 117, 142–155. doi:10.1016/j.actbio.2020.10.002

Brown, C. F. C., Yan, J., Han, T. T. Y., Marecak, D. M., Amsden, B. G., and Flynn, L. E. (2015). Effect of decellularized adipose tissue particle size and cell density on adipose-derived stem cell proliferation and adipogenic differentiation in composite methacrylated chondroitin sulphate hydrogels. *Biomed. Mat.* 10 (4), 045010. doi:10.1088/1748-6041/10/4/045010

Chan, L. K. Y., Leung, V. Y. L., Tam, V., Lu, W. W., Sze, K. Y., and Cheung, K. M. C. (2013). Decellularized bovine intervertebral disc as a natural scaffold for xenogenic cell studies. *Acta Biomater.* 9 (2), 5262–5272. doi:10.1016/j.actbio.2012.09.005

Chen, L., Liao, J., Klineberg, E., Leung, V. L., and Huang, S. (2017). Small leucine-rich proteoglycans (SLRPs): Characteristics and function in the intervertebral disc. *J. Tissue Eng. Regen. Med.* 11 (3), 602–608. doi:10.1002/term.2067

Cheung, H. K., Han, T. T. Y., Marecak, D. M., Watkins, J. F., Amsden, B. G., and Flynn, L. E. (2014). Composite hydrogel scaffolds incorporating decellularized adipose tissue for soft tissue engineering with adipose-derived stem cells. *Biomaterials* 35 (6), 1914–1923. doi:10.1016/j.biomaterials.2013.11.067

Cloyd, J. M., Malhotra, N. R., Weng, L., Chen, W., Mauck, R. L., and Elliott, D. M. (2007). Material properties in unconfined compression of human nucleus pulposus, injectable hyaluronic acid-based hydrogels and tissue engineering scaffolds. *Eur. Spine J.* 16 (11), 1892–1898. doi:10.1007/s00586-007-0443-6

Collin, E. C., Carroll, O., Kilcoyne, M., Peroglio, M., See, E., Hendig, D., et al. (2017). Marianna peroglio, eugene see, doris hendig, mauro Alini, sibylle grad, and abhay PanditAgeing affects chondroitin sulfates and their synthetic enzymes in the intervertebral disc. *Sig Transduct. Target Ther.* 2, 17049. doi:10.1038/sigtrans.2017.49

Craddock, R. J., Hodson, N. W., Hodson, M., Ozols, T., Shearer, J. A., Hoyland, Michael J., et al. (2018). Extracellular matrix fragmentation in Young, healthy cartilaginous tissues. *eCM* 35, 34–53. doi:10.22203/eCM.v035a04

Crapo, P. M., Gilbert, T. W., and Badylak, S. F. (2011). An overview of tissue and whole organ decellularization processes. *Biomaterials* 32 (12), 3233–3243. doi:10.1016/j.biomaterials.2011.01.057

Cui, J. H., Chang, H. G., and Kim, Y. C. (2012). The effects of monolayer subculture on the phenotype and growth of degenerated human intervertebral disc cells. *Tissue Eng. Regen. Med.* 9 (2), 92–100. doi:10.1007/s13770-012-0011-y

Demers, C. N., Antoniou, J., and Mwale, F. (2004). Value and limitations of using the bovine tail as a model for the human lumbar spine. *Spine* 29 (24), 2793–2799. doi:10.1097/01.brs.0000147744.74215.b0

DePalma, M. J., Ketchum, J. M., and Saullo, T. (2011). What is the source of chronic low back pain and does age play a role? *Pain Med.* 12 (2), 224–233. doi:10.1111/j.1526-4637.2010.01045.x

DeQuach, J. A., Mezzano, V., Miglani, A., Lange, S., Keller, G. M., Sheikh, F., et al. (2010). Simple and high yielding method for preparing tissue specific extracellular matrix coatings for cell culture. *PLoS ONE* 5 (9), e13039–11. doi:10.1371/journal.pone.0013039

Drury, J. L., and Mooney, D. J. (2003). Hydrogels for tissue engineering: Scaffold design variables and applications. *Biomaterials* 24 (24), 4337–4351. doi:10.1016/S0142-9612(03)00340-5

Erwin, W. M., Ashman, A., O'Donnel, O., and Inman, R. D. (2006). Nucleus pulposus notochord cells secrete connective tissue growth factor and up-regulate proteoglycan expression by intervertebral disc chondrocytes. *Arthritis Rheum.* 54 (12), 3859–3867. doi:10.1002/art.22258

Fernandez, C., Marionneaux, A., Gill, S., and Mercuri, J. (2016). Biomimetic nucleus pulposus scaffold created from bovine caudal intervertebral disc tissue utilizing an optimal decellularization procedure. *J. Biomed. Mat. Res.* 104 (12), 3093–3106. doi:10.1002/jbm.a.35858

Fiordalisi, M., Silva, A., Barbosa, M., Gonçalves, R., and Caldeira, J. (2020). Decellularized scaffolds for intervertebral disc regeneration. *Trends Biotechnol.* 38, 947–951. doi:10.1016/j.tibtech.2020.05.002

Francisco, A. T., Mancino, R. J., Bowles, R. D., Brunger, M., Tainter, D. M., Chen, Y-T., et al. (2013). Injectable laminin-functionalized hydrogel for nucleus pulposus regeneration. *Biomaterials* 34 (30), 7381–7388. doi:10.1016/j.biomaterials.2013.06.038

Freemont, A. J. (2009). The cellular pathobiology of the degenerate intervertebral disc and discogenic back pain. *Rheumatology* 48 (1), 5–10. doi:10.1093/rheumatology/ken396

Gawri, R., Shiba, T., Pilliar, R., and Kandel, R. (2017). Inorganic polyphosphates enhances nucleus pulposus tissue formation *in vitro*. *J. Orthop. Res.* 35 (1), 41–50. doi:10.1002/jor.23288

Gilbert, T. W., Freund, J. M., and Badylak, S. F. (2009). Quantification of DNA in biologic scaffold materials. *J. Surg. Res.* 152 (1), 135–139. doi:10.1016/j.jss.2008.02.013

Gilbert, T. W., Sellaro, T. L., and Badylak, S. F. (2006). Decellularization of tissues and organs. *Biomaterials* 27 (19), 3675–3683. doi:10.1016/j.biomaterials.2006.02.014

Gilbertson, L., Ahn, S. H., Teng, P. N., Studer, R. K., Niyibizi, C., and Kang, J. D. (2008). The effects of recombinant human bone morphogenetic protein-2, recombinant human bone morphogenetic protein-12, and adenoviral bone morphogenetic protein-12 on matrix synthesis in human annulus fibrosis and nucleus pulposus cells. *Spine J.* 8 (3), 449–456. doi:10.1016/j.spinee.2006.11.006

Gilchrist, C. L., Darling, E. M., Chen, J., and Setton, L. A. (2011). Extracellular matrix ligand and stiffness modulate immature nucleus pulposus cell-cell interactions. *PLoS ONE* 6 (11), e27170. doi:10.1371/journal.pone.0027170

Gilpin, A., and Yang, Y. (2017). Decellularization strategies for regenerative medicine: From processing techniques to applications. *BioMed Res. Int.* 2017, 1–13. doi:10.1155/2017/9831534

Graham, M. E., Gratzer, P. F., Bezuhly, M., and Hong, H. (2016). Development and characterization of decellularized human nasoseptal cartilage matrix for use in tissue engineering. *Laryngoscope* 126 (10), 2226–2231. doi:10.1002/lary.25884

Grenier, R., Périé, D., Gilbert, G., Beaudoin, G., and Curnier, D. (2014). Assessment of mechanical properties of muscles from multi-parametric magnetic resonance imaging. *JBiSE* 07 (08), 593–603. doi:10.4236/jbise.2014.78060

Gruber, H. E., Leslie, L., Ingram, J., Norton, H. J., and Hanley, E. N. (2004). Cell-based tissue engineering for the intervertebral disc: *In vitro* studies of human disc cell gene expression and matrix production within selected cell carriers. *Spine J.* 4 (1), 44–55. doi:10.1016/S1529-9430(03)00425-X

Guerrero, J., Häckel, S., Croft, A. S., Albers, C. E., and Gantenbein, B. (2021b). The effects of 3D culture on the expansion and maintenance of nucleus pulposus progenitor cell multipotency. *Jor Spine* 4 (1), 1–18. doi:10.1002/jsp2.1131

Guerrero, J., Häckel, S., Häckel, A. S., Croft, S., Hoppe, C. E., Albers, B., et al. (2021a). The nucleus pulposus microenvironment in the intervertebral disc: The fountain of youth? *eCM* 41, 707–738. doi:10.22203/eCM.v041a46

Hanai, H., Jacob, G., Nakagawa, S., Tuan, R. S., Nakamura, N., and Shimomura, K. (2020). Potential of soluble decellularized extracellular matrix for musculoskeletal tissue engineering - comparison of various mesenchymal tissues. *Front. Cell Dev. Biol.* 8, 1–15. doi:10.3389/fcell.2020.581972

Henry, N., Clouet, J., Fragale, A., Griveau, L., Chédeville, C., Véziers, J., et al. (2017). Pullulan microbeads/Si-hpmc hydrogel injectable system for the sustained delivery of GDF-5 and TGF-β1: New insight into intervertebral disc regenerative medicine. *Drug Deliv.* 24 (1), 999–1010. doi:10.1080/10717544.2017.1340362

Hensley, A., Rames, J., Casler, V., Rood, C., Walters, J., Fernandez, C., et al. (2018). Decellularization and characterization of a whole intervertebral disk xenograft scaffold. *J. Biomed. Mater Res. A* 106 (9), 2412–2423. doi:10.1002/jbm.a.36434

Hwang, P. Y., Chen, J., Jing, L., Hoffman, B. D., and Setton, L. A. (2014). The role of extracellular matrix elasticity and composition in regulating the nucleus pulposus cell phenotype in the intervertebral disc: A narrative review. *J. Biomechanical Eng.* 136 (2), 1–9. doi:10.1115/1.4026360

Hwang, P. Y., Jing, L., Chen, J., Lim, F. L., Tang, R., Choi, H., et al. (2016). N-cadherin is key to expression of the nucleus pulposus cell phenotype under selective substrate culture conditions. *Sci. Rep.* 6, 1–14. doi:10.1038/srep28038

Illien-Jünger, S., Sedaghatpour, D. S., Laudier, D. M., Hecht, A. C., Qureshi, S. A., and Iatridis, J. C. (2016). Development of a bovine decellularized extracellular matrix-biomaterial for nucleus pulposus regeneration. *J. Orthop. Res.* 34 (5), 876–888. doi:10.1002/jor.23088

Inoue, N., Alejandro, A., and Orías, E. (2012). Biomechanics of intervertebral disc degeneraion. *Orthop. Clin. N. Am.* 42 (4), 487–499. doi:10.1016/j.ocl.2011.07.001.Biomechanics

Inoue, T., Nakamura, T., Ikeda, T., and Takagi, K. (2005). Effect of extracellular matrix protein on the rate of proteoglycan synthesis in rabbit intervertebral disc cells. *J. Spinal Disord. Tech.* 18 (1), 52–57. doi:10.1097/01.bsd.0000128056.03461.6b

Jaworski, L. M., Kleinhans, K. L., and Jackson, A. R. (2019). Effects of oxygen concentration and culture time on porcine nucleus pulposus cell metabolism: An *in vitro* study. *Front. Bioeng. Biotechnol.* 7. (April): 1–12. doi:10.3389/fbioe.2019.00064

Jeong, C. G., Francisco, A. T., Niu, Z., Mancino, R. L., Craig, S. L., and Setton, L. A. (2014). Screening of hyaluronic acid-poly(ethylene glycol) composite hydrogels to support intervertebral disc cell biosynthesis using artificial neural network analysis. *Acta Biomater.* 10 (8), 3421–3430. doi:10.1016/j.actbio.2014.05.012

Kawakami, M., Matsumoto, T., Hashizume, H., Kuribayashi, K., Chubinskaya, S., and Yoshida, M. (2005). Osteogenic protein-1 (osteogenic protein-1/bone morphogenetic protein-7) inhibits degeneration and pain-related behavior induced by chronically compressed nucleus pulposus in the rat. *Spine* 30 (17), 1933–1939. doi:10.1097/01.brs.0000176319.78887.64

Kornmuller, A., Brown, C. F. C., Yu, C., and Flynn, L. E. (2017). Fabrication of extracellular matrix-derived foams and microcarriers as tissue-specific cell culture and delivery platforms. *JoVE* 2017 (122), 1–11. doi:10.3791/55436

Kushioka, J., Kaito, T., Chijimatsu, R., Okada, R., Ishiguro, H., Bal, Z., et al. (2019). A novel and efficient method for culturing mouse nucleus pulposus cells. *Spine J.* 19 (9), 1573–1583. doi:10.1016/j.spinee.2019.04.005

Lin, X., Fang, X., Wang, Q., Hu, Z., Chen, K., Shan, Z., et al. (2016). Decellularized allogeneic intervertebral disc: Natural biomaterials for regenerating disc degeneration. *Oncotarget* 7 (11), 12121–12136. doi:10.18632/oncotarget.7735

Ludwinski, F. E., Gnanalingham, K., Richardson, S. M., and Hoyland, J. A. (2013). Understanding the native nucleus pulposus cell phenotype has important implications for intervertebral disc regeneration strategies. *Regen. Med.* 8 (1), 75–87. doi:10.2217/rme.12.108

Martin, P. M., Grant, A. G., Hamilton, D. W., and Flynn, L. E. (2019). Matrix composition in 3-D collagenous bioscaffolds modulates the survival and angiogenic phenotype of human chronic wound dermal fibroblasts. *Acta Biomater.* 83, 199–210. doi:10.1016/j.actbio.2018.10.042

Masuda, K., Imai, Y., Okuma, M., Muehleman, C., Nakagawa, K., Akeda, K., et al. (2006). Osteogenic protein-1 injection into a degenerated disc induces the restoration of disc height and structural changes in the rabbit anular puncture model. *Spine* 31 (7), 742–754. doi:10.1097/01.brs.0000206358.66412.7b

Mercuri, J. J., Gill, S. S., and Simionescu, D. T. (2011). Novel tissue-derived biomimetic scaffold for regenerating the human nucleus pulposus. *J. Biomed. Mat. Res.* 96A (2), 422–435. doi:10.1002/jbm.a.33001

Murray, C. J., C Atkinson, K. B., Birbeck, G., Burstein, R., and Chou, D. (2013). The state of US health, 1990-2010. *Jama* 310 (6), 591–608. doi:10.1001/jama.2013.13805

Norbertczak, H., Ingham, E., Fermor, H. L., and Wilcox, R. K. (2020). Decellularized intervertebral discs: A potential replacement for degenerate human discs. *Tissue Eng. Part C. Methods* 26 (11), 565–576. doi:10.1089/ten.tec.2020.0104

O'Halloran, D. M., and Pandit, A. S. (2007). Tissue-engineering approach to regenerating the intervertebral disc. *Tissue Eng.* 13 (8), 1927–1954. doi:10.1089/ten.2005.0608

Peloso, A., Katari, R., Tamburrini, R., Duisit, D., and Orlando, G. (2016). Glycosaminoglycans as a measure of outcome of cell-on-scaffold seeding (decellularization) technology. *Expert Rev. Med. Devices* 13 (12), 1067–1068. doi:10.1080/17434440.2016.1249849

Piening, L. M., Lillyman, D. J., Lee, F., Lozano, A., Miles, J. R., and Wachs, R. A. (2022). Injectable decellularized nucleus pulposus tissue exhibits neuroinhibitory properties. *Jor Spine* 5. November 2021: 1–16. doi:10.1002/jsp2.1187

Priyadarshani, P., Li, Y., Yang, S., and Yao, L. (2016). Injectable hydrogel provides growth-permissive environment for human nucleus pulposus cells. *J. Biomed. Mat. Res.* 104 (2), 419–426. doi:10.1002/jbm.a.35580

Ramirez, F., and Rifkin, D. B. (2003). Cell signaling events: A view from the matrix. *Matrix Biol.* 22 (2), 101–107. doi:10.1016/S0945-053X(03)00002-7

Recuerda, M., Coté, S. P., Villemure, I., and Périé, D. (2011). Influence of experimental protocols on the mechanical properties of the intervertebral disc in unconfined compression. *J. Biomechanical Eng.* 133 (7), 1–5. doi:10.1115/1.4004411

Reginensi, D., Ortiz, D., Pravia, A., Burillo, A., Morales, F., Morgan, C., et al. (2020). Role of region-specific brain decellularized extracellular matrix on *in vitro* neuronal maturation. *Tissue Eng. Part A* 26 (17–18), 964–978. doi:10.1089/ten.tea.2019.0277

Robb, K. P., Shridhar, A., and Flynn, L. E. (2018). Decellularized matrices as cell-instructive scaffolds to guide tissue-specific regeneration. *ACS Biomater. Sci. Eng.* 4 (11), 3627–3643. doi:10.1021/acsbiomaterials.7b00619

Rosenzweig, D. H., Tremblay Gravel, J., Tremblay Gravel, D., Bisson, J. A., Ouellet, M. H., Weber, Haglund., et al. (2017). Comparative analysis in continuous expansion of bovine and human primary nucleus pulposus cells for tissue repair applications. *eCM* 33, 240–251. doi:10.22203/eCM.v033a18

Rothrauff, B. B., Yang, G., and Tuan, R. S. (2017). Guang Yang, and rocky S. TuanTissue-Specific bioactivity of soluble tendon-derived and cartilage-derived extracellular matrices on adult mesenchymal stem cells. *Stem Cell Res. Ther.* 8 (1), 1–17. doi:10.1186/s13287-017-0580-8

Roughley, P. J. (2004). Biology of intervertebral disc aging and degeneration. *Spine* 29 (23), 2691–2699. doi:10.1097/01.brs.0000146101.53784.b1

Rubashkin, M. G., Ou, G., and Weaver, V. M. (2014). Deconstructing signaling in three dimensions. *Biochemistry* 53 (13), 2078–2090. doi:10.1021/bi401710d

Schol, J., and Sakai, D. (2019). Cell therapy for intervertebral disc herniation and degenerative disc disease: Clinical trials. *Int. Orthop. (SICOT)* 43 (4), 1011–1025. doi:10.1007/s00264-018-4223-1

Séguin, C. A., Grynpas, M. D., Pilliar, R. M., Waldman, S. D., and Kandel, R. A. (2004). Tissue engineered nucleus pulposus tissue formed on a porous calcium polyphosphate substrate. *Spine* 29 (12), 1299–1306. doi:10.1097/01.BRS.0000127183.43765.AF

Shridhar, A., Amsden, B. G., Gillies, E. R., and Flynn, L. E. (2019). Investigating the effects of tissue-specific extracellular matrix on the adipogenic and osteogenic differentiation of human adipose-derived stromal cells within composite hydrogel scaffolds. *Front. Bioeng. Biotechnol.* 7. doi:10.3389/fbioe.2019.00402

Shridhar, A., Gillies, E., Amsden, B. G., and Flynn, L. E. (2017). Composite bioscaffolds incorporating decellularized ECM as a cell-instructive component within hydrogels as *in vitro* models and cell delivery systems. *Decellularized Scaffolds Organog. Methods Mol. Biol.* 1577, 183–208. doi:10.1007/7651_2017_36

Shridhar, A., Lam, A. Y. L., Simmons, C. A., Gillies, C. A., Flynn, E. R., and Flynn, L. E. (2020). Culture on tissue-specific coatings derived from α-amylase-digested decellularized adipose tissue enhances the proliferation and adipogenic differentiation of human adipose-derived stromal cells. *Biotechnol. J.* 15 (3), e1900118–10. doi:10.1002/biot.201900118

Spillekom, S., Smolders, L. A., Grinwis, G. C. M., ArkesteijnArkesteijn, T. M., Ito, K., Meij, B. P., et al. (2014). Increased osmolarity and cell clustering preserve canine notochordal cell phenotype in culture. *Tissue Eng. Part C. Methods* 20 (8), 652–662. doi:10.1089/ten.tec.2013.0479

Tang, G., Zhou, B., Li, F., Wang, W., Liu, Y., Wang, X., et al. (2020). Advances of naturally derived and synthetic hydrogels for intervertebral disk regeneration. *Front. Bioeng. Biotechnol.* 8, 1–13. doi:10.3389/fbioe.2020.00745

Tsai, T. T., Guttapalli, A., Oguz, E., Chen, L. H., Vaccaro, A. R., Albert, T. J., et al. (2007). Fibroblast growth factor-2 maintains the differentiation potential of nucleus pulposus cells *in vitro*. *Spine* 32 (5), 495–502. doi:10.1097/01.brs.0000257341.88880.f1

Tsuchiya, T., Balestrini, J. L., Mendez, J., Calle, E. A., Zhao, L., and Niklason, L. E. (2014). Influence of PH on extracellular matrix preservation during lung decellularization. *Tissue Eng. Part C. Methods* 20 (12), 1028–1036. doi:10.1089/ten.tec.2013.0492

Turner, A. E. B., Yu, C., Bianco, J., Watkins, J. F., and Flynn, L. E. (2012). The performance of decellularized adipose tissue microcarriers as an inductive substrate for human adipose-derived stem cells. *Biomaterials* 33 (18), 4490–4499. doi:10.1016/j.biomaterials.2012.03.026

Urban, J. P. G., and Roberts, S. (2003). Degeneration of the intervertebral disc. *Arthritis Res. Ther.* 5 (3), 120–130. doi:10.1186/ar629

Vadalà, G., Sowa, G., Hubert, M., Gilbertson, L. G., Denaro, V., and Kang, J. D. (2012). Mesenchymal stem cells injection in degenerated intervertebral disc: Cell leakage may induce osteophyte formation. *J. Tissue Eng. Regen. Med.* 6 (5), 348–355. doi:10.1002/term.433

Wachs, R. A., Hoogenboezem, E. N., Huda, H. I., Xin, S., Porvasnik, S. L., and Schmidt, C. E. (2017). Creation of an injectable *in situ* gelling native extracellular matrix for nucleus pulposus tissue engineering. *Spine J.* 17 (3), 435–444. doi:10.1016/j.spinee.2016.10.022

Wei, A., Brisby, H., Chung, S. A., and Diwan, A. D. (2008). Bone morphogenetic protein-7 protects human intervertebral disc cells *in vitro* from apoptosis. *Spine J.* 8 (3), 466–474. doi:10.1016/j.spinee.2007.04.021

Xu, J., Liu, S., Wang, S., Qiu, P., Chen, P., Lin, X., et al. (2019). Decellularised nucleus pulposus as a potential biologic scaffold for disc tissue engineering. *Mater. Sci. Eng. C* 99 (2018), 1213–1225. doi:10.1016/j.msec.2019.02.045

Xu, P., Guan, J., Chen, Y., Xiao, H., Yang, T., Sun, H., et al. (2021). Stiffness of photocrosslinkable gelatin hydrogel influences nucleus pulposus cell properties *in vitro*. *J. Cell Mol. Med.* 25 (2), 880–891. doi:10.1111/jcmm.16141

Yang, X., and Li, X. (2009). Nucleus pulposus tissue engineering: A brief review. *Eur. Spine J.* 18 (11), 1564–1572. doi:10.1007/s00586-009-1092-8

Yu, C., Bianco, J., Brown, C., Fuetterer, L., Watkins, J. F., Samani, A., et al. (2013). Porous decellularized adipose tissue foams for soft tissue regeneration. *Biomaterials* 34 (13), 3290–3302. doi:10.1016/j.biomaterials.2013.01.056

Yu, C., Kornmuller, K., Brown, C., Hoare, H., and Flynn, L. E. (2017). Decellularized adipose tissue microcarriers as a dynamic culture platform for human adipose-derived stem/stromal cell expansion. *Biomaterials* 120, 66–80. doi:10.1016/j.biomaterials.2016.12.017

Yuan, M., Leong, K. W., and Chan, B. P. (2011). Three-dimensional culture of rabbit nucleus pulposus cells in collagen microspheres. *Spine J.* 11 (10), 947–960. doi:10.1016/j.spinee.2011.07.004

Zhou, X., Wang, J., Huang, X., Fang, W., Tao, Y., Zhao, T., et al. (2018). Injectable decellularized nucleus pulposus-based cell delivery system for differentiation of adipose-derived stem cells and nucleus pulposus regeneration. *Acta Biomater.* 81, 115–128. doi:10.1016/j.actbio.2018.09.044

frontiers | Frontiers in Bioengineering and Biotechnology

TYPE Original Research
PUBLISHED 12 October 2022
DOI 10.3389/fbioe.2022.970235

Check for updates

OPEN ACCESS

EDITED BY
Rahul Gawri,
McGill University, Canada

REVIEWED BY
Amani Hassan,
McGill University, Canada
Derek H. Rosenzweig,
McGill University, Canada
Muhammad Farooq Rai,
Washington University in St. Louis, United States

*CORRESPONDENCE
Chathuraka T. Jayasuriya,
chathuraka_jayasuriya@brown.edu

SPECIALTY SECTION
This article was submitted to Tissue Engineering and Regenerative Medicine, a section of the journal Frontiers in Bioengineering and Biotechnology

RECEIVED 15 June 2022
ACCEPTED 03 October 2022
PUBLISHED 12 October 2022

CITATION
Desai S, Dooner M, Newberry J, Twomey-Kozak J, Molino J, Trivedi J, Patel JM, Owens BD and Jayasuriya CT (2022), Stable human cartilage progenitor cell line stimulates healing of meniscal tears and attenuates post-traumatic osteoarthritis.
Front. Bioeng. Biotechnol. 10:970235.
doi: 10.3389/fbioe.2022.970235

COPYRIGHT
© 2022 Desai, Dooner, Newberry, Twomey-Kozak, Molino, Trivedi, Patel, Owens and Jayasuriya. This is an open-access article distributed under the terms of the Creative Commons Attribution License (CC BY). The use, distribution or reproduction in other forums is permitted, provided the original author(s) and the copyright owner(s) are credited and that the original publication in this journal is cited, in accordance with accepted academic practice. No use, distribution or reproduction is permitted which does not comply with these terms.

Stable human cartilage progenitor cell line stimulates healing of meniscal tears and attenuates post-traumatic osteoarthritis

Salomi Desai[1], Mark Dooner[2], Jake Newberry[1], John Twomey-Kozak[1], Janine Molino[1], Jay Trivedi[1], Jay M. Patel[3], Brett D. Owens[1] and Chathuraka T. Jayasuriya[1]*

[1]Department of Orthopaedics, Warren Alpert Medical School of Brown University and the Rhode Island Hospital, Providence, RI, United States, [2]Department of Medicine, Division of Hematology Oncology, Rhode Island Hospital, Providence, RI, United States, [3]Department of Orthopaedics, Emory University, Atlanta, GA, United States

Meniscal tearing in the knee increases the risk of post-traumatic osteoarthritis (OA) in patients. The therapeutic application of tissue-specific mesenchymal progenitor cells is currently being investigated as an emerging biologic strategy to help improve healing of musculoskeletal tissues like meniscal fibrocartilage and articular hyaline cartilage. However, many of these approaches involve isolating cells from healthy tissues, and the low yield of rare progenitor populations (< 1% of total cells residing in tissues) can make finding a readily available cell source for therapeutic use a significant logistical challenge. In the present study, we investigated the therapeutic efficacy of using expanded cartilage-derived and bone marrow-derived progenitor cell lines, which were stabilized using retroviral SV40, for repair of meniscus injury in a rodent model. Our findings indicate that these cell lines express the same cell surface marker phenotype of primary cells (CD54+, CD90+, CD105+, CD166+), and that they exhibit improved proliferative capacity that is suitable for extensive expansion. Skeletally mature male athymic rats treated with 3.2 million cartilage-derived progenitor cell line exhibited approximately 79% greater meniscal tear reintegration/healing, compared to injured animals that left untreated, and 76% greater compared to animals treated with the same number of marrow-derived stromal cells. Histological analysis of articular surfaces also showed that cartilage-derived progenitor cell line treated animals exhibited reduced post-traumatic OA associated articular cartilage degeneration. Stable cell line treatment did not cause tumor formation or off-target engraftment in animals. Taken together, we present a proof-of-concept study demonstrating, for the first time, that intra-articular injection of a stable human cartilage-derived progenitor cell line stimulates meniscus tear healing and provide chondroprotection in an animal model. These outcomes suggest that the use of stable cell lines may help overcome cell source limitations for cell-based medicine.

KEYWORDS

meniscus repair, cartilage progenitor cell, stem cell, progenitor cell, cartilage, PTOA, regenerative medicine, rodent model

Introduction

The menisci are crescent shaped fibrocartilaginous tissues (Makris et al., 2011) that help to distribute axial load and provide knee joint stability (Fox et al., 2012). Meniscus injuries account for up to 20% of total knee injuries in young athletes, for whom the most sophisticated epidemiological data exist (Cameron et al., 2017; Kennedy et al., 2020). Specifically, meniscus tearing is one of the most common knee injuries occurring in 6—8% of active young adults annually in the U.S. (Baker et al., 1985; Jones et al., 2012) and it results in increased incidence rate of osteoarthritis (OA) (Englund et al., 2009). Tears compromise the ability of the meniscus to distribute loads in the joint, increasing cartilage-cartilage stresses, and starting a degenerative cascade. These injuries are treated clinically by arthroscopic surgical resection or suture repair, based on the nature and extent of tearing. However, due to the relatively hypovascular and hypocellular nature of meniscal fibrocartilage, its intrinsic healing capacity is limited, which is reflected in a high reoperation rate after meniscal repair of 16.5%–20.7% (Paxton et al., 2011). For these reasons, better stimulation of meniscal fibrocartilage healing could reduce reoperation and post-traumatic OA (PTOA) progression.

Mesenchymal progenitor cells derived from healthy articular cartilage, herein referred as CPCs, are a small subset of cells that are highly proliferative, chondrogenic, and migratory (Dowthwaite et al., 2004; Seol et al., 2014; Jayasuriya and Chen, 2015; Jayasuriya et al., 2016), making them a potentially useful resource for biologic cell therapy and cartilaginous tissue engineering applications (McCarthy et al., 2012; Seol et al., 2014; Bilgen et al., 2018; Park et al., 2020). Further, they are resistant to cellular hypertrophy and terminal differentiation (McCarthy et al., 2012; Twomey-Kozak et al., 2020), unlike mesenchymal progenitor/stem cells from bone marrow and osteoarthritic (diseased) cartilage tissue (Jayasuriya et al., 2018; Hu et al., 2019; Liu et al., 2020). We have recently demonstrated the efficacy of using stable CPC lines, either as such or in a collagen coated hydroxypropyl cellulose scaffold, to stimulate meniscus injury repair in rat and human *ex-vivo* organ culture model systems, respectively (Jayasuriya et al., 2019; Newberry et al., 2020).

In this study, we sought to validate our previous *ex-vivo* findings using a live animal model. To this end, our objective was to test the efficacy of intraarticularly injecting CPCs as a biologic cell therapy in order to accelerate healing of a meniscal tear injury in live rats. In particular, we hypothesized that CPC injections would accelerate meniscal healing and reduce the progression of PTOA. We opted to use one of the four previously generated and characterized stable CPC lines (CPCL3) for this purpose, considering the low natural abundance of primary CPCs in healthy articular cartilage (Jayasuriya et al., 2019). Our motivation was to report on the therapeutic efficacy of using this abundant and expandable CPC source for cartilaginous musculoskeletal tissue repair.

Materials and methods

Isolation and generation of human progenitor cell lines

The stable CPC line (CPCL3) used in this study was generated previously (Jayasuriya et al., 2019). A stable BM-MSC line (BM-MSCL) was generated in the same way by infecting with pRetro-E2 SV40 (Applied Biological Materials, Inc., Richmond, BC, Canada) according to the manufacturer. Primary CPCs (P-CPCs) were isolated from the non-arthritic articular cartilage of three different patients: 15-year, 18-year and 42-year-old, undergoing arthroscopy, with an approval from the IRB of Rhode Island Hospital (committee number 0070–17). Cartilage was diced followed by enzymatic tissue digestion using Pronase (Roche, Indianapolis, IN; 2.0 mg/ml in HBSS) and Collagenase type IA (Sigma-Aldrich, St. Louis, MO; 1.0 mg/ml in HBSS), similar to previously described method (Jayasuriya et al., 2019). P-CPCs were enriched by fibronectin adhesion (Williams et al., 2010; Jayasuriya et al., 2019) and adherent cells were cultured in Dulbecco's Modified Eagle's Medium supplemented with 10% Fetal Bovine Serum (FBS), 1% Pen Strep, 100 mM HEPES, 2 mM l-glutamine, 0.1 mM ascorbic acid, 0.1 mM sodium pyruvate, and 2.7 μM l-glucose (DMEM++) media and used for experiments as P-CPCs. Human Bone Marrow Mesenchymal Stem Cells (BM-MSCs) were purchased from American Type Culture Collection (ATCC) (PCS-500–012). Both BM-MSCL and CPCL3 were cultured and expanded in DMEM++ media for experiments conducted throughout this study.

Cell surface marker analysis

Cell surface marker analysis was performed to compare primary cells to stable cell lines. Cell suspensions were stained with antibody pre-conjugated with dye. CD90-FITC/PE (catalog # 130-114-901/130-114-902), CD54-PE (catalog # 130-120-780), CD49e-PE (catalog # 130-10-590), CD166-APC (catalog # 130-104-164), CD105-APC (catalog # 130-099-125), and IgG isotype-FITC/PE/APC controls (catalog # 130-113-761/130-113-762/130-113-758) from Miltenyi Biotec Inc., Auburn, CA. were

TABLE 1 List of forward and reverse primers, in 5′ to 3′ orientation, used for Real-Time Quantitative PCR. NCBI accession identification numbers of target sequences are included for each primer pair.

Gene	Forward seq.	Reverse seq.	Accession
SOX9	GGACCAGTACCCGCACTTGCA	GTTCTTCACCGACTTCCTCCGCCG	NM_000346.3
COL1A1	CAGGAGGCACGCGGAGTGTG	GGCAGGGCTCGGGTTTCCAC	NM_000088.3
COL2A1	CTCCCAGAACATCACCTACCACT	CGTGAACCTGCTATTGCCCT	NM_001844.4
Beta-Actin	GGACCTGACTGACTACCTCAT	CGTAGCACAGCTTCTCCTTAAT	NM_001101.4
MMP2	AGGAGGAGAAGGCTGTGTTC	TGGGGAAGCCAGGATCCATT	NM_004530.6
MMP13	ATGCGGGGTTCCTGATGTGG	GGCCCAGGAGGAAAAGCATG	NM_002427.4
ADAMTS-4	CCCCAGACCCCGAAGAGCCA	CCCGCTGCCAGGCACAGAAG	NM_005099.6
ADAMTS-5	GGCCGTGGTGAAGGTGGTGG	GCTGCGTGGAGGCCATCGTC	NM_007038.5
Mitochondrial Cytochrome B	TAGCAATAATCCCCATCCTCCATATAT	ACTTGTCCAATGATGGTAAAAGG	NC_012920.1

used according to manufacturer's protocol. Cells were washed in 5 ml of 1X PBS, spun down in a centrifuge at 300 g and resuspended in 100 µl of buffer (1X PBS, 0.5% Bovine Serum Albumin). Pre-conjugated antibody (10 µl) was added to the cell buffer and incubated in the dark at 4°C for 10 min. Flow cytometry was performed using an LSRII flow cytometer (BD Biosciences, Franklin Lakes NJ), and data were analyzed using FlowJo, Version10.7.2, (BD Biosciences, Franklin Lakes, NJ).

RNA expression analysis

Messenger RNA (mRNA) expression was quantified using real-time quantitative polymerase chain reaction (RT-qPCR). Total mRNA was isolated from cells *via* MagMAX™-96 for Microarrays Total RNA Isolation Kit (Thermo Fisher Scientific, Waltham, MA), according to manufacturer's protocol. mRNA was reverse transcribed into cDNA using iScript cDNA Synthesis Kit (Bio-Rad, Hercules, CA), according to manufacturer's protocol. RNA levels were calculated using the delta delta Ct (ΔΔCt) method and normalized to beta-actin, housekeeping gene. $X = 2^{-\Delta\Delta Ct}$, in which $\Delta\Delta Ct = (Ct_{\text{Exp target gene}} - Ct_{\text{Exp housekeeping gene}}) - (Ct_{\text{Ctl target gene}} - Ct_{\text{Ctl housekeeping gene}})$ and X = Relative transcript; Ct_{Exp} = Ct of experimental group, Ct_{Ctl} = Ct of control group. Data obtained from the three patient derived primary CPCs were pooled in order to compare their mRNA profile to that of CPCL3. Primer sequences used to test each gene are listed in Table 1.

Cell proliferation analysis

Cell proliferation assay was used to measure rates of proliferation between primary cells and cell lines. Cells were cultured for 48 h, and cell proliferation was measured using Click-iT™ Plus EdU Alexa Fluor™ 488 Flow Cytometry Assay Kit (Thermo Fisher Scientific, Waltham, MA), according to manufacturer's protocol. Cells (5.0×10^5) were stained with EdU for 2 h, fixed and then analyzed using Flow Cytometry. Data was analyzed using FlowJo.

Rodent meniscus injury model and treatment

All procedures used in this study were approved by the Institutional Animal Care and Use Committee (IACUC) of Rhode Island Hospital (committee number 0190–16). Skeletally mature male athymic RNU rats (12–15 weeks of age) were allowed to acclimate for 1 week prior to the surgery. Animals were anesthetized with isoflurane (3–5%) and the right knee was shaved and prepped thrice with surgical scrub followed by 70% alcohol. Pre-operatively, animals received cefazolin (20mg/kg) *via* intra-muscular injection as a prophylactic antibiotic and sustained release buprenorphine (1.2 mg/kg body weight) *via* subcutaneous injection to provide 72 h of analgesia. A medial side parapatellar arthrotomy was performed (by blunt dissection to minimize bleeding) on the right knee joints until the outer rim of the medial meniscus was exposed. Starting from the back rim of the medial meniscus, a full thickness 1.0 mm tear spanning from the red-red zone to the red-white zone was made using a micro scissor. The meniscus was left partially torn, and we ensured that it was not completely separated into two independent pieces. After the meniscal injury was induced, the synovial capsule was closed using 4–0 sutures, followed by muscle closure, and finally skin closure. VetBond skin glue was applied topically on the skin as an additional measure to close the wound site. Post-operatively, rats were housed two per cage and were permitted to bear weight as tolerated. Intra-articular injections of the CPCL3 or BM-MSCL treatments (1.6×10^6 of cells in 50 µL sterile PBS), were administered twice, at Week 1 and Week 4 post-surgery, through the patellar tendon into the joint space. We selected to inject 50 µL because studies have shown that up to

100 µL can be injected into the knee joints of rats (Yang et al., 2015; Fan et al., 2018). Administered cells were fluorescently labelled with Vibrant CM-Dil Cell-Labeling (Cat: V22888, Thermo Fisher Scientific, Waltham, MA) solution according to the manufacturer's instructions. The control group was administered with only the vehicle (50 µL of sterile PBS). Animals were euthanized 7-week following surgery for the postmortem analysis of relevant tissues.

Human DNA analysis

Athymic rats were euthanized 7 weeks after surgery and their organs (kidney, lungs, liver, spleen, and brain) were harvested and frozen immediately. These tissues were weighed and homogenized by Proteinase K digestion using DNeasy Blood and Tissue kit (Qiagen, Hilden, Germany), and DNA was isolated using the provided mini spin column according to the manufacturer's protocol. DNA was then quantified spectrophotometrically and used as template for PCR amplification of the human mitochondrial cytochrome B gene. Primer sequences for the gene product were obtained from Matsuda et al., 2005 (Matsuda et al., 2005). Amplified product was subjected to agarose gel electrophoresis and bands were observed under the UVP Bio-Doc Transilluminator.

Histology analysis

Seven weeks following surgery, athymic rats were euthanized, and their medial menisci, femoral condyles and tibial plateaus were harvested, and fixed in 10% Neutral Buffered Formalin followed by decalcification and processing. Samples were sectioned at 4 µm in transverse plane for histological assessment of the meniscus and in parasagittal plane for articular cartilage. Menisci were stained with Saf-O/Fast Green and adjacent sister sections (collected approximately every 150 µm) were stained with DAPI. Femoral condyle and Tibial Plateau were stained with Saf-O/Fast Green. Scoring of the femoral condyle and tibial plateau was conducted using Modified Mankin scoring. Histological scoring was performed independently by two different graders that were blinded to the animal identifier and their respective surgical treatment group. Their mean scores were used for analysis.

Statistical analysis

Statistical analysis was conducted using SAS version 9.4 (SAS Institute Inc., Cary, NC). Generalized linear models were used to compare all outcome measures between experimental conditions. Raw cycles-to-threshold of the synovial RT-qPCR were analyzed using a generalized linear model (GLM) with a Gaussian distribution and log link function, normalizing to the housekeeper gene within the model. The standard 2-to-the-negative-delta-delta formula was applied to the means and confidence intervals of relevant effects for presentation as normalized fold differences. GLM with a binomial distribution and logit link function was used to examine differences in Mankin score between experimental conditions and broken menisci while GLM with a Gaussian distribution and log link function was used to examine differences in the quantified size of defect area between experimental conditions. In the defect area analysis for the quantification of the size of the defect area was operationalized in two ways. In the first operationalization, animals in the 0-week control group, which were used to determine the reproducibility of the tear size, and animals with broken tears were excluded from the analysis since 7-week follow-up period was not collected for this set. In the second operationalization, 0-week control group was again excluded for the same reason and additionally, the missing value for the animals with broken tears was replaced with a variable that was 20% more than the maximum open area observed in the study. In all models, pairwise comparisons between experimental conditions were conducted within the GLM *via* orthogonal contrasts. The Holm test was used to protect against multiple comparisons and maintain a two-tailed familywise alpha of 0.05. Classical sandwich estimation was used to protect against possible model misspecification. Error bars in figures represent +1 standard deviation (SD) of the mean.

Results

Stable human mesenchymal progenitor cell lines maintain same cell surface marker profile as primary cells

In order to test the *in vivo* efficacy of treating meniscus tears with CPCs, we utilized the human cartilage progenitor cell line 3 (CPCL3), which was first reported for its ability to stimulate meniscal tear reunion, in explant culture (Jayasuriya et al., 2019). In the present study, we generated a human BM-MSC cell line (BM-MSCL) to which the *in vivo* repair efficacy of CPCL3 can be compared. We decided to use BM-MSCs as our control because they are among the most commonly studied progenitor populations that are used in pre-clinical investigations of cell-based musculoskeletal tissue repair. BM-MSCL was created using retroviral gene transfer of Large T antigen, which is the same procedure used to generate CPCL3. Flow cytometry results indicating the cell surface marker profiles of CPCL3 showed no notable differences from primary cells, suggesting that it exhibits phenotypic stability during monolayer culture expansion (Figure 1).

First, we confirmed the presence of cell surface fibronectin receptor (CD49e), which is a selection criterion for progenitor cells in cartilage (Williams et al., 2010). CPCL3 and primary CPCs derived from three females (15, 18, and 42 years old) showed ≥ 94% positivity for CD49e cell surface expression. Next, we analyzed mesenchymal progenitor cell associated markers Thy-1 (CD90), Endoglin (CD105)

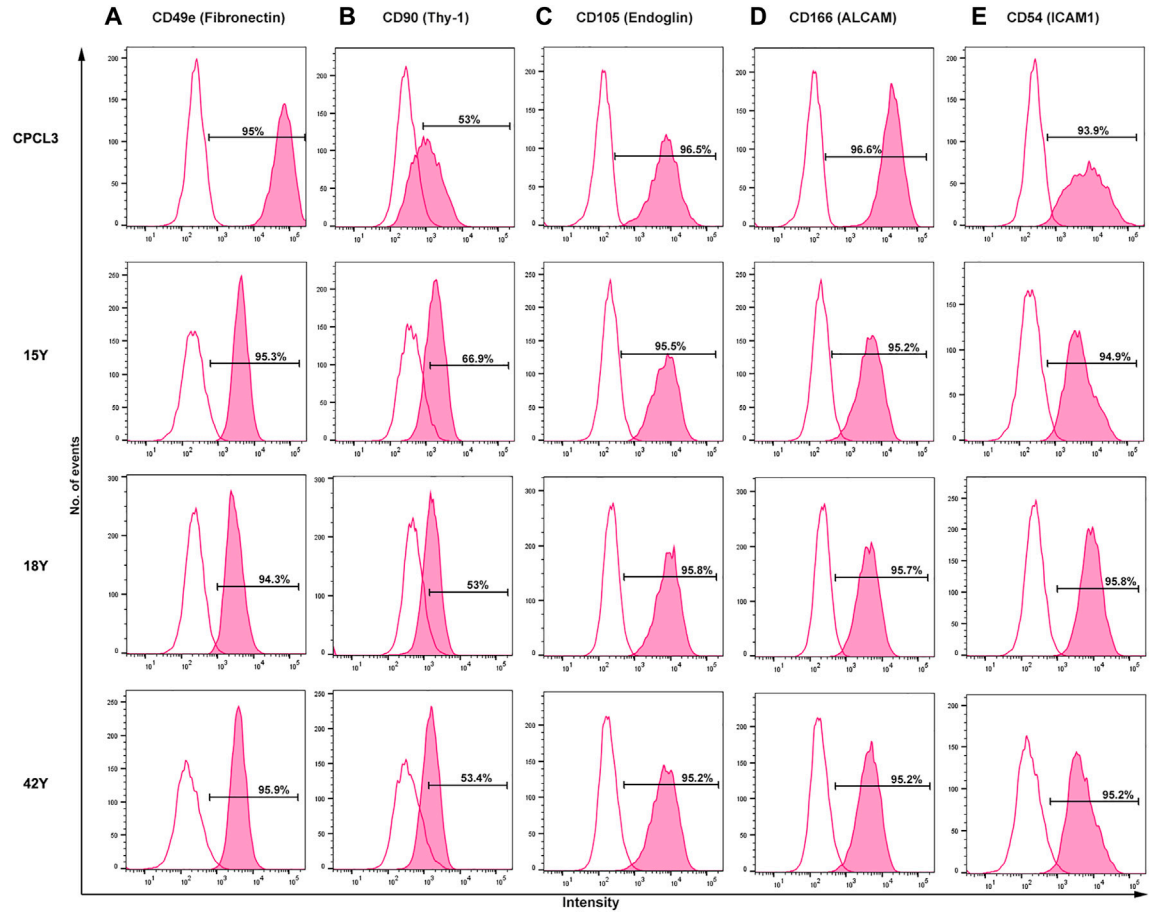

FIGURE 1
Side-by-side comparison of the cell surface marker profiles of the stable CPC line (CPCL3) and primary CPCs. Cell surface marker expression rates of **(A)** Fibronectin, **(B)** Thy-1, **(C)** Endoglin, **(D)** ALCAM, and **(E)** ICAM1 in CPCL3 and three primary CPC cell sources. Primary CPCs were independently collected and analyzed from three different individuals: 15-, 18-, and 42-years-old patients with no signs of degenerative joint diseases, such as osteoarthritis or rheumatoid arthritis. The empty peaks represent isotypic controls, for reference. Percent values indicated in the graphs represent positive staining rate, above isotype control, for each individual CD marker.

and ALCAM (CD166) as well as chondrocyte associated marker ICAM1 (CD54). CD90 showed positive expression in >50% of the cells constituting the stable CPC line, as previously reported (Jayasuriya et al., 2019; Twomey-Kozak et al., 2020), and in the primary CPCs isolated from all three patients. CD105 and CD166 were expressed in ≥ 95% of the stable CPC line and all tested primary CPCs. Chondrocyte associated marker ICAM1 (CD54) (Kienzle and von Kempis, 1998; Lee et al., 2009) was also highly expressed in all CPCs tested (≥93%).

Cell surface marker profiling of BM-MSCL was also performed and compared to that of primary BM-MSCs (Supplementary Figure S1). Results showed that the stable line exhibited no significant deviations in all tested markers (CD49e, CD54, CD90, CD105, and CD166) suggesting that BM-MSCL is phenotypically stable and does not deviate from its primary counterpart, with regards to its cell surface marker profile.

Stable CPCs exhibit lower collagen expression but higher *SOX9* expression and elevated proliferation capacity than primary CPCs

Gene expression profiling of master chondrogenesis regulator *SOX9* and collagens, which are central to the fibrocartilage extracellular matrix network composition, was performed *via* RT-qPCR in the stable cell lines and primary cells. The stable CPC cell line exhibited higher basal *SOX9* expression compared to that of primary CPCs (Figure 2A), and lower expression of type II and I collagen (*COL2A1, COL1A1*) (Figures 2B,C). Primary CPCs expressed approximately a 6-fold increase in *COL2A1* and a 2.5-fold increase in *COL1A1*, relative to CPCL3. BM-MSCL was also compared to primary BM-MSCs with regards to the expression of these key mediators of cartilage and fibrocartilage ECM synthesis.

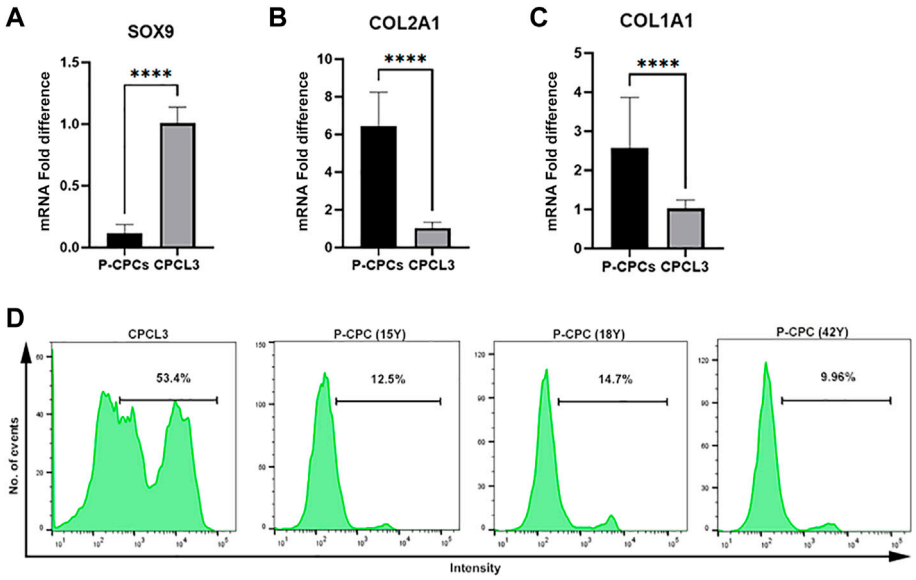

FIGURE 2
Comparison of chondrogenic marker expression and cell proliferation capacities of CPCL3 and primary CPCs. Fold differences in the mRNA expression of **(A)** *SOX9*, **(B)** type 2 collagen (*COL2A1*), and **(C)** type 1 collagen (*COL1A1*) between primary CPCs and the stable CPC line, CPCL3. N ≥ 4 per group. ****, $p \leq 0.0001$. **(D)** Cell proliferation assay results showing the proportion of proliferating cells in CPCL3 cultures and primary CPC cultures obtained from three different patients.

We found that primary BM-MSCs exhibited a 4-fold increase in *SOX9* over BM-MSCL (Supplementary Figure S2A). Primary BM-MSCs expressed approximately an 8-fold increase in *COL2A1* (Supplementary Figure S2B) and a 2.5-fold increase in *COL1A1*, relative to BM-MSCL (Supplementary Figure S2C).

The cell proliferation capacities of CPCL3 and BM-MSCL was compared to that of their primary cell counterparts, respectively. Primary CPCs and BM-MSCs show a reduced proliferation capacity following *in vitro* monolayer culture expansion, in comparison to the stable cell lines and measured by EdU cell proliferation analysis using flow cytometer (Figure 2D, Supplementary Figure S2D). Among analyzed CPCL3 cultures, the proportion of cells that stained positive for EdU was 53.4%, whereas primary CPCs ranged from 9.96—14.7% (Figure 2D). BM-MSCL cultures contained 37.5% of cells that stained positive for EdU, while only 2.6% of primary BM-MSCs stained positive (Supplementary Figure S2D).

Intra-articular injection of stable human cartilage-derived progenitor cells accelerate healing of a meniscal injury in athymic rats

To test our hypothesis that CPCs can accelerate meniscus tear repair in live animals, we implemented a medial meniscus tear model in RNU nude rats. A 1.0 mm radial tear was surgically created in the medial meniscus of the right hind limb, making sure that this injury did not sever the meniscus into two separate pieces (Figure 3A). Animals received an intra-articular injection of either CPCL3 (group 1), BM-MSCL (group 2), or saline alone (vehicle control, group 3). Cell treatments were divided into two separate injections (1.6×10^6 cells each) administered at Week 1 and Week 4, post injury. All animals were euthanized 7 weeks post-injury and the medial menisci from the surgical knee was carefully excised for analysis. All meniscal samples were fixed in their neutral resting position on a flat surface to prevent contortion of the injury site prior to embedding for sectioning. Samples were then uniformly sectioned along the transverse plane to reach the widest region, which allowed assessment of the extent of injury with respect to the total width of the meniscus.

Histology sections were used to qualitatively visualize the injury/repair site (Figures 3B–D). Outcomes revealed that none of the animals in the CPCL3-treatment group had medial menisci that were broken into two separate pieces upon harvest, whereas 36.4% of rats in the vehicle control group, and 16.7% in the BM-MSCL treatment group were, suggesting that the injury worsened over time in these animals (Table 2). Moreover, we quantified the remaining open area of the meniscal tears, in each experimental group (Figure 3E). Four animals were euthanized immediately following meniscal injury (at 0 weeks), to measure the open area of the injury immediately after it was created. This was done for two reasons: 1) To quantify the initial size of the injury before it has had a chance to heal or become worse with knee usage; 2) To validate the

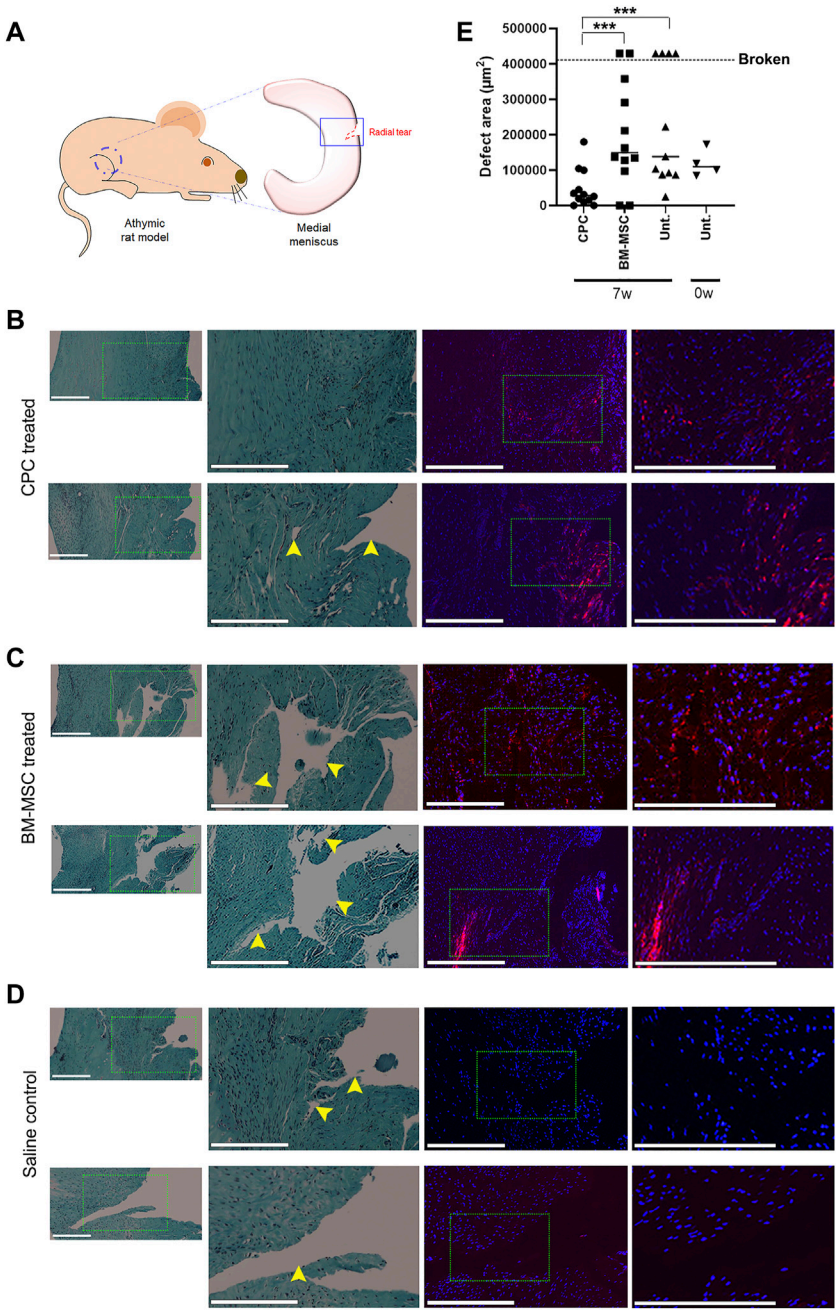

FIGURE 3
Intra-articular injection of CPCL3 following meniscus tearing stimulates fibrocartilage restoration and healing. **(A)** A radial tear was created in the outer third of the medial meniscus of skeletally mature athymic rats as shown in the diagram. Histology of meniscus tears 7 weeks following treatment with **(B)** CPCL3, **(C)** BM-MSCL, or **(D)** saline vehicle alone is shown. Left panels show sections stained with Safranin O/Fast green, while fluorescence imaging panels represent a sister section taken ~150—300 μm away from the aforementioned section that has been stained with Dapi. Rightmost fluorescent panels are higher magnification images of the select area inscribed by the dotted line in the Dapi stained image. Nuclei of all cells (both native meniscus cells and injected cells) are stained with Dapi (blue). In the cell treatment groups, a total of 3.2 million fluorescently labeled cells (red) were injected into the joint capsule following meniscus injury. **(E)** Open areas remaining within the meniscal tear channel was quantified by image analysis and compared across experimental groups. A 0-week control group was used to determine the open area of the meniscal tear before healing, or further tearing due to the *in vivo* environment, can take place. Data points above the dotted line indicates menisci that were broken in two at the time of harvest. Representative images in panels B, C and D were not obtained from these broken menisci samples. Scale bars represent 400 μm. N ≥ 8 per group. ***, $p \leq 0.005$.

TABLE 2 Prevalence of broken medial menisci by treatment condition. The prevalence of broken medial menisci differed by treatment condition. The saline control group experienced significantly more broken defects than the CPCL3-treated group (36.4% vs 0%, $p < 0.0001$). There were no statistically significant differences in the prevalence of broken menisci in the saline control compared to BM-MSCL group ($p = 0.30$).

Saline	BM-MSCL	CPCL3	Comparisons			
			p-values	Saline vs. BM-MSCL	Saline vs. CPCL3	BM-MSCL vs. CPCL3
4 (36.4%)	2 (16.7%)	0 (0%)	Unadjusted	0.30	<0.0001	<0.0001
			Adjusted	0.30	<0.0001	<0.0001

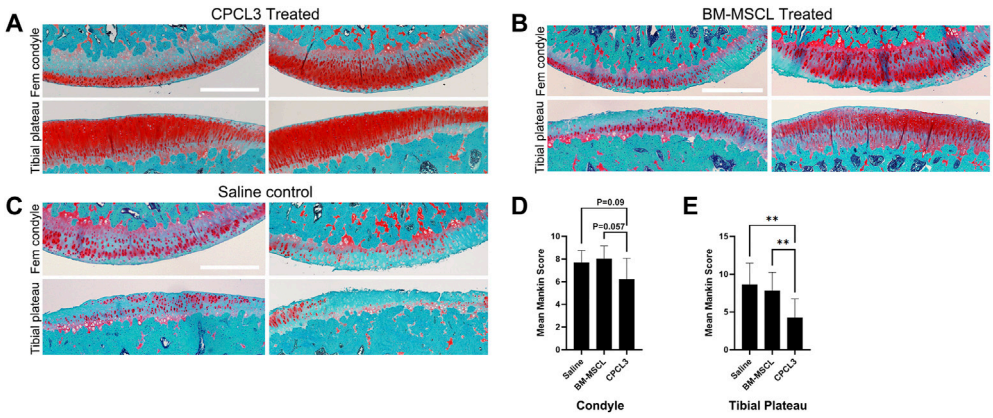

FIGURE 4
Animals with meniscus tears that were treated by intra-articular injection of CPCL3 exhibit reduced post-traumatic cartilage degeneration. The knee articular cartilage from the medial compartment of each knee that was subjected to a medial meniscus injury were sectioned and stained with Safranin O/Fast Green to visualize the extent of cartilage erosion. Staining of the medial femoral condyles and tibial plateaus of **(A)** CPCL3-treated, **(B)** BM-MSCL-treated, and **(C)** vehicle alone treated animals are shown. Both BM-MSCL-treated and vehicle alone treated animals show severe proteoglycan loss, indicated by diminished red staining in comparison to CPCL3-treated animals. Scale bars represent 500 μm. **(D)** Average modified Mankin scoring results of medial femoral condyles and **(E)** medial tibial plateaus of each experimental group are shown. N ≥ 8 per treatment group. **, $p \leq 0.01$.

reproducibility of the tear size from one surgery to the next. Outcomes showed that the extent of tissue reunification at the tear site was greatest in the CPCL3-treatment group, because it exhibited the least average open area. Since it is not possible to measure the exact open area in a completely severed meniscus, specimen that were found to have separated into two pieces were interpreted to have 20% larger open area than the largest unsevered meniscus that was observed in the study. We did this because it is a conservative adjustment that allows for the incorporation of these important outcomes into our quantitative analysis.

Posttraumatic cartilage degradation is significantly reduced following CPC treatment of meniscal tears

Articular surfaces of the injured and treated knees were inspected for signs of degradation resulting from the meniscal injury (Figures 4A–C). Independent blinded histopathology assessment was performed on the medial femoral condyles and medial tibial plateaus using a modified Mankin scoring system (Figures 4D,E). Mean femoral condyle scores showed that CPC-treated group exhibited improvement over the BM-MSCL-treated group and the saline control group. Tibial plateau scoring results indicated a significantly lower average Mankin score in the CPC-treated group compared to the vehicle alone control group, as well as the BM-MSCL-treated group, suggesting improvements in cartilage integrity in the CPC-treated animals. Relative basal mRNA expression of OA-associated proteinases *MMP2, MMP13, ADAMTS4,* and *ADAMTS5* was compared between CPCL3 and BM-MSCL (Figure 5). *MMP2, MMP13,* and *ADAMTS4* were significantly downregulated in CPCL3, suggesting that this reduction in catabolic enzyme production too may be a contributing factor to the difference in OA severity observed between these two treatment groups. Taken together with our previously published data demonstrating that *SOX9* is

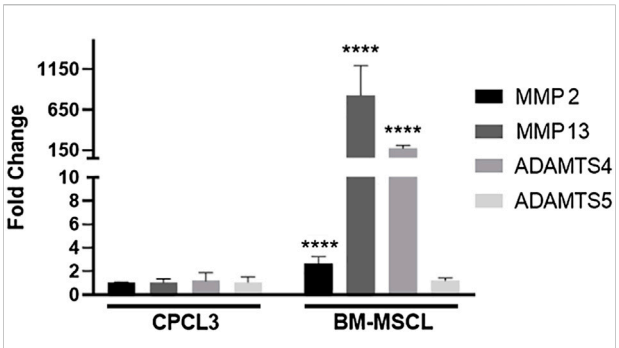

FIGURE 5
CPCL3 exhibits significant reduction in OA-associated catabolic enzyme expression, relative to BM-MSCL. Relative mRNA expression of collagenases and aggrecanases were compared between CPCL3 and BM-MSCL. Expression of *MMP2*, *MMP13*, and *ADAMTS4* are all elevated in BM-MSCL, while only *ADAMTS5* remained expressed at a comparable level between CPCL3 and BM-MSCL. N = 5 per group. ****, $p \leq 0.0001$.

upregulated in CPC lines compared to BM-MSCs (Jayasuriya et al., 2019), this suggests that CPCs are more anabolic and less catabolic than BM-MSCs, which may contribute to their improved efficacy for stimulating meniscus repair and preventing cartilage degradation.

Discussion

Cell-based meniscus repair strategies are currently being investigated using several musculoskeletal tissue specific mesenchymal cell sources; including progenitors derived from meniscus tissue itself, as well as synovium, adipose, and cartilage (Muhammad et al., 2014; Seol et al., 2017; Sun et al., 2020; Twomey-Kozak and Jayasuriya, 2020; Trivedi et al., 2022). CPCs are a promising cell-type for musculoskeletal tissue engineering applications given their inherently high chondrogenicity, propensity for colony formation, and resistance to chondrocyte hypertrophy (Dowthwaite et al., 2004; Fickert et al., 2004; Williams et al., 2010; McCarthy et al., 2012; Vinod et al., 2020). Further, these cells can be extracted from an available cell source (non-loadbearing cartilage), which is currently what is used for autologous chondrocyte implantation (ACI) (Ossendorf et al., 2011). However, a logistical hurdle for implementing these cells for therapy is their low natural abundance and the need to obtain sufficient expendable healthy cartilage tissue from which they can be extracted. Further, what little primary CPCs can be extracted from cartilage must undergo *in-vitro* expansion to obtain sufficient cell numbers for therapeutic use, which runs the risk of diminishing their proliferative capacity due to gradual replicative senescence that begins to set in during the extensive multiple-passage expansion of mesenchymal progenitor populations (Banfi et al., 2000; Baxter et al., 2004). These hurdles exist whether one seeks to use autologous (from same patient) or allogeneic (donor-derived) cell sources, unless a large amount of tissue can be made available from either source, which is rare. Here, we utilize a previously established stable CPC cell line (Jayasuriya et al., 2019; Newberry et al., 2020; Twomey-Kozak et al., 2020) to perform a proof-of-concept study set to test their therapeutic efficacy for fibrocartilage injury repair in a live animal model. The goal of this study was to determine whether a stabilized clonal CPC line can be used as an available alternative cell source for musculoskeletal joint tissue repair.

Prior to administering them into animals, the cell surface marker profiles and proliferative capacity of CPCL3 and the BM-MSCL control cell line, were examined. No significant differences in surface markers were found in both cell lines confirming that this aspect of their cell phenotype was consistent with their primary counterparts. When we compared the innate proliferation rate of the stable cell lines and primary cells, we discovered that even lightly expanded primary progenitor cells (passaged 4–6 times) exhibited significantly diminished proliferative capacity relative to the stable lines, both of which had been expanded from 7–10 passages, after the stabilization procedure. We also observed that CPCs consistently showed increased proliferative capacity, compared to BM-MSCs in the same class (i.e., stable CPC line compared to stable BM-MSC line; primary CPCs compared to primary BM-MSCs).

While our overall findings suggested a logistical advantage in using stable cell lines for therapy, due to their improved proliferative capacity, we carefully inspected whether these cells would proliferate uncontrollably in the joint space and/or migrate outside the joint capsule and engraft in off-target locations, such as vital organs in our athymic rat model. Gross inspection of the surgical knees of animals treated with either CPCL3 or BM-MSCL at the experimental endpoint of 7 weeks following surgery, showed the absence of any abnormal growths. Similarly, gross inspection of vital organs (kidney, liver, spleen, lungs, and brain) at the time of joint harvest revealed no such irregularities. As a secondary confirmation, DNA collected from homogenized organs were used as templates to run PCR using primers that only recognize and bind human DNA (specifically, the human Cytochrome B gene as done by Matsuda et al. (2005)). Results indicated no detection of this ubiquitous human-specific gene, signifying the absence of human cells (i.e., CPCL3/BM-MSCL) in these tissues (Supplementary Figure S3).

Intra-articular injection of stable CPCs significantly improved both meniscal tear healing and cartilage health outcomes in animals, compared to BM-MSCL treated animals. This strongly suggests that CPC treatment can safeguard against PTOA changes in the knee, following meniscal injury. We were surprised to find that in all performed outcome measures, the BM-MSCL treated animals showed no significant improvements over the control animals that were given vehicle only. To better

understand why there was such a significant difference in the treatment efficacy between CPCL3-treated and BM-MSCL-treated animals, we analyzed the expression profile of collagenases and aggrecanases that are produced by each cell type. We focused specifically on these catabolic genes because they are involved in cartilage turnover, and their differential expression may help to explain why CPCL3-treated animals showed less severe cartilage erosion. Our findings showed that CPCL3 exhibited significantly lower expression of catabolic proteinases *MMP2, MMP13,* and *ADAMTS4* compared to BM-MSCL. Relative to CPCL3, BM-MSCL exhibited >800-fold expression of *MMP13*, which has been reported to be the most potent cartilage eroding proteinase (Mitchell et al., 1996). Similarly, BM-MSCL exhibited 175-fold expression increase in *ADAMTS4*, which is also a prominent catabolic enzyme responsible for cartilage breakdown (Westling et al., 2002).

Interestingly, fluorescence imaging of meniscal sections from both cell treatment groups showed a wider distribution of administered cells throughout the meniscus than we expected. For instance, in some cases, cells were not found directly on the banks of the remnant tear channel, but rather they were found adhering to nearby adjacent regions of meniscus tissue. In the case of CPCs, this observation suggests that the mechanism by which these cells promote meniscus healing may (at least in part) involve their exertion of paracrine effect(s) that inspire native meniscal cells to form neo tissue and reunify the torn region. Identifying and examining these detailed mechanisms will be the subject of future investigation.

The athymic RNU rat model was selected for this proof-of-concept study to minimize any potential immune reaction/rejection due to the administered human cells. While we acknowledge that this is a study limitation, we opted for this model because it enabled us to first determine whether the stable cell therapies are capable of stimulating meniscal healing in an *in vivo* knee microenvironment, without having to consider immuno-rejection as an added complication. In the future, we anticipate designing studies that will be conducted in fully immunocompetent and large animals (both males and females), to further test the efficacy and translatability of this approach. Although we demonstrated that stable CPCs have higher proliferative capacity over primary CPCs, mRNA analysis revealed that CPCL3 exhibited detectably lower collagen I and II expression compared to primary CPCs, despite having higher *SOX9* expression. This may be considered a potential disadvantage of utilizing the stable CPC line for musculoskeletal tissue repair, over using primary CPCs. Further, future studies should focus on evaluating the long-term efficacy of using immortalized cells for cell-based therapy. Another limitation of our study was our inability to perform histological evaluation of the joint synovium, since the joint could not be kept intact considering that we needed to carefully excise the medial meniscus in order to conduct our quantitative analysis of the tear site, which required sectioning the tissue in the transverse plane. This means that the joint needed to be disarticulated, which ruptured the synovial capsule during sample preparation.

In conclusion, this is a proof-of-concept study demonstrating that a stable human cartilage progenitor cell line can facilitate meniscus tear healing and significantly reduce the severity of PTOA changes in knee articular cartilage. Futures studies will focus on evaluating the long-term safety and efficacy of utilizing stable CPCs for meniscus tissue repair. We will also determine safety and efficacy using an immunocompetent model. Lastly, we will explore strategies to scale up the success that we report here in rodents to a clinically relevant large animal model, similar in size to human patients. If success is demonstrated in the above anticipated studies, the opportunities for advancing the current state of cell-based biologic therapy for musculoskeletal tissue repair stands to gain significant ground. The implication of having a readily available stable cell source, that does not require an initial surgery to secure, that can be cryopreserved and kept for safe and effective repair for treating traumatic meniscus tears would dramatically change the way these injuries are currently addressed in the clinic.

Data availability statement

The raw data supporting the conclusions of this article will be made available by the authors, without undue reservation.

Ethics statement

The animal study was reviewed and approved by Rhode Island Hospital IACUC.

Author contributions

SD: Collection and assembly of data, data analysis and interpretation, manuscript writing and editing, final approval of manuscript. MD: Collection and assembly of data, data analysis and interpretation, manuscript editing, final approval of manuscript. JN: Collection of data, final approval of manuscript. JT: Collection of data, final approval of manuscript. JM: Statistical analysis, final approval of manuscript. JT: Collection of data, final approval of manuscript. J.M.P: Manuscript writing and editing, final approval of manuscript. BO: Provision of study material, manuscript editing, final approval of manuscript. CJ: Conception and design, data analysis and interpretation, manuscript writing, final approval of manuscript.

Funding

This research was supported by a Biologics Research Grant awarded to Jayasuriya and Owens from the Orthopaedic

Research and Education Foundation (OREF) sponsored by the Musculoskeletal Transplant Foundation (MTF) and Advance Clinical and Translational Research (Advance-CTR), Providence, RI (NIGMS/NIH grant U54GM115677). Partial support was provided by NIAMS/NIH grant R21 AR077326 and US Department of Defense grant W81XWH-20-1-0773. Facilities and imaging equipment support was provided by the COBRE for Skeletal Health and Repair at Rhode Island Hospital, Providence, RI (NIGMS/NIH grant P20GM104937). Histology core support was provided by the COBRE Histology and Imaging Core at the University of New England, Biddeford, ME (NIGMS/NIH grant P20GM103643). Flow cytometry support was provided by the Rhode Island COBRE Flow Cytometry Core, Providence, RI (NIGMS/NIH grant P20GM119943).

Acknowledgments

We acknowledge and thank Peter Cardona and his team at the University of New England for performing musculoskeletal tissue processing, sectioning, and staining.

Conflict of interest

The authors declare that the research was conducted in the absence of any commercial or financial relationships that could be construed as a potential conflict of interest.

Publisher's note

All claims expressed in this article are solely those of the authors and do not necessarily represent those of their affiliated organizations, or those of the publisher, the editors and the reviewers. Any product that may be evaluated in this article, or claim that may be made by its manufacturer, is not guaranteed or endorsed by the publisher.

Supplementary material

The Supplementary Material for this article can be found online at: https://www.frontiersin.org/articles/10.3389/fbioe.2022.970235/full#supplementary-material

SUPPLEMENTARY FIGURE S1
Side-by-side comparison of the cell surface marker profiles of the stable BM-MSC line (BM-MSCL) and primary BM-MSCs. Cell surface marker expression rates of **(A)** Fibronectin, **(B)** Thy-1, **(C)** Endoglin, **(D)** ALCAM, and **(E)** ICAM1 in BM-MSCL and primary BM-MSCs. Primary BM-MSCs were obtained from American Type Culture Collection, which dispenses cells collected from healthy human tissues. The empty peaks represent isotypic controls, for reference. Percent values indicated in the graphs represent positive staining rate, above isotype control, for each individual CD marker.

SUPPLEMENTARY FIGURE S2
Comparison of chondrogenic marker expression and cell proliferation capacities of BM-MSCL and primary BM-MSCs**.** Fold differences in the mRNA expression of **(A)** *SOX9*, **(B)** *COL2A1*, and **(C)** *COL1A1* between primary BM-MSCs and the stable BM-MSC line, BM-MSCL. N≥4 per group. ****, P≤0.0001. **(D)** Cell proliferation assay results showing the proportion of proliferating cells in BM-MSCL cultures and primary BM-MSC cultures.

SUPPLEMENTARY FIGURE S3
Off-target engraftment of stable human cell lines was not detected in the major organs of cell-treated athymic rats. Agarose gel electrophoresis was used to confirm that human DNA was absent in major organs that are common targets for cell engraftment and metastasis. Tissues from cell-treated animals were homogenized and the total DNA was used as templates for PCR amplification of the human mitochondrial cytochrome C gene. DNA that was directly extracted from each line was subjected to the same procedure described above and used as internal positive controls. Observed bands are marked with arrows. DNA ladder is labeled with "L". Data is representative of results observed in all experimental animals in each respective cell-treatment group.

References

Baker, B. E., Peckham, A. C., Pupparo, F., and Sanborn, J. C. (1985). Review of meniscal injury and associated sports. *Am. J. Sports Med.* 13 (1), 1–4. doi:10.1177/036354658501300101

Banfi, A., Muraglia, A., Dozin, B., Mastrogiacomo, M., Cancedda, R., and Quarto, R. (2000). Proliferation kinetics and differentiation potential of *ex vivo* expanded human bone marrow stromal cells: Implications for their use in cell therapy. *Exp. Hematol.* 28 (6), 707–715. doi:10.1016/s0301-472x(00)00160-0

Baxter, M. A., Wynn, R. F., Jowitt, S. N., Wraith, J. E., Fairbairn, L. J., and Bellantuono, I. (2004). Study of telomere length reveals rapid aging of human marrow stromal cells following *in vitro* expansion. *Stem Cells* 22 (5), 675–682. doi:10.1634/stemcells.22-5-675

Bilgen, B., Jayasuriya, C. T., and Owens, B. D. (2018). Current concepts in meniscus tissue engineering and repair. *Adv. Healthc. Mat.* 7 (11), e1701407. doi:10.1002/adhm.201701407

Cameron, K. L., Mauntel, T. C., and Owens, B. D. (2017). The epidemiology of glenohumeral joint instability: Incidence, burden, and long-term consequences. *Sports Med. Arthrosc. Rev.* 25 (3), 144–149. doi:10.1097/jsa.0000000000000155

Dowthwaite, G. P., Bishop, J. C., Redman, S. N., Khan, I. M., Rooney, P., Evans, D. J. R., et al. (2004). The surface of articular cartilage contains a progenitor cell population. *J. Cell Sci.* 117, 889–897. doi:10.1242/jcs.00912

Englund, M., Guermazi, A., and Lohmander, S. L. (2009). The role of the meniscus in knee osteoarthritis: a cause or consequence? *Radiol. Clin. North Am.* 47 (4), 703–712. doi:10.1016/j.rcl.2009.03.003

Fan, M. P., SiM.Li, B. J., Hu, G. H., Hou, Y., Yang, W., et al. (2018). Cell therapy of a knee osteoarthritis rat model using precartilaginous stem cells. *Eur. Rev. Med. Pharmacol. Sci.* 22 (7), 2119–2125. doi:10.26355/eurrev_201804_14745

Fickert, S., Fiedler, J., and Brenner, R. E. (2004). Identification of subpopulations with characteristics of mesenchymal progenitor cells from human osteoarthritic cartilage using triple staining for cell surface markers. *Arthritis Res. Ther.* 6 (5), R422–R432. doi:10.1186/ar1210

Fox, A. J., Bedi, A., and Rodeo, S. A. (2012). The basic science of human knee menisci: structure, composition, and function. *Sports Health.* 4 (4), 340–351. doi:10.1177/1941738111429419

Hu, N., Gao, Y., Jayasuriya, C. T., Liu, W., Du, H., Ding, J., et al. (2019). Chondrogenic induction of human osteoarthritic cartilage-derived mesenchymal stem cells activates mineralization and hypertrophic and osteogenic gene expression

through a mechanomiR. *Arthritis Res. Ther.* 21 (1), 167. doi:10.1186/s13075-019-1949-0

Jayasuriya, C. T., and Chen, Q. (2015). Potential benefits and limitations of utilizing chondroprogenitors in cell-based cartilage therapy. *Connect. Tissue Res.* 56 (4), 265–271. doi:10.3109/03008207.2015.1040547

Jayasuriya, C. T., Chen, Y., Liu, W., and Chen, Q. (2016). The influence of tissue microenvironment on stem cell-based cartilage repair. *Ann. N. Y. Acad. Sci.* 1383 (1), 21–33. doi:10.1111/nyas.13170

Jayasuriya, C. T., Li, J., Lemme, N., Terek, R., Ehrlich, M. G., Chen, Q., et al. (2018). Molecular characterization of mesenchymal stem cells in human osteoarthritis cartilage reveals contribution to the OA phenotype. *Sci. Rep.* 8 (1), 7044. doi:10.1038/s41598-018-25395-8

Jayasuriya, C. T., Twomey-Kozak, J., Newberry, J., Desai, S., Feltman, P., Franco, J. R., et al. (2019). Human cartilage-derived progenitors resist terminal differentiation and require CXCR4 activation to successfully bridge meniscus tissue tears. *Stem Cells* 37 (1), 102–114. doi:10.1002/stem.2923

Jones, J. C., Burks, R., Owens, B. D., Sturdivant, R. X., Svoboda, S. J., and Cameron, K. L. (2012). Incidence and risk factors associated with meniscal injuries among active-duty US military service members. *J. Athl. Train.* 47 (1), 67–73. doi:10.4085/1062-6050-47.1.67

Kennedy, M. I., Strauss, M., and LaPrade, R. F. (2020). Injury of the meniscus root. *Clin. Sports Med.* 39 (1), 57–68. doi:10.1016/j.csm.2019.08.009

Kienzle, G., and von Kempis, J. (1998). Vascular cell adhesion molecule 1 (CD106) on primary human articular chondrocytes: functional regulation of expression by cytokines and comparison with intercellular adhesion molecule 1 (CD54) and very late activation antigen 2. *Arthritis Rheum.* 41 (7), 1296–1305. doi:10.1002/1529-0131(199807)41:7<1296::aid-art21>3.0.co;2-8

Lee, H. J., Choi, B. H., Min, B. H., and Park, S. R. (2009). Changes in surface markers of human mesenchymal stem cells during the chondrogenic differentiation and dedifferentiation processes *in vitro*. *Arthritis Rheum.* 60 (8), 2325–2332. doi:10.1002/art.24786

Liu, W., Feng, M., Jayasuriya, C. T., Peng, H., Zhang, L., Guan, Y., et al. (2020). Human osteoarthritis cartilage-derived stromal cells activate joint degeneration through TGF-beta lateral signaling. *FASEB J.* 34 (12), 16552–16566. doi:10.1096/fj.202001448r

Makris, E. A., Hadidi, P., and Athanasiou, K. A. (2011). The knee meniscus: Structure–function, pathophysiology, current repair techniques, and prospects for regeneration. *Biomaterials* 32 (30), 7411–7431. doi:10.1016/j.biomaterials.2011.06.037

Matsuda, H., Seo, Y., Kakizaki, E., Kozawa, S., Muraoka, E., and Yukawa, N. (2005). Identification of DNA of human origin based on amplification of human-specific mitochondrial cytochrome b region. *Forensic Sci. Int.* 152 (2-3), 109–114. doi:10.1016/j.forsciint.2004.07.019

McCarthy, H. E., Bara, J. J., Brakspear, K., Singhrao, S. K., and Archer, C. W. (2012). The comparison of equine articular cartilage progenitor cells and bone marrow-derived stromal cells as potential cell sources for cartilage repair in the horse. *Vet. J.* 192 (3), 345–351. doi:10.1016/j.tvjl.2011.08.036

Mitchell, P. G., Magna, H. A., Reeves, L. M., Lopresti-Morrow, L. L., Yocum, S. A., Rosner, P. J., et al. (1996). Cloning, expression, and type II collagenolytic activity of matrix metalloproteinase-13 from human osteoarthritic cartilage. *J. Clin. Invest.* 97 (3), 761–768. doi:10.1172/jci118475

Muhammad, H., Schminke, B., Bode, C., Roth, M., Albert, J., von der Heyde, S., et al. (2014). Human migratory meniscus progenitor cells are controlled via the TGF-beta pathway. *Stem Cell Rep.* 3 (5), 789–803. doi:10.1016/j.stemcr.2014.08.010

Newberry, J., Desai, S., Adler, C., Li, N., Karamchedu, N. P., Fleming, B. C., et al. (2020). SDF-1 preconditioned HPC scaffolds mobilize cartilage-derived progenitors and stimulate meniscal fibrocartilage repair in human explant tissue culture. *Connect. Tissue Res.* 61 (3-4), 338–348. doi:10.1080/03008207.2019.1689966

Ossendorf, C., Steinwachs, M. R., Kreuz, P. C., Osterhoff, G., Lahm, A., Ducommun, P. P., et al. (2011). Autologous chondrocyte implantation (ACI) for the treatment of large and complex cartilage lesions of the knee. *Sports Med. Arthrosc. Rehabil. Ther. Technol.* 3, 11. doi:10.1186/1758-2555-3-11

Park, D. Y., Min, B. H., Park, S. R., Oh, H. J., Truong, M. D., Kim, M., et al. (2020). Engineered cartilage utilizing fetal cartilage-derived progenitor cells for cartilage repair. *Sci. Rep.* 10 (1), 5722. doi:10.1038/s41598-020-62580-0

Paxton, E. S., Stock, M. V., and Brophy, R. H. (2011). Meniscal repair versus partial meniscectomy: a systematic review comparing reoperation rates and clinical outcomes. *Arthrosc. J. Arthrosc. Relat. Surg.* 27 (9), 1275–1288. doi:10.1016/j.arthro.2011.03.088

Seol, D., Yu, Y., Choe, H., Jang, K., Brouillette, M. J., Zheng, H., et al. (2014). Effect of short-term enzymatic treatment on cell migration and cartilage regeneration: *in vitro* organ culture of bovine articular cartilage. *Tissue Eng. Part A* 20 (13-14), 1807–1814. doi:10.1089/ten.tea.2013.0444

Seol, D., Zhou, C., Brouillette, M. J., Song, I., Yu, Y., Choe, H. H., et al. (2017). Characteristics of meniscus progenitor cells migrated from injured meniscus. *J. Orthop. Res.* 35 (9), 1966–1972. doi:10.1002/jor.23472

Sun, H., Wen, X., Li, H., Wu, P., Gu, M., Zhao, X., et al. (2020). Single-cell RNA-seq analysis identifies meniscus progenitors and reveals the progression of meniscus degeneration. *Ann. Rheum. Dis.* 79 (3), 408–417. doi:10.1136/annrheumdis-2019-215926

Trivedi, J., and Jayasuriya, C. T. (2022). "Chapter 5 - meniscus tissue engineering and repair," in *Musculoskeletal tissue engineering*. Editor Y. Chen (Netherlands: Elsevier), 107–132.

Twomey-Kozak, J., and Jayasuriya, C. T. (2020). Meniscus repair and regeneration: A systematic review from a basic and translational science perspective. *Clin. sports Med.* 39 (1), 125–163. doi:10.1016/j.csm.2019.08.003

Twomey-Kozak, J., Desai, S., Liu, W., Li, N. Y., Lemme, N., Chen, Q., et al. (2020). Distal-less homeobox 5 is a therapeutic target for attenuating hypertrophy and apoptosis of mesenchymal progenitor cells. *Int. J. Mol. Sci.* 21 (14), 4823. doi:10.3390/ijms21144823

Vinod, E., Kachroo, U., Rebekah, G., Yadav, B. K., and Ramasamy, B. (2020). Characterization of human articular chondrocytes and chondroprogenitors derived from non-diseased and osteoarthritic knee joints to assess superiority for cell-based therapy. *Acta Histochem.* 122 (6), 151588. doi:10.1016/j.acthis.2020.151588

Westling, J., Fosang, A. J., Last, K., Thompson, V. P., Tomkinson, K. N., Hebert, T., et al. (2002). ADAMTS4 cleaves at the aggrecanase site (Glu373-Ala374) and secondarily at the matrix metalloproteinase site (Asn341-Phe342) in the aggrecan interglobular domain. *J. Biol. Chem.* 277 (18), 16059–16066. doi:10.1074/jbc.m108607200

Williams, R., Khan, I. M., Richardson, K., Nelson, L., McCarthy, H. E., Analbelsi, T., et al. (2010). Identification and clonal characterisation of a progenitor cell sub-population in normal human articular cartilage. *PLoS One* 5 (10), e13246. doi:10.1371/journal.pone.0013246

Yang, X., Zhu, T. Y., Wen, L. C., Cao, Y. P., Liu, C., Cui, Y. P., et al. (2015). Intraarticular injection of allogenic mesenchymal stem cells has a protective role for the osteoarthritis. *Chin. Med. J.* 128 (18), 2516–2523. doi:10.4103/0366-6999.164981

frontiers | Frontiers in Bioengineering and Biotechnology

TYPE Original Research
PUBLISHED 14 October 2022
DOI 10.3389/fbioe.2022.925838

Check for updates

OPEN ACCESS

EDITED BY
Andrea Vernengo,
AO Research Institute, Switzerland

REVIEWED BY
Jie Zhu,
Northwest A&F University, China
Donghee Lee,
University of Nebraska Medical Center, United States

*CORRESPONDENCE
Helen H. Lu,
hhlu@columbia.edu

SPECIALTY SECTION
This article was submitted to Biomaterials, a section of the journal Frontiers in Bioengineering and Biotechnology

RECEIVED 22 April 2022
ACCEPTED 07 July 2022
PUBLISHED 14 October 2022

CITATION
Brudnicki PAP, Gonsalves MA, Spinella SM, Kaufman LJ and Lu HH (2022), Engineering collagenous analogs of connective tissue extracellular matrix.
Front. Bioeng. Biotechnol. 10:925838.
doi: 10.3389/fbioe.2022.925838

COPYRIGHT
© 2022 Brudnicki, Gonsalves, Spinella, Kaufman and Lu. This is an open-access article distributed under the terms of the Creative Commons Attribution License (CC BY). The use, distribution or reproduction in other forums is permitted, provided the original author(s) and the copyright owner(s) are credited and that the original publication in this journal is cited, in accordance with accepted academic practice. No use, distribution or reproduction is permitted which does not comply with these terms.

Engineering collagenous analogs of connective tissue extracellular matrix

Philip A. P. Brudnicki[1], Matthew A. Gonsalves[1], Stephen M. Spinella[2], Laura J. Kaufman[2] and Helen H. Lu[1]*

[1]Biomaterials and Interface Tissue Engineering Laboratory, Department of Biomedical Engineering, Columbia University, New York, NY, United States, [2]Department of Chemistry, Columbia University, New York, NY, United States

Connective tissue extracellular matrix (ECM) consists of an interwoven network of contiguous collagen fibers that regulate cell activity, direct biological function, and guide tissue homeostasis throughout life. Recently, ECM analogs have emerged as a unique *ex vivo* culture platform for studying healthy and diseased tissues and in the latter, enabling the screening for and development of therapeutic regimen. Since these tissue models can mitigate the concern that observations from animal models do not always translate clinically, the design and production of a collagenous ECM analogue with relevant chemistry and nano- to micro-scale architecture remains a frontier challenge in the field. Therefore, the objectives of this study are two-fold— first, to apply green electrospinning approaches to the fabrication of an ECM analog with nanoscale mimicry and second, to systematically optimize collagen crosslinking in order to produce a stable, collagen-like substrate with continuous fibrous architecture that supports human cell culture and phenotypic expression. Specifically, the "green" electrospinning solvent acetic acid was evaluated for biofabrication of gelatin-based meshes, followed by the optimization of glutaraldehyde (GTA) crosslinking under controlled ambient conditions. These efforts led to the production of a collagen-like mesh with nano- and micro-scale cues, fibrous continuity with little batch-to-batch variability, and proven stability in both dry and wet conditions. Moreover, the as-fabricated mesh architecture and native chemistry were preserved with augmented mechanical properties. These meshes supported the *in vitro* expansion of stem cells and the production of a mineralized matrix by human osteoblast-like cells. Collectively these findings demonstrate the potential of green fabrication in the production of a collagen-like ECM analog with physiological relevance. Future studies will explore the potential of this high-fidelity platform for elucidating cell-matrix interactions and their relevance in connective tissue healing.

KEYWORDS

ECM model, collagen, biofabrication, green electrospinning, glutaraldehyde, crosslinking

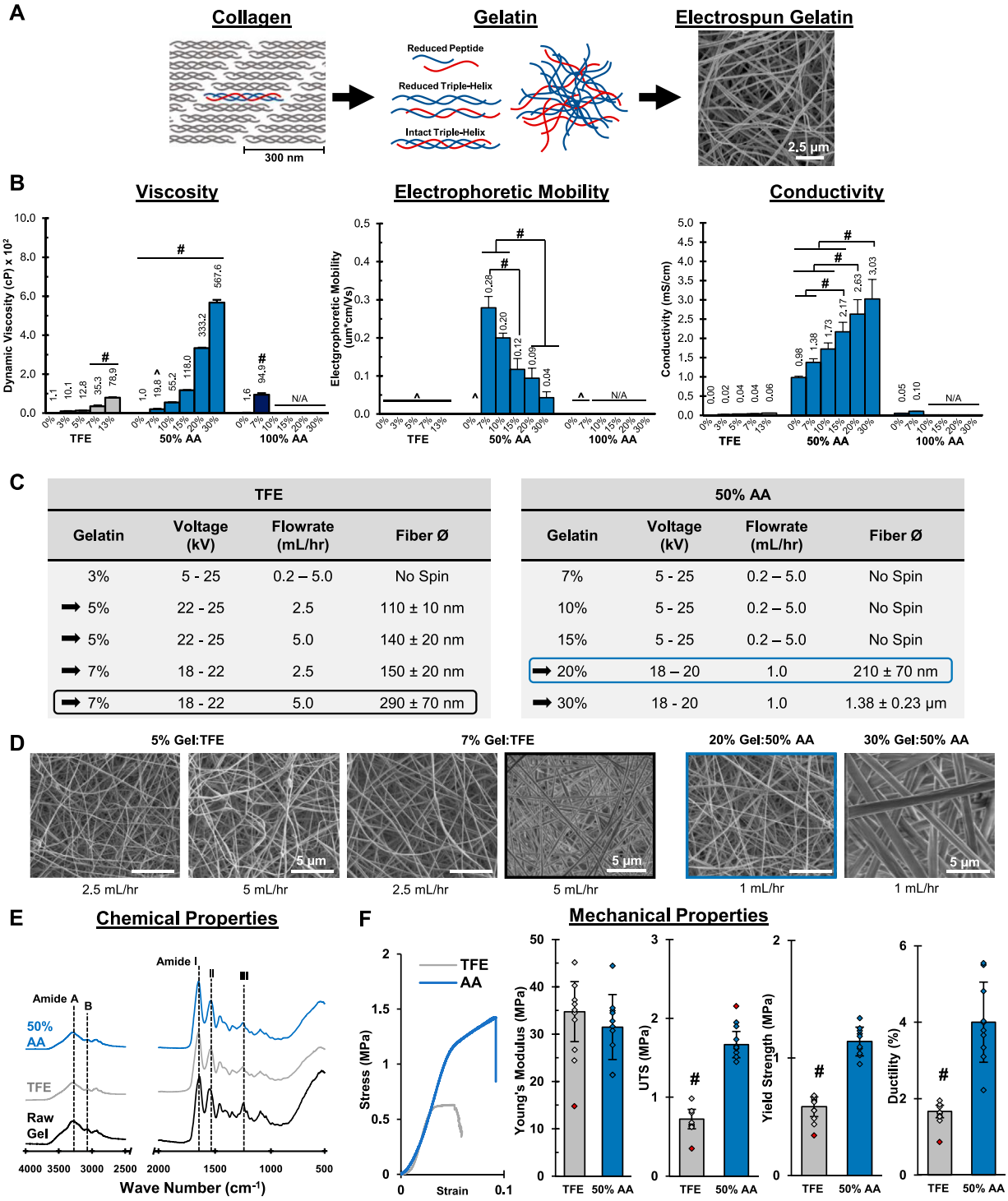

FIGURE 1
Mesh Fabrication: Solvent Optimization and Electrospinning. 50% acetic acid (AA) dissolves gelatin and supports mesh fabrication by electrospinning. The resulting mesh morphology, chemical composition and mechanical properties are comparable to meshes prepared in trifluoroethanol (TFE). **(A)** A schematic representing the structure of gelatin and its relationship to collagen. **(B)** Dynamic viscosity, electrophoretic mobility and conductivity measurements for gelatin solutions (n = 3). ^= Below Limit of Detection for Instrument. N/A = Not available due to sample gelling before analysis. **(C)** Successful electrospinning parameters using TFE and 50% AA. **(D)** Fiber morphology and diameter (n = 50) for meshes prepared from stable electrospins identified in part c. (SEM. 5,000x). **(E)** Chemical composition (FTIR-ATR). **(F)** Mesh tensile properties (n = 10). Red markers indicate sample outliers. #=p < 0.05.

Introduction

The extracellular matrix (ECM) is a diverse network of biopolymers that are organized and dynamically remodeled to meet the demands of physiological function. It can consist of over 300 different proteins, including over 20 types of collagens, several dozen proteoglycan and approximately 200 glycoproteins. (Frantz et al., 2010; Hynes and Naba, 2012; Theocharis et al., 2016). Each of these proteins may be organized with controlled interactions to impart structural and mechanical properties that are specific for the tissue of interest. Given this vast complexity, it is not surprising that a wide range of diseases can arise from disruption to the ECM's structure and composition. These include various cancers (Muschler and Streuli, 2010; Pickup et al., 2014), fibroproliferative diseases (Poli and Parola, 1997; Friedman, 2008), and many debilitating orthopaedic conditions, such as osteoporosis, osteoarthritis, chondrodysplasias, and intervertebral disk degeneration (Alberts et al., 2002; Parvizi, 2010). To better understand and treat these diverse diseases and conditions, an accurate model of the ECM is necessary to conduct physiologically relevant studies *in vitro*.

Among the proteins of the ECM, the most abundant are collagens, which make up over 30% of the total protein mass in the human body (Frantz et al., 2010; Fratzl, 2008). Among collagens, the most prevalent is type I, which is found in many connective and load-bearing tissues such as skin, tendons, ligaments, and bone (Vanderby and Provenzano, 2003). Collagen has a unique, hierarchical structure that provides mechanical support while also promoting cell attachment and activity through its chemistry. This structure is achieved through its triple-helical domains that are formed from three polypeptide chains (Figure 1) containing the amino acid sequence Glycine-X-Y, where X and Y are commonly proline and hydroxyproline (Shoulders and Raines, 2009). The hydroxyl groups of hydroxyproline assist in hydrogen bonding and enable interactions between adjacent peptides and fibrils, further building and stabilizing higher order collagen structures (Xu et al., 2019). The cyclic structure of these amino acids is partially responsible for driving the helical conformation of the tropocollagen monomer via steric hindrance (Shoulders and Raines, 2009; Ricard-Blum, 2011). Following this, tropocollagen molecules self-assemble into microfibril structures that are approximately 5 nm in diameter and several hundred nanometer long, which then further assemble into large fiber structures that are several hundred nanometer in diameter and several centimeter long. This final step, which is critical for creating collagen's high resilience to mechanical strain, is achieved through interchain crosslinks, which represent chemical or physical bonding between fibrils and most frequently from disulfide bond formation, transglutaminase conjugation of glutamine-lysine, lysyl oxidase crosslinking, and glycation (Siegel et al., 1970; Esposito and Caputo, 2005; Karsdal, 2019). While collagen fibrils themselves are not viscoelastic, through a slipping motion between the ordered fibrous structure, they can exhibit high levels of tissue deformation, which is a key characteristic of many connective tissues (Lorenzo and Caffarena, 2005; Shen et al., 2011). Beyond providing structural stability and supporting mechanotransduction and cell signaling throughout the ECM, collagen is also rich with many binding domains that support cell adhesion. It is decorated with ligands compatible with the many cell-surface integrins and discoidin domain receptors that support cell attachment, forming the critical connection between cells and the ECM (Theocharis et al., 2016). Given its high prevalence and unique chemical and physical properties, it is clear that collagen is a vital component of the ECM and is a critical feature when developing a bioactive analog of connective tissue ECM.

Despite the significant role collagen plays in cell-matrix interaction, the majority of *in vitro* studies rely on non-physiologic culturing substrates such as tissue culture polystyrene (TCPS) (Altering, 1966; Zeiger et al., 2013; Lerman et al., 2018). Since its adaption for eukaryotic cell culture in 1966, TCPS has been the standard platform for *in vitro* culture. Polystyrene is easy to synthesize, reproducible at scale, and its surface chemistry may be readily modified to accommodate a plethora of cell types. However, the chemical, structural, and mechanical properties of TCPS are radically different from collagenous ECM. Being a 2D substrate with a modulus on the scale of gigapascals, TCPS is orders of magnitude stiffer than all but the hardest of human tissues, such as bone and dentin (Kinney et al., 2003; Guimarães et al., 2020). Thus not surprisingly, long term stem cell culture on TCPS results in loss of stemness and drives these cells towards the osteogenic lineage (Tatullo et al., 2016; Gerardo et al., 2019). Similarly, the deleterious effect of cell passaging on phenotypic expression may be largely attributed to extended exposure to TCPS during *ex vivo* expansion (Gerardo et al., 2019; Rao et al., 2019). Furthermore, the lack of a fibrillar architecture coupled with the inherent difference in chemistry between TCPS and the native ECM at best attenuates, and at its worst, alters cell response beyond the realm of physiological relevance. Surface functionalization by coating with collagen or other ECM proteins (e.g., fibronectin) have mitigated these concerns but are costly and still result in cells being exposed to static and non-representative doses of the biomolecule (Lerman et al., 2018). These limitations significantly limit the applicability of TCPS and underscore the need for better models of the ECM.

Given the critical role of collagen architecture in directing cell response, significant focus has been directed towards the design and fabrication of ECM analogues with biomimetic organization (Lutolf and Hubbell, 2005; Moffat et al., 2009). To this end, electrospinning has been explored extensively for the generation of nano- and micro-scale fiber mesh using a variety of synthetic and biopolymers (Li et al., 2002; Ma et al., 2005; Sell et al., 2007;

Zhang et al., 2007; Subramony et al., 2013; Lee et al., 2017). In electrospinning, electrostatic forces are used to destabilize polymer solutions and cause the ejection of fine polymer strands that are then collected into a fibrous mat (Reneker and Chun, 1996; Reneker et al., 2000). These nano- and micro-fibrous substrates exhibit biomimetic architectures (diameter, alignment) that can be controlled at physiologically relevant scales, making electrospinning an ideal method for producing ECM analogues and targeting desired tissue architectures or states (Lee et al., 2017). As such, similar to TCPS, the collagen chemistry and bioactive domains that readily regulate and guide cell function are missing from these synethic, polymer-based systems. Alternatively, biological and synthetic polymer blends have also been explored (Jose et al., 2009; Kriegel et al., 2009). Here, the biopolymers introduce the biochemical features of the ECM to the analog, improving the system's biomimicry. Unfortunately, these systems still rely on synthetic materials to provide structural support and sufficient mechanical properties, which ultimately confound results when studying cell activity. Surface coatings and incorporation of growth factors (Chew et al., 2005; Boushell et al., 2019; Qu et al., 2019) have mitigated some of these concerns for regenerative medicine applications, but remain limited in scope and biological relevance as ECM analogues.

To better mimic the matrix composition, Matrigel®, consisting of a mixture of basement membrane proteins isolated from murine Englebreth-Holm-Swarm tumors, is commonly used (Kleinman et al., 1982). While it retains the natural basement membrane structure and composition after isolation *in vitro*, being derived from tumors, there is significant batch-to-batch variability and the isolated matrix often contains growth factors at non-physiologic concentrations and combinations (Vukicevic et al., 1992). Moreover, with a relatively low collagen I and high collagen IV content, compositionally it does not match the predominantly collagen I matrix intrinsic to connective tissues. While collagen-based hydrogels have also been used extensively for *in vitro* culture, their structural and mechanical properties are sub-physiologic, lacking both continuous fiber morphology and extended organization of the native ECM (Nöth et al., 2005; Oryan et al., 2018).

The feasibility of electrospinning collagen has also been explored, but largely with gelatin given the high cost of and difficulty solubilizing pure collagen (Huang et al., 2004; Zhang et al., 2005a). Gelatin is produced by hydrolyzing collagen, which breaks down its tertiary structure, yielding a heterogeneous polypeptide solution (Figure 1) with enhanced solubility (Harrington and Von Hippel, 1962). Most importantly, along with composition, it retains collagen's primary and secondary structure, which is rich with cell-binding motifs that support cell-matrix interactions (Ratanavaraporn et al., 2006; Davidenko et al., 2016). Furthermore, it is readily isolated from porcine and bovine connective tissues and thus inexpensive and easily obtainable. However, irrespective of the base material used, one drawback of using electrospinning to prepare the ECM analog is that it typically relies on harsh chemical solvents like trifluoroethanol (TFE), hexafluoroisopropanol, and dichloromethane. These solvents reduce substrate bioactivity and moreover, are associated with negative health and ecological effects, making them obstacles to large scale mesh production (Persano et al., 2013; Impurities, 2018). Recently, Mosher et al. (2021) identified the FDA Q3C solvent, acetic acid (AA) as a more biocompatible and "green" solvent for biofabrication. Thus, the first objective of this study is to optimize fabrication conditions using gelatin and AA as the solvent for the production of a fibrous collagen-like mesh.

Additional challenges in the production of collagen analogs include the fact that gelatin meshes require chemical stabilization or crosslinking following fabrication. Glutaraldehyde (GTA) is the most commonly used crosslinking agent, with highly reactive dialdehyde groups that readily bind to amines that are abundant in the amino acids that make up collagen's peptides (Bigi et al., 2001; Farris et al., 2010). Thus, adjacent gelatin fibers can be crosslinked by GTA, ultimately stabilizing the mesh architecture in aqueous environments (Figure 2A). However, GTA reactions are extremely difficult to control, resulting in highly variable mechanical properties and physical features between batches, resulting in a wide range of methods and approaches reported in literature (Zhang et al., 2006; Ju et al., 2010; Li et al., 2016). When applied in liquid form, GTA can partially or fully obliviate the fibrous architecture of the mesh during the crosslinking, resulting in flat sheets instead. While vapor crosslinking is better at preserving 3D fiber organization, vapor formation and interaction with mesh fibers is extremely difficult to control, being highly dependent on experimental setup and environmental conditions. Thus, the second objective of this study is to identify critical factors that impact GTA vapor crosslinking and determine the optimal parameters that will stabilize gelatin meshes without altering their biomimetic structure and chemical composition, all while remaining biocompatible.

This study aims to develop and standardize a method for fabricating a biomimetic collagenous ECM-like substrate. To this end, this ECM analog will be collagen-based, biocompatible, consist of continuous fibers, demonstrate both viscoelastic and elastic behavior, exhibit relevant mechanical properties, and remain stable for at least 14 days under cell culture conditions. After mesh development and characterization, biocompatibility will be tested using both cell-line and primary culture. It is anticipated that a high-fidelity collagen-based ECM analog will be fabricated under optimal electrospinning and crosslinking conditions, with physiologically relevant structural and mechanical properties reminiscent of the native collagenous ECM.

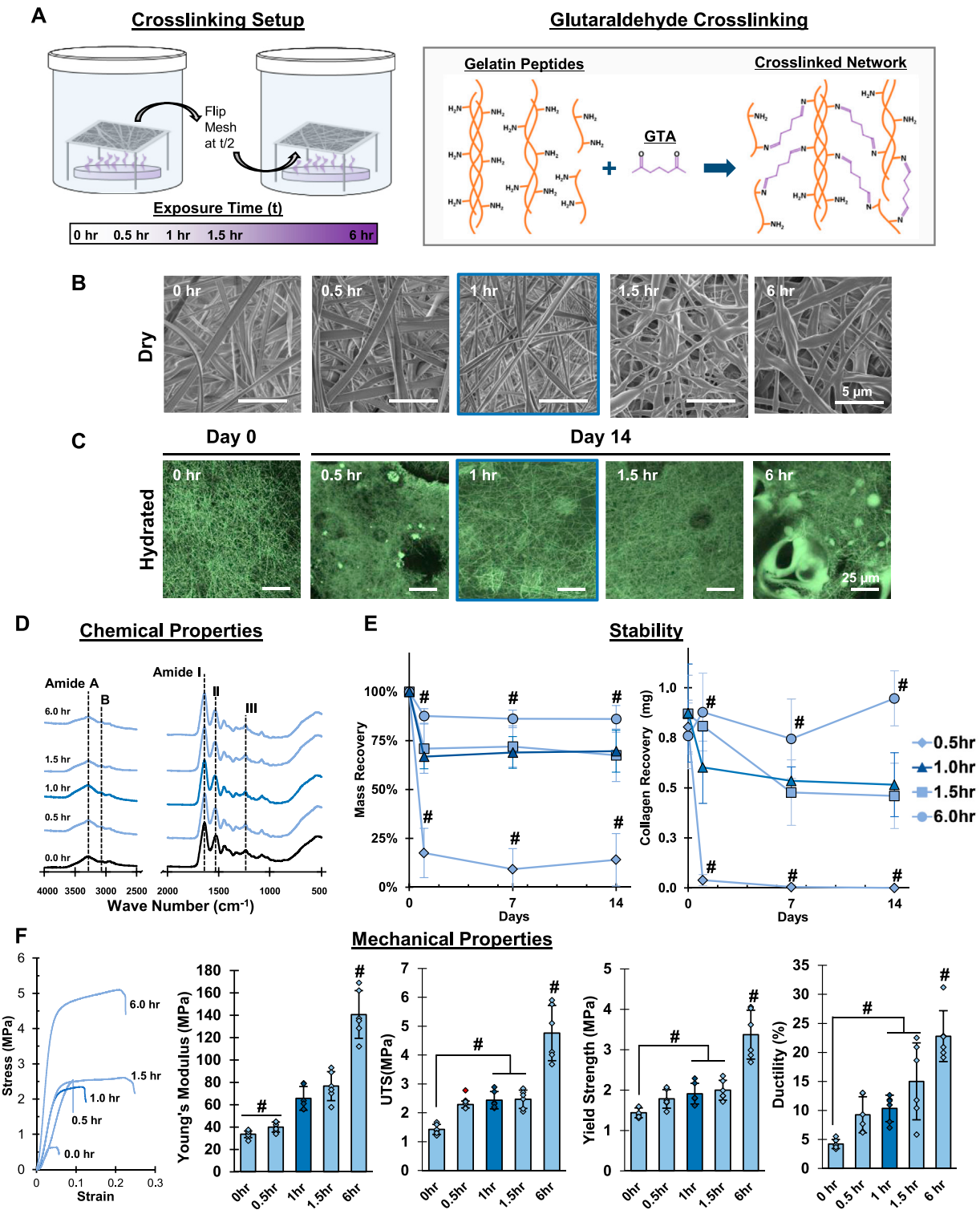

FIGURE 2
Mesh Fabrication: Crosslinking Duration. Glutaraldehyde exposure for 1 hour stabilizes meshes and enhances tensile properties without changing fiber morphology or chemistry. **(A)** Schematic of the crosslinking procedure and chemical reaction. **(B)** Dry morphology (SEM, 5,000x) and **(C)** hydrated morphology (CRM, 100x) of meshes after crosslinking. **(D)** Chemical composition (FTIR-ATR). **(E)** Mesh stability by mass recovery and gelatin recovery after incubation at 37°C in cell culture medium (14 days, n = 5). **(F)** Mesh tensile properties (n = 10). Red marker indicates outliers. #=$p < 0.05$.

Materials and methods

Mesh fabrication

Gelatin (porcine-derived, ~300 g bloom, type A) was dissolved in trifluoroethanol (TFE), 50% acetic acid (AA, prepared in deionized water) or glacial (100%) AA. Gelatin was solubilized in TFE (3, 5, 7, and 13% w/v), 50% AA (7, 10, 15, 20, and 30% w/v), and glacial AA (7, 10, 15, 20, and 30% w/v) by mixing at 45°C for up to 20 min (Fischer Brand Analog Vortex, setting 7) to accelerate dissolution. If the gelatin was not dissolved or had solidified after 20 min, the solution was considered not feasible for electrospinning. Next, the dynamic viscosity, electrophoretic mobility (EM) and conductivity of these solutions were determined. Solution dynamic viscosity (n = 3) was measured using a cone and plate rheometer under dynamic shear (TA instruments, New Castle, DE). Briefly, 2 ml of sample was placed on the instrument stage maintained at 22°C and a conical platen was lowered on top, ensuring full coverage. Next, a dynamic frequency sweep was conducted from 0.01–158 Hz and viscosity was calculated as the slope of the stress:strain rate curve. Electrophoretic mobility (n = 3) and conductivity (n = 3) were measured using the Zetasizer Nano ZS (Malvern) with disposable cuvettes (Malvern DTS1070) following the manufacturer's recommended protocol.

Next, the feasibility of electrospinning a fibrous gelatin mesh using the gelatin-solvent combinations described above were tested with a custom electrospinning device (Subramony et al., 2014). The gelatin solutions were loaded into a 5 ml syringe (Becton Dickinson, Franklin Lakes, NJ) fitted with a blunt-tipped 18-gauge stainless steel needle (Becton Dickinson). Once cooled to room temperature (~22°C), the loaded syringe was mounted onto a syringe pump (Harvard Apparatus, Holliston, MA) and electrospun at a set flow rate, voltage, relative humidity, and needle distance from a collection drum in a custom chamber. The drum was rotated at 500 rpm to promote even distribution of the collected fibers and uniform mesh thickness. The voltage and flow rate were optimized by identifying stable electrospins while adjusting the voltage from 5–25 kV and the flow rate between 0.2–5.0 ml/h. The chamber relative humidity was controlled at 40% and the travel distance between the needle and drum was fixed at 15 cm. The spins were considered stable when a fiber ejection persisted for greater than 15 min without user intervention.

Mesh characterization

Post fabrication mesh fiber morphology, chemical composition, and mechanical properties under tensile loading were determined. The electrospun meshes were first cored with a biopsy punch (Sklar Surgical Instruments, West Chester, PA) to obtain 10 mm discs. Fiber diameter (n = 50 fibers/group) and morphology (n = 5) were characterized by scanning electron microscopy (SEM, Zeiss Sigma VP, 2 keV, Carl Zeiss AG, Oberkochen, Germany). Prior to imaging, the samples were sputter-coated with gold-palladium using a 108 Auto Manual sputter coater (20 s, ~10 nm, Cressington Scientific, Watford, United Kingdom) to ensure sample conductivity. In addition to visual assessment of fiber continuity and morphology, fiber diameter was measured at ×10,000 magnification using ImageJ (National Institutes of Health, Bethesda, MD, n = 5 images per group, n = 10 fibers per image), as previously described (Lee et al., 2017).

Mesh chemical composition (n = 3) was confirmed by Fourier transform infrared spectroscopy in attenuated total reflectance mode (FTIR-ATR, Spectrum 100, Perkin Elmer, Waltham, MA). Spectra were collected at 100 scans with a spectral resolution of 4 cm^{-1}. Characteristic collagen peaks (Amide A, 3,306 cm^{-1}; Amide B, 3,076 cm^{-1}; Amide I, 1,646 cm^{-1}; Amide II, 1,520 cm^{-1}; Amide III, 1,234 cm^{-1}) (Muyonga et al., 2004; Nagai et al., 2010; Di Foggia et al., 2011; Cebi et al., 2016; Xu et al., 2017) were monitored in relation to solvent types, both pre- and post-electrospinning.

Sample mechanical properties (n = 6) were determined in tension according to the ASTM International standard test method D638-14 (Lu et al., 2005; Moffat et al., 2009). Briefly, 4 × 1 cm sections of mesh ranging from 0.1–0.3 mm thick were loaded onto a microtester device (Instron, Model 5,848, 10 N load cell, Norwood, MA), targeting a final gauge length of 2–3 cm. The samples were tested to failure at a strain rate of 5 mm/min. Young's modulus, yield strength, tensile strength, and ductility were calculated using a custom MATLAB code. Briefly, Young's modulus was measured as the slope of the linear region of the stress strain curve (0.2% strain offset) immediately following the toe region and prior to the onset of plastic deformation. The yield strength was calculated at the point where the stress strain curve was no longer linear, indicating plastic deformation. The tensile strength was calculated at the maximum stress measured in the curve the prior to sample failure. Lastly, the ductility was calculated by measuring the % elongation at the time of sample failure.

Mesh chemical crosslinking optimization

The electrospun gelatin meshes were chemically crosslinked using glutaraldehyde (GTA) and the effect of time, sample surface area, and ambient conditions were determined. To evaluate the effect of crosslinking time, as-fabricated meshes (6 × 6 cm) were secured in a custom bracket and placed inside of a beaker (2 L) containing 15 ml of GTA solution (Sigma G6403) and loosely covered (Figure 2A). The distance between the mesh-

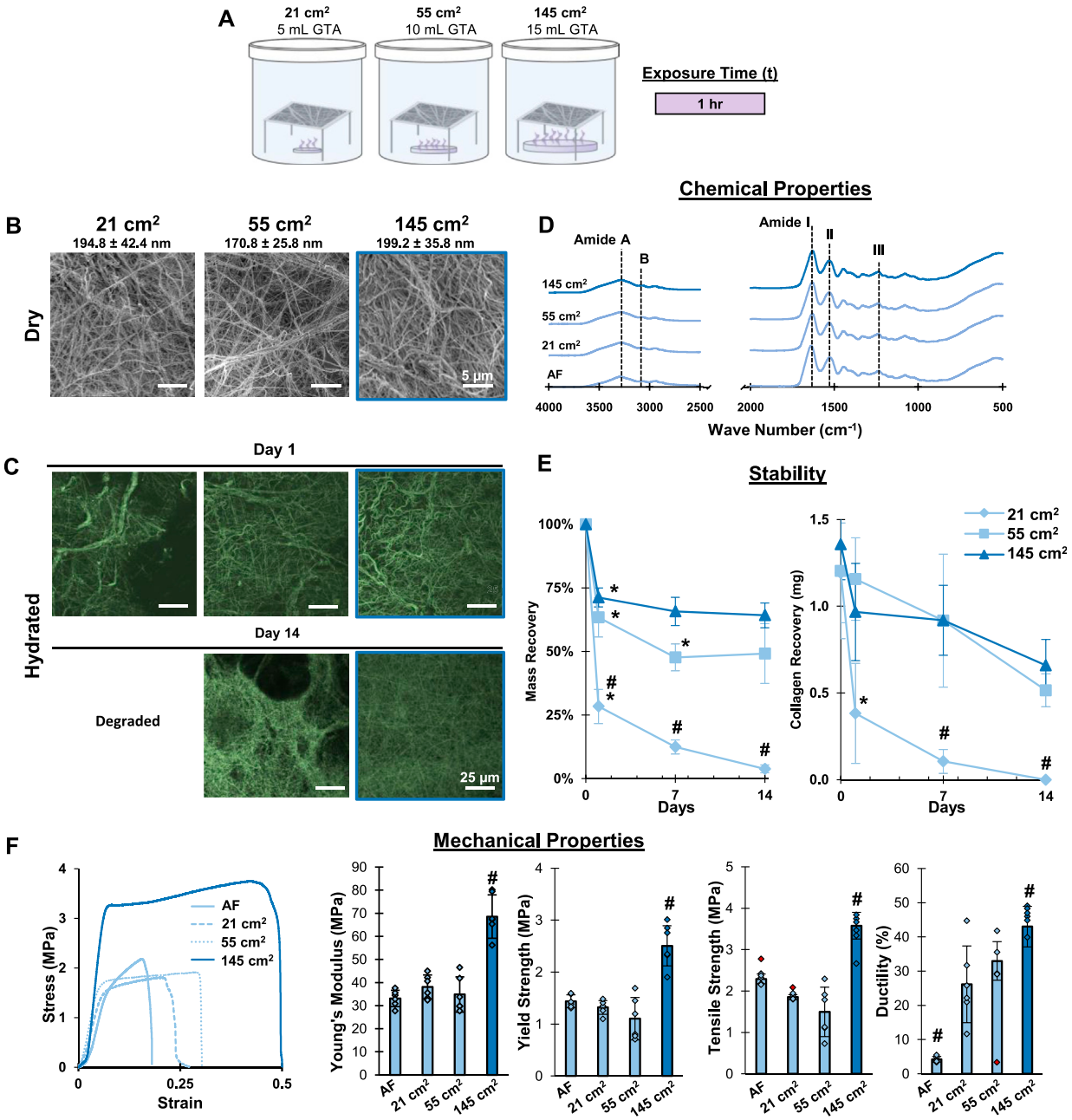

FIGURE 3
Mesh Fabrication: Crosslinking Surface Area. Crosslinking with the 145 cm² surface are a bath for 1 hour stabilizes gelatin meshes and enhances tensile properties without changing fiber morphology, chemistry, or causing pits/voids in the mesh surface. **(A)** Schematic of the crosslinking procedure. **(B)** Dry morphology (SEM, 2,500x) and **(C)** hydrated morphology (CRM, 100x) of meshes after crosslinking. **(D)** Chemical composition (FTIR-ATR). **(E)** Mesh stability by mass recovery and collagen recovery after incubation at 37°C in cell culture medium (14 days, n = 5). **(F)** Mesh tensile properties with representative stress-strain curves (n = 10). Red markers represent outliers. AF=As fabricated. #=p < 0.05 between groups. *=p < 0.05 overtime.

bracket system and the GTA bath was fixed at 6 cm. The mesh was exposed to the GTA vapors from the bath in a fume hood (Air Flow = 80 CFM) for 0.5, 1.0, 1.5, and 6 h to allow for crosslinking.

After identifying the optimal crosslink duration, the effect of surface area of the GTA bath was determined at 21 cm², 55 cm², and 145 cm². A similar set-up was followed as described above (Figure 3A), except, for the 21 and 55 cm² groups, GTA was

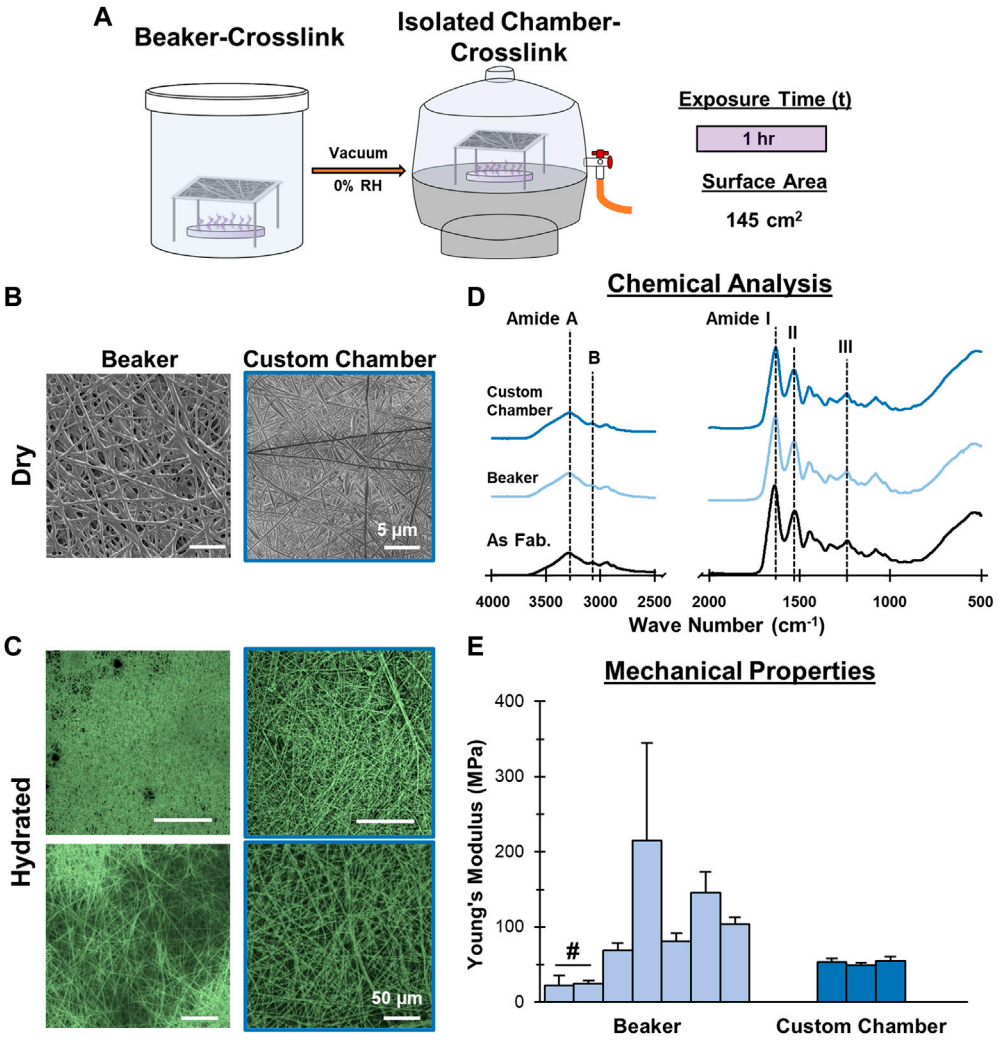

FIGURE 4
Mesh Fabrication: Crosslinking Environmental Conditions. Crosslinking inside a vacuum sealed chamber minimizes batch-to-batch variability. **(A)** Schematic of the crosslinking procedure. **(B)** Dry morphology (SEM, 2,500x) and **(C)** hydrated morphology (CRM, 100x, 300x) of meshes after crosslinking. **(D)** Chemical composition (FTIR-ATR). **(E)** Young's Moduli after crosslinking by beaker (7 batches) and the custom chamber (3 batches) (n = 10). #=p < 0.05.

poured into small and medium sized dishes with desired surface areas instead of the bottom of the glass beaker (glass beaker surface area was 145 cm^2). All meshes were then exposed to GTA baths for the optimal duration as determined above.

Lastly, to standardize ambient effects on crosslinking, gelatin meshes were chemically crosslinked by glutaraldehyde vapor deposition in a custom chamber (Figure 4A). Briefly, a 15 ml glutaraldehyde bath was placed in the custom chamber. A gelatin mesh (6 × 6 cm) was secured in a custom bracket and suspended 6 cm above the GTA bath with optimized surface area. The custom chamber was then sealed by applying a vacuum. After 3 min, the valve was closed and the chamber was isolated, allowing it to sit under vacuum for the optimal duration identified above. After half of the "optimal duration" had passed, the vacuum was slowly released to prevent GTA aerosolization and the mesh was flipped over. The vacuum was then reapplied as described above, allowing the mesh to sit under vacuum for the remainder of the prescribed time. Sample chemistry, structural and mechanical properties were compared between three batches of as-crosslinked meshes.

Optimal crosslinking parameters were determined by evaluating the impact the crosslink process had on mesh stability, fiber morphology, chemical composition, and mesh tensile properties. More specifically, the crosslinking

conditions should not alter the mesh fiber diameter, morphology and chemical composition from that observed in the as-fabricated meshes. In addition, the crosslinking process should enhance mesh mechanical properties and promote mesh stability by preventing loss of no more than 50% of its mass after incubation under cell culture conditions for up to 14 days. Finally, optimal crosslinking parameters should produce meshes with consistent chemical and physical properties without significant batch to batch variation.

Characterization of crosslinked meshes

Mesh fiber diameter, morphology, tensile properties, chemical composition and stability were evaluated as a function of crosslinking conditions. Fiber diameter and morphology were analyzed by SEM as described above. In addition, hydrated mesh morphology and stability (n = 2) were visualized by scanning confocal reflectance microscopy (CRM) (Paddock, 2002; Yang and Kaufman, 2009) on an inverted fluorescent microscope (Olympus Fluoview IX70 Confocal Microscope). The microscope was outfitted with ×20 (air) and ×40 (oil) objectives. Samples were illuminated (488 nm) and the reflected light was detected by a photomultiplier tube. Note that all meshes were compared to "0-h" group, which consists of meshes that had not undergone any crosslinking and were imaged in 100% ethanol to prevent dissolution.

Mesh mechanical properties (n = 6) and chemical composition (n = 3) were determined as described above. Mesh stability was evaluated qualitatively, through CRM imaging, and quantitatively by recording mesh mass and gelatin recovery after 14 days of incubation in Dulbecco's Modified Eagle's Medium (DMEM, Corning) supplemented with 10% fetal bovine serum (FBS, Atlanta Biologicals, Atlanta, GA), and 1% penicillin-streptomycin (P/S, 10,000 U/mL penicillin, 10 mg/ml streptomycin). Briefly, the mass of 1 cm^2 squares of mesh (n = 5) was measured at 0, 1, 7, and 14 days. After incubation, the samples were rinsed three times with deionized water and then dried using a CentriVap (Labconco, Kansas City, MO). Sample dry mass was recorded and mass recovery was calculated relative to the sample's starting mass. Mesh recovery was further determined using a hydroxyproline assay (Reddy and Enwemeka, 1996). Briefly, after dehydration, samples were digested for 18 h at 65°C with papain (8.3 activity units/mL) in 0.1 M sodium acetate, 10 mM cysteine-HCl, and 50 mM ethylenediaminetetraacetate. Next, samples were hydrolyzed by 2 N sodium hydroxide and incubated in Chloramine-T and Ehrlich's reagent. Absorbance was measured at 555 nm (TECAN SpectraFluor Plus) and gelatin content was calculated by correlating sample absorbance to a collagen standard curve.

Biocompatibility—Cells and cell culture

Biocompatibility of the gelatin mesh was assessed *in vitro* using both primary stromal cell culture and an established cell line. All cell culture was conducted in fully supplemented (F/S) media consisting of DMEM supplemented with 10% fetal bovine serum (FBS, Atlanta Biologicals, Atlanta, GA), and 1% penicillin-streptomycin (P/S, 10,000 U/mL penicillin, 10 mg/ml streptomycin). Crosslinked gelatin meshes (1 × 0.5 cm) were sterilized with 70% ethanol for 15 min, followed by rinsing in phosphate buffered saline (PBS, 2x, 5 min). After the second PBS rinse, meshes were pre-soaked in F/S media for 2 h to prepare meshes for cell attachment. Bone marrow derived stromal cells (MSC, Lonza, passage 4) (Bogdanowicz and Lu, 2017) or human osteoblast-like cells (HTB-85 Saos-2, ATCC, passage 8) were seeded onto meshes by dispensing 5 µL of concentrated cell stock suspension (1 M cells/ml) onto the mesh surface, targeting a seeding density of 50,000 cells/cm^2. Cells were allowed to attach for 20 min, after which 1 ml of F/S media was added and the samples were cultured at 37°C and 5% CO_2 for up to 28 days. Media was refreshed three times per week. After 6 days of culture, all groups were treated with 3 mM β-glycerophosphate, which was refreshed at each feed.

Cell response

Cell viability (n = 2) on the gelatin mesh was determined by Live/Dead staining (Molecular Probes, Eugene, OR) according to the manufacturer's protocol. Briefly, the samples were labeled with Live/Dead reagent warmed to 37°C for 2 minutes followed by rinsing in PBS. Next, all samples were imaged by confocal fluorescence microscopy (Olympus Fluoview IX70) at excitation/emission wavelengths of 473/519 nm for live imaging and 559/635 nm for dead imaging. All images are shown as an overlay of the live and dead channels.

Following cell culture, cells were lysed by rinsing the meshes with PBS and freezing them in 500 µL of 0.1% v/v Triton-X solution (Sigma-Aldrich). After one freeze/thaw cycle, samples were ultrasonicated for 10 s at 5 W (Misonix XL-2000, Farmingdale, NY) to promote cell lysis.

Cell proliferation (n = 5) was assessed using a Quanti-iT™ PicoGreen® dsDNA assay kit (Molecular Probes) according to the manufacturer's protocol. Fluorescence was measured using a microplate reader (SpectraFluor Plus, Tecan, Research Triangle Park, NC) at excitation and emission wavelengths of 485 and 535 nm, respectively. Total cell number per sample was determined by correlating measured fluorescence intensity to a DNA standard curve and using a conversion factor of 7.7 pg DNA/cell (Jiang et al., 2005).

Collagen content (n = 5) was assessed by using a hydroxyproline assay (Reddy and Enwemeka, 1996). Briefly, the sample were first desiccated for 12 h in a CentriVap

Concentrator to remove all liquid and digested for 18 h at 65°C with papain (8.3 activity units/mL) in 0.1 M sodium acetate, 10 mM cysteine-HCl, and 50 mM ethylenediaminetetraacetate. Collagen was hydrolyzed by mixing aliquots of the digested mesh with 2 N sodium hydroxide and heating to 250°C for 25 min. The resulting sample hydrolysate was oxidized at room temperature (25°C) for 25 min with buffered Chloramine-T reagent. Ehrlich's reagent (15% p-dimethylaminobenzaldehyde in 2:1 isopropanol/perchloric acid) was then added and absorbance was measured at 555 nm with a microplate reader. Hydroxyproline content was determined by correlating measured optical intensity to a bovine collagen I (Biocolor, Carrickfergus, United Kingdom) standard curve.

Matrix mineralization potential, as reflected in ALP activity (n = 5), was assessed using a colorimetric assay based on dephosphorylation of p-nitrophenyl phosphate (pNP-PO4) to p-nitrophenol (pNP) (Lu et al., 2003). An aliquot of lysed sample was mixed with pNP-PO_4 solution (Sigma-Aldrich) at a 1:1 v/v ratio and incubated at 37°C for up to 30 min. Absorbance was measured using a microplate reader at 405 nm after 5 min for Saos-2 cultures and after 30 min for MSC cultures. Sample ALP activity was determined by correlating measured optical intensity to a pNP standard curve and normalized to cell count and the time the sample was allowed to react.

Mineralization was further ascertained by energy dispersive x-ray analysis (EDS, XFlash® 6–30, Espirit 2.1 software, Bruker, Billerica, MA). Briefly, quantitative spectra were collected at ×10kV, ×500 magnification using the automated "fast" acquisition software settings. Spectra was then analyzed using the Espirit 2.1 software and Ca and P content (n = 3) was calculated in ppm relative to all elements detected. Mineral distribution (n = 2) was visualized by Alizarin Red and Von Kossa staining. Briefly, following incubation, the samples were rinsed 2x with PBS and then fixed in 10% neutral buffered formalin containing 1% cetylpyridinium chloride for 1 h at room temperature. After fixing, samples were rinsed 4x with deionized water and soaked overnight in 5% (w/v) polyvinyl alcohol (PVA). After soaking, samples were embedded in a block of PVA, frozen, and sectioned with a cryotome (10 µm, CM3050 S, Leica Biosystems, Wetzlar, Germany). After drying overnight, sections were cleared of PVA using deionized water and stained for calcium and phosphate content. To visualize Ca, meshes were stained with 2% Alizarin Red for 3 min, rinsed 4x with deionized water and allowed to airdry prior to imaging. To visualize phosphate, sections were covered with 5% $AgNO_3$ and exposed to UV light (365 nm) for 25 min. Following UV exposure, samples were rinsed 4x with deionized water and allowed to air dry. Once dry, all samples were imaged at 10x and 20x under light microscopy with a full spectrum color camera (Zeiss Axiovert 25, Oberkochen, Germany). During imaging, all acquisition settings remained constant to avoid biasing analysis.

Reagents

All reagents were purchased from Sigma-Aldrich unless otherwise noted.

Statistical analysis

All results are presented as mean ± standard deviation. The number of sample replicates are reported as "n." Multiple trials were conducted to ensure reproducibility and only data from representative trials are shown. One-way and two-way analysis of variance (ANOVA) were performed to evaluate statistically significance between sample groups and temporally, when appropriate. A Tukey–Kramer post-hoc test was used for all pair-wise comparisons ($p < 0.05$). All statistical analyses were performed using JMP IN statistical software (SAS Institute, Cary, NC, United States).

Results and discussion

Mesh fabrication: Gelatin-solvent interactions

The focus of this study was to identify ideal fabrication and crosslinking conditions for collagen-based materials prepared by electrospinning. We began by first optimizing the use of the "green" and biocompatible electrospinning solvent, acetic acid (AA). To achieve this, we evaluated the solution viscosity, electrophoretic mobility, and conductivity as a function of gelatin concentration in both 50% and glacial AA. For comparison, the traditional solvent trifluoroethanol (TFE) was used as a positive control (Figure 1). Both glacial and 50% AA were investigated because diluted AA can ionize, which impacts the solvency and solution conductivity (Angammana and Jayaram, 2011).

In TFE, gelatin solutions were slightly cloudy above 7% w/v, while this became evident at 10% w/v gelatin in 50% AA, indicating a decreasing solubility with increasing gelatin concentration. After dissolution, it was also observed that gelatin solutions above 7% in glacial AA began to form solid gels, suggesting poor solvency and that glacial AA is not suitable for electrospinning at higher gelatin concentrations. As expected, solution viscosity increased significantly with gelatin concentration for all solvents tested. The 5% and 7% gelatin in TFE solutions had viscosities of 12.8 and 35.3 cP, respectively, while 20 and 30% w/v gelatin in 50% AA exhibited viscosities of 333.2 and 567.6 cP, respectively. Because gelatin formed particulates at 13% w/v in TFE, higher concentrations were not evaluated. As well, because gelatin gelled in glacial AA above 7% w/v, viscosity, mobility, and conductivity were not measured. Typically, electrospun solutions with viscosity greater

than 100 cP are suitable for electrospinning because it indicates there are sufficient cohesive forces between solute particles to promote chain entanglement and that the solution can resist the applied electrostatic forces until a critical potential is achieved. At this critical potential, the solute will eject from the solution, forming a steady release of fine, smooth fibers (Fong et al., 1999; Ginestra et al., 2016; Amariei et al., 2017). While it is possible to electrospin gelatin at lower viscosities, the fiber ejection is often less stable due to the lower cohesive forces, resulting in the need for frequent user intervention during fabrication and increased variability in mesh morphology (Zeng et al., 2003; Nezarati et al., 2013).

Next, taking a closer look at the electrochemical properties, the mobility of gelatin in each sample was measured (Figure 1B). For all TFE samples, mobility measurements were below the limit of detection for the instrument, suggesting there were not enough particles with sufficient charge and/or the solution's ionic strength was too low be conductive. Interestingly, in 50% AA samples, the maximum mobility (0.28 μm * cm/Vs.) was observed in the 7% w/v gelatin solution, while mobility of 0.09 μm * cm/Vs. and 0.04 μm * cm/Vs. were measured in the 20% and 30% solutions, respectively. Since the mobility represents the ability of a solute to move in solution in response to an applied electric field (Davis and Cohn, 1939), it is an important factor for solution spinnability, which relies on polymer migration within the solvent prior to ejection. Thus, it is likely that a stable electrospin will result when solutions exhibit a moderate to low mobility. In this scenario, gelatin particles will migrate through solution quickly enough to eject, but slowly enough to promote polymer entanglement, which is critical for steady fiber ejection (Haider et al., 2018; Xue et al., 2019). If the mobility is too low, particles may fail to migrate and eject, while conversely, if the mobility is high, particles will migrate too quickly in solution, resulting in ejection before polymer entanglement can occur causing samples to electrospray as fine particles. In this study, the 20% and 30% w/v gelatin in 50% AA resulted in the most stable spins, as these solutions exhibited the lowest, but still non-zero mobility among all the samples.

In terms of conductivity, the TFE, 50% AA, and glacial AA neat solutions (no gelatin) had conductivities of 0.00 mS/cm, 0.98 mS/cm, and 0.05 mS/cm, respectively (Figure 1B). The TFE solutions exhibited an increase in conductivity with gelatin concentration, reaching a maximum conductivity of 36.5 μS/cm at 13% gelatin. As expected, conductivity of AA significantly increased when mixed with water. This is because diluting AA results in increased ionization, creating conductive acetate and hydronium ions. The conductivity for glacial AA increased slightly to 0.10 mS/cm with the addition of 7% gelatin, but was not measurable at higher concentrations due to the gelation of the samples. For 50% AA solutions, the conductivity increased with gelatin concentration, reaching 3.03 mS/cm in the 30% w/v gelatin sample, which is significantly greater than all TFE and glacial AA solutions tested. Conductivity is a vital characteristic for establishing a stable, reproducible electrospin (Uyar and Besenbacher, 2008; Angammana and Jayaram, 2011), as a sufficient number of ions must be present to permit the transfer of charge from the applied electric force that ultimately induce particle migration, entanglement, and ejection into continuous fibers. Zhang et al. (2005b) observed that increasing solution conductivity resulted in significant decreases in polyvinyl alcohol fiber diameter but, once above 2.75 mS/cm, resulted in bead formation along the polymer strand. Fong et al. (1999) reported that below a certain charge density threshold, which is analogous to solution conductivity, fiber ejection was not continuous and that bead formation would also occur in polyethylene oxide fibers, suggesting a minimum conductivity is also critical. These observations suggest that 50% AA is the best suited solvent for electrospinning, as it is electrically conductive and can support the building of the charge that is critical for inducing solute:solvent instability and causing fiber ejection.

Electrospinning stability relies on a balance between polymer chain mobility and entanglement while in the spin solution. Sufficient polymer entanglement is necessary to support steady polymer ejection while a sufficient polymer migration is necessary for solute movement and ejection. Here, we evaluated the solution viscosity, mobility and conductivity, to identify ideal solution properties. While mobility is a direct measure of particle movement the solution viscosity and conductivity are primarily indicative of particle entanglement and migration, respectively. Based on our analysis, 20% and 30% gelatin in 50% AA are most likely to result in stable electrospins due to their high conductivity, high viscosity, and moderate to low mobility. These properties in conjunction, will support polymer chain entanglement and migration, allowing for a steady fiber ejection. Interestingly, it was observed that gelatin in TFE did not follow this pattern, yet gelatin has previously been electrospun using TFE (Huang et al., 2004; Zhang et al., 2005a; Choktaweesap et al., 2007; Chuang, 2015). This is possible because, while each of these solution properties independently may not be ideal for electrospinning, they collectively can still support fiber formation, albeit with less stable fiber ejection. The instability is a direct consequence of the solution's low conductivity and viscosity, which result in insufficient solution charging to support mobility and evoke polymer chain entanglement, respectively. However, despite this, fiber ejection is still achieved due to the lower mobility of the polymer particles. This is because the lower mobility still allows particles to entangle and migrate, offsetting the low conductivity and viscosity. Conversely, if these solutions exhibited large mobility, gelatin particles would rapidly move and eject during the spin, resulting in electrospraying. Thus, even with sub-optimal solution characteristics, gelatin can be electrospun in TFE, albeit with less stable ejection that requires more user intervention and increased variability. In

contrast to TFE, the 50% AA gelatin solutions had significantly greater viscosity, mobility, and conductivity. These three solution properties worked in conjunction to allow for sufficient polymer chain entanglement and mobility, which should result in a steady ejection of polymer fibers with minimal user intervention required during fabrication.

Mesh fabrication: Electrospinning parameters

After characterizing solution properties, spinnability was evaluated at flow rates ranging from 0.25–5.0 ml/h and applied voltages ranging from 5–25 kV. These test parameters were chosen because they are reported to be stable electrospins (Moffat et al., 2009; Mosher et al., 2021). An electrospin was considered stable when a single, steady fiber ejection persisted without the need of user intervention for >15 min. Once stable spin conditions were identified, the resulting fibers were evaluated to ensure they retain the chemical properties of the source gelatin and are comprised of smooth fibers with physiologically relevant diameters and mechanical properties.

It was observed that gelatin prepared in TFE at 5% and 7% w/v produced stable spins after optimization of melt flow rate and applied voltage (Figures 1C,D), albeit with periodic user intervention and maintenance. When mixed in 50% AA, gelatin failed to electrospin at concentrations below 20% w/v. At 30% w/v, fibers appeared glassy and ribbon like, losing the cylindrical morphology (Figures 1C,D). These initial observations suggest that 7% and 30% w/v gelatin may be the upper limit for producing fibrous meshes in TFE and 50% AA, respectively. As shown in Figure 1C, all stable spins resulted in fibers with diameters averaging less than 300 nm, with the exception of 30% w/v gelatin in 50% AA. As expected, fiber diameter increased with gelatin concentration regardless of solvent tested. The greater solute per unit volume and higher viscosity that is associated with increasing gelatin concentration result in larger fibers along with decreased fiber stretching during ejection (Fridrikh et al., 2003; Zeng et al., 2003).

Given that the 20% w/v gelatin in 50% AA and 7% w/v gelatin in TFE were stable spins and had comparable fiber diameters, these two conditions were selected for further characterization (Figures 1E,F). FTIR-ATR analysis identified the characteristic gelatin or collagen peaks, including amide A (N-H stretch, 3,306 cm^{-1}), amide B (C-H stretch, 3,076 cm^{-1}), amide I (C = O and C-N stretch, 1,646 cm^{-1}), amide II (N-H bend and C-N stretch, 1,520 cm^{-1}), and amide III (N-H bend, C-N stretch, C-C and C = O in-plane bend, 1,234 cm^{-1}) (Muyonga et al., 2004; Nagai et al., 2010; Di Foggia et al., 2011; Cebi et al., 2016; Xu et al., 2017) All were evident in spectra for the source gelatin and in meshes prepared in TFE and AA, indicating that no chemical modifications occurred due to reacting with the solvent nor the electrospinning process.

For mechanical properties, both the TFE positive control and 50% AA group showed comparable Young's Moduli of approximately 30MPa, which is on the order of most biological tissues (Graham et al., 2004; Akhtar et al., 2011). Yield strength, ultimate tensile stress, and ductility were observed to be higher in the 50% AA mesh. The tensile properties of various hydrated collagen-based tissues have been reported to be in the range of 2–27 MPa (Eleswarapu et al., 2011), suggesting that the 50% AA mesh may be more representative of the softer tissues tested, while the TFE mesh was even weaker when tested wet under tension. The enhanced mechanical properties found in the 50% AA meshes may be due to carboxymethylation and subsequent crosslinking that can occur in AA, which is known to increase mesh mechanical properties (Yamauchi et al., 1988; Gómez-guillœn and Montero, 2001). Additionally, differences in solvent evaporation rate may impact the mechanical properties of the fibers by altering the polypeptide chain organization and ultimate crystallinity (Coppola et al., 2012). More specifically, because AA is less volatile than TFE, it will evaporate slower during the spinning process. This slower evaporation can allow polypeptide chains to rearrange to lower energy states, impacting sample crystallinity and enhancing mechanical properties. Lastly, SEM micrographs (Figure 1D, black-boxed and blue-boxed micrographs) showed that both meshes contained smooth, randomly oriented, nanofibers that appeared morphologically identical to many ECM tissues. Thus, gelatin was successfully electrospun in 50% AA with comparable modulus and morphology to traditional electrospinning methods (TFE). Moreover, the meshes were structurally and compositionally similar to natural ECM, supporting the use of this substrate as an ECM analog.

Mesh fabrication: Chemical crosslinking

Electrospun gelatin or collagen meshes require crosslinking to prevent dissolution and loss of structure in aqueous environments such as cell culture media. Therefore, the next part of this study centered on developing an optimized chemical crosslinking strategy that is reproducible and retains both morphological and chemical features of the as-fabricated mesh. Specifically, GTA is used to crosslink the meshes due to the ability of its dialdehyde groups to covalently bind primary amines present along the amino acids that make up gelatin, creating strong chemical crosslinks. To this end, the effects of crosslinking time, GTA bath surface area, and the impact of environmental conditions, including air flow and relative humidity, were evaluated. During each step of the optimization, the resulting mesh stability, fiber morphology, chemical composition, and tensile properties were analyzed. Along with the as-expected increase in mechanical properties due to crosslinking, the optimal crosslinking conditions were

defined as the production of physically stable meshes in dry and wet conditions with unaltered fiber morphology.

To evaluate the impact of crosslinking duration on the gelatin mesh, samples were exposed to GTA vapors for 0.5, 1.0, 1.5, and 6 h in a loosely-capped 2-L beaker containing 15 ml of GTA (Figure 2). A noticeable change in mesh morphology was observed at 1.5 h (Figure 2B, SEM). The fibers began to appear less cylindrical and woven and took on a flat, mat-like appearance. This became more apparent after 6 h, as the mesh fiber morphology and apparent pore size, which are critical features for recapitulating the native ECM, were starting to be irreversibly changed. Moreover, fibers began to merge together at 1.5 h, resulting in increases in the apparent fiber diameter. Furthermore, with increasing duration, meshes were becoming noticeably more brittle, making them difficult to handle.

Next, mesh stability was assessed in cell culture media, focusing on maintaining mesh morphology and mass over time. After 2 weeks, distinct fibers were retained in all groups except the 0.5-h group, where numerous pits and voids were observed, indicating 30 min crosslinking is insufficient for stabilizing gelatin *in vitro* (Figure 2C). In the 6-h group, large beaded structures were observed on the mesh surface. These beads are likely the result of GTA droplets, instead of fine vapors, becoming airborne during long crosslinking periods (beyond 1.5 h). These drops then contact the mesh, merging the nanofibers into larger structures disrupting fiber morphology. Thus, 0.5-h was insufficient for stabilizing the mesh, while 1.5 and 6 h were too long since abundant bead formation was observed. Furthermore, the 1-h group retained the most similar morphology to the as-fabricated day 0 mesh, which was imaged in 100% ethanol to preserve the mesh structure for comparison.

Meshes crosslinked for 6 h showed no significant change in mass, while the 1-h and 1.5-h groups showed 67% and 71% mass recovery after day 1, respectively (Figure 2E). Mesh mass stabilized thereafter for both groups, suggesting that the initial loss may be attributed to non-crosslinked gelatin. The lowest mass recovery (17%) at day 1 was found in the 0.5-h group, with significantly lower mass recovery over time, indicating the mesh was not sufficiently crosslinked. Along with mass recovery, gelatin recovery was also characterized (Figure 2E), which correlated well with the trends observed in mass recovery, indicating that the changes in mass recorded over time were due to loss of gelatin. In addition, this data further corroborated that meshes crosslinked for 0.5 h are unstable, while 1 and 1.5-h crosslinking demonstrated stability after day 1 and meshes crosslinked for 6 h remained stable through day 14. Reviewing the IR spectra, no discernible differences between as-fabricated and crosslinked meshes were observed, regardless of the duration (Figure 2D). This suggests that the chemical bonds formed during the crosslinking procedure may not be distinguishable by this method, but also confirms that other unintended modifications are not occurring during the crosslinking process. Following IR analysis, the tensile properties of the meshes, including Young's Modulus, yield strength, tensile strength, and ductility, were evaluated. As expected, mechanical properties increased with crosslinking time, with the highest value measured after 6 h. Notably, however, greater variability was found in the mechanical properties of the 6 h group, which is likely attributed to the increased mesh brittleness that is a result of overexposure to GTA.

Collectively these observations indicate that the ideal crosslinking duration is 1-h, which is sufficient for stabilizing the gelatin meshes without compromising fiber morphology and mechanical properties. Crosslinking for 0.5 h resulted in significant mass loss, while crosslinking for 1.5 and 6 h led to loss of fiber morphology and the mesh fibrous network. Thus, for all subsequent crosslinking optimization, 1 h was chosen as the ideal duration.

After determining an optimal crosslinking duration, the impact that the GTA bath surface area had on crosslinking was investigated. Increasing bath surface area increases vapor formation, thus impacting the crosslinking process. Thus, an optimal bath surface area will produce sufficient vapors to stabilize the meshes without altering their chemical or morphological features. To evaluate this, gelatin meshes were suspended over baths with surface areas of 21 cm^2, 55 cm^2, and 145 cm^2 and crosslinked for 1.0 h (Figure 3). Following crosslinking, no significant changes in fiber diameter nor fiber arrangement and morphology were observed among the different groups (Figure 3B). Imaging by CRM found loss in fiber morphology for the 21 cm^2 group after just 1 day of incubation in culture media (Figure 3C). Intact fibrous structures were observed in the 55 and 145 cm^2 setups by CRM, however, pitting and voids were found in the 55 cm^2 after 14 days of incubation. Mass recovery analysis found an 18% mass recovery for the 21 cm^2 after 1 day of incubation, while mass recovery was 62% and 71% for the 55 and 145 cm^2, respectively (Figure 3E). By day 14, meshes crosslinked with 21 cm^2 surface area fully dissolved, while 55 and 145 cm^2 groups remained relatively stable at 49% and 64% mass recovery, respectively. Similar trends were also observed after analyzing gelatin recovery for these samples using the hydroxy-proline colorimetric assay. Analysis by FTIR-ATR did not show any changes, indicating that chemically, gelatin remained unchanged and that GTA crosslinking was not detected in the IR spectra (Figure 3D). Mechanical properties were enhanced in the 145 cm^2 group but remained unchanged between the 21 cm^2, the 45 cm^2, and the as-fabricated mesh (Figure 3D). Thus, it was determined that 145 cm^2 surface area was required to fully stabilize the mesh and prevent loss of fiber morphology when crosslinking for 1 h and will be used in further optimization studies.

After identifying optimal duration and surface area parameters, significant variability was still observed in mesh mechanical properties. This variability was found to directly

A

Optimal Electrospinning Parameters			
[Gelatin]	Solvent	Flow Rate	Voltage
20-30%	50% AA	1mL/hr	18 - 22 kV

Optimal Crosslinking Parameters			
Solvent	Duration	Surface Area	Chamber
GTA	60 min. (30 min./side)	145 cm^2	Vacuum Chamber

B

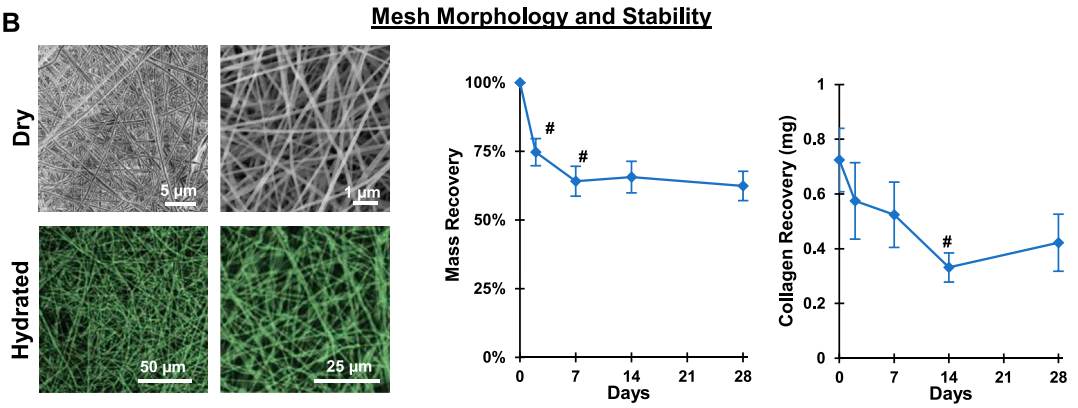

C

Optimized Mesh Properties						
Mesh State	Fiber Ø (nm)	Young's Modulus (MPa)	Yield Strength (MPa)	Tensile Strength (MPa)	% Ductility	Storage Modulus (KPa)
Dry	186.5 ± 55.0	41.2 ± 3.7	1.43 ± 0.17	1.78 ± 0.23	9.3 ± 3.1	N/A
Hydrated	N/A	1.08 ± 0.04	0.57 ± 0.03	0.83 ± 0.10	116.2 ± 15.0	1.70 ± 0.04

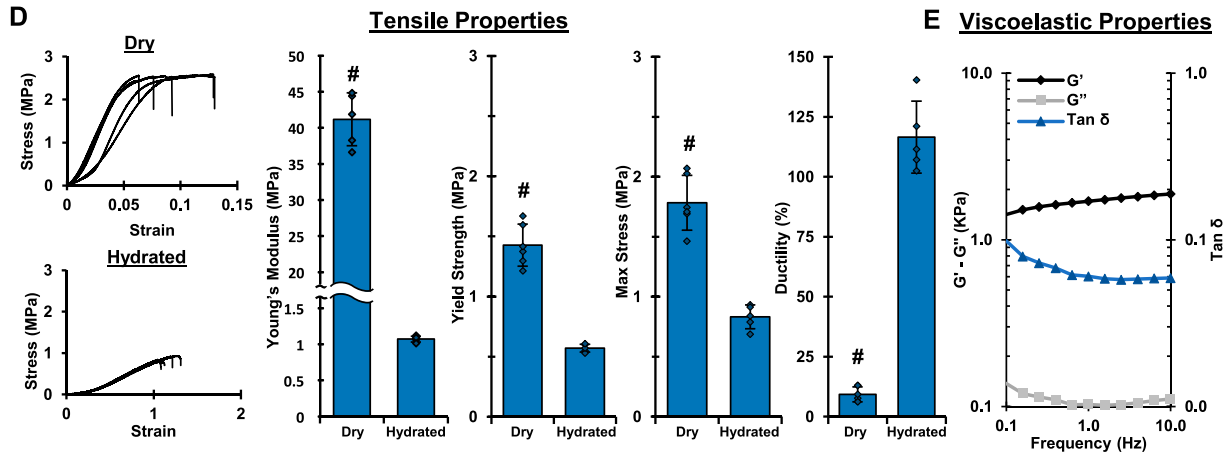

FIGURE 5
Optimal Fabrication: Electrospinning and Crosslinking. Gelatin electrospun in 50% acetic acid and crosslinked for 1 hr in a vacuum chamber results in stable, fibrous meshes with a conserved chemical composition. **(A)** Optimal electrospinning and crosslinking conditions. **(B)** Dry (SEM, 2,500x, 10,000x) and wet morphology (CRM, 100x, 300x) and stability of crosslinked gelatin meshes prepared using optimized parameters. **(C)** Table summarizing properties of optimized mesh. **(D)** Tensile properties after crosslinking and hydrating (n = 10). **(E)** Viscoelastic properties of hydrated gelatin meshes (n = 3). #=p < 0.05.

correlate with ambient conditions, such as air flow and humidity, during crosslinking. Suspecting that the loosely-capped beaker exposed the crosslinking to environmental conditions, a custom chamber that isolated the mesh during crosslinking, essentially eliminating humidity and air flow as variables, was developed (Figure 4). To test this new approach, meshes were placed into the custom chamber with a GTA bath with a surface area of 145 cm^2 and a vacuum was applied. Similar to the optimized beaker approach, the mesh was crosslinked 30 min per side (1 h total). To determine the impact of the chamber, mesh tensile

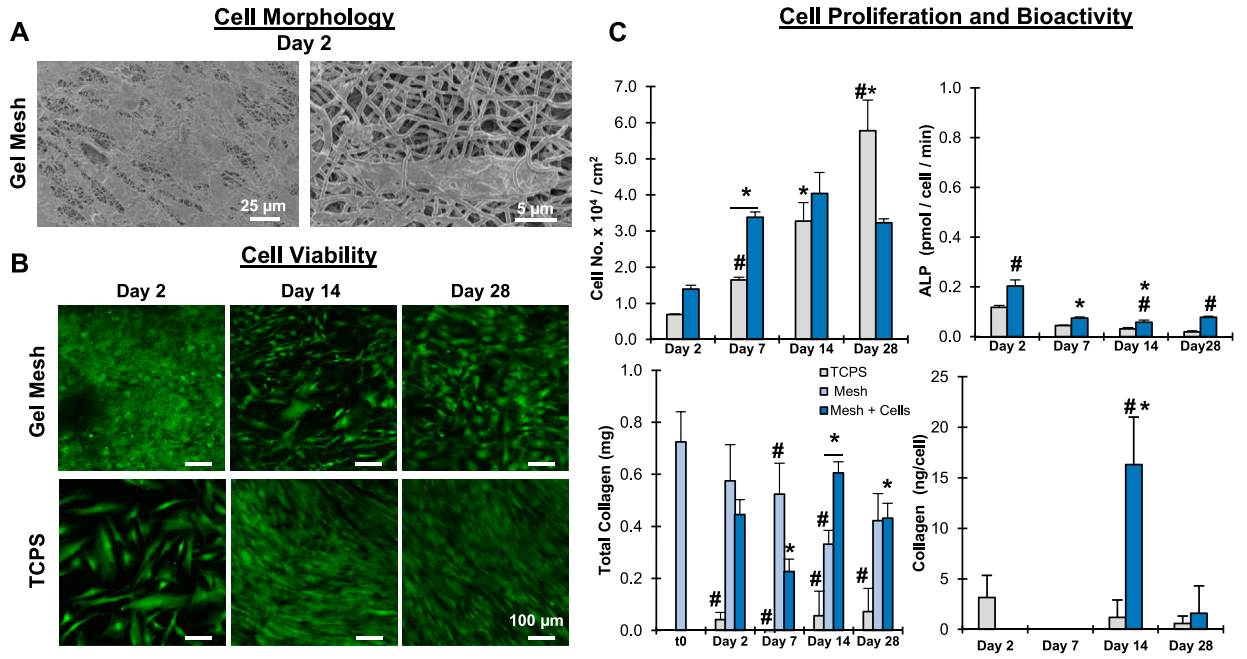

FIGURE 6
Mesh Biocompatibility: Stem Cells. Meshes were biocompatible and supported MSC attachment and growth. **(A)** Cell/matric interaction (Day 2, SEM, 500x, 2,500x). **(B)** Cell Viability **(C)** Cell proliferation, bioactivity, and matrix stability (n = 5). *= $p < 0.05$ between groups. #=$p < 0.05$ over time.

mechanical properties were evaluated (Figure 4E). Three separate batches were crosslinked in the custom chamber under vacuum and exhibited consistent mechanical properties, with Young's moduli of 53.1, 49.2, and 55.3 MPa. This is contrasted with 7 batches of mesh crosslinked using the optimized conditions in the loosely capped beaker, which had moduli ranging from 21.9–215.1 MPa. In addition to reduced variability in mechanical properties, no unintended changes in chemical composition by FTIR and the fiber morphology were observed. Using the custom chamber improved the reproducibility of mesh crosslinking by eliminating the influence that ambient conditions had on the production of GTA vapors and their subsequent interaction with the gelatin mesh.

Optimized fabrication protocol and biocompatibility

The processes described above allowed us to determine optimal fabrication and crosslinking conditions for the production of a biomimetic ECM analog using the "green" solvent, AA. Specifically, as shown in Figure 5, the optimal electrospinning conditions are: 20% w/v gelatin in 50% AA at 1 ml/h and 18–22 kV. The optimal setup and conditions for crosslinking includes placing the mesh over a GTA bath (15 ml, 145 cm^2) for 60 min (30 min per side) under vacuum in a custom chamber. Collectively, these optimal conditions resulted in a stable, fibrous mesh with physiologically relevant mechanical properties that may be used as a biomimetic alternative to current *in vitro* culture platforms (Figure 5). Optimized meshes exhibited Young's moduli of 41.2 and 1.08 MPa when dry and hydrated, respectively. Furthermore, when hydrated, the meshes were viscoelastic, with a storage modulus of 1.70 kPa. The hydrated meshes were highly elastic and ductile, properties that are similar to many natural ECM (Jiao et al., 2012). It is emphasized that our optimized protocol reproducibly yielded meshes that are chemically and morphologically comparable to collagen matrix and exhibit physiologically relevant physical properties. This is a significant improvement over other commonly utilized approaches for *in vitro* cell culture, including TCPS and synthetic polymer substrates, and demonstrates enhanced reproducibility over similar approaches currently presented in the literature.

To assess the biocompatibility of the crosslinked gelatin meshes, mesenchymal stromal cells (MSC) were cultured on the meshes and cell bioactivity and viability were evaluated (Figure 6). Meshes were consider biocompatible if they supported cell attachment, proliferation, and phenotypic response. It was observed that the MSC readily attached to the mesh fibrils (Figure 6A). Furthermore, the cells were observed both atop and beneath mesh fibrils, indicating that they can interact with, respond to, and penetrate the matrix. The stem cells remained viable and proliferated through the course of

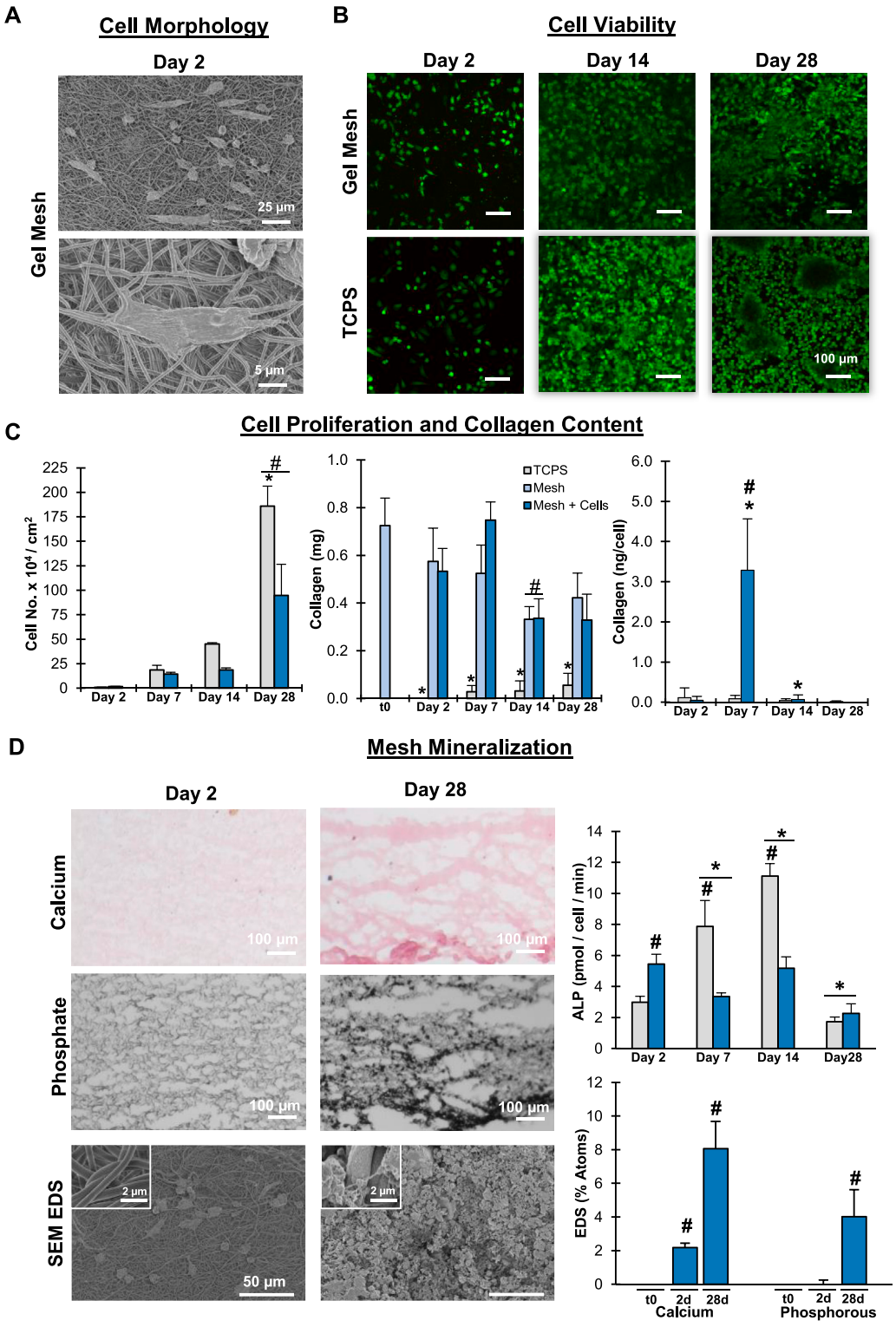

FIGURE 7
Mesh Biocompatibility: Human Osteoblast-like Cells. Meshes were biocompatible and supported Saos-2 cell attachment, growth, and matrix mineralization. **(A)** Cell/matrix interactions (day 2, SEM, 500x, 3,000x). **(B)** Cell Viability. **(C)** Cell proliferation and matrix stability (n = 5). **(D)** Matrix mineralization qualitatively by Von Kossa and Alizarin Red histological stains and quantitatively by alkaline phosphate activity (n = 5) and SEM EDS (SEM, 500x, n = 5 regions per mesh). #=p< 0.05 between groups, * = p < 0.05 over time.

the study, indicating the mesh did not negatively impact cell health and supports cell proliferation (Figures 6B,C). When normalized to surface area, cell proliferation was greater on the mesh than on TCPS through day 14. At day 14, proliferation on the mesh plateaued, suggesting cell-to-cell contact inhibition may be preventing further expansion. Conversely, on TCPS significant cell proliferation was observed to day 28. This is likely the result of cells spreading to the well-walls and possibly forming cell sheets, which were observed on TCPS but did not occur with mesh samples. Next, minimal ALP activity was observed during the course of the study, suggesting the stem cells are likely maintaining their naïve, undifferentiated state during culture. Collagen content was characterized and it was observed that the MSC did not appear to produce any new matrix, as collagen detected in cellular groups closely correlated with collagen measured in acellular groups. These results clearly demonstrate that gelatin meshes can successfully support stem cell culture prior to induction or differentiation studies.

The phenotypic response of a human osteoblast-like cell line on the matrix was also evaluated. Specifically, we were interested in determining if the gelatin mesh can act as a collagen-based platform for cell mediated mineralization. This is of interest because it models one route through which natural tissue mineralization occurs and thus could demonstrate the use of this platform for studying tissue mineralization. Similar to the MSC, the mesh readily supported attachment and proliferation of the osteoblast-like cells (Figure 7). When normalized to surface area, significant proliferation was observed in both mesh and TCPS groups after 28 days of culture. At 28 days, greater proliferation observed in the TCPS can be attributed to the formation of layers of cell sheets as well as cells expanding up the well-walls in the culture plate. Similar to the stem cell data, there was no discernable collagen production when compared to acellular meshes, suggesting the cells may not need to produce additional collagen matrix in the presence of the gelatin mesh. Significantly greater ALP activity was observed from cells cultured on the mesh compared to TCPS at day 2. Alkaline phosphatase is an enzyme critical for catalyzing the conversion of organic phosphate to inorganic phosphates in the body, the rate limiting step that makes up calcium-phosphate minerals in hard tissues (Orimo, 2010). Thus, this elevated activity is not just phenotypically expected, it also demonstrates the mesh can readily act as a base for supporting cell mineralization. Furthermore, it is to be expected that, under normal physiologic conditions, initial increases in ALP activity will be followed by decreases in activity after sufficient amounts of inorganic phosphates are produced. This pattern was observed in the mesh group. Conversely, steadily increasing ALP activity was observed in the TCPS group, which suggests non-physiologic ALP activity that may be related to culturing on TCPS. Mesh mineralization was further corroborated in the SEM/EDS analysis and histological staining (Figure 7D). Mineral nodules were evident on the mesh surface, which was accompanied by significant increases in calcium and phosphorous content on the mesh surface. The increases in CaP on the gelatin meshes may be attributed to cell mediated mineralization. Calcium and phosphate staining positively identified mineral on the mesh surface and through the mesh cross-section after 28 days of culture. Thus, it is clear the gelatin mesh was providing the collagen matrix framework that acts as a substrate for and is functionally similar to the *in vivo* sites for mineralization. This system offers a significant advantage when compared to other systems previously developed for substrate mineralization (Murphy and Mooney, 2002; Nandakumar et al., 2010). Alternative systems often utilize synthetic materials and surface coatings using concentrated simulated body fluid, an ion-rich solution comparable to blood plasma. These non-physiological factors impact the applicability of data collected on these systems when trying to study natural cellular processes. Conversely, in the work presented here, human osteoblast-like cells readily mineralized the surface of the biomimetic gelatin meshes while cultured under physiologically relevant conditions. Thus, the gelatin meshes support cell culture and viability, representing a more biomimetic culture system.

Conclusion

This study aimed to develop an ECM analog with high fidelity by systematically elucidating optimal fabrication and crosslinking conditions for collagen-based fibers. After optimizing gelatin electrospinning via the use of acetic acid, a "green" and biocompatible solvent, the effects of crosslinking conditions, including duration of exposure, surface area, and ambient conditions were investigated, culminating in optimal parameters for gelatin crosslinking post-fabrication. The resultant mesh is stable in both dry and wet conditions with little batch-to-batch variability, and retains as-fabricated architecture and native chemistry while enhancing mechanical properties. Moreover, the collagen platform supported the maintenance of human stem cells as well as the phenotypic production of a mineralized matrix by osteoblast-like cells. Future studies will explore the potential of this novel ECM analog for elucidating cell-matrix interactions and informing the design of tissue regeneration therapies.

Data availability statement

The raw data supporting the conclusion of this article will be made available by the authors, without undue reservation.

Author contributions

PB: Conceptualization; data curation; formal analysis; funding acquisition; investigation; methodology; validation; visualization; writing—original draft; writing—review and editing. MG: Data curation; formal analysis; investigation; writing—review and editing. SS: Methodology; investigation; resources; review and editing. LK: Methodology; investigation; resources; review and editing. HL: Conceptualization; data curation; funding acquisition; methodology; project administration; resources; software: supervision; validation; writing—original draft; writing—review and editing.

Funding

This work was supported by the National Institutes of Health (NIH-NIAMS 1R01-AR07352901A), the New York State Stem Cell ESSC Board (NYSTEM C029551), and the National Science Foundation Graduate Research Fellowship (DGE-1644869, PAPB). Defense Advanced Projects Agency (D20AC00004, HHL)

Conflict of interest

The authors declare that the research was conducted in the absence of any commercial or financial relationships that could be construed as a potential conflict of interest.

Publisher's note

All claims expressed in this article are solely those of the authors and do not necessarily represent those of their affiliated organizations, or those of the publisher, the editors and the reviewers. Any product that may be evaluated in this article, or claim that may be made by its manufacturer, is not guaranteed or endorsed by the publisher.

References

Akhtar, R., Sherratt, M. J., Cruickshank, J. K., and Derby, B. (2011). Characterizing the elastic properties of tissues. *Mat. TodayKidlingt.* 14 (3), 96–105. doi:10.1016/s1369-7021(11)70059-1

Alberts, B., Johnson, A., Lewis, J., Raff, M., Roberts, K., and Walter, P. (2002). "The extracellular matrix of animals," in *Molecular biology of the cell*. 4th edition (New York, NY: Garland Science).

AlteringRubin, Harry (1966). Altering bacteriological plastic petri dishes for tissue culture use. *Public Health Rep.* 81 (9), 843–844.

Amariei, N., Manea, L., Bertea, A., and Popa, A. (2017). "The influence of polymer solution on the properties of electrospun 3D nanostructures," in *IOP conference series: Materials science and engineering* (Bristol, UK: IOP Publishing).

Angammana, C. J., and Jayaram, S. H. (2011). Analysis of the effects of solution conductivity on electrospinning process and fiber morphology. *IEEE Trans. Ind. Appl.* 47 (3), 1109–1117. doi:10.1109/tia.2011.2127431

Bigi, A., Cojazzi, G., Panzavolta, S., Rubini, K., and Roveri, N. (2001). Mechanical and thermal properties of gelatin films at different degrees of glutaraldehyde crosslinking. *Biomaterials* 22 (8), 763–768. doi:10.1016/s0142-9612(00)00236-2

Bogdanowicz, D. R., and Lu, H. H. (2017). Designing the stem cell microenvironment for guided connective tissue regeneration. *Ann. N. Y. Acad. Sci.* 1410 (1), 3–25. doi:10.1111/nyas.13553

Boushell, M. K., Mosher, C. Z., Suri, G. K., Doty, S. B., Strauss, E. J., Hunziker, E. B., et al. (2019). Polymeric mesh and insulin-like growth factor 1 delivery enhance cell homing and graft– cartilage integration. *Ann. N. Y. Acad. Sci.* 1442 (1), 138–152. doi:10.1111/nyas.14054

Cebi, N., Durak, M. Z., Toker, O. S., Sagdic, O., and Arici, M. (2016). An evaluation of Fourier transforms infrared spectroscopy method for the classification and discrimination of bovine, porcine and fish gelatins. *Food Chem. x.* 190, 1109–1115. doi:10.1016/j.foodchem.2015.06.065

Chew, S. Y., Wen, J., Yim, E. K., and Leong, K. W. (2005). Sustained release of proteins from electrospun biodegradable fibers. *Biomacromolecules* 6 (4), 2017–2024. doi:10.1021/bm0501149

Choktaweesap, N., Arayanarakul, K., Aht-ong, D., Meechaisue, C., and Supaphol, P. (2007). Electrospun gelatin fibers: Effect of solvent system on morphology and fiber diameters. *Polym. J.* 39 (6), 622–631. doi:10.1295/polymj.pj2006190

Chuang, P. J. (2015). *Development and characterization of ion encapsulated liposomes for vesicle-mediated biomineralization*. Columbia University.

Coppola, M., Djabourov, M., and Ferrand, M. (2012). Unified phase diagram of gelatin films plasticized by hydrogen bonded liquids. *Polymer* 53 (7), 1483–1493. doi:10.1016/j.polymer.2012.02.016

Davidenko, N., Schuster, C. F., Bax, D. V., Farndale, R. W., Hamaia, S., Best, S. M., et al. (2016). Evaluation of cell binding to collagen and gelatin: a study of the effect of 2D and 3D architecture and surface chemistry. *J. Mat. Sci. Mat. Med.* 27 (10), 148. doi:10.1007/s10856-016-5763-9

Davis, B. D., and Cohn, E. J. (1939). The influence of ionic strength and pH on electrophoretic mobility. *J. Am. Chem. Soc.* 61 (8), 2092–2098. doi:10.1021/ja01877a036

Di Foggia, M., Taddei, P., Torreggiani, A., Dettin, M., and Tinti, A. (2011). Self-assembling peptides for biomedical applications: IR and Raman spectroscopies for the study of secondary structure. *Proteomics Res. J.* 2 (3), 231.

Eleswarapu, S. V., Responte, D. J., and Athanasiou, K. A. (2011). Tensile properties, collagen content, and crosslinks in connective tissues of the immature knee joint. *PLoS One* 6 (10), e26178. doi:10.1371/journal.pone.0026178

Esposito, C., and Caputo, I. (2005). Mammalian transglutaminases. Identification of substrates as a key to physiological function and physiopathological relevance. *FEBS J.* 272 (3), 615–631. doi:10.1111/j.1742-4658.2004.04476.x

Farris, S., Song, J., and Huang, Q. (2010). Alternative reaction mechanism for the cross-linking of gelatin with glutaraldehyde. *J. Agric. Food Chem.* 58 (2), 998–1003. doi:10.1021/jf9031603

Fong, H., Chun, I., and Reneker, D. H. (1999). Beaded nanofibers formed during electrospinning. *Polymer* 40, 4585–4592. doi:10.1016/s0032-3861(99)00068-3

Frantz, C., Stewart, K. M., and Weaver, V. M. (2010). The extracellular matrix at a glance. *J. Cell Sci.* 123 (24), 4195–4200. doi:10.1242/jcs.023820

Fratzl, P. (2008). *Collagen: Structure and mechanics, an introduction*. Collagen: Springer, 1–13.

Fridrikh, S. V., Yu, J. H., Brenner, M. P., and Rutledge, G. C. (2003). Controlling the fiber diameter during electrospinning. *Phys. Rev. Lett.* 90 (14), 144502. doi:10.1103/physrevlett.90.144502

Friedman, S. L. (2008). Mechanisms of hepatic fibrogenesis. *Gastroenterology* 134 (6), 1655–1669. doi:10.1053/j.gastro.2008.03.003

Gerardo, H., Lima, A., Carvalho, J., Ramos, J. R., Couceiro, S., Travasso, R. D., et al. (2019). Soft culture substrates favor stem-like cellular phenotype and facilitate reprogramming of human mesenchymal stem/stromal cells (hMSCs) through mechanotransduction. *Sci. Rep.* 9 (1), 9086. doi:10.1038/s41598-019-45352-3

Ginestra, P., Ceretti, E., and Fiorentino, A. (2016). Electrospinning of poly-caprolactone for scaffold manufacturing: experimental investigation on the process parameters influence. *Procedia CIRP* 49, 8–13. doi:10.1016/j.procir.2015.07.020

Gómez-guillœn, M., and Montero, P. (2001). Extraction of gelatin from megrim (Lepidorhombus boscii) skins with several organic acids. *J. Food Sci.* 66 (2), 213–216. doi:10.1111/j.1365-2621.2001.tb11319.x

Graham, J. S., Vomund, A. N., Phillips, C. L., and Grandbois, M. (2004). Structural changes in human type I collagen fibrils investigated by force spectroscopy. *Exp. Cell Res.* 299 (2), 335–342. doi:10.1016/j.yexcr.2004.05.022

Guimarães, C. F., Gasperini, L., Marques, A. P., and Reis, R. L. (2020). The stiffness of living tissues and its implications for tissue engineering. *Nat. Rev. Mat.* 5, 351–370. doi:10.1038/s41578-019-0169-1

Haider, A., Haider, S., and Kang, I-K. (2018). A comprehensive review summarizing the effect of electrospinning parameters and potential applications of nanofibers in biomedical and biotechnology. *Arabian J. Chem.* 11 (8), 1165–1188. doi:10.1016/j.arabjc.2015.11.015

Harrington, W. F., and Von Hippel, P. H. (1962). The structure of collagen and gelatin. *Adv. Protein Chem.* 16, 1–138. doi:10.1016/s0065-3233(08)60028-5

Huang, Z-M., Zhang, Y., Ramakrishna, S., and Lim, C. (2004). Electrospinning and mechanical characterization of gelatin nanofibers. *Polymer* 45 (15), 5361–5368. doi:10.1016/j.polymer.2004.04.005

Hynes, R. O., and Naba, A. (2012). Overview of the matrisome--an inventory of extracellular matrix constituents and functions. *Cold Spring Harb. Perspect. Biol.* 4 (1), a004903. doi:10.1101/cshperspect.a004903

Impurities (2018). Impurities: Guideline for residual solvents Q3C (R7). Contract No: 4.

Jiang, J., Nicoll, S. B., and Lu, H. H. (2005). Co-culture of osteoblasts and chondrocytes modulates cellular differentiation *in vitro*. *Biochem. Biophys. Res. Commun.* 338 (2), 762–770. doi:10.1016/j.bbrc.2005.10.025

Jiao, T., Clifton, R. J., Converse, G. L., and Hopkins, R. A. (2012). Measurements of the effects of decellularization on viscoelastic properties of tissues in ovine, baboon, and human heart valves. *Tissue Eng. Part A* 18 (3-4), 423–431. doi:10.1089/ten.tea.2010.0677

Jose, M. V., Thomas, V., Dean, D. R., and Nyairo, E. (2009). Fabrication and characterization of aligned nanofibrous PLGA/Collagen blends as bone tissue scaffolds. *Polymer* 50 (15), 3778–3785. doi:10.1016/j.polymer.2009.05.035

Ju, Y. M., San Choi, J., Atala, A., Yoo, J. J., and Lee, S. J. (2010). Bilayered scaffold for engineering cellularized blood vessels. *Biomaterials* 31 (15), 4313–4321. doi:10.1016/j.biomaterials.2010.02.002

Karsdal, M. (2019). *Biochemistry of collagens, laminins and elastin: Structure, function and biomarkers*. Academic Press.

Kinney, J., Marshall, S., and Marshall, G. (2003). The mechanical properties of human dentin: a critical review and re-evaluation of the dental literature. *Crit. Rev. Oral Biol. Med.* 14 (1), 13–29. doi:10.1177/154411130301400103

Kleinman, H. K., McGarvey, M. L., Liotta, L. A., Robey, P. G., Tryggvason, K., Martin, G. R., et al. (1982). Isolation and characterization of type IV procollagen, laminin, and heparan sulfate proteoglycan from the EHS sarcoma. *Biochemistry* 21 (24), 6188–6193. doi:10.1021/bi00267a025

Kriegel, C., Kit, K., McClements, D. J., and Weiss, J. (2009). Electrospinning of chitosan–poly (ethylene oxide) blend nanofibers in the presence of micellar surfactant solutions. *Polymer* 50 (1), 189–200. doi:10.1016/j.polymer.2008.09.041

Lee, N. M., Erisken, C., Iskratsch, T., Sheetz, M., Levine, W. N., Lu, H. H., et al. (2017). Polymer fiber-based models of connective tissue repair and healing. *Biomaterials* 112, 303–312. doi:10.1016/j.biomaterials.2016.10.013

Lerman, M. J., Lembong, J., Muramoto, S., Gillen, G., and Fisher, J. P. (2018). The evolution of polystyrene as a cell culture material. *Tissue Eng. Part B Rev.* 24 (5), 359–372. doi:10.1089/ten.teb.2018.0056

Li, H., Wang, M., Williams, G. R., Wu, J., Sun, X., Lv, Y., et al. (2016). Electrospun gelatin nanofibers loaded with vitamins A and E as antibacterial wound dressing materials. *RSC Adv.* 6 (55), 50267–50277. doi:10.1039/c6ra05092a

Li, W. J., Laurencin, C. T., Caterson, E. J., Tuan, R. S., and Ko, F. K. (2002). Electrospun nanofibrous structure: a novel scaffold for tissue engineering. *J. Biomed. Mat. Res.* 60 (4), 613–621. doi:10.1002/jbm.10167

Lorenzo, A. C., and Caffarena, E. R. (2005). Elastic properties, young's modulus determination and structural stability of the tropocollagen molecule: a computational study by steered molecular dynamics. *J. Biomech.* 38 (7), 1527–1533. doi:10.1016/j.jbiomech.2004.07.011

Lu, H. H., Cooper, J. A., Jr., Manuel, S., Freeman, J. W., Attawia, M. A., Ko, F. K., et al. (2005). Anterior cruciate ligament regeneration using braided biodegradable scaffolds: *In vitro* optimization studies. *Biomaterials* 26 (23), 4805–4816. doi:10.1016/j.biomaterials.2004.11.050

Lu, H. H., Kofron, M. D., El Amin, S. F., Attawia, M. A., and Laurencin, C. T. (2003). *In vitro* bone formation using muscle-derived cells: a new paradigm for bone tissue engineering using polymer-bone morphogenetic protein matrices. *Biochem. Biophys. Res. Commun.* 305 (4), 882–889. doi:10.1016/s0006-291x(03)00858-1

Lutolf, M. P., and Hubbell, J. A. (2005). Synthetic biomaterials as instructive extracellular microenvironments for morphogenesis in tissue engineering. *Nat. Biotechnol.* 23 (1), 47–55. doi:10.1038/nbt1055

Ma, Z., Kotaki, M., Inai, R., and Ramakrishna, S. (2005). Potential of nanofiber matrix as tissue-engineering scaffolds. *Tissue Eng.* 11 (1-2), 101–109. doi:10.1089/ten.2005.11.101

Moffat, K. L., Kwei, A. S., Spalazzi, J. P., Doty, S. B., Levine, W. N., Lu, H. H., et al. (2009). Novel nanofiber-based scaffold for rotator cuff repair and augmentation. *Tissue Eng. Part A* 15 (1), 115–126. doi:10.1089/ten.tea.2008.0014

Mosher, C. Z., Brudnicki, P. A., Gong, Z., Childs, H. R., Lee, S. W., Antrobus, R. M., et al. (2021). Green electrospinning solvents for biomaterials and biofabrication. *Biofabrication* 13 (3). doi:10.1088/1758-5090/ac0964

Murphy, W. L., and Mooney, D. J. (2002). Bioinspired growth of crystalline carbonate apatite on biodegradable polymer substrata. *J. Am. Chem. Soc.* 124 (9), 1910–1917. doi:10.1021/ja012433n

Muschler, J., and Streuli, C. H. (2010). Cell–matrix interactions in mammary gland development and breast cancer. *Cold Spring Harb. Perspect. Biol.* 2 (10), a003202. doi:10.1101/cshperspect.a003202

Muyonga, J., Cole, C., and Duodu, K. (2004). Fourier transform infrared (FTIR) spectroscopic study of acid soluble collagen and gelatin from skins and bones of young and adult Nile perch (Lates niloticus). *Food Chem. x.* 86 (3), 325–332. doi:10.1016/j.foodchem.2003.09.038

Nagai, T., Suzuki, N., Tanoue, Y., Kai, N., and Nagashima, T. (2010). Characterization of acid-soluble collagen from skins of surf smelt (*Hypomesus pretiosus* japonicus Brevoort). *Food Nutr. Sci.* 1 (02), 59–66. doi:10.4236/fns.2010.12010

Nandakumar, A., Yang, L., Habibovic, P., and van Blitterswijk, C. (2010). Calcium phosphate coated electrospun fiber matrices as scaffolds for bone tissue engineering. *Langmuir* 26 (10), 7380–7387. doi:10.1021/la904406b

Nezarati, R. M., Eifert, M. B., and Cosgriff-Hernandez, E. (2013). Effects of humidity and solution viscosity on electrospun fiber morphology. *Tissue Eng. Part C. Methods* 19 (10), 810–819. doi:10.1089/ten.tec.2012.0671

Nöth, U., Schupp, K., Heymer, A., Kall, S., Jakob, F., Schütze, N., et al. (2005). Anterior cruciate ligament constructs fabricated from human mesenchymal stem cells in a collagen type I hydrogel. *Cytotherapy* 7 (5), 447–455. doi:10.1080/14653240500319093

Orimo, H. (2010). The mechanism of mineralization and the role of alkaline phosphatase in health and disease. *J. Nippon. Med. Sch.* 77 (1), 4–12. doi:10.1272/jnms.77.4

Oryan, A., Jalili, M., Kamali, A., and Nikahval, B. (2018). The concurrent use of probiotic microorganism and collagen hydrogel/scaffold enhances burn wound healing: An *in vivo* evaluation. *Burns* 44 (7), 1775–1786. doi:10.1016/j.burns.2018.05.016

Paddock, S. (2002). Confocal reflection microscopy: the" other" confocal mode. *Biotechniques* 32 (2274), 274–276. 8.

Parvizi, J. (2010). *High yield orthopaedics: Collagen*. Elsevier Health Sciences.

Persano, L., Camposeo, A., Tekmen, C., and Pisignano, D. (2013). Industrial upscaling of electrospinning and applications of polymer nanofibers: a review. *Macromol. Mat. Eng.* 298 (5), 504–520. doi:10.1002/mame.201200290

Pickup, M. W., Mouw, J. K., and Weaver, V. M. (2014). The extracellular matrix modulates the hallmarks of cancer. *EMBO Rep.* 15 (12), 1243–1253. doi:10.15252/embr.201439246

Poli, G., and Parola, M. (1997). Oxidative damage and fibrogenesis. *Free Radic. Biol. Med.* 22 (1-2), 287–305. doi:10.1016/s0891-5849(96)00327-9

Qu, D., Zhu, J. P., Childs, H. R., and Lu, H. H. (2019). Nanofiber-based transforming growth factor-β3 release induces fibrochondrogenic differentiation of stem cells. *Acta Biomater.* 93, 111–122. doi:10.1016/j.actbio.2019.03.019

Rao, V. V., Vu, M. K., Ma, H., Killaars, A. R., and Anseth, K. S. (2019). Rescuing mesenchymal stem cell regenerative properties on hydrogel substrates post serial expansion. *Bioeng. Transl. Med.* 4 (1), 51–60. doi:10.1002/btm2.10104

Ratanavaraporn, J., Damrongsakkul, S., Sanchavanakit, N., Banaprasert, T., and Kanokpanont, S. (2006). Comparison of gelatin and collagen scaffolds for fibroblast cell culture. *J. Metals, Mater. Minerals* 16 (1).

Reddy, G. K., and Enwemeka, C. S. (1996). A simplified method for the analysis of hydroxyproline in biological tissues. *Clin. Biochem.* 29 (3), 225–229. doi:10.1016/0009-9120(96)00003-6

Reneker, D. H., and Chun, I. (1996). Nanometre diameter fibres of polymer, produced by electrospinning. *Nanotechnology* 7, 216–223. doi:10.1088/0957-4484/7/3/009

Reneker, D. H., Yarin, A. L., Fong, H., and Koombhongse, S. (2000). Bending instability of electrically charged liquid jets of polymer solutions in electrospinning. *J. Appl. Phys.* 87 (9), 4531–4547. doi:10.1063/1.373532

Ricard-Blum, S. (2011). The collagen family. *Cold Spring Harb. Perspect. Biol.* 3 (1), a004978. doi:10.1101/cshperspect.a004978

Sell, S., Barnes, C., Smith, M., McClure, M., Madurantakam, P., Grant, J., et al. (2007). Extracellular matrix regenerated: tissue engineering via electrospun biomimetic nanofibers. *Polym. Int.* 56 (11), 1349–1360. doi:10.1002/pi.2344

Shen, Z. L., Kahn, H., Ballarini, R., and Eppell, S. J. (2011). Viscoelastic properties of isolated collagen fibrils. *Biophys. J.* 100 (12), 3008–3015. doi:10.1016/j.bpj.2011.04.052

Shoulders, M. D., and Raines, R. T. (2009). Collagen structure and stability. *Annu. Rev. Biochem.* 78, 929–958. doi:10.1146/annurev.biochem.77.032207.120833

Siegel, R. C., Pinnell, S. R., and Martin, G. R. (1970). Cross-linking of collagen and elastin. Properties of lysyl oxidase. *Biochemistry* 9 (23), 4486–4492. doi:10.1021/bi00825a004

Subramony, S. D., Dargis, B. R., Castillo, M., Azeloglu, E. U., Tracey, M. S., Su, A., et al. (2013). The guidance of stem cell differentiation by substrate alignment and mechanical stimulation. *Biomaterials* 34 (8), 1942–1953. doi:10.1016/j.biomaterials.2012.11.012

Subramony, S. D., Su, A., Yeager, K., and Lu, H. H. (2014). Combined effects of chemical priming and mechanical stimulation on mesenchymal stem cell differentiation on nanofiber scaffolds. *J. Biomech.* 47 (9), 2189–2196. doi:10.1016/j.jbiomech.2013.10.016

Tatullo, M., Marrelli, M., Falisi, G., Rastelli, C., Palmieri, F., Gargari, M., et al. (2016). Mechanical influence of tissue culture plates and extracellular matrix on mesenchymal stem cell behavior: A topical review. *Int. J. Immunopathol. Pharmacol.* 29 (1), 3–8. doi:10.1177/0394632015617951

Theocharis, A. D., Skandalis, S. S., Gialeli, C., and Karamanos, N. K. (2016). Extracellular matrix structure. *Adv. Drug Deliv. Rev.* 97, 4–27. doi:10.1016/j.addr.2015.11.001

Uyar, T., and Besenbacher, F. (2008). Electrospinning of uniform polystyrene fibers: The effect of solvent conductivity. *Polymer* 49 (24), 5336–5343. doi:10.1016/j.polymer.2008.09.025

Vanderby, R., and Provenzano, P. P. (2003). Collagen in connective tissue: from tendon to bone. *J. Biomech.* 36 (10), 1523–1527. doi:10.1016/s0021-9290(03)00132-5

Vukicevic, S., Kleinman, H. K., Luyten, F. P., Roberts, A. B., Roche, N. S., Reddi, A. H., et al. (1992). Identification of multiple active growth factors in basement membrane Matrigel suggests caution in interpretation of cellular activity related to extracellular matrix components. *Exp. Cell Res.* 202 (1), 1–8. doi:10.1016/0014-4827(92)90397-q

Xu, M., Wei, L., Xiao, Y., Bi, H., Yang, H., Du, Y., et al. (2017). Molecular structural properties of extracted gelatin from Yak skin as analysed based on molecular weight. *Int. J. Food Prop.* 20 (1), S543–S555. doi:10.1080/10942912.2017.1300813

Xu, S., Gu, M., Wu, K., and Li, G. (2019). Unraveling the role of hydroxyproline in maintaining the thermal stability of the collagen triple helix structure using simulation. *J. Phys. Chem. B* 123 (36), 7754–7763. doi:10.1021/acs.jpcb.9b05006

Xue, J., Wu, T., Dai, Y., and Xia, Y. (2019). Electrospinning and electrospun nanofibers: Methods, materials, and applications. *Chem. Rev.* 119 (8), 5298–5415. doi:10.1021/acs.chemrev.8b00593

Yamauchi, M., Woodley, D. T., and Mechanic, G. L. (1988). Aging and cross-linking of skin collagen. *Biochem. Biophys. Res. Commun.* 152 (2), 898–903. doi:10.1016/s0006-291x(88)80124-4

Yang, Y-l., and Kaufman, L. J. (2009). Rheology and confocal reflectance microscopy as Probes of mechanical properties and structure during collagen and collagen/hyaluronan self-assembly. *Biophys. J.* 96 (4), 1566–1585. doi:10.1016/j.bpj.2008.10.063

Zeiger, A. S., Hinton, B., and Van Vliet, K. J. (2013). Why the dish makes a difference: quantitative comparison of polystyrene culture surfaces. *Acta Biomater.* 9 (7), 7354–7361. doi:10.1016/j.actbio.2013.02.035

Zeng, J., Haoqing, H., Schaper, A., Wendorff, J. H., and Greiner, A. (2003). Poly-L-lactide nanofibers by electrospinning–Influence of solution viscosity and electrical conductivity on fiber diameter and fiber morphology. *e-Polymers* 3 (1). doi:10.1515/epoly.2003.3.1.102

Zhang, C., Yuan, X., Wu, L., Han, Y., and Sheng, J. (2005). Study on morphology of electrospun poly (vinyl alcohol) mats. *Eur. Polym. J.* 41 (3), 423–432. doi:10.1016/j.eurpolymj.2004.10.027

Zhang, Y., Ouyang, H., Lim, C. T., Ramakrishna, S., and Huang, Z. M. (2005). Electrospinning of gelatin fibers and gelatin/PCL composite fibrous scaffolds. *J. Biomed. Mat. Res.* 72 (1), 156–165. doi:10.1002/jbm.b.30128

Zhang, Y., Su, B., Venugopal, J., Ramakrishna, S., and Lim, C. (2007). Biomimetic and bioactive nanofibrous scaffolds from electrospun composite nanofibers. *Int. J. Nanomedicine* 2 (4), 623–638.

Zhang, Y. Z., Venugopal, J., Huang, Z. M., Lim, C. T., and Ramakrishna, S. (2006). Crosslinking of the electrospun gelatin nanofibers. *Polymer* 47 (8), 2911–2917. doi:10.1016/j.polymer.2006.02.046

frontiers | Frontiers in Bioengineering and Biotechnology

TYPE Original Research
PUBLISHED 18 October 2022
DOI 10.3389/fbioe.2022.998774

Check for updates

OPEN ACCESS

EDITED BY
Mark Buckley,
University of Rochester, United States

REVIEWED BY
Anne Bernhardt,
Technical University Dresden, Germany
Girish Pattappa,
University Medical Center Regensburg, Germany

*CORRESPONDENCE
Martin J. Stoddart,
martin.stoddart@aofoundation.org

SPECIALTY SECTION
This article was submitted to Tissue Engineering and Regenerative Medicine, a section of the journal Frontiers in Bioengineering and Biotechnology

RECEIVED 20 July 2022
ACCEPTED 29 September 2022
PUBLISHED 18 October 2022

CITATION
Monaco G, Qawasmi F, El Haj AJ, Forsyth NR and Stoddart MJ (2022), Chondrogenic differentiation of human bone marrow MSCs in osteochondral implants under kinematic mechanical load is dependent on the underlying osteo component.
Front. Bioeng. Biotechnol. 10:998774.
doi: 10.3389/fbioe.2022.998774

COPYRIGHT
© 2022 Monaco, Qawasmi, El Haj, Forsyth and Stoddart. This is an open-access article distributed under the terms of the Creative Commons Attribution License (CC BY). The use, distribution or reproduction in other forums is permitted, provided the original author(s) and the copyright owner(s) are credited and that the original publication in this journal is cited, in accordance with accepted academic practice. No use, distribution or reproduction is permitted which does not comply with these terms.

Chondrogenic differentiation of human bone marrow MSCs in osteochondral implants under kinematic mechanical load is dependent on the underlying osteo component

Graziana Monaco[1,2], Feras Qawasmi[1,3], Alicia J. El Haj[4], Nicolas R. Forsyth[2] and Martin J. Stoddart[1,2]*

[1]AO Research Institute Davos, Davos, Switzerland, [2]Guy Hilton Research Centre, School of Pharmacy and Bioengineering, Keele University, Stoke-on-Trent, United Kingdom, [3]Hadassah Medical Center, Jerusalem, Israel, [4]Healthcare Technology Institute, Institute of Translational Medicine, University of Birmingham, Birmingham, United Kingdom

Chondrogenic models utilizing human mesenchymal stromal cells (hMSCs) are often simplistic, with a single cell type and the absence of mechanical stimulation. Considering the articulating joint as an organ it would be beneficial to include more complex stimulation. Within this study we applied clinically relevant kinematic load to biphasic constructs. In each case, the upper layer consisted of fibrin embedded hMSCs retained within an elastomeric polyurethane (PU) scaffold. These were randomly assigned to five base scaffolds, a cell-free fibrin PU base, viable bone, decellularized bone, 3D printed calcium phosphate or clinically used cement. This allowed the study of cross talk between viable bone and chondrogenically differentiating MSCs, while controlling for the change in stiffness of the base material. Data obtained showed that the bulk stiffness of the construct was not the defining factor in the response obtained, with viable and decellularized bone producing similar results to the softer PU base. However, the stiff synthetic materials led to reduced chondrogenesis and increased calcification in the upper MSC seeded layer. This demonstrates that the underlying base material must be considered when driving chondrogenesis of human cells using a clinically relevant loading protocol. It also indicates that the material used for bony reconstruction of osteochondral defects may influence subsequent chondrogenic potential.

KEYWORDS

osteochondral, chondrogenesis, crosstalk, tissue engineering, scaffold, signalling, mechanobiology

1 Introduction

Articular cartilage overlays the articulating surfaces of bones providing a low friction gliding surface to allow free movement and acts to protect the underlying bone, preventing damage from the high forces generated within joints (Sophia Fox et al., 2009). Cartilage defects are increasingly common and can be divided into three major classes: partial thickness defects, full thickness defects and osteochondral defects depending on the depth of the damage (Nukavarapu and Dorcemus, 2013). Cartilage defects present a unique clinical challenge due to their poor self-healing capacity, largely due to its avascular nature that impedes access of blood and bone marrow mesenchymal stem/stromal cells (MSCs) from the surrounding environment (Hunziker and Rosenberg, 1996; Buckwalter and Mankin, 1998). The crosstalk between the cartilage, underlying bone and any regenerating tissue will play a role on the resultant *de novo* tissue (Gomoll et al., 2010; Madry, 2010). Yet *in vitro* model systems generally lack this critical interaction, furthermore they also typically lack mechanical stimulation, a key aspect of cartilage biology. In many clinical trials of symptomatic cartilage defects, a modified autologous chondrocyte implantation (ACI) technique has been used with success by replacing the autologous chondrocytes with hMSCs seeded into collagen scaffolds (Wakitani et al., 2002; Wakitani et al., 2004; Kuroda et al., 2007). The substitution of chondrocytes with MSCs is also increasingly common as bone marrow aspirate harvest is relatively simple to obtain in comparison to cartilage biopsy required for chondrocyte expansion. MSCs as an alternative cell source for cartilage repair are relatively easy to isolate from a variety of tissues and represent an emerging ATMP treatment (Schneider et al., 2010; Bieback et al., 2011). However, in general current surgical treatments do not ensure consistent regeneration of hyaline cartilage, leading predominantly to fibrous tissue and hence remain controversial (Knutsen et al., 2007; Armiento et al., 2018). Therefore, there is a critical need to better study and understand healing mechanisms to achieve more effective therapies for cartilage regeneration through the development of new tissue engineering approaches. For this, to be successful, improved *in vitro* culture models will be required.

One of the major issues associated with *in vitro* MSCs chondrogenesis for cartilage therapy is their progression towards terminal differentiation and hypertrophy (Pelttari et al., 2006; Mueller and Tuan, 2008). It has been speculated that the rapid progression of MSCs towards hypertrophy during chondrogenic induction *in vitro* by using pellet culture, is caused by the loss of the important spatial and temporal signalling networks that exist for *in vivo* chondrogenically differentiating populations of cells (Pelttari et al., 2006). Accordingly, the interaction between cartilage and the subchondral bone is increasingly a focus of preclinical and clinical research (Gomoll et al., 2010; Madry et al., 2016). As such, the crosstalk and the organization of the cells within the tissue is essential for the tissue's normal development, homeostasis and repair. The ability to manage and reproduce the complex osteochondral unit from a cell point of view is still challenging but represents one of the key factors for a successful tissue regeneration. Since most tissues in the body, including osteochondral tissue, consist of more than one cell type, the development of a suitable co-culture system becomes an important requirement to finally achieve a functional cartilage regeneration both for clinical needs and for research purposes. Attempts have been made to establish osteochondral models.

Therefore, the aim of this study was the development of a more complex hybrid *in vitro—ex vivo* osteochondral model composed of an *ex vivo* bone explant cylinder underlying the *in vitro de novo* cartilage zone, represented by a fibrin poly (ester-urethane) (PU) construct asymmetrically seeded with hMSCs (Gardner et al., 2017a). This study primarily aimed to investigate the effect of bone and its putative biological and mechanical signals on the chondrogenic differentiation of human bone marrow MSC residing in the upper PU: fibrin scaffold. In parallel, the clinically relevant materials calcium phosphate and bone cement were used as a stiff osteochondral base in place of bone. In addition, the effect of joint-simulating mechanical load has been demonstrated to be beneficial for hMSC chondrogenesis (Li et al., 2010a). Therefore, the effect of mechanical loading was assessed, concomitantly with the presence of the bone and with its alternatives bases, on hMSC chondrogenesis seeded within the upper PU:fibrin scaffold. The aim of this study was to investigate if *ex vivo* bone affects the chondrogenic differentiation of hMSCs within a bilayer scaffold. We hypothesized that soluble signals from live bone would change the phenotype of the MSCs differentiating in the upper layer. Furthermore, we hypothesized that changing the 2 mm base material to a rigid material would modify the response to load compared to the soft PU base.

2 Materials and methods

2.1 Donor information

Human bone marrow aspirate was obtained with full ethical approval (KEK-ZH-NR: 2010-0444/0) and MSCs were isolated using standard methods (Gardner et al., 2015). See Table 1 for donor details. In brief, after Ficoll gradient separation mononuclear cells were seeded at a density of 50,000 cells/cm2 into culture flasks and left to attach for 96 h in αMEM supplemented with 10% FBS, 5 ng/ml basic fibroblast growth factor (bFGF) (Peprotech, Rocky Hill, United States) and 100 U/ml penicillin and 100 µg/ml streptomycin (Gibco, Carlsbad, United States). The medium was changed after 4 days and the attached cells were allowed to grow to 80% confluence before passaging. Expanded cells were seeded at density of

TABLE 1 Human sequences of self-designed oligonucleotide primers and probes used for real-time PCR analysis.

Donor	Donor site	Age (y)	Gender
Donor 1	vertebra (TH12/L2)	66	Female
Donor 2	Vertebra	22	Male
Donor 3	vertebra (TH7/9)	69	Male

3,000 cells/cm2 into fresh culture flasks and cultured in complete expansion medium.

2.2 Viable bone cylinder preparation from bovine knee joints

Bovine knee joints were collected from 6-month-old calves obtained from a local abattoir (Metzgerei Angst AG, Zurich, CH) within 48 h of slaughter. Drilling from the cartilage femur surface was performed by using the Bosch PBD 40 compact drilling machine supported by saline irrigation to constantly keep a hydrated environment during drilling. Osteochondral explants cylinders of 8 mm diameters were produced using a diamond coated custom-made trephine drill (Peertools AG, Ftan, CH). The cylindrical explants were washed with 1000 U/mL penicillin and 1,000 µg/ml streptomycin for 15 min. Then, the explants were further cut with an Exakt 300 band circular saw (Exakt Apparatebau GmbH & Co.KG, DE) to achieve cancellous bone cylinders with a final thickness of 2 mm and a diameter of 8 mm. These cylinders were soaked for 15 min in 1,000 U/ml penicillin and 1,000 µg/ml streptomycin and then for other 15 min in 100 U/ml penicillin and 100 µg/ml streptomycin. Cancellous bone cylinders were then transferred into 24 well plates and cultured in Dulbecco's modified eagle medium (DMEM-HG, 4.5 g/L-glucose; Gibco) supplemented with 10% fetal bovine serum (FBS, Gibco) and 100 U/ml penicillin and 100 µg/ml streptomycin, at 37°C and 5% CO_2 until the assembling with the upper MSC seeded PU-scaffold.

2.3 Decellularization of bone cylinders

Bone cylinders were exposed to five freezing-thawing cycles alternating between liquid nitrogen for five minutes and a 56°C water bath for five minutes (Jahn et al., 2010).

2.4 Seeding of fibrin-poly (ester-urethane) scaffolds

Elastomeric polyurethane (PU) scaffolds (2 mm height × 8 mm diameter) were created by salt leech synthesis. Scaffolds were asymmetrically seeded to better represent the superficial zone found in articular cartilage (Gardner et al., 2017a). Monolayer expanded MSCs (3 × 106 cells per scaffold) were resuspended in 37.5 µl of 33 mg/ml fibrinogen (Baxter, Vienna, Austria). The fibrin cell mixture was then rapidly mixed in the presence of the PU scaffold with an equal volume of 1 unit/ml thrombin (Baxter, Vienna, Austria). After 1 h at 37°C a further 500,000 cells were added to the surface of the scaffold and left to adhere. Scaffolds were cultured in a medium consisting of: Dulbecco's modified Eagle medium (4.5 g/L glucose (Gibco, Carlsbad, United States), 0.11 g/L sodium pyruvate, 50 µg/ml L-ascorbic acid 2-phosphate sesquimagnesium salt hydrate, 1 × 10-7 M dexamethasone, ITS + premix containing insulin 6.25 µg/ml, transferrin 6.25 µg/ml and selenious acid 6.25 ng/ml, bovine serum albumin 1.25 mg/ml and linoleic acid 5.35 µg/ml (Corning, Bedford, United States), 1% (v/v) Non-essential amino acids (Gibco, Carlsbad, United States), 100 U/mL penicillin and 100 µg/ml streptomycin (Gibco, Carlsbad, United States) and 5 µM 6-aminocaproic acid to reduce fibrin degradation (Kupcsik et al., 2009).

2.5 Preparation of 3D printed ceramic base

Osteoink calcium phosphate cement ink was use to 3D print the ceramic base as recommended by the manufacturer (Osteoink™, RegenHU, Villaz-St-Pierre, Switzerland). The ink is similar to the CE-marked ink developed by Innotere GmbH (Germany) and is mainly composed of α-tricalcium phosphate (α-TCP) with smaller amounts of hydroxyapatite, monetite, calcite and β-TCP, and a carrier liquid composed of triglycerides and surfactants (Heinemann et al., 2013). Setting of the cement occurs *via* α-TCP hydrolysis.

2.6 Preparation of the cement base

Acrylic casting resin SCS-Beracryl D-28 (Suter Kunststoffe AG, Fraubrunnen, Switzerland) was used to prepare the solid cement base as per manufactures instructions. In brief, the resin acrylic SCS-Beracryl D-28 and hardener was mixed in approximately equal weight proportions and mixed well. After casting, the samples were left to harden for 1 h.

2.7 Preparation of osteochondral combinations

hMSC seeded scaffolds were placed over the relevant base material and held together using a PU ring produced in the same manner as the upper PU scaffold. For an overview of the experimental Design, see Figure 1.

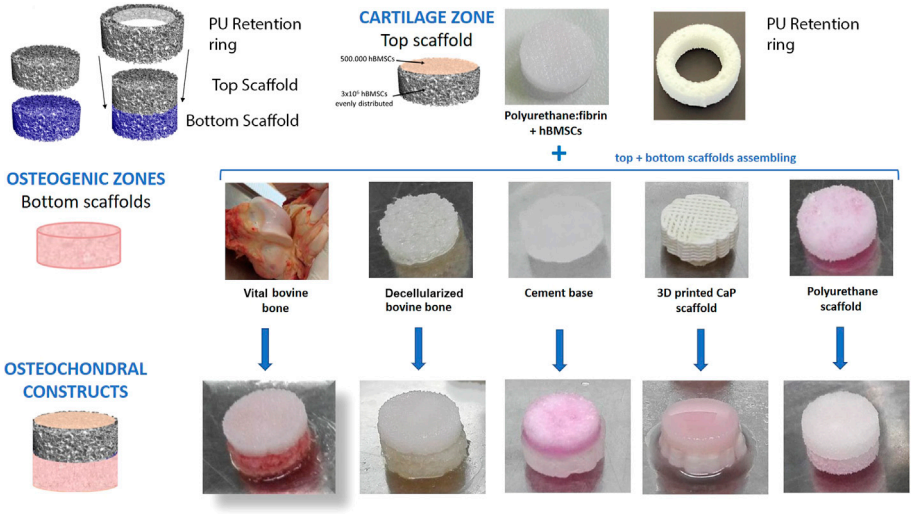

FIGURE 1
Overview of experimental design.

2.8 Application of multi-axial mechanical load

Osteochondral constructs were loaded using a custom-made multiaxial load bioreactor, designed to apply both dynamic shear and compressive loading, based on a tribological system analysis of natural articulating joints (Wimmer et al., 2004). Loaded scaffolds were exposed to 10% compression superimposed on top of a 10% pre-strain and shear loading (± 25°C) at 1 Hz for one hour a day five times a week over 7 and 28 days. 10% compression and 25°C rotation were chosen based on results from previous work (Li et al., 2010a). Load cells, located underneath the sample holders, were used to detect contact between the ceramic ball and scaffold in order apply 10% pre-compression before the initiation of 10% cyclic compression. Loading was carried out in an incubator at 37°C, 5% CO_2 and 80% humidity. Control scaffolds were kept in free-swelling culture conditions and harvested in parallel at the same timepoints of the loaded samples. The culture media was changed three times per week during the loading period.

2.9 Real Time PCR

RNA was isolated using TRI reagent and cDNA synthesized using Superscript VILO cDNA synthesis kit (Thermo Fisher) as per manufacturers recommendations. Either custom primers (Microsynth, Balgach, Switzerland) or Gene Expression Assays (Applied Biosystems, Carlsbad, United States) (Table 2) were used. Real Time PCR was performed using TaqMan® Master Mix and an Applied Biosystems QuantStudio 6 Flex Real-Time PCR System (Applied Biosystems, Carlsbad, United States. Data was analysed using the 2-ΔΔCt method to day 0 with human RPLP0 as the endogenous control.

2.10 Biochemical analysis

For biochemical analysis, one half scaffold was digested in 0.5 mg/ml Proteinase K (Roche, Basel, Switzerland) at 56°C for 16 h. Proteinase K (PK) was then deactivated with a 10 min incubation at 96°C, and the samples stored at -20°C for analysis. Total amount of glycosaminoglycans (GAGs) produced by cells, measured in both collected media and PK digests, was determined using the 1.9-dimethyl methylene blue (DMMB) assay and normalised to the DNA content of each PK digest measured using Hoechst 33,258 dye (Polysciences Inc., Warrington, United States).

2.11 Bone sectioning and viability assessment of osteocytes using lactate dehydrogenase activity staining

Bone cylinders were cut by using Leica annular saw (Leica AG, Glattbrugg,CH) to achieve sections of 250 µm–300 µm. Lactate dehydrogenase (LDH) staining solution (5% polypeptide base solution, 60 mM lactic acid (final conc. 5.4 mg/ml), 17.5 mg Nicotinamide adenine dinucleotide (NAD final conc. 1.75 mg/ml) was prepared (Jahn and Stoddart, 2011). The pH was brought to 8.00 and 30 mg Nitroblue Tetrazolium

TABLE 2 Details of source material from each donor used.

Gene	Primer forward (5′-3′)	Primer reverse (5′-3′)	Probe (5′ FAM- 3′ TAMRA)
COL2A1	5′-GGC AAT AGC AGG TTC ACG TAC A-3′	5′-GAT AAC AGT CTT GCC CCA CTT ACC-3′	5′-CCT GAA GGA TGG CTG CAC GAA ACA TAC-3′
COL10A1	5′-ACG CTG AAC GAT ACC AAA TG-3′	5′-TGC TAT ACC TTT ACT CTT TAT GGT GTA-3′	5′-ACT ACC CAA CAC CAA GAC ACA GTT CTT CAT TCC-3′
ACAN	5′-AGT CCT CAA GCC TCC TGT ACT CA-3′	5′-CGG GAA GTG GCG GTA ACA-3′	5′-CCG GAA TGG AAA CGT GAA TCA GAA TCA ACT-3′
RunX2	5′-AGC AAG GTT CAA CGA TCT GAG AT-3′	5′-TTT GTG AAG ACG GTT ATG GTC AA-3′	5′-TGA AAC TCT TGC CTC GTC CAC TCC G-3′
OC	5′-AAG AGA CCC AGG CGC TAC CT-3′	5′-AAC TCG TCA CAG TCC GGA TTG-3′	5′-ATG GCT GGG AGC CCC AGT CCC-3′
RPLP0	5′-TGG GCA AGA ACA CCA TGA TG-3′	5′-CGG ATA TGA GGC AGC AGT TTC-3′	5′-AGG GCA CCT GGA AAA CAA CCC AGC-3′
COMP	Applied Biosystems TaqMan Gene Expression Assay Hs00164359_m1		
PRG 4	Applied Biosystems TaqMan Gene Expression Assay Hs00981633_m1		
Sox9	Applied Biosystems TaqMan Gene Expression Assay Hs00165814_m1		
ALP	Applied Biosystems TaqMan Gene Expression Assay Hs00758162_m1		

RPLP0, ribosomal protein large P0 housekeeping gene; COL2A1, collagen type 2; COL10A1, collagen type 10; ACAN, aggrecan; RunX2, runt-related transcription factor 2; OC, osteocalcin; COMP, cartilage oligomeric protein; PRG, 4, Proteoglycan 4. Applied Biosystems TaqMan Human Assays on demand used for qRT-PCR., Sox9, SRY (sex determining region Y)-box 9 cartilage transcription factor; ALP, alkaline phosphatase.

(NBT, Sigma N5514) was then added. The bone sections were washed in PBS and placed in separate well where 500 µl of freshly prepared LDH staining solution was added. The sections were incubated at 37°C for 4 h in the dark, washed with warm (50°C–56°C) distilled water and then fixed with 4% paraformaldehyde at 4°C for 10 min. After a brief wash in deionized water, the sections were placed on glass slides and mounted with water based mountant (hydromount DAKO, National Diagnostics, HS-106).

2.12 Histological analysis

Methanol fixed PU/fibrin/MSC samples were frozen in OCT compound (R. Jung GmbH, Nussloch, Germany) before being sectioned (12 µm thick) on a cryotome (Carl Zeiss AG, Oberkochen, Germany) and adhered to Superfrost Plus slides (Thermo Fischer scientific, Waltham, United States). Slides were stored at −20°C.

2.13 Safranin O/Fast green staining

OCT compound was removed from the cryosections by rinsing in distilled water for ten minutes prior to Safranin O staining. This was followed by a twelve minute incubation in Weigert's Haematoxylin. The slides were then placed in lukewarm tap water for ten minutes, briefly washed in distilled water and then placed in 0.02% (v/v) fast green in 0.01% (v/v) acetic acid in deionised water for five minutes. Fast green staining was followed by thirty seconds in 1% (v/v) acetic acid and then five minutes in 0.1% (w/v) Safranin O solution (Chroma-Gesellschaft Schmid GmbH & Co., Münster, Germany). The slides were then dehydrated by immersing them in 96% ethanol twice (one minute each) and then 100% ethanol twice (two minutes each). Slides were then placed in 100% xylene for two minutes twice before being mounted using Eukitt mounting medium.

2.14 Von Kossa staining

OCT compound was removed from the cryosections by rinsing in distilled water for ten minutes prior to Von Kossa staining. This was followed by a thirty-minute incubation in 5% (v/v) Silver Nitrate (Sigma Aldrich, Sigma-Aldrich, Buchs, Switzerland) and parallel exposure to strong light. The slides were then rinsed three times ten minutes with deionized water and then placed in 5% (v/v) Sodium Thiosulfate (Sigma Aldrich, Sigma-Aldrich, Buchs, Switzerland) for ten minutes to fix the previous staining. The sections were washed again three times ten minutes with deionized water and counterstained per 10 min with 0.1% (v/v) Nuclear fast red (Fluka, St. Louis, United States). The slides were then washed as described in the previous steps and dehydrated by immersing them in 70% ethanol per ten seconds, 96% ethanol per one minute and then 100% ethanol twice (two minutes each). Slides were then placed in 100% xylene

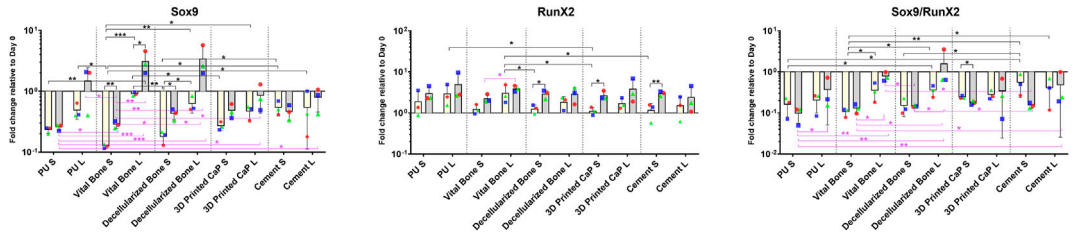

FIGURE 2
Gene expression of transcription factors SOX9 and RUNX2 in various scaffold systems under static (S) and loaded (L) conditions. Load generally led to an increase in both transcription factors. The load induced increase in SOX9 was most pronounced in the PU, vital bone, and bone dead groups. When considering the SOX9/RUNX2 ratio, the higher values were observed in the loaded groups with the bony bases. *$p < 0.05$, **$p < 0.01$, ***$p < 0.001$. Black significance bars designate differences on Day 7 among all groups or day 7 vs. day 28 within the same group. Purple significance bars designate differences on Day 28.

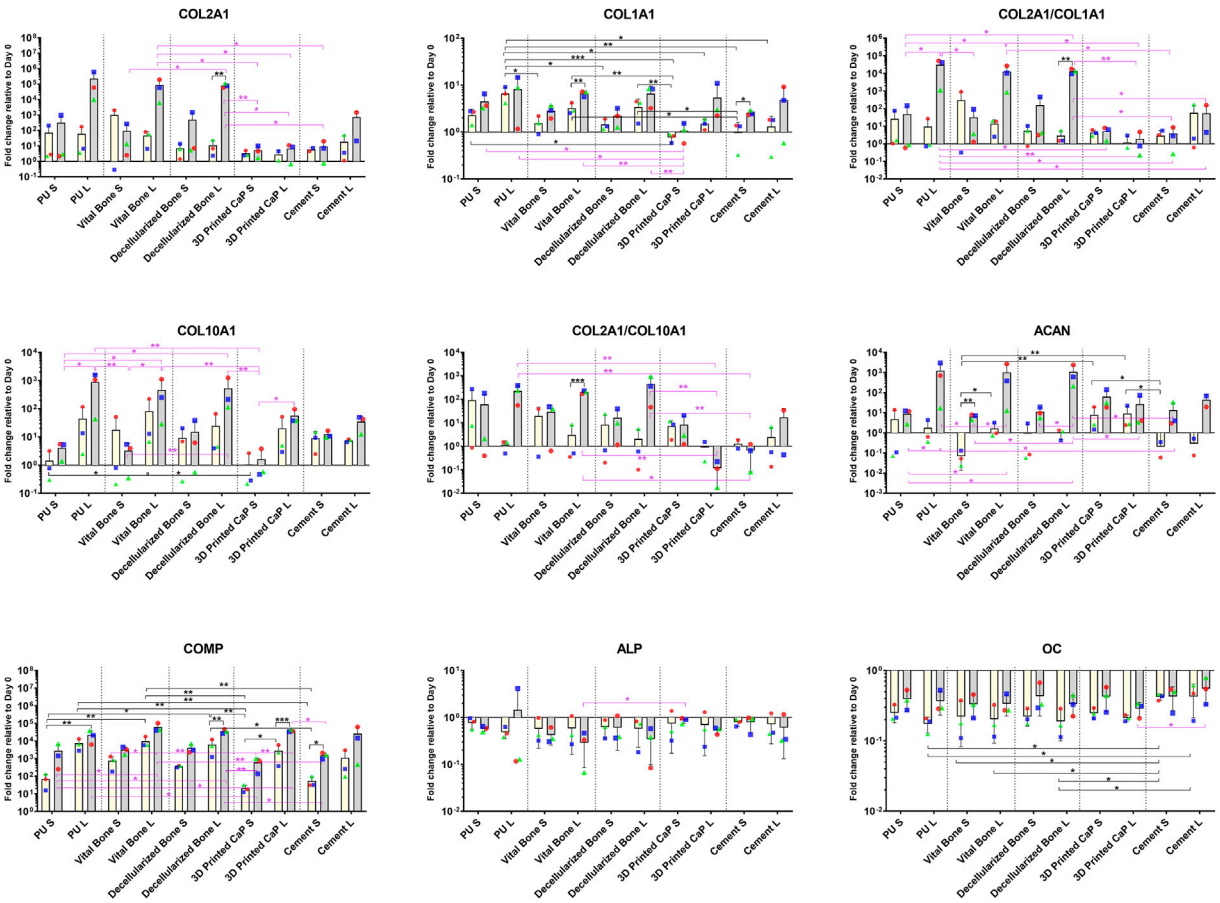

FIGURE 3
Gene expression of cartilage (COLA2A1, COMP, ACAN), hypertrophy (COL10A1) and bone (COL1A1, ALP, OC) related genes. Load generally led to an increase in all markers except ALP. Load combined with the PU, vital bone, and bone dead groups led to particularly favourable ACAN expression and improved COL2A1/COL1A1, COL2A1/COL10A1 ratios. *$p < 0.05$, **$p < 0.01$, ***$p < 0.001$. Black significance bars designate differences on Day 7 among all groups or day 7 vs. day 28 within the same group. Purple significance bars designate differences on Day 28.

for two minutes twice before being mounted using Eukitt mounting medium.

2.15 Statistical analysis

Data was analysed using 2-way ANOVA with Tukey multiple comparison, a p value > 0.05 was considered significant.

3 Results

3.1 Gene expression profiles of hMSCs seeded into fibrin-poly (ester-urethane) scaffolds after seven and twenty-eight days of culture

After 7 and 28 days of culture the gene expression profile of the MSCs in the upper scaffold was assessed (Figures 2, 3). Both transcription factors studied, SOX9 and RUNX2 were upregulated by mechanical load. The increase in Sox9 expression was most pronounced in the PU, viable bone and decellularized bone groups whereby day 28 expression had increased above day 0 levels. This led to a noticeable improvement in the SOX9/RUNX2 ratio, an indicator of chondrogenesis, in these groups (Figure 2).

Load also increased aggrecan and collagen 2 expression in the PU, viable bone and decellularized bone groups (Figure 3). While printed CaP and Cement based groups had a lower expression by day 28 and no noticeable response to load. By day 28, load induced a significant increase in collagen 10, which was most noticeable in the PU, viable bone and decellularized bone groups. The Col 2/Col 10 ratio demonstrates a significant benefit of load in the PU, viable bone and decellularized bone groups over time, the Col 2/Col 10 ratio decreased in the printed CaP group, indicating an unfavourable condition.

Investigating other pathways, Collagen 1 showed an increased expression, which was similar in all groups by day 28 (Figure 3). However, the PU, viable bone and decellularized bone groups also had a noticeable increased expression by day 7. ALP expression generally decreased with load, however few changes were significant. The expression of osteocalcin was generally higher with load in all groups, with no obvious differences between the groups. COMP expression levels generally increased over time in all groups and this was more pronounced with all loaded groups.

Taken together, the expression of cartilage related markers was increased by load and formed two clusters of expression. The PU, viable bone and decellularized bone groups showed a beneficial profile that was similar between the groups, whereas CaP and cement displayed a poorer chondrogenesis. The more bone related markers Col1, ALP, osteocalcin and Runx2 showed no specific base related trends.

3.2 Quantification of DNA content and sulphated glycosaminoglycan in fibrin-poly (ester-urethane) scaffolds and released into culture media

Under static conditions all groups showed a similar DNA content after 28 days of culture (Figure 4). This was largely unaffected by load, except for the vital bone and bone dead groups where a slight increase in DNA content was observed under loading conditions compared with static.

sGAG deposited in the scaffold: After 28 days of MSC chondrogenesis, no significant differences were observed in the sGAG deposition in PU, vital bone and bone dead groups (Figure 4). However, load led to a significant decrease ($^{**}p < 0.01$) of sGAG deposition in the 3D printed CaP group. A similar but not significant decrease was observed for the cement group. However, the sGAG deposition within the Cement group both under static and load conditions was significantly lower than the corresponding static or loaded vital bone ($^{**}p < 0.01$ and $^{*}p < 0.05$), bone dead ($^{**}p < 0.01$ and $^{*}p < 0.05$) and PU ($^{**}p < 0.01$) groups.

GAG per scaffold/DNA ratio at day 28: the scaffold sGAG/DNA ratio was investigated at day 28 to evaluate if the sGAG incorporated in the scaffold was due to higher MSC proliferation than differentiation (Figure 4). The scaffold sGAG/DNA ratio showed a similar trend observed for the GAG per scaffold. An overall reduction of the scaffold GAG/DNA ratio under loading was consistent among all the groups and was significantly more pronounced for bone dead ($^{*}p < 0.05$), 3D printed CaP ($^{**}p < 0.01$) and cement groups ($^{**}p < 0.01$). Under static conditions, PU led to the highest GAG/DNA level and this reached significance when compared with cement static ($^{*}p < 0.05$), with a tendency to higher GAG/DNA ratio when compared with the vital bone, 3D Printed CaP and cement loaded groups.

Within the loaded groups comparison, PU showed again the best scaffold sGAG/DNA ratio that was significantly higher compared with 3D Printed CaP ($^{**}p < 0.01$) and Cement ($^{*}p < 0.05$) groups. Cement loaded group showed the worst scaffold sGAG/DNA ratio significantly lower compared with PU ($^{**}p < 0.01$), bone dead ($^{*}p < 0.05$) and vital bone ($^{*}p < 0.05$) loaded. In addition, the cement load scaffold sGAG/DNA was a notably lower also in comparison with all the other static groups. 3D Printed CaP loaded group showed notably lower GAG/DNA then bone dead and PU static groups.

When using the PU: fibrin system, a large portion of the sGAG produced is released into the culture media. Therefore, GAG per media was also monitored and analyzed at each media change in order to investigate the trend of GAG release over 28 days of hMSCs chondrogenic differentiation (Figure 5). Over 28 days, an overall increase of sGAG per media was observed under loading conditions compared with comparable static conditions, with 3D Printed CaP ($^{*}p < 0.05$) and PU ($^{***}p < 0.001$) groups reaching significance. The cement base was the

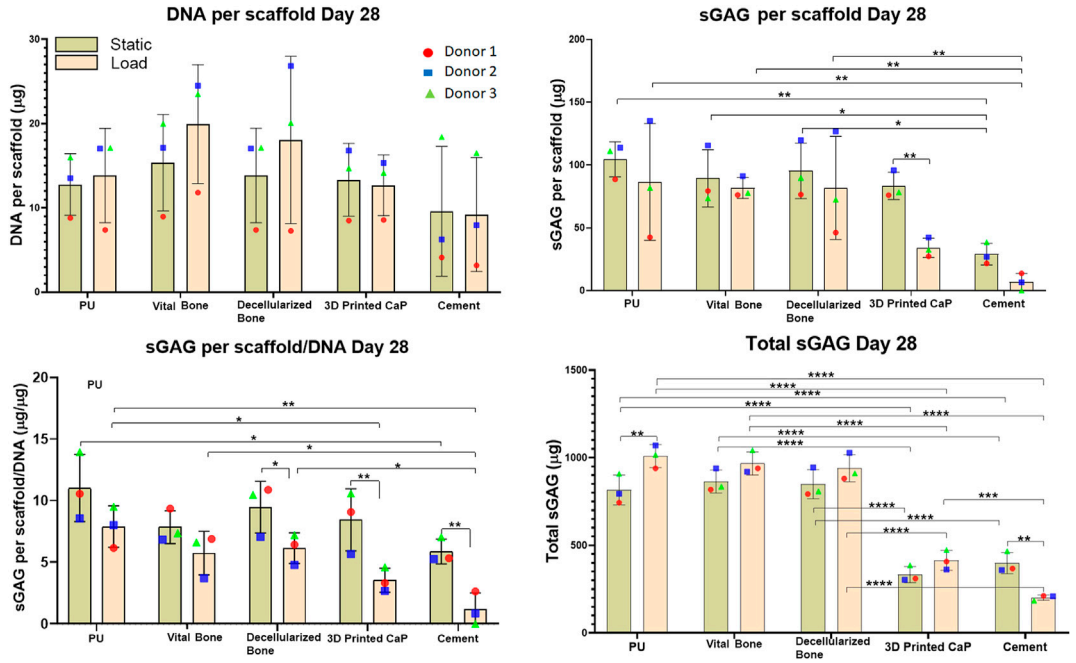

FIGURE 4
DNA, GAG per scaffold, Total GAG per scaffold/DNA, Total sGAG released into the media and total sGAG (media plus scaffold) produced over the entire 28-days. Load led to reduced sGAG per scaffold/DNA, mainly due to the load leading to an increased release of GAG into the medium. However, with the exception of the cement group, load led to an increase in total sGAG produced. The total sGAG produced was similar for PU, viable bone and decellularized bone, while the use of a 3D printed or cement base led to a significant reduction of total sGAG.

only group where a significant decrease ($^{**}p < 0.01$) was detected. Notably, the 3D Printed CaP and cement groups had a lower GAG production compared with the other three groups. Among the static groups, the highest media sGAG level was detected for vital bone group while among the loaded groups the highest media sGAG level was detected for PU. However, we did not find significant differences between PU, vital bone and bone dead groups by comparing either static or loaded conditions. Differently, PU ($^{****}p < 0.0001$), vital bone ($^{****}p < 0.0001$) and bone dead ($^{****}p < 0.0001$) groups released a significantly higher sGAG into the culture media compared with 3D Printed CaP and Cement either under static or under loading conditions. In addition, 3D Printed CaP loaded group showed significantly higher media sGAG ($^{**}p < 0.01$) compared with cement loaded group. No significant differences occurred under static conditions between 3D Printed CaP and cement even though 3D Printed CaP produced and released in the culture media more sGAG than the cement group.

3.3 Histology

In order to investigate the effect of the bone, the assessment of its viability over all the culture time was ensured by performing the lactate dehydrogenase viability staining at different timepoints. Viable bone was observed over the full 28 days, while the lack of LDH stained lacunae demonstrated the successful decellularization process (Figure 6).

Due to the large release of GAG into the medium, little safranin O-stained GAG matrix was observed in the upper scaffold after 28 days (Figure 7). However, von Kossa staining demonstrated considerable differences between the groups (Figure 7). While there was nonspecific staining of the cell free polyurethane base, there was no calcification observed in the upper cell seeded PU scaffold in any of the donors for the PU, viable bone and decellularized bone groups. However, with the exception of donor 3, there was significant von Kossa staining in the 3D printed calcium phosphate and cement groups. The 3D printed calcium phosphate demonstrated more calcification at the lower edge of the scaffold at the interface with the base, while the von Kossa staining was more evenly distributed throughout the scaffold in the cement group.

4 Discussion

Integration of kinematic load into *ex vivo* osteochondral culture models would allow a closer representation of the *in vivo* environment (Vainieri et al., 2018). This strategy could provide a new model to study healing or the regenerative

10.3389/fbioe.2022.998774

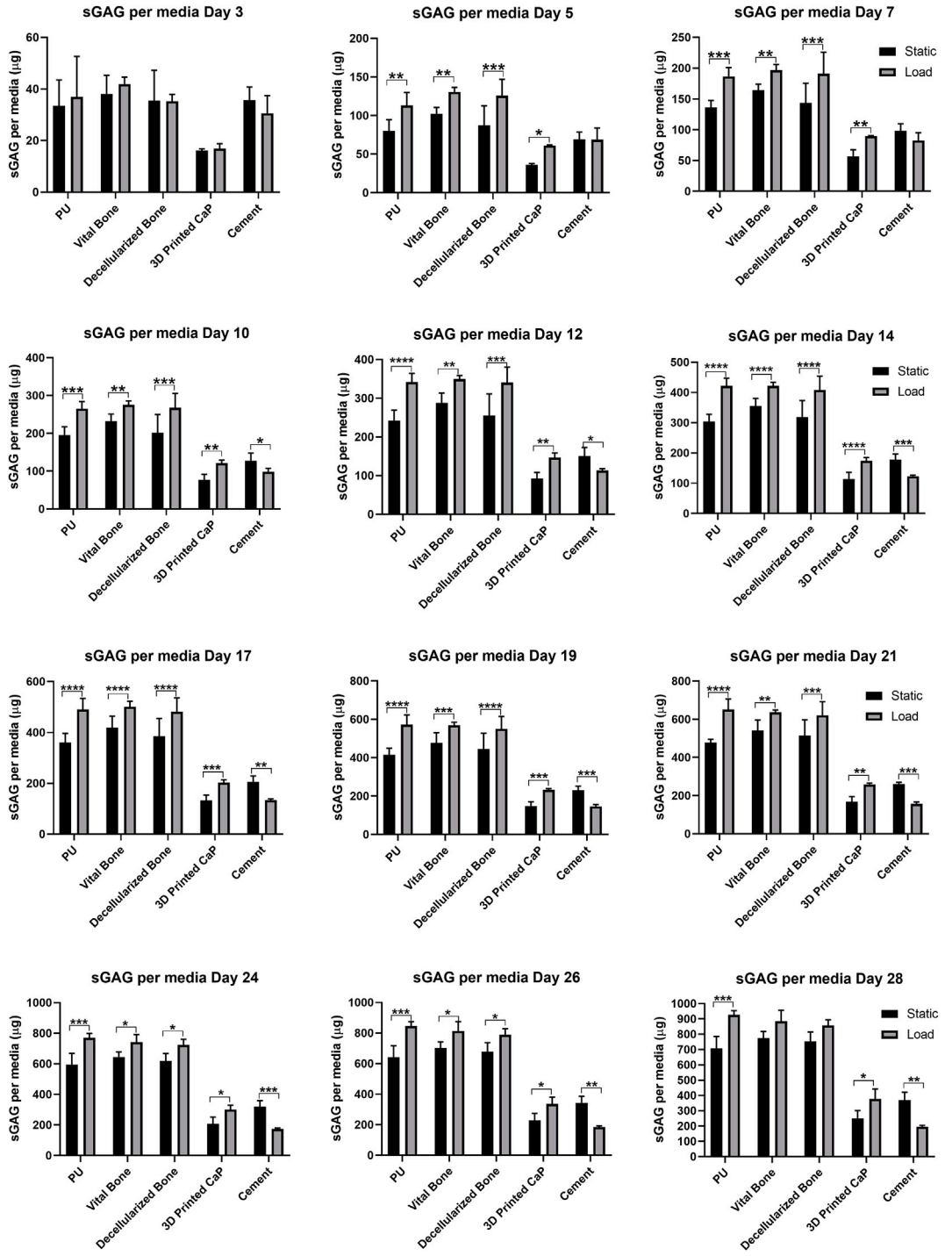

FIGURE 5
sGAG released into media by day. Media was sampled every two days and the sGAG contained within was quantified. By day 5 significant load induced differences were observed due to load and these were maintained throughout the experiment. *$p < 0.05$, **$p < 0.01$, ***$p < 0.001$, ****$p < 0.0001$.

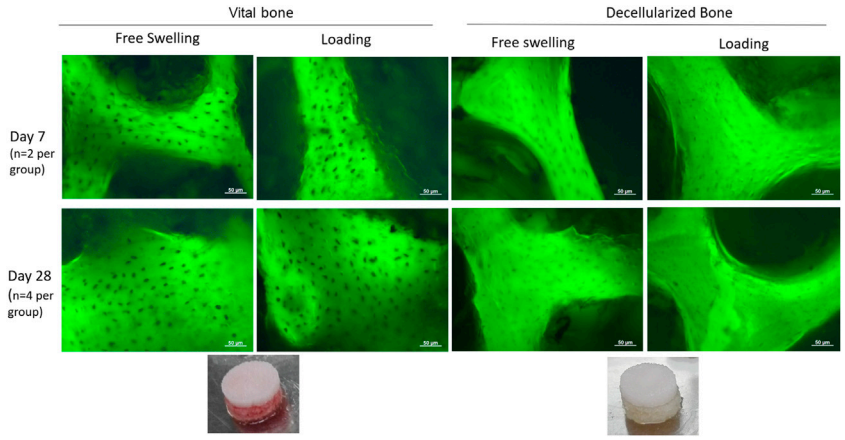

FIGURE 6
LDH staining of viable osteocytes within cultured bone explants. Dark spots indicate a viable osteocyte visible against the autofluorescent bone. Osteocytes in viable bone remained viable for up to 28 days, while the decellularization process was successful at removing all viable osteocytes.

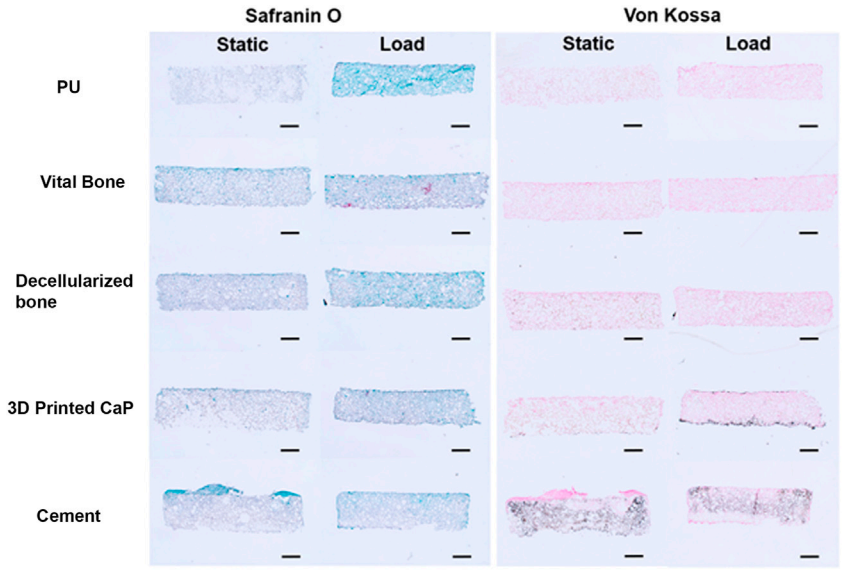

FIGURE 7
Example Safranin O and Von Kossa histology after 28 days of culture. Safranin O staining was minor due to the high resale of produced GAG into the culture medium. Von Kossa staining was observed at the interface (3D Printed CaP) or throughout (cement) the upper MSC laden scaffold. This was not observed when PU or bone was used as the base. (Scale bar = 1 mm).

processes of articular cartilage in a more joint-like environment, especially when various mechanical loading patterns can be applied to the model. In recent years, there has been a considerable effort to produce bioreactors and loading devices (Heath and Magari, 1996; Li et al., 2004; Lee et al., 2017; Meinert et al., 2017; Daly et al., 2018; Jonnalagadda et al., 2018; Nazempour and Van Wie, 2018). The bioreactors might be a supporting tool to expose cells seeded in a scaffold structure or *ex-vivo* explants, to different forms of mechanical load. This can be used to either develop tissue engineered implants or to better study the effect of mechanical load on tissue healing by simulating and predicting *in vivo* processes (Grad et al., 2011). It is quite challenging to achieve and faithfully reproduce complex *in vivo* load, as the motion pattern can

vary greatly even within the same joint (Grad et al., 2011). Nevertheless, even rudimentary mechanical stimulation is highly desirable. Within this study we applied compression and shear mechanical load to various osteochondral implant composites. The primary aim was to assess effect of load and the potential crosstalk between viable bone and MSC laden constructs. To control for the mechanical environment, decellularized bone, calcium phosphate printed base, and a cement base were used. The devitalized bone also offered a control to the viable bone soluble molecules produced by the viable cells. When considering the two main hypothesis, in the current study neither were proven correct.

We hypothesized that soluble signals from live bone would change the phenotype of the MSCs differentiating in the upper layer. When considering the two main experimental groups required for this analysis, viable bone base and decellularized bone base, no differences at the gene expression level could be detected. Other studies have demonstrated a soluble cross talk between osteoblasts, chondrocytes and MSCs (Funck-Brentano and Cohen-Solal, 2011; de Vries-van Melle et al., 2014a; Leyh et al., 2014; Glueck et al., 2015). There are reasons why this may not have been observed in this study. Potentially, biologically active molecules were leaching out of the decellularized bone driving a similar response to live bone. Alternatively, the distance between the bone and the MSCs in the upper scaffold may have been too great, with the soluble signals only affecting the MSCs in the lowest part of the scaffold. These effects may have been diluted out when using a destructive PCR analysis and suggest more spatial phenotyping would be required. Furthermore, studies which have shown the most dramatic effects utilized an osteochondral defect model (de Vries-van Melle et al., 2014a; de Vries-van Melle et al., 2014b) where the implanted material would have a more confined environment. While it is also possible that soluble molecules from bovine bone are not able to adequately stimulate human cells, an effect of bovine subchondral bone on human bone marrow MSCs has previously been observed (de Vries-van Melle et al., 2014a) suggesting the lack of signalling arises elsewhere. Therefore, an enclosed osteochondral defect model such as that developed by Vaineri et al. would lead to more reliable data (Vainieri et al., 2018). While no changes were observed with the PCR data, differences were seen at the histological level, particularly in the Von Kossa staining pattern. There is also the possibility that the total cell density is not sufficient, and the load induced fluid flow in this unconfirmed environment led to a washout of the secretome rather than a cross talk.

Furthermore, we hypothesized that changing the 2 mm base material to a rigid material would modify the response to load compared to the soft PU base. This also was not the case, as both the live and decellularized bone bases had similar responses to the softer PU base. This suggests there is a critical threshold above which the load response occurs and this is already reached when using the PU: fibrin scaffolds. As it has been previously shown that shear superimposed on compression leads to the mechanical activation of TGF β, this may be one of the key motion patterns required to drive the response (Gardner et al., 2017b). As frequency and amplitude has been shown to modify the chondrogenic response (Li et al., 2010b) it suggests the mechanical activation occurs in the liquid interface during the shear application, and then compression drives the activated TGF β protein into the scaffold. Once the bulk properties of the construct reach a threshold to allow this to occur, stiffening the construct further would not necessarily lead to increased protein activation.

Unexpectedly, the printed CaP and cement base groups led to a detrimental effect on the MSC chondrogenesis. Collagen 2 and aggrecan expression was decreased in comparison to the other three groups, and GAG production was reduced. No obvious difference in DNA content was observed between the groups, suggestion viability was not a reason for the reduced chondrogenesis. In both cases, an increase in calcium deposition was observed in the upper MSC laden scaffold, suggesting a more bony phenotype was induced. This was not apparent in the PCR data and we have not yet identified the underlying pathway involved. The exact mechanism may be different for the two materials, as they have different porosity and calcium content, which may affect nutrient availability and final medium composition respectively. The negative effect for the cement and printed CaP groups was most noticeable with reduced GAG production, and lower collagen 2 mRNA expression levels, these aspects need investigating further. This result may have a clinical significance as both of these materials are used clinically, and this data suggests detrimental effects on the developing cartilage when compared to natural bone graft. In the case of the 3D printed calcium phosphate base, it is possible that the material is affecting media calcium and phosphate levels. A study using a similar material from Innotere GmbH, Germany, demonstrated that 3D printed calcium phosphate materials decreased media calcium levels, while phosphorus levels were initially increased over the first 14 days (Kilian et al., 2020). In that study, the base material led to improved GAG and Collagen II production when using human chondrocytes. Therefore, it is possible the biological outcome is cell specific, but the influence of the base material should not be overlooked. The response to load is also likely to be cell specific. The negative effects seen could also be related to an induction of apoptosis and future studies should study this in more detail.

Therefore, we can conclude that within ten different conditions it is possible to categorize the ten experimental groups in two groups: PU, vital bone and bone dead belong to the group that showed similar chondrogenic potential that was increased by load, while 3D Printed CaP and cement groups produced and released less sGAG and were less responsive to loading.

In summary, the response of load was dependent on the material used as the subchondral bone component, with PU,

viable bone and decellularized bone showing similar profiles at the gene and protein level. The maintenance of viable osteocytes of 28 days shows the feasibility of this coculture approach and furthers studies will be performed to assess more regionalized differences. Data within this study suggests care should be taken when using printed calcium phosphate or cement as a filler for osteochondral defects as the chondrogenic response may be inhibited compared with natural bone.

Data availability statement

The raw data supporting the conclusions of this article will be made available by the authors, without undue reservation.

Ethics statement

The studies involving human participants were reviewed and approved by Zürich Kanton KEK-ZH-NR: 2010-0444/0. The patients/participants provided their written informed consent to participate in this study.

Author contributions

GM Project planning, data acquisition, data analysis, writing paper draft, final approval of the manuscript. FQ Project planning, data acquision, data analysis, final approval of the manuscript. NF Supervision, writing paper draft, final approval of the manuscript. AH. Supervision, writing paper draft, final approval of the manuscript. MS. Project planning, data acquisition, data analysis, supervision, funding acquisition, writing paper draft, final approval of the manuscript.

Funding

This study was funded by the AO Foundation.

Conflict of interest

The authors declare that the research was conducted in the absence of any commercial or financial relationships that could be construed as a potential conflict of interest.

Publisher's note

All claims expressed in this article are solely those of the authors and do not necessarily represent those of their affiliated organizations, or those of the publisher, the editors and the reviewers. Any product that may be evaluated in this article, or claim that may be made by its manufacturer, is not guaranteed or endorsed by the publisher.

References

Armiento, A. R., Alini, M., and Stoddart, M. J. (2018). Articular fibrocartilage - why does hyaline cartilage fail to repair? *Adv. Drug Deliv. Rev.* 146, 289–305. doi:10.1016/j.addr.2018.12.015

Bieback, K., Kinzebach, S., and Karagianni, M. (2011). Translating research into clinical scale manufacturing of mesenchymal stromal cells. *Stem cells Int.* 2010, 1–11. doi:10.4061/2010/193519

Buckwalter, J., and Mankin, H. (1998). Articular cartilage repair and transplantation. *Arthritis Rheum.* 41 (8), 1331–1342. doi:10.1002/1529-0131(199808)41:8<1331:AID-ART2>3.0.CO;2-J

Daly, A. C., Sathy, B. N., and Kelly, D. J. (2018). Engineering large cartilage tissues using dynamic bioreactor culture at defined oxygen conditions. *J. Tissue Eng.* 9, 204173141775371. doi:10.1177/2041731417753718

de Vries-van Melle, M. L., Narcisi, R., Kops, N., Koevoet, W. J., Bos, P. K., Murphy, J. M., et al. (2014). Chondrogenesis of mesenchymal stem cells in an osteochondral environment is mediated by the subchondral bone. *Tissue Eng. Part A* 20 (1-2), 23–33. doi:10.1089/ten.tea.2013.0080

de Vries-van Melle, M. L., Tihaya, M. S., Kops, N., Koevoet, W. J., Murphy, J. M., Verhaar, J. A., et al. (2014). Chondrogenic differentiation of human bone marrow-derived mesenchymal stem cells in a simulated osteochondral environment is hydrogel dependent. *Eur. Cell. Mat.* 27, 112–123. doi:10.22203/ecm.v027a09

Funck-Brentano, T., and Cohen-Solal, M. (2011). Crosstalk between cartilage and bone: When bone cytokines matter. *Cytokine Growth Factor Rev.* 22 (2), 91–97. doi:10.1016/j.cytogfr.2011.04.003

Gardner, O. F., Alini, M., and Stoddart, M. J. (2015). Mesenchymal stem cells derived from human bone marrow. *Methods Mol. Biol.* 1340, 41–52. doi:10.1007/978-1-4939-2938-2_3

Gardner, O. F. W., Musumeci, G., Neumann, A. J., Eglin, D., Archer, C. W., Alini, M., et al. (2017). Asymmetrical seeding of MSCs into fibrin-poly(ester-urethane) scaffolds and its effect on mechanically induced chondrogenesis. *J. Tissue Eng. Regen. Med.* 11 (10), 2912–2921. doi:10.1002/term.2194

Gardner, O. F. W., Fahy, N., Alini, M., and Stoddart, M. J. (2017). Joint mimicking mechanical load activates TGFβ1 in fibrin-poly(ester-urethane) scaffolds seeded with mesenchymal stem cells. *J. Tissue Eng. Regen. Med.* 11 (9), 2663–2666. doi:10.1002/term.2210

Glueck, M., Gardner, O., Czekanska, E., Alini, M., Stoddart, M. J., Salzmann, G. M., et al. (2015). Induction of osteogenic differentiation in human mesenchymal stem cells by crosstalk with osteoblasts. *BioResearch open access* 4 (1), 121–130. doi:10.1089/biores.2015.0002

Gomoll, A. H., Madry, H., Knutsen, G., van Dijk, N., Seil, R., Brittberg, M., et al. (2010). The subchondral bone in articular cartilage repair: current problems in the surgical management. *Knee Surg. Sports Traumatol. Arthrosc.* 18 (4), 434–447. doi:10.1007/s00167-010-1072-x

Grad, S., Eglin, D., Alini, M., and Stoddart, M. J. (2011). Physical stimulation of chondrogenic cells *in vitro*: a review. *Clin. Orthop. Relat. Res.* 469 (10), 2764–2772. doi:10.1007/s11999-011-1819-9

Heath, C. A., and Magari, S. R. (1996). Mini-review: Mechanical factors affecting cartilage regeneration *in vitro*. *Biotechnol. Bioeng.* 50 (4), 430–437. doi:10.1002/(sici)1097-0290(19960520)50:4<430:aid-bit10>3.0.co;2-n

Heinemann, S., Rossler, S., Lemm, M., Ruhnow, M., and Nies, B. (2013). Properties of injectable ready-to-use calcium phosphate cement based on water-immiscible liquid. *Acta biomater.* 9 (4), 6199–6207. doi:10.1016/j.actbio.2012.12.017

Hunziker, E. B., and Rosenberg, L. C. (1996). Repair of partial-thickness defects in articular cartilage: cell recruitment from the synovial membrane. *J. Bone Jt. Surg.* 78 (5), 721–733. doi:10.2106/00004623-199605000-00012

Jahn, K., and Stoddart, M. J. (2011). Viability assessment of osteocytes using histological lactate dehydrogenase activity staining on human cancellous bone sections. *Methods Mol. Biol.* 740, 141–148. doi:10.1007/978-1-61779-108-6_15

Jahn, K., Braunstein, V., Furlong, P. I., Simpson, A. E., Richards, R. G., and Stoddart, M. J. (2010). A rapid method for the generation of uniform acellular bone explants: a technical note. *J. Orthop. Surg. Res.* 5, 32. doi:10.1186/1749-799x-5-32

Jonnalagadda, U. S., Hill, M., Messaoudi, W., Cook, R. B., Oreffo, R. O., Glynne-Jones, P., et al. (2018). Acoustically modulated biomechanical stimulation for human cartilage tissue engineering. *Lab. Chip* 18 (3), 473–485. doi:10.1039/c7lc01195d

Kilian, D., Ahlfeld, T., Akkineni, A. R., Bernhardt, A., Gelinsky, M., and Lode, A. (2020). 3D Bioprinting of osteochondral tissue substitutes - *in vitro*-chondrogenesis in multi-layered mineralized constructs. *Sci. Rep.* 10 (1), 8277. doi:10.1038/s41598-020-65050-9

Knutsen, G., Drogset, J. O., Engebretsen, L., Grontvedt, T., Isaksen, V., Ludvigsen, T. C., et al. (2007). A randomized trial comparing autologous chondrocyte implantation with microfracture. Findings at five years. *J. Bone Jt. Surg.* 89 (10), 2105–2112. doi:10.2106/jbjs.g.00003

Kupcsik, L., Alini, M., and Stoddart, M. J. (2009). Epsilon-aminocaproic acid is a useful fibrin degradation inhibitor for cartilage tissue engineering. *Tissue Eng. Part A* 15 (8), 2309–2313. doi:10.1089/ten.tea.2008.0400

Kuroda, R., Ishida, K., Matsumoto, T., Akisue, T., Fujioka, H., Mizuno, K., et al. (2007). Treatment of a full-thickness articular cartilage defect in the femoral condyle of an athlete with autologous bone-marrow stromal cells. *Osteoarthr. Cartil.* 15 (2), 226–231. doi:10.1016/j.joca.2006.08.008

Lee, P. S., Eckert, H., Hess, R., Gelinsky, M., Rancourt, D., Krawetz, R., et al. (2017). Developing a customized perfusion bioreactor prototype with controlled positional variability in oxygen partial pressure for bone and cartilage tissue engineering. *Tissue Eng. Part C. Methods* 23 (5), 286–297. doi:10.1089/ten.tec.2016.0244

Leyh, M., Seitz, A., Durselen, L., Schaumburger, J., Ignatius, A., Grifka, J., et al. (2014). Subchondral bone influences chondrogenic differentiation and collagen production of human bone marrow-derived mesenchymal stem cells and articular chondrocytes. *Arthritis Res. Ther.* 16 (5), 453. doi:10.1186/s13075-014-0453-9

Li, K. W., Klein, T. J., Chawla, K., Nugent, G. E., Bae, W. C., and Sah, R. L. (2004). *In vitro* physical stimulation of tissue-engineered and native cartilage. *Methods Mol. Med.* 1, 325–352. Cellular and Molecular Tools. doi:10.1385/1-59259-810-2:325

Li, Z., Kupcsik, L., Yao, S. J., Alini, M., and Stoddart, M. J. (2010). Mechanical load modulates chondrogenesis of human mesenchymal stem cells through the TGF-beta pathway. *J. Cell. Mol. Med.* 14 (6A), 1338–1346. doi:10.1111/j.1582-4934.2009.00780.x

Li, Z., Yao, S. J., Alini, M., and Stoddart, M. J. (2010). Chondrogenesis of human bone marrow mesenchymal stem cells in fibrin-polyurethane composites is modulated by frequency and amplitude of dynamic compression and shear stress. *Tissue Eng. Part A* 16 (2), 575–584. doi:10.1089/ten.tea.2009.0262

Madry, H., Orth, P., and Cucchiarini, M. (2016). Role of the subchondral bone in articular cartilage degeneration and repair. *J. Am. Acad. Orthop. Surg.* 24 (4), e45–e46. doi:10.5435/jaaos-d-16-00096

Madry, H. (2010). The subchondral bone: a new frontier in articular cartilage repair. *Knee Surg. Sports Traumatol. Arthrosc.* 18 (4), 417–418. doi:10.1007/s00167-010-1071-y

Meinert, C., Schrobback, K., Hutmacher, D. W., and Klein, T. J. (2017). A novel bioreactor system for biaxial mechanical loading enhances the properties of tissue-engineered human cartilage. *Sci. Rep.* 7 (1), 16997. doi:10.1038/s41598-017-16523-x

Mueller, M. B., and Tuan, R. S. (2008). Functional characterization of hypertrophy in chondrogenesis of human mesenchymal stem cells. *Arthritis Rheum.* 58 (5), 1377–1388. doi:10.1002/art.23370

Nazempour, A., and Van Wie, B. J. (2018). A flow perfusion bioreactor with controlled mechanical stimulation: Application in cartilage tissue engineering and beyond. *J. Stem Cell Ther. Transpl.* 2, 015–034. doi:10.29328/journal.jsctt.1001011

Nukavarapu, S. P., and Dorcemus, D. L. (2013). Osteochondral tissue engineering: current strategies and challenges. *Biotechnol. Adv.* 31 (5), 706–721. doi:10.1016/j.biotechadv.2012.11.004

Pelttari, K., Winter, A., Steck, E., Goetzke, K., Hennig, T., Ochs, B. G., et al. (2006). Premature induction of hypertrophy during *in vitro* chondrogenesis of human mesenchymal stem cells correlates with calcification and vascular invasion after ectopic transplantation in SCID mice. *Arthritis Rheum.* 54 (10), 3254–3266. doi:10.1002/art.22136

Schneider, C. K., Salmikangas, P., Jilma, B., Flamion, B., Todorova, L. R., Paphitou, A., et al. (2010). Challenges with advanced therapy medicinal products and how to meet them. *Nat. Rev. Drug Discov.* 9 (3), 195–201. doi:10.1038/nrd3052

Sophia Fox, A. J., Bedi, A., and Rodeo, S. A. (2009). The basic science of articular cartilage: structure, composition, and function. *Sports health* 1 (6), 461–468. doi:10.1177/1941738109350438

Vainieri, M., Wahl, D., Alini, M., van Osch, G., and Grad, S. (2018). Mechanically stimulated osteochondral organ culture for evaluation of biomaterials in cartilage repair studies. *Acta biomater.* 81, 256–266. doi:10.1016/j.actbio.2018.09.058

Wakitani, S., Imoto, K., Yamamoto, T., Saito, M., Murata, N., and Yoneda, M. (2002). Human autologous culture expanded bone marrow mesenchymal cell transplantation for repair of cartilage defects in osteoarthritic knees. *Osteoarthr. Cartil.* 10 (3), 199–206. doi:10.1053/joca.2001.0504

Wakitani, S., Mitsuoka, T., Nakamura, N., Toritsuka, Y., Nakamura, Y., and Horibe, S. (2004). Autologous bone marrow stromal cell transplantation for repair of full-thickness articular cartilage defects in human patellae: two case reports. *Cell Transpl.* 13 (5), 595–600. doi:10.3727/000000004783983747

Wimmer, M. A., Grad, S., Kaup, T., Hanni, M., Schneider, E., Gogolewski, S., et al. (2004). Tribology approach to the engineering and study of articular cartilage. *Tissue Eng.* 10 (9-10), 1436–1445. doi:10.1089/1076327042500454

frontiers | Frontiers in Bioengineering and Biotechnology

TYPE Case Report
PUBLISHED 07 April 2023
DOI 10.3389/fbioe.2023.1024480

Check for updates

OPEN ACCESS

EDITED BY
Andrea Vernengo,
AO Research Institute, Switzerland

REVIEWED BY
Feng Li,
Qingdao University of Science and Technology, China
Amani Hassan,
McGill University, Canada

*CORRESPONDENCE
Ting Chen,
chenting88726@163.com
Guanning Shang,
cmushanggn@163.com

†These authors have contributed equally to this work

SPECIALTY SECTION
This article was submitted to Regenerative Medicine, a section of the journal Frontiers in Bioengineering and Biotechnology

RECEIVED 21 August 2022
ACCEPTED 31 March 2023
PUBLISHED 07 April 2023

CITATION
Zhang H, Hou B, Xia T, Ji L, Li J, Chen T and Shang G (2023), Primary sternal tumour resection and reconstruction with LARS mesh-bone cement sandwich by 3D-printing: Case reports. *Front. Bioeng. Biotechnol.* 11:1024480. doi: 10.3389/fbioe.2023.1024480

COPYRIGHT
© 2023 Zhang, Hou, Xia, Ji, Li, Chen and Shang. This is an open-access article distributed under the terms of the Creative Commons Attribution License (CC BY). The use, distribution or reproduction in other forums is permitted, provided the original author(s) and the copyright owner(s) are credited and that the original publication in this journal is cited, in accordance with accepted academic practice. No use, distribution or reproduction is permitted which does not comply with these terms.

Primary sternal tumour resection and reconstruction with LARS mesh-bone cement sandwich by 3D-printing: Case reports

He Zhang[1†], Bo Hou[1†], Tienan Xia[2], Lu Ji[3], Jiatong Li[1], Ting Chen[1*] and Guanning Shang[1*]

[1]Department of Bone and Soft Tissue Oncology, Department of Surgery, Shengjing Hospital, China Medical University, ShenYang, Liaoning, China, [2]Department of Orthopedics, Fifth People's Hospital of Shenyang, ShenYang, Liaoning, China, [3]Department of Gynecology and Obstetrics, Shengjing Hospital, China Medical University, ShenYang, Liaoning, China

Background: There are many reconstruction methods after sternal tumor resection, but the method that LARS mesh combines with bone-cement has not been reported.

Case report: A 54-year-old female patient and a 55-year-old male patient admitted to our department all presented with sternum masses, but neither presented with respiratory disorders. In women with limited manubrium sternum lesions, we resected the manubrium sternum completely. In men with sternal lesions, we removed part of the sternum and part of the sternocostal joint. The patients recovered well after surgery, and there were no respiratory complications and no tumor recurrence during the 1-year follow-up respectively.

Conclusion: We report two cases of sternal defect repair using LARS mesh combined with bone cement. This method is safe and stable, and can achieve satisfactory results.

KEYWORDS

sternal tumour, LARS, reconstruction, bone cement, 3D-printing, case reports

1 Introduction

Primary chest tumours are infrequent, accounting for less than 1% of primary bone tumours (Chaudhry et al., 2015; Ma et al., 2018), and only 20% of chest tumours arise from the sternum (Hann et al., 2018). Although primary sternal tumours are rare, their prevalence has increased in recent years. Among sternal tumours, malignancies such as chondrosarcoma are the most common. Benign lesions include chondromas, osteomas, and fibrous dysplasia (Gritsiuta et al., 2021). Afflicted patients often complain of a palpable chest mass accompanied by pain or cough.

Surgery is the primary treatment for sternal tumours when obvious clinical symptoms occur, whether malignant or benign. Radical resection is the optimal therapy for surgeons to guarantee non-tumour margins and low recurrence rates (Zhang et al., 2015). However, a larger excision area indicates a larger chest defect. The chest wall plays a critical role in thoracic stability and respiratory function. Reconstruction of chest defects should be considered to protect thoracic organs, restore cosmetic appearance, and prevent paradoxical ventilatory function (Zhang et al., 2015).

Reconstruction usually consists of two aspects: skeletal reconstruction and soft tissue reconstruction (Khullar and Fernandez, 2017). Soft tissue defects are usually resolved using primary closure or myocutaneous flaps, such as the latissimus dorsi, pectoralis major, serratus anterior, and rectus abdominis muscles. The optimal materials used in skeletal reconstruction are currently under debate, and no consensus has been reached. Such materials should have the properties of rigidity, biocompatibility, flexibility, and elasticity. Historically, various prosthetic materials used in reconstruction have included synthetic meshes, bioprosthetic materials, stainless steel, titanium plates, autografts, and homografts (Sandler and Hayes-Jordan, 2018). Each technique has its advantages and disadvantages. The choice of reconstruction method depends on the patient's state, the surgeon's preference, and the availability of materials.

In this cases, we support the use of an innovative ligament advanced reinforcement system (LARS)-bone cement sandwich as a prosthesis for reconstruction of the chest wall, which has not yet been reported in the literature. This new method achieved a good therapeutic effect, with uneventful recovery at the 1-year follow-up.

2 Case reports

2.1 Demographics

We report the cases of a 54-year-old female patient and a 55-year-old male patient who presented to our department with sternal masses, from March to May 2021; both patients were operated on by the same doctor. In the female patient, the lesion was located in the manubrium sternum, and was diagnosed as chondrosarcoma by postoperative pathology. In the male patient, the lesion was located in the middle of the sternum with involvement of the fourth rib, and was diagnosed as bone fibrous dysplasia based on postoperative pathology (Supplementary Table S1, Supplementary Figure S1). Both patients underwent preoperative chest 3-dimention computed tomography (slice thick 1 mm, 120 kV, 346 mA, FOV 500 mm) (Figure 1). Meanwhile, electrocardiography, pulmonary function tests, and other necessary examinations were conducted with normal results to ensure the surgery safety. Both patients denied other diseases. We made a 3D printed model based on the computed tomography data so as to determine the lesion and excision scopes, and to design the bone cement mould for surgery. 3D printing technology was achieved by mimics software, 3-matic software and 3D printer (RAISE 3D-n2, Shanghai Fuzhi Technology Co., LTD.). We imported the CT data into the mimics software to design 3D model according to the surgical requirement. Next, The modeled 3D data was imported to 3D-printer to manufacture 3D model using the polylatex (PLA). Serological examinations, including blood tests, liver and kidney function, and serum ions, were normal.

2.2 The sternum defect was repaired with polymethyl methacrylate (PMMA) and LARS ligament

2.2.1 Anaesthetic consideration

Both patients were placed in the supine position during the operation. The patients were anaesthetised using two-chamber endotracheal intubation after routine testing of blood oxygen and blood pressure and evaluating the electrocardiogram findings. The arterial catheter was indwelling for observation of blood gas analysis in surgery.

2.2.2 Resection

For sternal tumours, we ensured an adequate resection area according to individual principles, which meant the confirmation of

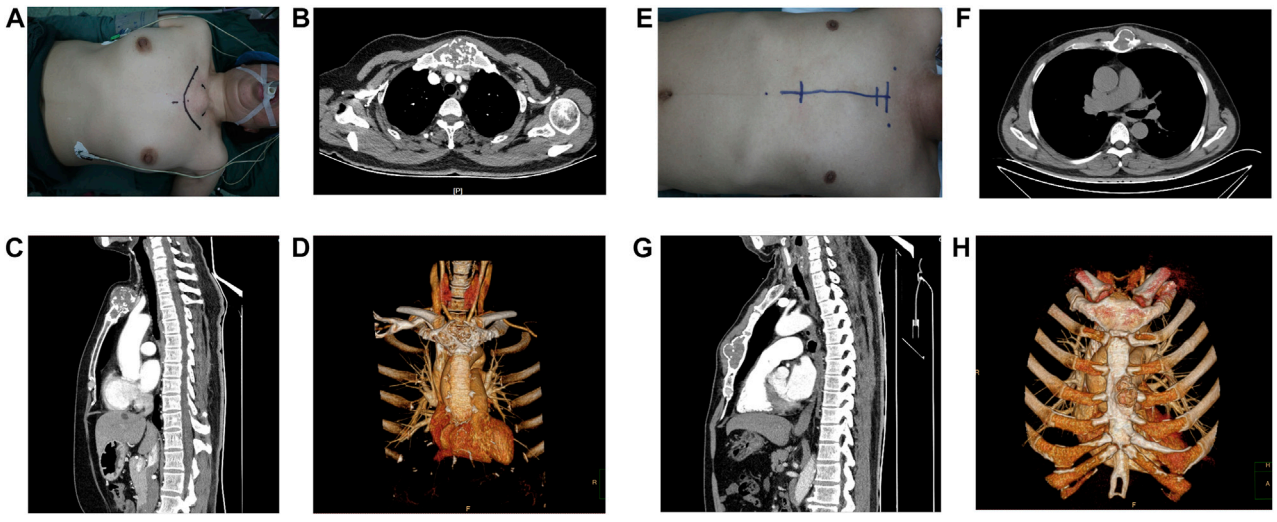

FIGURE 1
Appearance and preoperative images of the patients. **(A–D)** Female patient and **(E–H)** Male patient. **(A,E)** Appearance of the lesion and operative route on the body surface. **(B,C) (F,G)** The tumour is shown in cross-sectional and sagittal views **(D,H)**, **(D)** reconstruction of tumour on CT is demonstrated.

10.3389/fbioe.2023.1024480

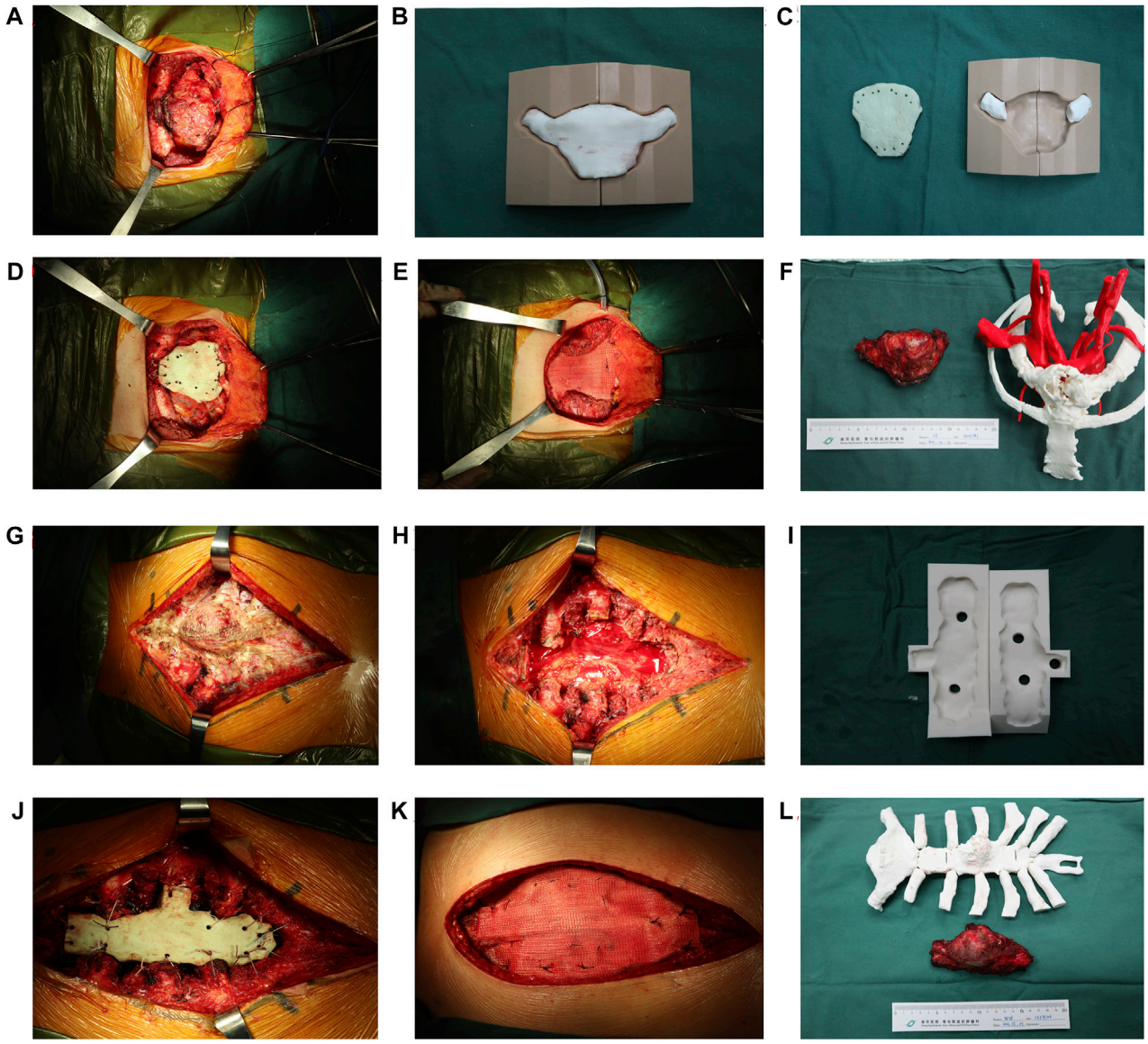

FIGURE 2
Surgical procedure of sternal tumour resection and reconstruction. **(A–F)** The female patient. **(A)** The lesion was exposed and separated. **(B–C)** Fabrication of sternal prosthesis by 3D-printing. **(D–E)** A "Sandwich" cement prosthesis is implanted in chest defect region. **(F)** The resected specimen and bone cement prosthesis were compared with the 3D-printing model. **(G–L)** The male patient. **(G–H)** The lesion is exposed and removed. **(I)** Fabrication of the sternal prosthesis by the 3D-printing mould. **(J–K)** A "Sandwich" cement prosthesis is implanted in the chest defect region. **(L)** The resected specimen and bone cement prosthesis as compared to the 3D-printing model.

incision and excision margin depended on intrinsic properties of tumours. Preoperative printing of the 3D model played a positive role in understanding the lesion scope and determining the surgical plan. For the female patient with a lesion limited to the manubrium sternum, the platysma muscle, sternocleidomastoid muscle, sternoclavicular joint, sternocostal joint, and the joint between the sternocleidomastoid and sternum were sequentially severed after exposure. For the male patient with a lesion located in the sternal body, we separated the sternal body from the manubrium sternum and bilateral third-sixth sternal costal joints. The residual costal stumps were proven to be non-tumourous on intraoperative pathology examination. The tumor histological characteristics of the female patient presented as lobulated hyaluronic cartilage nodules, which resembled normal cartilage to some extent. The margin of the tumor was white and yellow granular. The tumor histological characteristics of the male patient presented as no obvious boundary of osteocele, cystic fibrous changes, and the bone marrow cavity was occupied by grayish white or grayish red hyperplastic fibrous tissue.

2.2.3 Bone cement prosthesis and LARS ligament coverage

After removing the sternal lesions, bone cement was poured into a pre-made mould. The mould was fabricated using 3D printing

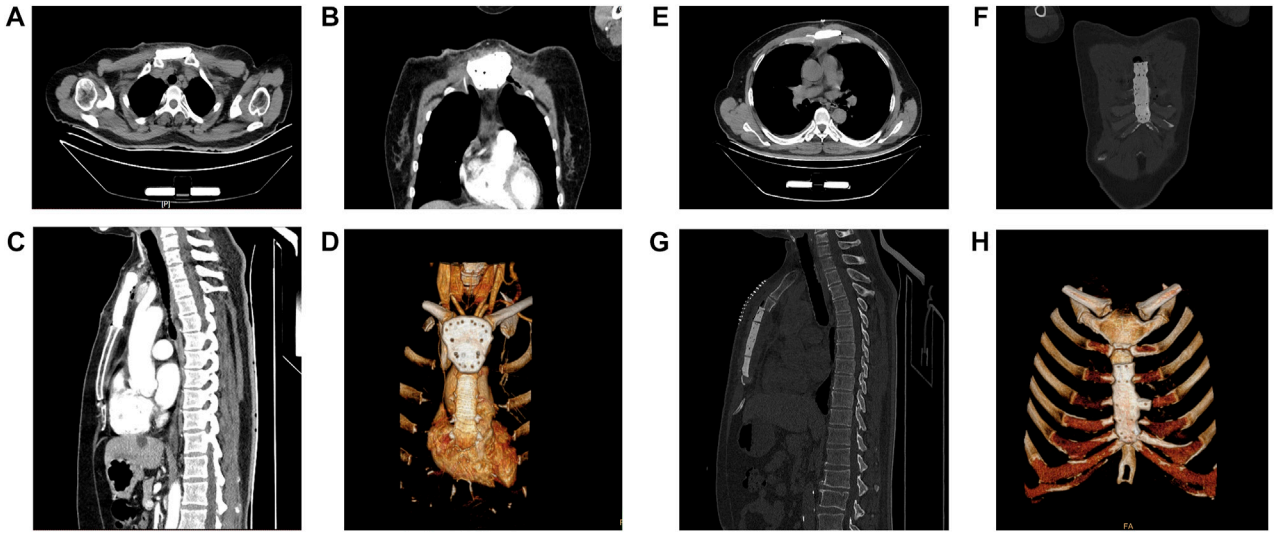

FIGURE 3
Postoperative computerized tomography (CT) images of the patients. **(A,E)** The CT images of sternal prosthesis in the transverse view.**(B,F)** The CT images of sternal prosthesis in the coronal view. **(C,G)** The CT images of sternal prosthesis in the sagittal view. **(D,H)** The 3D reconstruction of the sternal prosthesis on CT is demonstrated.

technology based on CT information to ensure its suitability. This mould is generally composed of two parts: the bottom and the cover. During fabrication, we first poured an appropriate amount of paste bone cement into the bottom and then covered it with a cover to ensure that the prosthesis surface was smooth. Subsequently, holes were drilled at the edge of the bone-cement prosthesis. The bone cement prosthesis was implanted in the sternal defect, and it was firmly fixed on the adjacent ribs and the residual sternum with non-absorbable wires. Next, the sternocleidomastoid muscle was sutured to the cement, which stabilised the sternocleidomastoid joint. We then fixed the LARS mesh to the surface of the cement prosthesis and the peripheral ligament on the pectoralis major muscles through interrupted non-absorbable sutures on the holes reserved in the cement. A drainage tube was inserted in both the patients during the operation. The surgical procedures were seen in Figure 2.

2.2.4 Postoperative care

Both patients were routinely transferred to the ward for primary care after surgery. They were provided with postoperative anti-inflammatory and analgesic therapy, and their respiratory function was closely monitored. When the drainage flow was less than 20 mL for 2 days, the drainage tube was removed. The average drainage time of the two patients was 8.5 days, and the average hospital stay was 16.5 days. No major postoperative complications occurred in either patient. The male patient experienced mild dyspnea on the night of surgery, which may have been caused by incision pain.

Postoperative pain management is extremely important in patients undergoing sternal resection. Furthermore, thoracic movement should be limited to avoid implant displacement. A small range of implant forward movements could be accepted, while implant back movements must be avoided, as this could lead to respiratory and circulatory failure. Both patients underwent chest tomography after drainage extubation that revealed sternal prosthesis located at proper position and cover the defect well (Figure 3). A follow-up 1 year postoperatively showed satisfactory cosmetic results and good self-assessment without any abnormal respiratory movements or dislocation of the prosthesis in either patient. The therapeutic procedure of this case report was seen in Figure 4.

3 Discussion

The sternum is a rare site for neoplasms, and surgery is the most important treatment for sternal tumours (Ersoz et al., 2014). Considering the role of the chest wall in respiratory function, protection of thoracic organs, and cosmetic appearance, reconstruction of large chest defects has reached a consensus, although the choice of material for chest reconstruction is still controversial (Wang et al., 2020).

It has been reported that various materials were used in chest reconstruction. Rigidity is the most important property that can prevent flail chest and protect organs (Nishida et al., 2015). In this case, the bone cement, titanium plates, and autografts could meet the requirements for rigidity. The autograft has rigidity with good self-compatibility, which makes it both resistant to infection and implantable (Drinnon et al., 2020). However, the corresponding incision exerts a significant pain burden on patients (Huang et al., 2015). Titanium plates have become a sophisticated material in recent years. The light weight, strength, durability, biocompatibility, and non-magnetic properties of titanium make it a preferable

FIGURE 4
The therapeutic course of our patient. The current case series is presented based on this sequence of events.

material for implants (Goldsmith et al., 2020). Nevertheless, there are still some limitations to the use of titanium plates in reconstruction. The lack of elasticity and tenacity of the titanium plates may increase the incidence of post-operative prosthetic dislocation (Voss et al., 2018). Meanwhile, titanium plates are often secured with screws on the ribs, which can result in unscrewing of the screws and dislocation of the prosthesis owing to the osteoporotic nature of the ribs (Ng, 2015). Furthermore, the high price of titanium may also be a considerable limitation (Divisi et al., 2021). Although the most common complication of PMMA is infection, LARS mesh could promote the adhesion and development of soft tissues, which could decrease risk of infection.

To overcome these bottlenecks, we proposed a new sandwich structure, referred to as PMMA, encapsulated with a LARS mesh. PMMA can provide sufficient support to the chest wall (Motono et al., 2019), is easy to manipulate, and less time-consuming to mould into sternal prostheses, due to the potential of a 3D-printing precast mould and the high plasticity of PMMA in the early period (Choi et al., 2021). In this case, we secured the prosthesis to the ribs with interrupted 1–0 sutures to reduce the incidence

of prosthesis displacement caused by the osteoporotic nature of the ribs.

In addition to PMMA, the LARS mesh is also essential for chest reconstruction. The restoration of respiration and movement of the upper limbs required micro-motion of the sterno-clavicular sternocostal joints, which was possible due to the elastic property of the mesh (Chaudhry et al., 2015). Traditional meshes, such as Marlex mesh, Prolene mesh, and Gore-Tex, are commonly used in clinics (Sandler and Hayes-Jordan, 2018; Motono et al., 2019; Tsuge et al., 2021). There was also a limitation of the technology. The absorption and shrinkage of traditional meshes can result in chest pain and wall deformities. Several studies have revealed a shrinkage range of bio-meshes from 7.6% to 50.8%, which was caused by degradation of the absorbable element of the mesh over time (Huang et al., 2015). Considering the limitations of traditional meshes, the LARS mesh was applied to wrap the PMMA prosthesis during surgery because of its remarkable strength, durability, elasticity, and bio-stability (Tiefenboeck et al., 2018; Naveen et al., 2020); this combination prevented absorption and shrinkage. The microporous structure of LARS also provides a scaffold that facilitates the adhesion of soft tissues (Trieb et al., 2004). Patients with LARS-PMMA sandwich prostheses had restored chest and shoulder strength, allowing normal respiration and movement of the upper limb. Although our treatment protocol has achieved satisfactory results, there are also some shortcomings as follows: 1) the particulate matter produced by the abrasion of the LARS ligament may cause an inflammatory reaction and its longevity may be shortened by long-term respiratory motion (Wei et al., 2019); 2) The bone cement may reduce the range of motion of the joint and may inhibit respiratory activity, and all synthetic materials remain permanently in the body after implantation, and there is also a risk of dislocation and deflection of the implanted prothesis (Chaudhry et al., 2015). Moreover, the loosening and fracture of the prosthesis may occur with prolonged implantation leading to chest wall deformity or even respiratory contradiction, although the probability is very low.

Besides chest wall reconstruction, soft tissue coverage of the prosthesis is necessary to prevent infection. In different situations, primary closure, skin grafts, myocutaneous flaps, and local advancement flaps may be used (Hameed et al., 2008). In this case, we covered the sternal prosthesis through a primary suture based on sufficient residual soft tissue.

4 Conclusion

Sternal tumours are rare, and are generally treated by tumour resection followed by chest defect reconstruction, which remains a challenging procedure. Bony and soft tissue reconstructions are two prominent aspects of maintaining chest cosmesis, respiratory function, and organ protection. The LARS-PMMA-LARS sandwich prosthesis has potential to be a suitable substitute for the sternum. Proper soft tissue reconstruction also promotes restoration of chest function and structure.

Data availability statement

The original contributions presented in the study are included in the article/Supplementary Material, further inquiries can be directed to the corresponding authors.

Ethics statement

Written informed consent was obtained from the individual(s) for the publication of any potentially identifiable images or data included in this article.

Author contributions

Conceptualization, HZ; image edition, TX; surgical assistant, TC; resources, LJ; data curation and writing—original draft preparation, JL; Follow up and investigation, BH; writing—review and editing, GS And all authors approved the final manuscript.

Funding

345 Talent Project of Shengjing Hospital, Shenyang Science and Technology Project (21-173-9-24) and China Postdoctoral Science Foundation, sponsor number: 2021M693912.

Conflict of interest

The authors declare that the research was conducted in the absence of any commercial or financial relationships that could be construed as a potential conflict of interest.

Publisher's note

All claims expressed in this article are solely those of the authors and do not necessarily represent those of their affiliated organizations, or those of the publisher, the editors and the reviewers. Any product that may be evaluated in this article, or claim that may be made by its manufacturer, is not guaranteed or endorsed by the publisher.

References

Chaudhry, I., Alhajji, Z., Aldulaijan, F., Mutairi, H., and Amr, S. S. (2015). Manubrioclavicular and manubriosternal reconstruction after radical resection for chondrosarcoma of manubriosternum: A modified surgical technique. *Ann. Thorac. Surg.* 99 (6), e137–e139. doi:10.1016/j.athoracsur.2015.02.119

Choi, C. W., Park, Y. K., Shin, H. K., Lim, J. W., and Her, K. (2021). Sternal resection and reconstruction for solitary plasmacytoma of the sternum: Case report. *J. Chest Surg.* 54 (5), 400–403. doi:10.5090/jcs.20.103

Divisi, D., Tosi, D., Zaccagna, G., De Vico, A., Diotti, C., and Crisci, R. (2021). Case report: A new tool for anterior chest wall reconstruction after sternal resection for primary or secondary tumors. *Front. Surg.* 8, 691945. doi:10.3389/fsurg.2021.691945

Drinnon, K. D., Sherali, S., Cox, C. T., and MacKay, B. J. (2020). Sternal tumor resection and reconstruction using iliac crest autograft. *Plast. Reconstr. Surg. Glob. Open* 8 (8), e3002. doi:10.1097/GOX.0000000000003002

Ersoz, E., Evman, S., Alpay, L., Akyil, M., Vayvada, M., Gurer, D., et al. (2014). Chondrosarcoma of the anterior chest wall: Surgical resection and reconstruction with titanium mesh. *J. Thorac. Dis.* 6 (10), E230–E233. doi:10.3978/j.issn.2072-1439.2014.09.30

Goldsmith, I., Evans, P. L., Goodrum, H., Warbrick-Smith, J., and Bragg, T. (2020). Chest wall reconstruction with an anatomically designed 3-D printed titanium ribs and hemi-sternum implant. *3D Print Med.* 6 (1), 26. doi:10.1186/s41205-020-00079-0

Gritsiuta, A. I., Bracken, A., Downs, P., Lara-Gutierrez, J., Beebe, K., Pechetov, A. A., et al. (2021). Surgical management of rare benign tumors of the sternum. *MOJ Clin. Med. Case Rep.* 11 (3), 88–94. doi:10.15406/mojcr.2021.11.00389

Hameed, A., Akhtar, S., Naqvi, A., and Pervaiz, Z. (2008). Reconstruction of complex chest wall defects by using polypropylene mesh and a pedicled latissimus dorsi flap: A 6-year experience. *J. Plast. Reconstr. Aesthet. Surg.* 61 (6), 628–635. doi:10.1016/j.bjps.2007.04.011

Hann, M. C., Pettiford, B., and Babycos, C. (2018). Novel chest wall reconstruction following excision of an xiphisternal chondrosarcoma. *Ochsner J.* 18 (2), 180–182. doi:10.31486/toj.17.0066

Huang, H., Kitano, K., Nagayama, K., Nitadori, J., Anraku, M., Murakawa, T., et al. (2015). Results of bony chest wall reconstruction with expanded polytetrafluoroethylene soft tissue patch. *Ann. Thorac. Cardiovasc Surg.* 21 (2), 119–124. doi:10.5761/atcs.oa.14-00195

Khullar, O. V., and Fernandez, F. G. (2017). Prosthetic reconstruction of the chest wall. *Thorac. Surg. Clin.* 27 (2), 201–208. doi:10.1016/j.thorsurg.2017.01.014

Ma, X. L., Wang, D. B., Ma, J. X., Wang, Y., Sun, L., Lu, B., et al. (2018). Custom-made prosthesis for reconstruction after radical resection for chondrosarcoma of manubrium. *Orthop. Surg.* 10 (3), 272–275. doi:10.1111/os.12388

Motono, N., Shimada, K., Kamata, T., and Uramoto, H. (2019). Sternal resection and reconstruction for metastasis due to breast cancer: The Marlex sandwich technique and implantation of a pedicled latissimus dorsi musculocutaneous flap. *J. Cardiothorac. Surg.* 14 (1), 79. doi:10.1186/s13019-019-0905-z

Naveen, N. B., Deckard, E. R., Buller, L. T., and Meneghini, R. M. (2020). Enhanced biomechanical performance of a modern polyester surgical mesh for extensor mechanism reconstruction in total knee arthroplasty. *J. Arthroplasty* 35 (11), 3311–3317. doi:10.1016/j.arth.2020.05.072

Ng, C. S. (2015). Recent and future developments in chest wall reconstruction. *Semin. Thorac. Cardiovasc Surg.* 27 (2), 234–239. doi:10.1053/j.semtcvs.2015.05.002

Nishida, Y., Tsukushi, S., Urakawa, H., Toriyama, K., Kamei, Y., Yokoi, K., et al. (2015). Post-operative pulmonary and shoulder function after sternal reconstruction for patients with chest wall sarcomas. *Int. J. Clin. Oncol.* 20 (6), 1218–1225. doi:10.1007/s10147-015-0844-1

Sandler, G., and Hayes-Jordan, A. (2018). Chest wall reconstruction after tumor resection. *Semin. Pediatr. Surg.* 27 (3), 200–206. doi:10.1053/j.sempedsurg.2018.05.008

Tiefenboeck, T. M., Boesmueller, S., Popp, D., Payr, S., Joestl, J., Binder, H., et al. (2018). The use of the LARS system in the treatment of AC joint instability - long-term results after a mean of 7.4 years. *Orthop. Traumatol. Surg. Res.* 104 (6), 749–754. doi:10.1016/j.otsr.2018.02.010

Trieb, K., Blahovec, H., Brand, G., Sabeti, M., Dominkus, M., and Kotz, R. (2004). *In vivo* and *in vitro* cellular ingrowth into a new generation of artificial ligaments. *Eur. Surg. Res.* 36 (3), 148–151. doi:10.1159/000077256

Tsuge, I., Saito, S., Sakamoto, A., and Matsuda, S. (2021). Anterior chest wall reconstruction after resection of a sternal tumor with a single mandibular plate and Gore-Tex® sheet. *Asian J. Surg.* 44 (3), 563–565. doi:10.1016/j.asjsur.2020.12.005

Voss, S., Will, A., Lange, R., and Voss, B. (2018). Mid-term results after sternal reconstruction using titanium plates: Is it worth it to plate? *Ann. Thorac. Surg.* 105 (6), 1640–1647. doi:10.1016/j.athoracsur.2018.01.057

Wang, H., Liu, Z., Chen, C., Liu, M., Xiao, Y., Zhang, J., et al. (2020). Sternal resection and reconstruction with a novel modularized prosthesis. *Ann. Thorac. Surg.* 110 (4), 1412–1416. doi:10.1016/j.athoracsur.2020.05.048

Wei, S., Liu, S., Han, F., Xu, F., and Cai, X. (2019). Clinical outcomes of a modified all-inside arthroscopic repair of anterior talofibular ligament for chronic ankle instability: A preliminary report. *Med. Baltim.* 98 (36), e16734. doi:10.1097/md.0000000000016734

Zhang, Y., Li, J. Z., Hao, Y. J., Lu, X. C., Shi, H. L., Liu, Y., et al. (2015). Sternal tumor resection and reconstruction with titanium mesh: A preliminary study. *Orthop. Surg.* 7 (2), 155–160. doi:10.1111/os.12169

Frontiers in
Bioengineering and Biotechnology

Accelerates the development of therapies, devices, and technologies to improve our lives

A multidisciplinary journal that accelerates the development of biological therapies, devices, processes and technologies to improve our lives by bridging the gap between discoveries and their application.

Discover the latest Research Topics

See more →

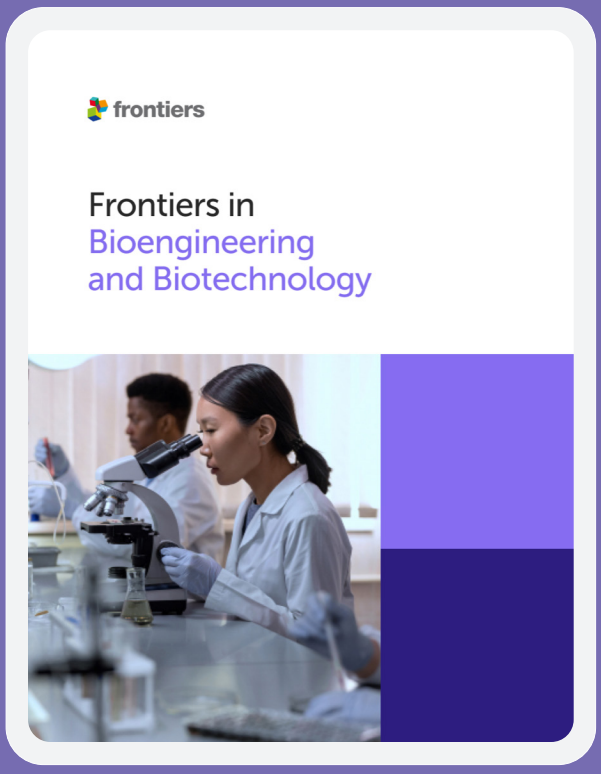

Frontiers

Avenue du Tribunal-Fédéral 34
1005 Lausanne, Switzerland
frontiersin.org

Contact us

+41 (0)21 510 17 00
frontiersin.org/about/contact